

Materials Recycling for Sustainability

Brajendra Mishra

Metallurgical & Materials Engineering
Colorado School of Mines
1500 Illinois Street, Golden, CO 80401, USA
Email: bmishra@mines.edu

Abstract: Resource productivity is a necessity for meeting the triple bottom-line for sustainability. Recycling and reuse of materials in all forms has the greatest impact on resource productivity. Pervasion of recycling concepts in the global society and technologies for materials recycling have to be based on principles of energy conservation, resource preservation, ecological management and economical growth advantages. Thus, recovery of metals and materials from secondary resources and industrial wastes is critical for the sustenance of the environment and economic growth of the materials industry. The technologies available for such recovery processes are also energetically favorable. Energy consumption in industrial processes will receive greater attention in the coming decades. While steel, aluminum and copper industries have made significant strides in metal production from metallic scrap, more effort is needed in industrialized as well as developing countries, both in metallic and non-metallic materials recycling. Current status of metal recovery from secondary sources and the technologies available has been reviewed. Of particular concern are wastes generated during metal processing in addition to post-consumer waste generation causing environmental hazards. Specific examples of technologies developed for materials recovery shall be discussed in context of resource sustainability.

Keywords: Recycling, Recovery, Sustainability, environment, conservation

1 INTRODUCTION

The development and growth in the agricultural and industrial endeavors of mankind have allowed the sustenance of the growing population on this planet that is now over 6 billion. The populace has gradually achieved higher economic well-being over the past two centuries. However, along with this tremendous improvement in quality of human life, the unprecedented industrial boom has also caused global warming, ozone depletion, soil sterilization, air contamination, pollution of water resources, etc. In addition, the natural resources that have sustained the industrialization are also dwindling. The solution to these environmental problems and resource depletion has to be global and cannot be effectively accomplished within local or national boundaries. Although industry is essential for our current and future growth, prospective development of the post-industrial era should be made in the frame of sustainable development to meet the basic needs of air, water and food for the 10 billion people that will live on this earth by the middle of this century. Developing technologies for recycling, minimization and safe storage of wastes and reutilization of products from

waste materials are useful and worthy concepts for environment protection, but not adequate for sustainable development. Reengineering the current production systems is another positive step but do not completely resolve the current and future environmental problems. Only, clean technology that may integrate recycling of the process wastes and products at the end of their 'life time cycle' should be applied to any industrial plant using 'cradle-to-grave' concept. Detailed analysis of resource recovery from red-mud is presented here, which is an integral part of primary aluminum production.

2 ALUMINA EXTRACTION

When the economic value from recycling waste and scraps can compete economically with manufacture of new products from virgin raw materials and resources, then and only then will recycling flourish as a business. The production of aluminum from secondary sources is the best example of resource conservation and productivity. Recycling aluminum results in 95% less air pollution and 97% less water pollution than producing primary or virgin aluminum

from ore. Recycling aluminum saves 95% of the energy necessary to mine bauxite ore, extract alumina, the raw materials needed to manufacture aluminum and produce metal from it.

Recycling 1 ton of aluminum saves the equivalent in energy of 2350 gallons of gasoline. This is equivalent to the amount of fuel needed to provide a typical home with electricity for a period of 10 years. Two-thirds of all aluminum ever made is still in use! Two largest areas of secondary market are cans and autos. Can recovery reached ~67% in early 1990's and is now at less than ~50%. Auto metal recovery, however, is at >90%, aided by regulations. Recovery of Al from autos has exceeded all other scrap sources since 2005. It takes 9350 cans to get the same amount of recovered aluminum as in 1 car. Thus, the case for aluminum recycling in the metallic form is well understood, the waste generated during primary production of aluminum at the alumina extraction stage from bauxite ores continues to be a significant problem.

The alkaline extraction of alumina from bauxite [Bayer Process] generates a major waste product known as *red-mud*. Approximately, a ton of red-mud is produced for every two tons of bauxite ore that is mined. The red-mud produced from Jamaican bauxite is rich in hematite, alumina and titanium oxide. It has been shown that over 90 wt. pct. alumina can be recovered from red-mud by soda-ash sintering and caustic leaching that can be reverted back to the Bayer Process. Hematite can be reduced with a degree of metallization of over 94 pct. or over 92% of the hematite can be partially reduced to magnetite. A completely reduced material could be charged through the tuyeres in an iron blast furnace or smelted to produce pig iron. A viable material balance has been included in this paper.

Attempts to separate magnetite by magnetic means are only partially successful as iron is mineralogically tied up with perovskite. This paper has described the successful efforts of iron and alumina recovery. The problems associated with the use of reduced red-mud, as an alternative to direct-reduced iron [DRI] has been discussed. Critical assessment of the recovery sequence chosen for the products has been described. Acid digestion of reduced as well as raw red mud has been attempted in an effort to separate it from other oxides. Electrolytic recovery of pure iron will be achieved from the acid-leached liquor. Acid digestion has shown that over 95 % of iron can be digested from the reduced red mud under proper conditions of acid concentration and temperature.

The pyrochemical extraction of alumina from bauxite leaves behind a process waste called red mud. Red mud produced from Jamaican bauxite is a conglomerate of about 12% aluminum oxide, 68% iron oxide, 7% titanium oxide, 6% calcium oxide, 3% silicon oxide and other trace elements as the balance.

The high amounts of aluminum oxide, iron oxide and titanium oxide make red mud attractive for metal recovery. This work has determined the possibility of extracting various value added products from red mud produced from North Coast Jamaican bauxite and the sequence of extraction for various products. In addition, intrinsic characteristics of the red mud have been identified and some potential commercial applications for the products have been recommended.

The composition of bauxite varies widely around the world and requires different conditions in the Bayer process for successful alumina extraction. After processing, these different bauxites result in varying red mud compositions. The U.S. Bureau of Mines has examined the extraction of these three constituents from Jamaican red mud (1). The sequence of removal of the value added products are a vital issue for success in extraction. The sequence thoroughly investigated in this work comprises the separate sintering and reduction steps to recover alumina followed by iron. The red mud is dried, sintered, leached and then washed to remove the alumina. The material is then reduced and magnetically separated and smelted, if necessary, to recover iron. The remaining non-magnetic portion of the separation is processed to recover titanium oxide. It should be noted that the removal of alumina, iron and titanium oxide leaves behind a material very similar in composition to Portland cement, providing an avenue for complete utilization of red mud in an ideal situation. The extraction process mentioned above demonstrates the use of well-established technologies. The processes succeed in both obtaining usable products from the red mud while concurrently reducing the amount of waste produced. Using the composition listed in Table 1, the aluminum industry can annually recover 27, 2.8 and 4.7 million tons of Fe₂O₃, TiO₂ and Al₂O₃, respectively, if such metal retrieval processes are effective (2).

Table 1: Composition of Dried North Coast Jamaican Bauxite and the Generated Red Mud and Trihydrate

Compound	% in Bauxite	% in Red Mud	% in Trihydrate
Al ₂ O ₃	56.4	11.7	11.0
SiO ₂	0.7	2.5	0.8
CaO	1.2	6.6	2.1
TiO ₂	4.3	7.1	6.7
Fe ₂ O ₃	35.1	67.7	77.2
Others (P, S, Cr, Mn, Zn, Cd)	2.3	4.4	2.3

The extraction of iron, the main constituent in red mud, is the focus of several papers. One investigator suggests separating the red mud (in slurry form) using high intensity magnetic separation. The

resulting magnetic product can be used as an ingredient for iron making or as a pigment for pottery making. The non-magnetic portion can be applied in building materials or supplemented back into the Bayer process. Recovery of the iron is low (3). Another investigator reduces the iron with chlorocarbons before magnetic separation and uses the resulting magnetic portion as feed for iron making (4). Another research suggests drying the red mud, blending with lime and ground coal and feeding the mixture into a machine that agglomerates it into ½ in. diameter balls. Subsequently, the balls are prereduced at high temperatures in a circular grate. The balls are then fed into a submerged-arc electric furnace for smelting and transported to a BOF where the high quality steel is produced. The final product yields about 98-99% iron (5). Another process entails mixing the red mud with $\text{Fe}_2(\text{SO}_4)_3$. This solution removes the sodium from the mud leaving behind material eligible for iron making (6). Simultaneous recovery of aluminum and sodium is performed by mixing the red mud with a solution of caustic soda and lime at 300°C at pressures of 4-9MPa. This solution is supplemented into the Bayer process for increased alumina recovery (7). One approach utilizes the amphoteric characteristics of aluminum by extracting it via treatment with sulfuric acid. It also attempts to extract the aluminum through biological leaching using sewage sludge bacteria (8). Another process that emphasizes titanium recovery, converts the red mud into sodium-aluminum fluoride compounds. The red mud is mixed with HCl and hydrofluoric acid to obtain silicic acid, which is then separated out. Evaporation leaves behind a material close to that of cryolite. The remaining material is mixed with the residual liquor, which dissolves the iron and aluminum. The titanium rich solid remaining can be further processed via chlorination (9). Synchronous recovery of aluminum, iron and titanium is investigated by a number of researchers. One method utilizes chlorination combined with fractional distillation to extract iron and titanium from red mud. The red mud can be leached prior to this to retrieve aluminum (10).

Favorable conditions for the recovery of iron and alumina from the simultaneous sintering and reduction tests include 1.5 hours at 900°C with a Na_2CO_3 to Al_2O_3 ratio of 1.45, a ratio of CaO to TiO_2 of 1.75 and a carbon addition slightly excess of stoichiometry. These conditions produce an alumina recovery of approximately 87% and an iron recovery of 78% based on initial starting composition. The results from the induction furnace experiment indicate that iron recovery reaches 95.5% of the magnetic portion before heating to 1480°C suggesting almost full reduction. The principal components after smelting include alpha iron, austenite and CaTiO_3 . This work offers a feasible route for the extraction of iron and alumina. However, because of its low grade even after several processing steps, titanium oxide proves not to be an option for

extraction (1). It should be noted that the presence of high level of lime does not allow the application of carbo-chlorination and Kroll Process for the recovery of titanium.

2.1 Analysis

2.1.1 Extraction of Iron: The processes to extract iron includes reducing the iron oxide to elemental iron or magnetite, magnetically separating the iron out of the red mud, evaluating the iron product for commercial use and smelting (if necessary) to recover iron as a value added product. Each of these steps depends on a number of variables that include the carbon content, temperature, time and the presence of a calcium oxide layer, which maintains a reducing atmosphere.

As temperature increases, reduction also increases as seen by the weight loss and products detected by the Moßbauer. Different temperatures prefer different oxide states. It is concluded that to achieve almost full reduction, temperatures around 1050°C should be used. It was found, in an attempt to ensure adequate energy for reduction, that small increases in temperature over 1050°C caused the iron to agglomerate (sinter) resulting in poor reduction. Time has no effect on the reduction conditions except that a minimum time is required for complete reduction, which was achieved in approx. 2 hours. A layer of calcium oxide does increase the amount of reduction in the iron as seen by the Moßbauer results and weight loss differences. As mentioned above, the calcium oxide layer promotes a more reducing environment by trapping the carbon monoxide evolved during reduction as well as by reacting with carbon dioxide to produce a carbonate.

Similar analysis was performed for the partially reduced material that was conducted in the temperature range of 500-650°C and using various forms of reductant. The results of the reduction experimentation are: The material is reduced to 95% elemental iron with the use of petroleum coke as a carbon source. The temperature of reduction is 1050°C. In addition, successful partial reduction to 92% magnetite has been accomplished by means of pine sawdust as a carbon source. The temperature of reduction is 550°C (11).

2.1.2 Magnetic Separation: A magnetic separation is performed to separate the reduced iron out of the remaining red mud. There were three methods investigated for magnetic separation process: crude wet, crude dry, and Davis Tube magnetic separation. Several tests are performed attempting to separate the non-magnetic from the magnetic portion of the red mud. The reduced red mud contains iron combined with titanium, aluminum, calcium, silicon oxides and residuals of sulfur, zinc, manganese, sodium, chromium and phosphorus. Figure 2 shows the

magnetic and the non-magnetic composition of two trials of Davis tube separation on red mud. It should be noted that iron, calcium, titanium and magnesium segregate to the magnetic product while sulfur, phosphorus, and silicon segregate to the non-magnetic product. Iron also distributes to the non-magnetic portion of the red mud. All other constituents appear to be about equally divided. Iron, calcium and titanium appear to be intimately mixed, or exhibit some type of affinity with each other, in all magnetic separations. It has been suggested that titanium is combined with iron in the bauxite ore.

Calcium oxide is supplemented to the Bayer process to perform a number of tasks, but can react with titanium oxide to form perovskite. This perovskite can attach itself to the iron. Thus, both calcium and titanium are carried with the iron during magnetic separation. Under the assumption that this affiliation occurred in the sintering portion of the extraction process; the magnetic separation was attempted on the raw red mud and trihydrate materials after being subjected to a full reduction only. The results of these separations showed no difference in the final compositions. In addition, aluminum and iron are

known to be combined in the bauxite ore (12). This combination can carry over to the red mud interfering with magnetic separation and leaching. Possibly during reduction, the manganese and sulfur react with the help of carbon to form manganese sulfide, a non-magnetic compound. The presence of iron in the non-magnetic product could be due to residual FeO remaining from reduction. Magnetic separation is not a completely successful procedure, as is readily apparent.

2.2 Material Balance

The separate sintering and reduction sequence is the optimum sequence for the extraction of alumina, iron and titanium oxide. A preliminary material balance is performed on the separate sintering and reduction sequence to obtain an estimate of the outcome of specific constituents and the weight loss and gain throughout the sequence. Table 2 shows the material balance flow sheet.

Table 2: Composition and Weight Change in Red Mud after Various Extraction Processes

Process	Fe ₂ O ₃	FeO	Fe	Al ₂ O ₃	TiO ₂	CaO	SiO ₂	Other	Wt.
Dried at 400°C 1hr.	67.7	-	-	11.7	7.1	6.6	2.5	4.4	100%
Sintered at 950°C 2hr. 50% xs. Soda	56.4	-	-	12.7	6.7	8	2.4	13.8	101%
Leached at 65°C 1.5hr. 100% xs caustic	66.0	-	-	5	8.1	11.1	2.5	7.3	81%
Washed at 100°C 15 min. 10g/l	69.3	-	-	2.8	8.4	12.5	1.9	5.1	70%
Reduced at 1050°C 2hr. 200% xs C	-	5.2	36.5	6.7	14.8	19.8	3.7	13.3	66%
Smelted at 1650°C	-	19	>90	-	29	22	7.5	22.5	64%

2.3 Blast Furnace Supplement

The red mud contains approx. 40% fully reduced iron, 5% iron oxide (FeO), 17% titanium oxide, 20% calcium oxide, 4% alumina and 2% silicon oxide after processing, the balance being constituents in order of decreasing quantity: manganese, sulfur, phosphorus, and sodium.

A potential application for alumina depleted and reduced red mud could be in the iron making blast furnaces. A preliminary calculation is made upon adding 100kg of red mud to 1000kg of iron ore. The total charge to the blast furnace consists of red mud, iron ore, coke and lime. The TiO₂ serves as a blast furnace hearth protector, acting as an acidic component enhancing the silica rich refractory. The red mud also contains calcium oxide that, if sufficient, can improve blast furnace efficiency by lowering the amount of

calcium oxide required to produce a specific basicity. Because the red mud is depleted of alumina, the slag melting point is not increased by this constituent. The slag is separated from the steel and cooled where these deleterious constituents are consequently entrapped in a glassy matrix. The red mud is in powder form and ought to be added to the furnace at the tuyere level. The sodium in the red mud should be kept to a minimum. This is performed through extensive washing, discussed previously. Sodium, a basic oxide, if present in the blast furnace can harm the acidic refractory. Due to its inherent pyrophoric behavior, the reduced red mud should be kept in a low oxidizing atmosphere prior to supplementation to avoid iron oxide formation. The principal benefit derived from this method for the alumina industry includes complete elimination of the red mud and the associated problems with it.

Table 3: Effect of reduced red mud charging in blast furnace in comparison to direct-reduced iron

Charging at blast-furnace tuyere-level: (per tonne hot-metal)

	<u>NO CHARGING</u>	<u>DRI-CHARGING</u>	<u>REDMUD-DRI CHARGING</u>
Fe°/Total Fe	0.00	25-30 %	20-25 %
Charged amount/thm	0.00	150	150
Production rate,t/m ³ /day	1.5	+ 25 %	+ 22 %
Coke rate, kg/thm	600	- 20 %	- 18 %
Fe/(SiO ₂ +Al ₂ O ₃)	10-15	23-25	25-28
Slag rate, kg/thm (const. basicity:1)	350	- 15 %	- 15 %
CaO/(SiO ₂ +Al ₂ O ₃) In the Fe-charge	0.16	0.01	2.25

The possible impact of using the reduced red mud on blast furnace performance parameters is shown in Table 3.

2.4 Acid Digestion

Acid digestion of raw red mud as well the reduced red mud without a prior alumina removal was done in sulfuric and hydrochloric acid. Table 6 shows the results of this digestion. It is evident that hydrochloric acid is more effective in leaching out iron and it is influenced by the acid concentration as well as the solid to leach solution volume ratio. These experiments have been done with a desire to increase

the iron recovery and to maintain a high concentration of iron in the leach liquor that can support an efficient iron recovery by electrowinning. The hydrochloric acid digestion also indicates that calcium is leached out but alumina and titanium oxide is left in the residue. Upto 93 pct. iron is recovered from the reduced material but only 70 pct. is recovered from the raw red mud. This investigation is being continued for iron recovery from the leach solution.

Table 4: Recovery of Iron by Acid Digestion

Expt.	Acid	Acid Conc. (wt%)	Acid Volume (ml)	Material	Weight of Material (g)	PPM of Fe	% Fe Digestion
A04	H2SO4	99%	700	Raw	25	7175	53%
A05	H2SO4	30%	700	Raw	25	1205	9%
A06	HCl	37%	700	Raw	25	9232	69%
A07	HCl	19%	1000	Raw	50	10798	58%
A08	HCl	37%	1000	Raw	25	6308	68%
A09	HCl	37%	500	Raw	25	9694	52%
A10	HCl	29%	500	Raw	25	8450	45%
A11	HCl	15%	1000	Raw	25	7014	75%
A12	HCl	15%	1000	Reduced	25	8541	89%
A13	HCl	15%	1000	Reduced	15	5262	93%
A14	HCl	15%	1000	Raw	15	3919	70%

3 CONCLUSION

- At least 90% reduction of the iron is achieved when the red mud is reduced at 1050°C for 2 hours using 200% excess carbon above the stoichiometry covered by a fine layer of calcium oxide. If partial reduction is conducted at 550°C, 92 pct. conversion to magnetite is achieved.
- The red mud, prior to processing, exhibits unusual magnetic characteristics caused by either inherent particle size or aluminum solubility in iron. Iron particles are found to be associated with calcium titanate particles. Magnetic separation, thus, is only partially successful.

Because of the inability to adequately magnetically separate iron after reduction, some alternative routes for utilization are suggested. These suggestions include using the red mud after prior processing in a blast furnace, smelting the red mud to recover pig iron and a slag rich in titanium.

References

1. Fursman, J.E. Mauser, M.O. Butler, and W.A. Stickney, 'Utilization of Red Mud Residues From Alumina Production', U. S. Bureau of Mines Report of Investigations 7454, [1970].
2. Piga, F. Pochetti and L. Stoppa, 'Recovering Metals from Red Mud Generated during Alumina Production', *JOM* 45(11), pp.55-59, [1993].
3. Braithwait, GB Patent No. 2078211-A. (Jan. 1982).
4. Agency of Ind. Sci. Tech., J Patent No. 52152896-A. (Dec. 1977).
5. Guccione, 'Red mud,' a Solid Waste, Can Now Be Converted To High-Quality Steel', *Eng. Min. J* 172(9), pp. 136-138, [1971].
6. Dakatos, M. Miskei, and J. Szolnoki, DE Patent No. 2747436. (May 1978).
7. Cresswell, and D.J. Milne, AU Patent No. 88102. (Sept. 1981).
8. Vachon, R. Tyagi; J-C. Auclair, and K.J. Wilkinson, 'Chemical and Biological Leaching of Aluminum from Red Mud', *Environ. Sci. Technol.* 28(1), pp. 26-30 [1994].
9. Vereinigte Aluminium-Werke., FR Patent No. 2117930-A. (Dec. 1971).
10. Baetz, R.C. Lightbourne, U.S. Patent No. 3690828. (Sept. 1972).
11. B. Mishra, A. Staley and D. Kirkpatrick, 'Recovery & Utilization of Iron from Red Mud', Bauxite Treatment Residues: Products and Processes' Light Metals 2001, Ed. J.L. Anjier, TMS Publications, Warrendale, PA, pp. 149-156, [2001]
12. Jacob, Jr., Bauxite: Proceedings of the 1984 Bauxite Symposium, Los Angeles, California, New York, N.Y.: Society of Mining Engineers of American Institute of Mining, Metallurgical, and Petroleum Engineers, pp. 349-369, [1984].

SUSTAINABLE CONSTRUCTION AS A RESEARCH AREA

Lech CZARNECKI* and Marek KAPROŃ**

*Professor, Ph.D. Eng., Warsaw University of Technology and Building Research Institute, Warsaw Poland

**MSc Eng., Building Research Institute, Warsaw Poland

l.czarnecki@itb.pl, L.Czarnecki@il.pw.edu.pl
m.kapron@itb.pl

Abstract: Sustainable development is one of the leading civilization ideas. This term means such a development that satisfies the present needs without a limitation of the possibility of satisfying the needs in the future. Sustainable development in construction is particularly important, as this branch of the industry is consuming enormous amounts of mass and energy. A new research area has been created by this idea. The new fields of investigation are involved with material, energetic, and environmental conditions, but also with such topics as protection against noise and the methods of the evaluation of the efficiency of waste materials storage. Implementation of the idea of sustainable development in the construction industry will be a source of scientific and engineering inspiration for many years to come.

1. Sustainable development – a challenge for civilisation

The leitmotiv of the renowned ICMR Akita International Conference since 1991 is the beneficial integration of separate idea into new concept, which could provide for sustainable development of human being. Authors try to reply to this Conference main idea on the arena of sustainable construction discussed as the research area.

The notion of sustainable development aspires to the role of a leading civilisation idea. Sustainable development *“implies meeting the needs of the present without compromising the ability of future generations to meet their own needs”* (UN, 1987) [1]. The term is the most frequently found expression in forecasts and similar studies. It follows from philosophical premises and – in Poland – it is a constitutional prerequisite: *“The Republic of Poland shall safeguard the independence and integrity of its territory and ensure the freedoms and rights of persons and citizens, security of citizens, safeguarding of Poland’s national heritage, and ensure the protection of the natural environment pursuant to the principles of sustainable development.”* Therefore, sustainable development constitutes a principle that is to be followed by the Republic of Poland, in turn safeguarding fundamental values. In the Environmental Protection Laws, the definition of sustainable development is expanded further: *such socio-economic development, in which – in order to equalise the opportunities to access the environment by individual communities or their members – both of contemporary generations and those still to come – a process of the integration of political, economic, and social actions takes place, maintaining the natural balance and continuity of vital natural processes* [2].

Brundtland’s definition of sustainable development [1] points out some ethical and ecological aspects. Cywiński, in his philosophy of sustainability [3], underlines the need to

generalise the definition of sustainable development and to also consider human spiritual needs. According to Cywiński, sustainable development fulfils the comprehensive, spiritual, and material needs of today’s people, without limiting the ability of future generations to satisfy their own respective needs. As a consequence, engineers must be prepared to respond not only to the ‘material’ question of ‘how’ but also be able to successfully cope with the ‘spiritual’ challenges of ‘why’. [4].

The principle of sustainable development can also be approached from the point of view of the caution that is included in the second law of thermodynamics. In Clausius’ version, the law implies that in isolated systems, processes can only occur if entropy is increased at the same time.

There have always been civilisations that have declined and fallen. In our times, the imperative of the constant growth of scale and sophistication might also bring about a disaster. Daly [5] formulated the following general principles of sustainability:

- renewable resources (e.g. water), including food (e.g. fish), must not be used faster than the rate at which they can be regenerated,
- non-renewable resources must not be used faster than they are replaced with renewable substitutes,
- pollution and waste must not be produced faster than they can be absorbed by nature, recycled, or rendered harmless.

The principles can be illustrated as follows [6]*.

Sustainable development is a life necessity. The above summary reflects a general research inspiration, comprising such areas in construction as the rationalisation of energy management (energy + mass), structural durability, maintenance, renovation, repairs, modernisation (including revitalisation), working life, reclaim and reuse, recycling and the influence on health and the environment. There is also an essential need to determine the “sustainability measures”, measurement or calculation methods, and the forecasting tools for the simulation and prediction of the “development of sustainability”.

*

Use of resources/Production of pollution and waste	Environmental impact	Sustainability
Faster than natural regeneration	Degradation	None
Equal to regenerative potential	Balance	Steady state
Slower than regenerative potential	Regeneration	Development

2. Key terms and definitions

In the Polish equivalent of sustainable development, “zrównoważony rozwój”, there is no lexical reference to sustainability. “To sustain” means “to keep in existence” and thus – a more literal translation of the term into Polish would incorporate an adjective with the meaning of “constant” or “permanent”. That was the case in the first Polish publications addressing the issue, which were published a dozen or so years ago. It is noteworthy that – at that time – a representative of the Building Research Institute brought that matter up [7], translating the Polish term “zrównoważony rozwój” literally, we could end up with “balanced development”. As can be seen, the Polish version focuses on the determinant of the development (equable), whereas the English term – on the expected results (sustainable). In other languages **développement durable** (French), **Nachhaltige Entwicklung** (German), **sviluppo sostenibile** (Italian), **duurzame ontwikkeling** (Netherlands), **Desenvolvimento Sustentável** (Portuguese), **устойчивое развитие** (Russian), **desarrollo sostenible** (Spanish) also rather the aspect of long-term durable development is stressed.

The term “sustainable development” in the construction-related literature is usually used to refer to the “construction that meets the requirements of sustainable development”. The approach reflects the conceptual scope of sustainable development, which includes the construction industry as one of its many elements. The drawback is the complexity of the term. A shorter version is used as: Sustainable Development in Construction. In English literature, much simpler terms are often used, both for structures (sustainable house, sustainable city, and sustainable structure) and actions (sustainable transport, sustainable design, and sustainable living). It seems that the sequence of “construction that meets the requirements of sustainable development → sustainable development in construction → sustainable development of construction” may also find its final form in “**sustainable construction**”. In anticipation of this notional evolution, the authors dared to use the term in the title of this study.

3. Construction that meets the requirements of sustainable development

The construction industry uses 42% generated power and emits 35% greenhouse gases. The branch of the concrete industry alone uses 20 billion tonnes of aggregates, 1.5 billion tonnes of cement and 800 million tonnes of water per year. That is a lot of matter. Implementing the principles of sustainable development in construction is a necessity, which has found its official acknowledgment in an initiative of the European Commission [9, 10], which announced a draft Regulation to replace the Directive 89/106/EEC. The regulation will introduce sustainable development for the construction industry as a seventh principal requirement: a civil structure should be designed, erected (and also used), and demolished in line with the requirements of sustainable development. As a matter of fact, it will be a superior requirement to all others. Although stipulating the development of construction to be sustainable is defined in an ecological

aspect, it is also determined by economic and social views. Sustainable construction has been classified as the second of the six development priorities. It is assumed that by the year 2020 the construction market will have been increased 3.5-fold with employment boosted by 70% [10].

The growing awareness of the importance of the influence of construction on environmental protection issues and energy saving makes the need to satisfy the comprehensive criteria of sustainable development particularly vital for buildings and civil structures. The basis for the harmonisation of the respective European requirements should be provided by the standards that were developed by the European Committee for Standardisation CEN, Technical Committee TC 350 “Sustainability of Construction Works”, in the following scope (shown in Fig. 1):

- evaluation of the effect of buildings on the natural environment,
- preparation of environmental declarations for construction materials/products,
- evaluation of the total life cycle of buildings and civil structures.

4. Sustainable construction – premises and research needs

In order to implement the concept of “construction that meets the requirements of sustainable development”, first of all, the requirements must be formulated specifically for the construction industry. In the year 2000, in Great Britain, a government policy for the sustainable development of construction was announced. Since that time, annual reviews have been performed to verify the policy. Nevertheless, it appears that there are still more questions than answers. In 2003, all of the sections of the report ended with a question mark [12]. In 2004, we could read the question again: *what is sustainable construction?*

The answer to the question was provided in a number of key points [13]:

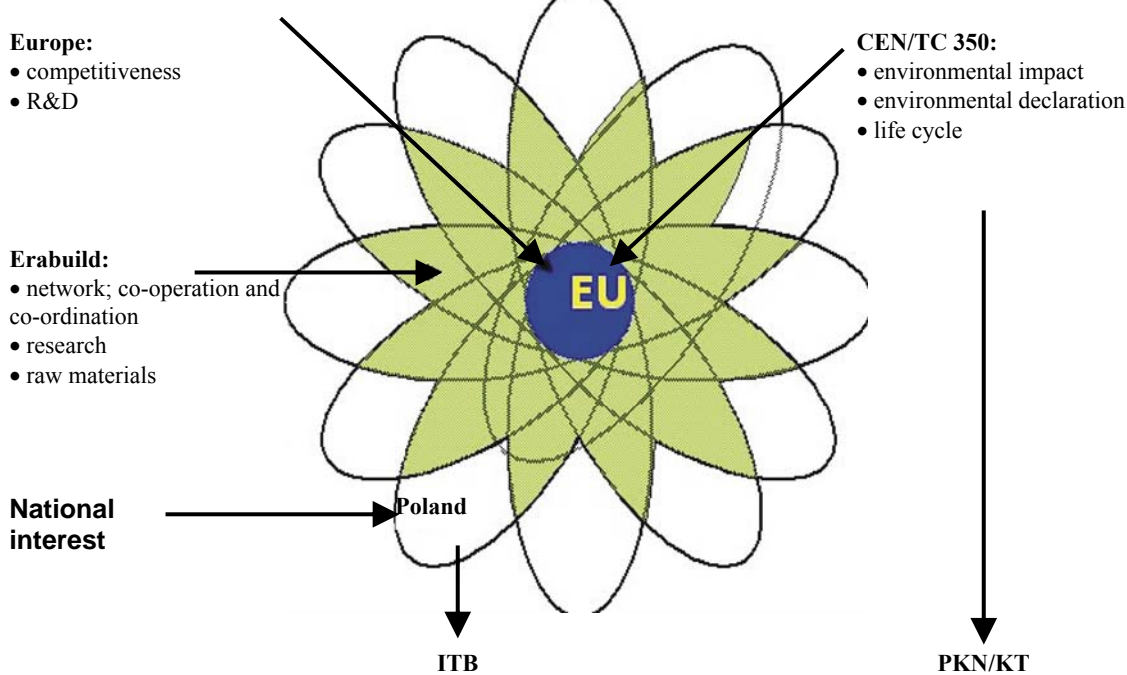
- cost-efficient design,
- using minimum energy in construction and use,
- producing no pollution,
- preserving the nature around and in turn enhancing biodiversity,
- preserving water resources,
- providing people with comfort and respecting the local “microclimate”.

The authors admit that most of these guidelines are no less than a simple business principle: minimise loss, maximise efficiency. A lack of new knowledge is distinctly felt [47]. As a result, in all of the European programmes, *sustainability* is one of the leitmotifs. COST – European Co-operation in the Field of Scientific and Technical Research, which determines research directions by definition, is engaged in the following two actions:

- Action C8: Best Practice in Sustainable Urban Infrastructure [14],
- Action C25: Sustainability of Constructions: Integrated Approach to Lifetime Structural Engineering [15].

Fig.1. Activities of CEN/TC 350 as a basis for the harmonisation of requirements

attempts by RILEM in this area have been very specifically orientated, e.g. Towards Sustainable Roofing, RILEM TC-166



In 2004, RILEM – The International Union of Laboratories and Experts in Construction Materials, Systems, and Structures, Technical Committee TC-92 ECM organised an international symposium "Materials and Systems for Sustainable Development" [16] under the direction of Kashino and Ohama. The symposium summed up the state of knowledge rather than attempting to solve any problems. Earlier, RILEM Technical Committee TC-165 worked on the definition of sustainable construction materials. However, their final report focused on the present situation and the technology regarding dismantling structures and the recycling of demolition waste [17]. Other

RMS [18].

Sustainable management of resources is an essential part of the latest theme (Theme 6: Environment) within the 7th Framework Programme [19]. In this context, it is surprising that in the policy of European Science Foundation (2007) – Looking Beyond the Endless Frontier - the concept of *sustainability* was not addressed [20].

5. Sustainable construction – research area

Sustainable construction is a rather rare example of a

Tab. 1. Developments in the research areas concerning construction material

Development factors (International Concrete, 1998)	Principal requirements (ER 89/106/EEC)	Sustainable Building, factors according to:		Research areas
		C.J.Kibert [22]	Sustainable Building Code	
sustainable development environmental impact energy saving reduced costs of erection, maintenance, dismantling, and recycling use of highly-suitable materials; optimisation of structural solutions big and growing share of repairs and modernisation in construction works design focused on the utility of the building/civil structure	structural safety: load- bearing capacity and stability fire safety hygiene, health, and environment safety of use protection against noise and vibration energy-saving properties and thermal insulation	minimum quantity of materials used (resource conservation) maximum reuse of components possibility to renovate components or materials environmental protection health comfort of use (quality)	demand for energy and emission of CO ₂ water use (dm ³ /person/day) effect of used materials and products on the environment evacuation of surface runoff waste management minimised pollution health and comfort construction process and building management ecology	performance criteria of construction materials methods of suitability assessment modification of materials and new material solutions material performance in service conditions – matching materials with structures recycling of construction materials; use of waste material
Material factors in the sustainable development of construction				

research theme in engineering. The inspiration for it did not follow from any direct practical needs, but rather from the central idea itself. Interpreting the idea, carrying out research and studies is for streamlining engineering activities. The versatility of the idea enveloped in sustainable development gave rise to a number of fundamental research directions, namely:

- material factors in the sustainable development of construction,
- energy factors in the sustainable development of construction,
- influence of a civil structure on the natural environment (ecology),
- influence of a civil structure on the internal environment (microclimate).

The first two research areas are the most extensive. An example of a direct interpretation of the research challenge contained in the concept of sustainable development is a study by K.Gertis* [21] that was presented at the conference "Low-energy or low-entropy buildings?" in 2002. The author states that two principal attitudes seem to have recently influenced the lines of thought of architects/building constructors:

- *absolutisation of the importance of the low-energy building,*
- *the primacy of an ecological and natural environmentally-friendly building;*

However, both terms are either undefined or vague.

As a result, Gertis states the following:

- *"natural environmentally-friendly" means a building with minimum flows of mass and energy (i.e. minimum increase of entropy),*
- *the most "ecological" action occurs when the flows of mass and energy are minimised (ideally: zero entropy increase),*
- *a low-energy building will be essential in the future, but it will not suffice,*
- *anyone familiar with thermodynamics (c.f. Section 2) will deduce that the notion of entropy is a key one.*

It is typical that Gertis did not introduce the notion of exergy in his study [45, 46, 47].

Accepting sustainable development as the main guideline for progress (Tab. 1) results in the creation of a new research area, concerning the material factors in the development (Fig. 2). The area comprises the following existing fields:

- performance criteria of construction materials,
- methods of suitability assessment,
- modification of materials and new material solutions,
- material performance in service conditions,

as well as certain aspects of ecology, waste management, and the recycling of used construction materials for the construction industry, and reuse of building materials.

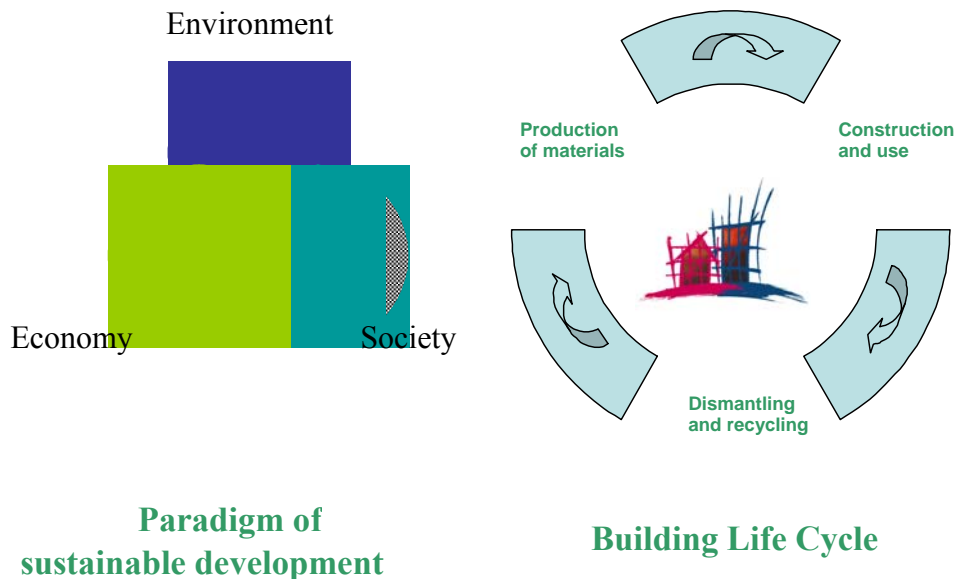
The mere comparison of the amount of waste and the amount of produced building materials is enough to show that – in the decades to come – waste management in the construction industry will become a civilisation challenge, just

like the repairs and modernisation of the existing assets and ensuing material needs.

The notion of sustainable development is a premise that spreads over the research and economic areas and – quite possibly – it will become a megatrend in the 21st century. At the same time, the implementation of this idea is linked with finding a solution for one of the most fundamental civilisational problems – waste management, including the concept of DFR - "design for recycling". It seems that the programme not only aims at rectifying the errors of the past and ensuring a better future for the next generations, but it will

Fig. 3. Material factors in the sustainable development of construction

also become a creative force of progress – "Smart Material Systems" [24].



Sustainable development is a task for creating a number of balances on various levels (Fig. 3). The most general perspective refers to the society, environment, and economy. As far as the construction industry is concerned, it refers to the comprehensive concept of an environmental impact over the whole life cycle of a civil structure or building (Life Cycle Assessment, LCA). Considering the nature of the construction industry, the material factors of structural durability and reliability are particularly important

* Director of the Fraunhofer Institute for Building Physics in Stuttgart.

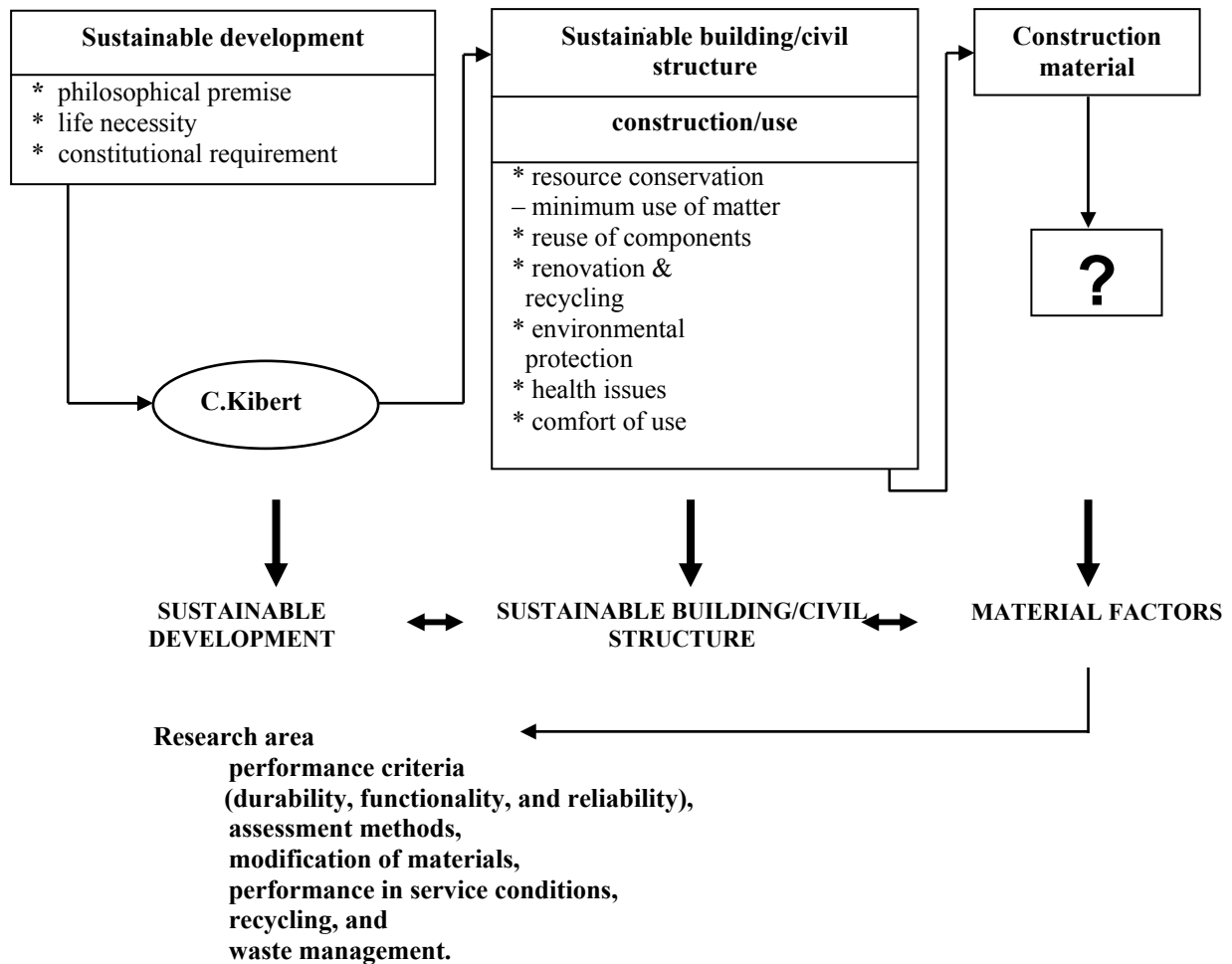


Fig. 2. The research area of the “material factors in sustainable development”

It is a vast, and multidisciplinary, task. It may be assumed that the message of sustainable development will be one of the main keynotes of the subsequent European Programmes. Sustainable development in construction in general – and factors determining the choice of materials in sustainable constructions in particular – are naturally becoming a paradigm of the research activity in the field of construction. It is an evolved consequence of the former paradigm – the principal requirements as set forth in Directive 89/106/EEC (1988). At the same time, it is a new approach, charting a new direction in the development of construction materials, which is referred to in Canada as “ISIS – Intelligent Sensing for Innovative Structures”. Some elements of the new approach include the “Structural Health Monitoring” and “Building Advanced Composite Materials”.

The specific nature of the construction industry makes durability and the reliability of material solutions understood as the material determinants of durability and the reliability of the construction, simply as a prerequisite. As far as the choice of materials is concerned, the central idea is their **compatibility**, which is understood as a choice of materials with regard to their physical and chemical properties so that the choice would ensure the load-bearing capacity and usability limits of each component of a given system within the designed time and conditions of use.

The policy of sustainable development sets new tasks for construction materials engineers. A sustainable building or

civil structure is to meet nine requirements as regards the time of the construction and period of use [10, 22, 23]:

- minimum quantity of materials used (resource conservation), including water,
- maximum reuse of components,
- possibility to renovate or recycle,
- environment protection,
- waste management,
- minimum emission of pollutants,
- construction process management and building management,
- health aspects,
- comfort of use (quality).

Recently, the survivability requirement is being increasingly brought up, especially when referring to a terrorist attack.

The task of waste management and its reuse for construction purposes became a part of the sustainable development idea. The amount of disposed and produced waste clearly shows that their reuse in the construction industry is becoming a necessity.

The research tasks, following from the concept of sustainable development, may be divided into two types:

- *intensive* – incorporating the demand for sustainable development into existing research themes,
- *extensive* – creating new fields of research.

The division is vague. However, one can argue that *material factors* belong to the first type, while energy factors to the second. The *intensive* tasks face a serious problem of how to

Tab. 2. Formulation matrix for the additional requirements to ensure sustainable material performance (based on [14])

Ecology		Economy		Social aspects		Assurance of sustainable material performance
Emission?		Cost/performance		Joint decision making		
Use of natural resources?		Tendency to incur costs		Transparency Responsibility		
Bio-diversification?		Organisational efficiency		Safety, health, and good mental state		
Balanced system – ecology		Balanced system – economy		Balanced system– social aspects		

define the types and levels of criteria; the notion of usefulness must be redefined to ensure sustainable development.

6. Sustainable development vs. performance concept; product performance criteria

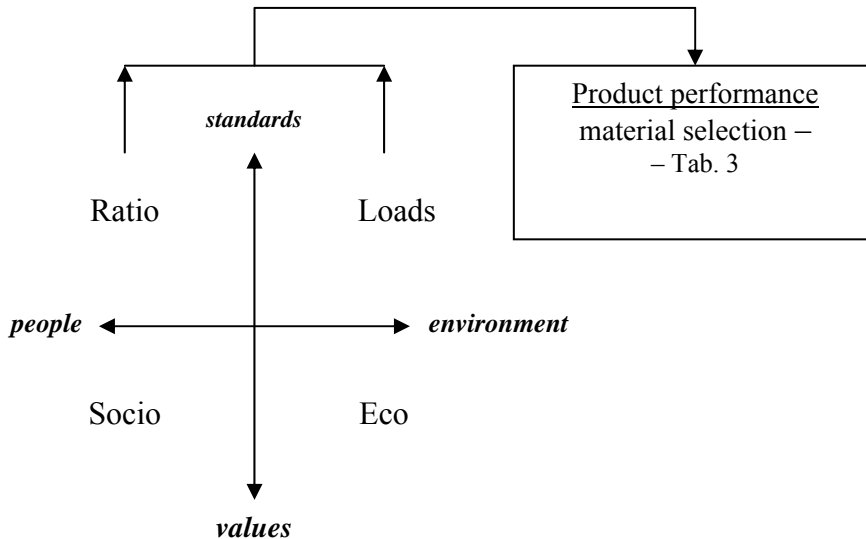
The idea of usefulness in the construction industry has a long tradition. Some aspects of the approach may be found in the Code of Hammurabi (1750 BC), and the writings of Vitruvius (dated 20-10 BC). However, only recently has there been the *performance concept*, i.e. evaluation and selection of materials according to their usefulness, becoming increasingly appreciated throughout the construction industry. In the European standard for concrete, which is accepted as a Polish standard (PN-EN 206-1), and in many other standards the notion was used in the title. The idea of performance was well grasped in the US building regulations of 1925 [25]:

“construction demands satisfactorily and economically, might be restricted from use, thus obstructing progress in the industry.”

The above statements have not lost their validity, and – in light of the sustainable development requirements – they have even become a particularly current necessity. It is especially significant with regard to substitute material solutions (alternative raw materials), and to those construction materials and products that are based on recycled ingredients or components. Moreover, sustainable development imposes the need to consider additional requirements and/or restrictions (Fig. 4 and Tab. 2). A restriction is also a situation when certain technical properties are not used in a given application or when they are redundant, and thereby generate irrational costs (energy input). This implies that there is a need [26], or even an obligation to develop a new research area (and knowledge/skills) to define the performance in terms of the properly selected (type and level) technical properties. The

final decision on the choice of a material solution, as a rule, will require an analysis or optimisation involving a number of criteria. There are examples of this approach in the literature, e.g. the *polyoptimal* method of designing environmentally-friendly buildings [27] considers the values of the total accumulated energy and CO₂ emission of construction materials and main technologies. It should become one of the fundamental activities of the leading research institutes in the field of the construction industry.

Fig 4. Defining the performance of a construction product as a derivative of basic principles of sustainable development (based on [14])



“Whenever possible, requirements should be stated in terms of performance, based upon test results for service conditions, rather than in dimensions, detailed methods, or specific materials. Otherwise new materials, or new assemblies of common materials, which would meet

The examples of the pursuit of a definition of *sustainable performance* are usually methods of assessing the environmental impact of buildings [28], which are used as a manual for auditors. As part of the activities of the CEN Technical Committee TC-350 [29], an extended term for “integrated building performance” was introduced (Fig. 5).

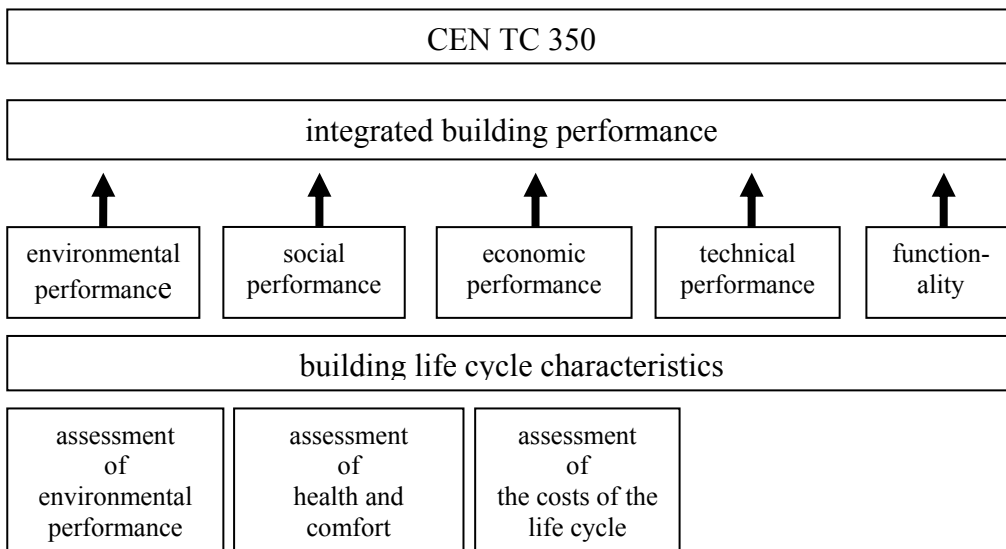


Fig. 5. A diagram representation of the term "integrated building performance" according to CEN TC-350 [29]

7. Sustainable construction industry – new fields of research

Energy factors in sustainable development have led to the creation of a few new fields of research, including a method for simulating the energy performance of buildings [30, 31] and a method for determining the energy profile of buildings (implementation of Directive 2002/91/EC) [32]. New terms have been coined, e.g. a "passive building" (Adamson, Feist), i.e. a building in which a comfortable interior climate can be maintained without an active heating and cooling system. Pilot projects have been realised to respond to the new notions [33] along with a whole new library of software to simulate and evaluate energy and environmental effects. The number of specialised programmes is so large that a validation method had to be developed [34].

New themes within the idea of sustainability include the recycling of construction materials, such as concrete [35], and

in this way (Fig. 6).

Sustainable development in construction opened a new research area, which is connected not only with material performance, energy factors [40], and environmental effects [41], but also protection against noise pollution [42] and the evaluation of the storage efficiency of waste material [43]. The introduction of the principle of sustainable development into the construction industry will provide a source of illuminating and important research inspiration for engineers for many years to come. A successful implementation of sustainable development in construction depends on the results, but it also – and to a large degree - depends on the availability of properly educated specialists. It has been found that – until now – only the British University of Strathclyde launched a *Masters' by Research in Sustainable Construction & Infrastructure* [44]. This should spur other universities to prepare similar relevant specialisation courses. In order to implement the concept of "construction that meets the requirements of sustainable development", first of all, the requirements must be formulated specifically for the construction industry.

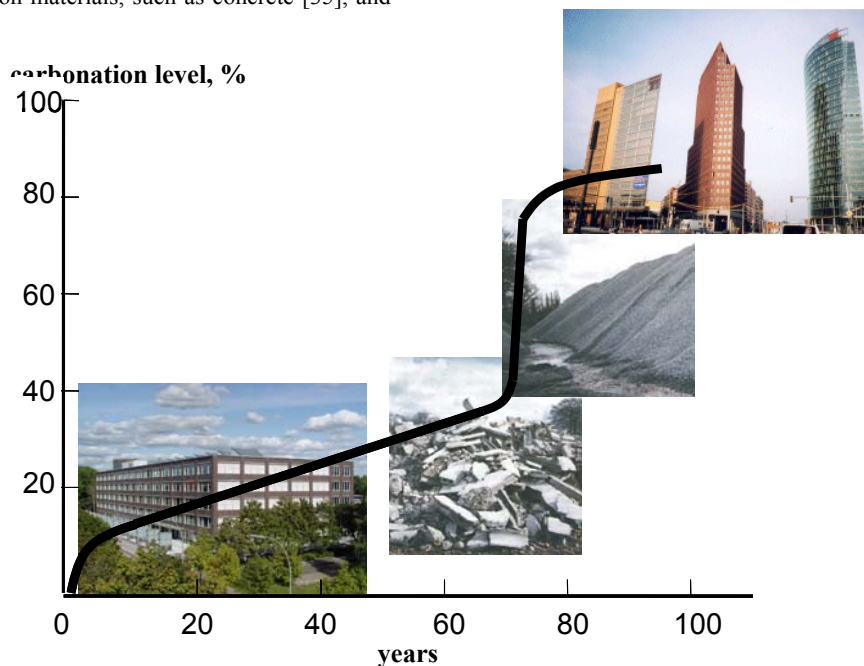


Fig. 6. Simulated carbonation of concrete, including its recycling.

the assessment of the durability of concrete [36] mixed with recycled concrete aggregate. *Sustainable concrete* has proven to be a satisfying field of research [37, 38]. Studies of concrete recycling show that the process of grinding causes such an expansion of the surface of concrete aggregate that it results in an irregular increase of carbonation intensity [39]; therefore, up to 90% of the carbon dioxide emitted while producing cement is assumed to be absorbed

References

- [1] United Nations, 1987: Report of the World Commission on Environment and Development, G. H. Brundtland Commission, General Assembly Resolution 42/187
- [2] Wierzbicki S.: Budownictwo zgodne z zasadami zrównoważonego rozwoju w świetle przepisów (in Polish)
- [3] Cywiński Z.: Current Philosophy of Sustainability in Civil Engineering, J. Prof. Issues in Eng. Educ. and Practice, 1/2007
- [4] Cywiński Z.: Zrównoważony rozwój a historia i dziedzictwo budownictwa, (in Polish) Pismo PG, 7/ 2007
- [5] Daly H.: Beyond Growth: The Economics of Sustainable Development, Boston, Beacon Press, 1996
- [6] Sustainability metric and indices. Wikipedia.org/wiki/sustainability
- [7] Wierzbicki S.: Budownictwo a stały rozwój środowiska ludzkiego. VII Ogólnopolska Interdyscyplinarna Konf. Nauk.–Tech: Ekologia a budownictwo, 1995, p. 19 -27 (in Polish)
- [8] www.eur-lex.europa.eu
- [9] Lead Market Initiative for Europe, COM 2007 – 860
- [10] Accelerating the Development of the Sustainable Construction Market in Europe, ibid
- [11] Tworek J.: Budownictwo spełniające wymagania rozwoju zrównoważonego w nowych dokumentach UE. Biuletyn ITB in UE 1/2008-04-25 (in Polish)
- [12] The UK Construction Industry: Progress towards more sustainable construction 2000- 2003, 2003, p. 23
- [13] Sustainable construction, Brief 2, 2004, p. 17 (www.defra.gov.uk)
- [14] Lahti P.: Towards Sustainable Urban Infrastructure, ESC, COST, 2006, p. 335
- [15] Action–C25: Sustainability of constructions: integrated approach to life – time Structural Engineering, COST, TUD, 2006- 2010
- [16] Kashino N., Ohama Y.[eds.]: Environment – Conscious Materials and Systems for Sustainable Development. RILEM Int. Symposium, Koriyama, 2004, p. 37
- [17] Hendriks C.F., Pietersen H.S.: The Sustainable Raw Materials – Construction and Demolition Wwaste. State-of-the-Art Report of RILEM TC165–SRM, RILEM, 2000, p. 216
- [18] Towards Sustainable roofing. Report CIB W83/RILEM TC 166 RMS, 2003, p.28
- [19] F-P7 Cooperation Work Programme 2008: Theme 6: Environment (including climate change), Activity 6. 2. Sustainable management of resources, 2008
- [20] Van der Meulen B.: Looking beyond the Endless Frontier” European Science Foundation. www.esf.org., 2007, p. 27
- [21] Gertis K.: Realistyczne rozważania zamiast wyidealizowanych życzeń: budynki niskoenergetyczne czy niskoentropowe? Konferencja ITB : Budownictwo spełniające wymagania zrównoważonego rozwoju, 2002 (in Polish)
- [22] Kibert C.J.: Establishing principles and a model for sustainable construction. Proceedings of the first Int. Conference CIB TG 16, Florida, 1999, p. 3 -12
- [23] Code for sustainable Homes Dept. Communities and Local Government. London, 2006, p. 28
- [24] Richard P., Cheyrezy M.H.: Reactive Powder Concrete With High Ductility and 200- 800 MPa Compressive Strength. In “Concrete Technology Past, Present and Future (P.K. Mehta ed.), SP- 144, American Concrete Institute, 1994
- [25] Gross J.: Developments in the application of the performance concept in building. NIST, Washington, 1985
- [26] Becker R.: Research and development needs for better implementation of the performance concept in building. Automation in Construction, 1999, p. 525- 532
- [27] Olędzka D., Węglarz A., Żmijewski K.: Projektowanie polioptymalnych budynków przyjaznych środowisku. Izolacje, 2007, p. 22- 24 (in Polish)
- [28] Panek A.: Metody oceny oddziaływania na środowisko obiektów budowlanych. Biblioteka Monitoring Środowiska. Warszawa, 2002 (in Polish)
- [29] Trinius E.: Sustainability of construction Works. CENTC 350
- [30] Narowski P.: Symulacje energetyczne budynków – czym są i do czego służą? Energia i Budynek, 2007, p. 4-13 (in Polish)
- [31] Bartkiewicz P.: Zakres praktycznego wykorzystania symulacji zużycia energii w budynkach, ibid., p. 14-17 (in Polish)
- [32] Kasperkiewicz K.: Opracowana w ITB koncepcja wdrożenia Dyrektywy 2002/91/WE. Doradca Energetyczny, 4/2008, p. 38-45 (in Polish)
- [33] www.passiv.de
- [34] Panek A., Domoń P.: Metodyka walidacji programów komputerowych stosowanych do wyznaczania charakterystyki energetycznej budynków. Energia i Budynek, 9/2007, p. 32-35 (in Polish)
- [35] Eguchi K. et al.: Application of recycled coarse aggregate by mixture to concrete construction. Construction and Building Materials, 2007, p.1542-1551
- [36] Levy S.M., Helene P.: Durability of recycled aggregates concrete a safe way to sustainable development
- [37] Ajdukiewicz A.: Beton a rozwój zrównoważony. Budownictwo, Technologie, Architektura, 3/2004, p. 38-44 (in Polish)
- [38] Czarnecki L.: Przyszłość betonu w warunkach zrównoważonego rozwoju. Materiały Budowlane, 1/2006, p. 22-24, 52 (in Polish)
- [39] Nielsen C.: Nordic Project; Concrete production – Best Available Technologies. Challenge for Sustainable Construction Seminar, Warszawa, 2006
- [40] Geryło R., Kasperkiewicz K.: Ograniczenie eksploatacyjnej energochłonności budynków w świetle postanowień europejskich, The Proceedings of the „Krynica 2008” (in Polish), Krynica, 2008.
- [41] Piasecki M., Prejzner H.: Ograniczenie negatywnego oddziaływania budynku na środowisko w świetle postanowień europejskich, The Proceedings of the „Krynica 2008” (in Polish), Krynica, 2008.
- [42] Niemas M., Nurzyński J., Szudrowicz B.: Zrównoważony rozwój budownictwa a problem ochrony przed hałasem, The Proceedings of the „Krynica 2008” (in Polish), Krynica, 2008.
- [43] Wysokiński L., Majer E.: Ocena właściwości przesłonowych iłów do budowy składowisk odpadów nową metodą, The Proceedings of the „Krynica 2008” (in Polish), Krynica, 2008.
- [44] Masters’ by Research in Sustainable Construction & Infrastructure. University of Strathclyde, www.strath.ac.uk
- [45] Rant Z.: Energy Value and Pricing. Strojnicki Vestnik, 1955, 1, 4-8
- [46] Torio H., Schmidt D.: More sustainable buildings through exergy analysis – Solar thermal and/or

ventilation systems? Proc. of Clima 2007 WellBeing
Indoors

[47] Czarnecki L.: Wyzwania inżynierii materiałów
budowlanych. Inżynieria i Budownictwo, (in Polish)
7/2008.

Functionalized Cucurbiturils and Their Biological Applications: Cucurbituril-Based Nanoparticles for Cancer Cell-Targeted Delivery of Hydrophobic Drugs

Kyeng Min Park,¹ Kyungwon Suh,² Hyuntae Jung,³ Don-Wook Lee,³ Youngjoo Ahn,² Jeeyeon Kim,² Kangkyun Baek², Jin Sook Jeong⁴ and Kimoon Kim*^{1,2,3}

¹Division of Advance Materials Science, ²National Creative Research Initiative Center for Smart Supramolecules and Department of Chemistry and ³School of Interdisciplinary Bioscience and Bioengineering Pohang University of Science and Technology (POSTECH), Pohang, 790-784, Republic of Korea, ⁴Department of Pathology, Dong-A University College of Medicine, Busan, 602-715, Republic of Korea
kkim@postech.ac.kr

Abstract: Cucurbituril-based nanoparticles (CB[6]NPs) serve as a new efficient delivery vehicle of hydrophobic drugs, which have unique features including (1) a high drug loading capacity and efficiency, (2) noncovalently tunable surface, (3) efficient delivery of hydrophobic drugs into a cancer cell by receptor-mediated endocytosis, and (4) facile release of drugs into cytoplasm, which enhances pharmaceutical effects of the drugs.

Key Words: Cucurbituril, Nanoparticle, Drug delivery, Supramolecular chemistry, Paclitaxel

1. INTRODUCTION

One of the major concerns regarding cancer treatment with clinically used hydrophobic drugs such as paclitaxel (PTX) is low therapeutic effects due to poor aqueous solubility and lack of specificity. This limitation can be overcome at least in part by targeted delivery of such drugs using nanomaterials such as liposomes [1], micelles [2] and nanoparticles (NPs) [3,4]. Although a wide range of nanomaterials made of various building blocks ranging from conventional lipids to polymer amphiphiles have been explored to date, the search for safe, efficient nano-sized vehicles for drug delivery continues [1-5]. Recently, amphiphilic macrocyclic molecules and nanomaterials therefrom have been investigated as a drug delivery vehicle by harnessing their hydrophobic cavities to encapsulate hydrophobic drugs, but most efforts have been focused on NPs made of cyclodextrins (CDs) or their derivatives [6,7].

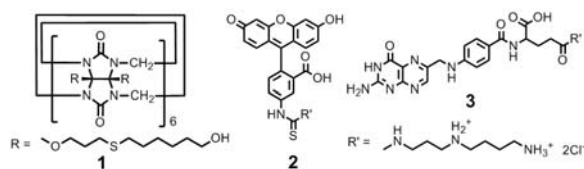
Cucurbit[6]uril (CB[6]), a member of the macrocyclic host family cucurbit[*n*]uril (CB[*n*]) comprising six glycoluril units has a hydrophobic cavity similar to that of α -CD. However, unlike CDs, it has two identical, carbonyl-fringed entrances to the cavity. Most importantly, CB[6] forms stable host-guest complexes with a wide range of small molecules, especially polyamines with extremely high binding affinity ($K > 10^6 \text{ M}^{-1}$) in aqueous solution [8-12]. Recent development of a direct functionalization method of CB[*n*] allowed us to synthesize a wide range of tailor-made CB[*n*] derivatives [13], and to explore their applications [14] including the synthesis of CB[6]-based vesicles[15] and polymer nanocapsules[16]. Recently, we have reported novel CB[6]-based NPs (CB[6]NPs) formed by a new CB[6]

derivative, which may serve as an effective vehicle for targeted intracellular delivery of hydrophobic drugs [17]. The unique features of CB[6]NPs include (1) hydrophobic drugs can be loaded inside the NPs with a high loading capacity and efficiency, (2) the surface of hydrophobic drug-loaded CB[6]NPs can be easily modified with a targeting ligand and/or fluorescent probe in a noncovalent manner by taking advantage of the strong host-guest interactions between CB[6] and polyamine derivatives, (3) drug-loaded CB[6]NPs can be efficiently delivered to a cancer cell and internalized by receptor-mediated endocytosis, and (4) hydrophobic drugs can be released into cytoplasm after receptor-mediated endocytosis, which enhances pharmaceutical effects of the drugs. Here, we report additional experimental details for CB[6]NPs.

2. EXPERIMENTS

2.1 Synthesis of a new CB[6] derivative ((3-(6-hydroxyhexanethio)propan-1-oxy)_{*n*}CB[6]) (1)

6-Mercaptohexanol (150 mg, 1.1 mmol) was added to a solution of (allyloxy)₁₂CB[6] (30 mg, 1.8×10^{-2} mmol) in methanol (2 mL) in a quartz tube and degassed with N₂. After the mixture was irradiated with UV light (254 nm and 300 nm) for 3 d, the solvent was removed under a reduced pressure. The crude product was recrystallized from diethyl ether (10 mL). The solid was washed with diethyl ether and dried under a reduced pressure to give **1** (50 mg, 89%).



Scheme 1: CB[6] derivative (**1**), FITC-spermidine conjugate (**2**), folate-spermidine conjugate (**3**)

2.2 Preparation of Nile Red loaded CB[6]NPs (CB[6]NPs \supset NR)

A solution of CB[6]NPs \supset NR was prepared with a solution of **1** (3.3 mg, 1.0×10^{-3} mmol) and Nile Red (10 μ g, 0.03 μ mol) in ethanol (100 μ L) a 20 mL glass vial and the solvent was evaporated under a reduced pressure to give a thin film. Addition of distilled H₂O (10 mL) to the vial followed by sonication for 30 min resulted in the formation of nanoparticles (1.0×10^{-4} M). The successful formation of Nile Red loaded CB[6]NPs was confirmed by transmission electron microscopy (TEM) and dynamic light scattering (DLS), fluorescence emission spectrometry and confocal laser scanning microscopy.

2.3 Preparation of **2** decorated CB[6]NPs \supset NR (**2**@CB[6]NPs \supset NR)

2 (0.60 mg, 1.0 equiv with respect to **1** forming CB[6]NPs) was added to the solution of CB[6]NPs \supset NR prepared by using the same procedure as above and the mixture was gently shaken for 1 h at room temperature to allow host-guest interactions between **2** and the accessible cavity of CB[6]NPs. The resulting solution was dialyzed against water to give **2**@CB[6]NPs \supset NR. The successful decoration of **2** on the surface of CB[6]NPs and Nile Red loading in the CB[6]NPs were confirmed by fluorescence emission spectroscopy and confocal laser scanning microscopy.

2.4 Targeted intracellular delivery of hydrophobic molecules using CB[6]NPs

HeLa cells were seeded on a poly-L-lysine coated cover glass in a 24-well plate at a density of 5×10^4 cells per well in 1 mL of folate deficient RPMI 1640 medium containing 10% fetal bovine serum (FBS) and 1% penicillin/streptomycin (PS) and incubated in a humidified 5% CO₂ atmosphere at 37 °C for 24 h. The culture medium was replaced with 1 mL of a fresh one including 100 μ L of water, CB[6]NPs \supset NR, **3**@CB[6]NPs \supset NR and **3**@CB[6]NPs \supset NR with a 1000-fold excess folic acid (1.3 mg, 0.2 μ mol). The final concentration of CB[6]NPs in the medium was 1.0×10^{-5} M. After 1 h incubation at 37 °C, the cells were washed with phosphate buffer saline (PBS) and fixed with 1% (w/v) para-formaldehyde solution. The cells on the cover glass were examined by a confocal laser scanning microscope. To understand the mechanism of the intracellular delivery, the same experiments were performed with **3**@CB[6]NPs \supset NR at 4 °C, instead of 37 °C.

2.5 Measurement of PTX loading capacity and efficiency of CB[6]NPs

CB[6]NPs \supset PTX were prepared with **1** (2.00 mg) and PTX (0.10 mg, 0.20 mg or 0.40 mg) in 5.00 mL of water by using the same procedure as CB[6]NPs \supset NR. The

samples were syringe-filtered through a polytetrafluoroethylene (PTFE) syringe filter having 1 μ m pore diameter to remove insoluble PTX and dialyzed against water. The filtrate was lyophilized and PTX in CB[6]NPs was extracted with chloroform. After removal of chloroform under the reduced pressure, the sample was dissolved in methanol to measure the amount of PTX by UV-visible spectroscopy. The experiment was performed 3 times to obtain mean \pm standard deviation (S.D.).

Loading capacity (%) = (weight of PTX loaded / weight of CB[6]NPs \supset PTX) \times 100

Loading efficiency (%) = (weight of PTX loaded / weight of initially added PTX) \times 100

2.6 In vitro cytotoxicity against HeLa cells to obtain IC₅₀ values

HeLa cells were seeded in a 96-well plate at a density of 5×10^3 cells per well in 200 μ L of folate deficient RPMI 1640 medium containing 10% FBS and 1% PS and incubated in a humidified 5% CO₂ atmosphere at 37 °C for 24 h. The cell culture medium was replaced with a fresh one containing various concentrations of PTX (0.01 - 4 μ g mL⁻¹) in CB[6]NPs \supset PTX and **3**@CB[6]NPs \supset PTX. The same experiment was performed with free PTX (0.01 - 4 μ g mL⁻¹) as a control. The cells were incubated for 1 h at 37 °C and the medium was again replaced with a fresh one and further incubated for 3 d at 37 °C. Subsequently, the cells were incubated in a fresh medium containing methylthiazolyldiphenyl-tetrazolium bromide (MTT) (0.5 mg mL⁻¹) for an additional 4 h at 37 °C, and then the medium was gently removed. The purple, water insoluble crystals formed by live cells remaining in the bottom of the wells were dissolved with 200 μ L of dimethyl sulfoxide and the solution was gently shaken for 10 min. UV absorption of the solution at 590 nm was measured by a multi-well plate reader. The experiment was performed 3 times to obtain S.D.

3. RESULTS AND DISCUSSIONS

3.1 Synthesis of CB[6] derivative (**1**)

The new CB[6] derivative, (3-(6-hydroxyhexanethio)propan-1-oxy)_nCB[6] (average $n = 11.4$) (**1**), was synthesized by photoreaction between (allyloxy)₁₂CB[6] and 6-mercaptohexanol in methanol. The product was a mixture of partially substituted **1** with a different degree of substitution. The MALDI-TOF mass spectrum of **1** revealed species with 9 - 12 substituents (3-(6-hydroxyhexanethio)propan-1-oxy) attached to a CB[6] core. The N/S ratio in elemental analysis suggested that the average degree of substitution is 11.4, which was consistent with the ¹H NMR integration.

3.2 Preparation of CB[6]NPs

CB[6]NPs were prepared by adding water to **1** dissolved in a minimum volume of ethanol and sonicating it for 30 min to allow to form NPs. The NPs have been characterized by TEM and DLS. A characteristic morphology of solid spherical NPs was observed by TEM. In the concentration range of 1×10^{-3} - 1×10^{-6} M, the average size of the spherical NPs determined by TEM is 190 ± 50 nm, which is consistent with 160 ± 40 nm determined by dynamic light scattering with samples dispersed in water.

3.3 Encapsulation of hydrophobic dyes

Having established a nanometer-sized solid particle nature of **1**, we decided to investigate whether the water-dispersed CB[6]NPs can encapsulate hydrophobic molecules inside similar to conventional polymer NPs [3-4]. A representative hydrophobic dye, Nile Red was chosen to investigate the loading properties of CB[6]NPs. Nile Red does not fluoresce in water, but emits red fluorescence in a hydrophobic environment. Nile Red loaded CB[6]NPs (CB[6]NPs \supset NR) were prepared by the same procedure as before, except using an ethanolic solution of Nile Red instead of pure ethanol. Confocal laser scanning microscopy showed strong red fluorescent dots dispersed in water, corresponding to the emission of Nile Red with λ_{max} at 609 nm as independently determined by emission spectroscopy. TEM and light scattering studies revealed little change in morphology and hydrodynamic radius of CB[6]NPs after loading of Nile Red. Taken together, we conclude that the hydrophobic molecules are successfully entrapped inside the CB[6]NPs.

3.4 Noncovalent surface modification of CB[6]NPs

The NPs are made of a CB[6] derivative with a cavity which is known to bind strongly with various guest molecules, in particular, polyamines including spermine ($K > 10^{-7} \text{ M}^{-1}$) and spermidine ($K > 10^{-6} \text{ M}^{-1}$) [4]. Taking advantage of the exceptional host-guest chemistry, a “tag” can be easily introduced to the surface of the CB[6]NPs in a noncovalent manner simply by treating with a tag-attached polyamine as we demonstrated with CB[6]-based vesicles [4c] and polymer nanocapsules [4d]. For example, we can decorate the surface of CB[6]NPs with the fluorescent probe fluorescein isothiocyanate (FITC) (**2**@CB[6]NPs), simply by adding 1 equivalent of FITC-spermidine conjugate (**2**) to a solution of CB[6]NPs, stirring the mixture for 1 h, and then dialyzing it against water to remove unbound **2**. The amount of accessible CB[6] cavities of CB[6]NPs was quantified by measuring the amount of unbound **2** recovered during the dialysis by fluorometry, which turned out to be $26 \pm 4\%$ of all the CB[6] derivative **1** constituting CB[6]NPs. The surface of the CB[6]NPs \supset NR can also be decorated with **2** using the same procedure (**2**@CB[6]NPs \supset NR). Confocal laser scanning microscopy (Figs.1a,b) showed green and red fluorescent dots corresponding to emission of **2** and Nile Red with λ_{max} at 521 and 609 nm, respectively. The emission band of **2** decorated on CB[6]NPs \supset NR was red-shifted by 6 nm with respect to that of free **2** (Fig.1d). The dots in FITC and Nile Red channels were well overlapped (Fig1), indicating that the surface of CB[6]NPs was successfully decorated with **2** while Nile Red was loaded inside CB[6]NPs. The TEM image (Fig.1e) showed that **2**@CB[6]NPs \supset NR maintained its spherical morphology and size even after the noncovalent surface modification using host-guest chemistry. Taken together, CB[6]NPs can entrap hydrophobic guest molecules inside the NPs, and at the same time, various “tag” units can be introduced on the surface of CB[6]NPs in a noncovalent manner without significant morphological changes.

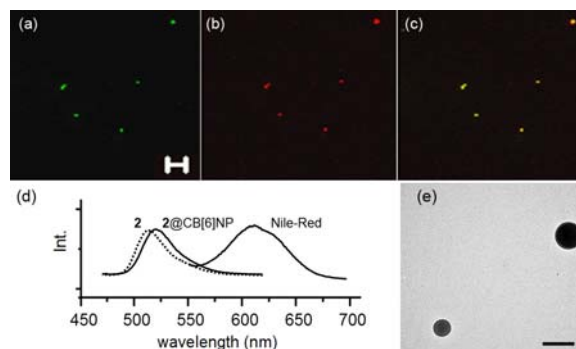


Figure 1: Confocal laser scanning microscopy images of **2**@CB[6]NPs \supset NR (a) FITC channel (scale bar = 5 μm), (b) Nile Red channel, (c) overlay of (a) and (b), (d) fluorescence measurement of free **2** (dashed line) and **2**@CB[6]NPs \supset NR (solid line) (e) TEM image of **2**@CB[6]NPs \supset NR (scale bar = 200 nm)

3.5 Selective intracellular uptake of CB[6]NPs

To demonstrate the potential utility of CB[6]NPs as a new vehicle for targeted drug delivery to tumors, an in vitro study was carried out using Nile Red as a model hydrophobic drug, and human ovarian carcinoma HeLa cells that have overexpressed folate receptors on the surface as a target cell. The cancer cells require excessive folic acid, a high affinity ligand to the folate receptors, for their rapid proliferation. We prepared folate-spermidine conjugate (**3**) [16] decorated CB[6]NPs \supset NR (**3**@CB[6]NPs \supset NR). The intracellular uptake of **3**@CB[6]NPs \supset NR and CB[6]NPs \supset NR into HeLa cells was examined by confocal laser scanning microscopy using 543 nm light for excitation of Nile Red. As illustrated in Fig.2, only **3**@CB[6]NPs \supset NR showed facile internalization into the cell after 1 h incubation at 37 $^{\circ}\text{C}$. No or only small translocation of CB[6]NPs \supset NR was observed without the targeting ligand (**3**) decorating the CB[6]NPs surface (Fig.2b), in the presence of excess amount of extra folic acid in the culture medium (Fig.2d), or incubation at 4 $^{\circ}\text{C}$ (Fig.2e), which suggested that the mechanism of the cellular uptake is most likely folate receptor-mediated endocytosis.

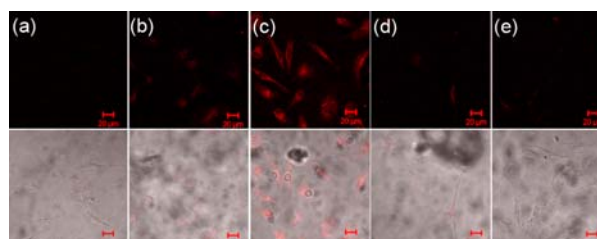


Figure 2: Confocal laser scanning microscopy images of (a) HeLa cells after incubation for 1 h at 37 $^{\circ}\text{C}$ with (b) CB[6]NPs \supset NR, (c) **3**@CB[6]NPs \supset NR, (d) **3**@CB[6]NPs \supset NR with a 1000-fold excess folic acid and (e) **3**@CB[6]NPs \supset NR after incubation for 1 h at 4 $^{\circ}\text{C}$.

3.6 Intracellular location of CB[6]NPs

To investigate the intracellular location of CB[6]NPs after endocytosis, we incubated HeLa cells with **2** (fluorescence probe) and **3** (targeting ligand) decorated CB[6]NPs (**(2+3)**@CB[6]NPs) and LysoTracker Red, a probe highly selective for cellular organelles with low internal pHs such as endosomes. As shown in Fig.3, a good overlap between the green dots and red dots independently observed by the FITC channel and

LysoTracker Red channel, respectively, of confocal laser scanning microscopy, indicated that CB[6]NPs were located predominantly at endosomes after endocytosis in the HeLa cells.

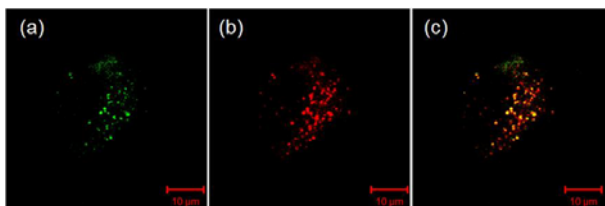


Figure 3 Confocal laser scanning microscopy images of HeLa cells incubated with (2+3)@CB[6]NPs for 1 h and then with LysoTracker Red for 30 min at 37 °C: (a) FITC channel, (b) LysoTracker Red channel and (c) overlay of (a) and (b).

Similarly, to monitor the behavior of Nile Red loaded in CB[6]NPs after endocytosis by confocal laser scanning microscopy, we incubated HeLa cells with (2+3)@CB[6]NPs⊃NR for 1 h at 37 °C, the surface of which was decorated with 2 and 3. Interestingly, as seen in Fig.4, Nile Red was distributed over the whole cell except the nucleus after 1 h incubation, while the green fluorescence from 3 decorating the surface of CB[6]NPs was localized, which indicated that after endocytosis, Nile Red was released into cytoplasm whereas CB[6]NPs appeared to remain in endosomes while maintaining their nanoparticle nature. At the moment, it is not clear how Nile Red is released from CB[6]NPs trapped in endosomes into cytoplasm. Nevertheless, considering that any drug loaded in nanomaterials must be released into the cytoplasm after endocytosis for efficient delivery, the facile release of the hydrophobic dye into cytoplasm increases the applicability of CB[6]NPs in targeted intracellular drug delivery.

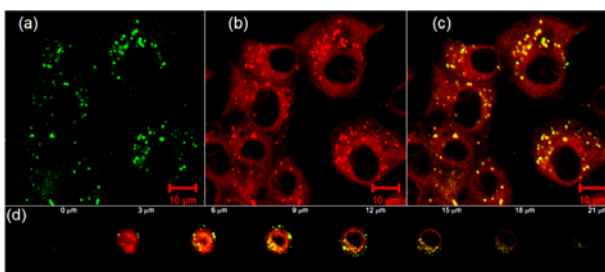


Figure 4: Confocal laser scanning microscopy images of HeLa cells incubated with (2+3)@CB[6]NPs⊃NR for 1 h at 37 °C: (a) FITC channel, (b) Nile Red channel, (c) overlay of (a) and (b) (scale bar = 10 μm), and (d) taken with different focal depths along the view axis.

3.7 PTX loading efficiency of CB[6]NPs

Encouraged by the series of observations, we then examined the delivery of hydrophobic drug PTX to HeLa cells using CB[6]NPs as a carrier and cell growth inhibition induced by cytotoxicity of PTX delivered by CB[6]NPs. We first determined the PTX loading efficiency of CB[6]NPs. In the case of CB[6]NPs⊃PTX prepared with 2.00 mg of CB[6] derivative 1 and 0.20 mg of PTX, PTX was loaded in CB[6]NPs with a loading capacity of $8.6 \pm 0.6\%$ (w/w) and a loading efficiency of $94 \pm 6\%$ (w/w), which was found to be the best condition for the preparation of CB[6]NPs⊃PTX for cell growth inhibition

assay. The PTX loading capacity and efficiency of CB[6]NPs are similar or higher than those reported for polymer based NPs such as hydrophobically modified glycol chitosan NPs [18] and stearate-grafted chitosan oligosaccharides NPs [19].

3.8 Cell growth inhibition of PTX loaded in CB[6]NPs

The cell growth inhibition induced by cytotoxicity of PTX delivered by CB[6]NPs with and without targeting ligands was evaluated by a standard MTT assay. First of all, the cytotoxicity of CB[6]NPs to HeLa cells is negligible at a concentration below $40 \mu\text{g mL}^{-1}$. Therefore, all the experiments were done with CB[6]NPs at a concentration of $40 \mu\text{g mL}^{-1}$ or below. HeLa cells were incubated with various concentration of free PTX, CB[6]NPs⊃PTX, or 3@CB[6]NPs⊃PTX in the cell culture medium for 1 h at 37 °C, and then incubated for another 3 days after replacing the culture medium with a fresh one. IC_{50} (50% of cell growth inhibition concentration) values after treatments were measured and compared in Table 1. The IC_{50} value of CB[6]NPs⊃PTX was $0.33 \pm 0.10 \mu\text{g mL}^{-1}$, which means that the PTX loaded in CB[6]NPs was approximately 3.8-fold more effective than free PTX ($\text{IC}_{50} = 1.24 \pm 0.20 \mu\text{g mL}^{-1}$) presumably due to internalization of CB[6]NPs⊃PTX into cells though nonspecific interactions, which was consistent with the nonspecific internalization of CB[6]NPs⊃NR into HeLa cells observed by confocal laser scanning (Figs.2b,d,e.). Most importantly, however, IC_{50} value of 3@CB[6]NPs⊃PTX was $0.08 \pm 0.02 \mu\text{g mL}^{-1}$, approximately 15.5-fold smaller than that of free PTX. The significantly enhanced cytotoxicity of 3@CB[6]NPs⊃PTX to HeLa cells may be attributed to facile internalization of 3@CB[6]NPs⊃PTX by folate receptor-mediated endocytosis followed by release of PTX into cytoplasm.

Table 1: IC_{50} values of PTX only, CB[6]NPs⊃PTX and 3@CB[6]NPs⊃PTX toward HeLa cells measured by MTT assay ($n = 3$).

	PTX	CB[6]NPs⊃PTX	3@CB[6]NPs⊃PTX
IC_{50} ($\mu\text{g mL}^{-1}$)	1.24 ± 0.20	0.33 ± 0.10	0.08 ± 0.02

4. CONCLUSIONS

We report novel nanoparticles CB[6]NPs made of a new CB[6] derivative, in which hydrophobic drugs can be loaded in a high loading capacity and efficiency. Their surface can be easily decorated in a nondestructive, noncovalent, and modular manner simply by mixing the NPs with tag-polyamine conjugates which can be used as a fluorescent probe or targeting ligand, by taking advantage of the exceptional ability of CB[6] to bind polyamines tightly. Moreover, we demonstrated the selective cellular uptake of targeting ligand-decorated CB[6]NPs by receptor-mediated endocytosis, and facile release of loaded hydrophobic dye molecules into cytoplasm after endocytosis. A significantly increased cytotoxicity of PTX using targeting ligand-decorated CB[6]NPs has also been demonstrated. Taken together, the remarkable abilities of CB[6]NPs make them a novel platform for efficient intracellular and cytoplasmic delivery systems for clinically available hydrophobic drugs

such as PTX, which opens possibility of practical applications of CB[6]-based nanomaterials as targeted drug delivery systems. Further work using animals is now in progress.

Acknowledgment - The CRI, WCU (Project No. R31-2008-000-10059-0) programs, and BK21 programs of the Korean Ministry of Education, Science and Technology (MOEST)

References

- [1] Torchilin, V. P., "Recent Advances with Liposomes as Pharmaceutical Carriers," *Nat. Rev. Drug Discov.*, Vol.4, pp.145-160, (2005).
- [2] Torchilin, V. P., "Targeted Polymeric Micelles for Delivery of Poorly Soluble Drugs," *Cell. Mol. Life Sci.*, Vol.61, pp.2549-2559, (2004).
- [3] Sinha, R., Kim, G. J., Nie, S. and Shin, D. M., "Nanotechnology in Cancer Therapeutics: Bioconjugated Nanoparticles for Drug Delivery", *Mol. Cancer Ther.*, Vol.5, pp.1909-1917,(2006).
- [4] Brannon-Peppas, L. and Blanchette, J. O., "Nanoparticle and Targeted Systems for Cancer Therapy", *Adv. Drug Delivery Rev.*, Vol.56, pp.1649-1659, (2004).
- [5] Peer, D., Karp, J. M., Hong, S., Farokhzad, O. C., Margalit, R. and Langer, R., "Nanocarriers as An Emerging Platform for cancer therapy," *Nat. Nanotech.*, Vol.2,pp.751-760, (2007).
- [6] Duchêne, D., Ponchel, G. and Wouessidjewe, D. "Cyclodextrins in Targeting Application to Nanoparticles", *Adv. Drug Delivery Rev.*, Vol.36, pp.29-40, (1999).
- [7] Bilensoy, E., Grürkaynak, O., Ertan, M., Şen M. and Hincal, A. A., "Development of Nonsurfactant Cyclodextrin Nanoparticles Loaded With Anticancer Drug Paclitaxel". *J. Pharm. Sci.*, Vol.97, pp.1519-1529. (2008).
- [8] Lee, J. W., Samal, S., Selvapalam, N., Kim, H.-J. and Kim, K., "Cucurbituril Homologues and Derivatives: New Opportunities in Supramolecular Chemistry" *Acc. Chem. Res.*, Vol.36, pp.621-630, (2003).
- [9] Kim, K. and Kim, H.-J., "Encyclopedia of Supramolecular Chemistry" ed. Atwood, J. L. Steed, J. W. and Marcel Dekker, New York, pp. 390-397, (2004).
- [10] Lagona, J., Mukhopadhyay, P., Chakrabarti, S. and Isaacs, L., "The Cucurbit[n]uril Family" *Angew. Chem., Int. Ed.*, Vol.44, pp.4844-4870, (2005).
- [11] Jeon, Y. J., Kim, S.-Y., Ko, Y. H., Sakamoto, S., Yamaguchi, K. and Kim, K., "Novel Molecular Drug Carrier: Encapsulation of Oxaliplatin in Cucurbit[7]uril and its Effects on Stability and Reactivity of the Drug" *Org. Biomol. Chem.*, Vol.3, pp.2122-2125, (2005).
- [12] Rekharsky, M. V., Ko, Y. K., Selvapalam, N., Kim, K. and Inoue, Y. "Complexation Thermodynamic of Cucurbit[6]uril with Aliphatic Alcohols, Amines, and Diamines" *Supramol. Chem.*, Vol.19, pp.39-46, (2007).
- [13] Jon, S. Y., Selvapalam, N., Oh, D. H., Kang, J.-K., Kim, S.-Y., Jeon, Y. J., Lee, J. W. and Kim, K. "Facile Synthesis of Cucurbit[n]uril Derivatives via Direct Functionalization: Expanding Utilization of Cucurbit[n]uril" *J. Am. Chem. Soc.*, Vol.125, pp.10186-10187, (2003).
- [14] Kim, K., Selvapalam, N., Ko, Y. H., Park, K. M., Kim, D. and Kim, J., "Functionalized Cucurbiturils and Their Applications", *Chem. Soc. Rev.*, Vol.36, pp.267-279,(2007).
- [15] Lee, H.-K., Park, K. M., Jeon, Y. J., Kim, D., Oh, D. H., Kim, H. S., Park, C. K. and Kim, K., "Vesicle Formed by Amphiphilic Cucurbit[6]uril: Versatile, Noncovalent Modification of the Vesicle Surface, and Multivalent Binding of Sugar-Decorated Vesicles to Lectin", *J. Am. Chem. Soc.*, Vol.127, pp.5006-5007, (2005).
- [16] Kim, D., Kim, E., Kim, J., Park, K. M., Baek, K., Jung, M., Ko, Y. H., Sung, W., Kim, H. S., Suh, J. H., Park, C. G., Na, O. S., Lee, D.-k., Lee, K. E., Han, S. S. and Kim, K., "Direct Synthesis of Polymer Nanocapsules with a Noncovalently Tailorable Surface", *Angew. Chem., Int. Ed.*, Vol.46, pp.3471-3474, (2007).
- [17] Park, K. M., Suh, K., Jung, H., Lee, D.-W., Ahn, Y., Kim, J., Baek, K. and Kim, K., "Cucurbituril-Based Nanoparticles: a New Efficient Vehicle for Targeted Intracellular Delivery of Hydrophobic Drugs", *Chem. Commun.*, pp.71-73, (2009)
- [18] Kim, J.-H., Kim, Y.-S., Kim, S., Park, J. H., Kim, K., Choi, K., Chung, H., Jeong, S. Y., Park, R.-W., Kim, I.-S, and Kwon, I. C., "Hydrophobically Modified Glycol Chitosan Nanoparticles as Carriers for Paclitaxel", *J. Control. Release*, Vol.111, pp.228-234. (2006).
- [19] You, J., Hu, F.-Q., Du, Y. -Z. and Yuan, H., "Polymeric Micelles with Glycolipid-like Structure and Multiple Hydrophobic Domains for Mediating Molecular Target Delivery of Paclitaxel" *Biomacromolecules*, Vol.8, pp.2450-2456. (2007).

Direct Writing of Hydrogel Microarrays in Microchannels Using Field Diaphragm-Assisted Microscope Projection Photolithography

Jin-Ming Lin* and Jiangjiang Liu

The Key Laboratory of Bioorganic Phosphorus Chemistry & Chemical Biology, Department of Chemistry, Tsinghua University, Beijing, 100084, China

E-mail: jmlin@mail.tsinghua.edu.cn

Abstract: In this work, we describe the fabrication, characterization and application of hydrogel microstructures patterned inside microchannels for use in bioassays. This method uses an ordinary fluorescence microscope for projection photolithography on poly(ethylene glycol) diacrylate (PEG-DA) to realize a rapid photopolymerization under UV light illumination. The cross-linked hydrogel microstructures have controlled morphology and determinate position inside microchannels, which offer controlled and selective encapsulation of various materials, even single cells. Our method provides a convenient, inexpensive and widely accessible technique for immobilization of cells and other biomolecules onto the solid surface inside microchannels, which is typically the critical step to perform microfluidic bioassays.

Key words: Hydrogel microarray, Poly(ethylene glycol) diacrylate; Microfluidic device

This work describes the direct writing of hydrogel arrays in microchannels using 1) microscope projection photolithography (MPP) to pattern solid surfaces with micron-scale features, 2) polymerization of poly(ethylene glycol) diacrylate (PEG-DA) to entrap biomaterials, and 3) microfluidic devices to perform bioassays. This photolithography provides a convenient, inexpensive and widely accessible technique for generating features down to 50 μm over a patterned area larger than 10 cm^2 . Based on the hydrogel arrays, a detection of DNA oligomer is demonstrated on a microfluidic device.

Microarray is an efficient tool for simultaneous detection of multiple analytes in medical diagnostics, screening in drug discoveries and investigations of molecules interactions.¹⁻³ In such researches and applications, immobilization of biomaterials on solid substrates plays a critical role. Current methods include soft lithography, photolithography, ink-jet printing and microfluidics.⁴⁻⁸ Despite their successes in biological researches, a simple, low-cost and easy operating method for immobilization of biomaterials is still under investigation.

MPP provided a rapid and convenient approach to control the illumination in photolithography. It allows the use of a standard commercial microscope to pattern solid substrates with micron-scale features⁹ or synthesize microparticles in a high through-put manner.^{10,11} Moreover, the previous researches on photolithography of PEG-DA showed that a variety of biomaterials could be encapsulated inside the polymerized hydrogel while keeping their bioactivities.¹⁰⁻¹⁵ Herein, we developed a maskless MPP and applied it for photolithography of PEG-DA in a direct writing manner to fabricate hydrogel arrays inside microchannels.

The principle of direct writing of hydrogel arrays in microchannels is schematically shown in Fig. 1a. We firstly fabricate poly-(dimethylsiloxane) (PDMS) molds with 200-1000 μm wide and 20-50 μm deep microchannels by stand soft lithography. After sealing the PDMS molds to glass slides, the microchannels are filled with solution of PEG-DA. An external fluorescence light source offering tunable and reliable control on light intensity is utilized for photolithography. Variation of field diaphragms and switch of objectives control the illuminated area of UV light beam

on glass surfaces with varying diameters of 50-250 μm . A shutter controls the illumination time at 100 ms, which is sufficient for polymerization of PEG-DA. One post could be synthesized at each illumination. In that case, a large area of hydrogel arrays is achieved by repeating illumination on PEG-DA solution at different locations in microchannels by stepping the microscope stage over the x-y plane (Fig. 1a and 1b). After removing the unpolymerized solution, hydrogel arrays with uniform sizes (50-250 μm in diameter) and good order are obtained (Fig. 1c and 1d). To confirm whether the PEG-DA hydrogel influence the fluorescence detection or not, hydrogel arrays entrapping fluorescein are fabricated. The fluorescence images show low back-ground and uniform fluorescence among different hydrogel posts (Fig. 1e and 1f). That means PEG-DA is a good matrix for fluorescence detection. It should be highlighted that field diaphragm is used in our experiment rather than masks which were widely used for photolithography in previous reports. Field diaphragm offers a direct and tunable control on the illumination area, including sizes and locations, and greatly improves the side wall roughness of hydrogel posts (< 500 nm). Moreover, the direct writing approach can pattern microchannels with complex features of arbitrary shapes, which is difficult or hardly to achieve when using masks. However, using field diaphragm can not generate features smaller than 20 μm in diameter even using a 100 \times object. Polymerization of an individual hydrogel post is fast (100 ms for illumination and 500 ms for manual stepping), but patterning over a large area still requires a relative long time (can be improved by using automatic stepper).

We fabricated a number of hydrogel arrays entrapping different biomaterials, including DNA oligomers, polystyrene beads and yeast cells (Fig. 2a-2e). Two different DNA oligomers were immobilized inside a single microchannel by two-step photolithography, which meets the detection of multiple analytes. To simplify the fabrication, no chemical modification is applied to enhance the strength between the hydrogel posts and glass surface.¹³⁻¹⁵ These hydrogel arrays could withstand gentle shear stress caused by streams at moderate flow rate (< 5 $\mu\text{L}/\text{min}$).

Therefore, bioassays are performed on microfluidic devices based on the hydrogel arrays.

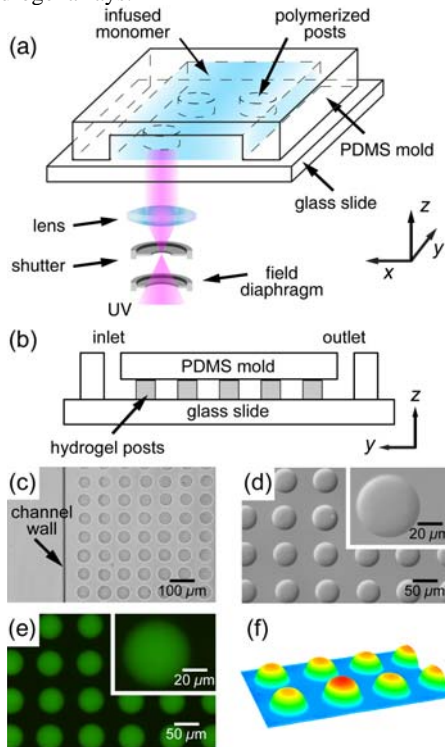


Fig. 1. (a) Schematic diagram of the configurations of the microfluidic device and the microscope for direct writing of hydrogel arrays in microchannel. (b) Schematic diagram of the cross view of the formed hydrogel arrays inside microchannel. (c) Bright field image of the hydrogel arrays patterned the glass surface inside a microchannel. (d) and (e) Differential interference contrast (DIC) and fluorescence images of arrayed microposts with uniform sizes. Fluorescein was added into the monomer solution. Insets: magnified area of individual micropost. (f) 3D contour plot of fluorescence intensity shows the uniformity of hydrogel posts in (e).

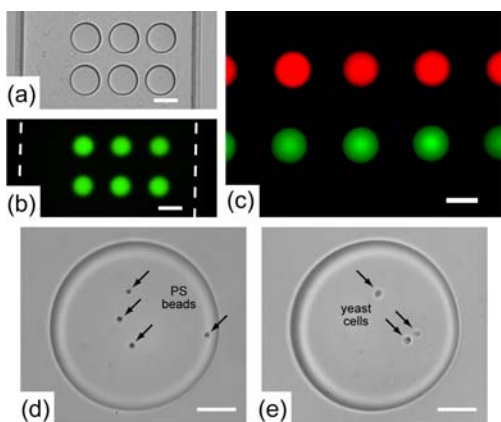


Fig. 2. Images of patterned hydrogel arrays show that a variety of biomaterials can be immobilized inside microchannels. (a) and (b) Bright field and fluorescence images of the same hydrogel arrays entrapping DNA oligomer labeled with 5'-FAM. Dashed line presents for the channel walls. (c) Fluorescence image of two sets of hydrogel arrays entrapping different DNA oligomers labeled with 5'-ROX and 5'-FAM, respectively. The two sets of hydrogel posts were fabricated inside the same microchannel. (d) and (e) Optical DIC images shows the entrapped polystyrene beads (2 μm in diameter) and yeast cells in hydrogel posts, respectively. Scale bars indicate 100 μm in (a), (b), and (c) and 25 μm in (d) and (e). FAM, 6-carboxyfluorescein; ROX, carboxy-X-rhodamine.

For demonstration, a detection of DNA oligomer is performed using the hydrogel posts entrapping probes. Fig. 3 shows the fluorescence images of hydrogel arrays after hybridization. Target oligomers were able to diffuse several micrometers into the hydrogel posts and hybridize with probe over the lateral and top surfaces. We simultaneously detected a series of samples in multiple microchannels with high sensitivity (detection limit, lower than 1 pM) and wide dynamic range

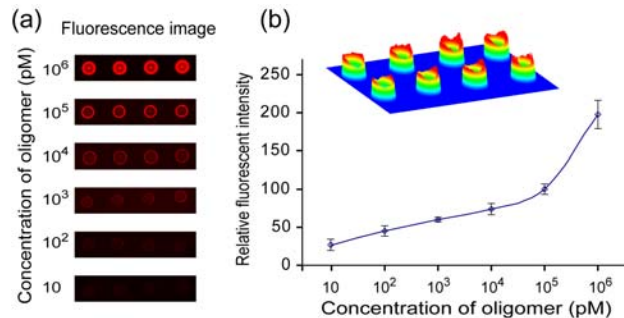


Fig. 3. Fluorescence detection of oligomer (5'-ROX-TCG AAT TGC C-3') on microfluidic device using the patterned hydrogel arrays containing probe (5'-Acrydite-C18-GGC AAT TCG A-3'). (a) Fluorescence images of the hydrogel arrays after hybridization of target oligomer with varying concentrations. (b) Plot of the increase in fluorescence intensity as a function of the concentration of oligomer. (Inset) 3D contour plot of fluorescence intensity of hydrogel arrays after 30 min incubation with 100 μM 5'-ROX labeled oligomer.

(over six orders of magnitude). The plot shown in Figure 3b was obtained from a microfluidic device with six parallel microchannels, each patterned with more than 50 hydrogel posts. The intensity contour plot of fluorescence over the hydrogel arrays shows low background and good uniformity of hybridization.

References

- (1) Koch, W. H. *Nat. Rev. Drug Discov.* **2004**, *3*, 749–761.
- (2) Terstappen, G. C.; Schlüpen, C.; Raggiacchi, R.; Gaviraghi, G. *Nat. Rev. Drug Discov.* **2007**, *6*, 891–903.
- (3) Schmitz, K.; Haggarty, S. J.; McPherson, O. M.; Clardy, J.; Koehler, A. N. *J. Am. Chem. Soc.* **2007**, *129*, 11346–11367.
- (4) Ramsay, G. *Nat. Biotechnol.* **1998**, *16*, 40–44.
- (5) Hughes, T. R.; et al. *Nat. Biotechnol.* **2001**, *19*, 342–347.
- (6) Majd, S.; Mayer, M. *Angew. Chem., Int. Ed.* **2005**, *44*, 6697–6700.
- (7) MacBeath, G.; Schreiber, S. L. *Science* **2000**, *289*, 1760–1763.
- (8) Su, J.; Bringer, M. R.; Ismagilov, R. F.; Mrksich, M. *J. Am. Chem. Soc.* **2005**, *127*, 7280–7281.
- (9) Love, J. C.; Wolfe, D. B.; Jacobs, H. O.; Whitesides, G. M. *Langmuir* **2001**, *17*, 6005–6012.
- (10) Dendukuri, D.; Pregibon, D. C.; Collins, J.; Hatton, T. A.; Doyle, P. S. *Nat. Mater.* **2006**, *5*, 365–369.
- (11) Pregibon, D. C.; Toner, M.; Doyle, P. S. *Science* **2007**, *315*, 1393–1396.
- (12) Peppas, N. A.; Hilt, J. Z.; Khadem Hosseini, A.; Langer, R. *Adv. Mater.* **2006**, *18*, 1345–1360.
- (13) Revzin, A.; Russell, R. J.; Yadavalli, V. K.; Koh, W. G.; Deister, C.; Hile, D. D.; Mellott, M. B.; Pishko, M. V. *Langmuir* **2001**, *17*, 5440–5447.
- (14) Zhan, W.; Seong, G. H.; Crooks, R. M. *Anal. Chem.* **2002**, *74*, 4647–4652.
- (15) Koh, W. G.; Itle, L. J.; Pishko, M. V. *Anal. Chem.* **2003**, *75*, 5783–5789.

Artificial Polymerases and Molecular Chaperones

Akira Harada

Department of Macromolecular Science, Graduate School of Science, Osaka University,
Toyonaka, Osaka 560-0043, Japan
E-mail: harada@chem.sci.osaka-u.ac.jp

Abstract: Cyclodextrins were found to initiate polymerization of lactones only by mixing cyclodextrins and lactones without solvents and co-catalysts. The product is a polyester-tethered cyclodextrin.

1 INTRODUCTION

In recent years, much attention has been focused on the development of renewable polymers from the view point of environmental protection and efficient utilization of natural resources. We are focusing our attention on renewable and biodegradable polymers like carbohydrates (polysaccharides) and polyesters. We chose cyclodextrins (CDs) as a catalyst and a cyclic component of renewable polymers.

Once, CDs attracted much attention of chemists as enzyme models, because of their unique inclusion properties and selective reactivities. However, the reactions of esters promoted by CDs have been limited to the hydrolysis of activated esters, like nitrophenyl esters. Although some acceleration and selectivities of ester hydrolysis by CDs have been reported, excess amount of CDs are required for these reactions. Accordingly, utilization of CDs as synthetic reagents has been limited. Now we found that CDs initiate ring opening polymerization of lactones in bulk without any solvents to give polyester-tethered CD.

Formation of Inclusion Complexes of CDs with Polyesters

Previously, we found that CDs formed inclusion complexes with some polyesters such as poly- ϵ -caprolactone (poly(ϵ -CL))^[1-2], poly(alkylene adipates) to give *pseudo*-polyrotaxanes.^[3] (Figure 1) Later, other researchers reported that some other polyesters are included in CDs.^[4]

While we were preparing inclusion complexes of poly(ϵ -CL) with α -CD, we found

that the polymer was easily hydrolyzed to give oligomers and monomers under mild conditions, although the polymer was not easily hydrolyzed under the same conditions.

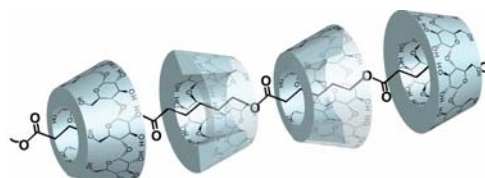
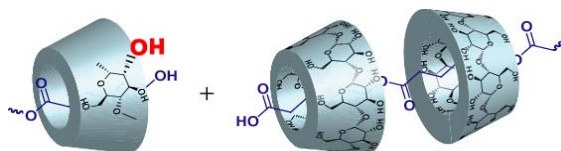


Figure 1. Inclusion complex of a polyester with α -CD.

Hydrolysis of Polyesters by Various Carbohydrates

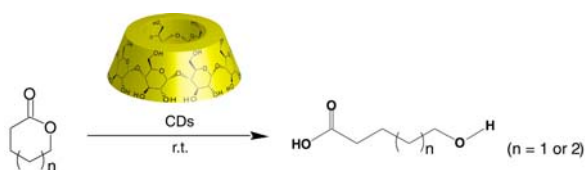
The GPC charts of the polyester after they were treated with various carbohydrates show that methyl glucoside, dextrin, dextran, and pululan did not cause any effects on the hydrolysis of the polyester. In contrast, the polyester has been easily hydrolyzed to its oligomers and monomer in CD under the same mild conditions.



Interactions of CDs with Lactones

We found that CDs selectively form inclusion complexes with some lactones, starting

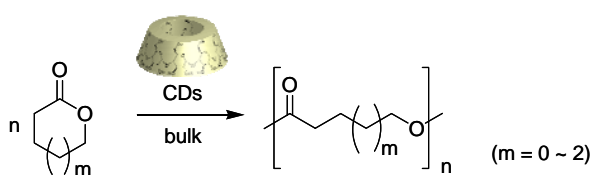
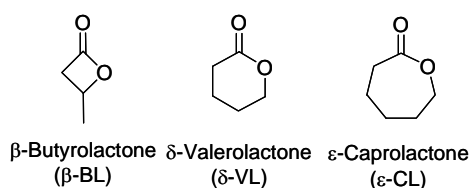
materials of the polyesters. In addition, we found that the hydrolysis of some lactones is promoted or suppressed according to the sizes of CDs.^[5]



Polymerization of Lactones by CDs

Polyesters are easily hydrolyzed by CDs in water. Lactones are also hydrolyzed by CDs in water. We thought that if lactones are heated with CDs in bulk without water, they might form polymers, because hydrolysis does not take place. We use α -, β -, γ -CD as catalysts and butyrolactone (β -BL), valerolactone (δ -VL) and caprolactone (ϵ -CL) as monomers.

Monomers



Experimental Procedure

First, CDs are placed in a Schlenk tube and dried CD at 75 C in high vacuum. Lactone is added onto the CD without any solvents. The mixture was heated at 100 C under an Ar atmosphere. The mixture became viscous and solidified. The reaction product was dissolved in dimethylformamide (DMF) and the solution was poured into THF to remove unreacted CD. The

polymer was obtained from the THF solution.(Figure 2)

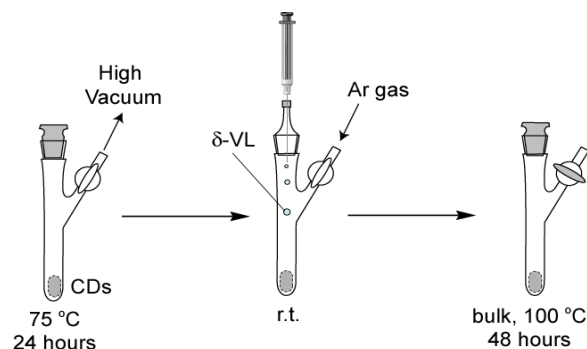


Figure 2. Polymerization of lactones with CD

Formation of Polymers

Poly(δ -VL) was obtained in high yields, almost quantitatively after 48 hours, although VL did not give any polymers without CD under the same conditions. γ -CD also gave a polymer, but in a lower yield. In contrast, α -CD did not give any polymers under the same conditions. These results suggest that polymerization took place by way of inclusion of lactone in a CD cavity.^[6-7](Figure 3)

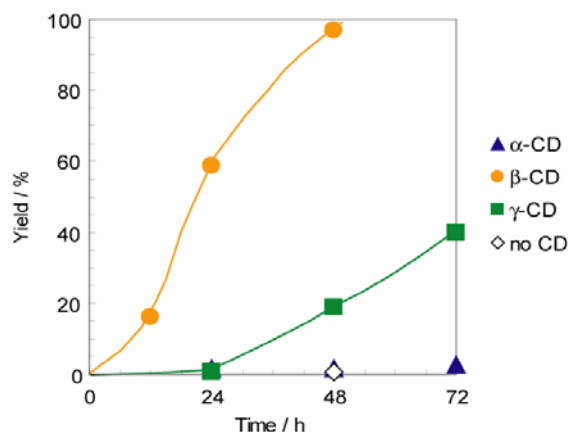


Figure 3. Polymerization of δ -VL with CDs.

Similar results were observed in the case of CL and CDs, but with lower yields than δ -VL/ The lower yields are due to the differences in reactivity of these lactones. (Figure 4)

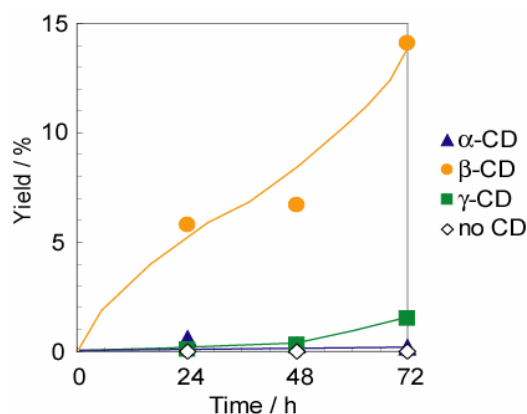


Figure 4. Polymerization of ϵ -CL with CDs.

In contrast, when butyrolactone, a smaller lactone, was used, the order of the polymer yields with CDs is α -CD, β -CD and γ -CD. A smaller lactone gave higher yields with a smaller CD (α -CD), and a larger lactone gave higher yields with a larger CD (β and γ -CD). These results indicate that the reactions took place by way of inclusion of lactones in CD cavities. (Figure 5)

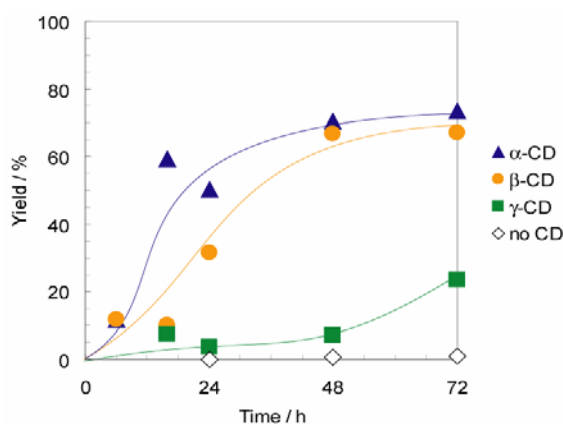


Figure 5. Polymerization of β -BL with CDs.

Initiators

When intact β -CD was used as an initiator, there is some induction period to start polymerization. In contrast, when inclusion complexes of δ -VL with β -CD was used as an initiator for the polymerization of VL, the polymerization reactions started smoothly and efficiently. When inclusion complexes of β -CD with adamantane, which is included in the β -CD cavity strongly, was used as an initiator, polymerization of lactones did not take place.

These results indicate that the formation of inclusion complexes is the rate determining step for the polymerization reactions. (Figure 6)

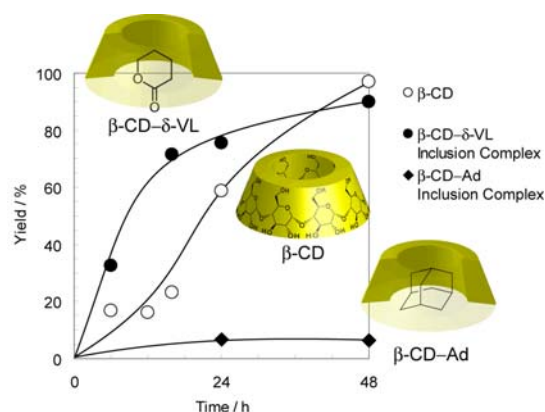


Figure 6. Polymerization of δ -VL with β -CD complexes

Structures of the polymers

There are some possibilities for the structures of the polymers formed. If inclusion polymerization takes place, *pseudo*-polyrotaxanes would be formed. If hydroxyl group acts as a nucleophile for lactone, polyesters covalently attached to CD would be formed.

The MALDI-TOF mass spectrum of poly(VL) obtained from the mixture of β -CD and δ -VL shows that each signal appears at interval of 100 amu, which corresponds to a δ -VL monomer unit from the signal of β -CD and that there are no other signals at lower molecular weight than β -CD. This indicates that each polymer has a single β -CD at the end of the polymer chain. (Figure 7)

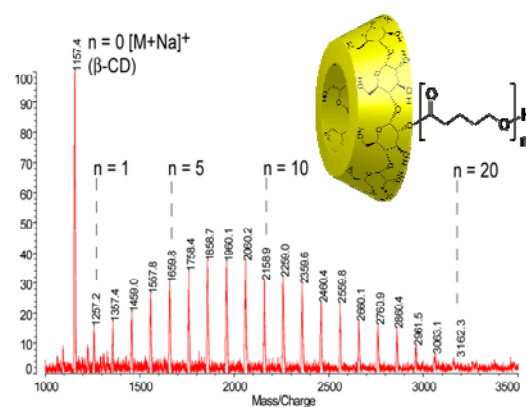


Figure 7. TOF mass spectrum of the product.

Other polymers, poly(ϵ -CL) and poly(β -BL), gave similar results.

CD Derivatives as Initiators

Dimethyl β -CD and triacetyl- β -CD showed no reactivity for the polymerization of these lactones. These results indicate that the inclusion of lactones in the CD cavity and secondary hydroxyl group plays an important role in initiating the polymerization.(Figure 8)

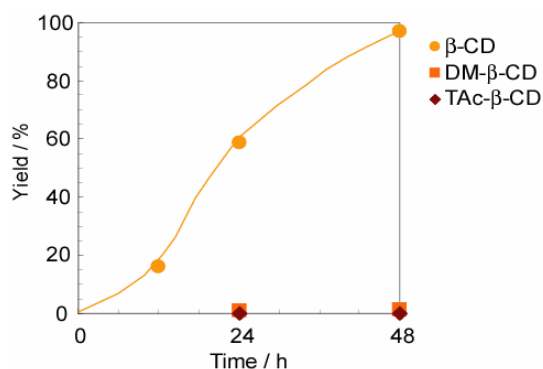
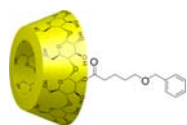


Figure 8. Polymerization of δ -VL with CD derivatives.

We have prepared a model compound, mono-2-(6-benzoxypentanoyl)- β -CD, according to the method reported previously.



The model compound was found to initiate polymerization of lactones to give polyesters, in spite of the fact that there is no hydroxyl group at the end of the polymer chain.

TOF-Mass spectrum of the product showed that the ester groups were inserted between CD and the polymer chain. This result indicates that the polymerization proceeds by way of inclusion and insertion of esters between CD and the polymer chain.

Mechanism

Continuous inclusion and insertion of the cyclic esters yield linear polyesters with CD. The possible mechanism of the formation of the polyester-tethered CD was shown in Figure 000.

However, path B is unlikely, because the model compound, (benzoxypentanoyl β -CD), was found to initiate polymerization of δ -VL even when there is no hydroxyl groups at the end of the polymer chain. (Figure 9)

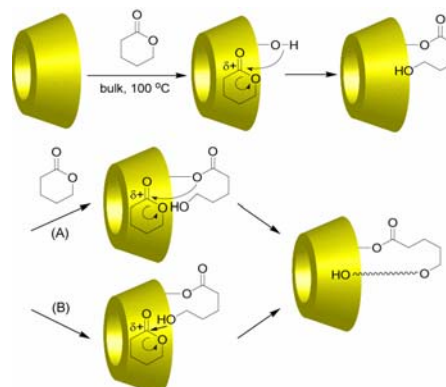


Figure 9. Proposed mechanism of the polymerization of lactone by CD.

Activation of lactones in CD

FT-IR spectra of CL, a mixture of CD and CL, and the inclusion complex showed that the IR band due to the ester carbonyl group shifted to lower frequency, when the lactone was included in a CD cavity. The spectra also showed that lactones are included in CD rings only by mixing CD and lactone. These results indicate that lactones are activated in a CD cavity by forming a hydrogen-bond between the carbonyl and the hydroxyl group of CD.(Figure 10)

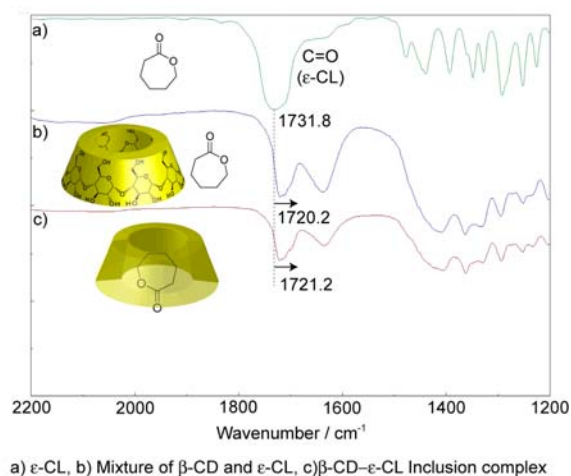


Figure 10. IR spectra of δ -VL with β -CD.

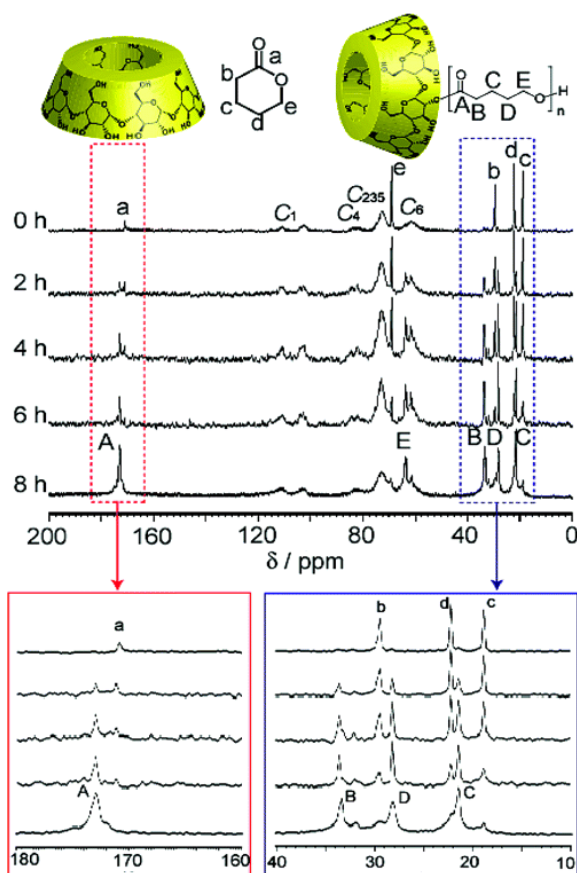


Figure 11. Time dependence of ^{13}C 1pda/MAS NMR spectra of the mixture of β -CD and δ -VL at $100\text{ }^{\circ}\text{C}$.

Figure 11 shows the 1pda/MAS NMR spectra of the mixture of β -CD and δ -VL recorded every 2 h at $100\text{ }^{\circ}\text{C}$. The 1pda/MAS NMR spectra support the polymerization behavior of δ -VL at $100\text{ }^{\circ}\text{C}$ in solid state because the 1pda/MAS NMR method, compared to the CP/MAS NMR method, enhances the peak intensity for mobile regions in the sample. Although the signals of poly(δ -VL) were not observed in the early stage, the peaks of poly(δ -VL) (A-E) increased with time and the peaks of δ -VL (a-e) decreased with time. Figure 12 shows the time-conversion curve for the polymerization of δ -VL using β -CD. The conversion of poly(δ -VL) increased with time, indicating the propagation of poly(δ -VL) in bulk.

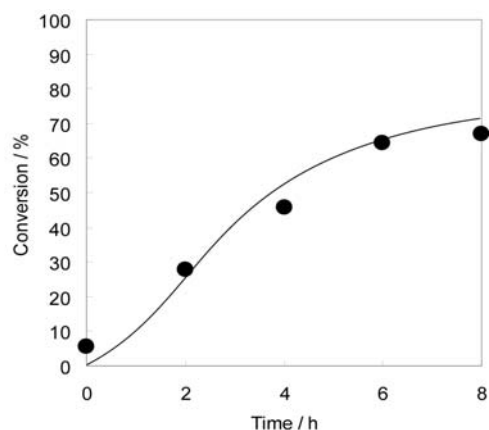


Figure 12. Time-conversion curve of the polymerization of δ -VL by β -CD.

Conclusion

In conclusion, CDs initiate ring opening polymerization of lactones selectively to give polyesters with a CD ring at the end of the polymer chain. Lactones are included in a CD cavity and activated by hydrogen bonding with one of the secondary hydroxyl group of CD.

References

- [1] A. Harada, T. Nishiyama, Y. Kawaguchi, M. Okada, M. Kamachi, *Macromolecules*, **1997**, *30*, 7115-7118.
- [2] A. Harada, Y. Kawaguchi, T. Nishiyama, M. Kamachi, *Macromol. Rapid Commun.*, **1997**, *18*, 535-539.
- [3] Y. Kawaguchi, T. Nishiyama, M. Okada, M. Kamachi, A. Harada, *Macromolecules*, **2000**, *33*, 4472-4477.
- [4] A. Harada, A. Hashizume, Y. Takashima, *Adv. Polym. Sci.*, **2006**, *201*, 1-43.
- [5] Y. Takashima, Y. Kawaguchi, S. Nakagawa, A. Harada, *Chem. Lett.*, **2003**, *32*, 1122-1123.
- [6] Y. Takashima, M. Osaki, A. Harada, *J. Am. Chem. Soc.*, **2004**, *126*, 13588-13589.
- [7] M. Osaki, Y. Takashima, H. Yamaguchi, A. Harada, *Macromolecules*, **2007**, *40*, 3154-3158.
- [8] M. Osaki, Y. Takashima, H. Yamaguchi, A. Harada, *J. Am. Chem. Soc.*, **2007**, *129*, 14452-14457.

Oxide Nanotubes for Fuel Cells and Batteries: Modeling of Porous Hosts

Professor W.H. Smyrl*

* Department of Chemical Engineering and Materials Science, Corrosion Research Center,
University of Minnesota,, Minneapolis, Minnesota 55455, USA
smyrl001@umn.edu

Abstract: Porous electrodes are essential for useful and practical electrochemical cells operated as fuel cells or batteries. High surface area is the focus for fuel cells, but small diffusion distances are more important for intercalation electrodes that are the central element for high energy and high rate batteries. Titanium dioxide nanotubes (TONT) serve as supports for catalysts such as Pt for the oxygen reduction reaction and have been found to offer enhanced durability in fuel cell environments. The TONT arrays also support Li^+ ion intercalation and the small wall thickness of the nanotubes (e.g. 100 nm) enable high rate insertion and release reactions. In order to design nanotube arrays with optimum geometric features, we have begun to analyze the intercalation processes by modeling approaches. The elements of diffusion, electronic and ionic conduction are incorporated into the analysis and that is the focus in the present discussion. Describing the relative importance of the individual elements is done by using the resistance to mass transfer approach. A multiple fin geometry is used to simulate nanotube arrays for the analysis. Results will be discussed for several practical examples.

Key Words: oxide nanotube arrays, intercalation rate, mass transfer resistance

1. INTRODUCTION

Porous electrode materials have a long history of development and use in electrochemical fuel cells and batteries. The interest for catalytic surfaces in fuel cells is to increase the electrochemically active area to yield practical total currents when the local current density is integrated over the area. The enhancement over a planar surface is the ratio of the reticulated area to that of the planar surface. Recent interest in nanostructured materials has enabled the design of new electrodes that are based on novel arrays of nanotubes for example. Titanium dioxide nanotube arrays are prepared in a robust and simple "one-pot" electrochemical anodic process (EAP). Titanium metal in the form of foils, films, sheets, plates, rods, and wires may be anodized in dilute aqueous HF at 20 volts for 20 minutes to yield nanotube arrays that are oriented perpendicular to the substrate surface (Lee et al. 2008). The amorphous titanium dioxide nanotubes (TONT) are not electrochemically active, but when heated at 300°C for 3 hours crystalline anatase is formed. The anatase array will host Li^+ ion intercalation. Of additional interest however, anatase arrays may be sputtered with low loadings of Pt that supports excellent rates of oxygen reduction in aqueous solutions. The Pt/TONT catalytic structure is more durable than Pt on carbon substrates, and is the subject of continuing

research in the laboratories at the University of Minnesota (Kang, et al. 2008, 2008).

Although the potential for intercalation into the high surface area nanotube arrays has been investigated very little, they remain interesting and our focus in the present discussion will be given to modeling and analysis of porous structures for intercalation processes. Nanotubes may be of interest for these applications, but the discussion here is not limited to those structures. Intercalation hosts in porous form are of interest for their short diffusion distance for intercalation in the solid host as well.

The thermodynamics of intercalation electrodes for electrochemical cells in a macroscopic sense is based on phase equilibria and reaction equilibria. In some respects, it is rather simple and can yield empirical correlations between the equilibrium potential and the concentration of guest species. Reversible insertion and release are the hallmarks of intercalation since the host lattice is perturbed but not disrupted by the process. In order to reveal the details of the process however, the microscopic structure and intercalation are studied and interpreted on the basis of models and theories such as the thermodynamics of the lattice gas.

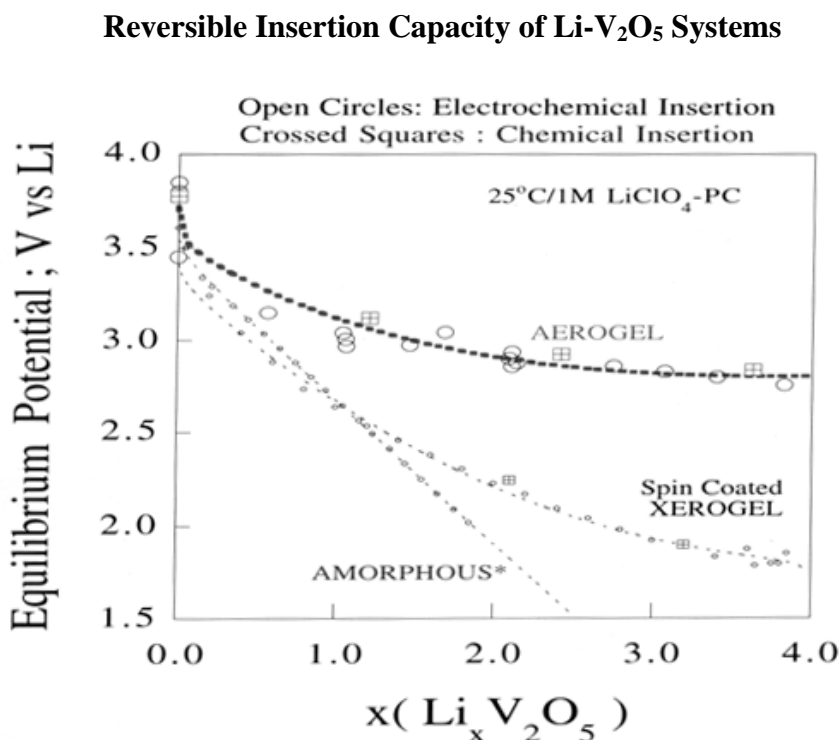
Variations of the equilibrium potential using the lattice gas approximation has been described in two excellent reviews by McKinnon and Haering (1983), and Coleman,

Dahn and McKinnon (1984). “Steps” in the equilibrium potential vs composition can be dealt with adequately with the theory of a two-dimensional lattice gas (Hill, 1962), as well as with multiple site – energy lattice gas models (McKinnon, et al. 1983). Treatments of staging in alkali metal –carbon systems have been discussed by Armand (1980), and by Dahn, et al. (1982). In addition to models of intercalation, thermodynamic quantities such as intercalation capacity, energy density, and specific energy are also of interest as figures of merit when one compares different host materials and different structures of the same material.

Although not the principal focus here, the thermodynamics of intercalation into various forms of vanadium pentoxide illustrate the connection between intercalation and structure in guest-host systems. That is, vanadium pentoxide is a host in several forms: (I) a crystalline solid (Delmas, et al. 1994); (II) an amorphous solid (Nabavi, et al. 1988); (III) an amorphous xerogel (Park, et al. 1994, 1995), and; (IV) a highly porous aerogel (Le, et al. 1995, 1996). The equilibrium potential of the host as a function of lithium ion concentration is shown in 1 for the V_2O_5 materials.

It would be a mistake to associate the surface aspects of

the oxide with the thermodynamics. The mistake is easily dismissed by referring to Figure 1. In particular, the enhanced thermodynamic properties of vanadium pentoxide (xerogel) over amorphous forms is not due to surface area because both are compact powders or films, and differ only in chemical composition and local structure. The xerogel material has retained 0.5 moles of water per mole of vanadium pentoxide and the water is chemically bound and retained during insertion and release (see quartz crystal microbalance results by Park, et al. 1994, 1995). The equilibrium potential – composition curve in Figure 1 was established by two independent techniques. First, insertion of lithium ions was controlled by coulombic titration, and release of lithium ions was controlled by the same process, and the two processes gave exactly the same curve. In addition, chemical intercalation by reaction of the oxide host with n-butyl lithium to a controlled composition gave exactly the same curve as that found by coulombic titration. This unequivocally establishes the importance of chemical composition and structure to be of paramount importance in these oxide materials. If one now looks at the difference between the xerogel and aerogel materials made in our laboratories, the thermodynamics are again influenced by chemical



Aerogel has the highest potential for reversible insertion capacity up to 4 Li per V_2O_5

Figure 1 Capacity of V_2O_5 sol-gel films.

composition and local structure. The curve for the aerogel was established both by coulombic titration and by chemical intercalation via reaction with n-butyl lithium. It was reported in the first-ever publications on vanadium pentoxide aerogel (Le, et al. 1995, 1996) that the water content was nearly the same as the xerogel (chemical analysis by Karl Fisher titration). The increased carbon – hydrogen content was due to retained solvent (acetone) material from the aerogel processing procedure. That is, acetone was used to replace pore water in the bicontinuous hydrogel to form an intermediate organogel, and then supercritical CO₂ replaced the acetone. Some acetone is retained in the structure and modifies the vanadium pentoxide. Other organic solvents (dioxane, acetonitrile, and butyl formate) were used to form organogels. When n-butyl lithium was used to chemically insert lithium ions in the liquid organogel intermediate step, and subsequently dried to form a xerogel (organically modified), one obtains exactly the same curve as for the acetone modified aerogel. This unequivocally eliminates the surface area and “surface sites” as being responsible for the difference between the aerogel and the ordinary xerogel (not modified organically). A recent review of vanadium oxide materials was reported from the Whittingham group (Chernova, et al. 2009).

2. INTERCALATION RATE ANALYSIS AND MODELING

In addition to the thermodynamic aspects of host-guest interactions, the rate and processes of intercalation are of importance in practical applications. The fundamental rate of insertion (release) may be divided into three general regions of behavior. In the first, at high rates of insertion or high frequencies for sinusoidal control, the insertion (release) is restricted to the surface and diffusion effects in the solid host (or the electrolyte) are of minor importance. In the kinetic region (Region I) of behavior, the surface reaction may be treated as a electrode kinetic process. At lower rates of insertion (release), or lower frequencies, diffusion in the solid host becomes dominant (Region II) and interfacial kinetics are of less importance. Diffusion in an adjacent electrolyte phase is usually much faster (especially for liquid electrolytes) and therefore does not control behavior, except for a few circumstances discussed below.

A third region of behavior (Region III) is that at much lower rates of insertion (release), or lower frequencies, where insertion (release) is not limited by either surface kinetics or by diffusion. In this third region, the concentration of the guest species is uniform in the solid and insertion/release changes the total concentration in the host. The third region is observed when the solid host is thin and the guest diffusion coefficient is large. General discussion of the three regions of behavior was clearly introduced by Ho, et al. (1980), and

extended to intercalation into conducting polymers by Hunter, et al. (1987). See also further discussion in Smyrl, et al. (1993).

The behavior of intercalation in porous guest/host systems has been discussed in an excellent series of papers by Atlung and coworkers (1979, 1980, 1982, 1985, 1989). In their analysis of insertion rate behavior, several characteristic times are found. The first characteristic time is the stoichiometric time, that is the time to complete the insertion of the guest species into a given amount of the host at the rate imposed experimentally, but with no imposed limits to the process. The second time is the diffusion time to penetrate the solid host of a given geometry (thin film, cylinder, or spherical shape). One may imagine other characteristic times that would be important when other controlling factors are considered, such as a characteristic conductivity time if ohmic limits are important either in the solid host or in the adjacent electrolyte phase.

For the purposes of the present paper, we will discuss the mass transfer limitations of intercalation into solid “fins”. The fins are rectangular in shape and perpendicular to the plane of the substrate. Therefore, for analysis of the intercalation it is relevant to compare insertion into the fins with insertion into a thin film on the same substrate. If the projected area of the thin film is A_{tf} , then the fins on the same substrate have the same projected area, i.e. $A_{fins} = A_{tf}$.

3. CHARACTERISTIC TIMES FOR INTERCALATION INTO THIN FILMS

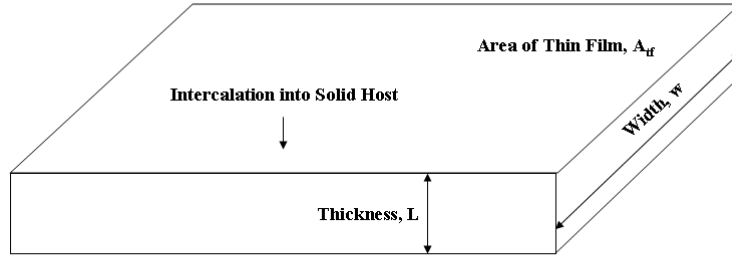
We begin the analysis of high rates of intercalation by considering compact thin films, as shown in Figure 2. The thickness of the film is L , the width is w , and the area of the thin film is A_f . The characteristic stoichiometric time for the thin film is (similar to Athung, et al., 1979-1989),

$$\tau_1 = \frac{nFLc^*}{i_o}$$

where n = charge on guest cation, F = Faraday constant, L = thickness, c^* = moles guest/cm³ host, i_o = amps/cm². This equation can be transformed to a more useful form by introducing the specific current (amps/gm host), i^* , and the molecular weight of the host, MW_{host} , and the mole ratio (moles guest/mole host), x

$$\tau_1 = \frac{nFLx}{i^*(MW_{host})} \quad [1]$$

Now, if $x = 1$, τ_1 is the time to intercalate 1 mole of guest into 1 mole of host, and the equation enables one to normalize the time by using the loading of the host (gms/cm²).



- **Mass transfer resistance for intercalation, R_{tf}**

$$R_{tf} = L/(nFD_{sol}A_{tf})$$

Figure 2 Intercalation into Thin Films.

It is noted in passing that c^* is either the maximum concentration of guest that may be intercalated or a fixed concentration that is to be achieved for a specific purpose.

A second characteristic time is the time for diffusion into the thin film host,

$$\tau_2 = \frac{L^2}{D_{solid}} \quad [2]$$

where D_{solid} is the diffusion coefficient of guest species (cm^2/sec), where the concentration of the guest is held constant at the outer surface with the electrolyte. The ratio of the two times helps to identify different regions of behavior. For example, at a fixed, high current density,

$$\frac{\tau_2}{\tau_1} = \frac{i_o L}{nFD_{sol}c^*} \gg 1 \quad [3]$$

the local concentration of guest in the (semi-infinite) solid may be shown to be

$$c_{solid} = \left(\frac{i_o}{nF} \sqrt{\frac{4t}{\pi D_{sol}}} \right) \text{erfc} \left(\frac{z}{\sqrt{4D_{sol}t}} \right) \quad [4]$$

Here, z is the normal distance from the surface into the solid, t is the time after the constant current density is imposed, and the complementary error function is a tabulated function in standard mathematical handbooks (Abramowitz and Stegun, 1964). Equation [4] is valid up to the time $t = t^*$, that is where the concentration at the surface c_{solid} ($z = 0$) equals c^* , and

$$c^* = \frac{i_o}{nF} \sqrt{\frac{4t^*}{\pi D_{solid}}} \quad [5]$$

Further, one can determine the ratio, U ,

$$U = \frac{\text{amount intercalated}}{\text{maximum amount that could be intercalated}} \\ = \frac{i_o t^*}{nF c^* L} = \frac{\pi}{4} \left(\frac{D_{solid} c^* nF}{L i_o} \right) = \frac{\pi}{4} \left(\frac{\tau_1}{\tau_2} \right) \quad [6]$$

In the limit, U is small given the condition imposed by equation [3], and it is concluded that the surface may be saturated at c^* quickly at high current densities. Before saturation, the surface concentration at short times is

$$c_{solid}^o = \frac{i_o}{nF} \sqrt{\frac{4t}{\pi D_{sol}}} \quad [7]$$

Equation [7] has considerable importance for characterization studies of thin films, and we will return to it below.

At small current densities at thin film hosts,

$$\frac{\tau_2}{\tau_1} < 1$$

the concentration distribution of the guest species will be given by equation [4], and the surface concentration will be given by equation [7] again. At long times, the distribution of the guest species will be given by

$$c_{sol} = \frac{i_o t}{L(nF)} + \frac{i_o L}{nF(D_{sol})} \left(\frac{3(L-z)^2 - L^2}{6L^2} + \dots \right) \quad [8]$$

where higher order terms are neglected because they are small. When $t = t^*$, the concentration at the surface will be $c_{sol} = c^*$ and

$$c^* = \frac{i_o t^*}{L(nf)} + \frac{i_o L}{3nF(D_{sol})} + \dots \quad [9]$$

Now,

$$U = \frac{i_o t^*}{nFc^* L} = 1 - \frac{i_o L}{3nFD_{sol}c^*} \quad [10]$$

$$= 1 - \frac{\tau_2}{3\tau_1} \quad [11]$$

and one may approach full utilization of the host species.

Returning to the short time behavior, it should be noted that the galvanostatic intermittent titration technique (GITT, see Weppner and Huggins, 1977, 1978) utilizes short, constant current pulses to change the composition in a host, followed by long relaxation times back to the new equilibrium state. During the short pulse, the composition-equilibrium relationship is perturbed by the imposed pulse, and one may approximate perturbation as a linear disturbance from equilibrium. Equation [7] can be used to show that the

potential will change with the square root of time, from which one may determine the diffusion coefficient of the guest species. Further, the composition dependence of the latter property may also be determined. GITT is a very useful technique with which to determine both the equilibrium composition relationship (thermodynamic) and the diffusivity (mass transfer) in a single set of measurements.

4. CHARACTERISTIC TIMES FOR INTERCALATION AT HIGH RATES INTO POROUS HOSTS

From Equation [2] it is clear that there are two paths to increase insertion rates into host materials, i.e., either increase the diffusion coefficient (normally not feasible) or reduce the diffusion distance L . In our previous work, we have chosen to pursue the latter path by generating high surface area aerogel forms of the host (vanadium pentoxide). The aerogel structure is formed from a bicontinuous precursor in which all of the solid is interconnected and all the pores are interconnected. One may start at any point in either phase and move to any other point in the same phase without crossing a phase boundary. One obtains a high surface area solid (aerogel) in which the solid "walls" have dimensions on the order of 10 - 20 nm. For diffusion distances given by thin "walls", the diffusion time is of the order of 1 second for a diffusion coefficient of 10^{-12} cm²/sec. This facilitates high rates of intercalation.

To make the discussion more quantitative, we refer to the schematic of a fin-slit geometry for the host in Figure 3. The height of an individual "fin" is L , its length is w , and its thickness is $2b'$. The separation between fins (i.e., the slit) is

$$R_{fin\ tip} = L/(nFD_{sol}A_{FIN})$$

$$R_{fin\ total}/R_{tf} = (A_{tf}/A_{fin\ total}) > 1$$

or $\rightarrow 1$ if $A_{tf} = A_{fin\ total}$

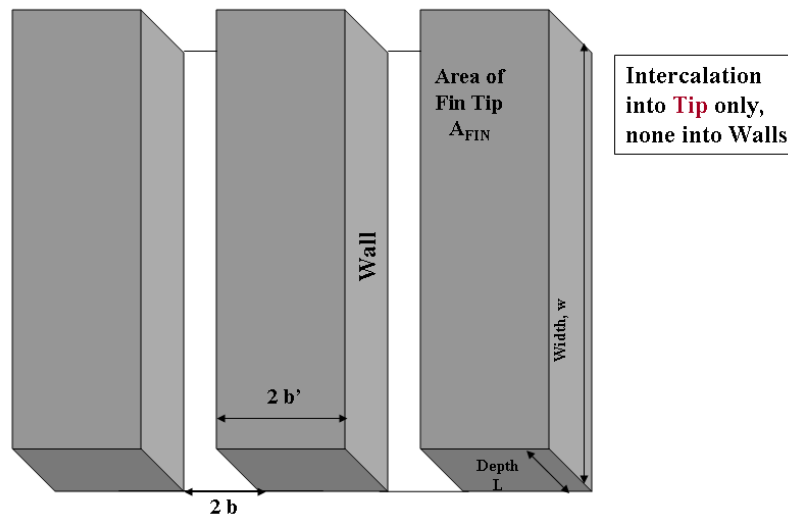


Figure 3 Intercalation into "Finned Surface"

2b. The total area of the fin, $A_{fin, total}$, is the sum of the tip area, A_{FIN} , and the wall area, A_w . The area of one end of an individual fin (i.e., $L \times 2b'$) is normally small compared to A_w and to A_{FIN} . Here, we assume that intercalation may occur into the fin but not into the bottom of the slit which is occupied by a current collector. The distance, z , is now taken to be zero at the top of the fin, and increases downward. The distance y , is taken to be orthogonal to z , and $y = 0$ at one edge of a fin. We treat one element of the finned electrode surface which includes one fin and one slit. The porosity of the electrode (i.e., void volume per unit total volume of the electrode) will be,

$$\varepsilon = b/(b + b') \quad [12]$$

Four new times are now relevant to describe the behavior. The first characteristic time is the stoichiometric insertion time,

$$\bar{\tau}_1 = \frac{b' c^* (nF)}{j_o} \quad [13]$$

Here, j_o is the average local current density, which is related to the current density, i_o , normalized to the external projected surface area by the relationship

$$j_o (2wL) = i_o (2b + 2b')w \quad [14]$$

Here, the ends of the fins and slits are neglected. The second characteristic time is

$$\bar{\tau}_2 = \frac{(b')^2}{D_{sol}} \quad [15]$$

which is the time for diffusion of the guest into the fin from the sides. The time for the guest species to diffuse into the electrolyte is

$$\bar{\tau}_3 = \frac{L^2}{D} \quad [16]$$

The time to diffuse across the slit (pore) is

$$\bar{\tau}_4 = \frac{b^2}{D} \quad [17]$$

$\bar{\tau}_3$ and $\bar{\tau}_4$ are expected to be much smaller than the other two, except as noted below. This means that the pores

(slits) are "well mixed", and the concentration of the bulk electrolyte is uniform everywhere in the pore as well. Ratios of these times dominate the behavior. Let $\bar{\tau}_3 \ll \bar{\tau}_2$ or $\bar{\tau}_1$, so that pores are well mixed in the z direction (also y direction since $\bar{\tau}_4$ is always smaller than $\bar{\tau}_1$). The behavior will be similar to that for the thin film, but modified for the new area, i.e., results are identical for the high current density limit where

$$\frac{\bar{\tau}_2}{\bar{\tau}_1} > 1 \gg \frac{\bar{\tau}_3}{\bar{\tau}_1} \quad [18]$$

In the low current density limit, the results are similar again when

$$1 > \frac{\bar{\tau}_2}{\bar{\tau}_1} \gg \frac{\bar{\tau}_3}{\bar{\tau}_1} \quad [19]$$

If $\bar{\tau}_3$ is larger, there can be concentration depletion within the pore (z -direction), and there are two general limits. First, there is a diffusion zone where the surface concentration of the guest equals c^* everywhere along the fin surface. In the other limit, the reaction zone, intercalation is possible, but depletion within the electrolyte prevents full utilization of the intercalation capacity of the fin near the bottom of the pore (slit).

5. MASS TRANSFER RESISTANCE FOR INTERCALATION

One may analyze the enhancement of insertion rate by comparing the mass transfer resistance of thin films compared to the finned surface. If one uses a concentration driving force (in the solid), the mass transfer resistance of a thin film is

$$\bar{R}_{TF} = \frac{L}{A_{tf} nF D_{sol}} \quad [20]$$

If the thin film is broken into an array of slits and fins, and if intercalation is only allowed into the tips of the fins (not interesting for practical reasons, but useful for discussion here), Case I, the mass transfer resistance for a single fin will be

$$\bar{R}_{FIN, TIP} = \frac{L}{nF A_{FIN, TIP} D_{sol}} \quad [21]$$

The resistance of the slit is infinite since no intercalation occurs at the bottom of a slit. The fins act in parallel, so that for the finned surface,

$$\begin{aligned} \frac{1}{\bar{R}_{TOTAL,FIN}} &= \sum \frac{1}{\bar{R}_{FIN,TIP}} \\ &= \frac{1}{\sum_{FINS} \left(\frac{L}{nFD_{sol} A_{FIN,TIP}} \right)} = \frac{nFD_{sol}}{L} \sum_{FINS} A_{FIN,TIP} \end{aligned}$$

and

$$\bar{R}_{TOTAL,FIN} = \frac{L}{nFD_{sol} A_{FIN,TOTAL}} \quad [22]$$

where $A_{FIN,TOTAL}$ is the total fin tip area. Now, the total resistance of the fin tips compared to the thin film resistance is

$$\begin{aligned} \frac{\bar{R}_{TOTAL,FIN}}{\bar{R}_{THIN,FILM}} &= \frac{\left(\frac{L}{nFD_{sol} A_{FIN,TOTAL}} \right)}{\left(\frac{L}{nFD_{sol} A_{FIN,TOTAL}} \right)} \\ &= \frac{A_{THIN,FILM}}{A_{FIN,TOTAL}} \end{aligned}$$

This ratio is greater than 1 since all the current is forced through a smaller total area (fin tips only). The ratio approaches 1 when the total fin area equals the area of the thin film.

Now consider the more interesting case of uniform intercalation in fins (walls plus tips), Case II. For one fin

$$R_{FIN}^* = \frac{b'}{nF \bar{A}_{FIN} D_{solid}} \quad [23]$$

where $2b'$ is fin thickness and

$$\bar{A}_{FIN} = A_{FIN,TIP} + A_{FIN,WALL}$$

Now,

$$\begin{aligned} \frac{1}{R_{FIN,TOTAL}^*} &= \frac{1}{\left(\sum_{FINS} \left(\frac{b'}{nF \bar{A}_{FIN} D_{solid}} \right) \right)} \\ &= \frac{(nFD_{solid} \bar{A}_{FIN,TOTAL})}{b'} \quad [24] \end{aligned}$$

where \bar{A}_{FIN} is identical for all fins. The total resistance,

$$R_{FIN,TOTAL}^* = \frac{b'}{nFD_{sol} \bar{A}_{FIN,TOTAL}}$$

may now be compared to the thin film

$$\frac{R_{FIN,TOTAL}^*}{\bar{R}_{THIN,FILM}} = \left(\frac{A_{THIN,FILM}}{\bar{A}_{FIN,TOTAL}} \right) \left(\frac{b'}{L} \right) \quad [25]$$

Now since both the first and second terms in [25] are less than 1,

$$\frac{R_{FIN,TOTAL}^*}{\bar{R}_{THIN,FILM}} \ll 1 \quad [26]$$

The total resistance to mass transfer of the "finned surface" would be much smaller than the thin film resistance because of two effects:

- (1) shorter diffusion distance (i.e., $b' \ll L$)
- (2) $A_{THIN,FILM} < \bar{A}_{TOTAL,FIN}$

Both effects are geometric and are independent of the diffusivity of the guest in the solid, D_{sol} .

6. DISCUSSION OF UTILIZATION OF INTERCALATION CAPACITY IN THIN FILMS AND POROUS HOSTS

Having developed the framework for analysis of intercalation into host materials in either thin film or in porous forms, one can proceed to discuss the utilization of capacity. The utilization, U , is defined as the fraction of the total capacity that has been filled under different conditions. In

Figure 4, U is plotted as a function of the ratio of the diffusion time to the stoichiometric time for a thin film in two limits. For small values of the ratio, U approaches unity, and at large values of the ratio, U approaches zero. There are two general cases. In the first case, the insertion rate is low (low discharge rate). The second case is for high discharge rates. In the limit of low discharge rates,

$$U = 1 - \frac{\tau_{diff(tf)}}{3\tau_{stoi(tf)}} \quad [27]$$

This function approaches unity when the ratio of the two characteristic times is small. Two specific examples are given as approximations as well. At high discharge (insertion) rates where the utilization approaches zero,

$$U = \frac{\pi\tau_{stoi(tf)}}{4\tau_{diff(tf)}} \quad [28]$$

The same utilization curve is obtained for porous host materials (fins) when the characteristic times for diffusion and stoichiometric discharge for the fins are used instead of the times for compact thin film hosts. It should be noted that equation [28] is identical to equation [6].

Another important case is depicted in Figure 5, where diffusion and electronic conductivity effects on utilization of porous hosts (fins) are compared. In the figure on the left, U is plotted as a function of the ratio of solid state diffusion time to stoichiometric discharge time, and on the right U is plotted as a function of the ration of conduction time to stoichiometric discharge time. In each figure, there are curves that trace the additional parameter of diffusion time divided by conduction time. At the bottom of Figure 5, a summary of important trends is included.

The utilization is a function of the ratio of time for diffusion (fin) to the stoichiometric time (fin), along with the influence of diffusion in the electrolyte as a parameter. The latter parameter is used in a ratio of diffusion time in the (porous) solid host to the diffusion time in the electrolyte-filled pore. The utilization approaches unity for short diffusion times in the solid, combined with short diffusion times in the electrolyte.

7. SUMMARY AND FINAL DISCUSSION OF THE RATE CAPABILITIES OF POROUS HOST MATERIALS

Characterization of porous intercalation electrodes in terms of the diffusion times and the stoichiometric discharge time incorporates the generality of the physical process as

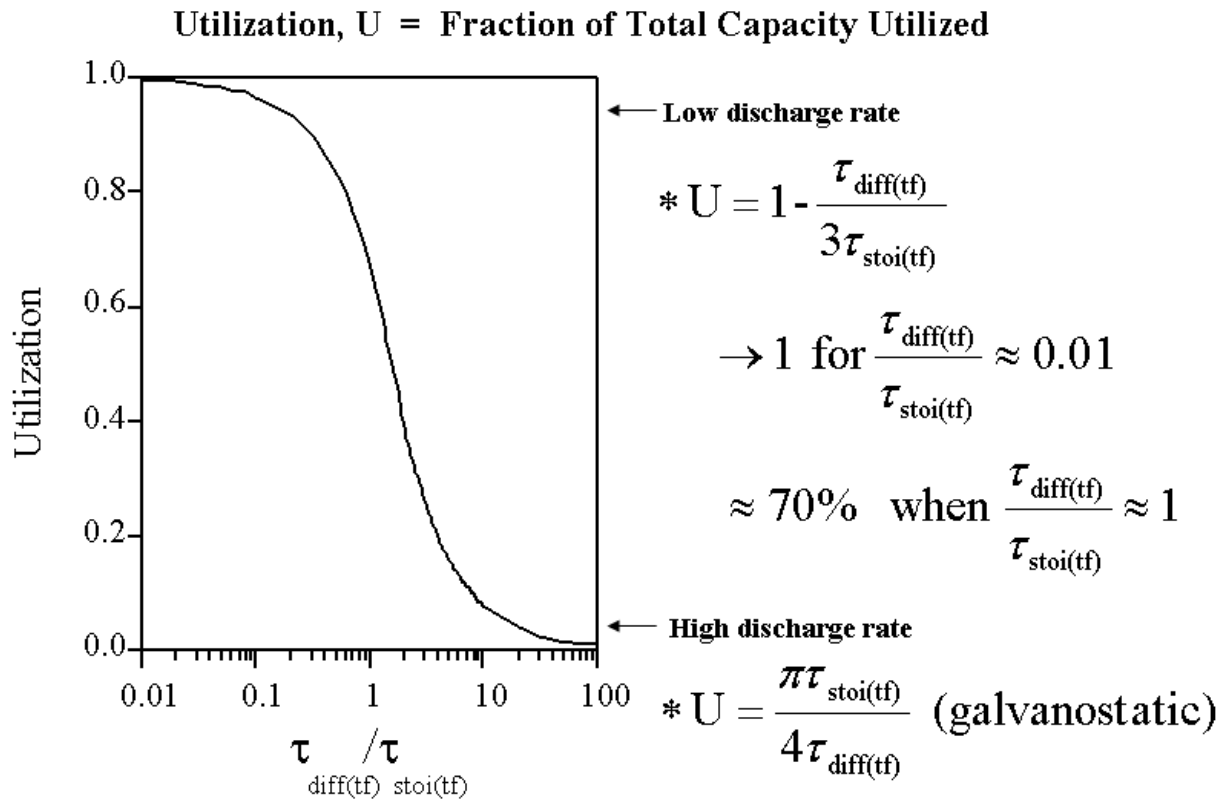


Figure 4 Intercalation into Thin Films.

Diffusion in Solid and in Electrolyte-filled Pores

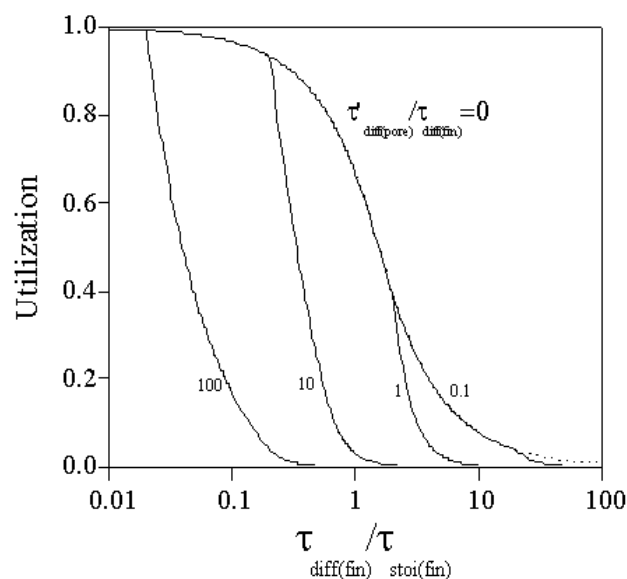


Figure 5 Intercalation into Porous Hosts.

well as the simplicity of the theoretical analysis in terms of the mass transfer resistance. The utilization equations can also be expressed as a function of the rate capability, the discharge rate, and the thickness of the electrode. For example, if the amount of solid host material in a “fin” is small relative to the amount of electrolyte in the “slit”, the discharge rate and utilization may be increased as the thickness of the fin is increased. However, as the relative amount of electrolyte becomes small, the utilization will decrease as the fin thickness is increased. The latter behavior is caused by depletion of the intercalate guest species in the electrolyte phase. That is, there is not enough guest species to support high rates of insertion because diffusion in the slit is limiting. Some aspects of porous intercalation host behavior have been observed previously by Atlung, et al. (1979-1982). A full discussion of this aspect is beyond the scope of the present treatment. A more complete analysis and description is available in the PhD thesis of Dr. Dinh Ba Le (University of Minnesota, 2004). A previous analysis with some limitations is available in a publication of West, et al. (1992).

ACKNOWLEDGEMENTS

It is a pleasure to recognize the collaboration on this work with Dr. Dinh Ba Le who is now at the 3M laboratories, Dr. Marco Georgetti and Dr. Mario Berrettoni of the University of Bologna, Dr. Elisa Frabetti, and Professor B.B. Owens who is now retired. Portions of this work were supported by the Office of Naval Research, by the U. S.

Department of Energy (Basic Energy Sciences), and by the Army Research Office.

REFERENCES

- [1] Abramowitz, M., and I.A. Stegun, Editors, *Handbook of Mathematical Functions*, Applied Mathematical Series 55, National Bureau of Standards, USGPO, Washington, D.C., 1964.
- [2] Atlung, S., K. West, and T. Jacobsen, *J. Electrochem. Soc.* **126**, 1311(1979)
- [3] Atlung, S., K. West, and T. Jacobsen, in *Materials for Advanced Batteries* (Eds. D.W. Murphy, J. Broadhead, and B.C.H. Steele), NATO Conference Series, Vol VI-2, Plenum Press, New York, 1980
- [4] Atlung, S. in *Solid State Batteries*, NATO ASI Series E, 129(1985)
- [5] Atlung, S., and K. West, *J. Power Sources*, **26**, 139(1989)
- [6] Weppner, W., and R.A. Huggins, *J. Electrochem. Soc.* **124** 1569-1578 (1977).
- [7] Weppner, W., and R.A. Huggins, *Ann. Rev. Mater. Sci.* **8** 269-311 (1978).
- [8] Chernova, N.A., M. Roppolo, A.C. Dillon, and M. S. Whittingham, *J. Mater. Chem.* **19**, 2526(2009)
- [9] Delmas, C., H. Cognac-Auradou, J.M. Cocciantelli, M. Menetrier, J.P. Doumerc, *Solid State Ionics* **69**, 257(1994)

- [10] Kang, S-H., T.-Y. Jeon, H.-S. Kim, Y.-E. Sung, and W.H. Smyrl, *J. Electrochem Soc.* **155**(10) (2008) B1058-B1065
- [11] Kang, S-H., Y-E. Sung, and W.H. Smyrl, *J. Electrochem Soc.* **155**(11) (2008) B1128-B1135
- [12] Le, D.B., S. Passerini, A.L. Tipton, B.B. Owens, and W.H. Smyrl, *J. Electrochem. Soc.* **142**, L102(1995).
- [13] Le, D.B., S. Passerini,, J. Guo, J. Ressler, B.B. Owens, and W.H. Smyrl, *J.Electrochem.Soc.* **143**, 2099(1996)
- [14] Le, D.B., PhD Thesis, University of Minnesota (2004)
- [15] Lee, W-J., M. Alhosan, S.L. Yohe, N.L. Macy and W.H. Smyrl, *J. Electrochem Soc.* **155**(9) (2008) B915-B920
- [16] McKinnon, W.R., and R.R. Haering, in *Modern Aspects of Electrochemistry* (Eds. R. White, J. Bockris, and B. Conway), Vol 15, Plenum Press, New York, 1983
- [17] Coleman, S.T., W.R. McKinnon, and J.R. Dahn, *Phys. Rev.* **29B**, 4147(1984)
- [18] Hill, T.L., *Introduction to Statistical Thermodynamics*, Addison-Wesley, New York, 1962
- [19] Armand, M.B., in *Materials for Advanced Batteries*, (Eds. D.W. Murphy, J. Broadhead, and B.C.H. Steele), Plenum Press, New York, 1980
- [20] Dahn, J.R., D.C. Dahn, and R.R. Haering, *Solid State Commun.* **42**, 179(1982)
- [21] Ho, C., I.D. Raistrick, and R.A. Huggins, *J.Electrochem.Soc.* **127**, 343(1980)
- [22] Hunter, T.B., P.S. Tyler, W.H. Smyrl, and H.S. White, *J.Electrochem.Soc.* **134**, 2198(1987)
- [23] Nabavi, M., Sanchez, C., F. Taulette, J. Livage, and A. De Guibert, *Solid State Ionics* **28-30**(Pt.2), 1183(1988)
- [24] Park, H-K., W.H. Smyrl, and M.D. Ward, *J.Electrochem.Soc.* **142**, 1068(1995)
- [25] Park, H-K., and W. H. Smyrl, *J. Electrochem. Soc.* **141**, L25 (1994)
- [26] Smyrl, W.H., and M. Lien, in *Applications of Electroactive Polymers*, (Ed. B. Scrosati), Chapman Hall, New York, 1993
- [27] West, K., T. Jacobsen, and S. Atlung, *J.Electrochem.Soc.* **129**, 1480(1982)

Diffraction-Based Plasmonic Methods for Chemical Sensing with Nanoparticles and Nanowire Arrays

Aaron R. Halpern,* Iuliana Sendroiu,* Naoya Nishi** and Robert M. Corn*

*Department of Chemistry, University of California-Irvine, Irvine CA 92697 USA

**Department of Energy and Hydrocarbon Chemistry, Graduate School of Engineering,
Kyoto University, Kyoto 615-8510 JAPAN

rcorn@uci.edu

Abstract: The use of diffraction gratings as an optical method for chemical modification of metal surfaces and detecting surface bioaffinity interactions for biosensor applications is explored. Nanoparticle gratings, nanowire gratings, and nanostructured metallic thin films are all used to create both localized and plane wave surface plasmons for the surface diffractions experiments.

Key Words: surface plasmon resonance, diffraction, biosensors

1 INTRODUCTION

Surface bioaffinity sensors have become invaluable tools for the rapid, multiplexed detection of biomolecules. By careful surface immobilization of capture probe biomolecules, we can create multiplex detection platforms that are highly selective towards a specific biomolecular targets present in complex test solutions. To monitor surface bioaffinity interactions, a variety of surface-sensitive spectroscopic methods have been developed. In particular, surface plasmon resonance (SPR) has emerged as an excellent alternative to traditional fluorescence-based measurements as it offers label-free detection without the need for modification of the target molecules prior to analysis. For example, the technique of SPR imaging (SPRI), where multiple probes are arrayed on a single planar gold thin film, has been successfully applied to measure the bioaffinity adsorption of DNA, RNA, antibodies, proteins and biomarkers.[1-2] In this talk, we will explore the use of diffraction gratings both as biosensors and as a general replacement method for SPR in the study of the chemical modification of metal surfaces.[3-6]

2 RESULTS AND DISCUSSION

Diffraction experiments were performed on Au and Pd gratings created on BK7 silica substrates using a 633 nm HeNe laser focused to a 0.5 mm beam width. Three different experimental geometries were employed: transmission, external

reflection, and total internal reflection (TIR). The TIR reflection geometry is shown in Figure 1.

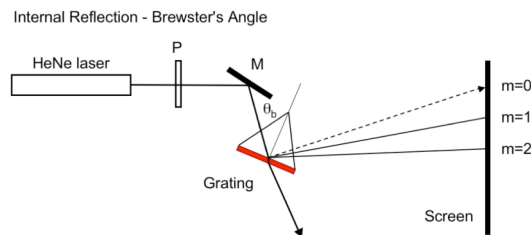


Figure 1: Total internal reflection geometry for diffraction grating experiments. From Ref. 3.

Figure 2 shows the TIR diffraction data obtained from an array of 100nm Pd nanowires spaced by 25 microns. The intensity of the diffraction from the nanowire arrays depended on the square of the nanowire width; diffraction was observed for nanowires with widths down to 25 nm, corresponding to 0.1% of the surface. The nanowire arrays yielded unique diffraction data over many orders (>60) with separate oscillating intensity patterns for even and odd order intensities. Note that diffraction orders appearing at angles greater than the critical angle show an enhancement. The oscillating intensity patterns are attributed to slight asymmetries in the 25 micron spacing of the nanowires in the array that is a direct consequence of the nanowire deposition process. With the use of a simple FT analysis, a value for the

asymmetry in the grating patterns can be obtained from the intensity patterns in the diffraction data. [3]

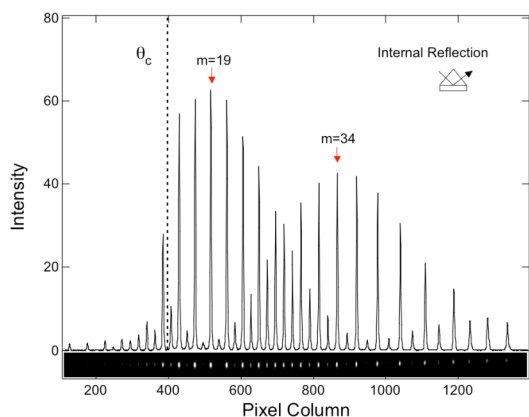


Figure 2: TIR diffraction data from a diffraction grating of 50 nm Pd nanowires, spaced by approximately 25 microns. From Ref. 3.

Figure 3 shows how nanoparticle diffraction gratings can be used in biosensor applications. To create surface bioaffinity sensors from these gratings, a DNA sandwich assay was used in which the presence of a target DNA molecule in solution was detected by the adsorption of a gold nanoparticle to a grating surface. As shown in Figure 3, one half of the complementary DNA sequence was attached to the gold nanoparticle, and the other half was attached to the surface. Target DNA solutions with concentrations as low as 10 fM were easily detected ex situ by the multiple orders of diffraction observed with a HeNe laser from these surfaces. No diffraction was observed in the absence of target DNA, demonstrating the lack of non-specific adsorption of nanoparticles to the surface.[4]

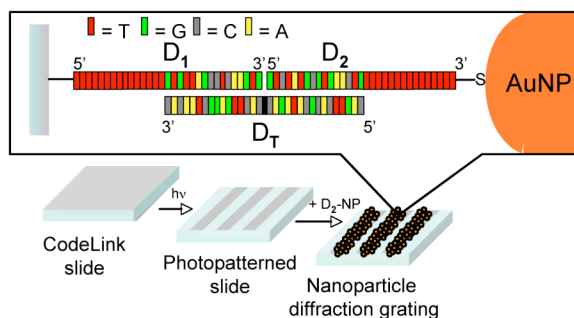


Figure 3: Three sequence DNA sandwich assay for the detection of target DNA from solution (DT) by the hybridization adsorption of gold nanoparticles (AuNPs) onto diffraction gratings. From Ref. 4.

Both the nanowire and nanoparticle diffraction experiments were performed at a single wavelength (633 nm). Figure 4 shows that diffraction observed from a collimated white light source from a Pd nanowire grating. For any given output angle, diffraction from different orders at different wavelengths can be observed. A more complete picture of the diffraction can be obtained by obtaining diffraction data over a range of wavelengths and output angles; an example of such a data set is shown in Figure 4. Note that any given wavelength, an intensity profile at different angles along the y-axis yields an even-odd diffraction pattern similar to that observed in Figure 1. We can

use these multi-wavelength diffraction experiments to identify the surface plasmon-enhanced diffraction from gold thin film gratings.



Figure 4: Multi-wavelength diffraction data from a Pd nanowire array. The x-axis of the image is wavelength (ca. 400-900 nm), and the y-axis is angle of incidence (ca. 40-45 degrees).

3 SUMMARY

In summary, we have shown that gratings created from Au nanoparticles, Pd nanowires and thin Au film metal nanostructures yield diffraction patterns that are easily observed and can be used for the characterization of surface modifications to the gratings with potential applications in surface bioaffinity sensing. The most sensitive surface bioaffinity measurements utilize both local and planar surface plasmons created on gold thin film gratings. Future work will incorporate various enzymatic amplification strategies on the grating surfaces for even higher specificity and sensitivity in the biosensor diffraction measurements.

Acknowledgments The authors gratefully acknowledge funding support from the National Institutes of Health (R01-GM059622) and the National Science Foundation (CHE-0551935).

References

- [1] Smith, E.A. and Corn, R.M., "Surface Plasmon Resonance Imaging as a Tool to Monitor Biomolecular Interactions in an Array Based Format," *Applied Spectroscopy*, **57** 320A-332A (2003).
- [2] Chen, Y., Nguyen, A., Niu, L. and Corn, R.M., "Fabrication of DNA Microarrays with poly-L-Glutamic Acid Monolayers on Gold Substrates for SPR Imaging Measurements," *Langmuir*, **25** 5054-5060 (2009).
- [3] Halpern, A.R., Nishi, N., Wen, J., Yang, F., Xiang, C., Penner, R.M. and Corn, R.M., "Characterization of Electrodeposited Gold and Palladium Nanowire Gratings with Optical Diffraction Measurements," *Analytical Chem.*, **81** 5585-5592 (2009).
- [4] Sendrou, I. and Corn, R.M., "Nanoparticle diffraction gratings for DNA detection on photopatterned glass substrates," *Biointerphases*, **3** FD23-FD29 (2008).
- [5] Lee, H.J., Wark, A. and Robert, M.C., "Enhanced bioaffinity sensing using surface plasmons, surface enzyme reactions, nanoparticles and diffraction gratings," *Analyst*, **133** 596-601 (2008).
- [6] Wark, A., Qavi, A., Lee, H.J. and Corn, R.M., "Nanoparticle-Enhanced Diffraction Gratings for Ultrasensitive Surface Plasmon Biosensing," *Analytical Chem.*, **79** 6697-6701 (2007).

Design and Preparation of Chemically Modified Electrodes for Selective Organic Electro-Preparative Synthesis

Yoshitomo Kashiwagi*, Uichi Akiba**, and Tetsuo Osa***

*Department of Physical Chemistry, Pharmaceutical Sciences, Ohu University, Tomita-machi, Koriyama, 963-8611 Japan

**Department of Life Science, Faculty of Engineering and Resource Science, Akita University, 1-1 Tegatagakuen-cho Akita 010-8502 Japan

***Professor Emeritus, Tohoku University (Home Address: 7-37-15 Sakura-ga-oka, Aoba-ku, Sendai 981-0961 Japan)
osa@mars.dti.ne.jp

Selective electro-preparative syntheses for various types of organic compounds have been reported by the present authors using the graphite felt electrode coating mediator-modified poly(acrylic acid) (PAA). The system can provide an ecologically clean process and will contribute to the development of green chemistry. Advantages of graphite felt (GF) electrode, PAA coating to GF, and mediator immobilization to PAA layer on GF are described. For the system using 2,2,6,6-tetramethylpiperidinyl-1-oxyl (TEMPO) as mediator, design of electrode system, some results of organic macro-electrolyses, and evaluation of the electrolysis data are being discussed.

Key Words: TEMPO, poly(acrylic acid), graphite felt, mediator-modified electrode, macro-electrolysis

1 INTRODUCTION

Organic macro-electrochemical synthesis has been expected to provide an ecological and green process, if a suitable electrochemical system is constructed. Since preparative chemical modified electrodes for this purpose were first reported in the mid-1970's [1], many results along the purpose have been published. We confirmed that a large surface area of electrode such as graphite felt (GF) immobilizing electrocatalytic mediator can construct the system with high current density, high current efficiency, and high regio- or stereo-selectivity without any wastes of reagents [2].

In 1960's, Osa, one of the present authors, successfully started the electrochemical regioselective reduction of benzene which has the highest negative reduction potential among the aromatic nuclei [3]. After then, Osa's group has carried out many specific

electrochemical trials. In 1986 when Bobbitt, J. M., University of Connecticut, USA, visited Sendai to cooperate with Osa's group, he brought GF and carried out to make reactive sites on the surface of GF by air or reagent oxidation to immobilize functional materials with Akiba and Osa. The reactive groups of the GF surface were introduced by the oxidation smoothly, but simultaneously were decomposed. Therefore, the density of the reactive groups on the GF surface could not exceed ca. 10^{-8} mol cm⁻². In 1987, Akiba found the use of poly(acrylic acid) (PAA) coating to the GF surface and attained our research objectives with satisfaction [4]. Since then, the modification method of many types of mediators on GF and the electrochemical oxidation and reduction of various kinds of substrates were mainly examined in acetonitrile containing supporting electrolyte of sodium perchlorate (NaClO₄). This electrochemical system is characterized to be able to

synthesize with high enantio- or stereo-selectivity, if achiral mediator-modified GF containing chiral additive of base in solution or chiral mediator-modified GF is used [5].

The design and preparation of electrode is, in general, essential to organic macro-electrochemical synthesis in the view-point of materials engineering for resources. Therefore, this paper is mainly discussed in the design and preparation of mediator-modified GF electrode.

2 DESIGN AND PREPARATION OF MEDIATOR-MODIFIED GRAPHITE FELT

2.1 Preferable property of graphite felt used in this study

To perform organic macro-electrolysis, large current passage is necessary. This objective can be attained by high current density electrolysis or by use of electrode having large surface area. The latter can be realized by sponge like metals, and felt, yarn or cloth of carbon materials. Carbon electrode materials have a long history of being used for industrial carbide production. Different carbon content and crystallinity of carbon electrode materials are commercially available from vitreous carbon to crystallized graphite of diamond providing a variety of shapes such as plate, ring, rod, yarn, fiber or felt. Graphite and carbon felt manufactured conventionally via pyrolysis of polyacrylonitrile by many companies are quite stable and have high surface areas (estimated to be ca. $0.7 \text{ m}^2 \text{ g}^{-1}$, density: 0.45 g cm^{-3}). We applied GF (WDF) brought by Bobbitt which was kindly gifted from National Electric Carbon Corp. Use of these materials for electrochemical reactions has been done by many researchers since the report by Bobbitt et.al. [6].

2.2 Preferable coating of poly(acrylic acid) on graphite felt

To increase the density of mediators at the surface of GF, we have adopted an indirect mediator modification using of polymer-coated electrodes. A coating of PAA layer to GF yielded a high loading ($20 \mu \text{ mol cm}^{-3}$ level) of mediators, after trials of a various kind of polymers [5]. This PAA coating GF has many favorable properties to prepare a polymer electrode as described below:

(a) Easy control of a layer thickness by dip-coating of

electrode from the different concentration of PAA methanol solution.

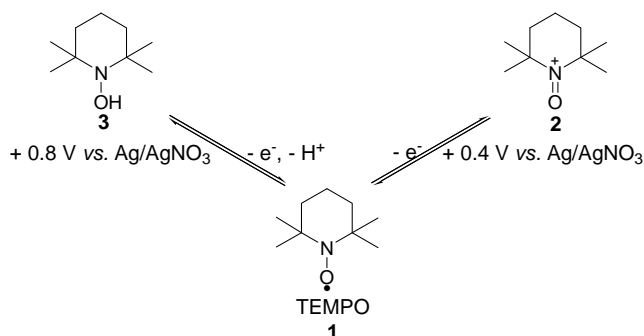
- (b) Strong physical adsorption of PAA to an electrode surface, particularly, to the GF surface.
- (c) Easy chemical immobilization of functional groups of mediators to the PAA layer by the reactions of carboxyl groups of PAA.
- (d) Control of hydrophilicity and lipophilicity by the quantity adjustment of free carboxylates of PAA.
- (e) In the absence of free carboxylates in the PAA layer, organic compounds in the electrolyte solution can be condensed in the PAA layer.
- (f) A suitable size of domain can be very important to construct a supramolecular structure.
- (g) Chemical stability of the PAA layer.

2.3 Advantageous mediators used for modified electrode

In general, the mediator-modified electrode has the following advantageous properties over bare electrode:

- (a) Electrochemical activation of electrochemically inactive substrates by depression of activation energy
- (b) Increase in the reaction rate (increase in the electric current) by increase in mediator density at electrode interface
- (c) Easy improvement of yield, selectivity and current efficiency of products by the control of electrode interface
- (d) Decrease in the amount of expensive mediators by immobilization to electrode
- (e) Attainment of clean and simple process, etc.

In order to achieve the above advantages, however, construction design at electrode interface such as highly efficient electron transfer or electric communications and high specificity is very important.



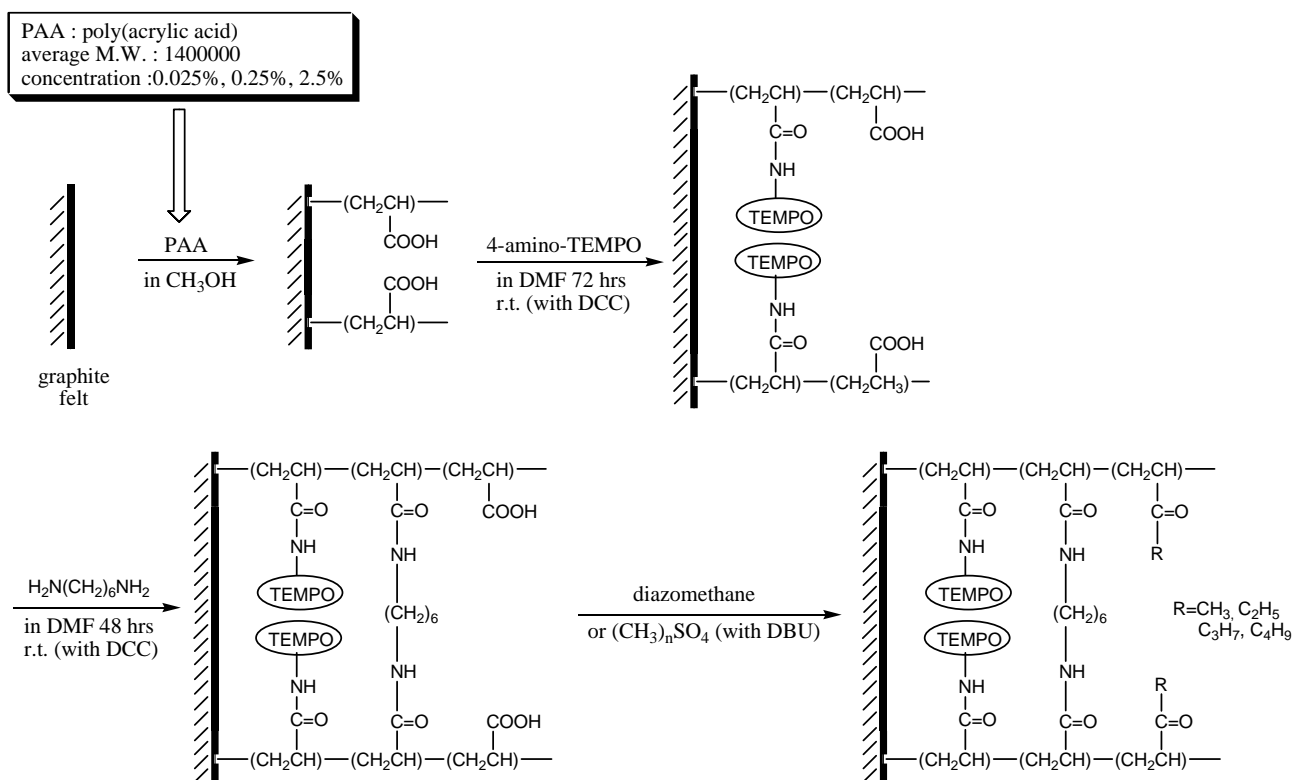
Scheme 1 A reversible redox system based on TEMPO.

The optimum mediators for the preparation of modified electrode should be the property of organic compounds or metal coordination compounds for the following reasons. First, these mediators can be covalently attached to the PAA layer strongly adsorbed on the electrode surface. Another point is that, due to the structural versatility of organic compounds or metal coordination compounds, the chemical structure of these mediators can be regulated to give a high degree of regio- and stereo-selectivity.

Here, we show a mediator mainly used by Kashiwagi et al. [5], The mediator, 2,2,6,6-tetramethylpiperidiny-1-oxyl (TEMPO) (1) constructs a reversible redox system as shown in Scheme 1. Oxoammonium salt 2 can be easily prepared from 1 by treating 1 with many methods such as positive halogen sources, *m*-chloroperbenzoic acid, high-valency metal salts, or electro-oxidation. Species 2 is a strong oxidation agent and is used for selective oxidation of several organic functional groups.

2.4 Modification of TEMPO to graphite felt as an example

The TEMPO-modified electrode was prepared according to our established method [5] (Scheme 2). A piece of GF (size: 1.0 x 1.0 x 0.5 cm) was usually dipped in 0.25 wt% PAA (average molecular weight: 1400000) methanol solution and then dried. The thickness of the PAA layer was ca. 40 nm. This layer was bonded to 4-amino-TEMPO to give a coverage of ca. 64% (by titration), cross-linked with hexamethylenediamine to give a coverage of 16%, and, finally, esterified perfectly (sometimes twice esterification) with methyl, ethyl, propyl or butyl group to remove any remained free carboxylate groups. The density of TEMPO on the electrode was $24 \mu\text{mol cm}^{-3}$. The effects of the PAA and TEMPO concentrations in methanol solution, and the effect of cross-linking of PAA with hexamethylenediamine or other diamines were carefully examined and the proper treatment conditions were obtained.



Scheme 2 Scheme for preparation of TEMPO-modified GF electrodes.

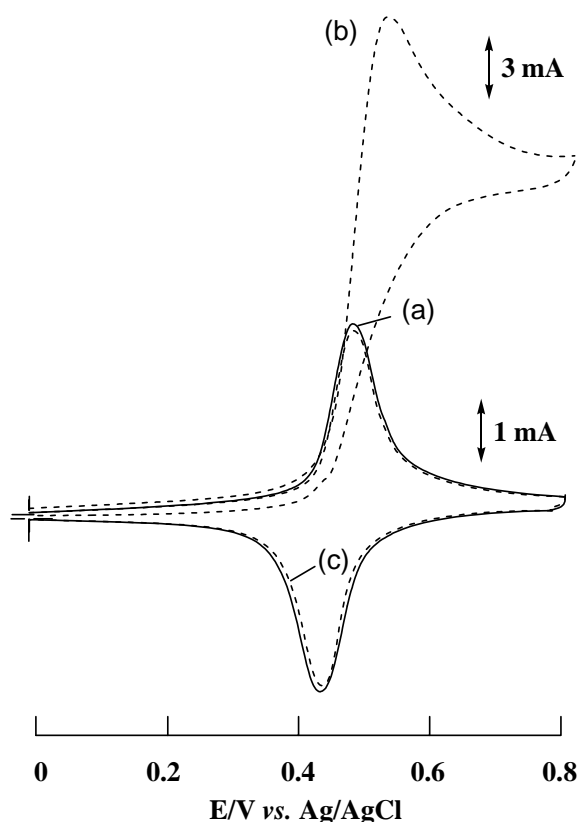


Figure 1 Cyclic voltammograms of TEMPO-modified GF electrode (1.0 x 1.0 x 0.5 cm) in 0.2 M NaClO₄ / CH₃CN at the scan rate of 10 mV s⁻¹. Curve (a) in both absence of 2-naphthol and (-)-sparteine; curve (b) in the presence of 10 mM 2-naphthol and 10 mM (-)-sparteine; curve (c) electrode after one macro-electrolysis in both absence of 2-naphthol and (-)-sparteine

Before macro-electrolysis of organic compounds, cyclic voltammetry was usually carried out. As an example, the cyclic voltammogram (CV) of TEMPO-modified electrode (size: 1.0 x 1.0 x 0.5 cm) itself in 0.2 mol l⁻¹ (M) NaClO₄ acetonitrile at scan rate 10 mV s⁻¹ is shown in curve (a) of Figure 1. The CV of 10 mM 2-naphthol on the electrode in the presence of 10 mM (-)-sparteine of chiral base afforded a well defined electrocatalytic peak at ca.+0.55 V vs. Ag/AgCl as shown in curve (b) of Figure 1. The stability of electrocatalytic activity is shown in curve (c) of Figure 1 in the absence of 2-naphthol and (-)-sparteine, after macro-electrolysis was carried out.

Table 1. Electrocatalytic Oxidation of Organic Compounds on TEMPO-modified Graphite Felt Electrode

substrate	product	η %	con. %	yield %	TON
		94.2	52.2	52.2	196
		95.6	33.1	33.1	124
		42.4	11.8	5.5	96
		98.6	100	100	410
		68.0	49.5	34.7	290
		95.2	98.6	98.6	410
		93.6	96.6	96.6	410
		93.5	70.9	68.9	284

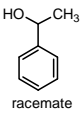
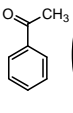
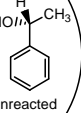
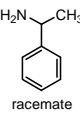
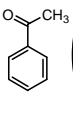
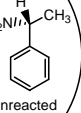
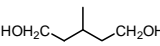
Table 2. Enantio- and Stereo-selective, Electrocatalytic Oxidations on TEMPO-modified Graphite Felt Electrode in the presence of (-)-sparteine

substrate	product	η %	con. %	yield %	%ee	TON
		95.1	53.8	52.4 (46.2)	99	87
		92.6	98.5	93.6	98	307
		88.8	93.6	93.6	99	384

3 ORGANIC MACRO-ELECTROLYSIS ON MEDIATOR-MODIFIED GRAPHITE FELT ELECTRODE

We usually carried out non-stereoselective electrolyses of organic compounds on TEMPO-modified PAA coating GF electrode (size: 5.0 x 2.0 x 0.5 cm) in a

Table 3. Enantio- and Stereo-selective, Electrocatalytic Oxidations on Chiral TEMPO-modified Graphite Felt Electrode

substrate	product	η %	con. %	yield %	%ee	TON
	 + 	99.1	50.7	50.4 (49.3)	99	74
	 + 	92.7	52.8	50.8 (47.2)	99	78
		97.0	99.2	96.5	99	71

conventional divided, H-type cell separated by a Nafion 117 membrane. The anode compartment contained 15-30 mmol of substrate, 30 mmol of 2,6-lutidine and several mmol of gas chromatography (GC) standard (tetralin or fluorene) in 40 ml of acetonitrile containing 0.2 M NaClO₄. The cathode was 40 ml of acetonitrile containing 0.2 M NaClO₄. The cell was operated at a constant potential of 0.8-1.0 V vs. Ag/AgNO₃ under nitrogen atmosphere. During electrolysis, samples were removed and analyzed by GC. After electrolysis, the electrolyte solution of acetonitrile was evaporated

and the residuals were extracted by organic solvent and dried. The residual materials were mainly reaction product, small amount of starting substrate, added base and NaClO₄ of supporting electrolyte. Therefore, any waste materials were not formed in this process. Isolation, identification and amounts of substrates and products were conducted by conventional methods.

Some results using the TEMPO-modified PAA coating GF electrode for preparative electrocatalysis are listed in Tables 1-3 where η is current efficiency (%), con. is conversion (%), and TON is turnover number. Table 1 contains the results for the oxidation of alcohols, thiols, naphthols, methyl-quinolines and amines by the TEMPO-modified PAA coating GF electrode. Table 2 lists the enantioselective oxidation of racemic alcohols, stereoselective lactonization of methyl-substituted diols and enantioselective coupling of naphthols in the presence of chiral base of (-)-sparteine as a deprotonating agent in an oxygen free and anhydrous acetonitrile solution. A chiral TEMPO-modified PAA coating GF electrode, where a chiral mediator is 1-aza-4-amino-2,2,7-trimethyl-10-isopropyl-spiro[5.5]-undecane-1-oxyl, was successfully used in the enantio- or stereo-selective electrocatalysis as shown in Table 3 [7-9]. Such a high selective electrocatalytic oxidation may proceed in a suitable size of domain in a PAA layer.

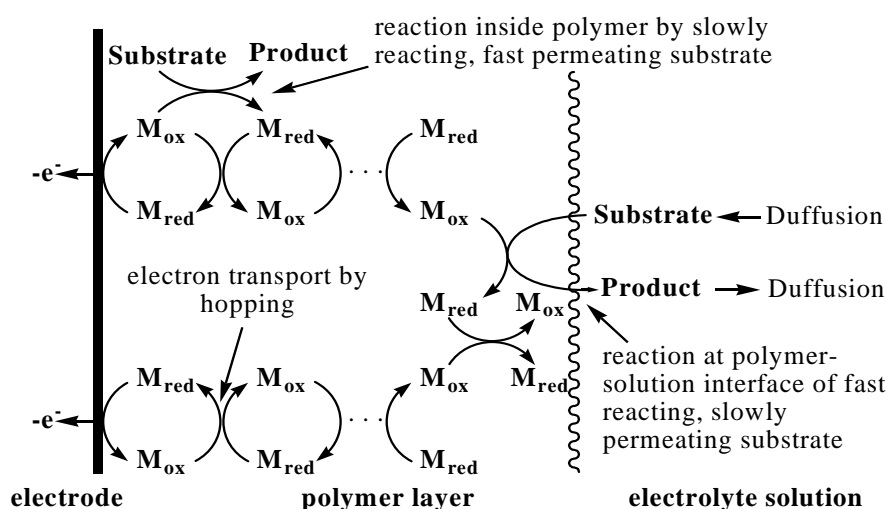


Figure 2 Plausible scheme electron transfer mechanism between electrode and substrate via a mediator-immobilized polymer layer.

4 EVALUATION OF ELECTROLYSIS DATA

The TEMPO-modified PAA coating GF electrode has high current density, high stability and long life. The current density of the electrode for organic compounds easily exceeds ca. 1 A l^{-1} . Therefore, when the substrate of molecular weight 100 is electrocatalytically oxidized by 2 electrons transfer, this electrochemical cell is estimated to provide a current charge concentration of ca. $3600 \text{ C l}^{-1} \text{ hr}^{-1}$, that is, ca. 2 g of product is produced per liter of electrolytic cell per hr. This value corresponds to that of a conventional organic reactor. Furthermore, conversion yield and current efficiency of product are also very high as well as low applied potential electrolysis using this mediator modified electrode.

The electron transfer mechanism between GF and substrate via PAA polymer layer can be schematically demonstrated in Figure 2.

5. CONCLUSIONS

It is demonstrated that the mediator-modified PAA coating GF electrode can provide an ecologically clean, green electrochemical system. This conclusion suggests to evoke important attention to electrochemical production of organic compounds in future.

References

- [1] a) Watkins, B. F., Behling, J. B., Kariv, E., and Miller, L. L., "Chiral electrode," *J. Am. Chem. Soc.*, Vol. 97, pp. 3549-3550, (1975). b) Firth, B. E., Miller, L. L., Mitani, M., Rogers, T., Lennox, J., and Murray, R. W., "Anodic and cathodic reactions on a chemically modified edge surface of graphite," *J. Am. Chem. Soc.*, Vol. 98, pp. 8271-8272, (1976).
- [2] Kuwana, T., Osa, T. and Kashiwagi, Y., "Organic Electrocatalysis," eds. by Rubinstein, I. and Fujihira, M., "Encyclopedia of Electrochemistry, Vol. 10, Modified Electrodes," Wiley-VCH, Weinheim, pp.695-705, (2007).
- [3] Misono, A., Osa, T., Yamagishi, T., and Kodama, T., "Selective Electro-reduction of the Benzene Nucleus," *J. Electrochem. Soc.*, Vol. 115, pp.266-267, (1968).
- [4] Osa, T., Akiba, T., Sagawa, I., and Bobbitt, J. M., "Electrocatalytic Oxidation of Nerol with Nitroxyl Radical Covalently Immobilized Poly(acrylic acid)

Coated on Carbon Electrodes," *Chem. Lett.*, Vol. 17, No. 8, pp.1423-1426, (1988).

- [5] Osa, T., "Construction of New Mediator System," pp.183-219 and references therein ed. by Osa, T., "New Challenges in Organic Electrochemistry," Gordon Breach Science Publishers, Amsterdam, (1998).
- [6] Bobbitt, J. M., Yagi, H., Shibuya, S., and Stock, J.T., "Electrochemistry of natural products. II. Electrolytic oxidation of some simple 1,2,3,4-tetrahydroisoquinoline phenols," *J. Org. Chem.*, Vol. 36, pp.3006-3010, (1971).
- [7] Kashiwagi, Y., Kurashima, F., Kikuchi, C., Anzai, J., Osa, T., and Bobbitt, J. M., "Enantioselective Electrocatalytic Oxidation of Racemic *sec*-Alcohols on Chiral 1-Azaspiro[5.5]undecane-*N*-oxyl Radical," *Tetrahedron Lett.*, Vol. 40, pp.6469-6472, (1999).
- [8] Kashiwagi, Y., Kurashima, F., Kikuchi, C., Anzai, J., and Osa, T., "Enantioselective Electrocatalytic Oxidation of Racemic Amines on Chiral 1-Azaspiro[5.5]undecane-*N*-oxyl Radical," *Chem. Commun.*, pp.1983-1984, (1999).
- [9] Kashiwagi, Y., Kurashima, F., Chiba, S., Anzai, J., Osa, T., and Bobbitt, J. M., "Asymmetric Electrochemical Lactonization of Diols on a Chiral 1-Azaspiro[5.5]undecane-*N*-oxyl Radical Mediator-modified Graphite Felt Electrode," *Chem. Commun.*, pp.114-115, (2003).

Integrated Biodevices Based on Microfabrication with Biomaterials

Tomokazu Matsue

Graduate School of Environmental Studies, Tohoku University, Sendai, Miyagi 980-8579, Japan
matsue@bioinfo.che.tohoku.ac.jp

ABSTRACT: Integrated biodevices using biomaterials such as proteins and living cells have been fabricated using microfabrication technology and the performance of the devices has been investigated using electrochemical methods. In this paper, I focus on the detection of the activity of recombinant cells with integrated devices. The gene expression inside the cells was successfully monitored by detecting amperometric signals triggered by reporter proteins. The electrochemistry-based device was applied to detection of hazardous materials. Also, this paper reports the novel integrated electrochemical devices for comprehensive bioanalysis.

Key Words: Integrated biodevices, Gene expression, Microfabrication, Comprehensive analysis

1 INTRODUCTION

The development of integrated biodevices using biomaterials such as proteins and living cells has received much attention in advanced biotechnology. Many biodevices developed so far are based on fluorescence detection since fluorescence measurement usually has a high sensitivity and a variety of tools for performing the measurements are commercially available. However, fluorescence detection has some drawbacks such as undesired fluctuations due to quenching or emission from other materials, shielding by a turbid solution or vessels, and need for labeling non-fluorescent species, which may cause toxic side effects in the analytes. Another form of detection utilized in biodevices is amperometric detection that offers sufficient sensitivity as well as specificity. In this paper, I will describe the recent progresses on the integrated biodevices based on electrochemical detection; especially detection of gene expression in recombinant cells. Living cell is itself an integrated sensing system by which highly sophisticated functional operation and parallel signal transduction pathways are systematically processed. Recent development of gene engineering technology enables the electrochemical detection of whole-cell reporter system in miniaturized devices. The miniaturized or integrated biodevices with recombinant cells are expected to provide improvement in throughput, sensitivity, and cost performance of the bioanalysis.

2 ELECTROCHEMICAL DEVICES FOR DETECTION OF GENE EXPRESSION

The availability of complete genome sequences has accelerated the study of gene functions on a genome-wide scale. DNA microarrays have enabled the survey of the intracellular gene network by comparing genome-wide transcriptional profiling in response to environmental stimuli. Since genetic

information encoded in the genome is ultimately manifested at the cellular level, global approaches for analyzing cell phenotypes would facilitate our understanding of cellular functions of genes. The currently developed cell-based microarrays enable comprehensive analysis of gene functions on a genome-wide scale from phenotypes of living cells. I will report here the fabrication and characterization of a microbial array chip composed of PDMS channels and a silicon substrate, simultaneous realization of the introduction of plasmid DNA into a bacterial host, and the monitoring of gene expression in the phenotypes of bacteria during the transformation process (Fig. 1) [1].

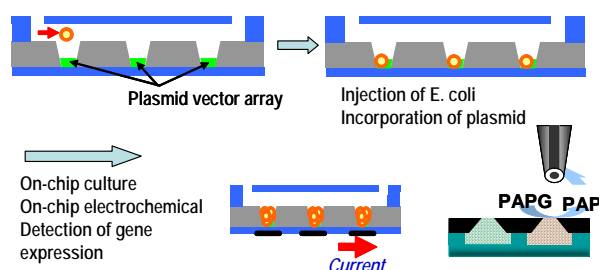


Fig. 1. Electrochemical gene-engineering using electrochemical detection of gene expression.

3 ELECTROCHEMICAL MONITORING SYSTEMS USING RECOMBINANT CELLS

E. coli cell is one of the most extensively used prokaryotic organisms for high-yield recombinant proteins production. Whereas several advantages are expected in *E. coli* as a host cell, the heterogenous proteins often form the insoluble aggregates in *E. coli* cell known as the inclusion body. For the efficient production of recombinant protein suitable for structural and functional studies, it is required to develop a

high-throughput screening of recombinant protein solubility in *E. coli* cells. We have applied the microbial array chip to screen the recombinant protein solubility in *E. coli* cells using scanning electrochemical microscopy (SECM) [2]. The β -Gal was used as a folding reporter by being fused to the model target protein maltose binding protein to demonstrate the electrochemical high-throughput screening of recombinant protein solubility assay (Fig. 2).

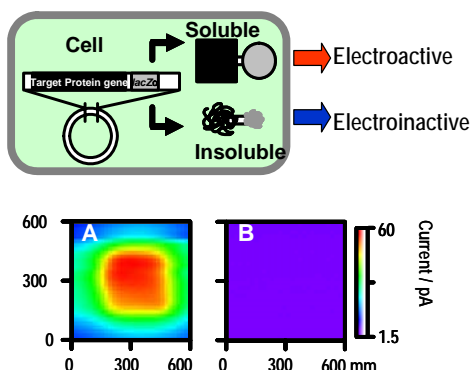


Fig. 2. Electrochemical recombinant protein solubility assay. Lower: Electrochemical Images of microbial chips. A. Wild *E. coli* expression soluble protein. B. Recombinant *E. coli* expressing insoluble protein.

Mutagens have been suspected of carcinogenicity, which induces DNA damages and causes gene mutation. To date, various mutagen screening methods utilizing bacteria have been introduced for practical use in the fields of healthcare and environment. The umu test utilizing the DNA repair process is one of the most sensitive mutagen screening systems. We have demonstrated mutagen screening systems with microbial array chips based on the umu test [3]. The chip has microstructures immobilized with genetically engineered bacteria which express β -Gal on exposure to mutagen to generate electrochemical responses (Fig. 3).

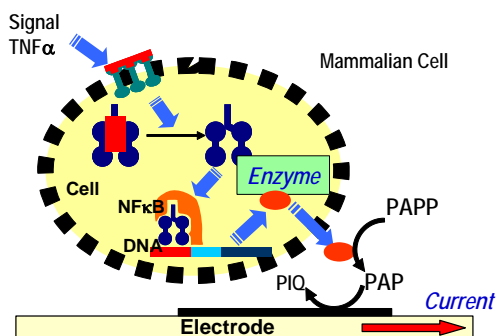


Fig. 3. Electrochemical cellular device for detection of intracellular signaling of mammalian cells.

4 ELECTROCHEMICAL MICROARRAY DEVICES FOR COMPREHENSIVE ANALYSIS

Although various cellular microarrays have been proposed, few studies have evaluated cellular functions under three-dimensional (3-D) culture conditions. We have investigated the in situ cellular signal transduction of 3-D cultured cells by applying electrochemical methods. These cells were genetically engineered to produce SEAP, and immobilized in an array of microholes on a chip. Cellular SEAP expression triggered by the exposure to $\text{TNF}\alpha$ was monitored using SECM and a cellular chip in parallel to realize a high-throughput screening system for cellular gene expression [4].

We also developed a novel multipoint addressable electrochemical device that consisted of orthogonally arranged row/column electrode arrays [5]. Using the device, the electrochemical responses at $n \times n$ crossing points were rapidly detected. The addressable device was combined with a microwell array to perform high-throughput screening of genetically engineered cells accommodated in the wells. The expression of the reporter protein—secreted alkaline phosphatase (SEAP)—from a single genetically engineered HeLa cell (HeLa-pSEAP) was rapidly detected with the addressable microelectrode/microwell array device. The electrochemical signals initiated by the expressed protein from 10×10 measurement points indicated the heterogeneity in the expression activity of individual cells.

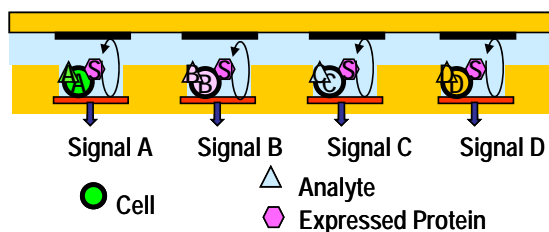


Fig. 4. Principle of an addressable microelectrode / microwell array for comprehensive electrochemical analysis.

References

- [1] K. Nagamine, S. Onodera, Y. Torisawa, T. Yasukawa, H. Shiku, T. Matsue, *Anal. Chem.*, **77**, 4279 (2005).
- [2] K. Nagamine, S. Onodera, A. Kurihara, T. Yasukawa, H. Shiku, R. Asano, I. Kumagai, T. Matsue, *Biotech. Bioeng.*, **96**, 1008 (2007).
- [3] N. Matsui, T. Kaya, K. Nagamine, T. Yasukawa, H. Shiku, T. Matsue, *Biosens. Bioelectron.*, **21**, 1202 (2006)
- [4] Y. Torisawa, N. Ohara, K. Nagamine, S. Kasai, T. Yasukawa, H. Shiku, T. Matsue, *Anal. Chem.*, **78**, 7625 (2006)
- [5] Z. N. Lin, Y. Takahashi, Y. Kitagawa, T. Umemura, H. Shiku, T. Matsue, *Anal. Chem.*, **80**, 6830 (2008); Z. Y. Lin, Y. Takahashi, T. Murata, M. Takeda, K. Ino, H. Shiku, T. Matsue, *Angew. Chem. Int. Ed. Engl.*, **48**, 2044 (2009).

From Nanolithography to Energy Assisted Writing – Is There a Limit to Magnetic Recording Density?

B. Terris*, T. Thomson*, R. Ruiz*, B. Stipe*, T. Strand*, C. Poon*, J. Katine*, H. Balamane*, N. Robertson*, H. Nemoto**, and A. Hirotsune**

*Hitachi Global Storage Technologies, San Jose Research Center, 3403 Yerba Buena Road, San Jose CA 95135 USA

** CentralResearchLaboratory,Hitachi,Ltd.,2880Kozu, Odawara,Kanagawa256-8510,Japan.

Bruce.Terris@HitachiGST.com

Abstract: As magnetic recording technology extends to ever higher areal density, it is possible the often predicted, and constantly increasing, density limit for “conventional” magnetic recording will be reached. This limit will likely be in the range of 750 – 1000 Gb/in². However, new technologies are being explored which may extend this limit toward 10,000 Gb/in², or 10 Tb/in² or beyond. These new technologies will require significant changes to the hard disk drive and ultimately they too will likely reach limits. In this paper we will discuss the technologies which are being pursued to achieve this density and to push the limit at least another factor of 10. These technologies include lithographically patterned single domain islands, novel forms of energy assisted recording including heat and microwaves, and novel data encoding and architecture schemes. The challenges and limits of these technologies will be discussed.

Key Words: Magnetic Recording, patterned media, nanofabrication, energy assisted recording

1. Introduction

Magnetic recording, invented over 100 years ago, has played a key role in the development of information storage technologies, including analog audio, video and digital data recording. Since the sale of the first magnetic hard disk drive by IBM in 1956, the capacity and storage density, i.e. the number of bits per square inch (bits/in²), have increased dramatically. The increase in density has required continuous scaling of the components of the disk drive to ever smaller dimensions. As a result of scaling, the head flies closer to the disk, write and read resolution is increased, write fields and field gradients from the head increase, the grains in the medium become both thinner and smaller in diameter, and the medium anisotropy is increased, all allowing for a growth in areal density and a corresponding increase in data rate.

Recording demonstrations at densities of around 600 Gb/in² have been reported on conventional perpendicular continuous granular media (CGM) and system designs have been discussed for Tbit/in² densities. This increase in density has been achieved by scaling the grain size in the media with the bit size, thus keeping the number of grains/bit approximately constant (not strictly true in recent years) and maintaining a sufficient signal to noise ratio. In order to prevent long term signal decay caused by thermally activated magnetization reversal, the magnetic anisotropy must increase with decreasing grain size.

Ultimately, the recording density will be limited by the inability of the write element to reverse grains having the required anisotropy for thermal stability. The individual magnetic grains must remain outside the superparamagnetic limit determined by the ratio of the

anisotropy energy to that of the thermal environment $K_uV/k_B T$. In the simplest possible case, the probability of thermal activated reversal is given by:

$$P(t) = e^{-t/\tau} \text{ where } \frac{1}{\tau} = f_0 e^{-\frac{K_u V}{k_B T}}$$

Here f_0 is the “attempt frequency” with values typically taken as in the range 10^9 to 10^{11} Hz. In order to have a robust media, we must ensure that $K_u V$ is large enough to keep any thermally activated reversal events to within a limit that allows the coding and error correction channel to retrieve the data without corruption. Together, thermal activation and the write field available from a recording head set quite strict limits on the magnetic anisotropy. If the anisotropy is too high (needed to ensure thermal stability) then the head field may not be able to reverse the grains and write data. Conversely, too low anisotropy leaves the grains vulnerable to thermal activated reversal although the writing becomes easier. Typically, a value of $K_u V/k_B T$ of 50-60 is required.

In order to push recording densities beyond the limits of conventional CGM, three classes of approaches have been proposed (fig 1):

(a) The first class of approaches, involves the use of lithographically patterned media [1]. In this case each bit is single magnetic domain and the switching volume for thermal stability is the bit volume rather than the grain volume. However, the bits must be of nearly identical size and spacing and arranged in a nearly perfect pattern. This approach thus uses a radically different media than used today, but has the advantage that head designs are similar to those in production today.

(b) In the second class an additional source of energy is introduced to assist the applied magnetic field in reversing the bit magnetization, thus allowing higher anisotropy media to be used. Until recently “energy assisted recording” was synonymous with heat assisted recording where locally heating the bit lowered the anisotropy during writing [2]. However, additional energy can also be provided by adding a radio frequency magnetic field [3]. The higher anisotropy enables smaller grains to be thermally stable, and adding a new energy source to the write element enables bits to be written with heads fabricated from existing pole materials.

(c) In the third class of approaches, the grain size and anisotropy are maintained at their present value, but the number of grains per bit is reduced. In the extreme limit, fractions of a bit per grain can be achieved, but at the expense of radical levels of signal processing and error correction. One such proposal use a two dimensional readback (TDMR) scheme to reconstruct the written data [4].

In this paper, we briefly review these different approaches to achieving high areal density and offer some comments on the possible limits of magnetic recording technology.

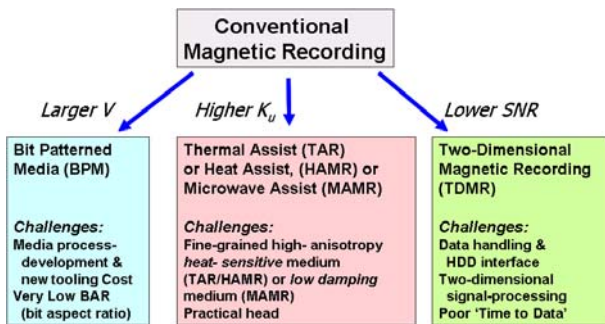


Figure 1. Schematic drawing of the three classes of approaches to achieve higher areal density recording.

2. Bit Patterned Media (BPM)

2.1 System Requirements

Date storage systems must be able to write and read information at low error rates, and current standards demand raw (uncorrected) rates of around 10^{-4} to 10^{-6} . In magnetic recording, the binary data are encoded by the presence or lack of a transition at a given clock cycle (Fig 1). However, there is a fundamental difference between continuous media and BPM in the method used for writing data to the disk. In CGM, the media are isotropic with the only structure due to grain-to-grain variations which occur on a 10 nm scale. Hence all locations on the disks are equivalent. Data are written to the disk by the write field gradient from the head, with the field gradient and media switching field distribution (SFD) defining the bit locations. In contrast, for BPM all the bit locations are defined by the disk, although the data values (such as magnetization up or down) are written by the head field. In this case, in order to correctly address the preexisting island locations, the head write field must be synchronized to the island locations. The implications for patterning are that the distributions of island sizes and positions must be tightly controlled. Micromagnetic models of BPM systems imply the standard deviations of

the distributions for island size and center-to-center distance need to be below 10% to achieve the desired error rates of 10^{-4} to 10^{-6} at 1 Tbit/in² density [5, 6], and similar tolerances are required for the magnetic anisotropy distribution. The requirements on these distributions will, of course, only become more stringent as densities increase towards 10 Tbit/in².

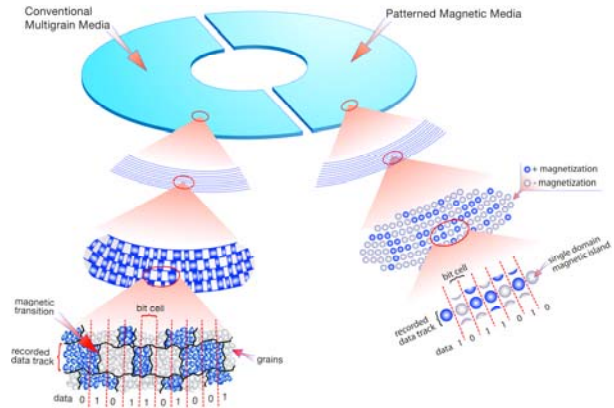


Figure 2. Schematic of recording on continuous granular media (left side) and on bit patterned media (right side)

2.2 Fabrication

One of the key advantages of conventional magnetic recording over other data storage technologies, such as DRAM and Flash, is the use of a continuous, featureless, recording medium. The magnetic write/read head is fabricated using conventional lithography processes, but even here the number of processing steps at the finest lithographic resolution are few compared to semiconductor based storage. The short, down track, dimension is not lithographically defined, but rather defined by thin film deposition processes used to form the write and read elements in the head. The track width is defined by lithography and typically requires only a few steps at the critical feature size of approximately 50 nm (half track pitch). Therefore, to the extent that the device price will depend on fabrication costs, disk drives have a huge advantage over semiconductor memory. This is borne out in the market place, where the price for disk drives is approximately \$0.20/GB and Flash memory around 20x more or \$4/GB. This cost disparity is even more remarkable when one considers the mechanical complexity of a disk drive.

The manufacturing process for BPM must therefore preserve this cost advantage if BPM is to be successful in the marketplace. The fabrication process currently envisioned for BPM would combine the use of e-beam lithography, possibly self-assembly, and nanoimprint lithography for the creation and replication of patterns. A single topographic master pattern, generated at considerable expense, is replicated by a two-generation nanoimprint lithography process, first to create a number of imprinting templates that are copies of the master pattern, and then to replicate the patterns from the imprinting templates onto millions of disks.

In order to create master templates for BPM, a new generation of rotary-stage e-beam writers will be essential. Rotary-stage writers produce large circular patterns with a continuously rotating stage, which avoids

the stitching errors between exposure fields inherent to conventional Cartesian (X-Y) e-beam lithography tools. Resolving the feature sizes needed for BPM (e.g. 12.5 nm diameter islands with 25 nm period for an areal density of 1 Tbit/in²) pushes the limits of e-beam lithography. Pattern densities as high as 4.5 Tbit/in² have been shown [7],

Once the e-beam pattern has been written into the resist, a pattern transfer process is used to convert it into a topographic pattern in the substrate, which will become the imprint stamper. The imprint process is then repeated using the stamper to define the pattern to be transferred into the recording medium. If a subtractive processing scheme is used then the resist is coated onto a medium that has been prepared by depositing a magnetic thin film, onto an unpatterned disk substrate. The etch/ion mill step then converts the continuous magnetic film into islands. However, most of the published work to date, has concentrated on additive processing. Here a blank disk is coated with resist and a reactive ion etch step is used to etch a specified depth into the disk substrate, leaving an array of pillars protruding from a recessed background on the substrate. A magnetic thin film, such as Co/Pd multilayers can then be blanket deposited on the patterned disk .

If patterned media is to be an extendable technology, beyond the limits of electron beam lithography, then new methods of creating large area arrays of magnetic islands must be explored. Block copolymer self assembly provides a route to achieving resolutions in the range of 10-100 nm, and recent work has suggested even higher resolution may be possible. The block co-polymer pattern would serve as an etch mask for transferring the pattern into an imprint master, most likely by etching.

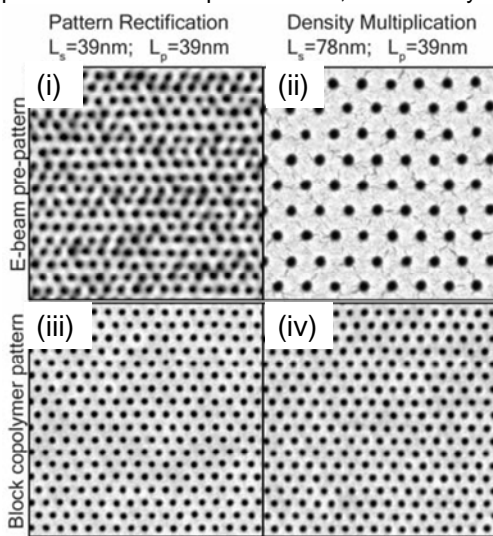


Figure 3 An example of guided self assembly along with density multiplication, after ref [8] (i) and (ii) show SEM images of developed e-beam resist with $L_s = 39$ and 78 nm. (iii) and (iv) show SEM images of the block copolymer film on top of the prepattern defined by the corresponding e-beam pattern above.

A guided self assembly method is more likely to succeed than a pure bottom-up approach in addressing challenges such as long range ordering, placement jitter, feature size distribution and pattern registration needed

to meet the specifications for patterned media applications. An example of guided self assembly is that of chemically pre-patterning the substrate as shown by recent results from Ruiz et al.[8] (Fig 3). Here electron beam lithography is used to create a chemically pre-patterned surface.

2.3 Magnetic properties

The magnetic properties needed for BPM are very different from those of CGM. Here the entire bit must switch as a unit rather than the individual grains. This leads to the requirement that the medium must be highly exchange coupled which is the antithesis of all conventional magnetic media developed to date. The other critical feature of patterned media is that each individual bit (island) switches at very similar values of applied field – that the switching field distribution (SFD) is very narrow. In one model, Schabes [6] showed that to successfully write data at densities of 2 Tbit/in² and assuming a lithography jitter of 1 nm required anisotropy distributions ($\sigma H_k/H_k$) in the range 4 – 7 % depending on challenging but realistic choices of head field gradient.

Several factors contribute to the SFD; there are intrinsic contributions due to material variations within the magnetic island under consideration and extrinsic contributions due to the fields from other islands in the array. The applied field needed to reverse a particular island depends on the sum of the magneto-static fields produced by the other islands in the BPM array. The contribution of these fields to the total SFD depends only on the geometry of the patterned array and the saturation magnetization (M_s) of the medium. An example of a measured SFD for Co/Pd islands is shown in Fig 5.[9] The contribution of magneto-static interactions to the total SFD increases significantly as island size (and period) decreases, ultimately approaching a sizeable fraction of $4\pi M_s$ for small (nm) island spacing.

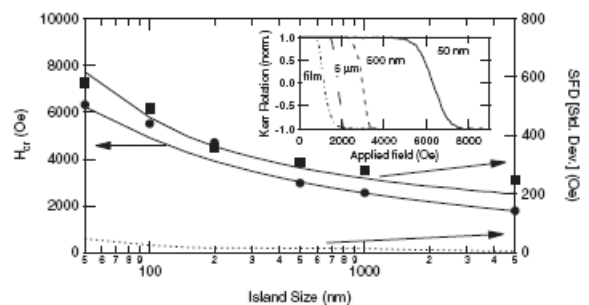


Figure 3 Left-hand axis: coercivity of island arrays as a function of island size (dots) and results of simulation (solid line). Right hand axis: switching field distribution (squares) and results of simulation (solid line). Also shown is the SFD standard deviation (dashed line) due only to differences in magnetostatic environment. The inset shows remanence curves for three island sizes and the continuous film. (ref [9]).

While magneto-static fields set the limit on the smallest SFD that can be obtained, island to island variation of magnetic properties provides the greatest challenge to creating patterned media with narrow SFD's. These island to island variations currently account for the largest fraction of the SFD. They originate from

microscopic variations in the local anisotropy. In highly exchange coupled continuous thin films (films with an area greater than a few tenths of a mm), reversal occurs by nucleation of a small reversed site, following which the remaining film is reversed by domain wall motion. Small, sub-exchange length, single domain islands reverse in a very different manner. In this case the islands cannot support domain walls and so reverse by rotation. The reversal field is therefore determined by the average anisotropy of the island and, of course, the temperature of the sample through thermal activation. Creating patterned media from an exchange coupled film results in a large number of nanoscale islands, each of which now roughly corresponds to a nucleation volume in the original film.[9] If the local anisotropy of the full film varies as a function of position, then the field required to switch individual islands will also vary.

3. Thermally (Heat) Assisted Recording (TAR or HAMR)

The second class of approaches to achieve higher areal density is to add a second energy source to the recording in order to reverse higher anisotropy materials. Materials with a large magnetic anisotropy, such as L₁₀ FePt [10], can support grains as small as 2.8 nm in diameter, compared to grains in current media of around 8 nm. However, the required write field for high-anisotropy materials is greater than the magnetic field that can be generated by a recording head.

Thermally (or heat) assisted magnetic recording (TAR or HAMR) overcomes this problem by heating the medium to near the Curie temperature during recording, thus reducing the required write field. Heating and cooling of the medium within around 1 ns is required in order to achieve the necessary data rates, to generate a large thermal gradient for achieving high linear density, and to ensure that the recorded data are thermally stable during cooling to ambient. It is desired that only a single track be heated, as heating adjacent tracks will result in thermally activated reversal and data loss. This requires the light (assuming optical heating) be confined to sub-40 nm spot for Tb/in² class density and such a spot size is far below the diffraction limit. The data are stored close to room temperature, where the high anisotropy ensures thermal stability (Fig 5).

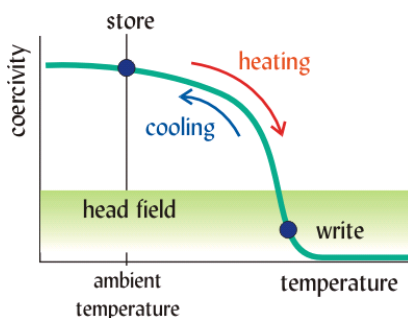


Figure 4. Schematic of thermally assisted recording concept.

There has been recent progress in developing such small spot, high efficiency, near field optical transducers integrated into magnetic recording heads. Challenger et al (Seagate) has reported the use of a grating to couple

a laser beam into on a planar solid immersion mirror (SIM) fabricated on a magnetic recording write head. [11] The SIM focuses the light onto a near field transducer located at the air bearing surface. Using this structure, data recording at 200 Gb/in² was demonstrated on granular FePt media.

We present here an alternative approach using a "c-aperture" integrated with a waveguide and magnetic write head. A waveguide delivers light to a plasmonic near-field transducer located at the air-bearing surface. The near-field transducer uses a low-loss metal (Au, Ag, Cu, etc.) with a size and shape necessary for the creation of resonant charge motion at the metal surface (surface plasmons) and includes a sharp tip to further enhance the charge motion in a localized region. The oscillating tip charge creates an intense near-field pattern, resulting in the localized heating of a disk placed in close proximity. For example, when polarized light is aligned with the ridge of a ridge slot waveguide (also known as the "c-aperture") an intense near field pattern is created at the end of the ridge.

Optimized ridge waveguides for use at 780nm wavelength were fabricated using electron beam lithography and a planar process on single-crystal quartz substrates to form a quartz aperture in a gold film. An example of this structure is shown in Figure 6. The resulting quartz sliders were mounted above CoPd super-lattice media and the disk was scanned using a static tester in recording experiments.

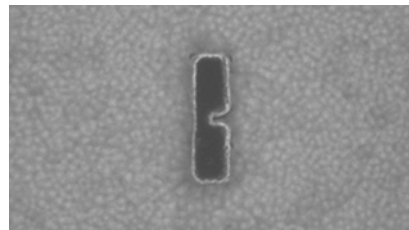


Figure 5 C-apertures in a gold film

In an integrated TAR head, a thin-film waveguide can be used to deliver light to the transducer. When designing an integrated TAR head, the exact means of light delivery, the type of near-field transducer, and the magnetic head design must all be jointly optimized. Figure 7 shows a schematic of the basic simplified head structure utilizing a Ta₂O₅ waveguide core with uniform rectangular cross section. Both Al₂O₃ and SiO₂ cladding materials were used. Ridge waveguides or related plasmonic transducers were fabricated at the end of the waveguide. The write pole (not shown) provides a strong magnetic field and field gradient without significantly reducing the optical efficiency of the head. As shown in Figure 7, the overall optical performance of the integrated head was modeled and shows that a 30nm spot size with 10% power efficiency can be achieved. By scanning a Pd thermistor tip with 100nm radius and recording the heating of the tip from near-field radiation, an image of near-field coupling can be generated (right side of Figure 7).

Light from an external 780nm wavelength diode laser was focused and end-fired into the top of the waveguide. Integrated heads were mounted on suspensions and recording was carried out using a quasi-static tester. The tester is particularly useful for TAR write/read

experiments as it combines many of the capabilities of a spin-stand and high resolution MFM in one apparatus. Nanosecond laser pulses and pulsed magnetic fields from the write pole were applied for recording experiments at sub-100nm track width. Images were generated by scanning the onboard reader element (70nm width) or the element from a second head (narrower width). Track squeeze images on high anisotropy Co/Pd media ($H_c > 11\text{kOe}$) down to 100nm track pitch are shown in Figure 8. Images of tracks at $< 25\text{nm}$ bit length show high fidelity and demonstrate $> 250\text{Gb/in}^2$ capability for TAR.

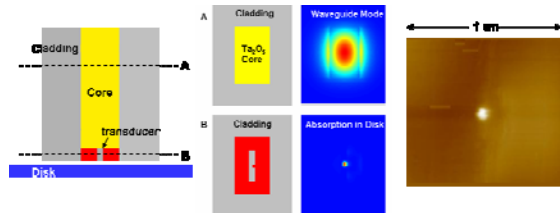


Figure 6 Concept of waveguide with c-aperture, modeling results of spot size, and scanning thermal microscope image of near field spot.

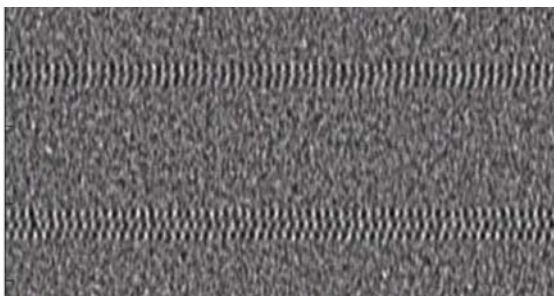


Figure 7. 150nm pitch tracks are shown at bottom and 100nm pitch tracks are shown at top.

4. Microwave Assisted Magnetic Recording (MAMR)

A second form of energy assisted recording is microwave assisted magnetic recording, or MAMR. In the case of MAMR the added energy for reversal comes from a radio frequency (RF), or microwave, magnetic field that is applied to the media in conjunction with the usual 'static' field from the write pole. The key new insight that makes MAMR interesting is that spin torque oscillators (STOs) can be used to generate very large, highly localized, RF magnetic fields [3]. There is no competing technology to do this.

Models suggest that if a well-tuned radio frequency (RF) oscillating magnetic field can be applied to the "idealized" media in conjunction with the normal pulsed magnetic field from the writer, then the media may be reversed with lower write fields than would otherwise be possible (fig. 9). This in turn opens the path to using finer grained media with higher anisotropies and commensurately better thermal stability than otherwise possible, and allows for improved areal densities (without the need for increased write field) as a consequence. There are three steps to the MAMR write process: (1) excitation of the magnetization precession in the media and RF pumping to increase the precession angle, (2)

switching of the media magnetization over an energy barrier into a reversed state upon application of a pulsed write field and (3) relaxation of precessional magnetization into the stable switched state.

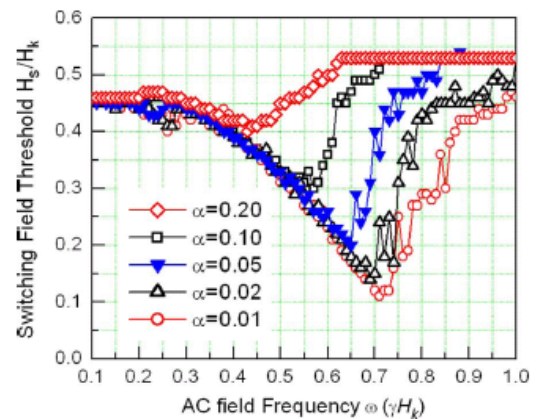


Figure 8 Calculated switching field threshold as a function of ac field frequency for a series of damping constant values. The pulsed reversing field is at 30 degree angle w.r.t. easy axis and the ac field amplitude is $0.1 H_k$. From ref. [3].

It is currently believed that RF magnetic fields on the order of 10-20% of the media anisotropy field H_k will be required for efficient MAMR, i.e., RF fields on the order of 2 kOe are required. Such large RF magnetic fields cannot be produced using microwave striplines or coplanar waveguides, and producing fields approaching anywhere near these levels would require extremely large input power (kW) as well as integration of RF compatible lead structures on the recording head. By contrast, an STO enables the required large local RF magnetic fields to be generated with the application of only small direct currents, on the order of a few milliamperes.

MAMR recording heads will thus incorporate an STO, with critical dimensions similar to the bit size, in the vicinity of the write pole. An STO is a thin film magnetic heterostructure that is rather similar to a CPP sensor, comprising a fixed layer that serves to polarize the incoming electrons and a free layer that can precess with large angle about its easy axis under the influence of the spin torque exerted by the spin-polarized electrons traversing the device. A thick free layer (on the order of 20 nm) is desirable for MAMR, since the magnitude of the RF magnetic field scales with the moment of the free layer. The incorporation of the high spin polarization magnetic materials will enhance the power efficiency of the STO. The frequency of the single mode precession of the STO depends on the anisotropy of the free layer as well as the magnitude of the applied direct current and external magnetic fields. Precession frequencies in the range 2 – 20 GHz have been observed in STOs already, and in principle this range can be readily extended by a factor of 2 or 3.

5. Two Dimensional Magnetic Recording (TDMR)

The final approach to high density recording is to reduce the number of grains per bit and operate at lower signal-to-noise. In this approach, two dimensional magnetic recording (TDMR) as shown in figure 10, a conventional recording medium with 20 Teragrains/in² is expected to record 10 Tb/in² (on average, each user bit is stored on 2 grains). Shingled-write, where each successive track partially overlaps and overwrites the previous track, with a specially designed “corner writer” will be necessary in order to maintain high write fields and to maximize both down-track and cross-track field gradients. Shingled-writing is viewed as essential even though it precludes “update-in-place” and may require a new interface protocol and a new, more complex, on-board data management system. Signal processing is done in two dimensions using information available across several adjacent tracks. This requires either an array head that reads many tracks simultaneously, or a single head that is progressively scanned to build up equivalent information in memory.

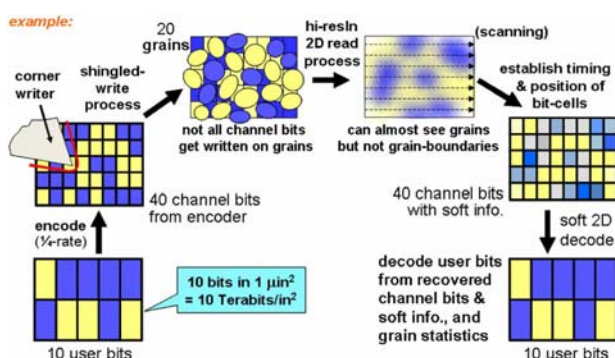


Figure 9 Example of TDMR recording proposal from ref. [4].

6. Outlook and Summary

We have introduced above a number of approaches to achieving areal densities beyond that possible with conventional magnetic recording media and systems. However, the growth in density cannot continue forever, assuming two dimensional storage and two level bits (up or down magnetization). This raises the question as to how far these proposed technologies can take us.

It is always dangerous to predict absolute limits, but a few challenges are worth noting:

- For TAR and MAMR, the grain size will be scaled with bit size. There will be some minimum number of grains required for obtaining the desired error rate, but this will depend partly on advances in signal processing (see TDMR). Using the anisotropy of L₁₀ FePt, the minimum stable grain diameter is around 3 nm [10]. Allowing for 0.5 nm of grain boundary, this implies 3.5 nm pitch or 9.6 nm² area. If we require 10 grains/bit, then the resulting density is around 7 Tb/in². In the extreme limit of adding TDMR with 2 grains/bit, this yields 35 Tb/in².
- A similar conclusion is drawn from an analysis of the lithography limits for BPMR. At 10 Tb/in² a square bit (bit aspect ratio 1), the bit cell is 8 nm x 8 nm, or 4 nm lithography. This is well beyond any lithography roadmaps, but is not physically

impossible with alternate lithographies such as self assembly. Extending this to 40 Tb/in² would require 2 nm lithography, and also 2 nm reader and writers. In addition, tolerances of 10% are required, which would now be atomic scale. While this may not be impossible, it would be quite a challenge!

In conclusion, we cannot state where the limit to magnetic recording will be, but a density in excess of a few tens of terabits per square inch appears to be beyond the envisioned engineering capabilities.

Acknowledgment We thank our many Hitachi colleagues in San Jose and in Japan for their contributions to this work.

References

- Terris, B.D. and T. Thomson, *Nanofabricated and Self-Assembled Magnetic Structures as Data Storage Media*. J. Phys D: Appl. Phys, 2005. **38**: p. R199-222.
- McDaniel, T.W., *Ultimate limits to thermally assisted magnetic recording*. Journal of Physics-Condensed Matter, 2005. **17**(7): p. R315-R332.
- Zhu, J.G., X.C. Zhu, and Y.H. Tang, *Microwave assisted magnetic recording*. IEEE Transactions on Magnetics, 2008. **44**(1): p. 125-131.
- Wood, R., et al., *The Feasibility of Magnetic Recording at 10 Terabits Per Square Inch on Conventional Media*. IEEE Transactions on Magnetics, 2009. **45**(2): p. 917-923.
- Richter, H.J., et al., *Recording on bit-patterned media at densities of 1 Tb/in(2) and beyond*. IEEE Transactions on Magnetics, 2006. **42**(10): p. 2255-2260.
- Schabes, M.E., *Micromagnetic simulations for terabit/in(2) head/media systems*. Journal of Magnetism and Magnetic Materials, 2008. **320**(22): p. 2880-2884.
- Yang, X., et al., *Challenges in 1 Terabit/ in.2 dot patterning using electron beam lithography for bit-patterned media*. J. Vac. Sci. Technol., 2007. **25**(6): p. 2202 -2209.
- Ruiz, R., et al., *Density multiplication and improved lithography by directed block copolymer assembly*. Science, 2008. **321**(5891): p. 936-939.
- Thomson, T., G. Hu, and B.D. Terris, *Intrinsic Distribution of Magnetic Anisotropy in Thin Films Probed by Patterned Nanostructures*. Phys. Rev. Lett., 2006. **96**: p. 257204.
- Weller, D. and A. Moser, *Thermal effect limits in ultrahigh-density magnetic recording*. IEEE Transactions on Magnetics, 1999. **35**(6): p. 4423-4439.
- Challener, W. et al., *Heat-assisted magnetic recording by a near-field transducer with efficient optical energy transfer*. Nature Photonics, 2009.

Electronic Design under New Alternatives to Solid-State Semiconductors

Carmen García, Antonio Rubio

Department of Electronic Design, Faculty of Telecommunication Engineers Campus Nord
UPC, c/ Gran Jordi Girona 1-3, 08034 Barcelona, Spain
cgarcia@eel.upc.edu, antonio.rubio@upc.edu

Abstract: This paper analyses the evolution of late and beyond CMOS technologies showing the relevant effect on the electronic design methods and rules due to the dramatic reduction of quality of the manufactured components. The paper argues that the main impact on such future technologies will be caused by the increase of the manufacturing defect ratio of components and circuits, the reduction of reliability through a huge increase of the error ratio and a drastic drop of the components quality. Consequently, new strategies of design have to be considered, among them the hierarchical fault tolerance that is presented in the paper. This fact will have implications in the design rules as we know them today.

Key Words: Technology evolution, integrated circuits, power consumption, low voltage operation, switching noise, thermal noise, manufacturing yield, fault tolerance.

1. INTRODUCTION

Today's most advanced integrated technology shows a miniaturizing level characterized by a manufacturing critical dimension of 32 nm. Following the scaling down of components predicted by Gordon Moore [1] we have seen a continuous miniaturization of the device sizes that in the last decade was located around the 350 nm generation. This last decade, from 350 to 90 nm nodes, the generations have been called the Pre-Giga transistor era. From 90 to 22 nm (a predicted feasible technology today) is called Giga transistor era and from 22 nm to the ultimate feasible size (presumably 12 or 6 nm) is called the Tera transistor era. The characteristics of the technology are evolving very fast due to the manufacturing constrains. For the Pre-Giga and older technologies, components were of high quality, with a low manufacturing defect rate that produced a high yield, because of the high voltage (>3.3 volts), the signal to noise figure (S/N) was very high allowing a robust logic, the "zero defects" objective could be reached thanks to an efficient test technology and, to summarize, in general we had highly reliable technologies.

For the Giga and Tera Eras things are changing. First, manufacturing is exhibiting critical levels of parameter variability due to manufacturing process limitations. Consequently, components are showing limited quality and causing a moderate if not low manufacturing yield. Moreover, because of the continuous reduction of the power supply voltage (<1.1 volts, because of the reliability requirements for the thin oxide of the transistors) switching noise is causing great problems and a significant performance limitation.

Finally due to the high speed and complexity of circuits test technology, the efficiency of years past is being lost and components may reach the market with faults.

As we mention in the following section, new nanotechnologies, based on the so-called emerging research devices (ERD) will keep the trend of miniaturization alive and will increase component density. These extremely sophisticated and powerful technologies, however, will not be rid of all these problems we have mentioned above, just the opposite. Quality will be extremely low, the defect rate will be very high, and voltage will be scaled so low that the S/N figure will easily reach 0 dB causing a high rate of transient, dynamic or soft errors. Yield will be practically zero and if we do not change design rules testing will be operative no longer.

In Section 2, the characteristics of the technology in the year 2020 and beyond are discussed, analyzing the potential manufacturing yield for those technologies. Section 3 deals with the key limiting aspect of these future technologies: reliability; the two main components of such limiting situation will be shown: power dissipation and thermal limits. Section 4 shows and analyzes the main mechanism to design acceptably robust systems even from low quality components: the use of fault tolerant redundant circuits. Section 5 introduces a new concept, the hierarchical fault tolerance technique, which presumably will be the future design paradigm with a continuous improvement of reliability thanks to the use of fault tolerant mechanisms in all the design flow level. Finally Section 6 summarizes a general discussion of the design future and draws several conclusions

2. THE TECHNOLOGY IN THE YEAR 2020 AND BEYOND

The International Technology Roadmap for Semiconductors (ITRS, [2]) predicts a potential CMOS technology capable of integrating 100 Giga-transistors in a single integrated circuit for the year 2020. This will imply the capability to integrate between 22 and 40 CPU cores or more than one thousand components like Silicon on Circuits cores or IPs. Components like Resonant Tunneling Devices [3], Single Electron Transistors [4], Molecular electronics [5], ferromagnetic logic [6], spin transistor logic [7] and memistors-based technologies [8] among others, that will be new at that time and are now under research will be ready for commercial applications. All these beyond CMOS technologies will exhibit critical dimension near to molecular or atomic sizes down to 1 nm. The main implication of such a reduced size of components will be a huge device density, around 10^{12} gates/cm² [9] and with a huge device error rate, around 10^8 higher than late CMOS technology (see figure 1). This will mean a practically null effective manufacturing yield.

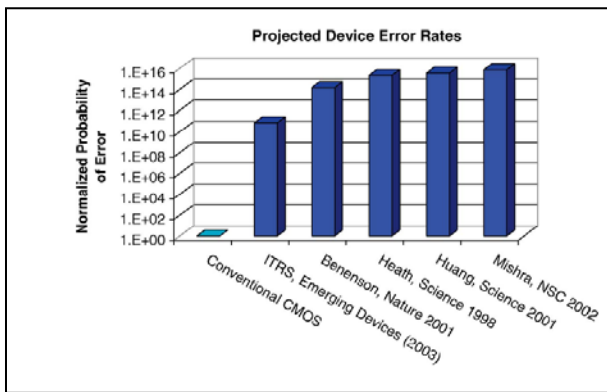


Figure 1. Projected device error rates for future technologies [9].

Probability of component defect	Number of devices			
	Error Prob.	10^6	10^8	10^{10}
10^{-6}	0.367	10^{-44}	0	0
10^{-8}	0.99	0.367	10^{-44}	0
10^{-9}	0.999	0.63	10^{-30}	0
10^{-10}	0.9999	0.99	0.367	10^{-44}
10^{-12}	0.99999	0.9999	0.99	0.367

Table 1. Yield prediction for different circuit complexities and component error probabilities.

Nowadays technologies (CMOS-based) are already showing a yield reduction trend. As a matter of example, a mature product yield for a 250 nm technology node was 90%; however, for a 45 nm technology node the effective yield is around 55%. This implies, as it is well accepted, a 5% average yield decrease per node [10].

In order to evaluate this yield (55%) in terms of component defect probability, assuming a component complexity of 10^9 components for the 45 nm technology we calculate a probability of 10^{-10} of component failure.

Table 1 shows the yield prediction for different complexities and component defect probabilities. Observe the sharp trend of yield towards zero when both components increase as predicted in Figure 1 [9]. As a matter of example of potential defect rates for future ERD, we can mention the results published in [11] where a chemically assembled electronic technology with a component density of 10^{10} gate-equivalents/cm² exhibit a 0.1 (10%) defect rate, and the molecular electronic memory shown in [12] that with a component density of 10^{11} bits/cm² shows a 0.25 (25%) defect rate. If all these technologies would be manufactured massively as we do today with CMOS, the yield would be dramatically unacceptable. However, there is still some hope for future technologies if practically perfect atomic positioning, as have been shown recently by using AFM. In the future it could be compatible with high complexity circuits and high production levels, in this case perhaps we could manufacture perfect components as Gordon Moore predicted in [13] "There is no fundamental obstacle to achieve device yields of 100%". However, in the next section we will discuss a critical problem for future technologies: power consumption.

3. A common danger for all future technologies: lack of reliability

In this section we will show that power dissipation is a current limitation for technologies and that there is an unavoidable limit: the thermal limit. Both will affect future circuits with a dramatic reduction of reliability.

3.1 Power dissipation limit.

Power dissipation is a key limiting drawback for modern technologies. As indicated in [14], modern CPUs dissipate around 100 watts getting close to the power density limit of 100 W/cm². The trend for the next decade is a huge increase in power density, around 20 times as much as that reached in 2006 for 2018 (see figure 2), and this would cause, even with efficient heat sinks, temperatures in the circuit of around 500 °C, a value that is not acceptable at all. The only solution for such complex technologies will be to reduce the power supply voltage which has a key impact on power dissipation. However, this effect will also have an impact on the error rate as the following section shows.

3.2 Low Voltage Design

There is a trend of reduction of the power supply voltage in CMOS technologies, due to the stress caused by the electric field in the thin oxide of the transistor. However, it is also a required condition if technologies keep increasing density in order to limit device temperature. Let us now evaluate the operation energy evolution for CMOS technologies until 2020 that is shown in figure 3.

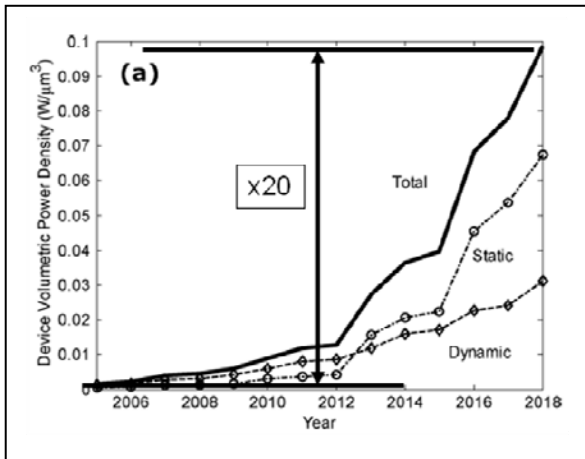


Figure 2. Forecast increase of power density in the next decade.

As the figure shows, the energy for an unitary operation (transition in a inverter gate) has been decreasing in the last decades predicting a value of 1 aJ (atto joule) in 2020. This trend agrees also with the switching energy predicted for Emerging Research Devices (Single electron transistors, molecular electronics ...) as indicated in ITRS [1].

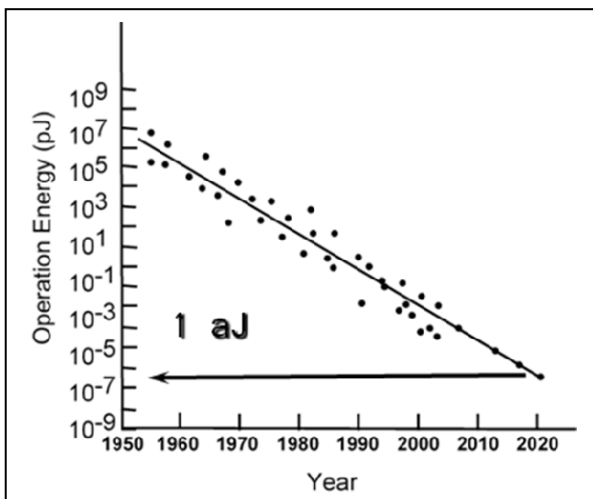


Figure 3. Evolution of the unitary operation energy for CMOS technologies.

The main noise source in modern digital circuits is the one caused by the digital circuit itself when it suddenly switches currents through parasitic components, called switching noise. In [15], a level of switching noise equivalent to 20% of the power supply voltage level in CMOS is predicted for 2020. In the case of digital circuits this voltage fluctuation causes a fluctuation in the propagation delay that is a cause of performance degradation. This could imply an error probability of 10^{-14} in every atomic processing cycle in the year 2020, according to [16]. New design strategies towards the reduction of transitions and even the implementation of clock-less circuits (asynchronous) are being developed. However, even with the advance of such future design strategies there is a factor that cannot be avoided, i.e. the thermal noise caused by molecular agitation of particles in

materials due to heat. Even though the level of thermal noise is lower than today's switching noise, it will be a key limit for future technologies (figure 4) as explained in the following section.

3.3 Thermal noise impact

Thermal noise is an unavoidable noise that for low voltage (low power) future technologies could imply a key limiting aspect. In [16], the error rate caused by thermal noise for a given energy operation was investigated. Figure 5 shows this relation, taken from [16], and the vertical arrow indicates the energy corresponding to the CMOS technology in 2020. This implies an error rate of 10^{-28} . If we consider now that the error rate for future ERD technologies is 10^8 times higher than for the CMOS, we obtain an error rate for processors made with ERD and working at low power of 10^{-20} . This error rate is equivalent to 5 errors per minute, which is too high to be considered a robust technology: it is unacceptable.

Transient faults or errors cause a temporary change in state of the system, without damaging any of the components. Because of their random and non-recurring nature, transient faults are difficult to solve, tolerate or isolate, hence they become a source of major concern, especially in critical real-time application areas.

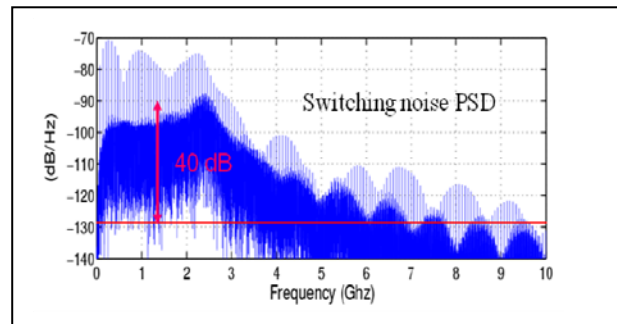


Figure 4. Comparison of switching noise and thermal noise levels.

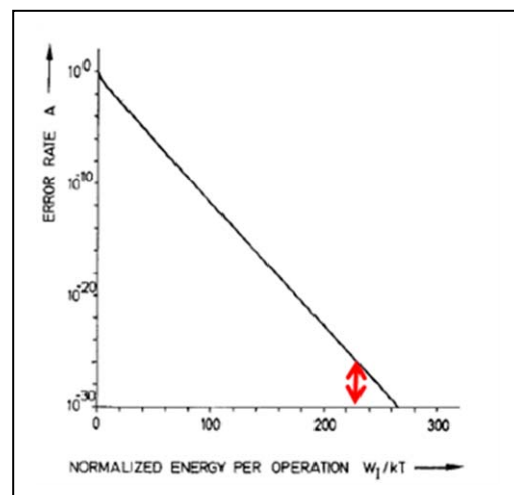


Figure 5. Error rate versus normalized energy per operation. Red arrow marks CMOS technology in 2020 operating at room temperature [16].

3.4 Unacceptable possible scenario

From the results shown above we can predict a low quality, unacceptable technological scenario for the future. We

have seen that in terms of manufacturing yield, with the techniques used until now we can expect a zero manufacturing yield. Perhaps in the future we will learn to position atom by atom in the right place. This would imply a 100% error-free manufacturing yield, but we do not know the efficiency of such a technology in terms of number of manufactured components per unit of time. Power supply is another limiting aspect; with the CMOS voltage scaling down trend we will reach temperatures higher than 500 °C. In case of drastic voltage reduction this would imply a dramatic reduction of performance in CMOS designs and an unacceptable error rate for ERD technologies in one or two decades. Until now integrated circuits have been designed considering a high quality component scenario, in such a way that with an efficient quality test procedure it was possible to have both a zero defect delivery to market and a high manufacturing yield. In the future, yield will decrease and test techniques could be inefficient (detecting all the components as defective). However, in 1956 [17], the solution to improve reliability of complex systems was already introduced by von Neumann: the use of fault tolerant systems. Fault tolerance implies redundancy of resources and this redundancy can be of hardware, of codes and of time. All three are equivalent and because future technologies will exhibit a huge number of component density we will consider hardware redundancy in the rest of the paper.

4. Fault tolerance techniques

4.1 Successful fault tolerance precedents

One of the most referenced examples related to fault tolerance of systems with a medium/high ratio of defective components is the reconfigurable architecture of TERAMAC designed by HP researchers [18]. In this example, a computer is organized from a reconfigurable structure made up of around 8 million components (220 thousand programmable logic cells, 145 thousand interchip elements and millions of crossbars). The system showed to be efficient to tolerate 10% of defective programmable cells. The principle of tolerance was based on reconfigurability; first a whole testing phase determined the set of defective components, later the systems were reconfigured using healthy components only, avoiding the use of defective ones. This is one of the principles of the reconfiguration technique, test-find-replace. The same technique is used in reconfigurable memories, which integrate sparse components, or even in multi-core systems where in every startup the systems test the cores and cancel the defective or marginal ones.

In spite of the apparent success of this technique, it cannot be used in computers that exhibit transient errors as are those caused by noise, the unavoidable source. The test of the whole systems takes time decades higher than the period of appearance of transient faults. Another drawback is that the method is not efficient if defect rate is very high, which is the case we expect in nanodevice architectures. In the scenario of nanosystems, we will find a significant number of defects at any level, section or subsection.

4.2 Other fault tolerant techniques adequate for transient errors

Hardware fault tolerant structures implemented through the use of massive redundancy have been reported previously [19,20,21]. The more relevant are: NAND multiplexing, N-modular redundancy (TMR) and averaging cells.

The NAND MULTIPLEXING technique was introduced by Von Neumann in 1956 [19]. The design is based on the implementation of a functional gate into three stages: executive stage, restorative stage and output stage. In each one of these stages the redundancy is given by N (with typical values of 100 or 1000). Figure 6, shows the results of this technique for three different levels of redundancy (N, 10, 100 and 1000). Observe that for high values of N the error probability is limited even for a significant individual gate error rate. However, many publications [20] have shown that this technique has a limitation, because the system is not able to tolerate global errors when the individual error rate is higher than 1% approximately.

The NMR or TMR TECHNIQUES. NMR, TMR are based on the use of a N-tuple or triple modular redundancy of the basic system. The system evaluates answers from the N or 3 modules and assumes as good the one voted in majority [19]. The system is simple and efficient but only for very low error rates as shown in figure 7.

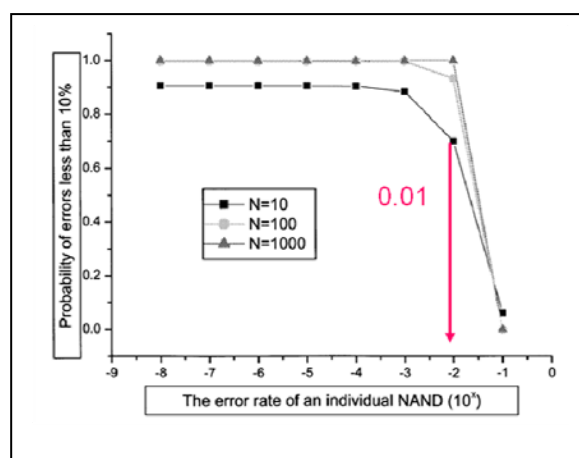


Figure 6. Error tolerance caused by NAND multiplexing versus individual error rate.

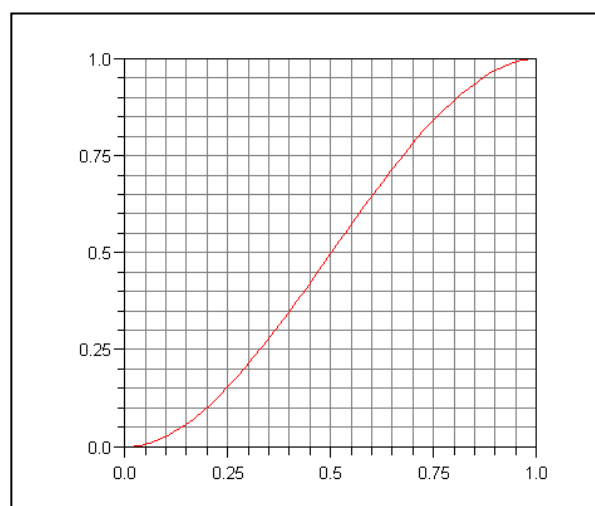


Figure 7. Error tolerance caused by TMR. The vertical axis is the error rate of the TMR system and the horizontal the error probability of each one of the three components.

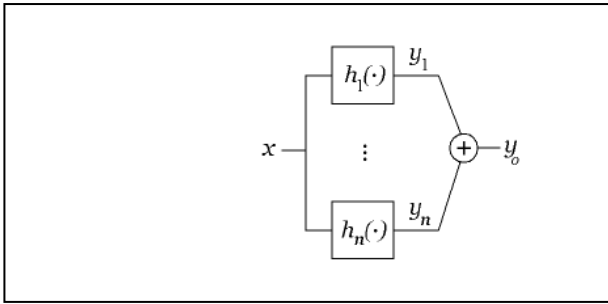


Figure 8. Schematic structure of the tolerant averaging cell

The AVERAGING CELL. This technique is based on the compensation of imperfect components. Published first in [21], it is a very efficient technique for even very high error rates, and it is adequate for molecular electronics where each component is implemented from a bunch of parallel molecules. The system exhibits a very high applicability for defect tolerance, deviation tolerance and noise tolerance. Figure 8 shows the basic structure of the cell and figure 9 shows the comparison of the error tolerance between the averaging cell with two different levels of redundancy and a NAND multiplexing with $N=100$. Observe that the NAND multiplexing is not efficient for individual error rates close to 0.01 and that the averaging cell satisfies the tolerance principle.

Figure 10 shows the comparison between the different fault tolerance mechanisms, including reconfigurability, showing how they cover different individual error rates with different efficiencies. This fact will be used in the following section to propose a new design technique.

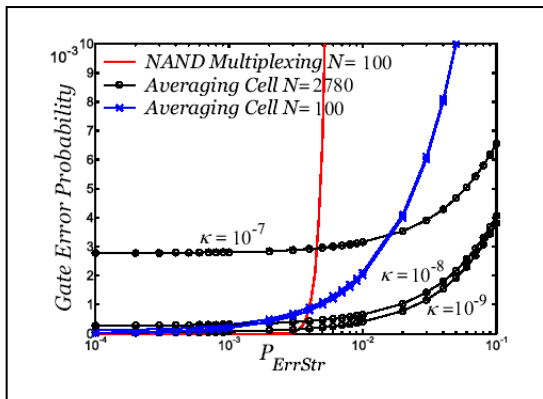


Figure 9. Comparison between Averaging cell and NAND multiplexing.

The main points we can conclude from these previous sections are: Fault tolerant techniques are not magical solutions for low quality components. The main effect of these mechanisms is that they usually reduce the error rate of the global block in comparison with the error rate of the individual components. The efficiency of this reliability improvement exhibits a limit for high error rate, at different levels for different mechanisms. The only one that is able to deal with very high error rate is the Averaging cell based on a compensating mechanism. Figure 10 shows that the required redundancy is very dependent of the individual error rate and the fault tolerance mechanism. All these concepts point to the proposal put forward in the following section.

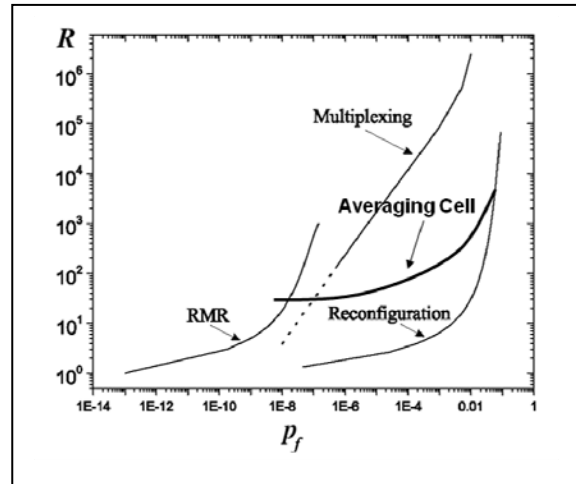


Figure 10. Comparison between the different tolerant mechanisms. Vertical axis is the redundancy factor, R , and the horizontal the component error probability.

5. Hierarchical fault tolerance strategy.

Because of the dramatic impact of very low quality components offered by future nanotechnologies, design methodologies have to take into account design for reliability improvement techniques in the same way than what happened in the past with the introduction of design for testability rules in design flow. In the future, designers will have to set the design of robust designs (adequately robust for the specific application) as their objective and this hardware will have to be implemented from very low quality and low reliable components.

As a practical solution, we propose the use of the hierarchical structure of the electronic design flow as a iterative mechanism of reliability improvement. This idea was first presented in [22]. Figure 11 shows an example of this strategy, where the different design flow levels (technology, transistors, circuit, gates, logic blocks ...) are used to improve the reliability (the arbitrary numbers inside the column give idea of a continuous reduction of the error rate). Also in order to illustrate the concept, different fault tolerant mechanisms are applied to every stage of the design.

For many years the mission of testing has been described as screening defects and to a lesser extent speed classification. Perhaps the common mission of tests and design has to be extended to screening for reliability.

Each design layer will base its structure on “components” coming from the previous layer with a given reliability (never perfect components). This layer not only will implement new components of a higher design hierarchy, but it will introduce fault-tolerant mechanisms (those adequate for the error rate level of the components) that will improve (not solve) the reliability offered to the next layer.

This will allow different orders of reliability improvement until the final level is reached with an adequate quality.

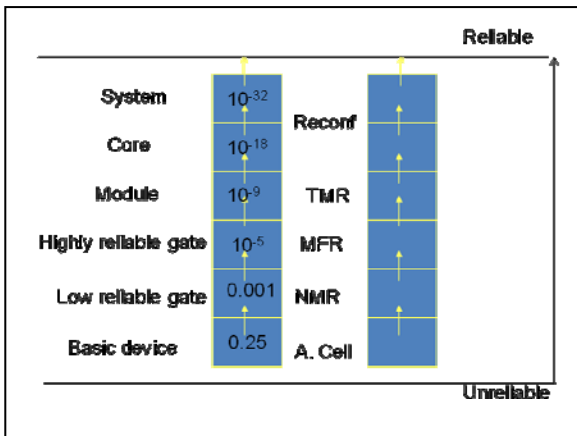


Figure 11. Example of hierarchical multiple coordinated fault tolerance strategy taking benefit from the well known hierarchical design flow.

6. CONCLUSIONS

We can accept the prediction that future technologies will exhibit components with a high defect rate and a high rate of transient errors. The sophisticated manufacturing process and the high level noise caused by the chip itself (switching noise) will be the main limiting point for CMOS technologies in the coming years. These drawbacks or limitations will be very likely solved with the evolution of technologies and new design styles. However there is one source of error that is unavoidable, the one caused by thermal noise. Thermal noise is the cause of a very high transient error rate, due to the equality of the noise and signals levels (the latter because of the necessary power dissipation limitation in order to operate within a feasible temperature range). In order to tolerate these errors the use of hardware redundant circuits like the ones introduced by von Neumann half a century ago will be required. All these mechanisms require massive redundancy, but this will not be a problem in such future technologies where we expect decades of higher component density. However, a detailed analysis of the mechanisms show there are not a panacea. NAND multiplexing as a matter of example with a level of redundancy $N=100$ is very efficient to tolerate transient error up to an individual error rate of around 0.01. Averaging cell needs a much higher redundancy factor, but it is adequate for very high error rate (even for levels close to 1). TMR is very efficient with a redundancy requirement of 3, but it fails when individual error rate takes moderate values. From all this the authors suggest a hierarchical fault tolerance strategy, where different fault tolerance mechanisms are used at different levels of component complexity. This implies an strategy of reliability-aware technique that can be implemented together with the hierarchical flow of electronic system design. Consequently, the solution for robust systems is not only in the hands of manufacturers, as in the past, but in each and every one of the basic steps of the design flow.

Acknowledgements

These results are part of research project TEC2008/01856 of the Science and Innovation Ministry in Spain, the project is also financed by FEDER funds.

REFERENCES

- [1] Gordon E. Moore "Lithography and the future of Moore's Law", Proc. SPIE, Vol. 2439; DOI:10.1117/12.209195
- [2] International Technology Roadmap for Semiconductors Report, www.sematech.org
- [3] P. Mazumder, et al., "Digital circuit applications of resonant tunneling devices", Proc. IEEE, April 1998, Vol. 86, issue 4. DOI: 10.1109/5.663544
- [4] R.H. Chen et al., "Single electron transistor logic", Appl. Phys. Lett. 68, 1954 (1996); DOI:10.1063/1.115637
- [5] Avi Aviram, "Molecular electronics, Science and Technology", Angewandte Chemie, Vol. 28, issue 4 (2003), DOI: 10.1002/anie.198905201
- [6] D.A. Allwood et al., "Submicrometer ferromagnetic NOT gate and shift register" Science 14, June 2002, Vol. 296, no. 5575, DOI: 10.1126/science.1070595
- [7] G. Zorpette, "The quest for the SPIN transistor", Spectrum IEEE, Vol. 38, issue 12 (2001), DOI: 10.1109/6.969357
- [8] D.B. Strukov et al., "The missing memristor found" Nature 453, (2008), DOI: 10.1038/nature.06932
- [9] AJ KleinOowski and David J. Lilja. "The NanoBox project: Exploring fabrics of selfcorrecting logic blocks for high defect rate molecular device technologies. In IEEE Symposium on VLSI, pages 1–10, 2004.
- [10] Source: Selantec 2007.
- [11] M. Mishra and S.C. Goldstein, "Defect tolerant at the end of the roadmap", Nano, Quantum and Molecular Computing, Springer, US, DOI: 10.1007/b116438
- [12] J.E. Green et al., "A 160-kilobit molecular electronic memory patterned at $10E(11)$ bits per square centimeter" Nature, 445 (2007), DOI: 10.1038/nature05462
- [13] G. Moore, "VLSI: Some fundamental challenges", IEEE Spectrum 1979.
- [14] E. Pop et al, "Heat Generation and transport nanometer-scale transistors" Proceedings IEEE, Vol. 94, issue 8, (2006), DOI:10.1109/JPROC.2006.879794
- [15] D. Andrade et al., "Power supply noise and logic error probability", Proc. European Conference on Circuit Theory and Design 2007, DOI: 10.1109/ECCTD.2007.4529559
- [16] K.U. Stein, "Noise-induced error rate as limiting factory for energy per operation in digital ICs", IEEE Journal Solid-State Circuits, Vol. 12, issue 5, 1977, pp. 527-530.
- [17] J. von Neumann et al., "Automata Studies", Annals of Mathematical Studies, Princeton University Press.
- [18] R. Amerson et al., "Teramac configurable custom computing", IEEE Symp. On FPGAs for Custom Computing Machines, 1995, DOI: 10.1109/FPGA.1995.477406
- [19] K. Nicolik et al., "Fault-tolerant techniques for nanocomputers", Nanotechnology 13, 357-362, 2002, DOI: 10.1088/0957-4484/13/3/323
- [20] K. Nicolik et al., "Architectures for reliable computing with unreliable nanodevices" IEEE Conf. on Nanotechnology, 2001, pp. 254-259, DOI: 19.1109/NANO.2001.966429
- [21] F. Martorell et al., "An analysis of internal parameter variations effects on nanoscaled gates" IEEE TR. On Nanotechnology, Vol. 7, no. 1, 2008, pp. 24-33, DOI:10.1109/TNANO.2007.913429
- [22] S. Cotozana et al., "A design exploration framework for reliable nano electronics", Proc. 2005 IEEE Conf. on Applied Specific Systems, Architecture Processors, pp. 260-267.

Direct Observation of Microscopic Magnetic Structures in Materials by Electron Phase Microscopy

A. TONOMURA

Advanced Research Laboratory, Hitachi Ltd., Hatoyama, Saitama 350-0395, Japan
Advanced Science Institute, RIKEN, Wako, Saitama 351-0198, Japan
Initial Research Project, Okinawa Institute of Science and Technology, Kunigami,
Okinawa 904-0411, Japan

akira.tonomura.zk@hitachi.com

Abstract: Electron phase microscopy based on the Aharonov-Bohm (AB) effect principle has been used to illuminate fundamental phenomena concerning magnetism and superconductivity by visualizing quantitative magnetic lines of force. These phenomena include the magnetization process of tiny magnetic heads for perpendicular recording.

Key Words: Quantum Phenomena, Electron interference, Phase

1 INTRODUCTION

Although electrons are detected as particles, they also show wave properties. Thanks to the development of brighter field-emission electron beams, we can now practically use the wave nature of electrons to directly image the quantum world by obtaining the phase information of electrons [1]. Projected magnetic lines of force can be quantitatively observed as phase contours of transmitted electrons by using holographic interference microscopy [2], since a phase shift of 2π is produced between two electron beams enclosing a magnetic flux of h/e due to the Aharonov-Bohm (AB) effect [3], and quantized vortices in superconductors can be dynamically observed by Lorentz microscopy [4].

This paper describes the challenges we faced in our efforts to investigate magnetic properties of magnetic heads used for perpendicular recording.

2 EXPERIMENTAL METHOD

We carried out experiments on the magnetic-field observation of magnetic heads and superconductors using 1-MV and 300-kV field-emission transmission electron microscopes. Projected magnetic lines of force of magnetic heads were directly observed as contour lines in the interference micrographs obtained from electron

holograms formed with electron biprisms [1].

3 EXPERIMENTAL RESULTS

Magnetic lines of force radiating outward from a tiny magnetic head were observed as holographic interference micrographs [6] (Fig. 1 (a)). This head is used for high-density perpendicular recording, so it must produce a very high and yet localized magnetic field. A strong magnetic field is rather simple to produce. However, this is not sufficient. We also need to be able to reproducibly control magnetic fields in any way we want. For example, we need to get a zero field outside the head, which sometimes poses difficulties, since the density of magnetic lines inside ferromagnets is a constant determined by the strength of the magnetization.

In the case of our FeNi head, straight magnetic lines inside the head were changed to "U-turn" lines [6] (Fig. 1 (b)) by reducing the applied magnetic field to zero. At the pole tip, which is used to localize magnetic fields, the magnetic lines formed a tiny closed circuit. The two distributions in (a) and (b) of magnetic lines are both symmetrical.

The problem is how to change straight lines into U-turn lines so that the outside magnetic lines disappear. The series of Lorentz micrographs in Fig. 2 show how this is done. When the applied magnetic

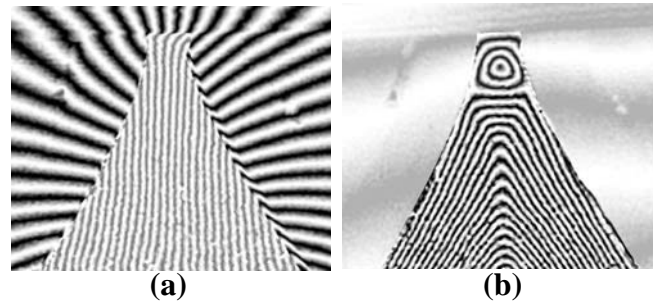


Figure 1 Interference micrographs showing magnetic lines of force of a FeNi magnetic head for perpendicular recording: (a) ON; (b) OFF.

Magnetic lines are produced radially from the magnetic head when it is magnetized in the upward direction by applying an external magnetic field ((a)). When the magnetic field is removed, magnetic lines outside the head almost disappear, since magnetic lines inside it form a closed circuit ((b)). These patterns are both symmetrical. The question arises how magnetic lines inside the head change from straight lines ((a)) to U-turn lines ((b)).

field was reduced from 120 to 80 Oe, the straight magnetic lines inside the head ((a)) begin to bend from below ((b)). This bent region moved upward ((c)) when the magnetic field was further reduced. The reason for this movement is evident from the pictures. The U-turn lines appeared from the lower left in (c), pushing the “bent magnetic lines” up.

The U-turn lines gradually moved upwards ((d) and (e)) and finally covered the whole head region ((f)). The “bent magnetic lines” finally changed into closed circles at the tip.

The leakage magnetic field gradually decreased from (a) to (f) and almost vanished in the remanent state (f), where all the magnetic lines inside the head were closed, restoring the pattern symmetry.

4 CONCLUSIONS

Thanks to recent developments in advanced technologies such as coherent yet bright electron beams, the wave nature of electrons can now be used to observe microscopic objects previously unobservable by conventional electron microscopy. Electron phase microscopy in a field-emission electron microscope is expected to play a more and more important role in future research and development not only in nanotechnology but also in biology, since microscopic information about materials reaching down even to atoms and molecules has become more pivotal.

References

- [1] Tonomura, A., “Direct observation of thitherto unobservable quantum phenomena by using electrons”, Proc. Natl. Acad. Sci. USA, Vol.102, No. 42, pp. 14952-14959, (2005).
- [2] Tonomura, A., Matsuda, T., Endo, J., Arii T. and Mihama K., “Direct observation of fine structure of magnetic domain walls by electron holography”, Phys. Rev. Lett., Vol.44, No. 21, pp. 1430-1433, (1980).
- [3] Aharonov, Y. and Bohm, D., “Significance of Electromagnetic Potentials in Quantum Theory”, Phys. Rev., Vol.115, pp. 485-491, (1959).
- [4] Harada, K., Matsuda, T., Bonevich, J., Igarashi, M., Kondo, S., Pozzi, G., Kawabe U. and Tonomura, A., “Real-time observation of vortex lattices in a superconductor by electron microscopy”, Nature, Vol. 360, pp. 51-53, (1992).
- [5] Tonomura, A., Akashi, T., Kasai, H., Mamishin, S., Yoshida, T., Matsuda, T., Tajima S., Tadatomo, H., Masui T. and Buzdin, A., (2009) to be submitted.
- [6] Kim, J. J., Hirata, K., Ishida, Y., Shindo, D., Takahashi, M. and Tonomura, A., “Magnetic domain observation in writer pole tip for perpendicular recording head by electron holography”, Appl. Phys. Lett., Vol.92, pp. 162501-1-162501-3, (2008).

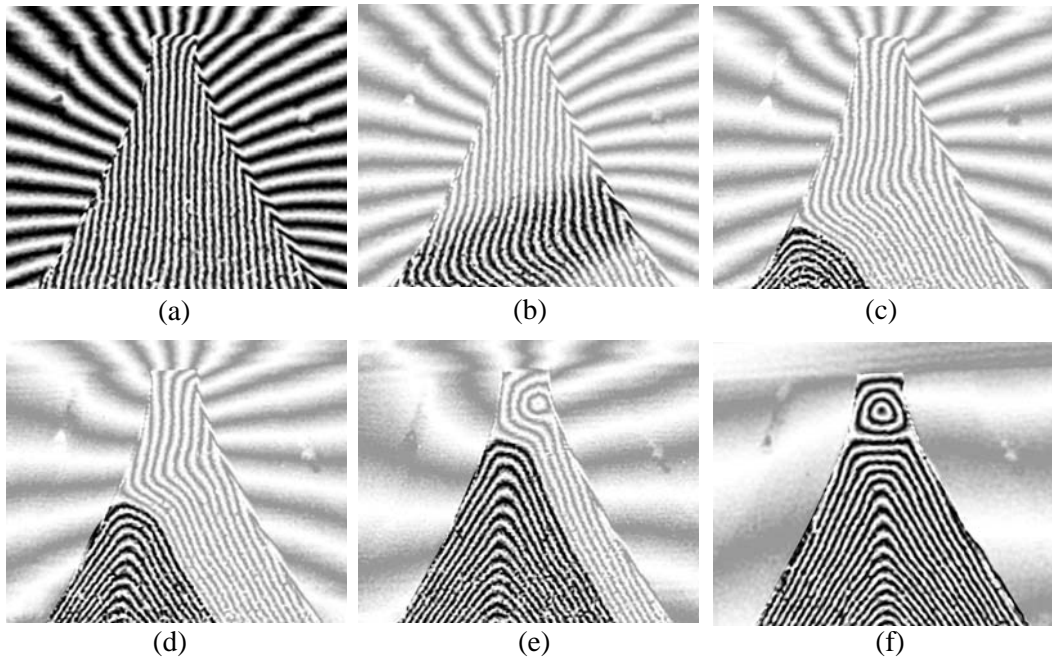


Figure 2 Interference micrographs showing how magnetic lines inside the head change from straight lines to U-turned lines when the applied magnetic field decreases: (a) $H = 120$ Oe; (b) $H = 80$ Oe; (c) $H = 60$ Oe; (d) $H = 35$ Oe; (e) $H = 15$ Oe; (f) $H = 0$ Oe. U-turn lines appear from the lower left ((c)) and move upwards pushing the region of bent magnetic lines ((d), (e)). The patterns of magnetic lines are no longer symmetrical. The bent magnetic lines form circular closed circuit in the remanent state in (f).

Modification of Titania Based Photocatalysts for Solar Chemical Conversion

Wonyong Choi, Yiseul Park, Jihee Park, Wooyul Kim, and Jungwon Kim

School of Environmental Science and Engineering, Pohang University of Science and Technology, Pohang 790-784, Korea

wchoi@postech.edu

Abstract: Solar energy utilization (solar chemical conversion) through semiconductor photocatalyst has been intensively investigated for both environmental and energy applications. However, pure titania has low activity for solar chemical conversion and its property should be modified in various ways. (1) TiO₂ samples sensitized with ruthenium complexes, fullerol were prepared and tested for the hydrogen generation and pollutant degradation under visible light irradiation. (2) TiO₂ surface was modified with alumina oxide or CNT to increase the efficiency of the photoinduced electron transfer. (3) The simultaneously platinized and fluorinated TiO₂ (F-Pt/TiO₂) was also compared with F-TiO₂ and Pt/TiO₂ for the generation of hydrogen under UV illumination. In the case of F-TiO₂/Pt, the hydrogen production was highly enhanced in the presence of 4-chlorophenol, which realized the simultaneous degradation of organic substrates and the production of hydrogen.

Key Words: solar chemical conversion, surface modification, photocatalyst

1 INTRODUCTION

Solar energy utilization through semiconductor photocatalysis has been intensively investigated for both environmental and energy applications.^[1] Heterogeneous photocatalytic reactions are mostly surface chemical reaction and the surface properties of the semiconductor play a critical role in determining the reaction efficiencies and mechanisms. The surface properties of TiO₂, the most popular semiconductor photocatalyst, are related with various parameters that include pH, surface charge, surface hydroxyl group density, particle size, crystalline phase, surface defects, surface metal deposits, and adsorbates or surface complexes. TiO₂ surface can be actively modified by manipulating the above parameters in order to optimize or control the photocatalytic reactions. This talk will introduce and discuss various examples that show how surface modification influences the photocatalytic activities in relation with pollutant degradation and hydrogen production.

TiO₂ was sensitized with Ru-complex dye and fullerol(water soluble C₆₀) to maximize the utilization of visible light. We can find the unique sensitization effect with fullerol that is absent in C₆₀. We introduce alumina oxide layer or CNT to the TiO₂ surface to enhance the electron transfer efficiency. The simultaneously platinized and fluorinated TiO₂ (F-Pt/TiO₂) was also compared with F-TiO₂ and Pt/TiO₂ for the generation of hydrogen under UV illumination.

2 EXPERIMENTAL

The methods of surface modification of TiO₂ include dye

sensitization, surface platinization, surface fluorination, surface complexation with fullerol, nafion coating with CNT.

Fullerol/TiO₂ sample was prepared by dispersing 0.1 g of TiO₂ powder in 100 mL aqueous fullerol solution (45 μM) at pH 3. The solution was stirred for 3 h, and then the fullerol/TiO₂ was collected by filtering. Al₂O₃-overcoated TiO₂ (Al₂O₃/TiO₂) was synthesized via a sol-gel method. Pt deposition on the surface of Al₂O₃/TiO₂ was done by the photocatalytic reduction. We also demonstrate that the visible light-sensitized production of hydrogen with a hybrid photoanode containing Ru(bpy)₃²⁺ (bpy = bipyridine), nafion (Nf: cation exchange resin that is perfluorinated polymer with sulfonate groups), and TiO₂ nanoparticles is highly enhanced with incorporating carbon nanotubes (CNTs) in the photoanode. Hybridizing Nf film with CNTs and TiO₂ nanoparticles enables the fabrication process of the sensitized photoanode to be free from the preparation of the derivatized sensitizers (*for surface anchoring*) as well as the heat treatment (*for sintering*). Pt deposition on the surface of TiO₂ was done by photocatalytic reduction of chloroplatinic acid (Pt content = 3.7 wt%) in the presence of methanol as an electron donor. For the fluorination of the TiO₂ surface, 10 mM NaF was added into the aqueous suspension of Pt/TiO₂ and then pH was adjusted to 3 to maximize the fluoride adsorption.

A 300-W Xe-arc lamp was used as the visible light source in the photocatalytic activity test. Light passed through a 10-cm IR water filter and a cutoff filter ($\lambda > 300$ or 420 nm), and then the filtered light was focused onto a 30(or 50) mL reactor.

3 RESULTS AND DISCUSSION

3.1 Fullerol-modified TiO₂ [2]

C₆₀-based sensitized photocatalysis that works through the charge transfer (CT) mechanism was proposed and tested as a new approach. By employing the water-soluble fullerol (C₆₀(OH)_x) instead of C₆₀, we demonstrated that the adsorbed fullerol activates TiO₂ under visible light irradiation through “surface-complex CT” mechanism that is largely absent in the C₆₀/TiO₂ system. While fullerene and its derivatives have been often utilized in TiO₂-based photochemical conversion systems as an electron transfer relay, their successful photocatalytic application as a visible light sensitizer of TiO₂ is not well established. Fullerol/TiO₂ exhibits the marked visible photocatalytic activity for not only the redox conversion of 4-chlorophenol, I⁻ and Cr(VI) but also H₂ production. The photoelectrode of fullerol/TiO₂ also generates an enhanced anodic photocurrent under visible light as compared with the electrodes of bare TiO₂ and C₆₀/TiO₂, which confirms that the visible-light induced electron transfer from fullerol to TiO₂ is particularly enhanced.

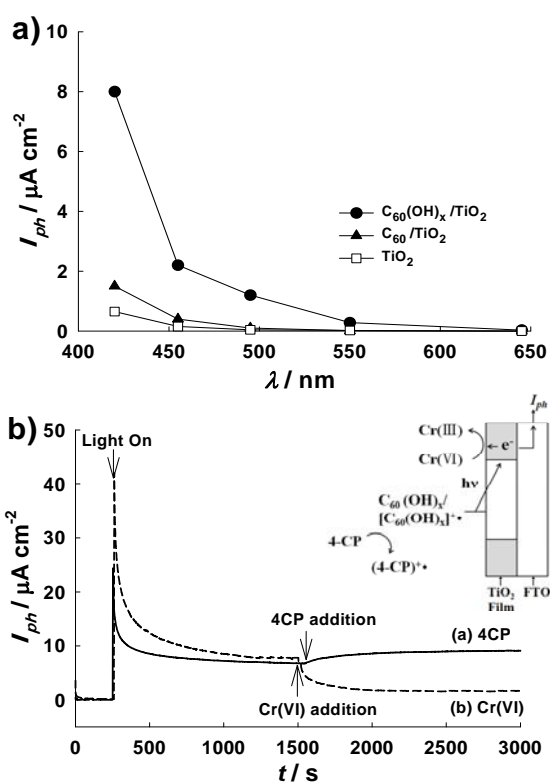
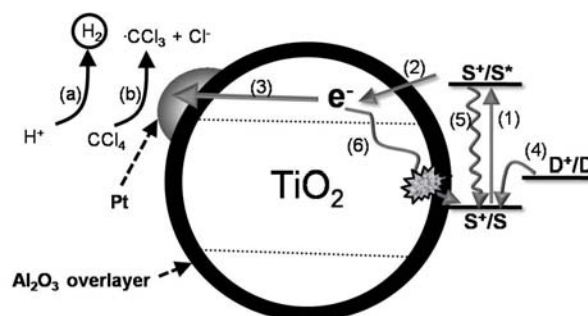


Figure 1. (a) I_{ph} generated from TiO₂, C₆₀/TiO₂, and fullerol/TiO₂ electrode as a function of the excitation wavelength. The wavelength in the abscissa refers to the cutoff λ of the long-pass filter (*i.e.*, irradiation $\lambda \geq$ cutoff λ). (b) I_{ph} change upon spiking an aliquot of 4-CP (250 μM) or Cr(VI) (200 μM) in the illuminated electrochemical reactor with the fullerol/TiO₂ electrode. [LiClO₄] = 10 mM, N₂-saturated condition, $\lambda > 420$ nm.

The surface complexation of fullerol/TiO₂ induced a visible absorption band around 400-500 nm, which was extinguished when the adsorption of fullerol was inhibited by fluorinating the surface of TiO₂. The transient absorption spectroscopic measurement obtained the absorption spectra that is ascribed to the fullerol radical cations (fullerol^{•+}) whose generation should be accompanied by the proposed CT. The theoretical calculation regarding the absorption spectra for the (TiO₂ cluster+fullerol) model also confirmed the proposed CT that involves the excitation from HOMO (fullerol) to LUMO (TiO₂ cluster) as the origin of the visible light absorption.

3.2 Dye-sensitized TiO₂ with thin overcoat of Al₂O₃ [3]

The essence of dye sensitization is the electron injection from the excited dye to conduction band (CB) of TiO₂ and the subsequent interfacial electron transfer. The main pathways are illustrated in Scheme 1. In this work, we prepared dye-sensitized TiO₂ nanoparticles that were loaded simultaneously with Pt and Al₂O₃ overlayer (Al₂O₃/TiO₂/Pt) and tested the visible photocatalytic activity for hydrogen production and the dechlorination of CCl₄ in aqueous colloidal solutions. Introducing a thin Al₂O₃ overlayer on the dye-sensitized TiO₂ significantly increased the visible light photocatalytic activity for hydrogen production and the degradation of chlorinated organic compound. The main role of the alumina overlayer is thought to retard the recombination between the CB electrons injected from the dye and the oxidized dye. The sensitized photocatalytic reactions should depend on the thickness of the barrier layer. When the barrier layer is too thick, the electron from the excited dye cannot efficiently tunnel into the CB of TiO₂. Fig. 2 shows the effect of the Al₂O₃ loading (in terms of Al/Ti atom ratio) on the sensitized photocatalytic activity and the photocurrent collection. For all three systems, the dependence on the Al₂O₃ loading is very similar. The overall sensitization efficiency rapidly increases with the alumina loading and then reaches a maximum beyond which the efficiency decreases with increasing the barrier layer loading. The optimal loading was found at Al/Ti = 0.009 and the activity was insignificantly low at Al/Ti = 0.18.



Scheme 1 Schematic representation of the electron transfer/recombination processes occurring on a dye-sensitized TiO₂ particle with Al₂O₃ overlayer for (a) H₂ production and (b) CCl₄ dechlorination.

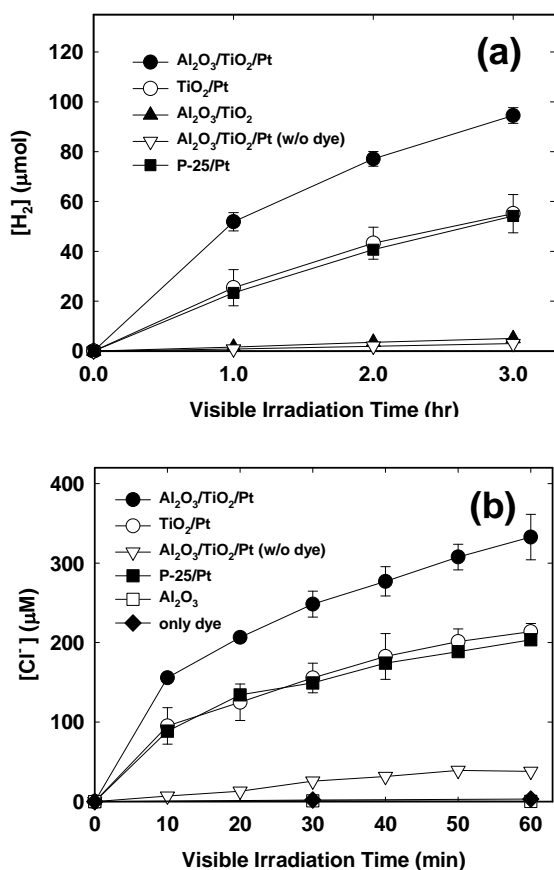
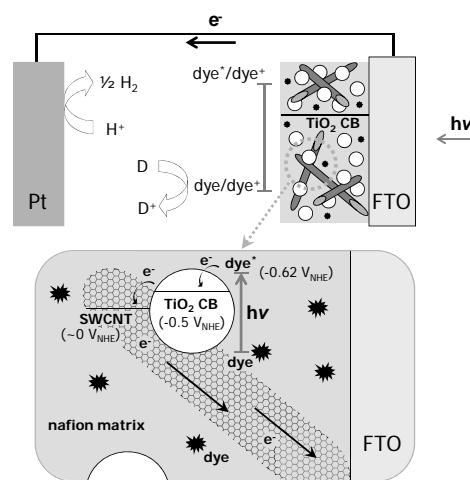


Figure 2. Time-dependent profiles of (a) hydrogen generation and (b) chloride production from CCl₄ degradation in the visible light-irradiated suspensions of Ru^{II}L₃-sensitized P25/Pt, TiO₂/Pt, Al₂O₃/TiO₂, and Al₂O₃/TiO₂/Pt. The experimental conditions were [catalyst] = 0.5 g/L, [Ru^{II}L₃] = 8.3 μM, Al/Ti atom ratio = 0.009, pH_i = 3, [EDTA] = 10 mM (for (a) H₂ generation), [CCl₄] = 1 mM (for (b) Cl⁻ generation), initially N₂-saturated, and λ > 420 nm irradiation.

3.3 CNT assisted H₂ production in dye-sensitized PEC system^[4]

A hybrid TiO₂ electrode that contains Nf resin and CNTs simultaneously was fabricated at low temperature (without the heat treatment that is commonly required in preparing TiO₂ photoelectrodes) and was used as a support for dye sensitizers that were bound to the electrode simply through the ion exchange process. The Nf matrix surrounding TiO₂ nanoparticles provides the binding sites for the sensitizers which little bind directly to the surface of TiO₂. Through this way, a complex process of dye derivatization, which is normally required to attach the surface anchoring groups (*e.g.*, carboxylate and phosphonate) to dye molecules, is not needed as long as the sensitizer dyes are cationic. While the photoinduced electron transfers within the sensitized {Nf/TiO₂} film are not efficient, the introduction of CNTs in the Nf matrix greatly enhanced the PEC activity of the hybrid electrode by

serving as an electron conduit that collects electrons from TiO₂ nanoparticles and transports them to the conducting electrode (FTO) base. Both the hydrogen production and the photocurrent generation were highly enhanced with CNTs present in the hybrid electrode. The hydrogen generation process in the proposed dye-sensitized PEC system is illustrated in Scheme 2. Fig. 3 compares the time profiles of the photocurrent generation and hydrogen evolution in the illuminated PEC system using {TiO₂}/Nf electrode with or without CNT. No hydrogen and photocurrent production were observed when either sensitizer or EDTA (electron donor) was absent. Note that both photocurrent and hydrogen production were greatly enhanced with {CNT+TiO₂}/Nf electrode (E1) while {TiO₂}/Nf electrode (E2) showed negligible activity.



Scheme 2. Illustration of the hydrogen evolution in the proposed PEC. The PEC consists of a nafion film hybridized with ruthenium bipyridyl complex, TiO₂ nanoparticles, and CNTs as a photoanode and a platinum electrode as a cathode. CNTs serve as *built-in nanowire* guiding electrons from the dye to FTO.

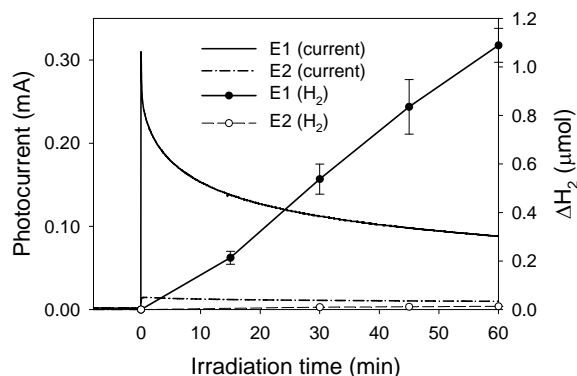


Figure 3. Time profiles of the photocurrent generation and hydrogen evolution in the illuminated dye-sensitized PEC employing the hybrid photoanode {TiO₂}/Nf/sensitizer with CNT (E1) or without CNT (E2). The weight ratio of CNT to TiO₂ in E1 electrode was 1:10. The sensitizer loading was the same in both E1 and E2.

3.4 Simultaneous H₂ production and organic pollutant degradation using F-TiO₂/Pt^[5]

The surface platinization and surface fluorination of TiO₂ have been studied independently and each modification method influences the photocatalytic activity in very different ways. The synergistic effect of two different surface species can exhibit the anoxic degradation of organic compounds. Furthermore, simultaneous modification can highly improve the hydrogen production in the presence of phenolic compounds. Fig. 4 shows the effect of single and simultaneous surface modification for hydrogen production. Simultaneously modified TiO₂ (F-TiO₂/Pt) showed the highest photoefficiency, and 4-chlorophenol (4-CP) in water has a synergistic effect on hydrogen production with acting as hole scavenger.

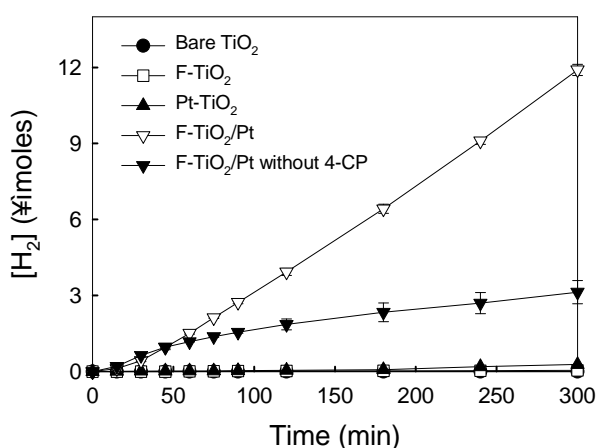


Figure 4. Hydrogen production with or without 4-CP in aqueous suspensions of bare TiO₂, F-TiO₂, Pt/TiO₂, and F-TiO₂/Pt under UV irradiation.

Highly synergistic effect of surface fluorination and platinization of TiO₂ is related to the substrate-surface interaction and the charge transfer/recombination processes. Surface Pt can serve as a temporary electron reservoir, and the surface complexation of phenolic compounds which can make null reaction is hindered by surface fluorides. Therefore the electrons trapped in surface Pt can be more easily transferred into H⁺ to produce hydrogen.

3 CONCLUSIONS

We have investigated solar chemical conversion through surface engineering of TiO₂. The visible light induced photocatalytic activity for the hydrogen production and pollutant degradation was achieved through complexation of fullerol/TiO₂. In dye-sensitized TiO₂ system, the introducing of alumina oxide or CNT to TiO₂ surface enhanced the photocatalytic activity through the efficient electron transfer. The surface engineering method can be also applied to

simultaneous production of hydrogen and degradation of pollutants.

Acknowledgment — This work was supported by Korea Science and Engineering Foundation (KOSEF) (No. R0A-2008-000-20068-0)

References

- [1] Hoffmann, M.R., Martin, S.T., Choi, W., Bahnemann, D.W., "Environmental Applications of Semiconductor Photocatalysis", Chem. Rev. Vol. 95, pp. 69-96, (1995); Choi, W., "Pure and modified TiO₂ photocatalysts and their environmental applications", Catal. Surv. Asia, Vol. 10, pp. 16-28, (2006)
- [2] Park, Y., Singh, N.J., Kim, K.S., Tachikawa, T., Majima, T., Choi, W., "Fullerol-titania charge transfer mediated photocatalysis working under visible light", Chem. Eur. J. (In press)
- [3] Kim, W., Tachikawa, T., Majima, T., Choi, W., "Photocatalysis of Dye-Sensitized TiO₂ Nanoparticles with Thin Overcoat of Al₂O₃: Enhanced Activity for H₂ Production and Dechlorination of CCl₄", J. Phys. Chem. C Vol.113, pp.10603-10609, (2009).
- [4] Park, J., Choi, W., "TiO₂-Nafion Photoelectrode Hybridized with Carbon Nanotubes for Sensitized Photochemical Activity", J. Phys. Chem. C (In press)
- [5] Kim, J., Lee, J. and Choi, W., "Synergic effect of simultaneous fluorination and platinization of TiO₂ surface on anoxic photocatalytic degradation of organic compounds", Chemical Communications, pp.756-758, (2008)

Change of the Influence of Long-distance Transportation
of Ionic Pollutants on the Atmospheric Environment of Japan
during Past Eight Years
-- Comparison of the Monitoring Results of Acid Precipitation
Carried Out at Wide Areas in (2000-2001), (2004-2005),
and (2007-2008) –

Toru Ozeki^{a*}, Ryoei Kikuchi^b, Nobuaki Ogawa^c

^a Hyogo University of Teacher Education, 942-1, Shimokume, Kato City, Hyogo 673-1494, Japan

^a ozeki@hyogo-u.ac.jp

^{b,c} Faculty of Engineering and Resource Science, Akita University,

1-1, Tegata Gakuen-cho, Akita 010-8502, Japan

^b ogawa@ipc.akita-u.ac.jp ,

^c kikuchi@akita-u.ac.jp

Abstract: Long-distance transportation of pollutants from Continental China to Japan is still serious problem. Previously, the transportation of acidic pollutant was mainly observed at the areas near west coast of Japan in winter due to seasonal monsoons. However, in recent years, other vast transportations by Jet streams have been observed from spring to early summer and acidic as well as alkaline pollutants have been transported. In order to characterize these transportations of pollutants, domestic and international collaborative research works have been carried out by our group. The first two were domestic wide-area researches inside Japan (2000 – 2001) and (2004 – 2005), and the third (2007 – 2008) was a Japan-Korea joint monitoring. In this report, changes of the character of long-distance transportation of ionic pollutants influencing the atmospheric environment of Japan during past eight years are presented.

Keywords: Long-distance Transportation, Ionic Pollutants, Atmospheric Environment,
Acid precipitation

1 Introduction

Acidification of precipitation (rain and snow) is still serious problem in East Asia where a vast amount of SO_x and NO_x are emitted and are transported across boundaries. So far in Japan,

heavy acidification of precipitation caused by the long distance transportation of acidic pollutants was observed in winter season only at areas close to the west coast of the Japan Island. Refs-[1 - 3] However, recently transportation of pollutants by

Jet streams from spring to early summer has increased and it has given serious problem since they bring acidic pollutants as well as alkaline pollutants case by case, depending upon routes on which Jet streams pass through.

Our group started study of acidic precipitation at Hyogo and Akita areas of Japan at 1991 and has continued the monitoring. In addition to the chemical analysis of precipitation samples, we have developed a statistical analytical method called as "Oblique Rotational Factor Analysis with Partially Non-Negative Constraints" to extract major independent pollutant groups from the compositional data of precipitation samples. Refs-[4-8]

In order to characterize the influence of transportation of pollutants upon atmospheric environments of Japan, the precipitation samples have been collected at various areas of the Japan through three wide area monitoring; WAM-1 from 2000 to 2001, WAM-2 from 2004 to 2005 and WAM-3 from 2007 to 2008. In these studies, the precipitation samples collected at week base were chemically analyzed. In this report, through the results of these three monitoring, changes of the character of long-distance transportation of ionic pollutants influencing the atmospheric environment of Japan during past eight years will be presented.

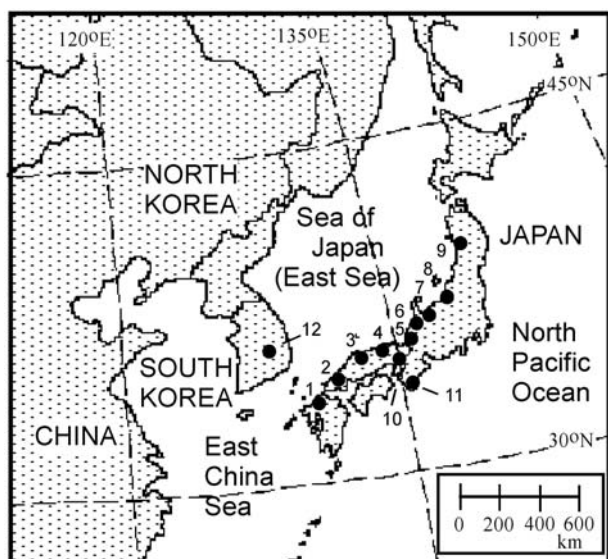


Figure 1 Location of sampling points of precipitation samples. (2000-2001, 2004-2005 and 2007-2008)

2 Experimental section

2.1 Sampling points and sampling period

Sampling points of three wide area monitoring (WAM) are shown in Fig.1: In WAM-1 from July 2000 to June 2001, 1 Fukuoka, 2 Hagi, 3 Yonago, 4 Tottori, 5 Fukui, 6 Ishikawa, 7 Toyama, 8 Kashiwazaki and 9 Akita; in WAM-2 from July 2004 to June 2005, 4 Tottori, 6 Ishikawa, 10 Hyogo and 11 Wakayama; in WAM-3 from July 2007 to June 2008, 5 Fukui, 6 Ishikawa, 9 Akita, 10 Hyogo, 11 Wakayama and 12 Daegu (Korea). Daegu is a city locating at the center of the Korean Peninsula.

2.2 Sampling method

In this study, rain and snow samples were collected in a cylindrical container of the inner diameter 22 cm made of plastic. A polyethylene bag was set inside the vessel and a precipitation sample was collected by a week base. Even when no precipitation occurred within a week, an old bag was replaced by a new one.

2.3 Chemical analysis

Analyzed quantities were: pH, electric conductivity (EC), concentrations of major nine ions (Na^+ , K^+ , NH_4^+ , Mg^{2+} , Ca^{2+} , SO_4^{2-} , NO_3^- , Cl^- , NO_2^-) and an amount of precipitation for week base samples. The concentrations of the major nine ions were measured by an ion chromatograph system. The water used was the Milli-Q water after doubly distillation. Reagents used were all of analytical grade. The chemical analysis was carried out according to the recommendations of the Japan Environment Agency. Ref-[9] The concentration unit used here is equiv L^{-1} .

2.4 Oblique rotational factor analysis with partially non-negative constraint

In order to extract major independent pollutant groups from the measured compositional data of the precipitation samples, we have applied "Oblique Rotational Factor Analysis with Partially Non-negative Constraint (ORFA-PNNC)" developed

by our group. The details of the procedure have been reported otherwise. Refs-[4, 5, 7]

3 Results and Discussion

3.1 WAM-1 (2000 – 2001)

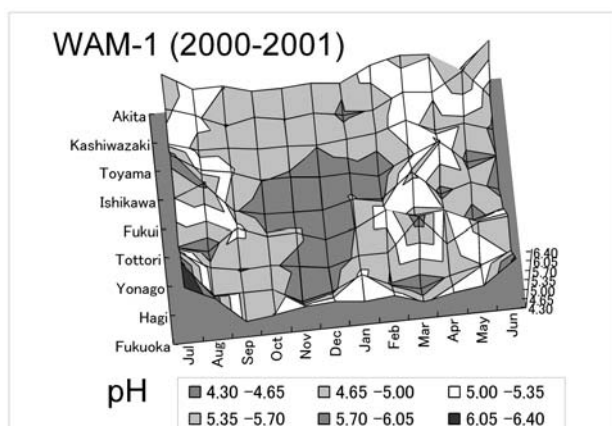


Figure 2 Regional and seasonal variation of pH in WAM-1 (2000-2001).

Fig.2 shows the three dimensional plots of regional and seasonal variation of pH of the precipitation samples collected at WAM-1. In winter season from October to February, pH values of the precipitation were low at all places locating near the west coast of Japan Island, but those at Ishikawa to Hagi were especially low. When the values of hydrogen ion concentration converted from pH were compared with the balance between the sum of the concentrations of acidic substances and that of alkaline substances, it is obvious that the balance between the acids and the alkalines determines the pH of precipitation samples.

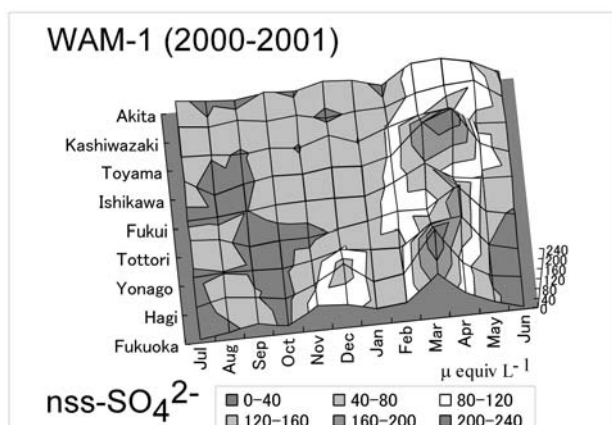


Figure 3 Regional and seasonal variation of nss-SO₄²⁻ ion concentration in WAM-1 (2000-2001).

When the regional and seasonal variation of nss-SO₄²⁻ ion concentration shown in Fig.3 is examined, a relatively high concentration area can be seen from November to February as shown by pale gray (40-80 u equiv L⁻¹). In the same season, high concentration of ammonium ion was also observed. It means that the sulfuric acid and the ammonium sulfate were transported to these areas by north western seasonal winds and they were acidifying the precipitation samples of winter.

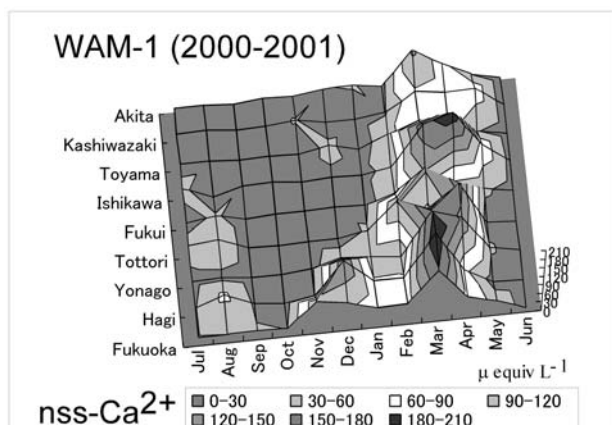


Figure 4 Regional and seasonal variation of nss-Ca²⁺ ion concentration in WAM-1 (2000-2001).

On the other hand, other very high concentration areas of nss-SO₄²⁻ ion, which are higher than 80 u equiv L⁻¹, are observed at March and April in Fig.3. These sulfate ions also seem to work as acid to precipitation samples. But, when the regional and seasonal variation of nss-Ca²⁺ ion concentration shown in Fig.4 is examined, this ion concentration also became very high from March to April. When the flow routes of Jet streams at January, March and April of 2001 were examined, it was found that these parts of ions were transported by Jet streams. Namely, a vast of pollutant substances were long distance transported from the Continent China to Japan Island by Jet streams. As a conclusion, the pollutant substances found in WAM-1 were transported by two ways: one was the northwestern seasonal wind and the other was the Jet streams.

The transportation by the former seasonal winds has been well known at the west coastal areas of the Japan Island in

winter. On the other hand, the latter transportation of pollutant containing calcium ion as major ion by Jet stream has been known as Eolian dust. The Eolian dust is working as an alkaline pollutant. But, through our study we have found that the acidic pollutant is also transported by Jet stream. However the acidic pollutant and alkaline pollutant transported by Jet streams do not come together. So, the net acidity of the precipitation seems to be determined by the balance of these two pollutant groups.

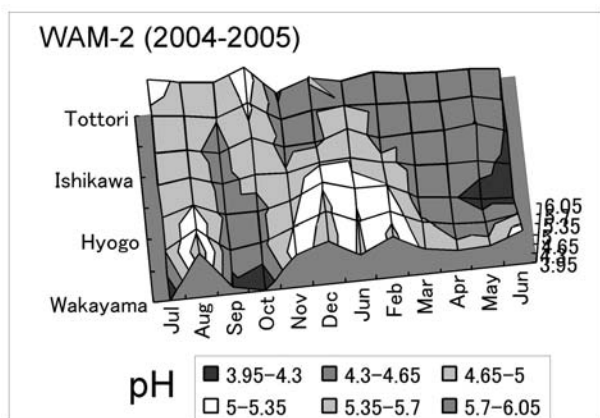


Figure 5 Regional and seasonal variation of pH in WAM-2 (2004-2005).

3.2 WAM-2 (2004 – 2005)

In the second wide area monitoring WAM-2 carried out from 2004 to 2005, precipitation samples were collected at areas locating at the west coast (Tottori and Ishikawa) as well as the areas locating at the east coast (Hyogo and Wakayama). As shown in Fig.5, pH values of the precipitation at winter were low only at west coast. This result is the one easily expected from the previous study WAM-1, because the acidic pollutants are transported by the northwestern seasonal wind. But, in this time, the precipitations from spring to early summer were acidified at all places from Tottori to Wakayama, even at the place where there was no emitting source. Transportation of the pollutants by Jet streams to wide areas of Japan seems to be the cause of this result.

In Fig. 6 and Fig. 7, the regional and seasonal variations of nss-SO_4^{2-} ion concentration and that of nss-Ca^{2+} ion are shown.

In the similar manner as WAM-1, very high concentration areas of nss-SO_4^{2-} ion and those of nss-Ca^{2+} ion were observed at March and April. However, in this monitoring WAM-2, the contribution of the nss-SO_4^{2-} ion concentration was larger than that of nss-Ca^{2+} ion concentration. In WAM-1 of 2000-2001, the contribution of the alkaline group was larger than that of the acidic group in spring and early summer, so the pH values of the precipitation samples of these seasons were relatively high. But, in WAM-2 of 2004-2005, the contribution of the acidic group became larger than that of alkaline group, thus the pH values of the precipitation of these seasons became low.

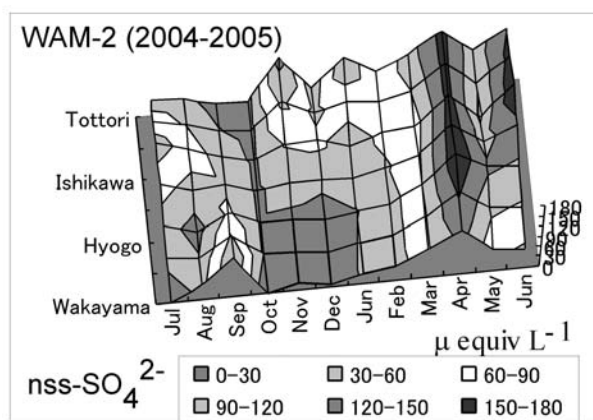


Figure 6 Regional and seasonal variation of nss-SO_4^{2-} ion concentration in WAM-2 (2004-2005).

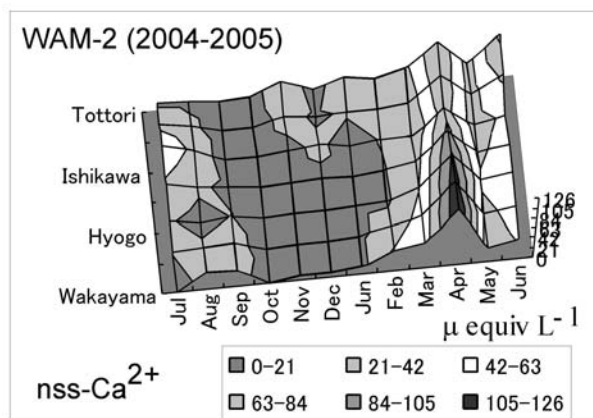


Figure 7 Regional and seasonal variation of nss-Ca^{2+} ion concentration in WAM-2 (2004-2005)

3.3 WAM-3 (2007 – 2008)

The third wide area monitoring WAM-3 was carried out

from July 2007 and June 2008. In this monitoring, precipitation samples were also collected at Daegu city of Korea. Regional and seasonal variation of pH of the precipitation samples are shown in Fig.8. Except for Daegu, the pattern of seasonal variation of pH shown in Fig.8 is very close to that of WAM-1 shown in Fig.2. The pH values of precipitation samples of winter season from November to February were very low at three points, Akita, Ishikawa and Fukui facing the west coast of the Japan Island.

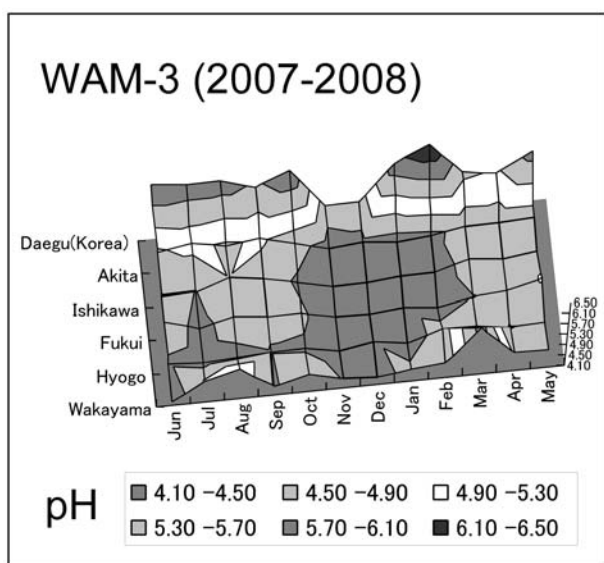


Figure 8 Regional and seasonal variation of pH. (WAM-3: 2007-2008).

The regional and seasonal variation of nss-SO_4^{2-} ion concentration and that of nss-Ca^{2+} ion are not shown here, but they have shown high concentration areas transported by the Jet streams in spring and early summer. However, in this time (WAM-3), the contribution of the alkaline group was rather larger than that of the acidic group. This is the reason why the pH values of the precipitation samples of spring and early summer were relatively high. Seasonal variation of pH in WAM-3 is much closer to the WAM-1 rather than the WAM-2.

As mentioned before, the acidic pollutants and the alkaline pollutants transported by Jet streams do not come together. So, the net acidity of the precipitation is determined by the balance of these two kinds of pollutant groups, and is depending upon

the routes of the Jet streams.

In this time, the precipitation samples of Daegu city in Korea were also collected. As can be seen in Fig.8, the pH values of precipitation samples of Daegu became higher than those of any other sampling points. In this stage, the reason of these high values of pH has not been fully understood. But, Fig.8 is closely examined, the pH values of the precipitation samples of Daegu at November and December (2007) were remarkably lower than the any other months. It means that the precipitation samples of Daegu city were also getting the influence of acidic pollutants in these months. These facts seem to tell us that the acidic pollutants were transported from westside of the Korean peninsula to Korea and Japan in winter season.

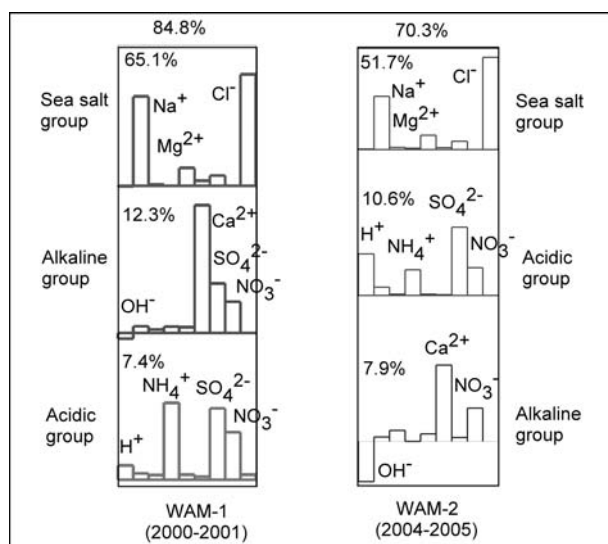


Figure 9 Comparison of compositions of the three factors extracted from precipitation samples of WAM-1 and those of WAM-2.

3.4 Analysis by the oblique rotational factor analysis with partially non-negative constraint

The data of WAM-1 and WAM-2 were analyzed by “Oblique Rotational Factor Analysis with Partially Non-negative Constraint”. In Fig.9, the compositions of the extracted three independent factor groups from the precipitation samples of WAM-1 and those of WAM-2 are compared. In either case, the three factors correspond to 1) sea salt origin

group, 2) an acidic group consisted of sulfuric acid and nitric acid and their ammonium salts, and 3) an alkaline group consisted of calcium ion as major ion. From Fig.9, it can be seen that the contribution of the acidic group increased in WAM-2 (10.6%) from WAM-1 (7.4%), but the contribution of the alkaline group decreased in WAM-2 (7.9%) from WAM-1 (12.3%). The detail of the results of this analysis will be discussed in the presentation.

4 Conclusions

In this study, the precipitation samples collected at various points in Japan and Korea were analyzed through three wide area monitoring. The pollutant groups contained in precipitation samples were transported long distance from the Continental China to the Japan Island across the Sea of Japan (the East Sea) by northwestern seasonal winds in winter and by Jet streams in spring and early summer. However, since the transportation routes by Jet streams vary time to time, it is difficult to expect whether a Jet stream brings acidic pollutant or alkaline pollutant. In recent years, the amount of emission of acidic pollutants at East Asia increases year after year. From this study, it is concluded that the continuous monitoring of the influence of Jet streams on the atmospheric environment of East Asia will be much more important.

The main characteristics of three wide area monitoring are as follows:

- (1) WAM-1 (2000-2001): the transportation of pollutants by the north western seasonal winds to Japan was large in winter, but that by the Jet streams was also very large in spring and early summer. The former pollutants were acidifying the precipitation samples of winter. For the precipitation of spring and early summer of 2001, the contribution of the alkaline pollutants brought by Jet streams were larger than that of the acidic pollutants.
- (2) WAM-2 (2004-2005): In this time, the contribution of the acidic pollutants brought by Jet streams was larger than that of the alkaline pollutant. So the precipitation samples of spring

and early summer of 2005 became acid rain.

- (3) WAM-3 (2007-2008): As a whole, nature of the precipitation samples was very close to that of WAM-1.

References

- [1] K.Murano, H.Mukai, S.Hatakeyama, O.Oishi, A.Utsunomiya, T.Shimohara, *Environ.Poll.*, 102, S1, 321, (1998).
- [2] N.Fukuzaki, T.Oshio, I.Noguchi, M.Matsumoto, S.Morisaki, M.Oohara, M.Tamaki, T.Hiraki, *Chemosphere*, 38, 411, (1999).
- [3] J.A.van Aardenne, G.R.Carmichael, H.Levy II, D.Streets, L.Hordijk, *Atmos.Environ.*, 33, 633, (1999).
- [4] T.Ozeki, K.Koide, T.Kimoto, *Environ. Sci. Technol.*, 29, 1638, (1995).
- [5] T.Ozeki, K.Koide, N.Ogawa, T.Adzuhata, M. Kajikawa, T.Kimoto, *Anal.Sci.*, 13, 169, (1997).
- [6] T.Ozeki, T.Okada, N.Ogawa, M. Kajikawa, *Anal.Sci.*, 17 SUPPLEMENT i457, (2001).
- [7] T.Ozeki, N.Ogawa, *Chemometrics and Intelligent Laboratory Systems*, 71, 61, (2004).
- [8] T.Ozeki, T.Ihara, T.Okada, R.Kikuchi, N.Ogawa, *BUNSEKI KAGAKU*, 53, 1427, (2004).
- [9] Japan Environmental Agency (JEA), Government of Japan, "Manual for acid deposition survey" 2nd ed.. Tokyo (2004).

Introduction to Rare – Earth Metal Resources in Thailand

P. Charusiri* C. Sutthirat* V. Daorerk*

* Earthquake and Tectonic Geology Research Unit (EATGRU), c/o Department of Geology, Faculty of Science, Chulalongkorn University, Bangkok 10330 Thailand

cpunya@chula.ac.th

Abstract: Geochemistry and mineralogy of rare earth mineral deposits in Thailand were investigated. Monazite and xenotime are significant rare earth minerals occurring with tin ± tungsten deposits of primary and secondary types. The former is recognized in granites and pegmatites of southern Thailand and the latter are observed near the former and in Quaternary fluvial and beach deposits. Geochemical analyses on granites suggest that the ilmenite – series granites yield more rare earth minerals than the magnetite - series granites. The younger and strongly hydrothermally altered granites contain more rare earth minerals. Three rare earth provinces are identified – primary, secondary, and tertiary provinces. The tertiary province represents the weathering crust of granites and pegmatites and is of important economic significance to explore. In southern Thailand it yields the highest RE metal contents (0.092%). The most important secondary provinces are in Songkhla and Yala of southern Thailand and can yield up to 0.045 % monazite and 0.196 % xenotime contents.

Key Words: Rare earth, Thailand, Granites, Ilmenite series, Alteration

1. INTRODUCTION

There is an increase in demands of rare earth metals year by year; particularly those used for information technology (IT) industries, special magnets, petroleum catalysts, and ceramic/glass uses. It is anticipated that their life-span has been shortened dramatically. This is mainly due to the efforts made to discover, to develop new deposits, and to make them productive. Continuous efforts are made to extend its life-span. However, the present – day quantity of consumed resources is totally different from that of the earlier 30-year time. Therefore, it is very difficult to secure and to maintain rare earth metal resources of the same number, and the innovation is vital in exploration and development of resources.

In this study we define rare earth (RE) metals following the definition proposed by Shannon [1] as a group of 17 chemically similar metals that includes the elements scandium and yttrium (atomic numbers 21 and 39, respectively) and the lanthanide elements (atomic numbers 57 through 71).

The main purpose of this study is to evaluate preliminary potentials of RE metals in Thailand. Additional aims are to determine their sources and classifications of RE metals. Therefore, all the relevant and existing published and unpublished reports and maps were compiled and reviewed for the first step. Then field work was conducted for geologic syntheses and samplings of

ores and granites. Selected samples of RE – bearing minerals, ores and rocks were analyzed geochemically and mineralogically. Interpretation of the result was done in the last step for RE metal appraisal.

2. GEOLOGIC AND TECTONIC SETTINGS

It has been widely accepted that many of the RE metals in Thailand are always associated with granites and pegmatites [2] and that only some special types of granites can give rise to such mineralization [3]. In Thailand the granites form as the north – south trending batholiths and stocks in the long (> 2,000 km) and curvilinear zones or belts. In term of geographical distribution, these granites can be subdivided into 3 major belts, namely Eastern, Central, and Western Belts (Fig.1). These granite belts extend northern to southern Yunan and southward to Malaysia. Based on the classification by Ishihara [4] which is relatively similar to that of Chappel and White [5], the granites of the Eastern Belt are mainly Triassic granites of I – type or magnetite – series whereas those of the Central and Western Belts belong to granites of both I – type or magnetite – series and S- type or ilmenite – series. The Central Belt granites occurred mainly in Triassic whereas those of the Western Belt are of Cretaceous to Tertiary. The S-type or ilmenite –series granites include fine – to coarse – grained biotite granites, biotite – muscovite granites, and tourmaline – muscovite granites. Only the biotite granites are usually porphyritic. Important accessory minerals include zircon, monazite, rutile, garnet, topaz and beryl.

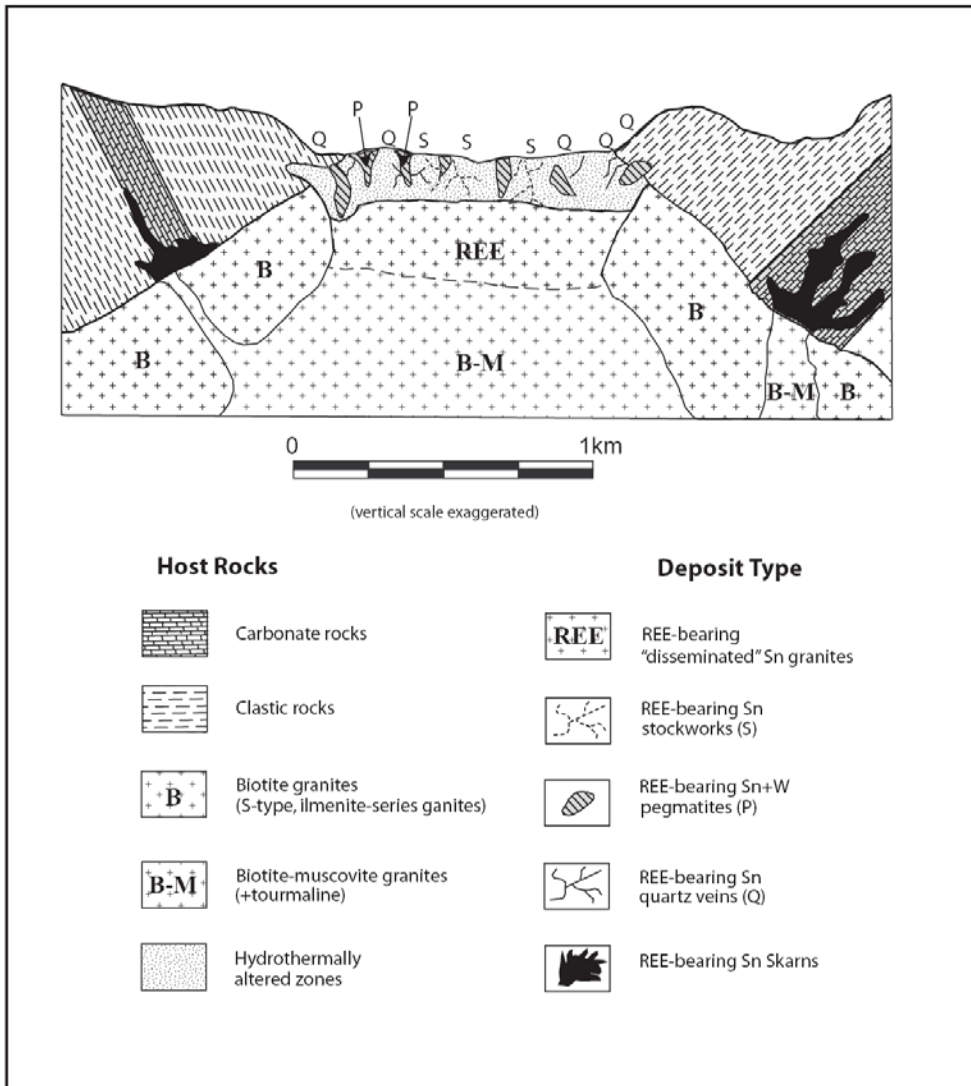


Fig. 1. Genetic model of the REE – bearing primary Sn± W deposits of Thailand (modified from Charusiri et al. [3]).

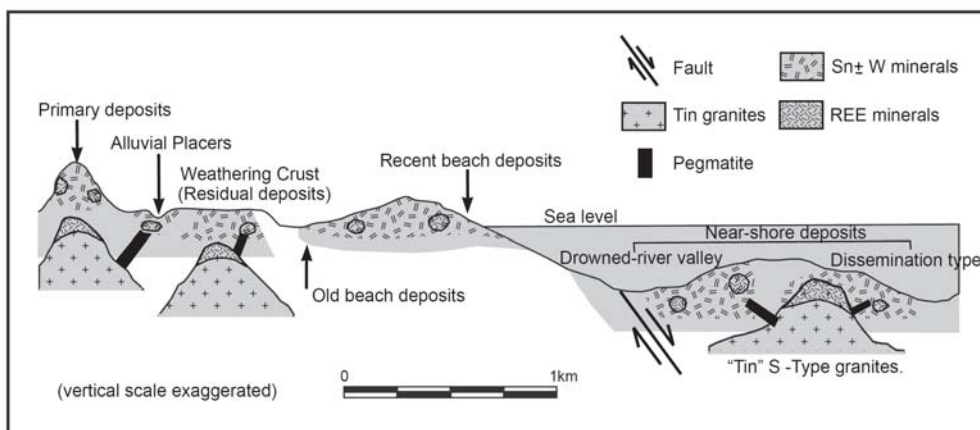


Fig. 2. Genetic model of the REE – bearing secondary Sn±W deposits of Thailand [3].

The magnetite - series granites include hornblende - biotite granites and biotite granites with strong to mild foliation and mainly porphyritic textures. Important accessory minerals are sphene, epidote and allanite (or orthite). In some places pyroxene are also present in minor amount. It is noted, based on our result, that the S-type or ilmenite – series granites with strong alteration can yield high REE contents (Figs. 1 and 2).

2. MINERALOGICAL INVESTIGATION

We compiled and reported RE metal contents from the analytical results of approximately 250 ore samples collected from various abandoned tin ± tungsten mines from both on land and sea beds. This also includes RE contents in ore samples collected from currently operated Au-Ag and Zn mines from various parts of the country. Mineral separation and processing were done to extract RE metal concentrates. XRD analysis and binocular microscopic determination were applied to evaluate their contents. Based upon our compiled data, particularly from the data by Praditwan [6] and Punggrassami [7], we found that both Zn and Au-Ag deposits contain no RE metals, and that only the tin ± tungsten alluvial and beach placer deposits host appreciable amounts of RE metals. Therefore unlike the other part of the world which bastnaesite is the most important ore for RE metals, in Thailand the most important RE ores are monazite and xenotime. Other RE minerals are samarskite, cassiterite, wolframite, zircon, microlite, columbite – tantalite, rutile, anatase, and ilmenite.

3. GEOCHEMICAL INVESTIGATION

In this study, results on the REE contents of about 150 granite and pegmatite samples from individual granite belts were reported. The analyses were performed using XRF, ICP OES and ICP MS methods [8]. It is quite likely that the granites of the Eastern Belt host small amounts of REE concentrations whereas those of the Central and Western Belts contain appreciable amounts of REE concentrations. We found that the granites of ilmenite – series granites, particularly those with the more evolved or differentiated melts can contain much more amounts of RE metal contents than the less evolved granites. Additionally, as very recently reported by Imai et al. [9], the weathering crust of the granites contain up to 1,000 ppm. It is quite likely that this kind of RE metal resources seems to be by far the most interesting one and requires detailed further detailed exploration for the commercial scale at present.

4. CLASSIFICATION OF RARE EARTH METAL RESOURCES

Based on the results reported above, we classify the RE metal resources into 3 provinces in Thailand, viz. primary, secondary and tertiary provinces (Fig. 3).

4.1 Primary Province

The primary RE metal province is the province where a group of RE metal deposits occurs principally in hard rocks, such as granites, pegmatites, and aplites. Charusiri et al. [3] and Imai et al. [9] recognized that the strongly differentiated or more evolved granites and the more altered granites and their minor intrusions contain more RE metal contents than the normal unaltered granites (Fig. 1). It is also found that the ilmenite – series (or S- type) granites contain more RE metal contents than the magnetite (or I – type) affinity for both of the altered and unaltered types. It is also recognized that the magnetite - series granites contain the varying total REE values from 512 to 778 ppm. Those of the more evolved granites vary from 634 to 997 ppm. The ilmenite-series granites have the total REE contents ranging from 712 to 887 ppm, and the more evolved granites show variation of total REE contents from 799 to 991ppm [8]. However, the strongly altered ilmenite – series granites have the total REE values from 832 to 1,092 ppm. However, as reported by Imai et al. [9], the REE value of the very strongly altered part of the ilmenite - series granites can be reached up to 1,525 ppm.

In addition, pegmatite can also be a host rock for RE metals. Geochemical analysis reveals that the altered pegmatite yields the RE metal contents of up to 0.02 and 0.05 % monazite and xenotime, respectively.

4.2 Secondary Province

Charusiri et al. [3] subdivided secondary RE metal deposits in Thailand into 3 groups; namely (1) alluvial placer deposits, (2) recent and old beach deposits, and (3) near – and off – shore deposits (Fig. 2). Particular interests are the Sn± W secondary deposit areas in the southern part of Thailand. Apart from cassiterite and wolframite, the other essential minerals are monazite, xenotime, zircon, columbite, tantalite, rutile, anatase, and ilmenite. The most important secondary provinces are alluvial placers in Songkhla and Yala of southern Thailand. The RE metal – bearing deposits contain up to 0.045 % monazite and 0.196 % xenotime contents [3].

4.3 Tertiary Province

A new type of rare earth elements (REEs) deposit has been discovered from the weathering crust of granites. Many of the deposits are located in southern Thailand. However, some of them are also found in the central part. In general this deposit type contains ΣRE_2O_3 within the range of 0.065% – 1.086% or at the average of 0.092% [9]. This type of REEs deposit was widely distributed with steady horizon and thickness of 3–4 m. The ore-bearing weathering crust (kaolinite) of the discovered REEs deposits belonged to the Cretaceous – Tertiary, S – type ilmenite – series granites. The new type of REEs deposit was suggested that chemical

weathering of the strongly evolved and altered granite weathering could lead to the enrichment of

the rare earth elements. Therefore, it is of economic

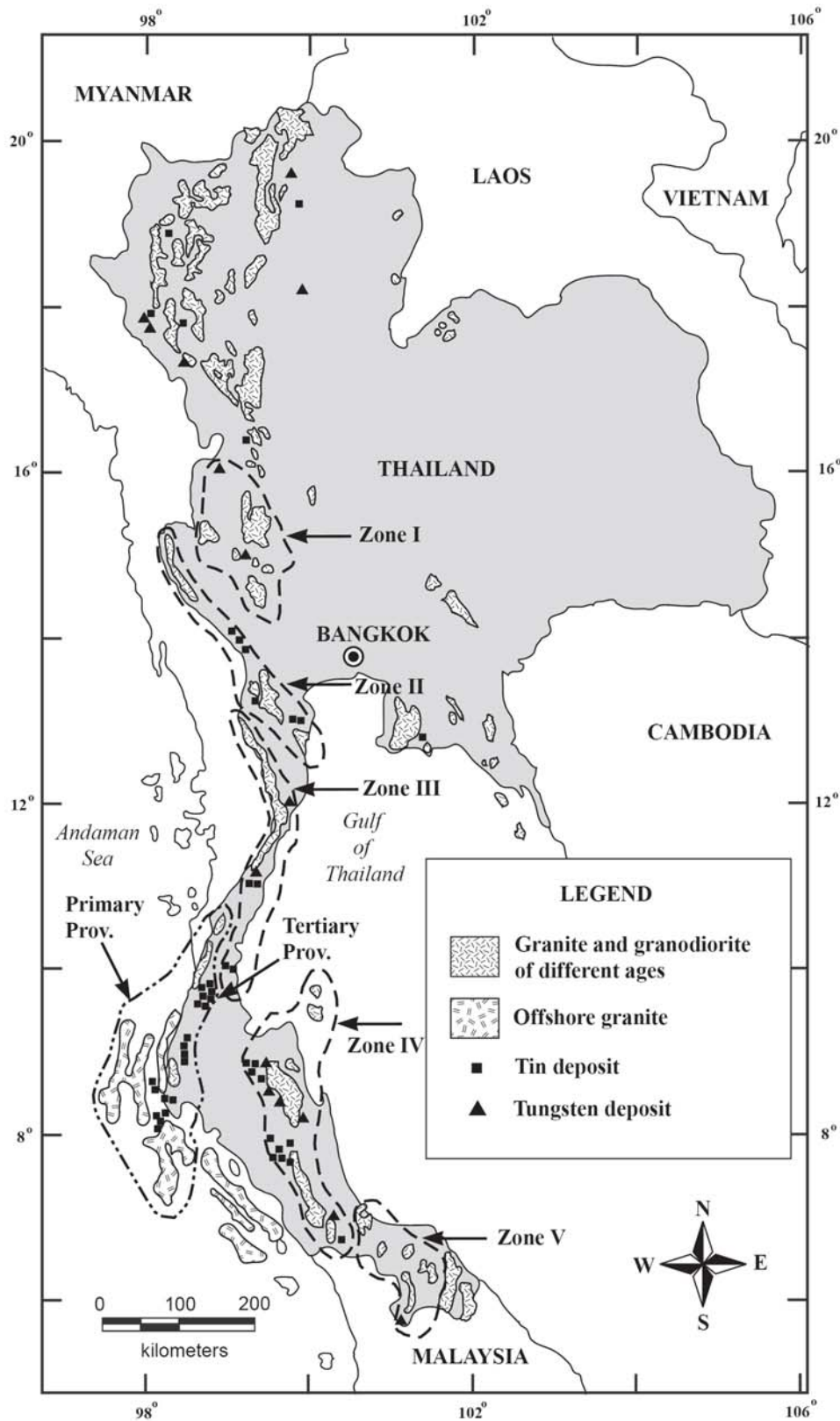


Fig. 3. Classification of REE provinces in association with Sn and W deposits and ilmenite – series granites in Thailand [3].

significance to explore REEs deposits in the in situ weathering zone of granites in Thailand.

5. DISCUSSION

Granites in Thailand show high REE contents in general. Total REE contents of weathered crust of granites in southern Thailand may reach 1,000 ppm. The total REE concentrations of weathering-crust granitic rocks appear higher than those of normal unaltered granitic rocks. However, REE contents of weathered crust of ilmenite – series granitic rocks are higher than those of the magnetite – series granites. The total REE contents of weathered crust of granitic rocks are elevated compared with the unweathered original granitic rocks.

In southern Thailand, Imai et al. [9] proposed that the total REE contents of weathered crust of granitic rocks are enriched at the lower part of the B zone in typical weathering profile. The chondrite-normalized REE patterns of the weathered crust of granitic rocks in southern Thailand are parallel to their unweathered part, while contents of each REE are higher in the weathered crust. This suggests that REE-bearing accessory minerals (monazite and xenotime) may be resistant against weathering, and may remain a residual phase. Thus, REE concentration should be elevated by removal of decomposed minerals.

Furthermore, it is observed that total REE contents are high in some hydrothermally altered granitic rocks through greisenization and argillization, and that kaolinite veinlets associated with hydrothermal Sn mineralization in the western granitic belt of southern Thailand. Some show HREE concentration higher than those of unweathered original granitic rocks in the western granitic belt of southern Thailand. Thus, the hydrothermally altered granitic rocks, and kaolinite veinlets associated with hydrothermal Sn mineralization in the western granitic belt of southern Thailand show relatively flat chondrite normalized REE pattern. According to Imai et al. [9], the REE pattern is similar to those of weathered crust of granitic rocks in Longnan area [10] [11] in China. The HREE concentration of greisens and hydrothermally altered granitic rocks, and kaolinized veinlets associated with Sn± W mineralization in the Western Granitic Belt are elevated compared with the unweathered original granitic rocks [10]. This is attributed to the leaching of LREE by hydrothermal solution, in addition to enrichment by removal of decomposed minerals. Furthermore, HREE is selectively enriched associated with clay minerals, such as kaolinite, most probably due to ion adsorption mechanism. The western granitic belt associated with Sn± W mineralization has a potential for the RE metal resources, particularly in hydrothermally altered granitic rocks and clay-enriched veinlets associated with hydrothermal deposits accompanied with ilmenite-series granitic rocks, in addition to REE-enriched weathered crust of granitic rocks and heavy mineral alluvium placers.

6. CONCLUSION

Monazite and xenotime are the most important RE metal minerals in Thailand. They are found more abundantly in ilmenite – series granites than magnetite – series granites. Secondary RE deposits yield high REE contents, as well as weathering crust of granites and altered ilmenite – series granites also contain high values of REE contents.

Acknowledgements “We thanked Isao Takashima (Akita University), Toshio Mizuta (Akita University) and Koichiro Watanabe (Kyushu University) for the long term co-operation and assistance. Thanks are extended to Geology Department, Chulalongkorn University for facilities provided. This research was fully supported by National Research Council of Thailand (NRCT) and Thailand Research Funds (TRF.), Bangkok through PC. Special thank goes to Sumet Phantuwongraj (Chulalongkorn University) for preparation of all figures.

References

- [1] Shannon, R. D., “Revised effective ionic radii and systematic studies of interatomic distances in halides and chalcogenides”. *Acta Crystallo.*, Sec A, 32, pp. 751-767, (1976).
- [2] Aranyakanon, P. “The cassiterite deposit of Haad Som Pan, Ranong Province, Thailand”. Report of Investigation, Department of Mineral Resources, Bangkok, Thailand, No.4, 182p, (1961).
- [3] Charusiri, P., Pungrassami, T., Sinclair, G., “Classification of rare-earth element (REE) deposits in Thailand: A genetic model”. *Journal of Geological Society of Thailand*, 1, pp.57-66, (2006).
- [4] Ishihara, S. “The magnetite – series and ilmenite – series granitic rocks”. *Mining Geology*, Vol. 27, pp.293-305, (1977).
- [5] Chappel, B. W. and White A.J.R., “Two contrasting granite types”. *Pacific Geology*, Vol. 8, pp.173-174, (1974).
- [6] Praditwan, J. “Study of Rare-earth minerals in tin tailings in Southern Thailand. Report of Investigation No. 78. SEATRAD .Centre, Malaysia, 21p, (1989).
- [7] Pungrassami, T., “Tin mineralization of the Thung Po – Thung Kamin mining district, Changwat Songkhla”. *Proceedings of the Conference on Application of Geology and the National Development*, Chulalongkorn University, Bangkok, November 1984, pp. 207-214, (1984).
- [8] Khantaprab, C., Pongsapitch, W., Charusiri, P., Pisutha-Arnont, V., Yumuang, S., Pungrassami, T., “Geological Assessment on the Potentials of the Rare – Earth – Bearing Mineral Resources in Thailand”. A final report submitted to National Research Council of Thailand, Bangkok, Thailand, 260 p. (in Thai with English abstract), (1998).
- [9] Imai, A., Sanematsu, K., Ishida, S., Watanabe, K., Boosayyasak, J., “Rare Earth Elements in weathered Crust in Sn – bearing Granitic Rocks in Southern Thailand” *Proceedings of the*

International Symposia on Geoscience Resources and Environments of Asian Terranes (GREAT 2008), 4th IGCP 516, and 5th APSEG, pp. 232-237, (2008).

[10] Wu, C-Y., Ishihara, S. "REE geochemistry of the southern Thailand granites". *Journal of Southeast Asian Earth Sciences*, 10, 81-94. (1994)

[11] Wu, C-Y., Huang, D-H., Guo, Z-X. 1990. REE geochemistry in the weathered crust of granites, Longnan area, Jiangxi province. *Acta Geologica Sinica*, 3, 193-210, (1990).

Mineralization in Indonesia – An overview and rare metal deposits

Emmy Suparka* and Isao Takashima**

* Department of Geology, Faculty of Earth Sciences and Technology, Institut Teknologi Bandung, Jalan Ganesha 10, Bandung, 40132, Indonesia.

** Mining Museum, Faculty Engineering and Resource Science, Akita University, 28-2 Tegataosawa, Akita 010-8502, Japan
emmy@gc.itb.ac.id

Abstract: Indonesia has various kinds of precious- and base- metal deposits (include rare metals), most of them that are closely related to Mesozoic- and Cenozoic- magmatic arcs. A few mineralization related to Paleozoic magmatic arc are also found. The types of mineral deposit present include : Porphyry Cu-Au, porphyry Mo, epithermal Au (low-sulphidation and high sulphidation types), skarn Cu-Au, volcanogenic massive sulphides (VMS), sediment- hosted Au, sedimentary-exhalative base metals, magmatic Sn deposits, Ni- and Fe- laterites, gold- and iron sand- placer deposits are also present. Some of the porphyry Cu-Au and skarn Cu-Au deposits have world-class ore bodies, and are economically important. The primary tin deposit (cassiterite) is closely associated with acidic igneous rocks (granitic) whilst nickel and iron as well occurs as lateritic deposits derived from ultramafic rocks.

Key Words : mineralization, Mesozoic - and Cenozoic- magmatic arcs, rear metal, Indonesia

1. INTRODUCTION

The Indonesian Archipelago consists of 13.000 islands, across a length of 5,200 km in the equator between 6°N to 11°S with the total on land area of more than 1,900,000 km². Geologically the Indonesian Archipelago is related to the interactions between the three major plates of the Pacific-, the Indian-Australian- and the Eurasian- plates. These phenomena give result to the presence of several magmatic arcs which are believed to be responsible for the formations of major mineralization in this archipelago. The eastern part of Indonesia (Halmahera and Papua) may be considered as part of the Circum-Pacific realm, whereas the remainder of the archipelago is closely related to convergent complex along the northeastern margin of the Indian-Australian plate (Hamilton, 1979). Indonesian metallogeny is dominated by porphyry Cu – Au and epithermal Au deposits. Most of these deposits belong to Mio-Pliocene in age (Carlile and Mitchell, 1994) and are generated in the island arc of the western Pacific region (Silitoe, 1994).

This paper provides an overview of mineralization related to Mesozoic- to Cenozoic- magmatic arc in Indonesia based on magmatic arc's configuration done by Carlile and Mitchell (1994) as it is seen in Figure 1. The distribution of mineralization including the type of mineralizations in each arc are briefly identified. Figure 2. displays the distribution of mineralized Late Cretaceous to Pliocene magmatic arcs (modified from Directorate of Mineral Resources (1991) and Carlile and Mitchell (1994).

2. LATE CRETACEOUS ARC

2.1 Sumatra-Meratus arc

This continental arc is represented by the Sumatra-Meratus arc which extends along the southern edge of Sundaland from north Sumatra through the tip of west Java to east Kalimantan. In Sumatra mineralization found consist of predominant tin deposits of the greissen/porphyry type (in this case are associated with W), and as placer deposits (with/without Ce). Other minerals found

include Au (skarn-, disseminated-, alluvial- types); silver, Cu-Zn, Cu-Mo, Cr-Mn, Pb-Zn, and small iron skarn deposits. Several gold prospects in the Meratus segment (at Timburu and Sungai Keruh) are hosted by quartz- and quartz-carbonate-veins, suggesting an epithermal type.

3. LATE MIOCENE AND PLIOCENE ARCS

3.1 Aceh arc

This arc is short; it has only a small potential in mineralization, but it differs from the adjacent western segment of the Sunda-Banda arc by its porphyry copper-molybdenum type mineralization and high sulphidation rather than low sulphidation epithermal type. (van Leeuwen et al, 1987 op cit Carlile and Mitchell, 1994).

3.2 Sunda-Banda arc

This arc is the longest arc in Indonesia, extending from North Sumatra through Java, Bali, to east of Damar. The western segment include west Java, a part of Central Java; it is present on the southern margin of Sundaland. This arc is very potential in mineralization. Nearly 20% of Indonesia's gold and about 14% of its copper deposits belong to this arc. The western part of Sunda-Banda arc is dominated by a low sulphidation epithermal vein system; minor sediment hosted gold mineralization is noted such as in Cikotok district. One of the most largest gold –silver deposit occurred in west Java (the Gunung Pongkor deposit) containing more than 100 tones of gold and 1000 tones of silver. Its belongs to a low sulphidation epithermal mineralization which is associated with Neogene calc-alkaline volcanism.

The mineralization type in the eastern segment of Sunda-Banda arc is different. The porphyry- type mineralization seems to be predominant such as the world class Batuhijau porphyry Cu-Au in Sumbawa island, and a number prospects with high sulphidation mineralization characteristics are known on Lombok, Sumbawa, Flores, and Wetar. The later contains stratiform, submarine exhalative baritic Au-Ag deposits at Lerokis

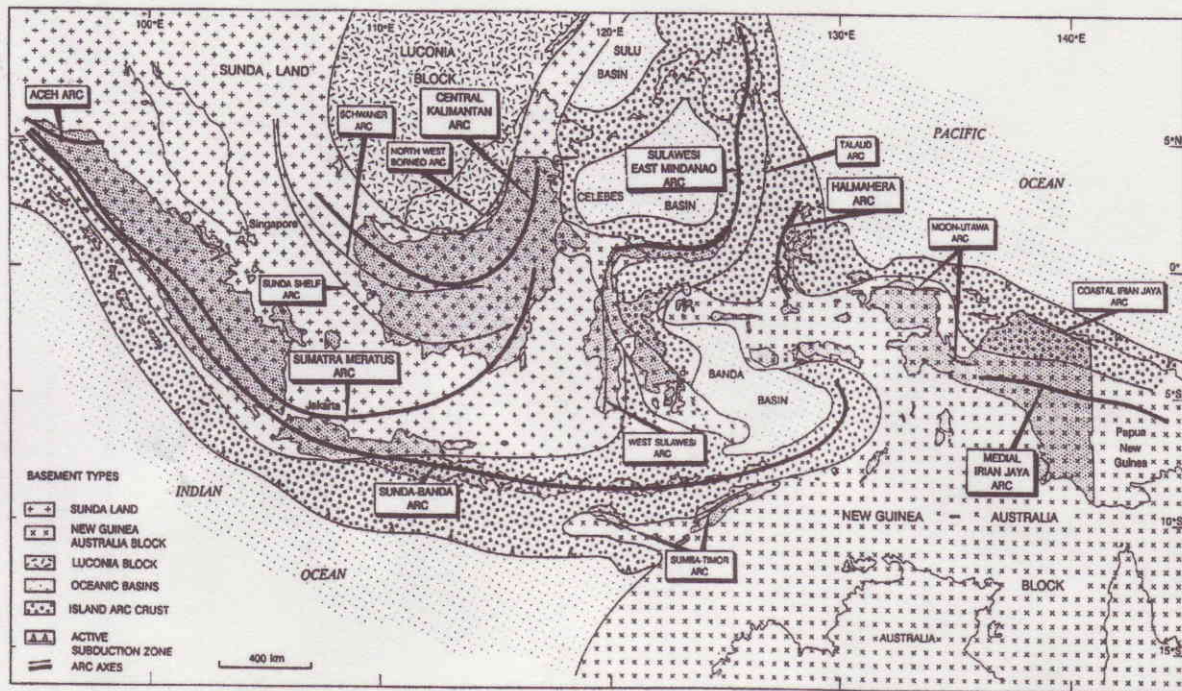


Figure 1. Major magmatic arc axes and crustal blocks in Indonesia (Carlile and Mitchell, 1994)

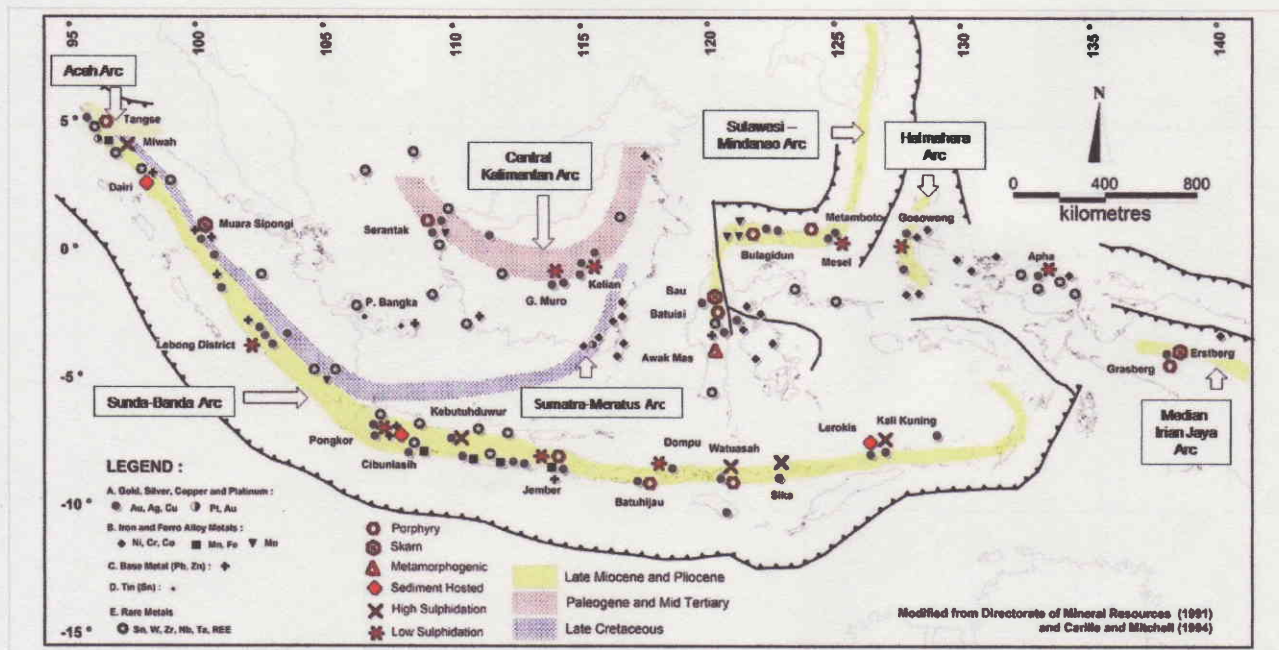


Figure 2. Distribution of mineralized Late Cretaceous to Pliocene magmatic arcs.

and Kali Kuning occur in ferruginous baritic sands, and clays in altered volcanic breccias, above and alongside mounds of Cu-rich massive sulphides. The deposits, then, are covered with fossiliferous sediment of an age of 4 Ma. The formation took place in submarine calderas at relatively shallow water depths (< 600 meters) in an emergent volcanic arc setting. The condition of the formation in a shallower depths, lower pressures and lower temperatures than those common for typical kuroko deposits may help explain the Au and Ag rich, Pb-Zn poor nature of Wetar deposits. It seems that shallow water submarine volcanic conditions facilitate the precious metals rather than the base metals.

3.3 Sulawesi-East Mindanao arc

The island arc segment, includes most of the north arm of Sulawesi and Bulagidun, high sulphidation deposit in Motomboto, sediment-hosted gold deposits in Mesel, and silver-barite± base metal (VMS) deposit at Binebase in Sangehe Island that has much similarity with VMS deposit in Wetar Island. The other sediment-hosted gold deposits are present at Ratatotok district (include Mesel and Lobongan). Skarn Au and porphyry molybdenum deposits are occurred at Bau (SW Sulawesi) and at Malala district (NW Sulawesi) in succession.

3.4 Halmahera arc

This arc is little explored and the only known mineralization is the Kaputusan porphyry copper-gold deposit on Bacan Island (Bering, 1986 op cit Carlile and Mitchell, 1994). Other deposits found in this island are ferro alloy metals (Ni-Cr-Co) laterites which are believed derived from weathered ultramafic rocks.

3.5 Medial Irian Jaya arc

More than 50% of Indonesia's gold deposits and about 70% of its copper deposits belong to this arc. There are four large deposits : the Grasberg, one of the largest gold-rich porphyry copper deposits in the world, and three major skarn ore bodies are located in an area of 100 square kilometers making up the Ertsberg mining district at the western end of the arc (MacDonald and Arnold, 1994; Mertig et al., 1994). The extension of these deposits to the eastern into Papua New Guinea are also contain world class deposits as it is reported by several authors .

4. PALEOGENE AND MID TERTIARY

4.1 Central Kalimantan arc

The Central Kalimantan arc represents the Mid Tertiary magmatic arc of Indonesia. The eastern and central section of the arc contains about 10% of Indonesia's gold without copper deposit. A number of four gold deposits occurred in this arc : Kelian, the largest Indonesian gold mine, which displays characteristic between epithermal and porphyry style mineralization (van Leeuwen et al., 1990, op cit Carlile and Mitchell, 1994); Long Laai, the skarn Au-Sn, it contains cassiterite in greissen and skarn, in, and adjacent to granodioritic intrusions (Hutchison, 1989, op cit Carlile and Mitchell, 1994; the mesothermal veins at Gunung Mas which are also associated with granite intrusions; The western segment contain only minor

mesothermal quartz veins mineralization which are closely associated with skarns, and deeper erosion level are inferred.

5. FUTURE RARE METALS AND RARE EARTH METALS EXPLORATION IN INDONESIA

Indonesia relatively rich in various metallic minerals such as precious-, base-, ferro alloy-, light- and rare- metals. The metallic mineral resources seem to be more and more economically important in the future. Rare metals are those which are relatively found in small amounts (compare to other metallic minerals) occurring in a very low concentrations, and is relatively very low in price. But since the year 2008, the Government of Indonesia especially the directorate which is responsible for mineral exploration (recently the Ministry of Energy and Mineral Resources, Geology Agency) pays attention about those rare metals by starting to put rare metals study as one of their agenda of mineral exploration. Figure 3 displays map showing rare metals occurrence in Indonesia compiled by Directorate of Mineral Resources (1991).

Indonesia supply more than 40% of Ni demand in Japan. Some of rare metals (Ni, Cr, Sn, Au) and rare earth resources had been surveyed by Japan Oil, Gas and Metals National Corporation (JOGMEC). Most of rare metals and rare earth are accompany with major base-metals. Beside the ore exploration, separation technique is another important research field. These are the best topics to cooperate with Akita University.

Acknowledgements: We are very grateful to the President of Akita University, the International Exchange Section, the OC of the ICRM2009 for inviting and facilitating the first author to come and joint the ICMR2009 conference. We also thank to Mr. Purnama Sendjaja in preparing all of the figures and provide most of the references.

References

- [1] Carlile, J.C., and Mitchell, A.H.G., "Magmatic arcs and associated gold and copper mineralization in Indonesia". *Journal of Geochemical Exploration*, 50, 91-142, (1994).
- [2] Crow, M.J., and T.M. Van Leeuwen, T.M., "Metallic mineral deposits". In: Barber A. J., Crow, M.J., Milsom, J.S (eds). *Sumatra, Geology, Resources and Tectonic Evolution*. Geological Society Memoir, 31, 147-174, (2004).
- [3] Hamilton, W., "Tectonics of the Indonesian region". U.S. Geol. Surv. Prof. Pap., 1078, United States Government Printing Office., 345pp., (1979)
- [4] MacDonald, G.D. and Arnold, L.C., "Geological and geochemical zoning of the Grasberg Igneous Complex, Irian Jaya, Indonesia". *Journal of Geochemical Exploration*, 50, pp.143-178, (1994).
- [5] Marcoux, E., A, and Milesi, J.P., "Epithermal gold deposits in West Java, Indonesia". *Journal of Geochemical Exploration*, 50, pp.393-408, (1994).
- [6] Mertig, H.J., Rubin, J.N., and J.R., Kyle, J.R., "Skarn Cu-Au orebodies of the Gunung Bijih (Ersberg) district, Irian Jaya, Indonesia". *Journal of Geochemical Exploration*, 50, pp.179-202, (1994).
- [7] Sewell, D.M. and Wheatley, C.J.V., "The Lerokis and Kali Kuning submarine exhalative gold-silver-barite deposits, Wetar

Island, Maluku, Indonesia". *Journal of Geochemical Exploration*, 50, pp.351-370, (1994).

[8] Sillitoe, R.H., "Indonesia mineral deposit-introductory, comments, comparisons and speculations". *Journal of Geochemical Exploration*, 50, pp.1-11, (1994).

[9] Soeharto, R.S., "Hasil eksplorasi logam di Jalur busur magmatic Sunda-Banda", Kolokium hasil kegiatan lapangan DSM, unpublished report, 20pp, (2000).

[10] van Leeuwen, T.M., "25 Years of mineral exploration and discovery in Indonesia". *Journal of Geochemical Exploration*, 50, pp.13-90, (1994).

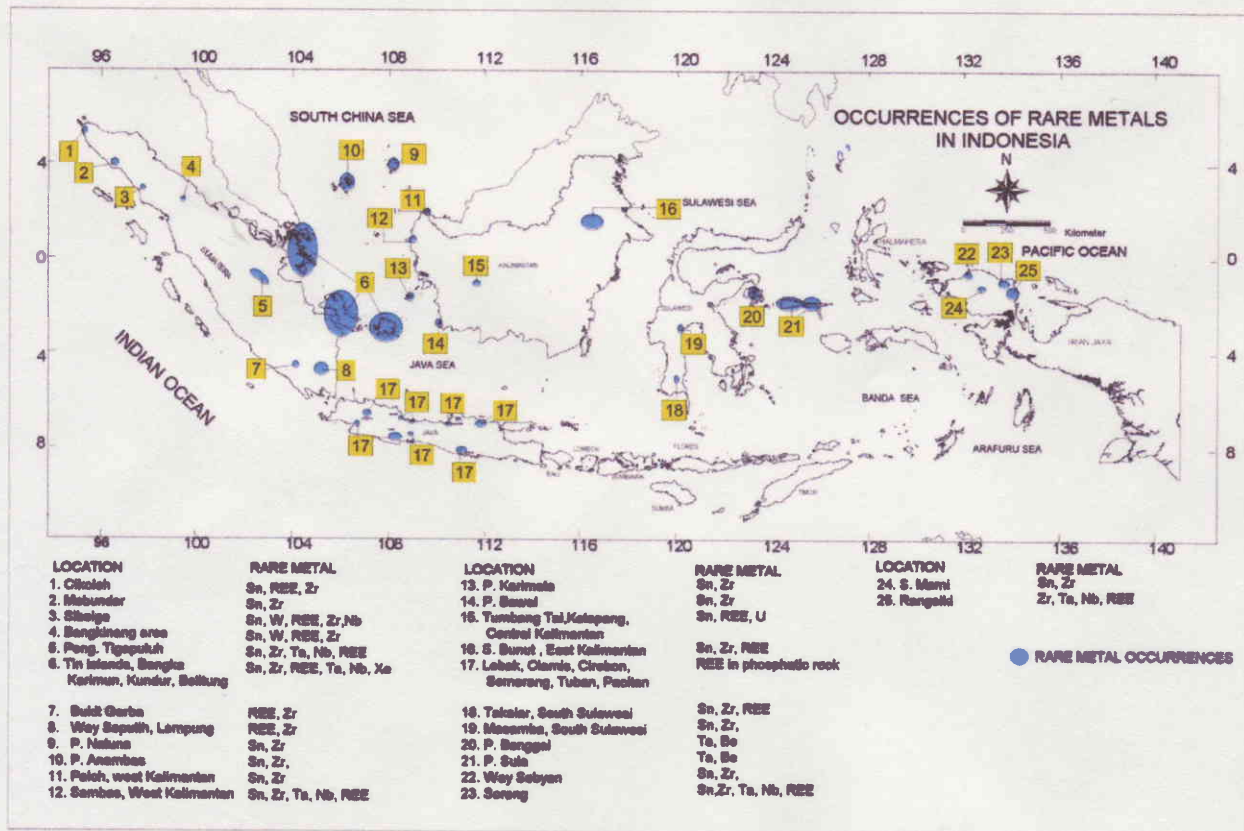


Figure 3. Occurrences of rare metals in Indonesia (Directorate of Mineral Resources, 1991)

Numerical Studies on Concrete Members to Detect the Defects by Impact-Echo Method

Sanghun LEE

Department of Civil and Environmental Engineering, Faculty of Engineering, Tohoku Gakuin University, 1-13-1, Chuo, Tagajo,
985-8537 Japan

leesh@tjcc.tohoku-gakuin.ac.jp

Abstract: In this study, PAM-CRASH, a finite element method structure analysis program, is applied to the analysis of the impact-echo method used to investigate defects in concrete structures. First, a model of concrete members is made, and a shock/dynamic analysis is performed. The result of the impact-echo method on the analysis is calibrated by comparing the experimental measurement with the impact-echo method for specimens under the same conditions. Furthermore, a shock/dynamic analysis is performed using models in which various defects are set, and the precision with which the size and position of the defects is identified by the impact-echo method is discussed.

Key Words: impact-echo method, size and position, defects in concrete members, PAM-CRASH

1. INTRODUCTION

Recently, the importance of maintenance of concrete structures has come to be recognized, and thinking about life cycle cost—not only about new social investment—is considered more important. In particular, nondestructive inspection has become an important technical method as it does not damage a structure when maintenance is carried out. When a concrete structure is inspected, it is important to gather as much information as possible. One of the advantages of nondestructive inspection is that it makes easy multiple inspections, which gather a wide range of information, possible without destruction of the structure. Conventional nondestructive inspection seeks only to ascertain the strength of the concrete. However, when a durability inspection is made, different information is needed in addition to that on concrete strength. There are many kinds of principles and methods involved in nondestructive inspection, and one tasked with carrying out an inspection should be well informed as to these methods.

One nondestructive inspection technique is the impact-echo method, used to detect voids in concrete. This method measures the reflection of an elastic wave caused when an impact is given to the surface of a concrete structure. The way the wave spreads throughout the concrete is analyzed, and the position of a void is identified [1].

In this study, PAM-CRASH, a finite element method (FEM) structure analysis program that uses the dynamic explicit integration method, is applied to the analysis of the impact-echo method used to investigate defects in concrete structures. First, a model of concrete members such as beams or slabs is made, and a shock/dynamic analysis is performed. The result of the impact-echo method on the analysis is

calibrated by comparing the experimental measurement with the impact-echo method for specimens under the same conditions. Furthermore the shock/dynamic analysis is performed using models in which various defects are included, and the precision with which the size and position of the defects identified by the impact-echo method is discussed.

2. IMPACT-ECHO METHOD

In the impact-echo method, an elastic wave is generated by the impact of a steel ball or a hammer positioned at an effective height above the surface of a concrete structure. The resulting elastic wave that spreads throughout the entire concrete structure is recorded by a sensor. This method is used to measure the position and dimensions of defects in concrete, as well as certain properties of the concrete, by analyzing the elastic wave received by a sensor. A great advantage of the impact-echo method is that it allows for nondestructive testing of a structure and is easier to conduct than conventional methods.

In this study, this impact-echo method is used mainly. As stated, in the impact echo method, a physical shock is given to a concrete surface, and an elastic wave is generated. Among the elastic waves produced, the P wave (a longitudinal wave), which has the biggest displacement, is used in the impact-echo method. From the property of the elastic wave, the resonance of the P wave produces a great number of reflections in the section between the concrete surface and the different boundary-surface of the matter properties. The frequency of the prominent peak is called the resonant frequency, and is detected when frequency analysis is carried out. The P wave received by a sensor on the surface of the concrete is converted into a frequency spectrum. Here, a fast Fourier transform (FFT) is

used. If a resonant frequency can be detected, the thickness of the concrete, or depth of the internal defect, can be calculated as

$$T = \frac{C_p}{2f_p} \quad (1)$$

where,

- T : Thickness of concrete (m)
- C_p : P-wave velocity (m/s)
- f_p : Frequency of P-wave reflections (Hz).

3. ABOUT PAM-CRASH

The modeling function and the mesh-generation function of midas FEA of software program are used to make a model, which in turn is analyzed using PAM-CRASH. Let the model made by midas FEA adapt itself to PAM-CRASH, and the time history of the acceleration response to shock impact acceleration is analyzed using PAM-CRASH, and a Fourier transformation is applied to the result, and the resonant frequency is obtained.

3.1 PAM-CRASH is...

PAM-CRASH is a FEM structural analysis program that uses the dynamic explicit integration method, and it can be applied to analysis for phenomenon that have strong nonlinearities, which in addition to shock/impact problems includes geometrical nonlinearity, material nonlinearity, and the contact problem.

3.2 Pre/Post processes

The FEM analysis solution for civil engineering/ building structures, midas FEA, is used as a pre-processor. This solution has a convenient user interface comprising a window environment, various geometric modeling functions at the CAD level, and an auto mesh-generation function. After analysis by PAM-CRASH, the results, for example the transient response of acceleration, can be expressed by a graph produced by a post-processor called PAM-VIEW.

4. VERIFICATION ANALYSIS

It is then verified whether the numerical analysis obtained by the three-dimensional finite element method using PAM-CRASH can be applied to the impact-echo method used to investigate defects in a concrete structure. A model of the specimen used in the experiment is constructed, and the time history of the response acceleration for the impact is calculated by a numerical analysis of PAM-CRASH, and the resonant frequency spectrum obtained from the result by FFT is compared with the result of the measurement of the resonant frequency spectrum obtained by experiment.

4.1 Analysis model

4.1.1 Modeling an impactor: In the impactor, two steel balls having different diameters (10 mm and 20 mm) are used, with masses of 4 g and 33 g, respectively. The elastic modulus and Poisson's ratio are $E=200$ kN/mm, $\nu = 0.3$, respectively, and the initial velocity of the ball is 30 m/sec. A model of an impactor is shown in Figure 1.

4.1.2 Modeling of specimens (concrete column): Models of three specimens (No. 1, No. 2, and No. 3) with lengths of 300

mm, 400 mm, and 600 mm, respectively, are shown in Figure 2. The cross section of each model is 100 mm × 150 mm. Specimen No. 4, which is a concrete beam with an internal defect, is shown in Figure 3. The size of the beam is 300 mm in length, and 100 mm × 150 mm in cross section. The defect is simulated by a thin rectangular void (70 mm × 10 mm × 10 mm). In addition, the defect position is set at the center of the specimen model, and its depth is 75 mm from the upper surface (shown in Figure 3).

The impactor with the 20-mm diameter steel ball is used for models No. 1, No. 2, No. 3, and that with the 10-mm diameter ball is used for No. 4. In addition, the impact point of the steel ball on the specimen model is the same point used in measuring the elastic wave. For specimen models No. 1, No. 2, and No. 3, the point is the center of the upper section. For Specimen No. 4, two points are measured, one is the center of the upper surface of the beam and the other is a point of 100 mm outward in the longitudinal direction.

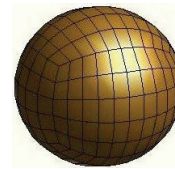


Figure 1. Model of an impactor

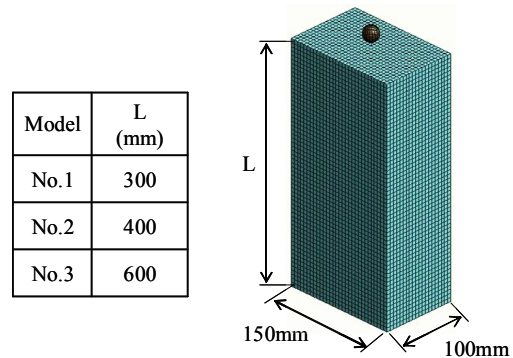


Figure 2. Model of a specimen

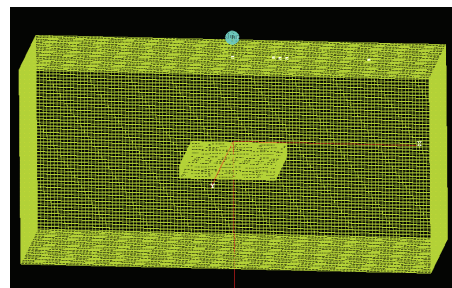


Figure 3. Model of a specimen with a defect

4.2 Material properties

The properties of the analytic model of PAM-CRASH are shown in Table 1, in which the impactor is assumed to be steel and the specimen is assumed to be concrete. The initial velocity of the impactor is 30 m/sec, and the time step of analysis is 1 μ sec.

The compressive strength of the concrete is assumed as 26 N/mm², which is the average value of the specimens used in the experiments [2], and the Young's modulus is estimated by Eq. (2) below, suggested by ACI for Young's modulus of concrete

$$E = 0.043w_c^{1.5}\sqrt{f'_c} \text{ MPa} \quad (2)$$

where,

E : Young's modulus of concrete (MPa)

w_c : Density of concrete (kg/m³)

f'_c : Compressive strength of concrete (MPa)

The relation with a bulk modulus and shear modulus is expressed as follows

$$\text{Bulk modulus} = \frac{E}{3(1-2\nu)} \quad (3)$$

$$\text{Shear modulus} = \frac{E}{2(1+\nu)} \quad (4)$$

where,

E : Young's modulus

ν : Poisson's ratio

4.3 Results of analyses

The time history of the response acceleration is obtained by analysis, and the resonant frequency spectrum is obtained by FFT, successively. The results of the FFT of the analyses are shown in Figure 4(a)~(e). The results are arranged and compared with the results of experiment as shown in Table 2.

When the propagation velocity (P-wave velocity) of models No. 1, No. 2 and No. 3 are compared with their average value, the deviation is settled within an error of less than 1%. From this, the P-wave velocity of models No. 1, No. 2, and No. 3 may be regarded as equal. The results of the experiment show

Table 1. Material properties

Model	Density $\times 10^6$ (kg/mm ³)	Young's Modulus (kN/mm ²)	Bulk Modulus (kN/mm ²)	Shear Modulus (kN/mm ²)
No. 1, 2, 3	2.35	24.6	13.6	10.2
No. 4	2.35	38.6	21.4	16.1
Impactor	7.85	200	-	-

Table 2. Results of analyses

Model	Length (mm)	P-Wave Speed	
		Analysis (m/s)	Experimental (m/s)
No. 1	300	3320	3090
No. 2	400	3351	3114
No. 3	600	3383	3110
No.4	75	3968	3621
	150	4211	4170

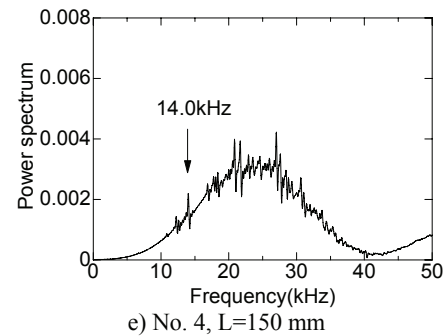
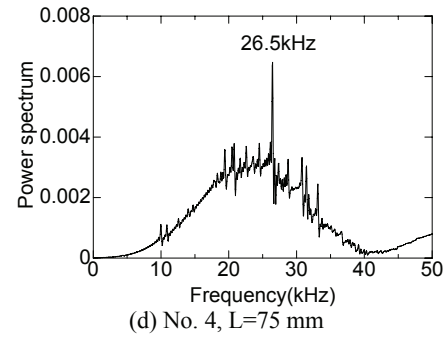
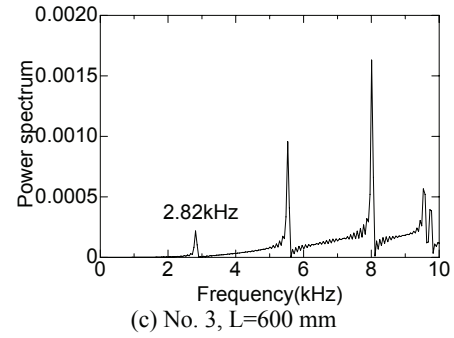
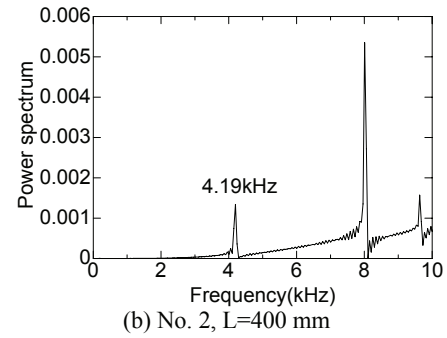
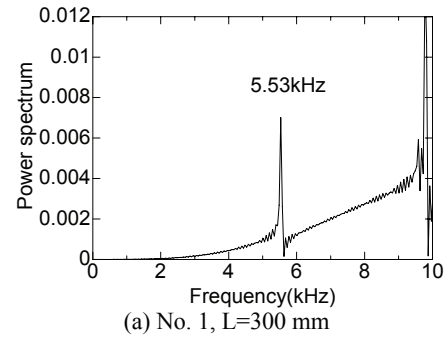


Figure 4. Results of analyses

the same tendency, too. Therefore, it can be said that the resonant frequency is a low value in all models and specimens when the measurement dimension is long. This shows that the method used in analysis and the experiment function as a measuring system together.

The numerical experiment using PAM-CRASH shows conclusively that an application of the impact-echo method is possible with good accuracy.

In addition, it is thought that the difference of resonant frequency obtained in the analyses results and the experimental results produced is because the properties of the material (density and elastic modulus, etc.) used for the analyses models and for the experimental specimens are different.

5. IDENTIFICATION OF POSITION AND SIZE OF INTERNAL DEFECT

Nine concrete models with three different defect widths and compressive strengths (an elastic wave) are analyzed using PAM-CRASH.

Time history data of response acceleration at the measuring point by impact analysis are converted by FFT, and examined to determine whether the defect position and size can be identified by the resonant frequency for the measurement dimension.

5.1 Analysis model

Let a 20-mm diameter steel ball (mass 33 g, $E=200$ kN/mm, $\nu=0.3$) shown in Figure 1 impact a concrete model at an initial velocity of 30 m/sec.

The size of the concrete model is 200 mm in length, and its section size is 50 mm \times 100 mm, the same in all models. The figures of each model are shown in Figure 5. The different point is the size of the defect in each model. The defect widths for No. 1, No. 2, and No. 3 are 25 mm, 50 mm, and 100 mm, respectively. The other size is 50 mm \times 100 mm for each model, and it is made so that the defect penetrates a concrete model.

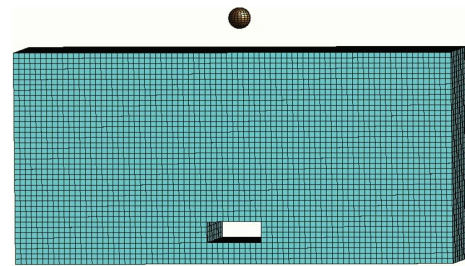
The five points of measurement are shown in Figure 6 and Table 4.

5.2 Material properties

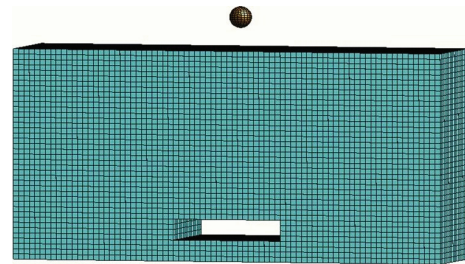
The properties of the impactor are the same as in Sec. 4 (shown in Table 1). The material properties are shown in Table 3. The material is divided into three types: A, B, and C according to the compressive strength of the concrete—18, 27, and 36 N/mm², respectively.

5.3 Results

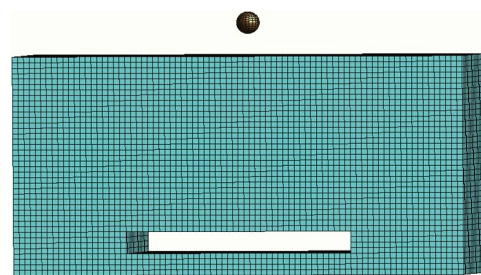
Figures 7-15 show the distribution of the peak magnitude of the power spectrum in the resonant frequency at measurement dimensions 80 mm and 100 mm in each point of measurement of the model, for each type of material (A, B, C).



(a) No. 1 (defect width = 25 mm)



(b) No. 2 (defect width 50 mm)



(b) No. 3 (defect width= 100 mm)

Figure 5. Models of analyses

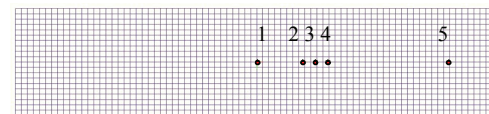
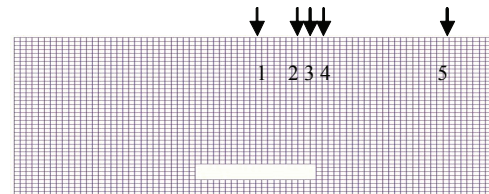


Figure 6. Points of measurement

Table 3. Material properties

Model Type	Compressive Strength (N/mm ²)	Young's Modulus (kN/mm ²)	Bulk Modulus (kN/mm ²)	Shear Modulus (kN/mm ²)
A	18	20.5	11.4	8.5
B	27	25.0	13.9	10.4
C	36	28.9	16.1	12.0

Table 4. distance of each point from center (mm)

Model Type	Point.1	Point.1	Point.1	Point.1	Point.6
No.1	0	10	12.5	15	80
No.2	0	20	25	30	80
No.3	0	40	50	60	80

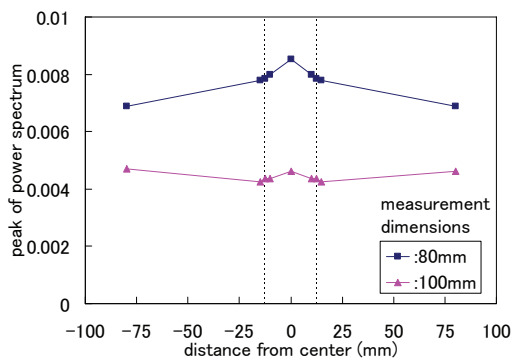


Figure 7. Peak magnitude of power spectrum in each position (defect width 25 mm, A type)

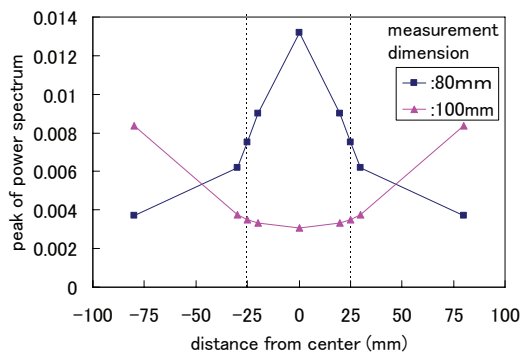


Figure 11. Peak magnitude of power spectrum in each position (defect width 50 mm, B type)

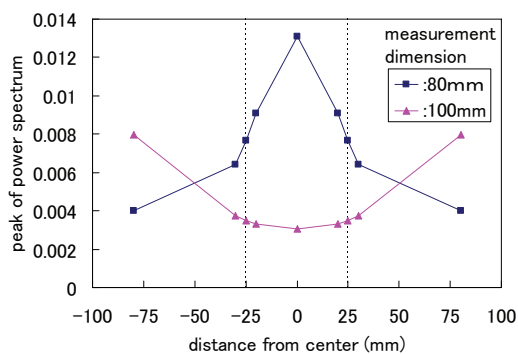


Figure 8. Peak magnitude of power spectrum in each position (defect width 50 mm, A type)

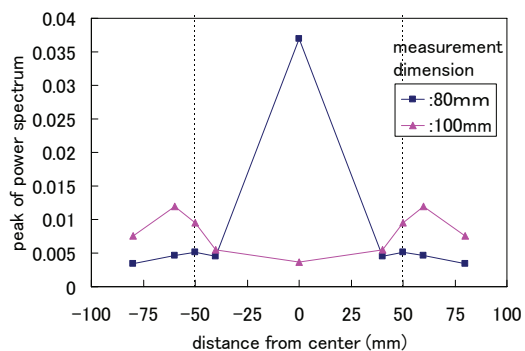


Figure 12. Peak magnitude of power spectrum in each position (defect width 100 mm, B type)

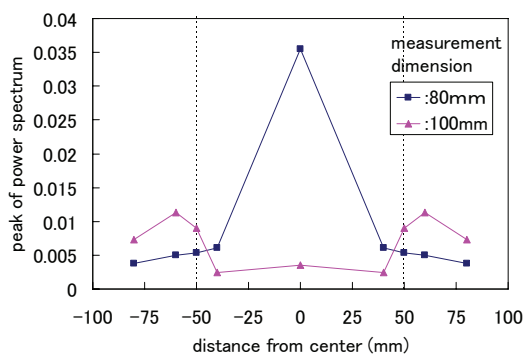


Figure 9. Peak magnitude of power spectrum in each position (defect width 100 mm, A type)

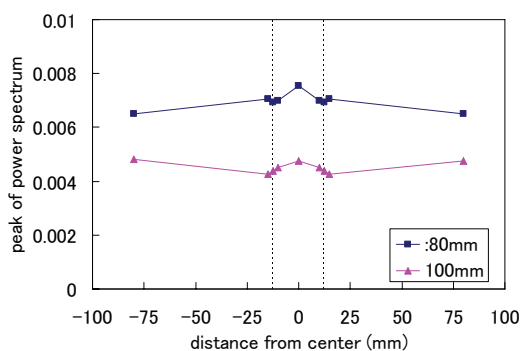


Figure 13. Peak magnitude of power spectrum in each position (defect width 25 mm, C type)

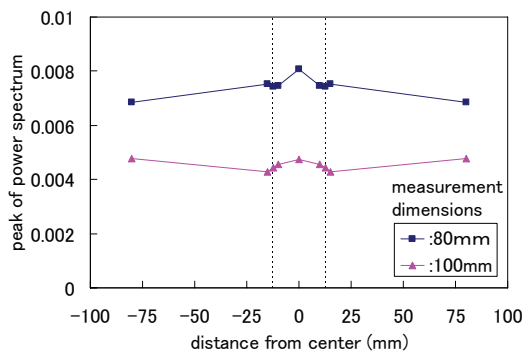


Figure 10. Peak magnitude of power spectrum in each position (defect width 25 mm, B type)

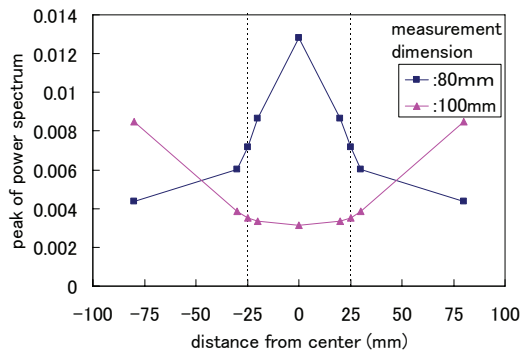


Figure 14. Peak magnitude of power spectrum in each position (defect width 50 mm, C type)

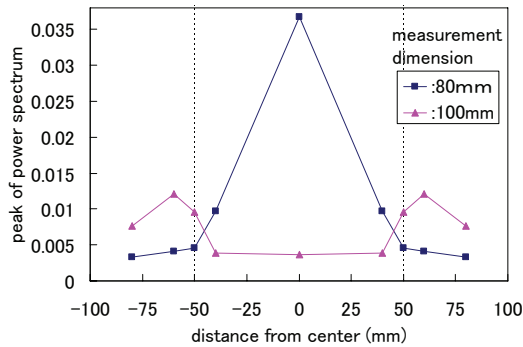


Figure 15. Peak magnitude of power spectrum in each position (defect width 100 mm, C type)

The result of the analysis for each defect width is written as follow.

Defect width 25 mm

Conceptually, it should be expected that the spectrum peak magnitude of the measurement dimension of 80 mm in the defect position is the reverse of that of 10 mm at the border of the defect. However, the result shows that the spectrum peak magnitude of measurement dimension 100 mm that should have been damped in the defect position was amplified in the defect position.

This goes against the expectation according to theory, but it may be said that it is not difficult to distinguish a defect area and sound area from a graph.

Defect width 50 mm

As it nears the defect center, the spectrum peak magnitude of the measurement dimension of 80 mm becomes larger, and the spectrum peak magnitude of measurement dimension 100 mm becomes smaller. This result accords with the theoretical expectation.

The position of the half values of the spectrum peak magnitude of the defect center becomes nearer in the boundary of a defect part and the sound area.

Defect width 100 mm

The magnitude of the spectrum peak in the center becomes stronger as the defect width becomes longer.

The boundary of the defect area and the sound area located near the position where the decrease line of the spectrum peak magnitude in measurement dimension 80 mm and the increase line of the spectrum peak magnitude in measurement dimension 100 mm intersect.

Summary

The graph of the spectrum peak magnitude for each defect width was compared, but a typical shape for the graph was not seen. The object that was near to a graph expected most was that with a defect 50 mm in width. In addition, a difference in strength of material was not seen.

As a result, even although the typical shape of a graph was not produced for a different defect-width model form, the possibility that the defect width can be identified by a border of the defect from the shape of the graph was confirmed.

6. CONCLUSIONS

The following knowledge was obtained through this study.

- (1) PAM CRASH is applicable to analysis at an experiment level using the impact-echo method.
- (2) It was recognized that the position and dimension of a defect could be supposed by this numerical experiment.
- (3) A difference in the strength of material was not observed in this study.

References

- [1] Sansalone, M. and Carino, N. J., "Detecting delaminations in concrete slabs with and without overlays using the impact-echo method," *ACI Materials Journal*, Vol.86, No.2, March-April 1989, pp.175-184.
- [2] Watanabe, M.; Lee, S. H.; and Ishikawa, M., "The inspection of the defect investigation system of the concrete structure using the impact-echo method," *Proceedings of the Annual Conference in H20, Tohoku Branch of JSCE*, I-34, 2009, pp.67-68, in Japanese.

Prospect of Demand for Concrete in Eastern Asian Countries in Terms of Statistics of Consumption of Cement in Europe and Japan

Masahiro OUCHI

Department of Infrastructure Systems Engineering, Kochi University of Technology
Tosa-yamada, Kami, Kochi 782-8502, JAPAN
ouchi.masahiro@kochi-tech.ac.jp

Abstract: Prospect of the demand for concrete in the eastern Asian main countries was discussed in terms of the statistics of the consumption of cement in the developed countries in the world like Japan and European countries as the preceding countries of the investment for the construction. The annual increasing rate of concrete was defined as the ratio of the annual consumption of cement to the accumulated consumption of cement. According to the statistics of some of the European developed countries, that is, U.K., France, Denmark, and Sweden, whose annual increasing rate was less than that of Japan, the annual increasing rate of concrete has been stable at around 0.01 to 0.02 for over ten years. The author assumed that the increasing rate would converge at 0.01 to 0.02 in Japan, Taiwan and Korea and estimated the consumption of cement in coming a few ten years.

Key Words: consumption of cement, demand for construction, increasing rate of concrete structures

1 INTRODUCTION

Prospect of the demand for concrete in the eastern Asian main countries was discussed in terms of the statistics of the consumption of cement in the developed countries in the world like Japan and European countries as the preceding countries of the investment for the construction. The reasons why the consumption of cement shall be the index are as follows:

- (1) Indispensable component of concrete: the most common construction material
- (2) Almost constant unit content in concrete : 300 kg/m³
- (3) Sufficient & reliable data from the early 20th century all over the world

The author assumed that the amount of consumption of cement shall be in proportion to the amount of structure constructed.

Asia's share of consumption of cement in the world has been increasing (Fig. 1). On the other hand, the consumption of cement in Japan and Taiwan is now decreasing and it is possible that the peak of the consumption may not break the record (Fig. 2).

The relationship between GDP and the consumption of cement per capita in all the countries and areas in the world in 2005 is shown to grasp the influence of the economic growth on the demand for the construction (Fig. 3). Also, the relationship in Asian main countries only is shown (Fig. 4). According to the regression curve, the peak for the demand for the construction can be found at GDP of around USD 20,000 per capita.

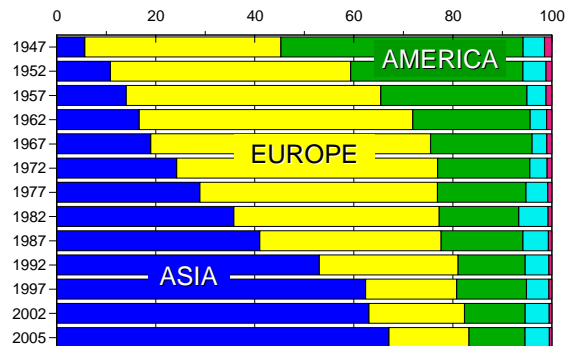


Fig. 1 Increasing and dominant Asia's share of consumption of cement in the world

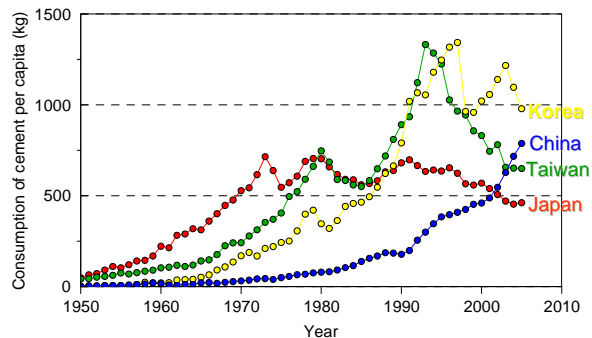


Fig. 2 Decreasing consumption of cement for over ten years both in Japan and Taiwan and just started decreasing in Korea

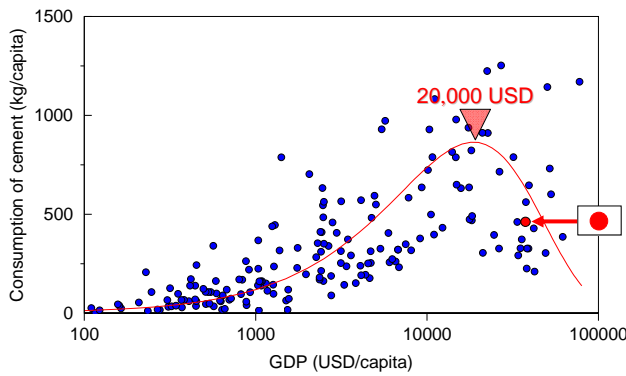


Fig. 3 Peak for demand for construction at GDP of USD 20,000 per capita as of 2005

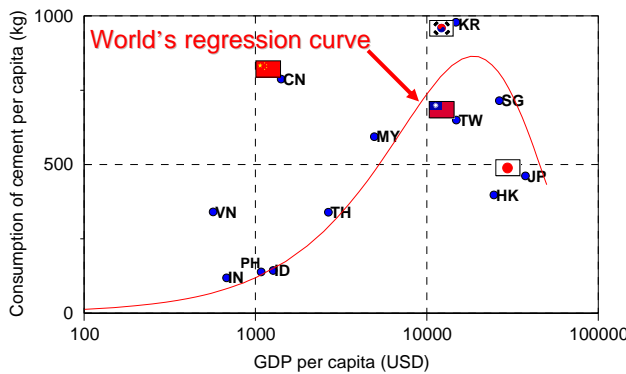


Fig. 4 Japan and Taiwan no longer in increasing demand for construction as of 2005

2 DEFINITION FOR ANNUAL INCREASING RATE OF CONCRETE

The potential for the demand for cement may be different in each country because the necessity for concrete structures is subject to the geological and weather conditions and to the status of the concrete material. The unified index for the demand for the construction and then the consumption of cement is indispensable.

The author assumed the relationship between accumulated and annual consumption of cement, in which the accumulation of the consumed cement may result in the stock of the infrastructure and it may affect the current amount of the consumption of cement as shown in Fig. 5.

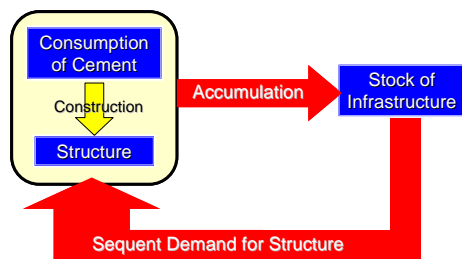


Fig. 5 Relationship between accumulated and annual consumption of cement

The author defined the annual increasing rate of concrete as the ratio of the annual consumption of cement to the accumulated consumption of cement (Fig. 6). The relationship between GDP per capita and the annual increasing rate of concrete in world's main countries as Asia, Europe and America is shown (Fig. 7). Larger GDP roughly corresponded to lower annual increasing rate of concrete.

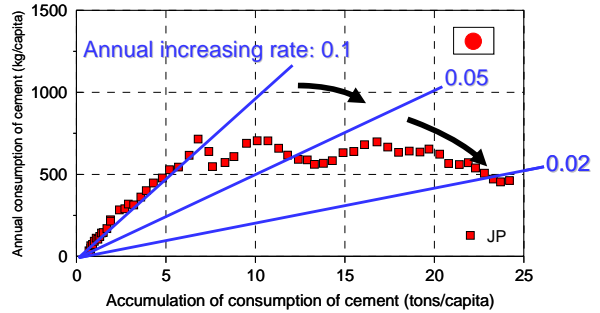


Fig. 6 Definition for annual increasing rate of concrete

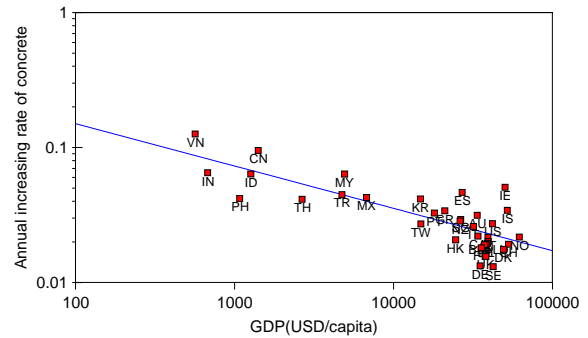


Fig. 7 Larger GDP roughly corresponding to lower annual increasing rate of concrete

The annual increasing rate of concrete in the main countries as of 2005 is shown (Fig. 8). The rate in France, Denmark, U.K., Germany and Sweden was smaller than that of Japan and the smallest of all the countries in the world.

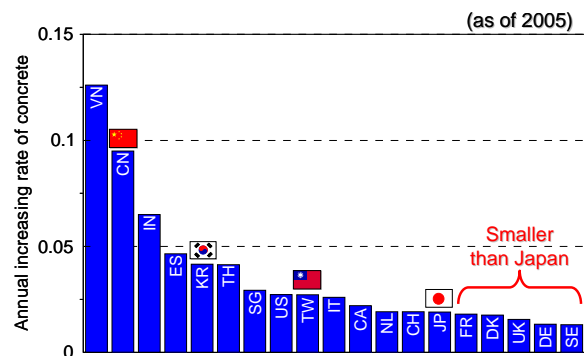


Fig. 8 Smaller annual increasing rate of concrete in France, Denmark, U.K., Germany & Sweden than in Japan as of 2005

The transition of the increasing rate of concrete in Japan since 1960 is shown (Fig. 9). The increasing rate had been constant at around 0.1 for over 10 years and then since 1973 it has been decreasing linearly along logarithmic scale for over 30 years in Japan. That was the case with most of the developed countries.

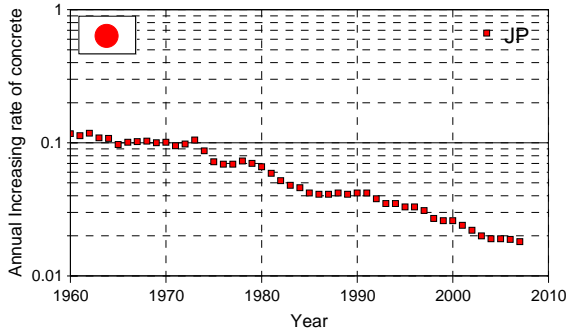


Fig. 9 Transition of the annual increasing rate of concrete in Japan

3 PROSPECT OF DEMAND FOR CONSUMPTION OF CEMENT IN JAPAN

According to the statistics of some of the European developed countries mentioned above, that is, U.K., France, Denmark, and Sweden, the annual increasing rate of concrete has been stable at around 0.01 to 0.02 for over ten years (Fig. 10). These values were the smallest of all the countries in the world.

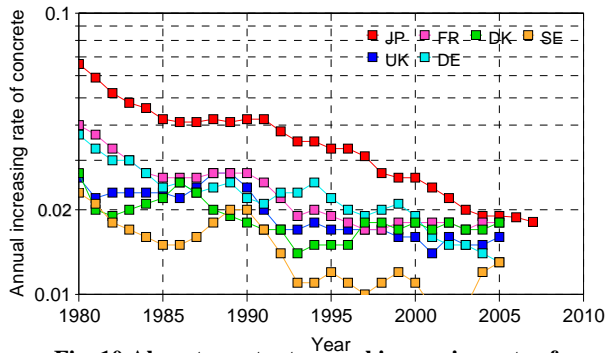


Fig. 10 Almost constant annual increasing rate of concrete at 0.01 to 0.02 for recent ten years in U.K., France, Denmark and Sweden

The author assumed that the annual increasing rate of concrete would converge at 0.01 to 0.02 in each country. By using the transition of the annual increasing rate of concrete as assumed in Fig. 11, the prospect of the consumption of cement in Japan in the near future is shown (Fig. 12). The expected bottom of the annual consumption of cement ranged from 40 to 60 millions subject to the converging annual increasing rate of concrete at ranging from 0.01 to 0.02.

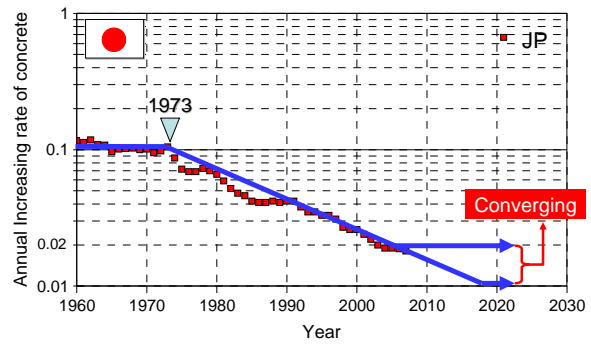


Fig. 11 Assumption for transition of the annual increasing rate of concrete in Japan

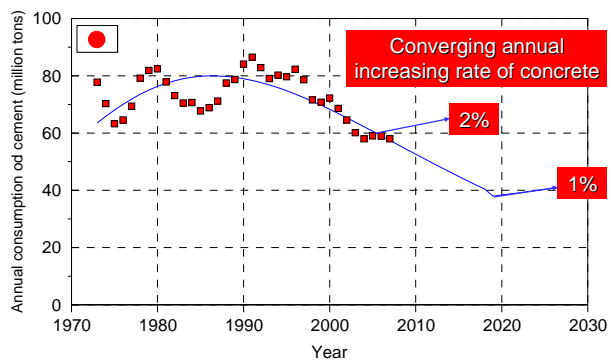


Fig. 12 Prospect of consumption of cement in Japan assuming annual increasing rate of concrete to converge at 0.01 to 0.02

4 PROSPECT OF DEMAND FOR CONSUMPTION OF CEMENT IN TAIWAN & KOREA

The prospect of the consumption of cement in Taiwan and Korea was also obtained by the same procedure with that of Japan (Figs 13 and 14). The logarithmic linear decreasing rate of the annual increasing rate of concrete was assumed as the same as that of Japan. Although the fluctuation of the increasing rate of concrete in Taiwan and Korea along the regression line was large compared with that of Japan, the line could be averagely fitted to that of Japan. By assuming that the annual increasing rate of concrete would converge at 0.01 to 0.02 in Taiwan and Korea, the bottom of the annual consumption of cement can be expected as 9 to 14 million tons in Taiwan (Fig. 15) and 25 to 40 million tons in Korea (Fig. 16).

The transition of the annual increasing rate of concrete in China was obtained (Fig. 17). The decrease in the annual increasing rate of concrete has not started yet as of 2006. Therefore, by assuming that the decrease in the annual increasing rate of concrete started in 2007, the prospect of the consumption of cement was obtained at this moment (Fig. 18). The bottom of the annual consumption was estimated as around 800 to 1,300 million tons.

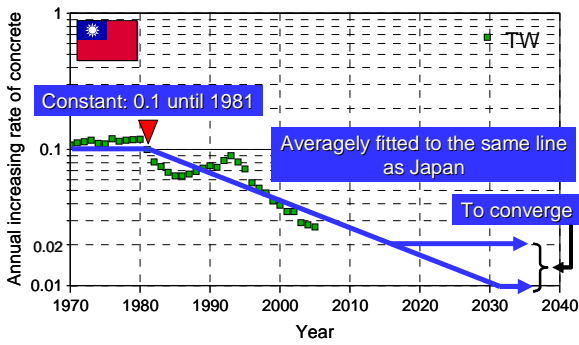


Fig. 13 Assumption for transition of annual increasing rate of concrete in Taiwan

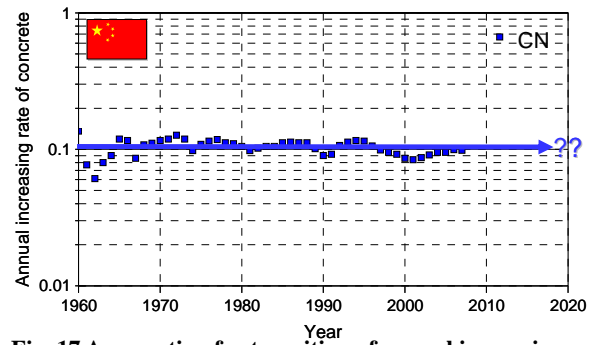


Fig. 17 Assumption for transition of annual increasing rate of concrete in China

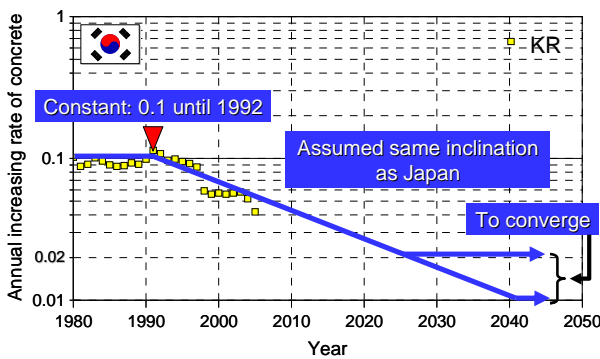


Fig. 14 Assumption for transition of annual increasing rate of concrete in Korea

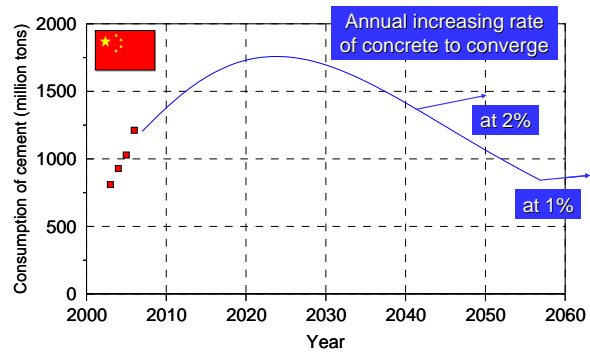


Fig. 18 Prospect of consumption of cement in China by assuming decrease in annual increasing rate of concrete starting from 2007

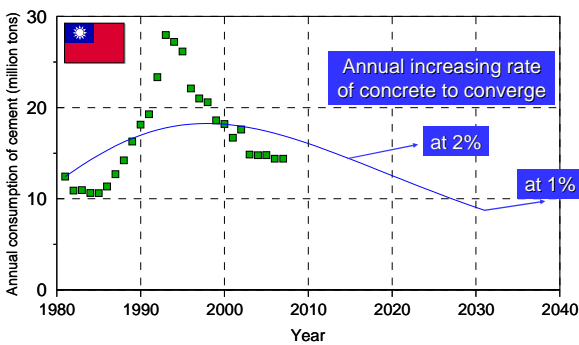


Fig. 15 Prospect of consumption of cement in Taiwan

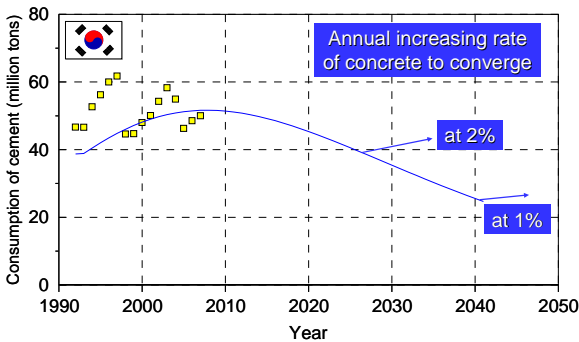


Fig. 16 Prospect of consumption of cement in Korea

5 TRIGGER OF DECREASE IN ANNUAL INCREASING RATE OF CONCRETE

It is necessary to know when the decrease in the annual increasing rate of concrete in each country started. So-called "The Trigger" of the decrease in the annual increasing rate of concrete was examined for each country in terms of the accumulated and annual consumption of cement (Fig. 19). Both in Japan and Taiwan, the accumulated consumption of cement per capita of around 7 tons was the trigger of the decrease. On the other hand, the decrease started at the accumulated consumption of around 10 tons per capita in Korea.

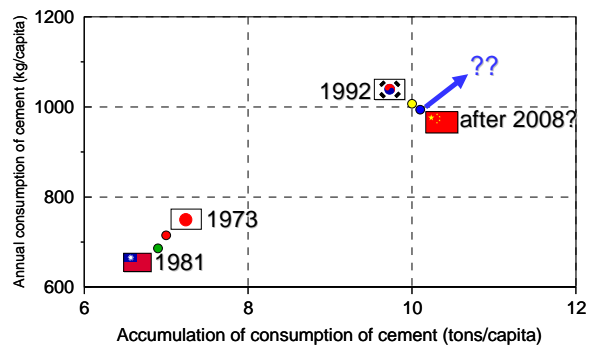


Fig. 19 Trigger of decrease in annual increasing rate of concrete in terms of accumulated and annual consumption of cement in each country

The decrease in the annual increasing rate of concrete in China has not started yet as mentioned above. However, the condition for the trigger was the quite similar to that of Korea in terms of the accumulated and annual consumption of cement.

6 SUMMARY

The prospects of the consumption of concrete in the near future in Japan, Taiwan and Korea were obtained by examining the statistical data of consumption of cement in the European preceding countries by using the index of the annual increasing rate of concrete.

The annual increasing rate of concrete was defined as the ratio of the annual consumption of cement to the accumulated consumption of cement. According to the statistics of the European developed countries, that is, U.K., France, Denmark, and Sweden, whose annual increasing rate was less than that of Japan, the annual increasing rate of concrete has been stable at around 0.01 to 0.02 for over ten years. By assuming the logarithmic linear decrease in

the annual increasing rate of concrete and the converging of the increasing rate at 0.02 to 0.01, the prospects of the consumption of cement in Japan, Taiwan and Korea were obtained.

Also, the trigger of the decrease in the annual increasing rate of concrete was examined for each country and needs more consideration and examination for its cause.

Acknowledgement The author acknowledges the CEMENT SHIMBUN (Cement Press), Tokyo, Japan for offering the latest statistics of the consumption of cement in the world.

References

[1] CEMBUREAU: World Cement Market in Figures 1913/1995

Trends for sustainable construction in Germany

Thomas A. BIER

Institut für Keramik, Glas- und Baustofftechnologie, Fakultät für Maschinenbau, Verfahrens- und Energietechnik, Technische Universität Bergakademie Freiberg, Leipzigerstrasse 28, D-09599 Freiberg, Germany

Thomas.bier@ikgb.tu-freiberg.de

Abstract: Based on European legislation, sustainable construction in Germany follows a guideline which focuses for example on “the design, construction and use of buildings and landholdings to sustainability, with the main emphasis put on the ecological and economic aspects.” In terms of construction this translates amongst others into longer life time of buildings, less use of building materials, energy efficient buildings and a safe environment with little risks to health. In the beginning of the chain design – construction – use of buildings are the construction materials and their respective raw materials. And there is logically an impact of this guideline on the use and manufacture of construction materials. Trends such as Manufacture of building materials with less energy and emissions, Building materials with higher mechanical performance and Building materials with improved thermal insulation are presented. Examples for each approach are presented and discussed in the light of its contribution to the sustainability of construction.

Key Words: Sustainability, Composite Cements, Thermal Insulation, Filler, High strength Concrete

1 INTRODUCTION

Together with the climate change due to CO₂ output by industrial processes and industrial economies a strong pressure has build up to reduce emissions, energy consumption and use of resources. The role of construction that is to say of buildings is shown in figure 1. The importance of an energy balance is demonstrated, in order to minimize the impact on the environment. The second possibility to reduce the impact of industrial processes lies in the construction materials production itself. These trends are not new as already 20 years ago the notion of green building materials or sustainable construction has been reported.

The discussion however can not only look into the production of building materials, but also has to include

the whole chain – the life cycle of construction materials e.g. of buildings.

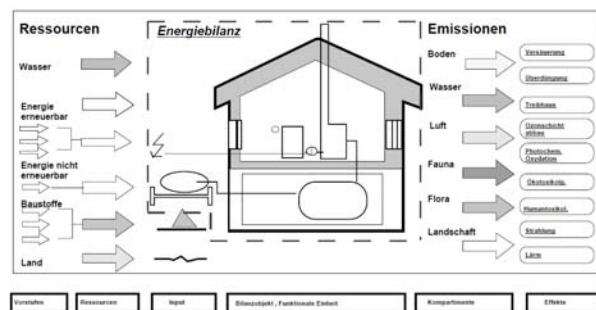


Figure 1: Energy balance of buildings and impact on environment from [2]

In Germany this approach has led to a guideline, based on European regulations, which spells out the areas of sustainable construction. In particular the

Energy saving law prescribes strict standards for energy conservation in new construction.

2 PRODUCTION

Production of building materials is always a high temperature, energy consuming process. For cement production the major raw material is limestone which adds additional CO₂ into the environment. This has led in cement production to a trend using more and more secondary fuels such as used oil, used tires, animal bone flour, waste plastics and even mud from waste water treatment plants. Some factories are nowadays using 100% secondary or waste fuels.

For cement production, however the major raw material is limestone which adds additional CO₂ into the environment. In terms of alternate raw materials there is not yet a major replacement. Industrial trends to lower CO₂ were described by E. Gartner [3]. Some of these trends starting to show up outside Germany such as the manufacture of different or modified clinker chemistries such as rapid setting cement, eco cement, and calcium sulphate based or calcium sulfo(aluminate) based cement. The production of such clinkers allows the reduction in sintering temperature and results in less CO₂ output.

The third and most common practiced approach in Germany is the replacement of clinker by latent hydraulic, pozzolanic or even inert, finely ground additives. This approach is aided by the European cement standard, which allows the addition of many different materials. Some suitable additives are shown in figure 2. Some additives can be used as such in cement production. For additives which are not specified in the standard, such as rice husk ash (RHA), approval by the German Institute for Construction techniques (DIBt) will be necessary.

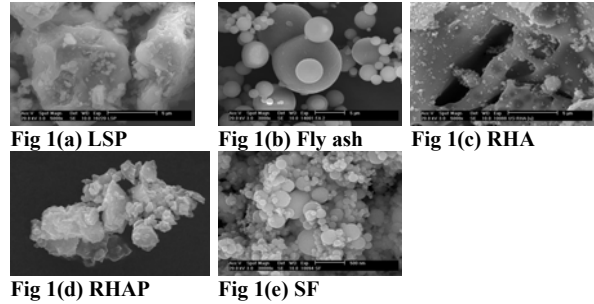


Figure 2: ESEM micrographs of various inorganic powder additives [4]

3 CONSTRUCTION

For construction two approaches are practised:

- High strength or ultra high strength concrete
- Thermal Insulation

3.1 High Strength Concrete

High strength concrete allows designing load bearing members with smaller cross sections and has a potential to last longer without or with little degradation. Therefore the impact on natural resources is diminished. The standards meanwhile specify high strength concrete up to 115 MPa as shown in table I:

Table I: Composition of high strength concrete

Concrete Strength			C55/67	C60/75	C70/85	C80/95	C100/115
Cement Content	CEM I 42,5 R	[kg/m ³]	420	340	420	-	-
	CEM I 52,5 R		-	-	-	450	450
Silica Fume s			-	30	40	45	45
Fly Ash f			-	80	-	-	100
W/C			0,32	0,35	0,32	0,28	0,26
HRWA			PCE or Melamin Naphthalene Type				
Retarder			-	-	-	-	yes
Aggregates	0/2 (Sand)	[kg/m ³]	650	640	630	660	830
	2/8 (round)		420	410	405	355	-
	8/16 (round)		790	880	765	-	-
	2/8 (crushed)		-	-	-	-	480
	8/16 (crushed)		-	-	-	760	770

High strength is achieved by lowering the porosity of the concrete through particle packing and reduction of the W/C ratio. Reduction of the W/C ratio to values around 0.2 can only be achieved by using a high range water reducing agent. The principle of high strength concrete is demonstrated through the schematic in figure 3.

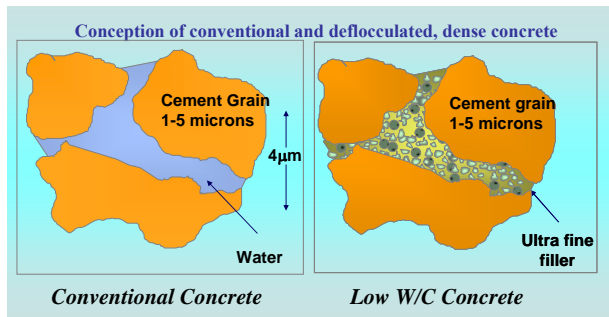


Figure 3: Principle of high strength concrete from [5]

The addition of fibres and further reduction in porosity leads to ultra high strength (UHPC) or powder reactive concrete (PRC) showing improved tensile and compressive strength with a high energy dissipation during loading. The mechanical behaviour of these materials is shown in figure 4:

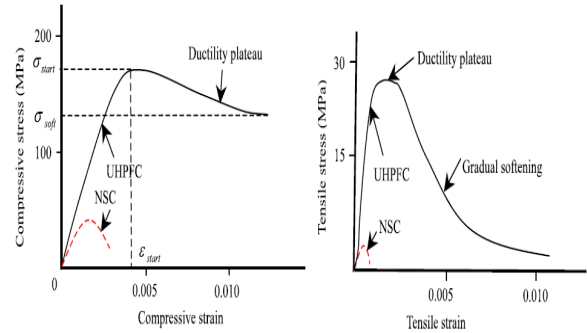


Figure 4: Comparison of stress-strain behaviour of UHPC and normal concrete (NC) [6]

An example of UHPC is given in figure 5. It shows a pedestrian bridge in Sakata (Japan) constructed with DUCTAL® a commercially available powder reactive concrete.



Figure 5: Pedestrian Bridge made from UHPC

3.2 Thermal Insulation

The most practiced approach and stipulated by law in Germany is the reduction in energy consumption in buildings by thermal insulation according to the energy savings regulation EnEV [7]. The principle is shown in figure 6.

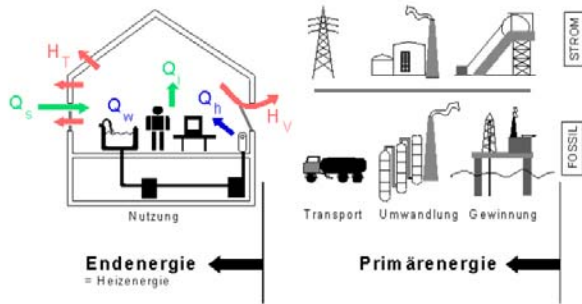


Figure 6: Energy flow from production to domestic use according to [8]

Most of the energy produced goes what domestic consumption is concerned into heating, cooling and hot water preparation (blue arrows). A large amount (red arrows) is lost to the environment through heat flow through the walls and openings of a building. Part of the sun's energy can be captured through sophisticated technology in window design, photo voltaic and solar heating of water (green arrow Q_s).

Figure 7 demonstrates the development of thermal insulation requirements and standards over the past 25 years. The upper line represents the steps which were introduced through building codes in Germany. The lower solid line shows the technical possibilities in construction. It is obvious that since about 10 years, the construction of buildings needing no outside energy is possible. However, the costs are still too high. Therefore the actual construction practice lies between regulation and optimum construction (red arrow).

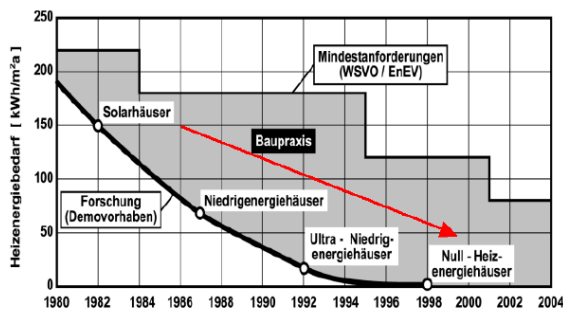


Figure 7: Comparison of energy saving according to ENEC, technological possible and practical construction knowledge



Figure 7: Example for exterior thermal insulation with Styrofoam

The practical application of Styrofoam panel – one of the very popular outside insulation materials - is shown in figure 8. The thermal insulation capabilities of various, additional insulation materials are shown in table II in terms of thermal conductivity.

Table II: Thermal conductivity for various insulating, building materials

Material	Density [kg/m ³]	λ -Value [W/(m K)]	k-Value [W/(m ² K)] Wall thickness 10 cm
Cellulose	35-60	0,045	0,45
Cork	120	0,04 - 0,05	0,4 - 0,5
Perlite	90-100	0,05 - 0,055	0,5 - 0,55
Sheep wool	20 - 80	0,037	0,37
Wood fibres	130 - 270	0,05 - 0,06	0,5 - 0,6
Schaumglas	125 - 150	0,045 - 0,06	0,45 - 0,6
Expanded Clay	400 - 1800	0,13 - 0,25	1,3 - 2,5
Styrofoam	15 - 50	0,03 - 0,04	0,3 - 0,4

4 SUMMARY

Sustainability is an important issue today, since only a careful handling of earth's resources will guarantee an environment for all human beings. Construction of buildings, however, is a basic need for humans in order to feel comfortable and significant resources – mostly

minerals and energy – are used to provide comfortable housing.

This paper shows some practiced aspects in construction, focussing on one hand on the manufacture of materials (mostly cement) and on the other hand on the use of these materials (construction of buildings)

For the manufacture of cement or other binders there is two ways.

- Development of new cement mineralogy such as CSA, belite cement or alinit cement
- Development of composite cements using naturally occurring pozzolanic materials or secondary raw materials

For Construction also two major trends can be observed:

- The minimization of energy produced by optimisation of thermal insulation and use of alternative energies in order to make buildings energy wise self sustainable
- The use of high performance building materials such as high strength concrete in order to minimize the use of natural resources.

References

[1] "Guideline for sustainable construction"; Ministry of Transport, Building and Housing, Germany, 2001

[2] N. Kohler "Grundlagen zur Bewertung kreislaufgerechter, nachhaltiger Baustoffe, Bauteile und Bauwerke"; 20.Aachener Baustofftag, Germany, 1998

[3] E. Gartner "Industrially interesting approaches to "low-CO₂" cements"; Cement and Concrete Research, 34, 2004, pp.1489-1498

[4] S. A. Rizwan, Th. A. Bier " Self-Consolidating Mortars Using Various Secondary Raw Materials"; ACI Materials Journal, 106, pp. 25-32, 2009

[5] Th. A. Bier, C. Parr, C. Revais "From Conventional Castables to Deflocculated Castables - A change in Raw Materials Perception"; ACERS 100th Annual Meeting, USA, 1998

[6] C. Wu, D.J. Oehlers, M. Rebentrost, J. Leach, A.S. Whittaker "Blast testing of ultra-high performance fibre and FRP-retrofitted concrete slabs"; Engineering Structures, 2009

[7] "Verordnung über energiesparenden Wärmeschutz und energiesparende Anlagentechnik bei Gebäuden (Energiesparverordnung ENEC)"; Bundesgesetzblatt, 2007, Teil I, Nr. 34

[8] K. Sedlbauer, K. Breuer, A. Kaufmann; "Der Mensch in Räumen – Risiko oder Behaglichkeit"; Fraunhofer-Institut für Bauphysik

Some Applications of Advance Technologies for Solving Transport Means Surveillance Problem in Vietnam

Le Hung Lan, Nguyen Thanh Hai, Dang Quang Thach, Nguyen Trung Dung

University of Transport and Communications Hanoi, Vietnam

lehunglan@ifpt.vn

Abstract: Currently, the monitoring, surveillance and management problem of transport means are very important and can be solved successfully in many developed countries. But in Vietnam due to different, complex conditions of transport infrastructure, weather conditions, financial potentiality, legislation, many similar systems imported from overseas companies can not be applicable. This paper proposes some successful solutions for this problem in Vietnam based on application of new technologies such as GPS, DSP and image processing. These solutions including the monitoring and management system for transport means in open-cast mining, monitoring and warning systems in long-distance buses, and surveillance systems by camera on the road.

Key Word: transport means surveillance, GPS, image processing

1 INTRODUCTION

In the industrialized countries such as Japan, USA, Europe,... science and technology actually become the important production. But for developing countries, science and technology applications meet many difficulties in practice, such as no comprehensive development in the industries, small-scale producing, redundant manual labor, the economic life is low,... Therefore, it needs a creative, certain activity in research and its applications. The management and surveillance transport means are the typical examples. When the transportation means do not run required road and speed may cause the serious consequences of human and material.

However, the use of solutions and systems available in developed countries is not feasible as mentioned before. The article introduces some experiences and results of the design and manufacture equipment in Vietnam: monitoring and warning of speed for long distance vehicles, monitoring and collecting traffic data, and monitoring system for transport means in open-cast mining.

2 SOLUTIONS FOR TRANSPORT MEANS SURVEILLANCE PROBLEM

2.1 The speed monitoring and warning system for long-distance buses

In Vietnam, the long-distance buses transport passengers have some following drawbacks, such as: often go through residential areas with limited speed, different transportation companies works at the same time on the same line causes over-speed driving to scramble for passengers.

The amount of accidents for this reason takes 50% of total accident number on the roads. So it is actuated to install the black box for speed monitoring and warning on the buses. The

main functions of this system are following: defining the vehicle location from speed sign on the road, comparing actual vehicle speed with allowed speed in this section and warning the driver, passengers and management center in the case of overspeed or taking a wrong road situation.

There are two forms of speed signs in Vietnam: fixed and mobile sign. The fixed signs are used at the city' entrances or curved sections, etc... and the mobile signs are often as maintenance.

For solving the proposed problem it is necessary to apply some new technologies: GPS technology for defining vehicle location and speed, GIS technology for calculating location in the digital map, GPRS/GSM technology for data transmission, RF technology for information transmission between vehicle and signs on the road. The system output is sound or light alarm with different levels depended on dangerous levels. The violated cases are also recorded and transmitted to management center to give evidence for driver punishment purpose.

On the mobile signs there are installed chip with standard ZigBee 802.15.4 for allowed speed information exchanging with on-board equipment within 30-50m distance and using solar energy. The on-board system operates by PsoC microprocessor from Cypress Inc. In the center the Webserver is designed for receiving data from onboard equipments via GPRS, and on-screen monitor allows the management of large numbers of vehicles are running the same time, alert and record events such as driving speeding, running with wrong road.

In addition, this system also allows the operating effectively the exploitation of transport such as the spaced between the vehicle, adjust the running time.

Equipment installed and tested on the vehicles which run on Highway 1A in Vietnam has started to find effective and help appropriate authorities bring out suitable policies contribute to reduce traffic accidents on this route.

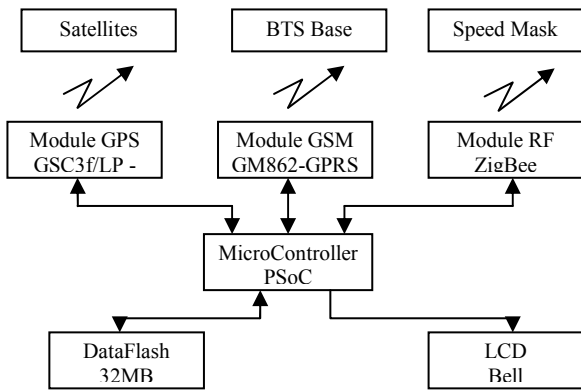


Figure 1 System architecture for speed monitoring and warning system for long-distance buses

2.2 Traffic surveillance and data collecting system

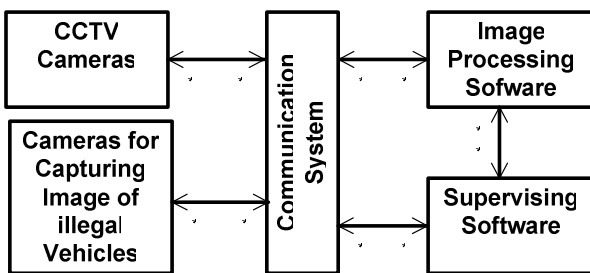


Figure 2 Components of Traffic Supervisor System

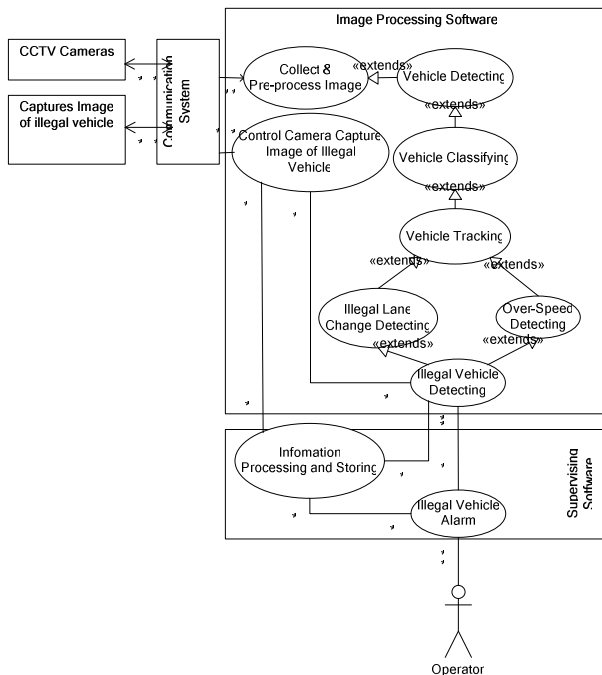


Figure 3. System Usercase

The system consists of two camera groups. The first group is using to collect overall images of traffic process in the monitoring zone for detecting the law violating cases. Then the second one records the images of violated vehicles for evidence.

The images collected by the first camera group are processed to determine vehicle flow structure, vehicle amount,

speed and trajectory. These data allow calculating some statistical parameters such as density, flow speed and detect the law violated situations such as over-speed, illegal lane-change, ...

The second camera group can be remote controlled via computer network to change angle in horizontal or vertical axis and zoom (Pan/Tit/Zoom – PTZ). The task of these cameras is to record the number plate of violated vehicles and the cameras are controlled by the monitoring software.

The image processing software is using to calculate the statistical parameters of vehicle flow, speed, and orbital vehicle running through observed area. The results allow detect violated vehicles, provide information on their position in the observed area, and control the second camera group record the number plate.

The monitoring software alerts the manager when occurring situations violate the traffic law, store, and processing information.

2.3 MANAGEMENT OF THE TRANSPORT MEANS IN OPEN-CAST MINING.

In open-cast mining of Vietnam, the truck team continuously transports land or coal daily from the coal mining to the coal storage was stipulated before on the craggy terrain. It is very difficult to manage operation of trucks in the mine face. The first difficulty is statistics on the number of times the truck running in a shift. Currently this work is being performed manually by hand as a complex process but does not guarantee accuracy due to process a large amount of data and not exclude gap in the management process can cause cheat in the statistics. The second difficulty is monitoring to ensure the vehicle with scoop up and pour on the right place. Cause of this problem comes from working conditions in coal mines, the vehicle moving in wide ranges, the monitoring is done manually, lack the number of staff to monitor ... so often happens event, i.e., the drive pour coal not in the regulation place, but in closer place to increase productivity, at the same time fraud amount of oil. Third difficulty is statistics the excavator productivity as well as production capacity of the company may refer to statistics on the number of trucks running.

From difficulties in managing activities of trucks, it needs to set up an automatic system in the counting statistics; check confirmed whether a truck goes right or not, statistics productivity of each excavator, and the productivity of the company periodically. Since then, reduce the subjective effect of people into management to manage more closely and avoid negative during implementation. Furthermore, system and created equipment must have the ability to work in severe environments of mines such as vibrate, damp, salty, dust, ... and with the reasonable price.

An overall solution may be setting: Design and installation on each truck a specific GPS device as black box. After each cycle of predetermined time, this device stored the time information, coordinates (a coordinate system) and speed of truck is calculated from the satellite signals. When change shift, the trucks are returning to management center and the data are automatical transformed to center by radio signal. At center, a computer paired with a device receiving radio signals from the trucks. Using software to control the pairing between the computer and device, all time data, coordinates and speed of all truck operating in a production shift recorded into the computer as a file text. There is software built to handle text files to implement the requirements such as automatically

calculating the number of trucks running, automatically confirm each trip is appropriate or not in accordance with regulations scoop up and pour, as well as defined road. Furthermore, some other statistics may require such as: excavator productivity, production capacity of individual workshops and company over time, activities time, breakdown time of the truck for management purpose.

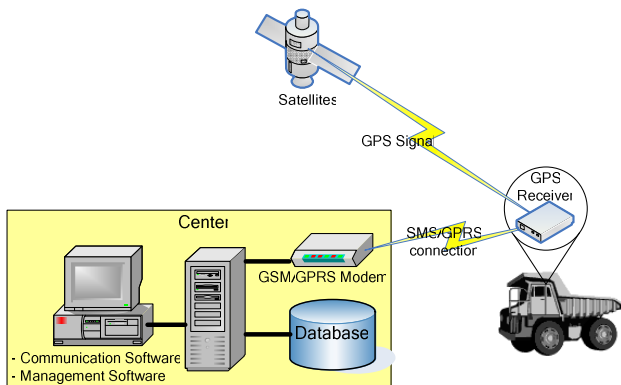


Figure. 4 System architecture for transport means management in open-cast mining

3. CONCLUSION

From three typical examples in the design and manufacture system which monitors transport means in Vietnam, it is showed that the applied research of science and technology in developing countries do not simply copy or import the original equipment of foreign company. It can only be successful and bring desired results when creatively, and finding a solution towards harmony in between advances technologies and the specific requirements of practice.

Reference

- [1] Le Hung Lan, KC03-21, State-level Research Project, Hanoi-Vietnam, (2006).
- [2] Le Hung Lan, KC.03.05/06-10, State-level Research Project, Hanoi-Vietnam, (2009).
- [3] Nguyen Thanh Hai, KC.06.02/06-10, State-level Research Project, Hanoi-Vietnam, (2009).
- [4] Le Hung Lan, "Management of the transport means in open-cast mining", Ministry-level research project, Hanoi-Vietnam, (2009).

The hybrids of cationic liposomes and biomaterials for gene delivery

Shubiao Zhang and Shengdi Fan

SEAC-ME Key Lab of Biotechnology and Bioresources Utilization, Dalian Nationalities University, Dalian 116600, China

zsb@dlnu.edu.cn, fsd@dlnu.edu.cn

Abstract: Gene transfer has been a critical step for gene therapy. Viral vectors and non-viral vectors are commonly used for gene transfer. It has shown that non-viral vectors have the advantages over viral ones as they are non-immunogenic, easy to produce and not oncogenic. However, they have the major limitation of inefficient transfection, the hybridized usage of non-viral vectors may provide a partial solution. Many novel cationic lipids have been synthesized to show high transfection efficiency and low toxicity. But they don't meet our requirements for gene delivery both *in vitro* and *in vivo*. So they were combined with cationic polymers (biomaterials) to give satisfied transfection results.

Key Words: Gene delivery, Cationic liposomes, Cationic polymers

1 INTRODUCTION

Gene therapy has been developed for the treatment of both acquired and inherited diseases such as severe combined immunodeficiency [1], cystic fibrosis [2], and Parkinson's disease [3], as well as an alternative method to traditional chemotherapy used in treating cancer [4]. This approach is based on the principle of correcting the basis of diseases at their origin by delivery and subsequent expression of exogenous DNA, which encodes for a missing or defective gene product [5]. Vectors are employed in many methods to protect nucleic acids and deliver them to targeted cells, as naked nucleic acids are easy to be degraded by nuclease.

After several accidents [6,7], non-viral vectors gained much more attention over viral ones for they are non-immunogenic, not oncogenic, easy to produce in large-scale and capable to deliver large genetic materials. However, nonviral gene carriers consistently exhibit significantly lower transfection efficiency compared with viral ones.

People have been designing and synthesizing a large amount of new compounds [8,9], at the same time the

hybridized utilization of non-viral vectors provides a solution to the problem. Hereunder cationic liposomes were combined with cationic polymers to deliver pDNA to cells, their hybridization showed synergistic effects for improving transfection to cells.

2 Experiments

2.1 Retardation

Interactions between plasmid DNA and liposomes/cationic polymers were investigated by electrophoresis of agarose gels. Lipoplexes (liposome-DNA complexes) or polyplexes (polymer-DNA complexes) were formed using pGFP-N2 vector at a final DNA concentration of 0.05 μ g/ μ L and at a lipid-to-DNA ratio varying from 0.5 to 8 of lipid to DNA (lane 1: Marker; lane 2: naked pDNA; lane 3: 0.5; lane 4: 1; lane 5: 1.5; lane 6: 2; lane 7: 3; lane 8: 4; lane 9: 6; lane 10: 8). The complexes were then loaded onto 0.8% agarose gels containing ethidium bromide (0.5 mg/ml). The gel running buffer was 40mM Tris acetate and 1mM EDTA. Electrophoresis was performed on a 0.8% agarose gel at 100V for 30 min. Fluorescent of the intercalated dye (ethidium bromide) was

measured using a gel imaging system (SYNGENE)

2.2 Transfection procedure

Transfection of pDNA was performed using cationic liposomes, cationic polymers and their hybrids. One day before transfection, cells were seeded in 100 μ l of growth medium (RPMI1640) without antibiotics to attain the required cell confluence at the time of transfection. Dilute liposomes or cationic polymers and pDNA in 25 μ l Opti-MEM without serum were mixed gently and kept for 20 min to give lipoplexes or polyplexes. Lipoplexes or polyplexes were added to plate wells, after cells were washed with PBS. The plate was shaken gently and incubated at 37°C in a humidified incubator with 5% CO₂ for 4-6 h, then cells were washed by PBS or DMEM and further cultured for 24-48 h. An inverted fluorescent microscope was used to image the expression of green fluorescent protein.

2.3 Cytotoxicity(MTT) assay

Cytotoxicity was evaluated by MTT assay. Cells were seeded at a density of 1×10^4 cells/well in 96-well plates, and incubated 12 h before treatment. The liposome and 50 μ l of DMEM medium were added to the well and incubated for 24 h at 37°C. After incubation, 50 μ l of 5 mg/ml MTT solution in PBS was added and incubated for an additional 4 h at 37°C. MTT-containing medium was aspirated off, and 150 μ l of DMSO was added to dissolve the formazan crystal formed by live cells. The absorbance was measured at 575 nm to determine cell viability as percentage of control.

3 Compaction of pDNA

DNA must be protected from the degradation caused by nuclease, so the interaction between non-viral vectors and DNA is a precondition to efficient transfection. To determine the binding strength of liposomes or cationic polymers to DNA, agarose gel electrophoresis was used to separate bound DNA from free DNA. Figure 1 shows that with the increase of N/P ratios the amount of retarded DNA is lowered. Complete binding of DNA was observed with liposomes or cationic polymers used, but cationic polymers can retard DNA more efficiently than liposomes (Fig.1 B and C). When combining liposomes and cationic polymers, synergistic binding between vectors and pDNA was observed.

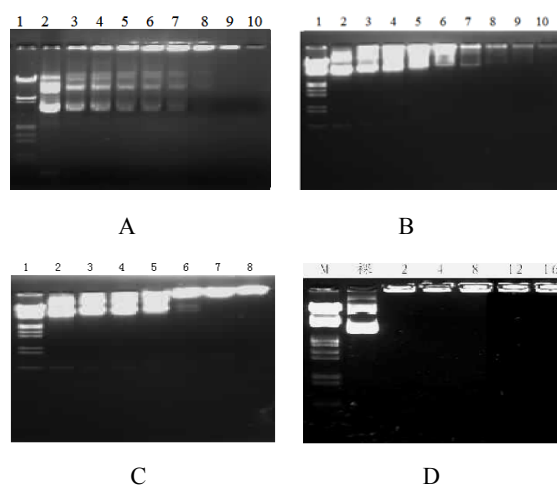


Fig.1 Gel electrophoresis of lipoplexes or polyplexes at various charge ratios, lane 1: marker (λ DNA/EcoR I + Hind III Markers from SABC), lane 2 naked DNA (1 μ g) and lanes 3-10: lipoplexes or polyplexes with progressively increasing proportions of N/P. A: cationic liposome 1; B: cationic liposome 2; C: cationic polymer; D: cationic liposome/ cationic polymer.

4 Transfection efficiency

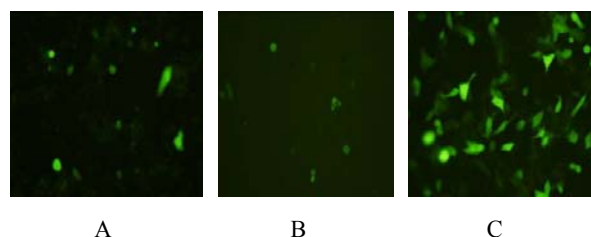


Fig.2 Transfection efficiency expressed by green fluorescent protein imaged using inverted fluorescent microscope, A: liposomes; B: cationic polymers; C: liposomes and cationic polymers.

The transfection efficiencies of cationic liposomes and polymers tested against Hela cells could be measured through the expression of green fluorescent protein under an inverted fluorescent microscope as shown in Fig.2. It has been speculated that cationic liposomes and polymers could transfect cells through endocytosis to pass cell membrane. The efficiencies of these non-viral vectors are very different depending on the chemical structures of lipids and polymers. In this study, cationic liposomes (Fig.2 A) could transfect Hela cells more efficiently than cationic polymers (Fig.2 B). The hybridized usage of cationic liposomes and cationic polymers, however, give much surprising transfection efficiency (Fig.2 C).

The cationic polymer we used in this study could compact DNA very efficiently as shown in Fig.1 C, after the formation of polyplexes the addition of liposomes provided modification by forming a layer outside the polyplex particles. This may partially explain the synergistic effect of cationic liposomes and cationic polymers.

5 Cytotoxicity

Since toxicity of the formulations to the cells is critical for transfection, we tested the viability of HeLa cells in the presence of formulations through MTT method. To assume that the cell viability of control is 100%, the relative cell viability of cationic liposomes or cationic polymers can be calculated through the following formula: $OD_{\text{test}}/OD_{\text{control}} \times 100$. The results shown in Fig.3 indicate that all the cell viability tested was over 95%, especially the introduction of polymers to the formulation did not cause additional toxicity to cells.

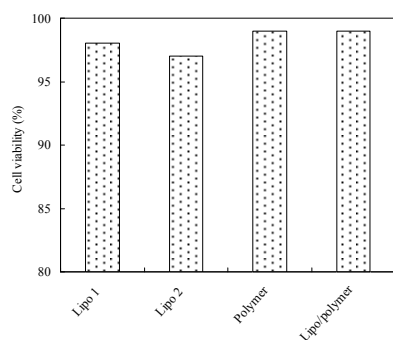


Fig.3 Toxicity, measured as percent viability, was evaluated with cationic liposomes, cationic polymer and liposome/polymer compared with control (100%).

In summary, this study provides a novel method to deliver pDNA to cells by using the hybrids of cationic liposomes and cationic polymers as a non-viral vector. The combination thereof indeed showed great improvement of transfection efficiency over either cationic liposome or cationic polymer alone. Though the past decade has seen tremendous progress in the design and synthesis of non-viral vectors for gene delivery as well as application of a battery of techniques, the hybrids of non-viral vectors provide another route to overcome the low transfection efficiency of non-viral vectors. The combined utilization of cationic liposomes and other non-viral vectors may provide the most exiting solution for gene delivery, for many advantages could concentrate on the delivery systems.

Acknowledgment The study was supported by Program for

New Century Excellent Talents in University and the National Natural Science Foundation of China (20876027)

References

- [1] Cavazzana-Calvo, M., Hacein-Bey, S., De.Saint Basile, G., Gross, F., Yvon, E., Nusbaum, P., Selz, F., Hue, C., Certain, S., Casanova, J. L., Bousso, P., Le Deist, F., Fischer, A. (2000) Gene therapy of human severe combined immunodeficiency (SCID)-X1 disease. *Science* 288, 669–672.
- [2] Boyd, A. C. (2006) Gene and Stem Cell Therapy. *Progress in Respiratory Research. Volume 3: Cystic Fibrosis in the 21st Century* (Bush, A., Alton, E.W.F.W., Davies, J. C., Griesenbach, U., Jaffe, A., Eds.) Karger: pp221-231, Chapter 29, Karger, New York.
- [3] Kaplitt, M. G., Feigin, A., Tang, C., Fitzsimons, H. L., Mattis, P., Lawlor, P. A., Bland, R. J., Young, D., Strybing, K., Eidelberg, D., Doring, M. J. (2007) Safety and tolerability of gene therapy with an adeno-associated virus (AAV) borne GAD gene for Parkinson's disease: an open label, phase I trial. *Lancet* 369, 2097–2105.
- [4] Zhang, S. B., Xu, Y. M., Wang, B., Qiao, W. H., Liu, D. L., Li, Z. S. (2004) Cationic compounds used in lipoplexes and polyplexes for gene delivery. *Journal of Controlled Release* 100, 165-180.
- [5] Liu, F., Huang, L. (2002) Development of non-viral vectors for systemic gene delivery *Journal of Controlled Release* 78, 259–266.
- [6] Hacein-Bey-Abina, S., von Kalle, C., Schmidt, M., Le Deist, F., Wulffraat, N., McIntyre, E., Radford, I., Villeval, J. L., Fraser, C. C., Cavazzana-Calvo, M., Fischer, A. (2003) A serious adverse event after successful gene therapy for X linked severe combined immunodeficiency. *N. Engl. J. Med.* 348, 255–256.
- [7] Woods, N. B., Bottero, V., Schmidt, M., von Kalle, C. I., Verma, M. (2006) Gene therapy: therapeutic gene causing lymphoma. *Nature* 440, 1123.
- [8] Ilies, M.A., Seitz, W.A., Caproiu, M.T., Wentz, M., Garfield, R.E., Balaban, A.T. (2003) Pyridinium-based cationic lipids as gene-transfer agents. *Eur. J. Org. Chem.* 21, 2645–2655.
- [9] Berh, J.P., Demeneix, B., Loeffler, J.P., Mutul, J.P. (1989) Efficient gene transfer into mammalian primary endocrine cells with lipopolyamine coated DNA. *Proc. Natl. Acad. Sci. U. S. A.* 86, 6982–6986.

A highly sensitive probe detecting low pH area of living cell based on modified β -cyclodextrin

Yoshihiko Kondo and Fumio Hamada

Department of Life Science, Faculty of Engineering and Resource Science, Akita University, Akita 010-8502, Japan.

y_kondo@ipc.akita-u.ac.jp

Abstract: Two kinds of rhodamine modified β -cyclodextrins (R-1 and R-2), which are coupled up ethylene diamine (EDA) and tetraethylene pentamine (TEPA) between Rh B and β -cyclodextrin, respectively, have been synthesized. R-1 and 2 work as a new fluorogenic probe for monitoring pH of Hela cells, and MTT of assay R-1, R-2, and rhodamine B indicate that less a cytotoxicity of those R-1 and R-2 than that of rhodamine B, where R-1 has much less one than that of R-2. The fluorogenetic probe capability of R-1 and R-2 was recognized in an area of acidic area in living cell, which is lysosome.

Key Words: Cyclodextrin; MTT assay; Fluorescence, Staining; Rhodamine dyes

1 INTRODUCTION

Cyclodextrins (CDs) are torus shaped cyclic oligosaccharides composed of six, seven and eight D-glucopyranose units (α , β , γ -CDs, respectively). A variety of organic compounds can be included in their central cavities in aqueous solution¹. Because of nontoxic property of CDs based on non-permeability of biological membrane, CDs are utilized in so many fields such as inclusion of molecules, DDS of anticancer and host as spectroscopy study in addition of chemical sensor detecting for organic molecules²⁻⁶. The pharmaceutical approach of CD is based on inclusion functionality and extended-release capability. On the other hand, modified CD such as fluorescent modified CD (FI-CD) has been used as molecular sensing probe for organic molecules⁷⁻⁸, because fluorescent moiety works as probe as fluorescence emission analysis and CD works as a cavity for guest molecules. Unfortunately, FI-CD has not been used as pharmaceutical application such as DDS carrier. In endocytotic system of a cell, there are some organelles showing acidic property. Those things are called as endosome and lysosome, where pH are 6.0 and 5.0-4.5, respectively⁹⁻¹¹. Derivatives of xanthene such as

fluorescein and rhodamine (Rh) dyes are widely employed as molecular probes in chemical biology, especially Rh dyes are used extensively in biotechnological applications such as fluorescence microscopy, flow cytometry, fluorescence correlation spectroscopy and ELISA, because Rh dyes are highly fluorescent and resistant to photo-bleaching¹²⁻¹⁶. It is well known that derivatives of Rh molecule such as rhodamine B (Rh B) can be taken in cellular without endocytosis because those dyes have positive charge, which show affinity for cell membrane of negative charge and endoplasmic reticular. On the basis of versatile functionality of Rh dyes, we study a synthesis of Rh B modified β -CDs (as shown in Figure 1), which has cell membrane permeability.

2 EXPERIMENTAL

2.1 Materials

CDs were a gift from Nihon Shokuhin Kako Co., Ltd. (Tokyo, Japan). Rhodamine B and 1-Hydroxybenzotriazole (1-HOBT) and dicyclohexylcarbodiimide (DCC) were commercially available (Tokyo Chemical Industry Co., Ltd.). Mono-6-(2-aminoethyl)-amino-6-deoxy- β -cyclodextrin and mono-[6-(11-amino-3,6,9-ethylene-amino)-6-deoxy]- β -cyclodextrin was synthesized according to the procedure reported previously.¹⁹

2.2 Preparation of R-1

Dicyclohexyl carbodiimide (DCC, 153 mg, 0.80 mmol) was added to a cooled solution (-20 °C) of rhodamine B (373 mg, 0.78 mmol) and 1-hydroxybenzotriazole (105 mg, 0.78 mmol) in 15 mL DMF and 10 mL pyridine. The reaction mixture was stirred at -20 °C for 2 h. To a stirred solution, mono-6-(2-aminoethyl)-amino-6-deoxy- β -cyclodextrin (500 mg, 0.39 mmol) was added portion wise. The solution was stirred for 30 min at -20 °C and then the reaction mixture was

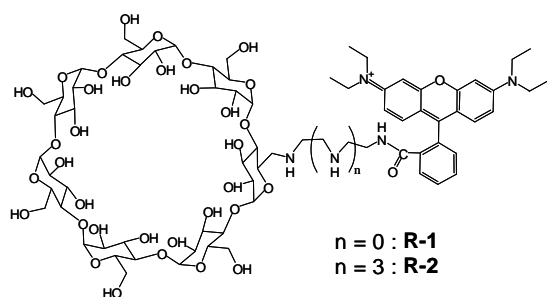


Figure 1 Structural formation of Rh B modified β -CyDs

stirred at room temperature for 24 hrs. The solution was evaporated in vacuo to small amount and then the residue was washed with acetone (300 mL). The resulting precipitates were collected and dried under vacuum overnight, to give 590 mg crude product. The crude product was dissolved in small amount of water and loaded on column chromatography on CM Sephadex C₅₀. After removal of impurities by elution with water, the fractions containing desired product were eluted of 2.5 % ammonia solution then it product were concentrated on a evaporation. Desired product was poured into acetone (300 mL), and resulting precipitates were collected and dried under vacuum overnight, to give a pink powder (770 mg, yield 20.1 %). ¹H MR (D₂O): δ = 7.83, 7.80 (d, d, 1H; rhodamine aromatic), 7.48 (s, br, 2H; rhodamine aromatic), 6.79 (br, 1H; rhodamine aromatic), 6.32 - 5.92 (m, 8H; rhodamine xthantan), 4.91 (s, 7H; C¹H of CD), 4.05 - 3.89 (m, amine CH₂), 3.93 - 3.09 (br, 48H; CD C²-C⁶H, rhodamine CH₂), 2.03 (t, 4H; amine CH₂) 1.83 (t, 2H; NH), 1.21 - 0.76 (m,br 12H; rhodamine CH₃) FAB MS: *m/z*: 1623.79 [*M*-H⁺+Na⁺] ((Calcd for C₇₂H₁₀₄N₄O₃₆: 1601.61) UV λ_{max} (H₂O) nm (log ε) 240 (5.157).

2.3 Preparation of R-2

Ethyl-3-(3-dimethylaminopropyl)-carbodiimide hydrochloride (EDC, 0.170 g, 0.887 mmol) was added to a cooled solution (-20 °C) of rhodamine B (373 mg, 0.78 mmol) and 1-hydroxybenzotriazole (108 mg, 0.77 mmol) in 15 mL DMF and 10 mL Piridine. The reaction mixture was stirred at -20 °C for 2 h. To a stirred solution was added portion wise, mono-[6-(11-amino-3,6,9-ethylene-amino)-6-deoxy]-β-cyclodextrin (500 mg, 0.38 mmol) in small amount of pyridine was added. The solution was stirred for 30 min at -20 °C and then the reaction mixture was stirred at room temperature for 2 days. The solution was decreased to solvent by evaporator then poured into acetone (300 mL). The precipitate was collected and dried under vacuum overnight, to give 680 mg crude product. The crude product was dissolved in water and purified by column chromatography on CM Sephadex C₅₀. After removal of impurities by elution with water, the fractions containing desired product were eluted of 2.5 % ammonia solution then it product were concentrated on a evaporation. Desired product poured into acetone (300 mL). The product was collected and dried under vacuum overnight, to give a pink powder (77 mg, yield 1.16 %). ¹H NMR (D₂O): δ = 7.82 (br, 1H; rhodamine aromatic), 7.74 (br, 2H; rhodamine aromatic), 6.89 (br, 1H; rhodamine aromatic), 6.48 - 5.84 (m, 8H; rhodamine xthantan), 4.92 (s, 7H; C¹H CD), 4.07 - 2.90 (br, 48H; CD C²-C⁶H, rhodamine CH₂), 2.57 - 2.25 (br, 20H;CH₂ amine), 2.10 (t, 6H; NH₂), 1.13 - 0.67 (br, 12H; rhodamine CH₃) FAB MS: *m/z*: 1752.96 [*M*-H⁺+Na⁺] Calcd for C₇₈H₁₁₉N₇O₃₆: 1730.808 λ_{max} (H₂O) nm (log ε) 240 (5.040).

2.4 Cell proliferation assay

Cell proliferation was evaluated using the colorimetric 3-(4,5-dimethylthiazo-2-yl)-2,5-diphenyl-tetrazolium bromide (MTT) assay. HeLa cells (1 x 10⁴ cells) were seeded in 96 well plates 24 h prior to adding 0.1 % DMSO containing drugs, then

were incubated an additional 48 h. After treatment, the cells received 10 μl of 5.5 mg/ml MTT and were incubated at 37 °C for 4 h. A 90-μl aliquot of extraction solution (40 % *N,N*-dimethylformamide, 2 % CH₃COOH, 20 % SDS and 0.03 *N* HCl) was added to each well and mixed thoroughly by overnight agitation at room temperature. Cell proliferation was determined by measuring optical density at 570 nm using a Model 550 microplate reader (Bio-Rad Laboratories, Hercules, CA, USA).

2.5 Fluorescence imaging

HeLa cells were cultured on 8-chamber slides for 20 h, and then incubated for 5 h in the presence or absence of the drugs. After removal of the medium, cells were fixed in 3.7% paraformaldehyde for 30 min. After washing, cells were mounted with aqueous mounting medium. Fluorescence images were observed using a fluorescent microscope IX70 (Olympus, Tokyo, Japan).

3 RESULTS AND DISCUSSION

3.1 UV-vis spectra and fluorescence spectra of rhodamine modified β-CDs

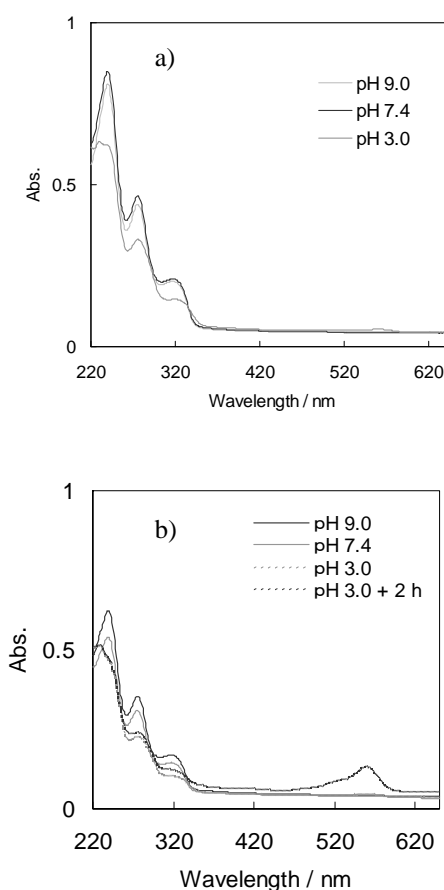


Figure 2 a) UV spectra of R-1 at the pH 9.0 (—), 7.4 (---) and 3.0 (·····). (b) UV spectra of R-2 at the pH 9.0 (—), 7.4 (---), 3.0 (·····) and 3.0 + 2 h (— · — ·).

UV-vis spectra of R-1 in different pH region were shown in Fig. 2(a), where a new peak at 570 nm appeared with small

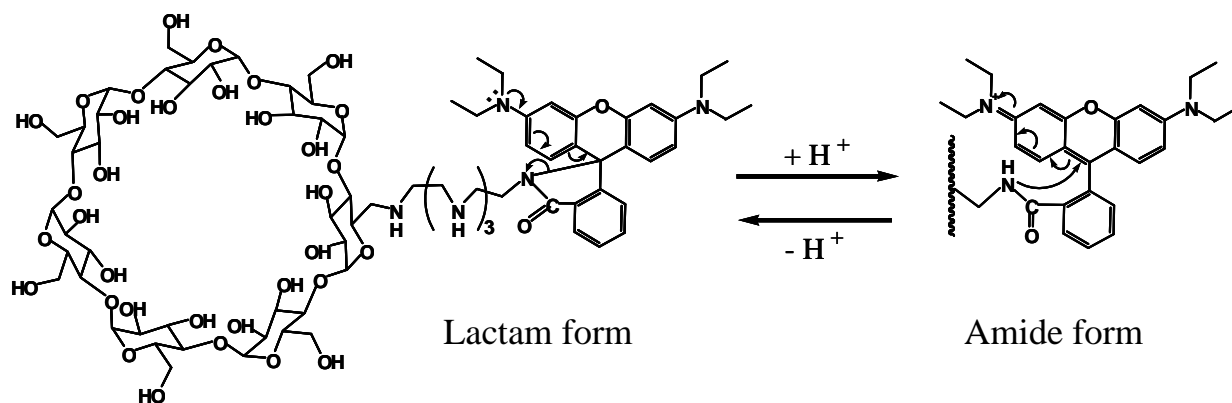


Figure 3 The structural conversion of amide and lactam form of R-2 at pH condition.

magnitude when R-1 was kept in pH 3.0 aqueous solution. On the other hand, the peak of R-2 at 560 nm was increased with high absorbance as shown in Fig. 2(b). The new peak was derived from amide form of R-2. The structural conversion of R-2 might be proceeded as shown in Fig. 3, because Walter Mier et al.¹⁷⁾ reported structures of the amide and lactam forms of the model compound such as rhodamine 101 conjugates, which exist in pH-dependent equilibrium. Fig. 4 shows the fluorescent intensity of R-2 at 560 nm in different pH region. As shown in Fig. 4, high fluorescent intensity was recognized in only at pH 3.0 region, which indicates amide form of R-2 existed in under at pH 3.0 region. These results suggested that R-2 shows fluorescent switching property in different pH region. These phenomena were utilized in the biological application.

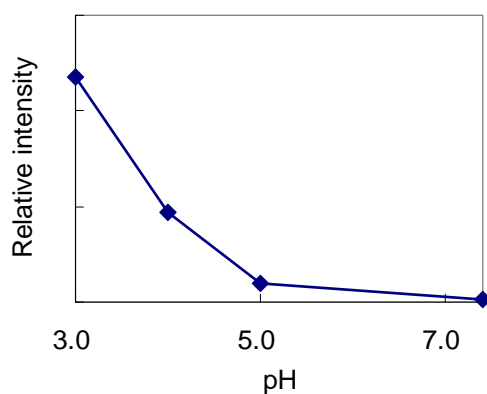


Figure 4 The pH variation of fluorescent intensity of R-2 at 560 nm. The concentration of R-2 was 30 μM , emission and excitation was 590 nm and 630 nm, slit width was 5 nm.

3.2 Cytotoxicity evaluation

Cytotoxicity of β -CD derivatives in human Jurkat cells and HeLa cells was evaluated by MTT assay¹⁸⁾ based on mitochondrial reduction of the yellow product. As shown in Figs. 5(a) and 5(b), cytotoxicity of Rh B, R-1 and R-2 were also investigated. The sequence of cytotoxicity of those compounds are R-1 < R-2 << Rh B. MTT assay shows modification of Rh B by CD reduces its cytotoxicity, where R-1 shows much better

than that of R-2 at the 100 μM . It seems that the cytotoxicity of those compounds for HeLa cells is less than that of Jurkat cells. It might be caused that a difference of surface area of those cell membrane derived from floating cell of Jurkat cells and adhesive cell of HeLa cells.

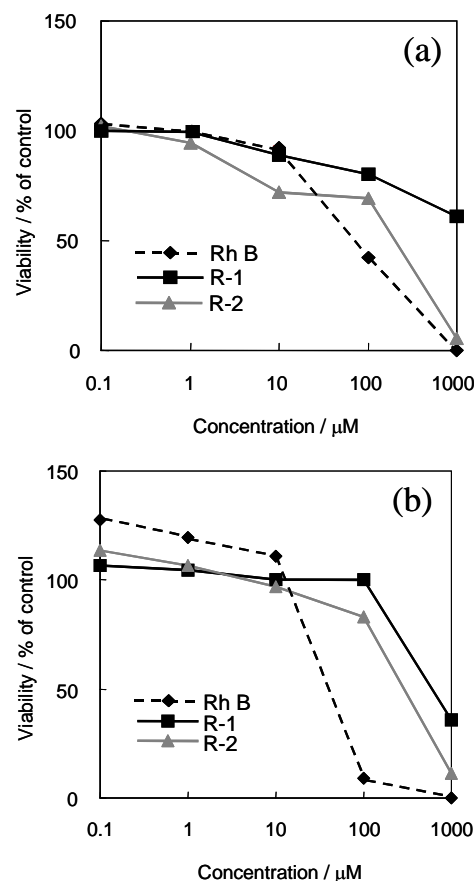


Figure 5 (a) The MTT assay of Rh B (---◆---), R-1 (—■—) and R-2 (—▲—) with Jurkat cells. (b) The MTT assay of Rh B (---◆---), R-1 (—■—) and R-2 (—▲—) with HeLa cells.

3.3 Fluorescence image of HeLa cells

A staining of living HeLa cells by R-2 was investigated. The pictures were taken by fluorescence microscope. Fig. 6(a)

shows a staining capability of Rh B for HeLa cells, where selective stainability was not recognized. On the other hand, outstanding selectivity of staining by R-2 for HeLa cells was recognized. Fig. 6(b) shows the staining result of R-2 for HeLa cells, where granulated fluorescence substance was recognized on the fringe of the nucleus and the light spot was partially recognized around neighborhood of the membrane. It means that endoplasmic reticula area is existing in acidic condition. To confirm the selectivity of R-2, Lyso Tracker blue, which stains lysosome with high selectivity, was used, where the light spot was partially recognized around neighborhood of the membrane .as same using R-2. These results suggested that R-2

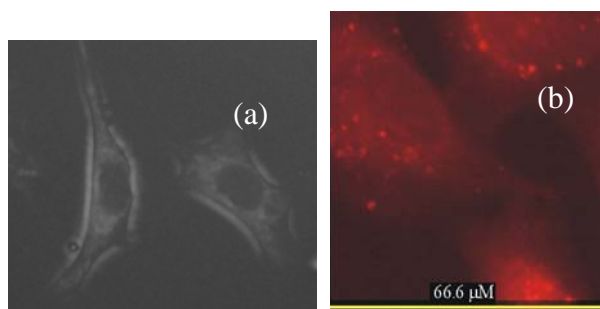


Figure 6 (a) The picture of living HeLa cells staining of Rh B. (b) The picture of living HeLa cells staining of R-2.

was incorporated into intracellular area by endocytosis action.

4 CONCLUSIONS

In conclusion, we declared that the fluorescent intensities of the titled compounds were affected by pH, where the lactam formation equilibrium would shift to charged amide form at low pH. It was shown that the intensity of R-2 was higher than that of R-1. It might be attributed to the longer length of linker because of the less affection by CD. Rh B is accumulated and kept in mitochondria of living cells, although R-1 and R-2 show different staining ability where coloring was observed in the area of outside of nucleus. That result looks like behavior of LysoTracker blue. It is known that Lysosome is low pH organelle at a region from 4.5 to 5. We assumed that the accumulation of R-1 and R-2 in lysosome was action of endocytosis. The reducing of cytotoxicity of R-1 and R-2 by comparison Rh B might be attributed to not passing through cell membrane. We concluded that R-2 could be used as sensor to identify acidic area in living cell with fluorescent image.

References

- [1] Peczuh, M. W.; Hamilton, A.D. *Chem. Rev.* **2000**, 100, 2479
- [2] Hirayama F.; Uekama K.; *Adv. Drug Deliv. Rev.* **1999**, 36, 125.
- [3] Arima H.; *Yakugaku Zasshi*, **2004**, 124, 451.
- [4] Tsutsumi T.; Hirayama F.; Uekama K.; Arima H. *J. Control. Release* **2007**, 3, 349.
- [5] Uekama K. *Chem. Pharm. Bull.* **2004**, 52(8), 900.
- [6] Tarrago-Trani M. T.; Storrie B., *Adv. Drug Deliv. Rev.* **2007**, 59, 782.
- [7] Kikuchi T.; Narita M.; Hamada F. *Tetrahedron* **2001**, 45, 9317.
- [8] Aoyagi T.; Nakamura A.; Ikeda H.; Ikeda T.; Mihara H.; Ueno A. *Anul. Chem.* **1997**, 69, 659.
- [9] Takenaka Y.; Nakashima H.; Yoshida N. *J. Mol. Struct.* **2007**, 871, 149.
- [10] Lincoln V. J.; Marcia L.W.; and Lan Bo C. *Proc. Natl. Acad. Sc. USA.* **1980**, 77, 990.
- [11] Walter M.; Barbro B.; Keith G.; William E. H. *Bioorg. Med. Chem.* **2002**, 10, 2543.
- [12] Lincoln V. J.; Marcia L.W.; and Lan Bo C. *Proc. Natl. Acad. Sc. USA.* **1980**, 77, 990.
- [13] Walter M.; Barbro B.; Keith G.; William E. H. *Bioorg. Med. Chem.* **2002**, 10, 2543.
- [14] Yatzeck M. M.; Lavis L. D.; Chao Tzu Yuan; Chandran S. S.; Raines R. T. *Bioorg. Med. Chem. Lett.* **2008**, 18(22), 5864.
- [15] Lavis Luke D.; Chao Tzu-Yuan; Raines Ronald T. *ACS Chem. Biol.* **2006**, 1 (4), 252.
- [16] Chandran S. S.; Dickson K. A.; Raines R. T. *J. Am. Chem. Soc.* **2005**, 127 (6), 1652.
- [17] Walter M.; Barbro B.; Keith G.; William E. H. *Bioorg. Med. Chem.* **2002**, 10, 2543.
- [18] Mosmann T. *J. Immunol. Methods* **1983**, 65, 55.
- [19] Beeson. C. J.; Czarnik, W. A. *Bioorg. Med. Chem.* **1994**, 2, 297.

Fluorescently labeled proteins as a tool for analyzing the dynamics of protein quality control in living cells

Hiroshi Kubota¹, Akira Kitamura², Hideaki Itoh¹, Masataka Kinjo², and Kazuhiro Nagata³

¹Department of Life Science, Faculty of Engineering and Resource Science, Akita University, ²Laboratory of Molecular Cell Dynamics, Graduate School of Advanced Life Science, Hokkaido University ³Department of Molecular and Cellular Biology, Institute for Frontier Medical Science, Kyoto University

hkubota@ipc.akita-u.ac.jp

Abstract: Proteins synthesized in living cells often fail to fold properly, and these misfolded proteins are potentially toxic to the cell due to existence of exposed hydrophobic surfaces. For example, misfolded proteins tend to aggregate each other and frequently capture other normal proteins into the aggregates. Protein misfolding caused by genetic mutations are often responsible for neuronal cell death in neurodegenerative diseases (e.g. Alzheimer's disease and Parkinson's disease), although molecular mechanisms are poorly understood. In living cells, there are two strategies to prevent the toxicity of misfolded proteins: one is prevention of aggregation by molecular chaperones and the other is degradation by proteases. These two systems coordinately monitor quality of proteins and decide the fate of proteins: reuse after refolding or destruction by protease digestion. We have used proteins tagged by green fluorescent proteins and derivatives to analyze the dynamics of misfolded proteins in living cells. The techniques we used include fluorescence correlation spectroscopy (FCS), fluorescence resonance energy transfer (FRET), fluorescence recovery after photobleaching (FRAP), fluorescence loss in photobleaching (FLIP), photoactivation and photoconversion. We introduce recent progress on the study of dynamics of misfolded proteins, particularly focusing on those achieved by these techniques.

Key Words: Fluorescently labeled protein, live cell imaging, protein dynamics, protein quality control

1 FLUORESCENTLY LABELED PROTEINS AND LIVE CELL IMAGING

Fluorescently labeled proteins are useful as a tag for cellular proteins. These fluorescent proteins include green fluorescent protein (GFP) and derivatives (e.g., RFP, YFP, CFP, BFP etc.) and have been used for time-lapse observation of cellular proteins. Recent progress on live cell imaging and related techniques allowed us to trace tracks of rapid movement of cellular proteins in living cells [1,2]. For example, fluorescence recovery after photobleaching (FRAP) is a microscopic method to measure mobility of fluorescently labeled molecule in living cells. In the FRAP analysis, fluorescently labeled proteins in a small region for a very short time and following movement from non-bleached area measured by recovery of fluorescence. Fluorescence loss in photobleaching (FLIP) is also a microscopic photobleaching technique for fluorescently labeled proteins in a living cell. Fluorescent proteins in a selected area are continuously bleached and decrease in fluorescence in a region of interest is measured during this analysis. The loss of fluorescent intensity

indicate movement of the bleached proteins from the bleached region to the measured region. Photoactivation and photoconversion are also useful to trace movement of fluorescently labeled proteins in living cells. Fluorescent proteins used in this analysis alter fluorescence intensity and wavelength after a short irradiation of laser beam. Movement of molecules emitting the activated or converted fluorescence is quantitatively analyzed.

Fluorescence resonance energy transfer (FRET) is useful to analyze intermolecular and intramolecular interactions and can be used in living cells. A pair of fluorescent proteins (e.g., YFP and CFP) is used to tag proteins, and interaction of the labeled proteins is evaluated by energy transfer between them. Since fluorescent intensities and lifetime of donor and acceptor are altered by energy transfer and the efficiency of energy transfer is highly dependent of the distance between donor and acceptor, degree of interaction between two selected proteins is estimated by the FRET analysis. This method has been widely applied for microscopic live cell imaging.

Fluorescence correlation spectroscopy (FCS) is a method to quantitatively analyze rapid movement of fluorescent

molecules. This method can be applied for fluorescent molecules in solution and living cells. FCS uses very thin laser beam on confocal microscopes to produce a very small detection volume and thus detects diffusion of fluorescent molecules at near single molecule level. After calculation of autocorrelation function, diffusion time and concentration of fluorescently labeled molecules are estimated. From the diffusion time, the size of molecule is calculated. Thus, FCS is useful to estimate size and concentration of fluorescently labeled molecules and complexes formed in living cells, including protein complexes and aggregates.

2 PROTEIN AGGREGATION AND QUALITY CONTROL

Living cells continuously synthesize large amount of proteins and the synthesized polypeptides often fail to fold properly. Misfolded proteins are potentially toxic to the cell due to existence of exposed hydrophobic surfaces, because they tend to aggregate and frequently capture other normal proteins into the aggregates. Genetic mutations cause protein misfolding and neuronal cell death in neurodegenerative diseases including Alzheimer's disease, Parkinson's disease, prion disease, polyglutamine disease and amyotrophic lateral sclerosis (ALS) [3,4]. However, molecular mechanisms for the toxicity of misfolded proteins are largely unknown. To prevent the toxicity, there are two systems controlling protein quality in living cells [5,6]. Firstly, molecular chaperones bind to misfolded proteins with masking hydrophobic surfaces and thus prevent aggregation [7-9]. If misfolded proteins are unable to refold by molecular chaperones or exceed cellular chaperoning capacity, misfolded proteins are degraded by ubiquitin-proteasome system and autophagy-lysosome system. These two systems coordinately monitor quality of proteins and decide the fate of proteins (reuse after refolding or destruction by protease digestion). Thus, the molecular chaperones and protein degradation systems are crucial for cell survival against the toxicity of misfolded proteins.

3 DYNAMICS OF PROTEIN AGGREGATION AND QUALITY CONTROL IN LIVING CELLS

Spectroscopic analyses including FRAP, FLIP, photoactivation, photoconversion, FRET and FCS are very useful to analyze aggregation and interaction of misfolded proteins occurred in living cells. FRET analysis of misfolding polyglutamine-expanded huntingtin and ALS-causing mutant superoxide dismutase 1 (SOD1) indicated that the latter is highly mobile in the inclusion (perinuclear large aggregate) while the former is mostly immobile in the similar aggregated structure [10,11]. FRAP analysis has been applied for analysis of protein interaction between aggregate and molecular chaperones. Analysis of interaction of HSP70, a cytosolic molecular chaperone, with polyglutamine aggregates by FRAP indicated that this chaperone transiently interact with polyglutamine aggregates. We have shown that

photoconversion and FLIP analysis are also useful to analyze aggregation and dynamics of misfolded proteins [12]. We have used FCS to analyze polyglutamine aggregation in soluble state (monomer, soluble oligomer and soluble aggregates) and found that soluble aggregates of polyglutamine-expanded protein are produced in cellular model of Huntington's disease. Intriguingly, depletion of CCT (also called TRiC), a cytosolic molecular chaperone, in cultured cells resulted in significant increase in soluble aggregates of polyglutamine-expanded proteins [13]. Since the depletion stimulates neuronal cell death [13-15], CCT is considered to protect cells from the toxicity of misfolded protein by preventing oligomer formation. We are currently analyzing dynamics of aggregation and interacting molecules of polyglutamine-expansion proteins, and ALS-linked SOD1 for comparison, using FCS (including fluorescence cross correlation spectroscopy), photoconversion and FRET techniques.

4 CONCLUSIONS

Although misfolded proteins are highly toxic to cells, how they exert the toxicity is largely unknown. Recent progress on the study of protein misfolding diseases including neurodegenerative diseases by live cell imaging and other analyses suggest that soluble species like misfolded monomers and oligomers are more toxic than large aggregates or inclusions. Further analysis including real-time spatio-temporal observation of misfolded proteins at various aggregation states (monomer, oligomer, large aggregate and inclusion) and interaction with other proteins (co-aggregating proteins, molecular chaperones, transporter and degradation-related proteins) may address how misfolded proteins kill neuronal cells in neurodegenerative diseases.

Acknowledgment This work is supported by a Grant-in-Aid for Scientific Research Programs from the Ministry of Education, Culture, Sports, Science and Technology of Japan and the Japanese Society for the Promotion of Science.

References

1. Lippincott-Schwartz J., Snapp E. and Kenworthy A. (2001) Studying protein dynamics in living cells. *Nat. Rev. Mol. Cell Biol.* **2**, 444-56.
2. Kim S.A. and Schwillle P. (2003) Intracellular applications of fluorescence correlation spectroscopy: prospects for neuroscience. *Curr. Opin. Neurobiol.* **13**, 83-90.
3. Ross, C. A. and Poirier, M. A. (2004) Protein aggregation and neurodegenerative disease. *Nat. Med.* **10 Suppl.**, S10-17
4. Chiti, F. and Dobson, C. M. (2006) Protein misfolding, functional amyloid, and human disease. *Annu. Rev. Biochem.* **75**, 333-366

5. Muchowski, P. J. and Wacker, J. L. (2005) Modulation of neurodegeneration by molecular chaperones. *Nat. Rev. Neurosci.* **6**, 11-22
6. Morimoto, R. I. (2008) Proteotoxic stress and inducible chaperone networks in neurodegenerative disease and aging. *Genes Dev.* **22**, 1427-1438
7. Bukau, B., Weissman, J. and Horwich, A. (2006) Molecular chaperones and protein quality control. *Cell* **125**, 443-451
8. Saibil, H. R. (2008) Chaperone machines in action. *Curr. Opin. Struct. Biol.* **18**, 35-42
9. Hartl, F. U. and Hayer-Hartl, M. (2009) Converging concepts of protein folding in vitro and in vivo. *Nat. Struct. Mol. Biol.* **16**, 574-581
10. Kim, S., Nollen, E.A., Kitagawa, K., Bindokas, V.P. and Morimoto, R.I. (2002) Polyglutamine protein aggregates are dynamic. *Nat. Cell Biol.* **4**, 826-831
11. Matsumoto, G., Stojanovic, A., Holmberg, C. I., Kim, S. and Morimoto, R. I. (2005) Structural properties and neuronal toxicity of amyotrophic lateral sclerosis-associated Cu/Zn superoxide dismutase 1 aggregates. *J. Cell Biol.* **171**, 75-85
12. Hirayama, S., Yamazaki, Y., Kitamura, A., Oda, Y., Morito, D., Okawa, K., Kimura, H., Cyr, D.M., Kubota, H. and Nagata, K. (2008) MKKS is a centrosome-shuttling protein degraded by disease-causing mutations via CHIP-mediated ubiquitination. *Mol. Biol. Cell.* **19**, 899-911.
13. Kitamura, A., Kubota, H., Pack, C. G., Matsumoto, G., Hirayama, S., Takahashi, Y., Kimura, H., Kinjo, M., Morimoto, R. I. and Nagata, K. (2006) Cytosolic chaperonin prevents polyglutamine toxicity with altering the aggregation state. *Nat. Cell Biol.* **8**, 1163-1170
14. Behrends, C., Langer, C. A., Boteva, R., Bottcher, U. M., Stemp, M. J., Schaffar, G., Rao, B. V., Giese, A., Kretzschmar, H., Siegers, K. and Hartl, F. U. (2006) Chaperonin TRiC Promotes the Assembly of polyQ Expansion Proteins into Nontoxic Oligomers. *Mol. Cell* **23**, 887-897
15. Tam, S., Geller, R., Spiess, C. and Frydman, J. (2006) The chaperonin TRiC controls polyglutamine aggregation and toxicity through subunit-specific interactions. *Nat. Cell Biol.* **8**, 1155-1162

Synthesis of Phenol- and Aniline-Based Oligomers as a Flexible Scaffold for Biomimetic Architectures

Hiroshi Katagiri

Graduate School of Science and Engineering, Yamagata University, 4-3-16 Jonan, Yonezawa, Yamagata 992-8510, Japan
kgri7078@yz.yamagata-u.ac.jp

Abstract: A double helicate having two spiroborate moieties was prepared from an ortho-linked hexaphenol and NaBH₄. The structure was determined in the solid state by X-ray analysis and in solution by ESI-MS and NMR. The optical resolution of the helicate was achieved by diastereomeric salt formation using an enantiomerically-pure ammonium salt. A chelation-assisted nucleophilic aromatic substitution methodology was applied to phenol-derived cyclic tetramers to displace the hydroxyl groups by benzylamino groups, which lead for the synthesis of the calixarenes comprised of aniline units. The structure was determined in the solid state by X-ray crystallography, which revealed a peptide-mimetic structure of hydrogen bond network.

Key Words: Oligophenol, Double helicate, Aniline, Hydrogen bond

1 INTRODUCTION

The metal-directed and hydrogen bonding-mediated self-assembly are an area of considerable current interest and research activity.[1] In particular, doubly- and triply-stranded helicates have attracted great attention due to its broad impact across a wide range of material science and biomimetic chemistry along with their aesthetic appeal.[2] In general, helicates are prepared from coordinating oligodentate strands with transition metals, and in few cases, typical metal cations such as lithium, sodium, and potassium.[3] However, to the best of our knowledge, boron has never been used as an assembling center for constructing a double-stranded helicate, although boric acid esters have been extensively utilized to date as a useful module for artificial supramolecular receptors and synthetic catalysts.[4,5]

In the viewpoint of cyclic aromatic oligomers, calix[n]arenes have provided versatile platforms for supramolecular host compounds depending on the introduction of hydrogen bond framework.[6] On the other hand, it has been well known that introduction of any substituents to the aromatic nucleus through cleavage of an aryl-oxygen bond is quite difficult. Therefore, it is not surprising that there have been only few examples of calixarenes bearing substituents other than those of -OR types at the lower rim. In this context, development of a method for introducing amino substituent to the lower rim is highly desirable because such substituent is a potential hydrogen bond framework attached to the skeleton directly.

We describe herein the synthesis and structure of a

double-stranded helicate consisting of achiral ortho-linked hexaphenol strands bridged by sodium and spiroborates which surprisingly appeared to be sufficiently inert to be resolved into enantiomers by diastereomeric salt formation. It also be described the transformation of the tetramethyl ethers of sulfinyl- and sulfonylcalix[4]arene to the tetraamino derivatives of the thia-, sulfinyl-, and sulfonylcalix[4]arene.

2 RESULTS AND DISCUSSION

2.1 Double Helicates Consisting of ortho-Linked Hexaphenol Strands Bridged by Spiroborate

We designed and synthesized the ortho-linked hexaphenol (H₆L) as the strands for helicates, since phenols, especially 2,2'-biphenols are known to form stable well-defined tetrahedral spiroborate complexes with boric acid (Fig. 1). The ligand H₆L was synthesized in a stepwise manner including the consecutive Suzuki coupling protocol. The boron complex of H₆L was prepared by heating a mixture of sodium borohydride and H₆L in 1,2-dichloroethane-ethanol at 80 °C.

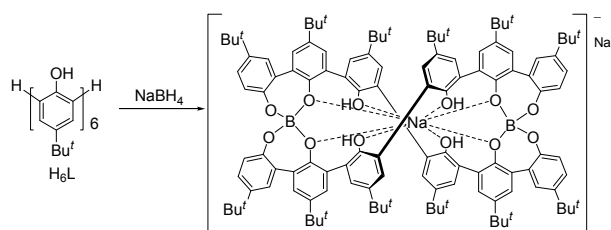


Figure 1. Synthesis of the helicate [B₂Na(H₂L)₂]⁻·Na⁺.

The X-ray single crystal analysis revealed the double-stranded helical structure of the complex, which has D_2 symmetry with three mutually perpendicular C_2 axes, and the two strands are C_2 symmetric and structurally identical, as shown in Fig 2. The two strands are bridged by the spiroborates formed from the terminal biphenol units and the boron atoms. Interestingly, an octacoordinated sodium cation is found at the center of the complex.

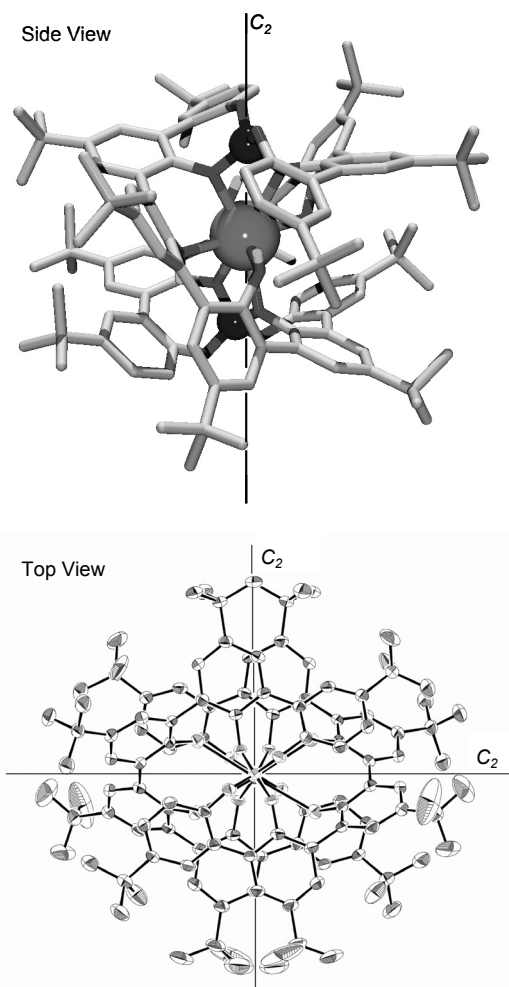


Figure 2. Crystal structure of the boron complex.

The formation of the boron complex was also confirmed by electrospray ionization (ESI) mass spectrometry (Fig. 3) and NMR studies of an acetone solution of the complex. (Fig. 4) Only one intense peak was observed at $m/z = 1819$ (negative mode) and 1865 (positive mode), which correspond to $[B_2Na(H_2L)_2]^-$ and $[B_2Na(H_2L)_2]^- \cdot 2Na^+$ species respectively, and each spectrum is in good agreement with simulated pattern. The 1H NMR spectrum of the complex in $[D_6]$ acetone is also consistent with the structure determined by X-ray in

the solid state; each strand is C_2 symmetric and the central biphenol units have two free phenolic protons. Moreover, the NOESY spectrum of the complex showed strong negative cross peaks between the two strands (Fig. 4). These cross peaks are attributed to the interstrand NOEs (distance approx. 2.5 Å), indicating that the complex holds the double-stranded helical trinuclear structure in solution.

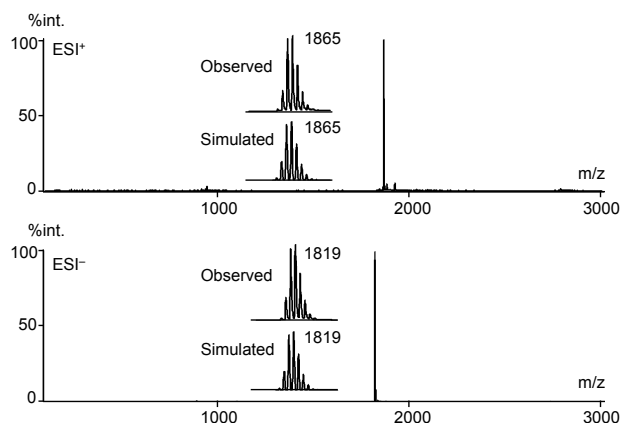


Figure 3. Electrospray ionization (ESI) mass spectra of an acetone solution of the boron complex.

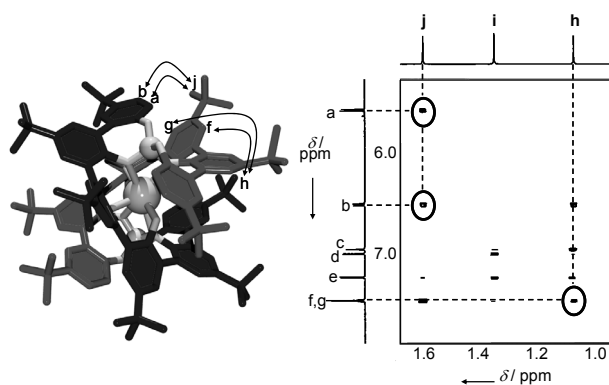


Figure 4. Partial NOESY spectrum of the boron complex in $[D_6]$ acetone at 25 °C.

To date, only a few example of the optical resolution of racemic helicates have been reported and they are usually based on the formation of diastereomeric ion pairs.[7] The optical resolution of the helicate $(\pm)\text{-}[B_2Na(H_2L)_2]^- \cdot Na^+$ was carried out by diastereomeric salt formation (Fig. 5). The cation exchange of the racemate was performed by adding a 10-fold excess of $(-)\text{-}N\text{-dodecyl-}N\text{-methylphedrinium bromide } ((-)\text{-}DME^+ \cdot Br^-)$ to a solution of the helicate in MeCN, and a white microcrystalline solid was precipitated within 24 h. The crystals of $(+)\text{-}313\text{-}[B_2Na(H_2L)_2]^- \cdot (-)\text{-}DME^+$ were collected by filtration and its diastereomeric excess (d.e.) was determined to be almost 99% by its 1H NMR (CD_2Cl_2 , 25 °C). The mother liquor was then evaporated to afford a white solid of the opposite diastereomer $(-)\text{-}313\text{-}[B_2Na(H_2L)_2]^- \cdot (-)\text{-}DME^+$ and the excess $(-)\text{-}DME^+ \cdot Br^-$; the d.e. was 66% as estimated by

^1H NMR in the same way.[8] The circular dichroism (CD) spectra of both the diastereomers showed almost all image Cotton effects in their patterns in the range of 240–330 nm except for the intensities, because the CD signals due to $(-)\text{-DME}^+\cdot\text{Br}^-$ are negligibly weak (Fig. 6).

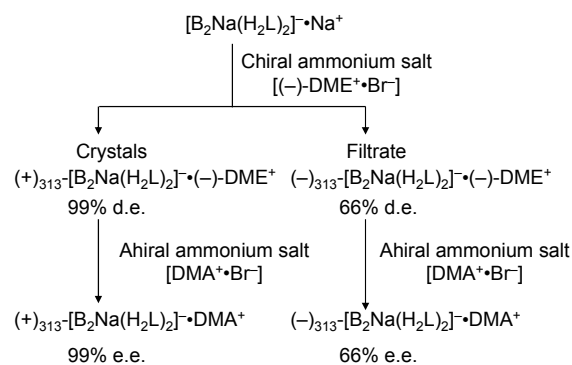


Figure 5. Optical resolution by formation of a diastereomeric salt followed by replacement with achiral ammonium salt.

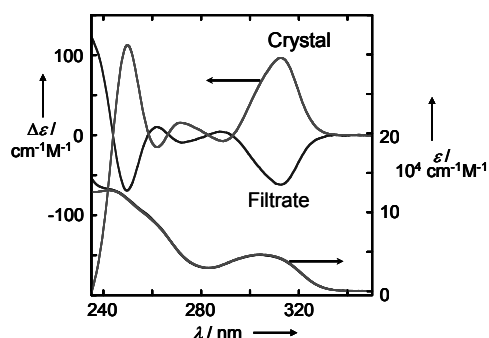


Figure 6. CD and UV/Vis spectra (CH_3CN , 25°C) of the boron complex of $(+)\text{-}313\text{-}[\text{B}_2\text{Na}(\text{H}_2\text{L})_2]^+\cdot(-)\text{-DME}^+$ and $(-)\text{-}313\text{-}[\text{B}_2\text{Na}(\text{H}_2\text{L})_2]^+\cdot(-)\text{-DME}^+$.

Finally, the resulting diastereomeric double-stranded helicates were successfully converted to the corresponding enantiomers when the optically active ammonium $(-)\text{-DME}^+$ was exchanged by dodecyltrimethylammonium bromide ($\text{DMA}^+\cdot\text{Br}^-$) as the achiral source (Fig. 5). Thus, the complex $(+)\text{-}313\text{-}[\text{B}_2\text{Na}(\text{H}_2\text{L})_2]^+\cdot\text{DMA}^+$ bearing only helical chirality without any other chiral factors, exhibiting the perfectly identical Cotton effects and UV/Vis spectra to these of $(+)\text{-}313\text{-}[\text{B}_2\text{Na}(\text{H}_2\text{L})_2]^+\cdot(-)\text{-DME}^+$ was obtained, suggesting that the helicate is really stereo-inert and may be enantiomerically pure.[9]

2.2 Calix[4]arenes comprised of aniline units

Chelation-assisted nucleophilic aromatic substitution ($\text{S}_{\text{N}}\text{Ar}$) reaction is one of the most useful methodologies for replacement of an ortho alkoxy group of aromatic substrates bearing substituents such as ester, sulfinyl, and sulfonyl groups by a C-, O-, or N-centered nucleophile (Fig. 7).[10] This type of substitution proceeds far more

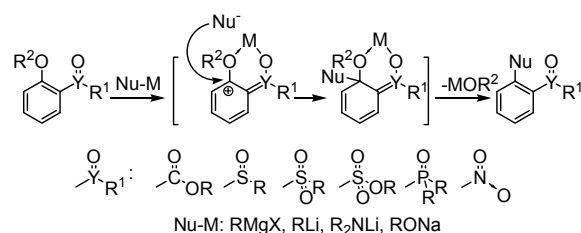


Figure 7. Chelation-assisted $\text{S}_{\text{N}}\text{Ar}$ reaction.

readily than the “classical” $\text{S}_{\text{N}}\text{Ar}$ process, because strong chelation of the substrate to the metal center of the nucleophile facilitates a Michael-type conjugate addition of the anionic moiety across the aromatic ring followed by displacement of the alkoxy group to afford the *ipso*-substitution product. Then, we extend the chelation-assisted $\text{S}_{\text{N}}\text{Ar}$ methodology to the thiacalix[4]arene family to displace the lower-rim hydroxy group by using sulfonyl or sulfinyl bridges as chelation-type activating groups. Treatment of the tetramethoxy derivative **1a** with lithium benzylamide in THF at room temp. for 2 h displaced all the methoxy groups with benzylamino substituents to give **2a** in high yield (Fig. 8). This indicates that the sulfonyl group even in a cyclic oligomer of alkoxybenzene is able to serve as an activating group for the $\text{S}_{\text{N}}\text{Ar}$. Although attempted hydrogenolytic removal of the benzyl moiety of **2a** was unsuccessful, treatment with NBS-BPO caused dehydrogenation to give imine **3a**, which was then hydrolyzed to tetraaminosulfonylcalix[4]arene TASO_2 with four free amino substituents at the lower rim. To our pleasure, the $\text{S}_{\text{N}}\text{Ar}$ process proceeded quite smoothly even via the SO route for the synthesis of tetraamino derivative TASO and TAS : By the same method used for **1a**, all the methoxy groups of **1b** were substituted by benzylamino groups to give **2b** in a comparable yield. Here again, the dehydrogenation with NBS-BPO afforded imine **3b**, which was then hydrolyzed to amine TASO . Treatment of TASO with $\text{LiAlH}_4\text{-TiCl}_4$ in THF at room temperature smoothly afforded TAS .

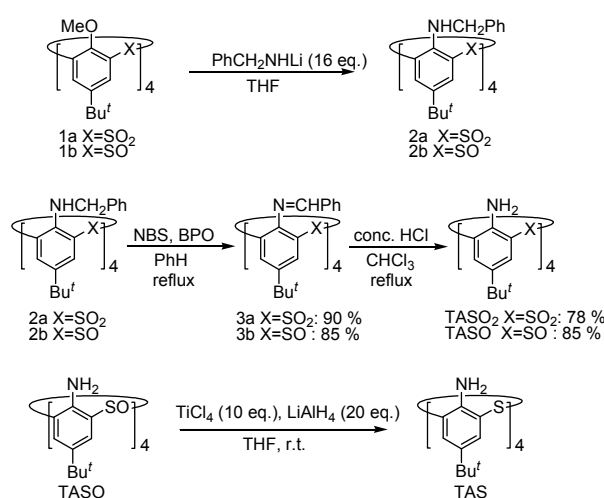


Figure 8. Reaction conditions and reagents.

The calix[4]arene analogues comprised of four aniline units bridged by S, SO, and SO₂ have some interesting structural features. The X-ray crystallographic analysis revealed that TAS adopts 1,3-alternate conformation with crystallographic symmetry (Fig. 9). The dihedral angle between the distal phenyl rings is 10.57(8)° to form an almost rectangular cavity. The intramolecular NH···S bonds are observed between an amino group and the ortho sulfides. This may cause the lone pair of amino group to direct toward outside the cavity.

Sulfinyl derivative TASO also adopts 1,3-alternate conformation with crystallographic symmetry. The dihedral angle between distal phenyl rings is 10.9(1)°, showing a quite similar cavity to that of TAS. Contrary to TAS, there are found not only intramolecular but also intermolecular hydrogen bonds, NH···O=S, between an amino group and sulfinyl oxygen atoms. This may let the lone pair of the amino group direct toward inside the cavity. The significant outcome of the intermolecular hydrogen bonds is that molecules of TASO form 2-dimensional molecular network. [11]

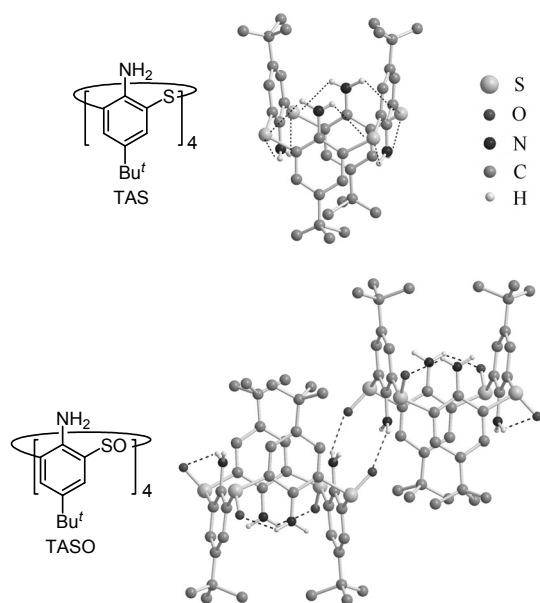


Figure 9. Crystal structure of TAS and TASO

3 SUMMARY

In summary, we have successfully prepared the spiroborate-based double helical complex using the simple ortho-linked hexaphenol as the ligand, and the helicate is stable in the solid state as well as in solution. Both enantiomers of the racemic helicates were resolved by diastereomeric salt formation using the optically active ammonium salt. We believe that various other optically active spiroborate-based double helicates can be prepared by the same strategy. It has also been shown here that

the chelation-assisted S_NAr methodology is applicable to the calix[4]arene analogues bearing sulfinyl and sulfonyl bridges for the synthesis of tetraaminocalix[4]arene derivatives, which should provide a new series of molecular platforms for functional materials and supramolecular assembly.

References

- [1] Lehn, J.-M., "Supramolecular Chemistry: Concepts and Perspectives," VCH, New York, (1995).
- [2] Albrecht, M. "Let's Twist Again" Double-Stranded, Triple-Stranded, and Circular Helicates," *Chemical Reviews*, Vol.101, No.11, pp.3457–3497, (2001).
- [3] Bell T. W. and Jousselein, H., "Self-assembly of a double-helical complex of sodium," *Nature*, Vol.367, pp.441–444, (1994).
- [4] Kobuke, Y., Sumida, Y., Hayashi, M. and Ogoshi, H., "Metal-Assisted Organization rather than Preorganization for the Design of Macrocyclic Hosts," *Angewandte Chemie International Edition in English*, Vol.30, No.11, pp.1496–1499, (1991).
- [5] Ishihara, K. and Yamamoto, H., "Bronsted Acid Assisted Chiral Lewis Acid (BLA) Catalyst for Asymmetric Diels-Alder Reaction," *Journal of the American Chemical Society*, Vol.116, No.4, pp.1561–1562, (1994).
- [6] Gutsche, C. D., "Calixarenes Revisited, Monographs in Supramolecular Chemistry," Stoddart, J. F., Ed. The Royal Society of Chemistry, Cambridge, (1998).
- [7] Rapenne, G., Dietrich-Buchecker, C. and Sauvage, J.-P., "Resolution of a Molecular Trefoil Knot," *Journal of the American Chemical Society*, Vol.118, No.44, pp.10932–10933, (1996).
- [8] "(+)-313" and "(–)-313" denote the signs of the Cotton effect at 313 nm.
- [9] Katagiri, H., Miyagawa, T., Furusho, Y. and Yashima, E., "Synthesis and Optical Resolution of a Double Helicates Consisting of ortho-Linked Hexaphenol Strands Bridged by Spiroborate," *Angewandte Chemie International Edition in English*, Vol.45, No.11, pp.1741–1744, (2006).
- [10] Hattori, T., Suzuki, M., Tomita, N., Takeda, A. and Miyano, S., "Chelation-assisted Nucleophilic Aromatic Substitution of 2-Sulfonylsubstituted 1-Methoxynaphthalenes by Grignard Reagents: Factors Determining the Activating Ability of the 2-Sulfonyl Substituents," *Journal of the Chemical Society, Perkin Trans. 1*, Vol.1997, No.8, pp.1117–1124, (1997).
- [11] Katagiri, H., Iki, N., Hattori, T., Kabuto, C. and Miyano, S., "Calix[4]arenes Comprised of Aniline Units," *Journal of the American Chemical Society*, Vol.123, No.4, pp.779–780, (2001).

A SELEX (Artificial Evolution) Approach to Light-Up Sensing Materials for Bioimaging

Shinsuke Sando,* Atsushi Narita, Masayoshi Hayami, and Yasuhiro Aoyama**

Department of Synthetic Chemistry and Biological Chemistry, Graduate School of Engineering, Kyoto University, Katsura,
Nishikyo-ku, Kyoto 615-8510, Japan

* Present Address; Inamori Frontier Research Center, Kyushu University, 744 Motoooka, Nishi-ku, Fukuoka
819-0395, Japan

**Present Address: Faculty of Science and Engineering, Doshisha University, 1-3 Tatara-Miyakodani, Kyotanabe-shi, Kyoto
610-0321, Japan

yaoyama@mail.dhoshisha.ac.jp

Abstract: By Using the SELEX technique, one can “evolve” a pool or library of randomized DNA or RNA sequences into specific binders (aptamers) toward a particular dyestuff, in this case a modified Hoechst dye. The latter, otherwise practically non-fluorescent, becomes highly fluorescent upon binding to the former. The aptamer-dye pair can be used as a light-up probe for gene sensing as well as transcription monitoring.

Key Words: SELEX, Gene Sensing, Transcription, Bioimaging

INTRODUCTION

The Nobel Prize in Chemistry for 2008 went to the discovery of green fluorescent protein (GFP) and its application. The application of GFP was in the fusion technology using thereof. Proteins of interest can be fused to GFP and afford, upon transcription/translation, fusion proteins with GFP. The target proteins can be monitored with GFP as a fluorescent tag. What we wanted to do is in-cell monitoring of RNAs. In analogy with the GFP-fusion technology, we need a fluorescent RNA tag. Unfortunately, however, fluorescent RNAs are not known. In these circumstances, we set up a two-step evolution strategy for “light-up” RNA-fluorophore pairs as a tag.

SELEX (Systematic Evolution of Ligands with Exponential Enrichment) is a selection-amplification procedure to evolve randomized nucleic acid sequences into effective binders (aptamers) for particular targets of interest (Figure 1). The object of this work is to generate a “light-up” fluorophore-aptamer pair based on down-modification of a conventional DNA-staining dye to suppress its affinity to the original dsDNA targets, followed by reselection of the aptamers that would bind to the modified dye.

RESULTS AND DISCUSSION

Giving up to create fluorescent RNAs themselves, we took an alternative approach, and set up a two-step “artificial” evolution strategy for “light-up” RNA-fluorophore pairs as a tag.

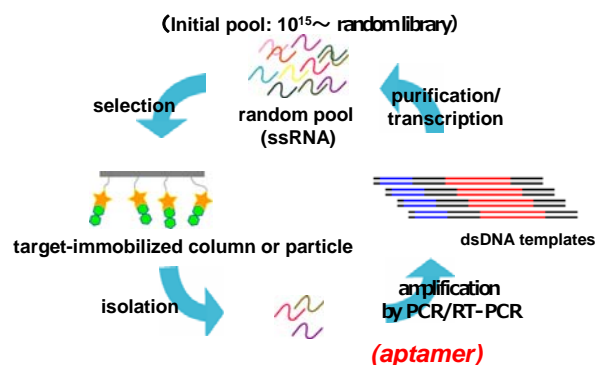
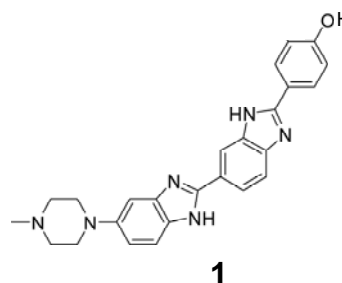
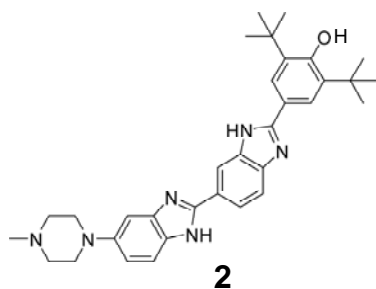


Figure 1. Schematic illustration of SELEX.



The first step is chemical evolution of dye stuffs. Hoechst 33258 (**1**) is a microenvironment-sensitive fluorophore whose fluorescence intensity is highly dependent on the micropolarity of the environment. It is practically nonfluorescent in water but is rendered highly fluorescent when bound to the minor groove of double-strand (ds) DNAs. As

a consequence, it is used as a stainer of nucleus in live cells. The Hoechst dye possesses a number of attractive features (light-up upon binding to nucleic acid, cell permeability, and low cytotoxicity) as an RNA imager. The problem is its high affinity to dsDNA. Our target is RNA in the cells. We thought that the affinity to dsDNA could be sterically controlled. In fact, upon introduction of two bulky *tert*-butyl groups on the benzene ring, the dye (compound **2**) loses its affinity to dsDNA.



The second step is biological evolution of random RNA sequences into particular ones that specifically bind to the *tert*-butyl-modified or “evolved” dye by using the *in vitro* selection (or in-test tube evolution) scheme known as SELEX. It is composed of two essential processes, selection of random sequences on the target by using, in the present case, target-immobilized magnetic particles and PCR (polymerase chain reaction) amplification of the binding sequences (aptamers). By repeating the selection/amplification cycles, one can exponentially enrich or evolve the strongly binding aptamers with K in the order of 10^6 M^{-1} and 10^8 M^{-1} for the DNA¹ and RNA² aptamers, respectively. Partial sequences of the aptamers, in light of their computer-predicted secondary structures, were also checked in search for the true dye-binding domain of the aptamers. In this way, we reached the shortest optimized (in terms of light-up property) sequences, i.e., 25-mer DNA aptamer **3** with $I/I_0 = 190^{45}$ and 29-mer RNA aptamer **4** with $I/I_0 \geq 50$,⁴⁶ where I_0 and I are fluorescence intensities of the modified dye when alone and when bound to the optimized aptamer, respectively. The aptamer-fluorophore (29-mer RNA aptamer-modified dye) pair can be used as a fluorescence tag. Transcription of luciferase gene fused with five successive 29-mer RNA tag sequences (Figure 3) in an *in vitro* transcription system can indeed be fluorescence-monitored in the presence of the modified dye (Figure 4).²

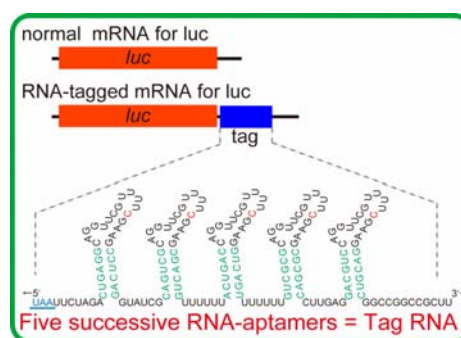
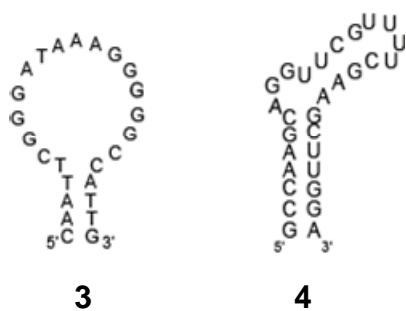


Figure 3. mRNA for luciferase fused with five successive 29-mer RNA tag sequences after the UAA stop codon.

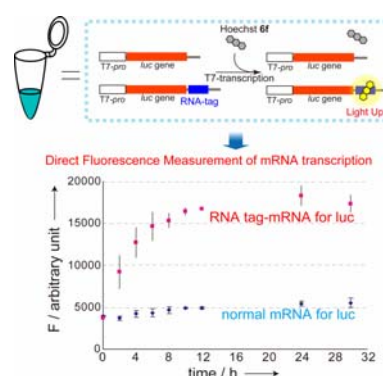


Figure 4. Fluorescence monitoring of the transcription of the tag-fused mRNA for luciferase (top trace shown in red) and that of normal luciferase (bottom trace shown in blue) in the presence of modified Hoechst dye **2**.

CONCLUDING REMARKS

Owing to its simplicity, the present strategy could be applied to other live cell staining fluorophores. This approach may lead to systematic generation of live cell compatible multicolor light-up fluorophore-aptamer pairs.

Acknowledgment—We thank Kazumasa Ogawa for his contribution in the early stage of this work. This work was supported by the Industrial Technology Research Grant Program of the New Energy and Industrial Technology Development Organization (NEDO) (to SS) and in part by a Grant-in-Aid from the Japan Society for the Promotion of Science (JSPS) and Japan Science and Technology Agency (JST).

References

- [1] Sando, S., Narita, A., Aoyama, Y. *ChemBioChem* **8**, 1795-1803 (2007).
- [2] Sando, S., Narita, A., Hayami, M., Aoyama, Y. *Chem. Commun.* 3858-3860 (2008).

Fabrication and application of 'plasmonic Ag nanosheet'

Kaoru Tamada*

* Research Institute of Electrical Communication, Tohoku University

2-1-1 Katahira, Aobaku, Sendai 980-8577 Japan

tamada@riec.tohoku.ac.jp

Abstract: Our latest effort to fabricate "*plasmonic silver nanosheet*" is presented in this paper. Uniformly sized silver nanoparticles ($d = 4.8$ nm) are deposited on the substrate as a homogeneous nanosheet composed of two dimensional crystalline domains, in which the distance between silver cores is accurately controlled by the thickness of the capping organic molecules. The silver nanosheet exhibits a significant shift of plasmon absorption band to the longer wavelength (ca. 50 nm) from the position in dispersion solution, while the peak width was rather reduced (sharpened) as an evidence of homogeneous coupling of local plasmons. This flexible, transferable nanosheet, which can trap and transport bulk light at nano-interface, promises new application in the field of bio- and opto-electronic devices.

Key Words: Silver nanoparticles, Local plasmons, Self-assembly

1 INTRODUCTION

Metal nanoparticles are one of key materials for future bottom-up nanotechnology due to their unique chemical, electronic, and optical properties [1-3]. Especially plasmonic studies excite a tremendous number of new applications in the field of optoelectronics and biosensing devices [4-6]. Gold nanoparticles are widely utilized in plasmonics due to their stable and inert property, however, silver nanoparticles are known to have a superior optical characteristics than gold. Silver exhibits much smaller imaginary part of the dielectric function for visible light compared with gold, which results in sharp plasmon absorption band and the electromagnetic enhancement factor excited at silver interface is more than 5 times larger than that at gold interface [7]. Only the weakness of silver is low resistance to oxidation, which causes unstable optical response occasionally. However, strongly adsorbed ligands such as alkanethiol, alkylamine and fatty acid can improve long-term stability of the silver particles preventing them being oxidized [8-10].

In this study, we fabricate homogeneous two dimensional crystalline sheet composed of uniformly sized silver nanoparticles. Silver nanoparticles are synthesized in our laboratory by thermal reduction of silver acetate precursor in the melt of myristic acid as a reaction medium as well as a capping agent (Fig.1) [11]. This simple method produces gram-scale homogeneous silver nanoparticles capped by myristates (AgMy) in good reproducibility. AgMy also exhibits unique property concerned with a ligand exchange. The particle is synthesized at more than 200 °C, i.e., myristate cappings can stay on silver nanoparticles at such high temperature, however,

they can be exchanged to thiol derivatives even

at room temperature. This characteristic of the particle enables us to control the thickness and surface functionality of capping layers on silver cores quite easily. Another advantage of our particle is its amphiphilic property. They can spread at air-water interface by forming a stable monolayer. The amphiphilicity of AgMy is mainly attributed to amphiphilic property of myristate cappings, however, even alkanethiolate-capped nanoparticles prepared by the ligand exchange can spread on water [11]. The two dimensional nanosheet composed of uniformly sized Ag nanoparticles with different core-to-core distance by capping thickness was utilized in this study.

2 EXPERIMENTALS

AgMy was purified by reprecipitation with ethanol in toluene (or hexane) to remove excess myristic acids before use. The particles as precipitates are separated from a top clear solution by low-speed centrifugation (15 °C, 6000 rpm, 10 min) and particle aggregates are removed from the redispersed toluene solution (or hexane) by high-speed centrifugation (15 °C, 20,000 rpm, 10 min).

For the ligand exchange, an AgMy solution (25 mg/ 50 ml) was mixed with an alkanethiol solution ($\text{CH}_3(\text{CH}_2)_n\text{SH}$, $n = 3, 7, 11, 17, 2$ mM, 50 ml) and stirred at room temperature for 3 hours, then purified by the same procedure as described above. The complete ligand exchange reaction was confirmed by FTIR measurements.

electromagnetic field on entire bulk surface without any expensive, complicated instrumentations (Fig. 5 right).

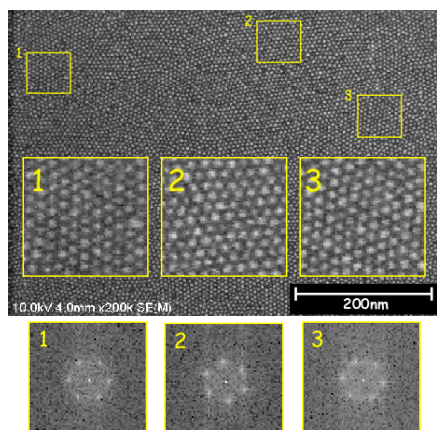


Fig. 4 SEM image and FFT images of AgMy film deposited at (B) in Fig. 2.

Another remarkable characteristic of our nanosheet is a tunable absorption band. By the ligand exchange to alkanethiolates with different chain length (AgC4, AgC8, AgC12, AgC18), we can control the distance between silver cores precisely, which leads to the different plasmon absorption band positions as shown in Fig. 6. As theoretically expected, the interparticle distance (edge to edge) and the plasmon band position (λ_{max}) have a logarithmic relation where λ_{max} shifts to longer wavelength as the interparticle distance becomes shorter [13].

Here we inform the other unique property of our nanosheet. When we measured reflection spectra of AgMy nanosheets deposited on Ag and Au thin layers (180 nm thick) at an incident angle of 5°, additional red-shift of plasmon absorption band with band sharpening was clearly detected, especially on gold substrate. These are certainly unexpected results.

There have been several studies concerning the interaction between nano-sized metal objects and metal thin layers [14-17]. Abe and Kajikawa have reported that two split resonance peaks are detected when p polarized lights are irradiated to gold thin layers with gold nanoparticles immobilized on surface at an incident angle of 45° [14]. One at the shorter wavelength (520 nm) corresponds to the absorption band of the particles in-plane, while another at the longer wavelength (600-700 nm) corresponds to the absorption band of the particles normal to the surface interacting with the gold thin layer. The experimental data well agreed with the theoretical expectation and the red-shift of plasmon band is interpreted by the electromagnetic interaction between the nanoparticle and the substrate occurring only by the irradiation of normal component of the light. There are a number of reports mentioning the interaction of periodic metallic array with metal thin film as well [15-17]. However, the phenomena they mentioned were with the array in the scale of light

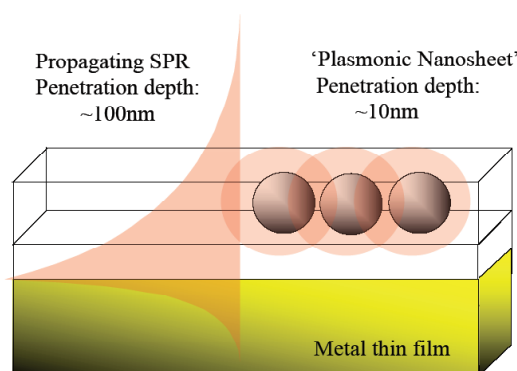


Fig. 5 Schematics of "plasmonic nanosheet".

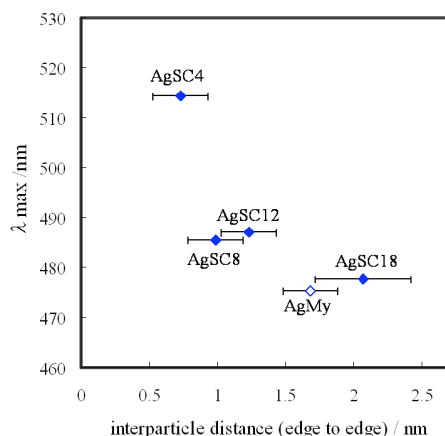


Fig. 6 Plasmon absorption band position (λ_{max}) vs. interparticle distance of plasmonic nanosheets

wavelength (e.g. 300 nm), i.e., the phenomena they found are completely different from our case but similar to the grating coupling.

Although further investigations are necessary to show the full picture, there is no doubt that the coupling of propagating SPR on gold thin film and LSPR on silver nanosheet is going on in our system. A simulational study of the two dimensional nanocrystalline structure may give an answer to our question.

At the end of the paper, we propose the application of the plasmonic nanosheet. The sheet can be simply integrated into conventional SPR biosensors to re-enhance the excitation light intensity from SPR set-up [19-20]. Here the LSR absorption band needs to be tuned to the wavelength of utilized light source. Since the photon energy must be too strong for organic dyes, QDs are a good candidate for a fluorescence marker. If the LSR of the sheet can excite propagating SPR without prism coupler, another possibility to improve the system will be proposed.

4 CONCLUSIONS

The improvement of chemical synthetic techniques enable us to have a great variety of nanostructured materials, e.g. nanoparticles, nanorods, nanowires, etc.^[21]. The advantage of these synthesized nanostructured materials is not only industrial productivity (cheap and easy) but also their small sizes; they can reach a few nm scale, which is definitely smaller than the one fabricated by top-down beam lithography. Even nanoimprint lithography reaches only tens of nm scale, which is still one-order larger than the nanomaterials chemically synthesized. However, a difficulty to control the spatial position on solid substrates has been a principle disadvantage of such bottom-up nanotechnology up to now.

When the object becomes so small, *self-assembly* or *self-organization* is the only way to construct long-range ordered regular arrays^[22]. In this paper, the fabrication and application of "*plasmonic nanosheet*", two dimensional crystalline films composed of uniformly sized silver nanoparticles are presented. This flexible, transferable nanosheet which can trap and transport bulk light at nanointerface promises new application in various field, not only biosensors but also optoelectronic devices such as LED and solar cells^[23-25].

Acknowledgment The part of this study has been done by collaboration with Prof. K. Okamoto, Kyoto University, JST-PRESTO.

References

- [1] Schmid, G., Talapin, D.V., Shevchenko, E.V., [Nanoparticles: From Theory to Applications], Weinheim, Germany, 251-298(2004).
- [2] Bohren, C. F., Huffman, D. R., [Absorption and scattering of light by small particles, vol. 1], John Wiley & Sons, Inc. New York (1998).
- [3] Toshima, N., Yonezawa, T., "Bimetallic nanoparticles - novel materials for chemical and physical applications", New J. of Chem. 22 (11), 1179-1201(1998).
- [4] Haynes, C.L., Van Duyne, R.P., "Nanosphere lithography: A versatile nanofabrication tool for studies of size-dependent nanoparticle optics", J. Phys. Chem. B 105(24), 5599-5611 (2001).
- [5] Kawata, S. [Near-field optics and surface polaritons], Springer, Berlin (2001).
- [6] Mirkin, C.A., Letsinger, R.L., Mucic, R.C., Storhoff, J.J., "A DNA-based method for rationally assembling nanoparticles into macroscopic materials", Nature 382 (6592), 607-609 (1996).
- [7] Knoll, W., "Interfaces and thin films as seen by bound electromagnetic waves", Annu. Rev. Phys. Chem. 49, 569-638 (1998).
- [8] Porter, L.A., Ji, D., Westcott, S.L., Graupe, M., Czernuszewicz, R.S., Halas, N.J., Lee, T.R., "Gold and silver nanoparticles functionalized by the adsorption of dialkyl disulfides", Langmuir 14(26), 7378-7386 (1998).
- [9] Nagasawa, H., Maruyama, M., Komatsu, T., Isoda, S., Kobayashi, T., "Physical characteristics of stabilized silver nanoparticles formed using a new thermal-decomposition method", Phys. Status Solid A 191, 67-76 (2002).
- [10] Yamamoto, M., Kashiwagi, Y., Nakamoto, M., "Size-controlled synthesis of monodispersed silver nanoparticles capped by long-chain alkyl carboxylates from silver carboxylate and tertiary amine", Langmuir, 22, 8581-8586 (2006).
- [11] Keum, C.-D., Ishii, N., Michioka, K., Wulandari, P., Tamada, K., Furusawa, M., Fukushima, H., "Agram scale synthesis of monodispersed silver nanoparticles capped by carboxylates and their ligand exchange", J. Nonlinear Opt. Phys. & Mater. 17(2), 131-142 (2008).
- [12] Taleb, A., Petit, C., Pilene, M.P., "Optical properties of self-assembled 2D and 3D superlattice of silver nanoparticles", J. Phys. Chem. B 102, 2214-2220 (1998).
- [13] Jain, P.K., Huang, W., El-Sayed, M.A., "On the universal scaling behavior of the distance decay of plasmon coupling in metal nanoparticle pairs: a plasmon ruler equation", Nano Lett. 7(7), 2080-2088(2007).
- [14] Abe, S., Kajikawa, K., "Linear and nonlinear optical properties of gold nanoparticles immobilized on a metallic surface", Phys. Rev. B 74, 035416 (2006).
- [15] Papanikolaou, N., "Optical properties of metallic nanoparticle arrays on a thin metallic film", Phys. Rev. B 75, 235426 (2007).
- [16] Zheng, Y.B., Juluri, B.K., Mao, X., Walker, T.R., Huang, T.J., "Systematic investigation of localized surface plasmon resonance of long-range ordered Au nanodisk arrays", J. Appl. Phys. 103, 014308 (2008).
- [17] Ghoshal, A., Kik, P.G., "Theory and simulation of surface plasmon excitation using resonant metal nanoparticle arrays", J. Appl. Phys. 103, 113111 (2008).
- [18] Johnson, P.B.; Christy, R.W., "Optical Constants of the Noble Metals", Physical Review B 6(12), 4370-4379 (1972).
- [19] Liebermann, T., Knoll, W., "Surface-plasmon field-enhanced fluorescence spectroscopy", Colloids and Surfaces A: Physicochemical and Engineering Aspects 171, 115-130 (2000).

[20]Roblek, R., Liu L., Schmid, E.L., Knoll, W.,
"Title: Multiplexed hybridization detection of quantum dot-
conjugated DNA sequences using surface plasmon enhanced
fluorescence microscopy and spectrometry", *Anal. Chem.* 76,
6160 (2004).

[21]Murphy, C.J., Gole, A.M., Hunyadi, S.E, Orendorff,
C.J., "One-dimensional colloidal gold and silver
nanostructures", *Inorg. Chem.* 45(19), 7544-7554 (2006).

[22]Ikezoe, Y., Kumashiro, Y., Tamada, K., Matsui, T.,
Yamashita, I., Shiba, K., Hara, M., "Growth of Giant Two-
Dimensional Crystal of Protein Molecules from a Three-Phase
Contact Line", *Langmuir* 24(22), 12836-12841 (2008).

[23] Okamoto, K., Niki, I., Shvartser, A., Narukawa, Y.,
Mukai, T., Scherer, A., "Surface-plasmon-
enhanced light emitters based on InGaN quantum wells",
Nature Materials 3(9), 601-605 (2004).

[24] Chandrasekharan, N., Kamat, P.V., "Improving the
photoelectrochemical performance of nanostructured
TiO₂ films by adsorption of gold nanoparticles", *J. Phys. Chem.*
B 104 (46), 10851-10857(2000).

[25] Rand, B.P., Peumans, P. Forrest, S.R., "Long-range
absorption enhancement in organic tandem thin-film solar cells
containing silver nanoclusters", *J. Appl. Phys.* 96(12),
7519-7526 (2004).

Synthesis and Properties of Dendritic-Linear Block Copolymer Having Multiple Interaction Sites

Mitsutoshi Jikei

Department of Engineering in Applied Chemistry, Akita University,
1-1, Tegatagakuen-machi, Akita-shi, Akita 010-8502, Japan
mjikei@gipc.akita-u.ac.jp

Abstract: Dendritic macromolecules have many terminal functional groups which can be used as multiple interaction sites. In this paper, a novel dendritic polyamide which has many carboxyl groups on the periphery was prepared as an initiator for atom transfer radical polymerization (ATRP) of 4-vinylpyridine. ATRP of 4-vinylpyridine was carried out by the dendritic initiator to prepare dendritic-linear copolymer. The resulting dendritic polyamide-b-poly(4-vinylpyridine) contains donor and acceptor sites for multiple hydrogen bondings. The effects of the hydrogen bonding on the thermal properties and association behavior in solution of the copolymer were investigated by DSC, NMR and light scattering experiments.

Key words: Dendrimer, multiple hydrogen bonding, dendritic polyamide, poly(4-vinylpyridine)

1 INTRODUCTION

Dendritic macromolecules are one of the most promising molecules for nano- and nanobiotechnology due to their unique size and three-dimensional architecture [1-6]. The unique shape of the dendrimers and dendrons allows to access unique molecular architectures, such as dumbbells, tadpoles and cylinders [7-15]. There are three strategies to prepare the dumbbell- and tadpole-shaped molecules. First of all, Fréchet and coworkers reported the preparation of linear and dendritic block copolymers by the coupling reaction of the benzyl ether dendrimers with poly(ethylene glycol) at the core [7-9]. The second one is the divergent approach from the terminal functional groups of linear polymers. The poly(ethylene oxide)-poly(lysine) dendrimer and polystyrene-poly(propylene imine) dendrimer were prepared by the divergent approach [10-12]. The last one is using the dendritic initiator reported by Hawker and Fréchet in 1996 [15]. The living/controlled polymerization is initiated at the core of the dendron to produce the tadpole-shaped copolymers. The nitroxide mediated radical polymerization, atom transfer radical polymerization and ring-opening polymerization of the N-carboxy- α -amino acid anhydrides have already been reported to date [13,15].

One of the unique features of dendrimers is the multivalency on the periphery. If the periphery is used as multiple interaction sites, a stable complex can be prepared from the dendrimer and other molecules via weak non-covalent interaction. In addition to hydrophobic interactions, hydrogen bonding is a key non-covalent interaction in nature because of its stability, dynamics and directionality. Although each hydrogen bond is weak compared to covalent bonds, the donor-to-acceptor interaction can be stabilized by multiple hydrogen bonding. In addition to biomolecules, such as nucleobases, stable multiple hydrogen bondings can be used as a key interaction to determine the properties of the synthetic

organic materials [16,17]. We have already reported the preparation of the carboxyl-terminated polyamide dendrimers and multiple hydrogen bonded complexes with poly(4-vinylpyridine) [18,19].

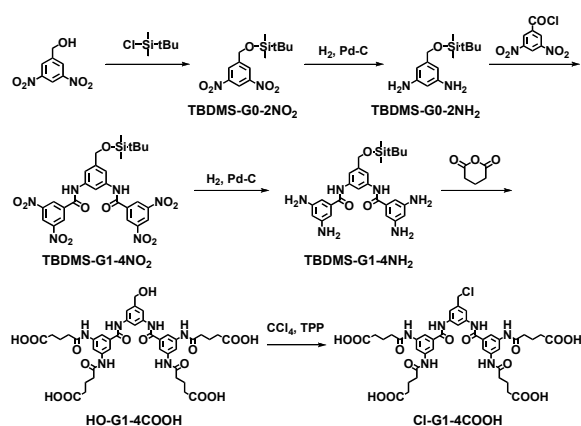
In this paper, we reported the preparation of dendritic polyamide-poly(4-vinylpyridine) copolymers [20,21]. The dendritic-linear copolymers have both donor and acceptor groups for multiple hydrogen bondings. Thermal and solution properties of the resulting copolymers were also investigated. It was found that both the multiple hydrogen bonding and solubility of each component affected the association behavior of the copolymer in solution.

2 EXPERIMENTS

2.1 Preparation of dendritic initiator

In a flask equipped with a magnetic stirrer, 3,5-dinitrobenzylalcohol (13.87 g, 70 mmol) and imidazole (4.77 g, 79 mmol) were dissolved in DMF (70 mL). A solution of t-butyldimethylchlorosilane (12.66 g, 84 mmol) in DMF (30 mL) was then added to the flask. After stirring at 40°C for 3h, the reaction solution was poured into water to precipitate the product. The precipitate was collected by filtration, washed with water and dried in vacuo at 50°C. The yield of TBDMS-G0-2NO₂ was 99 %. IR (KBr, cm⁻¹) ν 1594, 1545, 1471, 1342. ¹H NMR (DMSO-*d*₆) δ 8.71 (s, 1H), 8.55 (s, 2H), 4.97 (s, 2H), 0.94 (s, 9H), 0.13 (s, 6H).

In a flask equipped with a magnetic stirrer and a hydrogen inlet were added TBDMS-G0-2NO₂ (9.37 g, 30 mmol), Pd-C (3.19 g, 5 mol%) and ethanol (200 mL). The flask was degassed and purged several times with hydrogen and then stirred at room temperature for 48h. The mixture was filtered using Celite-545. The filtrate was evaporated and the residue was dried in vacuo at 50°C. The yield of TBDMS-G0-2NH₂ was 91 %. IR (KBr, cm⁻¹) ν 3309, 1596, 1472. ¹H NMR (DMSO-*d*₆) δ 5.76 (s, 2H), 5.71 (s, 1H),



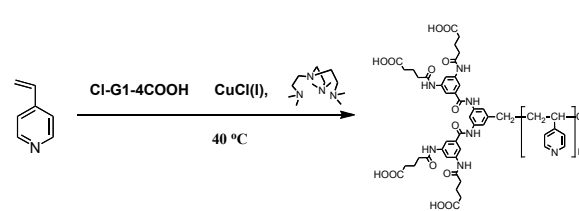
Scheme 1

4.97 (brs, 4H, NH₂), 4.39 (s, 2H, CH₂), 0.90 (s, 9H), 0.06 (s, 6H).

Into a flask equipped with a magnetic stirrer and a nitrogen inlet, TBDMS-G0-2NH₂ (2.52 g, 10 mmol) was dissolved in THF (100 mL). Triethylamine (3.33 mL, 24 mmol) and DNBC (5.53 g, 24 mmol) were added to the flask and the reaction mixture was stirred at rt under nitrogen. After 6h, the mixture was poured into water to precipitate the product. The precipitate was collected by filtration, washed with hot ethanol/n-hexane (1/2(v/v)) and dried in vacuo at 50°C. The yield of TBDMS-G1-4NO₂ was 88 %. IR (KBr, cm⁻¹) ν 1668, 1625, 1543, 1462, 1344. ¹H NMR (DMSO-*d*₆) δ 10.92 (s, 2H, amide H), 9.17 (s, 4H), 8.99 (s, 2H), 8.26 (s, 1H), 7.56 (s, 2H), 4.74 (s, 2H), 0.93 (s, 9H), 0.13 (s, 6H). Anal. Calcd for C₂₇H₂₈N₆O₁₁Si: C, 50.62; H, 4.41; N, 13.12. Found: C, 49.56; H, 3.68; N, 13.99.

In a flask equipped with a magnetic stirrer and a hydrogen inlet were added TBDMS-G1-4NO₂ (2.56 g, 4 mmol), Pd-C (1.70 g, 10 mol%), THF (100 mL) and ethanol (100 mL). Reductive hydrogenation was carried out in the same manner as TBDMS-G0-2NH₂. The yield of TBDMS-G1-4NH₂ was 79 %. IR (KBr, cm⁻¹) ν 3349, 1654, 1602, 1543, 1456. ¹H NMR (DMSO-*d*₆) δ 9.91 (s, 2H, amide H), 8.07 (s, 1H), 7.38 (s, 2H), 6.28 (s, 4H), 5.97 (s, 2H), 4.92 (s, 8H, NH₂), 4.64 (s, 2H, CH₂), 0.91 (s, 9H), 0.10 (s, 6H). Tm: 162.0-163.5°C. Anal. Calcd for C₂₇H₃₆N₆O₃Si: C, 62.28; H, 6.97; N, 16.14. Found: C, 61.78; H, 6.24; N, 17.36.

Into a flask equipped with a magnetic stirrer and a nitrogen inlet, TBDMS-G1-4NH₂ (1.04 g, 2 mmol) was dissolved in DMAc (15 mL). GAn (1.36 mL, 12 mmol) was added to the flask and the reaction mixture was stirred at rt under nitrogen. After 5h, the mixture was poured into water containing a small amount of hydrochloric acid to precipitate the product. The precipitate was collected by filtration, washed with water and dried in vacuo at 60°C. The yield of HO-G1-4COOH was 80 %. IR (KBr, cm⁻¹) ν 3304, 1709, 1671, 1605, 1558, 1455. ¹H NMR (DMSO-*d*₆) δ 12.09 (brs, 4H, COOH), 10.30 (s, 2H, amide H), 10.09 (s, 4H, amide H), 8.15 (s, 2H), 8.07 (s, 1H), 7.73 (s, 4H), 7.44 (s, 2H), 5.25 (s, 1H, OH), 4.48 (s, 2H), 2.37 (t, 8H), 2.28 (t, 8H), 1.81 (dt, 8H). ¹³C NMR (DMSO-*d*₆) δ 174.3, 171.1, 166.1, 143.4, 139.5, 139.3, 136.6, 114.1, 113.5, 112.8, 111.2, 63.1, 35.5, 33.1, 20.6. MALDI-TOF



Scheme 2

MS: *m/z* calcd for C₄₁H₄₆N₆O₁₅ 885.84 (M + Na⁺), found 884.14 (M + Na⁺). Tm: 153.0-154.0°C. Anal. Calcd for C₄₁H₄₆N₆O₁₅: C, 57.07; H, 5.37; N, 9.74; O, 27.81. Found: C, 56.95; H, 5.57; N, 9.82; O, 27.99.

Into a flask equipped with a magnetic stirrer, HO-G1-4COOH (0.129 g, 0.15 mmol) was dissolved in DMF (3 mL). A solution of triphenylphosphine (0.393 g, 1.5 mmol) and carbon tetrachloride (0.231 g, 1.5 mmol) in DMF (2 mL) was stirred at rt for 1h then added to the HO-G1-4COOH solution. The reaction mixture was stirred at rt for 48h. The mixture was poured into chloroform to precipitate the product. The crude precipitate was collected by filtration and dissolved in anhydrous methanol. The methanol solution was poured into chloroform to precipitate the product. The precipitate was collected by filtration, washed with chloroform and dried in vacuo at 60°C. The yield of Cl-G1-4COOH was 95 %. IR (KBr, cm⁻¹) ν 1713, 1671, 1604, 1556, 1455, 715. ¹H NMR (DMSO-*d*₆) δ 12.10 (brs, 4H, COOH), 10.41 (s, 2H, amide H), 10.12 (s, 4H, amide H), 8.15 (s, 3H), 7.74 (s, 4H), 7.57 (s, 2H), 4.74 (s, 2H), 2.37 (t, 8H), 2.28 (t, 8H), 1.81 (dt, 8H). ¹³C NMR (DMSO-*d*₆) δ 174.2, 171.1, 166.2, 139.7, 139.6, 138.2, 136.3, 116.1, 113.4, 112.8, 112.4, 46.6, 35.5, 33.0, 20.5. MALDI-TOF MS: *m/z* calcd for C₄₁H₄₅ClN₆O₁₄ 904.28 (M + Na⁺), found 904.20 (M + Na⁺). Tm: 158.5-160.0°C. Anal. Calcd for C₄₁H₄₅ClN₆O₁₄: C, 55.88; H, 5.15; Cl, 4.02; N, 9.54; O, 25.42. Found: C, 56.31; H, 5.21; Cl, 4.10; N, 9.22; O, 24.87.

2.2 Polymerization of 4-vinylpyridine

Into a flask equipped with a magnetic stirrer, a septum and a three-way stopcock adapter was added CuCl (3.0 mg, 0.03 mmol). The flask was degassed and purged with argon. Me₆TREN (69.1 mg, 0.3 mmol) and 4-vinylpyridine (0.65 mL, 6 mmol) were added to the flask via syringe. The flask was frozen and degassed and then purged three times with argon. The flask was heated at 40°C under argon. A solution of Cl-G1-4COOH (26.4 mg, 0.03 mmol) in methanol (0.5 mL) was added to the flask via syringe to initialize the polymerization of 4-vinylpyridine. After 24h, the reaction mixture was poured into ether to precipitate the product. The precipitate was collected by filtration, washed with ether and dried in vacuo at 40°C. The conversion of 17 % was determined by the recovery weight. IR (KBr, cm⁻¹) ν 1689, 1599, 1556, 1452, 1415. ¹H NMR (DMSO-*d*₆) δ 10.18 (brs), 8.24 (s), 7.76 (s), 6.58 (s), 2.35 (m), 1.81 (m), 1.53(s). The selected sample (No. 8 in Table 1) was purified by passing it through an alumina column to remove the residual copper catalyst for the characterization of the structure and properties.

Poly(4-vinylpyridine) was also prepared by ATRP initiated by 1-phenylethylchloride in the presence of CuCl

and Me₆TREN. Mn 80,200 (polystyrene standards).

3 RESULTS and DISCUSSION

The dendritic initiator, Cl-G1-4COOH, was prepared from 3,5-dinitrobenzylalcohol as the starting compound, as shown in Scheme 1. All of the intermediate compounds, TBDMS-G0-2NO₂, TBDMS-G0-2NH₂, TBDMS-G1-4NO₂, TBDMS-G1-4NH₂ and HO-G1-4COOH, were characterized by spectroscopic measurements. In the ¹H NMR spectra of Cl-G1-4COOH, the peak at 5.25 ppm attributed to the hydroxyl group of HO-G1-4COOH disappeared and the peak attributed to the methylene protons shifted toward a lower magnetic field from 4.48 to 4.74 ppm after the chlorination of HO-G1-4COOH. A broad peak at 12.10 ppm attributed to the carboxyl groups was also observed in the spectrum of Cl-G1-4COOH. The ¹³C NMR, IR and MALDI-TOF MS measurements of Cl-G1-4COOH also supported the formation of the proposed structure. Cl-G1-4COOH can act as a dendritic initiator for the atom transfer radical polymerization (ATRP) of vinyl monomers. Since the benzyl chloride group is located at the focal point, the resulting polymers by ATRP initiated by Cl-G1-4COOH should be tadpole-shaped dendritic-linear copolymers.

The living/controlled radical polymerization of 4-vinylpyridine initiated by Cl-G1-4COOH in the presence of Me₆TREN and CuCl was carried out, as shown in scheme 2. Since Cl-G1-4COOH was insoluble in 2-propanol, which was reported as a suitable solvent for the ATRP of 4-vinylpyridine, DMF, DMSO and methanol were examined as the solvent in this study. Overall, the conversion determined by the recovery weight was low even if the various reaction conditions, such as temperature, reaction period, solvents, concentration, and the ratio of the initiator to monomer, were examined. The low conversion is presumably due to the significant coordination of the monomer or polymer to the copper catalyst and/or the formation of salts with the carboxyl groups on Cl-G1-4COOH and Me₆TREN. The copolymer prepared in methanol has the molecular weight of 4700 which is close to the value (4455) calculated on the basis of the monomer/initiator ratio. In the ¹H NMR spectra of the copolymer measured in DMSO, the peaks attributed to pyridine, aromatic, methylene, methine and amide protons were observed. The peak attributed to the benzyl methylene protons at 4.7 ppm disappeared in the spectrum for the copolymer.

The resulting copolymers showed a single glass transition temperature (T_g) based on the DSC measurements, which implies that each component of the copolymer is miscible with each other. The T_g of the copolymer decreased with the molecular weight increasing. As the molecular weight of the copolymer increases, poly(4-vinylpyridine) becomes dominant in composition of the copolymer. Therefore, the T_g of the copolymer decreases with the molecular weight increasing and probably approaches the T_g of the poly(4-vinylpyridine) homopolymer (133°C).

The hydrodynamic radius of the copolymer in methanol, chloroform and DMF was measured by dynamic light scattering and particle size analyzer. The radius in methanol was quite large (29.9 μm), medium in chloroform (165 nm)

and relatively small in DMF (51 nm). Both the solubility of each component of the copolymer and the multiple hydrogen bonding between carboxyl and pyridine groups should influence the hydrodynamic radius. Generally, a strong hydrogen bonding is formed in non-polar solvents and the hydrogen bond becomes weak or dissociates in aprotic polar solvents, such as DMF. Since both components are soluble in methanol, intermolecular multiple hydrogen bonding could be formed between the carboxyl groups on the periphery of the initiator and vinylpyridine segments. The intermolecular multiple hydrogen bonding contributes to the formation of large aggregates or microgels. The medium radius in chloroform suggests the formation of small aggregates. We assume that the solubility of the dendron component significantly influences the formation of the small aggregates, as will be discussed in the following section. DMF is a good solvent for both of the components. Due to its high polarity, the effect of multiple hydrogen bonding might be negligible in DMF. Therefore, the hydrodynamic radius of the copolymer in DMF is the smallest in these solvents.

¹H NMR measurements at room temperature provide information about the solubility of each component of the copolymer in solvents. The peaks attributed to pyridine, aromatic and amide protons were observed in the spectrum measured in DMSO. The aromatic and amide protons were not detected by the measurement in chloroform. The spectrum in chloroform suggests that the polyamide dendron that originated from the initiator is insoluble in chloroform. Since insoluble particles were not observed, the dendron moiety could be surrounded and solubilized by the vinylpyridine segments in chloroform. In the spectrum measured in methanol, the aromatic protons were observed as weak and broad peaks while the amide protons were not detected. These weak and broad peaks imply the presence of a solute-solute interaction of P4VP-G1-4COOH which is presumably caused by the multiple hydrogen bonding.

According to the hydrodynamic radii and NMR data, we propose the structure of P4VP-G1-4COOH in solution (Figure 7). Since both components are soluble, large aggregates or microgels are formed in methanol through the

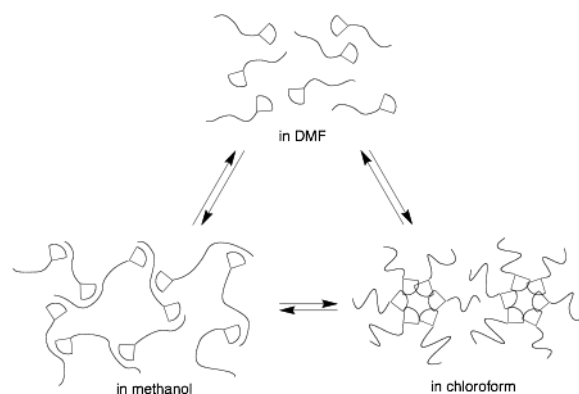


Figure 1. Proposed structural model for the dendritic polyamide-b-poly(4-vinylpyridine) copolymer in solution.

multiple hydrogen bondings between the carboxyl groups located on the periphery of the dendron and vinylpyridine segments. Micellar-type aggregates are formed in chloroform because the dendron is insoluble in chloroform. Since both components are soluble and the hydrogen bonding is negligible, the copolymer is dissolved in DMF without a strong solute-solute interaction.

4 CONCLUSIONS

A dendritic polyamide having carboxyl groups on the periphery initiated the atom transfer radical polymerization of 4-vinylpyridine to form tadpole-shaped dendritic-linear copolymers. The dendritic-linear copolymers have both donor and acceptor functions for multiple hydrogen bonding. The solubility, thermal and solution properties of the copolymers are influenced by the multiple hydrogen bonding. The solubility of the each component is also an important issue to explain the association form of the copolymer in solution. The structural model for the molecular interaction of the copolymer in the selected solvents was proposed on the basis of the hydrodynamic radii and NMR measurements.

5 REFERENCES

- [1] Jikei M, Kakimoto M 2001 *Prog. Polym. Sci.* **26** 1233
- [2] Fréchet J M J 2003 *J. Polym. Sci.: Part A: Polym. Chem.* **41** 3713
- [3] Tomalia D A 2005 *Prog. Polym. Sci.* **30** 294
- [4] Liang C, Fréchet J M J 2005 *Prog. Polym. Sci.* **30** 385
- [5] Jiang D-L, Aida T 2005 *Prog. Polym. Sci.* **30** 403
- [6] Crespo L, Sanclimens G, Pons M, Giralt E, Royo M, Albericio F 2005 *Chem. Rev.* **105** 1663
- [7] Gitsov I, Wooley K L, Fréchet J M J 1992 *Angew. Chem. Int. Ed. Engl.* **31** 1200
- [8] Gitsov I, Wooley K L, Hawker C J, Ivanova P T, Fréchet J M J 1993 *Macromolecules* **26** 5621
- [9] Gitsov I, Fréchet J M J 1996 *J. Am. Chem. Soc.* **118** 3785
- [10] Chapman T M, Hillyer G L, Mahan E J, Shaffer K A 1994 *J. Am. Chem. Soc.* **116** 11195
- [11] van Hest J C M, Delnoye D A P, Baars M W P L, van Genderen M H P, Meijer E W 1995 *Science* **268** 1592
- [12] van Hest J C M, Baars M W P L, Elissen-Román C, van Genderen M H P, Meijer E W 1995 *Macromolecules* **28** 6689
- [13] Aoi K, Motoda A, Ohno M, Tsutsumiuchi K, Okada M, Imae T 1999 *Polym. J.* **31** 1071
- [14] Zhang A, Shu L, Bo Zhishan Schülter A D 2003 *Macromol. Chem. Phys.* **204** 328
- [15] Leduc M R, Hawker C J, Da J, Fréchet J M J 1996 *J. Am. Chem. Soc.* **118** 11111
- [16] Kato T, Fréchet J M J 1989 *Macromolecules* **22** 3818
- [17] Sijbesma R P, Beijer F H, Brunsveld L, Folmer B J B, Hirschberg J H K K, Lange R F M, Lowe J K L, Meijer E W 1997 *Science* **278** 1601
- [18] Kouketsu T, Yokomachi K, Kakimoto M, Jikei M 2004 *High Perform. Polym.* **16** 611
- [19] Jikei M, Kouketsu T, Kakimoto M, Yamane Y, Ando I 2006 *High Perform. Polym.* **18** 421
- [20] Kouketsu T, Jikei M, Hayakawa T, Kakimoto M 2004 *J. Photopolym. Sci.* **17** 283
- [21] Jikei M, Itoh H, Kouketsu T, Hayakawa T, Kakimoto M 2006 *High Perform. Polym.* **18** 453
- [22] Xia J, Zhang X, Matyjaszewski K 1999 *Macromolecules* **32** 3531
- [23] Matyjaszewski K, Patten T E, Xia J 1997 *J. Am. Chem. Soc.* **119** 674

Developing a Recycling System by taking Advantage of using the RFID Technology

By Toyohisa Fujita, Nobuya Nakamura, Seiji Matsuo and Gjergj Dodbiba

The University of Tokyo, Graduate School of Eng. Dept. of Systems Innovation
113-8656 Tokyo, Japan
tfujita@sys.t.u-tokyo.ac.jp

Abstract: RFID (Radio Frequency Identification, IC tag) technology has been put to practical use in many areas. It is expected that RFID will also be used in designing or developing new recycling systems or in managing waste materials. It is also suggested that the technology using IC tags, which are able to store a relatively great amount of data related to the specification of the materials, can be used in various recovery or separation processes and be used at the surface contamination condition. Such a process can be effective since it not dependent of the physical properties of the materials to be processed. At first, the use of a microwave type IC tag, mounted on artificial parts to be separation, was investigated as a function of the speed and distance from the IC tag data reader. Next, if IC tags are utilized for the parts reuse and store of automobiles in order to increase the material recycling rate. Moreover, the environmental burden for automobile recycling has also been discussed.

Keywords: RFID, IC tag, Recycling, Reuse, Automobile

1 INTRODUCTION

There are some discrimination marks or methods such as bar codes, QR (quick response) codes, and IC tags. A bar code was developed in USA in middle of 20th century and was widely used because it is cheap. The information stored is however small and it is easy to misread due to the surface contamination. A QC code can store more information than a bar code because of the 2 dimensional codes; however, the data are not easily read if the surface is contaminated. A RFID system is composed of an IC tag (IC tip and an antenna) and a reader. There are two types of IC tags of an active type to oscillate and a passive type of no backup power source. An IC tag has no problem for the surface contamination and a IC tag reader can read large amount of information of several IC tags at once from the apart distance place. In these days RFID has been used in many areas, for example, production and transportation, library and finance systems. There are 3 types of IC tags for radio frequencies that are shortwave (13.56MHz), UHF (860 to 960 MHz) and microwave (2.45 GHz).

In this report, the use of a microwave type IC tag, mounted on artificial parts to be separation, was investigated as a function of the speed and distance from the IC tag data reader. A microwave type tag has also several benefits since it can be recognize the information of tag in water and at the several mm apart above metal surface. Next, if IC tags are utilized for the parts reuse and store of automobiles and the material recycling rate is increased, the environmental burden for automobile recycling has been discussed.

2 TRIAL OF A IC TAG UTILIZATION FOR PARTS SEPARATION

2.1 Concept of RFID system for reuse and recycle

In the future it would be effective to use RFID for a separation technology. If IC tags are attached on parts of electric appliances and machines and the parts are easily decomposed, the parts can be separated by the mechanical sorter after reading the record of IC tag in separation box when they are discarded. The concept is shown in Figure 1.

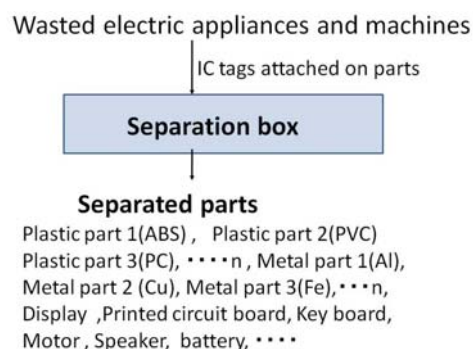


Figure 1. The concept of IC tag utilization for sorting the parts of the wasted electric appliances and machines.

On the other hand, if IC tags become smaller in size, i.e. less than mm, including antenna, as well as cheaper, IC tags might be fixed on many parts and also buried inside plastic materials. At present, the parts separation depends on the difference of physical property of shape, size, color, density and so on. However, this process cannot sort parts that have no

difference of physical property. If they are crushed and go to the material recycling process, the separation needs additional physical properties like magnetization, electric conductivity and surface property. To advance such separation processes, the RFID technology could be used. The scenario for using RFID for the separation is described in as follows. First, in the production process of goods, each parts would be attached the IC tag. In the IC tag, the ID number of each tag is written. And database servers that IC tag's ID and the name of material constructing the parts that the tag was attached are recorded would be installed.

In order to recycle the goods, they are separated or broken down to each part. In addition, the IC tag attached on the part is read to get the ID number of the IC tag in order to sort the goods by the construction material. To send the ID number to the database server, the name of material constructing parts could be gotten at once. The concept of separation apparatus is shown in Figure 2. In the separation, the air is blowing or a mechanical movement is utilized.

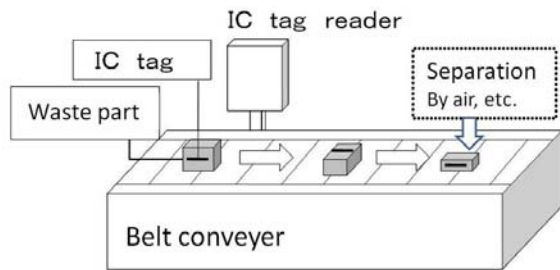


Figure 2 The concept of the separation apparatus using IC tag.

2.2 Experiment of IC tag reading

The used IC tag with antenna, the 3 kinds of direction of antenna of IC tag on reader and the experimental apparatus to recognize the IC tag content is shown in figure 3. The used RFID system is □-tip made in Hitachi Ltd. ¹⁾. The size is 0.4x0.4mm and uses the frequency of 2.45GHz. IC tag is set in the center of an antenna that is about 60mm length. It has a 128-bit ROM for storing the ID with no write-read and no anti-collision capabilities.

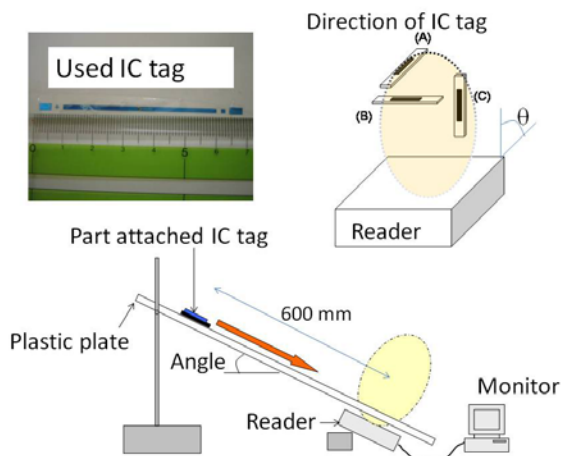


Figure 3 IC tag with antenna, three direction of IC tag and reader and experimental apparatus to recognize the IC tag

content.

The IC tag with antenna is fixed on the imitated part that is 50mm x 50mm (surface) x 3mm (thickness) plastic plate. The 3 kinds of direction of IC tag with antenna above reader is examined the reading percentage of IC tag content.

Table 1 shows the effect on passing speed of IC tag within the area covered by the reader. The passing speed until 3.5m/s of IC tag above the reader can be read 100% of IC tag content in A and B direction of figure 3. Table 2 shows the effect on direction of IC tag with antenna above the reader. When the C direction is perpendicular to the direction between IC tag with antenna and reader is used (Figure 3), the reading percentage of IC tag decreased to 80 to 90%. Table 3 shows the effect on the limit angle θ in Figure 3 between IC tag with antenna and reader and the distance between IC tag and reader to read 100%. The effect of angle between IC tag with antenna and reader is important.

The effect of length of antenna and reading distance is shown in Figure 4. More than 50 mm length antenna can be read 100% at distance of 600mm between IC tag and reader. The small antenna is convenient to attach the parts for reuse and recycling, however, 30mm length antenna is necessary at 150mm of short distance from the reader. This result is shown in the A and B direction case in Figure 3 and it also includes the same effect of direction of antenna

To reduce reading percentage in the direction between antenna and reader, the antenna is attached at the corner of box as shown in Figure 5. As the antenna has two dimensions direction, the reading percentage of IC tag is improved to 98% from 80-90 % in C direction (Figure 3), which condition are given in Table 2. As comparing the multiple readers that is two or three reader utilization, this method could be reduce the RFID system cost.

Table 1 Effect on passing speed of IC tag in the area of reader

Angle of plate inclination (degree)	22	28	55
Average passing speed of IC tag (m/s)	1.1	1.6	3.5
Reading percentage of IC tag (%)	100	100	100

Direction of IC tag with antenna on reader in Figure 3 is A and B. (Antenna of IC tag is parallel to reader.)

Table 2 Effect on direction of IC tag with antenna above the reader

Direction of IC tag with antenna above reader in Figure 3	A, B	C
Average passing speed of IC tag (m/s)	1.6	1.6
Reading percentage of IC tag (%)	100	80 - 90

Table 3 Effect on the limit angle θ in figure 3 between IC tag with antenna and reader and the distance between IC tag and reader to read 100%.

Angle θ between IC tag with antenna and reader (degree)	65	45	20
Distance between IC tag with antenna and reader (mm)	300	500	600

Passing speed of IC tag: 1.6m/s

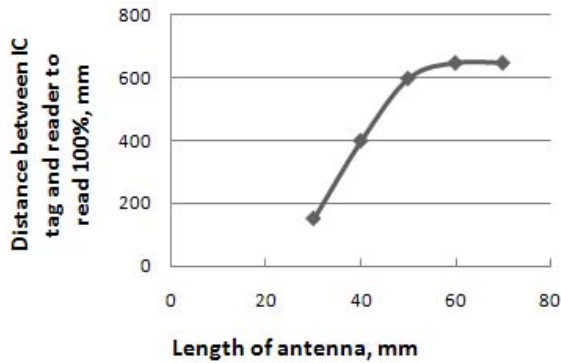


Figure 4 Effect of length of antenna and distance to read 100%. (Direction of IC tag with antenna on reader in figure 3 is A and B.)

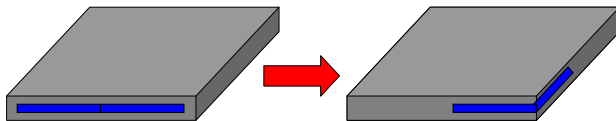


Figure 5 The improved attachment method of antenna to read in any direction between antenna and reader.

Table 4. Product Information Requirements and Availability for Reuse²⁾

Product info.	Product info. requirement	Ready availability of product info		Network RFID info.
		OEM	Third party	
static	Type	○	○	○
	Model	○	○	○
	BOM	○	×	○
	Reliability	○	×	○
	Dismantle Instructions	○	×	○
dynamic	Current BOM ⁽¹⁾	×	×	○
	Maintain History	×	×	○
	Parts replace history	×	×	○
	Usage-life	×	×	○
	Physical condition	×	×	×
	Functional condition	×	×	×

(1): BOM...Bill of Material

3 THE EFFECT OF RFID TECHNOLOGY FOR REUSE OF USED CARS

3.1 Concept of RFID system for reuse of used products

The scenario is to use the RFID technology for information management that is necessary for reuse of used products. Kulkarni et al. 2005 described the application of a networked RFID system for product recovery and management of laptops²⁾. In the process of the product recovery management, much product information like type of the product is required. The product recovery is owned by both Original Equipment Manufacturers (OEM) and third-parties. They both need much information as shown in Table 4. It shows a list of product information requirements for the product recovery decision. With using networked RFID, the information that is available enlarges. As above, complex managements of information are required to reuse or recovery products. If such process that is necessary to reuse or recovery take less time, the products that is reused or recovered would increase.

Then, what product is effective to bring in the RFID technology? It is like to be effective to use the RFID technology to manage used cars. Parts of used cars are comparatively reused at high rates. And the process to reuse cars is already developed. A car consists of many kinds of parts. Therefore, the management of information for reuse is quite complicated. The RFID technology is already used for stock managements and manufacturing managements. It has been proven that IC tag is effective and can be used for the management of reuse and recovery of used cars.

The reuse of parts is only possible during the period of production as shown in Figure 6. If the production stops, the parts have to go to material recycling.

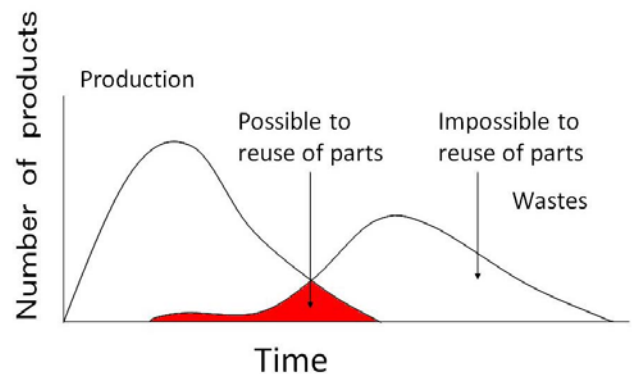


Figure 6 Relationship between production period and production number.

3.2 Reuse of automobile parts and environmental effects

Nowadays, some parts of used cars are well utilized. Photo 1 shows the storage of dismantled some parts like engine (a) and some car body parts like door (b). If the IC tag is fixed in each part and RFID system is carried out, the reuse of parts would be more effective and increase. In the near future the battery reuse will also increase as the utilization of hybrid and EV cars.

Funazaki et al. 2000 discussed the life cycle assessment and the details are shown in Tables 5 to 7^{3,4)}. Table 5 indicates the material composition of parts in an automobile. Here the automobile is divided into 4 parts. The energy and CO₂ emission to produce materials used in an automobile is shown

in Table 6. The weight of a used car is 1190kg. Table 7 shows the energy and the CO₂ emission during the production and the dismantling of the same automobile. The production energy and emission are much larger than the energy consumed during dismantling, transportation and landfill.

Next, the material recycle and parts reuse in an automobile life cycle are discussed the effects on the increase rate of parts reuse by IC tag utilization. The model of life cycle flow of car is shown in Figure 7. In the reuse priority model, the reuse rates are 80% for engine, 50% for suspension, brake etc. and 20% for interior and exterior body, respectively. The remainder goes to material recycling process using crushing. The automobile assumes to be reused and recycled after 10 years utilization. The parts recycling system and the parts reuse priority system using IC tag are compared with the CO₂ emission rate in the landfill rate. The results are indicated in Figure 8. Landfill rate 1 means no reuse and no recycle was carried out. Landfill rate 0 means that all materials go for reusing or to recycling process at the above rate. The reuse priority is more effective to reduce CO₂ emission than the recycle priority at low landfill rate.



(a) (b)

Photo 1. The storage of machine parts (a) and body parts (b) dismantled automobiles for reuse.

Table 5 Material composition of parts in an automobile ³⁾

	Iron (kg)	Non ferrous metals (kg)	Resin (kg)	Others (kg)
Engine parts	77.2	51.6	5.6	3.2
Suspension, brake etc.	208.5	20.7	1.7	3.0
Interior and exterior body	66.7	2.2	57.1	79.6
Body parts	384.1	4.0	0	8.4
Total	736.5	78.5	64.4	94.2

An automobile weight of 1190kg is utilized.

Table 6 Energy and CO₂ emission to produce materials used in an automobile ⁴⁾

	Energy for material production (GJ/kg)	CO ₂ emission (kg/kg)
Iron	0.035	2.77
Non ferrous metals	0.034	2.31
Resin	0.033	2.26
Others	0.025	1.97

An automobile weight of 1190kg is utilized.

Table7 Energy and CO₂ emission to produce and dismantle an automobile ⁴⁾

	Energy (GJ/kg)	CO ₂ emission (kg/kg)
Production	0.066	4.7
Crushing and separation	0.00073	0.031
Go to landfill	0.00036	0.016
Transportation after dismantle	0.00046	0.032

An automobile weight of 1190kg is utilized.

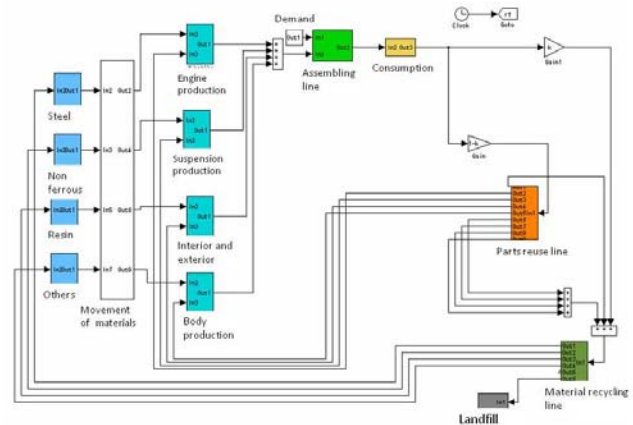


Figure 7 Model of life cycle flow of the automobile

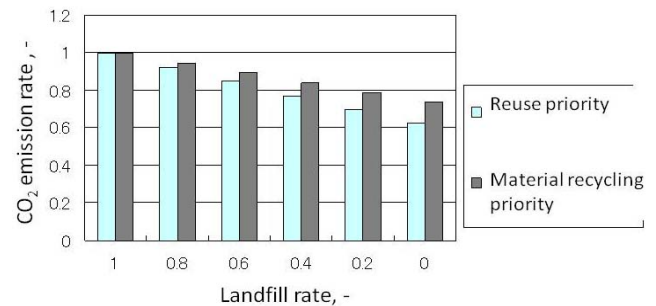


Figure 8 Comparison of CO₂ emissions to parts recycling and parts reuse priority system in the landfill rate.

4 Conclusions

A novel concept for sorting the parts of the wasted electric appliances and machines by using IC tags was introduced. The characteristics of IC tag (μ -tip) in RFID system were investigated. As the antenna has two dimensions direction, the reading percentage of IC tag is improved to 98% from 80-90 %. As comparing the multiple readers that is two or three reader utilization, this method could be reduce the RFID system cost. Based on the results presented in the paper, a design for the separation apparatus was put forward.

The IC tag is effective to increase the parts reuse rate of used automobiles. The reuse of parts is more effective alternative for reducing the CO₂ emission when compared with the recycling alternative, regardless the land filling rate.

References

[1] <http://www.hitachi.co.jp/Prod/mu-chip/jp/>, (2009)

- [2] Kulkarni, A.G., Parlikad, A. K. N. , McFarlane D. C. and Harrison, M. , "Networked RFID Systems in Product Recovery Management" Electronics and the Environment, 2005. Proceedings of the 2005 IEEE International Symposium, pp.66-71,(2005)
- [3] Funazaki, A., Taneda, K., "Life cycle assessment of an end-of life passenger car in 2002", JARI Research Journal, Vol.22, No.12, pp.606-609,(2000)
- [4] Funazaki, A., Taneda, K., "Life cycle assessment of end-of-life vehicles", Jidosha-gijyutu, Vol.56, No.7, pp.57-63,(2002)

Nanomechanics Characterization of Diamond-Like Carbon with Different Substrate Temperature by MPCVD

Kuen Ting*, Hui-Ching Wang**, Jung-Sheng Chen**, Ching-Hsin Chang**

*Graduate School of Engineering Technology, Lunghwa University of Science and Technology, Taoyuan, Taiwan

**Department of Applied Mathematics, National Chung Hsing University, Taichung, Taiwan

kuenting@mail.lhu.edu.tw

Abstract: Structural and nanomechanical properties of diamond-like carbon (DLC) thin films by microwave plasma chemical vapor deposition (MPCVD) with different substrate temperature are studied in this paper. Microstructure, surface morphology, hardness and Young's modulus of DLC thin films were characterized by Raman spectroscopy, scanning electron microscopy (SEM), atomic force microscopy (AFM) with nanoindenter, respectively. The ratio of the D-peak to G-peak (I_D/I_G) is found to remain approximate constant with the substrate temperature. The results demonstrate that substrate temperatures are not affected significantly by the intensity ratio of sp^2 and sp^3 . In addition, the surface roughness abruptly increases near the substrate temperature 600°C. The results also indicate that both Young's modulus and hardness increased as the substrate temperature increasing from 200°C to 500°C. When substrate temperature was 600°C, both values of Young's modulus and hardness drop to the values between 300 °C to 400°C. The results demonstrate that the nanomechanical properties of DLC thin films are significantly affected by different substrate temperature.

Keywords: MPCVD, Diamond-like carbon (DLC), Raman spectroscopy, Nanoindentation

1 INTRODUCTION

Diamond-like carbon (DLC) films have attracted extensive attention due to their high hardness, wear resistance, chemical inertness, and low friction coefficients, etc.[1,2]. In addition, DLC thin films possess excellent and stable field electron emission properties [3].

The DLC thin films have a variation of properties in between those of graphite and diamond [4]. The properties of DLC thin films vary with the concentration of sp^2 and sp^3 carbon in the films [5]. When DLC thin films have a high concentration of sp^3 carbon, it has been shown that the properties approach diamond [6].

MPCVD (Microwave Plasma Chemical Vapor Deposition) was successfully developed by methane-rich CH_4/H_2 mixtures with Ar or N_2 to prepare DLC films. The substrate temperature is the important parameter to the growth of DLC films. Kulisch et.al studied the influences of substrate temperature to the properties of DLC films in the range from 520 to 770 °C [7]. However the studies on the variations at the low substrate temperatures are limited. Thus, the aim of this paper is to study the nanomechanical properties of DLC films below 600°C substrate temperature.

Nanoindentation is an excellent method for measuring nanomechanical properties of both bulk and thin films. Zhang and Huan [8] have systematically investigated properties of the DLC coating on the different steel substrates by nanoindentation and nanoscratch tests. Fang and Chang [9] offered the result about nanomechanical characterization of DLC thin films deposited on a silicon substrate under various mixtures of methane-hydrogen gas by ECR-MPCVD using nanoindentation technique.

The main purpose of this study is to characterize microstructure, surface morphology, hardness and Young's modulus of DLC thin films fabricated by MPCVD with different substrate temperatures. In these investigations, Micro Raman spectroscopy, scanning electron microscopy, atomic force microscopy with nanoindenter to measure structural characteristics, surface roughness, hardness and Young's modulus.

2 EXPERIMENTAL DETAILS

Diamond-like carbon thin films were deposited onto 10mm square n-type silicon substrate (100) by MPCVD with the various substrate temperatures. The films were produced in a MUEGGE μ -Slan32 MPCVD system with reactant gases of hydrogen, methane and argon. For pretreatment process, the silicon substrates were scratched with a diamond powder of 1 μ m grain size in ethylate by ultrasonic cleaning machine. The time of all substrates scratched was 20min. The plasma for the films deposition was excited by microwaves at 2.45GHz. Before deposition, the chamber was pumped down below 10^{-5} torr using both a rotary pump and a turbo pump. A mixture of 4% H_2 and 1% CH_4 in Ar was used at a pressure of 10 torr, with a microwave power of 800W. Substrate temperature varied between 200°C and 600°C. The substrate temperature was determined by means of a thermo-couple located within the holder below its upper surface. The whole deposition process was performed for 3hrs. The parameters of the growth of DLC thin films are listed in Table 1.

Raman spectroscopy (MOF-iHR550, Jobin Yvon) was used to investigate structural characteristics of DLC thin films. The Raman spectra were detected at room temperature with blue light laser and $\lambda=488nm$ for excitation. Raman spectroscopy is a very effective way to study the detailed bonding structure of carbon films, largely because it can distinguish between the different allotropes of carbon [10].

Surface morphology namely topography and roughness was studied using PSIA XE-100 atomic force microscopy under ambient conditions. The average roughness of DLC thin films, R_a , was measured in contact mode.

Hardness and Young's modulus of DLC thin films were investigated using scanning probe microscopy in combination with depth sensing nanoindentation. The experimental equipment consists of a HYSITRON Triboscope attached to a PSIA XE-100 scanning probe microscope. The probe type is a Berkovich indenter.

DLC thin films were subjected to a depth-sensing nanoindentation, which is a reliable method for measuring the nanomechanical properties of thin films. [11,12]. By typical

continuous load-displacement curves during between loading and unloading are obtained from a Berkovich indenter, we can obtain the value of hardness and Young's modulus [13]. The hardness, H , is determined from maximum indentation load P_{\max} divided by the contact area A_c [14] :

$$H = \frac{P_{\max}}{A_c} \quad (1)$$

the contact area A_c is determined from shape function of probe. The contact area and the contact depth h_c relationship of the Berkovich indenter is

$$A_c = 24.5h_c^2 \quad (2)$$

then, the reduced modulus, E_r ,

$$E_r = \sqrt{\frac{\pi}{A_c}} \frac{S}{2\beta} \quad (3)$$

where S is the measured stiffness and β is a shape constant of 1.034 for the Berkovich indenter. The relationship of reduced modulus and Young's modulus is

$$\frac{1}{E_r} = \frac{1-\nu_f^2}{E_f} + \frac{1-\nu_i^2}{E_i} \quad (4)$$

where ν_f and E_f represent Poisson's ration and Young's modulus of test material, respectively ; ν_i and E_i represent Poisson's ration and Young's modulus of indenter, respectively. For diamond probe, $\nu_i=0.07$ and $E_i=1140\text{GPa}$ and $\nu_f=0.3$ for the DLC thin films [12]. The peak loads ranged from $1000\mu\text{N}$ to $5000\mu\text{N}$ at room temperature. Hardness and Young's modulus were obtained from the average load-displacement curves of six different tests.

3. RESULTS AND DISCUSSION

Figure 1 shows Raman spectra of five kinds of DLC thin films grown with different substrate temperature. The main two peaks of the curve correspond to the peaks for sp^3 (D-peak) and sp^2 (G-peak), the range represent $1250\text{-}1400\text{cm}^{-1}$ and $1500\text{-}1630\text{cm}^{-1}$, respectively [15]. In Figure 1, the D-peak was toward low Raman shift as the substrate temperature increased. The phenomena show that there exist the residual stresses in the DLC thin films during the growth process [16]. I_D and I_G represent the Raman intensity of D-peak and G-peak, respectively. The ratio of I_D/I_G provides the important information for the structure and chemical bonding of DLC thin films. Figure 2 displayed the ration of I_D/I_G as the constant versus to the substrate temperature. The substrate temperature is not affected significantly by the intensity ratio of sp^2 and sp^3 .

The surface average roughness R_a for 200°C , 300°C , 400°C , 500°C and 600°C are corresponding to the values of 0.22, 0.2, 0.24, 0.37, 5.93 as shown in Figure 3. The surface roughness is almost to be the constant between 200°C and 500°C . However, the roughness abruptly increases when the substrate temperature is 600°C . Figure 4 (a)-(e) demonstrate that surface topography for DLC thin films corresponding to the different substrate temperatures of 200°C , 300°C , 400°C , 500°C , 600°C .

The morphology of DLC thin films can be observed in the SEM as shown in Figure 5. The DLC film distributes uniformly on the substrate. The SEM image of cross-sectional surface of the deposited DLC thin films on silicon substrate is shown in Figure 6. From this micrograph, the coating can be viewed as successfully deposited continuously and uniformly on the substrate. The thickness of the thin film can be determined as $32.38\mu\text{m}$. The thickness of the DLC films is sufficient to conduct nanoindentation tests without the interferences of the substrate.

Young's modulus was measured by the nanoindentation technique at different applied loads and is shown in Figure 7. The values of Young's modulus are 49.76 to 62.45, 61.26 to 77.26, 80.4 to 96.12, 87.96 to 103.26 and 75.17 to 93.12 GPa corresponding to the temperatures of substrate temperatures 200 , 300 , 400 , 500 and 600°C . The hardness of the DLC films measured as a function of the load is plotted in Figure 8. Results indicate that the hardness ranged from 1.41 to 2.84, 2.24 to 3.46, 4.04 to 6.26, 5.23 to 8.31 and 2.53 to 5.27 GPa for the substrate temperatures of 200 , 300 , 400 , 500 and 600°C , respectively. It demonstrates that both Young's modulus and hardness increased with the applied load increased. Both Young's modulus and hardness increases with the substrate temperature between 200°C to 500°C . When substrate temperature increases to 600°C , both values of Young's modulus and hardness decreased to the values between 300°C to 400°C . The structure of the DLC thin films has a strong dependence on the substrate temperature. The more graphite phases may be produced in DLC thin films at higher substrate temperature[17]. Thus, the substrate temperature is near 600°C , both value of Young's modulus and hardness decreased due to more graphite produced. Young's modulus and hardness were obtained from the nanoindentation technique measured as a function of the contact depth is shown in Figure 9 and Figure 10. In the Figure 11 draws that the indent AFM image of DLC thin film at 400°C .

4. CONCLUSION

In this paper the characterizations of nanomechanics of DLC with different substrate temperature by MPCVD are investigated. The morphology, roughness, hardness and Young's modulus of DLC thin films are comprehensively studied. The surface roughness abruptly increases near the substrate temperature 600°C . The result indicates that both Young's modulus and hardness increased as the substrate temperature increase between 200°C to 500°C . When substrate temperature increases 600°C , both values of Young's modulus and hardness are reduced down to the values between 300°C to 400°C . This may be affected by the more graphite phase to be produced at higher temperature. Results confirm that the fabricated process on substrate temperature plays an important role in the nanomechanics of DLC thin film deposited on silicon substrate by MPCVD.

REFERENCES

- [1] G. Q. Yu, B.K. Tay, Z. Sun and L.K. Pan, "Properties of fluorinated amorphous diamond like carbon films by PECVD", *Applied Surface Science*, vol.219, pp.228-237, 2003.
- [2] X.W. Zhang, W.Y. Cheung, N.Ke and S.P. Wong," Optical properties of nitrogenated tetrahedral amorphous carbon films", *Journal of Applied Physics*, vol. 92, pp.1242-1247, 2002.
- [3] D.S. Mao, W. Li, X. Wang and X.H. Liu, "Diamond-like carbon films prepared by filtered arc deposition for electron field emission application", *Surface and Coatings Technology*, vol.137, pp.1-5, 2001.
- [4] R.E. Clausing, L.L. Horton, J.C. Angus and P. Koidl, *Diamond and diamond-like Films and Coatings*, vol.266, Plenum, New York, 1991.
- [5] T. Sharda, T. Soga, T. Jimbo and M. Umeno, "Biased enhanced growth of nanocrystalline diamond films by microwave plasma chemical vapor deposition" ,

Diamond and Related Materials, vol.9, pp.1331-1335, 2000.

- [6] R. Lossy, D.L. Pappas, R.A. Roy, J.P. Doyle and J. Bruley, "Properties of amorphous diamond films prepared by a filtered cathodic arc", *Journal of Applied Physics.*, vol.77, pp.4750-4756, 1995.
- [7] W. Kulisch, C. Popova, S. Boychevaa, M. Jelinekb, P.N. Gibsonc and V. Vorlicekb, "Influence of the substrate temperature on the properties of nanocrystalline diamond/amorphous carbon composite films", *Surface & Coatings Technology*, vol. 200, pp.4731 – 4736,2006.
- [8] T.H. Zhang and Y. Huan, "Nanoindentation and nanoscratch behaviors of DLC coatings on different steel substrates", *Composites Science and Technology*, vol.65, pp.1409-1413, 2005.
- [9] T.H. Fang and W.J. Chang, "Nanomechanical characterization of amorphous hydrogenated carbon thin films", *Applied Surface Science*, vol.252, pp.6243-6248, 2006.
- [10] P.K. Chu and L. Li, "Characterization of amorphous and nanocrystalline carbon films", *Materials Chemistry and Physics*, vol. 96, pp. 253-277, 2006.
- [11] S. R. Jian, T. H. Fang and D. S. Chuu, "Analysis of Physical Properties of III-Nitride Thin Films by Nanoindentation", *Journal of Electronic Materials*, vol.32, pp.496-500, 2003.
- [12] S. R. Jian, T. H. Fang and D. S. Chuu, "Nanoindentation investigation of amorphous hydrogenated carbon thin films deposited by ECR-MPCVD", *Journal of Non-Crystalline Solids*, vol.333, pp.291-295, 2004.
- [13] A. C. Fischer-Cripps, *Nanoindentation*, Springer-Verlag New York, 2004.
- [14] W.C. Oliver and G.M. Pharr, "An improved technique for determining hardness and elastic modulus using load and displacement sensing indentation experiments", *Journal of Material Research.*, vol.7, pp.1564-1583, 1992.
- [15] P. K. Chu and L. Li, "Characterization of amorphous and nanocrystalline carbon films", *Materials Chemistry and Physics*, vol.96, pp.253-277, 2006.
- [16] M. Vila, M. Amaral, F.J. Oliveira and R.F. Silva "Residual stress minimum in nanocrystalline diamond films", *Applied Physics Letters*, vol.89, 093109, 2006.
- [17] F. Liang and X.J. Yan, "Property, application and preparation of diamond-like film", *Chinese Physical Society*, vol.48, pp.1095-1102, 1999.

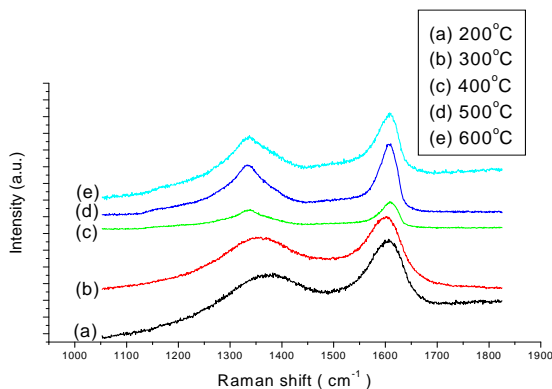


Figure 1 Raman spectra of five DLC thin films grown with different temperature.

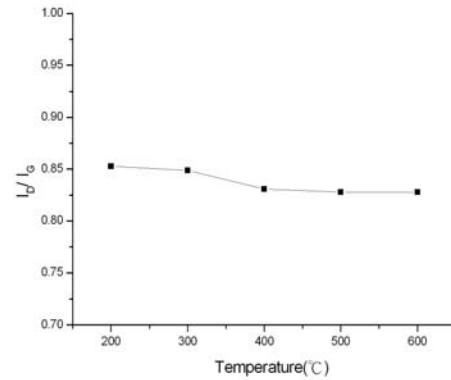


Figure 2 The relationship between I_D/I_G and temperatures

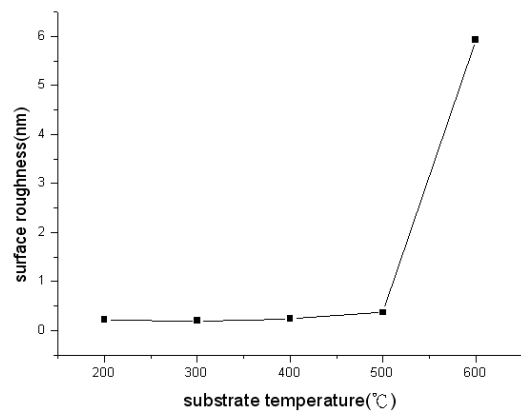
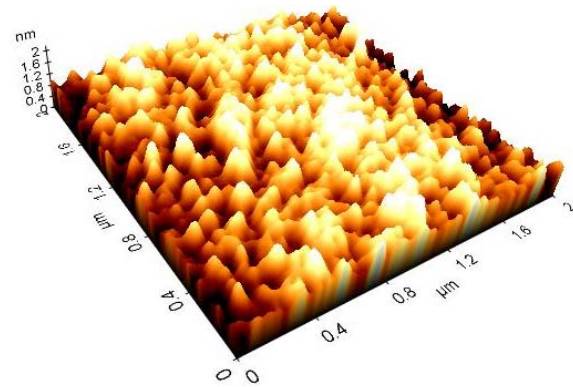
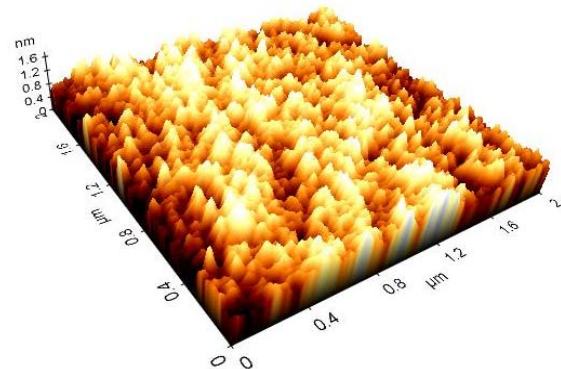


Figure 3 The relationship of surface roughness (R_a) and different substrate temperature.



(a) 200°C



(b) 300°C

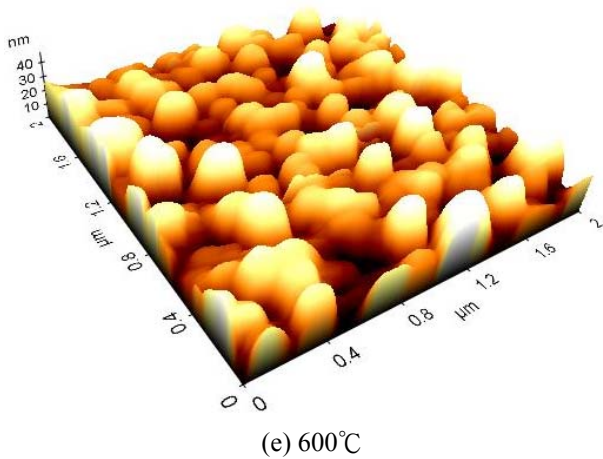
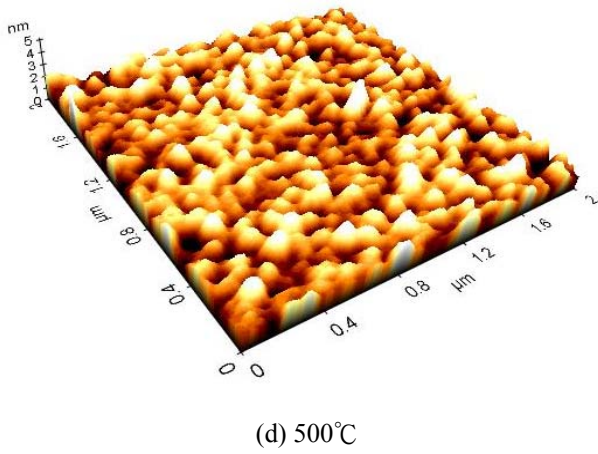
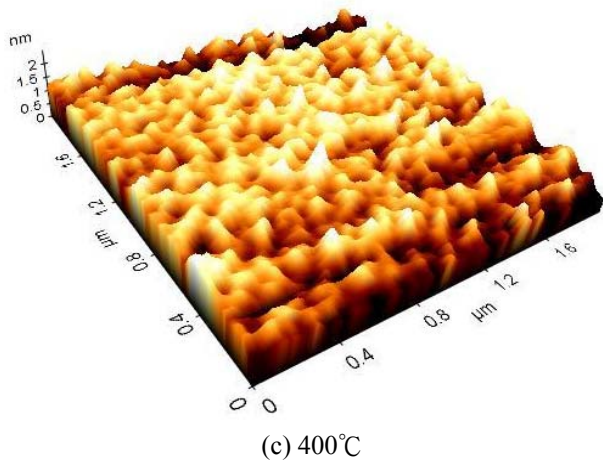


Figure 4 AFM images of DLC thin films with different substrate temperature : (a) 200°C , (b) 300°C , (c) 400°C , (d) 500°C , (e) 600°C .

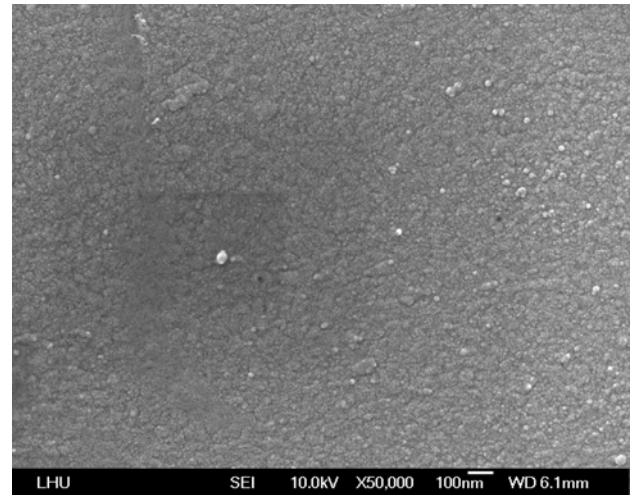


Figure 5 SEM micrograph of a DLC film deposited at 300°C .

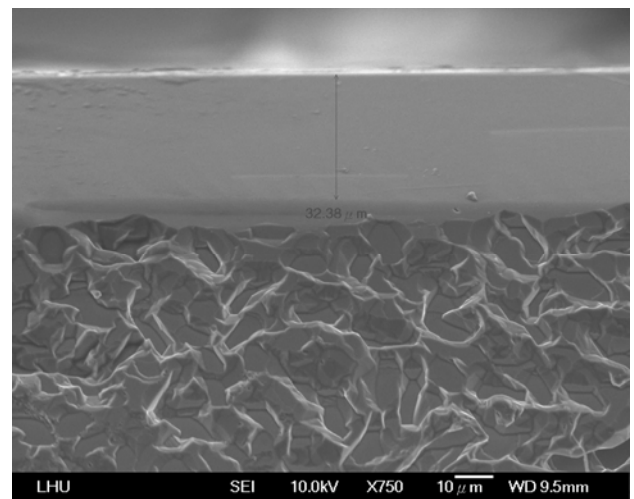


Figure 6 Cross-sectional image of a fracture surface showing the DLC film and the substrate.

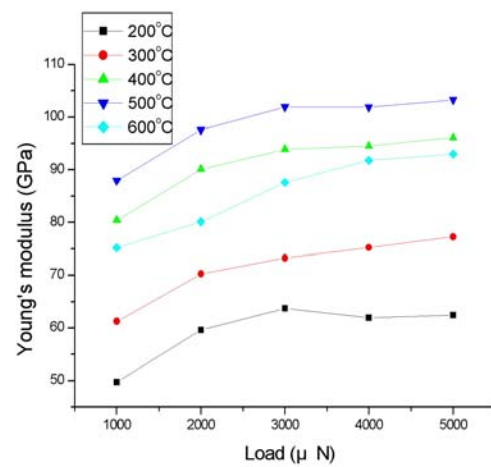


Figure 7 Young's modulus of DLC films measured as a function of the Load.

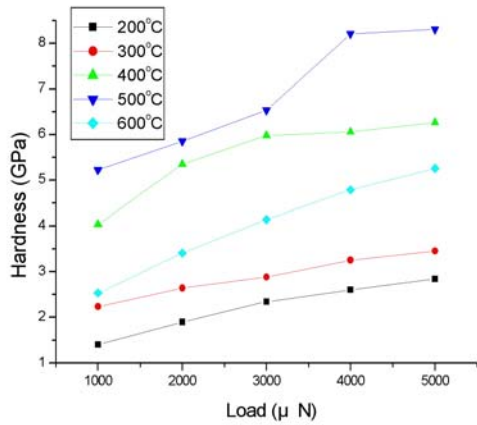


Figure 8 Hardness of DLC films measured as a function of the Load.

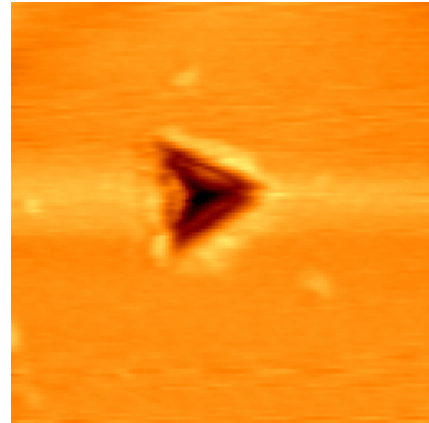


Figure 11 Indent AFM image of DLC thin film at 400°C.

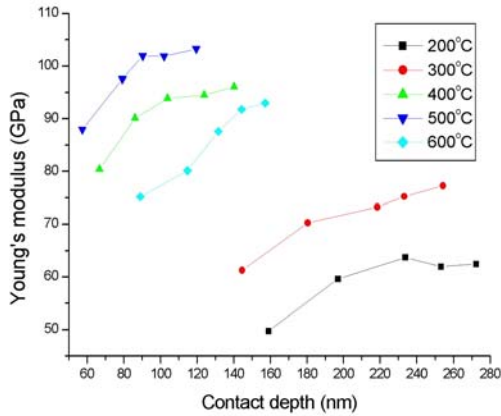


Figure 9 Young's modulus of DLC films measured as a function of the contact depth

Table1. Growth parameter of DLC thin films

Substrate	Silicon
Gas percentages	4% H ₂ 1% CH ₄ 95% Ar
Flow rate(sccm)	1000
Pressure(torr)	10
Substrate temperature(°C)	200;300;400;500;600
Microwave power(W)	800
Deposition time(hr)	3

Table2. Surface roughness of different substrate temperature

	200°C	300°C	400°C	500°C	600°C
Surface roughness Ra(nm)	0.22	0.2	0.24	0.37	5.93

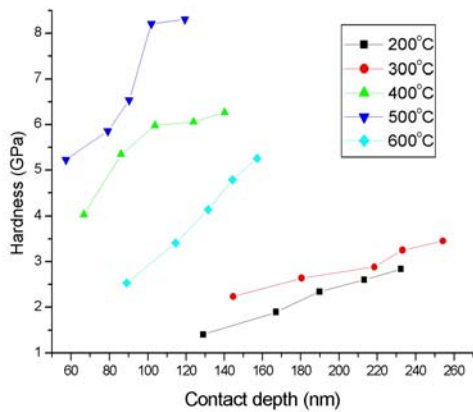


Figure 10 Hardness of DLC films measured as a function of the contact depth.

Characteristics of TiN thin films on mechanical details

Nguyen Thi Phuong Mai*

* Department of Precision Mechanical & Optical Engineering, Faculty of Mechanical Engineering, Hanoi University of Technology, 1 Dai Co Viet Road, Hanoi, Vietnam

maintp-mcx@mail.hut.edu.vn

Abstract: Microhardness and intrinsic stress are important technological parameters in depositing TiN thin film on mechanical details. In this study, the distribution of stress in measuring microhardness process is simulated by ANSYS. Thin TiN films, depositing by sputtering planar magnetron method by HUT, measured microhardness at high temperature, which simulated heat process used in high performance cutting operations; are in range 1600-1800HV at room temperature and reduced when temperature increased. The influence of Bias Voltage to Young module presented by calculating XRD patterns, which have good prediction with simulation results.

Key Words: TiN thin films, ANSYS, microhardness, Young module

1 INTRODUCTION

Titanium nitride (TiN) thin films are suitable in cutting, abrasive and erosive wear applications: cutting inserts, die and mold and other mechanical details. With this aim, ME in HUT designed and made a Planar Magnetron Sputtering (SPM) system. The SPM was put into a vacuum chamber of B.30 Vacuum equipment, Vacuum Dresden Co, as shown in Fig. 1.

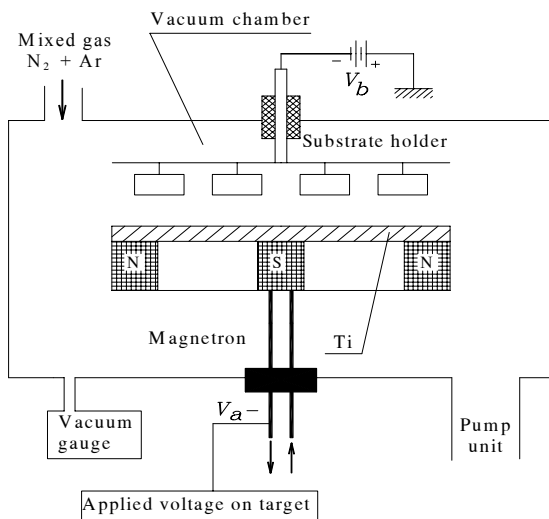


Figure 1: Schematic illustration of SPM system put in vacuum chamber

The PMS system was designed and made by Hanoi University of Technology (HUT) and Hochiminh National University (HNU) in Vietnam [1]. Substrates included both plates by 304 stainless steel and turned inserts. The optimal technical parameters were as follows: ratio by volume of the argon and nitrogen gas mixture was 8:1; current discharge 1.3 A; negative bias voltage – 100 V, applied voltage 1000 V.

The samples were analyzed by X-Ray Diffraction (XRD) using CuK α radiation - wavelength 1.5406 Å (Siemen D5000).

The microhardness was measured directly at high temperature (QM2, Nikon), both in air and in vacuum ($1.10^{-4} \div 5.10^{-5}$ Torr) over 90 min with a diamond indenter on the Vicker scale; a load 10 gf (0.098 N) for 30 sec was used, in the temperature from RT to 800°C.

Calculation stress

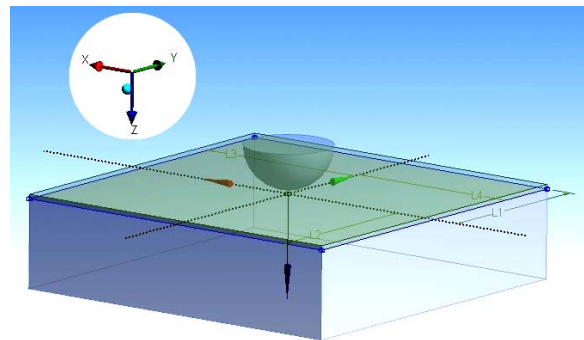


Figure 2. Deposited coating on a substrate

TiN thin films and mechanical details follows Hooke's law, the three-dimensional normal strains can be expressed by (1)

$$\begin{aligned} \varepsilon_x &= \frac{\sigma_x}{E} - \frac{\nu}{E} (\sigma_y + \sigma_z) \\ \varepsilon_y &= \frac{\sigma_y}{E} - \frac{\nu}{E} (\sigma_z + \sigma_x) \\ \varepsilon_z &= \frac{\sigma_z}{E} - \frac{\nu}{E} (\sigma_x + \sigma_y) \end{aligned} \quad (1)$$

Where $\varepsilon_x, \varepsilon_y, \varepsilon_z$ and $\sigma_x, \sigma_y, \sigma_z$ are normal strains and stresses in x, y and z direction, respectively. E is the Young's modulus, and ν is the Poisson ratio. Equation (1) can be rearranged for normal stresses σ_x, σ_y and σ_z yielding:

$$\begin{aligned}\sigma_x &= \frac{E}{(1+\nu)(1-2\nu)} [(1-\nu)\varepsilon_x + \nu(\varepsilon_y + \varepsilon_z)] \\ \sigma_y &= \frac{E}{(1+\nu)(1-2\nu)} [(1-\nu)\varepsilon_y + \nu(\varepsilon_x + \varepsilon_z)] \\ \sigma_z &= \frac{E}{(1+\nu)(1-2\nu)} [(1-\nu)\varepsilon_z + \nu(\varepsilon_y + \varepsilon_x)]\end{aligned}\quad (2)$$

The through-plane normal strain can be expressed by (Fig. 1)

$$\varepsilon_z = \varepsilon_z^z - \varepsilon_z^P \quad (3)$$

Where ε_z^z is the through-plane strain induced by through-plane stress, ε_z^P is the through-plane strain induced by in-plane stress. The strain ε_z is the strain that is measured when the film thickness changes due to thermal expansion. If there is no applied stress in any direction other than thermally induced stresses, and if the material is completely isotropic, then:

$$\varepsilon_x = \varepsilon_y = \varepsilon_z^z = \alpha \Delta T \quad (4)$$

where α is the coefficient of thermal expansion (CTE), ΔT is the temperature change. The last equation of (1) can be rearranged by substitution of eq. (4) as follows:

$$\varepsilon_z^P = \frac{-\nu}{(1-\nu)} (\varepsilon_x + \varepsilon_y) = \frac{-2\nu}{(1-\nu)} \alpha \Delta T \quad (5)$$

The through-plane normal strain ε_z can be represented by:

$$\varepsilon_z = \varepsilon_z^z - \varepsilon_z^P = \alpha \Delta T + \frac{2\nu}{(1-\nu)} \alpha \Delta T = \left(\frac{1+\nu}{1-\nu} \right) \alpha \Delta T \quad (6)$$

Therefore, the effective through-plane CTE ($\alpha_{1z,insitu}$) of the

deposited thin film on a rigid substrate can be represented as a function of the free CTE and Poisson ratio of the film by:

$$\alpha_{1z,insitu} = \left(\frac{1+\nu}{1-\nu} \right) \alpha = \left(\frac{1+\nu}{1-\nu} \right) \alpha_{1,free} \quad (7)$$

Where $\alpha_{1,free}$ is the CTE of free standing film, and equal to α in (6).

In case of a bilayer structure, and neglecting the effect of substrate curvature and assuming that the substrate is isotropic, the thin film structure can also expand or shrink in the in-plane direction by the amount which the substrate expands or contracts in the in-plane direction due to the substrate CTE. The in-plane expansion of the substrate also affects the stress in the thin film. Thus, eq. (5) can be modified for a bilayer by:

$$\begin{aligned}\varepsilon_{1x} = \varepsilon_{1y} = \varepsilon_{1z}^z &= \alpha_1 \Delta T - \alpha_2 \Delta T \\ \varepsilon_{2x} = \varepsilon_{2y} = \varepsilon_{2z}^z &= \alpha_2 \Delta T\end{aligned}\quad (8)$$

where 1 denotes the TiN thin film and 2 denotes the substrate. This equation holds as long as the free CTE of the thin film ($\alpha_{1,free}$) greater than or equal to the CTE of substrate (α_2). Equation (5) can be modified for a bilayer by:

$$\varepsilon_{1z}^P = \frac{-\nu}{(1-\nu)} (\varepsilon_{1x} + \varepsilon_{1y}) = \frac{-2\nu}{(1-\nu)} (\alpha_1 \Delta T - \alpha_2 \Delta T) \quad (9)$$

Thus, the effective through-plane CTE of the thin film on a substrate, such as a Steel 304 wafer, can be represented as a function of the free CTE of the thin film, the CTE of the substrate, and the Poisson ratio of the thin film by :

$$\alpha_{1z,insitu} = \left(\frac{1+\nu}{1-\nu} \right) \alpha_{1,free} - \left(\frac{2\nu}{1-\nu} \right) \alpha_2 \quad (10)$$

Equation (10) gives the measured CTE, $\alpha_{1z,insitu}$ as a function of the free film and substrate parameters. Usually the measured CTE can be as high as three times the free standing film value for the case of an incompressible film ($\nu = 0.5$) and low CTE substrate ($\alpha_2 = 0$).

The intrinsic stress and von Mises stress

In those cases, where the coating-substrate-compound can be considered as plate-like and the film thickness is small compared to the substrate thickness the following two assumptions

- the thin plate approximation is valid,
- the film-stress can be considered as being independent from the distance of the interface

This automatically yields a linear z-dependant stress within the substrate, stress distribution considered only the stress tensor components σ_{xx} , σ_{yy} , $\tau_{xy} = \sigma_{xy}$. In addition assume to have isotropic or transversely isotropic (with the c-axis parallel to the substrate normal) substrate materials of symmetry of revolution and homogeneous deposition conditions over the whole substrate surface, result in only one governing stress value σ_{rr} , which is rr the radial stress. While this stress is widely assumed to be homogeneous within the film it follows a linear z-dependant function within the substrate. This principle distribution of the σ_{rr} stress component occurs only under the above mentioned conditions. Unfortunately for most cases: coated tools, car components or massive lenses, the assumption of a plate-like film-substrate-compound is not valid and thus the stress distribution might be completely different from that one described above. This holds especially for the substrate. For the film, assume that $\sigma_{zz} = 0$ is valid and evaluate by combining the thin plate approximation with the isotropy condition for material properties and deposition process ($\sigma_{xx} = \sigma_{yy}$, $\sigma_{xy} = 0$) and the following transformation rules:

$$\begin{aligned}\sigma_{rr} &= \cos^2 \varphi \sigma_{xc} + \sin 2\varphi \sigma_{xy} + \sin^2 \varphi \sigma_{yy} = \sigma_{xx} \\ \sigma_{\varphi\varphi} &= \cos^2 \varphi \sigma_{yy} - 2 \cos \varphi \sigma_{xy} + \sin^2 \varphi \sigma_{xx} = \sigma_{xx} \\ \sigma_{r\varphi} &= \cos 2\varphi \sigma_{xy} - \sin 2\varphi (\sigma_{xx} - \sigma_{yy}) / 2 = 0\end{aligned}$$

the biaxial stress is homogeneous over the film thickness as long as the film is thin and there is no significant displacement, phase transition or other inelastic effect of any of the parts of the film causing local stress releases.

2 EXPERIMENTAL

The TiN thin films were sputtered in Vacuum chamber, using PMS. The substrates used Stainless Steel 304 and HSS drill cutting.

Considered the changing of intrinsic stress in the TiN films and influence to the microhardness, the bias voltage put on to the clamp of substrates changed from 0 V to minus 150 V. The other conditions still kept stability. The results received checking by X-Ray Diffraction (XRD) Equipment (Siemen D5000) using CuK α radiation with wavelength 1.5406 Å, some of them in Figure 3.

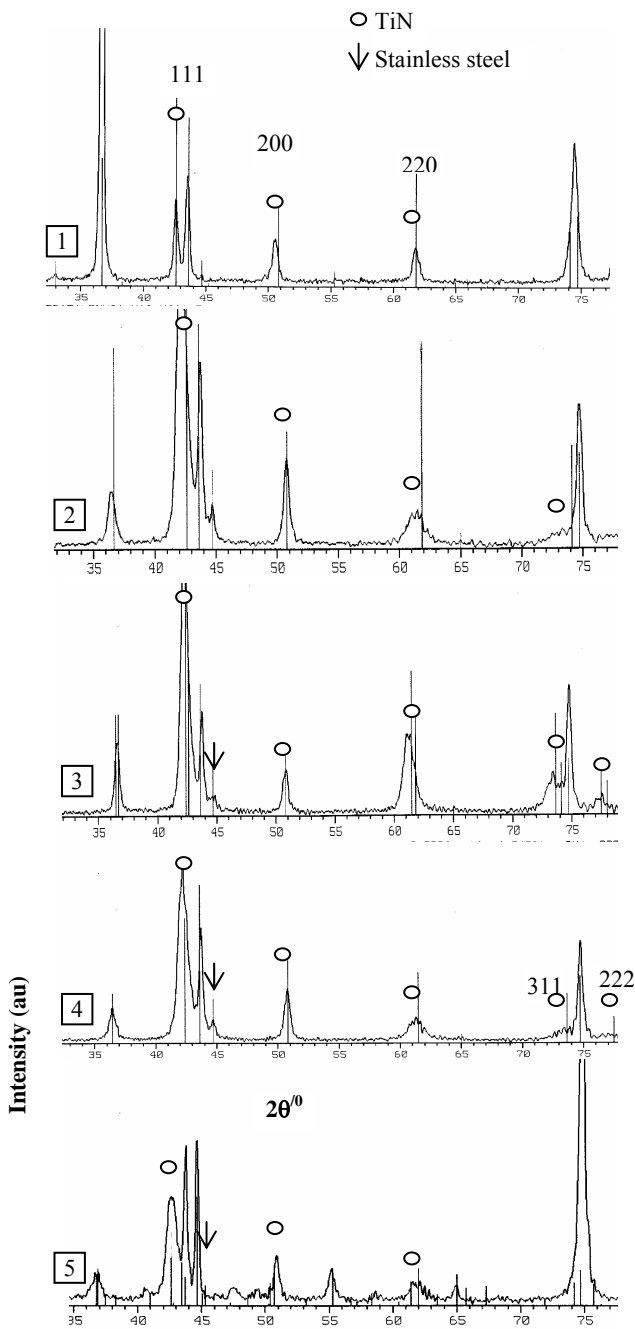


Figure 3. XRD patterns at difference Bias Voltages

Fig.3 shows the XRD patterns of TiN films from our experiments, at difference Bias Voltages.

Pattern number	1	2	3	4	5
Bias Voltage (V)	0	- 60	- 80	- 100	-120

From the XRD patterns, all the main peaks of TiN are appeared, the (200) orientation is predominate and peaks (111) and (311) were also detected with the peak (200) is higher than that of the TiN powder (ASTM-1420) in 4th pattern of Fig.3, that means the 200 plane of films more oriented on the surface.

The main peak of TiN is peak (200) at 42.596 2θ degree, hence the spectrum alters a little to smaller $\Delta 2\theta_{200} \approx -0.242$, the plane distance of 200 was expanded and the compressive stress 2578 GPa appeared in film. The others from 1st to 3rd pattern, the compressive stress increased from 327GPa to 1323 GPa. When the Bias Voltage rise to 120V, the intrinsic stress declined just over 1637 GPa. The results was shown in the Figure 4.

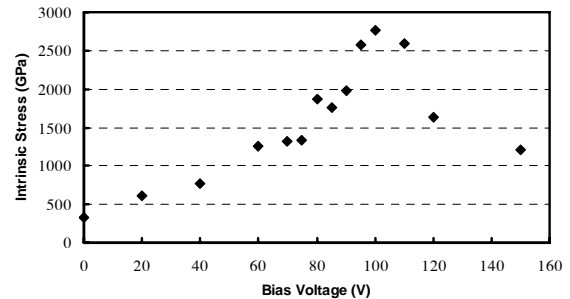


Figure 4. Intrinsic stress of TiN film on SS substrate when changing Bias Voltage

It seems the compressive stress rise nearly by linear function with Bias Voltage, reached the maximum at minus 100V, then reduced when the Bias voltage continue increase. After heating at 800⁰C the position of the peaks from TiN film really are unchanged compared with those before; but peak width at the half-maximum becomes smaller and the predominance of the (200) orientation reduced comparing with the (111) orientation, as seen in Fig. 5 comparing the qualitative five peak intensities of TiN films with the y -axis shows the intensity.

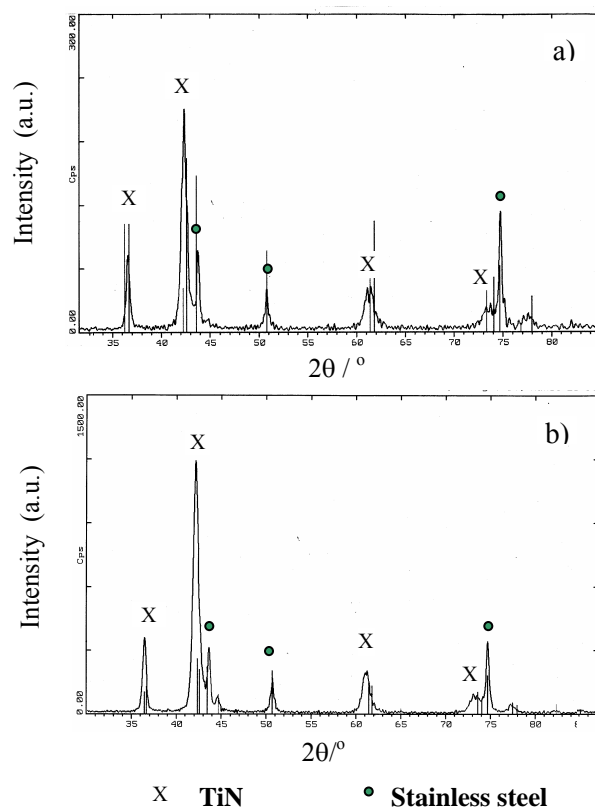


Figure 5 XRD pattern of TiN film (a) Before heating, (b) After heating

Starting with software ANSYS, simulation one layer thin film on substrate and measured with Diamond indenter radius 10 μm , thickness of TiN film only 1 μm , substrate was SS304. Simulated the process, which indenter touched to TiN film and distribution of intrinsic stress as in Fig. 6 and 3D demonstration in Fig. 7. The details calculation using ELASTICA software [4] as following:

	From	To	Points	Spacing
X	-2.7878	2.7878	\AA m	0.028018
Y	-2.7878	2.7878	\AA m	0.028018
Z	0	2.7878	\AA m	0.014009

Automatic range 2.5 times contact radius

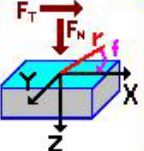
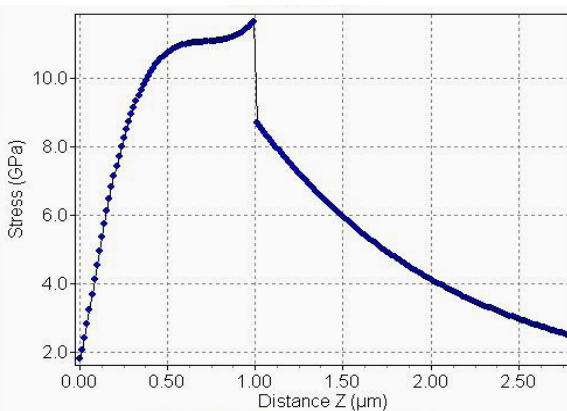
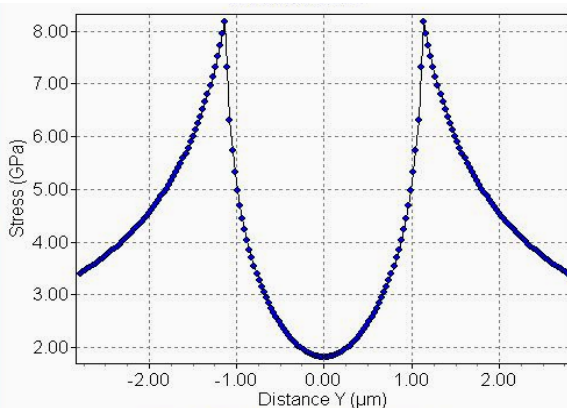
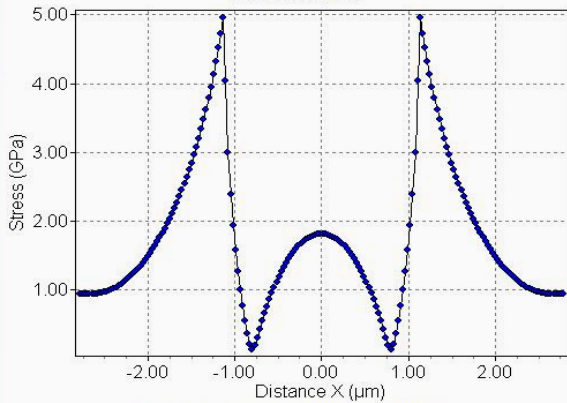



Figure 6. Intrinsic stress of TiN film on SS substrate calculation by ELASTICA software

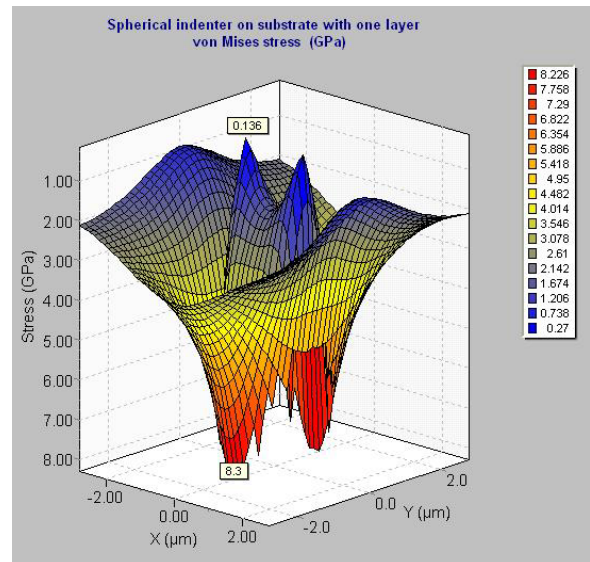


Figure 7. Intrinsic stress of TiN film on SS substrate calculation by ELASTICA software, in 3D demonstration

Calculation Range: From (μm) To (μm) Points Spacing (μm)
 X Direction: -2.78775 2.78775 200 0.0280176
 Y Direction: -2.78775 2.78775 200 0.0280176
 Z Direction: 0 2.78775 200 0.0140088

Current stress/deformation: von Mises stress
 Arrangement:

Elastic parameter:

	E-Modulus	Poisson's ratio	Thickness
Indenter:	1100.0 GPa	0.100	
Substrate:	200.0 GPa	0.300	infinite
Layer 1:	400.0 GPa	0.250	1.0000 μm

Shape parameters / Forces:

Indenter radius: 10 μm
 Normal force: 0.05 N Lateral force: 0 N

Internal stresses:

Layer 1 : XX: -2.01 GPa

Results for position:

X (μm)	Y (μm)	Z (μm)
0	0	0

Contact radius:	1.11511 μm
Contact area :	3.90646 μm^2
Mean contact pressure :	12.7995 GPa
Maximum contact pressure :	19.1992 GPa
Indentation depth (r=0):	0.1439 μm
Contact depth (r=a):	0.0470396 μm
Indenter deformation (r=0):	0.0302662 μm
Sample deformation (r=0):	0.113634 μm
Sample deformation (r=a):	0.0665943 μm

Stress XX :	-19.7021 GPa
Stress YY :	-17.6921 GPa
Stress ZZ :	-19.2167 GPa
Stress XY :	0.00000 GPa
Stress XZ :	-0.00001 GPa
Stress YZ :	0.00000 GPa
Principal stress S1 :	-17.6921 GPa
Principal stress S2 :	-19.2167 GPa
Principal stress S3 :	-19.7021 GPa
von Mises stress :	1.81661 GPa
Hydrostatic stress :	-18.8703 GPa
Max. shear stress :	1.005 GPa
Tresca stress :	2.01 GPa

Deformation U : -2.29342E-05 μm

Deformation V : 0.00000 μm
 Deformation W : 0.113628 μm
 Abs. deformation : 0.113628 μm

Strain ex : -2.61872 %
 Strain ey : -1.9906 %
 Strain ez : -2.46705 %
 Strain exy : 0.00000 %
 Strain exz : 0.00000 %
 Strain eyz : 0.00000 %
 Abs. strain : 3.35723 %

Energy density : 0.671104 J/m^3

Fig. 8 shows the microhardness of TiN coated SS304 substrate, which were automatically heat treated and measured directly from room temperature (RT) to 800°C over a time of 90 min. At the beginning of heating program, at RT the microhardness of the coated insert is 1783 kg/mm^2 . In the end ,when the temperature reached 800 °C, the microhardness had reduced by an exponential function to 492 kg/mm^2 .

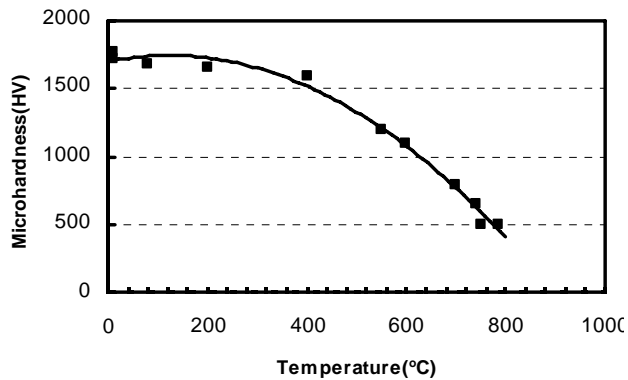


Figure 7: The reduction in microhardness with temperature of TiN film on SS 304 substrate

DISCUSSION

With simulation of intrinsic stress by Elastica software, it is more convenient for designing the parameters to receive the TiN thin film on SS and HSS substrates. The intrinsic stress corresponded with the experiments defining high (~1800 kg/mm^2) microhardness of TiN films. Direct measurement of the microhardness at high temperature (0 °C - 800 °C) over a range of time corresponding to the violent cutting conditions illustrated the influence of temperature on the working time of TiN films. The TiN films have high microhardness corresponding to abrasive resistance, although in our experiments, the modeling of machining time stretched to 90 min. Figure 7 shows that the microhardness reduced but was still higher than the microhardness of uncoated tool.

With high comprehensive stress in the TiN thin film, the coated tools have capacity using in high speed cutting regime.

CONCLUSIONS

- Using simulation software and experiments calculate and measure the high intrinsic stress of TiN thin films on mechanical details; considering SS and HSS substrates.
- The intrinsic stress change with difference parameters of TiN thin film sputtering and could control the intrinsic stress by changing Bias Voltages.

Acknowledgments

We would like to thanks the KC05-VN and the 21th century COE program-NUT for supporting the research.

References

- [1]. Mai,N.T.P., Long B.T., Ishizaki K., "Chacterization of TiN film deposited by planar magnetron sputtering method", Advances in Technology of Materials and Materials Processing Journal, (2003).
- [2]. Schwarzer N., "Modelling of the contact mechanics of thin films using analytical linear elastic approaches" geboren am 7., Eilenburg, (1966).
- [3]. Hegadekatte V., "Modeling and Simulation of Dry Sliding Wear for Micro-machine Applications" Hubli, Indien (2006)
- [4]. Chudoba T., Schwarzer N., ELASTICA, software demonstration package, Software ANSYS WORKBENCH (2007).

Non-volatile data storage beyond 2020

Leon Abelman¹, Niels Tas¹, Erwin Berenschot¹, and Miko Elwenspoek^{1,2}
¹*MESA⁺ and IMPACT Research Institutes,
University of Twente, The Netherlands*
^{1,2}*Freiburg Institute for Advanced Studies (FRIAS),
University of Freiburg, Germany*
l.abelmann@utwente.nl

Abstract: The continuous increase in capacity of non-volatile data storage systems will lead to bit densities of one bit per atom in 2020. Beyond this point, capacity can be increased by moving into the third dimension. We propose to use self-assembly of nanosized elements, either as a loosely organised associative network or into a cross-point architecture. When using principles requiring electrical connection, we show the need for transistor based cross-talk isolation. Cross-talk can be avoided by reusing the coincident current magnetic ring core memory architecture invented in 1953. We demonstrate that self-assembly of three-dimensional ring core memories is in principle possible by combining corner lithography and anisotropic etching into single crystal silicon.

Keywords: Data storage, self-assembly, ring core, magnetic

I. INTRODUCTION

The progress made in micro- and nanotechnology industry over the last six decades has relied heavily on thin film technology. Nanotechnology will continue to provide us with more, more powerful and smaller systems, primarily because of the ever reducing size of components.

The continuing decrease in size inevitably leads to the emergence of fundamental limits. Since the tiniest units of information are found in non-volatile storage systems (such as the hard disk), the first encounter with those limits was found in that area, where it expressed itself in the thermal stability of written bits [1]. Non-volatile data storage will therefore move away from magnetism, possibly in the direction of ferro-electrics [2] or phase-change [3]. Ultimately, we will store bits of information into single atoms [4].

Thin film technology is inherently two-dimensional, so we are accustomed to measuring progress in the number of transistors or stored bits per unit area. From a user point of view however, only the number of elements per unit volume is of interest. It seems to be in place to design new strategies which continue on the path towards increasing volumetric, rather than surface densities.

The key idea in this paper is to machine suitable nano-particles and assemble them in a self-assembly process. Each nanoparticle will have functionality to store one or more bits of information. When assembled in three-dimensional structures, the volumetric data density can grow far beyond the limit of two-dimensional storage.

By equipping particles with electronic functionality, we open the route towards three dimensional processors. On the long term, we can envision mixtures of particles with embedded digital electronics, non-

volatile memory and communication circuits, combined in cubic millimeter computers. In this paper we will limit ourselves to non-volatile data storage however.

II. CHALLENGES IN DATA STORAGE

The world of non-volatile data storage can be divided into two realms. On one side we have mechanically addressed memories, where information is addressed by physical movement of a read/write head. Since the bit dimensions are determined by the size of one single –or only a few– read/write heads and by positioning accuracies, the data density of these media is generally very high. Mechanical addressing is however relatively slow (ms), and usually applied in situations where large amounts of data need to be stored which are not needed frequently. The highest data density is found in magnetic hard disk storage. Predictions are that magnetic storage is limited to data densities of about 10 Tb/in² [5], which is another eight years from now at a growth rate of 40%. Probe storage technology [6] offers the possibility to increase the data density all the way up to one bit per atom [4]. At this point the data density will be in the order of 250 Tb/in², which will be in 2020 with an average growth rate of 60% per year. It is not clear however how areal data density will increase beyond this point.

On the other side, we have electrically addressed memories such as DRAM, FlashMemory, MRAM, Phase-Change RAM etc. Since every bit is connected to the outside world by means of wiring, data rates and access times are high (ns). The capacity, or better bit density, of these media is limited by lithography, and follows the semiconductor industry

roadmap. If the half-pitch linewidth is Λ , the minimum cell size is $4\Lambda^2$, and with multilevel storage at n bits per cell, the bit density becomes $n/4\Lambda^2$. The International Technology Roadmap for Semiconductors predicts that in 2020 Λ will be 11 nm (www.itrs.net). At a foreseen 4 bits per cell, the data density in electrically addressed storage will be 5 Tb/in². Consequently, electrically addressed memories will be far too expensive to take over the role of mechanically addressed memories in large capacity data storage systems in which access times of milliseconds are not an issue.

Areal data densities only give information about the relative cost of the system, but not about the final dimensions. From a user viewpoint, we are much more interested in capacity per unit volume. Assuming that in 2020 a probe recording system will fit into a package of about 1 mm thick, the volumetric data density at the atomic limit (250 Tb/in²) will be $4 \cdot 10^{20}$ bit/m³. This translates into a bit volume of (135 nm)³.

These volumetric data densities are very difficult to obtain with today's technology –let alone extend beyond that value–, mainly because the physical principle does not allow further decrease in bit size (holographic storage [7]), or the manufacturing costs become too high (stacking of FlashMemory cells [8]). It appears to us that there is currently no viable solution for high capacity storage above the 10^{20} bit/m³ limit, and radically new approaches need to be investigated. We propose to self-assemble a non-volatile 3D memory array from nanoparticles with electronic functionality and dimensions below 135 nm.

III. 3D CROSS-POINT STRUCTURES

To realize a three-dimensional storage system, the self assembled array of nano-particles needs to be addressed from the outside. One could use a random agglomerate of particles, all connected together, provided that the percolation is adequate (there are sufficient electrically connected paths through the network). By using proper encoding and data detection algorithms, information storage can be stored in an associative fashion [9, 10].

From an architectural point of view, it is however much simpler to start with crystals of particles, in which the position of every particle is exactly known by its three coordinates in the crystal. We can then simply use the cross-point architectures also used in two-dimensional solid state memories today (DRAM, Flash).

To address memory cells in a two-dimensional cross point architecture, we need to select two coordinates (bit and word lines). As a result, $2n$ address lines need to be connected for a n^2 bit memory. For a three-dimensional cross-point architecture, the situ-

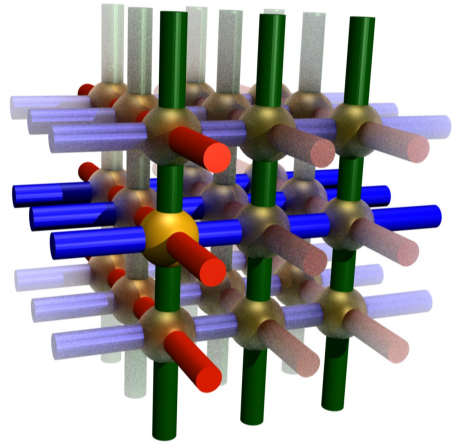


FIG. 1: Selecting a cell in a n^3 bit 3D array by three orthogonal planes reduces the number of connections to $3n$. The selected wires are displayed in bright colour.

ation is more favourable, with $3n$ lines addressing n^3 bit (figure 1), with the advantage getting bigger for larger memories. For example, a 8 Tbit memory would require about $3 \cdot 10^6$ connection wires in 2D, and only $6 \cdot 10^4$ in 3D.

The three-dimensional cross-point array will be connected by means of electronic circuitry including drivers and multiplexers. The connection of these circuits to the array will be on the plane level, requiring (self-)assembly onto three orthogonal sets of n electrodes. The spacing of the electrodes is relatively large (downwards of 135 nm), and the number of electrodes is limited ($n=2 \cdot 10^4$ for a 8 Tb memory, which be smaller than $(3 \text{ mm})^3$). Electronically, this does not seem to be a challenging task.

Although individual cells can be addressed by selecting three planes, read-out can also be done in parallel for increased data rate. By selecting two planes, a line of bits is addressed simultaneously and n bits can be read out on the lines of the third plane. This reduces the required data-rate per bit cell considerably. For a 8 Gb/s readout speed of a 8 Tb memory for instance, planes have to be addressed at a rate of only 400 kHz.

IV. ELECTRICALLY ADDRESSED

For large numbers of bit cells addressed in the cross-point architecture, we need to consider crosstalk. In two-dimensional cross-point solid state memories, every bit is addressed by connecting a voltage source to its word- and bit line. The current passing through the connection can be used to write or detect information. Since all memory elements conduct current, parasitic paths exist which shunt current around the memory element under interrogation. These parasitic currents reduce signal-to noise ra-

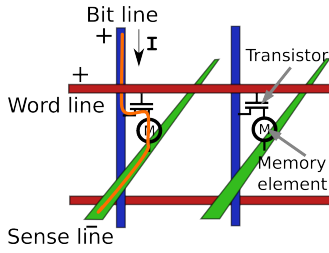


FIG. 2: 3D cross point architecture with transistors. M indicates the memory storage element, which can be based on various principles.

tio and strongly limit the array size. This can be avoided by integrating a diode within the memory cell. Since shunting currents pass in the opposite direction, parasitic currents are strongly suppressed. Even though the reverse currents through the diodes are very small, the combined effect through the many shunting paths can still be too large. In a 2×2 array for instance, there are only 6 parasitic paths, but this number increases rapidly with increasing array size. In general, the number of parasitic paths for a $n \times n$ array is A_n^{2n} , which can be calculated by iteration from

$$A_i^{2n} = \sum_{j=1}^{2n-1} A_{i-1}^j \quad (1)$$

$$A_2^{2n} = \left(\frac{1}{2}\right)^{2n} \sum_{j=1}^{2n-1} j \quad (2)$$

For large arrays the iteration can be approximated by $0.1 \cdot 2^{(n/2)}$ parallel paths. For a diode forward/reverse current ratio of 10^{11} , the maximum array size is limited to about 80×80 .

For larger arrays, we therefore need to move towards more aggressive rejection ratios, which can be achieved by using transistors rather than diodes. Since transistors are three-wire devices, an extra wire is connected, which - even though it can be shared between memory cells - complicates the architecture. Extending the cross-point architecture into three-dimensions however, there are three wires needed to address every bit, and the transistor geometry fits perfectly (figure 2).

In order to realize transistor functionality in the nanoparticles, there is some advantage in using semiconductor base materials such as silicon. Sources and drains can be defined by doping opposite faces of particles, or by assembly of n-doped and p-doped nanoparticles. Memory elements such as floating gates for charge storage (as in FlashMemory) or phase-change resistance wires exploiting the large difference in conductance between the amorphous and crystalline phase (as in PCRAM) can be incorporated at a third face or along edges of particles.

V. MAGNETICALLY ADDRESSED

Even though particles with active electronic functionality are extremely appealing, realisation of transistors inside nanoparticles or by assembly is technologically very challenging, since it requires excellent control over doping concentrations and interface quality. As a first step towards a three-dimensional storage system however, we can store data in a passive way, keeping the detection electronics outside the self-assembled structure. Therefore one needs to avoid the parasitic current paths.

A very elegant design of a three-dimensional cross point architecture without direct connection between the addressing wires was proposed by Jay W. Forrester [11] in 1951, based on the invention of the magnetic core memory in 1950 by An Wang and Way-Dong Woo [12]. In the magnetic ring core memory, data is stored in the direction of circulation of magnetisation of tiny magnetic rings. Information is written by means of the magnetic field of wires running through the center of the rings. Individual rings can be selected by passing currents only through wires selecting that ring (coincident current writing, invented by Forrester). Only in rings where two wires are actuated, the magnetic field is sufficiently high to induce switching. The rings therefore have to be able to discriminate between currents differing by a factor of two.

Depending on the direction of the current, clock or counterclockwise magnetisation patterns are written, representing “1” and “0” binary information. The use of magnetic ring cores was very elegant, since in such configuration the rotation of magnetisation is zero, and no magnetic stray fields emerge, therefore limiting the cross talk between elements.

In the 2D array, information was retrieved by attempting to overwrite information in the rings again and monitoring the change in flux. For this a current was applied to the two lines selecting a ring core (bit and word lines). A third wire (sense line) passing through all cores was used to detect a change in magnetic flux, causing an induced voltage. From the presence or absence of this pulse the magnetisation direction could be derived. When a pulse was detected, an opposite current was applied to restore the state of the magnetic element (write-after-read scheme, invented by Wang).

Writing of sub-micron ring cores can be achieved in a similar way as in macroscopic ring cores. Since the magnetic volume is orders of magnitude smaller however, we need to consider the stability of the magnetisation direction at room temperature. This stability is determined by the energy barrier for magnetisation reversal, which should be higher than 40 kT for 10 year data retention. Calculations [13] show that for ring diameters of 135 nm with wire diameters of 50 nm, the magnetic field is strong enough to overcome energy barriers of 120 kT.

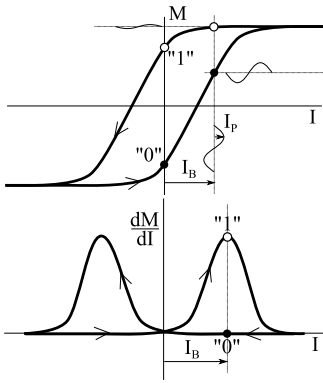


FIG. 3: High frequency modulation of the magnetisation can be used for non-destructive readout. a) Magnetisation curve b) Susceptibility

Writing as in the macroscopic system therefore seems to be possible. The situation is different for readout however. When the magnetisation reverses, the flux through the circuit formed by the sense line changes, causing an *emf*. The flux change is proportional to the ring core wire diameter squared, so decreases rapidly with shrinking dimensions. The noise on the sense lines is proportional the square root of the wire resistance, so the signal to noise ratio decreases with a power 2.5. Calculations show that this prohibits this type of destructive readout for nanometer scaled ring cores [13].

The main problem with destructive readout is that we get only one attempt to read out the information. Billing circumvents this problem by implementing a high frequency susceptibility measurement [14]. Rather than completely reversing the magnetisation in the core, a DC bias current I_B below the reversal threshold is passed through one of the addressing lines and small high frequency perturbation current I_P through another (figure 3a). Since the susceptibility (dM/dI) of the core depends on the direction of the current, the *emf* on the sense line can be used to determine the magnetic state of the ring (figure 3b). Calculations show that this method will allow for sufficient signal to noise ratio, but a trade-off needs to be made between wire diameter, modulation frequency and data rate [13].

VI. SELF ASSEMBLY

The relatively large dimension of 135 nm for bits required for a volumetric density of $4 \cdot 10^{20}$ bit/m³ suggest the use of nanotechnology. Fabrication of nanoparticles with those dimensions will be relatively cheap in 2020. Already today, methods exist to assemble these particles afterwards in large three-dimensional structures, similar to the way nature uses atoms and molecules to assembly larger structures.

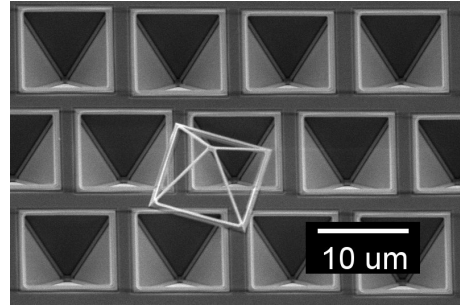


FIG. 4: Wireframe produced by corner lithography

The general concept is to fabricate large amounts of identical particles (spheres, cubes, tetrahedra, etc.) which are treated in such a way that they spontaneously self-assemble in liquid or gaseous environments. One method is to produce particles which have hydrophobic and hydrophilic surfaces. When immersed in water, the hydrophobic surfaces bind together, producing irregular or crystalline agglomerates. Glotzer [15] gives an excellent overview of the state of the art in this field, listing many different types of particles and realized assemblies.

Up to now, the particles are passive, which is useful if one wants to realize fluidic filters [16] or photonic crystals [17]. Although not yet demonstrated, several feasible paths to nanoparticles with internal degrees of freedom, or with electronic functions, with designed sterical and chemical anisotropy, are being considered - it is only a matter of time until they become available. Nanoparticles with a form commensurate with the crystal structure of silicon can be made by exploiting the great dependency of the etch rate in some high pH solutions. The technology allows for modification of the vertices, edges and faces of the tetrahedrons by means of corner lithography [18, 19]. Figure 4 shows an initial result of a free SiN wireframe produced by this method. The size of the particle is determined by the etched inverse structure in the Si, which can be seen below the particle. The dimensions are determined by lithography, and can be reduced below 100 nm. Since the particles are embedded in the support wafer before release, it is possible to deposit different materials in vertices, edges and faces.

Certainly nanoparticles can be modified to steer self-assembly into crystals so that regular structures similar to the cross-point structures shown in figure 1 can be grown. Parts of the nano-particles can for instance be made hydrophobic so that the assembly of amphiphilic particles into crystal structures similar to self-assembled structure in nature will become possible, see for instance [20–22]. Self-assembly of anisotropic nano-particles is currently in its infancy, however the emerging analogy with the growth of molecular crystals is quite encouraging. Regardless of the technique being used, it should in principle be

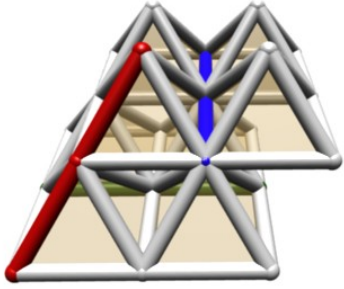


FIG. 5: Self assembly of pyramidal wire frames into units cells which can assemble into a 3D cross-point addressing architecture. Each unit cell contains eight smarticles. The addressing lines are shown in read, green and blue

possible to realize smarticles with transistor functionality or magnetic ring cores.

VII. RING CORE MEMORY

In the last part of this paper we will explore whether it would *in principle* be possible to realise a 3D magnetic ring core memory by means of self assembly of a limited number of substructures produced by corner lithography. Two functions need to be assembled, a three dimensional array of wires (the word, bit and sense lines) and magnetic ring cores. There are many different ways in which a three dimensional array of wires can be self assembled, starting from tetrahedra, cubes or pyramids for instance. To realise 3D cross point architectures, for each of those basic elements eight elements are needed to realise a unit cell (An example of pyramid unit cell is given in figure 5). Tetrahedra are the simplest elements, with exactly the right number of corner points.

Also the magnetic ring core has to be defined by vertices. An efficient method is using tetrahedra. Figure 6 shows a unit cell of eight tetrahedra, with addressing lines at the corners of a square magnetic ring. Of course, the addressing lines have to be located within the magnetic ring for inductive read-out, and should be electrically isolated from it. Placing the wires close to the magnetic ring has the advantage of an increase in field strength. The magnetic elements do not have to touch, since stray field coupling will lead to flux closure structures.

This particular solution requires 5 different types of elements. There are other solutions, with more favorable positioning of the magnetic core, but at this point it is sufficient to realise that in principle it is possible to construct a 3D magnetic ring core memory from a limited number of simple building blocks. Figure 7 shows an impression of such an architecture,

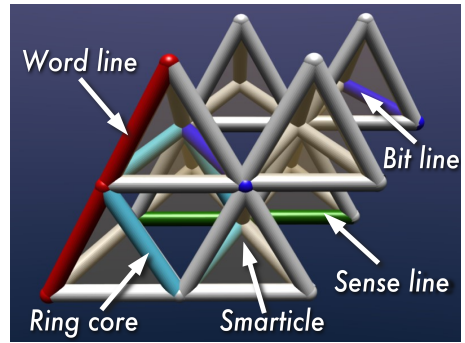


FIG. 6: By assembly of smarticles with different materials in the edges, a unit cell for a ring-core bit can be realized.

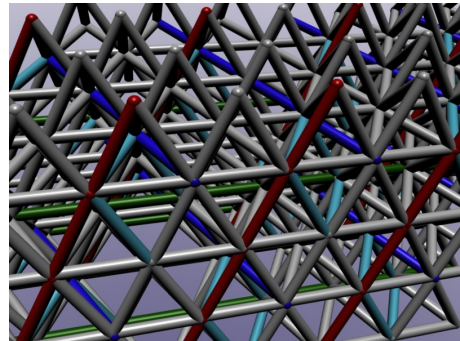


FIG. 7: Repetitive assembly of unit cells lead to a 3D ring core memory structure.

where the extension of the addressing lines can be clearly seen.

The technological challenges to realise a structure like this are formidable: We can make silicon tetrahedrons in a size range from a few tens of nanometers to a few micrometers, and we know ways to add electrical conductors of various metals along the edges. But these complex structures needs several types of tetrahedra. They have to be assembled in the right way. Furthermore they should conduct electrical current along lines passing a vast number of particles, whilst keeping the impedance low.

VIII. CONCLUSION

We expect the increase in data density for non-volatile, two-dimensional data storage to come to a halt when the bit spacing reaches atomic dimensions, which will be at a data density of about $4 \cdot 10^{20}$ bit/m². To continue the capacity of storage systems, we need to move from surface to volumetric storage. Using typical values for package sizes, one can estimate that the onset of three-dimensional data storage will have to start at a volumetric density of $4 \cdot 10^{12}$ bit/m³, or bit cell volumes of $(135 \text{ nm})^3$.

By adopting the cross-point architecture from to-

days solid state memories, and extending it into three dimensions, a simple addressing scheme can be made. If the memory cells are electrically addressed, transistors are required to reduce parasitic currents. Parasitic currents can be avoided by re-using the magnetic addressing strategies used in ring core memories from the early years of computer technology. We calculated that storing data into magnetic ring cores at sub micron dimensions is possible, using coincident current writing at current densities well below the electromigration threshold, and energy barriers largely sufficient for 10 years of data retention. The small size of the rings prevent destructive readout at sufficient signal-to-noise ratio, but a susceptibility technique, combined with frequency mixing can certainly be applied.

A promising strategy for the realisation of three-dimensional memories could be the self assembly of

artificial sub-micron elements (smarticles). We show that a ring core memory can in principle be (self-) assembled from eight tetragonal wire frame elements per memory cell, consisting of five different types of tetrahedra each having different combinations of conducting, non-conducting and magnetic edges. Other configurations are however possible.

We therefore believe that the concept of a self-assembled three-dimensional ring core memory is challenging, but technically feasible, and will provide an intriguing first step towards a solution for data storage beyond the atomic limit.

Acknowledgments

This work was supported by the Excellence Initiative of the German Federal and State Governments.

-
- [1] Charap, S. H., Lu, P. L., and He, Y. *IEEE Trans. Magn.* **33**(1), 978–983 (1997).
 - [2] Cho, Y., Hashimoto, S., Odagawa, N., Tanaka, K., and Hiranaga, Y. *Applied Physics Letters* **87**(23), 232907 – 1 (2005).
 - [3] Hamann, H. F., O’Boyle, M., Martin, Y. C., Rooks, M., and Wickramasinghe, H. K. *Nature Materials* **5**(5), 383 – 387 (2006).
 - [4] Bennewitz, R., Crain, J. N., Kirakosian, A., Lin, J. L., McChesney, J. L., Petrovykh, D. Y., and Himpfel, F. J. *Nanotechnology* **13**, 499–502 (2002).
 - [5] Thomson, T., Abelmann, L., and Groenland, J. P. J. In *Magnetic Nanostructures in Modern Technology*, Azzerboni, B., Asti, G., Pareti, L., and Ghidini, M., editors, NATO Science for Peace and Security Series Subseries: NATO Science for Peace and Security Series B: Physics and Biophysics, 237–306. Springer Verlag, Berlin (2007).
 - [6] Pantazi, A., Sebastian, A., Antonakopoulos, T. A., Bachtold, P., Bonaccio, A. R., Bonan, J., Cherubini, G., Despont, M., DiPietro, R. A., Drechsler, U., Durlg, U., Gotsmann, B., Haberle, W., Hagleitner, C., Hedrick, J. L., Jubin, D., Knoll, A., Lantz, M. A., Pentarakis, J., Pozidis, H., Pratt, R. C., Rothuizen, H. E., Stutz, R., Varsamou, M., Weismann, D., and Eleftheriou, E. *IBM J. Res. Dev.* **52**(4-5), 493–511 (2008).
 - [7] Ramanujam, P., Lohse, B., and Berg, R. *Proceedings of the SPIE - The International Society for Optical Engineering* **6252**, 62520 – 1 (2006).
 - [8] Morrow, P. R., Park, C.-M., Ramanathan, S., Kobrinsky, M. J., and Harmes, M. *IEEE Electron Device Letters* **27**(5), 335 – 337 (2006).
 - [9] Hopfield, J. *Proc Natl Acad Sci U S A* **79**(8), 2554–2558 (1982).
 - [10] McElice, R. J., Posner, E. C., Rodemich, E. R., and Venkatesh, S. S. *IEEE Trans Inf Theory* **IT-33**(4), 461–482 (1987).
 - [11] Forrester, J. W. *J. Appl. Phys.* **22**(1), 44–48 (1951).
 - [12] Wang, A. and Woo, W. D. *Journal of Applied Physics* **21**(1), 49–54 (1950).
 - [13] Due to restrictions in size, the calculations have been omitted here, but can be obtained from <http://eprints.eemcs.utwente.nl/15686>.
 - [14] Billing, H., Rüdiger, A., and Schilling, R. *Journal of Applied Physics* **37**(3), 1367–1373 (1966).
 - [15] Glotzer, S. C. and Solomon, M. J. *Nature Materials* **6**(8), 557 – 562 (2007).
 - [16] Seo, Y. H. *Applied Physics Letters* **90**(12), 123514 – (2007).
 - [17] Fleming, J., Lin, S., El-Kady, I., Biswas, R., and Ho, K. *Nature* **417**(6884), 52 – 55 (2002).
 - [18] Berenschot, E., Tas, N., Jansen, H., and Elwenspoek, M. In *3rd IEEE International Conference on Nano/Micro Engineered and Molecular Systems, NEMS 2008*, 729–732 (, Sanya, 2008).
 - [19] Sarajlic, E., Berenschot, J. W., Krijnen, G. J. M., and Elwenspoek, M. C. In *Proceedings of the 13th International Conference on Solid-State Sensors, Actuators and Microsystems 2005, Seoul*, volume 1, 27–30 (IEEE Computer Society Press, Los Alamitos, 2005).
 - [20] Murphy, C. J., Sau, T. K., Gole, A. M., Orendorff, C. J., Gao, J., Gou, L., Hunyadi, S. E., and Li, T. *Journal of Physical Chemistry B* **109**(29), 13857 – 13870 (2005).
 - [21] Park, S., Lim, J.-H., Chung, S.-W., and Mirkin, C. *Science* **303**(5656), 348–351 (2004).
 - [22] Rycenga, M., McLellan, J. M., and Xia, Y. *Advanced Materials* **20**(12), 2416 – 2420 (2008).

Recent study on Pt containing nanoparticles and Pt nanorods synthesized by wet chemical method and magnetic switching behaviors of CoPt patterned films

W. L. Pei*, G. W. Qin*, Y. P. Ren*, S. Ishio**

*Northeastern University, 3-11 Wenhua Road, Shenyang 110004, China

**Department of Materials Science and Engineering, Akita University, Japan

Qingw@smm.neu.edu.cn; Ishio@gipc.akita-u.ac.jp

Abstract: Pt and Pt alloy nanomaterials have many important potential applications, such as catalyst, sensor, magnetic recording materials. We present the recent study on the fabrication of one dimensional Pt and FePt nanomaterials and the magnetic switching behavior of CoPt pattern. Pt nanorods were synthesized by wet chemical method. The nanorods are sensitive to reactive parameters. The size, aspect rate, and morphology of the nanorod strongly relate to reactive temperature, time and surfactant. The micrograph of high resolution TEM shows the growth direction of the Pt nanorod is $\langle 100 \rangle$ direction, which means the functional group (amine) of the surfactant intensely interact on (111) surface and block the face to grow.

The CoPt pattern (10nm in height, 50 nm in diameter and 120 nm pitch) was fabricated by electron beam lithography and ion milling process. The switching field distribution (SFD) and magnetization switching process in the patterned films were studied by an in-filed magnetic force microscopy (MFM) technology. The angular dependence of switching field was discussed.

Key words: Nanorods, Wet chemical method, In-field MFM, Patterned film, Magnetization reversal

1 INTRODUCTION

One dimension Pt and Pt alloy nanomaterials have many important potential applications, such as catalyst, sensor, magnetic materials, and so on [1]. Recently, many research works have been devoted into these materials. Researchers have proposed some methods to fabricate one dimension Pt and FePt nanomaterials^[1-3]. The performances of the 1D nanomaterial strongly relate to size, size distribution and morphology of the 1D materials. It's a goal how to make 1D nanomaterials with uniform size, monodisperse, and controlled morphology. When we want to build a fine 1D nanostructure according to our idea, firstly we should understand the anisotropy growth mechanism. However, the mechanism still is not well-defined. There is not a general principle to guide how to produce Pt and FePt nanorod. In here, we tried to synthesize Pt nanorods by wet chemical process and discussed influence of reaction conditions on nanodods and the growth mechanism.

There is another important fabrication process for Pt based nanomaterials. That is a dry process like electron beam lithography and ion milling. The most of magnetic storage

devices like HDD and MRAM are fabricated by such process. Bit patterned media (BPM) is the most promising candidate for an extremely high density recording media at more than 2 Tbit/inch² [4]. Up to now the pattern media have successfully fabricated by dry process [5-6]. The magnetic properties, such as magnetic switching behavior, and switching field distribution (SFD) are very important issue to realize the BPM, because these properties will directly relate to magnetic recording performances. The value of magnetic switching field and the width of SFD are affected strongly by the fabrication method, because top-down method like ion milling sometimes induces a damaged layer with soft magnetic properties in patterned dots. A deeper insight into the basic mechanisms involved would be therefore beneficial for optimizing patterned structures. However, so far there are only little understands on these subjects because the patterned area that could be achieved is pretty small only in micro-range. It is very difficult to precisely measure these magnetic parameters by using some experimental methods, for example vibrating sample magnetometry (VSM). Therefore the reversal behaviors were

studied by micromagnetic modeling or Anomalous Hall effect (AHE) evaluation [7-8]. Recently, in-field MFM technology has been used to analyze switching filed distribution of patterned samples [9-10]. The technology employed in situ MFM observation in perpendicular magnetic field, which permits us to directly reveal the switch behavior in micro-range. In here, we tried to analyze the magnetization switching processes including the angular dependence of the switching field, and the effect of the damaged layer will be discussed.

2 EXPERIMENTAL

The Pt nanorods were synthesized by wet chemical method. Oleyl amine was used as surfactant and weak reducer, and Octadecene was employed as menstruum. Pt(acac)₂ was reduced to Pt nanomaterials at a function of reactive temperatures for different reactive time. The samples were characterized by the TEM and XRD.

Si/SiO₂/Ta(5nm) /Pt(10) /Ru (20)/ CoPt(10)/Pt(2)/Ta(10) films were deposited on SiO₂/Si substrates using a DC-magnetron sputtering system. The Ru as a seed layers resulted in the films with a large *K_u* and the *c* axis perpendicular to the film plane. Dot patterns were formed using high resolution e-beam lithography and reactive ion etching. The average diameter of dots in the present study was about 50 nm, with a periodicity of 120 nm. The uniaxial perpendicular magnetic anisotropy of the CoPt continuous film is about 1.3x10⁷ emu/cm³, and magnetization is 1140 emu/cm³. The magnetization configurations of dot arrays were observed by using in-field MFM observation technology explained in the references [6, 7].

3 RESULTS AND DISCUSSION

3.1 Pt nanorod produced by chemical method

The relationship between reactive temperature and the nanorod size is showing in figure 1. The synthesized nanomaterials were sensitive to reactive temperature. At the low temperature, the nanoparticles can not be completed nuclear-up process in a short time. With prolonging reactive time, the nanorods appeared. For high reactive temperature, the nanomaterials can be synthesized within short time. With prolonging reactive time, the nanorods were synthesized. The reactive time is also an important factor for synthesis of nanomaterials. By analysis of the sample synthesized at the same temperature and different time, we found that particle size and aspect ratio also gradually increased with prolonging reactive time.

By analysis of the high-resolution transmission micrograph,

as shown in Fig.2(d), the anisotropy mechanism of Pt nano-rod was revealed. It could be found that growth direction of the nanorod is $\langle 111 \rangle$ direction. We believed that the function group of Oleyl amine intensily interact on the (111) surface of nucleus, and block the nuclear grow up along $\langle 111 \rangle$ direction. Therefore, the nuclear grow up along $\langle 100 \rangle$ direction. It's very interesting thing that we also synthesized some T and L like nanomaterials. The synthesized mechanism was discussed as shown in figure 2. Fig.(a) shows nanorod, (b) shows nano-T, and (c) shows nano-L.

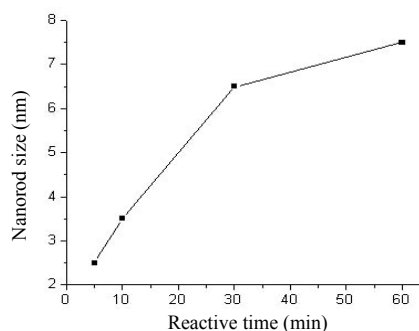


Figure 1. The relationship between reactive time and nanorod size.

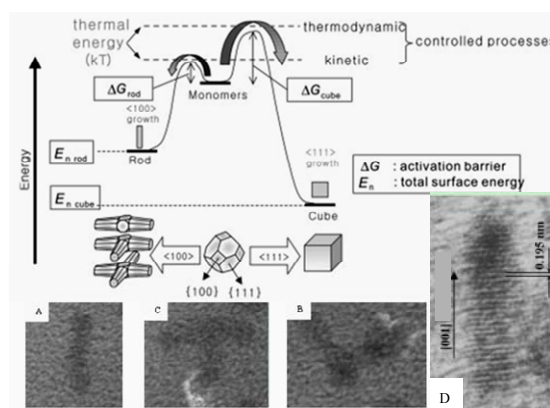


Figure 2. Mechanism of nanorod, nanoT and nano-L.

3.2 Switching behavior of CoPt patterned film

Fig.3 shows MFM images measured under a function of magnetic fields of the CoPt dot array (from remnant state to under -7 kOe magnetic field), where all images were taken at the same location of the sample. The first MFM image was scanned under a 0 magnetic field (remnant state). The magnetic morphology of CoPt dots shows all the dots have a single domain structure. It could be found that the dots switched step by step with the addition of magnetic field. Therefore, the dots array switching process was exactly defined by the figure.

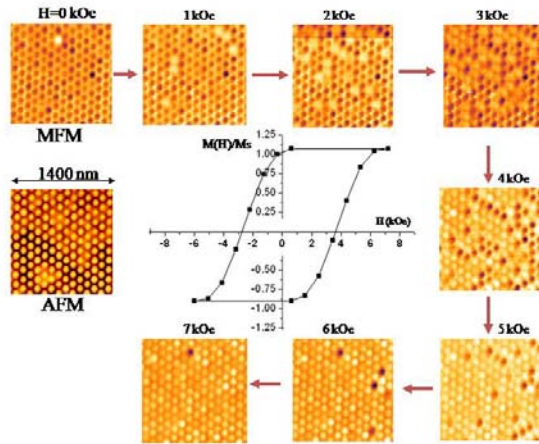


Figure 3. MFM images of CoPt dot array measured at remanent states. The inset shows a remanent magnetization curve obtained from MFM images.

Magnetization loop is a basic magnetic parameter. It's difficult to draw the loop of patterned simple by a normal method (VSM, and AGM) because the patterned area is pretty small. But the in-field technology could obtain the loop for the micro-range by a very simple method. By assuming the dots have a same volume, the relative remanent magnetization was obtained by

$$M(H)/M_s = (N_D - N_B) / (N_D + N_B), \quad (1)$$

where N_D and N_B are numbers of dots having upward magnetization (dark MFM contrast) and downward magnetization (bright MFM contrast). The magnetization loop could be obtained by counting the dots contrast and calculating according to equation 1, as in Fig.1. According to the loop, a remanent coercivity is estimated to be about 3 kOe.

Fig.4 (a) shows the statistic distribution of switching field of CoPt dot array. The half width of SFD is between 3 and 4 kOe as seen in the figure. The dipolar field from surrounding dots was calculated as about 1.3 kOe, which explains only a half of SFD obtained by experiment. Fig.4(b) shows a spatial distribution of switching field. MFM measurements at the remanent states were also done by changing directions of applied magnetic field. The sample was magnetized by electromagnet with a function of angles, and then we observed the sample at remanent state. Figure 5 shows the angle dependent remanent switching field. The angular range measured is from 0° to 90° . The angular dependence of switching field has not similarity to the Stoner-Wohlfarth model, but resemble to the curling model. Here the minimum in switching field is at 45° and is only 15% lower than the easy axis value rather than 50% lower at 45° predicted by the Stoner-Wohlfarth model, while the remanent coercivity increases with closing 90° . The methodology used for these

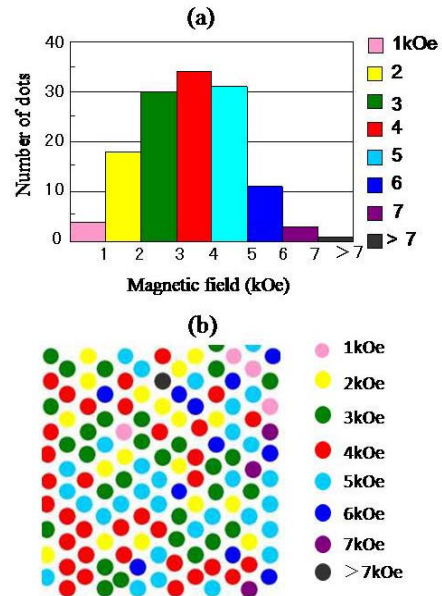


Figure 4. Switching field distribution of CoPt dot array (a) and switching field map (b).

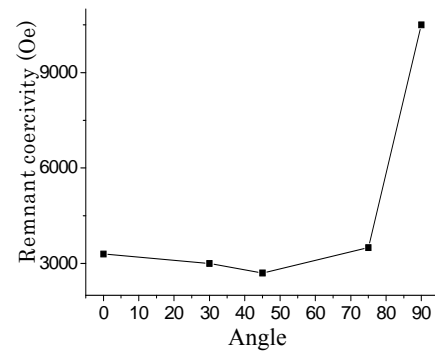


Figure 5. Angle dependence of switching field

measurements allows comparison of easy axis and hard axis switching. The easy axis coercivity was much smaller than that of hard axis, which may be explained by curing model, where the magnetization has a vortex-like structure.

There are many reports that suggest the soft magnetic layer is easily induced during fabrication process of bit pattern [11, 12]. According to LLG simulation, when such soft magnetic layer is formed around dots, the magnetization becomes a vortex-like structure surrounding hard magnetic inner core. As a result, the angle dependence of switching field becomes the curing like behavior just shown in Fig.5. We believe further improvement is necessary for the fabrication process of bit patterned media.

4 CONCLUSION

Pt nanorods were synthesized by wet chemical method. The rods size, aspect rate, and morphology strongly relate to

reactive temperature, time and surfactant. The micrograph of high resolution TEM shows the growth direction of the Pt nanorod is <100> direction, which means the functional group (amine) of the surfactant intensely interact on (111) surface and block the face to grow.

The SFD and magnetization rotation process of CoPt patterned film and Co nanorod film were studied by magnetic force microscopy. From the angular dependence of switching field, the existence of soft magnetic layer induced during fabrication process is suggested.

References

- [1] Y. Yu and B. Xu, *Appl. Organometal. Chem.* Vol. 20, pp. 638(2006).
- [2] Yanglong Hou, Hiroshi Kondoh, Renchao Che, Masaki Takeguchi, and Toshiaki Ohta, *Small*, Vol.2, No.2, pp. 235(2006).
- [3] E. Ramirez, L. Eradès, K. Philippot, P. Lecante, and B. Chaudret, *Adv. Funct. Mater.*, Vol.17, pp. 2219(2007).
- [4] B. D. Terris and T. Thomson, *J. Phys. D: Appl. Phys.*, Vol. 38, pp. R199 (2005).
- [5] T. Thomson, G. Hu, and B. D. Terris, *Phys. Rev. Lett.*, Vol.96, pp. 257204(2006).
- [6] K. Mitsuzuka, T. Shimatsu, H. Muraoka, N. Kikuchi*, and J. C. Lodder, *J. Magn. Soc. Jpn.*, *J. Magn. Soc. Jpn.*, Vol.30, pp. 100(2005).
- [7] N. Honda, K. Yamakawa, and K. Ouchi, *IEEE Tran. Magn.*, Vol. 43, No. 6, pp. 2142(2007).
- [8] K. Mitsuzuka, T. Shimatsu, H. Muraoka, H. Aoi, N. Kikuchi, and O. Kitakami, *J. Appl. Phys.*, Vol. 103, pp. 07C504 (2008).
- [9] J. Bai, H. Takahoashi, H. Ito, H. Saito, S. Ishio, *J. Appl. Phys.*, 2004, 96, 6690.
- [10] W. Pei, J. Yuan, T. Wang, Y. Fu, T. Washiya, T. Hasegawa, H. Saito, S. Ishio, and N. Honda, *Acta Materialia*, 2007, 55, 2959.
- [11] H. Takahoshi, H. Saito, S. Ishio, *J. Magn. Magn. Mater.*, Vol. 272-276, pp. e1313(2004).
- [12] Y. Kondo, T. Chiba, J. Ariake, K. Taguchi, M. Suzuki, M. Takagaki, N. Kawamura, B. M. Zulfkri, S. Hosaka, N. Honda, *J. Magn. Magn. Mater.*, Vol. 320, pp. 3157(2008).

Electrodeposition of Copper for Metallic Interconnects

Kimin Hong¹, Youngho Ryu¹, and Wonbae Bang¹
Byoungju Kang² and Seung-Hee Lee²
Seung Jin Yeom³

¹Department of Physics, Chungnam National University, Daejeon, 305-764, Korea

²Wezen Division, KC Tech, Anseong City, Gyeonggi-Do, 456-843, Korea

³Hynix Semiconductor, Icheon-si, Gyeonggi-Do, 467-701, Korea

kmhong@cnu.ac.kr

Abstract: We have studied the effect of organic additives on the properties of electroplated copper thin films for use as metallic interconnects of semiconductor devices. Depending on the species and concentration of the additives, surface roughness and electrical resistivity varied significantly. We also electroplated narrow trench patterns of which width is between 60 and 120 nm. We demonstrated successful gap-fill of the trenches by using three additives at appropriate concentrations.

Key Words: Electroplating, Metallic Interconnects, Copper, Organic Additives, Resistivity

1. INTRODUCTION

Electrodeposition of copper is now widely used in the semiconductor industry for fabrication of metallic interconnects. Most gap-fill process of copper interconnects are carried out using copper sulfate electrolyte. It is well known that organic additives in the electrolyte play an important role in achieving the super-fill or bottom-up fill process. Void-free super-fill and quality copper films are obtained using proper composition and concentrations of the additives¹. Commercially available additive makeups usually utilize three organic chemicals, generally called as accelerators, suppressors, and levelers. An accelerator enhances charge transfer rate contributing to the reduction of Cu^{++} to Cu^+ and increases plating current density. Typical accelerators are light molecules such as saccharine, bis-(3-sulfopropyl)-disulfide, disodium salt (SPSA) and their derivatives². Suppressors are usually polymers with the molecular weight range between 1,000 and 10,000 g/mol. They reduce current density during deposition. Polyethylene glycols with various molecular weights and their derivatives are known to have suppressing effects.

The difference between accelerators and suppressors can be easily characterized using cyclic voltammetry (CV)³. In this method, copper is alternately deposited on and stripped off a metallic electrode, typically Pt, as we apply an alternating voltage across a reference electrode and a working electrode. When we increase the concentration of an accelerator in a plating bath, the current density continuously increases. On the other hand, a suppressor prohibits metal deposition and the current density is reduced as we keep adding the suppressor in the bath. The third component, a leveler is known to be locally adsorbed at the top corners of the trenches and reduce the local growth rate. The fundamental role of organic additives on the super-fill process has been studied both theoretically and experimentally⁴⁻⁷.

Organic additives also have significant effect on the characteristics of plated copper such as grain size, crystalline orientation, and surface smoothness, which, in turn, determine the electrical resistivity⁸. We have reported the effects of an additive set on the electrical resistivity and gap-fill performance of 120 nm trenches⁹ and other metallic thin films^{10,11}. Since the line width of interconnects is being shrunk to as narrow as 30 nm, development of proper organic additives has risen as a challenging issue in semiconductor industry. This work is an attempt to develop additives for electroplating of narrow copper whose width is below 60 nm. We first tested commercially available additives and observed property changes depending on the composition of the electrolyte and concentration of the additive components. We then developed additive makeups composed of two and three organic chemicals. As a performance test of the new additive makeups, we plated thin films of copper, characterized electrical resistivity and surface roughness of them, and tested gap-fill capability of 30-60 nm wide trenches.

2. EXPERIMENTAL

A 20 nm thick Cu seed layer was deposited onto an N-type Si(100) substrate by electron-beam evaporation. The crystalline orientation of the Cu seed was mostly Cu(111), with the remainder being Cu(100). 30-60 nm wide trench patterns were fabricated with the standard semiconductor processes at Hynix Semiconductor. Electroplating was carried out using a conventional three terminal method, with an Ag/AgCl reference electrode, a platinum plate as a counter electrode, and the aforementioned copper seed layer and patterned wafers as working electrodes. A potentiostat (SI 1286, Solartron) was used as a power supply. The film thickness was controlled by adjusting the deposition time, and was confirmed using scanning electron microscopy (SEM).

The electrolyte we used was copper sulfate solution with 40-60 ppm of chloride ions. Since the properties of the copper deposits change considerably depending on the composition of the electrolyte, three different sets were prepared; UCL (Upper Control Limit), Target, and LCL (Lower Control Limit). The composition of the electrolytes is shown in Table 1.

Table 1. Composition of electrolytes

	Cu (g/L)	H ₂ SO ₄ (g/L)	Cl (ppm)
UCL	45	13	60
Target	40	10	50
LCL	35	8	40

Various organic additives have been used for manipulation of the properties of deposits and to test gap-fill capability of narrow trenches. The first was commercially available additive set, Viaform[®] by ATMI[®], which is composed of three chemicals; accelerator, suppressor, and leveller. We also prepared additive sets using PEG (polyethylene glycol) of various molecular weights.

Thickness of the thin films and feature fill capability was examined using damascene test structures by scanning electron microscopes (SEM, S-4800, Hitachi). Root-mean-square (RMS) surface roughness was measurement with an atomic force microscope (AFM, Nanoman, VEECO) in an area of 1 μm×1 μm. Resistivity of the thin films was measurement by using a four-point probe meter.

3. RESULTS AND DISCUSSION

3.1 Commercial Additives

First, we have analyzed effect of commercially available Viaform[®] additives on electroplated Cu thin films. 12 kinds of thin films were prepared with varying electrolyte composition and additive concentration. Table 2 shows the concentration of the Viaform[®] additives using the three electrolytes. In the Table, U, T, and L stand for UCL, Target, and LCL concentration of each additive. Plating was carried out for 10 s with the current density of 5 mA/cm².

Table 2. Electrolyte composition and additive concentration for the deposition of copper thin films.

Thin Film #	1	2	3	4	5	6	7	8	9	10	11	12
Electrolyte	LCL			Target			UCL					
Accelerator	0	L	T	U	0	L	T	U	0	L	T	U
Suppressor	0	L	T	U	0	L	T	U	0	L	T	U
Leveler	0	L	T	U	0	L	T	U	0	L	T	U

Measurement results of electrical resistivity and surface roughness of the thin film are summarized in Fig. 1. Thin film #1, prepared with LCL electrolyte and without additives, exhibited 1.8 μΩ•cm of resistivity and 37 nm of roughness. As we add the additives, resistivity increased to 2.1-2.5 μΩ•cm and roughness decreased to 5-10 nm. Additives in the Target electrolyte changed the resistivity

from 3.1 μΩ•cm to 1.6-2.5 μΩ•cm, while roughness was reduced from 37 nm to 6-9 nm. When the additives were used in the UCL electrolyte, the resistivity was 1.6-2.5 μΩ•cm and the roughness was 6-23 nm. Overall, the resistivity was in the range of 1.5-3.13 μΩ•cm and the roughness was in the range of 5-38 nm. The process Target, thin film #7, exhibited 2.5 μΩ•cm and 6.3 nm for resistivity and roughness, respectively. Note that the additives sometimes increase the resistivity depending on the composition of the electrolyte. However, it is clear that the additives have significant effect on the reduction of surface roughness.

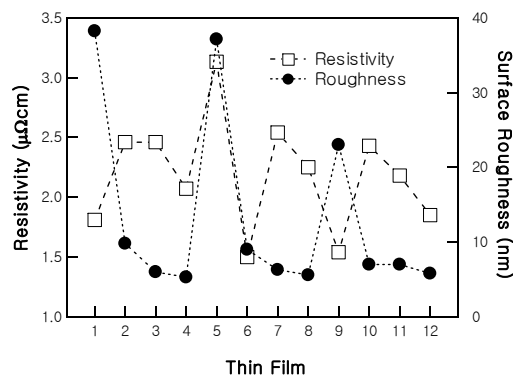


Figure 1. Electrical resistivity and surface roughness of the thin films with varying electrolyte composition and additive concentrations.

We have attempted gap-fill of 30 nm wide trenches using the electrolyte compositions of Table 2. With the 12 electrolytes the gap-fills have been successful for the aspect ratio of 1-2. For the aspect ratio higher than 2, there were voids in the trenches, as shown in Fig. 2. While Viaform[®] additives have demonstrated high gap-fill performance on low aspect ratio trenches, improvements in the electrolyte composition and the electroplating process are required.

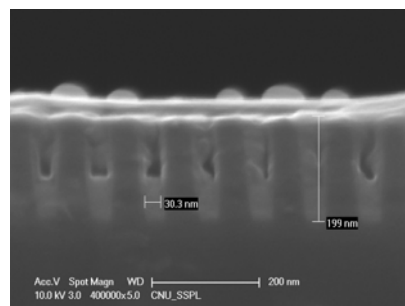


Figure 2. Cross-sectional view of 30 nm wide trenches with aspect ratio of 6 plated with an electrolyte containing Viaform[®] additives.

3.2 Development of two components additive makeup

First, we have tried an additive set of two chemicals: 1-20 mL/L of an accelerator and 5-20 mL/L of PEG (molecular weight 3,400 g/mol) as a suppressor. Fig. 3 shows the change of resistivity and thickness of the thin films as we vary the electroplating time (EP Time) when the concentration of the accelerator and suppressor were 2 mL/L and 5 mL/L, respectively. The plating current density was ~5 mA/cm². As we increase the plating time from 20 s

to 400 s, the thickness of the thin films increased from 150 nm to 1000 nm. As the thickness increased, the electrical resistivity was reduced from $10 \mu\Omega\cdot\text{cm}$ to $2 \mu\Omega\cdot\text{cm}$. Note that the resistivity is $\sim 2 \mu\Omega\cdot\text{cm}$ when the thickness is larger than 50 nm. In this range of the thickness, the surface roughness is $\sim 10\text{-}20$ nm.

While the electrical resistivity of the thin films was low enough, the gap-fill on 30-60 nm trenches was not successful. As we changed the molecular weight and concentration of PEG, no further improvement has been observed. We think that a two-component additive makeup has limitations in gap-fill of small features such as trenches narrower than 60 nm.

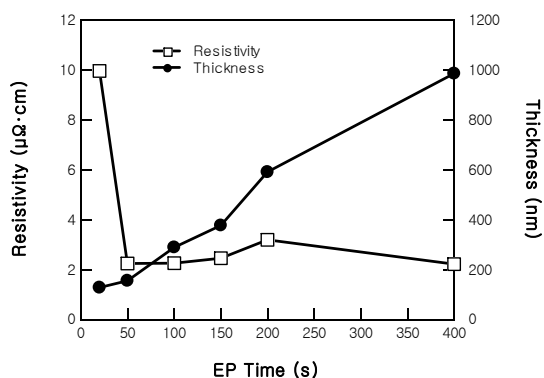


Figure 3. The changes of thickness and resistivity in the galvanostatically electroplated thin films with two additive components.

3.3 Development of three component additive makeup

In order to achieve a successful gap-fill of 30-60 nm trenches, we have made use of three component additive makeup where the suppressor was PEG (molecular weight 8,000 g/mol). Thickness of the thin films were controlled to 650 ± 5 nm. With this additive makeup the accelerator component had most considerable effect on the material property and gap-fill performance. Fig. 4 shows the effect of the accelerator on resistivity and surface roughness.

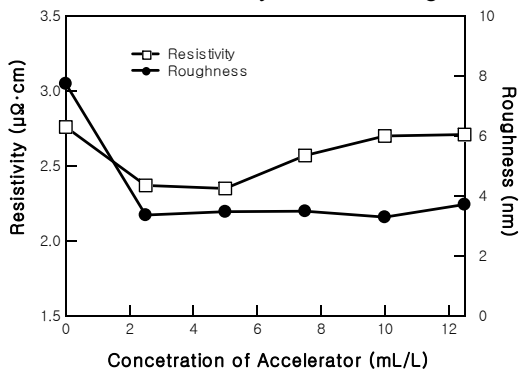


Figure 4. Changes of resistivity and surface roughness in the galvanostatically electroplated thin films as we increase the concentration of SPSA in the electrolyte.

When the accelerator was not included in the bath, the deposits show $\sim 3 \mu\Omega\cdot\text{cm}$ of resistivity and 6 nm of surface roughness. When 2.0-12.5 mL/L of the accelerator is added to the electrolyte, the surface roughness does not change

considerably. However, resistivity is reduced to $\sim 2 \mu\Omega\cdot\text{cm}$ within the range of the accelerator concentration.

Fig. 5 shows the gap-fill performance of 30 nm trenches as we vary the accelerator concentration. With the accelerator concentration below 10 mL/L, voids can be observed at the center of a few trenches, as shown in Fig. 5(a). With the concentration of 12.5 mL/L, the gap-fill does not exhibit voids, as can be seen in Fig. 5(b). However, when we increase the concentration above 15 mL/L, large voids appear at the center of most trenches, which is shown in Fig. 5(c). While the voids in Fig. 5(c) is evidently caused by the improper composition of the electrolyte, the root cause of the small voids at low concentration of the accelerator, i.e. Fig 5(a), needs careful analyses. One of the causes can be the aging of the seed layers, since the plating was carried out at least 3- weeks after the seed layers were fabricated. It is clear that the lag between seed layer fabrication and electrodeposition can cause formation of oxides on the seed surface. Another possibility is the imperfection of the side walls such as pin holes and defects. We need further investigation to understand this behavior.

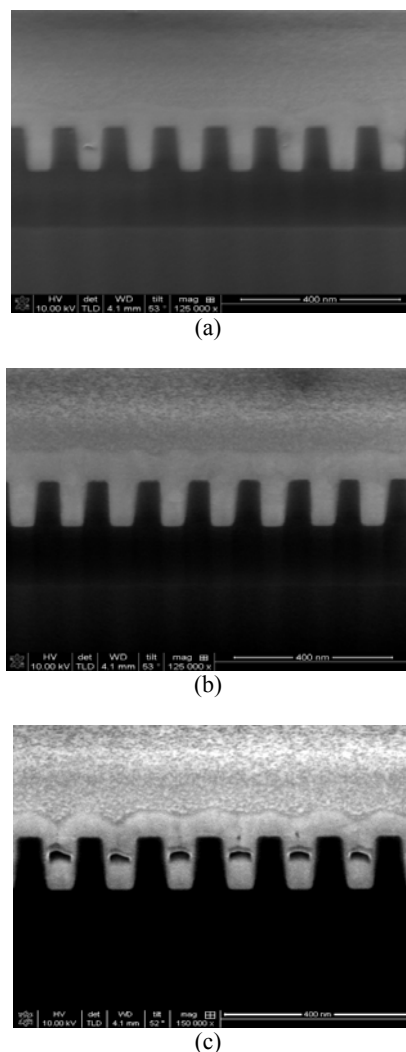


Figure 5. Gap-fill performance of 30 nm trenches as we vary the concentration of the accelerator: (a) 2.5 mL/L, (b) 12.5 mL/L, and (c) 20 mL/L.

Acknowledgment This work was in part supported by Fundamental R&D Program for Core Technology of Materials funded by the Ministry of Commerce, Industry and Energy.

References

- [1] D. Josell, B. Baker, C. Witt, D. Wheeler, and T. P. Moffat, *Electrochem. Solid-State Lett.*, 149 (12) C637-C641 (2002)
- [2] Alan C. West, *J. Electrochem. Soc.*, 147 (1) 227 (2000)
- [3] A. J. Bard and L. R. Faulkner, *Electrochemical Methods, Fundamentals and Applications*, Wiley, New York (2001)
- [4] Cao, P. Taephaisitphongse, R. Chalupa, and A. West, *J. Electrochem. Soc.*, 148, C466 (2001).
- [5] J. Reid and S. Mayer, *Proc. Adv. Metallization Conf.*, 53 (2000)
- [6] T. Moffat, J. Bonevich, W. Huber, A. Stanishevsky, D. Kelly, G. Stafford, and D. Josell, *J. Electrochem. Soc.*, 147, 4524 (2000).
- [7] J. Reid, S. Mayer, E. Broadbent, E. Klawuhn, and K. Ashtiani, *Solid State Tech.*, 43, 86 (2000).
- [8] G. B. McFadden, S. R. Coriell, T. P. Moffat, D. Josell, D. Wheeler, W. Schwarzacher, and J. Mallett, *J. Electrochem. Soc.*, 150 (9) C591 (2003)
- [9] Jinhan Lee, Jungju Lee, Jonghak Bae, Won Bae Bang, Kimin Hong, M. H. Lee, Sung G. Pyo, Sibum Kim, and Jin-Gyu Kim, *J. Electrochem. Soc.*, 153, C521 (2006).
- [10] Wonbae Bang and Kimin Hong, *Electrochem. Solid-State Lett.*, 10 (8) J86 (2007)
- [11] Stanko R. Brankovic, Ryan Haislmaier, and Natasa Vasiljevic, *Electrochem. Solid-State Lett.*, 10 (6) D67 (2007)

Synthesis and Vacuum Ultraviolet Spectral Properties of Nano-scaled phosphor

Yuhua Wang*, Zhaofeng Wang, Xue Yu and Qizheng Dong

Department of Materials Science, School of Physical Science and Technology, Lanzhou University, Lanzhou, 730000, PR China

* Corresponding author. Tel.: +86 931 8912772; fax: +86 931 8913554.

E-mail address: wyh@lzu.edu.cn. (Y.H. Wang)

Abstract

The nano-scaled red phosphor $\text{YBO}_3: \text{Eu}^{3+}$, green phosphor $\text{ZnSiO}_4: \text{Mn}^{2+}$ and blue phosphor $\text{BaMgAl}_{10}\text{O}_{17}: \text{Eu}^{2+}$ were synthesized by wet-chemical techniques. The morphologies and spectral properties of the three nano-phosphors under 147nm excitation were investigated. For $\text{YBO}_3: \text{Eu}^{3+}$, nano-sheets was obtained by solvent-thermal process, which reached 78.8% of the commercial red phosphor on emission intensity and exhibited better color purity than the latter. For $\text{ZnSiO}_4: \text{Mn}^{2+}$, different morphologies were obtained by hydrothermal method with varying ratio of CTAB to TEOS, among which the nano-spheres presented the strongest emission intensity and reached 86% of that of the commercial green phosphor. For $\text{BaMgAl}_{10}\text{O}_{17}: \text{Eu}^{2+}$, nano-rods were acquired using sol-gel process, which exhibited 78.15% of the commercial blue phosphor on emission intensity and the low y value of color coordinates, which indicated that the nano-rods were efficient for restricting the deterioration during application.

Key words: Synthesis, nano-phosphor, VUV

1. Introduction

The plasma display panel (PDP) was known as one of the promising flat panel display devices which utilized vacuum ultraviolet (VUV) exciting the phosphors, and a visible emission was generated^[1]. The representative tricolor commercial phosphors for PDP were $(\text{Y, Gd})\text{BO}_3: \text{Eu}^{3+}$, $\text{ZnSiO}_4: \text{Mn}^{2+}$ and $\text{BaMgAl}_{10}\text{O}_{17}: \text{Eu}^{2+}$ (BAM) due to their strong emission intensity and good color purity. However, there are still some deficiencies in these phosphors: The color purity $(\text{Y, Gd})\text{BO}_3: \text{Eu}^{3+}$ was poor and the decay time of $\text{ZnSiO}_4: \text{Mn}^{2+}$ was too long for the application, while the degradation of $\text{BaMgAl}_{10}\text{O}_{17}: \text{Eu}^{2+}$ was an outstanding problem during panel manufacture^[2].

Recently, many researchers have focused on the preparation and luminescent properties of nano-phosphors because of their small size effect, surface effect, and the quantum size effect, which made them promising to present different optical and electrical properties compared with bulk phosphors^[3]. Besides, to meet the requirement of the PDP manufacture procedure, nano-phosphors were convenient to brush the panel and they could get higher resolution to make the pictures more vivid.

With the expectation of improving the physical, chemical and luminescent properties of ordinary particles, many soft-chemical techniques have been adopted to synthesize nano-particles on the account of their good mixing of starting materials and relatively low reaction temperature^[4]. In this work, the nano-scaled $\text{YBO}_3: \text{Eu}^{3+}$, $\text{ZnSiO}_4: \text{Mn}^{2+}$ and $\text{BaMgAl}_{10}\text{O}_{17}: \text{Eu}^{2+}$ were respectively prepared by different soft-chemical methods, which were solvent-thermal, hydrothermal method and sol-gel process. Their morphologies and spectral properties under VUV excitation were investigated and discussed.

2. Experiments

2.1 $\text{YBO}_3: \text{Eu}^{3+}$ nano-phosphor

$\text{YBO}_3: \text{Eu}^{3+}$ nano-phosphor was synthesized by solvent-thermal method. The starting materials were Y_2O_3 (99.99%), Eu_2O_3 (99.99%) and H_3BO_3 (99.5%). Stoichiometric amounts of Y_2O_3 (95 wt %) and Eu_2O_3 (5 wt %) were dissolved in diluted nitric acid by heating, and drying to get a mixture of $\text{Y}(\text{NO}_3)_3$ and $\text{Eu}(\text{NO}_3)_3$. Stoichiometric amount of H_3BO_3 was added in the mixture. The mixture was dissolved in 50ml of mixed water and ethanol hybrid solution (the relative volume ratio of water to ethanol are adjusted for 1:0, 1:1, 1:2 and 1:3, respectively) under ultrasonic mixing for 1h. The initial pH value was adjusted to 8 with ammonia, since the reaction was a process of producing H^+ and weak alkaline conditions were propitious to reaction production. The solution was transferred into a 100ml Teflon-lined, stainless steel autoclave. The solution was heated at 230°C and the reaction time was 3 h. White precipitates were collected, filtered and washed with distilled water and ethanol several times, and dried in an oven at 80°C to get the finally product.

2.2 $\text{ZnSiO}_4: \text{Mn}^{2+}$ nano-phosphor

$\text{Zn}_2\text{SiO}_4: \text{Mn}^{2+}$ nano-phosphor was synthesized in an autoclave equipped with a Teflon reaction vessel by hydrothermal method. All the reagents are of analytical grade. $\text{Zn}(\text{CH}_3\text{COO})_2 \cdot 2\text{H}_2\text{O}$ (99.0%), $\text{Mn}(\text{CH}_3\text{COO})_2 \cdot 4\text{H}_2\text{O}$ (99.0%) and $(\text{C}_2\text{H}_5\text{O})_4\text{Si}$ (SiO_2 , 28.4%) (TEOS) were used as sources of zinc, manganese, and silicon, respectively. In a typical procedure, firstly, TEOS was dissolved in a mixture solution of distilled water and ethanol, ammonia hydroxide was added as the catalyst for the hydrolysis with vigorous stirring for an hour. $\text{Zn}(\text{CH}_3\text{COO})_2 \cdot 2\text{H}_2\text{O}$ and $\text{Mn}(\text{CH}_3\text{COO})_2 \cdot 4\text{H}_2\text{O}$ was dissolved in the distilled water and stirred continuously until complete dissolution occurred. Then the TEOS solution was slowly added into the above aqueous $\text{Zn}(\text{CH}_3\text{COO})_2$ and $\text{Mn}(\text{CH}_3\text{COO})_2$ solution. After being stirred for half an hour, the mixture solution was transferred into the Teflon reaction vessel of the autoclaves and heated at different temperature for 2 h. After cooling down to room temperature naturally, the resultant products were collected by filtration, washing and drying. To control the morphology and the particle sizes of the phosphor, the cetyl-tri-methyl-ammonium bromide (CTAB) as the surfactant molecules was adopted into the solution of $\text{Zn}(\text{CH}_3\text{COO})_2$ and $\text{Mn}(\text{CH}_3\text{COO})_2$. The phosphor was obtained through the same procedure of hydrothermal as above.

2.3 $\text{BaMgAl}_{10}\text{O}_{17}: \text{Eu}^{2+}$ nano-phosphor

$\text{BaMgAl}_{10}\text{O}_{17}: \text{Eu}^{2+}$ was synthesized by sol.-gel process. The starting materials Eu_2O_3 (99.99%), $\text{Al}(\text{NO}_3)_3 \cdot 9\text{H}_2\text{O}$ (99.0%), $\text{Ba}(\text{NO}_3)_2$ (99.5%) and $\text{Mg}(\text{NO}_3)_2 \cdot 6\text{H}_2\text{O}$ (99.0%) were weighted as the nominal composition of $\text{Ba}_{0.9}\text{MgAl}_{10}\text{O}_{17}: 0.1 \text{Eu}^{2+}$. Then, citric acid were dissolved in deionized water and adjusted PH value to 3 by $\text{NH}_3 \cdot \text{H}_2\text{O}$. And then a stoichiometric amount of starting materials were dissolved in the citric solution. After all of the materials dissolved, adjusted the PH value to 5 and heated to 60°C with ceaselessly stirring about half an hour to gain the sol. The sol was placed in room temperature for about 40 min in succession. Then dried it in a muffle oven at 120°C and the volume of the gel expanded greatly and the puffy and porous dried gel was obtained. Finally

grinded the gel in agate mortar and sintered at the temperature range of 850°C to 1300°C for 4 h under a reducing atmosphere (5% H₂/N₂ mixture gas) to obtain the product.

2.4 Characterizations

The X-ray diffraction (XRD) patterns were obtained on a Rigaku D/max-2400 X Ray diffractometer. The morphology of the powders was examined by Transmission Electron Microscopy (TEM) performed with a Hitachi H-800 transmission electron microscope using an accelerating voltage of 200 kV and JEOL-5600 Scanning Electron Microscope (SEM). The emission spectra were measured at room temperature by FLS-920T fluorescence spectrophotometer with a VM-504-type vacuum monochromator. A deuterium lamp was used as the lighting source.

3. Results and discussions

3.1 YBO₃: Eu³⁺ red nano-phosphor

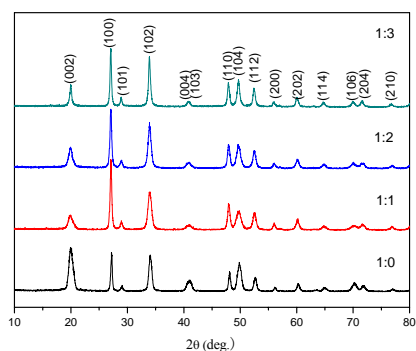


Figure 1: XRD patterns of the YBO₃: Eu³⁺ samples prepared with different ratios of water to solvent

Figure 1 shows XRD patterns of the samples synthesized with different ratios of water to solvent. All the diffraction peaks could be indexed to the JCPDF card (No. 83-1205), and there is no second phase observed. As shown in the Fig.1, the relative intensity of the diffraction peaks for the solvent-thermal (SO) samples are different from the sample prepared by hydrothermal reaction (HR, the 1:0 samples). The (002) peak is the strongest for the HR samples but the (100) peak becomes strongest when the solvent was introduced in the reaction systems, indicating the appearance of a preferred orientation.

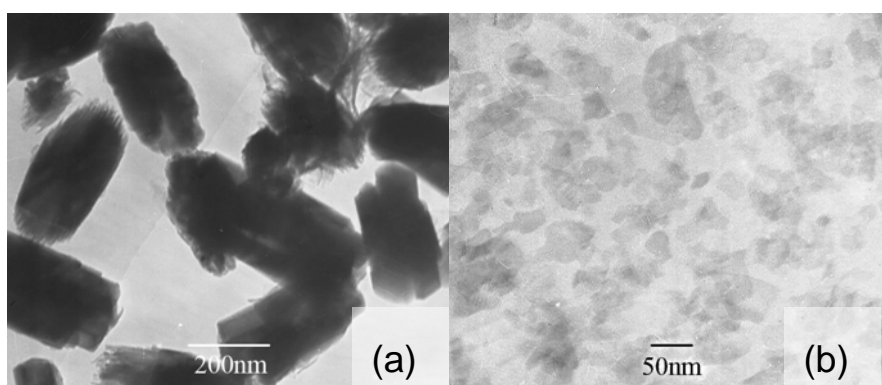


Figure 2: The TEM images of YBO₃: Eu³⁺ phosphors prepared by different reaction (a) HR Samples; (b) SO samples

The TEM photographs of the SO and HR samples are shown in Fig.2. In Fig.2(a), we could find that the HR particles are rod-like with size of 150nm in diameter and 300nm in length. By the addition of solvent, the

morphology changes into nano-sheets about 50nm, and it represents better dispersion than that of HR samples. The possible reason is that solvent and water present different physical properties, such as boiling point, viscosity, dielectric constant and thermal conductivity, and these differences could influence crystallization environment leading to different morphology and agglomeration state of products^[5].

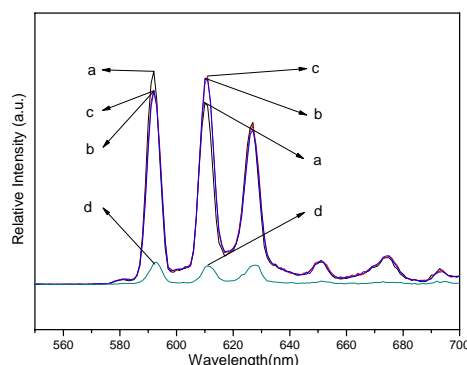


Figure 3: Emission spectra of $\text{YBO}_3: \text{Eu}^{3+}$ nano-phosphors prepared at different ratios of water to solvent (a) 1:0; (b) 1:1; (c) 1:2; (d) 1:3 ($\lambda_{\text{ex}}=147\text{nm}$)

Under 147nm excitation, the emission spectra of the SO samples with different ratios of water to solvent are shown in Fig.3. All spectra consists of sharp lines ranging from 580 to 700 nm, which are associated with the transitions from the excited $^5\text{D}_0$ level to $^7\text{F}_J$ ($J=1, 2, 3, 4$) levels of Eu^{3+} activators^[6]. It is observed that the strongest red emission is at the water to solvent ratio of 1:2, and the PL intensity of 1:3 samples is lower obviously than the others. It can be due to the existence of a small amount of OH^- coordinated to lanthanide ions at the surface of phosphors prepared by the wet chemical method. Adding excessive amount organic solvent (over 1:3) lead to large number of OH^- adhering on the surface of phosphor, which result in the poor PL intensity^[7]. It was found that the ratio of red emission (611nm) intensity to orange emission (592nm) intensity (R/O) is 1.11, which is the highest value among above samples. It predicts that the SO sample (solvent at 1:2) has the best color purity.

3.2 $\text{ZnSiO}_4: \text{Mn}^{2+}$ green nano-phosphor

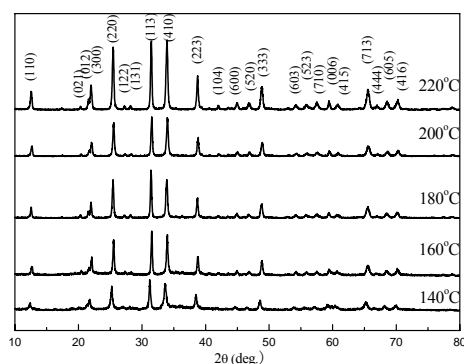


Figure 4: XRD patterns of the $\text{Zn}_2\text{SiO}_4: 0.06\text{Mn}^{2+}$ samples prepared at different reaction temperature.

Figure 4 shows the XRD patterns of the $\text{Zn}_2\text{SiO}_4: 0.06\text{Mn}^{2+}$ phosphors prepared at different reaction temperatures. All the diffraction peaks can be indexed to pure hexagonal structured Zn_2SiO_4 (JCPDF card, No. 37-1485). The $\text{Zn}_4\text{Si}_2\text{O}_7(\text{OH})_2\text{H}_2\text{O}$ is not detected as that reported by Ref.^[8] in the hydrothermal procedure below 280°C, which means that there is no intermediate phase in our hydrothermal procedure even at a low reaction temperature. The XRD result shows that single phase of $\text{Zn}_2\text{SiO}_4: \text{Mn}^{2+}$ prepared at 220°C represents the best crystallinity.

When the adoption of CTAB in the hydrothermal procedure as the surfactant molecules, it was found that the size and the morphology of the $\text{Zn}_2\text{SiO}_4: \text{Mn}^{2+}$ phosphors could be controlled as shown in Fig. 5(a)-(d). When the CTAB/TEOS=0.01 was adopted, the rod-like particles show the trends to the sphere-like shaped (Fig. 5(b)). This is

an interim morphology from rod-like to spheres. When the concentration of CTAB increased to CTAB/TEOS=0.05, TEM micrograph (Fig. 5(c)) shows that the willemite phosphors are nano-spheres with the diameter about 60 nm. The nanoparticles dispersed well without agglomerated. When larger amount of CTAB are introduced, nanoparticles aggregates can be observed in the final products.

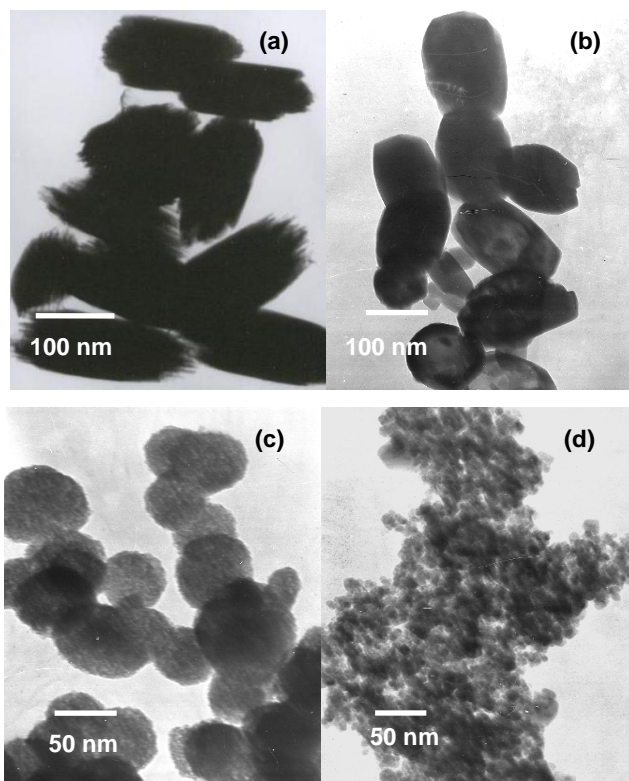


Figure 5: TEM micrographs of the $\text{Zn}_2\text{SiO}_4:0.06\text{Mn}^{2+}$ samples synthesized at different conditions. (a) Without CTAB, (b) CTAB/TEOS=0.01, (c) CTAB/TEOS=0.05, (d) CTAB/TEOS=0.20.

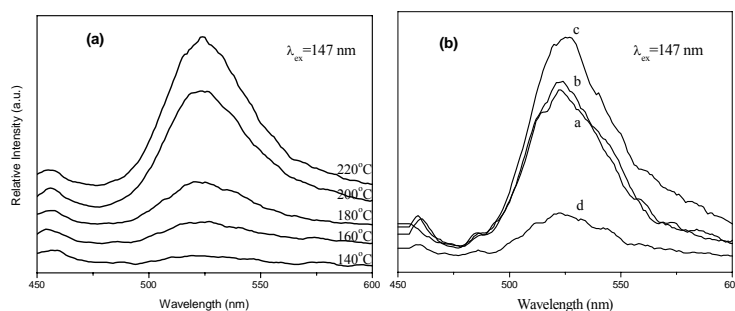


Figure 6: The emission spectra of $\text{Zn}_2\text{SiO}_4:0.06\text{Mn}^{2+}$ phosphors (a) synthesized at different reaction temperature, (b) different ratio of CTAB to TEOS of sample a-d

The relative intensities of $\text{Zn}_2\text{SiO}_4:0.06\text{Mn}^{2+}$ samples at different reaction temperatures under the 147 nm excitation are given in Fig. 6(a). The strongest broad band emission at about 523 nm was observed, which is attributed to the ${}^4\text{T}_1 \rightarrow {}^6\text{A}_1$ transition of Mn^{2+} . It shows that the luminescence intensity increases when the temperature increases. This phenomenon would be ascribed to the higher crystallinity according to the XRD results as discussed previously.

The PL intensity among different morphology of the phosphors was also investigated. Fig. 6(b) presents emission spectra for the samples with different morphology under VUV excitation. The green luminescence is the conventional green of $\text{Zn}_2\text{SiO}_4: \text{Mn}^{2+}$ phosphor, occurring at about 523 nm. As can be seen in Fig. 6(b), the shape change of phosphors has a certain extent influence on their luminescent intensity. It can be seen that the highest PL

intensity was obtained when the $\text{Zn}_2\text{SiO}_4: \text{Mn}^{2+}$ phosphor has uniform spherical morphology (sample c) due to the unique properties of sphere morphology.

3.3 $\text{BaMgAl}_{10}\text{O}_{17}: \text{Eu}^{2+}$ blue nano-phosphor

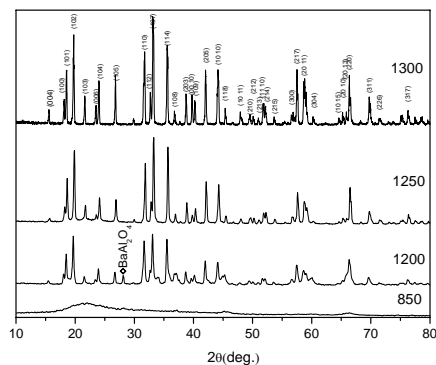


Figure 7: XRD patterns for $\text{BaMgAl}_{10}\text{O}_{17}: \text{Eu}^{2+}$ under different reaction temperatures

Figure 7 shows the typical XRD patterns of the sol-gel derived $\text{BaMgAl}_{10}\text{O}_{17}: \text{Eu}^{2+}$ samples under different reaction temperatures for 4 h. At 850°C , the sample is amorphous. When the temperature rises to 1200°C , the BAM phase begins to form but still has an impurity peak (BaAl_2O_4). Farther rising to 1250°C , the impurity peak disappeared and forms a well BAM phase. It matches well with JCPDF card (No. 26-0163) of BAM. When the temperature rises to 1300°C , it is also single-phase with the crystallinity much improved.

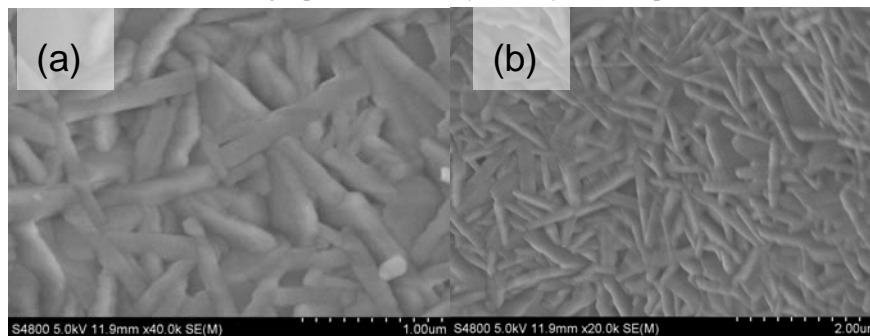


Figure 8: SEM images of BAM phosphors synthesized at (a) 1250°C , (b) 1300°C

As shown in Fig.8, the images exhibit the SEM micrographs of the BAM samples under 1250°C (a) and 1300°C (b). As $\text{BaMgAl}_{10}\text{O}_{17}$ has the crystal structure of β -alumina, the particle takes the form of hexagonal platelets when the crystal freely grows^[9]. In our work the images of (a) and (b), the nanorods could be obviously seen and has a homogeneous grain size at 80-100nm in diameter and 0.8-1 μm in length. This morphology is different from that bulk BAM synthesized by other methods which has irregular morphology, such as the solid-state method, oxalate co-precipitation process, microwave irradiation synthesis methods^[10-12].

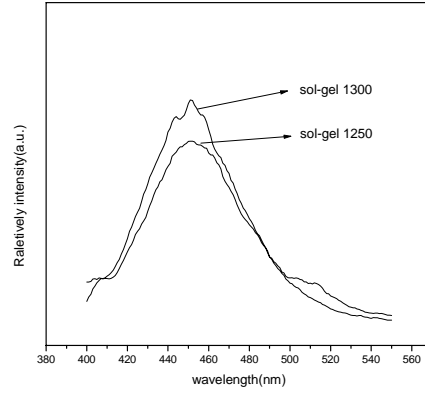


Figure 9: Emission spectra of $\text{BaMgAl}_{10}\text{O}_{17}:\text{Eu}^{2+}$ blue nano-phosphors synthesized by sol-gel method under 1250°C and 1300°C ($\lambda_{\text{ex}}=147\text{nm}$)

Figure 9 illustrates the comparison of the emission spectra of BAM nano-phosphors synthesized by sol-gel method under 1250°C and 1300°C by 147 nm excitation. As shown in Fig.9, a broad emission band could be seen and it attributes to the $4f^65d \rightarrow 4f^7$ ($^8S_{7/2}$) transition of Eu^{2+} . With the temperature increasing from 1250°C to 1300°C , the emission intensity of these nano-phosphors by 147 nm excitation enhanced about 22%. This is consistent with the result of XRD due to the improvement of the crystallinity.

3.4 Comparison to commercial phosphor

Table 1 shows the ratio of emission intensity and the color coordinates of the tri-color nano-phosphor compared with commercial phosphor. The emission intensity of nano-scaled $\text{YBO}_3:\text{Eu}^{3+}$, $\text{ZnSiO}_4:\text{Mn}^{2+}$ and $\text{BaMgAl}_{10}\text{O}_{17}:\text{Eu}^{2+}$ reaches 78.8%, 86%, 78.15% respectively compared with the commercial phosphor. The color coordinates of nano-scaled $\text{YBO}_3:\text{Eu}^{3+}$ and $\text{ZnSiO}_4:\text{Mn}^{2+}$ is superior to commercial bulk phosphor and more close to the National Television Systems Committee (NTSC). For nano-scaled $\text{BaMgAl}_{10}\text{O}_{17}:\text{Eu}^{2+}$, the y value of the coordinates is lower than the value of both commercial phosphor and NTSC which means that it is useful for restricting the decrease of BAM efficiency during application.

Table 1: The ratio of emission intensity and color coordinates of the tri-color nano-phosphor compared with commercial phosphor

Nano-scaled phosphor	$\text{YBO}_3:\text{Eu}^{3+}$	$\text{ZnSiO}_4:\text{Mn}^{2+}$	$\text{BaMgAl}_{10}\text{O}_{17}:\text{Eu}^{2+}$
Ratio (compared with commercial phosphor in emission intensity)	78.8%	86%	78.15%
Color coordinates of nano-scaled phosphor	(0.644,0.356)	(0.219,0.646)	(0.143,0.068)
Color coordinates of commercial phosphor	(0.645,0.355)	(0.248,0.649)	(0.144,0.069)
Color coordinates of NTSC	(0.67,0.33)	(0.21,0.71)	(0.147,0.08)

4. Conclusion

The nano-scaled phosphors $\text{YBO}_3:\text{Eu}^{3+}$, $\text{ZnSiO}_4:\text{Mn}^{2+}$ and $\text{BaMgAl}_{10}\text{O}_{17}:\text{Eu}^{2+}$ were synthesized by solvent-thermal, hydrothermal and sol-gel processes respectively and the relating morphologies of the phosphors were nano-sheet, nano-sphere and nano-rod. By 147nm excitation, the $\text{YBO}_3:\text{Eu}^{3+}$ nano-sheets exhibit 78.8% on emission intensity of that of commercial phosphor and better color purity than the latter; The $\text{ZnSiO}_4:\text{Mn}^{2+}$

nano-spheres show the strongest emission intensity than ZnSiO₄: Mn²⁺ of other morphologies and reaches 86% of that of the commercial phosphor; The BaMgAl₁₀O₁₇: Eu²⁺ nano-rods represent 78.15% of the emission intensity of commercial phosphor, and obtained low γ value of the BAM nano-rods suggesting that it was helpful for enhancing the thermal stability. All of the results indicated that the tricolor nano-scaled phosphors had an optimistic application prospect in PDP.

Acknowledgements This work is supported by the “National Natural Science Foundation of China (10874061)”, “the Project of the combination of Industry and Research by the Ministry of Education and Guangdong Province (Grant No.0712226100023)” and “the Research Fund for the Doctoral Program of Higher Education (RFDP No.200807300010)”.

Note In this paper, the data of YBO₃: Eu³⁺ nano-phosphor is provided by Qizheng Dong, the data of ZnSiO₄: Mn²⁺ nano-phosphor is provided by Xue Yu, and the data of BaMgAl₁₀O₁₇: Eu²⁺ nano-phosphor is provided by Zhaofeng Wang.

Reference

- [1] I. Y. Jung, Y. Cho, S. G. Lee and S. H. Sohn, “Optical properties of the BaMgAlO: Eu phosphor coated with SiO for a plasma display panel,” *Appl. Phys. Lett.* 87, 191908 (2005)
- [2] K. B. Kim, K. W. Koo, T. Y. Cho, and H. G. Chun, “Effect of heat treatment on photoluminescence behavior of BaMgAl₁₀O₁₇: Eu phosphors,” *Mater. Chem. Phys.* 80,682 (2003)
- [3] Y. H. Wang, F. Li, “Synthesis of BaAl₁₂O₁₉:Mn²⁺ nanophosphors by a reverse microemulsion method and its photoluminescence properties under VUV excitation,” *J. Lumin.* 122-123, 866-868 (2007).
- [4] Y. Zhou, J. Lin, M. Yu, S. Wang, H. Zhang, “Comparative study on the luminescent properties of Y₃Al₅O₁₂:RE³⁺ (RE: Eu, Dy) phosphors synthesized by three methods,” *Mater. Lett.* 56, 628 (2002).
- [5] S. Yin, M. Shinozaki, T. Sato, “Synthesis and characterization of wire-like and near-spherical Eu₂O₃-doped Y₂O₃ phosphors by solvothermal reaction,” *J. Lumin.* 126 (2007) 427–433.
- [6] R. T. Wegh, H. Donker, K. D. Oskam, and A. Meijerink, “Visible quantum cutting in LiGdF₄: Eu³⁺ through downconversion,” *Science* 283 (1999) 663.
- [7] H. Maas, A. Currao, G. Calzaferri, “Encapsulated lanthanides as luminescent materials,” *Angew. Chem. Int. Ed.* 41 (2002) 2495.
- [8] H. F. Wang, Y. Q. Ma, G. S. Yi, and D. P. Chen, “Influence on the Growth and Changes of Several Phenotypes of Cultured Rat MsC Transfected by DCN Gene,” *Mater. Chem. Phys.* 82, 414 (2003).
- [9] D. Ravichandran, S. T. Johnson., “A polymer solution process for synthesis of (Y,Gd)₃Al₅O₁₂:Ce phosphor particles,” *S. Taya, J. Non-Cryst. Solids.* 351,697 (2005).
- [10] S. S. Lee, Hee Jin Kim, Song-Hb Byeon, Jung-Chul Park, and Dong-Kuk. Kim, *Mater. Interfaces.* 44, 4300-4303 (2005).
- [11] Z. H. Zhang, Y. H. Wang, “coprecipitation synthesis and photoluminescence of BaMgAl₁₀O₁₇: Eu²⁺ phosphor for PDP application,” *Mater. Sci. Forum.* 475-479, 1701-1704 (2005).
- [12] K. T. Kuo, S. P. Lee, S. Y. Chen, B. M. Cheng, H. C. Lu, C. C. Ting, “Effect of microwave irradiation on surface characteristics and luminescent properties of BaMgAl₁₀O₁₇ : Eu blue phosphors,” *J. Chem. Solid.* 69,362-365 (2008).

Several Algorithms in Computer Graphics

Yong-Kui Liu Heng-Bo Zhang

College of Computer Science and Engineering, Dalian Nationalities University, Dalian Development Zone 116600, China
Tel./Fax: 86-41187656170. E-mail: ykliu@dlnu.edu.cn

Abstract: Three fundamental algorithms of computer graphics are presented first. The first one is an algorithm for approximating the curve with a curve-intersecting poly-line. The idea can also be used for surface approximating. The second one is an efficient algorithm for line clipping against convex windows. It sets a basis for polygon clipping. The third one is an algorithm for recognition of the chain code of curves with the method of computer graphics. The testing results show that the new algorithms not only can recognize both the perfect and the noise chain codes, but also with a high speed. Then the advantages of the hexagonal grid over the traditional square grid for graphics display and our research works on the attempt for implementing the hexagonal grid display are introduced. Finally, an application of graphical technique on processing and recognizing of NaXi Pictographs used by Chinese national minority NaXi are introduced.

Key Words: Computer graphics, algorithm, optical material

1 INTRODUCTION

Nowadays computer graphics are getting widely used. The fundamental algorithms of computer graphics are the basis of graphical systems. They are called repeatedly in each graphical application, so the efficiency of them is very important. These algorithms have been researched for a long time, so it is difficult to get even a little progress.

Many applications need new functions of computer graphics, and new 2D and 3D displays.

2 SEVERAL FUNDAMENTAL ALGORITHMS OF COMPUTER GRAPHICS

2.1 The Approximation of the Circle-intersecting Poly-line^[1]

The traditional approximation method to the circle is expressed by the inner polygon as shown in Fig.1.

We have put forward the new method of using the arc-intersecting polygon instead of the inner polygon. The approximation error is reduced as shown in Fig.2.

In realizing the algorithm, no other change is needed except the addition of ΔR to the radius R of the circle. It is the same to use the traditional algorithm on a circle with the radius $R+\Delta R$. After calculating, the result shows that when

$$\Delta R = \frac{1 - \cos \frac{a}{2}}{1 + \cos \frac{a}{2}} R$$

the largest error between the polygon and the circle arc will be the minimum. When compared with the traditional method of approximating the circle with the inner polygon, the error is

reduced almost by half.

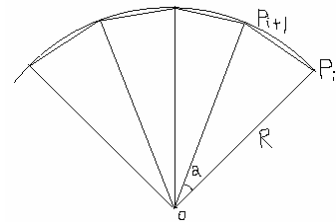


Fig.1 Traditional approximation to the circle by the inner polygon

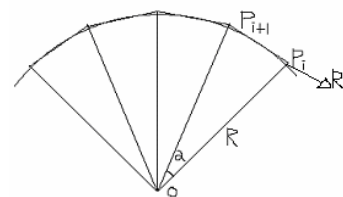


Fig.2 Approximation of the circle by the arc-intersecting polygon

2.2 The approximation of the general curve intersecting poly-line

For the approximation of the general curve, most researchers study how to choose points on the curve to obtain the least amount of errors or how to use less points in the case of the definite error. For instance, the algorithm presented by Pikaz and Dinstein uses the least number of definite points under the condition of definite error.^[2]

This section will extend the idea of the last section to the approximation of any general curve, which means to approximate the curve with the curve-intersecting poly-line.

The parameter curve is presented :

$$P(t) = [x(t), y(t)], \quad 0 \leq t \leq 1$$

The traditional method of approximation to the parameter curve is to choose example points evenly on the curve $P(t_i), (i=0,1,\dots,n, \quad 0 \leq t_i \leq 1)$, then connect these points in turn to form the poly-line. When the parameter value gets dense enough, this poly-line can be used to replace the parameter curve.

Now choose two neighboring points on the curve $P_i = P(t_i), \quad P_{i+1} = P(t_{i+1})$, then the unit normal of the two points will be :

$$n_i = (-\dot{y}(t_i), \dot{x}(t_i)) / \|n_i\|$$

$$n_{i+1} = (-\dot{y}(t_{i+1}), \dot{x}(t_{i+1})) / \|n_{i+1}\|$$

the equation of the line passing through the points P_i, P_{i+1} will be :

$$\frac{y - y_i}{x - x_i} = \frac{y_{i+1} - y_i}{x_{i+1} - x_i}$$

after calculating, the equation will be as follows:

$$Ax + By + C = 0$$

where, $A = y_{i+1} - y_i, \quad B = -x_{i+1} + x_i, \quad C = (x_{i+1} - x_i)y_i - (y_{i+1} - y_i)x_i$ the distance from the point $P(t)$ on the parameter curve to the line $P_i P_{i+1}$ will be

$$D(t) = \frac{|Ax(t) + By(t) + C|}{\sqrt{A^2 + B^2}}$$

after calculating :

$$D'(t) = |A\dot{x}(t) + B\dot{y}(t)| / \sqrt{A^2 + B^2}$$

suppose $D'(t) = 0$, the result of t^* can be obtained. When there is more than one result, choose the one between t_i and t_{i+1} . $P(t^*)$ is the farthest point of the i th segment of the curve from the approximating line segment. The distance is $D(t^*)$.

To approximate the curve by the curve-intersecting poly-line, we choose to move the line $P_i P_{i+1}$ to the direction of $P(t^*)$. The moved line intersects with the two normal lines n_i, n_{i+1} (at P_i and P_{i+1} on the curve) at R_i, R_{i+1} , as shown in Fig.3. Suppose the excursion distance is $\Delta R_i, \Delta R_{i+1}$, then two new points will be obtained after the excursion :

$$R_i = P_i + \Delta R_i \cdot n_i, \quad R_{i+1} = P_{i+1} + \Delta R_{i+1} \cdot n_{i+1}$$

The largest distance from the curve to the line $P_i P_{i+1}$ is $D(t^*)$, therefore, when the distance from the moved line $R_i R_{i+1}$ to the original line $P_i P_{i+1}$ is $D(t^*)/2$ (in Fig.3 $\|PT\| = D(t^*)/2$), the distance error from the parameter curve $P(t)$ to the line $R_i R_{i+1}$ became the minimum, $D(t^*)/2$. Let $\alpha = \angle R_i P_i T$,

$$\cos(\alpha + \pi/2) = \frac{n_i \cdot \overrightarrow{P_i P_{i+1}}}{\|\overrightarrow{P_i P_{i+1}}\|}$$

then

$$\sin \alpha = -\frac{n_i \cdot \overrightarrow{P_i P_{i+1}}}{\|\overrightarrow{P_i P_{i+1}}\|}$$

So, the excursion ΔR_i of the point P_i is

$$\Delta R_i = \frac{\|\overrightarrow{P_i R_i}\|}{\cos \alpha} = \frac{\overline{P_i T}}{\cos \alpha} = \frac{D(t^*)}{2 \cos \alpha} = \frac{D(t^*)}{2 \sqrt{1 - \sin^2 \alpha}}$$

then the point R_i is determined.

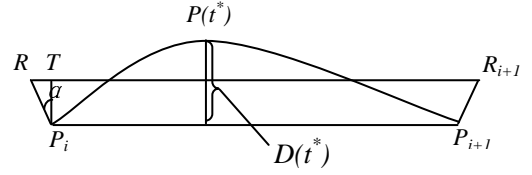


Fig. 3 The calculation of line segment moving and the points excursion

To compare the efficiency of the coded algorithms, we coded the new algorithm and the traditional algorithm. The experimental results show that the approximation error of the new method is significantly less than the traditional one. After analysing the experimental results, we can see that the largest distance error is reduced almost by half, mostly distributed in the range of 50% ~ 53%. The experimental results support our theoretical proposition.

On the other hand, under the same limited largest error, the points needed by the new algorithm are 65% ~ 74% less than the traditional one.

It still needs to be pointed out that the new technique for curve approximation may be applied directly to the surface approximation. For instance, Coons Surface can be approximated by the technique of approximating its borderline curve, therefore it can be treated by treating with the borderline curve.

2.3 An algorithm for line clipping against convex windows

A well-known algorithm for line clipping against convex windows is Cyrus-Beck algorithm^[3]. Firstly, it divide the intersections into two groups by the product of the vector of line and the vector of the window's edge. Then, it searches for the minimum product in the group which the product is bigger than zero and the maximum product in the other group, which is the endpoint of visible part. However it can not be used for concave window, so Cyrus-Beck algorithm only can apply for the line clipping against convex window.

This section proposes an efficient algorithm for line clipping against general polygon. For this algorithm, firstly, we choose a reference point (X_f, Y_f) on the line to be clipped or on its extension. This reference point must be in the left of the leftmost endpoint of the polygon or below the most lowest endpoint. Then we calculate the slope of the reference point to each vertices of the polygon. The expression is as follows:

$$vs_i = \frac{y_i - Y_f}{x_i - X_f}$$

(x_i, y_i) is the i th vertices and one of X_f and Y_f can be chosen as zero, so the calculation is one subtraction and one division.

Then we could judge whether the slope of the line to be clipped is between the slopes of the two adjacent vertices. If it is true, the line to be clipped intersects the edge between the two adjacent vertices; Otherwise they don't intersect, as shown in Fig.4. If they intersect, then calculate the intersection.

In this paper, we use this algorithm for the detection and calculation of the polygon's intersections. This algorithm has

very simple detection condition.

A similar method to find out the intersections is presented by Skala^[4]. It uses a product of the vectors are calculated to determine whether the line to be clipped is between two adjacent vertices which define the edge.

From above description, we can determine whether an intersection is entry or exit point when it is calculated. The method is that judging a intersection is entry or exit point depend on the order of intersection order is odd or dual on the line to be clipped. the odd is entry point, the dual is exit point. We could get the intersections order on the line to be clipped by the x or y coordinates value of the intersection. If we get a intersection's x coordinates value, finding the intersection is on the line to be clipped, the intersection doesn't be inserted into the polygon link. But removing that intersection may change the odd or dual order of the other intersections. Our method is, if the direction of the line to be clipped is form A to B for example, the useless intersections on the extension of both sides A and B don't be saved, but the number of the useless intersections on the extension of side A should be remained to keep the correct order of the useful intersections.

In the clipping algorithm, we determine which parts of the line to be clipped are in the polygon window by the order of the intersections. But if the line to be clipped crosses one or more vertices of the polygon, the rule doesn't apply. it is a special cases, but need to be analysed. we discuss the cases

later in this paper.

For testing the efficiency of the new algorithm, it is compared with Cyrus-Beck method and Skala method in term of calculations needed. Table 1 lists the calculations needed by the methods for clipping a line against an edge of the window. It is obvious that the new method needs less calculations than the other methods.

Based on the new method, a software package for "Intersection" "Difference" and "Union" operations between regions was developed. The regions can consist of more than one concave polygon with holes.

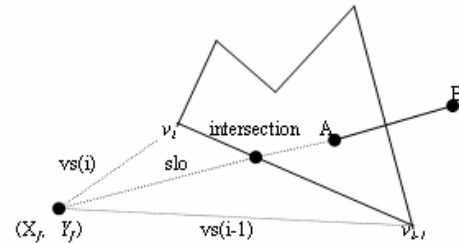


Fig.4 Finding intersection by the Slope Method (slo represents the slope of the line to be clipped)

Table 1. Comparison of calculations needed to clip against one edge of the window by the new method and the existing methods

Methods	Edge Calculations	Clipping by an edge without intersecting with the line to be clipped			Clipping by an edge intersecting with the line to be clipped		
		Division Multiplication	Addition and subtraction	Comp arison	Division Multiplication	Addition and subtraction	Comp arison
Cyrus-Beck method		5	6	6	5	6	6
Skala method		2	1	4	5	6	4
The new method		1	1	4	5	6	4

2.4 Recognition of the chain code of curves with the method of computer graphics

Straight lines and curves are the most basic patterns that we always encounter. They are usually represented in chain code shown in Fig.5. The recognition of the chain code of a straight line has been fully discussed. Freeman^[5] suggested the following criteria which the chain code of a line must meet: (1) At most two basic directions are present and these can differ only by unity, modulo eight. (2) One of these values always occurs singly. (3) Successive occurrences of the principal direction occurring singly are as uniformly spaced as possible. After that, a number of properties that the chain code of a line has have been proved^[6,7], and Wu^[8] presented an algorithm to recognise whether a chain code is the chain code of a line according to the properties. In 1995, Yuan and Suen^[9] proposed an O(n) algorithm for identifying straight line from a chain code.

For the recognition of curves, a method often used is Hough Transform method^[10] which works on the image-based patterns (not on chain code). Since the properties of the chain code of a curve are more complicated than those of a line, it seems that there is not an efficient method for the recognition of the chain codes of curves, though there are some works on it. For example, in 1998, Zingaretti et al. ^[11] proposed a fast method for chain coding of region boundaries and

Giraldoetal.^[12](in 1999) presented their research achievements on finding out the properties of the chain code or digitisation of circular and other curve contours In this section, a new concept of recognising the chain code of curve patterns with the method of Computer Graphics is proposed and the algorithms for recognising the chain codes of line, circle and ellipse are given.

2.4.1 A New Concept for Recognition of the Chain Codes of Lines and Curves

In this section we propose a new concept — pattern recognition with the method of computer graphics, to recognising the chain codes of line or curves. That is, the parameters of line or curves (e.g. the endpoints of the line) are first obtained by analysing the chain code. Then with these parameters as input, the line or curve drawing algorithm is used to generate the line or curve. Meanwhile the generated line or curve is compared with the chain code. If they match each other, the chain code is of a line or a curve; otherwise it is not. Since the line and curve drawing algorithms are high-speed and use only integer arithmetic, the recognition algorithms based on them is also speeded up. The eight Freeman code values have the following (Table 2) orresponding relationship with the movements generated by curve drawing algorithm along the curve (see Fig.5).

In program, this relationship can be implemented with only a CASE statement. Considering the possible noise in the input pattern (then in the chain code), some small deviation of

the chain code from the curve generated by the drawing algorithm is tolerated by the curve recognising algorithm. How much deviation can be tolerated is controlled by a threshold T which can be set by the user according to the demands of applications. For example supposing T is set to 2, if the deviation between the chain code and the generated curve is greater than 2 pixel-sizes, it is believed that the chain code is not of the curve being recognised. In the following sections, the method is given in detail for the recognition of line, circle and ellipse.

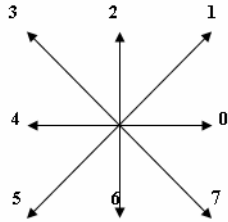


Fig.5. Freeman chain code

2.4.2 Recognition of the Chain Code of a Line with a Line Drawing Algorithm

Suppose that the chain code consists of n symbols of Freeman code and it is put in an array $C[1:n]$. First the chain code is traversed to determine the endpoints (suppose the starting endpoint of the line is $(0,0)$) of the line for the line drawing algorithm. Meanwhile, the chain code is checked against the Freeman's first two criteria described in Section 1. Then the line drawing algorithm such as the Bresenham's line algorithm^[14] is used to generate the points along the line path. If the deviation between the generated point (x_g, y_g) and the point (x_c, y_c) defined by the chain code is greater than T , the chain code is not of a line. Based on the above discussion we obtain the following recognition algorithm (Fig.6).

2.4.3 Recognition of the Chain Code of a Circle with a Circle Drawing Algorithm

First we need to find the radius R from the chain code. Then supposing that the circle is centred at the origin of the coordinate system, i.e. point $(0,0)$, we seek the code that is at the top of the circle, i.e. the code corresponding to the point $(0,R)$ which is the point the circle drawing algorithm starts at. Finally the circle drawing algorithm, starting from the point $(0,R)$, is used to check the chain code, starting from the code corresponding to $(0,R)$, code by code. If a deviation between the point given by any code element and the corresponding point generated by the drawing algorithm is greater than T , the chain code is not believed to be a circle. If no such a deviation has been found by the time the drawing algorithm finishes, the chain code is believed to be a circle. To sum up, the algorithm has the following three steps:

Find the radius R .

Seek the starting code element corresponding to $(0,R)$.

Check each code element in the chain code by circle drawing algorithm starting from $(0,R)$ to see if the code is on a circle.

2.4.4 Comparison of the Algorithms

To evaluate the new algorithm for line recognition, We compare it with two typical line recognition algorithms — Wu's algorithm^[7] and Yuan and Suen's algorithm^[8]. To compare the time complexity of the algorithms, we mainly consider the time complexity for the algorithm to deal with the third criterion of a line described in Section 1, because this criterion is the most difficult to deal with and all the algorithms

consume most of their time on it. The first two criteria are easy to deal with and the algorithms have almost the same time complexity to deal with them.

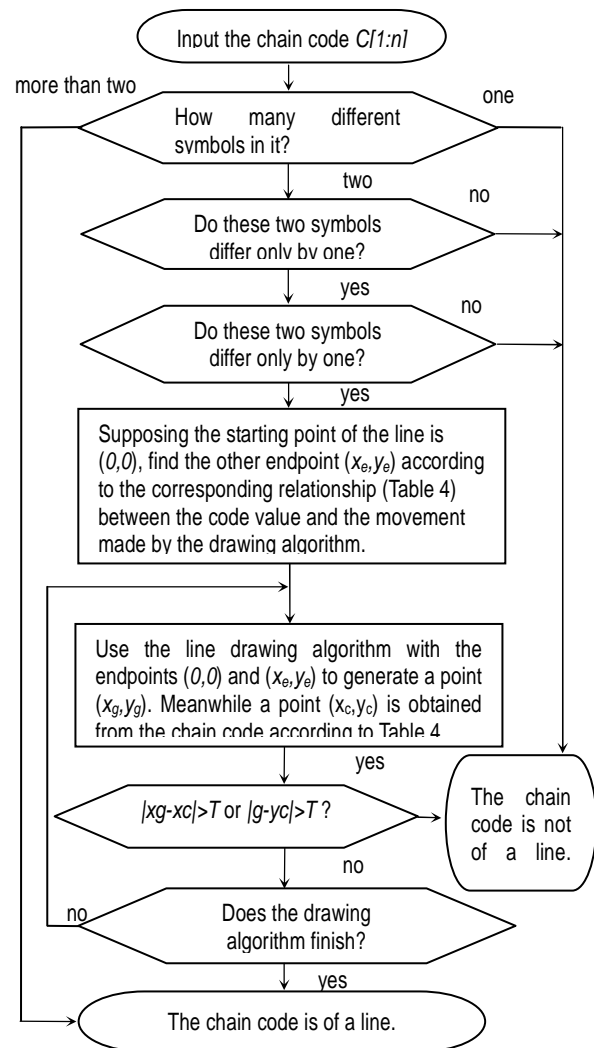


Fig.6. The new recognition algorithm for the chain code of a line

Wu's algorithm represents the traditional line recognition algorithm. Generally more than one passes to go through the chain code are needed by it, except some special lines such as vertical or horizontal lines. The Yuan and Suen's algorithm and the new algorithm need just one pass scan to the chain code. But the Yuan and Suen's algorithm requires a great number of calculations to calculate the upper and lower bounds and the angles for the code elements during the scan, and float arithmetic is used. The new algorithm uses the line drawing algorithm to deal with the third criterion. We know that the Bresenham's line drawing algorithm^[14] uses the minimum calculation of only 3 integer additions and 1 integer comparison for each point.

Addition to the least calculation, the new algorithm has another main advantage, i.e. it can be used to recognise the chain code with noise by adjusting the threshold value T , while the other two algorithms can not. The above comparison is summarised in Table 3.

For the recognition of the chain codes of circle and ellipse, works have been done^[12, 13] on finding out the properties of the chain code of the curves. Because the properties of the chain

code of circle or ellipse are much complex than that of straight line, it is difficult to develop an efficient recognition algorithm based on them. The new circle and ellipse recognition algorithm proposed in this paper has the same advantages as the new line recognition algorithm has, i.e. only a small

amount of integer calculations of 4 or 5 additions and one comparison are used, which is decided by the circle^[15] and ellipse^[16] drawing algorithms, and the new algorithms can be used to recognise the chain code with noise.

Table 2. Relationship between the Freeman code value and the corresponding movement made by the curve drawing algorithm

Freeman code value	0	1	2	3	4	5	6	7
Movement by curve drawing algorithm	x+1→x	x+1→x y+1→y	y+1→y	x-1→x y+1→y	x-1→x	x-1→x y-1→y	y-1→y	x+1→x y-1→y

Table 3. Comparison of the line recognition algorithms

	Number of scans	Arithmetic used	Calculation for each code	Capability
Wu's algorithm	More than one passes	Integer	Middle	Not tolerated for noise
Yuan and Suen's algorithm	One pass	Float	More	Not tolerated for noise
New algorithm	One pass	Integer	Least	Can be justified to tolerate noise

3 HEXAGONAL GRIDS FOR GRAPHICS DISPLAY

Mathematicians have demonstrated that the best disposition of a discrete set of points on the plane can be reached if the points are on a hexagonal grid^[13]. In recent years, studies by scientists in computer graphics and image processing have shown the advantages of the hexagonal grid over the square grid.

Let R indicate the set of real number. Let u and v be two linearly independent vectors of R^2 . The set $S=(u,v)$ of all vectors a of R^2 of the form $a=mu+nv$ (where m and n are integers) is called a lattice of points of R^2 . In a lattice S every vector of the grid can be unequivocally identified by the ordered pair of (m,n) . The two most common lattice classes are the square grids $S_4((1,0),(0,1))$ and the hexagonal grids $S_6((1,0),(\frac{1}{2}, \frac{\sqrt{3}}{2}))$, as shown in Fig.7.

On the hexagonal grid, digitizations display a better connectivity and are perceived as being approximated by small polylines, whereas on the square grid, digitizations are still perceived as being approximated by pixels. Such a perception of single pixels disturbs the impression of continuity of the discretized line. This is due to the fact that in the square grid a pixel's neighbours are not placed all at the same distance, as the diagonal neighbours lie at a distance that is $\sqrt{2}$ times greater than the distance of the vertical and horizontal neighbours. Moreover, two diagonal neighbours in the square grid have only one point in common, whereas two horizontal or vertical neighbours of the square grid, and all the neighbours of a pel in the hexagonal grid, have one segment in common with their neighbour. This fact produces thickness variations in square digitizations, leading to a greater edge "business" and to a thinner average width in a line's discretization.

We have developed algorithms for drawing line, circles and ellipses and for line clipping on hexagonal grids^[14,15]. Some algorithms for image processing on hexagonal grids are also developed, such as the algorithm for digital sampling etc.

Now we discuss some issues related with realizing hexagonal grid display. In fact, there are only small difference

between the square grid display and the hexagonal grid display. The difference is that the start point for each line of scan is on the same vertical line for the square grid, while for the hexagonal grid the scanning for the odd lines starts half pixel behind that for the even lines.

We are familiar to the square grids and may be feel inconvenient to use hexagonal grids. To make it easier, we may design the coordinates as shown in Fig.8 which we call Hexagonal-square coordinates. However this is not a coordinate system to develop algorithms. The method we use is to develop algorithms based on the hexagonal grids. The input hexagonal-square coordinates are converted into the hexagonal grids simply by $x = x - y \text{ DIV } 2$ (where DIV means integer dividing) at the beginning of the algorithms, and the results are converted back to the hexagonal-square coordinates by $x = x + y \text{ DIV } 2$ at the end of the algorithms. The y coordinate is not changed. In this way the user can use the hexagonal-square coordinates.

These works lay foundations for implementing hexagonal grid display.

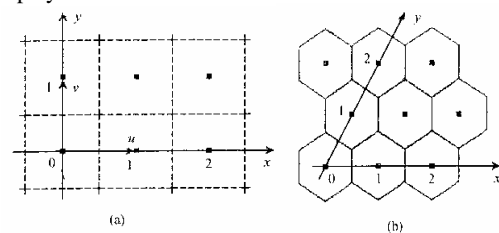


Fig.7 Square grids and the hexagonal grids

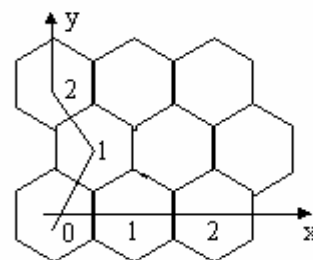


Fig.8 Hexagonal-square coordinates

4 PHYSICAL 3-D DISPLAY NEEDS FOR NEW OPTICAL MATERIALS

The world we live in is three-dimensional. Scenes should also been displayed three dimensionally. Researches have been made into displaying virtual 3D scenes on plane screens. However, real physical 3D displays have not been made by now. In this section, our tentative ideas of developing a real physical 3D display are introduced, which requires a new optical material.

The display medium of real physical 3D display we imagine should be consist of a transparent cube which can be divided into $L \times M \times N$ small cubes called voxel, where L , M and N are separately the lengths of the cube in X , Y and Z directions. Each voxel can be stimulated separately with different colors. When a voxel is stimulated, the others behind it will be covered even though they are also stimulated. The voxels can be controlled (by laser, electricity, or others) from the back surface and the bottom surface of the transparent cube.

We need such materials.

There would be many advantages of the physical 3D display. The scene displayed is three-dimensional and various sides of it can be seen from different viewpoint. Moreover the algorithms for processing graphics and images are much more simple than on a virtual 3D display, because some procedures for virtual scene such as hidden surface removal should be made on the physical 3D display. For example, the inner parts of object are easy to be displayed by removing the surface. That can be done by resetting the front voxels from the viewpoint.

When it is used as a TV set, the program is made by four cameras working simultaneously, from four directions of front, up-front, left-front and right-front. The program is digitized by modeling.

5 NAXI PICTOGRAPHS

NaXi pictograph, which is the only hieroglyph in use now, is important for researching into the evolution of the characters used by human being. Following is some words of NaXi pictograph.



NaXi pictograph has been processed by hand, which is very inefficient. We developed a NaXi pictograph processing system which includes the pictograph outline font lib, the coding and input module, the embedded module and so on. It meets the needs of informational processing of NaXi pictograph. In view of the complexity of coding NaXi pictograph, the Initial Simplification Input Method is proposed for raising the efficiency and speed. For rapidly inputting mass pictograph, we have made effective researches on automatically recognizing NaXi pictograph. The NaXi pictograph font discrimination theory based on Bayesian method is presented. With that NaXi Pictograph characters can be divided into two classes, namely NaXi Hieroglyph and NaXi Ideogram, thus we can recognize those by respective method. With this method, the difficulty of recognizing can be reduced and the efficiency and the correct rate can be raised.

The development of the NaXi Pictograph Information Processing System fills the gaps in this field.

6 CONCLUDING REMARKS

Three algorithms are proposed and proved to be efficient. The advantages of the hexagonal grid over the traditional square grid for graphics display and our research works on the attempt for implementing the hexagonal grid display are introduced. The conceiving of developing a physical 3D display is also introduced, which needs new optical materials. Finally, an application of graphical technique on processing and recognizing of NaXi Pictographs used by Chinese national minority NaXi are introduced.

Acknowledgement This work was supported by the National Natural Science Foundation of China (60675008), the Scientific Fundation of Liaoning Province and the State Ethnic Affairs Committee of China.

References

- [1] Liu Yong-Kui. Algorithm for Circle Approximation and Generation[J]. Computer-Aided Design, 1993, 25(3): 169-171.
- [2] Pikaz A, Dinstein I. Optimal polygonal approximation of digital curves[J]. Pattern Recognition, 1995, 28(3):373~379.
- [3] Cyrus M, Beck J. Generalized two- and three-dimensional clipping[J]. Computer & Graphics, 1978; 3(1): 23-28
- [4] Skala V. $O(\lg N)$ line clipping algorithm in E^2 [J]. Computers & Graphics. 1994, 18: 517-524.
- [5] H.Freeman. Boundary Encoging and Processing[M]. In Picture Processing and Psychopictorics, Academic Press, New York, (1970).
- [6] S.H.Y.Hung. On the Straightness of Digital Arcs[J]. IEEE Transactions on Pattern Analysis and Machine Intelligence, 1985, 7(2): p.203-215.
- [7] M.Gaafar. Convexity Verification, Block-chords and Digital Straight Lines[J]. Computer Graphics and Image Processing, 1977, 6(4): p.361-370.
- [8] L.D.Wu. On the Chain Code of a Line[J]. IEEE Transactions on Pattern Analysis and Machine Intelligence, 1982, 4(3): p.347-353.
- [9] J.Yuan and C.Y.Suen. An Optimal $O(n)$ Algorithm for Identifying Line Segments from a Sequence of Chain Code[J]. Pattern Recognition, 1995, 28(5): p.635-645.
- [11] P.Zingaretti, M.Gasparroni and L.Vecci. Fast Chain Coding of Region Boundaries[J]. IEEE Transactions on Pattern Analysis and Machine Intelligence, 1998, 20(4): p.407-414.
- [12] A.Giraldo, A.Gross and L.J.Latecki. Digitizations Preserving Shape[J]. Pattern Recognition, 1999, 32(3): p.365-376.
- [13] C.A.Rogers. Packing and Covering[M]. Cambridge: Cambridge University Press, 1964. 98-123.
- [14] Liu Yong-Kui. The Generation of Straight Lines on Hexagonal Grids[J]. Computer Graphics Forum, 1993,12 (1):27-31.
- [15] Liu Yong-Kui. The Generation of Circular Arcs on Hexagonal Grids[J]. Computer Graphics Forum, 1993, 12 (1):21-26.

Space Charge Effects on Breakdown of Oil-paper Insulation for Ultra-high Voltage Transformer

Zhou Yuan-xiang*, Li Guang-fan**, Sun Qing-hua*, Wang Yun-shan*,
Li Jin-zhong**, Jiang Xin-xin*, Qiu Yu-zhou*, Wang Ning-hua**

*State Key Lab of Control and Simulation of Power Systems and Generation Equipments,
Dept of Electrical Engineering, Tsinghua University, Beijing, China 100084;

**China Electric Power Research Institute, Haidian District, Beijing, China 100192

Zhou-yx@tsinghua.edu.cn

Abstract: The structural features, insulation level and special problems of power transformer for Ultra-high Voltage (UHV), which means 1000 kV AC and 800 kV DC power transmission project in China, are presented in this paper. The space charge effect is the key problem of insulation system in UHV equipments. This paper studied the space charge characteristics of oil-paper insulation materials by Pulsed Electro-Acoustic (PEA) method. The breakdown and creeping discharge of oil-paper insulation were also experimentally studied. The connections between space charge and breakdown in oil-paper were discussed. The results showed that the space charge inside oil-paper insulation resulted in an electrical field distortion up to 40%. The space charge dissipated fast when depolarized and this phenomenon played a key role in oil-paper insulating performance in condition of polarity reversal under UHV. Breakdown and creeping discharge experiments of oil-paper insulation during the polarity reversal showed that polarity reversal effect existed in oil-paper insulation systems.

Key Words: UHV, Transformer, Space Charge, Oil-paper Insulation

1. INTRODUCTION

The first 1000 kV Transmission Pilot Project in China, including two substations, one switching station and more than 650 km line, has just finished building in 2008. However, the insulation design of UHV power transformers cannot be extrapolated simply from 500 kV transformers. Ultra high voltage, large capacity, large size and space charge also brings special request to the structural style.

Moreover, principles of insulation coordination in 1000 kV transmission project is different from 750 kV or lower voltage class projects. And some insulation design can't be checked by the test voltage specified in the technical specification due to different principles of insulation coordination among different windings of UHV power transformers and other reasons such as large size.

Power transformers and converter transformers used in UHV transmissions as the central apparatuses have drawn

much attention. The research works on oil-paper insulation under UHV is one of those hot spots. Failures of oil-paper insulation, such as breakdown or creeping discharge, will bring damage to the insulation system. It has been proved that space charge has strong impacts on electrical field distribution and breakdown in insulation materials [1].

In traditional AC power transformers, oil-paper insulation operates under AC voltage for most of the time, and its distribution of electrical field is determined by dielectric constants of transformer oil and pressboard [2, 3]. The rate of dielectric constants of transformer oil and pressboard is about 0.5, and dielectric constants do not vary much along with the changes of electrical field or temperature. Therefore, the electrical field in transformer oil is twice than in pressboard, and most of the voltage is endured by transformer oil. However, it differs in converter transformers, especially for the distribution of DC electrical field, which is determined by electric conductivity. Under this situation, electrical field in pressboard is much higher than in transformer oil. Moreover, the electric conductivities of both transformer oil and pressboard vary in a large scale along with the range of electrical field, temperature and moisture content. Taken account of the complex structures of converter transformers, the electric conductivity of pressboard is anisotropic [4]. In a word, distribution of electrical field of converter transformers is more complex than traditional transformers due to the existence of DC electrical field, which varies along with electrical field, temperature and moisture content. Thus more research works are needed.

Since DC electrical field shows up in valve side winding of converter transformers, polarity reversal effect should be taken into account [5]. Polarity reversal effect was found out in DC subsea cable using cross-linked polyethylene (XLPE) as insulating material during 1970s [6]. Polarity reversal effect in DC cable means that, after the cable is applied one polarity DC voltage for a period of time, the breakdown strength of electric field with another polarity will decrease due to the effect of space charge accumulated in XLPE. Nowadays in UHV transmissions, polarity reversal effect caused by space charge limits the time of fast polarity reversal operation (about hundreds of millisecond).

Space charge accumulation and its effect on insulation are different under DC and AC respectively. In condition of high

voltage direct current (HVDC), space charge accumulation is easy to occur remarkably in insulation materials, which will lead to serious electrical field distortion and affect the insulating performance of material. [1, 7] The high voltage convert transformers and other equipments mainly use transformer oil and paper as insulation materials at present. Their insulation design bears not only AC operating voltage but also HVDC. The insulation accidents in operating of convert transformer account for about 50% of the total breakdowns. [3] At present the effect that space charges take on the insulation of converter transformers is short of direct basis. The effect mechanism of space charge in converter transformers also has insufficient evidence [2]. The study on space charge measurement technology is a hot issue nowadays. The studies on space charge property of PE are relatively numerous [8- 10]. On the other hand, concerning oil-paper insulation, although there are a few of studies on its space charge property [11, 12], they basically concentrate on cables. Space charge property of oil-paper insulation used in convert transformers is ignored.

In this paper, the structural features and insulation level of power transformer for 1000 kV power transmission project in China as well as special problems during the insulation test are presented in detail. The experiments on space charge, creeping discharge and breakdown in UHV oil-paper insulation are showed and space charge effects in UHV transformer are discussed.

2. UHV POWER TRANSFORMER

The operating voltage of UHV power transformer is up to 1000 kV, which means higher technical difficulty for design and manufacture. The insulation design of UHV power transformer cannot be extrapolated simply from 500 kV transformers. Many new problems have come out and special technologies should be taken. Breakdown processes in dielectric solids are very complicated and they are influenced by many factors. It is difficult to use one theory to explain all phenomena. However, space charge plays the key role in the breakdown process of oil-paper insulation.

So far, there is no international standard on the insulation level of UHV transformer. Fig.1 gives the drawing of UHV power transformer of China. The insulation level of 1000 kV power transformer of China is as follow: the lightning impulse withstand voltage is 2250 kV; the switching impulse withstand

voltage is 1800 kV; and the power frequency withstand voltage is 1100 kV/5min.

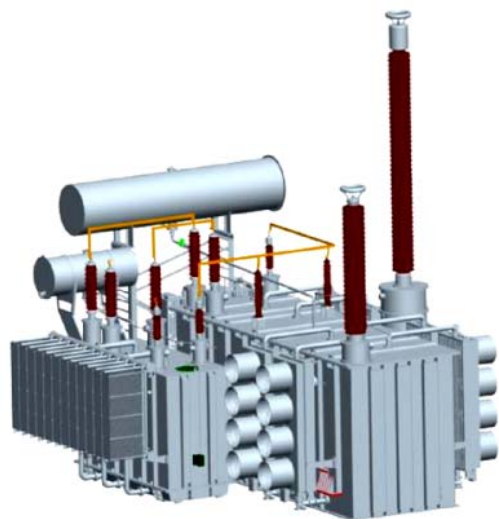


Figure 1. Master drawing of UHV power transformer of China.

Table 1 shows the insulation level of UHV transformers in the world. Japanese UHV transformer has the same capacity as that in China, but it uses the split type. The three transformers are developed by Toshiba, Mitsubishi, and Hitachi. And there are some problems in both design process and field test, which shows the great technique difficulty. Monomer structure is used in China. So the technique is more difficult and the difficulties are different from that in Japan. In the term of capacity and voltage of UHV power transformer of China, there is no precedent in the world [13].

Due to the high voltage, big capacity, and large size of UHV transformer, the stray parameters of the test circuit have great influence on the front time of voltage waveform in lightning impulse test. The standard waveform of the lightning impulse test voltage is $(1.2 \pm 30\%) / (50 \pm 20\%) \mu\text{s}$. Because of the big capacity and large size of the UHV transformer, the front time of the wave is inevitably extended, exceeding relevant standard greatly. The wave-front steepness mainly affect the longitudinal insulation of the winding. So the prolonging of wave front time may lead to relaxation of test on certain longitudinal insulation and strictness of test on main insulation. Therefore, in the process of UHV transformer's design, development, and test, great importance should be attached to the influence of the prolonging of wave front time of lightning impulse voltage waveform on the equipment insulation performance.

3. SAMPLE PREPARATION AND EXPERIMENT

DESIGN

The samples used in the space charge and breakdown experiments were made of sulphate electrical pressboard with the thickness of $320 \mu\text{m}$. Work the cardboard to a circular sample which is qualified to the PEA Space Charge measurement System [14] and do vacuum pumping for 24 hours. Then immerse the sample in clean transformer oil and dry in vacuum at $60 \text{ }^\circ\text{C}$. This kind of treatment method is used to simulate the partial circumstances in the oil-paper insulation of convert transformer.

In the space charge measurement, negative direct current field strength was applied from -5 kV/mm to -50 kV/mm respectively on samples under $20 \text{ }^\circ\text{C}$ for 30 minutes. The space charge accumulation and dissipation were measured during polarization and depolarization in order to observe the influence of field intensity on space charges.

Devices used in breakdown of oil-paper insulation were designed according to GB/T 1408.2-2006 [15]. Both High voltage electrode and ground electrode were immersed in transformer oil as well as the sample to avoid flashover during experiments. The samples used in breakdown experiments were $320 \mu\text{m}$ in thickness with a diameter of 150 mm.

The size of sample used in creeping discharge experiments is $100 \times 100 \times 1.5 \text{ mm}$. The treatment progress is the same as described before. The device for this experiment is showed in Fig. 2. The electrodes were placed in container made of organic glass filled with transformer oil. And the distance between two electrodes was adjusted to 5 mm. In this experiment, the pre-stressing electrical field was -6 kV/mm , 0 kV/mm or $+6 \text{ kV/mm}$. After pre-stressing, a positive DC voltage was applied till breakdown. These experiments were repeated several times to get average breakdown strength.

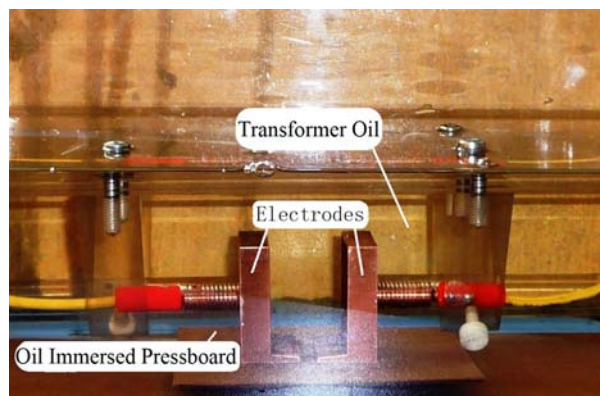


Figure 2. Device used in creeping discharge experiment.

Table 1. The main technical parameters of UHV transformers in China, Japan, Former Soviet and Italy

main technical parameter	China	Japan	Former Soviet	Italy	
Maximum voltage U_m /kV	1 100	1 100	1 200	1 050	
Rated power/MVA	1 000/1 000/334	1 000/1 000/400	667/667/180	400/400/-	
Rated voltage/kV	$(1050/\sqrt{3})/(525/\sqrt{3} \pm 5\%)/110$	$(1 050/\sqrt{3})/(525/\sqrt{3} \pm 5\%)/147$	$(1 150/\sqrt{3})/(500/\sqrt{3})/20$	$(1 000/\sqrt{3})/(400/\sqrt{3})/12.2$	
Cooling method	OFAF	ODAF	—	—	
Out-leading type	bushing	GIS	bushing	cable	
Voltage Regulating Method	neutral point off-circuit-tap-changing	neutral point on-load voltage regulation	single-phase autotransformer	step up transformer single-phase autotransformer	
Insulation level	(Full wave/Chopped wave)/kV	2 250/2 400	1 950	2 550/2 800 2 250/2 550	2 250
	SI/kV	1 800	1 425	2 100 1 800	1 800
	AC(5min)/kV	1 100	1 100	1 100(1 min) 1 000(1 min)	$1.5 \times 1 050/\sqrt{3}$ (1 h)
	(Full wave/Chopped wave)/kV	1 550/1 675	1 300	1 550/1 650	1 300
	SI/kV	1 175	—	1 230	—
	AC(1min)/kV	630	550(5 min)	630	—
	LV wave/Chopped wave)/kV	650/750	750	—	95
	AC(1min)/kV	275	325	—	—
	neutr al point wave/Chopped wave)/kV	325	—	—	—
	AC(1min)/kV	140	185	—	—
No-load loss P_0 /kW	≈ 200	350	310	—	
No-load current I_0 /%	≈ 0.05	0.35	—	—	
Load loss P_k /kW	1 420~1 450	3 395	1 100	—	
Short-circuit impedance U_k /%	≈ 18	18	12.5	15	
Noise/dB(A)	78~80	65	—	—	
Size/m	12×4.15×4.9	10.5×3.1×4.1(split type)	—	10×4.1×4.6	
Weight/t	375	200(every cabinet)	390 (with oil)	275 (without oil)	

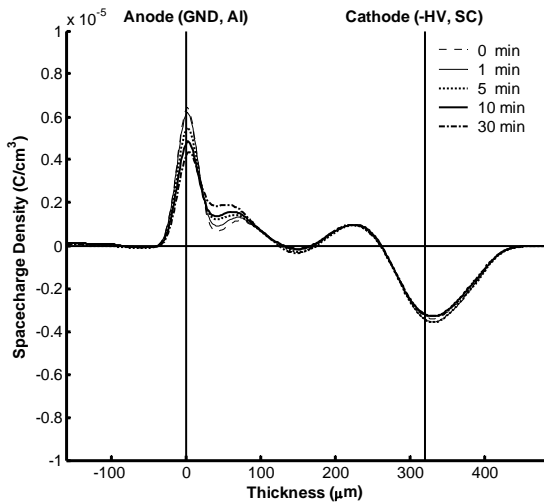


Figure 3. Space charge distribution of oil-paper in 30 minutes with a -5 kV/mm applied field.

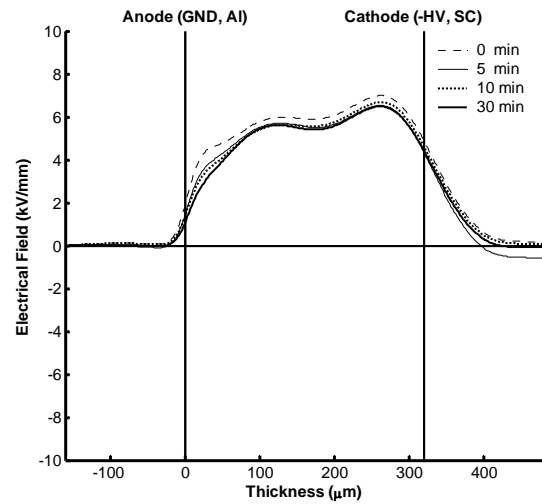


Figure 4. Field intensity distribution of oil-paper in 30 minutes with a -5 kV/mm applied field.

4. SPACE CHARGE IN OIL-PAPER INSULATION

4.1 Space Charge Phenomena in Oil-paper Insulation

Fig. 3 shows the result of space charge accumulation in oil-paper insulation materials. Space charge distribution and movement in the sample could be observed clearly when the sample was applied with -5 kV/mm field. Space charges in material could lead to partial electrical field distortion, thereby affecting material's insulation property. Fig. 4 illustrates field intensity distribution in sample shown in Fig. 3. Applied field stress was -5 kV/mm, however, the maximum field stress in material exceeded -7 kV/mm. The electrical field distortion rate exceeded 40%.

When the field reached -55 kV/mm as show in Fig. 5, the anode had a very obvious positive charge injection phenomenon. Although this great charge injection into both electrodes of the material was observed, space charge packet phenomenon like other materials such as low density polyethylene (LDPE) was not observed [16- 18]. It can be understood by referring to oil-paper insulation bipolar injection model from reference [8].

It was observed that the conductivity of oil-paper became larger gradually while the polarization time getting longer. The quantity of inductive charges at both electrodes got smaller obviously before breakdown. Meanwhile, conduction current in the material reached 40 μ A and the material got breakdown. These changes indicate that intensity degradation induced by space charges appears in the oil-paper insulation under high field.

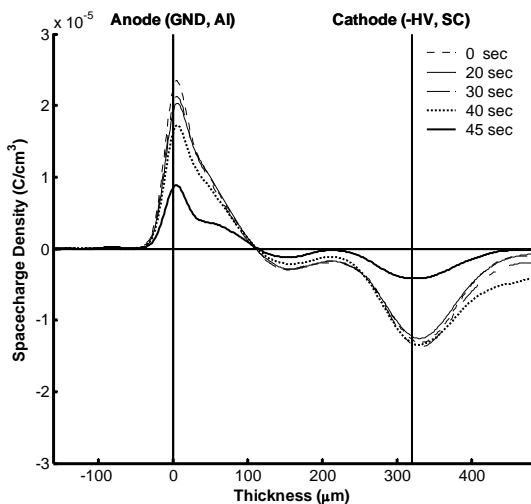


Figure 5. Space charge distribution of oil-paper till breakdown with applied field of -55 kV/mm.

4.2 Space Charge Dissipation Property in Oil-paper Insulation during Depolarization

Fig. 6 shows space charge dissipation of oil-paper sample after a -15 kV/mm field applied for 30 minutes. After the field was removed for 30 seconds, space charges in the material and inductive charges accumulated at electrodes dissipated quickly to background noise magnitude.

Comparing the similar experiment of low density polyethylene (LDPE) [19], it can be found that in LDPE, space charges dissipated much slower after depolarization than in oil-paper.

The conductivity of oil-paper is 5×10^{-12} S/m while that of polyethylene is over 10^{-15} S/m [20], therefore space charge in oil-paper insulation dissipated easier compared with other high polymers such as polyethylene. As is known to all, polarity reversal effect of insulation material caused by space charge will lead to hiking up the insulation destroying probability and reducing breakdown voltage [21]. If direct current electrical equipments with oil-paper insulation take a reversal of polarity, as show in Fig. 6, they can basically avoid polarity reversal effect caused by space charge when the interval of polarity reversal is more than 30 seconds. This phenomenon and its mechanism have vital importance of further study, especially on the polarity reversal effect of oil-paper insulation. This phenomenon also proves that oil-paper insulation has a good long-term insulating performance behavior because, at the very least, the space charges are not easy to accumulate.

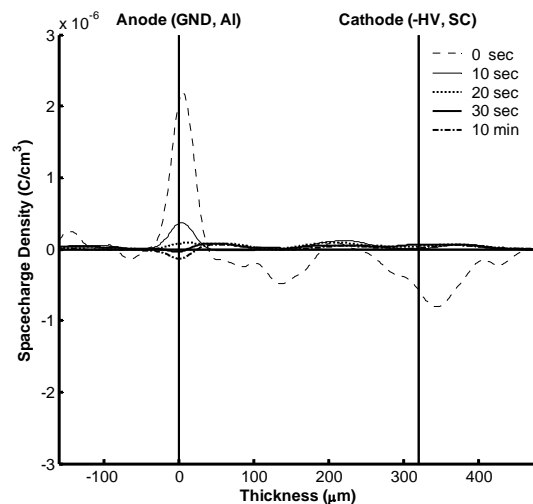


Figure 6. Space charge dissipation after a -15 kV/mm applied field for 30 minutes.

5. BREAKDOWN AND CREEPING DISCHARGE IN OIL-PAPER INSULATION

5.1 Breakdown of Oil-paper Insulation

Fig.7 gives the breakdown strength of oil-paper insulation after pre-stressing as well as deviations. The data where pre-stressing electrical field is 0 kV/mm represents the breakdown strength of samples without pre-stressing, simply intitule as E_0 hereinafter.

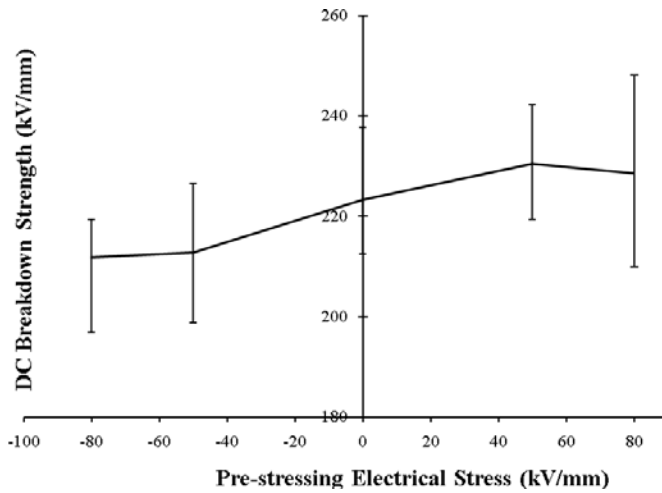


Figure 7. DC breakdown strength of oil-paper insulation after pre-stressing.

It is show in Fig.7 that, after the samples were pre-stressed by a positive DC voltage, their breakdown strength increased by a maximum of 3%. On the other hand, the breakdown strength of samples pre-stressed by a negative DC voltage decreased by a maximum of 5%.

Fig.7 indicates that polarity reversal effect exists not only in polymers such as XLPE, but also in oil-paper insulation system. In these experiments, space charge accumulated when the samples were pre-stressed by a negative DC voltage [22], became hetero when the positive voltage was applied and increased the electrical field in both interfaces between electrodes and oil immersed pressboard. Thus, the breakdown strength decreased than E_0 , which was similar to what happened in XLPE.

5.2 Creeping Discharge of Oil-paper Insulation

Fig. 8 gives the creeping discharge strength of oil-paper insulation in experiments described in Fig.2. The distance between two electrodes was 5 mm.

Fig.8 indicates that after pre-stressing, the creeping

discharge strength of oil-paper insulation increased by a maximum of 20% in both negative and positive polarity of pre-stressing. In these experiments, the conductivity of oil-paper insulation is relatively larger than XLPE, and the flow of transformer oil takes away part of the space charge accumulated on the surface of pressboard. Moreover, the transportation of space charge may bring in homogenization to the surface of pressboard. Therefore, the creeping discharge strength increased.

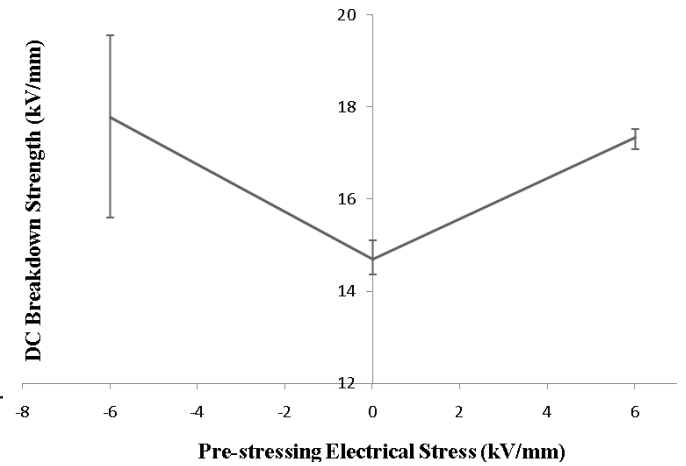


Figure 8. The creeping discharge strength of oil-paper insulation after pre-stressing.

However, it is not reasonable to assume that space charge could certainly increase the creeping discharge of oil-paper insulation. In fact, when too much space charge accumulates on the surface of pressboard, partial discharge will take place and insulation system will be damaged.

6. CONCLUSIONS

In this paper, special problems of ultra high voltage power transformers were raised, and space charge phenomena in oil-paper insulation was studied. Space charge effects on oil-paper insulation used in converter transformers were emphasized.

1. Due to the high voltage, big capacity, and large size of UHV transformer, the stray parameters of the test circuit will prolong the front time of lightning impulse waveform, thus the validity of lightning impulse overvoltage test needs more attentions.
2. The space charge distribution and dissipation process in oil-paper insulation which is used in transformers were directly observed by the PEA system, and the space charge characters under varied fields was investigated. The electrical field

distortion rate caused by space charge exceeded 40%.

3. The conductivity of oil-paper material is much larger as compared to polymers, and the space charge dissipates very fast when being depolarized. Therefore there is almost no space charge in oil-paper after the applied field is removed for more than 30 seconds. This property of oil-paper insulation has great theoretical and practical engineering significance.

4. Breakdown and creeping discharge of oil-paper insulation were studied, and based on measurements of space charge in oil-paper insulation, effects of space charge on breakdown and creeping discharge were discussed. The results showed that space charge accumulated under DC electrical field did have some effects on the performance of oil-paper insulation as follows:

- a) As in XLPE insulation, polarity reversal effect exists in oil-paper insulation too. Breakdown strength of oil immersed pressboard can be affected by space charge.
- b) Space charge can also affect the creeping discharge of oil-paper insulation, but more researches are needed to get a full knowledge about the mechanism.
- c) Space charge should be taken account of carefully during the design and manufacture of converter transformers.

Acknowledgment – This paper is supported by the Program for New Century Excellent Talents in University of China (NCET-04-0095), the National Natural Science Foundation of China (NSFC 50877040), as well as Specialized Research Fund for the Doctoral Program of Higher Education (SRFDP 200800030040). And we are also grateful for the technical support and cooperation from Professor Takada and Tanaka of Musashi Institute of Technology, Japan.

References

- [1] Mizutani T., “Space charge measurement techniques and space charge in polyethylene,” *IEEE Transactions On Dielectrics and Electrical Insulation*, Vol.1, No.5, pp.923-933, (1994).
- [2] Hang X. D., Zhai Y. D., “CONVERTER TRANSFORMER USED FOR HVDC TRANSMISSION,” *High Voltage Apparatus*, Vol.38, No.3, pp.5-6, (2002).
- [3] Wang X., Cao X. L., “Summarize of UHVDC Station Transmit Electricity Equipments,” *Electrical Engineering*, No.5, pp.9-14, (2006).
- [4] Lu X. D., Chen S. K., Sun D. H., Fang Z. Q., “The Study on Numerical Method for Anisotropic Nonlinear DC Electric Field,” *TRANSACTIONS OF CHINA ELECTROTECHNICAL SOCIETY*, Vol.14, No.4, pp.60-64, (1998).
- [5] HAMMER F., KUCHLER A., “Insulating systems for HVDC power apparatus,” *IEEE TRANSACTIONS ON ELECTRICAL INSULATION*, Vol.27, No.3, pp.601-609, (1992).
- [6] Li Y., Takada T., “Progress in Space Charge Measurement of Solid Insulating Materials in Japan,” *IEEE Electrical Insulation Magazine*, Vol.10, No.5, pp.16-28, (1994).
- [7] Hanley T. L., Burford R. P., Fleming R. J., et al, “A General Review of Polymeric Insulation for Use in HVDC Cables,” *IEEE Electrical Insulation Magazine*, Vol.19, No.1, pp.13-24, (2003).
- [8] Ahmed N. H., Srinivas N. N., “Review of Space Charge Measurements in Dielectrics,” *IEEE Transactions on Dielectrics and Electrical Insulation*, Vol.4, No.5, pp.664-656, (1997).
- [9] Fukuma M., Fukunaga K., Maeno T., “Space Charge Dynamics in LDPE Films Immediately Before Breakdown,” *IEEE Transactions on Dielectrics and Electrical Insulation*, Vol.8, No.2, pp.304-306, (2001).
- [10] Liu R. S., Takada T., Takasu N., “Pulsed Electroacoustic Method for Measurement of Charge Distribution in Power Cables under both ac and dc Electric Fields,” *Journal of Physics D: Applied Physics*, Vol.26, No.6, pp.986-993, (1993).
- [11] Peter M., Marc J., “Space Charge Measurements on Impregnated Paper: A Review of the PEA Method and a Discussion of Results,” *IEEE Electrical Insulation Magazine*, Vol.13, No.3, pp.26-35, (1997).
- [12] Ciobanu R., Schreiner C., Pfeiffer W., et al, “Space charge evolution in oil-paper insulation for DC cables application,” *Proceedings of 14th International Conference on Dielectric Liquids*, pp.321- 324, (1994)
- [13] WUHAN HIGH VOLTAGE RESEARCH INSTITUTE OF SGCC . UHV transmission technical documentation[Z]. Wuhan: WUHAN HIGH VOLTAGE RESEARCH INSTITUTE OF SGCC, 2005.

- [14] Wang N. H., Gao B., Zhou Y. X., et al, “A Practical Space Charge Testing System Realized by the Pulse Electro-acoustic Method, *Electrical Measurement & Instrumentation*,” Vol.41, No.11, pp.12-15, (2004).
- [15] Electrical strength of insulating materials – Test methods-Part 2:Additional requirements for tests using direct voltage, GB/T 1408.2-2006, Nov. 2006.
- [16] Wang N. H., *Morphology Effects on Space Charge Characteristics of Low Density Polyethylene*, Beijing: Tsinghua University, 2007
- [17] Jones J. P., Llewellyn J. P., Lewis T. J., “The Contribution of Field-Induced Morphological Change to the Electrical Aging and breakdown of Polyethylene,” *IEEE Transactions on Dielectrics and Electrical Insulation*, Vol.12, No.5, pp.951-966, (2005).
- [18] See A., Dissado L. A., Fothergill J. C., “Electric field criteria for charge packet formation and movement in XLPE,” *IEEE Transactions of Dielectric and Electrical Insulation*, Vol.8, No.6, pp.859-866, (2001).
- [19] Wang N. H., Zhou Y.X., Liu H.B., et al, “Effects of crystallinity on the space charge properties of polyethylene,” *Journal of Electrostatics*, Vol.63, No.6-10, pp.649-656, (2005).
- [20] Zhou Y.X., Wang N.H., Yan P., et al. “Effect of Annealing Condition on DC Conduction in Polyethylene Films, *High Voltage Engineering*. Vol.28, No.120, pp.5-7, (2002).
- [21] Mizutani T., Suzuoki Y., Matsukawa Y., et al, “Space Charge and High Field Phenomena in Polyethylene,” *IEEE Dielectrics and Electrical Insulation Society, 1992 Annual Report, Conference on Electrical Insulation and Dielectric Phenomena*, New York: IEEE Dielectrics and Electrical Insulation Society. Pp.55-60, (1994).
- [22] Zhou Y. X., Wang Y. S., Li G. F., Wang N. H., Liu Y. Y., Li B., Li P., Cheng H. C.. “Space Charge Phenomena in Oil-paper Insulation Materials under High Voltage Direct Current,” *Journal of Electrostatics*, Vol.67, No.2-3, pp.417-421, (2009).

Reduction of Excess Activated Sludge by Ferrite Particles: Process and Possibilities

Mahmudul Kabir*, Masafumi Suzuki* and Noboru Yoshimura*

*Department of Electrical, Electronic and Computer Systems Engineering,

Faculty of Engineering and Resource Science, Akita University,

1-1, Tegata-Gakuen-Cho, Akita, 010-8502 Japan

Tel:(+81)-18-889-3027, E-mail: kabir@ipc.akita-u.ac.jp

Abstract: Activated sludge method is widely being used for waste water treatment in many countries including Japan. This method is very useful, as its running cost is very cheap. However, every year a large amount of excess sludge is being produced in the Waste Water Treatment Plants (WWTPs) which is a serious problem in terms of both economical and environmental problems. So, the experiments on reduction of excess sludge are carried out in many countries. We have introduced Magneto-ferrite treatment on activated sludge in order to reduce excess sludge in the laboratory scale. This magneto-ferrite treatment is a new approach for reduction of excess sludge by using ferrite particles and permanent magnets. First, we determined the parameters for this method and then with the parameters, we observed the effect of this new method on activated sludge with the running method of Conventional Activated Sludge (CAS) of a Waste Water Treatment Plant (WWTP). Two miniature WWTPs were used at the laboratory, which one was run with magneto-ferrite treatment while another was run without any treatment. The observations showed good results in reduction of excess sludge growth. The growth of excess sludge was controlled at 42% comparing to that of non-treatment system running WWTPs with CAS. The results showed good possibilities of reducing sludge in the arena of biological waste water treatment. A rotary treatment plant was introduced which showed a good possibilities of this method.

Keywords: Magneto-ferrite treatment, Excess activated sludge, Zero emission

Nomenclature:

WWT	Waste Water Treatment	CAS	Conventional Activated Sludge
WWTP	Waste Water Treatment Plant	EA	Extended Aeration
BOD	Biochemical Oxygen Demand	COD	Chemical Oxygen Demand
MLSS	Mixed Liquor Suspended Solid	VCC	Viable Cell Coefficient

1 INTRODUCTION

Biological analysis method is the most widely used method for the WWT. The method is widely used to treat waste water in all over the world for the low running cost of this method [1]. The method uses biological groups of living organisms which possess good settling characteristics. The groups of these living organisms are used to be gathered in floc. In general, they are called activated sludge. The living organisms decompose the biological nutrients from the waste water and thus purify the waste water from biological waste. The diagram of the WWT using activated sludge can be found in Fig.1 [2-4]. In order to separate big wastes from waste water, it is run under some primary processes and then waste water is finally put to the aeration tank where activated sludge is kept. Oxygen is supplied to decompose the biological waste in the aeration tank. From the aeration tank, the treated water is supplied to the settling tank where water is separated from activated sludge by settling the sludge naturally. The treated water is taken out as effluent and the activated sludge is returned to the aeration tank. The excess activated sludge is discarded from settling tank when it is necessary. There are a lot of merits of using activated sludge method to treat waste water but the system has some demerits, too. The main disadvantage of the activated sludge method is the production of excess sludge which is being

produced through the WWT process. There are several works done by the many scientists to treat the excess sludge [2-5]. These must byproducts are dewatered, dried and finally burnt into ashes. Some are used in farm lands as compost fertilizer. The dump places for ashes and the high cost to treat the excess sludge are huge burdens to our society on the basis of both economical and environmental problems. Some statistics showed that the availability of dump places for sludge waste will be difficult in next 6.1 years in Japan. In urban places for Japan, the situation is worse as the limit was found to be about 2.3 years [6].

It is clear from the Fig.1 that the value of C_1 is greater than the value of C_0 and the subtraction of BOD of waste water is responsible for the increase of activated sludge. The probable amount of excess sludge can be expressed by the following equation [2-4];

$$\Delta X = a S_r - b X \quad \dots\dots (1)$$

It can be understood from the above equation that the zero emission is possible when aS_r is less or equal to bX . There are some reports informing the success in order to control the gross yield coefficient of BOD 'a' by adding fallen leaves in the aeration tank with sludge. But, the mechanism is no yet clearly understood. Some efforts were carried out to increase the self

decay of activated sludge prolonging the aeration period [7]. However, these attempts are dependant on biomass and difficult to achieve good results at every time. Again, prolonging of the aeration period brings the excess economical burden. However, recently, a new approach has been started to minimize this excess sludge. A part of activated sludge is treated under cell lysis. The treated sludge or a part of the treated sludge becomes to be equal to biological waste. This treated sludge is sent to the aeration tank and is decomposed by the non-treated activated sludge and thus the excess sludge can be minimized.

If we consider 'W' is to be the amount of activated sludge for the treatment of cell lysis and 'h' is to be the diverting rate of treated sludge to activated sludge then from the eq. (1) the amount of 'W' can be calculated in the following way.

$$W = \Delta X / (1 - h) \quad \dots\dots (2)$$

Thus, it is possible to reduce the excess sludge theoretically. Several reports regarding to cell lysis in order to reduce excess sludge were published including ozonation, milling process with beads, revolving disks methods etc. [1-4,7-10]. But, however, the methods are still on the process and a new and effective technology method is still a demand in this new branch. We have developed a new process to minimize the production of excess sludge with the ferrite particles. This magneto-ferrite method was explained in other paper [11, 12]. We determined the necessary parameters to perform this new method. We will discuss the effect of magneto-ferrite method using two miniature WWTPs. The two WWTPs were run for a fixed period of time with CAS and EA process [11, 12]. Magneto-ferrite effect was applied for about 4 weeks in the case of CAS and found more than half of excess sludge reduced comparing to the control for first 2 weeks. But, the reduction speed of the excess sludge lowered a little bit from then. The possible reason was the increase of BOD produced by the magneto-ferrite treatment which may increase the overall production of the activated sludge of the relevant aeration tank. However, in the overall, about 42% of excess

sludge reduction was possible with magneto-ferrite treatment of sludge comparing to the non-treated sludge.

The growth of the excess sludge is limited in EA method comparing to the other running methods of WWTPs. Moreover, it is very suitable for the laboratory experiments for its less production of the excess activated sludge. It was continued for about 10 weeks and found no significant evidence of excess sludge in the treated aeration tank. These two types of running processes for the WWTPs proved the effectiveness of the magneto-ferrite system in order to reduce the excess sludge in the laboratory level tests.

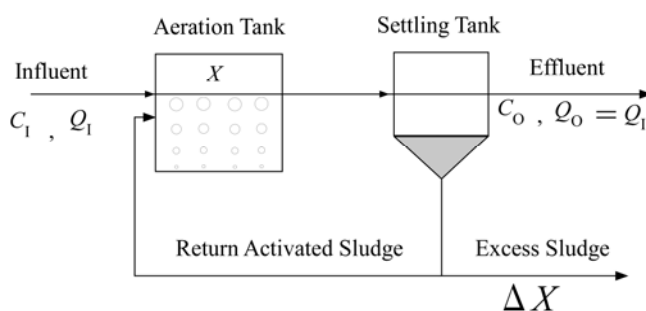
Again, we considered the practical application of magneto-ferrite treatment. A rotary treatment plant was proposed and magneto-ferrite treatment was applied in activated sludge in lab scale. The result showed good possibilities of application of magneto-ferrite treatment.

2 EXPERIMENTAL

A miniature WWTP has a reservoir for influent, an aeration tank and a settling tank as described in Fig.2 (a). The waste water was supplied to the aeration tank with a pump. The amount of air supplied in the aeration tanks was at a rate of 3.0L/min. While being in the aeration tank, the activated sludge decomposed the biological waste from the waste water and thus deduced the BOD of the influent. At the same time, one of the parts of the BOD supplied the nutrients for the growth of the activated sludge which resulted to the excess activated sludge. The treated water was sent to the settling tank. Sludge also came with the water into this tank. The sludge was sent back to the aeration tank as return sludge. While sending back the sludge to the aeration tank, magneto-ferrite treatment was applied. The treated sludge was sent to the aeration tank. In our laboratory, we used the same type of two miniature WWTPs to evaluate the effect of magneto-ferrite treatment on the excess sludge in which only one WWTP was exposed to magneto-ferrite treatment and the other WWTP was kept without any treatment. It can be seen that the miniature WWTP with the magneto-ferrite treatment was named with system 2 shown in Fig.2 (a). Thus with the help of the two miniature WWTPs the validity of this method can be evaluated at the same room temperature and humid conditions. A brief explanation of the magneto-ferrite devices will be introduced here.

The magneto-ferrite system's diagram model can be seen in Fig.2 (b). Two permanent magnets were placed in on a plate. The plate was connected to a shaft of a motor with a joint. The circular rotation of the motor is changed into linear motion with the shaft of the joints. Two test tubes were fixed on the way of the magnetic flux. The capacity of the test tubes is 100ml. Adequate ferrite particles were kept in the test tubes. The activated sludge from the settling tank was let to come to the test tube, treated and then sent back to the aeration tank. The amount of the activated sludge for treatment was controlled in a way so that the activated sludge can be kept in the magnetic flux for about 3 hours. Thus the activated sludge was happened to get the magneto-ferrite effect for 3 hours and the microbes of the sludge get disrupted.

The rotary magneto-ferrite treatment plant can be seen in Fig.2(c). Two permanent magnets were set up on a rotor which was coupled with the shaft of a motor. A round shaped receiver was fixed on the top of the rotor. A fixed amount of ferrite particles with activated sludge were kept in the receiver. A stirrer made of free plastic which had two ferro plate installed in it was placed in the receiver. The material of the receiver is



Here,

C_1 : BOD of waste water [kg/m³]

Q_1 : amount of influent [m³/d]

Q_0 : amount of effluent [m³/d]

C_0 : BOD of effluent [kg/m³]

X : amount of activated sludge [kg]

ΔX : excess sludge [kg/d]

Fig.1. A model diagram of a miniature WWTP

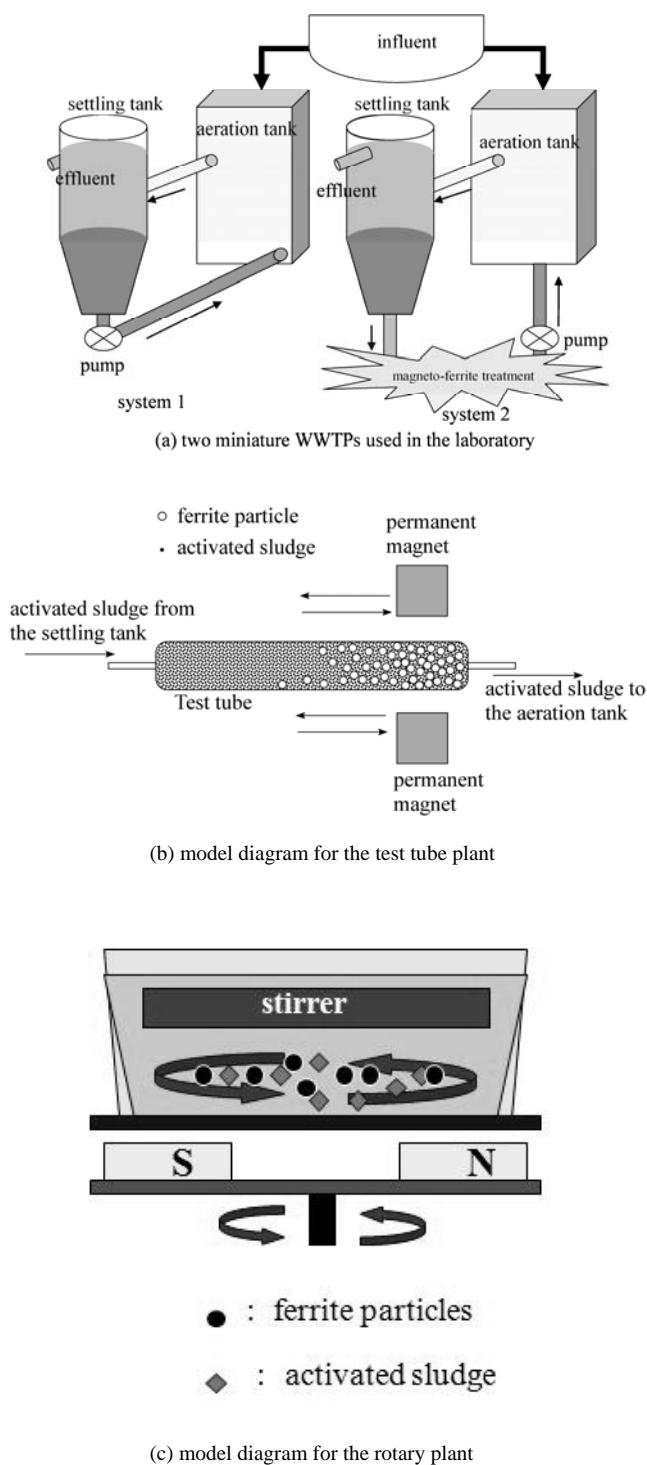


Fig. 2 Model diagrams of the laboratory apparatus and the magneto-ferrite treatment

PVC. The rotor circles when the shaft of the motor starts to move. At the same time, the stirrer and the ferrite particles of the receiver start to move with the magnets. The activated sludge was oppressed and stirred in the receiver. The collision was occurred with ferrite particles which caused the break down of the cell wall of micro organisms. Thus the sterilization is performed and the organic compounds are to be hydrolyzed in the solution. It will plug into the reduction of activated

sludge.

3 METHODS

Two miniature WWTPs were run for CAS and EA processes. The biological parameters used in this experiment were shown in Table 1. We measured the MLSS for aeration tanks of both WWTPs. We cast out the excess sludge when the value of MLSS had crossed the level described in Table 1. The amount of the removed sludge was measured after the processes of dewatering and drying of sludge. Their values evaluated the effect of magneto-ferrite treatment. One thing is to be noted that the measurement of BOD takes about 5 days, so we preferred to measure COD instead of measuring BOD for relevant measurements. In this experiment, we used a COD meter to measure the COD of effluent. The COD removal efficiency was calculated for both treatment and non-treatment of magneto-ferrite effect. Here is the equation to calculate the value of COD removal efficiency.

$$\text{COD removal efficiency [\%]} = (\text{COD}_{\text{influent}} - \text{COD}_{\text{effluent}}) \times 100 / \text{COD}_{\text{influent}} \dots\dots(3)$$

The methods to carry out the experiments will be described below;

1. Certain amount of artificial waste water was put in the reservoir.
2. The waste water was sent to the aeration tank by a pump (Cassette Tube Pump SMP-23, Tokyo Rikakikai Co.). The amount of the waste water is controlled by this pump according to the two methods described in Table 1.
3. The activated sludge which had gathered in the settling tank was sent back to the aeration tank by a pump (Roller Pump; Furue Science Co.) for a fixed period of time. It is to be noted that magneto-ferrite effect is applied on system 2 whether another system was kept without any of the treatment.
4. In order to verify the effect of the magneto-ferrite treatment, the MLSS was measured periodically for the each of the aeration tanks. The excess sludge was removed if necessary, then dried and measured the amount of the sludge.
5. The COD of the effluent was measured periodically by a COD meter (Quick COD; Central Kagaku Co.)

3.1 Experimental conditions

The experimental conditions were described below. The experiments were performed to make clear the effect of the magneto-ferrite treatment; so the major conditions were kept same for both control (system 1) and system 2. However, the values of MLSS of the two aeration tanks were little different at the initial stage which was not so big in amount and was acceptable.

The ingredients of the artificial influent were as follows;

- 1) Peptone 0.5g/L
- 2) Glucose 0.5g/L
- 3) East 0.25g/L
- 4) Ammonium Dihydrogenphosphate ($\text{NH}_4\text{H}_2\text{PO}_4$) 7mg/L
- 5) 25% Ammonia water 1ml/L

The pH (6-8.5) was measured regularly of the activated sludge and controlled the value with NaOH dropping if needed. These chemical products are available in any place.

Table 1. The factors for the experiments

	CAS	EA
BOD-Sludge Loading	0.4	0.15
BOD-Volume Loading	0.2	0.05
MLSS	2000 mg/L	3000 mg/L
COD of Influent	300 mg/L	150 mg/L
Amount of Influent	4.48 L/d	3.36 L/d
Aeration rate	3.0L/min	

3.2 Experimental conditions for test tube plant

For CAS, the COD of the influent was controlled at 300mg/L and for the EA method it was controlled at 150 mg/L.

From the previous experiments, we came to the conclusions that these are the most effective conditions to get the best results from the magneto-ferrite effects [11, 12].

Ferrite particles ~50µm, 30g
 Magnetic flux 165 mT
 Revolving speed of the motor of the permanent magnets 1.5-1.8 roll/s
 Volume of the test tubes 100ml
 Treatment time 12h/d
 Running time 1min×2 times (in 1 hour)

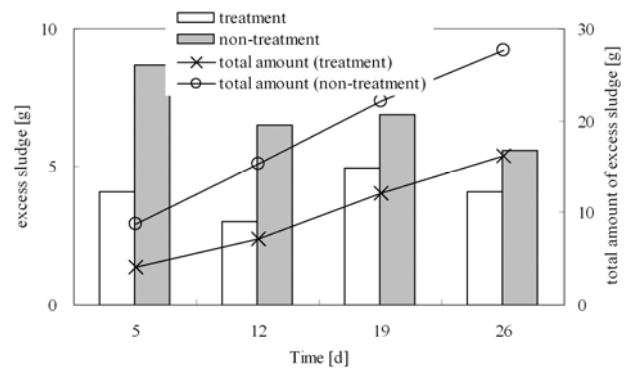
3.3 Experimental conditions for rotary plant

The experiments were carried out to determine the parameters of the rotary treatment plant. The shape and the volume of the receiver were 17cm × 5 cm and 870ml respectively. It can treat about 200ml at a time. The magnetic flux was 30-50mT and the speed of rotor was 90rpm. The amount of influent and COD of influent were 3.36L/d and 400mg/L. The experiments were carried out in CAS method. However, the treatment time was shrunk to 1 hour. Again, as this system can treat a large amount of sludge at a time comparing to test tube plant, the running time of this plant was only 4h/d. The size and the shape of the ferrite particles were same with the test tube plant. 50g of ferrite particles were used to run this system.

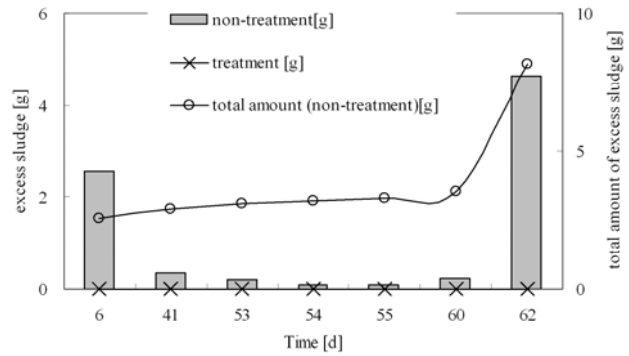
4 RESULTS AND DISCUSSION

4.1 Test tube plant

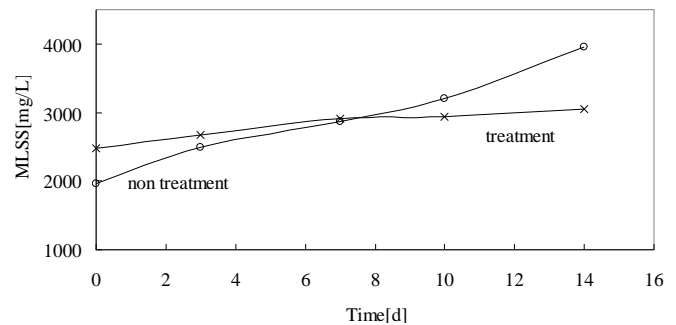
The experiments were carried out for about 4 weeks for CAS. When we run the miniature WWTP, the activated sludge will be grown up gradually while purifying the waste water. According to the methods, the MLSS of both two aeration tanks were measured periodically and controlled accordingly to Table 1. So, we drew up the excess sludge from the both aeration tanks and compared the amounts of the dried sludge. The amount of the excess sludge removed from the two systems can be found in Fig. 3(a). It can be seen that for the first 2 weeks, the amount of excess sludge was about half comparing to the non treated sludge. As the whole conditions but the magneto-ferrite effect were same for the two aeration tanks, it is clear that the excess sludge was disrupted by magneto-ferrite treatment system. However, the difference in the amount of the excess sludge was getting closer to the non-treatment aeration tank's sludge. The BOD of the system 2



(a) for CAS



(b) for EA



(c) for rotary plant

Fig. 3 Experimental results, (a), (b): discarded sludge amount for test tube plant and (c) MLSS for rotary plant

was not only from the waste water, but it can be understood that the treated activated sludge was also contributed in the increasing of BOD of the relevant aeration tank. Thus the input BOD was greater than the non treated aeration tank (system 1) comparing to the system 2. This reason may influence the increase of excess sludge in system 2. So, a less amount of BOD is preferable to check the validity of the magneto-ferrite treatment to activated sludge in laboratory environment. However, the total amount of the excess sludge was 16.2g for the system 2 which was about 42% of the amount of excess sludge of system 2 (27.7 g).

In the same way, we observed the sludge growth in operating with EA method for treatment and non-treatment of magneto-ferrite effect. The MLSS of two systems were

controlled according to the amount of Table 1. The observations for both systems were carried out for about 10 weeks. The MLSS of the aeration tanks of two systems were measured periodically and removed the excess sludge when it was necessary. Sometimes, for other experiments, a short volume of activated sludge was removed from the aeration tank of system 1. The excess sludge was removed from the aeration tank, dried and measured the amount like the previous running process. The values of the amount of the discarded sludge can be found in Fig. 3(b). It is clear that no excess sludge was found in system 2 which had been exposed to magneto-ferrite treatment for 10 weeks. The values of initial stage of two systems were 2744 mg/L (system 1) and 3084 (system 2), respectively. The average of the MLSS for both aeration tanks were 3303 (system 1) and 2843 (system 2). The standard deviation value for both aeration tanks' MLSS were 351 for magneto-ferrite treatment and 546 mg/L for non-treatment system. These figures also proved the effectiveness of magneto-ferrite treatment on the excess sludge.

We checked the ferrite particles after 10 weeks after applying the EA method. The ferrite particles were collected, dried and observed by a photo microscope. The particles were found in the same size and shape of the initial stage of the experiment. Again the Viable Cells of the test tubes of the magneto-ferrite treatment were measured by the Easicult. The VCC was calculated. The method of calculating VCC can be found in other paper [11]. The viable cells were found 10^7 cells/ml for the control and 10^5 - 10^6 cells/ml after 3 hours of application of magneto-ferrite treatment. It proved that 90-99% sterilization was still possible after more than 10 weeks of the starting stage.

4.2 Rotary treatment plant

It is essential to increase the amount of activated excess sludge to be treated and reduced as the production of sludge in WWTPs is much larger than the laboratory scale. It can be understood that a larger plant should possess the following characteristics;

1. It can be applicable easily,
2. The setup cost is low and sound in economic,
3. It can be usable with the WWTPs easily.

Comparing to test tube plant, the rotary plant was capable of treating more activated sludge at a time. So, the total running was less than test tube plant. The experiment method was similar to the test tube plant. The experiment period was for about two weeks. Only MLSS of the two aeration tanks (system 1 and 2) were measured to evaluate the treatment effect. Fig.3 (c) shows the result of the experiments. It can be seen that the activated sludge had been increasing with time in system 1 but, however, it was well controlled in system 2. A simple calculation of activated sludge from the MLSS values has showed that in system 2 (with magneto ferrite treatment) only 3.8g of sludge had increased while the non treated aeration tank had increased 13.4g. So, it can be said that with this rotary plant, a total of 72% reduction has been possible in this experiment.

The magneto-ferrite treatment was applied for only 4hrs/d, which showed a good result. These results proved that our new method is quite effective to reduce excess activated sludge in miniature WWTPs. It also points towards the new possibilities of this magneto-ferrite treatment. The method can be applied not only in the reduction of activated sludge but it can be used in the sterilization of the water of swimming pool, ballast tank of a cargo boat etc. As this process is a non-thermal sterilization method, many other uses can be expected. Again,

this process can be used as a hydrolyzed method of activated sludge. Activated sludge is well known by products for its water retention ability. So, dewatering is very important process for the treatment of excess sludge. Our method can be helpful in it. One thing is to be noted that if this method can be success in reducing even 1% of excess sludge, it can save about ¥8 billion.

5 CONCLUSION

We examined the effectiveness of magneto-ferrite treatment in the reduction of excess with two miniature WWTPs. Test tube plant and a rotary plant were introduced and experiments were carried out to evaluate their effectiveness in lab scale. The growth of excess sludge was found in control with magneto-ferrite treatment. The magneto-ferrite treatment has pointed out several possibilities in the view of both economical and environmental aspects.

Reference

- [1] Wei Y, Van Houten RT, Borger AR, Eickelboom DH, Fan Y. Minimization of excess sludge production for biological waste water treatment. *Water Res*; vol.37, no.18, pp.4453-4467 (2003).
- [2] Ide T. Water treatment engineering, Tokyo: Gihodo Shuppan (1990)[in Japanese].
- [3] Editors: Eckenfelder WW, Grau P. Activated sludge process design and control: Theory and practice, Lancaster: Technomic Publishing Co. (1998).
- [4] Miyoshi Y. Ideas and techniques of sewage and waste water treatment, Tokyo: Ohmsha; pp.55-169 (2006) [in Japanese].
- [5] Sawada Y, Nagashima S, Uchida T, Kawashima N, Takeuchi S, Akita M, Nagaoka H. Basic study on sludge concentration and dehydration with ultrasonic exposure. *Jpn J Appl Phys.*, vol.44, no.6B, pp.4678-4681 (2005).
- [6] Ministry of the Environment, Government of Japan. Press release on the 8th November, (2005).[in Japanese].
- [7] Publisher: Yoshida T. Technologies for minimization of sludge and reduction of sludge growth, Tokyo: NTS (2000) [in Japanese].
- [8] Sano A, Bando Y, Yasuda K, Nakamura M, Senga A, Kiyokawa E. Enhancement in biodegradability of excess sludge by using centrifugal vibration mill. *J Chem Eng Jpn*; vol.38, no.6, pp.446-449 (2005).
- [9] Yasui H, Shibata M. An innovative approach to reduce excess sludge production in the activated sludge process. *Water Sci Technol.* vol. 30, no.9, pp.11-20 (1994).
- [10] Ghyoot W, Verstraete W. Reduced sludge production in a two-stage membrane-assisted bioreactor. *Water Res.*, vol. 34, no.1, pp.205-215 (1999).
- [11] M. Kabir, M. Suzuki and N. Yoshimura: "Reduction of Excess Sludge by Ferrite Particles," *Jpn. J. Water Treat. Biol.*, vol.43, no.4, pp.189-197 (2007).
- [12] M. Kabir, M. Suzuki and N. Yoshimura: "Reduction of Excess Sludge by Magneto-Ferrite Treatment: Observation on Lab Scale WWTPs," *IEEJ Trans.Elec. Electron. Engg.*, vol.4, no.4, pp.584-586 (2009).

Quasicrystals and Tiling Semigroups

Akihiro Yamamura

Department of Computer Science and Engineering,
Faculty of Engineering and Resource Science, Akita University,
1-1, Tegata-Gakuen, Akita, 010-8502 Japan
yamamura@ie.akita-u.ac.jp

Abstract: In this paper, we survey researches on algebraic structures related to tilings and connections to structures of quasicrystals. We then introduce the concept of inverse semigroups and groupoids. We also introduce Kellendonk's tiling semigroups as an adequate tool to work on aperiodic tilings. We briefly touch on the relationship between tiling semigroups and quasicrystals. Furthermore, we introduce the author's previous researches on inverse semigroups. Lastly, some plausible direction is shown to study algorithmic aspects of tiling semigroups.

Key words: Quasicrystals, Aperiodic tilings, Inverse semigroups, Tiling semigroups, Algorithmic problems

1 INTRODUCTION

In this paper, we survey current research on algebraic structures of quasi-crystals and related algorithmic problems. The structures of crystals are described by their symmetry, and group theory is the fundamental tool to work on it.

A *space group* is the set of geometrical symmetry operations that take a 3-dimensional periodic object into itself. In mathematical terms, a space group is a discrete cocompact group of isometries of an oriented Euclidean space. It is well known that space groups or crystallographic groups describe symmetric structures of crystals of which structures are captured by a periodic repetition of a unit cell each with an identical shape. The numerous space groups in 3 dimensions are enumerated by Barlow, Fedorov and Schönflies [2, 3, 25], and close relationship between the structure of crystals and such groups have been examined extensively.

On the other hand, quasicrystals allow aperiodic structures, and so, group theory does not fit into the study of structures of quasicrystals be-

cause group theory works only to study symmetry of objects. Generalizing a group, we obtain a concept of an inverse semigroup which is an ideal tool to study partial symmetry.

1.1 Quasicrystals

In 1984, D. Shechtman and his coworkers reported the discovery of a quasicrystal that is a phase of an aluminium-manganese alloy which produces a sharp diffractogram with a unambiguous fivefold symmetry in [23], and since then numerous such objects have been found by now. The discovery of these aperiodic forms in nature gave big influence on the study of crystallography and solid state physics.

While such a physical object had not observed until 1984, aperiodic tilings were already discovered by mathematicians in the early 1960s. Surprisingly they could be applied to the study of quasicrystals. The Penrose tiling [18] is the best-known example of such an aperiodic set of tiles and presents theoretically interesting problems in many areas of mathematics.

1.2 Erlangen program

In mathematics, Klein [12] proposed that the study of geometry is to capture structure-preserving bijections. Klein proposed that group theory to abstract the idea of symmetry of shape or objects. This is called the Erlangen program and has greatly promoted the study of symmetry group of geometry. Crystals are typical physical objects possessing symmetric structures, and can be classified and characterized via group theory. Thus, from the standpoint of view of Erlangen program, crystals should be investigated using group theory, whereas quasicrystals need some other mathematical concept to understand them because quasicrystals does not fall into the domain of study of symmetric objects. To study solids such as quasicrystals, group theory is not a right mathematical tool. We need something else to examine quasicrystals and inverse semigroups and groupoids provide adequate vehicle for us to study non-periodic objects.

2 INVERSE SEMIGROUPS AND GROUPOIDS

Instead of groups, inverse semigroups, the generalization of groups in algebra, or groupoids, the generalization of groups in category theory, are an appropriate tool for studying quasicrystals. Let us introduce the concept of an inverse semigroup and a groupoid here.

2.1 Origins

Partial one-to-one mappings of a non-empty set constitute an algebraic system called the *symmetric inverse semigroup*. Conversely any abstract inverse semigroup is embedded in the symmetric inverse semigroup of a certain set (known as *Wagner-Preston theorem*, see [19]) Thus, the theory of inverse semigroups is an ideal tool to formalize and study algebraic structure of a system of partial one-to-one morphisms and local properties of mathematical objects. As a matter of fact, inverse semigroup theory was initiated to study local properties of manifolds by Wagner [26]. Ehresmann [5] also considered inverse semigroups with some extra assumptions in the context of topology and differential geometry

under the name of *pseudogroups*. After the introduction of the concept, numerous researches had been done mainly on its algebraic structure. Against its first motivation, only a little attention had been paid to the theory of partial automorphisms of a specific mathematical structure, such as groups, rings, vector spaces, topological spaces, manifolds, or graphs. The significance of partial automorphisms in other areas of mathematics has been rediscovered recently. For instance, the study on the relationship between C^* -algebras, groupoids, and inverse semigroups can be found in [17]. Furthermore, it is requested to expand the Erlangen program to include study of partial symmetry or aperiodic symmetry of geometric objects and applications to solid state physics. Inverse semigroups and groupoids are ideal mathematical tools to treat such a non-group based symmetry. The reader is referred to [13] for historical account and detailed information on the theory of inverse semigroups and relationship between inverse semigroups and groupoids.

2.2 Regular semigroups

A semigroup S is called *regular* if for each x in S there is an element x' in S such that $xx'x = x$ and $x'xx' = x'$. An element satisfying this property is called an *inverse* of x . An element e of a semigroup is called an *idempotent* if $e^2 = e$. A regular semigroup was introduced in the influence of von Neumann's study of quantum physics.

2.3 Inverse semigroups

A regular semigroup S is called an *inverse semigroup* if each x in S has a unique inverse. It is known that an inverse semigroup is a regular semigroup whose idempotents commute. Hence, the set of idempotents in an inverse semigroup forms a *semilattice*, that is, a commutative semigroup in which every element is an idempotent. The inverse of x in an inverse semigroup is denoted by x^{-1} , and the semilattice of idempotents of S is denoted by $E(S)$. We note that $s^{-1}E(S)s \subset E(S)$ for every s in an inverse semigroup S since $(s^{-1}es)(s^{-1}es) = s^{-1}ss^{-1}ees = s^{-1}es$ for every $e \in E(S)$. An inverse semigroup S has the *natural partial order* defined as follows. For $a, b \in S$, $a \leq b$ if there exists $e \in E(S)$ such

that $a = eb$. It is easy to see that $a \leq b$ if and only if there exists $f \in E(S)$ such that $a = bf$. The order relation is compatible with multiplication: if $a \leq b$ then $sa \leq sb$ and $as \leq bs$ for every $s \in S$. It is easy to show that if $s \leq e$ for $s \in S$ and $e \in E(S)$ then $s \in E(S)$.

2.4 Representations

Let X be a non-empty set. Let $I(X)$ be the set of partial one-to-one mappings on X . We introduce a multiplication in $I(X)$. For $\alpha, \beta \in I(X)$, the product $\alpha \circ \beta$ is the partial one-to-one mapping on X defined by $\text{Dom}(\alpha \circ \beta) = (\text{Ran}(\alpha) \cap \text{Dom}(\beta))\alpha^{-1}$, $\text{Ran}(\alpha \circ \beta) = (\text{Ran}(\alpha) \cap \text{Dom}(\beta))\beta$, and $x(\alpha \circ \beta) = (x\alpha)\beta$ for $x \in \text{Dom}(\alpha \circ \beta)$. Here, $\text{Dom}(\alpha)$ and $\text{Ran}(\alpha)$ denote the *domain* and the *range* of the mapping α , respectively. Then $I(X)$ forms an inverse semigroup, and is called the *symmetric inverse semigroup* on X . The product $\alpha \circ \beta$ is denoted by $\alpha\beta$. The following is well known (see [13, 19]).

Proposition 2.1 *Let $\alpha \in I(X)$. Then $\alpha \in E(I(X))$ if and only if α is the identity mapping on its domain.* \square

Suppose \mathbb{X} is a mathematical structure. Recall that a group G acts on \mathbb{X} if there exists a homomorphism (called *representation*) of G into the automorphism group $\text{Aut}(\mathbb{X})$, where $\text{Aut}(\mathbb{X})$ consists of all bijective morphisms of \mathbb{X} . We also say that a semigroup S acts on \mathbb{X} , if there exists a homomorphism (called *representation*) of S into the endomorphism monoid $\text{End}(\mathbb{X})$, where $\text{End}(\mathbb{X})$ consists of all morphisms of \mathbb{X} into \mathbb{X} .

Similarly, we say that an inverse semigroup S acts on \mathbb{X} if there exists a homomorphism of S into the inverse monoid $\text{Paut}(\mathbb{X})$ of partial one-to-one morphisms of \mathbb{X} . Here, a partial one-to-one morphism means an isomorphism between substructures of \mathbb{X} . Such a homomorphism is called an *action* of S on \mathbb{X} , or a *representation* of S into $\text{Paut}(\mathbb{X})$. This is the reason that inverse semigroups is a generalization of a group in the sense that it captures wider sense of symmetry of objects.

2.5 E-unitary inverse semigroups

If a group H is a homomorphic image of an inverse semigroup S , then we say that S is an *in-*

verse semigroup coextension of H . We say that an inverse semigroup coextension S of H has the *same set of generators as H* if both S and H are generated by X and $\sigma \circ \iota_S = \iota_H$, where ι_S and ι_H are the natural mappings, and σ is a homomorphism of S onto H .

An inverse semigroup coextension S of H is called *E-unitary* if $\sigma^{-1}(1) = E(S)$. In such a case, the group H is the *maximal group homomorphic image of S* . We remark that the maximal group homomorphic image H of an inverse semigroup S has the universal mapping property: for any homomorphism ρ of S into any group Q , there exists a homomorphism ν of H into Q such that $\nu \circ \sigma = \rho$. An inverse semigroup S is called *E-unitary* if any element above an idempotent is an idempotent (see [13]). It is easy to see that an inverse semigroup is E-unitary if and only if it is an E-unitary coextension of its maximal group homomorphic image. An inverse semigroup with zero is called *0-E-unitary* if $0 \neq e \geq s$, where e is an idempotent, implies s is an idempotent.

2.6 Groupoids

A *groupoid* is a small category in which every morphism is invertible (see [7]). Any inverse semigroup S can be endowed with a groupoid structure ([24]) and we denote it by $\text{Gpd}(S)$ in this paper. The set of objects of $\text{Gpd}(S)$ is $E(S)$. For $e, f \in E(S)$, a morphism of e to f is any element $s \in S$ such that $e = ss^{-1}$ and $f = s^{-1}s$. The inverse of the morphism s is given by s^{-1} . If $e \in E(S)$, then e is the *identity morphism* of the object e . The *trace product* of an inverse semigroup S is the groupoid product in $\text{Gpd}(S)$, that is, the trace product for s_1, s_2 in S is defined to be s_1s_2 if and only if $s_1^{-1}s_1 = s_2s_2^{-1}$ in S . Then s_1s_2 is a morphism from $s_1s_1^{-1}$ to $s_2^{-1}s_2$ since $(s_1s_2)(s_1s_2)^{-1} = s_1s_2s_2^{-1}s_1^{-1} = s_1s_1^{-1}s_2s_2^{-1} = s_1s_1^{-1}$ and $(s_1s_2)^{-1}(s_1s_2) = s_2^{-1}s_1^{-1}s_1s_2 = s_2^{-1}s_2s_2^{-1}s_2 = s_2^{-1}s_2$. Using the terminology in semigroup theory, we define the trace product s_1s_2 if and only if there exists $e \in E(S)$ such that $s_1 \mathcal{L} e \mathcal{R} s_2$, where \mathcal{L} and \mathcal{R} are Green's relations (see [13]). Furthermore, $\text{Gpd}(S)$ is endowed with an order structure. Both inverse semigroups and groupoids are useful tools to analyse partial symmetry in mathematical objects.

3 TILING SEMIGROUPS

A tiling semigroup is invented by J.Kellendonk [9, 10, 11] to model solids. Each tile represents a particular atom or molecule. Such tilings are assumed periodic in crystals, however, quasicrystals can be modelled aperiodic tiling such as Penrose tilings.

Kellendonk showed that the appropriate C^* -algebra are obtained as follows. An algebraic object is constructed from the tiling. This is a 0-unitary inverse semigroup called the tiling semigroup. A topological groupoid is derived from the tiling semigroup. Then a C^* -algebra is constructed from the topological groupoid (see [17, 21]). It is a basic problem to determine the spectrum of a particle moving in a solid. For quasicrystals, the associated tiling is aperiodic and K-theoretical method in the C^* -algebra is a powerful tool. The reader is referred to [13].

A *tile* is a connected bounded subset of \mathbb{R}^n which is the closure of its interior. An *n-dimensional tiling* is an infinite set of tiles which cover \mathbb{R}^n overlapping at their boundaries. A *pattern* is a finite subset of a tiling which is a union of tiles. Usually a pattern is assumed to be connected. Let T be a tiling in \mathbb{R}^n . A *doubly pointed pattern* is a triple (p_2, P, p_1) , where P is a pattern, p_1, p_2 are tiles in P . Two doubly pointed patterns are equivalent if there is a translation τ of \mathbb{R}^n such that

$$\tau(P) = Q, \tau(p_1) = q_1, \tau(p_2) = q_2.$$

The equivalence class containing (p_2, P, p_1) is denoted by $[p_2, P, p_1]$ and called a *doubly pointed pattern class*. The *tiling semigroup* $S(T)$ consists of all doubly pointed pattern classes with the following multiplication. Let $[p_2, P, p_1]$ and $[q_2, Q, q_1]$ be two doubly pointed pattern classes. Suppose that there are translations τ_1 and τ_2 of \mathbb{R}^n such that $\tau_1(P)$ and $\tau_2(Q)$ are patterns and $\tau_1(p_1) = \tau_2(q_2)$. Then the product of $[p_2, P, p_1]$ and $[q_2, Q, q_1]$ in $S(T)$ is defined by

$$[\tau_1(p_2), \tau_1(P) \cup \tau_2(Q), \tau(q_1)].$$

Otherwise, the product is defined to be 0.

Theorem 3.1 *With the multiplication defined above, $S(T)$ forms a 0-E-unitary inverse semigroup.* \square

The inverse semigroup $S(T)$ is called a *tiling semigroup of the tiling T*. The reader is referred to [13] for more information.

4 ALGORITHMIC PROBLEMS

The author has been studying algorithmic problems on inverse semigroups. In this section we introduce some of these results and future research related algorithmic problems, aperiodic tilings and quasicrystals. An extensive survey on algorithmic problems is given in [14].

4.1 Undecidability of Markov property

In combinatorial group theory HNN extensions of groups play a crucial role to show the existence of finitely presented groups with unsolvable word problem, the solvability of the word problem of one relator groups, the existence of finitely presented non-Hopfian groups, the Higman embedding theorem and the undecidability of Markov properties.

Markov [15, 16] showed the undecidability of Markov properties for the class of finitely presented semigroups. Later Adyan [1] and Rabin [20] obtained the same result for the class of finitely presented groups. Similar results for other classes of algebras were obtained by several authors; Addison and Feeney for cancellation semigroups, Bokut for associative and Lie algebras, and Macintyre for skew fields. In 1978 Vazhenin announced the similar result for the class of inverse semigroups but no proof had been known until the paper [28] was published.

A property \mathcal{P} of finitely presented inverse semigroups is called *Markov* if it satisfies:

- (i) there is a finitely presented inverse semigroup S_1 with \mathcal{P} and
- (ii) there is a finitely presented inverse semigroup S_2 which cannot be embedded in any finitely presented inverse semigroup with \mathcal{P}

The followings are examples of Markov properties of finitely presented inverse semigroups: triviality, commutativity, finiteness and freeness.

The author obtained the following result in [28] employing the concept of an HNN extension of an inverse semigroup. Hereafter, the concept is studied by other scholars [4, 6, 8, 22].

Theorem 4.1 *Let \mathcal{P} be a Markov property of inverse semigroups. Then there is no algorithm which decides whether or not a finitely presented inverse semigroup satisfies the property \mathcal{P} .*

Besides undecidability of Markov properties, undecidability of several non-Markov properties is also shown in [28], furthermore, the author has been studying various algorithmic problems on inverse semigroups since then [29, 30, 31, 32, 33].

4.2 Future work

Wang [27] discusses algorithmic problems related to aperiodic tilings. After his work, various approaches to algorithmic issues on tilings have been examined. However, as far as the author knows, algorithmic issues on aperiodic tilings related to quasicrystals and tiling semigroups have not studied so far. It quite interesting to investigate relationship among structures of quasicrystals, aperiodic tilings such as The Penrose tiling, and the related tiling semigroups and topological groupoids. From the point of view of the author, the algorithmic issues derived from quasicrystals may give a big impact on several open problems on algorithms of inverse semigroups and groupoids.

References

- [1] Adyan, S.I., “On algorithmic problems in effectively complete classes of groups” *Dokl. Akad. SSSR*. **123** (1958) 13-16
- [2] Barlow, W., “Über die geometrischen Eigenschaften starrer Strukturen und ihre Anwendung auf Kristalle”, *Z. Kristallogr*, **23** (1894) 1–63
- [3] Fedorov, E.S., “Symmetry of Regular Systems of Figures”, *Zap. Mineral. Obch.*, **28** (1891) 1–146
- [4] Dombi, E.R., Gilbert, N.D., Ruskuc, N., “Finite presentability of HNN extensions of inverse semigroups”, *Internat. J. Algebra Comput.* **15** (2005) 423–436.
- [5] Ehresmann, C., “Gattungen von lokalen Strukturen,” *Jahresber. Deutsch. Math.-Verein.* **60** (1957) 49-77.
- [6] Gilbert, N.D., “HNN extensions of inverse semigroups and groupoids”, *J. Algebra*, **272** (2004) 27–45.
- [7] Higgins, P.J., *Notes on categories and groupoids*, Van Nostrand Reinhold Math. Stud. **32** (1971)
- [8] Jajcayova, T., *HNN extensions of inverse semigroups*, (Ph.D Thesis, University of Nebraska-Lincoln, 1997).
- [9] Kellendonk, J., “Noncommutative geometry of tilings and gap labelling”, *Rev. Math. Phys.* **7** (1995) 1133–1180
- [10] Kellendonk, J., “The local structure of tilings and their integer group of coinvariants”, *Com. Math. Phys.* **187** (1997) 115–157
- [11] Kellendonk, J., “Topological equivalence of tilings”, *J. Math. Phys.* **38** (1997) 1823–1842
- [12] Klein, F., “Vergleichende Betrachtungen über neuere geometrische Forschungen”, *Mathematische Annalen*, **43** (1893) pp. 63-100
- [13] Lawson, M.V., *Inverse semigroups: The theory of partial symmetries*, World Scientific, Singapore, (1998).
- [14] Margolis, S.W., Meakin, J.C., Sapir, M.V., “Algorithmic problems in groups, semigroups and inverse semigroups,” in *Semigroups, Formal Languages and Groups*, Kluwer, Dordrecht, (1995) 147-214.
- [15] Markov, A., “On the impossibility of certain algorithms” in the theory of associative systems, *Dokl. Acad. Sci. SSSR* **55** (1947) 583-586
- [16] Markov, A., “Impossibility of algorithms for recognizing some properties of associative systems”, *Dokl. Akad. Nauk SSSR* **77** (1951) 953-956
- [17] Paterson, A.L.T., *Groupoids, inverse semigroups, and their operator algebras*, Birkhäuser, Boston, (1999).

- [18] Penrose,R., “Role of aesthetics in pure and applied research” *Bull. Inst. Maths. Appl.* **10** (1974) 266
- [19] Petrich,M., *Inverse Semigroups*, Wiley, New York (1984)
- [20] Rabin, M.O., “Recursive unsolvability of group theoretic problems”, *Ann. Math.* **67** (1958) 172-194
- [21] Renault,J., *A groupoid approach to C^* -algebras*, Lecture Notes in Mathematics **793** Springer-Verlag Berlin (1980)
- [22] Rodaro,E., Cherubini,A., “Decidability of the word problem in Yamamura’s HNN extensions of finite inverse semigroups”, *Semigroup Forum* **77** (2008) 163–186.
- [23] Shechtman,D., Blech,I., Gratias,D., Cahn,J.W., “Metallic Phase with Long-Range Orientational Order and No Translational Symmetry”, *Phys. Rev. Let.* **53** (1984) 1951–1954
- [24] Schein,B.M., “On the generalized groups and generalized heaps,” *Amer. Math. Soc. Transl. (2)* **113** (1979) 89-122.
- [25] Schönflies,A.M., *Theorie der Kristallstruktur*, Gebr. Bornträger, Berlin (1891)
- [26] Wagner,V.V., “Generalized groups,” *Dokl. Akad. Nauk* **84** (1952) 1119-1122.
- [27] Wang,H., “Proving theorems by pattern recognition II”, *Bell Systems Tech. J.* **40** (1961) 1–42.
- [28] Yamamura,A., “HNN extensions of inverse semigroups and applications”, *Internat. J. Algebra Comput.* **7** (1997), 605–624.
- [29] Yamamura,A., “HNN extensions of semi-lattices”, *Internat. J. Algebra Comput.* **9** (1999) 555–596.
- [30] Yamamura,A., “Locally full HNN extensions of inverse semigroups”, *J. Austral. Math. Soc.* **70** (2001), 235–272.
- [31] Yamamura,A., “Presentations of Bruck-Reilly extensions and decision problems”, *Semigroup Forum* **62** (2001) 79–97.
- [32] Yamamura,A., “A class of inverse monoids acting on ordered forests”, *J. Algebra* **281** (2004), 15–67.
- [33] Yamamura,A., “Embedding theorem for HNN extensions of inverse semigroups,” *Journal of Pure and Applied Algebra* **210** (2007) 521–536.

Passive Oxide Films and Their In-situ Detection

Toshiaki Ohtsuka

Division of Materials Science and Engineering, Graduate School of Engineering, Hokkaido University

Kita 13 Nishi 8, Kita-ku, Sapporo 060-8628 Japan

ohtsuka@eng.hokudai.ac.jp

Abstract: The passive oxide film electrochemically formed on iron was investigated by in-situ ellipsometry and Raman spectroscopy. The thickness of the passive oxide on iron increases with potential under both stationary and non-stationary conditions. The growth may be followed by the field-assisted ionic migration mechanism coupled with non-stationary dissolution of ferric ions from the oxide. From spectroscopic ellipsometry, a light-absorption edge was estimated at 2.6 eV, which may be a band gap energy of the semiconducting passive oxide. When Fe^{2+} ions exist in the solution, the anodic deposition of $\text{FeOOH}\cdot\text{H}_2\text{O}$ takes place, resulting in formation of an outer hydrous layer a few 10 nm thick. The Raman spectra of the passive oxide correspond to those of Fe_3O_4 and $\gamma\text{-Fe}_2\text{O}_3$.

Key words: Passivation, Oxide Film, Ellipsometry, Raman spectroscopy, In-situ condition

1 INTRODUCTION

The passivation of metals is a one of the key phenomena of corrosion protection of metals. In the passive state, thin stable oxide films a few nm thick are formed on the metals. It may be desired that the detection of the passive oxide is made under in-situ condition, because the passive oxide is only stable in aqueous solution under anodic bias condition and some change may be expected if the passivated metals are transferred to other conditions such as vacuum. In this paper, we describe application to the passivated iron of optical techniques combined with electrochemistry: three-parameter ellipsometry¹⁾ for the precise determination of thickness and spectroscopic property, and Raman spectroscopy²⁾ for the composition identification.

2 EXPERIMENTAL

The ellipsometer used is rotating-analyzer type automated ellipsometer.¹⁾ From the ellipsometer, one obtained three parameters of $\tan \Psi$ (relative amplitude ratio of p- to s-polarized light), Δ (relative phase retardation between p- and s-polarized lights), and reflectance. From the three parameters, unique set of three unknowns of n_2 (real part of complex refractive index), k_2 (imaginary part) and d (thickness) of the passive oxide film under in-situ condition. Spectroscopic property of the passive oxide was measured from the ellipsometry at various wavelength of incident light. The ellipsometric cell was made of acryl resin equipped with two optical glass windows for incidence and reflection light.

For Raman spectrometer a single monochromater was used, equipped with band-edge filter and multi-channel CCD detector. The electrochemical cell for the Raman measurement was made of a polychlorotrifluoroethylene cylinder with 100 mm diameter.

An area of 60 mm in diameter and 50 mm in length was drilled in the cylinder from a sidewall. The drilled area was covered by an optical flat quartz glass 0.5 mm thick was used for the cell and filled by electrolyte solution. The polychlorotrifluoroethylene rod with 10 mm diameter at the top of which iron disc electrode was fixed was inserted from another side into the cell part through a hole with two sealing O-rings. The electrode surface was fixed at a position 3 mm from the glass window. The measurement was made at room temperature of 25°C.

Iron sheet 99.99% pure and 1mm thick was used for electrode. The electrolytes were a borate buffer solution at pH 8.4 of 1:1 mixture of 0.3 mol dm^{-3} (M) H_3BO_3 and 0.075 M $\text{Na}_2\text{B}_4\text{O}_7$ aqueous solutions and an acidic phosphate solution of mixture of 0.3 M H_3PO_4 and 0.3 M NaH_2PO_4 . The electrolyte solutions were prepared from milli-Q water and analytical grade reagents.

3 RESULTS

3.1 Thickness and growth of passive oxide

The thickness of the passive film formed on iron in neutral borate solution at pH 8.4 and acidic phosphate solution after 1h potentiostatic oxidation at individual potentials is shown in Fig.1, where the thickness was estimated by three-parameter ellipsometry with light of 460 nm wavelength.³⁾ The passive oxide linearly grows with potential. When one compares between the passive oxide formed in acidic phosphate solution and in neutral borate solution, the thickness is about half thinner in the acidic phosphate solution than that in neutral borate solution. The linear increase of the thickness is explained by

field assisted ionic migration model proposed by Cabrera and Mott.⁴⁾ The smaller thickness in the acidic solution may be explained by a higher stationary passive current which should be equal to the stationary migration current through the oxide film.⁵⁾ The results in Fig. 1 is assumed for the thickness to reach a stationary value in the acidic phosphate solution and, however, the thickness in the neutral borate solution increases further after 1 h constant potential oxidation.³⁾ Figure 2 shows that thickness increase with time (t) in logarithmic scale at 1.5 V vs. RHE at the same solution where the thickness linearly increases with $\log(t)$, accompanied by a decrease of $\log(i)$; i is current density of the passivated iron.

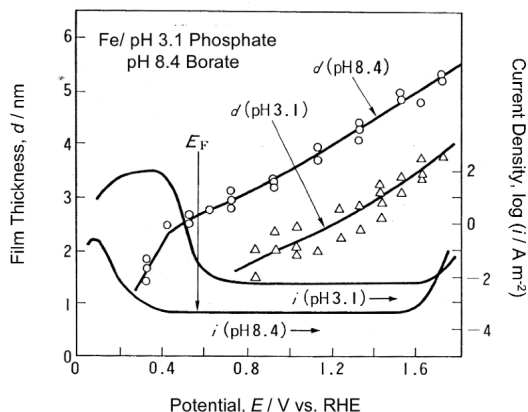


Fig. 1 Thickness of passive oxide film on iron formed in neutral borate solution at pH 8.4 and in acidic phosphate solution at pH 3.1 for 1 h under potentiostatic condition. The thickness was estimated by ellipsometry with light at 460 nm wavelength. The current density (CD) was taken after 1 h potentiostatic oxidation at individual potentials.

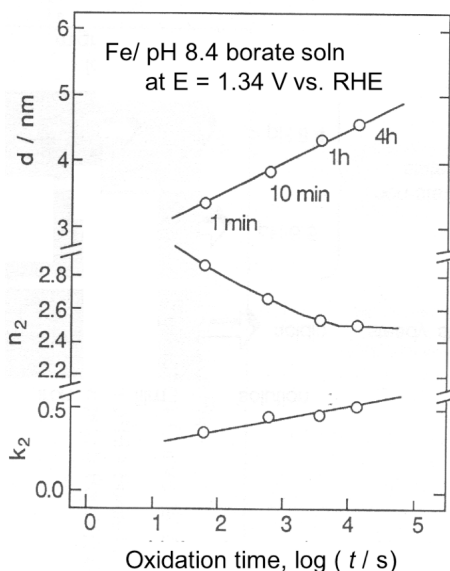


Fig. 2 Change of thickness and complex refractive index, $N_2 = n_2 - jk_2$, of the passive oxide film on iron with time at constant potential of 1.34 V vs. RHE. The thickness and complex refractive index were measured by ellipsometry with light at 460 nm wavelength.

The non-stationary growth was also pursued by the ellipsometry, as shown in Fig. 3,⁶⁾ where the film growth was measured during potential increase in sweep in passive potential region. The thickness increases with potential applied and the growth rate of dd/dE (d ; thickness and E ; potential) depended on the sweep rate, dE/dt . It was seen that the higher sweep rate induces smaller thickness and larger current. The relation may be explained by a model proposed by Vetter⁷⁾ and Sato et. al.⁵⁾ In the model non-stationary dissolution of ferric ions from the oxide was assumed at the oxide/ solution interface and the dissolution was combined with the high field ionic migration in the oxide film.

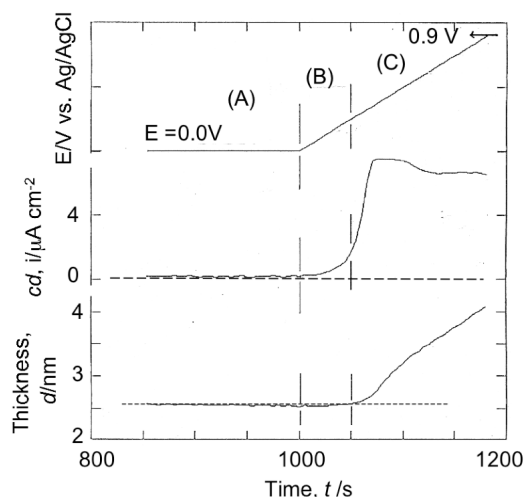


Fig. 3 Transient change of thickness of passive oxide during a potential sweep from 0.00 V vs. Ag/ AgCl/ Sat. KCl to 0.90 V following the constant potential oxidation at 0.00 V for 1000 s in neutral borate solution at pH 8.4.

3.2 Spectroscopic Property

If the ellipsometric measurement was done at multi-wavelength light, the spectroscopic data of the complex refractive index was obtained. From the spectroscopy of the k_2 values (imaginary part of the complex refractive index) one can calculate the light absorption coefficient (α) in unit of m^{-1} as the following.

$$\alpha = 4\pi k_2 / \lambda$$

where λ is wavelength of light. Figure 4 shows the spectroscopy of light absorption.⁸⁾ The relation between the light absorption and the photon energy of incident light can be approximated as the following in the near region of band gap energy with assumption of direct transition from the valance to conduction band.

$$\alpha^2 = K(h\nu)$$

The band gap in the passive oxide film is estimated from an extrapolation to the photon energy axis to be 2.6 eV.

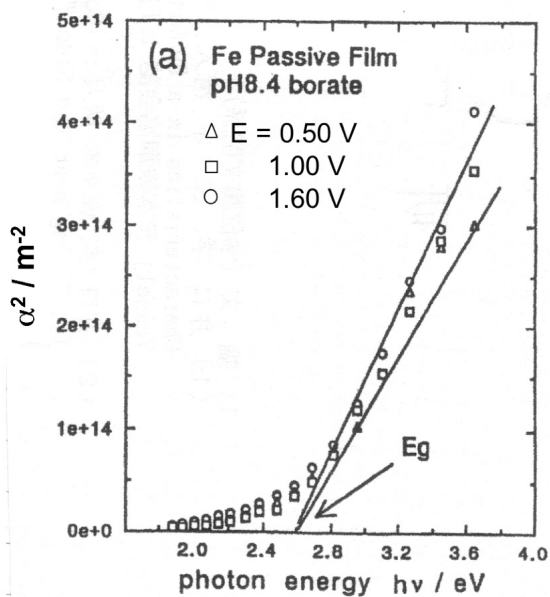


Fig. 4 Square of light absorption coefficient, α^2 , of the passive oxide films formed at 0.50, 1.00, and 1.60 V vs. RHE in neutral borate solution at pH 8.4 vs. photon energy. The absorption coefficient was estimated from the k_2 value in the complex refractive index measured by multi-wavelength ellipsometry.

3.3 Outer Hydrated Layer

The much thick passive oxide film has been reported in the neutral solution, when one oxidized at potential sweep from the active potential region. We believe that the thicker oxide may be formed by effect of Fe^{2+} dissolved in aqueous solution. The Fe^{2+} dissolved can be deposited as FeOOH which is oxidized from Fe^{2+} in the solution. The effect of Fe^{2+} dissolved was examined in the experiment where the iron was oxidized in the neutral borate solution containing Fe^{2+} at given concentrations. Figure 5 shows a thickness increase with time at 0.80 V vs. Ag/AgCl/Sat. KCl in the solution containing Fe^{2+} at 0.00, 0.25, and 0.50 mM.⁹⁾ During the initial 10 s oxidation, the initial film is formed to thickness of about 4 nm and thickness remains almost constant until 900 s without Fe^{2+} ions in the solution. When the Fe^{2+} ions are contained in the solution, the film linearly grows in thickness with time to thickness over 10 nm and the growth slopes are proportional to Fe^{2+} concentration. The result in Fig. 5 may be explained from anodic deposition from Fe^{2+} in the solution to $\text{FeOOH} \cdot x\text{H}_2\text{O}$ ¹⁰⁾ which was gradually formed on the passive oxide. The initial passive oxide is spontaneously formed with the application of potential in the passive region and, however, the deposition from Fe^{2+} is relatively slow process and may be controlled by a diffusion of Fe^{2+} ions in the solution.

Nagayama and Cohen estimated the thickness of the passive film by electricity measurement in which they performed a relatively slow transient from the active to passive state.¹¹⁾ The thickness estimated is about doubly larger than a thickness by ellipsometry. Noda and Sato indicated from ellipsometry that the passive oxide grown by the slow transient from the active to passive state consists of two layers, the inner

of which may be compact and the outer hydrated and loose.¹²⁾ The results reported indicate that Fe^{2+} dissolved in the initial slow transient from the active to the passive state results in a thick hydrated layer due to an anodic deposition from Fe^{2+} in neutral aqueous solution.

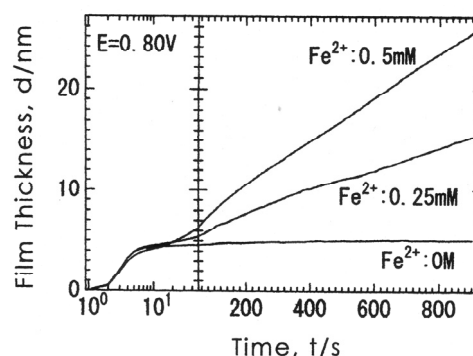


Fig. 5 Film growth of passive oxide film in neutral borate solution at pH 8.4 containing Fe^{2+} at concentration of 0.00, 0.25, and 0.50 mM at 0.80 V vs. Ag/AgCl/Sat. KCl. The thickness was measured by ellipsometry with light of 632.8 nm wavelength.

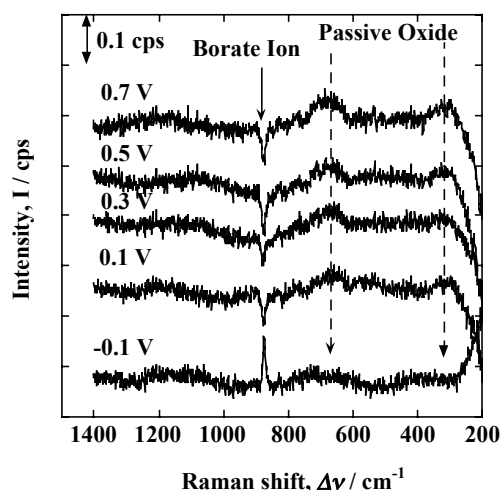


Fig. 6 In-situ Raman spectra of the passive oxide film on iron in neutral borate solution at pH 8.4. The spectra plotted was calculated from subtraction of a spectrum for bare reduced iron from those for the passivated iron at the individual potentials. The positive or negative strong peak at 880 cm^{-1} corresponds to borate ions in the electrolyte solution.

3.4 Raman Spectroscopy

The Raman spectra of the passive oxide formed was measured in the cell designed for in-situ measurement. The results are shown in Fig. 6 where the passive oxide is formed in neutral borate solution by step-wise potential increase in the passive potential region. The Raman spectrum was measured after the iron electrode was kept for 1 h at each potential. The accumulation time with CCD camera for detection of Raman scattering light was 1000 s with irradiation of Ar ion laser light of 514.5 nm wavelength at about 100 mW out-put power. The Raman spectra shown in Fig. 6 are difference signals which are

obtained by subtraction of the Raman signal on reduced bare iron from those on the passive iron. An intense Raman peak at 875 cm^{-1} was observed, which corresponded to the strongest Raman peak of borate ions in the electrolyte solution. In addition to the Raman peak of borate anions, the difference spectra in Fig. 6 exhibit a small and broad peak at about 670 cm^{-1} , and the peak intensity increases as potentials increase from 0.02 cps to 0.04 cps. Another faint peak is observed at 320 cm^{-1} and also increases with potential.

When we measured the passivated surface under ex-situ condition in air soon after removal of the electrode from the electrolyte solution, we observed clearer Raman peaks, which are given in Fig. 7. In Fig. 7, the background signal is not appreciable and the Raman peak at 670 cm^{-1} is clearly distinguishable. In addition, a small peak at about 320 cm^{-1} can be observed. The ex-situ spectrum is almost the same as that previously reported.²⁾

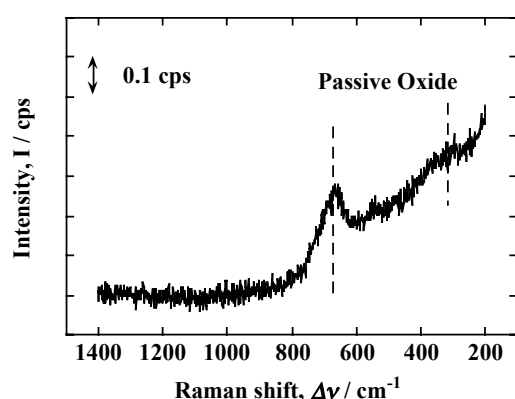


Fig. 7 Ex-situ Raman spectrum of the passive oxide film on iron in neutral borate solution at pH 8.4. The spectrum was measured in air immediately after the passivated iron was removed from the solution.

Although the spectra measured are broad and do not exhibit clear peaks, the passive oxide may basically be considered an amorphous-like Fe(III) oxide and oxyhydroxide. In the Raman spectra of iron oxides and oxyhydroxides, Fe_3O_4 , $\gamma\text{-Fe}_2\text{O}_3$, and $\delta\text{-FeOOH}$ possess the strongest peak at a Raman shift of about $600\text{--}700\text{ cm}^{-1}$ in the individual Raman peaks; for example, the strongest peak of Fe_3O_4 is 670 cm^{-1} , $\gamma\text{-Fe}_2\text{O}_3$ is 680 cm^{-1} , and $\delta\text{-FeOOH}$ is 700 cm^{-1} .^{2, 13, 14, 15, 16)} From the second peak at $300\text{--}400\text{ cm}^{-1}$ observed under the ex-situ condition as well as the in-situ condition, one can select the compounds of Fe_3O_4 and $\gamma\text{-Fe}_2\text{O}_3$ as candidates for the passive oxide. The assignment is in agreement with the presumption derived by Graham et al., from the results by SIMS and XPS.¹⁷⁾ They assumed that the passive oxide film was composed of Fe_3O_4 at the oxide/metal interface and $\gamma\text{-Fe}_2\text{O}_3$ at the oxide/solution interface. Our results support this estimation. The spectra in this work indicate that the passive film is not largely hydrated, although the oxide is formed in the aqueous solution. Ohtsuka et al. discussed the dehydration of the hydrated oxide film induced by a high electric field crossing the passive oxide film on iron as well as nickel¹⁸⁾ and titanium¹⁹⁾. The hydration-dehydration change will be examined further.

4 CONCLUSION

1. The thickness of the passive oxide on iron increases with potential under both stationary and non-stationary conditions. The growth may be followed by the field-assisted ionic migration mechanism coupled with non-stationary dissolution of ferric ions from the oxide.
2. From spectroscopic ellipsometry, a light-absorption edge was estimated at 2.6 eV, which may be a band gap energy of the semiconducting passive oxide.
3. When Fe^{2+} ions exist in the solution, the anodic deposition of $\text{FeOOH}\cdot\text{H}_2\text{O}$ takes place, resulting in formation of an outer hydrous layer a few 10 nm thick.
4. The Raman spectra of the passive oxide correspond to those of Fe_3O_4 and $\gamma\text{-Fe}_2\text{O}_3$.

References

- [1] T. Ohtsuka, *Denki Kagaku (J. Jpn Electrochem. Soc.)*, 60 (1992) 1123.
- [2] T. Ohtsuka, *Transaction JIM*, 37 (1996) 67.
- [3] K. Azumi, T. Ohtsuka, and N. Sato, *Denki Kagaku (J. Jpn Electrochem. Soc.)*, 53 (1985) 700.
- [4] H. Cabrera and N. F. Mott, *Rep. Progr. Phys.*, 12 (1949) 163.
- [5] N. Sato and T. Noda, *Electrochim. Acta.*, 22 (1977) 839.
- [6] T. Ohtsuka and Ohta, *J. Material Sci. and Engineering*, A198 (1995) 169.
- [7] K. J. Vetter and F. Gorn, *Electrochim. Acta*, 18 (1973) 321.
- [8] K. Azumi, T. Ohtsuka, and N. Sato, *J. Electrochem. Soc.*, 113 (1986) 1326.
- [9] T. Ohtsuka and H. Yamada, *Corrosion Sci.*, 40, (1998) 1131.
- [10] T. Ohtsuka and J.-S. Ju, S. Ito, and H. Einaga, *Corrosion Sci.*, 36 (1994) 1257.
- [11] M. Nagayama and M. Cohen, *J. Electrochem. Soc.*, 110 (1963) 670.
- [12] N. Sato, K. Kudo, and T. Noda, *Z. Phys. Chem. N. F.*, 98 (1975) 271.
- [13] J. Gui and T. M. Devine, *Corrosion Sci.*, 37, 1177 (1995).
- [14] N. Boucherit, A. Hugot-Le Goff, and S. Joiret, *Corrosion Sci.*, 32, 497 (1991).
- [15] T. Ohtsuka, K. Kubo, and N. Sato, *Corrosion*, 42, 476 (1986).
- [16] R. J. Thibreau, C. W. Brown, and R. H. Heidersbach, *Appl. Spectrosc.*, 32, 532 (1978).
- [17] M. E. Brett, K. M. Parkin, and M. J. Graham, *J. Electrochem. Soc.*, 133, 2031 (1986).
- [18] T. Ohtsuka and S. Iida, *Corrosion Sci.*, 49, 1408 (2007).
- [19] T. Ohtsuka and N. Nomura, *Corrosion Sci.*, 39, 1253 (1997).

Application of PVDF Pressure Gauge for Pressure Measurements of Non-ideal Explosives

Kenji MURATA and Yukio KATO

Nippon koki. Co., Ltd.2-1 Dobu, Nagasaka, Nishigo-mura,
Nishishirakawa-gun, Fukushima,961-8686, JAPAN

Kmurata@nippon-koki.co.jp

abstract : Manganin pressure gauge has been widely used for pressure measurements of shock wave in condensed matter and detonation in condensed explosive. However, recording time of manganin gauge is limited to a few microsecond. This short recording time is not long enough to measure detonation pressure of non-ideal explosive which has long reaction zone length. We developed pressure gauge composed of PVDF sensing element which has longer recording time compare with manganin pressure gauge.

In this study, detonation pressure profile was measured by PVDF pressure gauge for non-ideal explosives consisted of a packed bed of aluminum particles of different size saturated with neat nitromethane. The results of pressure measurements by PVDF pressure gauge show the existence of the extended reaction zone behind leading shock wave, which is considered to be the results of significant interplay between detonations in nitromethane in interstitial pores and shock waves in metal particles. The results of pressure measurements also revealed important pressure increase due to aluminum particle reaction when aluminum particle size is smaller than 16 micrometer. The result of this study showed that PVDF pressure gauge is very useful tool to measure detonation pressure of non-ideal explosives which have very long reaction zone length.

Key word: PVDF sensor, Detonation pressure measurements, Explosive

Effect of temperature and corrosive environment on cyclic fatigue and final fracture behavior of 2524 aluminum alloy

Yi Danqing^{a, b} Zhou Mingzhe^a Liu Huiqun^{a, b} Wang Bin^{a, b} Yang Sheng^{a, b}

^a School of Materials Science and Engineering, Central South University, Changsha, Hunan, 410083, P.R. China

^b Key Lab of Nonferrous Materials, Ministry of Education, Central South University, Changsha, Hunan 410083, P.R. China

danqing123456@126.com

Abstract: The effect of temperature and environment (air, humidity and 3.5wt% NaCl salt spray) on cyclic fatigue life and fracture mechanism on 2524 aluminum alloy was investigated by scanning electron microscopy (SEM), transmission electron microscopy (TEM) and fatigue property testing. The results showed that temperature has a detrimental influence on cyclic fatigue life. The cyclic fatigue strength $n=10^6$ at elevated temperature (100°C) decreased by 30Mpa compared to that at cryogenic temperature (-55°C). Moreover, temperature also remarkably affected the feature of dislocation, second-phase particles and grain boundary. The fracture surface at cryogenic temperature showed crystallographic morphology. The dominant deformation process at ambient and elevated temperature was a combination of predominantly transgranular and local intercrystalline fracture mechanism. The fractographic features revealed the fatigue crack growth behavior of the alloy in three environments, more brittle striations were observed in humidity air and salt spray. The increased crack growth rate was attributed to a combination of hydrogen embrittlement and anodic dissolution at the tip of crack.

Keywords: 2524 alloy; temperature; corrosion; cyclic fatigue; hydrogen embrittlement

1. Introduction

Aluminum alloys found a wide variety of uses in airplane industry because of their remarkable combination of low density, high corrosion resistance, easy workability, high electrical and heat conductivity. In the past decades, innovation and progress related to the processes and property of aluminum

alloys greatly contributed to the design and manufacture of new-type civil and military aircraft. Novel aluminum alloys and tempers, for example, have been used in Boeing 777 aircraft to obtain an improved combination of strength, ductility and damage tolerance over those alloys used in previously designed aircrafts [1].

Fatigue is a very important issue to be considered in the design

of mechanical components subjected to constant and variable amplitude loading. Mechanical, metallurgical and environmental factors affected the fatigue resistance of structural components[2]. Normally fatigue is the primary cause for 80-90% of all engineering failures [3].

Corrosion pits were found to initiate crack growth in structures subjected to fatigue loading. A number of studies have addressed this by experimentally observing and modeling the growth of corrosion-initiated fatigue cracks in aluminum alloys [4-8]. A fracture mechanics approach for life prediction has been employed where the researchers have adapted the special case of pits serving as initial flaws. It has repeatedly been observed that multiple crack-nucleating pits can lead to the failure of individual test samples [9-12]. Cycling heating and cooling could also result in fatigue of structure components, i.e. thermal fatigue. It is thus important that materials using for aircraft's structure have good thermal fatigue resistant performance. Abelkis[13] found that 2024 aluminum alloy performed a better fatigue property at 219K than that at room temperature. Srivatsan [14,15] observed similar results in 2524-T3 alloy, which has initial hardening followed by rapid softening to failure at elevated temperature.

2524 aluminum alloy is a relatively new Al-Cu-Mg alloy and used as fuselage skin replacement of 2024 alloy[16,17]. The objective of this paper is to document the influence of temperature and corrosion environment on fatigue property of 2524 aluminum alloy. The high-cycle fatigue properties and final fracture characteristics of the alloy at four temperatures are evaluated. The fatigue crack propagation of the alloy in humid air and salt spray were investigated compared to the test conducted in the lab air.

2. Experiment

2524 alloy for this study was provided by Northeast Light Alloy Co. Ltd. with final condition being 2.2mm thick alclad sheet. The chemical composition of the material is listed in Table 1. Axial test specimens were machined from as-received 2524-T4 alloy plate according to China standard GB 3075-82 for stress amplitude-controlled high-cycle fatigue test. The stress axes of the specimens was parallel (longitudinal) to the rolling direction. The measured gauge of the specimen is 15mm in length. All mechanical tests were loaded up to failure on a fully automated, closed-loop servohydraulic mechanical test machine (INSTRON-8032). Fracture surface of the cyclically deformed and failed specimens were examined by KYKY-2800

type scanning electron microscope (SEM) to characterize the topographic features of the fatigue fracture surface. Disks of 3mm in diameter and around 0.5mm in thickness were cut from the fatigue test samples near the fracture surface for TEM observation. Electropolished solution was a mixture HNO₃ and methanol (1:3 in volume). TEM foils were examined by TecnaiG²20 transmission electron microscope operating at 200kV.

Table 1 The chemical composition of 2524 alloy (wt%)

	Cu	Mg	Mn	Fe	Si	Al
wt%	4.0-4.23	1.4-1.42	0.56-0.6	≤0.08	≤0.06	bal.

3. Results and discussion

3.1 The influence of temperature

3.1.1 S-N curves: S-N curves for as-received 2524 alloy at four different temperatures (-55°C, 25°C, 100°C, 150°C) were given in Fig.1. It can be found that fatigue life (N_f) is inversely proportional to the temperatures at the same stress level. The cyclic fatigue strength of 10^6 cycles at elevated temperature (100°C) decreased by 30MPa than that at the cryogenic temperature (-55°C). The fatigue behavior of alloy at 150°C at higher stress level is discussed below.

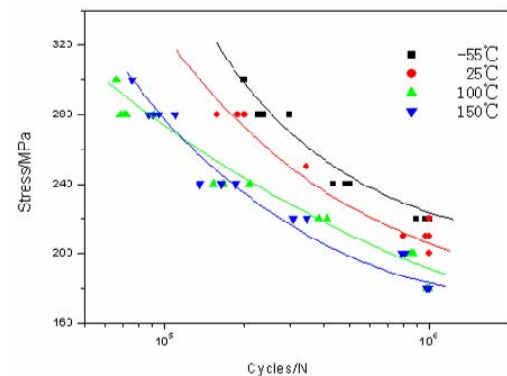


Fig.1 Fatigue S-N curves of 2524 alloy at different temperatures

3.1.2 Fracture analysis: Figs.2-4 show fractographic morphology of different stages of crack growth in the 2524 alloy studied together with fatigue life N_f . The fatigue life was tested at -55°C, 25°C, 100°C and 150°C. Fig.2 illustrates the cases that the crack originated from surface at different temperature. Normally, the crack source comes from the surface, where the maximum tension stress occurs. For the alclad alloy, the crack initiated at the pure aluminum layer because of its lower yield strength [18,19]. Fig.3 illustrates the fatigue crack propagation area. As shown, the fracture surface at cryogenic temperature exhibits a crystallographic fracture

pattern, which was not observed at room temperature and above. The overload region of all samples comprised of macroscopic voids and shallow dimples.

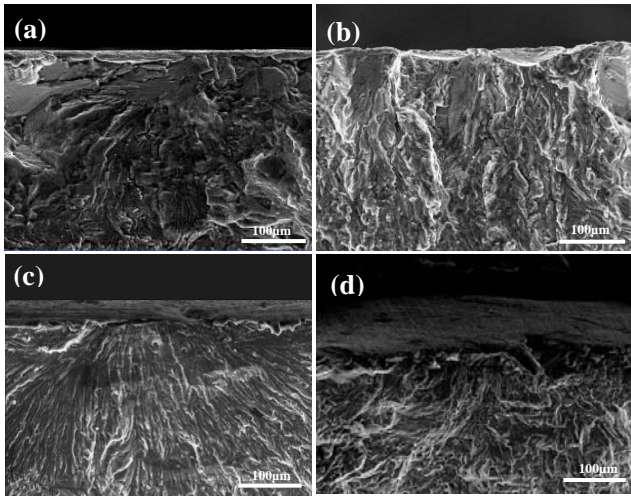


Fig.2 Fractograph of fatigue initiation zone of 2524 alloy at $\sigma_{max}=280$, with (a) -55°C $N_f=297541$ (b) 25°C $N_f=111957$ (c) 100°C $N_f=72198$ and (d) 150°C $N_f=90688$

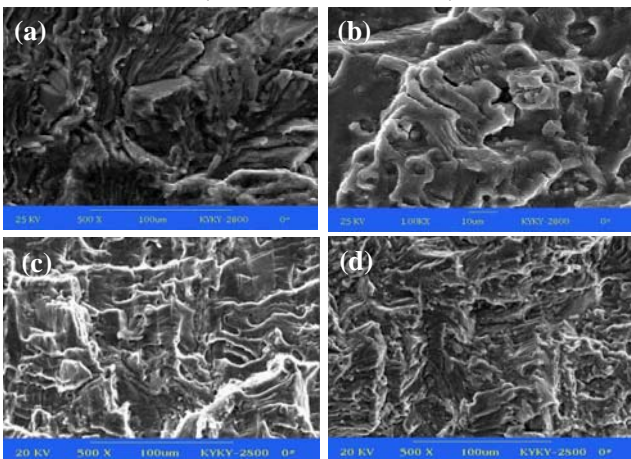


Fig.3 Fractograph of fatigue crack growth of 2524 alloy at $\sigma_{max}=280\text{MPa}$, with (a) -55°C $N_f=297541$ (b) 25°C $N_f=111957$ (c) 100°C $N_f=72198$ and (d) 150°C $N_f=90688$

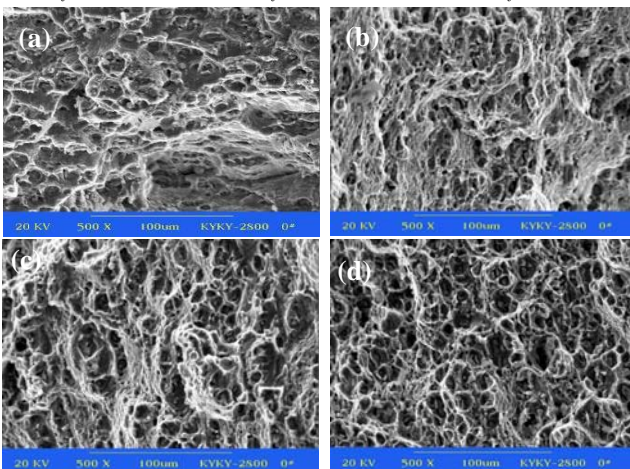


Fig.4 Fractograph of rapid crack growth zone of 2524 aluminum alloy at $\sigma_{max}=280$, with (a) -55°C $N_f=297541$ (b) 25°C $N_f=111957$ (c) 100°C $N_f=72198$ and (d) 150°C $N_f=90688$

3.1.3 TEM microstructure: Fig.6 illustrates the TEM images of 2524 alloy after fatigue test at different temperatures. As seen in Fig.6, the dislocation density is lower at cryogenic temperature than that at room temperature because more energy is needed for the generation and movement of dislocation at low temperature. With the increase of temperature, more dislocations were easily to move and then piled up at grain boundary; small cracks formed in consequence after applying cyclic stress.

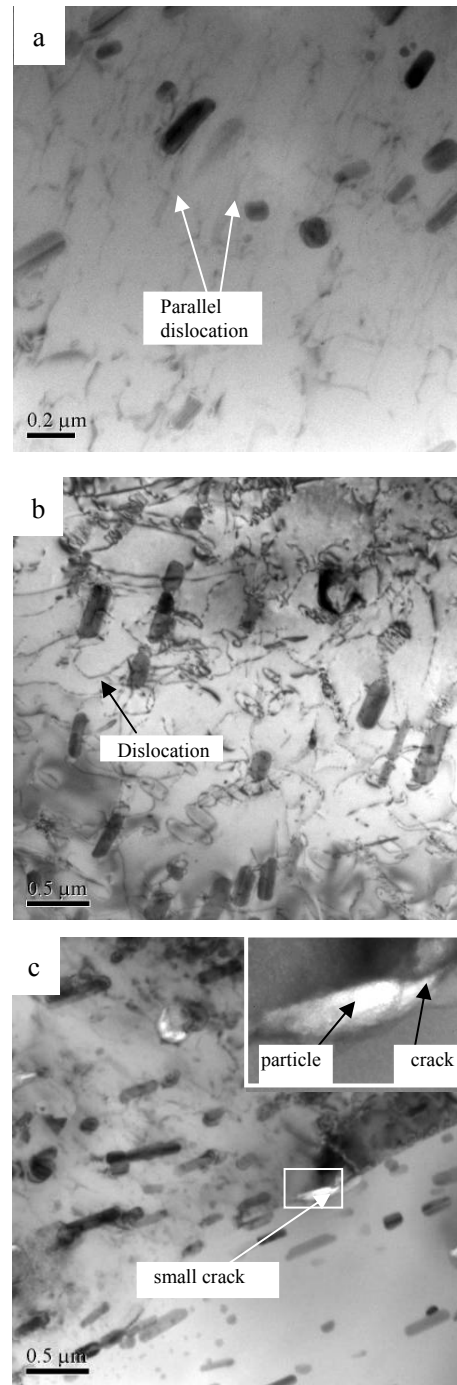


Fig 6 TEM of 2524 Al alloy at $\sigma_{Max} = 280\text{MPa}$ (a) -55°C $N_f=297541$ (b) 25°C $N_f=111957$ (c) 100°C $N_f=72198$

3.1.4 Effect of temperature on fatigue mechanism: During the fatigue process, the formation of

fatigue crack took most of the fatigue life, in order to analyze the effect of temperature on fatigue life, here we focus on micro-crack formation as a function of temperature. According to the dislocation slipping mechanism, there were three stages during fatigue process: (a) fine slip lines formed by the motion of dislocations, (b) formation of slip band; (c) formation of micro-crack. In this paragraph, the micro-rheological stress mechanism was introduced to analyze the effect of temperature on the fatigue properties of the alloy[20,21], the stress τ is given by[22]:

$$\tau = \tau_p + \tau_s + \tau_l + \tau_j + \tau_D \quad (1)$$

where τ_p is the lattice resistance, τ_s , τ_l , τ_j and τ_D are the resistance caused by dislocation stress field, dislocation intersect, jogging, and point defects respectively. The τ_s , τ_l are long-range resistance which is insensitivity to temperature, while τ_j and τ_D are short-range resistance sensitive to temperature. At ambient temperature, both the lattice resistance τ_p and short range resistance are small where the movement of dislocations to be ease. However the pile-up of dislocations at grain boundary would cause local stress concentration and micro-crack formation. On the other hand, the thermal vibration of the lattice at cryogenic temperature is decreased, where the long-range resistance being remained, while temperature sensitive factors τ_j and τ_D increased, causing larger lattice resistance. Compared with the case of the ambient temperature, the mobility of dislocations is decreased at the same stress level (Fig.6). Lower density of dislocations means less micro stress concentration of the alloy, so the time of micro-crack formation was longer. Moreover, the dislocation accumulation rate at grain boundaries tends to be slower, which means longer time for the dislocations to move in neighbor grains. At higher temperature, the energy for dislocation to start moving decreased, and dislocations movement occurred and piled up at the grain boundaries. After fewer loading times, they could cause the stress concentration and then resulted in micro-cracks (Fig.6 c), which led to a short fatigue life at the same stress level compared with the case of lower temperature. As known, the slip bands could be recovered during the fatigue process, but at higher temperatures, the formation of an oxide of Al_xO_x will occur in a short time, by synergism of temperature and oxygen in the ambient air, and caused a reduction of the recovery of the slip bands, which produced unrecovery plastic deformation of the alloy. The synergism mechanism of all the factors mentioned above caused a shorter fatigue life of alloy at higher temperatures.

It is worth to mention that, at higher stress level, the alloy has a better fatigue property at 150°C than that at 100°C. During the fatigue process at 150°C, higher temperature and stress induced the precipitation of second phase. The increase of dislocation moving resistance by precipitates improved the fatigue performance at 150°C[23]. However, at lower stress level, by the precipitates coarsening during the long period fatigue process, the mechanism mention at last paragraph become the dominate mechanism.

According to the work of Cedirc[24], for naturally aged 2024 Al-Cu-Mg alloy, although the fatigue stress was large enough, the dislocation can cut through the GP zone and form the fracture surface with steps. At cryogenic temperature, because of high resistance to dislocations movement, it is very hard for dislocation slip to transmit from one grain to neighbor grain. The different grains have different orientations, the crack will propagate along a route with least resistance so the cryogenic fracture shows coarsening steps pattern. With the increase of temperature, dislocations' mobility increase, the stress concentration caused by the piled up dislocations near the grain boundaries could start more slip bands in the neighbor grains, and the nearly grains with lower deflexion angle become easier to crack, so the fracture morphology shown smoother patterns. As seen in Fig.2 to Fig.4, the cryogenic fracture surface is characterized by some cleavage feature and plates (Fig.2a, Fig.3a). At ambient temperature and higher temperatures, striations were observed paralleling the cracking direction, and some micro-cracks can be seen near the grain boundaries especially at high temperature. That is because at higher temperatures, the binding force of atoms decreased, so the cracks were easily formed at the area. Large amount of oxide were observed at the fracture surface, after treated at 150°C.

3.2 The influence of corrosion environment

3.2.1 Fatigue crack propagation (FCP): FCP rate of 2524 Al alloy in three different environments (lab air, humid air and salt spray) were shown in Fig.7 and Fig.8. The humid air and salt spray environment accelerate the fatigue crack propagation. At the first stage of fatigue crack propagation, humid air accelerates the FCP significantly. The FCP rate in humid air is almost two times than that in ambient air. While at the steady-state stage, the FCP in humid air is 40% faster than that in ambient air. Based on the Paris relationship (Eq.1), an environment factor γ was introduced here for amendment, seen in Eq.2. Linear regression fitted results of the environment factor γ were 1.324 and 1.528 for humid air and salt spray

environment respectively.

$$da/dN = c\Delta k^n \quad (2)$$

$$da/dN = \gamma c\Delta k^n \quad (3)$$

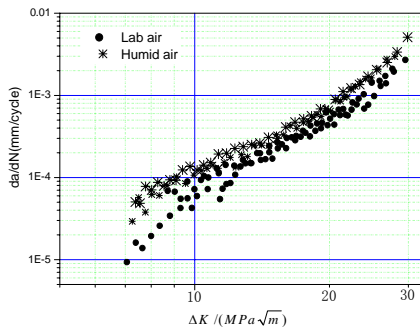


Fig.7 Crack growth rate of alloy in lab air and humid air

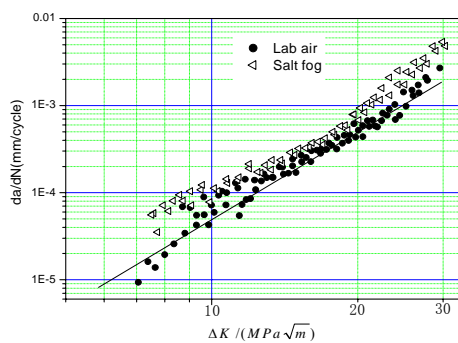


Fig.8 Crack growth rate of alloy in lab air and salt spray

3.2.2 Fracture morphology: The SEM observation of fatigue fracture surface ($\Delta K = 10\text{MPa}\sqrt{\text{m}}$) is presented in Fig.9. It can be seen that in ambient air the striations were evenly spaced indicating stable growth of cracks through the microstructure. In contrast to the case above, the fractographs of tested samples in the other two environments show more brittleness feature, and some micro-cracks were observed as pointed by white arrows in Fig.9. For the salt spray tested samples, the fractured surface was covered by a layer of corrosion products. The striations exhibit brittleness feature. The width between the striations in salt spray environment was the largest at the same stress level, which was consist to the FCP rate results (Fig.7, 8).

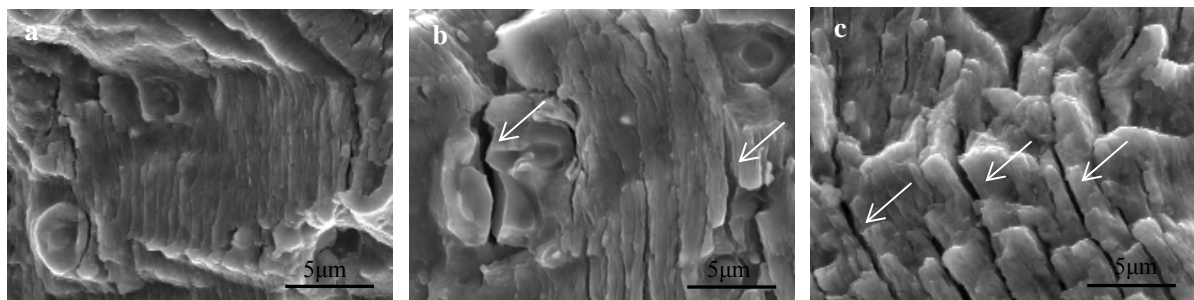


Fig.9 Fatigue fractographs for 2524 alloy, where $\Delta K = 10\text{MPa}\sqrt{\text{m}}$, with (a) in lab air; (b) humid air; and (c) salt spray

3.3 Fatigue Mechanism

During the fatigue process, plastic deformation accumulated at the plastic zone beyond the fatigue crack tips, then caused the crack propagation and the plastic deformation striations formed. According to the hydrogen embrittlement theory [25,26], if there was water vapor in the environment, some reactions would occur at the fresh fracture surface during the fatigue process as follows::

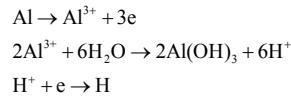


Fig.10 gives a schematic of hydrogen embrittlement during the fatigue process. The activated H atoms could diffuse through dislocations to the tip of cracks, and then caused the brittleness at the plastic zone beyond the crack tips, which resulted in the stress for decreasing the crack propagate, so the FCP rate increased simultaneously. At the initial stage of crack propagation, lower FCP rate led to less surface, so the exposed fresh surface per cycle was very limited, which means that the amount of activated H atoms transporting to the plastic zone per cycle was high. So the effect of hydrogen embrittlement on the FCP rate at lower stress intensity factor range is remarkable (Fig.7). With the propagation of fatigue crack, the flux of activated H atoms to the plastic zone per cycle became smaller, so the effect of hydrogen embrittlement on the FCP rate at high stress was less significant.

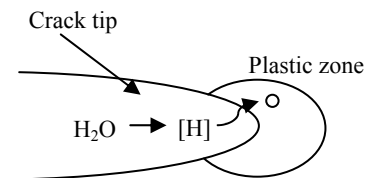
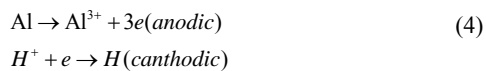


Fig 10 Schematic of hydrogen embrittlement in corrosive environment

Similar to the fatigue propagation in the humid air, the fresh fracture surface exposed in salt spray environment, in which cell reaction occurred during the fatigue process, as presented in Eq.4, the salt spray is the electrolyte, and the fresh surface of the alloy was the anode of corrosion microbattery. The anode metal dissolved into the electrolyte which caused pits at the surface of alloy. The stress concentration at the pits accelerated the crack propagation rate. In another hand, the dissolving occurring at the crack tip promoted the hydrogen brittleness, and then increased the FCP rate of the alloy. The co-action of pit stress concentration and hydrogen brittleness contribute to the highest FCP rate in this experiment.



4. Conclusions

By the use of fatigue test machine, SEM and TEM, the fatigue performance and fracture behavior of 2524 aluminum alloy were studied at four temperatures and in three classical environment (ambient air, humid air and salt spray), we can conclude as follows: (1) The fatigue life of the alloy increased with the decrease of temperature, the better fatigue performance at lower temperatures is due to higher dislocation motion resistance. (2) The fatigue crack propagation rate increased in humid and salt spray environment, environment factor γ of meliorated Paris relationship are 1.324 and 1.528 for humid air and salt spray environment respectively. (3) Hydrogen brittleness mechanism of activated H atoms transporting to the plastic zone is the main reason for the FCP acceleration in humid air environment, and the acceleration of FCP rate in the salt spray environment is due to the hydrogen brittleness and anode dissolving synergism.

Acknowledgements

This research was jointly supported by The National Key Basic Research Program of China (grant Number, 2005CB623705) and China Aluminum Company Research Program (grant Number CHALCO-2007-KJ-09). The authors would like to thank both of them.

References

[1] Payne J, MIAC Newsl 1995, December: 4-6
 [2] Pellpoux RM, In: Proceedings of Conference fatigue. Montreal, 1993
 [3] Ilston JM, Dinwoodie JM, Smith AA, Concrete timber and metals, New York: Van Nostraand Reinhold; 1979.

[4] Du Quesnay DL, Underhill PR, Britt HJ. Int J Fatigue 2003, 25: p.371-377
 [5] Medved JJ, breton M, Irving PE. Int J Fatigue 2004, 26: p.71-80
 [6] Sankaran KK, Perez R, Jata KV. Mater Sci Eng 2001, A297: p.223-229.
 [7] Dolley EJ, Lee B, Wei RP. Fatigue Fract Eng Mater Struct 2000, 23: p.555-560
 [8] Zamber JE. MS Thesis. Purdue University, 1997
 [9] Bray GH, Bucci RJ, Colcin EL, Kulak M. ASTM STP 1298. ASTM, 1997, p.89-103
 [10] Perez R. Corrosion/fatigue metrics. ICAF97 symposium on fatigue in new and ageing aircraft, Edingburgh, Scotland, 1996, p.215-229
 [11] Pao PS, Gill SJ, Feng CR. Scripta Mater 2000, 43: p.391-396.
 [12] Tuegel EJ. Report AFRL-VA-WP-TR-2003-3088. Air Force Research laboratory, Air Force Material Command, Wright-Patterson Air Force Base, Ohio; 2003
 [13] Abelkis PB, Harmon M B ,Hayman E L. ASTM Special Technical Publication, 1985, p.257-273
 [14] Srivatsan TS, Kolar D, Magnusen P. Materials Science and Engineering A, 2001, 314: 118-130
 [15] Srivatsan TS, Kolar D, Materials and Design, 2002, 23:129-139
 [16] Starke EA, Staley Jr and JT, Prog. Aerospace Sci. 1996, 32: p.131
 [17] Cassada W., Liu J., Taley J.: Advanced Materials Processes, 2002, 162: p.27.
 [18] Edwards PR, Earl MG, RAE Technical Report of Aeronautical Research Council, Farnborough, 1977.
 [19] Truckner WG, Staley JT, Bucci RJ, et al. USAF Technical Report AFML-TR-96169, 1976, 10.
 [20] Xu H. Fatigue Strength [M], Beijing, Higher Education Publishing Company, 1988
 [21] Feng D., Metal Physics [M], Beijing, Science Press, 1999
 [22] Basinski ZS, Christian JW. Advanced Cryogenic Engineering, 1954, 2: p.90-92
 [23] Yang S., Study on the microstructure of 2E12 aluminum alloy during the attended time [D].
 [24] Cedric G, Christine SB, Jean P, etal. Scripta Materialia, 2005, 53: p.1333-1337
 [26] Stanzl-Tschegg SE, Mayer HR, Tschegg EK. Materials Science and Engineering A, 1991, p. 45-54
 [27] Harvey C. Voris and Min-Ten Jahn, Journal of Material Science, 1989, 25: p.4708-4711

Interface Atomic Structures and Properties of Ceramics

Yuichi Ikuhara^{1,2,3}

¹ Institute of Engineering Innovation, The University of Tokyo, Tokyo 113-8656 Japan.

² Nanostructures Research Laboratory, Japan Fine Ceramic Center, Nagoya 456-8575, Japan.

³ WPI Advanced Institute for Materials Research, Tohoku University, Sendai 980-8577, Japan
 ikuhara@sigma.t.u-tokyo.ac.jp

Abstract: Interfaces in ceramics play an important role on the various properties. It has been known that the addition of small amount of dopants strongly improve the mechanical and functional properties in polycrystalline ceramics. Z-contrast images obtained by scanning transmission electron microscopy (STEM) is powerful technique to experimentally determine the atomic site of the dopants segregated at grain boundaries. As the image intensity in the Z-contrast is approximately proportional to the square of the atomic number, STEM technique is especially well suited for understanding the role of heavy impurities in grain boundaries composed of much lighter ions. In this paper, the results obtained by high-angle annular dark field STEM (HAADF-STEM) are demonstrated for well-defined grain boundaries in ZnO and Al₂O₃ bicrystals doped with Y and Pr. In addition, several examples are also demonstrated to characterize the dislocation core structures in ceramics, interface structures of SrTiO₃ superlattice and the ion site in lithium battery by HAADF-STEM

1. Introduction

Grain boundaries and interfaces of crystals have peculiar electronic structures, caused by the disorder in periodicity, providing the functional properties, which cannot be observed in a perfect crystal [1, 2]. In the vicinity of the grain boundaries and interfaces around the order of 1 nanometer, dopants or impurities are often segregated, and they play a crucial role in the material properties. We call these dopants “function providing elements”, which have the characteristics to change the macroscopic properties of the materials drastically.

To obtain a guideline for designing material by the atomic scale modification, an understanding of the atomistic mechanism for the functional properties is required as well as precise measurement of the present state of trace elements segregated in the nanoscale region. In recent nano-characterization technologies, there has been remarkable progress by Scanning Transmission Electron Microscopy (STEM) utilizing the spherical aberration (Cs) corrector [3]. The technique enables us not only to identify the location of the dopants but also to analyze the local electronic state for the single atomic column on grain boundaries and interfaces. In this paper, we focus our attention on grain boundaries and interfaces of various ceramics, to which “function provided elements” are doped, and introduce the latest results of the microstructure analyzed in detail by STEM. Furthermore, by the first principles calculation based on these observation results, the analyzed results of the mechanism of the “function providing elements” will be described as well.

2. Scanning Transmission Electron Microscopy (STEM)

STEM (Scanning Transmission Electron Microscopy) is a technique to scan a specimen by an electron probe, which is focused down to 1 nm or less on the sample. The STEM image is formed with the collected scattered electrons in each probe position by the Annular Dark Field (ADF) detector at the bottom of the sample on the monitor in synchronism with the scanning probe [4]. The atomic resolution image can be obtained by focusing the electron probe down to below the atomic column interval. The advantages of this method are those: there is no inversion of the image contrast with the defocusing and the change in the sample thickness, and thus

the positions of the atomic columns can be determined directly from the image. These excellent characteristics are very useful to determine the complicated atomic structures in the grain boundaries and interfaces. In addition, the intensity of the image obtained by detecting the electrons scattered to higher angles is known to correspond to about the square of the atomic number Z . The contrast of High Angle Annular Dark Field (HAADF) –STEM is therefore called “Z-contrast” as well, making it possible to observe the element distribution at an atomic column level in the region where local composition is changed. Figure 1 shows an example of HAADF-STEM image for SrTiO₃ projected along the [001]. As seen in Fig. 1, the contrast of Sr atoms ($Z=38$) is brighter than that of Ti atoms ($Z=22$), which indicates that atomic species can be discriminated in the one image. Moreover, in recent years, by

SrTiO₃

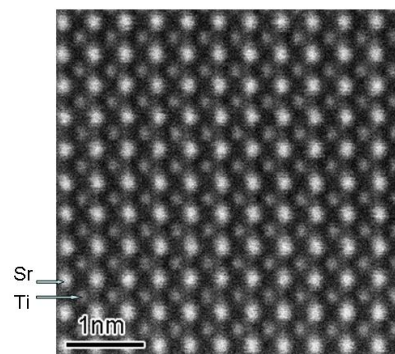


Fig.1 HAADF-STEM image for SrTiO₃ projected along the [001] direction, in which the contrast of Sr atoms ($Z=38$) is brighter than that of Ti atoms ($Z=22$).

combining STEM method with the Cs correction technology, drastic improvement in resolution has become possible. At present, with the STEM using the Cs corrector, the electron probe diameter of 1 Å (0.1 nm) or less has been already achieved [5]. Furthermore, since the intensity of the electron probe can be increased by the Cs correction technology, there are advantages that the S/N ratio of the STEM image will be increased and hence the image quality also can be improved drastically. STEM method using the Cs corrector is thus

expected as a powerful tool to characterize the atomic structures in grain boundaries and interfaces.

3. Results and Discussions

(1) Grain Boundary of Pr-doped ZnO Varistor^{6, 7)}

As an example of the grain boundary segregation in electro ceramics, Pr doped ZnO grain boundary is shown in this section. Since ZnO ceramics show high nonlinear current-voltage characteristics by doping secondary elements such as Pr and Bi, they are widely used for varistors. It has been reported that Pr and Bi etc., doped to ZnO ceramics segregate in grain boundaries and it is believed that they have an important role for providing varistor properties. However, its segregation behavior has not been understood in detail at an atomic level. It is therefore required to characterize an atomic level analysis of the Pr segregation in ZnO grain boundaries to clarify the atomistic mechanism of the varistor properties.

Figure 2 shows a HAADF-STEM image of the Pr-doped $\Sigma 7$ grain boundary (JEOL JEM-2100F (200 kV) with Cs corrector (CEOS), Univ. Tokyo) [6]. Here, Σ represents the degree of geometrical coherency at grain boundaries [1]. The small Σ number indicates high coherency, and the large Σ number indicates low coherency at grain boundaries. As described above, in HAADF-STEM image, the atomic column position emerges as white dots. Pr that has the higher atomic number than Zn, shows the brighter contrast. Accordingly, the bright spots, indicated by the arrows at the grain boundary, show the segregated Pr atoms. It can be recognized from the image that Pr does not have the wide distribution but segregates only at the special atomic sites. With substituting Pr atoms, suggested from the HAADF-STEM image, to the Zn sites in the $\Sigma 7$ grain boundary, the most stable atomic structure was calculated by the first principles method as shown in Fig. 3 [7]. It is confirmed from Fig. 3 that the experimentally observed Pr atoms segregate at the most stable position in the grain boundary. In addition, by the systematic first principles calculations, it was found that due to Pr presence in the grain boundary, acceptor type defects such as Zn vacancy and interstitial O atom are easily formed as well [6, 7]. These defect formations must be related with the mechanism of the varistor properties, which is believed to be an important role of Pr addition. Furthermore, it has been shown by the similar calculations that Pr segregates preferentially at the Zn sites (the locally tensile sites), in which the bonding length at the grain boundary is long [7].

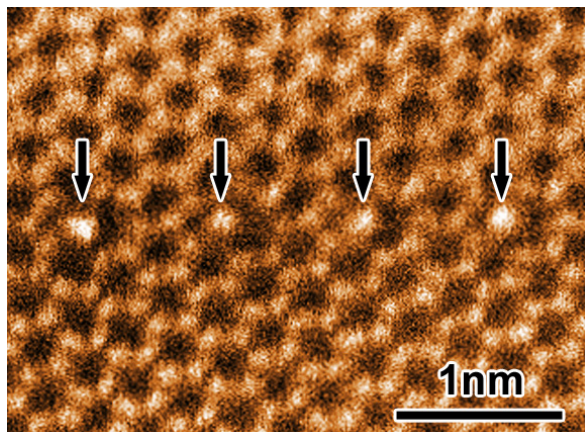


Fig.2 HAADF-STEM image of Pr-doped ZnO $\Sigma 7$ grain boundary, showing that Pr segregation sites can be observed as bright spots indicated by the arrows [6].

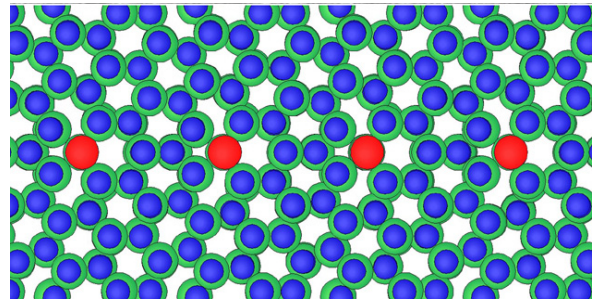


Fig.3 The stable atomic structure of Pr-doped ZnO $\Sigma 7$ grain boundary obtained by the first principles calculation (green circle: O, blue circle: Zn, red circle:Pr) [7].

(2) Grain Boundary of Y-doped Alumina Ceramics⁸⁾

It has been known that the high temperature strength of alumina ceramics is improved drastically by doping small amount of rare earth elements such as Y and Lu [8, 9]. Although it has been proposed that these minor doping elements segregate in the grain boundaries in the alumina polycrystal and prevent grain boundary sliding at high temperature, there are many unknown issues regarding the intrinsic mechanism yet. Here, the grain boundary structure of the Y-doped alumina was observed by STEM method. The results demonstrate the grain boundary strengthening mechanism by Y. Figure 4 shows HAADF-STEM image of the Y-doped $\Sigma 31$ alumina grain boundary (JEOL JEM-2100F (200 kV) with Cs corrector (CEOS), Univ. Tokyo) [8]. Here, $\Sigma 31$ grain boundary can be classified into a general grain boundary. It can be recognized that very strong contrast is observed at the particular atomic sites along the grain boundary. It corresponds to the position of Y atoms segregated in the grain boundary cores, which indicates that Y atoms segregate selectively and periodically only at the special sites in the grain boundary cores.

Figure 5 shows the results of the theoretical analysis by the first principles calculation based on this structure, showing the electron density distribution around the Y atoms segregated in

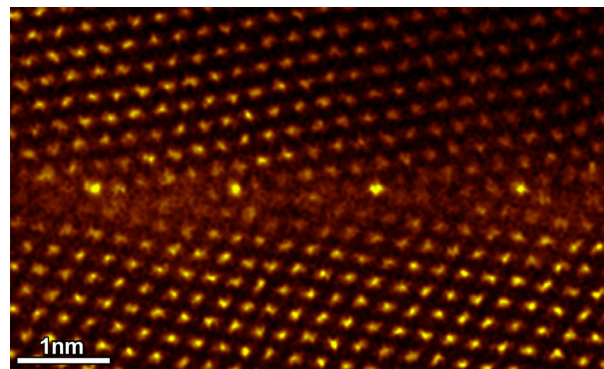


Fig.4 HAADF-STEM image of Y-doped $\Sigma 31$ [0001] tilt grain boundary in alumina. The brightest columns indicate the presence of the heavy Y ions.

the center of the seven member ring [8]. From Fig. 5, it is recognized that the electron distribution is oriented around Y atoms to form covalent-like chemical bonds in the seven member ring, which is confirmed to be significant by comparing with the fact that the bonds without segregation are mainly ionic bonding [8]. In this way, it has become evident

that due to the segregation of rare earth elements in the grain boundaries, surrounding chemical bonds change drastically, which has the effect to improve the grain boundary strength. In other words, it is believed that the effect of rare earth element doping to alumina ceramics is originated from the change in the local chemical bonding state at the grain boundary.

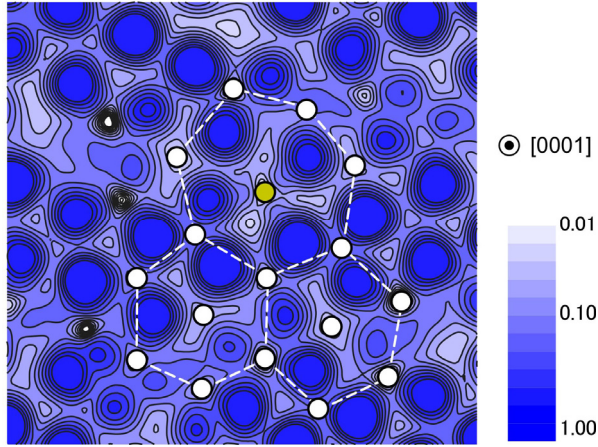


Fig.5 Electron density map around Y atoms segregated in Σ_{31} Al_2O_3 grain boundary, which was obtained by the first principles calculation [8].

(3) Dislocation Structure of Sapphire¹⁰⁾

To understand the mechanical properties of sapphire, many studies have been performed for the dislocations so far. It has been shown that the basal dislocation is dissociated to two partial dislocations. However, there are many unknown matters concerning the structure at the atomic level, and the atomistic mechanism of dislocation gliding has not been quantitatively understood yet. Since sapphire is composed of Al and O, an analysis of sublattice including the oxygen is required to understand its dislocation core structure at the atomic level. Therefore, using the Cs-corrected STEM, the dislocation core structure including the oxygen column was directly observed by combining BF and HAADF-STEM techniques.

Figure 6 shows (a) the crystal structure model of sapphire crystal viewed from $[1100]$ direction, (b) the HAADF-STEM and (c) the Bright Field (BF) STEM images (VG HB603U STEM (300 kV) with Cs corrector (Nion), ORNL) [10]. By STEM, the BF and the HAADF image can be obtained from the same area simultaneously. As shown in the crystal structure model, the atomic columns of Al and O can be distinguished with the present incident axis. In the HAADF-STEM image shown in (b), the positions of the O columns and the Al columns are apparently discriminated. Although the S/N ratio of the HAADF-STEM image is lower than the one of the BF-STEM image of (c), the atom position can be determined directly, since the image is the image under incoherent conditions. On the other hand, the S/N of the BF-STEM image is pretty high, and the BF-STEM image is optically equivalent to the image obtained by high-resolution transmission electron microscopy (HRTEM) due to the reciprocity theorem. Although, the contrast of BF-STEM image varies widely according to the defocusing and the thickness of the sample, accordingly, by taking the BF-STEM image and the HAADF-STEM image simultaneously to compare their contrast, the correspondence of the contrast of the BF-STEM image and the atom position can be determined directly. Under

the present observation condition, the position of the bright contrast in the BF-STEM image directly corresponds to the atomic column position. The structure determination including so far as the light element like oxygen thus becomes possible by simultaneous observation utilizing the image formation by both HAADF and BF STEM imaging.

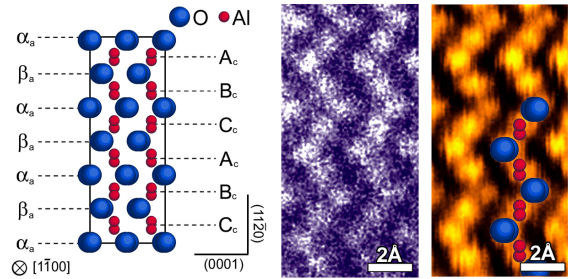


Fig.6 (a) Atomic structure model of sapphire projected along $[1100]$ direction, (b) HAADF and (c) BF-STEM images of a sapphire single crystal viewed from $[1100]$ direction [10].

The basal dislocation of sapphire has the Burgers vector of $\mathbf{b} = 1/3\langle 1120 \rangle$, but it has been confirmed that the dislocation core is dissociated by climb mechanism along the $[0001]$ direction and is composed of partial dislocations of $\mathbf{b}_1 = 1/3\langle 0110 \rangle$ and $\mathbf{b}_2 = 1/3\langle 1010 \rangle$ and stacking faults on the $\{1120\}$ plane [11]. Figure 7 shows the BF-STEM image of each dislocation edge of the dissociated partial dislocations (VG HB603U STEM (300 kV)). In the BF-STEM image, since the oxygen column and the aluminum column can be identified, the atomic columns at the dislocation edge can be directly determined. As apparent from the experimental image, two partial dislocations terminate at the aluminum and the oxygen atomic columns, respectively. It is thus shown that each partial dislocation core has the structure with local composition shift of aluminum surplus or oxygen surplus from the stoichiometric ratio.

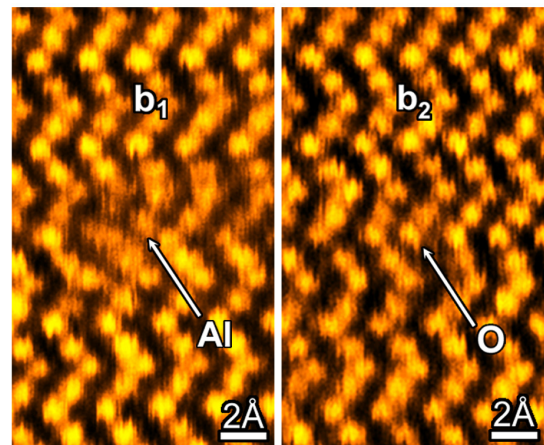


Fig.7 BF-STEM images of the core structures of the dissociated basal dislocations (b_1 and b_2), indicating that each core terminates at Al and O, respectively [10].

In case of ionic crystals, although the structure like this has been considered to be energetically unstable, the present results first demonstrate that the nonstoichiometric local structure can exist in the crystal. If the perfect dislocation is composed of two partial dislocations, the stoichiometric ratio is

satisfied in total. In other words, the stoichiometry is maintained when the basal dislocation glides. By the direct observation of the dislocation core structure like this, the gliding mechanism of the basal dislocation of sapphire can be understood [10], which will bring a great breakthrough to the study of ceramics dislocation in future. The development of the new functional materials utilizing the ceramics dislocation also has already developed [12]. It is expected that STEM observation, which combines the BF image with the HAADF image, will become a useful means in future.

(4) Interface Structure of $\text{SrTiO}_3/\text{Nb-SrTiO}_3/\text{SrTiO}_3$ Superlattice¹³⁾

Figure 8 shows HAADF-STEM image of the $\text{SrTiO}_3/\text{Nb-doped SrTiO}_3/\text{SrTiO}_3$ superlattice film (JEOL JEM-2100F (200 kV) with Cs corrector (CEOS), Univ. Tokyo) [13]. As described above, since the image intensity of HAADF-STEM image is proportional to about the square of Z , it is recognized that Sr ($Z=38$) columns are observed brightly compared with the Ti ($Z=22$) columns. In this case, Nb-doped SrTiO_3 layers deposited at every 24 unit cell are observed as stripe contrast (Fig. 8(a)). Figure 8 (b) and (c) show the magnified HAADF-STEM image around the Nb-doped SrTiO_3 layer and a line profile of the image intensity of the Sr atomic row and the Ti atomic row in the same region. From these figures, it is recognized that the image intensity does not change in the Sr atomic row; however, the image intensity becomes high in the Ti atomic row at the Nb-doped SrTiO_3 layer. Taking into consideration that the atomic number of Nb is 41, it is considered that Nb exists at the Ti sites by substitution. On the other hand, since the atomic numbers of Nb and Sr are close, whether Nb exists in the Sr sites or not cannot be judged only by the contrast of the HAADF-STEM image. Then, the solubility energy of Nb was calculated by the first principles PAW (Projector Augmented-Wave) method. It is then clarified that the solubility energy of Nb to the Sr sites is 7.6 eV higher compared with the one to the Ti sites. This result

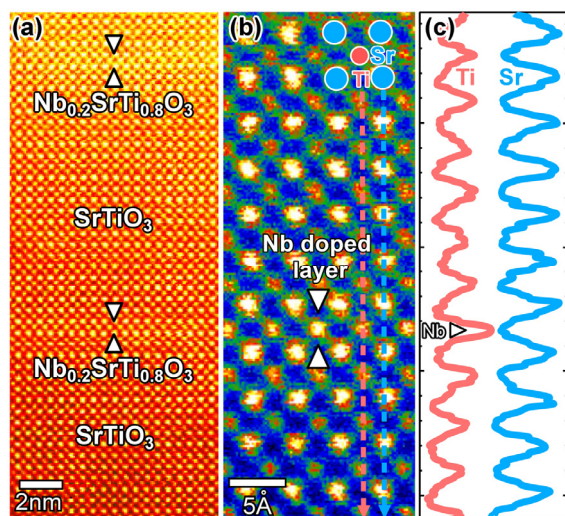


Fig.8(a) HAADF-STEM image of $\text{SrTiO}_3/\text{Nb-SrTiO}_3$ superlattice, (b) magnified image of the region (a) and (c) image intensity profile of Ti and Sr layers [13].

also shows the solubility of Nb to the Ti sites.

Figure 9 shows the spectra of Ti- $L_{2,3}$ ELNES (Energy Loss Near Edge Structure) obtained from the SrTiO_3 layer and the Nb-doped SrTiO_3 layer in the $\text{SrTiO}_3/\text{Nb-doped SrTiO}_3/\text{SrTiO}_3$ superlattice. The upper figure corresponds to the experimental spectra, and the bottom figure corresponds to the theoretically calculated spectra. Although four peaks (t_{2g} , e_g split) are apparent in the spectra obtained from the SrTiO_3 layer, it is recognized that the peaks are broadened in the spectrum from the Nb-doped SrTiO_3 layer. Comparing the theoretical ELNES calculated by the first principles relativistic multi-electron method with the experimental ELNES, it is found that the change in the experimental spectra is due to the transition from Ti^{4+} to Ti^{3+} which is accompanied by the Nb doping.

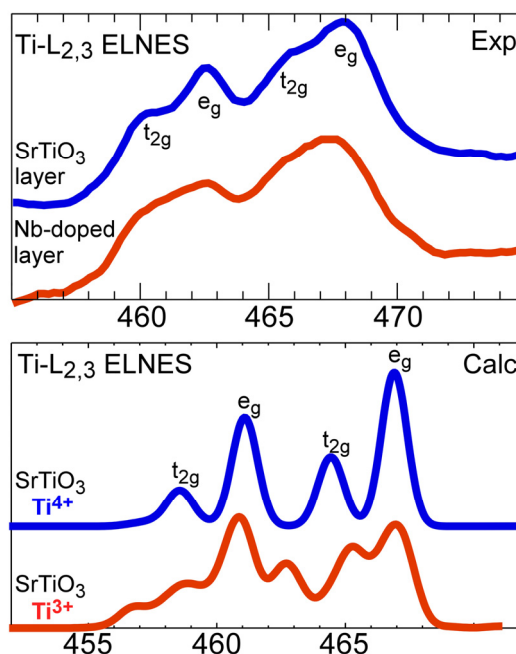


Fig.9 (top) Experimental and (bottom) theoretically calculated Ti- $L_{2,3}$ ELNES obtained from the SrTiO_3 layer and the Nb-doped SrTiO_3 layer in the $\text{SrTiO}_3/\text{Nb-doped SrTiO}_3$ superlattice. The calculations were made by the first principles relativistic multielectron method.

(5) Direct observation of Li ion site in lithium battery¹⁴⁾

Li battery is widely used for the battery of cellular phone and personal computer. Recently, it is also intensively studied for the application of the automobile battery. The properties of Li battery is strongly dependent on the positive electrode active material, and cobalt or nickel-compounds such as LiCoO_2 or LiNiO_2 have been mainly used as industrial products so far. However, it has been pointed out that they have problems on the stability, lifetime and reliability. LiFePO_4 with the stable olivine structure is therefore expected as the lithium battery for the next generation. Since the properties of the positive electrode active material is related to the behavior of Li ions in the crystal, direct visualization of Li site is needed to understand the mechanism of the properties. But, it is

impossible to directly observe Li atoms even by HAADF-STEM technique because the atomic number 3 for Li is too small to scatter electrons. We therefore exchanged a part of Li sites with Fe atoms in LiFePO₄ crystal by chemical modification–annealing technique, and tried to directly observe the Li sites by HAADF-STEM. Figure 10 shows HAADF-STEM image for the LiFePO₄ crystals observed along the [010] direction (JEOL JEM-2100F (200 kV) with Cs corrector (CEOS), Univ. Tokyo). In the sample, about 15% of Li sites were substituted by Fe atoms [14]. In Fig. 10, the model crystal structure composed of Fe, Li, P, O is shown, and the inset shows the simulated HAADF image for the olivine with 15% Li-Fe exchange. As can be seen in the image, Li sites, which is substituted by Fe atoms, can be observed as weak spots in the center of hexagonal framework composed of Fe and P. It is also found that such exchange defects appear to be locally aggregated rather than homogeneously dispersed in the crystal. In addition, the distribution of the exchange defect was not homogeneous in the vicinity of the grain boundaries, which indicates that the direct visualization of Li sites will clarify the behavior of lithium ions, conductor and breakdown mechanism of lithium battery in the future.

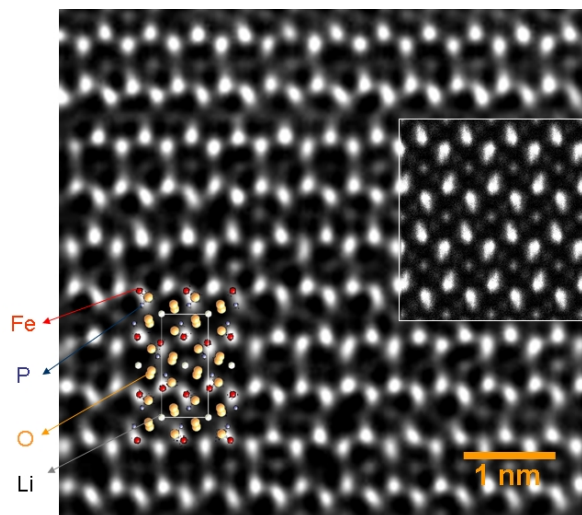


Fig.10 HAADF-STEM image for the LiFePO₄ crystals, in which a part of Li sites was substituted by Fe atoms, showing that some of the Li columns have a bright contrast in significant intensity [14]. The inset shows the simulated HAADF image for the olivine with 15% Li-Fe exchange.

IV. Conclusion

Various kinds of dopants have been used for industrial materials to improve the functional and mechanical properties. However, many of such dopants have been considered and selected on the basis of the long-term experience and empirical background, and it is hence unclear for the effect of the function provided dopants on the atomistic mechanism. If the atomistic mechanism can be intrinsically understood, it will be possible to reasonably design material by controlling atoms, electrons and function providing elements in the materials. The appearance of Cs corrected STEM enables us to determine the location of the dopants and the local electronic state at a single

atomic level.

In this paper, we introduce our recent results obtained for ceramic grain boundary and interface by Cs corrected STEM. Several examples are demonstrated for the grain boundaries of varistor and structural ceramics, dislocation in alumina, oxide superlattice, lithium battery and so on. These results indicate that the atomistic mechanism of the properties can be unraveled by combination of STEM characterization and the first principles calculations. This approach must be a breakthrough for new materials science and engineering in the next generation.

Acknowledgement

The authors would like to acknowledge the collaboration with N. Shibata, T. Mizoguchi, Y. Sato, A. Nakamura, H. Ohta, S.-Y. Choi, S.-Y. Chung, K. Matsunaga, W. Y. Ching, M.F. Chisholm, S.J. Pennycook, T. Yamamoto and T. Hirayama. Part of this work was supported by the Grants-in-Aid for Scientific Research on Priority Areas “Nano Materials Science for Atomic-scale Modification” (No.19053001) from the Ministry of Education, Culture, Sports, Science and Technology (MEXT).

References

- ¹ Y. Ikuhara Ed. “Physics of Ceramics” *Nikkan-Kogyo –Shinbun Pub.Co.* (1999).
- ² Y. Ikuhara, *J. Ceram. Soc. Jpn.*, **110**, 139 (2002).
- ³ M. Haider, H. Rose, S. Uhlemann, B. Kabius and K. Urban, *J. Electron Microsc.*, **47**, 395 (1998).
- ⁴ S. J. Pennycook and D. E. Jesson, *Phys. Rev. Lett.* **64**, 938 (1990).
- ⁵ P.D. Nellist, M.F. Chisholm, N. Dellby, O.L. Krivanek, M.F. Murfitt, Z.S. Szilagy, A.R. Lupini, A.Y. Borisevich, W.H. Sides and S.J. Pennycook, *Science*, **305**, 1741 (2004).
- ⁶ Y. Sato, J. P. Buban, T. Mizoguchi, N. Shibata, M. Yodogawa, T. Yamamoto, and Y. Ikuhara, *Phys. Rev. Lett.* **97**, 106802 (2006).
- ⁷ Y. Sato, T. Yamamoto and Y. Ikuhara, *J. Am. Ceram. Soc.*, **90**, 337 (2007).
- ⁸ J.P. Buban, K. Matsunaga, J. Chen, N. Shibata, W.Y. Ching, T. Yamamoto and Y. Ikuhara, *Science*, **311**, 212 (2006).
- ⁹ H. Yoshida, Y. Ikuhara and T. Sakuma, *Acta Mater.* **50**, 2955 (2002).
- ¹⁰ N. Shibata, M.F. Chisholm, A. Nakamura, S.J. Pennycook, T. Yamamoto and Y. Ikuhara, *Science* **316**, 82 (2007).
- ¹¹ A. Nakamura, T. Yamamoto and Y. Ikuhara, *Acta Mater.* **50**, 101 (2002).
- ¹² A. Nakamura, K. Matsunaga, J. Tohma, T. Yamamoto and Y. Ikuhara, *Nature Mater.*, **Vol.2**, 453 (2003).
- ¹³ H. Ohta, S.W. Kim, Y. Mune, T. Mizoguchi, K. Nomura, S. Ohta, T. Nomura, Y. Nakanishi, Y. Ikuhara, M. Hirano, H. Hosono and K. Koumoto, *Nature Mater.* **Vol.6**, 129 (2007).
- ¹⁴ S.-Y. Chung, S.-Y. Choi, T. Yamamoto and Y. Ikuhara, *Phys. Rev. Lett.*, **100**, 125502 (2008).

The dependences of shoulder induced, pin induced and combined flows on rotation speed and forward speed during friction stir welding/processing

S Cui and Z W Chen

Department of Mechanical and Manufacturing Engineering, AUT University, Auckland, NZ
song.cui@aut.ac.nz, zhan.chen@aut.ac.nz

Abstract. The influences of processing parameters and the measurable thermomechanical responses on the individual and combined flows forming the different processed zones during friction stir welding/processing has not been clearly understood in literature and have been investigated in this study. Experimentally, a cast Al-7Si-0.3Mg alloy was used to provide readily identifiable processed zones. A series of friction stir experiments covering a wide range of tool forward and rotation speeds were conducted followed by the measurement of individual and combined stir areas. It has been found that the basic modes of material flow did not change but the relative volume of each flow depended on both forward and rotation speeds. The trends observed with the present data explain how pin rotation relates to the material transportation mechanism and the associated torque required. The present data also explains how forward speed, not rotation speed, relates to specific energy and the volume of the total stir zone.

Key Words: stir zone, deformation, dendrites, torque, specific energy

1 INTRODUCTION

Friction Stir Welding (FSW) is a relatively new solid-state joining technique which has been applied quite widely in the last few years. During FSW, a rotating non-consumable tool, usually with a threaded pin, is inserted into the joining seam between two metal plates and then the tool travels along the joining seam. Frictional heat generated between the tool and base metal causes the later to plasticize and this plasticized material is then transported by the rotating tool to the back, completing the weld. Based on the same FS thermomechanical principle, friction stir processing (FSP) has been explored for microstructure refinement and defect elimination. The first study was conducted by Mishra et al's [1] demonstrating superplasticity of cast aluminum alloy after FS and marked the beginning of FSP.

Through the intensive plastic deformation, FSP can be used to modify the microstructure either locally or in the surface region where the processed thickness under the surface can be quite large. Furthermore, in principle, through the pre-placement of nano or micro particulates, composite materials can be produced using FSP. Ma's [2] recently reviewed the research on FSP, demonstrating the potential of FSP for various microstructure modifications and defect elimination. It is clear that, however, the understanding of the detailed flow phenomena during FSP for attaining the best refined microstructure and for control of FS parameters for the desired microstructure in various processed zones is insufficient and further research is needed.

FSW/P is a fully coupled thermo-mechanical process and the associated physical phenomenon is complex. Understanding of various thermo-mechanical and metallurgical phenomena during FSW/P has recently been updated in a comprehensive review [3]. However, how the most important parameters, welding speed (v) and rotation speed (ω), affect heat input and material flow forming the stir zone is quantitatively not very clear. From the recent conceptual model relating FSW process variables to heat generation suggested by Colligan and Mishra [4], it is clear that no reliable quantitative relationships have been established to describe how v and ω are

related to maximum temperature, temperature distribution and flow volume.

On the more mechanical side, the mechanism of material flow during FSW/P has been a major subject of study for more than 10 years. Many researchers have observed the change in flow volumes as welding parameters are altered [5-12], although no precise quantification on flow volumes or study on how the individual and combined flow volumes are affected by v and ω have been conducted. On the thermal side, torque (M), power ($P=M\omega$) and specific energy ($E_s=M\omega/v$) are measurable quantities that are often related to temperature and heat input [8,13-15]. How these variables relate to flow volumes has not yet been established, despite some suggestions made [8].

In this study, we aim to quantify how v and ω affect both the individual flow and the combined flow forming the various zones. A cast aluminium alloy was used in the present study, as FSP is a technique that can potentially be used for refining the normally coarse cast microstructures and eliminating porosity normally associated with casting. During friction stir (FS) experiments, M was measured and thus E_s could be calculated. These measured variables could then be related to v and ω and then to flow volumes, to gain a better understanding of their interrelationships.

2 EXPERIMENTAL PROCEDURES

FSW experiments were conducted using a milling machine. Tool tilt angle was kept constant at 2.5° , v and ω were set varied from 28 to 450 mm/min and 250 to 1400 rpm, respectively. A356 (Al-7Si-0.3Mg) cast aluminium alloy was used. Plates were machined from cast ingots to yield a consistent dimension of 290 mm \times 85 mm \times 6.35 mm to obtain comparable results. M for each weld was recorded using a *LowStir*TM device and E_s could then be calculated. After FS experiments, cross sectional metallographic samples were prepared for metallographic examination following the normal metallographic procedure. Using FS samples of a cast alloy, the deformed dendrites enable a flow marking to be made and thus a more quantitative analysis on various zones could be conducted.

Figure 1 shows a cross section of a FS sample. The total stir area has been outlined. Outside of this area undeformed $\alpha(\text{Al})$ dendrites (appearing dark) and Al-Si eutectic (appearing light grey) can be identified. Inside the stir area, a solid line divides the shoulder induced zone above and the pin induced zone (nugget) below. This dividing line can normally be made, starting from the retreating side (right side in Fig. 1a), where the deformed dendrites induced by the tool shoulder is more towards the advancing side (left) but those induced from pin has an appearance of coming slightly from below (Fig. 1b). Referring to the nugget, RSM (rotational shear material) is the heavily deformed material deposited from tool pin thread spaces and the surrounding is the less deformed material mechanically affected or dragged by RSM and pin thread crests [16]. Area of each individual zone (shoulder - A_{sh} , nugget - A_{ng} , RSM - A_{RSM}) and total stir area, A_{st} , for each sample were measured by manually counting after superimposing fine grids on each macrograph.

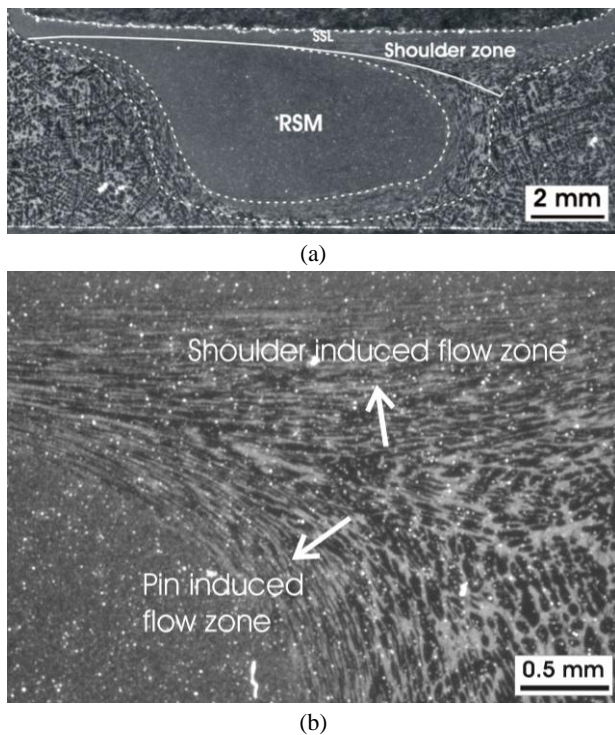


Figure 1. Cross section (advancing side on the left) of A356 cast alloy FS sample made using $v = 28$ mm/min, $\omega = 710$ rpm. The solid line marks the division of shoulder induced (above) and pin induced (below) flow zones. SSL denotes surface shear layer and RSM denotes rotational shear material.

3 RESULTS AND DISCUSSION

3.1 General features of friction stir flow

Macrographs of welds conducted at $v = 224$ mm/min, with ω varied from 250 rpm to 1400 rpm are shown in Figure 2, a to e, respectively. These macrographs show that the commonly observed onion ring structure in FS nugget is absent, meaning that the out flow from thread spaces forming the nugget zone in the present case differs from those identified for the case of forming onion rings [17]. Non-ring nugget structure is, however, not uncommon and can be identified in FS nuggets presented in literature for FSW/P of similar cast alloys [18-21]. The metallographic evidence for the detailed material flows forming the non-ring nugget has been described [16]. Basically, RSM deposited to the nugget from thread spaces in the trailing-advancing side and the lower part (due to the screwing effect), thus forming a L-shaped RSM region in the nugget. The rest of the nugget is primarily the result of flow

dragged by the RSM and the thread crests. The feature of L-shape RSM is clear in Figure 2, although the individual flow volume forming the region changed as ω changed.

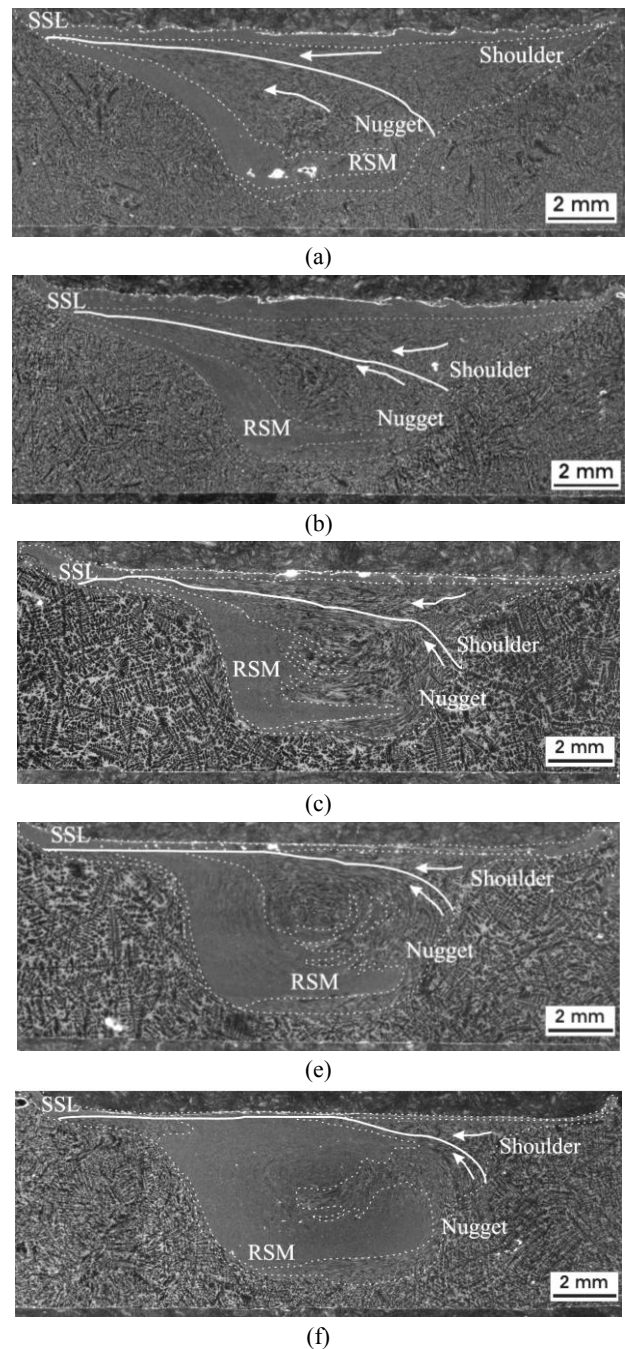


Figure 2. Cross section views of FS samples conducted at $v = 224$ mm/min, with rotation speed of (a) 250 rpm, (b) 500 rpm, (c) 710 rpm, (d) 1000 rpm, and (e) 1400 rpm respectively. Various zones have been outlined.

As already described, RSM is the result of the intensive shear deformation. In other words, the original coarse dendrites have been heavily deformed and recrystallized in this RSM region. Very fine silicon particles, which originally were present in the interdendritic regions as the result of eutectic solidification during casting, have now evenly distributed in the RSM region due to FS mixing. Figure 3 shows these features, comparing dendritic cast structure outside the nugget zone to the fine silicon particles evenly distributed in the deformed $\alpha(\text{Al})$ matrix in the RSM region. It is thus important to gain knowledge on how processing conditions can be formulated to increase the amount of RSM.

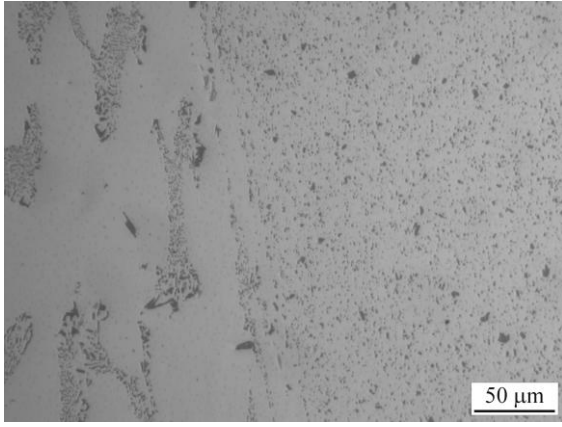


Figure 3. A micrograph taken in an FS location. In the left portion (the thermomechanically affected zone), slightly deformed dendrites are seen and the right portion (RSM) is the highly deformed $\alpha(\text{Al})$ with fine Si particles evenly distributed.

3.2 Effects of tool speeds on flow volumes

At low ω (Figure 2a), it is clear that the area of RSM is small (thin L-shape). This is reasonable as at a low ω transported volume of material (RSM) through thread spaces should be low. Small voids inside this RSM area can be identified (Figure 2a). The rounding flow (dragged by RSM and pin thread crests) filled almost the rest of the nugget meanwhile the shoulder flow was sufficient, thus the total stir zone was fulfilled without forming further voids. With the increase in ω (Figure 2b to 2e), the production in and transportation through thread spaces of RSM became more and more effectively, resulting in a higher volume of RSM flow and thus an increase in nugget area. Accompanying this is the smaller shoulder induced flow which largely sequentially followed the pin induced flow [22].

If ω is kept constant, increasing v has the similar effect to decreasing ω for the generation and transportation of RSM. This can be seen by comparing Figure 2c to Figure 4 where the samples were from FS experiments using $\omega = 710$ rpm but different v values. The increase in v from 224 to 450 mm/min resulted in a thinner RSM region. On the other hand, when v decreased to 28 mm/min, the thread spaces were very effective, producing a very high amount of RSM, as can be seen in Figure 1a.

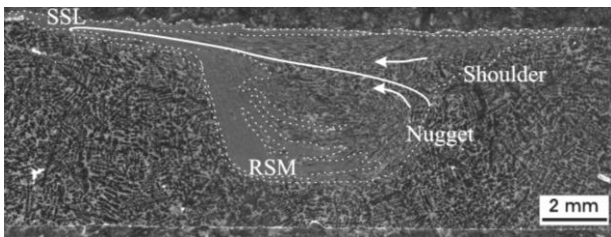
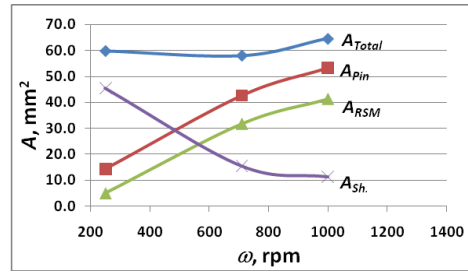
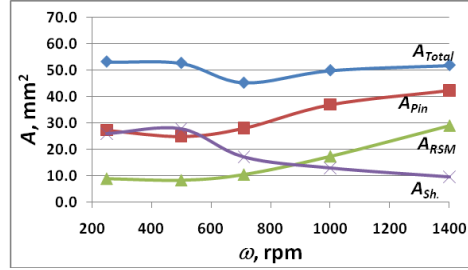


Figure 4. Cross section views of FS sample conducted at $v = 450$ mm/min, with rotation speed of 710 rpm. Various zones have been outlined.

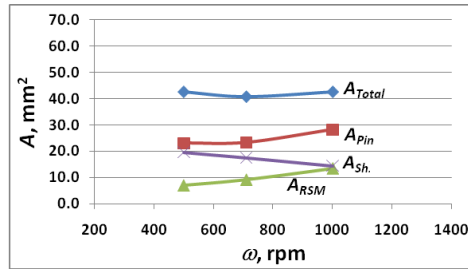
The relationships between ω and various zone areas, at various constant v values, are shown in Figure 5a to c. A trend of decreasing the total stir zone area as v increases is clear. On the other hand, increasing ω affects little the total stir zone area. A_{ng} and A_{RSM} increased, while A_{sh} decreased, as ω increased, quantitatively confirming the trend described above. An important feature of these data and the metallographic observations is that the more effective the production and transportation mechanisms of RSM are, when ω increases, the higher the RSM flow volume is and the lower the shoulder flow is needed for the completion of the total stir zone.



(a)



(b)

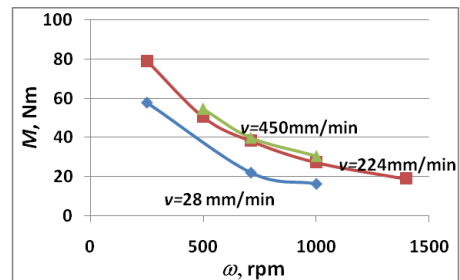


(c)

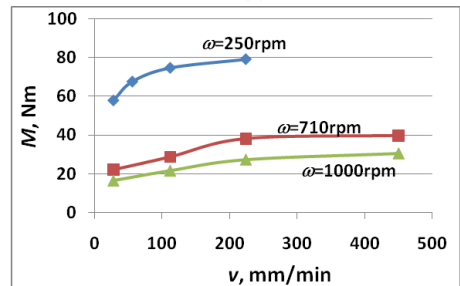
Figure 5. The effects of rotational speed (ω) on A_{st} , A_{ng} , A_{RSM} and A_{sh} at (a) $v = 28$ mm/min, (b) $v = 224$ mm/min, (c) $v = 450$ mm/min.

3.3 Tool speeds, torque/energy and flows

M values and calculated E_s values are given in Figure 6 and Figure 7, respectively, each plotted vs v and ω . The trends are similar to those recently established in literature [8,13-15], although that the decay function of E_s vs v is almost not affected by ω values, meaning $E_s = f(\omega, v) \approx f(v)$, is clear observed in the present data (Figure 7b).



(a)



(b)

Figure 6. The relationships between (a) torque and rotation speed and (b) torque and linear speed.

Examining data in Figure 5 and Figure 6a, it may be suggested that at low ω , the relatively large shoulder flow requires a high M value, while the effective production and transportation of RSM at high ω values requires only a low M value. By examining data shown in Figure 5 and Figure 7b, it can be concluded that E_s (heat input per unit length) is positively related to the volume of the total stir zone. This is reasonable, as the volume of the workpiece which has become plasticized should be a function of heat input.

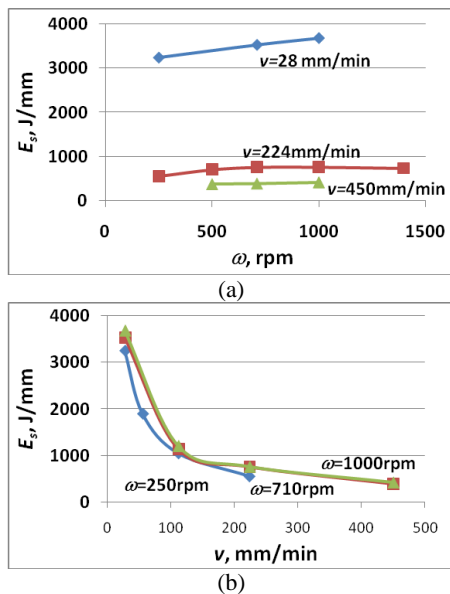


Figure 7. The relationships between (a) specific energy and rotation speed and (b) specific energy and linear speed.

4 CONCLUSIONS

The basic modes of pin induced (RSM and rounding) and shoulder induced flows did not change but the individual flow volume varied significantly, depending on tool speeds. In general, increasing ω increased the volume of RSM flow with the volume of rounding flow almost unaffected, thus the size of nugget increased. However, the overall friction stir volume was a weak function of ω . At low ω values, the large shoulder flow required a high M value. At high ω values, the effective production and transportation of RSM required a relatively low M value. E_s (heat input) values related well to the size of the total stir zone, likely to be primarily the result of E_s relating well with the size of total plasticized volume during FSW/P. Thus the total stir zone is primarily a function of v , affected little by ω .

References

[1] Mishra, R.S., Mahoney, M.V., McFadden, S.X., Mara,

N.A. and Mukherjee, A.K., Scripta Materialis, Vol. 42, pp.163-168, (2000)

[2] Ma, Z.Y., Metallurgical and Materials Transactions A, Vol.39, pp.642-658, (2008).

[3] Nandan, R., DebRoy, T. and Bhadeshia, H.K.D.H., Progress in Materials Science, Vol.53 980-1023, (2008).

[4] Colligan, K.J. and Mishra, R.S, Scripta Materialia, Vol.58, pp.327-331, (2008).

[5] Yang, B.C., Yan, J.H., Sutton, M.A. and Reynolds, A.P., Materials Science and Engineering A Vol.364 pp.55-65, (2004).

[6] Lee, C.Y., Lee, W.B., Kim, J.W., Choi, D.H., Yeon, Y.M. and Jung, S.B. 2008, Journal of Materials Science, Vol.43 pp.3296-3304, (2008)

[7] Liu, F.C. and Ma, Z.Y., Metallurgical and Materials Transactions A, Vol.39, pp.2378-2388 (2008)

[8] Yan, J., Sutton, M.A. and Reynolds, A.P., Science & Technology of Welding & Joining, Vol. 2008/725-36, (2005).

[9] Peel, M., Steuwer, A. and Withers, P., Metallurgical and Materials Transactions A, Vol.37, pp. 2195-2206 (2006).

[10] Xu, S. and Deng, X., Acta Materialia, Vol.56, pp.1326-1341 (2008).

[11] Ren, S. R., Ma, Z.Y. and Chen, L.Q., Scripta Materialia, Vol.56, pp.69-72, (2007).

[12] Arbogast, W.J., Scripta Materialia, Vol.58, pp.372-376, (2008).

[13] Reynolds, A.P., Tang, W., Khandkar, Z., Khan, J.A. and Lindner, K., Science & Technology of Welding & Joining, Vol.10, pp.190-199, (2005).

[14] Pew, J.W., Nelson, T.W. and Sorensen, C.D., Science & Technology of Welding & Joining, Vol.12, pp.341-347 (2007).

[15] Long, T., Tang, W. and Reynolds, A.P. 2007 Science & Technology of Welding & Joining, Vol.12, pp.311-317, (2007).

[16] Chen, Z.W. and Cui, S., in Proceedings of the 7th International Symposium on Friction Stir Welding (Awaji Island), TWI, (ISBN 13-978-1-903761-06-9), (2008).

[17] Chen, Z.W. and Cui, S., Scripta Materialia, Vol.58, pp.417-420, (2008).

[18] Ma, Z.Y., Sharma, S.R. and Mishra, R.S., Scripta Materialia, Vol.54, pp.1623-1626. (2006).

[19] Nakata, K., Kim, Y.G., Fujii, H.T., Tsumura, T. and Komazaki, T., Materials Science and Engineering A, Vol.437, pp.274-280, (2006).

[20] Amirizad, M, Kokabi, A.H., Abbasi Gharacheh, M., Sarrafi, R., Shalchi, B. and Azizieh, M, Materials Letters 60, 565-568, (2006).

[21] Mahmoud, T.S., Gaafer, A.M. and Khalifa, T.A., Materials Science and Technology, Vol.24, pp.553-559, (2008)

Chen, Z.W., Peris, R., Maginness, R. and Xu, Z.P., International Journal of the Society of Materials Engineering for Resources, Vol.20, pp.4081-4086 (2006).

Pipeline Design of Settling Slurries Containing Mixed Sized Particles by Using the Wasp Method

Naoki Kamiyama*, Isamu Sato**, and Hiroshi Sato**

** Department of Earth Science and Technology Faculty of Engineering and Resource Science, Akita University, 1-1 Tegata Gakuen-cho, Akita, 010-8502 Japan

*Graduate School of Mining and Engineering, Akita University, Japan
hsato@ipc.akita-u.ac.jp

Abstract: The designer of hydraulic transport of coarse solid particles in pipes has to determine the important factors of critical deposit velocity and hydraulic gradient, because they govern the most economic mode. However, the factors are dependent on not only the transport conditions such as pipe diameter, solids density, and concentration, but also the range of particle sizes. It should be also noted that uniform sized particles are seldom encountered in the transport system of crushed minerals, coal, and sand, while the serious attrition of the coarse particles through pumps and pipes may lead the discrepancy between the predicted and measured pressure losses of the flow.

In this paper the effects of fine solids component on the critical deposit velocity, hydraulic gradient, hydraulic power requirement, and specific energy consumption are discussed for commercial practice of slurry transport of multi-sized particles by using the Wasp method. The results show that the hydraulic gradient decreases with increasing the vehicle portion of fine particles in slurries and the software developed in this approach can be useful in design applications.

Key Words: pipeline design, settling slurry, Wasp's method

Nomenclature

C	Delivered concentration
C_D	Drag coefficient of solid particle
D	Pipe diameter
d	Particle diameter
d_o, d_i	Particle diameters of coarse and fine solids
g	Gravitational acceleration
i	Hydraulic gradient for slurry
iw	Hydraulic gradient for water flowing alone at the same velocity as slurry
K_D	Coefficient of the Durand-Condolios equation
L	Length of pipeline
q	In-situ concentration
q_H, q_V	Heterogeneous and vehicle portions of q
q_o, q_w	In-situ concentrations at the center line and at $z = 0.92D$ in a pipe
Re	Reynolds number
Rm	Fraction of fine solid particles
V	Mean velocity of slurry
V_c	Critical Velocity
Vcd	Critical deposit velocity
Vt	Terminal velocity of a solid particle
V_*	Friction Velocity
z	Vertical coordinate
α, β	Swanson's shape factors
γ, γ_s	Specific weights of water and solids

δ	Specific gravity of solid particles
μ, μ_{sl}	Viscosities of water and slurry
ρ, ρ_s, ρ_{sl}	Densities of water, solids, and slurry
ϕ	Head loss parameter
ψ	Modified Froude number

1 INTRODUCTION

Coarse particle transport as heterogeneous flow has strong economic advantages, especially for short-distance coal-slurry pipelines¹⁾, because the substantial cost of the pipeline system are incurred in preparation and dewatering if fine size solids are allowed. However, after passing through slurry pumps, or the centrifugal types which can produce higher flow rate than reciprocating pumps, coarse coal particles are broken down into finer size ones. The particle size distribution occurred with the attrition of solids affects the flow behavior of the solid-liquid mixture in pipes, as shown schematically in Figure 1.

Moreover, the addition of a large amount of fine particles to the coarse particle slurry changes the physical properties such as the density and viscosity of the vehicle portion which carry the solids, and also leads the decrease of the settling velocity of solids. It is consequently most likely that the hydraulic gradient i and critical deposit velocity V_{cd} of slurry are dependent on the particle size distribution.

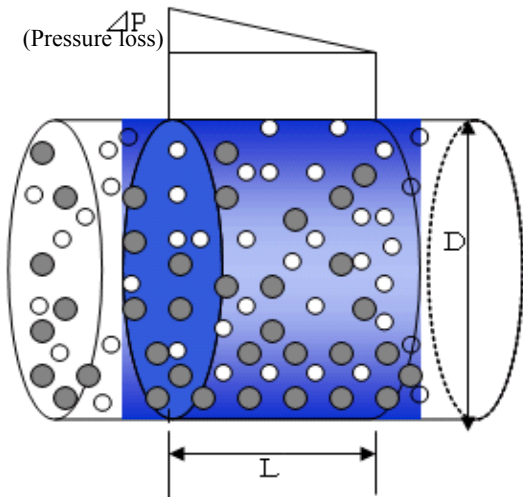


Fig. 1 Flow conditions of a mixed-sized slurry

However, many correlations for estimating i and Vcd have been developed upon the data from the experiments with narrow-size or single size particles of solids, mostly sand in water. In spite of using the representative diameter²⁾ of d_{50} on a weight or mass accumulation curve and the weighted diameter $d_w (= \sum x_i \cdot d_i)$ calculated both with portions x_i and mean sizes of particles d_i , Wasp et al.³⁾ suggested a unique method for evaluating the hydraulic gradient i of heterogeneous flow with size distribution. In the flow regime, Liu⁴⁾ discussed the Wasp method and concluded that "it appears to be accurate and most useful when the slurry consists of a wide spectrum of particle sizes, as in the case of crushed minerals and coal."

Since the calculation of the hydraulic gradient i of slurry should be iterated, according to the Wasp method, it is essentially expected for pipeline designers to apply the software of it. In this study, the effects of the portion of fine particles in the settling slurries on the hydraulic gradient i , the hydraulic power requirement E , and the Specific Energy Consumption (SEC) were discussed by using the original program. As a result, it was concluded that the valuable parameters of i , Vcd , and the SEC related to the transport cost decreases with increasing the fraction of the fine particles on the same conditions of flow as the single size coarse slurry.

2 Application of the Wasp method

Wasp et al.³⁾ illustrated the satisfactory results for predicting pressure losses along the pipeline of the coal-water mixture. It is likely that the good agreement between the predicted and experimental data resulted from the experimental relationship of viscosity of slurry to the concentration of solids. Therefore, it is important to modify the Wasp method and develop it for generalizing the evaluation procedure to make application to the other minerals except to coal.

2.1 Settling velocity of solid particles

The settling velocity of various sizes of solids can be determined in the wide range of particle Reynolds number from the Stokes to the Newton regions by the Swanson equation⁵⁾:

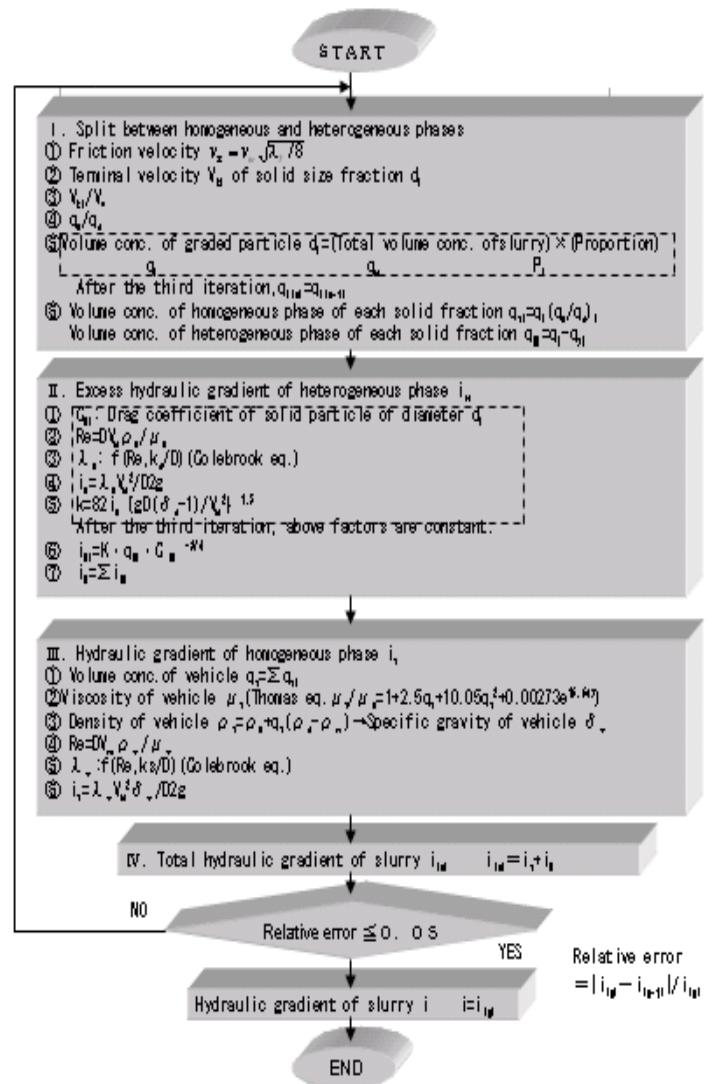


Fig. 2 Flowchart of the Wasp method for hydraulic gradients

Particle size	Homogeneous phase	Heterogeneous phase	Volume concentration
d_1	q_{H1}	q_{H1}	q_1
d_2	q_{H2}	q_{H2}	q_2
d_3	q_{H3}	q_{H3}	q_3
⋮	⋮	⋮	⋮
d_i	q_{Hi}	q_{Hi}	q_i
⋮	⋮	⋮	⋮
d_n	q_{Hn}	q_{Hn}	q_n
			Volume concentration of solids $q = \sum q_i$

Fig. 3 Slurry constitution of homogeneous and heterogeneous Parts

$$v_t = \frac{v_N}{\alpha} \left[\frac{1}{1 + (\sqrt{48\beta} \mu / d \rho v_N)} \right] \quad (1)$$

where,

$$v_N = \sqrt{4gd(\rho_s - \rho)/3\rho}$$

and α and β are Swanson's shape factors of the solids. It should be stressed that the viscosity μ and density are not of water but of the vehicle phase of the suspension.

2.2 Viscosity of slurry

The viscosity of homogeneous suspensions increases with the increase of the concentration q of the solids. If the effects of the sphericity and size distribution of the solid particles are so small to be negligible, the viscosity of the suspension μ_{sl} is expressed by the Thomas equation for the Newtonian fluids ⁶⁾.

$$\mu_{sl}/\mu = 1 + 2.5q + 10.05q^2 + 0.00273e^{16.6q} \quad (2)$$

2.3 Pressure losses in heterogeneous flow

Wasp et al.⁷⁾ proposed the same type as the Durand-Condolios equation for evaluating the frictional pressure losses of heterogeneous suspension flow of uniformly size-graded particles in horizontal pipes:

$$\phi = K_D \psi^{-1.5} \quad (3)$$

where,

$$\phi = (i - i_w)/(i_w C) \quad (4)$$

and

$$\psi = V^2 \sqrt{C_D} / \{gD(\delta - 1)\} \quad (5)$$

Wasp et al.⁷⁾ also suggest that $K_D=82$ be used, in spite of $K_D=81$ in the Durand-Condolios equation ⁸⁾ and $K_D=83$ recommended by Liu ⁴⁾ in Eq. (3). It is worth noting that the value of K_D is dependent on the experimental conditions. According to Wasp et al., Eq.(3) becomes

$$\phi = 82 \psi^{-1.5} \quad (6)$$

3 Calculation procedure of the Wasp method

The procedure is composed of four calculation blocks in Figure 2. If a mixed-sized slurry of different sizes of d_1, d_2, \dots, d_n with corresponding volume concentration q_1, q_2, \dots, q_n flows in a horizontal pipe, each size fraction of slurry can be divided into the homogeneous "vehicle" and the remainder of heterogeneous parts, q_{v1} and q_{H1} respectively, as shown in Figure 3. For each size fraction of solids, the vehicle part is assumed to constitute a fraction of q_w/q_o , while the heterogeneous part is assumed to constitute a fraction $(1-q_w/q_o)$, the remainder of the vehicle.

The criteria q_w/q_o can be represented by ⁷⁾:

$$\log_{10}(q_w/q_o) = -4.5(Vt/V_{*}) \quad (7)$$

The hydraulic gradient of the heterogeneous parts of each size fraction i_{Hi} is evaluated by using Eq.(6). The total hydraulic gradient of heterogeneous part i_H is taken as the sum of i_{Hi} .

Conversely, the vehicle parts of each size fraction are

added up to form the total component of the homogeneous suspension, for which the hydraulic gradient i_v can be evaluated with the parameters of μ_{sl} and ρ_{sl} .

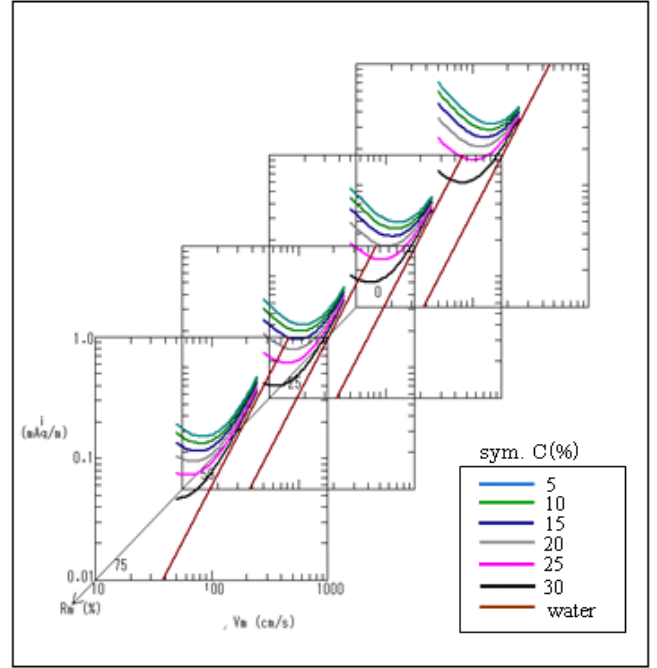


Fig. 4 Effects of fines content on hydraulic gradient for mixed-sized slurry flow in a 25 mm diameter pipe ($D=25(\text{mm})$, $d_0=2(\text{mm})$, $d_1=0.05(\text{mm})$)

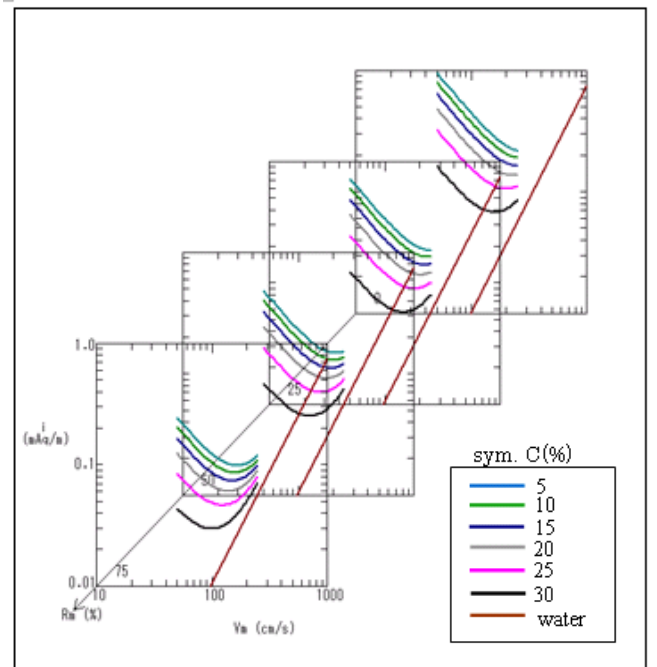


Fig. 5 Effects of fines content on hydraulic gradient for mixed-sized slurry flow in a 100 mm diameter pipe ($D=100(\text{mm})$, $d_0=2(\text{mm})$, $d_1=0.05(\text{mm})$)

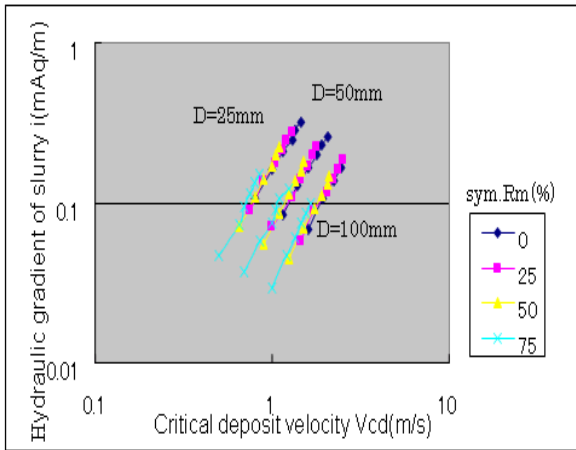


Fig. 6 The relationships between minimum hydraulic gradients and critical deposit velocities for mixed-sized slurry flow ($d_0=2(\text{mm})$, $d_1=0.05(\text{mm})$)

4 Pipe Line Design

In designing a slurry pipeline, following items must be determined after selecting a pipe size:

- hydraulic gradient (frictional pressure loss)
- critical deposit velocity
- energy requirement
- Specific Energy Consumption (SEC).

For illustrative purposes, the basic items were evaluated for sand-water slurry ($\delta=2.65$) flowing in the pipes of 25, 50, and 100 mm inside diameters. To investigate the effect of the component ratio of fine particles to coarse particles of solids, the mixed sand which composed of 50 μm and 2 mm particles was discussed at delivered volume concentrations C between 5 to 30 %, whereas $C=25\%$ is a commonly used concentration in practice, according to Jacobs⁸⁾.

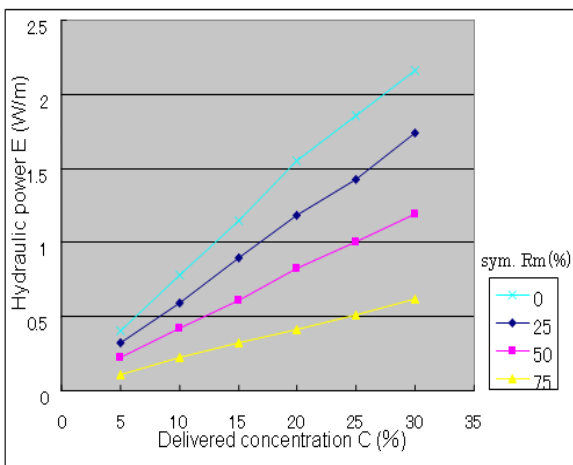


Fig. 7 Hydraulic power vs. delivered concentration for different fractions of fine solids in a 25 mm diameter pipe ($D=25(\text{mm})$, $d_0=2(\text{mm})$, $d_1=0.05(\text{mm})$)

4.1 Critical deposit velocity

In commercial pipe pipelines, settling slurries are transported at a velocity somewhat higher (by at least 0.3 m/s⁹⁾) than the critical deposit velocity V_{cd} at which solid particles form a stationary bed on the pipe bottom, because the risk of pipeline blockage increases below the point.

From Eq.(6), a velocity for minimum hydraulic gradient can be obtained by taking the derivative of the hydraulic gradient i with respect to the mean velocity of slurry flow V :

$$V_C = 3.4C^{1/3} \left\{ gd(\delta - 1) \sqrt{C_D} \right\}^{1/2} \quad (8)$$

The velocity V_c corresponds to the critical deposit velocity of the settling slurry of a given concentration, according to Gover¹⁰⁾, Sato and Kawahara¹¹⁾. It can be expected that the mixed sized slurry of coarse solid particles together with a portion of fine solids make a high density medium that enables suspension of coarse particles at reduced flow velocities.

4.2. Hydraulic power requirement

The hydraulic power required to transport slurry at a velocity of V m/s in the pipe of diameter D m over a unit distance can be represented by:

$$E = Q(\Delta p/L) = 9.807 \times 10^{-3} i \cdot \gamma \cdot V^2 \cdot \pi D^2 / 4 \quad (9)$$

The energy should be applied to selecting the size of the operating motor in the pipeline system.

4.3 Specific Energy Consumption (SEC)

The Specific Energy Consumption (SEC) is defined as the energy required to transport a unit mass of solids over a unit distance¹²⁾, and calculated by:

$$SEC = i \gamma Q / (9.807 \times 10^{-3} M_s) \quad (10)$$

In Eq.(10), M_s is the solid flow rate (in kg/s) through a pipeline, given as:

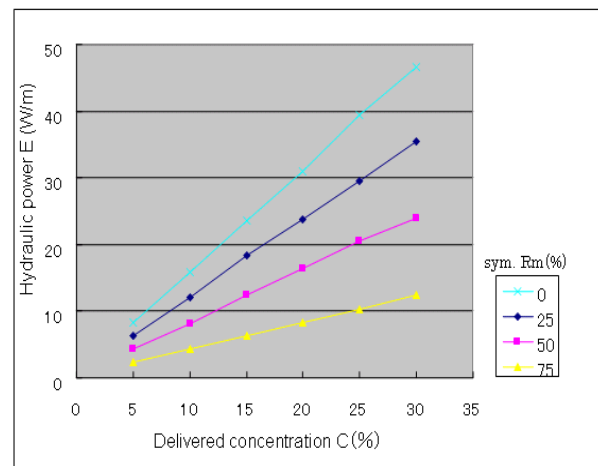


Fig. 8 Hydraulic power vs. delivered concentration for different fractions of fine solids in a 100 mm diameter pipe ($D=100(\text{mm})$, $d_0=2(\text{mm})$, $d_1=0.05(\text{mm})$)

$$M_s = QC \gamma_s \quad (11)$$

Substituting Eq.(11) into Eq.(10), the SEC in kWh/(t·km) is given by:

$$SEC = 2.724 i / (C \cdot \delta) \quad (12)$$

5 Analytical Result and Discussion

5.1 The effect of the component ratio on the hydraulic gradient and the critical deposit velocity

Figures 4 and 5 show the i - V curves computed by the Wasp method for slurries consisting of two grades of sand at volumetric concentrations ranging from 5 to 30 vol.%. With an increase in both of pipe diameter and the fraction of fine sand, the hydraulic gradients decrease. This suggests that the adding fine sand to coarse sand in 25 vol.% gives about 14 % reduction of the hydraulic gradient.

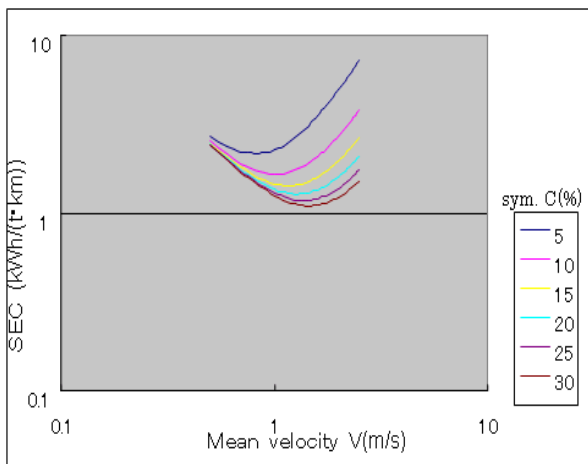


Fig. 9(a) Specific Energy Consumption (SEC) at different concentrations of uniform coarse solids in a 25 mm diameter pipe ($D=25(\text{mm})$, $d_0=2(\text{mm})$)

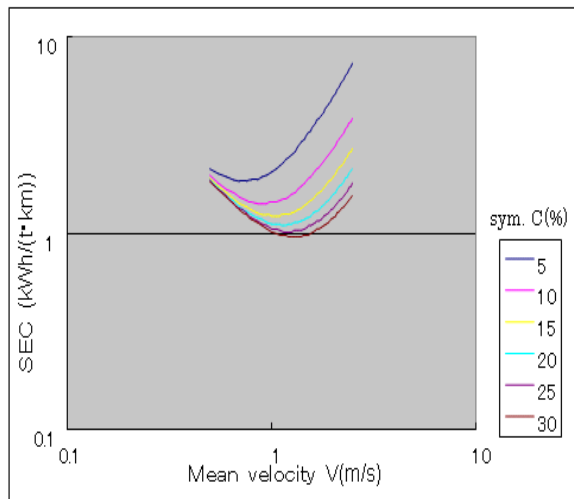


Fig. 9(b) Specific Energy Consumption (SEC) at different concentrations of mixed-sized slurry for 25% fines content in a 25 mm diameter pipe ($D=25(\text{mm})$, $d_0=2(\text{mm})$, $d_1=0.05(\text{mm})$, $R_m=(25\%)$)

Moreover, an increase in the ratio of the fine sand component causes a decrease in the value of the critical deposit velocity V_{cd} , as shown in Figure 6.

5.2 The effect of the component ratio on the hydraulic power requirement

The hydraulic power required for transporting the slurry over a unit distance of the pipeline decreases with an increase in the fraction of fine sand, as shown in Figures 7 and 8, while the pipeline of diameter in 100 mm requires a twentyfold energy in compared with the pipe diameter of 25 mm.

5.3 The effect of the component ratio on the Specific Energy Consumption (SEC)

By using the Wasp method, the SEC values were computed for three pipe sizes of 25, 50, and 100 mm diameters at various delivered volume concentrations. Figures 9 to 11 show the SEC vs. the mean velocity curves. In each curve, a

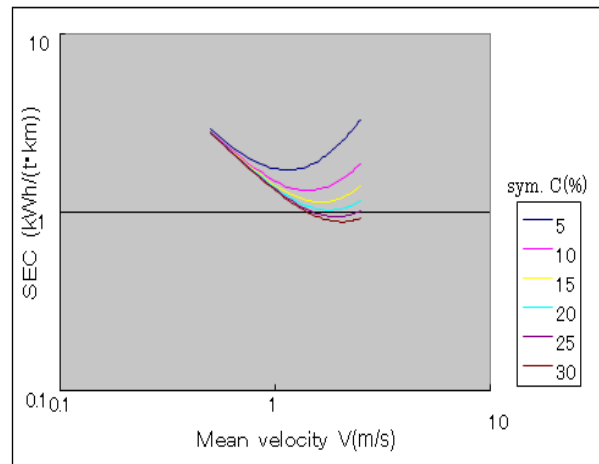


Fig. 10(a) Specific Energy Consumption (SEC) at different concentrations of uniform coarse solids in a 50 mm diameter pipe ($D=50(\text{mm})$, $d_0=2(\text{mm})$)

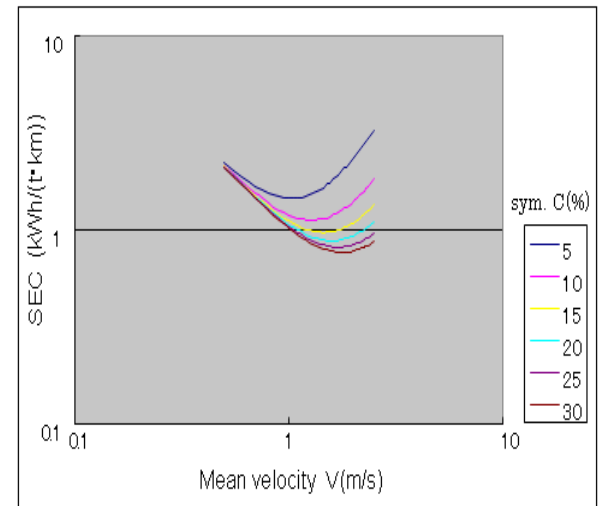


Fig. 10(b) Specific Energy Consumption (SEC) at different concentrations of mixed-sized slurry for 25% fines content in a 50 mm diameter pipe ($D=50(\text{mm})$, $d_0=2(\text{mm})$, $d_1=0.05(\text{mm})$, $R_m=(25\%)$)

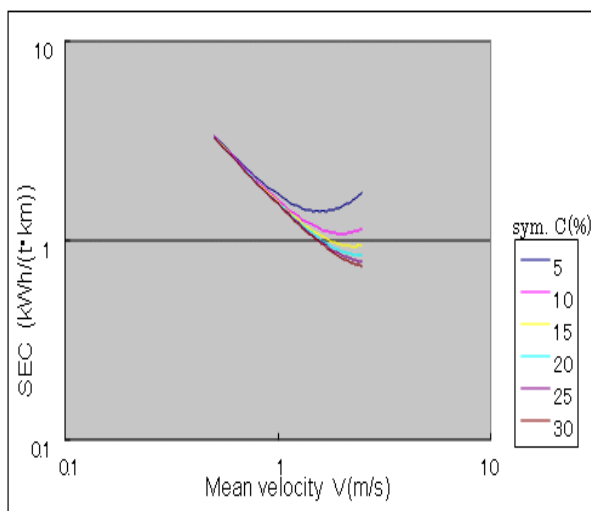


Fig. 11(a) Specific Energy Consumption (SEC) at different concentrations of uniform coarse solids in a 100 mm diameter pipe ($D=100(\text{mm})$, $d_0=2(\text{mm})$)

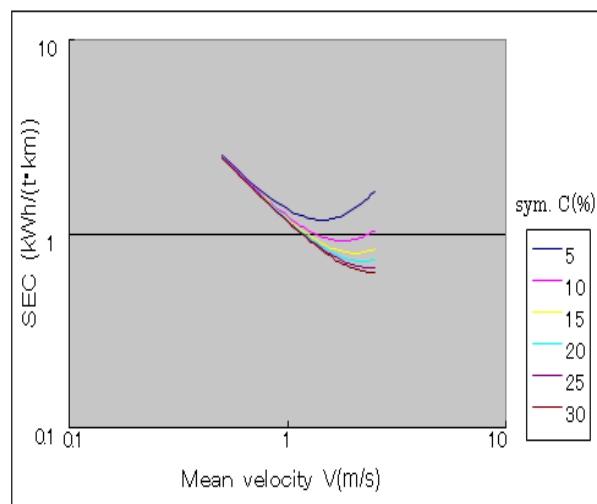


Fig. 11(b) Specific Energy Consumption (SEC) at different concentrations of mixed-sized slurry for 25% fines content in a 100 mm diameter pipe ($D=100(\text{mm})$, $d_0=2(\text{mm})$, $d_1=0.05(\text{mm})$, $R_m=(25\%)$)

minimum point, or an optimum condition, is observed. As the concentration is increased, the velocity at this minimum point increases, while the SEC decreases at the point.

It should be noted that the amount of reduction in the SEC is dependent on the pipe diameter and the fraction of the fine particles. Although a twice increase in pipe diameter results in about 30 % increase in the mean velocity for flowing the slurry at the optimum conditions, a 25% increase in the fraction of fine particles reduces the SEC by 14 %.

6 Conclusions

- (1) In mixed-sized slurry, an increase of fraction of fine particles to the coarse particles causes a decrease in critical deposit velocity, hydraulic gradient, hydraulic power requirement, and the Specific Energy Consumption (SEC).
- (2) The hydraulic power required for slurry flow is dependent on the pipe diameter. A fourfold increase in diameter results in about a twentyfold increase in energy.
- (3) As the concentration increases, the velocity at the minimum point on the SEC-V curve increases, although the SEC decreases.
- (4) At the concentration ranging from 5 to 30 vol.%, a 25% increase in the fraction of fine particles make possible reduction of the SEC by 14%.

References

- [1] Elsibai, N. G., Snoek, P. E., and Pitts, J. D., "How Particles Size Affects the Cost of Short Distance Coal-Slurry Pipelines," *Oil and Gas Journal*, Vol.80, No30, pp.253-259, (1982).
- [2] Kao, D. T. T. and Hwang, A. L. Y., "Determination of Particle settling Velocity in Heterogeneous Suspension and its Effect on Energy Loss Prediction in Solid-Liquid Freight Pipelines", *J. of Powder & Bulk Solid Tech.* Vol. 4, No. 1, pp.31-40, (1980).

- [3] Wasp, E. J., Regan, T. J., Withers, J., Cook, P. A. C., and Clancey, J. T., "Cross Country Coal Pipe Line Hydraulics," *Pipe Line News*, Vol. 35, pp.20-28, (1963).
- [4] Liu, H. : *Pipeline Engineering*, Lewis Publishers, pp. 131-143, (2003).
- [5] Sato, H., Otsuka, K., and Cui, Y., "A Model for the Settling Slurry Flow with a Stationary Bed in a Pipe," *Proc. 1st ASME-JSME Fluid Engng Conf., Liquid-Solid Flow, FED-Vol. 118*, pp.53-63, (1991).
- [6] Thomas, D. G., "Transport Characteristics of Suspension:VIII. A Note of the Viscosity of Newtonian Suspensions of Uniform Spherical Particles," *J. of Colloid Sci.*, Vol. 20, pp.267-277, (1965).
- [7] Wasp, E. J., Kenny, J. P., and Gandhi, R. L., : *Solid-Liquid Flow, Slurry Pipeline Transportation*, pp.93-94, (1977).
- [8] Jacobs, B. E. A. : *Design of Slurry Transport Systems*, Elsevier Science Publications LTD, pp.25-36, (1991).
- [9] Hanks, R. W., "The Influence of Non-Newtonian Rheology in Mixed Homogeneous-Heterogeneous Slurry Flow," *Proc. 5th Tec. Conf. on Slurry Transport*, pp.251-260, (1980).
- [10] Govier, G. W. and Aziz, K., : *The Flow of Complex Mixtures in Pipes*, Robert E. Krieger Pub. Co. pp.617-771, (1972).
- [11] Sato, H. and Kawahara, M. "Critical Deposit Velocity of Slurry Flow Including Single-Size Solid Particles," *Proc. 2nd Int. Cof. on Multiphase Flow '95-Kyoto*, pp.IA3-23-IA3-30, (1995).
- [12] Senapati, P. K., Mishra, B. K., and Parida, A., "Slurry Pipelines for Fly Ash, bulk solid handling, Vol. 26, No. 8, pp.556-562, (2006).

Research on Utilization of Woody Residues from Bio-Ethanol Production Research and Development on High-Solids and Efficient Saccharification for Bio-Ethanol Production from Woody Biomass

Hironori Kobayashi, Takehiko Takahashi, Kazushi Ito, Arata Ito, Yukio Enda
and Junichi Kobayashi

Department of Machine Intelligence and Systems Engineering, Akita Prefectural University

84-4, Tsuchiya-aza-ebinokuchi, Yurihonjo, 015-0055, Japan

takehiko_takahashi@akita-pu.ac.jp, m10a005@akita-pu.ac.jp

Abstract: Bio-ethanol production from lignocellulosic biomass, comprising cellulose, hemicellulose and lignin, includes an enzymatic hydrolysis process to convert cellulose and hemicellulose to sugar. The developments of an enzymatic hydrolysis process to achieve high concentration saccharification in short time have economical advantages. In this study, the enzymatic hydrolysis process with a wet mill was carried out using sample of Japanese cedar wood powder. And then a solids-liquid separation by the filter press was carried out using the residue after the enzymatic hydrolysis process. As a result of this, the enzymatic hydrolysis process with the wet mill increased an initial saccharification speed and maximum saccharification ratio of holocellulose at 10% of solids concentration. And the residue and glucose solution collected were slightly affected by changes in wood powder finely ground.

Key Words: Saccharification with a wet mill, Cellulowood powder, Solid-liquid separation

1. INTRODUCTION

Biomass energy has been examined as a technology corresponding to global warming¹⁾. Biomass energy is energy that can be reproduced by plants. Wood and grass biomass include tree prunings, scrap wood, rice hull, rice straw, cleared brush, and other waste sources. Their use as automobile fuel use is desirable. Woody biomass comprises cellulose, hemicelluloses, and lignin. Holocellulose, which includes cellulose and hemicelluloses, can be processed into monosaccharides using hydrolysis; monosaccharides can be processed into ethanol through yeast fermentation. Lignin disturbs saccharification and yeast fermentation.

Accordingly, it is necessary to eliminate remaining lignin for saccharification²⁾. Various hydrolytic methods can produce monosaccharides from holocellulose. Among them, hydrolysis using enzymes is the most environmentally friendly.

Enda et al.³⁾ developed an inner power ring mill for manufacturing ethanol. The inner power ring mill can mill Japanese cedar chips using high ballistic force. Japanese cedar powder achieved an 80% saccharification ratio for enzymic saccharification using an inner power ring mill with 20 μm average grain diameter. However, knowledge of a technology to collect lignin-based residues from a saccharified solution is not yet available.

Ethanol fermentation of the sample powder used by Enda et al. required a 20% saccharification ratio to accomplish a greater than 10% ethanol ratio. Furthermore, a glucose ratio of 20% was achieved during enzyme saccharification using a

sample powder ratio of 35%. A glucose ratio of 20% was necessary to generate an ethanol ratio higher than 10%. However, it is confirmed that the saccharification ratio is impaired by the high powder sample ratio became clear. Action of the enzyme was obstructed by high ratios of sample powder. Moreover, the saccharified solution includes lignin-based residues. The glucose included in the residue is difficult to convert into ethanol. Moreover, for use of the residue as a functional material, technology to collect residues during or after enzyme saccharification is necessary.

In saccharification, sample powder finely ground increases the contact area of the sample powder and the enzyme, which improves saccharification. However, because the sample powder is finer, separation of the saccharified solution and residue becomes difficult. An appropriate technology to collect residues is therefore demanded.

For this study, enzyme saccharification was performed using a sample powder milled using the inner power ring mill. This study examines injected sample powders according to the progress of saccharification. A saccharification method using finely ground sample powder during enzyme saccharification was examined. This study investigated the change of grain size by wet milling and its relation to the saccharification ratio. The sample powder used during enzyme saccharification was finely ground; its influence on residue collection was investigated. We used a gear pump during saccharification processing and circulated the powder through the saccharification liquid. The mill effect on improvement of the saccharification ratio was examined. In addition, we examined

the influence of sample powder miniaturization on collection of the saccharified solution after saccharification. Solid–liquid separation used a filter press as described in an earlier report⁴⁾. Furthermore, this study measured collection ratio of the saccharified solution and residue to investigate its influence on residue collection ratio by miniaturization.

2. EXPERIMENTAL METHODOLOGY

2.1 Enzyme saccharification experiment

This experiment was done to evaluate the saccharification ratio when finely ground powder was used in enzyme saccharification. The powder was circulated in a saccharified solution; experiments were performed using finely ground powder and the gear pump and churning in a saccharification tank. Figure 1 portrays a circuit diagram of the experimental device. An earlier report⁴⁾ described churning of the saccharified solution using a screw. Furthermore circulation with the gear pump was added by this investigation. A gear pump (Koyo Particularity Co.) was incorporated in circulation. The circulation flow rate was 5.0 l/min. The experiment was performed in the following saccharification conditions: churning of the sample powder in the tank; churning and circulation of the saccharified solution in the tank; churning and saccharification of the sample powder in the tank; churning, circulation, and saccharification of the sample powder in the tank. The Japanese cedar sample powder density was 10 w/v% for buffer. For experiments with enzyme saccharification, the enzyme density was 10% for the Japanese cedar sample powder. The saccharification experiment conditions were the following.

Saccharification time: 48 hr
 Saccharification temperature: 50°C
 Buffer solution: acetic acid (pH 5.0), 10 l, 20 l
 Churning speed: 100 rpm

Samples were gathered during a regular examination. Grain size distributions were measured (HRA-X-100; Nikkiso Co. Ltd.). The saccharification ratio was measured using a UV brightness absorption meter (Hitachi Ltd.).

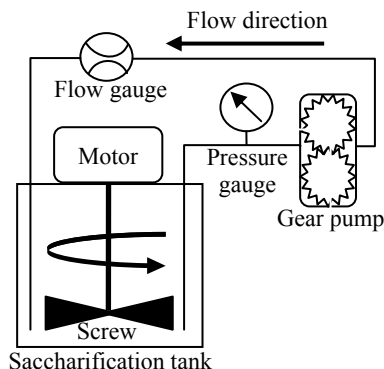


Fig. 1 Attachment diagram of saccharification experiment

2.2 Solid–liquid separation experiment

Solid–liquid separation was done using a filter press. The principal circulation saccharified solution after enzyme saccharification, including solid bodies, was filter pressed using pneumatic transportation with a pump. After the saccharified solution passed the filter in the filter press, the residue and saccharified solution with particles smaller than the mesh diameter flow out into the low-pressure side as a suspension. The residue that cannot pass the filter remains on the high-pressure side as a residue. The suspension and the solid body—dehydrated cake—can then be collected.

The solid–liquid-separation experimental procedure is presented in Fig. 2. A diagram of solid–liquid separation by the filter press is depicted in Fig. 3. The first solid–liquid separation in residue and saccharified solution experiment used a filter press in saccharified solution after enzyme saccharification. Distilled water was added to the collected residue. Then the suspension solution produced after the first solid–liquid separation was used for collection of glucose included from the residue. The suspension was separated to residue and the saccharified solution by a second filter press solid–liquid separation. The gear pump's influence on the collection ratio of finely ground residue was evaluated. Measurements were made of the quantity of glucose and grain diameter distribution of the sample powder after enzyme saccharification, the quantity of the collected residue, the saccharified solution quantity, and the glucose quantity.

3. EXPERIMENTAL RESULT

3.1 Enzyme saccharification experiment

The effect of the finely ground sample powder is portrayed in Fig. 4. For churning of the sample powder in the tank, few changes were detected in the average diameter. It is confirmed that the churning and circulation of the sample powder, the average diameter of the finely ground particles. Furthermore, the average diameter at the start of the experiment was 27 μm, but the average diameter became 10 μm after 8 hr. The results show the effects of the finely ground sample powder with gear pump circulation in the tank. For churning and enzyme saccharification in the tank, the time was about 2 hr for average particle diameter of 10 μm, which more finely ground than the average diameter size in the case of churning and circulation in the tank. Cellulose constituting the sample powder disappeared through enzymic saccharification; the sample powder bonding became weak. It was probably destroyed by churning. Fine grinding was superior in the combined case of churning, circulation and saccharification of the sample powder in the tank: for the average diameter of 10 μm, the time was 15 min, which is 1/8 of the time necessary for churning and saccharification of sample powder in the tank. Probably, the bonding of the finely ground sample powder was degraded by enzyme saccharification.

Additional circulation shortened the time for powder with average diameter size of 10 μm . Fine grinding using the gear pump is more efficient: probably, fine grinding using the gear pump is equivalent to fine grinding by churning.

The influence on the saccharification ratio by performing fine grinding of the sample powder using a process of enzymic saccharification is presented in Fig. 5. Improvement of the saccharification ratio was confirmed in a short time using circulation. It increased the enzyme contact area: the finely ground sample powder promoted enzymic saccharification.

Furthermore, the saccharification ratio measured 48 hr later reached 81%, but it was only 62% when circulation was not used, confirming that circulation improved the saccharification ratio by about 20%. Why the saccharification ratio is improved by fine grinding of sample powder must be investigated in future studies.

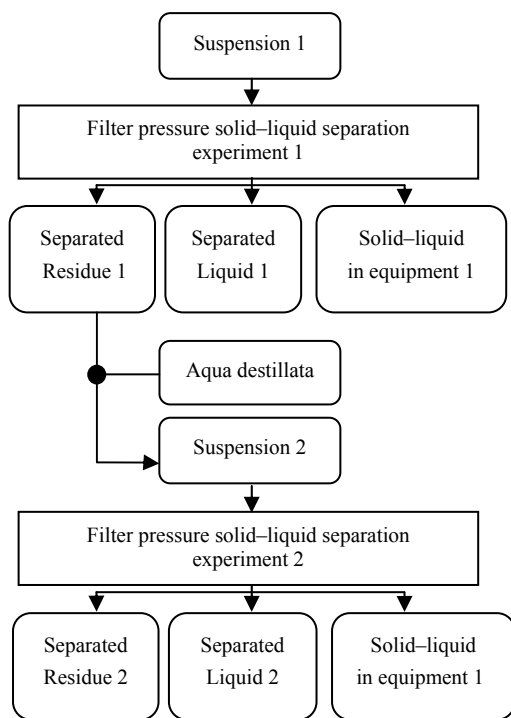


Fig. 2 Pressure solid-liquid separation experiment flowchart

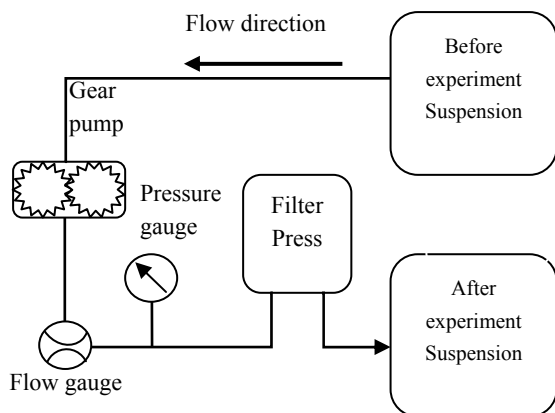


Fig. 3 Attachment diagram of pressure solid-liquid separation experiment

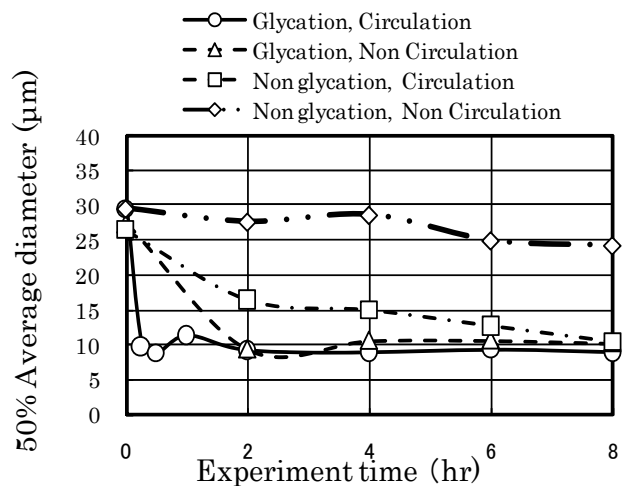


Fig. 4 Effect of wet mill on the average diameter of powder during enzymatic hydrolysis

3.2 Solid-liquid separation experiment

The suspension after enzymic saccharification was done using solid-liquid separation. Therefore, collection of the saccharified solution and residue was performed.

The mass balance of enzymic saccharification of circulation is depicted in Fig. 6. The mass balance before enzymic saccharification was measured using 1000 g sample powder, 100 g enzymic solution (34% of the enzyme was glucose), and 10,000 g buffer solution. The estimated mass balance quantity before enzymic saccharification was converted into glucose by the sample powder, and it was measured. The saccharification ratio and water content ratio of saccharified solution were thus measured, and glucose was estimated. The collection ratio of glucose and the collection ratio of residue of solid-liquid separation experiment are presented in Table 1. The collection ratio of glucose was measured using the first and the second total of a solid-liquid separation experiment. The collection ratio of residue was demanded by the second collection residue of a solid-liquid separation experiment.

For the glucose ratios collection, no difference was found between non-circulation and circulation. The residue collection ratio did not decrease even using circulation, probably because the average diameters of both were 10 μm .

Mass balances of residue and glucose were measured after the solid-liquid separation experiment. The residue mass balance is portrayed in Fig. 7. The glucose mass balance is presented in Fig. 8. When solid-liquid separation was performed twice, 9% of the residue was not collected, but 17% of glucose was collected. Regarding the glucose that was not collected during solid-liquid separation, 42% was included in the first collection residue; 25% was included in the second collection residue. Glucose was collected from throughout the collection residue, but the number of solid-liquid separation times should be examined because the residue was lost.

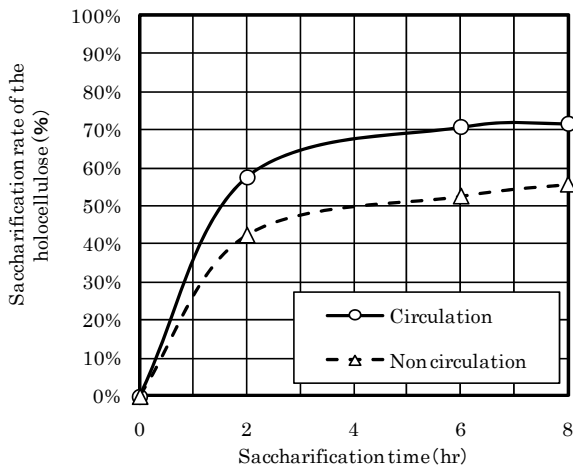


Fig. 5 Effect of wet mill on the saccharification ration of holocellulose

Table 1 Collection ratio at filter pressure solid-liquid separation experiment

	Circulation	Non Circulation
Glucose (amount of glucose after saccharification was defined as 100%)	73.1%	75.3%
Solid residue (amount of solid residue after saccharification was defined as 100%)	65.0%	54.0%

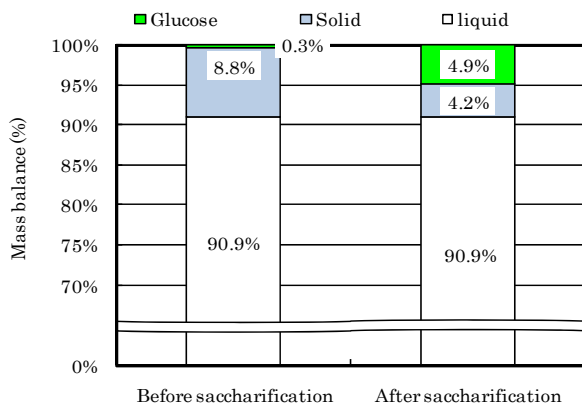


Fig. 6 Variation of mass balance during saccharification

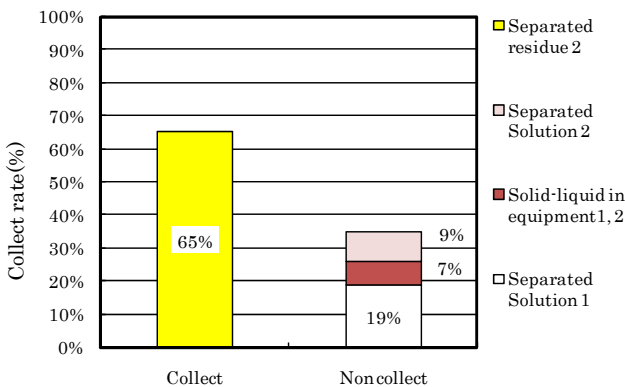


Fig. 7 Mass balance of solid residue after solid-liquid separation experiment in twice using saccharification residue at saccharification experiment with circulation

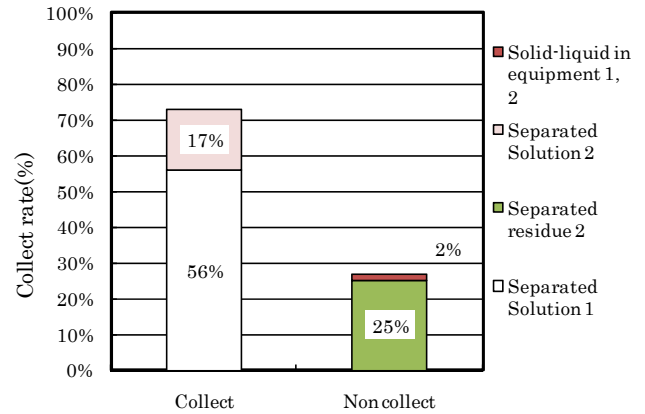


Fig. 8 Mass balance of glucose solution after solid-liquid separation experiment in twice using saccharification residue at saccharification experiment with circulation

4. CONCLUSION

For this study, technical examination was made of enzyme saccharification of a sample powder milled in the inner power ring mill. The influences on the saccharification ratio and collection ratio of residue were examined when the sample powder was finely ground during enzyme saccharification. Results confirmed that the average diameter became 10 μm . The saccharification ratio was improved 10 points, from as 70% to 80%. Saccharification was effective when the sample powder was finely ground during enzyme saccharification. For finely ground sample powders, it is necessary to examine the reason why the saccharification ratio improved.

References

- [1] Daisei Y, "Farthest Advance of the Bio-ethanol," (2004).
- [2] Japan Alcohol Association "Production Technology of the Bio-ethanol," (2007).
- [3] Enda Y, Kobayashi J, Takahashi T, Ito K, Ito A, "A Study for High Glucose Concentration Solution From Cellulosic Woody Biomass by Inner Power-Ring Mill," Bio-mass Scientific Meeting, Vol. 4, pp. 104-105, (2009).
- [4] Kobayashi H, Takahashi T, Ito A, Enda Y, Kobayashi J, "A Study of Saccharide Collecting Process from Residue of Bio-Ethanol Production using Wet Crushing," Symposium on Environmental Engineering Vol. 18, pp. 183-186, (2008).

Metal recovery from effluent water of metallurgical refining process by cementation and solvent extraction

Kazutoshi Haga¹, Hisayoshi Umeda², Atsushi Sasaki², Kunihiko Takahashi²
Yasushi Takasaki¹ and Atsushi Shibayama¹

¹ Faculty of Engineering and Resource Science, Akita University, Akita 010-8502, Japan

² Yokohama Metal Co., Ltd., Kanagawa 229-1132, Japan

m9008032@wm.akita-u.ac.jp

Abstract: Effluent waters from metallurgical refining process are usually treated by hydrometallurgical processes incorporating leaching, cementation, electrowinning, neutralization, precipitation to extract and recover precious and base metals from waste materials. In the current study, we focused on the possibility of recovering previous metals namely; (Cu, Au, In, Pd, Pt) from the effluent water by cementation and solvent extraction steps. Fe, Al, and Zn powders were used for precious metal cementation, and LIX-84I, D2EHPA, and TBP as organic extractants with kerosene were used in solvent extraction. 99% of Cu, 96% of Pd, 85% of Au were recovered by Fe powder at (Cu/Fe) mole ratio of 2, and 99.6% of Cu, 99.5% of Pd were recovered by Al powder at (Al/Cu) mole ratio of 2. Also 90% of Au, and 60% of In, were recovered by solvent extraction using D2EHPA and TBP, respectively.

Key Words: Metal recovery, Cementation, Solvent extraction

1 INTRODUCTION

Due to decline in existing resources and increased utilization of precious metals such as gold (Au), silver (Ag), platinum (Pt), palladium (Pd) in many applications including catalysis, electronics, jewelry, etc, sourcing of these metals from secondary resources such as industrial wastes are being developed. Most of such metals contained in waste materials are recovered through hydrometallurgical processes, by leaching, cementation, electrowinning, neutralization/precipitation process [1-6]. The effluent water generated after hydro metallurgical processing is usually acidic with high nitrate-nitrogen concentration from nitric and hydrochloric acids used in the process. At the same time, the effluent water contains high concentration of copper (Cu) and indium (In), with Au, Pd and Pt at lower concentrations.

Currently the treatment of such effluent water is difficult due to its low pH and most treatment facilities use burning as treatment option. Such operations treat the effluent water from the hydrometallurgical process as waste water, even though it

contains high Cu and In with other elements (Au, Pd, Pt). There exists a need to develop a treatment process option to treat such effluent water for precious metals recovery and decrease environmental load.

The current study was focused on the possibility of recovering Cu, Au, In, Pd, and Pt from the effluent water by cementation followed by neutralization/precipitation and solvent extraction with LIX-84I, D2EHPA ($C_{16}H_{35}O_4P$) and TBP ($[CH_3(CH_2)_3O]_3PO$) as organic extractants with kerosene to recover the metals from the effluent water.

2 EXPERIMENTAL

2.1 Effluent water sample

Table 1 shows initial metal concentration of effluent water from metal refining and recycling operation used in this work. The effluent water also contain many other metals such as nickel, lead, tin, bismuth, and so on, however, in this study, Cu, which initially has a very high concentration and the other four valuable and most expensive metals (Au, Pt, In, Pd) are being

investigated as the five metals of interest. The concentration of Au, Pt, Pd and In ranged between 0.01 to 10 mmol/L and that of Cu at approx. 200 mmol/L was present in the effluent water. The same effluent water contains high concentration of chloride, nitric and ammonium ions from reagents used in acid leaching and adsorption processes.

Table 1 Initial concentration of metals in effluent water

Metal	Cu	Au	In	Pd	Pt
Conc. (mmol/L)	218.32	0.06	9.37	1.51	0.14

2.2 Cementation

Separation of dissolved metals in effluent water by cementation was performed by the addition of iron (Fe), aluminum (Al), and zinc (Zn) metal powders. The metal powders were added at 1 or 2 (Metal/Cu) mol/mol ratio, into 250mL of effluent water in a 300mL beaker. A (Metal/Cu) mole ratio of 1 and 2, so each metal powder was added at 0.2 and 0.4mol/L respectively. 5mL of samples were drawn from the solution at different times between 10 to 360 min for metals concentration analysis.

2.3 Precipitation

Recovery of metals from solution by precipitation technique usually involves pH adjustment or sulfide addition to form solid products for separation. A 100mL of effluent water was put into 200mL glass beaker and pH was adjusted to target pH by addition of NaOH (10M) and slowly rotated on magnetic stirrer. After pH adjustment, the solid precipitates were allowed to settle. This was followed by filtration and both solids and solution fraction were analyzed by ICP-AES to monitor distribution of the metals and evaluate efficiency of precipitation process.

2.3 Solvent extraction

Recovery of metals from effluent water by solvent extraction was performed using LIX-84I (2-hydroxy-5-nonylacetophenone oxime), D2EHPA (Phosphoric Acid Di(2-Ethylhexyl) Ester) and TBP(Tri Butyl Phosphate).

A 50mL of effluent water and diluents (60vol% organic extractant and 40vol% kerosene) were added into 200mL separating funnel and placed on a mixer for 10min. After

mixing, the solution was allowed to separate into organic and inorganic phases. The phases were then separated and analyzed by ICP-AES for metals in the aqueous solution.

3 Result and discussion

3.1 Cementation

3.1.1 Iron cementation

Figure 1 shows change of metal concentration during iron cementation at different Fe/Cu molar additions. Concentration of Au was observed to decrease in the first 10 min, and concentration of Cu and Pd decreased after 60 min. At 360 min of reaction time, concentration of Au decreased up to 85% and that of Cu and Pd in solution decreased by more than 90% for (Fe/Cu) ratio of 1, but recovery was further improved by over 5% for (Fe/Cu) ratio of 2.

However, the recovery of In and Pt were not achieved in this process. For In, this could be due to its lower standard electrode potential when compared to other precious metal, so recovery is difficult by cementation. Concentration of Au decreased in the first 10 min but re-dissolved into solution as cementation progressed, this could be attributed to metal oxidation by effect of dissolved oxygen. Pure Pt metal has high standard potential and can be recovered by cementation on the electro chemical principal. However, in this effluent water system, Pt concentration only decreased by up to 18% and this could be due to formation of cyanogens complex, which has low standard electrode potential making it difficult for cementation.

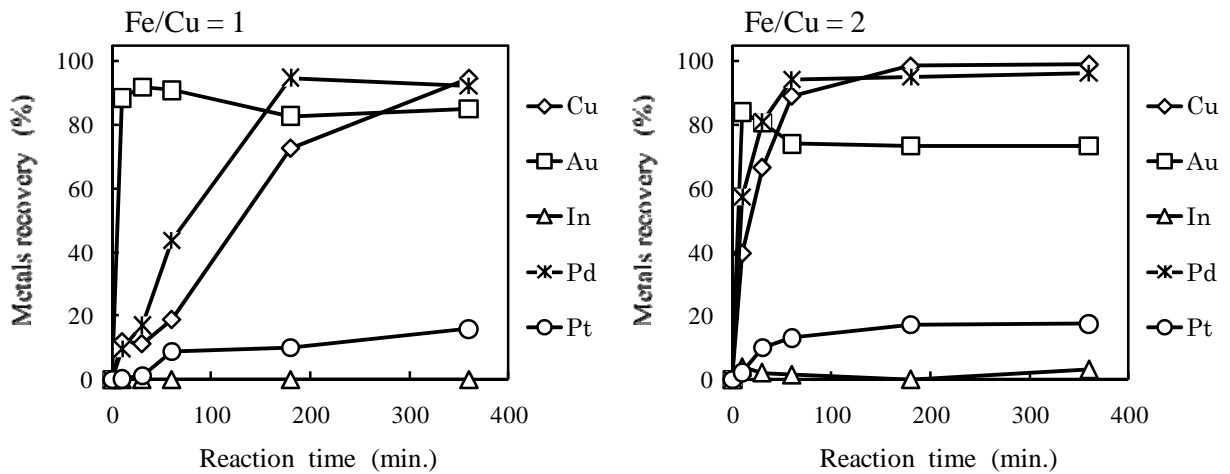


Figure 1: Change of metals recovery by iron cementation

3.1.2 Aluminum cementation

Figure 2 shows change of metal concentration by aluminum cementation. When (Al/Cu) ratio is 1, only Pd concentration decreased and other metals remained constant, due to low amount of Alminum. When (Al/Cu) ratio is increased to 2, Cu, Au and Pd concentrations similarly decreased and results obtained was similar to iron cementation in the previous section. Concentration of Cu, Au, and Pd has been reduced by more than 80% in solution, with Pd approaching 99% recovery. The result also indicates that In and Pt can not be recovered by aluminum cementation.

3.1.3 Zinc cementation

Figure 3 shows change of metal concentration by zinc cementation. Unlike in iron and aluminum cementation, Cu, Au and Pd can not be easily recovered by zinc cementation. However, In concentration in zinc cementation solution reduced by more than 99%. Solution pH in iron and aluminum cementation was around pH 3, however, in zinc cementation the solution pH increased to pH 5.6. Standard electrode potential of In is lower compared to other precious metals and is not easily removed by cementation, but in the current case, it could be concerned to precipitation as indium hydroxide.

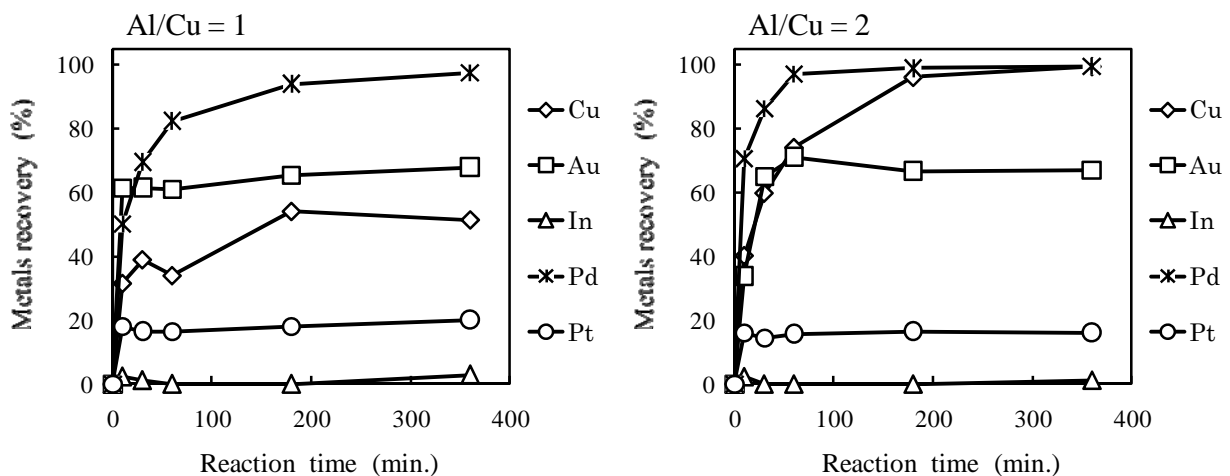


Figure 2: Change of metals recovery by aluminum cementation

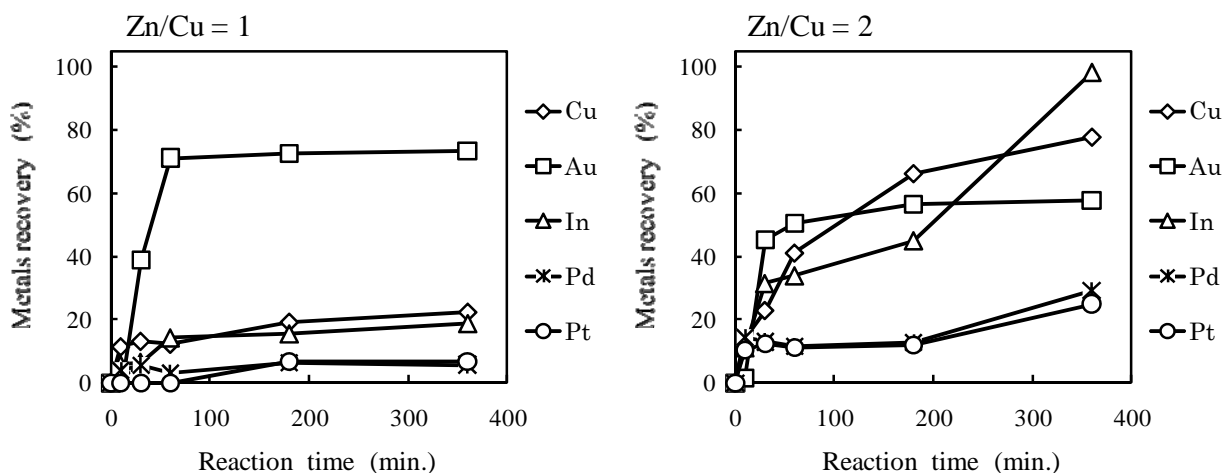


Figure 3: Change of metals recovery by zinc cementation

3.2 Precipitation

Recovery of metals dissolved in solution by precipitation as a function of pH is shown in Figure 4. It can be seen from this result that concentration of Cu, In decreased as solution pH is increased from below pH 1 to above pH 5. Cu and In concentrations were reduced in the solution at pH 4.2. 95% of Cu and 98% of In have been recovered from the effluent water at pH 5.2. However, concentrations of Au, Pd and Pt remained constant indicating that the following metals can not be recovered in the precipitation process by pH control.

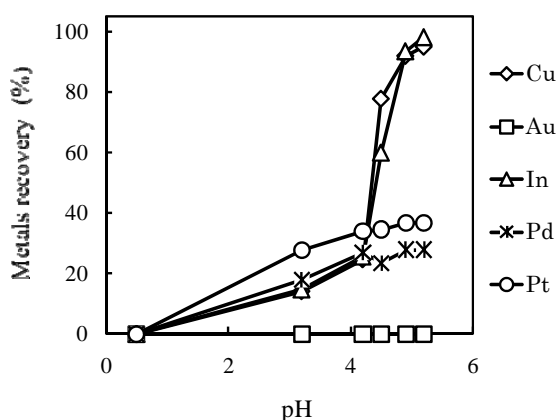


Figure 4: Recovery of metals dissolved in solution by precipitation as a function of pH

3.3 Solvent extraction

3.3.1 Using LIX-84I extraction

Figure 5 shows extraction of metals contained in effluent water using LIX-84I. 50% of Au can be extracted by

LIX-84I. In general, LIX-84I is used as an organic extractant for Cu recovery. However, in the current result Cu recovery was low because of the effluent water containing high Cu concentration. Extraction of In and Pt were difficult with LIX-84I.

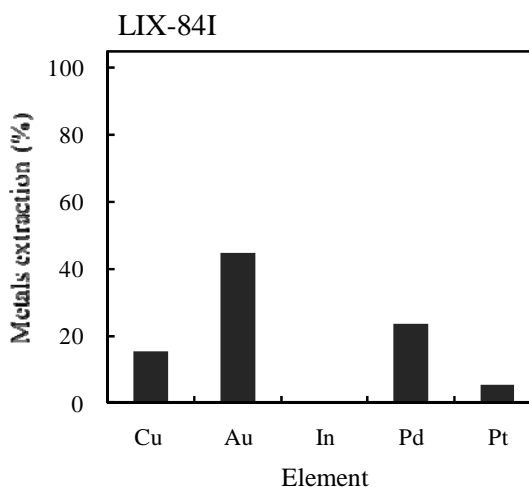


Figure 5: Extraction of metals containing in effluent water using LIX-84I

3.3.2 Using D2EHPA extraction

Figure 6 shows extraction of metals (Cu, Au, In, Pd, Pt) using D2EHPA as extractant directly from the effluent water and experimental conditions. The result shows that extraction of In was at 85%, even though the initial concentration of the In was significantly different at 9.37 mmol/L (In) was selectively extracted under the same extraction conditions. Extraction of Cu and Au reached

only about 10%, but Pd and Pt were not extracted from the effluent water.

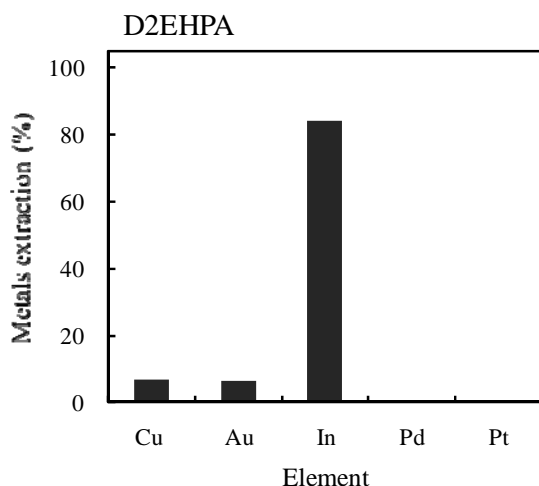


Figure 6: Extraction of metals containing in effluent water using D2EHPA

3.3.3 Using TBP extraction

Figure 7 shows extraction of metals using TBP as extractant. The result shows that 85% of Au was extracted by TBP. A low of about 5% extraction was achieved for In and Pt, however, Cu and Pd were not extracted by TBP.

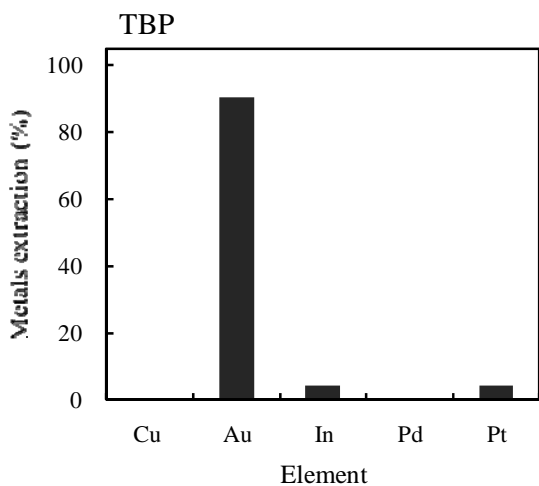


Figure 7: Extraction of metals containing in effluent water using TBP

4 Conclusion

The findings as discussed in this work, to investigate a metal recovery process consisting; cementation, precipitation and solvent extraction from effluent water of metallurgical refining process is summarised below;

- 1) Recovery of Cu, Au, Pd by cementation process using iron and aluminum powder recovered up to 99%, 85%, 96% for the three metals respectively with iron, and similarly up to 99%, 70% and 100% was recovered with aluminum. However, Cu, Au and Pd metals were not successfully recovered with zinc cementation. But very high recovery of up to 99.5% In was achieved with zinc cementation of the effluent water.
- 2) In precipitation process, Cu and In concentrations were reduced in the solution at pH 4.2. 95% of Cu and 98% of In have been recovered from the effluent water at pH 5.2.
- 3) In solvent extraction process, three of the extractants used had different extraction capabilities for different metals. With LIX-84I extraction of all metals did not exceed 50% under current investigation conditions, however, extraction of copper approached ideal recovery. When using D2EHPA, In was selectively extracted from the solution with concentrations exceeding 85%. The third extractant, TBP selectively extracted Au concentration up to as high as 90%.

References

- [1] Jirang Cui, Lifeng Zhang, Metallurgical recovery of metals from electronic waste: A review. *Journal of Hazardous Materials* 158 (2008) 228–256.
- [2] Eric Jackson, Hydrometallurgical Extraction and Reclamation, E.G. West (ed.) *Ellis Horwood Series in Industrial Metals*, 1986.
- [2] Zhike Wang, Donghui Chen, Liang Chen, Gold cementation from thiocyanate solutions by iron powder *Minerals Engineering* 20 (2007) 581–590.
- [3] Jurjen Kramer, Willem L. Driessen, Klaus R. Koch, Jan Reedijk, Highly selective extraction of platinum group metals with silica-based (poly)amine ion exchangers applied to industrial metal refinery effluents *Hydrometallurgy* 64 (2002) 59–68.
- [4] The chemistry of Metals Recovery using LIX® Reagent, Mining Chemicals and Technology, cognis (www.cognis.com)

[5] Gordon M. Ritcey, G. M. Ritcey (eds), Solvent Extraction in Hydrometallurgy: Present and Future. *TSINGHUA SCIENCE AND TECHNOLOGY* (Ottawa, Canada), 11(2) (2006) 137-152.

[6] Kathryn C. Sole, Angus M. Feather, Peter M. Cole, Solvent extraction in southern Africa: An update of some recent hydrometallurgical developments. *Hydrometallurgy* 78 (2005) 52–78.

Recovery of Pt and Pd from PGM mine tailings by magnetic separation

Jan. Pana. Rabatho, William Tongamp, Yasushi Takasaki and Atsushi Shibayama

Faculty of Engineering and Resource Science, Akita
University Tegata-Gakuen-cho, Akita 010-8502, Japan

d9508002@wm.akita-u.ac.jp (J.P. Rabatho)

Abstract: An application of a dry magnetic separation process to recover platinum (Pt) and palladium (Pd) contained in PGM(platinum group metals) flotation tailings in South Africa was investigated in this work. The concentrations of Pt and Pd in the tailings were 0.7 g/t and 0.2 g/t in mainly SiO₂, Fe₂O₃ and MgCr₂O₄ minerals according to XRD patterns. A dry coil magnetic separator with its strength varied from 120 to 240 mT was used to separate the tailings into magnetic, middling and non-magnetic fractions in a two-stage operation. The results show that around 2 wt% of the tailings could be recovered as the magnetic fraction of Pt and Pd concentrations of 40 g/t respectively. About 8 wt% of the tailings reported to the middling section giving Pt and Pd concentration in that fraction as 25 and 16 g/t respectively. XRD studies of the three fractions from magnetic separation show that Fe₂O₃ and MgCr₂O₄ as main phases in the magnetic and middling fractions indicating that Pt and Pd fine grain particles are interlocked in MgCr₂O. This process could be optimised to increase the Pt and Pd concentrations from 40 to over 50 g/t of PGM flotation tailings and offer as the additional resource for recovering the valuables metals.

Key words: Platinum group metals; Flotation tailing; Magnetic separation.

1. INTRODUCTION

South Africa, the largest producer of platinum group metals, still has more than two thirds of the world's platinum reserves. But with the growth in the platinum market driven by the demand in PGMs in a variety of applications as catalyst, jewellery, autocatalyst, and other industrial use, there is a growing trend to develop the processes for recovering PGMs contained in the resources such as low grade deposits, industrial wastes and millions of tonnes of mine flotation tailings.

This project was targeted to develop the process for recovering PGMs in the flotation tailings held in tailing dams in South Africa. Millions of tons of tailing contain the mixture of UG-2 and Merensky projects containing about 10% chromite from the UG-2 operation. The association of the PGMs with the chromite has been known since the early 1920s [1,2]. Detail studies of this reef by McLaren and De Villiers [3], Von Gruenewaldt [4], Gain [5] have shown that the PGMs are not evenly distributed but associate with base metals. The PGMs with particle size ranging from (2-5µm)

are enclosed within the chromite. Recently the recovery of PGMs from the same tailings by flotation has been reported [6]. The average grade of the concentrate produced during flotation was 45 g/t. NiS-FA discussed elsewhere [7], used as a collector for platinum, palladium and rhodium. The analytical results shown in table 1 indicated that the original sample contains chromite that contained Pd, Pt and Rh interlocked between the grain boundaries of the chromite and coarse silica [8-15]. However, amongst other losses due to the fine grain sizes of Pt during washing and flotation of the ore caused Pt to be misreported in the tailing.

This paper discusses the concentrations of Pt, Pd and Rh in the flotation tailing produced in South Africa. The recovery of chrome is also possible as the sample contains about 10% chromium. The platinum bearing minerals tend to be found in the chromitite layers and can be separated by dense medium separation.

2 EXPERIMENTAL

2.1 Sample

The sample used in this work was flotation tailings with a d_{50} size of 45 μm . It contains Pt (0.7 g/t, Pd (0.2 g/t) and Rh (5.0 g/t) as given in Table 1. Powder X-ray diffraction analysis of the original sample is shown in Figure 1 indicating Fe_2O_3 and MgCr_2O_4 as the main phases.

Table 1. Chemical content of the main elements in the tailings sample

Metal grade (g/t)			
Pt	Pd	Rh	Cr (%)
0.7	0.2	5	10

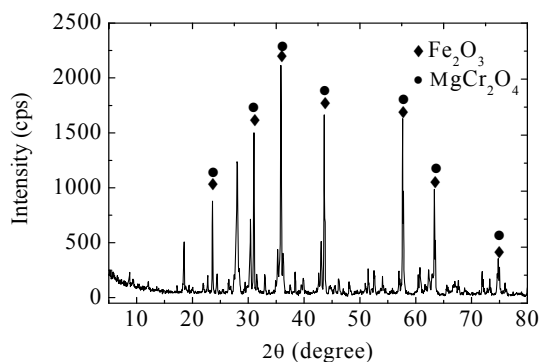


Figure 1. The X-ray diffraction pattern of PGM tailings sample.

2.2 Processing for PGM recovery

2.2.1 Sizing classification

The PGM tailings sample was first separated into different size fractions to evaluate the contents of Pt, Pd, Rh and other metals like chrome in them. The separation was obtained by using laboratory sieves to three groups; screen sizes are +100 μm , -100+32 μm and -32 μm .

2.2.2 Magnetic separation

In this section, the PGM tailings sample was separated into another three fractions; (1) highly magnetic materials, (2) middling and (3) the non-magnetic fractions. Magnetic separator was used and the separation was achieved by placing dry batch samples of 100g in a plastic tray inclined at 5 to 10° subjected to the magnetic force or intensity ranging between 120 and 240 mT (milli Tesla). Physical observation with assistance of hand brush was made to spread the material evenly on the tray in the three different fractions.

First at the magnetic strength of 240 mT the 100 g batch samples were separated into the magnetic, middling and non-magnetic fractions. The magnetic fraction from the first stage was subject to the second stage magnetic separation with the magnetic strength at 120 mT, and the middling from second stage magnetic separation was mixed with one from the first stage and obtained a highly magnetic fraction. Each of the three fractions was analyzed for their phase and chemical compositions.

2.2 Characterization and chemical analyses

Characterization of all solid samples was performed by using X-ray diffraction (XRD) analysis equipment with Cu $K\alpha$ radiation source (Rigaku Co., Japan) and the standard scanning speed of (5°/min) was used to analyze the sample. This includes original sample, samples from sizing operation and different fractions obtained from magnetic separation.

Chemical analysis of both solid and solution samples were obtained by using an Inductively Coupled Plasma – Optical Emission Spectroscopy (ICP-OES, SPS 3000, Seiko instrument Inc, Japan). However, prior to ICP analysis and due to low content of Pt, Pd, and Rh in the sample and high content of silica and chromium. All sample fractions including sizing classification and magnetic separation were treated using the nickel button fire assay (NiS-FA) technique [7].

3 RESULTS AND DISCUSSIONS

3.1 Separation by size classification

Analytical results of the distribution of Pt, Pd, Rh and chromium in all the three size fractions showed no indication of the valuable metals concentrated into one of the size fractions. Concentration of each of the elements remained consistently similar to the original values given in Table 1, indicating that further classification of the tailings samples into different sizes could not be recommended in any process development for the recovery of the valuable metals. The characterization by XRD gave peaks similar to that of original sample (Figure 1).

3.2 Magnetic separation

The purpose of the magnetic separation stage was to maximize the magnetic materials and rejection of the gangue materials in a two stage. In the first stage of magnetic separation, up to 6 wt% of the material (6g/100g sample)

reported to the magnetic fraction and over 5 wt% (5g/100g of sample) of material reporting to the middling fraction. The treatment of the different fractions by NiS-FA for concentration of Pt, Pd, Rh followed by ICP analysis evaluated to 25 g/t and 15 g/t Pt in the magnetic and middling fractions respectively (Table 2) from below

1 g/t in the original tailings sample. Pd also increased to 15 g/t in the magnetic fraction but was below 2 g/t in the middling fraction. This separation was achieved at a magnetic strength of 240 mT.

Table 2. Concentrations of Pt and Pd in the magnetic and middling fractions

Sample	1 st Mag-separation		2 nd Mag-separation	
	Metal grade (g/t)		Metal grade (g/t)	
	Pt	Pd	Pt	Pd
Magnetic	25.0	14.8	42	41
Middling	15.4	1.32	25	16

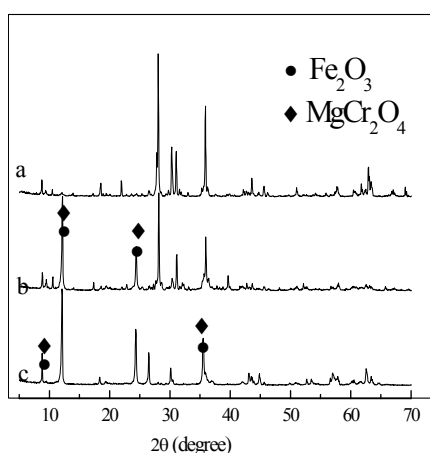


Figure 2. The XRD patterns; (a) non-magnetic, (b) middling, (c) magnetic fractions

With a view for improving Pt recovery to around 40 g/t in the magnetic fraction, the magnetic fraction obtained from the first stage was treated in the second stage magnetic separation with the strength at 120 mT to obtain two fractions; magnetic and non-magnetic fractions. Chemical analysis and the evaluation of the magnetic fraction in the second stage improved the Pt recovery to 42 g/t (2 wt% or

2g/100g sample) and the Pd recovery to 41 g/t as shown in Table 2. Total middling weight combined from the first and second stage magnetic separations is 8 wt% (up to 8g/100g sample). The X-ray diffraction in Figure 2, indicates that both middling (Fig. 2(b) and magnetic (Fig. 2(c) fractions contain high magnetic materials (Fe_2O_3 , and MgCr_2O_4). However, much higher Pt and Pd contents in the magnetic fraction can be attributed to much lower gangue minerals such as silica when its peak disappears in magnetic fraction as compared to the non-magnetic and middling. This result further supports the high content of Pt and Pd in the magnetic fraction.

Preliminary results in the current work also indicated that the sample contains high Rh with the concentration of about 100 g/t. As the testwork is progressed, we will continue to evaluate such result and recommend the development of the concentration process by magnetic separation. According to these results, it is pretty clear that the PGM tailings sample can be treated in a magnetic separator to obtain the magnetic fraction with both Pt and Pd at the concentration of 40 g/t.

4 CONCLUSION

The results obtained in the current work indicate that a dry magnetic separation process could be applied to recovery Pt, Pd, Rh contained in PGM mine flotation tailings. The observations can be summarized as follows:

- (1) Chemical and XRD studies showed original material contained 0.7 g/t Pt and 0.2 g/t Pd with SiO_2 , Fe_2O_3 , and MgCr_2O_4 as main mineral phases.
- (2) The separation by sizing for investigation of Pt and Pd in the size ranges (+100 μm), (-100+32 μm) and (-32 μm) showed the equal distribution of the metals in all size fractions.
- (3) A magnetic strength of 240 mT recovered up to 6 wt% of material into the magnetic fraction giving 25 g/t Pt and 14.8 g/t Pd. Also over 5 wt% recovered as the middling fraction with 15 g/t Pt and 1.3 g/t Pd.
- (4) Further separation of magnetic fraction obtained at 240 mT at the lower magnetic strength (120 mT) saw weight recovery reduced to 2 wt% of total material but Pt and Pd concentrations increased to 40 g/t respectively.
- (5) All chemical analysis by ICP was followed by first preparing samples by using the NiS-FA Pt and Pd concentration procedure.

(6) Since UG-2 is known to contain high Rh, the metal will be considered in the recovery process investigated. Preliminary results indicate Rh at around 5 g/t in the tailings sample.

More work is in progress to include Rh and also further increase Pt and Pd recovery to above 50 g/t. The data could possibly allow the development of a magnetic separation process to recover Pt, Pd and Rh in the flotation tailings and compare viability against other processes like flotation recovery.

References

- [1]. Wagner, P.A. "The chromite of the Bushveld Complex." South African Journal of Science vol. 20. pp. 223-235. (1923).
- [2]. Wagner, P.A. "The platinum deposit and mines of South Africa." London, Oliver & Boyd, 326 pp. (1929).
- [3]. McLaren C.H., De Villiers J.P.R., "The platinum group chemistry and mineralogy of the UG-2 chromitite layer of the bushveld complex." *Economic Geology*, 77, 1348–1366. (1982).
- [4]. Von Gruenewaldt G., Hatton C.J., Merkle R.K.W., Gain S.B., "Platinum group elements-chromitite association in the bushveld complex." *Economic Geology*, 81, 1067–1079. (1986).
- [5]. Gain, S.B. "The geologic setting of the platinumiferous UG-2 Chromitite layer on the farm Masandagshoek, eastern Bushveld Complex." *Economic Geology*, vol. 80. pp. 925–943. (1985).
- [6]. Talbot, B "Tailings scavenging—the complete story. International Platinum Conference platinum Adding value", The South African Institute of Mining and Metallurgy, (2004).
- [7]. Juvonen R, Lakomaa T, Soikkeli L, "Determination of gold and the platinum group elements in geological samples by ICP – MS after nickel sulphide fire assay: difficulties encountered with different types of geological samples." *Talanta* 58, 595–603. (2002).
- [8]. Vermaak, C.F., Hendriks, L.P., "A review on mineralogy of the Merensky reef with specific reference to new data on the precious metal mineralogy." *Econ. Geol.* 71, 1244–1269. (1976).
- [9]. Cole S., Ferron Cj., "A review of the beneficiation and extractive metallurgy of the platinum group elements, highlighting recent process innovations, the geology, geochemistry, mineralogy and mineral beneficiation of platinum group elements." Canadian Institute of mining and metallurgy, Special volume 54, 811–818. (2002).
- [10]. Watson, J.H.P., Rassi, D., Bahaj, A.S., "The Recovery of gold and uranium from gold ore leached residues by HGMS." *IEEE Transactions on magnetic* MAG-19 (5), 2136–2136. (1983).
- [11]. Wagner P.A., "The chromite of the bushveld complex," *South African Journal of science*, 20, 223–235. (1987).
- [12]. Juvonen R., Lakomaa T., Soikkeli L., "Determination of gold and platinum group elements in geological samples by ICP-MS after nickel sulphide fire assay; difficulties encountered with different types of geological samples." *Talanta*, 58, 595–603. (2002).
- [13]. Gareth P. Hatch., Richard E. Stelter., "Magnetic Design consideration for devices and particles used for biological high gradient magnetic separation (HGMS) systems." *Journal of magnetism and magnetic materials*. 225, 262–276. (2001).
- [14]. Walklate J.R., Jeram H., "The development of a metallurgical flow sheet to treat tails. The journal of the Southern African Institute of Mining and Metallurgy," 108, 57–65. (2008).
- [15]. Venter W.J.C., Guest R.N., Svoboda J., "The use of gravity and magnetic separation to recover copper and lean lead from Tsumeb flotation tailings". *The journal of the South African Institute of Mining and Metallurgy*, 88, 21–26. (1988).

Spontaneous Traveling Wave of Oil/water System –Transducer of Chemical Potential into Work –

Akihisa Shioi*, Takahiko Ban, Youichi Morimune, Daishi Mori, Katsuhito Oomiya

Department of Chemical Engineering & Materials Science, Doshisha University
1-3 Tatara Miyakodani, Kyotanabe, Kyoto 610-0321 Japan
phone:81-774-65-6839, FAX:81-774-65-6803
ashioi@mail.doshisha.ac.jp

Abstract: Some kinds of oil/water interfaces generate traveling wave along a glass surface. The aqueous and organic phases contain cationic surfactant, octadecyltrimethylammonium chloride, and an anionic chemical, respectively. This curious phenomenon has been studied by several researchers including the present authors. The spatiotemporal pattern formation may be useful for the direct energy conversion of chemical potential into work. We report recent research progresses in this oil/water system and propose a simple mathematical model based on the experimental results. Both of the experimental and theoretical considerations indicate that the traveling wave is produced by an excitable kinetics: Quasi-periodical oscillation due to the adsorption of cationic surfactant on glass followed by the desorption due to chemical reaction operates as a pace-maker of the interfacial motion. This sometimes develops into traveling waves.

Key Words: Chemomechanical Energy Transduction, Nonlinear Dynamics, Oil/Water Interface

1. INTRODUCTION

A heat engine can turn chemical potential into work with a cycle, ideally the Carnot cycle. A continuous energy transduction requires a reset of a system into the initial state that can get into the next cycle. A living system also carries out many kinds of continuous chemomechanical energy transductions, for example, with molecular motors and in a heart cell motion. In these chemical systems, the reset of the physicochemical state into the initial one is necessary for the continuous energy conversion. In contrast to the heat engine, however, the reset is achieved by an oscillatory or an excitable nature based on nonlinear dynamics [1]. In a laboratory, one can design a chemical system which shows an oscillatory or excitable kinetics [2,3]. These artificial chemical systems can turn chemical potential into work continuously, and hence it may be utilized as an energy transducer which seems to have the similar characteristics to a biological system. For example, such a chemical system begins to move or changes the dynamical mode responding to the surrounding chemical conditions [4]. It exhibits a motion like a chemotaxis, and sometimes a coupling of the chemical systems generates a cooperative motion with a larger scale than the elementary system [5]. The kinetic energy is provided by chemical reactions. Such kinds of spatiotemporal pattern formation are only seen for an open system which reacts and moves through an exchange of matter with the surroundings. Thus, the chemical reaction as an energy source often proceeds near or in the vicinity of the surface of the chemical system.

Oil/water interface containing surfactant is one of the simplest examples which can show the spatiotemporal pattern formation [6,7]. Although many oil/water systems with such the characteristics are reported, the most typical example is that discovered by Dupeyrat and Nakache around 1980 [8,9]. The aqueous phase contains cationic surfactant, octadecyltrimethylammonium chloride $C_{18}TAC$, while I_2 and KI are dissolved in the organic phase. A contact line of the oil/water interface along the glass surface moves oscillatory and often develops into a macroscopic wave propagation. Although this is one of the oldest examples, the wave amplitude is completely macroscopic such as 1 cm. Thus, this oil/water system is a favorite with a scientist who would like to study the spatiotemporal pattern formation as a continuous energy transducer [10,11].

In this paper, the authors introduce outstanding experimental results of this oil/water system with the review of preceding studies [12,13]. On the basis of the results, a mathematical description of the nonlinear dynamics is proposed, which is introduced with more general basis than that in the previous papers [14,15]. We show that the description gives a fundamental insight of this phenomena. The model well explains many characteristics of this oil/water system, though some disagreements are present. Furthermore, we show that the interfacial dynamics can be controlled electrochemically.

2. EXPERIMENTS

The experimental procedure is essentially the same as

those reported elsewhere [12,13]. Octadecyltrimethyl ammonium chloride $C_{18}TAC$ was dissolved in water, and the reactive chemical species was dissolved in nitrobenzene. Both solutions are poured into a glass container with cylindrical shape, and the motions of the contact line and the interface were observed. I_2 and KI in organic phase were used mostly as the reactive matter. Di(2-ethylhexyl) phosphate DEHP was sometimes employed.

For the electrochemical experiments, nitrobenzene containing DEHP was contacted with an aqueous phase with Ba^{2+} , for which its hydroxide was used. After the equilibrium was attained, a requisite amount of $C_{18}TAC$ was dissolved in the aqueous phase. After a few minutes, an electric potential was applied between Ag/AgCl electrodes, each of which was immersed in the aqueous or in the organic phase. The current between platinum electrodes each of which was in the aqueous or in the organic phase was observed. The interfacial and the contact line motion was observed. The voltage was controlled by a potentiostat. In the electrochemical system, the electrolyte tetrabutyl ammonium tetraphenylborate TBATPB of 5 mM is added in the oil phase for reducing the impedance. All of the experiments were performed at room temperature 22-26 °C.

3. CONTACT LINE MOTION

We focus on the contact line motion without the applied voltage. The electrochemical system is mentioned at the last section of this paper.

Figure 1 shows a typical examples of the traveling wave which appears in the contact line of oil/water interface and the glass surface. The wave pattern strongly depends on chemical conditions, such as concentrations of dissolved chemicals, pH of aqueous phase and the reactive chemical species in nitrobenzene. The dependency is quite complicated. However, the simplest mode of the contact line motion is the oscillatory motion, a sequence of the upward and the downward motions, without a traveling wave. The formation of such a oscillatory dynamics, which is denoted as the pacemaker in this paper, is quite difficult, since a weak perturbation apt to transform the motion into a traveling mode. However, the pacemaker is sometimes obtained with an experimental procedure; a little aqueous solution with a regulated pH is added on the organic phase. After that, $C_{18}TAC$ -containing solution was gently poured on the oil/water system. In this experiment, a restricted portion of the contact line sometimes exhibits an oscillatory motion without traveling. A schematic representation is shown in Figure 2. The characteristics were dependent on the pH in the aqueous solution which was added at first and

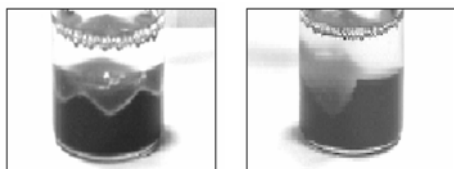


Figure 1 Traveling wave dependent on pH. Diameter of the glass container was 3.1cm, and the depth of the aqueous and the organic phases was 1.3 cm each. Concentrations of $C_{18}TAC$ and iodine were 50 mM and 25 mM, respectively.

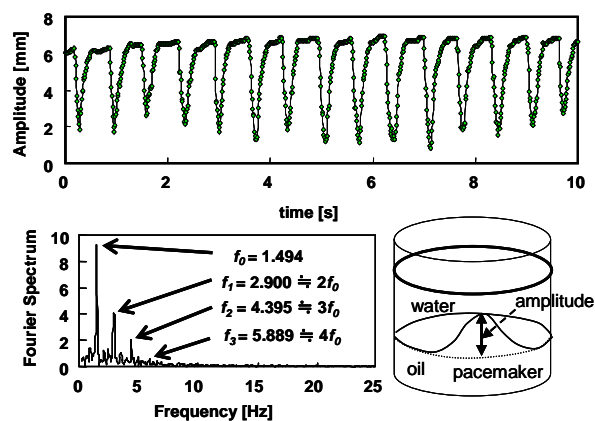


Figure 2 Vertical position of contact line at the position of pacemaker (top) and its Fourier spectrum (bottom left). The experimental setup is schematically shown in the bottom. 10mM $C_{18}TAC$ and 5 mM I_2 are used. KI is the saturation.

concentrations of $C_{18}TAC$ and I_2 . We measured the amplitude of the motion along a vertical sidewall of the glass container for the most successful experiment. The result is shown in Figure 2 with the Fourier spectrum. The pattern is constituted of the quasi-periodic pulses. The downward change is instantaneous, while the upward one seems to show a relaxation behavior. In the other experiments, we can also observe the instantaneous upward change followed by a slower downward motion. However, we can conclude that a quasi-periodic pulses with an instantaneous change followed by a slower decay constitute the dynamics of the pacemaker.

4. MATHEMATICAL MODEL

We introduce a mathematical model for the pacemaker. The obtained equations are the same as reported elsewhere [13]. However, the previous derivation is based on the consideration on the molecular level, which can explain the upward pulses. In the experiments, both the upward and the downward pulses are observed. Therefore, we derive the nonlinear differential equation on the basis of more phenomenological discussions. The present way for the derivation can lead to the both results, the upward and the downward pulses. However, it does not mention the molecular picture of the wetting dynamics

An instantaneous change of the contact line motion suggests the presence of the autocatalytic nature in this process. The contact line motion reflects the change in surface energy of the glass which is responsible for the wetting dynamics. The oscillatory wetting is schematically shown in Figure 3. $C_{18}TAC$ is a cationic surfactant and adsorbed on the glass surface. As a result, the surface energy varies, and the first step of the wetting begins. Then, the adsorption layer is desorbed by the chemical reaction with the reactive matter in organic phase. This also affects the surface energy. If the overall desorption rate is diffusion limited, the contact line motion itself may accelerate the desorption rate, because the mass transport coefficient of the reactive matter increases as the contact line moves more violently. Thus, the contact line motion which is produced by the desorption is amplified by the motion itself. The overall reaction rate of this autocatalytic process is expressed by

$$r_1 = \frac{C_A}{\frac{1}{k} + \frac{1}{K(|u|)}} \quad (1)$$

where C_A denotes the concentration of the reactive matter. k is the chemical reaction rate constant between the adsorbed $C_{18}TAC$ and the reactive matter. $K(u)$ stands for the mass-transport coefficient which is an increasing function of $|u|$, an absolute value of the velocity of the contact line motion. We simply assume the increasing function to be $K(|u|) \propto |u|$. It yields

$$r_1 = \frac{\kappa \Theta(u) |u|}{1 + \frac{|u|}{k'}} \quad (2)$$

where the constant value and C_A is included in κ . The Heaviside step function $\Theta(u)$ is multiplied since this autocatalytic process operates for either the upward or the downward change. Here, we consider the upward pulse.

After the autocatalytic process have occurred, further chemical reaction between the remaining $C_{18}TAC$ and the reactive matter proceeds. This is a simple relaxation process, and the rate is determined by the height to which the autocatalytic wetting reaches. This is illustrated in Figure 3, and the rate for surface energy change is given by

$$r_2 = \chi v = \chi \int_0^t u dt \quad (3)$$

If one considers the downward one, $-\Theta(-u)$ is necessary

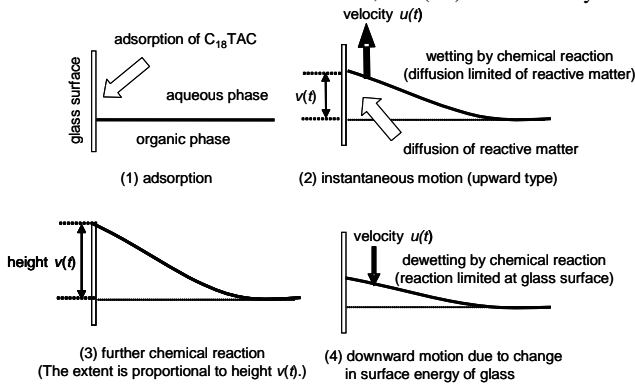


Figure 3 Schematic representation of contact line motion. This illustrates that case where the upward change is instantaneous.

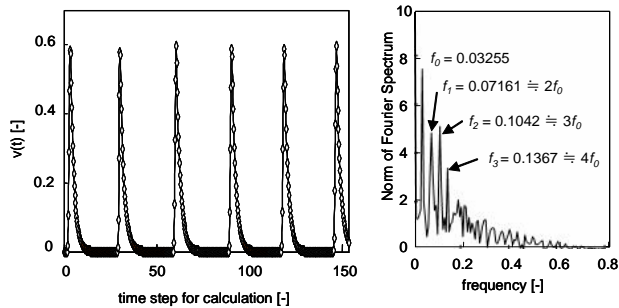


Figure 4 Numerical calculation of eq.4. The Runge-Kutta method of the fourth order is used. The amplitude (left) and its Fourier spectrum (right) are shown. $\chi = 5$, $\kappa = 20$, $\mu = 10$, $10^{-5} < \xi(t) < 10^5$.

instead of $\Theta(u)$. In this case, the diffusion-limited process is contained in the dewetting process.

In the process shown in Figure 3, the glass surface returns to the initial state via a cyclic change. When the first process (wetting by the lower phase) starts again, the motion gets into the next cycle. The quasi-periodic change is thus generated.

What occurs on the molecular scale is dependent on the experimental conditions. This determines whether the autocatalytic process appears in the upward or downward change. When the upward change is instantaneous, i.e., it includes the autocatalytic process, an explanation of molecular level is given elsewhere [13]. The understanding in the literature cannot be applied when the downward motion is instantaneous. However, the sequence of pulses as shown in Figure 2 can be generated only by the above mentioned autocatalytic process included.

Following the theory of wetting [16], the force driving the contact line is determined by the difference in interfacial energies between the water-glass and the oil-glass interfaces. In the present case, the difference varies with the adsorption and desorption of surfactants, and hence the nonzero ad/desorption rate generates the driving force. Thus, we may consider that the driving force, which is proportional to du/dt , is expressed by

$$\frac{du}{dt} = -\mu u - \chi v + \frac{\kappa \Theta(u) u}{1 + \frac{u}{k}} + \xi(t) \quad (4a)$$

$$\frac{dv}{dt} = u \quad (4b)$$

Here, the first term of the right hand side of eq.4a represents the dissipation due to the viscosity. The last term $\xi(t)$ is the noise. Unless the noise is present, eqs.4 has a stationary point $(u,v) = (0,0)$ which is not stable for the perturbation of $u > 0$. Thus, the term $\xi(t)$ generates a quasi-periodic sequence of the pulses.

Figure 4 shows an example of the calculation result with its Fourier spectrum. The calculated and experimental patterns (Figures 2 and 4) are symmetric with respect to the horizontal axis. The direction of pulses, whether it is upward or downward, is not essential in this model, because we did not consider the autocatalytic process on a molecular level. It gives what occurs at the glass surface microscopically, and hence either the upward or the downward pulse is specified. Although the upward pulse has already been discussed on a molecular level [13], the understanding of the downward one requires a further experimental and theoretical considerations. Except this point, the calculation reproduces outstanding characteristics included in the pacemaker; for example, a quasi-periodic pattern and a instantaneous change followed by a relaxation-like decay are reproduced.

Eq.4 mentions that the contact line motion is excitable, which requires a noise for the onset. There are two kinds of possible noise sources. One is the initial turbulence due to pouring the solutions. The irregular motion of the contact line operates as the noise. Once the motion develops into an oscillatory motion and/or into a traveling wave, the motion itself works as the noise (perturbation) for the following motion. This results in quasi-periodic or continuous motion of the contact line. The other noise source is due to the

chemical Marangoni instability in the oil/water interface. When the reactive chemical in organic phase is selected appropriately, the spontaneous Marangoni instability is seen. This induces an interfacial flow. When the flow reaches the sidewall made of glass, the contact line shape is perturbed. This is the other kind of the noise source. This type of noise source is accomplished by the use of phenylboronic acid and DEHP as the reactive chemical. Then, the chemical reaction between phenylborate and C₁₈TAC causes the chemical Marangoni instability which gives a perturbation to the contact line. This perturbation, the noise, triggers the contact line motion due to the chemical reaction of DEHPA and C₁₈TAC [15]: Eq.4 gives an excursion of (u,v) when a noise disappears. The excursion returns (u,v) to the stable point (0,0). This corresponds to the reset of the glass surface shown in Figure 3. If the noise continuously operates, it moves the point (u,v) into the next cycle. Thus, the quasi-periodic cycle is generated.

The traveling wave as shown in Figure 1 can be reproduced by coupling of the aligned oscillators, the dynamics of which is expressed by eq.4: Please consider the case that a large number of oscillators align along a vertical glass wall. If the oscillators move independently, random deformation of the contact line develops. This deformation increases the interfacial area and the excess energy. Thus, the neighboring oscillators tend to synchronize with each other to reduce the randomness of the deformation. This effect is most simply expressed by the addition of $\partial^2 u(x,t)/\partial x^2$, where x denotes the spatial coordinate along the intact contact line before the onset of the motion. Then, traveling waves are generated by the modified equation. Details are discussed

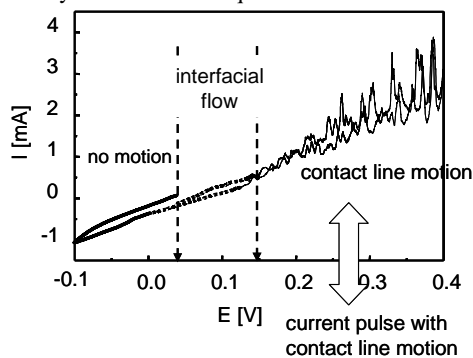


Figure 5 current-voltage diagram. Sweep rate is 1 mV/s. Organic phase contains 5 mM TBATPB and 5 mM DEHPA. Aqueous phase contains 1 mM Ba(OH)₂ and 5 mM C₁₈TAC.

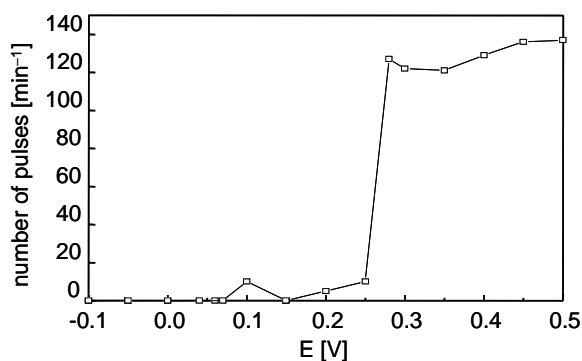


Figure 6 The number of pulses against applied voltage is shown. Chemical compositions are the same as those of Fig. 5.

elsewhere. [14]

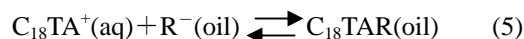
5. ELECTROCHEMICAL SYSTEM

The spontaneous motion of the oil/water system requires the transport of ionic molecules such as octadecyltrimethyl ammonium ion C₁₈TA⁺ and an appropriate noise. When the chemical potential change due to the chemical reaction and mass transport is enough to cause the motion, it begins quite spontaneously without any supply of energy. In a certain experimental condition, however, the chemical potential change is not sufficient. Then, the intrinsic instability hardly appears as the motion, and an applied field such as the electric field, which supplies an energy to develop the instability, may catalyze the process. In other words, the motion of oil/water interface can be controlled electrically. Then, one can design the chemomechanical energy transducer whose onset is triggered by an external electric field. In such a system, for example, the chemical potential is transformed into work only at a certain applied voltage. The authors tried to make such a novel system by the method mentioned in the experimental section.

Figure 5 shows a current-voltage diagram with sweeping the applied voltage between the reference electrodes. When the applied voltage is low, no outstanding motion appears in the contact line and in the interface. As increasing the voltage, an irregular interfacial flow is generated, and at last the contact line motion appears beyond a threshold voltage. The interfacial flow is probably due to the Marangoni instability induced by the electrically assisted ion transport across the interface. This instability operates as the noise source for the contact line motion caused by the reaction between C₁₈TAC and DEHP. The contact line motion accompanies the irregular pulses in the current as shown in Figure 5. We confirmed that the number of pulses in the current is regarded as an index of the violence in the contact line motion.

The interfacial dynamics may not follow the applied voltage under its sweeping state. Thus, we also carried out the experiment with a constant voltage. The threshold voltage for the contact line motion exists also in this experiment. We counted the number of current pulses for the initial 1 minute which is shown in Figure 6. The number of pulses begins to rise beyond a threshold voltage. When DEHP concentration is increased, the threshold becomes unclear, and the pattern of Figure 6 exhibits a gradual rise against the voltage. In particular, the threshold disappears at DEHP concentration beyond 50 mM. Therefore, either the higher applied voltage or the larger DEHP concentration, at least, is able to cause the contact line motion.

The current pulses, i.e., the contact line motion, is caused by the reaction between C₁₈TA⁺ and DEHP⁻; we confirmed that C₁₈TAC and DEHP are necessary for generation of the pulses. Thus, we consider a following chemical reaction



Here, R⁻ denotes the concentration of DEHP ionized in organic phase. The change in the Gibbs free energy of the chemical reaction ΔG is

$$\Delta G = \Delta G^0 + RT \ln \left(\frac{C_{C_{18}TAR(oil)}}{C_{C_{18}TA^+(aq)} C_{R^-(oil)}} \right) - F\Delta\phi \quad (6)$$

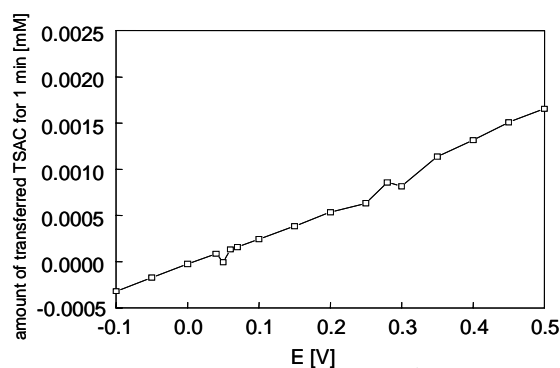


Figure 7 Amount of transferred $C_{18}TA^+$ against the voltage. Chemical compositions are the same as those of Figure 5.

Here, ΔG_0 is the standard Gibbs free energy change. T and $\Delta\phi$ denote the temperature and the electric potential across the interface, respectively. R and F are the Gass constant and the Faraday constant, respectively. C_i is the concentration of the corresponding chemical species. Positive values of the current are defined so that the cation moves from the aqueous to the organic phase. Thus, it occurs when the chemical reaction proceeds toward the right. $\Delta G < 0$ is the necessary condition from the thermodynamics. However, it is not the sufficient one. This is clearly shown in Figure 7, where the molar amount of $C_{18}TA^+$ moved from the aqueous to the organic phases is calculated by the average current divided by the Faraday constant. It is simply proportional to the applied voltage, i.e., the Ohm's law is satisfied over the entire voltage range. This means that the current flows across the interface independently of the contact line motion. Thus, $\Delta G < 0$ is satisfied independently of the voltage. This suggests that ΔG under a certain critical value $\Delta G_{cr} < 0$ is required for the contact line motion. This condition can be satisfied by controlling the external voltage and/or the chemical compositions. This gives a complicated dependency of the motion on them. Although further study is necessary for the elucidation of the details, electrically regulated contact line motion may explore the applications of the chemomechanical energy transducer with the oil/water system.

6. CONCLUSION

The spatiotemporal pattern formation in an oil/water system was discussed with a mathematical model. Cationic surfactant octadecyltrimethylammonium chloride is dissolved in the aqueous phase. The reactive chemical in organic phase was mainly I_2 and KI . The contact line shows an oscillatory motion and sometimes develops into a traveling wave. A pacemaker of this motion is clearly observed in the experiment where the procedure was carefully designed. The dynamics of the pacemaker essentially agrees with the authors' mathematical model. This contains a chemical wetting, the rate of which was accelerated by the mechanical perturbation of the contact line. Then, the contact line motion due to the chemical wetting grew in the autocatalytic manner. We also showed that the electrochemical control of this motion is possible. The present system is one of the simplest systems which can turn chemical potential into work. The electrochemical control may explore the applications of the

chemomechanical energy transducer.

References

- [1] Keener, J., Sneyd, J., "Mathematical Biology," Springer-Verlag, New York, (1998).
- [2] Epstein, I. R., Pojman, J. A., Steinbock, O., "Introduction: Self-organization in nonequilibrium chemical systems," CHAOS, Vol. 16, 037101, pp. 1-7, (2006).
- [3] Mikhailov, A. S., Showalter, K., "Control of waves, patterns and turbulence in chemical systems," Physics Reports, Vol. 425, pp. 79-194, (2006).
- [4] Kuramoto, Y., "Chemical Oscillations, Waves, and Turbulence," Springer-Verlag, New York, (1984).
- [5] Ban, T. and Shioi, A., "Autonomous Motion of Liquids Interface Controlled by Chemical Reaction," NOVA Science Publishers, Inc., New York, (2008).
- [6] Sumino, Y., Kitahata, H., Yoshikawa, K., Nagayama, M., Nomura, S. M., Magome, N., Mori, Y., "Chemosensitive running droplet," Physical Review E, Vol. 72, No. 4, 041603, pp.1-8, (2005).
- [7] Dupeyrat, M, Nakache, E., "Direct conversion of chemical energy into mechanical energy at an oil water interface," Bioelectrochemistry and Bioenergetics, Vol. 5, No. 1, pp.134-141, (1978).
- [8] Dupeyrat, M, Nakache, E., "Chemical reactions and oscillating potential difference variations at an oil-water interface," Bioelectrochemistry and Bioenergetics, Vol. 9, No. 5, pp.583-590, (1982).
- [9] Kai, S., Muller, S.C., Mori, T., Miki, M., "Chemically driven nonlinear waves and oscillations at an oil-water interface," Physica D, Vol. 50, No. 3, pp. 412-428, (1991).
- [10] Magome, N., Yoshikawa, K., "Nonlinear Oscillation and Ameba-like Motion in an Oil/Water System," The Journal of Physical Chemistry, Vol. 100, pp.19102-19105, (1996).
- [11] Kuragane, S., Fujii, T., Ban, T., Shioi, A., "Spontaneous wave driven by chemical autophobing with oscillatory dynamics at glass/oil/water interfaces," Colloids and Surfaces A, Vol. 311, No. 1-3, pp. 16-25, (2007).
- [12] Shioi, A., Katano, K., Onodera, Y., "Effect of solid walls on spontaneous wave formation at water/oil interfaces," Journal of Colloid and Interface Science, Vol. 266, No. 2, pp. 415-421, (2003).
- [13] Shioi, A., Ban, T., Suzuki, S., "Noise-induced kinetic model for autonomous motion of the contact line in oil-water systems with chemical reactions," Physical Review E, Vol. 77, No. 3, 036208 pp.1-7, (2008).
- [14] Shioi, A., Ban, T., Suzuki, S., "Model of traveling wave formed by autonomous motion of contact line with oil/water interface," Chemical Physics Letters, Vol. 467, No.1-3, pp.210-215, (2008).
- [15] Ban, T., Suzuki, S., Abe, S., Shioi, A., "Anionic control of autonomous motion of oil/water interface with cationic surfactant," Chemistry Letters, Vol. 36, No.8, pp. 1040-1041, (2007).
- [16] de Gennes, P. G., Brochard-Wyart, F, Quere D, "Gouttes, Bulles, Perles et Ondes", Yoshioka Shoten, Kyoto, (2003) (Japanese translation)

Fabrication of porous zinc oxide ceramics having a sustainable antibacterial activity under dark conditions

Ken Hirota^{*}, Maiko Sugimoto^{*}, Masaki Kato^{*}, Kazuhiko Tsukagoshi^{*},
Tooru Tanigawa^{*} and Hiroshi Sugimoto^{**}

^{*}Department of Molecular Chemistry & Biochemistry, Faculty of Science & Engineering, Doshisha University, Kyo-tanabe, Kyoto 610-0321, Japan.

^{**}Research and Development, Meisui Co. Ltd., Nishi-ku, Osaka 550-0002, Japan

khirota@mail.doshisha.ac.jp

Abstract: Fabrication of porous ZnO ceramics has been tried from two application viewpoints: 1) bulk materials with an easy-handling and a biochemical safety and 2) sustainable antibacterial activity under dark conditions. Fine ZnO powders were hydrothermally treated in $0.5 \sim 3 \text{ mol}\cdot\text{l}^{-1}$ $\text{Zn}(\text{NO}_3)_2$ aqueous solutions at $110^\circ\text{-}180^\circ\text{C}$ for $3 \sim 20 \text{ h}$. After washing, drying, and uniaxial pressing, the ZnO powders thus prepared were sintered at $400^\circ \sim 600^\circ\text{C}$ for 1 h in air.

Sustainability of antibacterial activity for the ceramics, evaluated using a colony count method with *Escherichia coli* bacteria, was related to the physical properties of ZnO powders and process conditions, such as, surface areas, lattice constants, excess oxygen contents, and pH values of Na-P-buffer solution. Furthermore from ESR study and chemical photoluminescence analyses, it has been cleared that radical oxygen of super-oxide ($\cdot\text{O}_2^-$) originated from the surface of ZnO might exhibit antibacterial activity even in the dark.

Keywords; Zinc oxide ceramics, Hydrothermal treatment, Antibacterial activity, Radical oxygen of super-oxide ($\cdot\text{O}_2^-$)

1 INTRODUCTION

Up to now, several intensive studies have revealed that some metal oxides (TiO_2 [1], SiO_2 [1], MgO [2], CaO [2], CeO_2 [3], and ZnO [1,2,4,5]) show bacteriostatic, antimicrobial, or biocidal action [6]; for example, it is well-known that illuminated suspensions containing TiO_2 are effective at killing *Escherichia coli* (*E. coli*), which activity is originated from its photocatalytic disinfection [7]. However, the disadvantage of utilizing TiO_2 is that UV light is required to activate the photocatalyst and initiate the killing of the bacteria and viruses [8,9].

Among above-mentioned metal oxides, *in vitro* antibacterial activity and efficacy of regular zinc oxides (for examples, high purity fine powders commercially available) were carefully examined. Sawai [2] reported that after quantitative evaluation of antibacterial activities of some metal oxide powders (ZnO , MgO and CaO), ZnO was the most effective for *Staphylococcus aureus*, which might be due to strong affinity to their cells. Sawai *et al.* [10~15] have

investigated the antibacterial behaviors related ZnO-based substances intensively, *i.e.*, ZnO-CaO solid solutions [10], carbon powders containing ZnO [11], mixtures of ZnO and MgO powders [12], developing a quantitative evaluation method [13], and identification of reactive oxygen species (ROS) generated from ZnO [14,15].

Recently, eco-toxicity of ZnO nanoparticle suspensions on a broad spectrum of microorganisms have been examined precisely by Jones *et al.* [5] and Adams *et al.* [1] They reported that the antibacterial behavior of ZnO increased with increasing nanoparticle concentration and with decreasing particle size; the particle concentration was observed to be more important than the particle size. And that the use of dispersant did not affect much on the antibacterial activity of ZnO nanofluids but enhances the stability of the suspensions. In addition, they described that the presence of ZnO nanoparticle damaged the membrane wall of the bacteria. Among these antibacterial materials-related literatures, little information is available about fabrication of metal oxide ceramics; this might be due to the heating process, which is required for conventional ceramic

processing to fabricate bulk materials by sintering fine powders, resulted in the degradation of their antibacterial behaviors [16]. Therefore, there has been no report on the fabrication of metal oxide ceramics with strong antimicrobial activity.

On the other hand, for corresponding to an increasing demand for home appliances, health-related and industrial applications, new antimicrobial or antibiotic materials being active and sustainable under dark conditions are much required. Even though, ZnO nanoparticles show the growth inhibition of bacteria in the dark, our preliminary experimental results indicated that the repeated-use of ZnO reduced their antibacterial activity remarkably.

The purpose of this study was to fabricate new porous bulk ZnO ceramics having a strong inhibition of bacteria growth in the dark sunshade from a viewpoint of i) bulk materials with an easy-handling and a biochemical safety and ii) sustainable antibacterial activity.

2 EXPERIMENTAL PROCEDURE

2.1 Antibacterial test

Sustainability of antibacterial activity for various kinds of ZnO materials in the dark was evaluated with a colony count method using *Escherichia coli* bacteria (*E. coli*: IFO 3972) on nutrient agar medium in a Na-P-buffer solution as the same as usual method. An antibacterial activity f was defined as the following equation: $f = -\log(N/N_0)$, where N and N_0 the number of the colonies after and before the addition of ZnO, respectively; $N_0 = 10^7/\text{ml}$, $10^6/\text{ml}$, or $10^5/\text{ml}$ was utilized. If the value of f is 7 under the condition of $N_0 = 10^7/\text{ml}$, all the colonies were perfectly disappeared after an antibacterial activity test. This evaluation was repeated up to seven times to investigate the sustainability of antibacterial activity for the ZnO materials prepared in the present study.

2.2 Fabrication of porous ZnO ceramics

A fabrication of porous bulk ZnO ceramics was tried as almost the same process as conventional ceramic processing. Fine ZnO powders (Sakai Chemical Co. Ltd., Osaka, "NANO FINE", an average particle size P_s of ~ 20 nm (Fig. 1(a)), BET surface area of ~ 52 m²/g, and purity of 98.5%), were used as the starting material. As the preliminary experiment, they were uniaxially pressed into compacts at 98 MPa and then sintered at 400° to 600°C for 1 h in air; the best sintering temperature was determined to be 500°C. And then two kinds of sintering patterns were selected; i) a simple pattern with a linear temperature increasing rate of 200°C/h up to 500°C (Pt.1) and ii) a step-by-step pattern (470°C/1h-485°C/1h-500°C/1h) (Pt. 2), respectively.

2.3 Hydrothermal treatment

As the above mentioned porous ZnO ceramics sintered at 500°C exhibited an antibacterial activity only after a few culture tests, hydrothermal treatment of ZnO powders were tried to improve their antibacterial activity, which was based on the idea that the surface of ZnO could be modified chemically and be functionally graded by the hydrothermal process under a high pressure. Before our study, Xu *et al.* [17] reported hydrothermal synthesis of zinc oxide powders with controllable morphology, however, they did not investigate nor mention about the antibacterial behavior of these powders.

After an uniaxial pressing, fine ZnO powder-compacts with an aqueous solution of $\text{Zn}(\text{NO}_3)_2 \cdot 6\text{H}_2\text{O}$ or $\text{Zn}(\text{CH}_3\text{COO})$

$\cdot 2\text{H}_2\text{O}$ were put into a high-pressure stainless container and heated for 3 to 20 h at 110° to 180°C; the concentration of aqueous solution was varied from 0.5 to 3 mol·l⁻¹. After the hydrothermal treatment, the samples were rinsed with pure water for several times until the pH value of rinsed water reached around 7 and then dried at 120°C for 10 h in air. Hydrothermally treated ZnO powders were also sintered at 500°C for 1 h in air as described in 2.2.

2.4 Characterization of ZnO materials

Various kinds of analytical measurements were utilized; a field-emission type scanning electron microscope (FE-SEM, JEOL Ltd., "JSM-7001FD"); X-ray diffraction (XRD, Rigaku Co. Ltd., Osaka, "Rint 2200"); spectrochemical analysis for determination of excess oxygen contents (Horiba Co. Ltd., Kyoto, "EMGA-620W/C"); an absorption measurement system for BET surface areas of powders (Shimadzu, Kyoto, "ASAP 2010"); X-ray photoelectron spectroscopy (XPS, Shimadzu, "AXIS-165"); electron spin resonance spectroscopy (ESR, JEOL Ltd., "FR80") on the samples in the dark by a spin-trap method under the conditions: a microwave of 9.226 GHz with an electric power of 10 mW, using trap agents of a new dimethylpyrroline-*N*-oxide (DMPO)-type spin trap "CYPMPO" (Radical Research Inc., Tokyo) for super-oxide radical anion ($\cdot\text{O}_2^-$) and dimethylpyrroline-*N*-oxide (DMPO, Dojindo Laboratories, Kumamoto) for hydroxyl radical ($\cdot\text{OH}$), and scavengers of super-oxide dismutase (SOD, Wako Pure Chemical Industries Ltd., Osaka) for $\cdot\text{O}_2^-$ and dimethyl sulfoxide (DMSO, Sigma Aldrich, Tokyo) for $\cdot\text{OH}$; and a chemical photoluminescence (chemiluminescence: CL) method (Tohoku Electric Industries Co. Ltd., Sendai, "CLD-100FC") for identification of ROS by detecting luminescence in the mixed solutions of luminol (concentration: 10^{-6} mol/l) (Nacalai Tesque, Kyoto) and diluted ZnO suspensions (10^{-11} mol·l⁻¹). The diluted ZnO suspension had been prepared by adding the ZnO powder into a carbonate buffer solution (NaOH - NaHCO_3) with pH 10.8. Luminescence in the mixed solutions could be detected when the luminol was oxidized by ROS generated from ZnO suspension. In this method, the same reagents as ESR, scavengers such as SOD for $\cdot\text{O}_2^-$, DMSO for $\cdot\text{OH}$, furthermore, catalase (Sigma Aldrich) for hydrogen peroxide H_2O_2 and sodium azide (NaN_3 , Nacalai Tesque) for singlet oxygen $^1\text{O}_2$, respectively, were used.

3 RESULTS AND DISCUSSION

3.1 Characteristics of ZnO ceramics

As-received ZnO powder was heated using a linear sintering pattern (Pt.1) at 400°, 500°, and 600°C for 1 h in air. Thus obtained ceramics were evaluated from the points of view of antibacterial activity f ; Table 1 (i) shows the results as a function of sintering temperature. In this case, the number of bacteria before testing $N_0 = 10^7/\text{ml}$ was adopted. The ceramics sintered at 400° and 500°C, in which the particle size P_s of the latter was ~ 30 nm, exhibited an f value of ~ 6 after the 1st antibacterial test, indicating that almost all bacteria were disappeared, only ~ 10 bacteria were remained after the testing, *i.e.*, antibacterial activity of 99.9999%. However, the ZnO ceramics fabricated at 600°C indicated a value f of 5, a little lower antibacterial activity than those sintered at 400° and 500°C. In general, the higher sintering temperature gives ceramics the higher density and strength. Therefore, we

selected 500°C as a sintering temperature for the fabrication of porous ZnO ceramics. Then, sustainable antibacterial activity of ZnO ceramics sintered at 500°C was examined; the results after the 2nd antibacterial test decreased drastically to a value f of 2, as the same result obtained using as-received ZnO powder. Therefore, a simple ceramic processing using as-received ZnO powder was thought not to produce ZnO ceramics having a sustainable antibacterial activity in the dark sunshade.

3.2 Antibacterial activity of ZnO ceramics via hydrothermally treated powders

In order to enhance the sustainable antibacterial activity of ZnO ceramics, the ZnO powder was modified by hydrothermal treatment in aqueous solutions of zinc nitrate or zinc acetate [18,19]. As described in experimental procedure 2.3, after hydrothermal treatment (HT) ZnO powders were rinsed and then dried. XRD analysis revealed that the HTed sample was single phase of ZnO (JCPDS:#36-1451) and from the FE-SEM observation, ZnO particles, for example, after HT(3M-Zn(NO₃)₂/120°C/7h), grew from 20 to ca 30 nm (Fig. 1 (b)).

i) Sintering pattern: HTed ZnO powders were compacted and heated at 500°C for 1 h in air under two different sintering patterns, *i.e.*, a linear pattern (Pt.1) and a step-by-step pattern (Pt.2). The latter sintering pattern gave a better sustainable antibacterial activity; *i.e.*, the antibacterial activity f of ZnO ceramics sintered by Pt. 1 using hydrothermally treated ZnO powders in a 3 mol·l⁻¹ Zn(NO₃)₂·6H₂O solution at 120°C for 3 h (Pt.1, HT:3M/120°C/3h) reached 7 until the 3rd of antibacterial test and then dropped to 0, however, that of ceramics made under the condition of (Pt.2, HT:3M/120°C/3h) could maintain more than 6 up to 5 times of test.

In addition, difference in microstructure of ceramics depended on sintering patterns was investigated from the viewpoint of their mechanical properties. Figure 1 (c) shows a SEM photograph for fracture surface of ZnO ceramics (Pt.2, HT:3M/120°C/3h), indicating that the porous ceramics composed of homogeneous ZnO grains (~100 nm). The step-by-step sintering pattern (Pt. 2) gave a little higher bending strength to the ZnO ceramics than Pt. 1. The difference might be originated from the higher energy totally supplied to enhance the bonding among ZnO grains. However, the difference in properties of sustainable antibacterial activity could not be clearly explained.

ii) Difference of Zn salts: Then the difference in ZnO ceramics (Pt.2) derived from ZnO powders prepared hydrothermally in the Zn(NO₃)₂·6H₂O or Zn(CH₃COO)₂·2H₂O

solutions was investigated; up to 3 times of antibacterial test, there was no difference between them (HT:1M/120°C/10h), however, nitrate-salt-derived ZnO ceramics gave a higher f values than the acetate-salt-derived ZnO at more than 4 times of test. From these results, hereafter, hydrothermal treatment of ZnO powders was conducted in nitrate salt solutions.

iii) Solution concentration: Both 1 and 3 mol·l⁻¹ of Zn(NO₃)₂·6H₂O solutions were used for preparation of hydrothermally treated ZnO powders. A higher concentrated nitrate salt solution resulted in ZnO ceramics (Pt.2, HT:120°C/3h) with a higher f values (≥ 6) even after the 5th test.

iv) HT temperature: Table 1 (i) shows the effect of hydrothermal treatment temperature on the sustainable antibacterial activity of ZnO ceramics (Pt.2, HT:3M/3h). Only HT temperature of 120°C maintained f value of 6 even after the 5th antibacterial test; higher HT temperatures than 120°C tend to decrease the antibacterial activity. From this result, HT temperature was determined to be 120°C.

v) Soaking time of HT: ZnO ceramics made from hydrothermally treated powders with various kinds of soaking time from 3 to 20 h during HT were examined on the sustainable antibacterial activity. In Table 1 (ii), up to the 3rd antibacterial test, a little difference between soaking time was observed, however, more than 4 times test, we could find some effect of soaking time on the antibacterial activity. The optimal soaking time for hydrothermal treatment was thought to be 7 hours.

vi) pH values: During antibacterial test, the pH values of penetrated culture of bacteria were monitored with a slight suspect of their effect on antibacterial activity. Table 1 (ii) summarized the antibacterial activity f and pH values as a function of number of testing (n). Here, ZnO ceramics were fabricated under the conditions of hydrothermal treatment in a 3 mol·l⁻¹ Zn(NO₃)₂·6H₂O solution at 120°C for 7 h and sintering at 500°C for 1 h in air by the step-by-step pattern. There is no relationship between antibacterial activity f and pH values, as previously reported on the antibacterial behavior of TiO₂⁶.

3.3 Mechanism of antibacterial activity of ZnO in the dark sunshade

To investigate the mechanism of the sustainable antibacterial activity of ZnO ceramics (Pt.2, HT:3M/120°C) under dark conditions, ESR, CL, and conventional colony count methods were utilized.

i) ESR study: this measurement was conducted in the sunshade as described before. Figure 2 shows the ESR

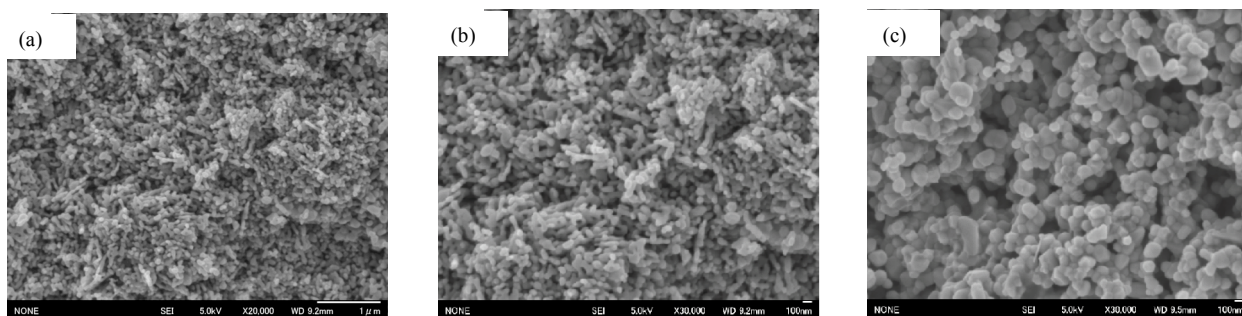


Fig. 1 FE-SEM photographs of ZnO powders:(a) NANO FINE, (b) after sintering (Pt.2) without hydrothermal treatment, and (c) after sintering (Pt.2) using the hydrothermally treated (3M/120°C/7h) powder.

Table 1

(i) Dependence of antibacterial activity $f = -\log(N/N_0)$ on the testing number n as a function of hydrothermal temperature

Testing number n	1	2	3	4	5
Hydrothermal conditions					
120°C-3 h	7.0	7.0	5.0	6.0	6.0
150°C-3 h	7.0	7.0	7.0	4.0	-
180°C-3 h	1.0	-			

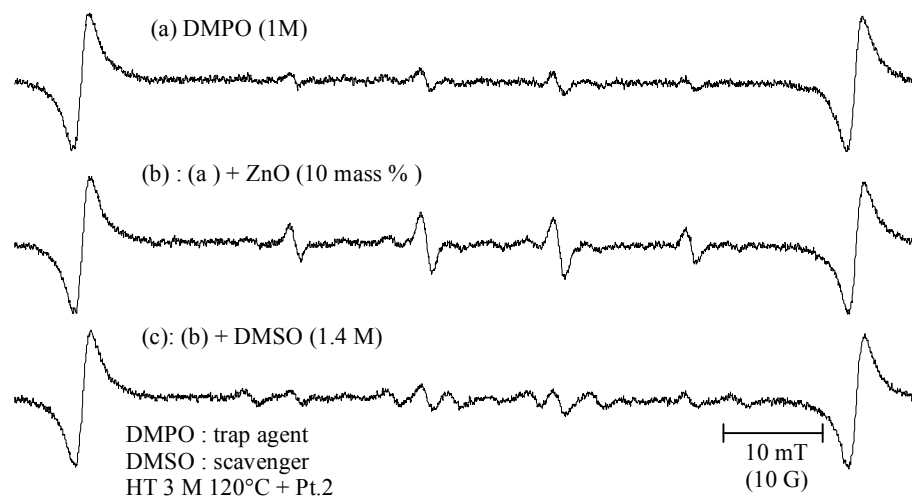
(ii) Dependence of antibacterial activity $f = -\log(N/N_0)$ on the testing number n as a function of hydrothermal soaking time

Testing number n	1	2	3	4	5	6	7
Hydrothermal soaking time							
3 h	5.9	1.9	3.2	0.5	-	-	-
7 h	6.0	4.7	5.6	4.4	2.7	2.1	0.4
pH value	7.6	8.9	10.4	9.2	8.3	8.1	8.0
10 h	5.4	5.7	5.9	0.6	-	-	
20 h	3.8	4.8	5.4	5.4	3.2	1.5	-

spectrum of samples; (a): 1-M DMPO, (b): 1-M DMPO + 10 mass% ZnO powder pulverized from ceramics, and (c): (DMPO+ZnO)+1.4-M DMSO. DMPO is a trap agent for hydroxyl radical ($\cdot\text{OH}$) (Fig. 2(a)) and when ZnO ceramic powder was added, the intensities of 4 spectra in the middle range were increased a little (Fig. 2 (b)), however, when 1.4-M DMSO, a scavenger of $\cdot\text{OH}$, was added again to sample (b), 4 spectra were reduced (Fig. 2 (c)), indicating that ZnO ceramics have generated hydroxyl radical ($\cdot\text{OH}$). In other ESR measurements, ESR 7 spectra originated from hydroxyl radical ($\cdot\text{OH}$) were observed. At the same time one spectrum for radical oxygen of super-oxide ($\cdot\text{O}_2^-$) in the sample containing of 100 mM CYPMPO, a newly developed trap agent for radical oxygen of super-oxide ($\cdot\text{O}_2^-$), was also detected. When an SOD scavenger of $\cdot\text{O}_2^-$ was added into sample (a), all intensities of spectra were decreased clearly. From these ESR results, it should be stated that confirmations of $\cdot\text{OH}$ and $\cdot\text{O}_2^-$ due to ZnO, respectively, have been made.

ii) CL measurement: Chemical photoluminescence (chemiluminescence: CL) profiles for ZnO samples containing some kinds of scavengers are presented in Fig. 3 (a) to (d):(a) ZnO with a scavenger SOD for $\cdot\text{O}_2^-$, (b) with catalase for H_2O_2 , (c) with DMSO for $\cdot\text{OH}$, and (d) with NaN_3 for $^1\text{O}_2$. By comparing these 4 data, it might be concluded that with the addition of scavenger SOD and catalase to ZnO, the CL intensities were much suppressed, suggesting that both $\cdot\text{O}_2^-$ and H_2O_2 were generated by the ZnO in the dark sunshine. However, as a little decrease in the CL peak was also observed in the sample (c) containing ZnO with DMSO; it was indicated that generation of $\cdot\text{OH}$ by ZnO was not necessary a negative phenomena. From these, it might be stated that from CL measurements ZnO ceramics could generate $\cdot\text{O}_2^- > \text{H}_2\text{O}_2 > \cdot\text{OH}$.

iii) Colony count methods: Antibacterial activity f of ZnO ceramics with radical scavengers are investigated. Figure 4 summarized the f values in relation to the combination of

Fig. 2 ESR-confirmation of $\cdot\text{O}_2^-$ generation by ZnO. Microwave: frequency $f = 9.226$ GHz and power = 10 mW.

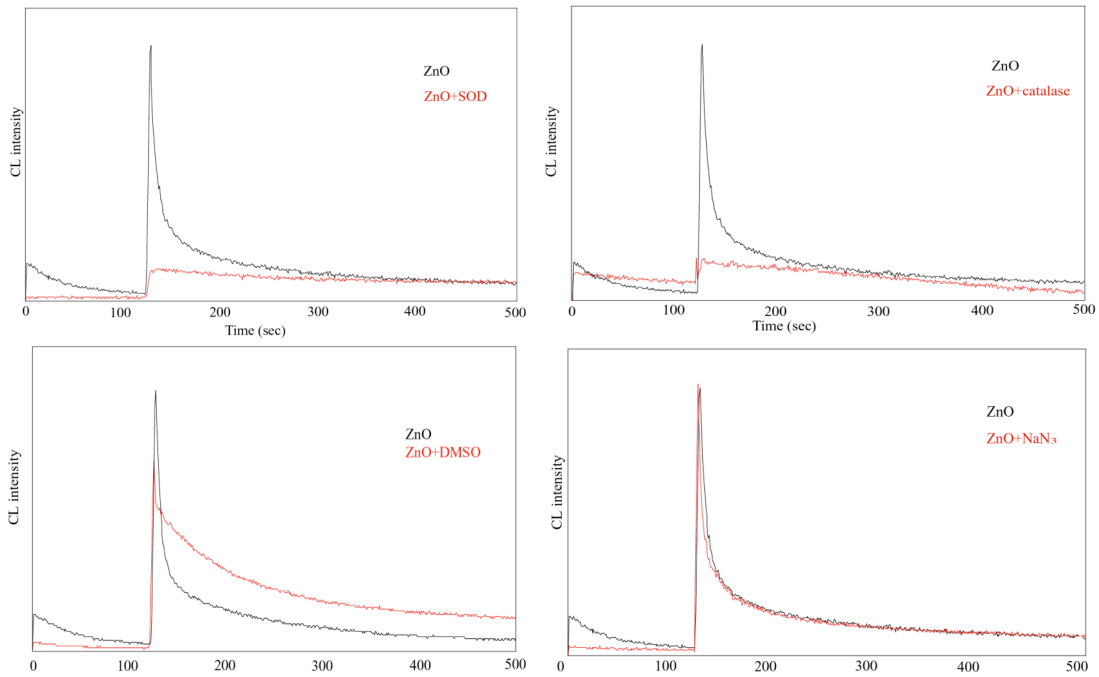


Fig. 3 CL profiles of ZnO (Pt.2, HT:3M/120°C/7h):(a) with SOD, (b) with catalase, (c) with DMSO, and (d) with NaN₃.

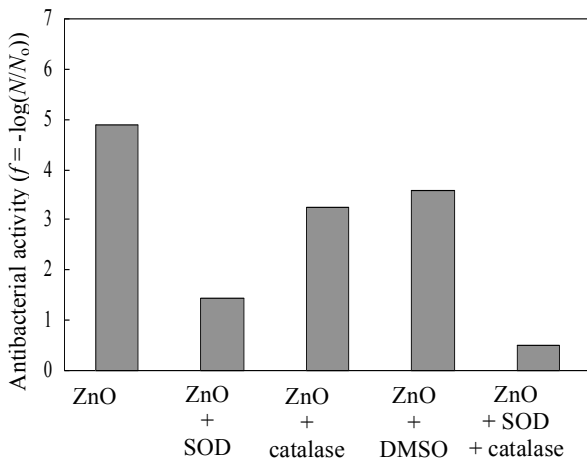


Fig. 4 Antibacterial activity (f) of the ZnO ceramics, fabricated under the conditions (Pt.2, HT:3M/120°C/7 h), depressed by adding radical scavenger.

ZnO and scavengers, proving clearly that with the addition of SOD or both SOD and catalase, f values were much decreased than those with the single addition of DMSO or catalase, *i.e.*, SOD suppressed the generation of $\cdot\text{O}_2^-$ from ZnO.

From these 3 experimental data, we might reach the conclusions that hydrothermally treated ZnO could generate

$\cdot\text{O}_2^-$ repeatedly in the dark sunshade. This ROS generation resulted in sustainable antibacterial activity of ZnO ceramics.

iv) Other characteristics of porous ZnO ceramics:

Table 2 summarized the physical properties of ZnO materials prepared in the present study, oxygen contents δ measured by spectrochemical analysis, BET surface areas, lattice constants (a and c) of hexagonal ZnO by XRD, and binding energy determined by XPS. These parameters were measured and considered for the first time to have much relationship between the antibacterial activity or the sustainability of ZnO, however, we could not find any relationship among them.

4 CONCLUSIONS

Different from the antibacterial activity of TiO₂ under UV light, newly developed ZnO ceramics have been found to exhibit sustainable antibacterial activity even in the dark sunshade. These ceramics were fabricated by sintering ZnO powders at low temperature of 500°C for 1 h in air, in which powders were prepared by treating ZnO hydrothermally in a 3 mol·l⁻¹ zinc nitrate solution at 120°C for 7 h. The sustainable antibacterial activity of thus fabricated ZnO ceramics might be originated from the generation of super-oxide anion ($\cdot\text{O}_2^-$). Based on this study, much investigation for new applications using its antibacterial activity is expected to start in future.

Table 2 Characteristics of ZnO ceramics

Sample	Excess oxygen content δ	ZnO _{1+δ}	Surface area (m ² ·g ⁻¹)	Lattice parameters a (nm)	c (nm)	Lattice volume v (nm ³)	Binding energy (eV)
NANO FINE ZnO	-0.0400	ZnO _{0.960}	52.0	0.3248	0.5205	0.047554	89.42
After sintering (Pt.2)	-0.0758	ZnO _{0.924}	9.27	0.3236	0.5185	0.047022	89.04
HT 3 h + Pt.2*	-0.0316	ZnO _{0.968}	1.78	0.3244	0.5195	0.047345	89.67
HT 5 h + Pt.2*	-0.0247	ZnO _{0.975}	0.374	0.3249	0.5206	0.047592	89.82
HT 10 h + Pt.2*	-0.0121	ZnO _{0.989}	-	0.3243	0.5195	0.047316	89.88

*, Hydrothermal treatment was performed in a 3 M Zn(NO₃)₂·6H₂O solution at 120°C for 3 to 10 h and then sintered at 500°C for 1 h in air using a step-by-step pattern.

cf: ZnO (JCPDS#36-1451): $a=0.3250$, $c=0.5206$ nm, and $v=0.047621$ nm³: binding energy of Zn (ZnO) 3p 89.0 eV.

References

- [1] Adams, L.K., Lyon, D.Y. and Alvarez, P.J.J., "Comparative Eco-Toxicity of Nanoscale TiO₂, SiO₂, and ZnO Water Suspensions", *Water Research*, Vol.40, pp.3527-3532, (2006).
- [2] Sawai, J. and Yoshikawa, T., "Quantitative Evaluation of Antifungal Activity of Metallic Oxide Powders (MgO, CaO and ZnO) by an Indirect Conductimetric Assay", *J. Appl. Microbiol.*, Vol.96, pp.803-809, (2004).
- [3] Thill, A., Zeyons, O., Spalla, O., Chauvat, F., Rose, J., Auffan, M. and Flank, A.M., "Cytotoxicity of CeO₂ nanoparticles for Escherichia coli", Physico-chemical insight of the cytotoxicity mechanism", *Environ. Sci. Technol.*, Vol.40, pp.6151-6156, (2006).
- [4] Zhang, L., Jiang, Y., Ding, Y. Povey, M. and York, D., "Investigation into the Antibacterial Behaviour of Suspensions of ZnO Nanoparticles (ZnO nanofluids)", *J. Nanoparticle Res.*, Vol.9, pp.479-489, (2007).
- [5] Jones, N., Ray, B., Ranjit, K.T. and Manna, A.C., "Antibacterial Activity of ZnO Nanoparticle Suspensions on a Broad Spectrum of Microorganisms", *FEMS Microbiol. Lett.*, Vol.279, pp.71-76, (2008).
- [6] Stoimenov, P.K., Klinger, R.L., Marchin, G.L. and Klabunde, K.J., "Metal oxide nanopartilces as bactericidal agents", *Langmuir*, Vol.18, pp.6679-6686, (2002).
- [7] Cho, M., Chung, H., Choi, W. and Yoon, J., "Linear Correlation Between Inactivation of *E. coli* and OH Radical Concentration in TiO₂ Photocatalytic Disinfection", *Water Research*, Vol.38, pp.1069-1072, (2004).
- [8] Kuhn, K. P., Chaberny, I.F., Massholder, K., Stickler, M., Benz, V.W., Sonntag, H. G. and Erdinger, L., "Disinfection of surfaces by photocatalytic oxidation with titanium dioxide and UVA light", *Chemosphere*, Vol.58, pp.71-77, (2003).
- [9] Sunada, K., Kikuchi, Y., Hashimoto, K. and Fujishima, A., "Bactericidal and detoxification effects of TiO₂ thin film photocatalysts", *Environ. Sci. Technol.*, Vol.32, pp.726-728, (1998).
- [10] Yamamoto, O., Shimura, T., Sawai, J., Kojima, H. and Sasamoto, T., "Effect of CaO Doping on Antibacterial Activity of ZnO Powders", *J. Ceram. Soc. Jpn.*, Vol.108, No.2, pp.156-180, (2000).
- [11] Yamamoto, O., Nakakoshi, K., Sasamoto, T., Nakagawa, H. and Miura, K., "Adsorption and Growth Inhibition of Bacteria on Carbon Materials Containing Zinc Oxide", *Carbon*, Vol.39, pp.1643-1651, (2001).
- [12] Yamamoto, O., Sawai, J., Hotta, M., Kojima, H. and Sasamoto, T., "Influence of mixing ratio of ZnO and MgO powders on antibacterial activity", *J. Mater. Sci. Soc. Jpn.*, Vol.35, pp.258-261, (1998). (in Japanese)
- [13] Sawai, J., "Quantitative Evaluation of Antibacterial Activities of Metallic Oxide Powders (ZnO, MgO, and CaO) by Conductimetric Assay", *J. Microbiol. Methods*, Vol.54, pp.177-182, (2003).
- [14] Sawai, J., Kawada, E., Kanou, F., Igarashi, H., Hashimoto, A., Kokugan, T. and Shimizu, M., "Detection of Active Oxygen Generated from Ceramic Powders Having Antibacterial Activity", *J. Chem. Eng. Jpn.*, Vol.29, No.4, pp.627-633, (1996).
- [15] Sawai, J., Shoji, S., Igarashi, H., Hashimoto, A. and Koguran, T., "Hydrogen Peroxide as an Antibacterial Factor in Zinc Oxide Powder Slurry", *J. Fermentation and Bioengineering*, Vol.86, No.5, pp.521-522, (1998).
- [16] Sawai, J., Yamamoto, O., Hotta, M., Kojima, H. and Sasamoto, T., "Antibacterial Activity of Heat-Treated ZnO powders against *E. coli* and *S. aureus*", *J. Chem. Soc. Jpn.*, Vol.9, pp.633-635, (1998). (in Japanese)
- [17] Xu, H.Y., Wang, H., Zhang, Y.C., He, W.L., Zhu, M.K., B. Wang, and H. Yan, "Hydrothermal Synthesis of Zinc Oxide Powders with Controllable Morphology", *Ceramics International*, Vol.30, pp.93-97, (2004).
- [18] Tiller, J.C., Liao, C.J., Lewis, K. and Klibanov, A.M., "Designing surfaces that kill bacteria on contact", *Proc. Natl. Acad. Sci. USA*, Vol.98, pp.5981-5985 (2001).
- [19] Lin, J., Qui, S., Lewis, K. and Klibanov, A.M., "Bactericidal properties of flat surfaces and nanoparticles derivatized with alkylated polyethylenimines", *Biotechnol. Prog.*, Vol.18, pp.1082-1086, (2002).

Origin and transportation course of heavy metal elements in the particulate matter (PM) at the Hachimantai mountain range at the Northern Japan

Ryoei Kikuchi*, Yuko Sasaki*, Asami Oba*, Ayako Sato*, Makoto Takada*,
Takashi Kimoto** Toru Ozeki*** and Nobuaki Ogawa*

* Faculty of Engineering and Resource Science, Akita University,

1-1, Tegata Gakuen-cho, Akita 020-8502, Japan

** Kimoto Electric Co. Ltd., 3-1, Funahashicho Tennojiku, Osaka 543-0024, Japan

*** Hyogo University of Teacher Education, Yashiro-cho, Katou-gun, Hyogo 673-1494, Japan

ogawa@ipc.akita-u.ac.jp

Particulate matter (PM) was collected at the Hachimantai mountain range in northern Japan. In the present study, the origin and transportation course of the heavy metal elements was discussed for PM_{fine} and PM_{coarse} , determined by using PIXE (Particle Induced X-ray Emission) and back trajectory analyses. The result shows that the PM_{fine} emitted mainly from artificial sources, compared with the PM_{coarse} from natural sources, since the EF value of PM_{fine} was higher than PM_{coarse} . When the air mass was transported from Chinese Continent to the Hachimantai mountain range, elements from artificial sources were high concentration.

Keyword: Particulate matter (PM), PIXE, Enrichment factor, Heavy Metal, Back trajectory

1. Introduction

Particulate matter (PM) in the atmosphere may be derived from anthropogenic sources such as motor vehicles, biomass and fossil fuel combustion, and natural sources such as soils and sea spray [1,2]. Characterization of the fine particulates in the PM is becoming increasingly important to researchers due to their potential impacts on human health [3], transnational migration and influence on climate forcing and global warming [4].

Asia is one of the major sources of not only mineral dust but also anthropogenic aerosols. Especially, Northeast Asia was known to emit a large amount of anthropogenic pollutants due to its high population density and increasingly high rate of energy consumption. Because the Japanese Islands locate in

the latitude region of northeast Asia, many studies on the influence of long-range transport have been actively performed. Many previous works examined the contributions of emission sources to $PM_{2.5}$ and PM_{10} aerosols in the northeast Asia region [5].

In a Japan, also many studies on the influence of long-range transport have been performed [6-9]. However, there are few papers that clarify the origin of the PM by using the Enrichment Factor analysis, the ratio of the specific element, and the back trajectory analysis.

The purpose of present study is to clarify the origin of the PM at the Akita Hachimantai mountain range by using the enrichment factor analysis, the ratio of the specific element, and the back trajectory analysis.

2. Experimental

Figure 1 shows the site used for sampling of PM. The PM was sampled at the Akita Hachimantai Kogen Hotel (39°59'N, 140°48'E, 960 m a.s.l.) using a PM sampler (PM2.5/10-DX; Kimoto Electric Co. Ltd.) from 2004 to 2006. As a filter for PM sampling, a cellulose mixed-type ester filter (pore size 0.8 μm , ϕ 47 mm, White AAWP; Millipore Corp.) was used. Various elements, sampled on the filter were analyzed by particle induced X-ray emission (PIXE) analysis in the Nishina Memorial Cyclotron Center, Japan Radioisotope Association at Takizawa-mura, Iwate Prefecture, Japan. To estimate air mass movement, 72 h back trajectories were determined by the secondary approximation method on an 850 hPa weather chart corresponding to each sampling time.

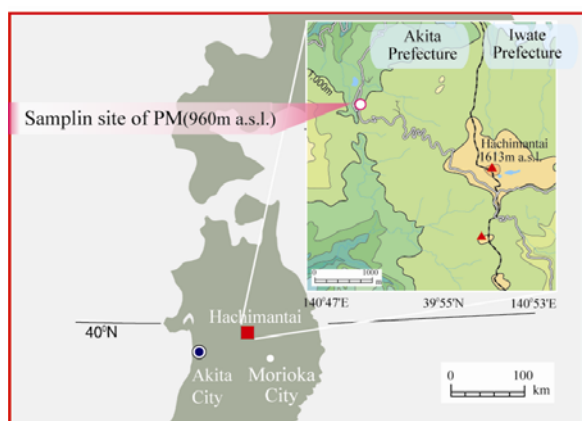


Figure 1 Sampling site location.

3. Results and Discussion

3.1 General characteristic of PM

Table 1 shows the various elements in the fine ($d < 2.5 \mu\text{m}$, $\text{PM}_{2.5}$) and coarse ($10 \mu\text{m} > d > 2.5 \mu\text{m}$, $\text{PM}_{10-2.5}$) atmospheric particles. Figure 2 shows the enrichment factor (EF value) [10] of PM_{fine} and $\text{PM}_{\text{coarse}}$ for each element (standard element is Fe). The elements with higher concentration ($> 10 \text{ngm}^{-3}$) were Na, Mg, Al, Fe, K and Ca and the EF values was less than ten. The elements with lower concentration ($< 10 \text{ngm}^{-3}$) were Ti, Mn, V, Cr, Ni, Cu, Zn, Pb, As and Se and the EF values was more than ten except for Ti, Mn and V. The element with EF value of more than ten is the crust origin mainly and less than ten is emitted from anthropogenic source [11]. From Figure 2 and Table 1, it is found that crust origin elements were Na, Mg, Al, Fe, K, Ca, Ti and V and anthropogenic source elements were Cr, Ni, Cu, Zn, Pb, As and Se. The group of Al, Si, Ca, Ti

and Fe (mainly originating from crust) were found to be 91.5, 324.2, 87.8, 7.56 and 77.9ngm^{-3} , respectively. These elements concentrations were 1 or 2 orders low, compared to that of the other regions except for Si [12-16]. These results suggested that the EF values were low because the surface in the Hachimantai mountain range is covered with vegetation. Moreover, the group of Cr, Cu, As and Se (mainly originating from combustion of the fossil fuel and emitting from the vehicles and factory) concentrations were found to be 1.2, 1.1, 0.16 and 0.09ngm^{-3} , respectively. These elements concentrations were also 1 or 2 orders low, compared to the other regions. These results suggest that these elements (Cr, Cu, As and Se) concentration is lower because there is no industrial area near the Hachimantai mountain range and it is far away from the Chinese continent regarded as the pollutant source. The atmospheric environment in the Hachimantai mountain range has shown the characteristics of the atmosphere of relatively pure rural site. However, even in National Park PM included the anthropogenic origin elements.

Table 1 The concentration of elements (ngm^{-3}) measured in the coarse and fine fractions of particles at Hachimantai mountain range over period from 2004 to 2006.

Elements	This study		PM10 Asia			PM10 eastern Mediterranean	
	PM10-2.5	<PM2.5	This study rural	Tokyo urban*	Gwangju urban*	Erdemli†	Sde Boker‡ arid
Na	86.9	35	121	562	185	-	-
Mg	19.5	7.1	26.6	-	144	-	-
Al	74.3	17.2	91.5	833	319	-	-
Si	237	87.2	324	-	114	-	-
S	135	846	981	-	-	1637	2646
Cl	32.1	4.45	36.6	4440	-	5492	1199
K	50.3	89.1	139	457	535	360	599
Ca	66.2	21.6	87.8	1380	349	1888	6744
Ti	4.8	2.76	7.56	108	19	27.1	126
V	0.06	0.14	0.2	5.87	4	8.7	9.8
Cr	0.55	0.63	1.18	10.8	-	5.7	-
Mn	1.59	2.05	3.64	42.9	18	7.6	24.9
Fe	51.9	26	77.9	1220	408	351	1293
Ni	0.21	0.61	0.82	6.29	5	3.7	5.7
Cu	0.49	0.62	1.11	67.1	11	9.7	-
Zn	1.15	4.62	5.77	261	57	-	30.6
As	0.02	0.14	0.16	2.47	-	-	-
Se	0.02	0.07	0.09	1.1	-	-	-
Br	0.12	0.28	0.4	21.8	-	-	-
Rb	-	0.14	0.14	1.47	-	-	-
Sr	0.08	-	0.08	-	-	-	-
Pb	3.1	6.45	9.55	-	30	-	-

Concentration are expressed in ngm^{-3}

*Mizohata et al.(2000)

†Lee et al.(2008)

‡Rodriguez et al.(2002)

*Kock et al.(2007)

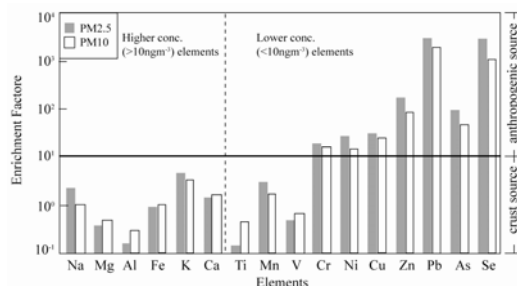


Figure 2 EF values for various elements in the PM.

□:the PM_{10} , ■:the $\text{PM}_{2.5}$

3.2 Identification of origin of As

Figure 3 shows the back trajectories when As contained in the sampled PM. The air mass of the event including As was transported from a Chinese continent and the Korean peninsula. For identification of origin of As, it is effective to use the As/V ratio [17]. The As/V ratio by the coal, the oil and the gasoline combustion is 4.8, 0.02, and 1.1, respectively [17]. The event including V was only one event (23-25 June 2005) and the As/V ratio was 0.81. Therefore, this result suggested that origin of As of this event was mainly the gasoline combustion in Chinese continent and Korea peninsula, since there is no industrial area near the Hachimantai mountain range and the total number of vehicles is low in the mountain area.

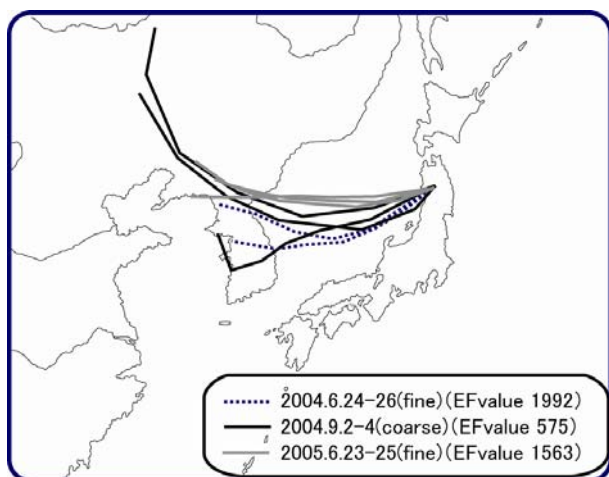


Figure 3 The back trajectories when As was collected.

3.3 Identification of origin of Pb

Figure 4 shows the back trajectories when Pb contained in the PM. The air mass of the event including Pb was transported from the Chinese continent, the Korean peninsula and Japanese Islands. For identification of origin of Pb, it is effective to use the Pb/Br ratio [17]. The Pb is an anthropogenic origin when the Pb/Br ratio ranges from 0.8 to 4.7, and is the metal refinement origin in case of more than 4.8. From Figure 4, it was suggested that Pb in PM at Akita Hachimantai mountain range has both of the anthropogenic and the metal refining origins. Furthermore, when the air mass was transported over the Japanese Islands, it is find out that air mass was mainly passed over the large-scale industrial area

in Japan.

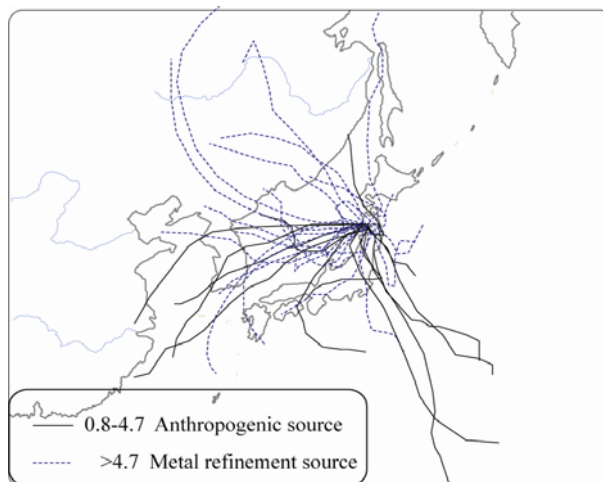


Figure 4 The back trajectories when Pb was collected.

3.4 Identification of origin of Se

Figure 5 shows the back trajectories when Se contained in the PM. The air mass of the event including Se was transported mainly from the Chinese continent and the Korean peninsula. For identification of origin of Se, it is effective to use the Se/S ratio [17]. The Se is coal combustion and vehicles origin when the Se/S ratio ranges from 0.00014 to 0.00088. The origin of Se was mainly coal combustion and vehicles from the Chinese continent and the Korean peninsula.

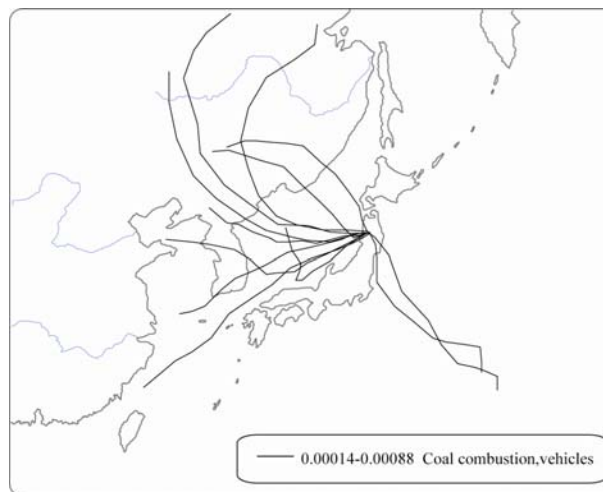


Figure 5 The back trajectories when Se was collected.

4. Conclusions

The elements concentrations of mainly originating from crust were 1 or 2 orders low compared with the industrial regions except for Si. The EF values of these elements were low, because the surface in the Hachimantai mountain range is

covered with vegetation. Moreover, elements concentrations of mainly originating from combustion of the fossil fuel and emitting from the vehicles were also 1 or 2 orders low compared with the industrial regions. The origin of As and Se were mainly gasoline and coal combustion from Chinese continent and Korea peninsula, respectively.

The atmospheric environment in the Hachimantai mountain range has shown the characteristics of the atmosphere of relatively pure rural site but the PM contained the elements from anthropogenic origin.

References

- [1] Cohen, D.D., "Characterisation of atmospheric fine particles using IBA techniques," *Nuclear Instruments and Methods in Physics Research*, 14, pp.136-138, (1998).
- [2] Cohen, D.D., Graham, M.B. and Kondepudi, R., "Elemental analysis by PIXE and other IBA techniques and their application to source fingerprinting of atmospheric fine particle pollution," *Nuclear Instruments and Methods in Physics Research* 109, p.218, (1996).
- [3] Dockery, D.W., Pope, C.A., Xu, X., Spengler, J.D., Ware, J.H., Fay, M.E., Ferris, B.G. and Speizer, F.E., *New England Journal of Medicine* 329, 1753. (1993).
- [4] IPCC, 2001. The Third Assessment Report of Working Group I of the Intergovernmental Panel on Climate Change: Technical Summary, Lead Authors, Albritton, D. L. (USA), Meira Filho, L.G., (Brazil), Shanghai, 17-20 January (2001).
- [5] Han, J.S., Ghim, Y.S., Moon, K.J., Ahn, J.Y., Kim, J.E., Ryu, S.Y., Kim, Y.J., Kong, B.J. and Lee, S.J., "Concentration variations of trace elements in Gosan, Jeju during the polluted period in November 2001 and the yellow sand period in spring 2002," *Journal of Korean Society for Atmos. Environ.* 20, pp.143-151, (2004).
- [6] Kikuchi, R., Adzuhata, T., Okamura, T., Ozeki, T., Kajikawa, M. and Ogawa, N., "A pollution of fog by ionic components and insoluble substances at Akita Hachimantai mountain range." *Int. Soc. Mater. Eng. Resour.*, 9, pp.28-31, (2001).
- [7] Kikuchi, R., Inotsume, J., Yoshimura, K., Ogawa, N., Sera, K. and Ozeki, T., "Transport course of insoluble substances of fog water in Akita Prefecture in Northern Japan," *Int. J. PIXE*, 23, pp.81-87, (2003).
- [8] Saitoh, K., Sera, K. and Shirai, T., "Characterization of atmospheric aerosol particles in a mountainous region in northern Japan," *Atmospheric Research*, 89, pp.324-329, (2008).
- [9] Yamada, E., Funoki, S., Abe, Y., Umemura, S., Yamaguchi, D. and Fuse, Y., "Size Distribution and Characteristics of Chemical Components in Ambient Particulate Matter," *Anal. Sci.*, 21, pp.89-94, (2005).
- [10] Kim, K. H., Choi, G. H., Kang, C. H., Lee, J. H., Kim, J. Y., Youn, Y. H. and Lee, S. R., "The chemical composition of fine and coarse particles in relation with the Asian Dust events," *Atmospheric Environment*, 37, pp.753-765, (2003).
- [11] Fang, G.C., Wu, Y.S., Chen, J. C., Fu, P. P. C., Chang, C. N. and Chen, M. H., "Metallic elements study on fine and coarse particulates during daytime and nighttime periods at a traffic sampling site," *Science of the Total Environment*, 345, pp.61-68 (2005).
- [12] Mizohata, A., Ito, N. and Kasuya, Y., "Characterization of the atmospheric particulate matter observed at the sites near the heavy traffic road in Tokyo," *J. Jpn. Soc. Atmos. Environ.* 35, pp.77-102 (2000). (in Japanese).
- [13] Lee, H., Park, S., Kim, S. And Kim, J., "Source identification of PM2.5 particles measured in Gwangju, Korea," *Atmos. Res.* 88, pp.199-211 (2008).
- [14] Rodriguez, S., Querol, X., Alastuey, A. and Plana, F., "Sources and processes affecting levels and composition of atmospheric aerosol in the western Mediterranean," *J. Geophys. Res.* 107, pp.47-77 (2002).
- [15] Kocak, M., Mihalopoulos, N. and Kubilay, N. N., "Chemical composition of the fine and coarse fraction of aerosols in the northeastern Mediterranean", *Atmos. Environ.* 41, pp.7351-7368 (2007).
- [16] Andreae, T. W., Andreae, M., Ichoku, C., Maenhaut, W., Cafmayer, J., Karnieli, A. and Orlovsky, L., "Light scattering by dust and anthropogenic aerosol at a remote site in the Negev Desert, Israel", *Geophys. Res.* 107. (2002).
- [17] Arditoglou, A., C. Samara, "Levels of total suspended particulate matter and major trace elements in Kosovo: a source identification and apportionment study", *Chemosphere*, 59, 669-678 (2005).

Observation of the scavenging effect for ionic pollutants in the case of that the air mass brought the precipitation in Japan after precipitating in Korea

Takanori Tanie*, Nobuhisa Tamura*, Ryuzi Nakata**, Kaoru Fuzinaga***, Toru Ozeki****, Dong Uk Kim****, Heejun Lim****, Nobuaki Ogawa*

*Faculty of Engineering and Resource Science, Akita University,

1-1 Tegata Gakuen-cho Akita 010-8502, Japan

**Fukui University, 3-9-1, Bunkyo, Fukui 910-1193, Japan

***Kanazawa Institute of Technology, 7-1, Ohgigaoka Nonoichi Ishikawa 921 - 8501, Japan

****Hyogo University of Teacher Education, 942-1, Shimokume, Kato-shi, Hyogo 673-1494, Japan

*****Daegu National University of Education, #1797-6 Daemyung 2 dong,

Namgu, Daegu, Korea

*****Gyeongin National University, 969-17 Gyesan-dong Gyeyang-gu, Incheon, Korea

ogawa@ipc.akita-u.ac.jp

In order to clarify the scavenging effect of pollutants of the air mass transported from the Chinese Continent via South Korea to Japan by precipitation, the precipitates were collected in South Korea (Daegu and Incheon) and five sites of Japan (Akita, Ishikawa, Fukui, Hyogo, and Wakayama). When the air mass brought the precipitate in South Korea also brought the precipitate at the sampling sites in Japan, the concentration of nss-SO₄²⁻ ion in the precipitation at Japan was decreased, compared with that in Korea. However, when the air mass which did not bring the precipitation in South Korea brought the precipitation only in Japan, the concentration of nss-SO₄²⁻ in the precipitation in Japan was high more than the above result. These results suggested that the nss-SO₄²⁻ ion was scavenged from air mass by the precipitation in Korea.

Key Words: Precipitation, Same air mass, nss-SO₄²⁻, NO₃⁻, Scavenging effect

1. Introduction

In recent years, more concern is with the increase in the emission amount of sulfur oxide and nitrogen oxides by rapid industrial development in East Asia area [1-3]. For Japanese site, especially for the region located in the coast of the Sea of Japan, the air mass brought precipitate is mainly transported from the Chinese Continent and Korean Peninsula (about 60%). Therefore, this fact means that the acid rain problem has to keep being esteemed from now on in the Japan. On the other hand it is well known that these pollutants in air are scavenged from atmosphere by wet deposition such as rain, snow and fog. The purpose of the present study is to evaluate

the scavenging effect of ionic pollutants in the case that, the air mass brought the precipitate in Japan after precipitating in Korea.

2. Experimental

Every one week precipitate was collected in South Korea (Daegu (35.9°N, 128.6°E) and Incheon (37.3°N, 126.4°E)) and five sites of Japan (Akita (39.7°N, 140.1°E), Ishikawa (36.5°N, 136.6°E), Fukui (36.1°N, 136.2°E), Hyogo (34.9°N, 135.0°E) and Wakayama (34.1°N, 135.1°E))(Fig.1). The pH of collected rain water was measured with pH meter

(HM-30S; TOA Co. Ltd.) and electric conductivity (EC) using conductivity meter (CM-4-S; TOA Co. Ltd.). Ions concentrations of rain water were measured by ion chromatography system (ICA-5000; TOA Co. Ltd.). Transport course of air mass was estimated by using “metex” of Center for Global Environmental Research [4].



Figure 1 Sampling sites of one week precipitation.

3. Results and Discussion

Table 1 shows the volume-weighted mean concentration of various ions of one week precipitate in seven sites. For precipitation at Daegu, the pH value was higher than other sites since precipitation was neutralized by NH_4^+ and Ca^{2+} . In the Incheon, pH value of precipitation was lowest since concentration of Ca^{2+} was lower, compared with precipitation of Daegu and these of nss-SO_4^{2-} and NO_3^- was nearly equal, compared with precipitation at Daegu. In the five sites of Japan, the concentration of Na^+ and Cl^- was higher at coast of Japan Sea (Akita, Ishikawa and Fukui) since sea-salt particle was abundant in the air mass which passes over the Sea of Japan.

Figure 2 shows the various ionic concentrations and change when or after the air mass brought the precipitate in South Korea and the precipitate sampling area in Japan. The concentration of nss-SO_4^{2-} ion decreased from 10 to 51% at the sampling sites in Japan compared with that in Korea.

However, when the air mass which did not bring the precipitation in South Korea, brought the precipitation only in

Japan, the concentration of nss-SO_4^{2-} ion in the precipitation in Japan was higher than the above result. These facts suggested that nss-SO_4^{2-} ion in the air was scavenged from air mass by the precipitation in Korea.

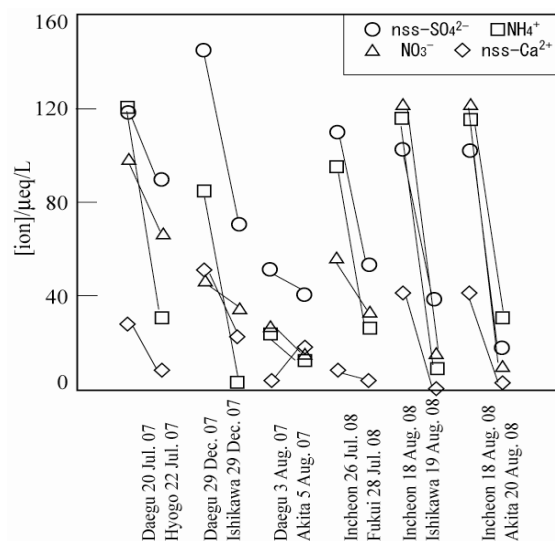


Figure 2 The various ions concentrations change when the air mass brought the precipitation in South Korea also brought the precipitation at the sampling sites in Japan.

4. Conclusion

The results in this study suggested that when the same air mass brought precipitation by South Korea and Japan, nss-SO_4^{2-} ion was scavenged from the air mass by the precipitation of South Korea.

References

- [1] J. Li et al., “Quantifying the human health benefits of curbing air pollution in Shanghai”, *Journal of Environmental Management* 70, 49–62 (2004)
- [2] J. N. GALLOWAY et al., “Nitrogen mobilization in the United States of America and the People's Republic of China”, *Atmos. Environ.*, 30, 1551-1561(1995)
- [3] Zhifang Xu et al., “Chemical and strontium isotope characterization of rainwater in Beijing, China”, *Atmos. Environ.*, 43, 1954-1961(2009)
- [4] <http://www.adorc.gr.jp/adorcjp/index.html>

Table 1 Volume-weighted mean concentration of various ions and pH.

	pH	Cl^-	NO_3^-	nss-SO_4^{2-}	Na^+	NH_4^+	nss-Ca^{2+}
		µeq/L					
Daegu (n=38)	5.86±0.76	47±65	69±125	102±147	44±75	42±52	121±420
Incheon (n=13)	4.17±0.08	21±25	66±76	105±118	16±23	63±65	28±36
Akita (n=65)	4.60±0.13	131±234	20±20	38±28	92±161	22±45	9±18
Ishikawa (n=60)	4.30±0.11	142±202	33±33	52±65	115±152	31±63	18±37
Fukui (n=65)	4.44±0.08	132±273	25±26	43±54	100±205	18±23	8±18
Hyogo (n=64)	4.38±0.01	18±15	28±28	43±46	19±22	15±16	9±13
Wakayama (n=40)	4.54±0.12	40±36	26±33	42±52	29±27	19±21	8±8

Geology, Mineral Resources and Mining Activity of Mongolia

Jargalan Sereenen* and Altankhuyag Dorj-Unden**

* School of Geology and Petroleum Engineering, Mongolian University of Science and Technology

**Department of Geology, Ministry of Mineral Resources and Energy

jrgln_s@yahoo.com; d_altankhuyag@yahoo.com

Abstract: Mongolia is land locked country, located at the center of Central Asia, between Russia and China. Its geology is complicated, consisting of various types of rocks, formed during wide period of geological evolution from Archean to Quarternary. Mongolia's mining industry has great potential. Its mineral resources are largely unexplored and unexploited. In total, about 80 types of minerals have been discovered in Mongolia and has sizable reserves of coal, copper, fluorspar and gold. In 2003 the minerals sector accounted for 9% of GDP, 53.5% of gross industrial output, 56.7% of export revenues whereas today this sector produces 28.2% of GDP, 64.3% of total industrial output, 80.7% of export earnings. Present situation of Mongolian mining activity is very complicated ranging from Mongolian version 19's century American gold rush (so called Ninjas) to middle size mining inherited from socialist period mining activity (middle and small size dredges) recent high technology mining operations (Boroo gold mine)

INTRODUCTION

Mongolia is located at the central part of Central Asian Orogenic Belt, between the Siberian platform in the north and Sino-Korean and Tarim terrains in the south. Geological structure of the Mongolia is represented by collages of continental blocks, ancient island arc terrains, subduction complexes and fragments of oceanic crust that amalgamated during late PreCambrian, Paleozoic and Mesozoic. Long history of Mongolian geological setting from Archean to Cenozoic is characterized by diversity of tectonic environments. In the course of geological evolution sedimentary, magmatic and metamorphic geologic formations developed, and correspondingly genetically and paragenetically they are associated with

various types of mineral resources.

Here we are going to introduce about main mineral resources, their distribution and recent situation of mining activities in Mongolia.

Geologic survey and mineral deposit investigation of Mongolia is started in the beginning of 20th century, but systematic study began since 1939, when geological survey of Mongolia is established. Since that time geological prospecting in Mongolia has identified over 500 mineral deposits, 6000 occurrences of about 80 different types of minerals, such as copper, gold, iron, zinc, lead, fluorite, phosphate and coal etc. Main mining activity is undertaken on the gold, copper, coal and fluorite deposits (Figure-1).

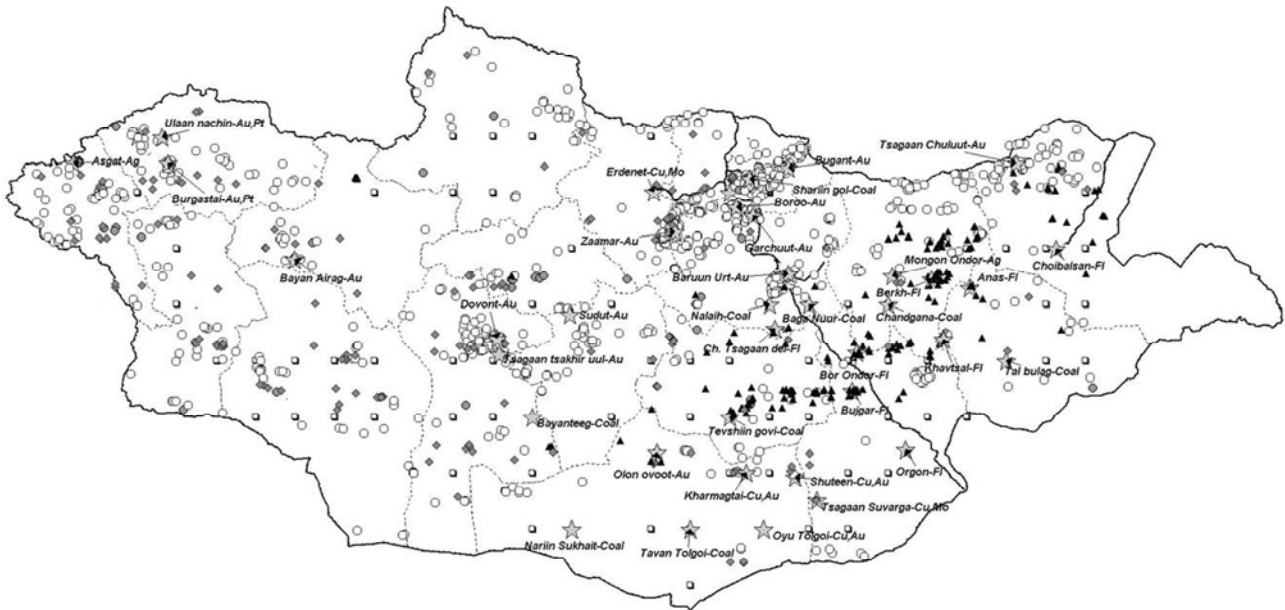


Figure-1. Distribution map of gold, silver, copper, fluorspar and coal deposits of Mongolia. Open circle is gold; gray circle is silver; diamond is copper; triangle is fluorspar and rectangle is coal. Stars are main active deposits and mining areas with name and type of deposit

GOLD AND SILVER

Gold deposits and occurrences are widely distributed in whole country. The biggest gold producing area is North Khentii gold belt which contains Zaamar gold field, Boroo cluster of deposits, newly discovered Gatsuurt gold deposit, Yoroo gol gold district etc. Other main gold producing areas area Bayanhongor gold belt, Khangai gold belt, Mongol Altai gold belt and South Khentii gold belt.

Silver is mainly accompanying product of gold. There are two big silver deposits in Mongolia one is Asgat deposit which is located at the west Mongolia. Another one is Mongon Ondor deposit, located south east part of Mongolia.

COPPER

Copper is the one of main metal, producing in Mongolia. There are 3 main belts of copper mineralization: South Mongolia, Central Mongolian and North Mongolian. South Mongolian copper belt occupies almost whole area of Gurvansaihan island arc terrane, which hosts 6 major porphyry deposits such as Tsagaan Suvarga, Oyu Tolgoi,

Shuteen, Kharmagtai etc and more than 45 occurrences. Major Cu-Au, Cu-Mo deposits are the Oyu Tolgoi, Tsagaansuvarga, Kharmagtai and Shuteen. The Oyu Tolgoi is newly found deposit and it is huge in size occupying over 12 km long north northeast-trending zone, with six porphyry Cu ± Au deposits as: South, Southwest, and Central Oyu Tolgoi, and Hugo Dummett South and North and Heruga.

The Erdenet Cu-Mo deposit located at the north Mongolian copper belt. The ore body of the deposit extends over 2 x 1 km area, with a maximum vertical thickness of 560m, including 100-300 m thick secondary Cu-enriched supergene zone at the top. The Erdenet Cu-Mo porphyry deposit was found 30 years ago and has being mined since 1978. The deposit has 1.3 billion tons of ore containing 0.51% of copper and 0.015% of molybdenum (Jargalsaikhan, 1996) and produces 450-480 thousand metric tons of copper concentrate (assaying 27% Cu) and over 2800 metric tons of molybdenum concentrate (assaying at least 50% of molybdenum) per year.

FLUORSPAR

The fluor spar mineralization is wide spread in the east and south-east part of Mongolia. Main part of fluor spar is formed during late Mesozoic to late Jurassic and early Cretaceous time. There two main types of fluor spar deposits: one is epithermal fluorite veins and other one is metasomatic ore bodies. Biggest deposits are Bor Undur, Berkh, Orgon, Khar Airag, Chuluut Tsagaan Del etc.

COAL

Coal is the leading mineral and the principal source of heat and energy of Mongolia. More than 40 coal deposits were discovered and 20 of them have being actively mined. Main coal deposition is found in Carboniferous, Permian, Jurassic and Cretaceous sediments. Carboniferous and Permian age coals are mainly hard-coal and Jurassic and Cretaceous age are brown-coal. The biggest coal deposits are Tavan Tolgoi (hard-coal), Baga nuur (brown coal), Nalaikh, Shariin gol, Shivee ovoo etc.

MINING

Mining history dates back to the early 1900's: gold mining was being initiated in 1901 Mongol-Or association conducted surveys on the Yuroo, Shariin Gol, Haraa, Yamaat, Nyalkh, and Tolgoit at the north Khentii gold belt and coal mining being developed 1912. In 1943-1948 the Yugzur, Tumentsogt and Burentsogt tungsten mines were built and mining of fluor spar began. The "Mongol-Oil" enterprise developed the Zuunbayan oil field starting in 1950. In the 1970's and 1980's Modot placer tin, Tolgoit placer gold, Khajuu Ulaan, Khar Airag, Orgon Bor-Ondor, Berkh fluor spar; the Erdenet copper molybdenum and Baganuur coal mines began operation.

In the early 1990 in Mongolia political change has occurred. The country has embarked on the road to a market economy. The transition from planned economy to market economy is accompanied by much economical difficulties. Once a foreign journalist said that Mongolia is a country of "Beggars sitting on the Gold". To recover this economic crisis Mongolian government made a decision

to develop mining of gold and compiled the Program named "Gold-2000". According to this program gold operating and mining activity has abruptly increased, and now there are more than 200 companies, engaged on this business. In early 1990's annual gold production was around 500 kg and statistical report of Mongolia informed that gold production is reached up to 15184kg (535599.8ounces) in 2008. It should be noted that over 95% of gold production comes from placer deposit operation.

In 2003 the minerals sector accounted for 9% of GDP, 53.5% of gross industrial output, 56.7% of export revenues whereas today this sector produces 28.2% of GDP, 64.3% of total industrial output, 80.7% of export earnings. It builds the bulk of the fiscal revenues and accounts for the major part of currency reserves of the country. In addition, it employs over 30 thousand people. Present situation of Mongolian mining activity is very complicated ranging from Mongolian version 19's century American gold rush (so called Ninjas) to middle size mining inherited from socialist period mining activity (middle and small size dredges) recent high technology mining operations (Boroo gold mine).

Removing Arsenic from Acid Mine Drainage by Microbubble Flotation

Danni Dai*, Gjergj Dodbiba*, Kazuya Sunaka**, Chiharu Tokoro**, Toyohisa Fujita*,

*Department of Systems Innovation, School of Engineering, The University of Tokyo, 7-3-1, Hongo, Bunkyo-ku, Tokyo, 113-8656 Japan

**Department of Resources and Environmental Engineering, School of Creative Science and Engineering, The University of Waseda, 3-4-1, Okubo, Shinjuku-ku, Tokyo, 169-8555, Japan
tt086393@mail.ecc.u-tokyo.ac.jp

Abstract: The mine drainage of the strong acidity that contains arsenic of the high concentration is drained from Horobetsu sulfur mine. This mine drainage flows into Lake Toya and affects a wide range of water quality of Lake Toya. The processing method of Horobetsu mine consists of a co-precipitation method with iron hydroxide, since the wastewater contains a large amount of Fe. Furthermore, it is processed with neutralization. In this study, the objective was to find a better way to remove arsenic from mine drainage of Lake Toya by microbubble flotation. Arsenic was effectively removed when mole ratio with sulfur of sulfating agent and arsenic was 6 and pH2.5. The experimental results suggested that arsenic was removed from 10ppm to 1.5ppm.

Key Words: Arsenic; Sulfuration; Microbubble Flotation

1 INTRODUCTION

The depletion of the water resource is serious issue in developing countries. Various elements such as arsenic, iron, manganese and ammonium ions contaminate the underground water that is an excellent resource, when compared with the surface water which is generally polluted easily. The problem of arsenic contamination in groundwater poses a serious threat in these areas because ground water is the main source of drinking water [1]. Arsenic is a notorious pollutant and therefore the treatment of arsenic contaminated waters is of great interests [2].

The arsenic problem is especially serious in some Asian countries such as Thailand and Bangladesh. Arsenic is a very toxic element, since at even low concentration it can cause many complications to humans. The arsenic unites easily with the protein in the body, and obstructs the enzyme in the protein. The toxic symptom is caused by 5 - 50 mg, and the fatal dose is 5 - 7 mg/kg [3].

The influence of arsenic is a serious situation in natural environmental pollution, destruction, and the human body. In February 1, 1997, the environmental standards value was restricted at 0.01 mg/L and the drainage standard value was set at 0.1 mg/L [4].

The mine drainage of the strong acidity that contains arsenic of the high concentration is drained from Horobetsu sulfur mine. This mine drainage flows into Lake Toya, and has a big influence on the acidification of the water quality of Lake Toya. It is necessary to remove arsenic efficiently and economically for resident's health and environmental protection.

The processing method of mine drainage coming from Horobetsu mine, includes a coprecipitation method with iron hydroxide, since the content of Fe in waste water is relatively high and a neutralization process. However, a large amount of sludge that contains arsenic is generated in this method. It has the problem in the final disposal. In this work, a new method is introduced. It combines a sulfuration and microbubble flotation in order to remove arsenic from the mine drainage. The condition of

removing arsenic efficiently and economically was considered by the experiment under various conditions such as the amount of the sulfide addition, time, pH and xanthate concentration.

2 EXPERIMENTAL

2.1 Microbubble Flotation

Flotation is a very well-known beneficiation method. Microbubble generated during the flotation have a diameter of 10 μ m. Following are the characteristic of the microbubble:

- Neither the union nor the absorption of the bubble happen. It stays in water for a long time like a single gas, and are stable for a relatively long period.
- The surfacing speed is extremely slow, and it is excellent in diffusive of horizontal direction.
- It is easy to be dissolved to water because it stays in water for a long time, and the surface area of the bubble for each unit volume is large.
- It has adsorbent to the underwater float because it electrifies electrically.

2.2. Xanthates and PAX [5]

Xanthates are water-soluble chemicals that are used primarily in the mining industry. Xanthates can be obtained by reacting an alcohol with carbon disulphide and an alkali such as sodium hydroxide or potassium hydroxide. The alcohols employed are not unique. They can form ethyl, butyl (isobutyl, normal butyl, secondary butyl), propyl (isopropyl, normal propyl) and amyl (isoamyl, normal amyl, secondary amyl) xanthates, in dry forms, such as powder, granules, pellets, tablets or flakes. Xanthate is the common name for chemical reagents used in the flotation of base and precious metals, which is the standard

method for separating valuable minerals, such as gold, copper, lead or zinc minerals, from non-valuable minerals, such as limestone or quartz (gangue).

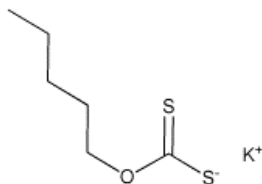


Fig.1 Potassium Amyl Xanthate structure

2.3. Sulfide reaction

A sulfide reaction by H_2S is shown with arsenic sulfide as example.

The arsenic exists in the form of As(III) and As(V).

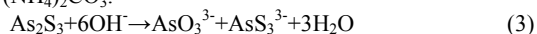
As(III) precipitates yellow arsenic trisulfide by the acidic solution.



As(V) happens the reductive reaction by H_2S , and the arsenic trisulfide is precipitated as (1).



As_2S_3 melts easily in alkaline solution such as NaOH, NH_3 , and $(NH_4)_2CO_3$.



If these solutions are made acidic, As_2S_3 is precipitated again.

2.4 Materials

The element and the concentration of Horobetsu mine drainage are shown in Table 1. $NaSH \cdot nH_2O$ was used as sulfating agent, H_2SO_4 and NaOH were used to adjust pH. In some cases, potassium amyl xanthate (PAX) was used as surfactant.

Table 1 The element and the concentration of Horobetsu mine drainage

As	10ppm
Fe	380ppm
pH	1.8

2.5 Methods

After pH was adjusted, the sulfating agent was adjusted to prescribed concentration and the xanthate were added to Horobetsu mine drainage. The arsenic solution treated with NaHS was injected into the microbubble flotation. The sample was then stirred for 30 minutes, and the flotation separation of the arsenic sulfide was done. The concentration of each element was then measured with ICP-OES. The microbubble flotation is shown in Fig. 2.



Fig.2 The microbubble flotation machine

3 RESULTS AND DISCUSSION

3.1 The effect of sulfating agent addition on the remaining As concentration

The arsenic exists in the form of As(III) and As(V). In general, As(III) generates arsenic sulfide with the next expression.



As(III) exists as H_3AsO_3 ion under the acid condition and exists as $H_2AsO_3^-$ under the alkali condition.



When As(III) exists in the solution as $H_2AsO_3^-$, soluble AsS_3^{3-} and insoluble As_2S_3 are generated by the addition of sulfating agent. Therefore, it is necessary to do sulfide processing of As(III) by the acidic condition.



As(V) is reduced to As(III), and generates arsenic sulfide by the sulfating agent.

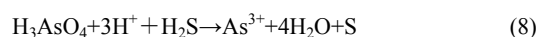


Figure 2 shows the effect of sulfating agent addition on the remaining As concentration in Horobetsu mine drainage in pH 2.5. Figure 3 shows the removed ratio of As in Horobetsu mine drainage in pH 2.5.

When the S/As molar ratio was 6, a better removal effect was observed. The As concentration went down from 8.9 ppm to 3.1 ppm, and the removal ratio is about 70%. However, the result of Horobetsu mine drainage in pH 2.5 had not arrived at the drainage standard value (i.e., As = 0.1 ppm).

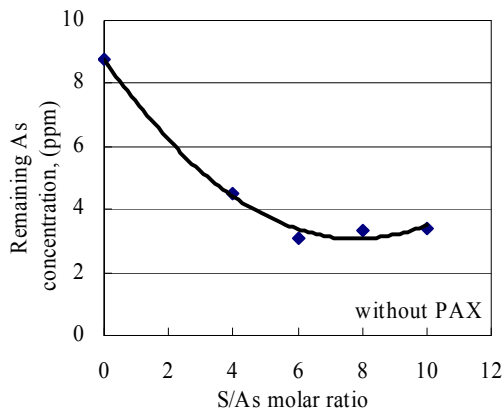


Fig.2. The effect of sulfating agent addition on the remaining As concentration in pH 2.5

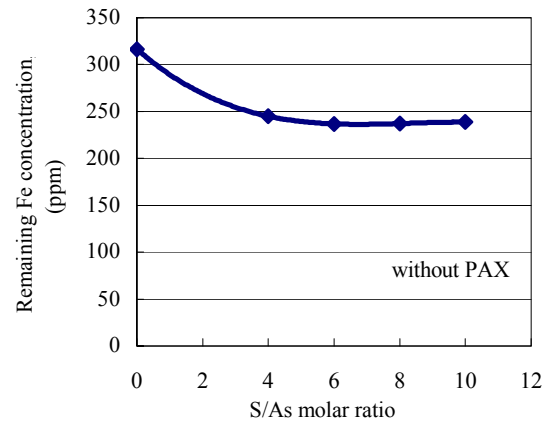


Fig.4. The effect of sulfating agent addition on the remaining Fe concentration in pH 2.5

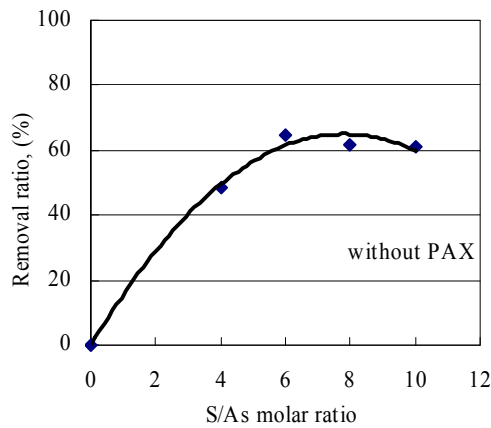


Fig.3. The removal ratio of Fe in Horobetsu mine drainage in pH 2.5.

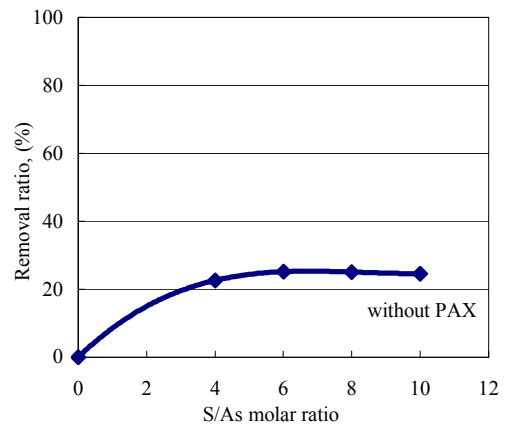


Fig.5. The removal ratio of Fe in Horobetsu mine drainage in pH 2.5.

3.2 The effect of sulfating agent addition on the remaining Fe concentration

Figure 4 shows the effect of sulfating agent addition on the remaining Fe concentration in Horobetsu mine drainage in pH 2.5. Figure 5 shows the removal ratio of Fe in Horobetsu mine drainage in pH 2.5.

In pH 2.5, the Fe concentration went down from 336 ppm to 245 ppm, and the removal ratio is about 25%. It hardly influenced the remaining Fe concentration for the decrease in the As concentration by the amount of the sulfating agent addition. The separation removal of As and Fe becomes possible.

3.3 The effect of pH on the remaining As concentration

Figure 6 shows the effect of pH on the remaining As concentration of Horobetsu mine drainage when the S/As molar ratio was 6. The experimental results indicated that when pH was higher, the removal effect of arsenic was better. When pH was 3, the As concentration went down from 8.896 ppm to 0.067 ppm. The result of Horobetsu mine drainage arrived at the drainage standard value (As=0.1 ppm). When pH was 2.5 and 2, the remaining As concentration was 3.123 ppm and 4.213 ppm, respectively. The result of Horobetsu mine drainage in pH 2.5 had not arrived at the drainage standard value (As=0.1 ppm).

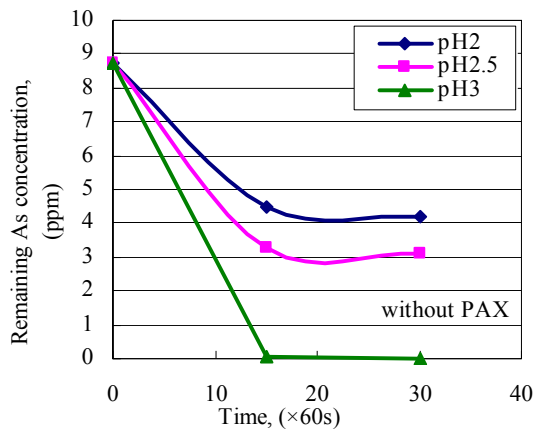


Fig.6. The effect of pH on the remaining As concentration when the S/As molar ratio was 6

3.4 The effect of pH on the remaining Fe concentration

Figure 7 shows the effect of pH on the remaining Fe concentration of Horobetsu mine drainage when the S/As molar ratio was 6. It was found that when pH was higher, the removal effect of Fe was lower. When pH was 3, the Fe concentration went down from 336 ppm to 158 ppm, and the removed ratio was about 50%. On the other hand, when pH was 2.5 and 2, both results were almost the same. The remaining Fe concentration was 336 ppm to 245 ppm, and the removed ratio was about 25%.

When pH was 3 or more, a part of Fe(II) was oxidized to Fe(III). The hydroxide precipitate is generated. So it is necessary to process it at pH 2.5 or less. By the result of 3.3, the remaining As concentration in pH 2.5 was better than in pH 2. So, it was thought that the best removal effect was in pH 2.5.

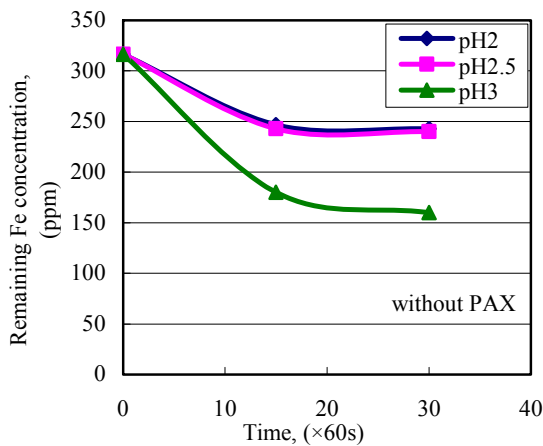


Fig.7. The effect of pH on the remaining Fe concentration when the S/As molar ratio was 6.

3.5 The effect of xanthate concentration on the remaining As concentration

Figure 8 shows the effect of xanthate concentration (PAX = 1g/kg) on the remaining As concentration of Horobetsu mine drainage when the S/As molar ratio was 6 in pH 2.5.

The better removal effect was shown in PAX = 1 g/kg when

passing for 30 minutes. When without PAX, the As concentration went down from 8.896 ppm to 3.123 ppm. On the other hand, when PAX = 1 g/kg, the As concentration went down from 8.896 ppm to 2.302 ppm. However, the result of Horobetsu mine drainage had not arrived at the drainage standard value.

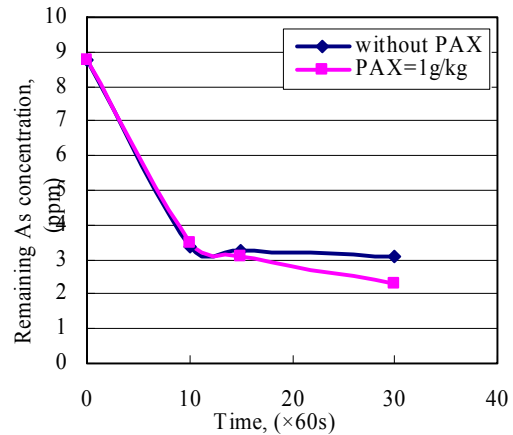


Fig.8. The effect of xanthate concentration on the remaining As concentration when the S/As molar ratio was 6 in pH 2.5.

3.6 The effect of xanthate concentration on the remaining Fe concentration

Figure 9 shows the effect of xanthate concentration (PAX = 1g/kg) on the remaining Fe concentration of Horobetsu mine drainage when the S/As molar ratio was 6 in pH 2.5.

When PAX = 1 g/kg and without PAX, both results were almost the same. The remaining Fe concentration was 336 ppm to 245 ppm, and the removed ratio is about 25%. It hardly influenced remaining Fe concentration by PAX.

The removal of As and Fe becomes possible when PAX was added into Horobetsu mine drainage.

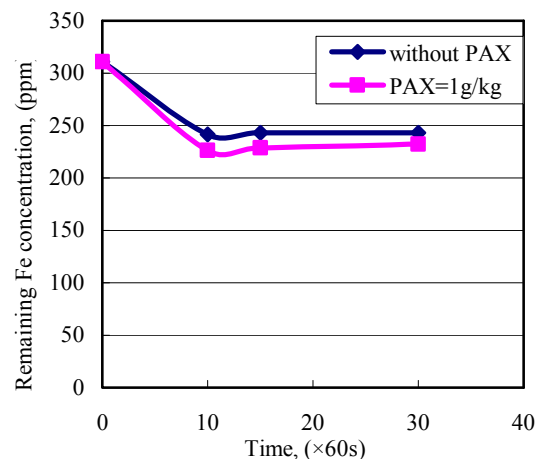


Fig.9. The effect of xanthate concentration on the remaining Fe concentration when the S/As molar ratio was 6 in pH 2.5.

4. CONCLUSIONS

In Horobetsu mine drainage, when the S/As molar ratio was 6, a better removal effect was shown in pH 2.5. The As concentration went down from 8.896 ppm to 3.123 ppm. At higher, the removal effect of the arsenic was better. When pH was 3, the As concentration went down from 8.896 ppm to 0.067 ppm. However, when pH was 3, the Fe concentration went down from 336 ppm to 158 ppm, the removal ratio was about 50%. On the other hand, when pH was 2.5 and 2, both results were almost the same. The remaining Fe concentration was 336 ppm to 245 ppm, and the removal ratio was about 25%. When pH was 3 or more, a part of Fe(II) was oxidized to Fe(III) and the hydroxide precipitate is generated. So, it is necessary to process it at pH 2.5. The separation removal of As and Fe becomes possible in pH 2.5. The better removal effect was shown in PAX=1g/kg. The As concentration went down from 8.896 ppm to 2.302 ppm, and the remaining Fe concentration was 336 ppm to 245 ppm, the removal ratio is about 25%. It hardly influenced the remaining Fe concentration. The separation removal of As and Fe becomes possible when PAX was put into Horobetsu mine drainage. In the future, we will research the more effective experimental conditions for removal arsenic until the drainage standard value (As=0.1 ppm).

Acknowledgment: The authors would like to acknowledge JOGMEC, Water re-use promotion center and Aqua Tech for their support during this work.

References

- [1] G.S. Murugesan, M. Sathishkumar. K. Swaminathan, Arsenic removal from groundwater by pretreated waste tea fungal biomass, *Bioresource Technology* 97 (2006) 483-487
- [2] Diana Q.L. Oliveira, Maraisa goncalves, Luiz C.A.Oliveira, Luiz R.G.Guilherme, Removal of As(V) and Cr(VI) from aqueous solutions using solid waste from leather industry, *J. Hazard. Mater.* 151 (2008) 280-284
- [3] APEC Virtual Center for Environmental Technology Exchange, <http://www.apec-vc.or.jp/e/>
- [4] AMRON Solution Business, <http://www.amron.co.jp/index.asp>
- [5] PAX, Xanthate, <http://www.3dchem.com/molecules.asp?ID=316>

Synthesis of a Pb-Fe based Adsorbent and its Application in the Adsorption of Mo in Nitric Acid Solution

Gjergj Dodbiba*, I-Chen Wu, Yu-Chen Lee, Toyohisa Fujita

Department of Systems Innovation, The University of Tokyo, Japan

dodbiba@sys.t.u-tokyo.ac.jp

Abstract: The incorporation of molybdenum is of particular concern in the vitrification of high-level radioactive liquid waste (HLLW). Thus, in order to eliminate molybdenum (Mo) from HLLW, a Pb-Fe based adsorbent was synthesized. The sintering temperature was considered to be the main parameter when synthesizing the adsorbent. The morphology of the synthesized adsorbent was investigated by using an X-ray diffractometer. Then, the adsorption behavior of Mo from a 3M HNO₃ solution was investigated. The experimental results pointed out that the synthesized adsorbent has a relatively high adsorption capacity for Mo(VI) from the HNO₃ solution.

Key Words: molybdenum, HLLW, adsorbent, sintering

1. INTRODUCTION

In order to minimize the long-term radiological risk and facilitate the management of high-level radioactive liquid waste (HLLW), several multi-cycle partition processes have been developed, [1-7]. Mo is one of the main fission products, since it is 10 wt% of the total amount of FP in a spent fuel, [8]. Thus, the removal of Mo will also significantly reduce the amount of HLLW to be disposed, as well as improve the vitrification of HLLW.

Various materials or composites have been synthesized in order to remove Mo from HLLW, [4, 8]. Although the above mentioned composites can extract Mo from the HLLW, other materials, such as a Pb-Fe based adsorbent, could be a feasible alternative. In this work, on the other hand, a series of Pb-Fe based adsorbents have been synthesized in order to adsorb Mo from HLLW. Moreover, the adsorption capacity of the synthesized adsorbents in adsorbing Mo in nitric acid (HNO₃)

aqueous solution was investigated as function of the calcination temperature of precipitate.

2. EXPERIMENTAL

2.1. Synthesis of the Pb-Fe based Adsorbents

Each Pb-Fe based adsorbents was precipitated (at 25 °C) by adding sodium hydroxide (NaOH) in a mixture of 1 mol/L lead nitrate Pb(NO₃)₂ and 1 mol/L ferric nitrate (Fe(NO₃)₃ · 9 H₂O) aqueous solutions, until pH of the mixture was adjusted to a desired value. The suspensions were then filtered and the precipitates were dried at 70 °C for over 72 hrs. Finally, each precipitate was ground by using an agate mortar with pestle to obtain a fine powder, which has been used as an adsorbent. In same cases, prior to the adsorption experiment, the prepared powder was also calcinated at a given temperature. The synthesized adsorbents were characterized by means of a X-ray

diffractometer (XRD: Mac Science, MO3XHF), and a scanning electron microscope (SEM: Keyence, VE-8800).

2.2. Chemical Composition of the Solution

The simulated HLLW waste stream used in this work was a 3 mol/L aqueous solution of nitric acid. Ammonium molybdate $(\text{NH}_4)_6\text{Mo}_7\text{O}_{24}$ was, on the other hand, added to adjust the concentration of Mo in solution. Except where noted, the concentration of Mo in solution was adjusted to 9.5 mmol/L. In some other cases, the adsorption of Mo from solution was studied by changing the concentration of HNO_3 in solution from 0.1 to 6 mol/L.

2.3. Adsorption Procedure and Measurements

A known amount of the Pb-Fe based adsorbent and 20 mL of ca. 9.5 mmol/L Mo in HNO_3 aqueous solution were mixed into a 50 mL clear glass vials with lid and shaken mechanically for ca. 2.5 hrs. Then, the two phases are separated by filtration using a filter unit (pore size of 0.20 μm). Finally, the concentration of Mo in the solution was analyzed by using an inductively coupled plasma-optical emission spectrometer, ICP-OES (PerkinElmer, OPTIMA 5300DV). Next, the experimental results were reported in terms of the sorbed concentration (i.e. mass adsorbate/mass adsorbent), which is also known as adsorption capacity. The sorbed concentration q was calculated by the following equation, (Eq. 1):

$$q = (C_0 - C) \cdot \frac{V}{M}, \quad (\text{mg/g}) \quad (1)$$

where C_0 and C are aqueous concentration of adsorbate (in mg/L) before and after adsorption, respectively; V is the volume of solution (in L); M is the mass of the adsorbent (in g).

3. RESULTS AND DISCUSSIONS

The sorbed Mo concentration was investigated as a function of the calcination temperature of the Pb-Fe based adsorbent. Finally, the equilibrium relationship between the sorbed concentration of Mo and the concentration of Mo in solution (i.e. adsorption isotherm) was described.

3.1. Adsorption of Mo: Effect of Calcination Temperature of the Pb-Fe based Adsorbent

In this set of experiments, the effect of the calcination temperature of the Pb-Fe based adsorbent on the sorbed concentration of Mo was investigated. Thus, the adsorbents were first precipitated at pH 9 and, then, either dried at 70 °C for over 70 hrs. or calcinated at one of the following temperatures for 1 hr., i.e. 180, 210, 280, 350, 410, 500, 660, 700 or 800 °C, respectively. Next, each adsorbent was added in a 3 mol/L HNO_3 aqueous solutions. The concentration of adsorbent in each solution was 100 g/L, whereas the initial Mo concentration (i.e. C_0) was 9.6 mmol/L (i.e. 916.6 mg/L). The samples were then mechanically stirred for 2 hours. After filtering each solution, the concentration of Mo remaining in solution was analyzed by means of ICP-OES.

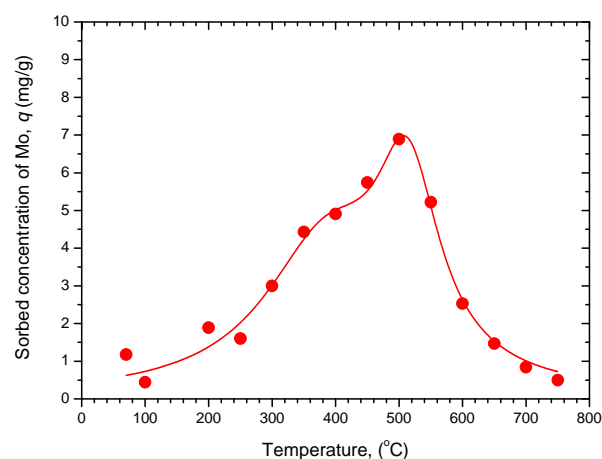


Fig. 1. Sorbed concentration of Mo as a function the calcination temperature of the Pb-Fe based adsorbent; (*Experimental conditions*: Solution: 3 mol/L HNO_3 ; Initial concentration of Mo: 9.6 mmol/L (i.e. 916.6 mg/L); Concentration of Pb-Fe based adsorbent: 100 g/L; Contact time: 2 hrs.).

The experimental results are shown in Fig. 1. Referring to the experimental results, the calcination temperature of the Pb-Fe based adsorbent had a great influence on the sorbed concentration of Mo. Fig. 1 shows that when the adsorbent was calcinated at 500 °C, before being used in the experiment, the sorbed concentration was the greatest, i.e. 6.9 mg/g. It was found that the calcination of the adsorbent at 500 °C, prior to

the adsorption experiments, substantially increases the sorbed concentration of Mo from the 3 mol/L nitric acid solution. In other words, the Pb-Fe based adsorbent was precipitated at pH 9 and then calcinated at 500 °C, before being used in all subsequent experiments.

3.2. Characterization of the Synthesized Adsorbents

Following is a series of quantitative and qualitative analysis carried out to characterize the Pb-Fe based adsorbent.

3.2.1. XRD analysis: In order to better understand the results of the TG/DTA analysis, an X-ray diffraction analysis was carried out. The aim was to observe the structure evolution of the Pb-Fe based adsorbent as a function of the calcination temperature. Thus, the Pb-Fe based adsorbent was precipitated at pH 9, and then various fraction of it were heated at 70, 280, 500, 700 or 800 °C for 1 hr., before being analyzed by using a XRD diffractometer (Mac Science, MO3XHF). The diffraction patterns for the Pb-Fe based adsorbents, calcinated at various temperatures are given in Fig. 2.

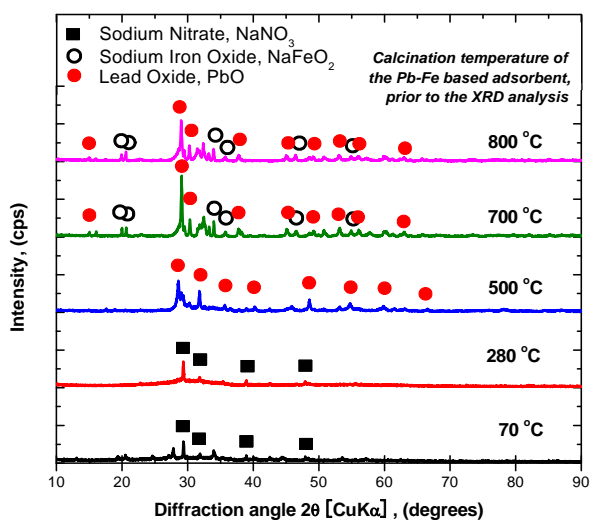
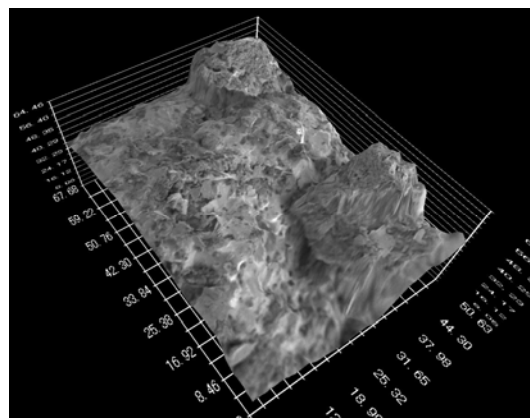


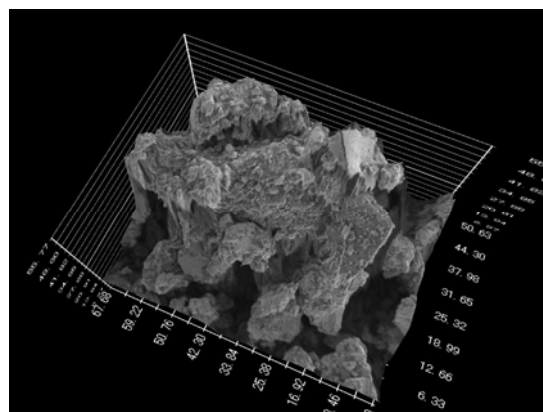
Fig. 2. XRD pattern of the Pb-Fe based adsorbent, after fired at various temperatures for 1 hr. *Note:* All the XRD analyses were performed at room temperature.

X-ray diffraction analysis indicated that when the adsorbent is calcinated at a temperature lower than 300 °C, its structure is almost amorphous. For instance, Fig. 2 shows that when adsorbent is heated at 70 °C or 280 °C there is no crystalline structure, except for the sodium nitrate, a salt formed during the precipitation of the adsorbent. Moreover, Fig. 2 also shows

that when the adsorbent is calcinated at 500 °C, the crystalline structure of lead oxide (PbO) appeared. Furthermore, Fig. 2 also shows the XRD patterns for Pb-Fe based adsorbents calcinated at 700 and 800 °C respectively. It can be seen that at relatively high calcination temperature sodium iron oxide (FeNaO₂) was formed together with PbO.



(a) before calcination (i.e. only drying at 70 °C)



(b) calcination at 500 °C

Fig. 3. 3D scanning electron micrographs of the Pb-Fe based adsorbent, before (a) and after (b) calcination at 500 °C for 1 hr. (*Note:* Unit on X, Y and Z axes is µm).

3.2.2. SEM analysis: Figure 3 shows 3D scanning electron micrographs of the Pb-Fe based adsorbent, precipitated at pH 9, before (Fig. 3a) and after (Fig. 3b) calcination at 500 °C for 1 hr. The SEM micrographs were taken by using a scanning electron microscope (SEM: Keyence, VE-8800). The difference in texture of the adsorbent, before and after calcination, can be clearly observed indicating the crystalline structure of the adsorbent after calcination, which is also

appeared to be more porous (Fig. 3). Moreover, an estimation from SEM micrographs is that the particle size of the synthesized adsorbent ranged from 10 to 30 μm .

Considering the results presented in Sections 3.2.1 and 3.2.2, the authors suggest that calcination of adsorbent leads to a change in structure and therefore the affinity of the adsorbent's surface to Mo ions is greatly enhanced. The reason is that the oxygen atom in adsorbent surface, which the main species is PbO, has a great affinity of for Mo ions.

3.3. Adsorption isotherm of Mo on the Pb-Fe based adsorbent

Generally speaking, the amount of material sorbed per unit of adsorbent is called sorbed concentration, q , (Eq. 1). For a given amount of adsorbate and adsorbent in solution, there exists a unique sorbed concentration, [9]. The equilibrium relationship between the sorbed concentration q (in mg/g) and the adsorbate concentration C in solution (in mg/L) is called adsorption isotherm. Figure 4 shows adsorption of Mo on Pb-Fe based adsorbent, which was precipitated at pH 9 and then calcinated at 500 °C for 1 hr. The specific surface area of the adsorbent, measured by using an Automatic Surface Area Apparatus (SIBATA, ASA-2500), was 17.1 m^2/g .

In order to collect the data to construct this isotherm, various amount of the Pb-Fe adsorbent were added in 3 mol/L HNO_3 solution, containing 10.6 mmol/L Mo (i.e. 1018 mg/L), and mixed for 3 hrs. The concentration of Mo remaining was then measured by ICP-OES. By knowing the initial concentration, the sorbed concentration q was calculated, (Eq. 1).

One of most commonly used isotherm is the Langmuir isotherm, which linearized form is given by Eq. (2), [10].

$$\frac{1}{q} = \frac{1}{q_m K_{ads}} \left(\frac{1}{C} \right) + \frac{1}{q_m} \quad (2)$$

where q_m is the maximum capacity of the adsorbent for adsorbate, (mass adsorbate/mass adsorbent, mg/g); and K_{ads} is a measure of affinity of adsorbate for adsorbent.

The inset in Fig. 4 shows the linear graph of the Langmuir isotherm of Mo in 3 mol/L HNO_3 aqueous solution. The data

have then been extrapolated using the least-squared linear regression in order to calculate the maximum capacity of the adsorbent (q_m). The linearized form of this specific Langmuir isotherm is given in Eq. 3. Moreover, it was found that the maximum capacity of the Pb-Fe based adsorbent for Mo in 3 mol/L HNO_3 aqueous solution was 34.7 mg/g, (Fig. 4).

$$\frac{1}{q} = 5.23 \left(\frac{1}{C} \right) + 0.03 \quad (3)$$

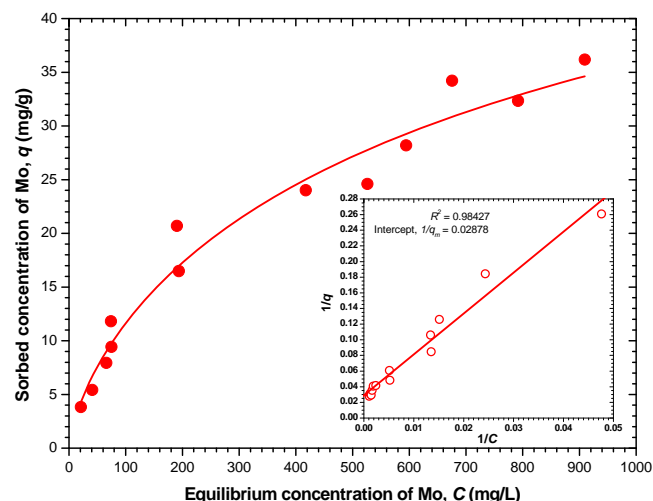


Fig. 4. Adsorption of Mo on the Pb-Fe based adsorbent, calcinated at 500 °C for 1 hr. *Inset*: Linear graph of the Langmuir isotherm; (Experimental conditions: Solution: 3 mol/L HNO_3 ; Initial concentration of Mo: 10.6 mmol/L (i.e. 1018 mg/L); Contact time: 3 hrs.).

4. CONCLUSIONS

A series of Pb-Fe based adsorbents, able to adsorb molybdenum (Mo) from high-level nuclear waste (HLW) were synthesized. The adsorbents were precipitated by adding sodium hydroxide in mixture of 1 mol/L lead nitrate and 1 mol/L ferric nitrate aqueous solutions. In addition, the adsorbents were also calcinated.

The adsorption capacity of the synthesized adsorbent in adsorbing Mo in HNO_3 solution was investigated as function of the calcination temperature of the adsorbent. The main finding of this work was when the Pb-Fe based adsorbent was

calcinated at 500 °C, prior to the adsorption experiments, the sorbed concentration of Mo was the greatest. The equilibrium relationship between the sorbed concentration of Mo and the concentration of Mo in solution was described according to the Langmuir isotherm, which indicated that maximum capacity of the Pb-Fe based adsorbent for Mo in 3 mol/L HNO₃ solution was 34.7 mg/g.

Acknowledgements

The present study includes the result of “Development of separation technology of transuranium elements and fission products by using new extractants and adsorbents” entrusted to Japan Atomic Energy Agency by the Ministry of Education, Culture, Sports, Science and Technology of Japan (MEXT). Moreover, the technical support provided by Mr. Shinya Sakae and Mr. Kazuhiro Fukawa of the University of Tokyo in carrying out the ICP-AES and XRD analysis is also gratefully acknowledged and appreciated.

References

- [1] Koch, L., 1986. Minor actinide transmutation - a waste management option. *Journal of the Less Common Metals*, Vol. 122, 371 - 382.
- [2] Schulz, W.W., Horwitz, E.P., 1988, TRUEX process and the management of liquid TRU waste. *Separation Science and Technology*, Vol. 23, No. 12-13, 1191 - 1210
- [3] Eccles, H., 2000. Nuclear fuel cycle technologies - sustainable in the twenty first century? *Extraction and Ion Exchange*, Vol. 18, No. 4, 633 – 654
- [4] Fujii, T., Yamana, H., Watanabe, M., Moriyama, H., 2001. Extraction of molybdenum from nitric acid by octyl(phenyl)-N,N-diisobutylcarbamoylmethyl-phosphine oxide. *Solvent Extraction and Ion Exchange*, Vol. 19/1, 127 - 141
- [5] Mathur, J.N., Murali, M.S., Nash, K.L., 2001. Actinide partitioning-A review. *Solvent Extraction and Ion Exchange*, Vol. 19, No. 3, 357-390.
- [6] Zhang, A., Wei, Y., Kumagai, M., Koma, Y., 2005. A new partitioning process for high-level liquid waste by extraction chromatography using silica-substrate chelating agent impregnated adsorbent. *Journal of Alloys and Compounds*, Vol. 390, 275 - 281.
- [7] Sasa, T., Nishihara, K., Sugawara, T., Okamoto, Y., Oigawa, H., 2008. Actinide reformer concept. *Progress in Nuclear Energy*, Vol. 50, No. 2-6, 353 - 358
- [8] Zhang, A., Kuraoka, E., Kumagai, M., 2006. Removal of Pd(II), Zr(IV), Sr(II), Fe(III), and Mo from simulated high level liquid waste by extraction chromatography utilizing the macroporous silica-based polymeric materials. *Separation and Purification Technology*, Vol. 50, 35 - 44.
- [9] Langmuir I., 1916. The constitution and fundamental properties of solids and liquids. *Journal of the American Chemical Society*, Vol. 38, 2221 - 2295
- [10] Benjamin, M.M., 2002. Water Chemistry, *McGraw-Hill*, New York.

Copper Recovery from Printed Circuit Board by Carbonization

Hiroyuki Ono, Gjergj Dodbiba, Toyohisa Fujita

Department of Systems Innovation, School of Engineering, The University of Tokyo
7-3-1 Hongo, Bunkyo-ku, Tokyo 113-8656, Japan
ono1@dowa.co.jp

Abstract: In an attempt to raise the copper grade of Printed Circuit board (PCB) by removing other components, carbonization treatment was investigated. The crushed PCB without surface-mounted parts was carbonized under nitrogen atmosphere. After screening, the char was classified by size into oversized pieces, undersized pieces and powder. The copper foil and glass fiber pieces were liberated and collected in undersized fraction. The liberation of copper foil from the oversized pieces was also investigated. The copper foil was liberated easily from glass fiber by stamping treatment. Liberation rate of copper foil was high at high carbonized temperature. The experimental results indicated that 90% of oversized char was liberated and the copper foil recovery from PCB carbonized at 1073K was 110kg/t. The copper recovery from char powder by flotation was also investigated. 15% of the copper grade and 80 % of the copper recovery were obtained, whereas the removal rate of silicon was 55%.

Key Words: Carbonization, Printed Circuit Board, Recycling

1 INTRODUCTION

Recently, it has been required to recycle valuable resources from wastes to conserve limited resources. Especially Waste Electrical and Electronic Equipments (WEEEs) should be recycled because they have many kinds of valuable materials. Most WEEEs include Printed Circuit Boards (PCBs). In Japan, about 30 km² per year of Printed Circuit board (PCB) has been produced [1]. PCBs are normally separated from WEEEs and picked up by hand and sold to non-ferrous metal market because PCBs include high grade of copper and other precious metal such as gold, silver and palladium [2]. However, PCB also has impurities such as silicon, aluminum and calcium which are slag materials in non-ferrous smelting process, and other harmful elements such as lead, bromine and antimony. Low grade PCBs are sold after removal of invaluable parts or sometimes landfilled without any treatment.

Recovery of metal from PCB has been studied by several methods such as crushing, separation method and leaching method [3-7]. Glass fiber recovery has also been studied [8].

In this paper, carbonization treatment was studied to remove glass fiber from low grade PCBs. Carbonization is a pyrolysis treatment of solids in absence of air. Pyrolysis of PCB has been studied but these studies were mainly investigated about the pyrolysis gas and char constituent [9-12]. Resin in PCB is pyrolyzed and metal is not oxidized by carbonization. It is therefore expected to recover copper efficiently in post process.

2 EXPERIMENTAL METHOD

2.1 Carbonization and separation

PCBs of 3-20mm in size, which were crushed by using a biaxial shear cutter and rotor crusher, were used for experiment. Surface mounted parts were removed from crushed PCBs. 100 g of crushed PCB was spread over a stainless tray made of

SUS430 and set in an electric furnace with 17L of furnace volume. PCBs were heated with 50K/min. of heating rate and carbonized at 673, 873, or 1073K for 1hour. 15L/min. of nitrogen gas was blown into the furnace to keep 2.5% of oxygen concentration due to air leakage into the furnace. PCB char was air-cooled after carbonization.

PCB char was screened by sieves and weight ratio with each particle size was measured. From char pieces with size over 4mm, copper foil, glass fiber and other parts were hand-picked and recovery of copper foil was measured.

Separation tests were conducted for parts in which copper foil and glass fiber keep multi-layered form to liberate copper foil with cutter mill, ball mill and stamp mill. 20g of multi-layered parts was tested with each test. Parts with the size over 4mm were screened after separation test and liberated copper foil and glass fiber were hand-picked to measure each weight.

2.2 Flotation

For the powder of PCB char carbonized at 1073K with size under 0.5mm, copper upgrade was investigated by flotation. Char was ground with pestle and mortar to prepare powder of particle size under 150, 75 and 44 μ m. Flotation reagents were 0.5mol/L sulfuric acid and 1mol/L sodium hydroxide as pH adjustor, sodium hydrogen sulfide (NaHS, purity 70%) as surfactant, Potassium Amyl Xanthate (PAX, purity 90%) as collector and Methyl Isobutyl Carbinol (MIBC) as frother. The dosage of MIBC was 1.4kg/t. NaHS and PAX are dissolved in ionic exchange water to obtain 5wt% and 1wt% solution.

Denver type flotation cell of 200cm³ was used. 5g of powder was added in 150 cm³ of deionized water while stirring by impeller at 350rpm. Next, NaHS solution was added. After 15 minutes, PAX was added and pH was regulated by pH adjustor. After 15 minutes, MIBC was added and 1.5mL/min. of air was introduced under the cell. The floated froth was

collected for 10 minutes. The froth and tailing were filtered and dried at 363K for 12hours. After measuring the weight, several elements such as copper, silicon and calcium were analyzed with X-ray Fluorescence Analyzer (XRF, Rigaku Supermini) and copper grade and recovery were calculated. Fig.1 shows the experimental flow.

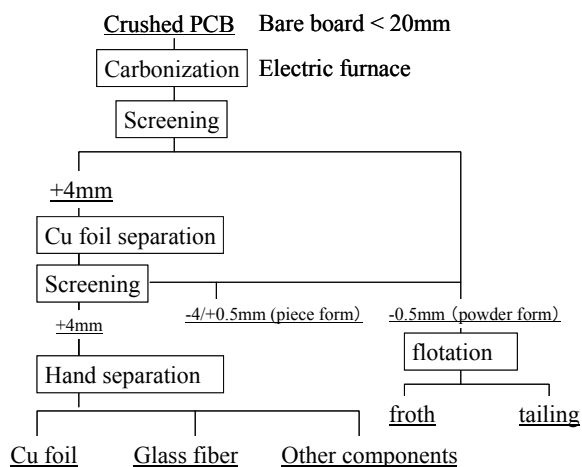


Figure 1. Experimental flowsheet

3 RESULTS AND DISCUSSIONS

3.1 Carbonization condition

Char with size over 4mm was composed of copper foil, glass fiber, other parts, and multi-layered parts at any carbonized temperature. On the other hand, copper foil and glass fiber were liberated among char with size under 4mm. It is expected to recover copper foil efficiently from char with size under 4mm with eddy current separator or electrostatic separator.

As a result of separation tests for multi-layered parts, both copper foil and glass fiber were pulverized with cutter mill. Most parts kept multi-layered form with ball mill. Multi-layered parts decreased gradually with back and forth shaker, but most parts were pulverized by abrasion and copper foil hardly increased.

On the other hand, copper foil and glass fiber were liberated by stamping. Table 1 shows the result of separation test by stamping with pestle at a rate of 150 times per minute.

Table 1. Results of stamping treatment: relationship between stamping time and recovery of copper foil for char carbonized at 873 and 1073K.

carbonized temperature (K)	stamping time (min.)	classification (wt.%)			
		multi-layered form	Cu foil	glass fiber	-4mm
873	0	100	0	0	0
	5	34	6	32	27
	10	19	8	36	35
1073	0	100	0	0	0
	5	38	9	10	41
	10	4	17	5	74

It is concluded that stamping treatment was the best way for copper foil liberation. Copper foil liberation of char carbonized at each temperature was compared. Fig. 2 shows the breakdown of the char after stamping treatment. Parts with size over 4mm were classified with copper foil, glass fiber, other parts and multi-layered parts. Most parts keep multi-layered form for char carbonized at 673K. Glass fiber was liberated most from char carbonized at 873K. Copper foil was liberated most from char carbonized at 1073K. Especially, multi-layered

parts were broken down most and glass fiber was selectively crushed to powder for the char. Copper foil yield was 110 kg/t-PCB and copper recovery was 55% in case of carbonization at 1073K. More copper foil was liberated from char carbonized at higher temperature. Carbonization at high temperature was effective to recover copper foil.

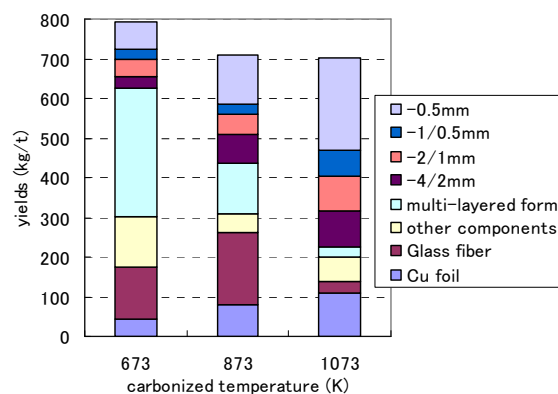


Figure 2. The yield and breakdown of char at each carbonized temperature after stamping treatment for 10min.

3.2 Flotation for powder of PCB char

Copper grade of char carbonized at 1073K with size under 0.5mm was 10% and copper distribution in the char was 12%. Fig. 3 shows the X-ray diffraction pattern of PCB char carbonized at each temperature. The peak of Cu, Pb, SiO₂ and Sb₂O₃ were observed. So it is expected that copper is separated from SiO₂ by sulfurization and flotation.

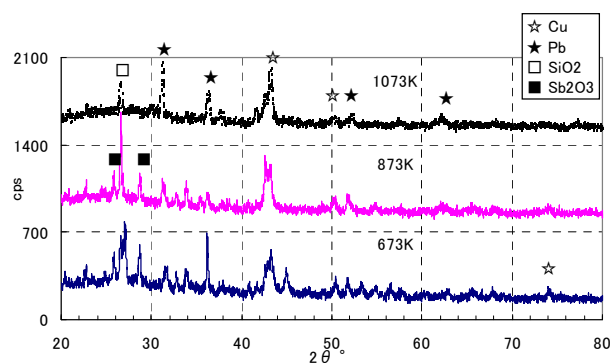


Figure 3. X-ray diffraction pattern of PCB char with size under 0.5mm

Fig. 4 shows the grade and recovery of copper in froth as a function of NaHS dosage. The flotation tests were carried out for the powder grounded to particle size under 150µm by adding 10kg/t PAX and adjusting pH at 6. NaHS dosage in the 5 to 50 kg/t range has little effect on copper grade and recovery. So it is concluded that 5kg/t of NaHS is enough.

Fig. 5 shows the grade and recovery of copper in froth as a function of PAX dosage. The flotation tests were carried out for the powder grounded to particle size under 150µm by adding 5kg/t NaHS and adjusting pH at 6. The grade of copper increased with increasing PAX dosage in the 2 to 10 kg/t range, but the recovery slightly decreased. So it is concluded that the optimum dosage of PAX is 10kg/t.

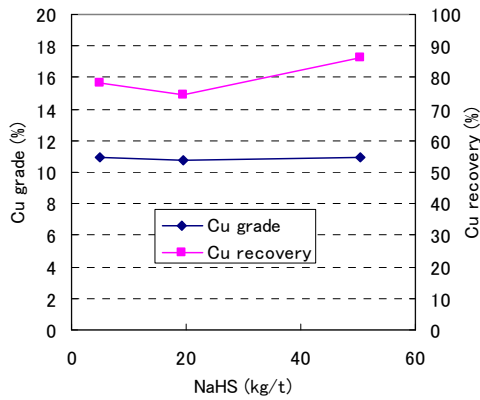


Figure 4. Effect of NaHS dosage on the flotation (particle size under 150 μ m, pH6, 10kg/t PAX)

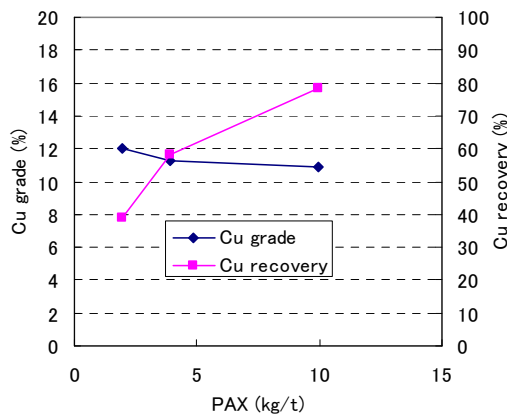


Figure 5. Effect of PAX dosage on the flotation (particle size under 150 μ m, pH6, 5kg/t NaHS)

Fig. 6 shows the grade and recovery of copper in froth as a function of pH. The flotation tests were carried out for the powder grounded to particle size under 150 μ m by adding 5kg/t NaHS and 10kg/t PAX. The recovery was highest and the grade increased from 10 to 12% at pH 10. No pH adjuster was added at pH 6. Considering the grade, recovery and reagent dosage, it is concluded that optimum pH is 10. Optimum dosage of PAX is 10kg/t.

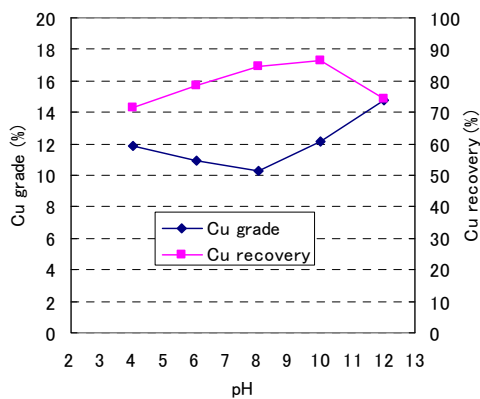


Figure 6. Effect of pH on the flotation (particle size under 150 μ m, 5kg/t NaHS, 10kg/t PAX)

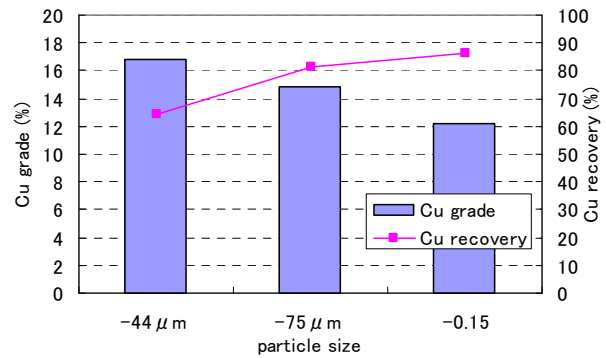


Figure 7. Effect of particle size on the flotation (pH10, 5kg/t NaHS, 10kg/t PAX)

Fig. 7 shows the grade and recovery of copper in froth as a function of particle size. The flotation tests were carried out by adding 5kg/t NaHS and 10kg/t PAX adjusting pH at 10. The grade increased with the smaller particle size, but the recovery decreased. Considering the grade and recovery, under 75 μ m was optimum grinding size. At this optimum condition, the copper grade increased from 10 to 15%, the copper recovery was 80% and silicon and calcium removal rate was both 55%. Though this copper grade was not enough for copper smelting material, the flotation was effective for the recovery of copper from the powder of PCB char.

4 CONCLUSION

Copper with foil form can be liberated from carbonized PCB by stamping treatment. High temperature carbonization was effective for copper foil liberation. Glass fiber was crushed to powder selectively by stamping treatment and 110kg/t of copper foil was liberated from PCB carbonized at 1073K.

Copper grade was raised from 10 to 15% by flotation for char powder carbonized at 1073K with size under 0.5mm and 80% of the copper recovery was obtained on the condition: particle size under 75 μ m, 5kg/t of NaHS, 10kg/t of PAX and pH10.

References

- [1] Ministry of Economy, Trade and Industry in Japan, Statistics of Machine, (2008).
- [2] Jirang Cui, Lifeng Zhang, "Metallurgical recovery of metals from electronic waste: A review" *Journal of Hazardous Materials* 158, pp.228–256, (2008).
- [3] Hugo Marcelo Veit, Andr'ea Moura Bernardes a, Jane Zoppas Ferreira, Jorge Alberto Soares Ten'orio, C'elia de Fraga Malfatti, "Recovery of copper from printed circuit boards scraps by mechanical processing and electrometallurgy" *Journal of Hazardous Materials* B137, pp.1704–1709, (2006).
- [4] C. Eswaraiah, T. Kavitha, S. Vidyasagar, S.S. Narayanan, "Classification of metals and plastics from printed circuit boards (PCB) using air classifier" *Chemical Engineering and Processing* 47, pp.565–576, (2008).
- [5] Jiang Wu, Jia Li, Zhenming Xu "Electrostatic separation for multi-size granule of crushed printed circuit board waste using two-roll separator" *Journal of Hazardous Materials* 159, pp.230–234, (2008).
- [6] Jae-Min Yoo, Jinki Jeong, Kyoungkeun Yoo, Jae-chun Lee, Wonbaek Kim, "Enrichment of the metallic components from waste printed circuit boards by a mechanical separation process using a stamp mill" *Waste Management* 29, pp. 1132–1137, (2009).
- [7] O.A. Fouad, S.M. Abdel Basir, "Cementation-induced recovery of self-assembled ultrafine copper powders from spent etching solutions of printed circuit boards" *Powder Technology* 159, pp.127 – 134, (2005).
- [8] Yanhong Zheng, Zhigang Shen, Chujiang Cai, Shulin

Ma, Yushan Xing, "The reuse of nonmetals recycled from waste printed circuit boards as reinforcing fillers in the polypropylene composites" *Journal of Hazardous Materials* 163, pp.600–606, (2009).

[9] William J. Hall, Paul T. Williams, "Separation and recovery of materials from scrap printed circuit boards" *Resources, Conservation and Recycling* 51, pp.691–709, (2007).

[10] Chiang Hung-Lunga, Lin Kuo-Hsiung, Lai Mei-Hsiu, Chen Ting-Chien, Ma Sen-Yi, "Pyrolysis characteristics of integrated circuit boards at various particle sizes and temperatures" *Journal of Hazardous Materials* 149, pp.151–159, (2007).

[11] Guido Grause, Masaaki Furusawa, Akitsugu Okuwaki, Toshiaki Yoshioka, "Pyrolysis of tetrabromobisphenol-A containing paper laminated printed circuit boards" *Chemosphere* 71, pp.872–878, (2008).

[12] Guan Jie, Li Ying-Shun, Lu Mai-Xi, "Product characterization of waste printed circuit board by pyrolysis" *J. Anal. Appl. Pyrolysis* 83, pp.185–18, (2008).

The use of Micro-bubble for Separating Plastic Mixtures

Cyou Shin*, Gjergj Dodbiba and Toyohisa Fujita

Department of System Innovation, The University of Tokyo, Japan
shincyou1983@yahoo.co.jp

Abstract: The aim of the research presented in this article is to investigate the performance when separating a mixture of two plastics acrylonitrile-ethylene-styrene (ABS), polyvinyl chloride (PVC) or Teflon by the use of the micro-bubble. All of the plastics mentioned above have a greater density than the water. However, ABS, which is hydrophobic, adheres to the micro-bubble will float, whereas the other two kinds of plastics still sink. After the experiments, the recoveries of the ABS and PVC in experiment 1 were both 100 %, whereas the recoveries of the ABS and Teflon in experiment 2 were 98 % and 96 %. Therefore, the separation can be finished successfully.

Key Words: Micro-bubble, Separation, ABS, PVC, Teflon

1. INTRODUCTION

Large production, large consumption, and large disposal of goods are noticeable in various economical activities in our daily lives, which keep the fast development of the economic activities. However, in contrary, it also leads to depletion of resources. Therefore, the recycling of the resources becomes more and more important for the sustainable development of the society.

The world production of the plastics in 2006 was 2.4 hundred million ton, whereas the total consumption was 2.1 hundred million ton. In Japan, the production in 2006 and 2007 were 14,049kt and 18,000kt respectively, the growth rate of which was 1.1%, however, the growth of the consumption was 0.8% off, so the application of the recycle of the waste plastic is essentially. [1].

Early studies on plastic wet separation were focused on adding some wetting agent to the mixture of plastics to change selectively one component of the mixture plastic to behave as hydrophobic or hydrophilic, [2-3]; or adding surfactant to change surface tension of the solution to the value between the

two solids to make one kind of the plastic in the mixture becomes hydrophilic, [4]. Later researches were also concerned with combined different surface treatment to achieve separation using a treatment in which wet oxidization which was combined with depressant adsorption to improve the separation, [5].

The aim of the research presented in this paper is to develop a laboratory-scale separator employing micro-bubble to recover plastics such as polyvinyl chloride (PVC), Teflon and acrylonitrile-ethylene-styrene (ABS).

2. EXPERIMENTAL

2.1 Materials

Three different kinds of plastics, i.e. ABS, PVC and Teflon were selected for investigation as they are widely used in our daily lives. Each of the plastic samples was first cut into flakes of 4 - 6 mm in size. Since the samples were of different colors and of sufficiently large size, at the end of the each experiment, the results of the separation could be analyzed by manual sorting. The densities of the samples were measured by using

pycnometer and the results are listed in Table 1 together with other characteristics.

Table 1 Properties of the plastic samples

Property	ABS	PVC	Teflon
Density, (g/cm ³)	1.06	1.4	2.1
Color	black	blue	white
Price, (USD/ton)	1700	970-1040	-

2.2 Experiment

Two different types of mixture were chosen for separation by using two different types of micro-bubble machine.

2.2.1 Mixture 1, ABS and PVC: This experiment was carried out by artificial mixture of ABS (white) and PVC (blue). The sizes of them have been introduced above, the densities of them have been listed in Table 1, and the proportion is shown in Table 2.

Table 2 Composition of ABS and PVC mixture

Component	Quantity	Weight, (g)
ABS	42 pieces	1.095g
PVC	26 pieces	1.003g

A photo of the laboratory-scale separation system is shown in Fig. 1. The separating system was composed of a micro-bubble machine, a magnetic stirrer and a beaker. The micro-bubble machine (AURA TEC OM4-MDG-020(OG)) was a device to give the solution stable air bubbles. The input tube would absorb the solution in the beaker and the micro-bubble would be discharge by the output tube. The working pressure and the impact of the output could also be adjusted. The magnetic stirrer was used for stirring the solution and helping the plastic flakes to contact with the micro-bubble abundantly.

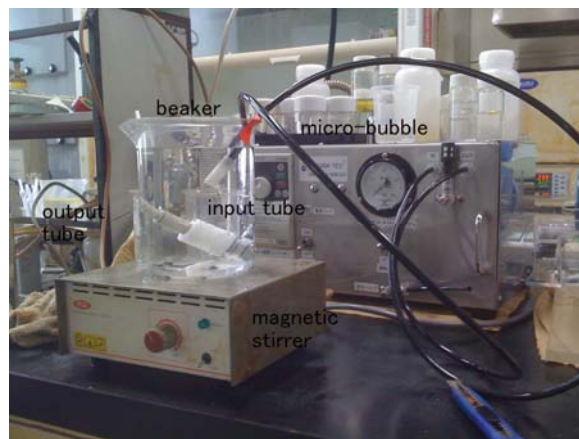


Fig. 1. Separating system

In operation, the output tube and the input tube were placed in the beaker (volume = 2 L, diameter = 150 mm) and fixed at the suitable position. After the beaker was filled with water (volume = 1.5 L), the micro-bubble machine was switched on. The working pressure and the impact of the output were adjusted at 0.27 MPa and 55Hz, which had been proved to be the optimum setting for the separation. After running the micro-bubble machine for 4 minutes, the magnetic stirrer was turned on.

During the experiment, although the density of the ABS and PVC is larger than that of the water, the ABS became hydrophobic and adhered to the micro-bubbles (Fig. 2). While, even if the PVC was also adhering the micro-bubbles (Fig. 3), the effect of the micro-bubbles was a little and could be neglected because the density of PVC was too much larger than that of water.



Fig. 2. ABS was adhered to the micro-bubbles



Fig. 3. PVC was adhered to the micro-bubble too, but still sinking

2.2.2 Mixture 2, ABS and Teflon: The experiment was carried out using artificial mixture flakes of ABS (black) and Teflon (white). The size of the specimen has been mentioned above, the densities of them have been listed in Table 1, and the proportion is shown in Table 3.

Table 3 Composition of the ABS and Teflon mixture

Component	Quantity	Weight, (g)
ABS	54 pieces	1.52
Teflon	28 pieces	1.55

The laboratory-scale separation system was shown in Fig. 4. The separating system was composed of a micro-bubble machine, a separating cell (11cm x 11cm x 45cm) and a collecting cell (30cm x 23.5cm x 10cm). It should be noted that the input tube was set in the collecting cell and the output tube was in the separating cell, which made the whole system recyclable and the separating cell was made of colorless acrylic resin for easily observation.



Fig. 4. Separating system 2

2.2.3 Procedure: The sample was introduced from the top of the separating cell after running the micro-bubble machine for 4 minutes. Both of the mixtures sank at first due to the gravity but after contacting the micro-bubbles, the ABS floated due to its hydrophobic properties and discharge to the collecting cell, (Fig. 5), and the water would be recycled by the input tube. On the other hand, the Teflon sank to the bottom of the cell directly, (Fig. 6).



Fig. 5. ABS adhered to micro-bubbles

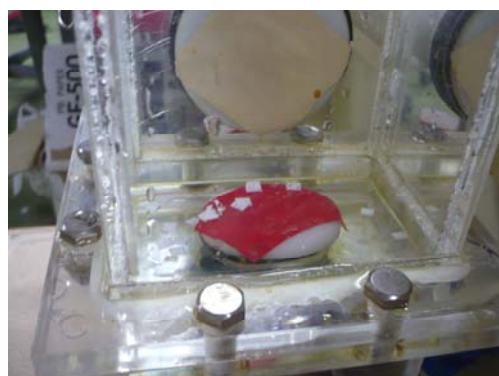


Fig. 6. Teflon flakes sinking at the bottom of the separation cell

3. RESULTS AND DISCUSSION

The results of the experiment 1 and experiment 2 are shown in the Tables 4 and 5. Respectively, the separation of the ABS and PVC was efficiently accomplished and high-purity products recovered. It should be noted that no chemical reagent was used in the experiment, and therefore there was no need to wash the samples after the separation.

Table 4 Separation result of ABS and PVC mixture

Components	Float product		Sink product	
	Grade, (%)	Recovery, (%)	Grade, (%)	Recovery, (%)
ABS	100	100	0	0
PVC	0	0	100	1

The results of experiment 2 are shown in Table 5. The recovery of ABS was 98%, whereas the recovery of Teflon was 96%. During the experiment 2, the recoveries of ABS and Teflon were less than those of in the experiment 1. The reason is clear that the some flakes of ABS adhered to the wall of the separating cell, (Fig. 7). In addition, some flakes of the Teflon were discharged to the collecting cell due to the lack of time to become wet. Therefore, if a long agitation can be applied, the separating efficiency will sure be improved.

Table 5 Separation result of ABS and Teflon

Components	Float product		Sink product	
	Grade, (%)	Recovery, (%)	Grade, (%)	Recovery, (%)
ABS	96	98	2	2
Teflon	4	4	98	96



Fig.7. Flake adhere to the wall

4. SUMMARY AND CONCLUSIONS

The aim of this research is to separate PVC or Teflon from ABS. It is worth doing it because PVC will corrode the equipment when utilizing waste plastics for charging into blast furnaces, [6] and the price of the Teflon is far much higher than

that of the ABS. The result of the experiment showed that ABS was able to be adhered to the micro-bubbles and became hydrophobic despite being denser than water. On the other hand, PVC or Teflon was little influenced. The recoveries of the ABS and PVC in experiment 1 were both 100 %, whereas the recoveries of the ABS and Teflon in experiment 2 were 98 % and 96 %, respectively. These results indicated that the separation of plastics by micro-bubbles was a very efficient, cost-effective and eco-friendly technique, since high separation results can be achieved without the use of surfactants.

References

- [1] China Plastics Industry, 1005-5770 (2008) 03-0001-22, 1005-5570 (2009) 03-0001-22 (in Chinese),
- [2] Saitoh, K., Nagano, I., Izumi, s., 1976. New separation technique for waste plastics. *Resource Recovery and Conservation* 2, 127-145
- [3] Valdez, E. G., Wilson, W. J., 1979. Separation of plastics by floatation. US Patent NO. 4167477.
- [4] Buchan, R., Yarar, B., 1995. Recovering plastics for recycling by mineral processing techniques. *Journal of Metal* 2, 52-55
- [5] Fraunholz, N., Kooijman, S. J. M., Dalmijn, W. L., 2000. Flotation of plastics using combined treatments. In: *Proceedings of the XXIth International Mineral Processing Congress*, vol. B, July 23-30, 2000 Rome, pp. B12a-49-B12a-55.
- [6] G. Dodbiba, A. Shibayama, T. Miyazaki and T. Fujita, *Physical Separation in Science and Engineering*, 2003, Vol.12, NO.2, pp. 71-86

Recovery of Platinum from Cobalt-Rich Crust – Proposal of an In-situ Recovery Method

Li Pang Wang*, Daisuke Sato*, Gjergj Dodbiba*, Jun Sadaki*, Toyohisa Fujita*,
Atsushi Shibayama** and Hajime Hishita***

*Department of Systems Innovation, School of Engineering, The University of Tokyo, 7-3-1, Hongo, Bunkyo-ku, Tokyo, 113-8656 Japan

**Department of Material Process Engineering and Applied Chemistry for Environment, Faculty of Engineering and Resource Science, Akita University, 1-1, Tegata-Gakuen-Cho, Akita, 010-8502 Japan

***Deep-Sea Technology Team, Metals Mining Technology Group, Japan Oil, Gas and Metals National Corporation, Kanagawa, 212-8554 Japan

tt67102@mail.ecc.u-tokyo.ac.jp

Abstract: In order to recover trace of platinum (Pt) from Cobalt-Rich-Crust (CRC), a fundamental study of liberating CRC by electrical disintegration was carried out. The characteristics of electrical disintegration of CRC performed in distilled water and conductive solution were investigated. The results showed with the increase of the thickness of CRC, the applied voltage for the electric breakdown was also increased. Higher applied voltage made the particle size of CRC fragments smaller. When electrical disintegration was performed in conductive solution, the applied breakdown voltage and electric energy consumption needed was greatly increased since the majority of the current passed through the solution instead of CRC. However, it could be prevented by using coated discharge electrode, which makes electrical disintegration of CRC perform in seawater possible. Based on the result from the fundamental study, an in-situ recovery method of recovering Pt from CRC was proposed.

Key Words: Cobalt-Rich Crust, Platinum, Recovery, Electrical disintegration

1 INTRODUCTION

Cobalt-Rich Crust (CRC) is a kind of mineral deposit distributed on the slope or top of seamounts in the Middle and South of the Pacific Ocean at a depth of 800-2400 m. The main contents of CRC are oxides of manganese (Mn) and iron (Fe), as well as trace amounts of cobalt (Co), nickel (Ni), copper (Cu) and platinum (Pt). With the increase of Pt demand and for the safety supply of Pt, CRC is also considered to be a new Pt mineral resource in the future. However, since the Pt grade in CRC is extremely low (0.1-1 g/t in average), in order to recover 1 gram Pt, 1-10 ton CRC is needed to be excavated, crushed and smelted, which consumes a lot of energy and produces large amounts of solid wastes. For recovering Pt from CRC, more economical and effective method is required.

Liberation is very important for the separation of different materials in mineral beneficiation and recovery. Conventional liberation method for mineral processing is by mechanical comminution. Mechanical comminution disintegrates the material at random fragmentation or along the fragile fraction of its structure, however, crushed fragments include different kinds of components.

Different from mechanical comminution, electrical disintegration employs high voltage impulse to disintegrate the material. The high voltage current flows along the grain boundaries of minerals with different electrical parameters in it. Joule heat or the impact of the high voltage current causes the cracking along the boundary to make a precious separation of the different materials along the boundaries and gangue materials. It

is considered that electrical disintegration could selectively liberate the CRC compared with mechanical comminution.

For Pt recovery from spent catalysts, chloride containing solutions such as aqua regia or hydrochloric acid (HCl) with the addition of oxidant such as hydrogen peroxide (H₂O₂) has been used to leach out the Pt. Pt in the leach liquor is then separated by solvent extraction. In the recent years, seaweed biosorption or activated carbon adsorption has also been studied to remove toxic metals such as lead and cadmium as well as to recover valuable metals such as precious metals from various wastes due to their high adsorption capacity for the metal ions. It is considered that they could also be applied to recover the Pt from CRC.

In this study, the characteristics of liberating CRC by electrical disintegration in distilled water and conductive solution were investigated. Also the leaching conditions of Pt from CRC by HCl and H₂O₂ as well as the separation and recovery of Pt by seaweed and activated carbon were studied. Finally, an in-situ recovery method of recovering Pt from CRC was proposed.

2 MATERIAL AND APPARATUS

2.1 Materials

CRC samples obtained from the Japan Oil, Gas and Metals National Corporation (JOGMEC) were used in this study. The CRC samples were excavated from seamount near the Minamitori Island of Japan in the West Pacific Ocean. An illustration of one as-received CRC sample is shown in Photo 1. The as-received CRC samples composed of CRC and substrate rock. The substrate rock fractions were cut by band-sawer (LUXO, DIA V-19) and

removed off. Only the CRC fractions were used as experiment material. The chemical composition of the CRC fraction including Pt, Fe, Mn, Co, Ni and Cu is shown in Table 1.



Photo 1: - An illustration of one as-received CRC sample (Black fraction: CRC; brown fraction: substrate rock)

Table 1: Chemical composition of the CRC fraction

Pt	Fe	Mn	Co	Ni	Cu
0.22g/t	15.7%	16.4%	0.29%	0.35%	0.1%

2.2 Apparatus

The schematic diagram of the experimental setup of electrical disintegration in this study is shown in Fig.1. The specific parameters of the impulse high voltage generator are shown in Table 2. The impulse high voltage generator was manufactured by Pulse Electronic Engineering Co. Ltd., Japan. Electrical disintegration experiment on CRC was performed under wet conditions that the sample was immersed in liquid, since hazardous ozone would be produced when the high voltage was applied in the atmosphere. The CRC sample was placed between a rod-shape stainless electrode and a ground copper plate. The rod-shape electrode was 1 cm diameter with head sharpened. The former study shows head sharpened electrode possesses higher electricity discharging ability than round one. A coil type ammeter was placed around the ground code electrode and connected to the oscilloscope. The voltage between the impulse high voltage generator and ground electrode was measured by a probe connected to the oscilloscope. When the sample was broken by the impulse, the consumed energy E was calculated from the equation (1) by using products of the sum of the voltage V per period Δt and the sum of current I per voltage applied period Δt measured by the oscilloscope. [1,2]

$$E = \sum VI \Delta t \quad (1)$$

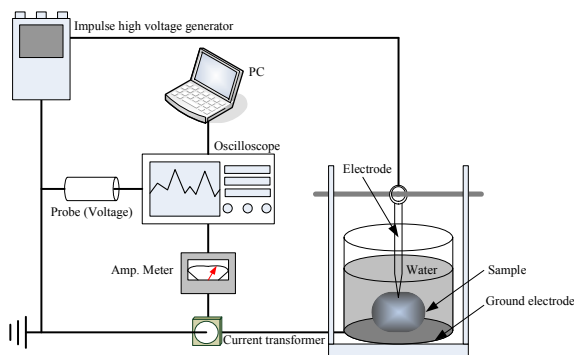


Figure 1: Schematic design of the experimental setup of electrical disintegration system [1]

Table 2: Specific parameters of impulse high voltage generator

Nominal Voltage	80 kV
Electrostatic Capacity	0.25 μ F
Maximum Charge Energy	800 J
Utilization Factor	more than 80 %

3 RESULTS AND DISCUSSIONS

3.1 Electrical Disintegration of CRC in distilled water

First of all, electrical disintegration of CRC in distilled water was performed. CRC samples were cut to different size by band-sawer. The sizes of CRC samples are shown in Table 3. Before experiment, these CRC samples were immersed in distilled water to force out the air existing in the cracks of the CRC.

Table 3: Size of CRC samples used for electrical disintegration in distilled water

Sample No.	Length (mm)	Width (mm)	Thickness (mm)	Weight (g)
S-1	50	20	20	37.5
S-2	50	20	60	79.6
S-3	50	20	25	42.3

For samples S-1, S-2, impulse voltage was applied and increased gradually until the breakdown occurred to find the least impulse voltage that was needed for the breakdown of CRC of different thickness. Meanwhile, higher impulse voltage was also applied to sample S-3 to be compared with the result of sample S-1 of almost the same thickness that was disintegrated by the least impulse voltage. The wave shapes of voltage and current during electrical disintegration were read from the oscilloscope, and the electricity consumption was also calculated according to equation (1). The CRC fragments after electrical disintegration were sieved and their size distribution was measured.

As an example, the photograph of sample S-3 before and after electrical disintegration is shown in Photo 2. It is clear to see that block CRC sample was liberated after electrical disintegration.

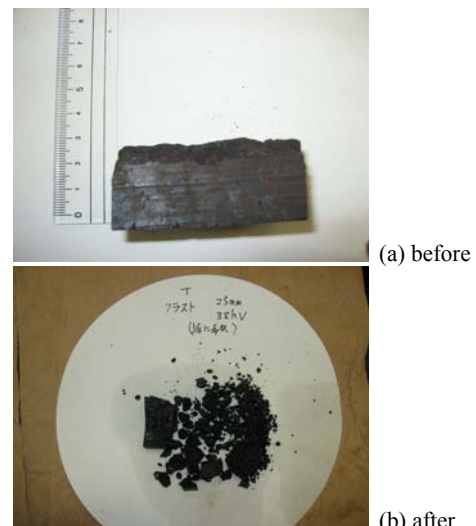


Photo 2: Sample S-3 before (a) and after (b) electrical disintegration

The characteristic values of electrical disintegration in distilled water of each CRC sample read from oscilloscope is shown in Table 4. The results showed that an increase in CRC thickness also increased the applied voltage needed for electric breakdown to occur. The value of intensity of breakdown is obtained from the maximum voltage divided by the sample thickness. The lower the intensity of breakdown the easier the breakdown occurs. The intensity of breakdown of S-2 is lower than S-1 and S-3, which implies that the ratio of crack friction in S-2 is higher than S-1 and S-3. When the least voltage needed for the breakdown to occur is applied, the energy consumption is almost the same. If applied voltage is higher than the least needed for the breakdown to occur, the energy consumption is also increased.

The size distribution of each CRC sample after electrical disintegration is shown in Fig.2. It is found that higher applied voltage made the size of CRC fragments smaller.

Table 4: Characteristic values of electrical disintegration in distilled water of each CRC sample

Sample No.	S-1	S-2	S-3
Thickness	20 mm	60 mm	25 mm
Weight	37.5 g	79.6 g	42.3 g
Applied Voltage	40 kV	60 kV	60 kV
Disintegration Time	20 μ s	30 μ s	20 μ s
Maximum Voltage	33 kV	50 kV	50 kV
Maximum Current	1.7 kA	2.2 kA	2.8 kA
Intensity of Breakdown	1.7 kV/mm	0.8 kV/mm	2.0 kV/mm
Energy Consumption	119 kWh/t	129 kWh/t	795 kWh/t

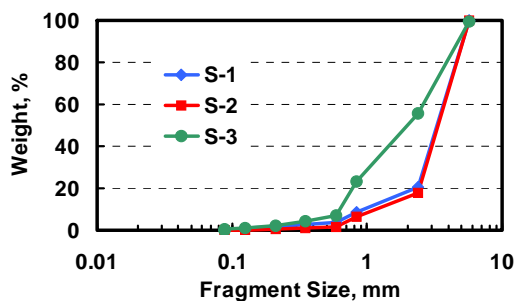


Figure 2: Size distribution of CRC fragments of S-1, S-2 and S-3 after electrical disintegration in distilled water

3.2 Electrical Disintegration of CRC in conductive solution

At first, in order to realize the effect of conductivity on the least applied voltage that make breakdown occur, electrical disintegration was performed in various solutions with different sodium chloride (NaCl) concentrations under the condition that the gap between the discharge electrode and the ground electrode was set to be 10 mm, whereas no CRC sample was put between the electrodes. The conductivity of each solution was measured. The result is shown in Table 5. It was found that with an increase in NaCl concentrations, the conductivity of solution and the least applied voltage needed for the breakdown to occur also increased.

Table 5: Conductivity of various NaCl solution concentrations and applied voltage that make breakdown occur needed

NaCl conc.(mol/l)	0.48	0.24	0.12	0.06	0.03
Conductivity (mS/cm)	47.9	25.0	13.2	7.05	3.48
Applied Voltage (kV)	—*	38	25	17	15

* breakdown not occurred

Second, one CRC sample (50mm x 20mm x 25mm) was put into above solutions and 80 kV applied voltage was discharged. Also the CRC sample was immersed into these solutions before the experiment to force out the air existing in the cracks of the CRC. As a result, the breakdown of the CRC sample occurred only in 0.03 NaCl solution. The characteristic values of electrical disintegration in 0.03 mol/l NaCl solution are shown Table 6. It was found that when electrical disintegration was performed in conductive solution, the applied breakdown voltage and electric energy consumption needed were greatly increased

Table 6: Characteristic values of electrical disintegration in 0.03 mol/l NaCl solution

Thickness	25 mm
Weight	31 g
Applied Voltage	80 kV
Disintegration Time	20 μ s
Maximum Voltage	45 kV
Maximum Current	2.7 kA
Intensity of Breakdown	1.8 kV/mm
Energy Consumption	636 kWh/t

The above experiments were performed by using bare discharge electrode. It was considered that the majority of the current flowed through the conductive solution instead of the CRC, thus the breakdown of CRC never occurred. In order to prevent the current from flowing through the conductive solution, a modified discharge electrode fully coated by resin except for the top of sharpened head was introduced as shown in Photo 3.



Photo 3: Resin-coated discharge electrode

Electrical disintegration of CRC in seawater by using electrode with and without resin-coated were carried out. The result is shown in Table 7. For the CRC sample with thickness of 10 mm, the breakdown of CRC in seawater never occurred when using bare electrode even the energy consumption was 1000 kWh/t. When using resin-coated electrode, the breakdown of CRC in seawater occurred when 80 kV voltages was applied. The energy consumption was 340 kWh/t. It is suggested that the

modified resin-coated discharge electrode could effectively prevent the current from flowing through the conductive solution and make the breakdown of CRC occur at lower applied voltage and energy consumption, which makes electrical disintegration of CRC in seawater possible.

Table 7: Characteristic values of electrical disintegration in seawater with and without electrode resin-coated

Electrode	not-coated	coated
Thickness	10 mm	10 mm
Weight	8.48 g	13.4 g
Applied Voltage	76 kV	80 kV
Disintegration Time	20 μ s	20 μ s
Maximum Voltage	32 kV	36 kV
Maximum Current	3.0 kA	4.4 kA
Intensity of Breakdown	3.2 kV/mm	3.6 kV/mm
Energy Consumption	1000 kWh/t	340 kWh/t
Breakdown	Not-happened	happened

3.3 Pt leaching from CRC by HCl and H₂O₂

The leaching conditions of Pt from CRC by HCl and H₂O₂ including parameters such as HCl concentration, H₂O₂ addition amount, leaching temperature, leaching time and solid-liquid ratio were investigated. The results showed more than 95 % Pt in the CRC was leached out by using HCl solution higher than 0.5 mol/L at a temperature of 30 °C for over 15 min with solid-liquid ratio less than 10 g/L when more than 1 vol.% H₂O₂ (30 wt.% H₂O₂ aqueous solution utilized) was added. Meanwhile, more than 95 % of other metals contained in CRC were leached out except for Fe.

3.4 Pt adsorption from CRC leaching solution by seaweed and activated carbon

Four kinds of seaweeds (*Undaria pinnatifida*, *Laminaria angustata*, *Enteromorpha linza* and *Gloiopeltis tenax*) and activated carbon were utilized as Pt adsorbent. Their adsorption abilities for Pt ion as well as selective adsorption properties for other coexisting metal ions contained in CRC (including Fe, Mn, Co, Ni and Cu) were investigated by using artificial solutions.

The results showed that all seaweeds achieved their best Pt adsorption capacity only at pH 2, whereas activated carbon possessed a high Pt adsorption ability over a wide pH range from pH 0 to 6 as well as in HCl solution up to 3 M. In selective adsorption except for Pt and Fe, other metal ions contained in CRC were rarely adsorbed by all seaweeds at pH 2. Only Pt was adsorbed by activated carbon in 3M HCl solution. All seaweeds and activated carbon possess high selective adsorption ability for Pt in low pH solution. It is found that seaweed and activated carbon are both effective adsorbents for recovering Pt from HCl leaching solution of CRC.

3.5 Proposal of an in-situ Pt recovery method

Based on the results from above fundamental studies, an in-situ Pt recovery method for recovering Pt from CRC is proposed. The schematic diagram is shown in Fig.3. One triple pipe is pulled down from ship to the CRC at seamount in deep sea. The triple pipe includes three parts, that is, resin-coated electrode, internal pipe and external pipe. In front of the triple pipe is a leak-proof rubber sucking disk. The resin-coated electrode is to perform electrical disintegration to liberate the CRC. Pt leaching solution including HCl and H₂O₂ is introduced through the

external pipe to leach the Pt from the liberated CRC fragments. The liberated CRC fragments and Pt leaching solution are air-lifted through the internal pipe to the adsorption tank in ship. Seaweed or activated carbon is added into the adsorption tank to selectively adsorb the Pt from the leaching solution.

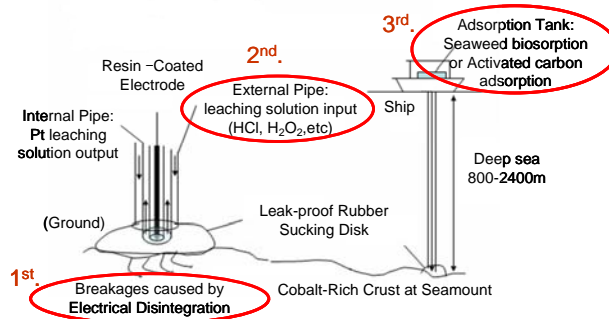


Figure 3: A schematic diagram of proposed in-situ Pt recovering system

4 CONCLUSIONS

In this present study, fundamental studies including CRC liberated by electrical disintegration, Pt leached out by HCl and H₂O₂, Pt adsorbed by seaweed and activated carbon were carried out. The results showed resin-coated discharge electrode could prevent the majority of the current from flowing through the conductive solution when electrical disintegration was carried out in conductive solution, which makes electrical disintegration of CRC in seawater possible. More than 95% Pt contained in CRC could be leached out by 0.5 mol/L HCl and 1 vol.% H₂O₂ in 30°C after 15 minutes. Except for Pt and Fe, other metal ions contained in CRC were rarely adsorbed by all seaweeds at pH 2. Only Pt was adsorbed by activated carbon in 3M HCl solution. All seaweeds and activated carbon possess high selective adsorption ability for Pt in low pH solution. Based on the results, an in-situ Pt recovery method was proposed.

Acknowledgement Financial support and experimental materials from the Japan Oil, Gas and Metals National Corporation (JOGMEC) is acknowledged. Also the present research work was supported in part through the GCOE Program, “Global Mechanical Systems Innovation,” by the Ministry of Education, Culture, Sports, Science and Technology, Japan.

References

- [1] Wang, L. P., Sato, D., Dodbiba, G., Okaya, K., Sadaki, J., Fujita, T., Shibayama, A. and Hishita, H., “Fundamental Study on the Electrical Disintegration of Cobalt-Rich-Crust for Platinum Recovery,” Resources Processing, Vol.56, No.1, pp.26-32 (2009). (in Japanese)
- [2] Yoshimi, I., Shibayama, A., Fujita, T., Abe, K., Miyazaki, T., Sato, M. and Yen, W. T., “Liberation of Materials by Electrical Disintegration for Recycling,” Int. J. Soc. Mater. Eng. Resour., Vol.10, No.1, pp.66-70 (2002).

DEM Simulation on Strength and Deformation Characteristics of Fiber-Cement-Stabilized Soil

Hiroshi Takahashi* and Naoki Konda*

*Department of Environmental Studies, Graduate school of environmental studies, Tohoku University
6-6-20, Aoba, Aramaki, Aoba-ku, Sendai, 980-8579 Japan

htaka_fy07009@mail.kankyo.tohoku.ac.jp

Abstract: Fiber-cement-stabilized method is an effective way to recycle high water content. The modified soil by this method has several features such as high failure strength and high failure strain. Furthermore, it has already confirmed that this modified soil has high dynamic strength. However, the quality of the modified soil produced by this method is not constant and depends on the water content of the mud. Experiments to obtain the strength characteristics of the modified soil are necessary, but they are ineffective and uneconomic. In this study, a model to analyze deformation and strength characteristics of the soil was developed by using Distinct Element Method (DEM). Before the model of fiber-cement-stabilized soil is developed, the model of conventional cement-stabilized soil was developed, and next, fiber element was added to the model. By using the developed model, numerical simulation on strength and deformation was carried out. It was confirmed through the comparison between experimental results and simulated ones that the new model developed here was almost reasonable.

Key Words: Fiber-cement-stabilized soil, Distinct Element Method (DEM), Soil Improvement, Recycling

1 INTRODUCTION

In Japan, strong earthquakes have occurred frequently and ground damages are serious problems. Generally, the ground damages are divided into two types. One is liquefaction. If the soil around structures is shaken by earthquake, the pore water pressure in the soil will increase and the connections between soil particles will be broken. Then, the soil behaves like liquid, and it makes the structures be suspended in the liquefied soil. The other is a landslide. If the strength of soil is decreased by earthquake, the surface soil on embankment will slide down.

By the way, recently, many kinds of construction wastes are recycled to create recycling society. High-water content mud discharged from construction sites is not exception. Previously, cement-stabilized method was used to recycle the high-water content mud. In this method, cement was added to improve the strength and modified soil was used as embankment soil or landfill materials. However, although the strength of modified soil is very high, the failure strain is extremely small compared with the one of ordinary soil. That is, cement-stabilized soil is hard but brittle. In

addition, it is already reported that the durability of cement-stabilized soil for drying and wetting is very low. Therefore cement-stabilized soil does not have enough failure strength and failure strain for the use of embankment soil and landfill materials.

In order to increase the quality of modified soil which is recycled from high-water content mud, we have already developed a new recycling method by using paper debris (fragments of newspaper) and powder polymer[1]. Since the paper debris is mixed in the mud, the modified soil is called fiber-cement-stabilized soil. It was already confirmed that the failure strength and failure strain of fiber-cement-stabilized soil were much larger than those of cement-stabilized soil[1]. This means that fiber-cement-stabilized soil is the best for embankment soil and landfill materials.

The principle of fiber-cement-stabilized soil method is as follows: Fig. 1 shows the concept of new recycling system of the construction sludge by using paper debris and polymer. Fig.1(a) shows the initial construction sludge. Soil particles are free to move in the water. Therefore, the construction sludge behaves as "fluid". After the paper debris is added in

the construction sludge, the water is absorbed in the paper debris and the superficial water content of the construction sludge decreases as shown in Fig.1(b). After the mixtures of water and paper debris are agitated, then powder polymer is added and mixtures are still agitated. Then powder polymer solves in the water and attaches on the surface of the soil particles. Furthermore, the clusters of soil particles are made by the bridging effect as shown in Fig.1(c). Finally, the chemical flocculants are added to produce the modified soils. If the modified soils are used for planting, it is not necessary to add the cement. However, if the modified soils are used as landfill materials, the addition of the cement is needed to obtain the necessary strength.

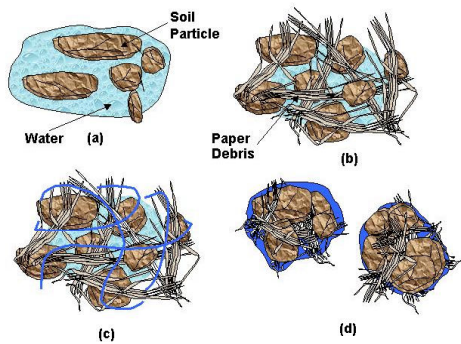


Fig.1 A concept of new recycling system for high water-content mud

The modified soil by this method has several features such as high failure strength and high failure strain[1]. Furthermore, it has already confirmed that this modified soil has high dynamic strength[2]. However, the quality of the modified soil produced by this method is not constant and depends on the water content of the mud. Experiments to obtain the strength characteristics of the modified soil are necessary, but they are ineffective and uneconomic. Therefore, the purpose of this study is to develop a model to predict the deformation and strength characteristics of modified soil by using Distinct Element Method(DEM).

2 Development of simulator by using Distinct Element Method

In this study, Distinct Element Method (DEM) is used to develop the simulator. DEM is often used to analyze the behavior of granular materials [3]. The principle of DEM is to analyze the motion of elements by obtaining an equation of motion for each element and by solving the equation of motion in the time region using difference approximation method. In this study, DEM is applied for the modified soil by

assuming that the modified soil is an aggregation of many elements. In the calculation of DEM, an equation of motion is given in each element to analyze the behavior of elements. In order to derive the equation of motion, it is necessary to estimate the forces acting among elements. Usually, the model as shown in Fig.2 is used. When the two elements contact each other, a spring and a dashpot are introduced between two elements in the normal and tangential direction. The spring and dashpot indicate the effect of elasticity and viscous resistance, respectively. Furthermore, a slider is set in the tangential direction to consider the frictional effect. In this study, two-dimensional analysis was assumed. So, the shape of the element was assumed to be circle.

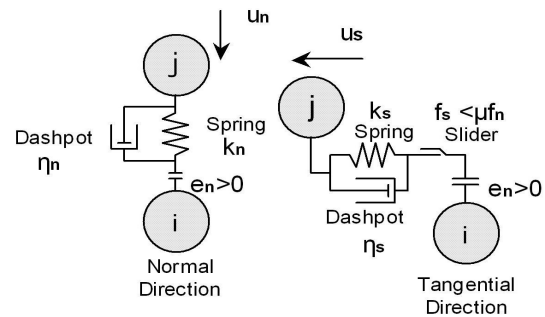


Fig.2 DEM model

In order to realize the modified soil by many elements in the simulation, it was assumed that the elements contacting each other are bonding state[4,5]. In this bonding state, when the elements come closer, repulsive force will act by the spring between elements, and when the elements move apart, tensile force will act by the spring between elements. If the force acting between elements is beyond the limitation, the connection is cut and after that, the tensile force does not act even if the elements are apart. The part which the connection is cut is regarded as a micro crack and the whole breakage of the modified soil is occurred by growing the micro cracks. If either tensile force or shear strength is beyond the limitation, it is assumed that connection between elements is cut. The failure criterions are expressed as follows:

$$\sigma > S \quad S: \text{tensile strength}$$

$$\tau > c + \sigma \cdot \tan \phi \quad c: \text{cohesive force}$$

$$\phi: \text{internal friction angle}$$

3 Simulation of cement-stabilized soil

3.1 Modeling of cement-stabilized soil

Fig.3 shows the results of unconfined compression test for cement-stabilized soil and fiber-cement-

stabilized soil made from same high water content mud. The initial water content of the mud was 150%. Additive amount of paper debris, powder polymer, chemical flocculants and cement were 60kg/m^3 , 7kg/m^3 , 1kg/m^3 and 100kg/m^3 , respectively.

Fiber-cement-stabilized soil has higher failure strength and failure strain compared with cement-stabilized soil. The difference between these two soils is the existence of fiber materials. That is, fiber-cement-stabilized soil contains fiber materials, on the other hand, cement-stabilized soil does not contain fiber materials. Therefore, it can be considered that the strength features of fiber-cement-stabilized soil come from the connections between soil particles and fiber materials.

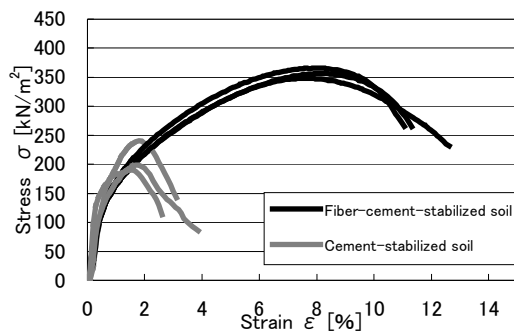


Fig.3 Stress-strain diagram for fiber-cement-stabilized soil and cement-stabilized soil

Since the difference between fiber-cement-stabilized soil and cement-stabilized soil is the fiber, it is effective to make a model of cement-stabilized soil firstly and then to add the fiber model to the cement-stabilized soil model. In addition, by dividing the fiber model from the cement-stabilized soil model, it will become easier to analyze the relationship between the actual amount of fiber materials and simulation parameters. So, before developing the fiber-cement-stabilized soil model, the cement-stabilized soil model was developed. In order to develop the cement-stabilized soil model, unconfined compression test was carried out on computer, and by comparing the simulated results with the experimental ones, the most accurate parameters in DEM simulation were determined.

In DEM simulation, it can be considered that tensile strength, cohesive force and internal friction angle will affect the results of unconfined compression test, because they are key factors related to the breaking of connections between elements. Furthermore, it is considered that a spring constant and damping ratio will affect Young's modulus. Therefore, many simulations were carried out by changing above five

parameters (spring constant in normal direction, damping ratio, tensile strength, cohesive force and internal friction angle), and the most appropriate values for these parameters were determined by trial and error method.

By the way, tensile strength, cohesive force and internal friction angle are physical properties which can be obtained by carrying out the soil tests, and the actual properties should be used in the simulator. However, it is well-known that if the above mentioned physical properties obtained by the soils tests are used in DEM simulation, the object will be broken by smaller force than actual failure force [6]. Therefore, it is reported that actual physical properties obtained from the soils tests should not be used directly and they have to be determined by trial and error method based on the actual physical properties obtained from the soils tests.

3.2 The results of simulation

Figs.4-8 show the effect of above mentioned parameters on failure stress. Spring constant in normal direction does not affect the failure stress. But, as it affects the gradient of stress-strain curve, failure strain decreased with increasing the spring constant. Damping

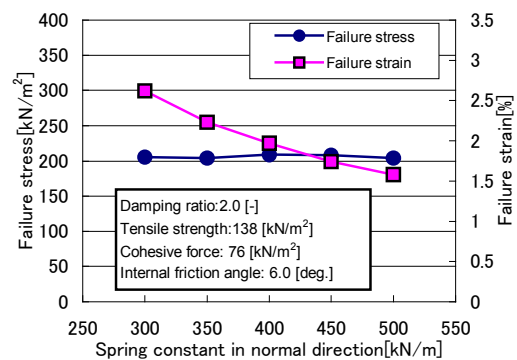


Fig.4 Relationship between spring constant of normal direction and failure stress

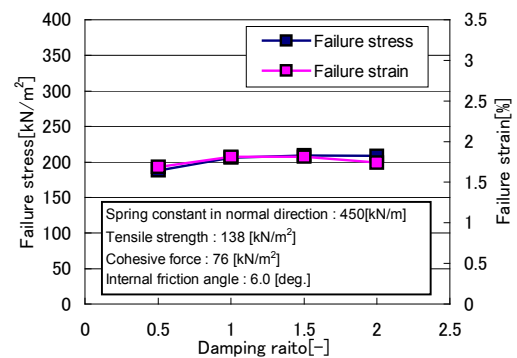


Fig.5 Relationship between damping ratio and failure stress

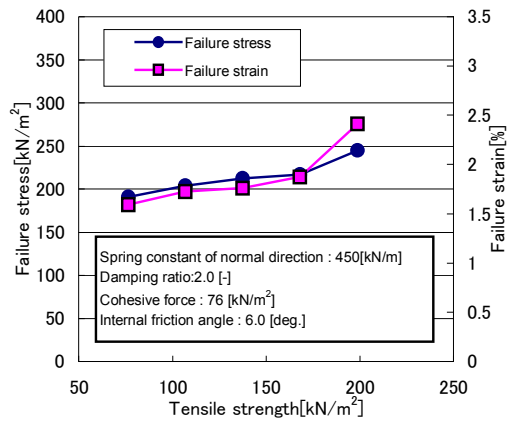


Fig.6 Relationship between tensile strength and failure stress

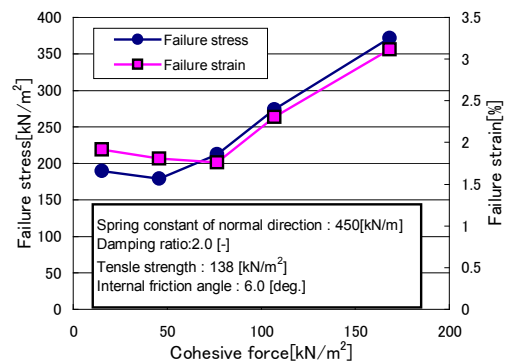


Fig.7 Relationship between cohesive force and failure stress

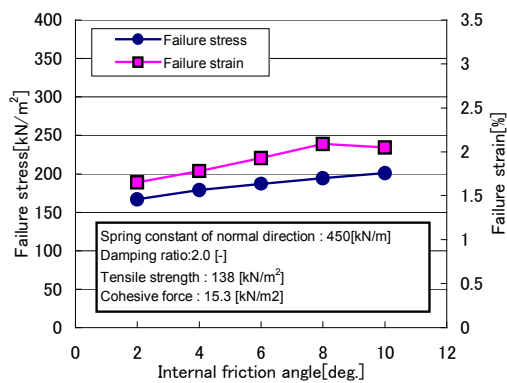


Fig.8 Relationship between internal friction angle and failure stress

ratio does not affect failure properties neither even if it was set at very high values. Tensile strength, cohesive force and internal friction angle that are factors in failure criterion related to the connection between elements affect the failure properties largely. From the

results in Figs.6-8, the most appropriate parameters were determined by comparing the simulated results with the experimental ones for unconfined compression tests by trial and error method.

3.3 The problems of the cement-stabilized soil model

Table 1 shows the values of parameters used in this simulation. These values were determined by trail and error method.

Fig.9 shows the simulation result of unconfined compression test obtained by using the parameters shown in Table 1. By setting the parameters accurately, it is possible to coincide with the simulated result and experimental one for failure stress and failure strain. However the whole stress-strain curve of simulation result is much different from the one of experimental result. In the experimental result, stress increases plastically with increasing the strain, and then it decreases gradually after reaching the peak value (failure stress). On the other hand, in the simulation result, stress decreases elastically with increasing the strain, and then stress decreases rapidly after reaching the peak value(failure stress), so the simulation result is just like the one of unconfined compression test for rocks. This tendency appeared no matter how the parameters were set. That is, this model cannot simulate the strength properties of cement-stabilized soil appropriately. There are several reasons why simulated results disagree with experimental results. One of the reasons is the difference of loading speed. In the experiments, the loading speed was 1 mm/min based on the test standard. On the other hand, the loading speed in the simulation was 10,000 mm/min and this is much larger than that in the experiments. Of course, it is the best to coincide both loading speed, but there are two reasons why such a huge loading speed was used in the simulation. The one is the simulation cost(time). Since the time interval of calculation was 10^{-6} sec., it will take about 1 month to complete the simulation by personal computer(PC) if the loading speed is set to be 1 mm/min, and this is unrealistic. The other reason is the effect of damping ratio on the failure stress and failure strain. It is considered that damping ratio is related to the loading speed, but as mentioned before, failure properties is not affected by the damping ratio. So, it was assumed that the effect of loading speed in the simulation is small. By considering two reasons, large loading speed was used in the simulation to reduce the simulation cost(time). The experiment by high loading speed was carried out, but reasonable results were not obtained as yet. So, in the next step, the effect of loading speed should be investigated. The other reason is that the soil features are not well modeled in the simulation. That is, it is necessary to develop a new

model to simulate the behavior of cement-stabilized soil accurately.

Table1 Parameters used in this simulation

Spring constant	450 [kN/m]
Damping ratio	2.0 [-]
Tensile strength	138 [kN/m ²]
Cohesive force	76 [kN/m ²]
Internal friction angle	6.0 [deg.]

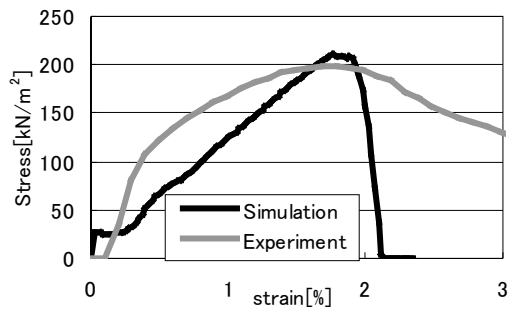


Fig.9 Comparison between experimental results and simulated ones

3.4 Improvement in the model

In order to simulate the plastic properties of cement-stabilized soil, two improvements were added to conventional model.

It is considered that the concept of connection between elements for soil is different from that for rock. For example, in direct shear test apparatus, even if the soil breaks by shear, the soil particles still keep the connection at the failure plane. On the other hand, if the rock breaks by shear, connection between rock particles are absolutely cut. Therefore, it can be considered that connections between soil particles are occurred by interstitial material such as water. In order to simulate this effect, the improvement that forces acting between elements were assumed by “pore spring” and “element spring”, and “pore spring” was added to the conventional model. Fig10 shows the new dynamical model with pore spring and element spring. Element spring acts only when elements are compressed regardless of the existence of connection between elements. Pore spring always acts if elements connect each other, but if the connections are broken, pore spring acts only when the elements are compressed. By adding this technique, it will be possible to simulate the effect by interstitial material. In addition, the criterion was modified. In the convention model, connection is broken if the forces acting between elements are beyond the limit in normal direction or tangential

direction. But, as mentioned above, soil particles keep connecting even if the slide occurs by the shear. For this reason, the criterion in tangential direction was deleted. Therefore, connections between elements will be broken only when the forces in normal direction are beyond the failure limit.

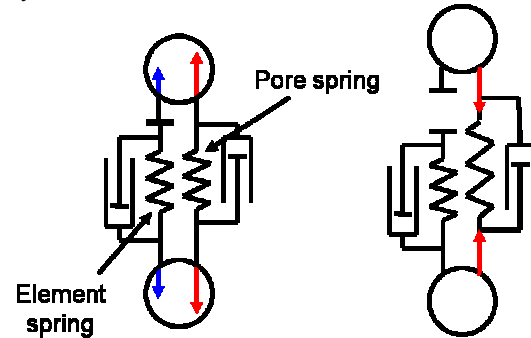


Fig.10 Modified contact model used in this simulation

3.5 The simulation result with modified model

By using the modified model of cement-stabilized soil, the most accurate parameters were determined. The effects of these parameters on the simulation results of unconfined compression tests on computer showed the same tendency as the one by conventional model. The most accurate parameters were determined by trial and error method. Table 2 shows the values of the parameters and Fig.11 shows the simulation results of unconfined compression test obtained by using the new model with the parameters shown in Table 2.

As well as the conventional model, by setting the parameters accurately, it is possible to coincide with the simulated result and experimental one for failure stress and failure strain. Furthermore, the stress decreases gradually after reaching the failure stress just like experimental result. However, elastic increasing of the stress with increasing the strain like rocks still appears in this result. So, in order to simulate the plastic behavior of cement-stabilized soil, more improvement is necessary for this model.

Table2 Parameters used in this simulation

Element spring constant of normal direction	400 [kN/m]
Pore spring constant of normal direction	200 [kN/m]
Damping ratio	2.0 [-]
Tensile strength	45.9 [kN/m ²]
Cohesive force	107 [kN/m ²]
Internal friction angle	4.0 [deg.]

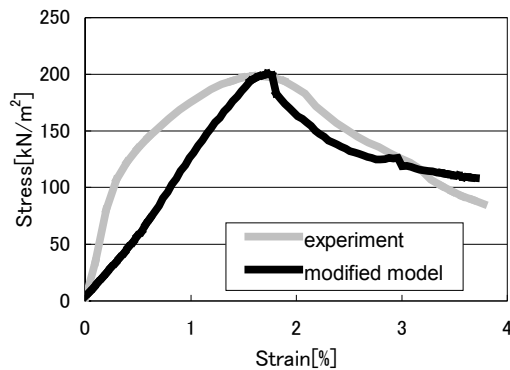


Fig.11 Comparison between experimental results and simulated ones obtained by modified model

4 Modeling of fiber-cement-stabilized soil

As mentioned above, adding the fiber model accurately to the cement-stabilized soil model, it is considered that the model of fiber-cement-stabilized soil will be developed because the large failure stress and failure strain of fiber-cement stabilized soil come from the existence of fiber materials. In the ordinary DEM simulation, the force will act only on particles in contact with. However, as the fiber materials and soil particles intertwine each other, the force will act on distantly-positioned particles by fiber materials. Therefore, in order to model this effect, following techniques are considered.

(1) In the fiber-cement-stabilized soil model, the connections by fiber materials are added between distantly-positioned elements.

(2) Considering the properties of fiber material, it is assumed that another force which is different from the one by spring will act on elements connected by fiber materials.

A new model of fiber-cements-stabilized soil with these techniques is now under consideration.

5 Conclusions

In this study, firstly the cement-stabilized soil model was developed, and then the fiber model was considered. By using the developed model, DEM simulations for unconfined compression tests were carried out. The conclusions were summarized as follows:

(1) The values of simulated failure stress and failure strain were almost the same as the experimental ones. So, it is possible to predict the failure stress and failure strain of cement-stabilized soil by using the developed model. However, there is a large difference between simulated stress-strain curve and the one in the experimental results.

(2) By adding the pore spring to the cement-stabilized soil model, and improving the failure criterion of connections between elements, the stress decreased gradually after reaching the failure stress like experimental result. But elastic increasing of stress like rock still appears. Therefore, further modification is still necessary.

(3) The concept of fiber-cement-stabilized soil model was described.

References

- [1]Mori M., Takahashi H., Ousaka A., Horii K., I Kataoka, Ishi T. and Kotani K., "A Proposal of New Recycling System of High-Water Content Mud by using Paper Debris and Polymer and Strength Property of Recycled Soils", J. of the Mining and Materials Processing Institute of Japan, Vol.119, No.4-5, pp.155-160, (2003).
- [2]Takahashi H., Takahashi K. and Mori M., "Experimental Study on Dynamic Strength of Fiber-Cement-Stabilized Soil", Proc. of the 4th Symposium on Sediment-Related Disasters, Vol.1, pp.1-5, (2008).
- [3]Cundall P.A. and Strack O.D.L., "A discrete numerical model for granular assemblies", Geotechnique, 29[1], pp.47-65, (1979).
- [4]Izumi W., "Numerical Simulation on Breaking of Boulders by Hydraulic Breaker", Graduate Thesis, Tohoku University, (2001).
- [5]Sato T., "Study on Mechanism of Rock Breaking by Disc Cutter", Master Thesis, Tohoku University, (2003).
- [6]Hakuno M., "Hakai no Simulation", Tokyo: Morikita Shuppan Co.Ltd., pp.10-55, (1997).

A New Recycling System of Waste Gypsum Board Paper : Application of Waste Gypsum Board Paper for Soil Improvement

Hiroshi Takahashi* and Hirokazu Kanahama*

* Department of Environmental Studies, Graduate School of Environmental Studies, Tohoku University, 6-6-20, Aoba-Aramaki, Aoba-ku, Sendai, 980-8579 Japan
htaka@mail.kankyo.tohoku.ac.jp

Abstract: We have already developed a new recycling system for the construction sludge by using paper debris (fragments of the newspaper) to increase the recycling rate of the construction sludge. In this study, the applicability of waste gypsum board paper instead of paper debris was investigated. The waste gypsum board paper was crushed by hammer mill and crushed paper was used in fiber-cement-stabilized-soil method. It was found that the failure strength and failure strain of soil specimens by using crushed paper are almost the same as those of soil specimens by using fragments of old newspaper. That is, it was confirmed that the crushed paper can become a substitute of the fragments of old newspaper. As the price of old newspaper is increasing rapidly, this means that the cost reduction will be possible.

Key Words: Gypsum Board Paper, Fiber-Cement-Stabilized Soil, Soil Improvement, Recycling

1 INTRODUCTION

Construction sludge is the typical high water-content mud and is produced more than 10 million ton per year from the construction sites in Japan. However, as the water content of the construction sludge is very high, it is very difficult to reuse the construction sludge directly. Consequently, the recycling rate of the construction sludge is extremely low. Therefore, we have already developed a new recycling system of high water-content mud by using the paper debris (fragments of the newspaper) and polymer in order to increase the recycling rate of the construction sludge [1,2]. By using this system, 200-500% water content mud has been modified to the landfill materials by 20-30 minutes mixing process. Since the paper debris is mixed in the mud, the modified soils are called fiber-cement-stabilized soils. When the water content in the mud is very high, a large amount of paper debris is necessary in this recycling system. However, recently, the price of paper debris is increasing rapidly, resulting in the increase of the recycling cost. Therefore, a new material which can be used as a substitute of the paper debris is strongly desired.

By the way, the amount of waste gypsum board discharged from the dismantling sites is increasing every year. However, since the waste gypsum boards are one of the difficulty processing materials and many local governments have troubles to process them. The gypsum boards consist of gypsum and board papers. Although there are some methods to recycle gypsum, most of the board papers are not recycled because if

the gypsum powder is attached on the surface of the board papers, recycling of board paper to the ordinary paper is very difficult.

In this study, the use of gypsum board paper is focused as a substitute of paper debris. If the board paper can be used as a substitute of paper debris, the reduction of the recycling cost and the increase of the recycling rate of gypsum board paper will be possible. Furthermore, there is no problem in our new recycling system even if the gypsum powder is attached on the surface of the board papers.

Therefore, the purpose of this study is to investigate the possibility to use the gypsum board paper as a substitute of paper debris in the fiber-cement-stabilized soil method.

2 PRINCIPLE OF FIBER-CEMENT-STABILIZED SOIL METHOD

Fig. 1 shows the concept of new recycling system of the construction sludge by using paper debris and polymer. Fig.1(a) shows the initial construction sludge. Soil particles are free to move in the water. Therefore, the construction sludge behaves as "fluid". After the paper debris is added in the construction sludge, the water is absorbed in the paper debris and the superficial water content of the construction sludge decreases as shown in Fig.1(b). After the mixtures of water and paper debris are agitated, then powder polymer is added and mixtures are still agitated. Then powder polymer solves in the water and attaches on the surface of the soil particles. Furthermore, the

clusters of soil particles are made by the bridging effect as shown in Fig.1(c). Finally, the chemical flocculants are added to produce the modified soils. If the modified soils are used for planting, it is not necessary to add the cement. However, if the modified soils are used as landfill materials, the addition of the cement is needed to obtain the necessary strength.

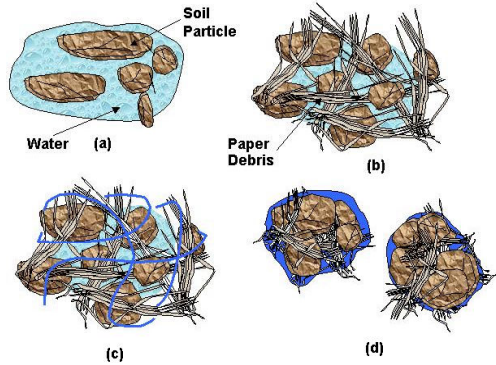


Fig.1 A concept of new recycling system for high water-content mud

3 SPECIMENS

Fig.2 and Fig.3 show the ordinary paper debris and gypsum board paper discharged from intermediate treatment plants, respectively.



Fig.2 Ordinary paper debris used in the fiber-cement-stabilized soil method



Fig.3 Gypsum board paper discharged from intermediate treatment plants

Ordinary paper debris is made in the special paper factories and the size of it is about 15mm squares. As the paper debris is thin and is easy to be broken up into fibrous, this can absorb the water in the mud. On the other hand, as shown in Fig.3, the board paper is a little hard and cannot absorb the water in the mud, it can be considered that this board paper does not fit in the fiber-cement-stabilized soil method in this state. That is, a criteria whether the paper is suitable for fiber-cement-stabilized soil method is the ability of water absorb. Therefore, we tried to crush the board paper and to obtain the crushed materials. In this experiment, a hammer mill as shown in Fig.4 was used. This machine can control the size of the crushed materials by changing the mesh size of the filter installed to the outlet of the machine. In this study, the crushing size was defined by the mesh size of the filter. Crushing size was 3mm, 6mm and 11mm. Fig.5 and Fig.6 show the photographs of crushed board paper and the one obtained by microscope.



Fig.4 Hammer mill used in this study



Fig.5 Crushed board paper (crushing size is 3mm)



Fig.6 Photograph obtained by microscope (100 times)

As shown in Fig.5, the crushed board paper is just like cotton. Furthermore, as shown in Fig.6, the massive board paper is broken up into fibrous state. So, it is considered that the crushed board paper will fit the fiber-cement-stabilized soil method.

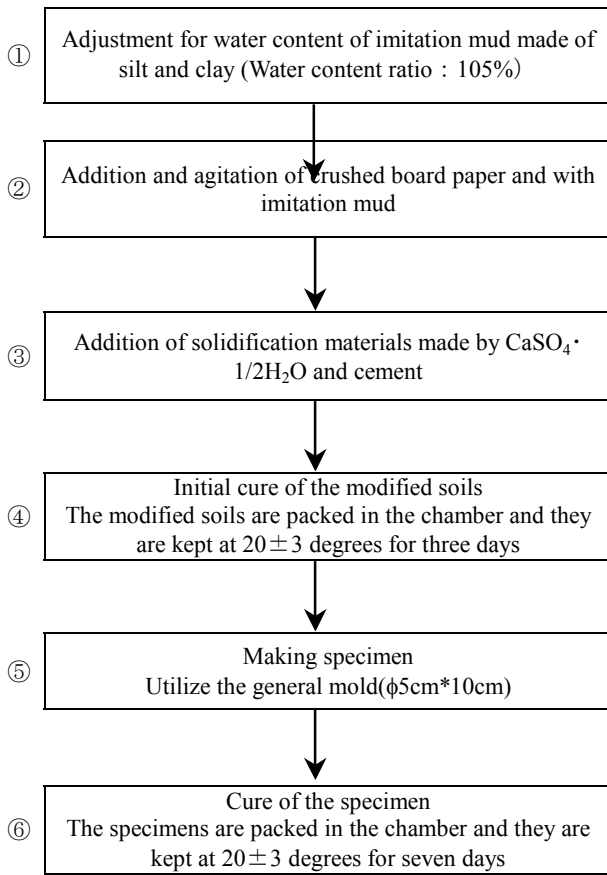


Fig.7 Flowchart of making specimen of fiber-cement stabilized soil.

Fig.7 shows the flowchart of making specimen of the fiber-cement-stabilized soil. Silt and clay were mixed by the weight ratio of 40:60, and the imitation mud was made by adding the water. The amount of water was adjusted so that the water content becomes 105%. In creation of the fiber-cement-stabilized soil, crushed board paper mentioned above was mixed with the imitation mud. The addition rate of crushed board paper was changed as 25, 65 and 85 kg/m³. The next, the solidification material by CaSO₄·1/2H₂O and cement were mixed. Solidification material by CaSO₄·1/2H₂O was made by heating the gypsum powder in the electric furnace at 180 degrees for 1 hour. The addition ratio of solidification material by CaSO₄·1/2H₂O and cement was changed as [200:50], [150:60] and [80:80](kg/m³). Then, specimens were made by using the fiber-cement-stabilized soil and the standard mold of 50mm diameter*100mm height. Then, they were cured for 7 days at 20±3 degrees.

In each unconfined compression test, 3 specimens were used and the unconfined compressive strength of the specimens were measured. Then, averaged value was calculated.

4 EXPERIMENTAL RESULTS ON STRENGTH

Prior to the unconfined compression tests, the target value for the failure strength and failure strain were set in order to obtain the optimum addition rate of crushed board paper and solidification materials. The target values were determined as follows according to the previous research[3]:

Failure strength = more than 200 kN/m²

Failure strain = more than 5 %

Fig.8 shows an example of the relationship between addition rate of crushed board paper and failure strength with the crushing size as a parameter. Fig.9 shows an example of the relationship between addition rate of crushed board paper and failure strain with the crushing size as a parameter. As shown in Fig.8, the failure strength increased with increasing the addition rate of crushed board paper and all experimental results satisfied the target value. The effect of crushing size on the failure strength was not observed. Failure strain increased a little with increasing the addition rate of crushed board paper or

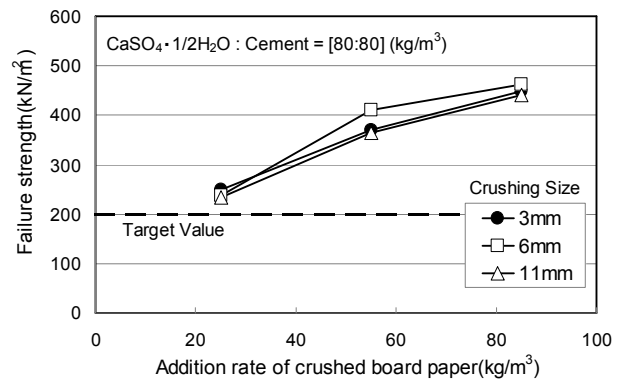


Fig.8 Relationship between addition rate of crushed board paper and failure strength

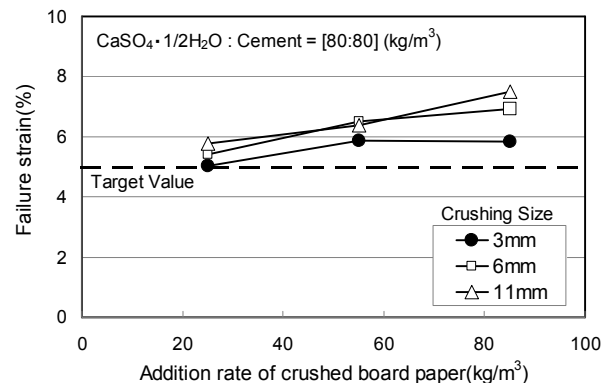


Fig.9 Relationship between addition rate of crushed board paper and failure strain

showed almost constant regardless of the addition rate of crushed board paper. The effect of crushing size on the failure strain was the same as the one for failure strength. Since the effect of crushing size on strength characteristics was not observed, we concluded that the 11mm was the best for crushing size in this experiment, because smaller size crushing requires the longer time for crushing.

Fig.10 shows the effect of the ratio of solidification material on failure strength. As the solidification ability of cement is larger than that of $\text{CaSO}_4 \cdot 1/2\text{H}_2\text{O}$, the failure strength of fiber-cement-stabilized soil increased with increasing the amount of cement. If the ratio of solidification material is [80:80], only 25kg/m^3 crushed board paper is enough to satisfy the target value. In our previous system, about 55kg/m^3 paper debris is necessary for 105% water content mud. 25kg/m^3 crushed paper is about half of the one for ordinary paper debris.

Fig.11 shows the effect of the ratio of solidification material on failure strain. When the ratio of solidification material is [80:80], all results satisfy the target value regardless of the addition rate of crushed board paper. Therefore, it is considered that if the minimum crushed board paper is desirable, the ratio of solidification material should be [80:80].

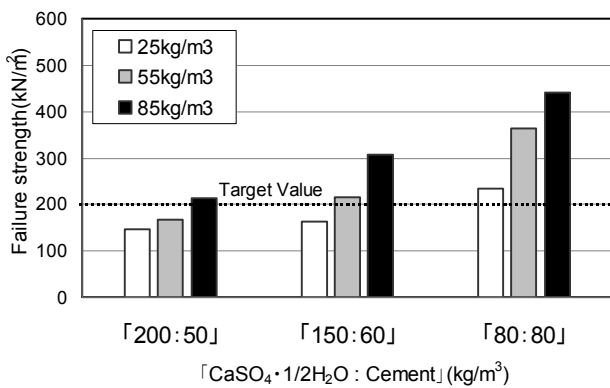


Fig.10 Effect of the ratio of solidification material on failure strength

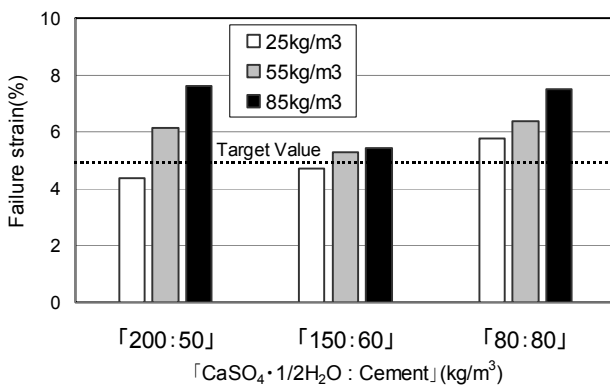


Fig.11 Effect of the ratio of solidification material on failure strain

Fig.12 shows the comparison between the failure strength of modified soils by using ordinary paper debris and the one of modified soils by using crushed board papers. Fig.13 shows the comparison between the failure strain of modified soils by using ordinary paper debris and the one of modified soils by using crushed board papers. The failure strength of modified soils by using crushed board papers is a little less than that of modified soils by using ordinary paper debris, but they are close each other and the difference is a quite small. Furthermore, the failure strain of modified soils by using crushed board paper is larger than that of modified soils by using ordinary paper debris.

Fig.14 and Fig.15 show the photographs of modified soils by using ordinary paper debris and crushed board paper, respectively. These photographs were taken after unconfined compression tests were over. As shown in these figures, the soil particles and fiber materials are intertwined well each other and structure is both similar. By considering above mentioned results, it can be concluded from these figures that the crushed board paper can become a substitute of paper debris and can be applicable to the fiber-cement-stabilized soils method.

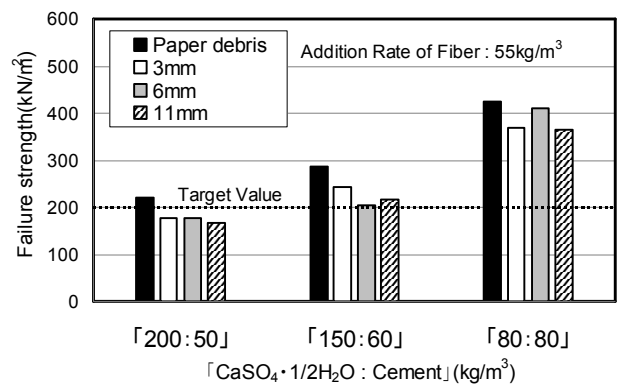


Fig.12 Comparison between the failure strength of modified soils by using ordinary paper debris and the one of modified soils by using crushed board paper

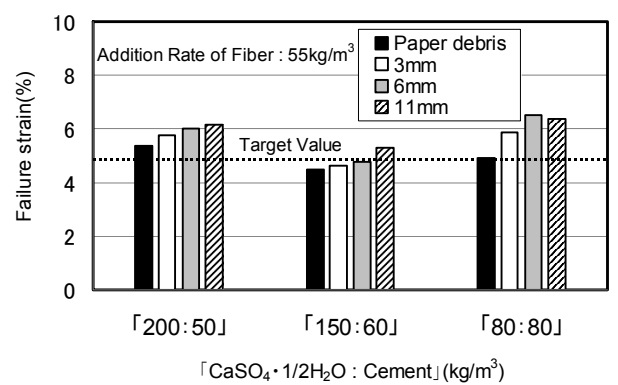


Fig.13 Comparison between the failure strain of modified soils by using ordinary paper debris and the one of modified soils by using crushed board paper



Fig.14 Photograph of modified soils by using ordinary paper debris



Fig.15 Photograph of modified soils by using crushed board paper

5 CONCLUSIONS

In this study, the applicability of gypsum board paper to the fiber-cement-stabilized soil method was experimentally investigated. First of all, the board paper was crushed by the hammer mill and modified soils were made by using crushed board paper. It was confirmed through the unconfined compression tests that the crushed board paper can be used as a substitute of paper debris and can be applicable to the fiber-cement-stabilized soil method.

ACKNOWLEDGMENT

This study is financially supported by Miyagi Prefecture 3 R new technical research development subsidy. The authors appreciate their financial support.

References

- [1] Mori M., Takahashi H., Ousaka A., Horii K., I Kataoka, Ishi T. & Kotani K., "A Proposal of New Recycling System of High-Water Content Mud by using Paper Debris and Polymer and Strength Property of Recycled Soils," *J. of the Mining and Materials Processing Institute of Japan*, Vol.119, No.4-5, pp.155-160, (2003).
- [2] Takahashi H., Mori M., Kumakura K., Otani M., and Ishi T., "Study on the Recycling System of Lightweight Fiber-Stabilized Landfill Materials from High-Water Content Construction Sludge", *J. of the Society of Materials Engineering for Resources of Japan*, Vol.16, No.1, pp.21-26, (2003).
- [3] Mori M., Takahashi H. and Kumakura K., "An Experimental Study on the Durability of Fiber-Cement-Stabilized Mud by Repeated Cycle Test of Drying and Wetting," *J. of the Mining and Materials Processing Institute of Japan*, Vol.121, No.2-3, pp.37-43, (2005).

Material conversion from various incinerated ashes using alkali fusion method

Takaaki Wajima* and Katsuyasu Sugawara*

* Faculty of Engineering and Resource Science, Akita University, Akita 010-8502, Japan
 wajima@gipc.akita-u.ac.jp

Abstract: Conversion of three different types of incineration ash, coal fly ash (CFA), paper sludge fly ash (PSFA) and industrial waste incineration fly ash (IWIFA) into useful materials using the alkali fusion method is attempted. The chemical and mineralogical compositions of these ashes differed. The order of Ca content in the ash was IWIFA > PSFA > CFA, while the Si and Al contents in the ashes were CFA > PSFA > IWIFA. CFA was mainly composed of quartz [SiO₂] and mullite [3Al₂O₃·2SiO₂], PSFA mainly of gehlenite [Ca₂Al₂SiO₇], anorthite [CaAl₂Si₂O₈] and talc [Mg₃Si₄O₁₀(OH)₂], and IWIFA mainly of portlandite [Ca(OH)₂], halite [NaCl] and sylvine [KCl]. Zeolites (zeolite-X, -A, -P and hydroxysodalite), hydrogrossular (katoite), and calcite were synthesized from the ashes. With an increasing Ca content of the ash, the Si concentration in the solution decreased, and the main product phases changed from zeolite (aluminosilicate) to hydrogrossular (calcium aluminosilicate), and finally to calcite (calcium carbonate).

Key Words: Alkali fusion, Incinerated ash, Waste recycling

1 INTRODUCTION

The global environment suffers from mass production, mass consumption and mass waste production that far exceed the purification ability of the earth. It is therefore necessary to make efforts toward environmental restoration. To this end, development of materials for environmental conservation and resource technology of solid waste are important subjects for material scientists and engineers. For a resource-poor nation such as Japan, it is desirable to develop resource recovery technology for solid wastes, and establish a sustainable society that is oriented towards the recycling of resources. Substantial research is being conducted into the recovery of industrial wastes as resources.

Incineration fly ash is one form of industrial solid waste with potential for recycling. Over 17 million tons of incineration fly ash from incinerators, coal fired power stations, etc. is discharged annually in Japan, and this amount increases every year. A small portion of incineration fly ash is used as cement fill, while a large portion is deposited in landfills [1]. The large daily output and limited landfill capacity have caused a variety

of environmental problems. “Law for the Promotion of Effective Utilization of Resources [1991]“ and “Fundamental Law for Establishing a Sound Material-Cycle Society [2000]“ established by the Japanese government makes it obligatory to reuse incineration fly ash. Thus, new effective ways to reuse this ash need to be developed quickly.

One of the most effective utilizations is to convert the ash into useful material. Many researchers have reported the conversion of incineration fly ashes into materials such as zeolite, tobermorite and hydrogrossular, to be used for environmental purification [2-10]. The most common method used for the conversion of fly ash into useful materials involves a hydrothermal process whereby the fly ash is mixed with an alkali solution such as sodium hydroxide at different temperature, pressure and reaction time conditions. In particular, there is much research into the conversion of coal fly ash, whose main components are SiO₂ and Al₂O₃, into zeolitic compounds. Hydrothermal treatment of coal fly ash with alkali gives various types of zeolites such as Na-P1, Na-A and hydroxysodalite, where the zeolite zone is formed like an egg white, covering the

central core of fly ash particles [11]. However, their structural heterogeneity, together with the poor properties as ion exchangers of stable zeolites, limits their applications. In order to overcome these shortcomings, a variation of the process in which an alkaline fusion stage is introduced prior to the conventional zeolite synthesis, usually known as the fusion method, has been suggested [12, 13]. This significantly improves the zeolitization process and the product is typically confirmed as highly crystalline zeolites from the faujasite group. Therefore, it is considered that alkali fusion would be an effective method for material conversion from fly ash. Little information is available, however, on this conversion using incineration fly ash other than coal fly ash. The conversion of the ash into useful material products depends largely on the chemistry of the raw ash, and it is important to clarify the products arising from different ashes when alkali fusion is used.

In the present study, conversion of three different types of incineration fly ashes, coal fly ash (CFA), paper sludge fly ash (PSFA) and industrial waste incinerated fly ash (IWIFA), into useful materials using the alkali fusion method was attempted. The synthesis procedures were undertaken under identical conditions, using NaOH as the activation reagent, and the products and synthesis reactions were compared.

2 EXPERIMENTAL

2.1 Incinerated ash

Three different incinerated ashes (CFA, PSFA, and IWIFA) discharged in Japan were used in this study. Powder X-ray diffraction (XRD, XRD-DSC-XII, Rigaku) was used to determine the crystalline phases present in the ashes. Chemical compositions of the ashes were analyzed by X-ray fluorescent spectrometry (XRF, XRF-1700, Shimadzu).

2.2 Alkali fusion

Material conversion from the ash using alkali fusion was carried out as shown in Figure 1. 10 g of the ash was mixed with 12 g of NaOH powder and ground to obtain a homogeneous mixture. This mixture was then heated in a nickel crucible in air at 600 °C for 6 h. The resultant material was cooled to room temperature and ground again to obtain powdered fused

material. 0.5 g of fused material was added to 2 mL of distilled water in a 10 mL tube made of polymethylpentene (TPX), followed by an aging process with vigorous agitation by reciprocal shaker at room temperature, in order to obtain the aged material. After 24 h of agitation, the aged material was heated in a water bath at 80 °C for 0 - 48 h. After heating, the solids were filtered, washed with distilled water, and dried overnight in a drying oven at 60 °C. The products were determined by XRD (RINT2500, Rigaku), and the concentrations of Si, Al and Na in the filtrate were analyzed by inductively-coupled plasma (ICP-AES, ICPS-7500, Shimadzu).

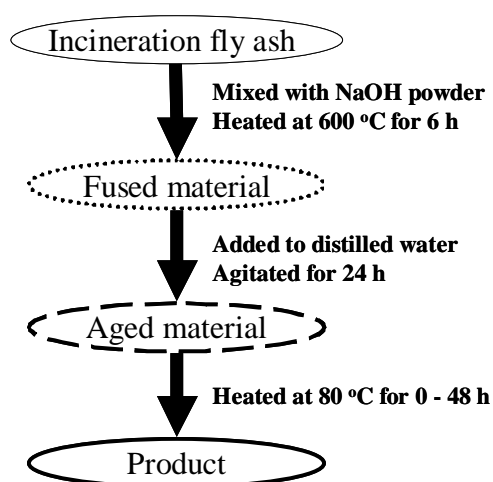


Figure 1 Flow chart of our experiments.

3 Results and discussion

3.1 Characterization of incinerated ash

Table 1 shows the chemical compositions of CFA, PSFA and IWIFA, and Figure 2 shows XRD patterns of CFA, PSFA and IWIFA. The chemical and mineralogical compositions of these ashes are different. The main components of CFA are SiO₂ (53.0 %) and Al₂O₃ (19.3 %), while those of PSFA are SiO₂ (30.1 %), Al₂O₃ (15.6 %) and CaO (38.4 %). IWIFA has a high CaO content (60.9 %) and other minor elements (< 15 %). The order of Ca content in the ash is IWIFA > PSFA > CFA, while those of Si and Al are CFA > PSFA > IWIFA. CFA is mainly composed of quartz [SiO₂] and mullite [3Al₂O₃·2SiO₂], PSFA is mainly composed of gehlenite [Ca₂Al₂SiO₇], anorthite [CaAl₂Si₂O₈] and talc [Mg₃Si₄O₁₀(OH)₂], and IWIFA is mainly composed of portlandite [Ca(OH)₂], halite [NaCl] and sylvine [KCl]. With an increasing Ca content, the main minerals in the

ash changed from silicate or aluminosilicate to calcium aluminosilicate, and finally to calcium hydroxide. It is noted that IWIFA is high chloride content while CFA and PSFA are not.

Table 1 Chemical compositions of CFA, PSFA and IWIFA.

Oxide (wt. %)	CFA	PSFA	IWIFA
SiO ₂	53.0	30.1	4.7
Al ₂ O ₃	19.3	15.6	2.5
CaO	4.8	38.4	60.9
Fe ₂ O ₃	12.3	2.3	2.4
MgO	0.9	5.5	1.2
K ₂ O	1.4	0.2	4.1
Na ₂ O	-	-	2.7
TiO ₂	2.8	3.6	2.0
SO ₃	0.4	0.6	1.3
P ₂ O ₅	1.9	0.8	0.6
SrO	0.8	-	0.1
MnO	0.1	-	-
ZnO	0.1	0.4	4.1
ZrO ₂	-	0.1	-
CuO	-	0.2	0.2
PbO	-	-	0.4
Cl	-	-	12.2
Total	97.8	97.9	99.2

3.2 Products obtained from the various ashes

Figure 3 shows XRD patterns of the products synthesized from (a) CFA, (b) PSFA and (c) IWIFA at various reaction times. Before heating, aged material from CFA indicated amorphous broad peaks in the range between 20 and 40°. In aged material from PSFA, peaks of calcite appeared, together with an amorphous peak. Calcite and hydrocalumite peaks were confirmed in aged material from IWIFA. When alkali fusion was applied to incinerated ashes, almost all the Si and Al content was transformed into amorphous phases, and the Ca content was precipitated as calcium compounds (calcite and hydrocalumite) in aged material. It is noted that no mineral phases that had been present in raw ashes remained in any of the aged materials, due to the destruction of the mineral structures by alkali fusion.

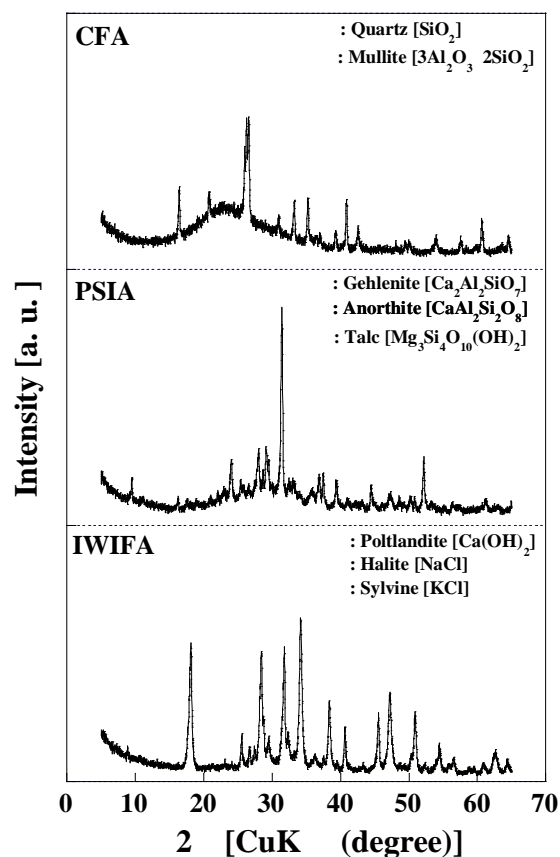


Figure 2 XRD patterns of CFA, PSFA and IWIFA.

After heating aged material from CFA, zeolites such as zeolite-X, zeolite-A and hydroxysodalite were synthesized (Fig. 3 (a)). Zeolite-X and -A have high cation exchange capacities and are value-added materials utilized as molecular sieves or catalysts, while hydroxysodalite has a low cation exchange capacity and a low added value [2]. Zeolite-X and -A were synthesized before 6 h of reaction time, and the amounts formed decreased with longer reaction times. In contrast, hydroxysodalite was frequently identified after 12 h of reaction. Since zeolite-X and -A are metastable phases, zeolite-X and -A are easily transformed into hydroxysodalite after 12 h of reaction. After heating aged material from PSFA, the amount of calcite decreased, and katoite, hydrocalumite and zeolite-P appeared, regardless of the reaction time (Fig. 3 (b)). Katoite is known as hydrogrossular, and could be very useful for the fixation of hydrogen chloride (HCl) gas at high temperatures [14 - 18]. After heating aged material from IWIFA, the amount of hydrocalumite decreased and only calcite appeared, regardless of the reaction time (Fig. 3 (c)).

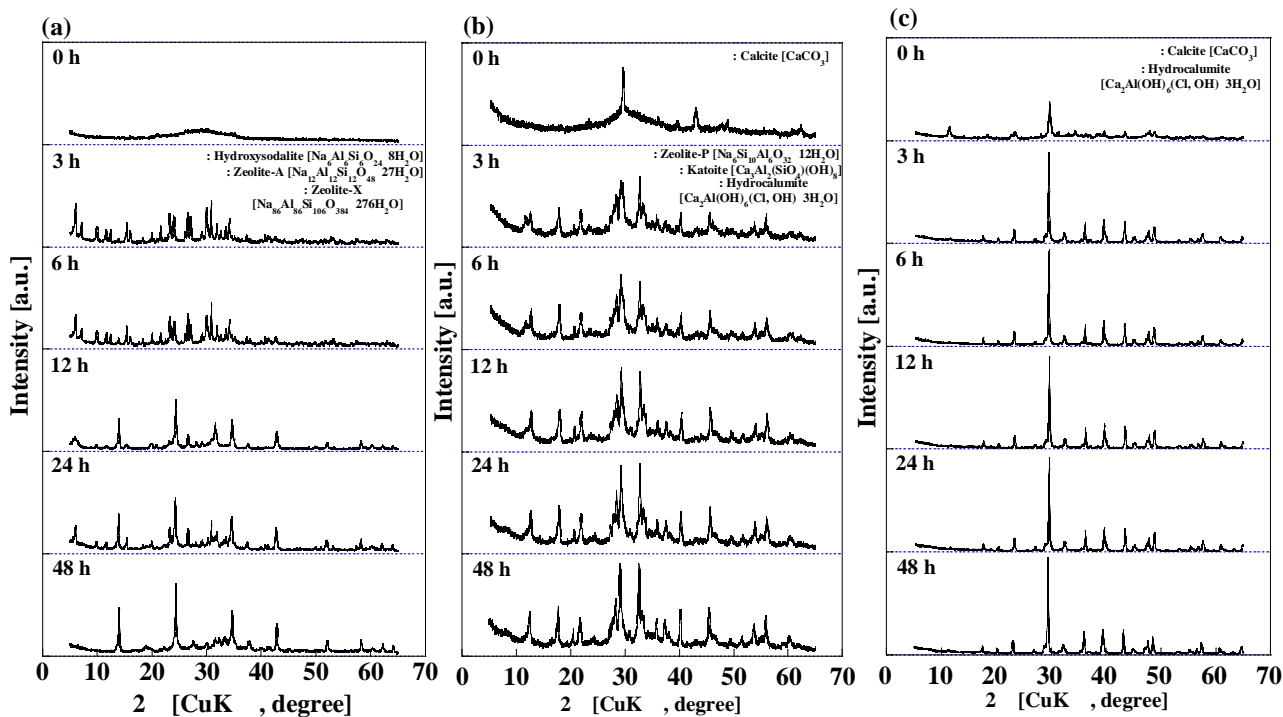


Figure 3 XRD patterns of the products synthesized from (a) CFA, (b) PSFA and (c) IWIFA at various reaction times.

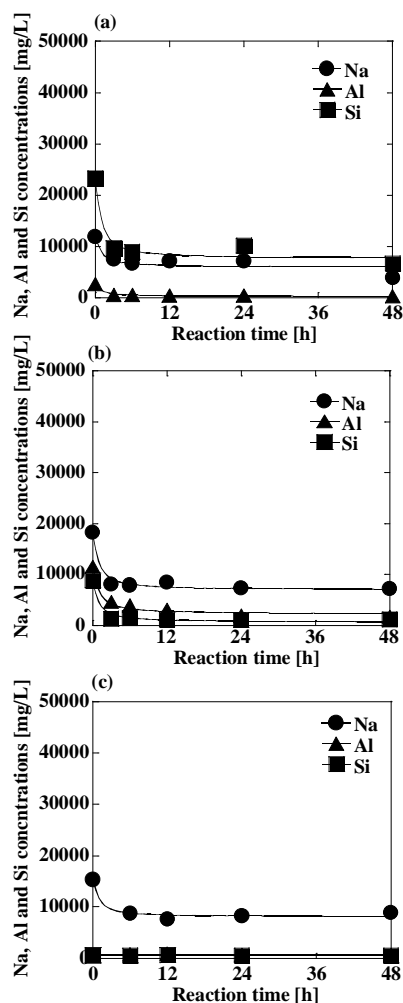


Figure 4 Na, Al and Si concentrations in reaction solution during the synthesis from (a) CFA, (b) PSFA and (c) IWIFA.

Figure 4 shows Na, Al and Si concentrations in reaction solution during the synthesis from (a) CFA, (b) PSFA and (c) IWIFA. In the case of CFA, the concentration of Si was higher than that of Al during the synthesis, due to the high Si content in raw ash. In the case of PSFA, the concentration of Si was lower than that of Al, although the Si content in raw ash was higher than that of Al. Calcium was more reactive with Si than Al, and the Si content in the solution decreased due to the reaction with Ca, due to the high content of Ca in raw ash. In the case of IWIFA, the contents of Si and Al in the solution from IWIFA were far lower than those in the solutions from CFA and PSFA, due to the low contents of Si and Al in raw IWIFA. The content of Na in the solution from CFA was lower than those in the solutions from PSFA and IWIFA, due to the creation of zeolite containing sodium.

In summary, the following mechanism for the conversion from CFA, PSFA and IWIFA using alkali fusion is proposed, as shown in Figure 5. Regardless of mineral compositions of incinerated ashes, Si and Al in the ash were transformed into soluble phases, dissolving in the solution. CFA has high Si and Al contents, and a low Ca content. After aging, most of the Si and Al has dissolved into the solution, and precipitates out as aluminosilicates

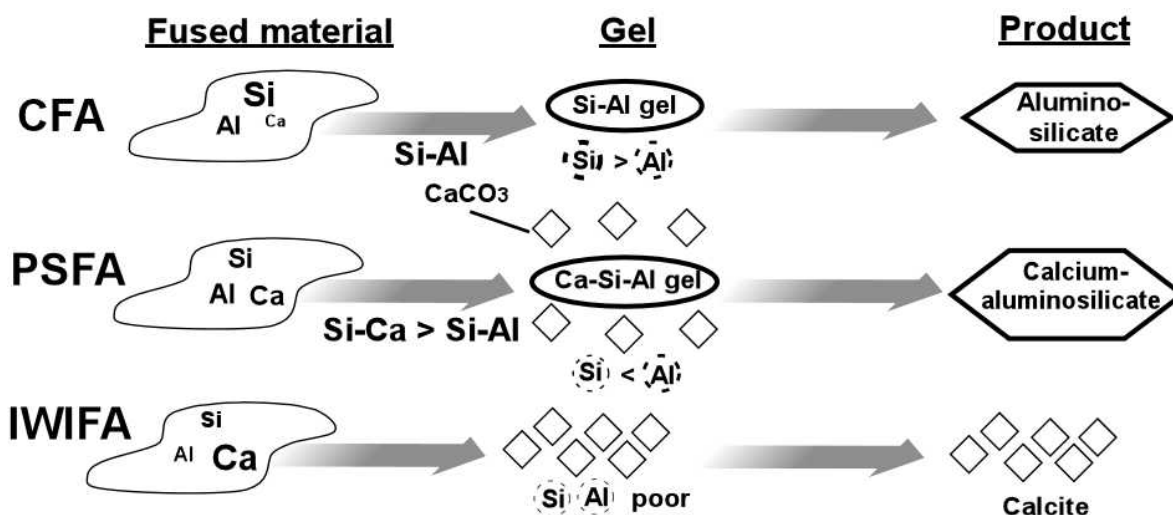


Figure 5 Proposed mechanisms for the material conversion from CFA, PSFA and IWIFA using alkali fusion.

to crystallize into zeolite by heating at 80 °C. PSFA contains Si and Al, and is higher in Ca than CFA. After aging, Si and Al have dissolved into the solution, and Ca reacts with Si to precipitate as calcium aluminosilicate gel, or precipitates as calcite. The reaction between Ca and Si is preferable to that between Si and Al, and the Si content in the solution is lower than the Al content. By heating at 80 °C, some of the aged material, such as calcium aluminosilicate gel and calcite, is transformed into katoite, and other parts are transformed into zeolite-P and hydrocalumite. IWIFA contains a high amount of Ca and is low in Si and Al. After aging, the dissolution of Si and Al into the solution is low, and Ca precipitates out as calcite and hydrocalumite. By heating at 80 °C, the amount of hydrocalumite is decreased, and only calcite is crystallized.

4 Conclusion

Conversion of three different types of incineration ashes, CFA, PSFA and IWIFA, into useful materials using the alkali fusion method was attempted. The chemical and mineralogical compositions of these ashes are different. The order of the Ca contents in the ashes is IWIFA > PSFA > CFA, while the Si and Al contents in the ashes are in the order CFA > PSFA > IWIFA. CFA is mainly composed of quartz [SiO₂] and mullite [3Al₂O₃·2SiO₂], PSFA is mainly composed of gehlenite [Ca₂Al₂SiO₇], anorthite [CaAl₂Si₂O₈] and talc [Mg₃Si₄O₁₀(OH)₂], and IWIFA is

mainly composed of portlandite [Ca(OH)₂], halite [NaCl] and sylvine [KCl]. When the Ca content of the ash increases, the main minerals in the ash are changed from silicate or aluminosilicate to calcium aluminosilicate, and finally to calcium hydroxide. Zeolites (zeolite-X, -A, -P and hydroxysodalite), hydrogrossular (katoite), and calcite were synthesized from the ashes. With an increasing Ca content in the ash, the Si concentration in the solution decreases, and the main product phases are changed from zeolite (aluminosilicate) to hydrogrossular (calcium aluminosilicate), and finally to calcite (calcium carbonate).

These results show that control of the Ca content in the ash is important for the conversion of incinerated ashes into useful materials using alkali fusion.

References

- [1] Ministry of Environment, Government of Japan, Survey Report on the Actual Conditions of the General Waste Management, Tokyo, Japan, 2006.
- [2] Querol, X., Moreno, N., Umaña, J. C., Alastuey, A., Hernández, E., López-Solar, A. and Plana, F., "Synthesis of Zeolites from Coal Fly Ash: an Overview," International Journal of Coal Geology, 50, pp. 413-423, (2002).
- [3] Molina, A. and Poole, C., "A Comparative Study using Two Methods to Produce Zeolites from Fly Ash," Minerals Engineering, 17, pp. 167-173, (2004).
- [4] Wajima, T., Kuzawa, K., Ishimoto, H., Tamada, O. and Nishiyama, T., "The Synthesis of Zeolite-P, Linde Type A, and Hydroxysodalite Zeolites from Paper Sludge

- Ash at Low Temperature (80 °C): Optimal Ash-leaching Condition for Zeolite Synthesis,” *American Mineralogist*, 89, pp. 1694-1700, (2004).
- [5] Wajima, T., Haga, M., Kuzawa, K., Ishimoto, H., Tamada, O., Ito, K., Nishiyama, T., Downs, R. T. and Racovan, J. F., “Zeolite Synthesis from Paper Sludge Ash at Low Temperature (90 °C) with Addition of Diatomite,” *Journal of Hazardous Materials*, B132, pp. 244-252, (2006).
- [6] Wajima, T. and Ikegami, Y., “Zeolite Synthesis from Paper Sludge Ash via Acid Leaching,” *Chemical Engineering Communications*, 195, pp. 305-315, (2008).
- [7] Wajima, T., Ishimoto, H., Kuzawa, K., Ito, K., Tamada, O., Gunter, M. E. and Racovan, J. F., “Material Conversion from Paper Sludge Ash in NaOH, KOH, and LiOH solutions,” *American Mineralogist*, 92, pp. 1105-1111, (2007).
- [8] Wajima, T., Shimizu, T. and Ikegami, Y., “Zeolite Synthesis from Paper Sludge Ash with Addition of Diatomite,” *Journal of Chemical Technology and Biotechnology*, 83, pp. 921-927, (2008).
- [9] Yao, Z., Tamura, C. Matsuda, M. and Miyake, M., “Resource Recovery of Waste Incineration Fly Ash: Synthesis of Tobermorite as Ion Exchanger,” *Journal of Material Research*, 14, pp. 4437-4442, (1999).
- [10] Fujita, S., Suzuki, K. and Shibasaki, Y., “The Mild Hydrothermal Synthesis of Hydrogrossular from Coal Ash,” *Journal of Material Cycles and Waste Management*, 4, pp. 41-45, (2002).
- [11] Shigemoto, N., Shirakami, K., Hirano, S. and Hayashi, H., “Preparation and Characterization of Zeolites from Coal Ash,” *Journal of the Chemical Society of Japan*, 5, pp. 484-492, (1992).
- [12] Shigemoto, N., Hayashi, H. and Miyaura, K., “Selective Formation of Na-X Zeolite from Coal Fly Ash by Fusion with Sodium Hydroxide prior to Hydrothermal Reaction,” *Journal of Material Science*, 28, pp. 4781-4786, (1993).
- [13] Shigemoto, N., Sugiyama, S., Hayashi, H. and Miyaura, K., “Characterization of Na-X, Na-A, and Coal Fly Ash Zeolites and their Amorphous Precursors by IR, MAS NMR and XPS,” *Journal of Material Science*, 30, pp. 5777-5783, (1995).
- [14] Shingu, H., Suzuki, K., Yamasaki, T., Fujita, S., Ogawa, N., Fukuda, T., Sataka, S. and Shibasaki, Y., “Flue Gas Purification at High Temperatures using Alkali Minerals,” *Journal of the Clay Science Society of Japan*, Vol. 44, No. 4, pp. 171– 175, (2005).
- [15] Fujita, S., Suzuki, K., Okawa, M., Shibasaki, Y. and Mori, T., “Reaction of Hydrogrossular with Hydrogen Chloride Gas at High Temperature,” *Chemistry of Materials*, 13, pp. 2523– 2527, (2001).
- [16] Fujita, S., Suzuki, K., Shibasaki, Y. and Mori, T., “Synthesis of Hydrogarnet from Molten Slag and its Hydrogen Chloride Fixation Performance at High Temperature,” *Journal of Material Cycles and Waste Management*, 4, pp. 70– 76, (2002).
- [17] Fujita, S., Suzuki, K., Mori, T. and Shibasaki, Y., “A New Technique to Remove Hydrogen Chloride Gas at High Temperature using Hydrogrossular,” *Industrial and Engineering Chemistry Research*, 42, pp. 1023– 1027, (2003).
- [18] Fujita, S., Ogawa, N., Yamasaki, T., Fukuda, T., Sakata, S., Suzuki, K., Shibasaki, Y. and Mori, T., “A New Sorbent, Hydrogarnet, with Purging HCl Gas at High Temperature,” *Chemical Engineering Journal*, 102, pp. 99– 104, (2004).

Extractability of PGM from mixed metal solution with New Derivative of Thiacalix[6]arene

Yoshihiko Kondo*, Mitsuhiro Akama**, Manabu Yamada**, Chunbin Li***,

Atsushi Shibayama**** and Fumio Hamada*

*Department of Life Science, Faculty of Engineering and Resource Science, Akita University, Akita 010-8502, Japan.

**Department of Material-Process and Applied Chemistry for Environments, Faculty of Engineering and Resource Science, Akita University, Akita 010-8502, Japan.

***Akita University Venture Business Laboratory, Akita 010-8502, Japan.

****Department of Material-Process Engineering in Applied Chemistry, Faculty of Engineering and Resource Science, Akita University, Akita 010-8502, Japan.

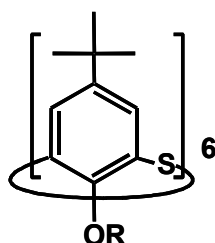
y_kondo@ipc.akita-u.ac.jp

Abstract: Two kinds of new thiacalix[6]arene derivatives modified at the lower rims were synthesized. (TC6A-CH₂COOH (**1**) and TC6A-CSN(CH₃)₂ (**2**)) The extraction abilities of TC6A derivatives for metal cations from platinum-group metals (PGM) solution or standard solution have been investigated. Nine metal cations (Rh, Pd, Pt, Zr, Ce, Ba, Al, La, Y) were contained in the PGM solution. Compound **1** showed high selectivity for Pd and Zr cations. The extractabilities of **1** for those metals were over 70%, although extractabilities for other metals were below 10%. Compound **1** also showed stripping extraction ability by 7N HCl. The stripping rate was ca. 70% for Pd cation. On the other hand, **2** showed great selectivity for Pd cation. The extractability of **2** for Pd cation was ca. 100%, although extractabilities for other metal cations were below 10%.

Key Words: Thiacalixarene, platinum-group metals, liquid-liquid extraction, host-guest chemistry

1 INTRODUCTION

Considerable attention has been recently focused on thiacalix[n]arenes (TCnAs) because of their capability of making a host-guest complexation with organic compounds or metal cations.¹ TCnAs are composed of benzene rings, linked via sulfur bridges instead of methylene units, which itself can make host-guest or supramolecular complexation with metal cations because sulfide groups has affinity for metal cations.² We have already reported the more selective extraction of rare metals with *p*-*tert*-butyl-TC6A than those of *p*-*tert*-butyl-TC4A.³ We would like to report here the synthesis of new TC6A derivatives such as TC6A-OCH₂COOH (**1**) and TC6A-OCSN(CH₃)₂ (**2**) (as shown in Figure 1) and extraction ability of metal cations from the rare metal mixture solution



TC6A-OCH₂COOH (**1**):

R = CH₂COOH

TC6A-OCSN(CH₃)₂ (**2**):

R = CSN(CH₃)₂

Figure 1. Structural formula of thiacalix[6]arene derivatives

with those TC6A derivatives. The rare metal mixture solution, which was named as PGM (Platinum Group Metals) solution, was prepared from automotive catalyst residue including nine rare metals (Rh, Pd, Pt, Zr, Ce, Ba, Al, La, Y).⁴ Those metal cations were existed as variously concentration in the PGM solution as shown in Table 1. The concentration of metal cations in aqueous layer was measured by inductively coupled plasma atomic emission spectrometry (ICP-AES). In the results, **1** showed high selective extractability of Pd at 70% and Zr at 90%. On the other hand, in the case using **2**, the extraction ability was shown only Pd at 100% and other metal cations at below 10%.

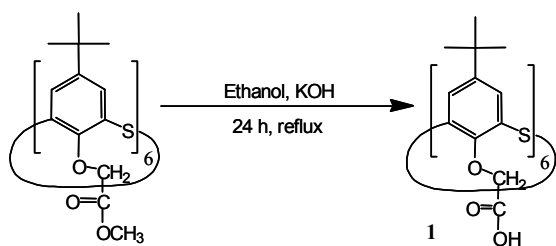
2 EXPERIMENTAL

2.1 Materials

Two metal solutions were prepared. One kind of the metal solution was leaching solution from an automotive catalyst residue into HCl (11.6 M) and H₂O₂ (1.0 vol. %), named as PGM solution. The PGM solution was containing nine metal cations (Rh, Pd, Pt, Zr, Ce, Ba, Al, La, Y) and strong acidity (pH: 0.13). Those metal concentrations in the PGM solution were variously, as shown in Table 1. Another one was the solution of containing single metal for comparison with the PGM solution. The metal solution was diluted to 10 ppm from nine kinds of standard metal solutions (1000 ppm, KANTO CHEMICAL CO., INC.) each other.

2.2 Preparation of 5,11,17,23,29,35-hexa-*tert*-butyl-37,38,39,40,41,42-hexakis[(carboxyl)methoxy]-2,8,14,20,26,32-hexathiocalix[6]arene (TC6A-CH₂COOH) (1)

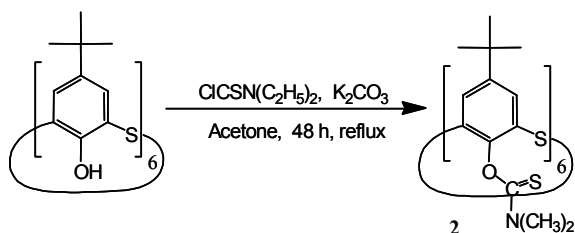
A mixture of TC6A-CH₂COOCH₃ (1.08 g, 1.0 mmol)² and NaOH (1.10 g, 27.5 mmol) in ethanol (250 ml) was stirred and refluxed for 24 h. After cooling to the room temperature, 4N H₂SO₄ (100 ml) was added to the reaction mixture for adjusting to pH 1.0 in ice-water bath. Precipitates were collected by filtration and dissolved in acetone. After undissolved matter was filtrated, the solvent was removed in vacuo to give a pure compound of TC6A-CH₂COOH (Yield: 0.84 g, 94.0 %). The structure of compound was determined by ¹H NMR (DPX-300, BURUKER BIOSPIN K. K.), FT-IR (SPECTRUM 2000, PerkinElmer Co., Ltd.) and elemental analysis (CHN coder, Yanaco New Science Inc.). ¹H NMR (300 MHz, CD₂Cl₂): δ = 6.52-8.00 (12H, br s, aromatic-H), 4.48-5.07 (12H, br s, OCH₂CO), 0.70-1.56 (12H, m, *tert*-butyl-H). IR (KBr): 3401 (O-H), 2963 (C-H), 1745 (C=O) cm⁻¹. Anal. Calcd for C₇₂H₈₄O₁₈S₆·C₃H₆O: C, 59.73; H, 5.99. Found: C, 59.54; H, 6.00.



Scheme 1. Synthesis of TC6A-CH₂COOH (1)

2.3 Preparation of 5,11,17,23,29,35-hexa-*tert*-butyl-37,38,39,40,41,42-hexakis[*N,N*-dimethylthiocarbamoyl]-2,8,14,20,26,32-hexathiocalix[6]arene (TC6A-CSN(CH₃)₂) (2)

A mixture of TC6A (0.200 g, 0.19 mmol), K₂CO₃ (0.230 g, 1.67 mmol) and *N,N*-dimethylthiocarbamoyl chloride (0.274 g, 2.22 mmol) in acetone (20.0 ml) was stirred and refluxed for 48 h under the nitrogen atmosphere. After cooling to the room temperature, 4N H₂SO₄ (100 ml) was added to the reaction mixture for adjusting to pH 1.0 in ice-water bath. Precipitates were collected by filtration and dissolved in acetone. After



Scheme 2. Synthesis of TC6A-CSN(CH₃)₂ (2)

undissolved matter was filtrated, the solvent was removed in

Table 1. The composition and concentration of metal cations in PGM solution.

Metal cation	Concentration (ppm)
Rh	320.9
Pd	711.1
Pt	450.7
Zr	177.9
Ce	4706
Al	2161
Ba	2438
La	655.1
Y	38.25

vacuo to give a white crude product. The crude product was recrystallized from chloroform-ethanol mixture solution to give a pure product of TC6A-CSN(CH₃)₂ (Yield: 0.18 g, 61.0 %). The structure of compound was determined by ¹H NMR (DPX-300, BURUKER BIOSPIN K. K.), FT-IR (SPECTRUM 2000, PerkinElmer Co., Ltd.), mass spectrum (JMS-700, JEOL) and elemental analysis (CHN coder, Yanaco New Science Inc.). ¹H NMR(300 MHz, CD₂Cl₂): δ = 8.10- 6.70 (12H, br m, aromatic-H), 4.25- 2.10 (36H, br m, N(CH₃)₂), 2.00- 0.75 (54H, *tert*-butyl-H). IR (KBr): 2963 (C-H), 1222 (C=S) 1095 (C -N) cm⁻¹. FAB-Mass: 1603.6, [M+H⁺]. Anal. Calcd for C₇₂H₁₀₈O₆S₁₂: C, 58.41; H, 6.42; N5.24. Found: C, 56.83; H, 6.13; N5.17.

2.4 General procedure of liquid-liquid extraction

A chloroform layer of TC6A derivatives and PGM solution were shaken at 600 stroke/min in separating funnel at room temperature for 30 min. Basically, the molar and volume ratio were 1 : 1. On the other hand, a chloroform layer of TC6A derivatives and standard solution were stirred at 500 rotate/min with sample tube at room temperature for 24 h. The molar and volume ratio were 1 : 1. The concentration of metal cations in aqueous layer was measured by inductively coupled plasma atomic emission spectrometry (ICP-AES, SPS3000, SII). The extractability (*E*%) was calculated by Eqs. I and II.

$$E\% = C_{\text{org}} / C_0 \times 100 \quad (\text{I})$$

$$C_{\text{org}} = C_0 - C_{\text{aq}} \quad (\text{II})$$

where *C*₀ and *C*_{aq} are initial and final concentration (ppm) of metal cation in aqueous layer, respectively.

2.5 General procedure of stripping extraction

A chloroform layer after liquid-liquid extraction from standard solution and 7N acid solution made from HCl, HNO₃ or H₂SO₄ were stirred at 500 rotate/min with sample tube at room temperature for 24 h. On the other hand, a chloroform layer after liquid-liquid extraction from PGM solution and 7N acid solution were shaken at 600 stroke/min with separating

funnel at room temperature for 30 min. The volume ratio for the stripping extraction was 1 : 1. The concentration of metal cations in aqueous layer was measured by inductively coupled plasma atomic emission spectrometry (ICP-AES, SPS3000, SII). The stripping extractability ($SE\%$) was calculated by Eq. III,

$$SE\% = C_w / C_{org} \times 100 \quad (III)$$

where C_w is final concentration (ppm) of metal cation in aqueous layer after stripping extraction, C_{org} is calculated concentration (ppm) of metal cation in organic layer as shown in Eq. II

3 RESULTS AND DISCUSSION

3.1 Extraction ability of TC6A derivatives from PGM solution

PGM solution was diluted fifty times distilled water for liquid-liquid extraction. The total concentration of all metal cations was 2.92 mM in the PGM solution. A chloroform layer of TC6A derivatives (2.92 mM) and PGM solution as an aqueous layer were shaken at 600 stroke/min in separating funnel at room temperature for 30 min. The volume ratio for the extraction was 1 : 1. Figure 2 shows extraction ability of TC6A derivatives for metal cations from PGM solution. Compound **1** showed selective extraction ability for Pd and Zr cations, which was 70% and 91%, respectively. The extraction of another metal cations was below 5%. Compound **2** showed great selective extraction ability for only Pd cation. The extraction rate of Pd cation was 100%. It was shown that **2** has obtained a high affinity for Pd cation.

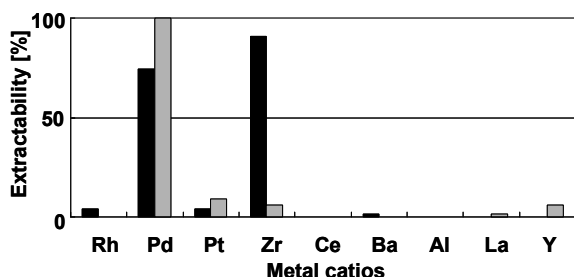


Figure 2 Extraction of metal cations from the adjusted PGM solution by **1** TC6A-OCH₂COOH (**1**) and **2** TC6A-OCSN(CH₃)₂ (**2**)

3.2 Extraction ability of TC6A derivatives from standard solution

The extractability of **1** from standard solution at several pH were shown in Figure 3. The adjustment of pH for standard solution was made with 5N NaOH and the solution was measured to concentration of metal cations. The Pd standard solution over pH 2.3 and Al standard solution over pH 3.2 were not used for liquid-liquid extraction because those concentrations were changed after adjustment of pH. Pd and Zr cations were extracted ca. 100% at the pH 2.0. The extraction

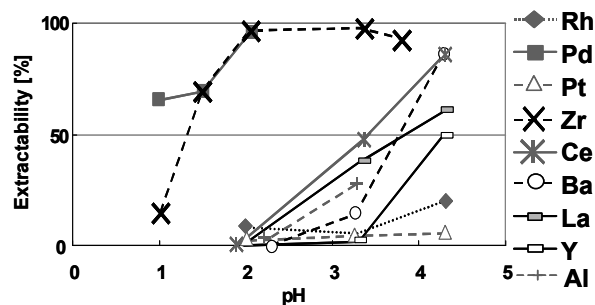


Figure 3 Extractability of **1** from standard solution at several pH.

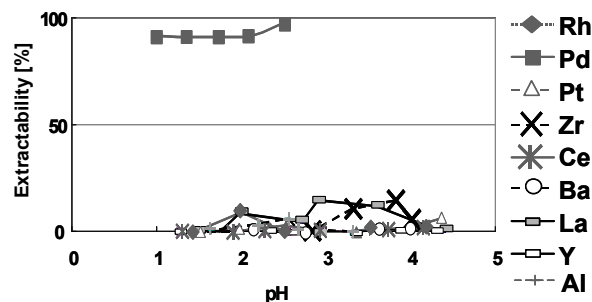


Figure 4 Extractability of **2** from standard solution at several pH.

abilities for the La and Y cations were shown from pH. 2.0 and 3.3, respectively, and those extraction rates were about 50% at pH 4.3. The extraction of Pt, Rh and Al cations were not too high. However, Ce and Ba cations were extracted about 90% at pH 4.3, though those extraction rates were 0% under pH 2.0. It was suggested that extraction of Ba and Ce were improved by co-extraction mechanism of alkali metal cations⁵. On the other hand, as shown in Figure 4, the extraction ability of **2** was indicated from standard solution at several pH. Compound **2** showed extraction ability for only Pd, although other metal cations were extracted below 15% at every pH. It was shown that **2** has obtained high selective extractability for only Pd cation.

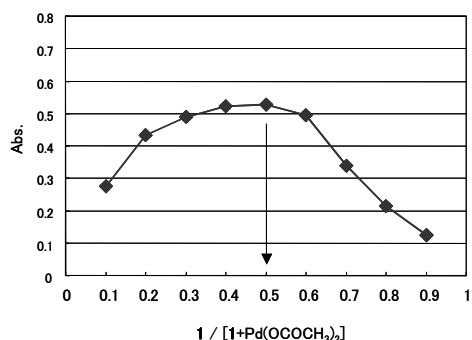


Figure 5 Continuous variation plots for the formation of Pd²⁺ complex

We determined the ratio of **1** and Pd cation in the complex by the continuous variation plots method. As illustrated in Figure 5, the compound **1** and Pd²⁺ has its maximum absorbance at [**1**] / [**1** + Pd(OCOCH₃)₂] = 0.5 at 500 nm. The result shows that **1** forms a 1 : 1 complex with Pd²⁺ in CHCl₃.

3.3 Stripping Extraction

Figure 6 shows stripping of Pd cation from loaded TC6A derivatives with various stripping solutions. The stripping rate of 80% from loaded **1** was achieved by 7N HCl. The other stripping solution could not strip from loaded **1**. On the other hand, Pd cation from loaded **2** was not stripped by all 7N acid solution. According to these results, it was suggested that the complexation ability of **2** for Pd cation was strong. In order to discuss for the application, we also tried to strip of some metal cations from loaded TC6A derivatives after extraction from PGM solution, as shown in Figure 7. The stripping rate of 71% of Pd and 4.7% of Zr cations from loaded **1** were achieved by 7N HCl. The 29% of Pd was stripped from loaded **2** by 7N HNO₃.

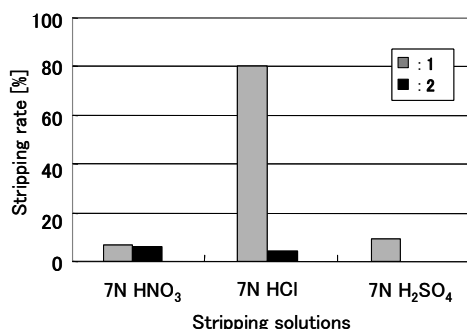


Figure 6 Stripping rate of Pd cation from loaded TC6A derivatives by several stripping solution

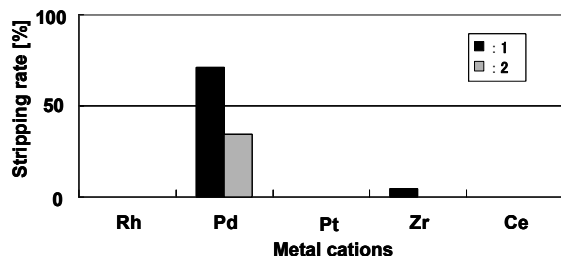


Figure 7 Stripping rate of several metal cations from loaded **1** by 7N HCl and loaded **2** by 7N HNO₃

4 CONCLUSIONS

In this study, two kinds of new TC6A derivatives are prepared. Compound **1** shows high selectivity for Pd and Zr cation from standard solution or PGM solution. The stripping rate of 80% from loaded **1** was achieved by 7N HCl. On the other hand, Compound **2** can extract only Pd cation at ca. 100% from standard solution or PGM solution. However, the effective stripping was not observed with several 7N acid solutions. According to those results, it seems that TC6A derivatives can be usefulness for the recycle process of rare metals.

Acknowledgement

This study was supported by Industrial Technology Research Grant Program in 2006 from New Energy and Industrial Technology Development Organization (NEDO) of Japan.

References

- [1] Naoya Morohashi, Fumitaka Narumi, Nobuhiko Iki, Tetsutaro Hattori, Sotaro Miyano, "Thiacalixarenes", *Chem. Rev.*, **106** (2006) 5291.
- [2] a) Yoshihiko Kondo, Ken Endo, Tomohiro Nimi, Fumio Hamada, "New Crystal Structure of *p*-tert-butylthiacalix[6]arene Complexes with Toluene and Benzyl Alcohol", *Int. J. of the Soc. of Mat. Eng. for Resources*, **11**, 16-28 (2003). b) Yoshihiko Kondo, Ken Endo, Nobuhiko Iki, Sotaro Miyano, and Fumio Hamada, "Synthesis and Crystal Structure of *p*-tert-Butylthiacalix[8]arene : A New Member of Thiacalixarenes" *Journal of Inclusion Phenomena and Macrocyclic Chemistry*, in press. c) Yoshihiko Kondo, Ken Endo, and Fumio Hamada, "Potassium-Thiacalix[8]arene Assembly: Structure and Guest Sorption Profiles" *Chem. Commun.* 711-712 (2005). d) Ken Endo, Yoshihiko Kondo, Yasuhiro Aoyama and Fumio Hamada, "Guest-binding properties of functionally crystal based on metal complex of *p*-tert-butylthiacalix[6]arene", *Tetrahedron Lett.*, **44**(7), 1355 (2003). e) Manabu Yamada, Yoshihiko Kondo, Nobuhiko Iki, Chizuko Kabuto, Fumio Hamada, "Hydrophobic and metal coordination interacted architecture based on *p*-tert-butylthiacalix[4]arene-potassium complex and its vapor absorption capability", *Tetrahedron Lett.*, **49**(24) (2008) 3906.
- [3] Manabu Yamada, Atsushi Shibayama, Yoshihiko Kondo, Fumio Hamada, "Selective extraction of precious metal from automotive catalyst residue by thiacalix[6]arene derivatives", *Int. J. of the Soc. of Mat. Eng. for Resources.*, **15** (2007) 13-15.
- [4] S. Harjanto, Y. Cao, A. Shibayama, I. Naitoh, T. Nanami, K. Kasahara, Y. Okumura, K. Liu, T. Fujita, "Leaching of Pt, Pd and Rh from Automotive Catalyst Residue in Various Chloride Based Solutions, Materials Transaction", **47** (2006) 129-135.
- [5] K. Ohto, M. Yano, K. Inoue, T. Nagasaki, M. Goto, F. Nakashio, S. Shinkai, Effect of coexisting alkaline metal ions on the extraction selectivity of lanthanide ions with calixarene carboxylate derivatives, *Polyhedron.*, **16** (1997) 1655-1661.

Mn-oxides as Adsorbents for Molybdenum in Nitric acidic solution

Jayappa Manjanna*, Gjergj Dodbiba*, Takahiro Kikuchi**, Seiji Matsuo*, Toyohisa Fujita*

* Department of Systems Innovation, The University of Tokyo, Tokyo 113-8656

** Japan Atomic Energy Agency, Ibaraki 319-1194

jmanjanna@rediffmail.com

Abstract: Mn-oxides viz., Mn_3O_4 , Mn_5O_8 and α - Mn_2O_3 were prepared by calcination at different temperatures, of the precipitate obtained using $MnCl_2$ and NaOH at pH ~10. The adsorption of molybdenum on these oxides, using a stock-solution of 10 mM Mo(VI) in 3M HNO_3 solution, was conducted with different amounts of solid (adsorbents)-to-liquid ratio. Mn_3O_4 was found to adsorb 100% of Mo when the solid-to-liquid ratio was close to 100 g/ L, whereas Mn_5O_8 and α - Mn_2O_3 adsorbed about 45% and 25%, respectively. However, due to the oxidizing nature of HNO_3 , Mn_3O_4 was oxidized to γ - MnO_2 along with partial dissolution, ~20%. Therefore, although the removal of Mo by Mn_3O_4 was successful (which is comparable to our previous results using α - Fe_2O_3), the accompanying dissolution behavior needs to be addressed.

Keywords: Vitrification, high-level radioactive liquid waste (HLLW), Molybdenum, adsorption, Mn-oxides

1 INTRODUCTION

High-level radioactive liquid waste (HLLW) is generated from the reprocessing of spent-fuel in nuclear reactors. After cooling for several years to take-off decay heat, this liquid waste will have to be concentrated and solidified (i.e., *vitrification* - glass formation process) for ultimate disposal in the deep geological repositories.

The presence of molybdenum (Mo), one of the main fission-product, FP, accounting to about 10 wt.% of the total FP [1], in the HLLW is known to interfere in the vitrification process, thereby affecting the long-time integrity of vitrified solid to be disposed. Therefore, the removal of Mo from the liquid waste, prior to vitrification, is highly advantageous

[1–3]. Furthermore, the removal of Mo will significantly reduce the amount of HLLW to be disposed, as well as improve the vitrification of HLLW. Hence we have focused on the development of suitable adsorbents for Mo from a simulated (highly acidic) liquid waste solution i.e., 3M HNO_3 . In this study, we used synthetic Mn-oxides to compare with our previous results with Fe-oxides. Manganese oxides crystallize in several different structures with varied proportion of Mn in different oxidation states (+2, +3 and +4). The stable and well-known oxides are easy to prepare, and extensive studies have been carried out to prepare these oxides from various precursors with the aim of controlling the particle size and microstructure [4–10] and/or for a particular application, mainly as catalyst [9, 11, 12].

As revealed in this study, although the Mo removal by Mn-oxide was possible, these oxides undergo partial dissolution (~20% over a period of 2 h). Here we report these findings with detailed synthetic conditions of Mn-oxides. We used 3M HNO₃ wherein known amount of Mo was added, as a simulated (highly acidic) HLLW solution.

2 MATERIALS AND METHOD

2.1 Synthesis/Characterization of Mn-oxides

MnCl₂ 4H₂O (198 g) was dissolved in 2 L of water (0.5 M; pH ~4.5). Then 30% of NaOH was added slowly over a period of about 4 h with constant stirring to ensure the complete precipitation of Mn ions i.e., until the solution attained pH ~10. The precipitate was kept stirred for another ~12 h with the mother liquor at room-temperature (RT). Then it was filtered, washed with plenty of water and dried at 90 °C/24 h. To study the temperature effect, this 'as prepared' sample was calcinated at 300 °C and 600 °C for 24 h in air.

The samples were characterized using X-ray diffraction (XRD) with Ni-filtered Cu K_α radiation, Thermogravimetry (TG)/ Differential thermal analysis (DTA) with a heating rate of 4 °C/min in air, Field emission-scanning electron microscope (FE-SEM), and BET single-point method for specific surface area.

2.2 Mo adsorption on Mn-oxides

A stock-solution of Mo(VI) was prepared by dissolving 0.883 g of (NH₄)₆Mo₇O₂₄ 4H₂O salt in 500 ml of 3M HNO₃ solution.

To a 5 ml of the stock-solution, a known amount of the oxide (with varying solid-to-liquid ratio) was added, and interacted for 2 h at RT. The liquid sample was collected through syringe-filter (0.2 μm), and analyzed for Mo and Mn by inductively coupled plasma-optical emission spectroscopy (ICP-OES).

For comparison, adsorption time and/or temperature was also varied in some cases.

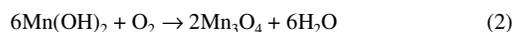
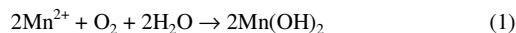
Adsorption capacity (*q*) was calculated as: $q = (C_0 - C) * V / M$ where C₀ and C are initial concentration of Mo (mg/L = ppm) before and after adsorption, V - solution volume (L) and M - mass of adsorbent (g). Therefore, the unit of *q* is mg/g i.e., 'mg' of Mo adsorbed per 'g' of adsorbent. In some cases, only the % of adsorption i.e., $(C_0 - C) * 100 / C_0$ was calculated.

3 RESULTS AND DISCUSSION

3.1 Nature of Mn-oxides

Based on the TG/DTA data (Fig.1) and the XRD pattern (Fig.2) analysis, the as prepared oxide was Mn₃O₄. It was converted (oxidized) to Mn₅O₈ on heating to 300 °C and then to α-Mn₂O₃ at 600 °C.

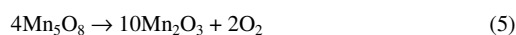
As indicated in Fig.2, all of the peaks can be indexed to the corresponding JCPDS patterns: 24-0734 (Mn₃O₄), 30-1218 (Mn₅O₈) and 31-0825 (α-Mn₂O₃). The formation of Mn-oxides here from the starting Mn²⁺ ions can be written as [4-10]:



As-prepared sample, tetragonal *hausmannite*, belongs to normal spinel structure with Mn²⁺ and Mn³⁺ ions distributed in tetrahedral and octahedral sites as [Mn²⁺]₄[Mn³⁺]₆O₄²⁻. On heating to about 300 °C, the monoclinic Mn₅O₈ structure, Mn₂²⁺Mn₃⁴⁺O₈²⁻, was formed by oxidation



On further heating of this mixed valence oxide at about 600 °C, the stable cubic α-Mn₂³⁺O₃ bixbyite-C structure was formed



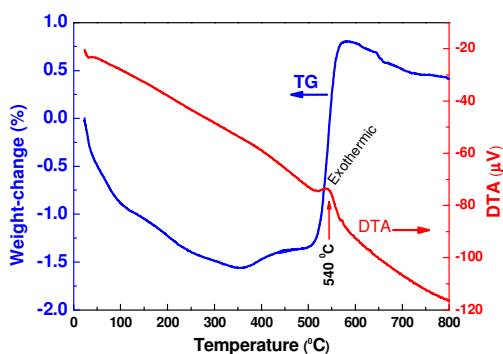


Figure 1. TG/DTA of the 'as prepared' Mn-oxide
($\text{Mn}_3\text{O}_4 \rightarrow \alpha\text{-Mn}_2\text{O}_3$)

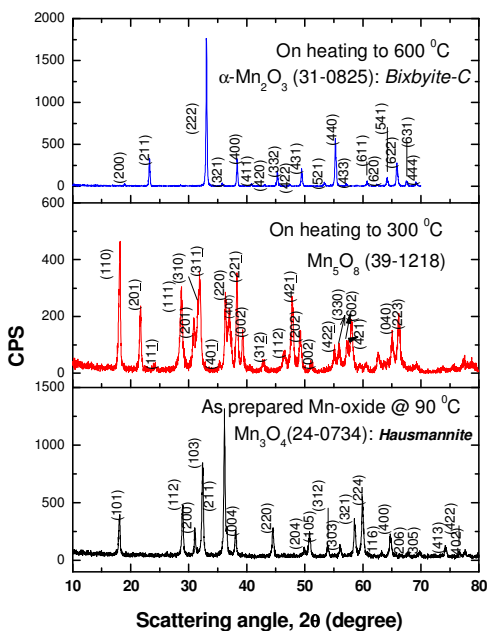


Figure 2. Powder XRD patterns of Mn-oxides
($\text{Cu } K_{\alpha}$ radiation)

The specific surface area determined by the single-point BET method are about $20 \text{ m}^2/\text{g}$ for Mn_3O_4 , $16 \text{ m}^2/\text{g}$ for Mn_5O_8 and $10 \text{ m}^2/\text{g}$ for $\alpha\text{-Mn}_2\text{O}_3$. This is due to the increased particle size as can be seen from the FE-SEM micrographs, Fig.3. The majority of Mn_3O_4 particles are $<100 \text{ nm}$, and we can also see few nano-rods shaped particles. In the case of $\alpha\text{-Mn}_2\text{O}_3$, the particles were relatively large and uniform. The morphology of the particles is an important property for the adsorption. However, from our previous experience with Fe-oxides samples [13], it was found that the adsorption of Mo(VI)

depends not only on surface area but also on other microstructural and/or surface features of adsorbents.

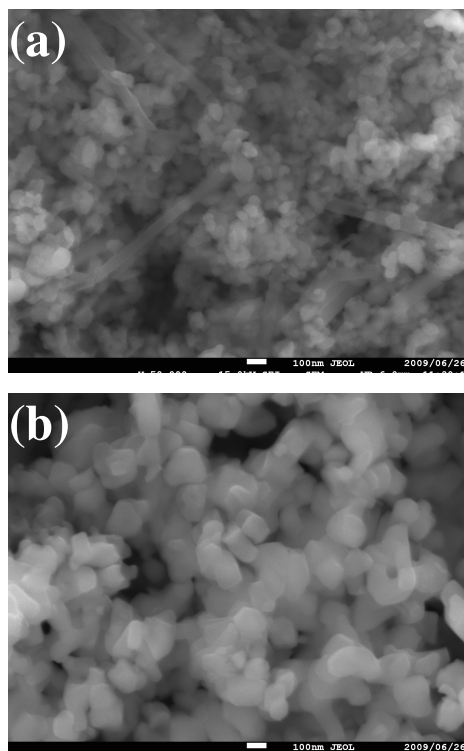


Figure 3. FE-SEM micrographs of (a) as prepared oxide, Mn_3O_4 and (b) on calcined at $600 \text{ }^\circ\text{C}$,

3.2 Mo adsorption

Mo(VI) is known to be present as cation in this highly acidic solutions ($>1 \text{ M}$). The possible species are: H_3MoO_4^+ or HMoO_3^+ and their dimeric forms: $\text{H}_2\text{Mo}_2\text{O}_6^{2+}$ and $\text{H}_3\text{Mo}_2\text{O}_6^{3+}$. With an increase in acidity, the divalent mononuclear cations MoO_2^{2+} and $\text{H}_2\text{MoO}_3^{2+}$ are reported to form by dehydration and gradually become the predominant species [1].

Fig.4 shows the amount of Mo adsorbed per gram of the adsorbent (Mn-oxides) i.e., adsorption capacity, q as a function of adsorbent amounts i.e., solid-to-liquid ratio. It is clear that the q was much higher for the as-prepared sample (Mn_3O_4) when compared to the other two adsorbents. The efficiency of these Mn-oxides to remove/adsorb Mo from 3M HNO_3 solution can be shown as: $\text{Mn}_3\text{O}_4 > \text{Mn}_5\text{O}_8 > \alpha\text{-Mn}_2\text{O}_3$, which may be attributed, tentatively, to their morphology.

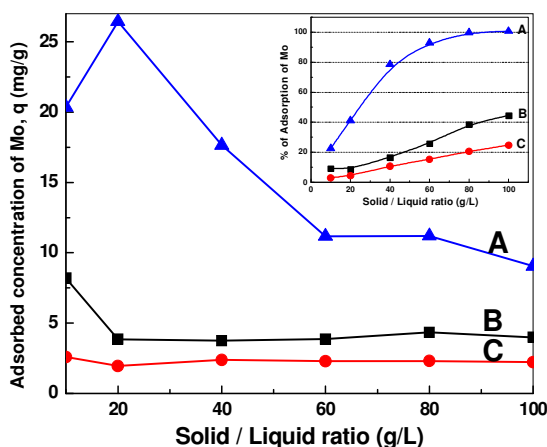


Figure 4. Adsorption of Mo in 3M HNO₃ solution in 2 h at RT by Mn-oxides: A Mn₃O₄, B Mn₅O₈ and C

For all the adsorbents, in general, the adsorption capacity is highest when the solid-to-liquid ratio is low (ca. 10g/L). Under this condition, the entire surface and/or all the active sites on the adsorbent are available for adsorption as the surface area to volume ratio is low. However, when the solid-to-liquid ratio high ca. 100 g/L, the surface area to volume ratio is also high, thereby, the efficiency decreased.

The inset of Fig. 4 shows the percentage (%) of Mo removed from a fixed volume of stock-solution (5 mL). It is clear that the % removal of Mo increased with increasing solid-to-liquid ratio. Using Mn₃O₄, complete (100%) removal of Mo was possible when the solid-to-liquid ratio was close to 100g/L. In the case of Mn₅O₈ and α-Mn₂O₃, the Mo adsorbed was about 45% and 25%, respectively.

Based on the efficient adsorption capacity observed here when the solid-to-liquid ratio is low, it may be suggested that the multi-step method is useful for complete utilization of adsorbents. Nevertheless, the mode of operation depends on many factors in the actual system.

3.2 Effect of adsorption time and temperature

It was also seen that the maximum time needed for adsorption is not more than 30 min. There was no significant

change in the adsorption capacity and/or % of adsorption even when the interaction time varied from few hours to 1 day.

However, the temperature influences the adsorption behavior. It was seen that as the temperature was increased from RT to 90 °C, there was about 50% increase in the % of adsorption, especially when the solid-to-liquid ratio is low. We are conducting further studies to calculate at the adsorption activation energy.

3.3 Oxidation / Dissolution of Mn₃O₄ in 3M HNO₃

Although Mn₃O₄ was found to be efficient adsorbent among other Mn-oxides, it was oxidized to γ-MnO₂ phase during its interaction with 3M HNO₃ solution (within 30 min). Simultaneously, there occurred dissolution of about 20% the oxide in 2 h. This is a major set-back to qualify this oxide as adsorbents under the prevailing situation. However, efforts are on to stabilize this oxide by suitable modifying the drying temperature.

Fig. 5 shows the XRD, SEM and TG/DTA data of γ-MnO₂ phase obtained by treating Mn₃O₄ in nitric acid solution for 36 h. The γ-MnO₂ phase here is almost similar to that of electrolytic manganese dioxide (EMD) material in alkaline battery cells [14]. We hope to use this material in our future studies for some suitable applications ca. cathode materials for rechargeable Li metal or Li ion batteries [for example, 15] and/or catalyst [for example, 16] as it can be easily obtained.

4 SUMMARY

Mn-oxides viz., Mn₃O₄, Mn₅O₈ and α-Mn₂O₃ were prepared and characterized for their application as adsorbents for Mo in 3M HNO₃ solution (a simulant high level liquid waste from unclear industry). The Mn₃O₄ obtained at low-temperature (90 °C/ 24 h) was found to be effective. The 100% adsorption of Mo was seen with Mn₃O₄ when the solid-to-liquid ratio was close to 100 g/L. In fact, the adsorption capacity (mg of Mo adsorbed per g of adsorbent)

was found to decrease with increasing solid-to-liquid ratio. The highest capacity was realized when it is ≤ 20 g/L.

Although the adsorption results obtained here are comparable to our previous findings on α -Fe₂O₃ (calcined ~ 500 °C) as adsorbent, however, the major set-back here is the dissolution ($\sim 20\%$) and oxidation of the adsorbent, Mn₃O₄ \rightarrow γ -MnO₂, during its interaction with HNO₃ solution. Therefore, now we are trying to stabilize the material by suitably modifying the synthetic conditions.

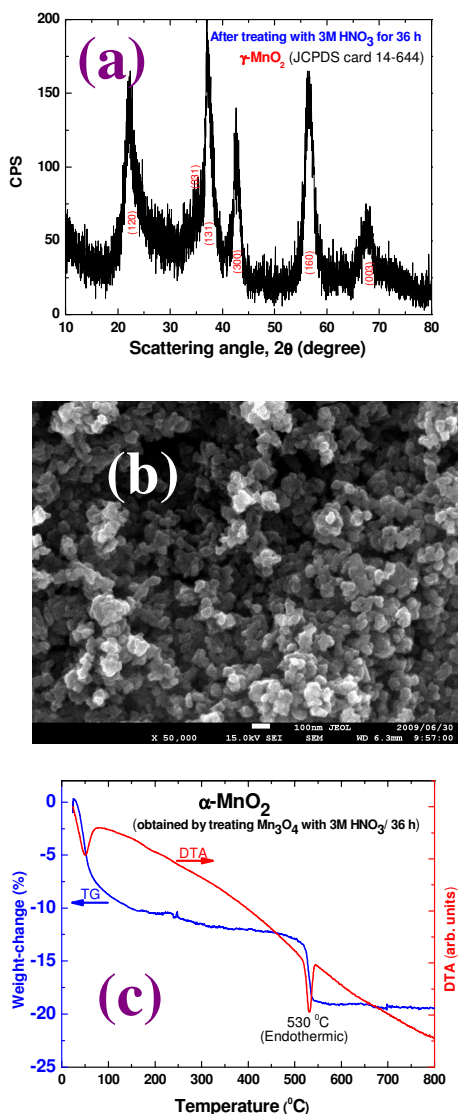


Figure 5. (a) XRD pattern, (b) SEM micrograph and (c) TG/DTA plots, of the Mn-oxide after treating with 3M HNO₃ for 36 h. (Mn₃O₄ \rightarrow α -MnO₂)

References

- [1] Zhang, A., Wei, Y. and Kumagai, M. "Properties and mechanism of Molybdenum and Zirconium Adsorption by a Microporous Silica-Based Extraction Resin in the MAREC Process", *Solvent Extraction and Ion Exchange*, Vol.21, No.4, pp.591–611, (2003).
- [2] Fujii, T., Yamana, H., Watanabe, M. and Moriyama, H. "Extraction of Molybdenum from Nitric Acid by Octyl(phenyl)-N,N-diisobutylcarbamoylmethyl-phosphine oxide", *Solvent Extraction and Ion Exchange*, Vol.19, No.1, pp.127–141, (2001).
- [3] Zhang, A., Kuraoka, E. and Kumagai, M. "Removal of Pd(II), Zr(IV), Sr(II), Fe(III), and Mo from Simulated High Level Liquid Waste by Extraction Chromatography Utilizing the Macroporous Silica-Based Polymeric Materials", *Separation and Purification Technology*, Vol.50, pp.35–44, (2006).
- [4] Gibot, P. and Laffont, L. "Hydrophilic and Hydrophobic Nano-sized Mn₃O₄ Particles", *Jour. of Solid State Chemistry*, Vol.180, pp.695–701 (2007).
- [5] Yang, L.-X., Zhu, Y.-J., Tong, H., Wang, W.-W. and Cheng, G.-F. "Low-temperature Synthesis of Mn₃O₄ polyhedral nanocrystals and magnetic study", *Jour. of Solid State Chemistry*, Vol.179, pp.1225–1229, (2006).
- [6] Fritsch, S., Sarrias, J., Rousset, A. and Kulkarni, G.U., "Low-temperature Oxidation of Mn₃O₄ Hausmannite", *Material Research Bulletin*, Vol.33, No.8, pp.1185–1194, (1998).
- [7] Al Sagheer, F.A., Hasan, M.A., Pasupulety, L. and Zaki, M.I., "Low-temperature Synthesis of Hausmannite Mn₃O₄", *Jour. of Materials Science Letters*, Vol.18, pp.209–211, (1999).
- [8] Punnose, A., Magnone, H. and Seehra, M.S., "Synthesis and Antiferromagnetism of Mn₃O₈", *IEEE Transactions on Magnetics*, Vol.37, No.4, pp.2150–2152, (2001).
- [9] Ren, T.-Z., Yuan, Z.-Y., Hu, W. and Zou, X. "Single crystal Manganese oxide hexagonal plates with Regulated Mesoporous structure", *Microporous and Mesoporous Materials*, Vol.112, pp.467–473, (2008).

- [10] Xiong, Y., Xie, Y., Li, Z. and Wu, C. "Growth of Well-Aligned γ -MnO₂ Monocrystalline Nanowires through a Coordination-Polymer-Precursor Route", *Chemistry–A European Jour.* Vol.9, No.7, pp.1645–1651, (2003).
- [11] Jana, S., Praharaj, S., Panigrahi, S., Basu, S., Pande, S., Chang, C.-H. and Pal, T. "Light-induced Hydrolysis of Nitriles by Photoproduced α -MnO₂ Nanorods on Polystyrene Beads", *Organic Letters* Vol.9, No.11, pp.2191–2193, (2007).
- [12] Jana, S., Pande, S., Sinha, A.K. and Pal, T. "Synthesis of Superparamagnetic β -MnO₂ Organosol: a Photocatalyst for the Oxidative Phenol Coupling Reaction", *Inorganic Chemistry* Vol.47, No.13, pp.5558–5560, (2008).
- [13] Gjergji, D., Lee, Y.-C. and Fujita, T (unpublished results) – Personal communication.
- [14] Simon, D.E., Morton, R.W. and Gislason, J.J. "A Close look at Electrolytic Manganese Dioxide (EMD) and The γ -MnO₂ & ϵ -MnO₂ Phases using Rietveld Modeling", *JCPDS - International Centre for Diffraction Data, Advances in X-ray Analysis*, Vol.47, pp.267–280, (2004).
- [15] Komaba, S., Kumagai, N. and Chiba, S. "Synthesis of Layered MnO₂ by Calcination of KMnO₄ for Rechargeable Lithium Battery Cathode", *Electrochimica Acta*, Vol.46, pp.31–37, (2000).
- [16] Han, Y.-F., Ramesh, K., Chen, L., Widjaja, E., Chilukoti, S. and Chen, F. "Observation of the Reversible Phase-Transformation of α -MnO₂ Nanocrystals during the Catalytic Combustion of Methane by in Situ Raman Spectroscopy", *Jour. of Physical Chemistry C*, Vol.111, pp.2830–2833, (2007).

Method for displaying false colors on the liquid crystal display by switching two colors

Chikako Ishizawa* and Makoto Nishida*

* Department of Computer Science and Engineering, Faculty of Engineering and Resource Science, Akita University,
1-1, Tegata-Gakuen-Machi, Akita, 010-8502 Japan
ishizawa@ie.akita-u.ac.jp

Abstract: There is a problem that images open to the public on the Internet are illegally copied. This study proposes a method to display false colors against the problem. The proposed method is able to display the same color as the original one by switching two different colors. The approach gives the same effect with the copy prevention because a color copied as the image is quite different from the original one. We examined the presence of flicker against two elements on the liquid crystal display: the color and the speed of switching. The experimental results show that false colors were well displayed when the color in the low level brightness was switched at the same speed as the refresh rate of the display. Additionally, RGB values of the perceived color were examined. It was found that the perceived color was a similar to the middle one of the switched two colors. However, the RGB values were different from those of the middle color. The finding indicates that an original color is never restored by using those false colors of the copied image.

Key Words: color mixture, switch of colors, flicker, copy prevention

1 INTRODUCTION

There is a problem that images open to the public on the Internet are illegally copied. Any method has not come to prevent the copy completely though the digital watermark^[1] and the cryptography^[2] have been proposed. The image data is copied easily because the image data is captured into the video memory of the computer when the image open to the public on the Internet is displayed. For example, data in the video memory is copied by pressing the print screen key of the computer.

On the other hand, there are three kinds of cones in the retina of human's eyes^[3]. Each of cones has high sensitivity for light of the short wavelength (about 380 nm to 490 nm), the middle wavelength (about 490 nm to 570 nm), and the long wavelength (about 570 nm to 780 nm), respectively. The color is perceived by the reaction of these cones. For instance, a yellow, which is the color in the middle of red and green, is perceived by reaction of the two cones when red light (long wavelength region) and green light (middle wavelength region) enter into eyes at the same time. Moreover, the yellow is also

perceived when the red and green light change in short time.

Therefore, the purpose of this study is to develop the method for displaying false colors so that the image copied from the video memory will be different from the one displayed on the display. The proposed method has an advantage of displaying the target color by switching different two colors. It is expected that the approach has the same effect with the copy prevention because the color recognized as the image data is quite differs two colors used in the switching process.

However, it is difficult to change color quickly in the liquid crystal display^[4]. Additionally, flicker appears at switching because the liquid crystal display is the hold type display^[4]. Therefore we examined the presence of flicker against the color and the speed of switching on the liquid crystal display.

2 EXPERIMENT

2.1 Experimental conditions

Figure 1 shows the outline of the experimental conditions. Seventeen testers examined images, and the presence of flicker was evaluated. Testers were eight men of his twenties, eight women of her twenties, and a woman of her thirties. Figure 2

shows the criterion of flicker.

The liquid crystal display (EPSON LD1952G; size: 1280×1024 pixel; dot pitch: 0.294 mm × 0.294 mm; the graphics mode: True Color; response time: about 25 ms; maximal luminance: 250 cd/m²; luminance contrast: 700:1) and the personal computer (CPU: Pentium^(R)4 (3.2 GHz); Memory: 1 GByte) were used. The liquid crystal display was set up in a general indoor environment; it is about 450 lx under the fluorescent lamp. The distance between the liquid crystal display and the tester was about 40 cm. The refresh rates of the liquid crystal display were both 60 Hz and 75 Hz.

2.2 Color of switching

The colors used for the experiment are shown in Table 1. Main colors were red, green, blue, yellow, cyan, and magenta. The brightness level (RGB value) of each color was 255, 191, 127, and 63. The number of color was twenty-four.

Two different colors at the same brightness level were selected from the twenty-four colors and used for the experiment. For instance, G1, B1, Y1, C1, and M1 were combined with R1, respectively. The total number of combinations were sixty. Then, the presence of flicker was evaluated to the sixty combination's colors in the switching.

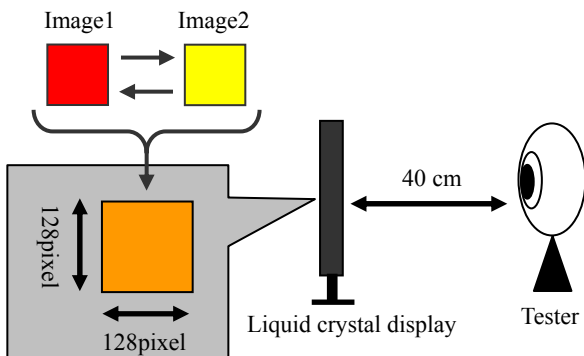


Fig.1 Experimental conditions.

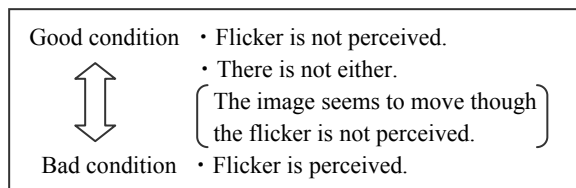


Fig. 2 Criterion of flicker.

- (1) The speed increases from 20 frame/seconds to 120 frame/seconds every 1 frame/seconds.
- (2) The speed decreases from 120 frame/seconds to 20 frame/seconds every 1 frame/seconds.

Fig.3 Conditions for the change of speed.

2.3 Speed of switching

The switching speed was changed every 1 frame/seconds to all the switch of the sixty combinations. When the switching speed changes consecutively, the previous states of the color or flicker will affect the present state. Therefore, the speed of switch was changed under the conditions shown in Figure 3.

3 RESULTS AND DISCUSSION

3.1 Flicker against the colors of switching

Table 2 shows the number of "flicker is not perceived" regarding the switching of the sixty combination's colors. The lower the brightness level became, the more decrease the flicker became under the conditions of the refresh rate of both 60 Hz and 75 Hz.

It is found that there was no combination of colors that all testers judged as "Flicker is not perceived". However, the evaluation of the following combination was high under the conditions of the refresh rate of both 60 Hz and 75 Hz. They were the combination of the red and the magenta, the green and the yellow, the yellow and the cyan; the brightness level was 63. These three combinations have common features that G values of two colors are the same. Therefore, it is guessed that the flicker is not recognized easily when two colors with the same

Table 1. Experimental colors.

Color	RGB Value			
	R	G	B	
Red	R1	255	0	0
	R2	191	0	0
	R3	127	0	0
	R4	63	0	0
Green	G1	0	255	0
	G2	0	191	0
	G3	0	127	0
	G4	0	63	0
Blue	B1	0	0	255
	B2	0	0	191
	B3	0	0	127
	B4	0	0	63
Yellow	Y1	255	255	0
	Y2	191	191	0
	Y3	127	127	0
	Y4	63	63	0
Cyan	C1	0	255	255
	C2	0	191	191
	C3	0	127	127
	C4	0	63	63
Magenta	M1	255	0	255
	M1	191	0	191
	M1	127	0	127
	M1	63	0	63

G value are switched. Further, there is found to be no difference of evaluation between men and women.

3.2 Flicker against the speed of switching

As a result of the experiment, the speed of switching with a little flicker to the sixty combinations were around 60 frame/seconds in the refresh rate of 60 Hz, and the around 40 frame/seconds and the around 75 frame/seconds in the refresh rate of 75 Hz. Additionally, the difference between men and women, and the different of the conditions for the change of speed were never found in the evaluation results.

Figure 4 shows the results regarding the three combinations obtain high evaluation by the testers. The condition, flicker is not perceived, was evaluated in the ranges of the switching speed from 30 frame/seconds to 105 frame/seconds (the refresh rate of 60 Hz) and from 35 frame/seconds to 120 frame/seconds (the refresh rate of 75 Hz). The speed that is obtained high evaluation in all of the three combinations were 61 frame/seconds and from 74 frame/seconds to 76 frame/seconds among these speeds. The flicker caused in the case with different response time will be evaluated in the future.

Table 2. The number of testers judging “flicker is not perceived” regarding to the switching of the sixty combinations.

Combination of colors	The refresh rate of 60 Hz				The refresh rate of 75 Hz			
	RGB Values				RGB Values			
	63	127	191	255	63	127	191	255
The red and the green	4	2	0	0	5	0	0	0
The red and the blue	7	2	1	0	9	0	0	0
The red and the yellow	4	2	0	0	4	0	0	0
The red and the cyan	4	3	0	0	2	0	0	0
The red and the magenta	11	4	3	0	14	1	0	0
The green and the blue	5	3	0	0	3	0	0	0
The green and the yellow	10	3	0	0	11	1	0	0
The green and the cyan	8	4	2	0	8	1	0	0
The green and the magenta	6	4	0	0	8	0	0	0
The blue and the yellow	4	3	0	0	0	0	0	0
The blue and the cyan	4	4	0	0	2	0	0	0
The blue and the magenta	5	3	0	0	9	0	0	0
The yellow and the cyan	9	4	1	0	12	0	0	0
The yellow and the magenta	6	3	0	0	3	0	0	0
The cyan and the magenta	4	4	0	0	4	0	0	0

More than half of testers.

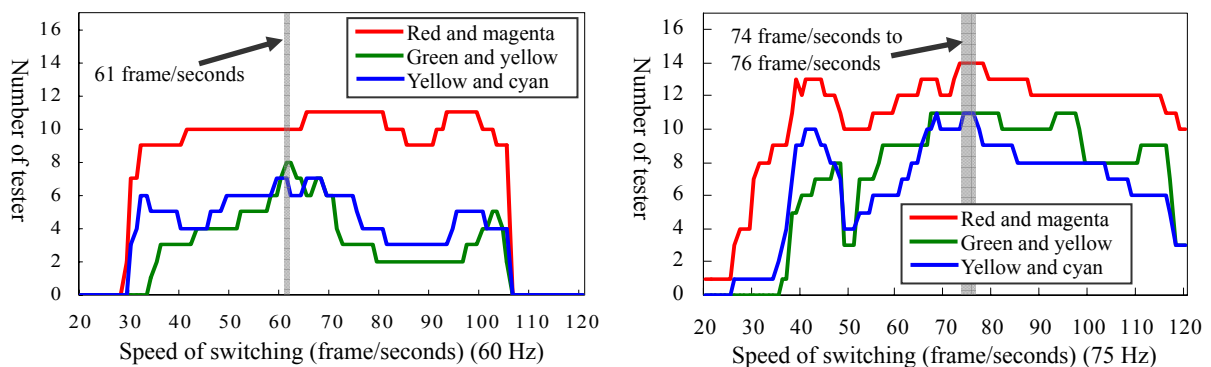


Fig.4 The number of testers judging “flicker is not perceived” regarding the switching speed. The refresh rate of 60 Hz (left) and the refresh rate of 75 Hz (right).

4 APPLICATION TO THE COPY PREVENTION OF THE IMAGE

Based on the above findings, it was tried to apply the method for displaying false colors against the copy prevention of the image by the following three procedures.

Step 1) It was supposed that an original image was a single color; the images shown in Figure 5 were made by using the colors of the three combinations obtained high evaluation (see 3.1).

Step 2) The image 1 and image 2 were alternately switched and displayed. The image 3 and image 4, and the image 5 and image 6 were also switched. The display and experimental conditions were same in the previous experiment (see 2). The refresh rate of the liquid crystal display and the switching speed were set to the 60 Hz and the 61 frame/seconds, respectively. Moreover, the still image that was able to change RGB value was displayed next to the switched image.

Step 3) Testers evaluated the presence of the character in the switched image. The number and details of the testers were the same in the experiment described in 3.1. In addition, the color, called false color, of the switched image was examined by changing RGB value of the still image.

As the result, the character in the image disappeared by switching the image, and the image of the single color was perceived.

Table 3 indicates the evaluation result of the character. When the image 5 and image 6 were switched, twelve testers perceived the characters because flicker was perceived around the characters. However, the characters and flicker were not perceived in the switching of other images at all.



Fig.5 Images used for the switching.

Figure 6 shows typical examples of the false colors. All false colors are looked like the middle color of the switched two colors. However, the RGB value of the false color and the middle color was different. Therefore, the results suggest that it is difficult to restore an original image from the copied image.

5 CONCLUSION

In the present study, the method for displaying false colors on the display was proposed to prevent the copy of image. The experimental results show that false colors were well displayed when the color in the low level brightness was switched at the same speed as the refresh rate of the display. It was also found that an original color is never restored by using those false colors of the copied image. It is future work to examine the difference between restored image and original one.

Acknowledgement

The authors thank Dr. Y. Kageyama, Mr. T. Takahashi, and Ms. M. Suzuki, Akita University, for the help in conducting the experiment.

References

- [1] Ono, T., "Digital watermarking and contents protection", Ohmsha, (2001).
- [2] Shin, K., Aonuma, H., "Securing Intellectual and Artistic Property Rights of Digital Contents during Storage, Distribution and Consumption.", Information Processing Society of Japan Magazine, Vol.40, No.5, pp.480-485, (1999).
- [3] The Vision Society of Japan, "Vision information processing handbook", Asakura Publishing, (2007).
- [4] Ohishi, I., Hatada, T., Tamura, T., "Base of display", Kyoritsu Shuppan, (2004).

Table 3. Evaluation results.

Combination of image	Character is not seen.	Character is seen.
Image 1 and Image 2	17	0
Image 3 and Image 4	17	0
Image 5 and Image 6	5	12

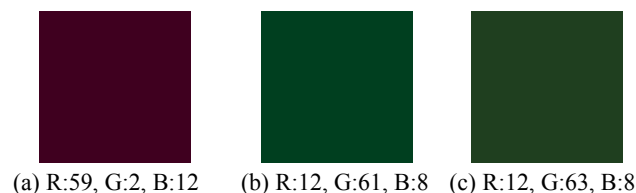


Fig.6 Example of the false color and the RGB values; (a) The switching of the image 1 and image 2, (b) The switching of the image 3 and image 4, (c)The switching of the image 5 and image 6.

Reflection Response from a Finite Plane Crack Lying in Elastic Half-Space Subjected to SH Periodic Impact Load

Kimihisa MIURA*

*Department of Mechanical Engineering
Faculty of Engineering and Resource Science, Akita University
1-1, Tegata-Gakuen-Cho, Akita, 010-8502, JAPAN
kmiura@ipc.akita-u.ac.jp

Abstract: Here, the new simple analytical method named EAEA (The exact analytical element approach) is developed. EAEA is our original analytical method which we connect analytically several exact solutions for the transient boundary problem and solve precisely and rationally the more complicated problem. By using this method, the Cagniard method, the Wiener-Hopf technique and the method of images, we are finally analyzing the reflection response from a finite plane crack lying in elastic half-space subjected to SH periodic impact load. In this paper the most important subject is to observe the resonance phenomenon of the finite length crack by the periodic impact load. The relationship between transient wave reflection response from the finite crack and the impact periodic frequency is examined by the exact analysis and the numerical calculation.

Key Words: Transient Reflection Analysis, SH Periodic Impact Load, Finite Plane Crack

1 INTRODUCTION

Recently, for the transient wave propagation problem of the elastic material we are confirming the possibility of the engineering application using the new simple analytical approach which connects several exact solutions and calculates numerically by using the small computer system and finally represents the precise and rational transient response^{(1)~(5)}. This approach is named EAEA by us. The transient wave propagation analysis is used widely in the industrial field as the fundamental engineering analytical approach of the health monitoring of the structures and the non-destructive testing^{(6)~(8)}. Therefore we are considering that our offering analytical method from now on will become the new effective simulation approach for many engineering problems. Here, we consider reflection response from a finite plane crack lying in elastic half-space subjected to SH periodic impact load. We are analytically connecting three solutions of SH transient problem for the elastic half-space and the elastic thick plate, and SH transient reflection problem from a micro plane crack in the elastic half-space. The Cagniard method⁽⁹⁾ gives the exact solution of the anti-plane deformation problem which SH impulsive load acts on the free surface of an elastic half-space.

After considering the secondary boundary condition on the crack surface, the transient reflection response from a micro plane crack is given by the Wiener-Hopf technique⁽¹⁰⁾. And the transient response for the elastic thick plate is given by the method of images⁽¹¹⁾. In this paper, by using EAEA we investigate the resonance phenomenon of the finite crack. When resonance phenomena of the structure are examined, the required engineering keyword is the natural frequency of the structural element at the resonance position, and the most important property included in the external force is the central frequency of the periodic impact load. If it is assumed that the crack doesn't vibrate and its size doesn't change by the impact, and the elastic material and the crack are in one body, we can consider that the effect of the finite length crack by periodically repeated impact load is appeared within the transient reflection response field from the finite crack. Here, as one of the specific example of the numerical experiment to investigate such resonance phenomena, we consider a SH transient problem. SH impulsive load, which is represented as the Dirac's delta function and is repeated periodically, is applied on the free surface of the elastic half space with a finite plane crack. The relationship between the transient wave reflection response from the crack and the impact periodic frequency of the load is examined by the exact analysis and the numerical calculation.

2 ANALYSIS

We consider the transient response for an anti-plane deformation problem which SH periodic impact load acts on the free surface of the homogeneous isotropic elastic half-space with a finite plane crack like Fig.1. The symmetric finite crack surface is parallel to the free surface of the half-space and the crack tips coordinates are $(\pm x_c, h)$. On advancing the analysis by using EAEA, we connect analytically SH transient problems for the elastic half-space and the elastic thick plate, and SH transient reflection problem from a micro plane crack in the elastic half-space.

2.1 SH transient analysis for elastic half-space

First, we consider that SH impulsive load acts on the free surface of the elastic half-space for the no crack case. The equation of motion of the SH mode is

$$\frac{\partial^2 w}{\partial x^2} + \frac{\partial^2 w}{\partial y^2} = \frac{1}{c^2} \frac{\partial^2 w}{\partial t^2} \quad (1)$$

where, w is z direction displacement and c is the phase velocity as following

$$c = \sqrt{\mu/\rho} \quad (2)$$

μ is the modulus of transverse elasticity and ρ is the mass density of the material.

The constitutive equations for the stresses are

$$\tau_{yz} = \mu \frac{\partial w}{\partial y} \quad (3)$$

$$\tau_{xz} = \mu \frac{\partial w}{\partial x} \quad (4)$$

The boundary condition on the free surface of the half-space is

$$[\tau_{yz}]_{y=0} = Q\delta(x)H(t) \quad (5)$$

where, $\delta(x)$ is the Dirac's delta function and $H(t)$ is the Heaviside's step function.

The initial conditions are

$$[w]_{t=0} = [\dot{w}]_{t=0} = 0 \quad (6)$$

Two pairs of the integral transforms are defined as following

The Fourier integral transform

$$\mathcal{F}[w] \equiv \bar{w}(s\xi) = \int_{-\infty}^{\infty} w(x) e^{-is\xi x} dx \quad (7)$$

$$\mathcal{F}^{-1}[\bar{w}] \equiv w(x) = \frac{1}{2\pi} \int_{-\infty}^{\infty} \bar{w}(s\xi) e^{is\xi x} d(s\xi) \quad (8)$$

The Laplace integral transform

$$\mathcal{L}[w] \equiv w^*(s) = \int_0^{\infty} w(t) e^{-st} dt \quad (9)$$

$$\mathcal{L}^{-1}[w^*] \equiv w(t) = \frac{1}{2\pi i} \int_{Br} w^*(s) e^{st} ds \quad (10)$$

where, Br of Eq.(10) stands for the integral of Bromwich-Wagner.

Applying the Fourier Laplace double transforms to Eq. (1)~(6) and considering the boundary condition (5), we obtain the

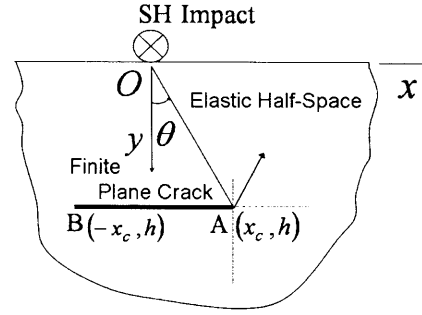


Figure 1 Finite crack lying in the elastic half-space subjected to SH periodic Impact load

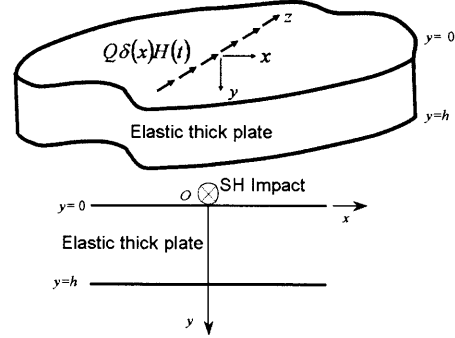


Figure 2 Elastic thick plate subjected to SH impact load

transformed solutions. Furthermore, applying the Cagniard method to evaluate exactly the double inversion, we finally obtain the following exact solutions for the stress components

$$\tau_{yz} = \frac{Q}{2\pi} H(t - vR) \frac{2yt}{R^2 \sqrt{t^2 - v^2 R^2}} \quad (11)$$

$$\tau_{xz} = \frac{Q}{2\pi} H(t - vR) \text{Im} \left[\frac{\xi_+}{\sqrt{\xi_+^2 + v^2}} \frac{\partial \xi_+}{\partial t} - \frac{\xi_-}{\sqrt{\xi_-^2 + v^2}} \frac{\partial \xi_-}{\partial t} \right] \quad (12)$$

and for the strain energy

$$U = \frac{1}{2\mu} (\tau_{yz}^2 + \tau_{xz}^2) \quad (13)$$

where

$$v = 1/c \quad (14)$$

$$\xi_{\pm} = \frac{\pm y \sqrt{t^2 - v^2 R^2} + ixt}{R^2} \quad (15)$$

$$R = \sqrt{x^2 + y^2} \quad (16)$$

2.2 SH transient analysis for elastic thick plate

We consider the homogeneous isotropic elastic thick plate with the thickness h like Fig.2. SH impulsive load acts on the free surface and we assume that the boundary condition and the initial condition are same as the preceding section.

Then the boundary conditions are

$$\tau_{yz} |_{y=0} = Q\delta(x)H(t) \quad (17)$$

$$\tau_{yz} |_{y=h} = 0 \quad (18)$$

Considering the boundary condition (17),(18) and applying the Fourier Laplace double transforms to the basic equations, we obtain the transformed solutions. Furthermore, applying the Cagniard method to evaluate exactly the double inversion, we finally obtain the following exact solutions for the stress components

$$\tau_{yz} = \frac{Q_t}{\pi} \sum_{n=1}^{\infty} [\tau_{yz1} - \tau_{yz2}] \quad (19)$$

$$\tau_{xz} = \frac{Q}{2\pi} \sum_{n=1}^{\infty} [\tau_{xz1} + \tau_{xz2}] \quad (20)$$

where

$$\tau_{yz1} = \{y + 2(n-1)h\} \frac{H(t - vR_{2(n-1)})}{R_{2(n-1)}^2 \sqrt{t^2 - v^2 R_{2(n-1)}^2}} \quad (21)$$

$$\tau_{yz2} = \{y - 2nh\} \frac{H(t - vR_{2n})}{R_{2n}^2 \sqrt{t^2 - v^2 R_{2n}^2}} \quad (22)$$

$$\tau_{xz1} = H(t - vR_{2(n-1)}) \text{Im} \left[\frac{\xi_{2(n-1)+}}{\sqrt{\xi_{2(n-1)+}^2 + v^2}} \frac{\partial \xi_{2(n-1)+}}{\partial t} - \frac{\xi_{2(n-1)-}}{\sqrt{\xi_{2(n-1)-}^2 + v^2}} \frac{\partial \xi_{2(n-1)-}}{\partial t} \right] \quad (23)$$

$$\tau_{xz2} = H(t - vR_{2n}) \text{Im} \left[\frac{\xi_{2n+}}{\sqrt{\xi_{2n+}^2 + v^2}} \frac{\partial \xi_{2n+}}{\partial t} - \frac{\xi_{2n-}}{\sqrt{\xi_{2n-}^2 + v^2}} \frac{\partial \xi_{2n-}}{\partial t} \right] \quad (24)$$

$$R_{2(n-1)} = \sqrt{x^2 + \{y + 2(n-1)h\}^2} \quad (25)$$

$$R_{2n} = \sqrt{x^2 + (y - 2nh)^2} \quad (26)$$

$$\xi_{2(n-1)}(t) = \frac{\pm \{y + 2(n-1)h\} \sqrt{t^2 - v^2 R_{2(n-1)}^2} + ixt}{R_{2(n-1)}^2} \quad (27)$$

$$\xi_{2n}(t) = \frac{\pm (y - 2nh) \sqrt{t^2 - v^2 R_{2n}^2} + ixt}{R_{2n}^2} \quad (28)$$

and n is the frequency which the transient waves go and return through the plate vertically to the free surface.

Therefore, the solution for the strain energy is

$$U = \frac{1}{2\mu} (\tau_{yz}^2 + \tau_{xz}^2) \quad (29)$$

2.3 SH transient reflection analysis from a micro plane crack in the elastic half-space

We consider SH transient reflection response from a micro plane crack in the elastic half-space. The boundary condition and the initial condition are same as the preceding section. We assume that there is a micro plane crack with angle ϕ from the horizontal line at the coordinate (x_c, y_c) in the elastic half-space like Fig.3 and this crack is assumed to be able to reflect only one transient wave ray. Since we could get the exact solutions of the transient problem for the elastic half-space in the section 2.1, when the wavefront reaches at the crack tip on

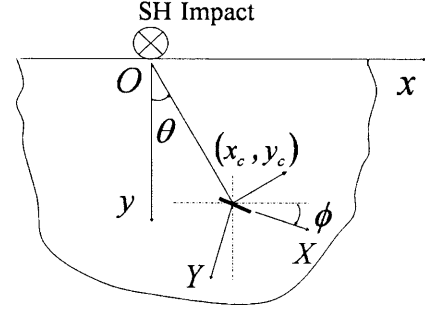


Figure 3 Reflection of SH transient waves from a micro plane crack

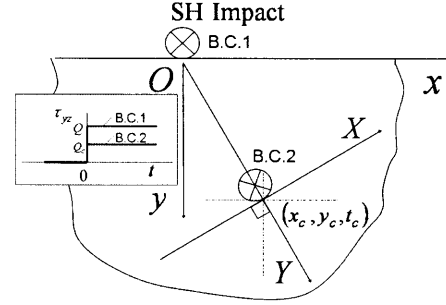


Figure 4 Boundary conditions B.C.1 for the half-space and B.C.2 for the micro plane crack

the time $t_c = vR_c$, we can numerically calculate the transient response which will become a new wave source at the crack tip. Where, the distance R_c from the wave source to the crack tip is

$$R_c = \sqrt{x_c^2 + y_c^2} \quad (30)$$

Here, we consider the secondary wave source subjected on the micro plane crack surface. As the principal plane of the stress, the plane crack angle ϕ is given like $\phi = -\theta$. As shown in Fig.4 considering the geometrical attenuating of the response of the wavefront generated at the wave source, the secondary boundary conditions with the $X-Y$ coordinate system are as following

$$\tau_{yz}|_{Y=0} = Q_c \delta(X) H(t - t_c) \quad (31)$$

$$\tau_{xz}|_{Y=0} = 0 \quad (32)$$

where,

$$Q_c = Q \cos \Phi / \pi R_c \quad (33)$$

$$\Phi = \arctan(x_c / y_c) + \phi \quad (34)$$

When we consider these boundary condition, the wave normal of the transient wave incident to the crack is right angle with a micro plane crack surface, therefore $\Phi = 0$. Furthermore we can describe the geometrical diagram of the wave propagation like Fig.5 and we can obtain the analytical solution of the reflection response from the micro plane crack as following

at $t < t_c$

$$\begin{bmatrix} \tau_{yz} \\ \tau_{xz} \end{bmatrix} = \begin{bmatrix} \tau_{yz}(x, y, t) \\ \tau_{xz}(x, y, t) \end{bmatrix}_1 \quad (35)$$

at $t \geq t_c$

$$\begin{bmatrix} \tau_{yz} \\ \tau_{xz} \end{bmatrix} = \begin{bmatrix} \tau_{yz}(x, y, t) \\ \tau_{xz}(x, y, t) \end{bmatrix}_1 + \begin{bmatrix} \cos \phi + \sin \phi & \cos \phi - \sin \phi \\ \sin \phi - \cos \phi & \sin \phi + \cos \phi \end{bmatrix} \begin{bmatrix} \tau_{yz}(x_r, y_r, t - t_c) \\ \tau_{xz}(x_r, y_r, t - t_c) \end{bmatrix} \quad (36)$$

The bottom suffix 1 of the right hand side the first term stands for the no crack case and (x_r, y_r) is

$$\begin{bmatrix} x_r \\ y_r \end{bmatrix} = \begin{bmatrix} \cos \phi & -\sin \phi \\ \sin \phi & \cos \phi \end{bmatrix} \begin{bmatrix} X \\ Y \end{bmatrix} \quad (37)$$

where, the relationship between (x_r, y_r) and the calculation point coordinate (x, y) are

$$\begin{bmatrix} x \\ y \end{bmatrix} = \begin{bmatrix} x_r \\ y_r \end{bmatrix} + \begin{bmatrix} R_x + R_2 \\ R_y + R_2 \end{bmatrix} \quad (38)$$

$$R_2 = R_1 - R_c \quad (39)$$

$$R_x = R_1 + R_c \sin \theta - R_2 \quad (40)$$

$$R_y = \sqrt{R_c^2 - R_c^2 \sin^2 \theta} - R_2 \quad (41)$$

where, R_1 and R_2 are the radiuses of the original wavefront and the reflected wavefront from the crack tip at the arbitrary calculation time t_1 , respectively.

2.4 SH transient reflection analysis from a finite plane crack in the elastic half-space

We consider the elastic half-space with a finite plane crack represented as the segment AB like Fig. 6. The boundary condition and the initial condition at the origin are same as the preceding section. As shown in this figure, the wave field from the origin is cut off at the AC plane and the BG plane. The reflected wave field from the elastic thick plate is cut off at the AD plane and the BH plane. The transient reflection wavefronts from the crack tips are tangentially contact with the transient wavefront from the origin at the C line and the G line and with the wavefront from the plate at the D line and the H line. In this analysis, the AC, BG plane and the AD, BH plane become the discontinuous plane of the response. Here, the discontinuities at the AC, BG plane are gradually decreased to zero toward the AE, BI plane, respectively by the assumption of the additional wave propagation. We consider the same operation from the AD, BH plane to the AF, BJ plane, respectively.

3 NUMERICAL CALCULATION

In EAEA, when we analyze the problem contain the characteristic dimension such as the plate thickness or the crack length, we use, not the Cagniard method, but the method of images and the analytical connection such as the Wiener-Hopf technique. That is, the application of the Cagniard method is limited only the transient problem for the fundamental elastic half-space. Therefore the load of our numerical calculation

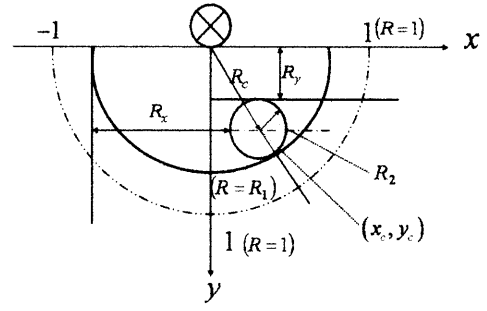


Figure 5 Image of the transient reflection response from a micro place crack

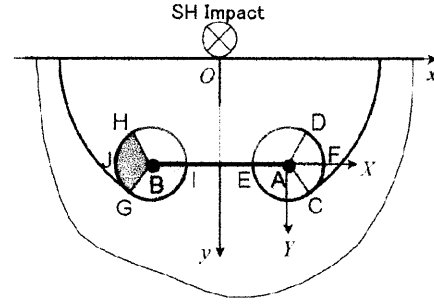


Figure 6 Explanation of the analytical connection of the transient problems for the elastic half-space, the thick plate and the micro plane crack

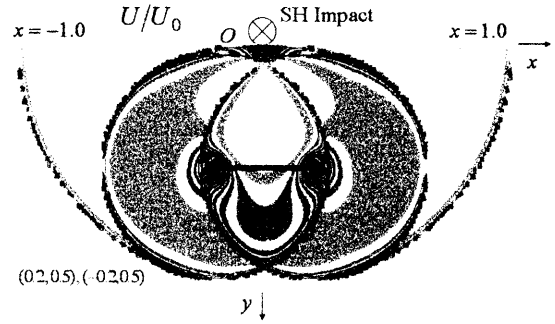


Figure 7 Transient reflection response of the strain energy with the crack tips coordinates $(-0.2,0.5),(0.2,0.5)$

drastically reduced. Here, the phase velocity of SH wave is $c = 1.0$, but the generality is not lost and we can freely set the crack length. Although we can calculate the stresses, the strain energy and the displacement, as we can explain the acoustic wave propagation we calculate only the transient response of the strain energy which is represented as the scalar value. In our analysis by using Eq.(5) we consider the step impact, but the analysis by using the delta impact is better for the case of the periodic impact since it doesn't contain the extra wave information. Then in the numerical calculation we did some analytical manipulations, that is, we replaced the step function σ_s within the exact solution by the step impact load with the delta function σ_δ as following

$$\sigma_s = H(t - vR) \quad (42)$$

$$\sigma_\delta = \exp(-10\sigma_s) \quad (43)$$

And the periodic frequency was made to change from 1 to 320

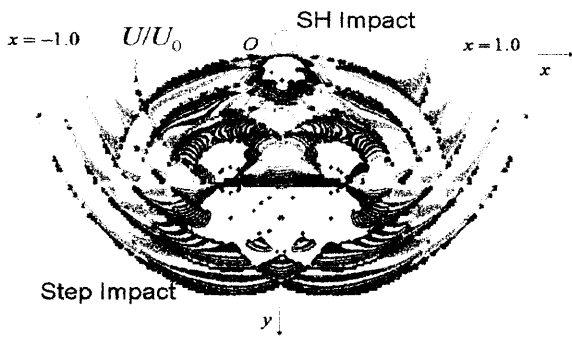


Figure 8 Transient reflection response from the finite crack for 5 times periodic step impact

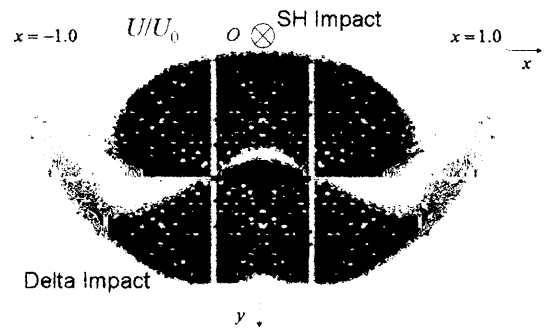


Figure 10 Transient reflection response from the finite crack for 320 times periodic delta impact

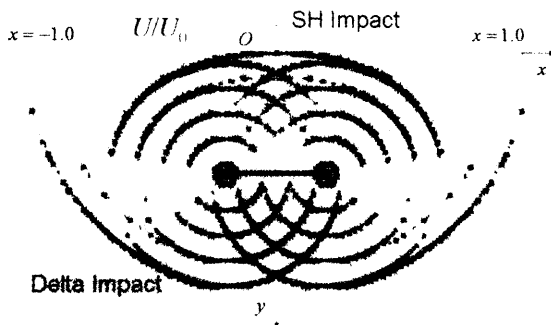


Figure 9 Transient reflection response from the finite crack for 5 times periodic delta impact

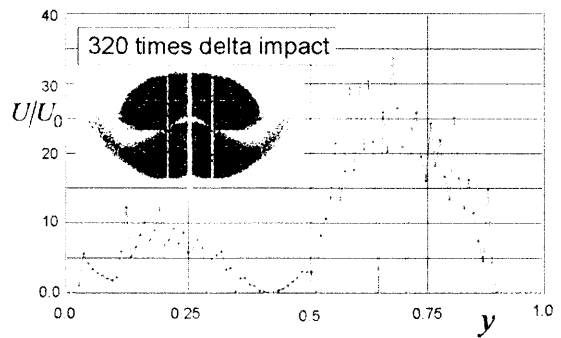


Figure 11 Variation of the strain energy for 320 times periodic delta impact for y coordinate at $x = 0.0$

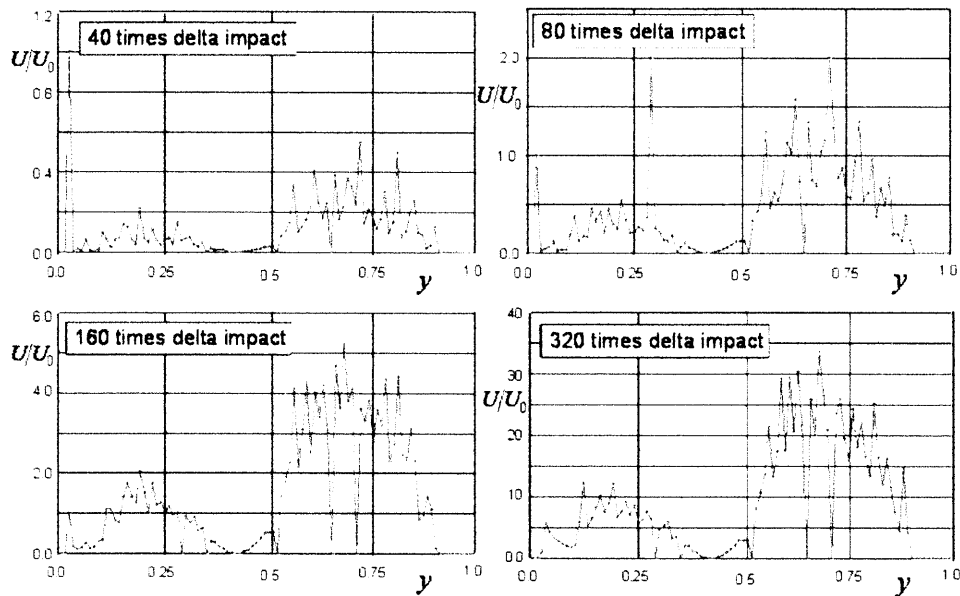


Figure 12 Comparison of the transient responses between the periodic frequencies 40, 80, 160 and 320 times

times. Fig.7 is the transient reflection response from the finite crack with the tips coordinates $(\pm 0.2, 0.5)$ for 1 time step impact. The response values are positive and the colors are alternately changed in every 0.002 for $0 \leq U/U_0 \leq 0.02$. U_0 is the response value of the strain energy U at the coordinate $(0,0.01)$. The reflected wavefront which generated at one crack tip propagates along the crack and go through another

tip. But the reflection from another tip newly does not occur. Fig.8 is the transient reflection response from the finite crack subjected to 5 times periodic step impact. Fig.9 is the transient reflection response from the finite crack subjected to 5 times periodic delta impact and this figure is comprehensively and effectively representing the reflection response more than Fig.8.

Precise measurement of air-refractive-index fluctuation using laser frequency shift

Tuan Banh Quoc*, Lan Le Hung** and Masato Aketagawa*

* Department of Mechanical Engineering, Nagaoka University of Technology, 1603-1 Kamitomioka, Nagaoka, Niigata, 940-2188 Japan

** Department of Cybernetics, University of Transport and Communication, #1 Lang Thuong, Dong Da, Hanoi, Viet Nam
bqtuan79@stn.nagaokaut.ac.jp

Abstract: Commercial laser interferometers suffer a big uncertainty from the air-refractive-index fluctuation (Δn_{air}). This paper presents a method to measure Δn_{air} using a Fabry-Perot cavity, in which an external cavity laser diode (ECLD) is used as the light source and its frequency is controlled to track the resonance of the Fabry-Perot cavity. The Pound-Drever-Hall method and an ultra low thermal expansion material (ULTEM) with thermal expansion coefficient of 2×10^{-8} /K are used to control ECLD frequency and to reduce the deformation of the optical path length within the temperature fluctuation range of 10 mK, respectively. Δn_{air} can be derived from the ECLD frequency shift with an estimated uncertainty of 10^{-9} order.

Key Words: frequency shift, air refractive index, Fabry-Perot cavity

1. INTRODUCTION

Since the ultraprecise manufacturing industries require machining and positioning tolerances of sub-nanometer order or less due to the progress of nanotechnology^[1], numerous commercial displacement measuring optical interferometers using heterodyne^[2] and homodyne^[3] techniques are widely used for positioning techniques in the semiconductor industry because of their wide dynamic range and high resolution. However, optical influences of environmental fluctuations, such as the thermal expansion of optical devices, change in the refractive index and so on, cause very serious scattering of the sub-nm values detected by the displacement interferometer. Therefore, to achieve sub-nanometer precision of displacement interferometers, it is very important to minimize the influence of these optical fluctuations. In the normal air environment, the air-refractive-index fluctuation (Δn_{air}) is a dominant factor causing the measurement uncertainty. This kind of environmental influence can be calculated by numerical method given by Edlen^[4] or Ciddor^[5]. These methods are quite simple but the measurement speed is low owing to the time response of environmental sensors, and resolution is limited to 10^{-8} order^[5]. It is not satisfied to the requirement of sub-nanometer displacement precision. The paper presents a method for a precise measurement of Δn_{air} by utilizing a

Fabry-Perot cavity (FPC) supported with an ultra low thermal expansion material (ULTEM) and an external cavity laser diode (ECLD). The resonant of the FPC (means a minimum intensity peak of reflection light from the FPC) is locked by controlling the ECLD frequency (Pound-Drever-Hall method^[6]). Δn_{air} can be derived from the ECLD frequency change. The experimental results, taken in two conditions: large and small refractive index fluctuation, respectively, show a good agreement of Δn_{air} measurement compared with the numerical method mentioned above, in reference 5, with the estimation uncertainty of 10^{-9} order. There is a possibility to improve the measurement uncertainty level down to 10^{-10} order if the signal-to-noise of the control system is improved.

2. MEASUREMENT PRICIPLES

Fig. 1 shows the schematic diagram of the measurement system. In the system, an ECLD is used as light source for the measurement of Δn_{air} . A 633 nm linearly polarized laser beam is emitted from the ECLD, and phase-modulated by the electro optical modulator (EOM). After that, the beam passes through a mode matching lens (L_M) to adjust the beam waist in order to reduce the mode output of the Fabry-Perot cavity. Cavity mirrors are mounted on the ULTEM in order to reduce the cavity length deformation caused by thermal disturbance. The laser beam bounces between two cavity mirrors back and forth,

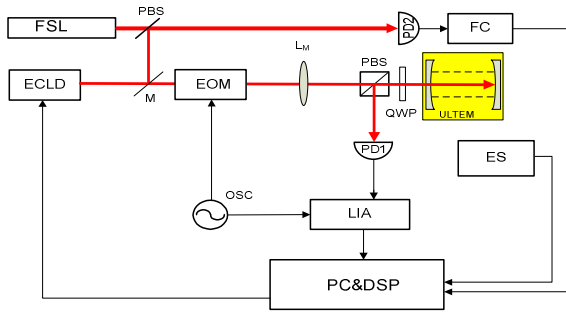


Fig. 1 Schematic of Δn_{air} measurement system using the FPC. ECLD: external cavity laser diodes, EOM: electro optical modulators, FSL: frequency stabilized laser, PBS: polarized beam splitter, QWP: quarter wave plate, M: mirror, L_M : mode matching lens, ES: environmental sensors, ULTEM: ultra low thermal expansion material, PD1 and PD2: photo diodes, LIA: lock-in amplifier, FC: frequency counter, OSC: oscillator, PC&DSP: personal computer & digital signal processor.

and then, the reflection beam goes through a quarter wave plate (QWP) and a polarizing beam splitter (PBS). Intensity of the reflection beam is measured by a high speed photodetector 1 (PD1). The measured signal from PD1 is proportional to the instantaneous frequency error, as measured with respect to the cavity's stable resonant frequency. This error signal is then processed by a lock-in amplifier and ELCD frequency is controlled by a digital signal processor (DSP) to eliminate the error. The PD2 and the frequency counter (FC) are utilized to measure the beat frequency Δf between the ECLD and the FSL. The environmental sensors such as: thermometer, hygrometer and barometer are placed near the optics so that the Δn_{air} is also measured by Ciddor's calculation. A performance of the Δn_{air} measurement between theoretical method and experimental method can be taken in the real time.

The mathematical model of the system is explained in detail as below:

The electric field of the ECLD laser to the FPC can be written as

$$E_1 = E_0 \cos(\omega t) \quad (2.1)$$

where: ω is angular frequency of the ECLD, E_0 : amplitude of electric field E_I . The light is modulated by EOM with modulation signal $f(t)$ at modulation frequency ω_m and modulation index a

$$f(t) = a \cos(\omega_m t) \quad (2.2)$$

The incident beam to the FPC is

$$E_i = E_0 \cos[\omega t + m \sin \omega_m t] \quad (2.3)$$

After some mathematical calculation, the incident beam can be

rewritten as

$$E_i \approx E_0 \{J_0(m) \cos(\omega t) - J_1(m)[\cos(\omega - \omega_m)t - \cos(\omega + \omega_m)t]\} \quad (2.4)$$

or in exponential way E_i is expressed by

$$E_i = E_0 [J_0(m) e^{i\omega t} + J_1(m) e^{i(\omega + \omega_m)t} - J_1(m) e^{i(\omega - \omega_m)t}] \quad (2.5)$$

where $J_n(m)$ is the n^{th} -order Bessel function.

The modulated signal is incident to the FPC, after that it interfere with the reflection light after through cavity. The amplitude reflection coefficient of the cavity is a function of frequency of incident light ω and cavity resonant frequency ω_{res} as:

$$F(\omega_e) = E_{ref} / E_i = \frac{r_1 r_2 \left[\exp\left(i \frac{\omega_e}{F.S.R}\right) - 1 \right]}{1 - (r_1 r_2)^2 \exp\left(i \frac{\omega_e}{F.S.R}\right)} \quad (2.6)$$

where $\omega_e = \omega - \omega_{res}$ and F.S.R is free spectral range of the cavity.

The reflection signal from cavity can be written as:

$$E_{ref} = E_0 \left[F(\omega_e) J_0(m) e^{i\omega t} + F(\omega + \omega_m) J_1(m) e^{i(\omega + \omega_m)t} - F(\omega - \omega_m) J_1(m) e^{i(\omega - \omega_m)t} \right] \quad (2.7)$$

The beat signal of E_i and E_{ref} generates an error signal and the intensity of the error signal is measured by photodetector as

$$I_e(t) = -2J_0(m)J_1(m)Im[F(\omega_e)F^*(\omega_e + \omega_m) - F^*(\omega_e)F(\omega_e - \omega_m)] \sin(\omega_m t) \quad (2.8)$$

At the resonant point, error signal is completely null value. When the laser frequency ω is different resonant frequency of the cavity, then the null point will be shifted. Detecting this shift value can be done by a control system, from that, laser frequency is adjusted to adapt the shift of the resonant point.

Under the locking condition of the interferometer, the intensity output of the LIA must be null^[6]. The null point is locked by a control system that adjusts the ECLD frequency to lock some dark fringes of the interferometer. Therefore, the following condition is satisfied:

$$n_{air} L = \frac{\lambda}{2} N = \frac{c}{2f} N \quad (2.9)$$

where n_{air} , L , λ , f , N , and c are the air-refractive-index, the separation between two cavity mirrors, the vacuum wavelength of the ECLD, the frequency of the ECLD, the interference fringe order and the speed of light, respectively. Equation (2.9) shows that one of the null cross-points of the LIA coincides with the N -th dark fringe of the interferometer. At the null cross-point with N -th fringe order, we can rewrite equation

(2.9) as

$$\frac{\Delta n_{air}}{n_{air}} = -\frac{\Delta f}{f} - \frac{\Delta L}{L} + \frac{\Delta N}{N} \quad (2.10)$$

where Δn_{air} , ΔL , Δf and ΔN are the shifts or fluctuations against n , L , f and N , respectively. In the system, since the N -th order null cross-point must be maintained by tuning the ECLD frequency so that the change in the ratio of $\Delta N/N$ can be neglected. Meanwhile, a selection of L (or N) and a reduction of the noise in the control of the specific null cross-point can eliminate $\Delta N/N$ with 10^{-10} order. Then, we can obtain

$$\frac{\Delta n_{air}}{n_{air}} \approx -\frac{\Delta f}{f} - \frac{\Delta L}{L} \quad (2.11)$$

Equation (2.11) indicates that $\Delta n_{air}/n_{air}$ can be derived from $\Delta L/L$ and $\Delta f/f$. In the system, two cavity mirrors are fixed on the ULTEM plate. If the ULTEM thermal expansion ratio α is $10^{-7} \sim 10^{-8}/K$ then $\Delta L/L$ should be of $10^{-9} \sim 10^{-10}$ order against the temperature change ΔT of 1mK \sim 10 mK then $\Delta n_{air}/n_{air}$ can be written as

$$\frac{\Delta n_{air}}{n_{air}} \approx -\frac{\Delta f}{f} \quad (2.12)$$

From equation (2.12) under the conditions $\alpha = 2 \times 10^{-8}/K$, $\Delta N/N \leq 10^{-10}$, $\Delta T \leq 10$ mK and $\Delta L/L \leq 10^{-10}$, $\Delta n_{air}/n_{air}$ can be calculated from $\Delta f/f$ with the resolution of 10^{-9} order or less, which is limited by the uncertainty of $\Delta N/N$, $\Delta L/L$ and $\Delta f/f$.

3. EXPERIMENTAL RESULTS

The environmental sensors (ES, Thermometer: Takara Thermistor DS100, Resolution 1 mK, response time 1 s; Hydrometer: Delta OHM, Inc., HD2101.1, Resolution 0.1 %, response time 1 s; Barometer: Tokyo Suzuki Co. Ltd., T-60, Resolution 1 Pa, response time 1 s) were used in order to calculate the Δn_{air} using Ciddor calculation. Data from these sensors were recorded by a data acquisition system at the same time of the measurement by the interferometers. In this experiment, maximum sampling rate for Ciddor calculation was 1 Hz. In the experiment, sampling rates of the ECLD frequency shift Δf was 100 Hz. The ECLD (New focus, velocity 6304, linewidth of 300 kHz) was used. The FSL (Spectra Physics, 117A He-Ne laser) and frequency counter (Pendulum, Inc. CNT-90) were used to measure the ELCD frequency change. Modulation frequency of ~ 6 MHz was applied to the EOM with the modulation index of 1.8 rad. The LIA consisted of a mixer (R&K, M1xca double balanced mixer) and a low pass filter (NF Electronic Instrument E-3201, cutoff frequency = 1 kHz) which were used to for demodulation process. The cavity's mirrors were set on the ULTEM with thermal expansion coefficient of $2 \times 10^{-8}/K$ (Nippon Steel, Nexcera). The optical path length between two mirrors was calculated through the measurement free spectral range (FSR) of the FPC. In the system, the FSR of the FPC was

approximately 1.5 GHz, equivalent to the optical path length of 99.9 mm.

The experiment was taken under two conditions: unstable and stable environments. In the unstable case, an air disturbance flow was introduced to the interferometers area causes large pressure and temperature changes. In the stable case, interferometers are covered by a shield box in order to minimize the fluctuation of the temperature, humidity and pressure. For each case, experimental data was compared with Ciddor calculation in term of the measurement tendency and uncertainties

3.1 Large refractive index fluctuation

Fig. 2 shows temperature and pressure variations under the condition of large air turbulence. In the experiment, the intensity of the air turbulence flow was varied periodically, so that we can see temperature and pressure are also changed according to the disturbance. The temperature, pressure and humidity changes are about 30 mK, 6 Pa and 1% in the measurement duration of 150 s, respectively. Fig. 3 shows a comparison of the Δn_{air} measurement using the FPC and the Ciddor calculation. A good correlation between the time variations of $\Delta f/f$ determined from the proposed method and $\Delta n_{air}/n_{air}$ calculated from the Ciddor method can be seen. However, due to the low response speed of the ESs in the system, the Ciddor calculation may not respond in the high speed change of Δn_{air} .

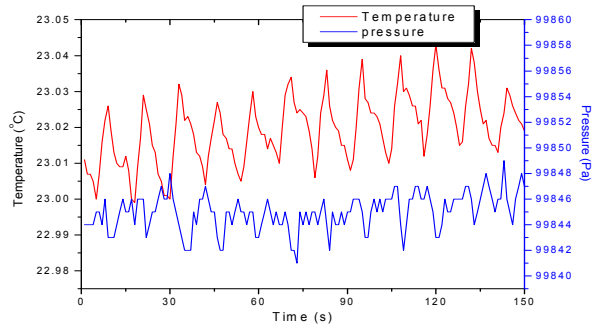


Fig. 2 Temperature and pressure change under the air disturbance flow

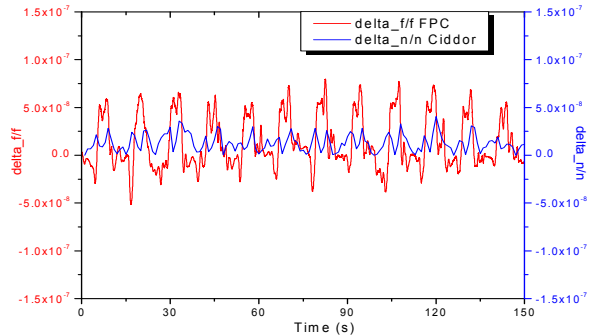


Fig. 3 Experimental result of Δn_{air} measurement using the FPC method in large refractive index fluctuation. A comparison with Ciddor method.

3.2 Small refractive index fluctuation

The measurement of Δn_{air} under disturbance flow showed that the FPC resonant condition is changed according to the Δn_{air} so that, tracking resonant of interferometer by changing laser frequency, Δn_{air} can be derived. In order to investigate more characteristics of the measurement method, the experiment was taken under stable conditions where fluctuation of temperature, pressure and humidity is minimized. A small shield box was used to cover the FPC; the box included some coppers wall mounted inside so that, temperature gradient inside the box might be less. Fig. 4 shows temperature and pressure variations under the stable condition. Temperature, pressure and humidity fluctuation are approximately 5 mK, 8 Pa and 1 %, respectively. Fig. 5 shows the comparison result between the Ciddor calculation and the FPC methods. In Fig. 5, the FPC method variation is almost similar to the Ciddor calculation. In our system, the FPC method is faster than Ciddor's method that is limited by the low measurement speed of the ESs.

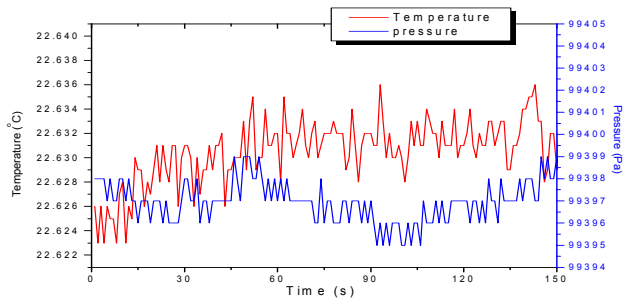


Fig. 4 Temperature and pressure change under the stable condition

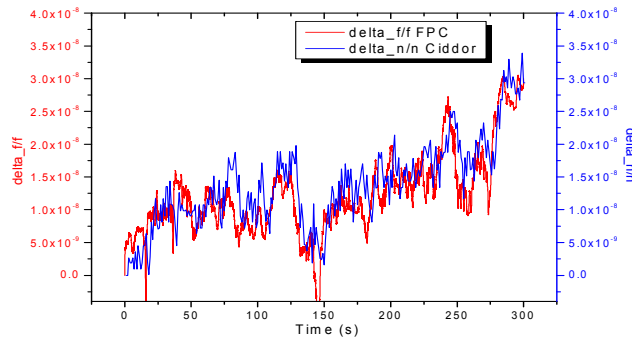


Fig. 5 Experimental result of Δn_{air} measurement using the FPC method in small refractive index fluctuation condition. A comparison with Ciddor method.

From the experimental result in stable conditions, measurement uncertainty is calculated. From equation (2.10), the uncertainty of Δn_{air} measurement using interferometers depends on three factors: an uncertainty of laser source, a signal to noise ratio (SNR) of the LIA, and a deformation of the optical path length. The estimation uncertainty of the interferometer methods can

be represented in the following equation:

$$U_{\Delta n_{air}/n_{air}} = \sqrt{\{U_{\Delta f/f}\}^2 + \{U_{\Delta L/L}\}^2 + \{U_{\Delta N/N}\}^2} \quad (3.1)$$

In this equation, $U_{\Delta f/f}$, $U_{\Delta L/L}$ and $U_{\Delta N/N}$ are the uncertainties of $\Delta f/f$, $\Delta L/L$, and $\Delta N/N$, respectively. $U_{\Delta f/f}$ is limited by the frequency linewidth of the ECLD and the frequency stability of the FSL. The $U_{\Delta f/f}$ is estimated of approximately 1×10^{-9} order. The deformation of the optical path length depends on the ULTEM and the temperature change. Because the temperature change and the thermal expansion ratio of the ULTEM were 8 mK and 2×10^{-8} /K, respectively, the $U_{\Delta L/L}$ in the experiment was 3×10^{-10} order. $U_{\Delta N/N}$ is concerned with the SNR of the LIA output and N (or L). In the experiment, the estimation of $U_{\Delta N/N}$, after some mathematical calculations, is about 8.7×10^{-10} order. Finally, the total uncertainty of the Δn_{air} measurement is approximately of 1.4×10^{-9} order.

4. CONCLUSIONS

The paper presented experimental investigations of interferometer configurations for Δn_{air} measurement. The fixed FPC on an ULTEM with the ELCD was used to detect Δn_{air} through the shift of the ECLD frequency. From the results comparison between the proposed method (using laser frequency shift) and the theoretical method (Ciddor calculation, using environmental sensors), this work confirmed that the FPC method was constructed successfully on the ULTEM even though it was though that difficult to align and fix the optics on the ULTEM. The resolution of the proposed method can be 10^{-9} order or less. It is satisfied to the requirement of the precise displacement measuring system with sub-nanometer resolution. In addition, the measurement speed of the proposed method is much higher than that of Ciddor calculation; the measurement speed depends on the maximum sampling time of the frequency counter. It turns out that the proposed system can respond to very high speed change of the air refractive index.

References

- [1] International Technology Roadmap for Semiconductors, <http://public.itrs.net/>.
- [2] Agilent Technologies, 5301 Stevens Creek Boulevard, Santa Clara, CA 95051, USA
- [3] Ranishaw Plc. Old Town, Wotton-under-Edge, Gloucestershire, GL12 7DW, United Kingdom.
- [4] B. Edlen, "The Dispersion of Standard Air" J. Opt. Soc. Am. Vol. 43, pp. 339 (1953).
- [5] P. E. Ciddor, "Refractive index of air: new equations for the visible and near infrared", App. Opt., Vol. 35, pp. 1566, (1996).
- [6] R. W. P. Drever and J. L. Hall, "Laser Phase and Frequency Stabilization using an Optical Resonator", Applied Physics B, Vol. 31, pp. 97, (1983).

Influence of interface anisotropy on microstructure and soft magnetic properties of Fe₆₅Co₃₅ thin films

Li Yan-Bo ^{a)}, Liu Xi ^{a)}, Li Zheng-Hua ^{a)}, Fu Yu ^{a)}, A. S. Kamzin ^{b)},
Wei Fu-Lin ^{a)*}, Yang Zheng ^{a)}

^{a)} (Key Laboratory for Magnetism and Magnetic Materials of the Ministry of Education Research Institute of Magnetic Materials, Lanzhou University, Lanzhou 730000, China)

^{b)} (Ioffe Physico-Technical Institute of Russian Academy of Sciences, St. Petersburg 194021, Russian Federation)

Abstract:

Fe₆₅Co₃₅/under-layer bilayer films were successfully prepared with different under-layer materials (Co₉₃Fe₇, Fe, Co and Cu). X-ray diffraction (XRD) analysis and magnetic measurements suggest that Fe₆₅Co₃₅ thin films deposited on different under-layers show different texture. Moreover, the in-plane anisotropy and soft magnetic properties of Fe₆₅Co₃₅ thin films with (200) texture are better than that of Fe₆₅Co₃₅ thin films with (110) texture. Investigations of several typical samples by conversion electron Mossbauer spectrum (CEMS) reveal that the magnetization vector of Fe₆₅Co₃₅ thin films have small deviation from the film plane, and the deviation from the film plane of Fe₆₅Co₃₅ thin films with (110) texture are bigger than that of Fe₆₅Co₃₅ thin films with (200) texture. Further study exhibits that this phenomenon is caused by the interface anisotropy induced by magnetostrictive effect at the interface between Fe₆₅Co₃₅ thin films and under-layers.

Keywords: Fe₆₅Co₃₅ thin films, interface anisotropy, soft magnetic properties

* Corresponding author: e-mail: weifl@lzu.edu.cn

1 Introduction

The need for new soft magnetic materials with high saturation magnetization $4\pi M_s$ for heads in order to record on future high coercivity media is widely recognized. The bcc $\text{Fe}_{1-x}\text{Co}_x$ alloy system have been studied extensively because they have the highest saturation magnetization up to $\mu_0 M_s \geq 2.45$ T in the composition range of $0.3 \leq x \leq 0.5$.^[1-2] However, it is difficult to obtain good soft magnetic Fe-Co films for its large magnetostriction constant ($\lambda_s = 4.0-6.5 \times 10^{-5}$).^[3] Recently, an improvement of soft magnetic properties for Fe-Co films by using an under-layer^[2-7] has been reported. Nevertheless, discussions about the effect of interface anisotropy on microstructure and soft magnetic properties of Fe-Co film are still few now.

In the present work, the effect of interface anisotropy at the interface between Fe-Co thin film and under-layers on microstructure and soft magnetic properties of Fe-Co film was studied. The reason that different under-layers have different influence on improving of soft magnetic properties for Fe-Co film was also discussed.

2 Experiments

The $\text{Fe}_{65}\text{Co}_{35}$ single layer and $\text{Fe}_{65}\text{Co}_{35}$ /under-layer bilayer films were deposited at 360 °C onto glass substrate (Corning 7059) in a CMS-18 four-gun DC/RF magnetron sputtering system. The under-layer materials are $\text{Co}_{93}\text{Fe}_7$, Fe, Co and Cu. The thickness of $\text{Fe}_{65}\text{Co}_{35}$ main layer maintains 100 nm and that of under-layer is 0-10 nm. The background pressure of the sputtering system was 4×10^{-5} Pa. A magnetic field of

240 Oe was applied to induce an in-plane uniaxial magnetic anisotropy during film deposition. The $\text{Fe}_{65}\text{Co}_{35}$ main layer and $\text{Co}_{93}\text{Fe}_7$ under-layer were deposited by co-sputtering from pure Fe and Co targets. The Fe, Co and Cu under-layers were prepared by conventional sputtering method. The film deposition rate was monitored by a quartz crystal oscillator. The film structure was investigated by X-ray diffraction (XRD) using $\theta-2\theta$ scan method with $\text{Cu K}\alpha$ radiation. The composition of films was determined by using an inductively coupled plasma (ICP) technique. Macro- and micro-magnetic properties were measured by vibrating sample magnetometer (VSM) and conversion electron Mossbauer spectroscopy (CEMS) with ^{57}Fe at room temperature, respectively.

3 Results and Discussions

3.1 Soft magnetic properties

Figure 1 shows typical magnetic hysteresis loops of 100 nm $\text{Fe}_{65}\text{Co}_{35}$ films deposited (a) directly on glass substrate and on 1 nm of (b) Fe, (c) $\text{Co}_{93}\text{Fe}_7$, (d) Cu under-layer. The $\text{Fe}_{65}\text{Co}_{35}$ films without an under-layer show anisotropic in-plane hysteresis loops with $H_{ce}=41$ Oe and $H_{ch}=26$ Oe, respectively. The soft magnetic properties of $\text{Fe}_{65}\text{Co}_{35}$ films are much improved by using an under-layer. The $\text{Fe}_{65}\text{Co}_{35}$ films with 1 nm $\text{Co}_{93}\text{Fe}_7$ and Cu under-layer show a well-defined uniaxial magnetic hysteresis loops with $H_{ce}=11-14$ Oe and $H_{ch}=1-2.5$ Oe. The $\text{Fe}_{65}\text{Co}_{35}$ films with Fe under-layer have $H_{ce}=14$ Oe and $H_{ch}=7.5$ Oe, but the magnetic anisotropy of films is not very clear.

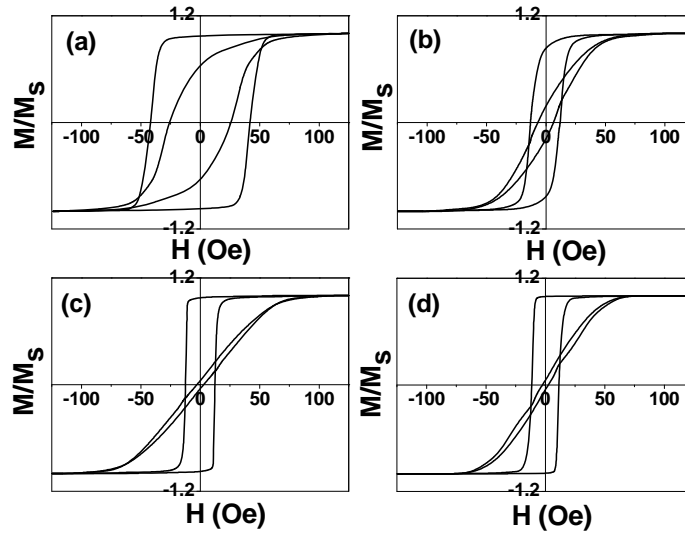


Fig. 1 Typical magnetic hysteresis loops along easy axis (H_{ce}) and hard axis (H_{ch}) direction for 100 nm $Fe_{65}Co_{35}$ films deposited (a) directly on glass substrate, and on 1 nm of (b) Fe, (c) $Co_{93}Fe_7$, (d) Cu under-layer.

It has been reported ^[8-9] that some fcc metallic under-layers such as Cu, Ag and NiFe with (111) texture significantly improve soft magnetic properties of Fe-base thin films, but the bcc metallic under-layers do not have or have a little this effect. Our experimental results are in good agreement with these reports.

In order to further explore the cause of different under-layers have different effect on improving of soft magnetic properties for $Fe_{65}Co_{35}$ film, several typical samples were investigated by CEMS measurement.

3.2 CEMS analysis of typical samples

Through CEMS measurement, we can obtain information regarding the angle between the magnetization vector and the incident γ ray, and also regarding the magnetic ordering state. So, CEMS is a useful method for our investigation.

If the CEMS spectra are gotten, the direction of the magnetization vector can be estimated from the intensity ratio of six lines with the following equation:

$$\frac{I_{2,5}}{I_{1,6}} = \frac{4 \sin^2 \theta}{3(1 + \cos^2 \theta)} \quad (1)$$

where θ is the angle between the incident γ ray and the magnetization vector. $I_{1,6}$ and $I_{2,5}$ are, respectively, intensity of the first (or sixth) and the second (or fifth) peak in the six line pattern. For $Fe_{65}Co_{35}$ thin film samples, the direction of incident γ ray is just the normal of film plane. Therefore, $\theta=90^\circ$ means the magnetization vector is parallel to the film plane, and $\theta=0^\circ$ means the magnetization vector is perpendicular to the film plane.

Figure 2 shows the CEMS spectra of four typical samples (a) $Fe_{65}Co_{35}$ (100nm)/ $Co_{93}Fe_7$ (3nm), (b) $Fe_{65}Co_{35}$ (100nm)/Co (3nm), (c) $Fe_{65}Co_{35}$ (100nm)/Fe (1.5nm) and (d) $Fe_{65}Co_{35}$ (100nm)/Cu (10nm) with different under-layers. With the equation (1), the angle θ between the magnetization vector and the normal of film plane can be determined: (a) 76.74° , (b) 76.74° , (c) 70.06° , (d) 67.03° (shown in Table 1). It is seen that $\theta < 90^\circ$ is true for all typical samples. Hysteresis loops in figure 1 exhibit excellent soft magnetic

properties implying that $\text{Fe}_{65}\text{Co}_{35}$ film has low anisotropy dispersion and the magnetization vector should lie in film plane. However, this is inconsistent with the results of CEMS measurement. The contradiction indicates that the magnetization vector of $\text{Fe}_{65}\text{Co}_{35}$ thin films have a small deviation from the film plane and, interestingly, the deviation from the

film plane of $\text{Fe}_{65}\text{Co}_{35}$ thin films with (110) texture are larger than that of $\text{Fe}_{65}\text{Co}_{35}$ thin films with (200) texture. The presence of the perpendicular component of the magnetization vector for $\text{Fe}_{65}\text{Co}_{35}$ film is probably caused by the interface anisotropy at the interface between the $\text{Fe}_{65}\text{Co}_{35}$ film and under-layer.

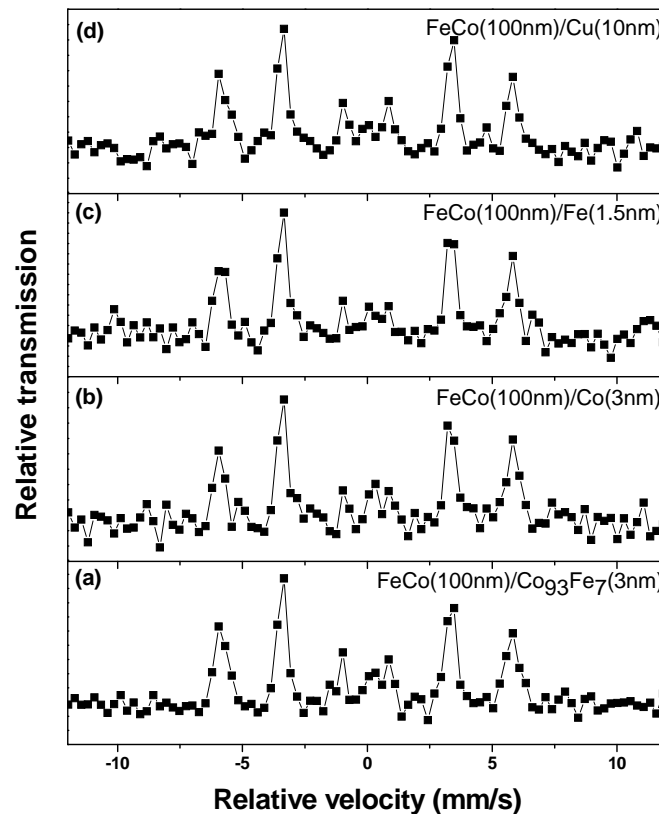


Fig. 2 CEMS spectra of typical samples: (a) $\text{Fe}_{65}\text{Co}_{35}$ (100nm)/ $\text{Co}_{93}\text{Fe}_7$ (3nm), (b) $\text{Fe}_{65}\text{Co}_{35}$ (100nm)/Co (3nm), (c) $\text{Fe}_{65}\text{Co}_{35}$ (100nm)/Fe (1.5nm), (d) $\text{Fe}_{65}\text{Co}_{35}$ (100nm)/Cu (10nm).

3.3 Discussions on interface anisotropy

It is well established ^[10] that interface anisotropy is caused by changes in the electronic structure associated with the

reduced symmetry and modified inter-atomic interactions, or by stress via the magnetoelastic interactions. Here we will focus on the latter one in this discussion.

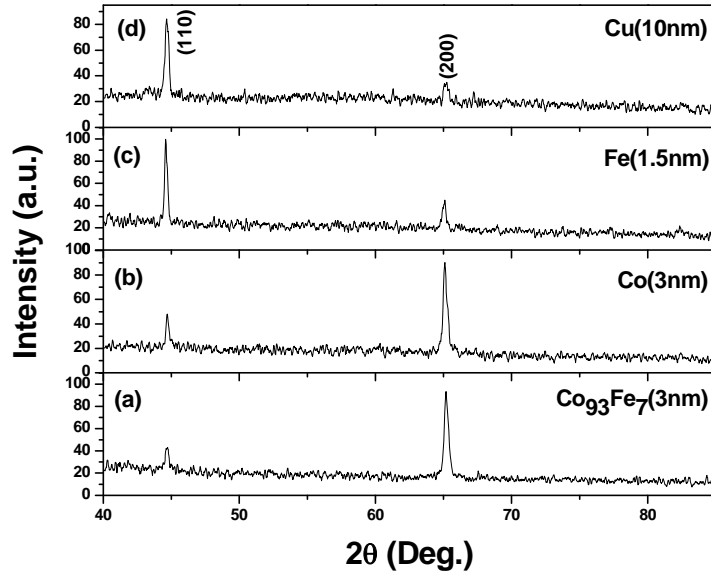


Fig. 3 XRD pattern for typical samples: (a) $\text{Fe}_{65}\text{Co}_{35}$ (100nm)/ $\text{Co}_{93}\text{Fe}_7$ (3nm), (b) $\text{Fe}_{65}\text{Co}_{35}$ (100nm)/Co (3nm), (c) $\text{Fe}_{65}\text{Co}_{35}$ (100nm)/Fe (1.5nm), (d) $\text{Fe}_{65}\text{Co}_{35}$ (100nm)/Cu (10nm).

Figure 3 exhibits the XRD pattern of the typical samples (a) $\text{Fe}_{65}\text{Co}_{35}$ (100nm)/ $\text{Co}_{93}\text{Fe}_7$ (3nm), (b) $\text{Fe}_{65}\text{Co}_{35}$ (100nm)/Co (3nm), (c) $\text{Fe}_{65}\text{Co}_{35}$ (100nm)/Fe (1.5nm) and (d) $\text{Fe}_{65}\text{Co}_{35}$ (100nm)/Cu (10nm). Obviously, the (200) texture is predominant for samples (a) and (b), while the (110) texture is predominant for samples (c) and (d). In our previous work^[11], it has been found out that, as the intensity ratio of $I(110)/I(200)$ decrease, the coercivity along hard axis of $\text{Fe}_{65}\text{Co}_{35}$ films with different under-layers decrease on over trend. In other words, it seems that, with the texture changing from (110) to (200), the soft magnetic properties of $\text{Fe}_{65}\text{Co}_{35}$ films improve better.

The value of the lattice parameter of bcc bulk $\text{Fe}_{65}\text{Co}_{35}$ alloy without stress and lattice deformation is found to be $a_0=2.858\pm 0.002 \text{ \AA}$.^[6,12] It is assumed that the ideal value of spacing distance d_0 of (200) or (110) plane for $\text{Fe}_{65}\text{Co}_{35}$ film is the same as that for bulk $\text{Fe}_{65}\text{Co}_{35}$ alloy. With the following geometric relations,

$$d_0 = a_0/2 \quad \text{for (200) plane} \quad (2)$$

$$d_0 = a_0/\sqrt{2} \quad \text{for (110) plane} \quad (3)$$

the spacing distance d_0 of (200) or (110) plane for bcc $\text{Fe}_{65}\text{Co}_{35}$ film without stress and lattice deformation is calculated and shown in Table 1. According to the Bragg's Law,

$$2d \sin \theta = n\lambda \quad (4)$$

where d is the spacing distance, λ is the wavelength of X-ray, θ is the diffraction angle and n is the diffraction order, the real spacing distance d of (200) or (110) plane for the four typical samples is calculated, too.

Table 1 shows the situation of relative lattices deformation of (200) or (110) plane for typical samples (a) $\text{Fe}_{65}\text{Co}_{35}$ (100nm)/ $\text{Co}_{93}\text{Fe}_7$ (3nm), (b) $\text{Fe}_{65}\text{Co}_{35}$ (100nm)/Co (3nm), (c) $\text{Fe}_{65}\text{Co}_{35}$ (100nm)/Fe (1.5nm) and (d) $\text{Fe}_{65}\text{Co}_{35}$ (100nm)/Cu (10nm). From Table 1, we can see that the relative lattices deformation of $\text{Fe}_{65}\text{Co}_{35}$ films with different texture is different. Furthermore, the relative lattices deformation of $\text{Fe}_{65}\text{Co}_{35}$ films

with (110) texture is bigger than that of Fe₆₅Co₃₅ films with (200) texture. This implies that the stress induced by lattices deformation

at the interface between the Fe₆₅Co₃₅ film and under-layer is different.

Table 1 Relative lattices deformations for typical samples.

Samples	Texture	Maximum peak	d (Å)	d ₀ (Å)	(d-d ₀)/d ₀	θ	H _{ce} (Oe)	H _{ch} (Oe)
(a)	(200)	65.209°	1.431	1.429	1.4%	76.74°	15.6	5.3
(b)	(200)	65.116°	1.432	1.429	2.1%	76.74°	15.6	5.6
(c)	(110)	44.607°	2.031	2.021	4.9%	70.06°	25.9	5.0
(d)	(110)	44.675°	2.028	2.021	3.5%	67.03°	36.2	13.8

Note: θ is the angle between the magnetization vector and the normal of Fe₆₅Co₃₅ film plane.

It has been reported [12-13] that the stress induced by lattices deformation has an intimate correlation with the coercivity of Fe-Co film, and has an influence on the soft magnetic properties via magnetoelastic anisotropy induced by magnetostrictive effect. It should be noted that, in Table 1, with the increasing of lattices deformation, the angle θ between the magnetization vector and the normal of Fe₆₅Co₃₅ film plane decrease while the coercivity increase. The results are similar to that observed by Masakatsu Senda et al. [14] This indicates that the appearance of the perpendicular component of the magnetization vector and the variation of soft magnetic properties of Fe₆₅Co₃₅ films deposited on different under-layers can be attributed to the stress induced by lattice deformation. For Fe₆₅Co₃₅ films with (200) texture, due to the stress induced by lattices deformation is smaller, and the interface anisotropy induced by magnetostrictive effect is smaller, hence the perpendicular component of the magnetization vector is smaller. The situation for Fe₆₅Co₃₅ films with (110) texture is exactly opposite. Through a simple comparison, it is easy to understand that the in-plane anisotropy and soft magnetic properties of Fe₆₅Co₃₅ films with (200) texture both are better than that of Fe₆₅Co₃₅ films with (110) texture. The reason that different under-layers have different

influence on improving of soft magnetic properties for Fe₆₅Co₃₅ film is revealed simultaneously.

4 Conclusions

Fe₆₅Co₃₅/under-layer bilayer films were successfully prepared with different under-layer materials (Co₉₃Fe₇, Fe, Co and Cu) by the method of magnetron sputtering. VSM measurement and XRD analysis reveal that the soft magnetic properties of Fe₆₅Co₃₅ films improve better with the texture changing from (110) to (200). CEMS measurement exhibits that the magnetization vector of Fe₆₅Co₃₅ thin films have small deviation from the film plane and the deviation from the film plane of Fe₆₅Co₃₅ thin films with (110) texture are larger than that of Fe₆₅Co₃₅ thin films with (200) texture. The results from calculations of lattices deformation show that the lattices deformation of Fe₆₅Co₃₅ films with different texture is different, and the lattices deformation of Fe₆₅Co₃₅ films with (110) texture is bigger than that of Fe₆₅Co₃₅ films with (200) texture. The appearance of the perpendicular component of the magnetization vector and the difference of soft magnetic properties of Fe₆₅Co₃₅ films deposited on different under-layers can be attributed to the interface anisotropy induced by

magnetostrictive effect at the interface between Fe₆₅Co₃₅ thin films and under-layers.

References

- [1] R. M. Bozorth, *Ferromagnetism* (IEEE, New York, 1993).
- [2] H. S. Jung, W. D. Doyle, J. E. Wittig, J. F. Al-Sharab and J. Bentley, *Appl. Phys. Lett.* **81**, 2415 (2002).
- [3] Fu Yu, Cheng Xiaofeng and Yang Zheng, *Phys. Stat. Sol. (a)* **202** 1150, 2005
- [4] C. L. Platt, A. E. Berkowitz, David J. Smith and M. R. McCartney, *J. Appl. Phys.* **88** 2058, 2000.
- [5] Jung H. S., Doyle W. D. and Matsunuma S., *J. Appl. Phys.* **93** 6462, 2003
- [6] Platt C. L., Howard J. K. and D. J. Smith, *J. Magn. Mater.* **269** 212, 2004
- [7] Y. Fu, T. Miyao, J.W. Cao, Z. Yang, M. Matsumoto, X.X. Liu and A. Morisako, *J. Magn. Mater.* **308** 165, 2007
- [8] Inturi V. R. and Barnard J. A., *J. Appl. Phys.* **79** 5904, 1996
- [9] Jiang Hai, Chen Yingjian, Chen Lifan and Huai Yiming, *J. Appl. Phys.* **91**, 6821, 2002
- [10] Bland J. A. C., Hope S., Choi B. and Bode P., *J. Appl. Phys.* **85** 4613, 1999.
- [11] Fu Yu, Cheng Xiaofeng and Yang Zheng, *Phys. Stat. Sol. (a)* **203** 963, 2006
- [12] Vas'ko Vladyslav A., Rantschler James O. and Kief Mark T., *IEEE Trans. Magn.* **40** 2335, 2004.
- [13] Shimatsu T., Katada H., Watanabe I., Muraoka H. and Y. Nakamura, *IEEE Trans. Magn.* **39** 2365, 2003.
- [14] Masakatsu Senda and Yasuhiro Nagai, *J. Appl. Phys.* **68**, 3508, 1990.

Proposal of Command Input Interface Using Lip Motion Features

Yoshiyuki Sato* ** Yoichi Kageyama* and Makoto Nishida*

* Department of Computer Science and Engineering, Faculty of Engineering and Resource Science, Akita University,
1-1, Tegata-Gakuen-Machi, Akita, 010-8502 Japan

** Logizard Co., Ltd., 5th Fl., Kourinkaikan, 3-6-23 Shibakouen, Minato-ku, Tokyo, 105-0011 Japan
i98247@ie.akita-u.ac.jp

Abstract: Lip motion features are of practical use in identifying individuals; therefore, it is important to develop non-contact type interface and allow for individual differences (accents or dialects) in commands. In this paper, we propose a method to identify commands by analyzing three kinds of lip motion features: lip width, lip length, and ratio of width and length. The analysis is made on the basis of these features' relative values obtained from the primary and object frame. The proposed method has three steps. First, the lip motion features were automatically extracted on the basis of both positions and shapes of lip in each frame of facial images. The approach adopted fuzzy reasoning in order to consider obscurity in image data such as shade on the face. Secondly, standard patterns were created from features of six utterances per command. The standard patterns facilitate the reduction of the relative difference in the lip motion features. Thirdly, similarities among commands were computed by Dynamic Time Warping (DTW), and then command with the largest similarity was selected as the target one. Our experimental results for twenty kinds of commands regarding electric appliance control, spoken by nine persons, suggest that the proposed method provides results suitable for identifying various commands.

Key Words: lip motion features, DTW, command input interface, standard pattern

1 INTRODUCTION

In recent years studies about the individual identification using biometrics, such as a fingerprint and a vein are performed and they are already put to practical use[1][2]. However, the interface that performs an identification and command input by non-contact has not yet been developed. For a representative example of non-contact type system, sound recognition[3]-[6] is developed; the accuracy obtained by sound recognition falls under the noisy conditions[7]. There are also problems that the sound recognition is impossible when a user cannot utter words, and that the utterance contents are known to the third person.

On the other hand, "the lips" are the biometrics that have both physical and motion features: the shape and the movement of lips with the utterance[8][9]. When the width and length of lips of facial images are used for identification or command input, there are advantages described below:

(1)There is little danger that utterance contents are identified even if looked at the state of the data acquisition by

anyone because the lip motion features can be acquired without voice.

(2)The system is able to be used under the environment with many noises.

(3)Special equipment, such as used for the vein certification, is never needed; the lip motion features are obtained with the aid of commercial common cameras.

(4)The lip motion features is able to be acquired without touching the input device; it is hygienic approach.

(5)The lip motion data will be changed even if the registration information was taken illegally by the third person.

In our previous research, it is cleared that the lip motion features are able to be extracted by pursuing the characteristic points set on the lips outline[8]. We also found that the lip motion features included individual differences and features unique to words[5][8][9]. The findings suggest that command input interface on the basis of lip motion features extracted from each image of utterance is constructed.

In the case that we construct a versatile command input

interface, it is required to keep good accuracy of identification when the number of users and of commands increase. The system that applies the images around the lip to command input for controlling the household electrical appliance was suggested [10]; the examination regarding the increase of the number of users and of commands was not done. When the same speaker utters the same contents, differences of the movement of lips may occur; however it is important that the system is robust to the influence of these differences.

Therefore, we aim at development of versatile command input system and propose a command identification method on the basis of the lip motion features obtained from animated utterance data. The proposed method works in three steps. First, the individual identification using the lip motion features is performed, and then commands that control the household electrical appliance are continuously input. Since only the registered data spoken by the identified user is used for the process, there is little influence that the increase in the number of users gives the accuracy of the command identification. The proposed method divided commands into the plural groups in order to reduce the influence of the increase in the number of commands. Secondly, standard patterns were created from features of six utterances per command in order to reduce the quantity of registration data. Thirdly, command identification using the distance computed by Dynamic Time Warping (DTW)[6][11], as a degree of similarity, is performed. The DTW distances are computed from three kinds of lip motion features: lip width, lip length, and ratio of width and length. Our experimental results for twenty kinds of commands regarding electric appliance control suggest that the proposed method provides results suitable for identifying various commands.

2 DATA PREPARATION

2.1 Data acquisition

The animation data that users spoke commands was obtained with CCD video camera (SONY: DCR-VX2100). The details of image data are shown in **Table 1**. The number of users was nine (id01 to id09). The conditions of acquiring data were described below:

- The distance between each user and the CCD video camera was about 60cm.
- The data acquisition was performed under a common fluorescent lamps, i.e., about 800 lx.
- The user closed his/her mouth except for the utterance period.
- The utterance period in the animation data was decided on the basis of operator’s visual interpretation.

Table 1. The details of facial image data.

image data	
Frame rate	30fps
Frame size	320×240pixel
Composition of data	RGB 8bit



Figure 1. An example of facial image data.

- The user practiced the utterance before the data acquisition.

We obtained still images converted from the above animation data. **Figure 1** shows an example of facial image data. Input data for the experimentation was created from three animation data of each command. Registration data for the experimentation was also created from six animation data of each command. The input data and the registration data were acquired on the different days. The interval of the data acquisition is about 2-10 days per user.

2.2 Contents of utterance and grouping process

In the system assumed in this paper, command identification was performed in three steps: "choice of a place", "choice of a household appliance", and "check of switching". Therefore, when command input is performed, the target group of the commands of each step is able to be selected before command identification. In addition, individual identification is performed before command input, so that the data spoken by the identified user is only used for the command identification. That is, the influences of the increase in the number of users and commands will be reduced by selecting the target group of the command in each process.

In this paper, we assume a system performing only the on/off change of the household appliance of each room. The number of commands used for experimentation was twenty. Then, these commands divided into five groups (group1 to group5). **Table 2** indicates the details of the commands and groups. Group 1 is user’s name. Group 2 is password set freely by each user. Group 3 consists of nine words that mean places in a house; “living”, “entrance”, “kitchen”, “bathroom”, “bedroom”, “passage”, “nursery”, “lavatory”, and “toilet”. Group 4 consists of seven words that mean an electric appliance; “air-conditioner”, “bath”, “ventilation fan”, “light”, “TV”, “Video”, and “washing machine”. Group 5 consists of two words that mean check of switching; “Yes” and “No”.

Table 2. List of commands set in the study.

group	commands
group 1	name
group 2	password
group 3 (Place)	"living", "entrance", "kitchen", "bathroom", "bedroom", "passage", "nursery", "lavatory", "toilet"
group 4 (electric appliance)	"air-conditioner", "bath(hot water supply system)", "ventilation fan", "light", "TV", "video", "washing machine"
group 5 (check of switching)	"yes", "no"

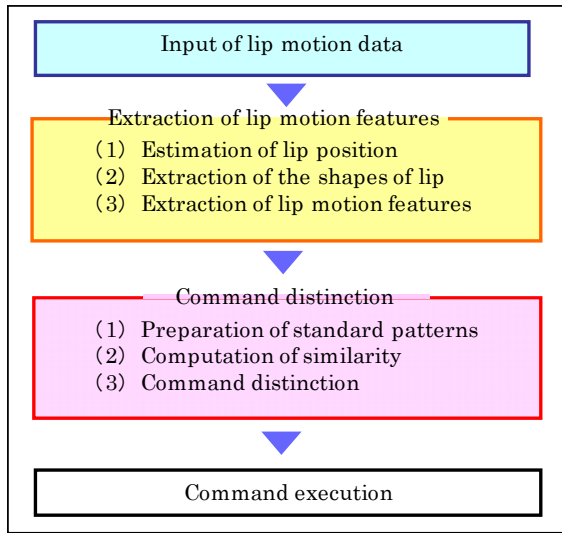


Figure 2. Flowchart of the command identification.

Here, all commands are spoken in Japanese.

3 COMMAND IDENTIFICATION METHOD

Figure 2 shows the flowchart of the command identification proposed in this study. The proposed method has two steps. First, the lip motion features were extracted from the facial image data. Next, command identification was performed with the extracted features.

3.1 Extraction of the features

The lip motion features were automatically extracted on the basis of both positions and shapes of the lip in each frame of facial images[12][13]. The process used color information: psychometric quantities of a metric hue angle (h_{ab}) and a rectangular coordinates (a^*), which are defined in CIE 1976 $L^* a^* b^*$ color space[14]. This color space has a characteristic that it is robust against a change of the luminosity, and it is effective for the extraction of the lips from the facial images. The approach adopted fuzzy reasoning in order to consider obscurity in image data such as shade on the face. Fuzzy reasoning was performed by using membership function made from histogram of a^* and h_{ab} . After applying fuzzy reasoning,

the pixel having membership values for “lip class” were extracted as “lip”.

Figure 3 shows the outline of lip motion features. The features used for the analysis consist of three features: “StX” as lip width, “StY” as lip length, and “StR” as ratio of width and length. The distance between the camera and a user would be different whenever command input is performed. In order to reduce the influence caused by the difference in distance, these features are computed on the basis of relative values obtained from the primary and object frame.

3.2 Command identification algorithm

As shown in **Figure 2**, the command identification algorithm works in three steps.

- (1) Preparation of standard patterns: standard patterns were created from features of six utterances per command. In this paper, the number of data used for registration was decided in consideration of the user’s stress in the data acquisition. **Figure 4** shows the flowchart of the process of making standard patterns. The process consists of three steps. First, the average number of the frame of the registration data is computed as “standard frame number”. Secondly, normalizing of the number of frames is performed by removing some frames from, or adding some frames to, each registration data. Here, the number of processed frames is called D; the D is the difference between the standard frame number and the number of frame of each registration data. The average of the parameter of six registration data is computed in each frame as the parameter of standard pattern. The standard pattern facilitates the reduction of the relative difference in the lip motion features.
- (2) Computation of similarity: first, the proposed algorithm computes a distance between input data and standard patterns with the DTW. **Figure 5** shows an outline of DTW. Here, the distance computed with the DTW was defined as “DTW distance”. There are differences of the utterance speed; even when the same person utters the same contents, the utterance speeds are changeable. The DTW is suitable for reducing the influence of the change in the utterance speed[6][11]. The DTW distance is computed from each feature. And then, the total of DTW distance of three features was used for command identification as “similarity”.
- (3) Command identification: the command with the largest similarity was selected from commands in the group, as the target one.

4 EXPERIMENTAL CONDITIONS

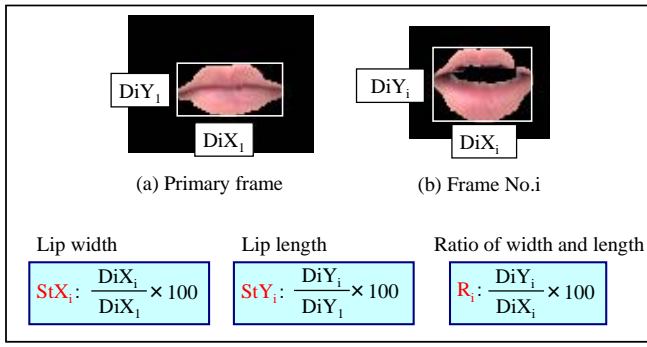


Figure 3. Outline of lip motion features.

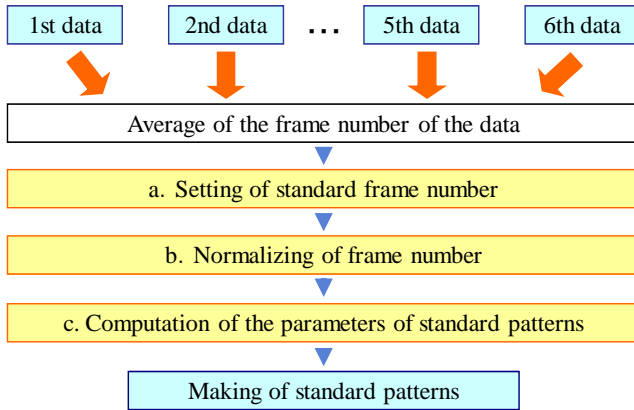


Figure 4. Flowchart of the process of making standard patterns.

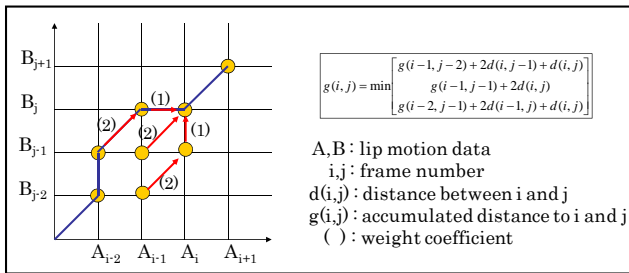


Figure 5. Outline of DTW.

4.1 Examinations regarding integration of features

In this paper, a total of the DTW distance, computed from three kinds of features (StXi, StYi and StRi), was used for command identification. To examine the use of combining three features, the experiments were performed on the conditions described below:

- simulation A : use a total of the DTW distance computed from three kinds of features (proposed method)
- simulation B : use the DTW distance computed from StXi
- simulation C : use the DTW distance computed from StYi
- simulation D : use the DTW distance computed from StRi

4.2 Examinations regarding process of making standard patterns

To examine the significance of the process of making standard patterns, the experiments were performed on the

conditions described below:

- simulation 1 : use the DTW distances between input data and standard patterns (proposed method)
- simulation 2 : use the average of DTW distances between input data and each registration data (used for comparison)

4.3 Examinations regarding command grouping

To examine the effectiveness of command grouping, the experiments were performed on the following conditions.

- simulation I : eighteen commands, except for name and password, were divided into three groups (group 3 to group 5) (proposed method)
- simulation II : eighteen commands, except for name and password, were used for the experiment without grouping

The individual identification was assumed to be performed before command identification. The name and the password were therefore excluded from the grouping process.

5 EXPERIMENTAL RESULTS AND DISCUSSION

5.1 Examinations regarding integration of features

The results for the use of combining three features are shown in **Figure 6**. The total accuracy of command identification with the combining three features (simulation A; proposed method) is achieved to be 90.2%. The total accuracies with each feature (simulation B to D) are 76.3% (simulation B; StX), 76.1% (simulation C; StY), and 75.9% (simulation D; StR), respectively. For the Group1 (name) and Group2 (password), the accuracy of the command identification in which three features are combined (simulation A: proposed method) is achieved to be 100%. On the other hand, the results of command identification with each feature (simulation B to D) include the failure cases, respectively. For example, when id03 spoke his own name, two of three input data failed in identification with using StRi (simulation D).

The above-described results show that the integration of three features is useful for command identification.

5.2 Examinations regarding process of making standard patterns

The results for the use of standard pattern are shown in **Figure 7**. The total accuracy of command identification without standard patterns (simulation 2: comparison method) is achieved to be 90.7%. The total accuracy of command identification with standard patterns (simulation 1: proposed method) is 90.2%, the accuracy is almost equal to the one acquired by the compared method. Additionally, Group1 (name) is perfectly identified with the proposed method. The results given by the compared method include the failure cases.

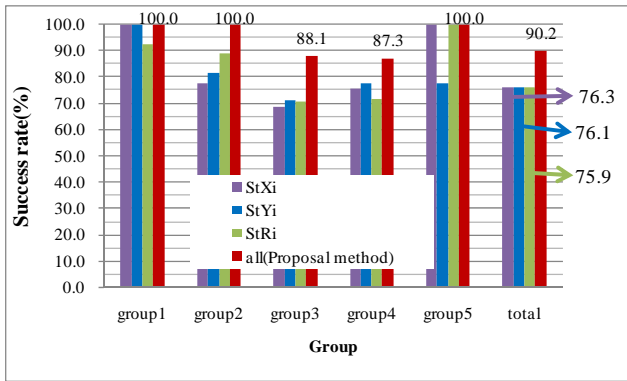


Figure 6. Experimental results for the use of combining three features.

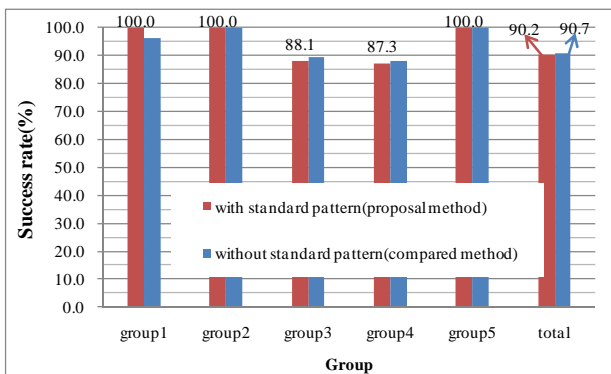


Figure 7. Experimental results for the use of standard patterns.

For example, when id03 spoke his own name, one of the three input data failed in the identification in which the compared method was used (simulation 2). Because individual identification is performed before command identification in the proposed method, it is necessary to correctly do individual identification. The experimental results suggest that the process of making standard pattern is effective for command identification.

Pay attention to the quantity of the registered data for the command identification, the total quantity of data used for the compared method (without making standard patterns) was about 1.15MB. The data used for the proposed method (with making standard patterns) was achieved to be about 198KB. It became clear that the process of making standard pattern can reduce about 84% of the data.

5.3 Examinations regarding command grouping

The results for the grouping of commands are shown in **Figure 8**. The total accuracy of command identification without grouping (simulation II) is 73.5%. The total accuracy of command identification with grouping (simulation I: proposed method) is achieved to be 89.1%; the results show that the

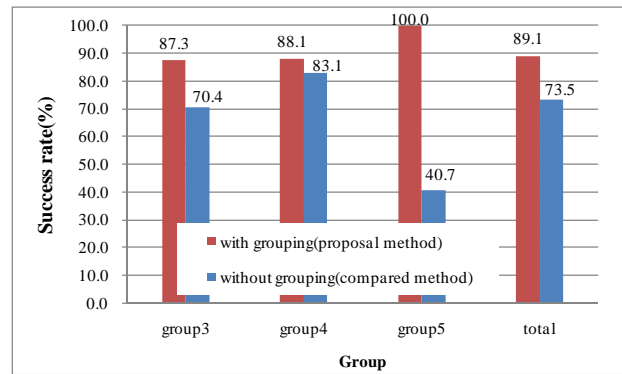


Figure 8. Experimental results for the grouping of commands.

Table 3. Examples of command identification (id05).

Feature \ Command	all (Proposal method)	StXi	StYi	StRi
bedroom	0	1	3	0
bathroom	3	3	3	3
nursery	3	3	3	3
entrance	3	3	1	0
kitchen	3	3	1	1
living	3	3	3	3
toilet	3	3	3	3
passage	3	3	2	3
lavatory	3	3	3	3

accuracy of command identification was able to be raised about 15.6% with the grouping of commands. Therefore, these results suggest that the grouping of commands is effective for the command identification.

5.4 Failure cases of command identification

Table 3 shows an example of commands identification. All of input data (three of three times) failed in command identification in the case that id05 uttered “bed room (Shi-n-shi-tsu)”. The differences of lip motion between input data and registration data cause failures in command identification. However, the results with “StYi” show that all of input data succeeded in command identification. Then, we will examine the weight of each lip motion features.

When id 08 uttered “passage (Ro-u-ka)”, all of the input data failed in command identification, too. **Figure 9** shows a typical example of the similar features of standard patterns. These patterns are very similar, hence the failure identification will happen. When the irregular data is involved in the registration data, it is found that the differences between each registration data cause failures in command identification. Therefore, we are planning to develop a procedure of data rejection. That is, when a user registers the new command, the new data will be rejected when it is similar to the data already

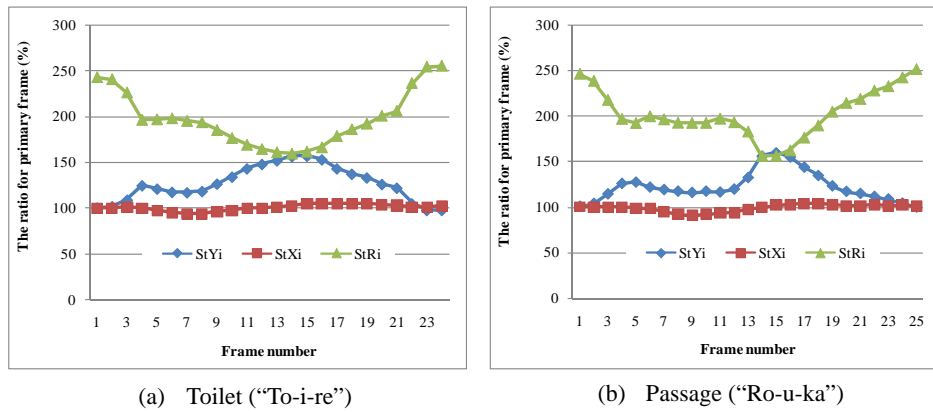


Figure 9. Similar features of the standard pattern (id08 spoke “To-i-re” and “Ro-u-ka”).

registered. And, the registration data will be rejected and a user will be requested to register the data again when the registration data involve irregular data.

6 CONCLUSION

In this paper, the command identification method that uses the lip motion features was proposed. The contribution of this paper is threefold; each of them includes several advantages as follows:

First, the proposed method combined three kinds of lip motion features: lip width, lip length, and ratio of width and length. The accuracy of command identification with combined three features was better than the one with each single feature. Therefore, combining lip motion features is effective to improve the accuracy of command identification.

Secondly, standard patterns were made from six registration data per command. Standard patterns are able to reduce the quantity of data needed for the command identification without decreasing the accuracy.

Finally, the proposed method divided commands into the plural groups. The accuracy of command identification with command grouping was better than the one without grouping. Therefore, grouping of commands is good for reducing the influence of the increase in the number of commands.

These results indicate that the proposed method is useful to construct the non-contact type interface of command input using image processing.

Acknowledgement

The authors thank Ms. C. Ishizawa, Mr. T. Takahashi, and Mr. J. Narita, Akita University, for the help in conducting the experiment. We also express our sincere appreciation to Mr. H. Endo and many colleagues, Logizard Ltd.

References

- [1] Seto, Y., “Biometrics Technology in Cyber-Security”, Kyoritsu Publishing Company (2002)
- [2] Robert, W.F., Ulrich, D., “BioID: A Multimodal Biometric Identification System”, IEEE Trans. Comput., Vol.33, No.2, pp.64-68 (2000)
- [3] Nakagawa, S., “A Survey on Automatic Speech Recognition”, T. IEICE Japan. Vol.J83-D- II, No.2, pp.433-457 (2002)
- [4] Ogihara, A., Shintani, A., Doi, N., and Fukunaga, K., “HMM Speech Recognition Using Fusion of Visual and Auditory Information”, T.IEE Japan, Vol.115-C, No.11, pp.1317-1324(1995)
- [5] Sato, Y., and Nishida, M., “A Study on Individual Discernment Using the Speech Sound and Movement Feature of Lip in Speech”, IEEJ Trans. EIS, Vol.125-C, No.8, pp.1282-1289 (2005)
- [6] Furui, S., “Digital Speech Processing”, Tokai University Press (1985)
- [7] Manabe, H., Hiraiwa, A., and Sugimura, T., “Mime Speech Recognition : Recognition of 5 Japanese Vowels without Generating Voice Using Electromyography”, T. IEICE Japan, Vol.J88-D- II, No.9, pp.1909-1917 (2005)
- [8] Ishi, M., Sato, K., Nishida, M., and Kageyama, Y., “Feature Extraction and Analysis for Lip Reading in Continuous Image”, T.IEE Japan, Vol.119-D, No.4, pp.465-472 (1999)
- [9] Konda, M., Nishida, M., Ishi, M., and Sato, K., “Application of the Feature of Lip Motion in Continuous Image to Personal Identification”, T.IEE Japan, Vol.120-C, No.5, pp.765-766 (2000)
- [10] Nakanishi, T., Terabayashi, K., Umeda, K., “Mouth Motion Recognition for Intelligent Room Using DP Matching”, IEEJ Trans. EIS, Vol.129-C, No.5, pp.940-946 (2009)
- [11] Yahagi, T., “Digital Signal Processing of Speech and Images”, CORONA PUBLISHING CO., LTD. (1996)
- [12] Shirasawa, Y., Nishida, M., and Kurisu, S., “Estimation of Lip Position Robust against Zoom and Face Direction”, ITE, Vol.59, No.12, pp.1816-1821(2005)
- [13] Shirasawa, Y., Nishida, M., and Nishi, K., “A Study on Lip Extraction Due to Fuzzy Reasoning by Using Color Information”, IEEJ Trans. EIS, Vol.125-C, No.9, pp.1430-1437 (2005)
- [14] The Color Science Association of Japan, “Handbook of Color Science”, University of Tokyo Press (1998)

Extraction Method of Brain Regions with Balloon models for Imaging Diagnosis Support of Alzheimer-Type Dementia

Momoyo Ito[†], Makoto Nishida[‡] and Ikuro Namura^{*}

[†] Graduate School of Engineering and Resource Science, Akita University,
[‡] Faculty of Engineering and Resource Science, Akita University, ^{*} Akita University Health Administration Center,
Gakuenmachi 1-1, Tegata, Akita-shi 010-8502, Japan
j01208@ie.akita-u.ac.jp

Abstract: A system which is an image diagnosis support system for Alzheimer-type Dementia (ATD) has been constructed; it extracts temporal lobe regions and an intracranial region as interest regions from a T2-weighted MR frontal image, and uses the cerebral atrophy rates at the regions of interest. In this paper, the extraction of temporal lobe regions and intracranial region is specifically discussed, and the regions of interest extraction method using Balloon model a kind of deformable models is proposed. We show the potential of our method using actual diagnosis images.

Key Words: MRI, T2-weighted image, Balloon models

1. Introduction

In recent years, Alzheimer-type Dementia (ATD), a kind of senile dementia, has been a social problem; large-scale research studies to determine whether brain imaging can help predict the onset and monitor progression of ATD for prevention and cure of the disease have been launched worldwide [1]. In a normal group (age-related cerebral atrophy group), intracranial regions show whole-brain atrophy, while in ATD, the temporal lobe region including the hippocampus atrophies remarkably [2]. Therefore, comparison of the rate of intracranial region atrophy to that of the temporal lobe region makes a difference for normal groups and ATD. Our purpose is to construct an image diagnosis support system for ATD which extracts temporal lobe regions and an intracranial region as interest regions from a T2-weighted MR frontal image used in usual imaging diagnosis of ATD and which uses the cerebral atrophy rate at the regions of interest. In this paper, we propose an extraction method of temporal lobe region and intracranial region fitting to the individual brain shape and size using Balloon models.

2. Regions of interest

In usual daily imaging diagnosis of brain atrophy, doctors check cerebrospinal fluid (CSF) which increases with brain atrophy on T2-weighted MR images. CSF is easy to check because of its brighter color than other brain matter on T2-weighted MR images by comparison with other kinds of MR images. Figure 1 depicts the intracranial region (Fig. 1(b)) and the temporal lobe region (Fig. 1(c)) of a T2-weighted MR frontal image showing the hippocampi and the temporal lobes clearly. The temporal lobe regions are defined as presented in Fig. 1(d). The temporal lobe regions are at the right and lower left part of the intracranial region and are defined by three features as

follows:

- 1) A space to an insular from the lateral sulcus
- 2) A space around the hippocampus
- 3) An outline of the intracranial region

A part of the temporal lobe region's boundary partly makes the intracranial region's boundary. Precision extraction of the temporal lobe region is effective in intracranial region's extraction.

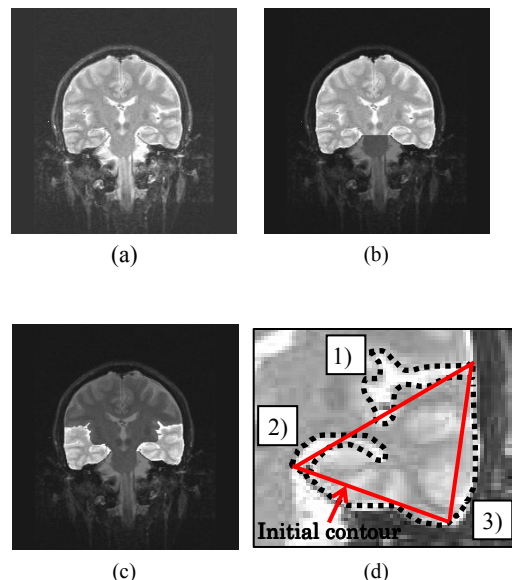


Fig.1 Region of interest and these features. (a) Original image. (b) Intracranial region. (c) Temporal lobe regions. (d) Three features of temporal lobe region and initial snake contour.

3. Method for extraction of the regions of interest

Some extraction methods of brain region are proposed by Kaeriyama et al [3] and Hayashi et al [4]. These methods used T1-weighted MR image which has clear contrast between CSF and brain matter, and were able to extract a brain matter image by binarization based on the brightness of T1-weighted MR image. However, T2-weighted MR image has low contrast between CSF and brain matter, therefore it is difficult to detect a region of interest by binarization. The proposed method comprises three steps as shown in Fig. 2. Figure 2 shows a flow chart of our method. In step 1, brain structures of a T2-weighted MR image are enhanced. In step 2, Balloon Snakes search the temporal lobe region fitting to individual brain structure. In step 3, the intracranial region is detected with the temporal lobe regions based on results obtained during the second step.

Step 1 Brain structure enhancement

T2-weighted MR image is easy to check CSF which is important for diagnosis of ATD, while it has low contrast, brain structures around the temporal lobe region are not clear. This leads to a problem: edges which feature the temporal lobe region are obscure and it is hard to detect the temporal lobe region. In this step, brain structures on a T2-weighted MR image are enhanced as preprocessing for extraction of the temporal lobe region. Following is the brain structure enhancement algorithm:

- 1) Binarize the T2-weighted MR image with Otsu's method [5]. Otsu's method is an automatic thresholding method based on image's histogram shape.
- 2) Extract a maximum region from the binarized image and eliminate noises of the maximum region. This region is used as an image mask template.
- 3) Mask an original MR image with the image mask template and extract an objective image including a brain stem.
- 4) Equalize a histogram of the objective image and remove noises on the image by median filter.

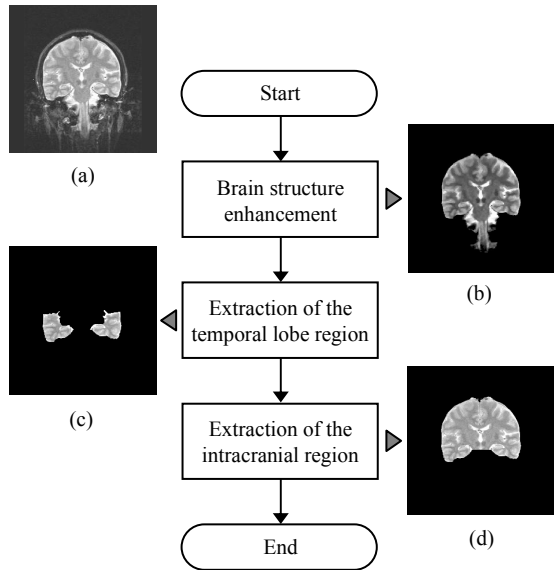


Fig.2 Flow chart of the proposed method. (a) Original image. (b) Enhanced image. (c) Temporal lobe regions. (d) Intracranial region.

Step 2 Temporal lobe region extraction using Balloon models

Snake, one of the deformable models, was introduced by Kass et al. [6]; it had abilities of free-form extraction and connecting nodes on obscure and broken contours like T2-weighted MR images. In our proposed method, an initial contour is set with a triangle approximated to a shape of the temporal lobe region using three points selected manually by an operator along the three temporal lobe region's features (Fig. 1(d)). The initial contour is in the temporal lobe region; it is needed to push the initial contour toward the outline of the temporal lobe region. Balloon models were introduced by Choen et al. [7] to add a pressure force to normal Snakes to expand or contract a contour. Accordingly, the proposed method uses the pressure force with the normal Snake energy function. The Balloon model's energy function is defined as

$$E_{\text{BalloonModel}} = \int_0^1 \{E_{\text{int}}(v(s)) + E_{\text{image}}(v(s)) + E_{\text{balloon}}(v(s))\} ds \quad (1)$$

The contour is a curve $v(s) = (x(s), y(s))$, $s \in [0, 1]$, where x and y are the coordinate functions, and s is the parametric domain. The contour moves through the image domain to minimize the energy function: E_{int} , E_{image} and E_{balloon} denote the internal energy, the image energy and the balloon energy respectively; these three energies are defined as the following.

$$E_{\text{int}} = \alpha(s) \left| \frac{\partial v(s)}{\partial s} \right|^2 + \beta(s) \left| \frac{\partial^2 v(s)}{\partial s^2} \right|^2 \quad (2)$$

$$E_{\text{image}} = -|\nabla I(v(s))|^2 \quad (3)$$

$$E_{\text{balloon}} = -\gamma(s) \bar{n}(v(s)) \quad (4)$$

Therein, $\alpha(s)$ and $\beta(s)$ are weight parameters that control the Snake's elasticity and rigidity. Equation (3) represents the negative gradient of a potential function, where $I(v(s))$ is a MR gray-level image, and ∇ is the gradient operator. Equation (4) presents the presser force: $\bar{n}(v(s))$ is the normal unit vector to the curve at point $v(s)$ and $\gamma(s)$ is a weight parameter that controls the presser force. Three weight parameters are set as $\alpha(s) = 30.0$, $\beta(s) = 30.0$, $\gamma(s) = 30.0$ from our experience; the searching area is local 3×3 pixels area around each point of $v(s)$.

Step 3 Intracranial region extraction

The temporal lobe region is included in the intracranial region. If the Balloon models extract the temporal lobe region accurately, it leads to good extraction of intracranial region. In this step, the intracranial region is extracted with right and left temporal lobe regions detected in step 2; the processing flow is shown in Fig. 3.

4. Experimental results

Experiment was carried out on actual diagnosis MR images. MR image data were scanned using a SMT-100X 1.0T (Shimadzu Corp.); these are 512×512 pixels 16 bit gray-level

T2-weighted frontal brain images. We translated the images to 256×256 pixel 8-bit gray-level by linear quantization.

Figure 4 shows the use of proposed method for extraction of regions of interest. Figures 4(a), (e) show initial contour setting by one operator. Figures 4(b), (f) show the temporal lobe extraction results. The Balloon model's contour detects the

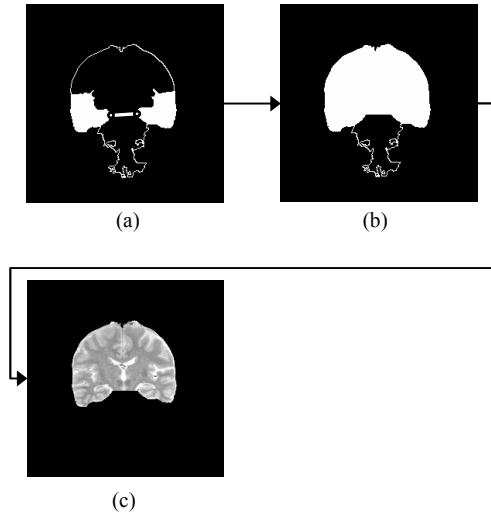


Fig.3 Flow of a extraction of a intracranial region. (a) Link of the left and right temporal lobe region. (b) Template of the intracranial region. (c) Intracranial region.

shape of the temporal lobe region fitting to individual brain shape and size. Although the proposed method can detect the temporal lobe regions, it missed the detection of the upper lateral sulcus: a part of the first temporal lobe's feature reflects the temporal lobe region's atrophy well; it is shown with a circle in Fig. 4(c), (g). It is suggested that the Balloon model's contour converged on edges between temporal lobe's brain matter and space to an insular from the lateral sulcus before the contour reaches a desirable boundary. Figures 4(d), (h) show the intracranial region extraction results. The results show excellent intracranial region boundary. These results show that our proposed method provided good conditions for extraction of the temporal lobe regions and excellent results for extraction of the intracranial region.

5. Conclusion

In this paper, an extraction method of temporal lobe region and intracranial region using Balloon models was proposed. This method was able to detect the temporal lobe regions along three features defined in chapter 2 fitting to individual brain shape and size, and extraction the intracranial region along brain structure. However, this method was unable to extract the upper lateral sulcus using only Balloon models. In future works, we improve this method to extract temporal lobe region with an Active Appearance Models [8] introduced by Cootes *et al.*; it has abilities to represent an object statistically and to search for an object if the object has individual differences.

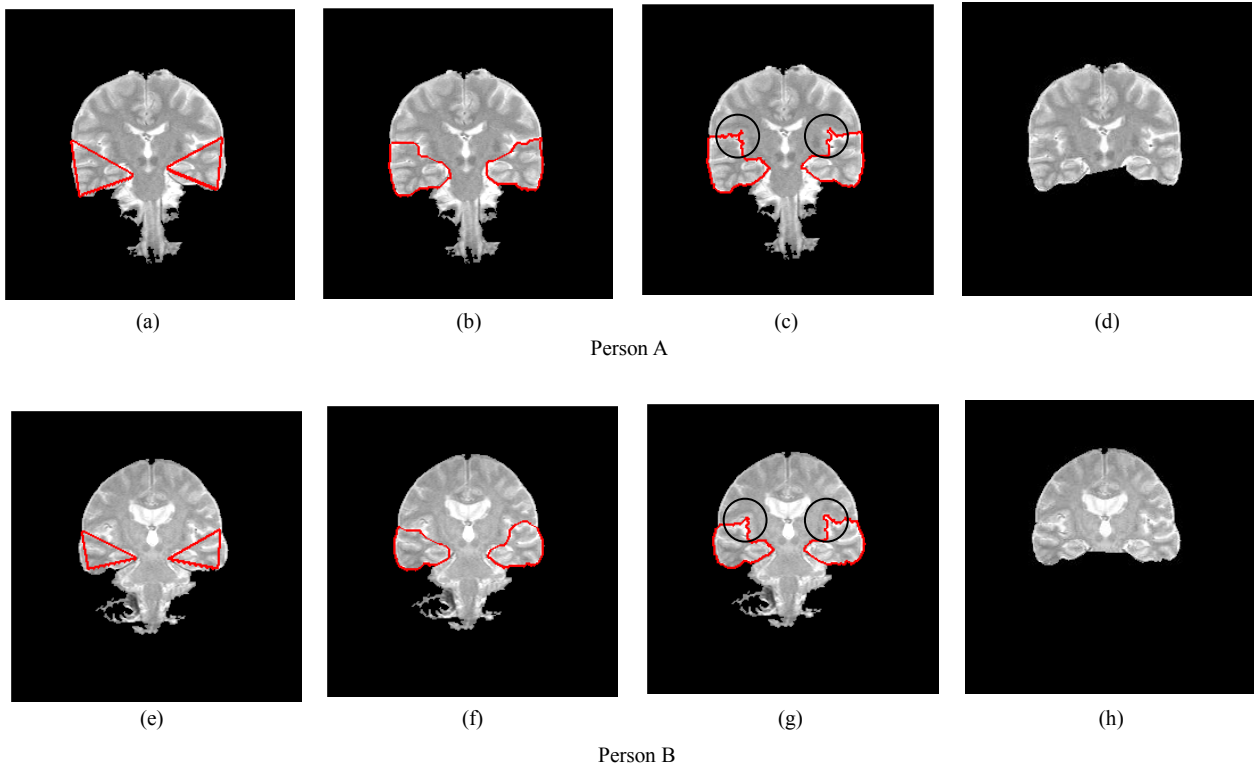


Fig.4 Extraction results of temporal lobe region and intracranial region. (a),(e): Initial contour. (b),(f): Temporal lobe extraction result. (c),(g): Manual extraction result. (d),(h): Intracranial extraction result. \circ : Upper lateral sulcus.

References

- [1] S. G. Mueller, M. W. Weiner, L. J. Thal, et al.: “Ways toward an early diagnosis in Alzheimer’s disease: The Alzheimer’s Disease Neuroimaging Initiative (ADNI)”, *Alzheimer’s & Dementia*, 1: pp. 55–66, (2005).
- [2] Y. Kuroda: “Alzheimer’s Disease”, Iwanami Paperbacks, (1998) (in Japanese).
- [3] T. Kaeriyama, N. Kodama, T. Kaneko, T. Shimada, H. Tanaka, A. Takeda and I. Fukumoto : “Improvement in the Performance of CAD for the Alzheimer-type Dementia Based on Automatic Extraction of Temporal Lobe from Coronal MR Images”, *Med Imag Tech*, Vol.22, No.2, pp.99-106 (2004) (in Japanese).
- [4] N. Hayashi, S. Sanada and M. Suzuki : “Development of Automated Segmentation Method for the Posterior Portion of the Temporal Lobe on Coronal MR Images”, *JJRT*, Vol.59, No.11, pp.1407-13 (2003) (in Japanese).
- [5] M. Takagi and H. Shimoda: “HANDBOOK OF IMAGE ANALYSIS”, University of Tokyo Press (2004) (in Japanese).
- [6] M. Kass, A. Witkin and D. Terzopoulos: “Snakes: Active Contour Models”, *IJCV*, 1(4), pp. 321–331, (1987).
- [7] L. D. Cohen: “On active contour models and balloons”, *CVGIP:IU*, 53(2), pp. 211–218, (1991).
- [8] T. F. Cootes, G.J. Edwards and C.J. Taylor: “Active Appearance Models”, in *Proc. European Conference on Computer Vision 1998* (H.Burkhardt & B. Neumann Eds.). Vol. 2, pp. 484–498, Springer, (1998).

Network Anomaly Detection Based on R/S Pox Diagram

Akinori Takahashi*, Ryuji Igarashi*, Hiroshi Ueda**, Yukio Iwaya*** and
Tetsuo Kinoshita****

* Department of Computer Science and Engineering, Akita University,
1-1, Tegata Gakuen-cho, Akita City, Akita 010-8502, Japan
Phone:81-18-889-2964, Fax:81-18-837-0408, igarashi@ie.akita-u.ac.jp

**Library and Information Technology Center, Gunma University

***Research Institute of Electrical Communication, Tohoku University

****Graduate School of Information Sciences, Tohoku University

akinori@ie.akita-u.ac.jp

Abstract: A method is proposed in this paper to detect attack traffic or anomaly by utilizing an R/S analysis. Our study so far indicates that a LS(Level Shift) or a cycle superimposed on a discrete time series provides a dispersion on the R/S pox diagram. The LS is well expressed by both H_{Sup} and H_{Inf} , the slope of the upper- and the lower-most plots group of the diagram. By utilizing them as the indices of the anomaly, validity of the proposal is tested at first by a Bernoulli trial simulation and then with the traffic data of "1999 DARPA Intrusion Detection Evaluation Data Set". Tested attacks are TCP SYN Flood, UDP Storm, and Smurf and our investigations show that H_{Inf} is suitable for the detection of flooding attacks arriving during a short period. A need for further investigations is also discussed.

Key Words: Anomaly Detection, Hurst Parameter, Pox Diagram, DoS Attack

1 INTRODUCTION

The Internet in current society is an important infrastructure. Therefore, to maintain the quality of the Internet, comprehensive measures to maintain that must be taken because an amount of malicious traffic such as Dos or DDoS prevails[1] among normal traffic. These kinds of flooding attacks often cause a congestion collapse or a disorder in the internet, revealing an anomaly in the traffic. The detection of anomalies is useful from TE(Traffic Engineering) point of view. The anomaly detection in this context is the detection of abrupt changes in traffic flow[2]. As to packet traffic, however, a care must be paid because, owing to recent studies, it is not consistent with conventional Poisson processes but it is said to obey 2nd order SS(self-similar) processes[3]. The most remarkable nature of the SS is that the burstiness of the traffic holds over decades of time scale, i.e. traffic fluctuations never disappear however long observation is aggregated. This means that the self-similarity causes an unfavorable effect of giving false alarms whereas the traffic fluctuation is within a normal level.

A number of studies have already been reported to try to evaluate the traffic properties prescribed by self-similarity origin packet flow[1],[4-7]. Deterioration of 99.9% file

transmission time delay, for example, was reported to have relevance with the self-similarity when the upper layer traffic was regulated by TCP[4]. Some studies indicate that the SS process is caused by phase transitions of flow from non-congestion to congestion state[5]. An investigation of the change of the degree of traffic self-similarity under DDoS attack[1] or real time derivation of SS parameter H in order to apply it to traffic control[6-8] has been being attempted. Those preceding works suggest the importance and usefulness as well to practice anomaly detections by taking account of SS nature of the traffic.

We have reported that the R/S pox diagram employed to estimate a Hurst parameter H represents a characteristic configuration depending on the scale of LAN, the nature of traffic, and observation time scale[9]. A remarkable feature is the dispersive configuration of the diagram when a traffic is subjected to a LS(level shift) or a cycle. We expressed the dispersion aperture by the upper- and the lower-most plots group of the diagram. The slope H_{Sup} of the upper-most plots group and H_{Inf} of the lower-most plots group are indices of the dispersion and are no more the Hurst parameter to estimate the self-similarity. Our preceding study shows that H_{Inf} especially provides a definite feature when traffic is being interfered with continual flow increase by, for example, DoS attacks[10].

In this paper we report the characteristics of H , H_{Sup} , and H_{Inf} in case traffic time series is mixed with such flooding attack as appears continually having a cycle within the flooding duration. That which was investigated mainly capabilities by making use of H , H_{Sup} , and H_{Inf} . The confirmation of the proposal is practiced by using a simulation and a real data of “1999 DARPA Intrusion Detection Evaluation Data Set”(1999 DARPA Data Set).

The paper consists of five sections. In section 2 a brief introduction of the R/S analysis including the derivation of H , H_{Sup} , and H_{Inf} is described. In section 3 a simulation which imagines the attack traffic is practiced and a method to detect the anomaly is proposed. In section 4 a detection result tested with “1999 DARPA Data Set” is described. A conclusion is stated in section 5.

2 EVALUATION QUANTITIES DERIVED FROM POX DIAGRAMS

2.1 R/S analysis

What is called an R/S analysis, a graphical method conventionally used to estimate the self-similarity parameter H , was at first introduced for the analysis of Nile River flow fluctuations by H. E. Hurst[12]. Mathematical foundation thereafter was established by B. B. Mandelbrot[13] and the analysis has been widely used in various walks of research fields. An application to communication fields especially for packet traffic communications was first practiced by Leland et al.[3] in the late 20th century. The R/S is a statistic and the self-similarity parameter H named after Hurst is estimated graphically by using an R/S pox diagram[3], [14], [15]. The derivation process of H with respect to the packet traffic is conceptually depicted in Fig.1.

A packet flow interpreted as random points placed on a time axis is captured every small time interval Δt and then the count is transformed to a discrete time series X_t , $t = 1, 2, \dots, N_W$.

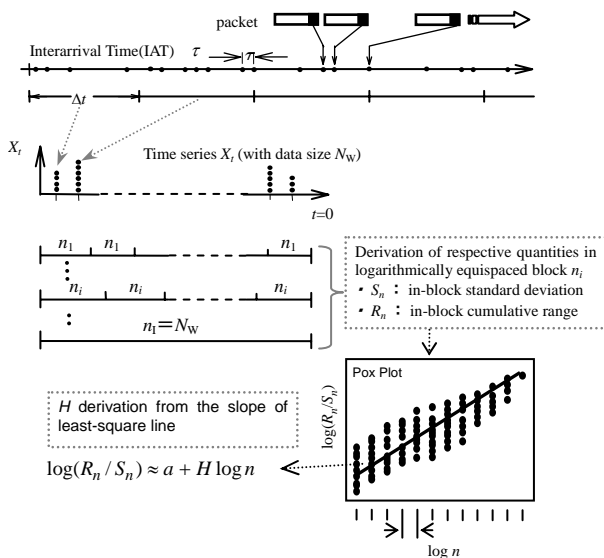


Fig.1 H derivation procedure in an R/S analysis.

The R/S analysis let us to divide the time series into non-overlapped n blocks and then to derive a cumulative range R_n and a standard deviation S_n within every block thus constructing a relationship between $\log\{R_n/S_n\}$ and $\log n$. In the derivation process a cumulative sum W_k , ($k=1, \dots, n$) is successively obtained as in Eq. (3). The Hurst parameter H is determined as the slope of the line on $\log\{R_n/S_n\}$ v.s. $\log n$ graph.

$$(\bar{X})_n = \sum_{k=1}^n X_k / n \dots\dots\dots (1)$$

$$S_n = \sqrt{\sum_{k=1}^n X_k^2 / n - (\bar{X})_n^2} \dots\dots\dots (2)$$

$$W_k = \sum_{j=1}^k X_j - k(\bar{X})_n \dots\dots\dots (3)$$

$\{0, W_1, \dots, W_k, \dots, W_n\} \rightarrow k = 1, \dots, n$

$$R_n = \max\{0, W_1, \dots, W_k, \dots, W_n\} - \min\{0, W_1, \dots, W_k, \dots, W_n\} \dots\dots\dots (4)$$

The stochastic property of X_t is subjected to a change according to time scale or aggregation level Δt , which has been discussed from the early days of this field. Observation of X_t with higher aggregation so that the size N_W ranges over days, weeks, months, or years, provides a diurnal variation. This is a definite non-stationarity. At smaller Δt the diurnal variation tends to disappear and X_t tends to become an uncorrelated process. However, the intervention of such anomalous traffic as attack or unusual user application may also cause a non-stationarity with this small Δt . Therefore, a care must be taken to properly choose the Δt . The criteria how to set Δt is another problem and this will be discussed elsewhere. In our present study Δt was set to 0.001s and the size N_W was chosen to become 5000. This comes from a need to estimate a significant H by the R/S analysis[14], in which is recommended to use at least more than 500~1000 points. Our selection $\Delta t=0.001$ s and $N_W=5000$ realize less than 1s H derivation and is suitable for a real time derivation[8].

2.2 Dispersion index H_{Sup} and H_{Inf} of pox diagram

Whereas the pox diagram of an FGN(Fractional Gaussian Noise), a theoretically constructed 2nd order SS process, shows a monotone variation as depicted in Fig.2 (a), that of a real traffic provides a definite dispersion with an aperture between H_{Sup} and H_{Inf} . In Fig.2 (b) is illustrated an example of intentional flooding attack in our laboratory. Clearly seen is the dispersion in the pox diagram[9],[10]. Our study so far tells that a LS makes an increase in H_{Sup} and a cycle makes a decrease in H_{Inf} .

The dispersion illustrated in Fig.2 (b) is proposed hereafter as a dispersion index of the pox diagram. Each index is H_{Sup} or H_{Inf} and determined as below, where either $\max(R_n/S_n)$ and $\min(R_n/S_n)$ are those of upper- and lower-most plots group respectively. Intercepts a_{Sup} and a_{Inf} are not apparently made use of in this context.

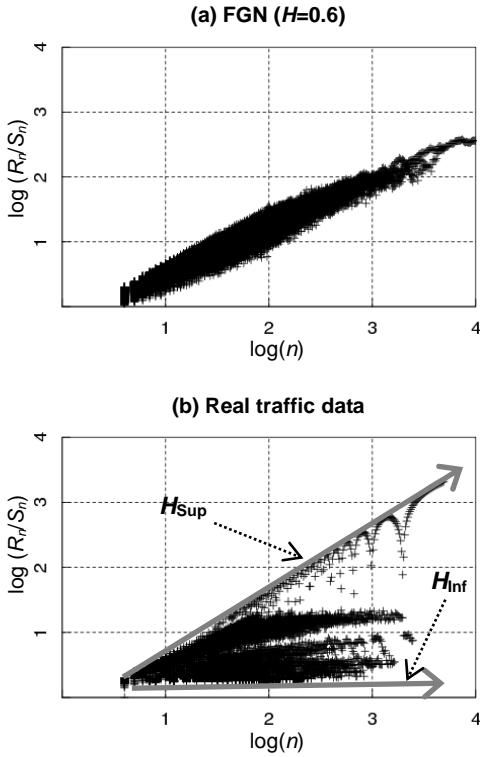


Fig.2 Example of a pox diagram of either (a) FGN(Fractional Gaussian Noise) or (b) real traffic. Characteristic quantities H_{Sup} , and H_{Inf} of the pox diagram are also depicted in (b).

$$\log\{\max(R_n/S_n)\} = a_{Sup} + H_{Sup} \log n \dots\dots\dots (5)$$

$$\log\{\min(R_n/S_n)\} = a_{Inf} + H_{Inf} \log n \dots\dots\dots (6)$$

Since the decrease of plots in the pox diagram at larger n makes statistical fluctuations increase[14], H_{Sup} and H_{Inf} are derived for $\log n < 3$. Although H_{Sup} and H_{Inf} are slopes of the plotted lines each of them hereafter is called a “dispersion index”.

3 ANOMALY DETECTION SIMULATION USING THE DISPERSION INDEX

The performance of the dispersion indices H_{Sup} and H_{Inf} is discussed as below in terms of abrupt excess of packets and the periodicity of packet arrival in the excess duration.

3.1 Characteristics with respect to the change of packet arrival rate

The case imagined here is that in which packet arrivals increase abruptly during the observation as represented in Fig.3. Assumed in Fig.3 is the case where Δt is sufficiently small so that packets arrive sparsely and obey a Poisson process. This means that the probability z_1 and z_2 of packet arrival during Δt becomes $z_1 = p_1 \Delta t$ and $z_2 = p_2 \Delta t$ over the former and the latter half of total duration $N_W = 5000$, where p_1 and p_2 are packet arrival rates respectively. This also means that packet arrival is regarded as Bernoulli trial and the block length $n_1 = n_2 = n = N_W/2$ with the small probabilities z_1 and z_2 prescribes the binomial

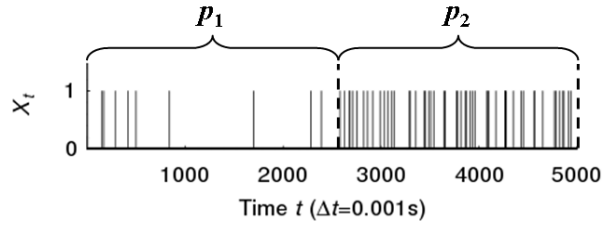


Fig.3 Simulation of the traffic time series X_t in which the packet arrival rate is subjected to a change after the center of the total duration 5000 data points. The former half is set at p_1 [pps] and the latter half at p_2 [pps], where $p_1 < p_2$.

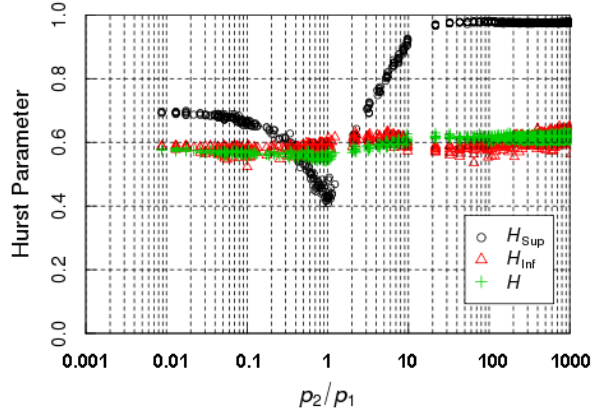


Fig.4 Variation of each of H_{Sup} , H_{Inf} , and H with respect to the ratio of p_2 to p_1 .

distribution $B_{n,z_1}(x) = {}_n C_x z_1^x (1-z_1)^{n-x}$, $B_{n,z_2}(x) = {}_n C_x z_2^x (1-z_2)^{n-x}$ respectively. With the R-Langrange randomly placed x points are easily obtained under the binomial mean $\mu_1 = n_1 z_1$ and $\mu_2 = n_2 z_2$. Customarily random arrival of x points over n -sized block should be generated successively by a Monte Carlo simulation. However, in the above situation where only one packet arrives at the most, the Poisson process can be well approximated by a Bernoulli trial thus validating our simulation. In addition the practice above makes the simulation time reduce more than the consecutive Monte Carlo simulation.

The simulation illustrated in Fig.3 is similar to the LS discussed in ref.[16]. Precisely speaking, however, it is the same with the statistical hypothesis testing for the change point detection[17].

In Fig.4 is represented the dispersion indices H_{Sup} , H , and H_{Inf} with respect to p_1/p_2 under the constant $p_1 = 91.6$ pps. Since two kind of LS are assumed, namely an increase and a decrease after the change point as represented in Fig.3, the increased LS corresponds to $p_1/p_2 > 1$ and the decreased one to $p_1/p_2 < 1$. Clearly seen is the remarkable variation of H_{Sup} between a bottom and asymptotes over two decades before and after $p_1/p_2 = 1$. This suggests that the variation of H_{Sup} sufficiently reacts to LS.

3.2 Characteristics with respect to periodic packet arrival

Since flooding attacks like DoS or DDoS cause numerous number of packets to arrive in so short a period, the interarrival

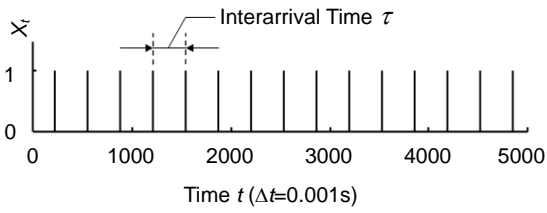


Fig.5 Time series X_t in case packet arrivals are periodic with its periodicity τ . Packets are positioned so sparse that each of them appears one at a time at the most, which explains why X_t in this figure resides between 0 and 1.

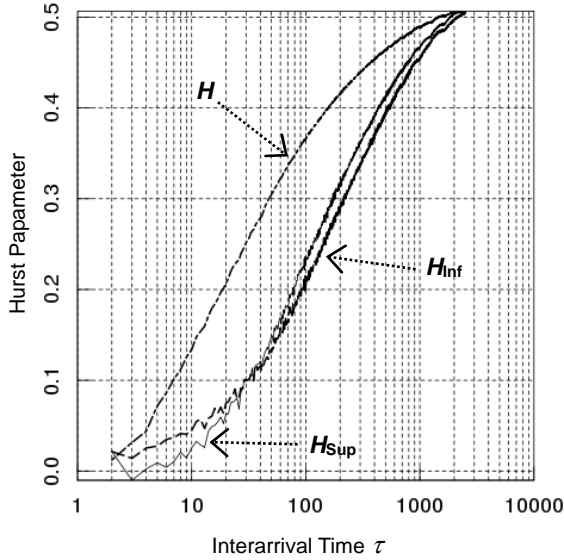


Fig.6 Variation of each of H_{Sup} , H_{Inf} , and H against the interarrival time t . Each quantity appears a definite relationship with respect to t when it is regarded as a dispersion index of the pox diagram.

time of them are regarded periodic. This assumption leads us to investigate the response of the dispersion indices to packet train having a period τ as exemplified in Fig.5. The case imagined is that in which at the most only one packet arrives during the small time Δt . This explains why X_t in this figure resides between 0 and 1.

Represented in Fig.6 is the simulation result of the variation of H_{Sup} , H , and H_{Inf} with respect to τ . Monotone variation to each of them is obtained over two decades on logarithmic τ scale and every one of them shows an asymptote to both larger and smaller end of τ . Each variation appears a detectability of periodic packet arrival.

3.3 Effects of attacking period ratio to calculation window size

To practice a real time H_{Sup} , H , and H_{Inf} derivation, the effect of size N_w and step size ΔN_w of calculation window should be investigated because the ratio p so defined as $p = \Delta N_w / N_w$ describes the performance of immediateness and periodicity detectability. Conceptual advancement of the window is depicted in Fig.7. In case the indices H_{Sup} , H , and

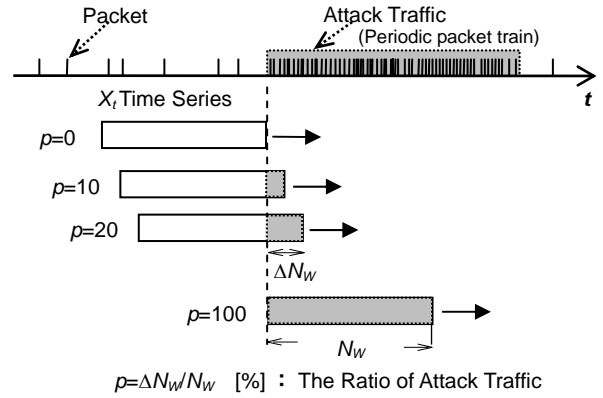


Fig.7 Ratio p [%] of the period of attacking packets to the calculation window of the R/S analysis.

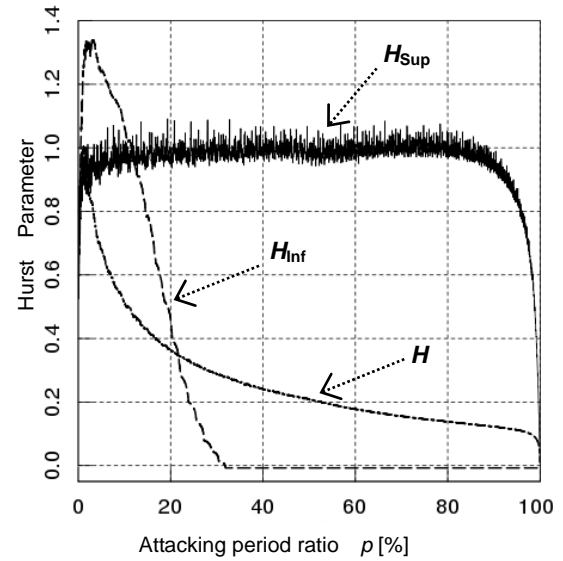


Fig.8 Variation of dispersion indices H_{Sup} , H_{Inf} , and H against the attacking period ratio p .

H_{Inf} show rapid variation, this is favorable to change point detections[17]

When the indices maintain a definite relation to p then this is preferred to periodicity detection. Represented in Fig.8 is sufficient immediateness of all indices H_{Sup} , H , and H_{Inf} . The periodicity may be evaluated by either H , or H_{Inf} because either of them shows a monotone variation with respect to p . H_{Inf} in this case is superior to H because H_{Inf} shows more linear and rapid variation than that of H .

From the reasons above H_{Inf} is chosen as an index to detect anomaly. In addition H_{Inf} converges around $p = 30$ %. This means the window needs to let some numbers of attack packets in to evaluate the attack period τ . This may probably provides characteristic in favor of false alarm[16].

4 PERFORMAMNCE EVALUATION

As stated in 3.3 better way of anomaly detection is it should be sensitive to anomalies with false alarms as least as possible. From this point of view the employment of H_{Inf} is

recommended. An evaluation using “1999 DARPA Data Set”[11]is practiced as below. Attempted are 5th week Monday data (TCP SYN Flood-18:04:04, UDP Storm-20:00:27, Smurf-13:18:12) because these are the important in the TCP/IP communications.

4.1 Method proposal

A decision criterion $E(t)$ is so defined that it represents “Attack $\{E(t)=1\}$ ” or “Non Attack $\{E(t)=0\}$ ” by comparing H_{Inf} with a threshold α as below. We set α as $\alpha=0.3$. Although this α is most suitable as to the data employed, careful discussion should be done with respect to the appropriate way to determine it.

$$E(t) = \begin{cases} 1, & H_{Inf}(t) < \alpha \\ 0, & H_{Inf}(t) \geq \alpha \end{cases} \dots\dots\dots (7)$$

The confirmation of the periodicity spectrum as represented in Fig.9 assures the validity of using these data because every spectrum resides within $2 < \tau < 20$ and this satisfies the detectable range simulated as in Fig.6.

4.2 Result

Represented in Fig.10 is the detection result using 5th week Monday data all through 24 hours, the time series X_t , $H_{Inf_SYN}(t)$ for SYN packets, $H_{Inf_UDP}(t)$ for UDP packets, and $H_{Inf_ICMP}(t)$ for ICMP packets downward respectively. In the X_t graph the total traffic is gray-colored, whereas the attack traffic is black-painted. The “Alert” expresses an anomaly detected with the criterion prescribed in Eq.(7). The results are

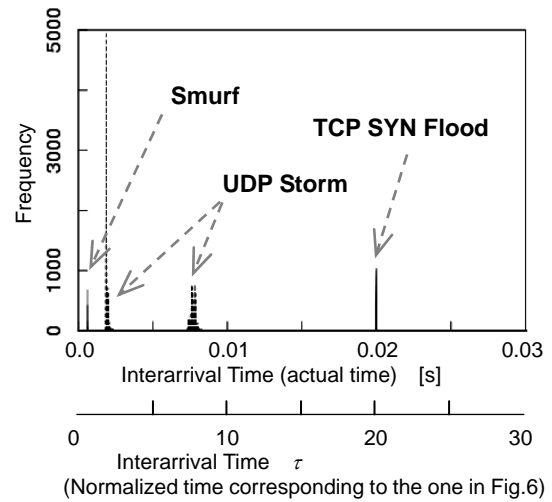


Fig.9 Attack time interval of the attacking traffic (Attack period τ).

self-explanatory in Fig.10. The duration of TCP SYN Flood and UDP Storm are around several minutes and this makes the detection easy. Despite the short duration of Smurf, this also could be detected.

The result for the “DARPA Data Set 4th week Monday through 5th week Friday”is represented in Table 1, where “Detected” means those which are detected with the proposed method, “DoS Attack” means those which actually are the DoS

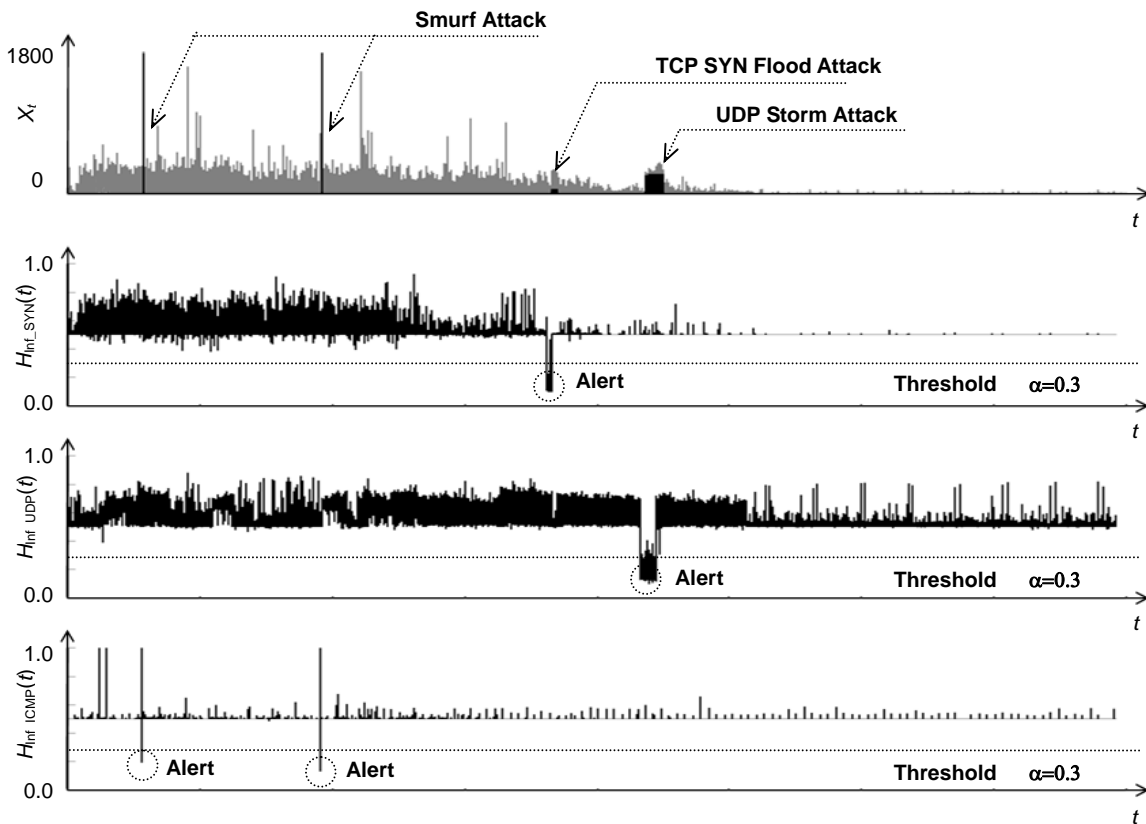


Fig.10 Example results of the dispersion index H_{Inf} derived from the time series X_t of the DARPA 5th week Monday traffic.

attack, and “Detected False” means those which are not set as that attack name. To be noticed is that the “Detected False” are almost attacks, for example Ping of Death or Teardrop, which do not coincide only by attack names. Such exception as DNS commute traffic which provides truly a false, however, must be paid an attention. Further study, however, is left to follow.

Table 1 Results of the detection attempt.

	Detected	DoS Attack	Detected False
H_{Inf_SYN}	5	4	1
H_{Inf_UDP}	7	3	4
H_{Inf_ICMP}	6	5	1

5 CONCLUSION

In the present paper the detection of traffic anomaly caused by such flooding attacks as TCP SYN Flood, UDP Storm, and Smurf was attempted by proposing evaluation indices derived from the R/S pox diagram. Investigated agents were H_{Sup} derived from the upper-most plots group of the diagram, H derived conventionally from the diagram, and H_{Inf} derived from the lower-most plots group of the diagram. With the purpose of detecting not only the change point(attack onset time) but also the attack period τ , H_{Inf} was chosen as the index. To confirm the validity the “1999 DARPA Data Set” is used and the proposal showed a successful result not only for those tried above but for other flooding attacks with an exception to the DNS commute traffic. Further tests should be necessary, however, for the time scale Δt , the window size N_w and its step size ΔN_w to derive the evaluation index, and the detection threshold α .

Acknowledgment—This study was partially supported by the Nation-wide Cooperative Research Projects of Research Institute of Electrical Communication, Tohoku University (H19/A25).

References

[1] Li, M., "Change Trend of Averaged Hurst Parameter of Traffic under DDoS Flood Attacks", Computers & Security, Vol.25, Issue 3, pp.213-220, (2006).
 [2] Thottan, M. and Ji, C., "Anomaly Detection in IP Networks", IEEE Transaction on Signal Processing, Special Issue of Signal Processing in Networking, Vol.51, No.8, pp.2191-2204, (2003).
 [3] Leland, W.E., Taqqu, M.S., Willinger, W. and Wilson, D.V., "On the Self-Similar Nature of Ethernet Traffic", Computer Communications Review, Vol.23, No.4, pp.183-193, (1993).
 [4] Sumida, Y., Ohsaki, H., Nurata, M. and Miyahara, H., "Effects of Upper-Layer Protocols on Self-Similarity of Network Traffic", Trans of IEICE B, Vol. J82-B, No.6, pp.1126-1137, (1999).
 [5] Fukuda, K., Takayasu, M. and Takayasu, H., "Analysis of Minimal Model of Internet Traffic", Proc. of Traffic and Granular Flow'01, pp.381-400, (2001).
 [6] Hagiwara, T., Doi, H., Tode, H. and Ikeda H., "High-Speed Calculation Method of the Hurst Parameter Based on Real Traffic", IEICE Transactions on Information and

Systems, Vol.E84-D, No.5, pp.578-587, (2001).

[7] Roughan, M., Veitch, D. and Abry, P., "On Line Estimation of the Parameters of Long-Range Dependence", IEEE GLOBECOM'98, pp.3716-3721, (1998).
 [8] Igarashi, R., Takahashi, A., Ueda, H., Nasuno, Y., Iwaya, Y., Sakata, M., and Kinoshita, T., "A Proposal for Real Time Hurst Parameter Derivation", IEEJ Trans. EIS, Vol.127, No.6, pp.968-969, (2007).
 [9] Nasuno, Y., "A study of IP Network Base Build Technology for Voice Communications", Ph.D Thesis, Tohoku University(Department of Electrical and Communication Engineering, Graduate School of Engineering), A3TD2009, (2006).
 [10] Takahashi, A., Igarashi, R., Ueda, H., Nasuno, Y., Iwaya, Y., and Kinoshita, T., "Online Network Observation to Detect Traffic Anomaly", IEICE technical report 10, pp. 57-62, (2007).
 [11] available at "1999 DARPA Intrusion Detection Evaluation Data Set", <http://www.ll.mit.edu/mission/communications/ist/corpora/ideval/data/1999data.html>
 [12] Hurst, H.E., "Long-Term Storage Capacity of Reservoirs", Trans. Amer. Soc. Civil Eng., Vol. 116, pp.770-799, (1951).
 [13] Mandelbrot, B.B. and Wallis, J.R., "Robustness of the Rescaled Range R/S in the Measurement of Noncyclic Long-Run Statistical Dependence", Water Res. Res., Vol.5, No.5, pp.967-988, (1969).
 [14] Beran, J., Sherman, R., Taqqu, M.S. and Willinger, W., "Long-Range Dependence in Variable-Bit Rate Video Traffic", IEEE Transactions on Communications, Vol.43, No.2/3/4, pp.1566-1579, (1995).
 [15] Taqqu, M.S., Teverovsky, V. and Willinger, W., "Estimators for Long-Range Dependence: An Empirical Study", Fractals, Vol.3, No.4, pp.785-798, (1995).
 [16] Dang, T. and Molnar, S., "On the Effects of Non-Stationarity in Long-Range Dependence Tests", Periodica Polytechnica, Ser. El., Vol.43, No.4, pp.227-250, (1999).
 [17] Basseville, M. and Nikiforov, I., "Detection of Abrupt Changes-Theory and Applications", Prentice Hall, Englewood Cliffs, New Jersey, (1993).

A CG Contents Production System for Explaining Human Motions in a Digital Museum

Takeshi Shibata*, Takashi Yukawa † , Takaaki Kaiga* ‡ , Hiroshi Yokoyama**, and
Hideo Tamamoto **

*Graduate School of Engineering and Resource Science, Akita University, 1-1, Tegata-Gakuen-Cho, Akita, 010-8502 Japan

† North Asia University

‡ Warabi-Za

**Department of Computer Science and Engineering, Akita University

shibata@ie.akita-u.ac.jp

Abstract: The traditional folk dances should be preserved and exhibited in order to bequeath these dances to the next generations. A digital museum is a good candidate for this purpose because we can exhibit dances using a CG reproduction technique. We can preserve and reproduce dances by using motion capture system. When exhibiting the dances in the digital museum, we have to not only reproduce dances, but also add exhibition effects to the reproduced contents. It is difficult to decide exhibition effects because a high degree of CG techniques is required. The proposed system can define exhibition effects by using the GUI and generates a camerawork automatically. The exhibition effects are described in XML, and the camerawork is generated so that the targets of the body sites to be explained are well observed. We implement the proposed system and show how effectively it works.

Key Words: Human Motion Analysis, Computer Graphics, Digital Museum

1 INTRODUCTION

Nowadays, some Japanese folk dances are on the verge of extinction. These Japanese folk dances are intangible cultural assets. In order to safeguard these assets from being extinguished, we should archive and exhibit them, as the tangible cultural assets are done in a museum. Since these intangible assets are not physical objects, it is difficult to archive and exhibit them in a museum.

We are interested in the digital museum where the intangible assets can be exhibited. In the digital museum, cultural assets are digitalized and archived as digital data. These data are exhibited by using visualization techniques and network techniques [1,2].

There are some studies on the techniques of digitalizing the assets or the techniques of constructing the digital museum. Since these studies target the tangible cultural assets, we should discuss a new technique for the intangible cultural assets. The human motion like dances are difficult to archive and exhibit, because they are represented by time-space data.

We proposed a technique for archiving and displaying folk dances by using motion capturing system and CG techniques [3]. The human motion, including a folk dance, can be digitized by motion capturing system and archived as human motion data. We can display dances by using archived data and a character

animation. We can use these archived data in the digital museum.

When exhibiting dances, it is important not only to display human motions, but also to attach the explanations based on the study of museum curators. This is because the audiences can be aware of the worth of the assets by reading attached explanations. We call the contents of attached explanations the human motion exhibition contents.

In order to attach the explanations, a contents creator has to prepare the explaining effects such as explanation text, target body parts, and a camerawork. We define these effects as exhibition scenarios. Setting the exhibition scenarios requires a high degree of CG techniques and only a CG specialist can do that. The exhibition contents have to be able to display the motion which is explained. The contents creator should prepare the camerawork so that the camera position and camera rotation may change according to the postures of target parts.

Hence, we propose a system for creating CG contents to exhibit dances in the digital museum, so that even a contents creator without a high degree of CG techniques can easily create these contents.

The proposed system includes the GUI (Graphical User Interface) for setting an exhibition scenario, and the function of automatic camerawork generation. This system can save the exhibition scenario as an XML (Extensible Markup Language)

file. This created file is exhibited on the proposed viewer that can run on a web browser.

2 ARCHIVING THE HUMAN MOTION BY USING A MOTION CAPTURING SYSTEM

In this study, we use Motion Start Wireless, which is the magnetic wireless motion capturing system made by Ascension Technology, for digitalizing the human motion. We attach 15 sensors on a human body and capture the data at the ratio of 30 frames per second. We use a frame as a time unit in this paper.

Each sensor of the motion capturing system can get the data of 6 dimensions. This data contains the position data (X,Y,Z) in 3 dimensions and the rotation data (azimuth, elevation, roll) described by Euler angle in 3 dimensions.

We call each segment a body part, which is shown as a rectangle in figure 1. This figure also shows the names of body parts. The captured data describes the position and rotation of the body part where the sensor is attached. Since body shape of an actor is different from the one of a CG character, the captured data cannot be used as it is. We standardize the data by adjusting the rotation data to the CG character. In this paper, we use the standardized data.

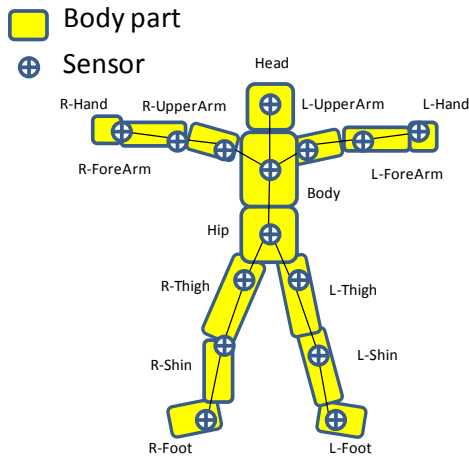


Figure 1: Sensors on CG character

3 EXHIBITION CONTENTS

The CG animations, which represent the human motion and to which the effects are attached for explanation, is called exhibition contents in this paper. We call an explanation effect an exhibition scenario. In this section, we propose a method to represent the exhibition scenario, and we propose a method to automatically generate a camerawork.

3.1 Exhibition Scenario

The exhibition scenario consists of the following information; 1) captured human motion data (MoCap data), 2) sound data for BGM, and 3) some explanation scenes.

The explanation scene contains a start time of explanation, an end time of explanation, body parts of explanation target

(target parts), explanation text, and exhibition effects such as parameters for generating a camerawork.

The exhibition scenario is described by XML tags, because we can redefine afterwards, or share the tags easily. Table 1 shows the list of the tags defined for exhibition scenario.

Table 1. Tags for exhibition scenario

Tag	
<mdml>	The language to describe the exhibition scenario
<scenario>	Exhibition scenario
<motion>	Motion capture file name
<bgm>	BGM file name
<scene>	Explanation scene
<shot>	Shot parameter for camerawork
<segment>	Target parts
<speed>	Animation speed
<description>	Explanation article

3.2 Automatic Camerawork Generation Method

We consider the camerawork consists of the time series of a camera angle. The camera angles contains a camera position and a camera rotation. The proposed system generates the camerawork in each explanation scene.

Each camera angle should display the human motion to be explained. Figure 2 shows the images from two different angles. In this explanation scene, the motion, where the left arm is stretched forward from the posture that the elbow is pulled, is explained. We can see from this image that the side view image is better than the front view image to understand how the left arm moves. In this subsection, we propose a method for generating a camerawork that can display a side view as shown in figure 2(b).

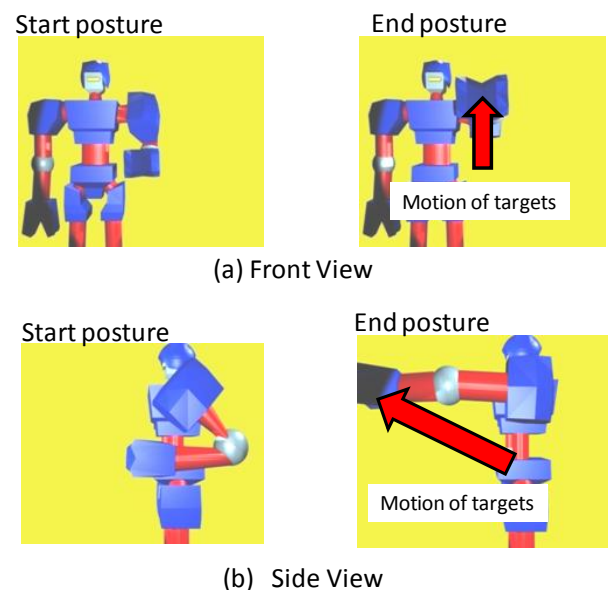


Figure 2: Two images from two angles

The time period during which a camera is not rotated is called a shot. The camerawork is generated by the following three steps; 1) segmenting the explanation scene as some shots, 2) deciding the camera angle in each shot, and 3) interpolating each camera angles between shots.

3.2.1 Segmenting the Scene as Shots: If the number of frames in the explanation scene is less than 200, we consider the length of the scene to be too short and we segment it into one shot. If not, we segment the scene as some shots. The less the posture of a character moves in a shot, the better the movement of a character is displayed, because the camera rotation is not changed during a shot. As shown in figure 3, we employ the time period during which the postures of the character are similar to each other as a candidate of a shot. We find out the candidates by using the modified Self Organizing Map [4], which can cluster the postures. When a candidate of a shot is too short, the animation has a poor view, because the camera swings. If the length of candidate is less than threshold, we combine two adjacent candidates. We employ 90 frames as a threshold.

3.2.2 Deciding the Camera Angle: The camera angle that

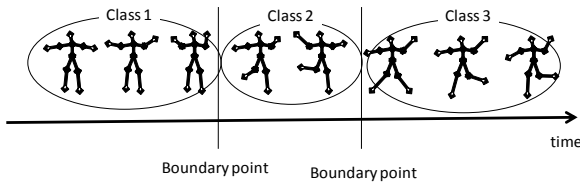


Figure 3: The result of clustering

is appropriate for explanation should be able to widely display the motion of target parts. That means the trajectory of target parts is widely distributed on the screen. We use the principle component analysis (PCA), which can derive the axis so that the variance of input data is maximized on it. We can obtain the plane where the trajectory is widely distributed by using PCA. The camera angle is decided so that the direction of a camera may coincide with a normal vector of the obtained plain.

In this paper, we consider the trajectory can be represented as time series of positions of target parts. We analyze the trajectory by PCA. The first principal component obtained by PCA means an axis where the trajectory the most widely distributed. And the second principle means the axis the second widely distributed. For this reason, the plane P formed by the first principle and the second principle, will become a screen.

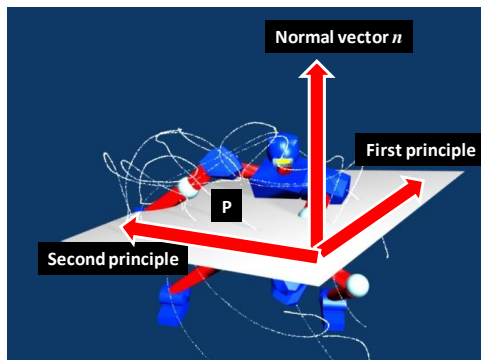


Figure 4: The result of PCA and camera rotation

We decide the camera rotation as a normal vector of plane P in figure 4. The normal vector n of plane P can be obtained by an exterior product of the first principle and the second principle. In order to display the motion of the target parts widely on the screen, the center of trajectory is displayed on the center of a screen. The distance between a camera and a center of trajectory is decided so that all target parts may be included in the screen. Figure 5 shows these conditions, where c is a center of trajectory, d is a distance between a camera and a center of trajectory, and n is a normal vector of a display plane.

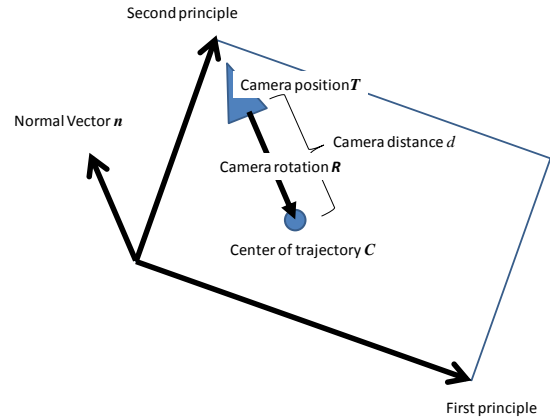


Figure 5: The condition of camera angle

The camera rotation R and camera position T can be calculated by equations (1) and (2).

$$T = c + dn \quad (1)$$

$$R = \text{sign}(d) n \quad (2)$$

3.2.3 Interpolation of Camera Angles: Since the camera angles are decided in each shot, we should generate a camerawork between two adjacent shots. The camerawork is generated by using the linear interpolation.

4 PROPOSED SYSTEM

We implemented the proposed system. When this system is used, a user can generate an exhibition scenario by only inputting MoCap data and explanation scene. We can see this exhibition scenario by using the viewer.

The proposed system generates a camerawork automatically and replaces the default camerawork with the generated camerawork, when the contents creator inputs the explanation scene into the system. The contents can be made by repeating the input and the confirmation on GUI.

4.1 Structure of the Proposed System

Figure 6 shows the structure of the proposed system. This system contains a contents editor, a scenario processor, a camerawork generator, a MoCap database, and a contents viewer. The contents editor contains a scenario editor, and a scene editor. A contents scenario can be set by the contents editor.

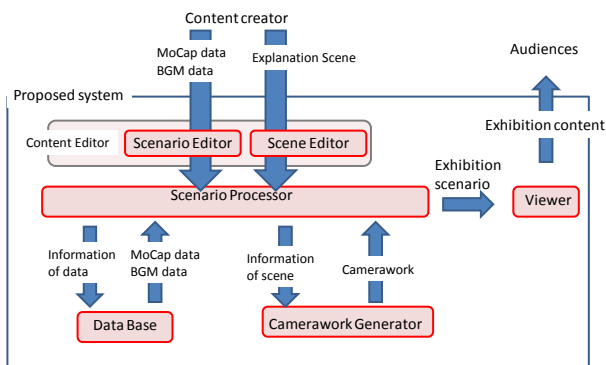


Figure 6: Structure of proposed system

4.2 Contents Editor

The contents editor offers the human interface for creating the contents. In this system, the contents editor consists of two parts, a scenario editor and a scene editor.

4.2.1 Scenario Editor: Figure 7 shows the scenario editor. The scenario editor contains a menu bar, a simple viewer, and a time line. A user can retrieve the MoCap data to be exhibited from a database by using a menu bar. The menu bar can be also used to load BGM file, to load a scenario already created, or to save a current scenario.

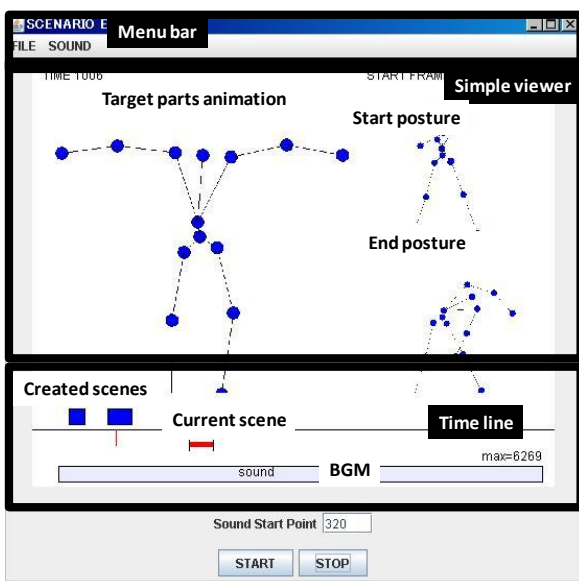


Figure 7: Scenario Editor

The current period of an explanation scene is displayed on the time line by red line. The user can point the start time of an explanation scene and the end time of an explanation scene by sliding the red line. The time line also displays created scenes, and a time period of BGM. The time period of BGM to be played can be changed by sliding the BGM period line.

4.2.2 Scene Editor: The user can insert an explanation scene, delete the scene, or reedit the scene by using a scene editor. The scene editor is shown in figure 8. The scene editor contains

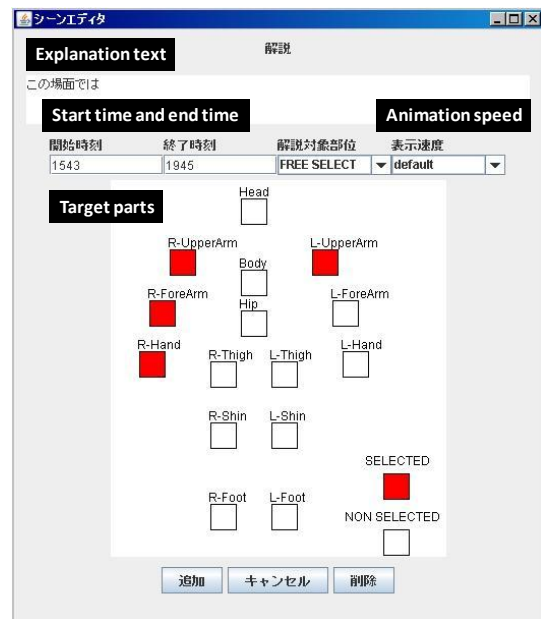


Figure 8: Scene Editor

input areas for explanation text, a scene period, target parts, and an animation speed.

The user writes explanation text into the text area on the top of the scene editor. The start time of the scene and the end time of the scene are inputted into the text field on the middle of the scene editor. If sliding the red line on the scenario editor, the start time and end time change according to the red line. We can select the target parts from the choice box or from the character displayed on the bottom of the scene editor.

4.3 Scenario Processor

The scenario processor manages the scenario. The scenario processor reconstructs the scenario according to the user's input. When the new scenario is created, the scenario processor loads the MoCap data from a database and generates a default camerawork. When the explanation scene is inserted, the scenario processor gets the information including the start time of the scene, the end time of the scene, and the target parts. Then the scenario processor enables the camerawork generator. The scenario processor replaces the generated camerawork with a default camerawork. The scenario processor can write and load the exhibition scenario.

4.4 Camerawork generator

The camerawork generator is enabled by the scenario processor. The camerawork generator generates a camerawork from the information of scene period and target parts by using the method which has been already explained in section 3.

4.5 Database

This database contains the human motion data which is captured by magnetic motion capture system. In this paper, the human motion is archived in the BVA format, the simple format for motion data.

4.6 Contents Viewer

The contents viewer can display the exhibition scenario as a CG animation. As shown in figure 9, the contents viewer contains the CG animation display area, and the time line. The audience can control the animation time by sliding the time line.

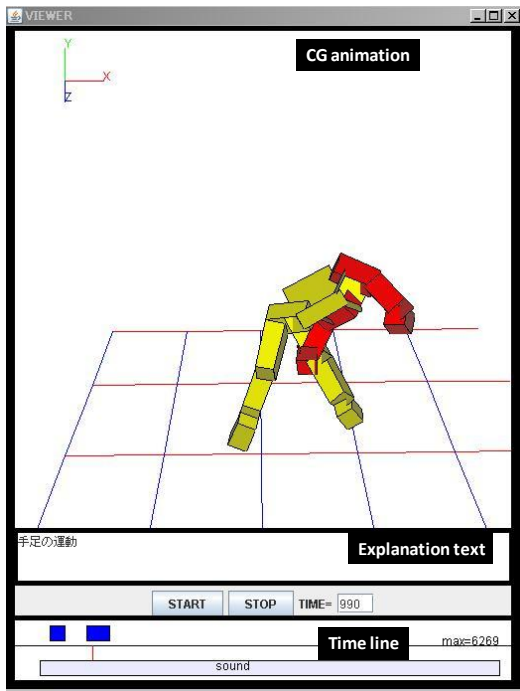


Figure 9: Content Viewer

This viewer represents the human motion as a CG animation by using the CG character and the MoCap data. The camerawork coordinated by the scenario processor is used for this CG animation. If a BGM is set in the contents scenario, it is played. While explaining a scene, the target parts are colored red. The other effects like an animation speed are also applied into the animation. This viewer can run on a web browser.

5 EXPERIMENTAL

We created the exhibition contents by using the proposed system. This contents is based on the leaning DVD for dancing [5]. The contents exhibit the "Rokogi", which is a dance motion in "soran-bushi". "Rokogi" is a motion which imitates the motion that a fishing boat is rowed powerfully.

This scenario contains 4 explanation scenes. In the first scene, the motion of stamping the right leg is explained. In the second scene, the motion of pulling the both arms is explained. In the third scene, the direction of a character's face is explained. In the fourth scene, all body parts are displayed and nothing is explained.

The generated exhibition scenario is shown in figure 10. The MoCpa data which is exhibited in the contents is defined by a mocap tag. The scenario contains scene tags describing the explanation scene, segment tags describing the target parts, and speed tags describing the animation speed. This result includes the enough information for generate an exhibition contents.

The exhibition contents can be exhibited by the viewer that can run on a web browser. Screen shots of exhibition contents are shown in figure 11. In the explanation scene, the target parts are colored red. The target parts are illustrated from the angle

```

<mdml>
<scenraio>
<mocap type="-i" name="soran1"/>
<scene begin="400" end="500">
<shot begin="400" end="500"/>
<segment parts="R-Thigh:R-Shin:R-Foot"/>
<speed fps="10.0"/>
<description>
    右足を出し、体を右から左に押し出す
</description>
</scene>
<scene begin="500" end="570">
<shot begin="500" end="570"/>
<segment parts="R-UpperArm:R-ForeArm:R-Hand:L-
UpperArm:L-ForeArm:L-Hand"/>
<speed fps="15.0"/>
<description>
    手を大きく広げ、船を胸まで引く
</description>
</scene>
<scene begin="570" end="650">
<shot begin="570" end="650"/>
<segment parts="Head"/>
<speed fps="30.0"/>
<description>
    目と顔は左斜め前方をしっかりと見、目的地を見据える
</description>
</scene>
<scene begin="650" end="730">
<shot begin="650" end="730"/>
<segment parts="Hip:Body:L-UpperArm:L-ForeArm:L-Hand:R-
UpperArm:R-ForeArm:R-Hand:Head:R-Thigh:R-Shin:R-Foot:L-Thigh:L-
Shin:L-Foot"/>
<speed fps="30.0"/>
<description>
    「それぞれ」の掛声のもと、4回で目的地にたどり着くよう力いっ
    ぱい漕ぐ
</description>
</scene>
<scene begin="780" end="1123">
<shot begin="780" end="880"/>
<shot begin="880" end="976"/>
<shot begin="976" end="1123"/>
<segment parts="L-UpperArm:L-ForeArm:L-Hand"/>
<speed fps="30.0"/>
<description>
</description>
</scene>
</scenraio>
</mdml>

```

Figure 10: Created exhibition scenario

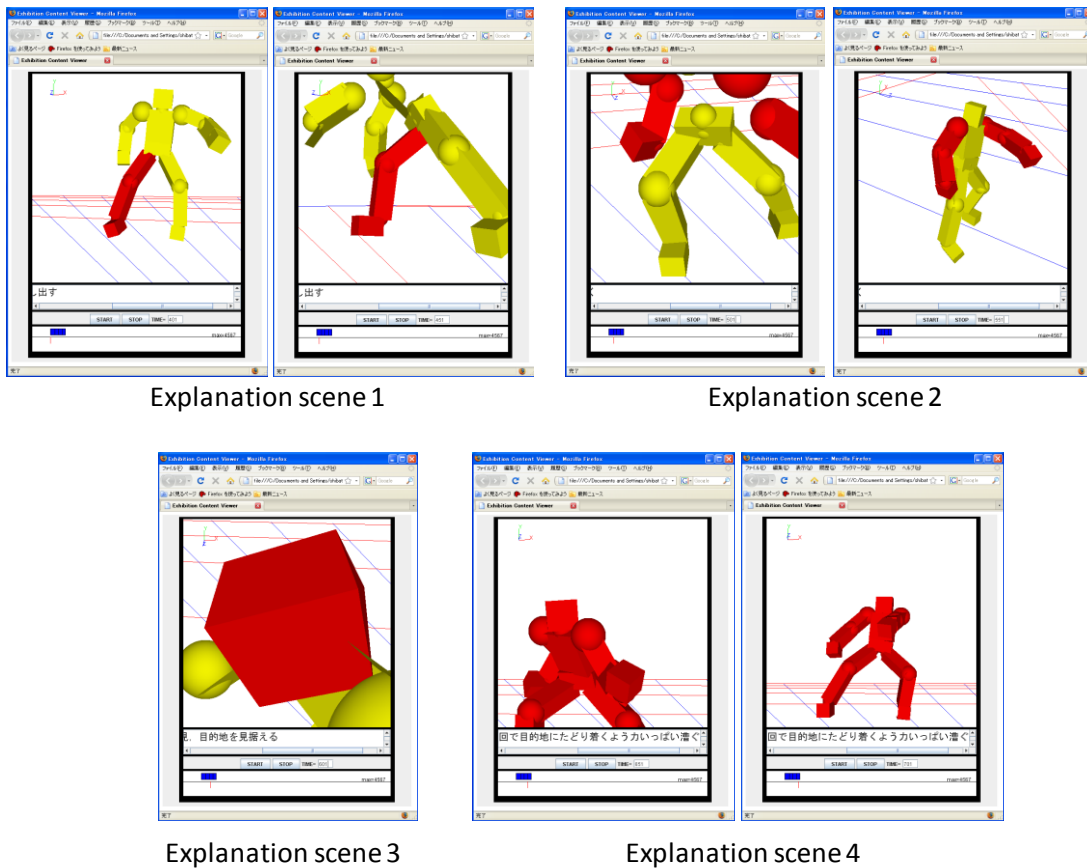


Figure 11: Screen shots of exhibition content

where the motion of the target parts is displayed widely. The explanation text defined with the description tag is displayed on the viewer. We can see the CG animation at the defined speed.

6 CONCLUSION

In order to safeguard the Japanese folk dances from being extinguished, we should archive and exhibit them. We have paid attention to the digital museum, because we can exhibit the intangible cultural assets.

The motion capture technique can be used to archive the human motion in the digital museum. However, it is difficult to attach the explanation and effect to the CG animation that represents the human motion for exhibition contents.

In this paper, we proposed a system that creates the exhibition contents easily. We implemented the system and showed how effectively the system works.

The tuning of camerawork generator and considering the MoCap data format are the future works.

Acknowledgment— This study was aided by Grant-in-Aid for Scientific Research (C) (Research Project Number 20500084) in 2008 fiscal year.

References

[1] Takeshi Oishi, Tomohito Masuda, Ryo Kurazume, and Katsushi Ikeuchi, "Digital Restoration of the Original Great

Buddha and Main Hall of Todaiji Temple," Transactions of the Virtual Reality Society of Japan, Vol. 10, No. 3, pp. 429-436, (2005), in Japanese.

[2] Miki Abe, Hisakazu Hada, Masakazu Imai, and Hideki Sunahara, "A proposal of the Automatic Exhibition Scenario Creation System," The Institute of Image Information and Television Engineers Technical Report, Vol. 26, No. 24, pp. 13-18, (2002), in Japanese.

[3] Hideo Tamamoto, Takashi Yukawa, Takaaki Kaiga, Kazutaka Mitobe, Kaeshi Miura, and Noboru Yoshimura, "Development of Digital Contents Production Techniques for Bequeathing Folkloric Performing Arts in Cooperation among Industry, Academia and Local Government," Vol. 91, No. 4, pp. 303-308, (2008), in Japanese.

[4] Takeshi Shibata, Takashi Yukawa, Kaiga Takaaki, Hiroshi Yokoyama, Hideo Tamamoto, "A Proposal of the CG Contents Production Tool for Explaining the Human Motion", IPSJ SIG Technical Report, (2008), CH-80-1 pp.1-8 in Japanese.

[5] Warabi-Za, "Learning DVD New So-ran Bushi," WDAF02001, (2002), in Japanese.

A Novel Detection System for Second Harmonic Ultrasonic Pulse Waves Using Bonded Ring Type Double-Layered Piezoelectric Transducer

Makoto Fukuda and Kazuhiko Imano

Department of Electrical and Electronic Engineering, Faculty of Engineering and Resource Science, Akita University, 1-1 Tegata Gakuen-machi, Akita 010-8502, Japan
mfukuda@gipc.akita-u.ac.jp

Abstract: A novel detection system for second harmonic ultrasonic pulse waves is constructed by modifying an existing double-layered piezoelectric transducer (DLPT). The DLPT composed of two PbTiO₃ thickness-mode piezoceramic concave disks, one is conventional type and another is ring type concave transducer, is employed. Since the switch for electrical connection used in the conventional double-layered piezoelectric transducer system is not required, a simple system for detecting second harmonic ultrasonic pulse waves is constructed. Furthermore, for real time detection of second harmonic ultrasonic pulse waves, pulse inversion averaging which is cancelled fundamental component is carried out. As the result, enhanced second harmonic ultrasonic pulse waves are displayed on an oscilloscope in real time.

Key Words: Ultrasonic, Second harmonic pulse wave, Double-layered piezoelectric transducer

1 INTRODUCTION

Acoustic harmonic components are generated in an acoustic medium when the ultrasonic wave intensity is larger than the threshold of a nonlinear effect. Their characteristics and application to nondestructive testing for harmonics were discussed previously, and imaging methods using second harmonic pulse waves have increasingly become a topic of interest in this field [1, 2]. Efficiency of second harmonic generation in acoustic medium is lower compared to the fundamental component, and hence, a method of detecting the second harmonic component with high sensitivity is required to

enhance the dynamic range in the frequency of the second harmonic pulse wave.

Several transducers for harmonic wave detection have been developed. Several transducers having resonance frequencies of both the fundamental and second harmonic component have been reported. A LiNbO₃ plate with a ferroelectric inversion layer fabricated by heat treatment has been reported [3]. Transducers arranged coaxially [4] or stacked [5] on their acoustic radiated surfaces for transmitting the fundamental pulse wave or receiving the harmonic pulse wave, respectively, have also been reported.

A method of generating short ultrasonic pulse waves using a double-layered piezoelectric transducer (DLPT) has been reported by authors [6]. The DLPT in electrically parallel connection has the advantage of transmitting fundamental pulse waves with the higher sensitivity of the fundamental frequency compared to case of a conventional single transducer. Moreover, the DLPT in electrically series connection has the higher sensitivity in second harmonic component frequency. In our previous DLPT system, switching the electrical connection in parallel or series for a DLPT allows the effective transmitting of fundamental pulse waves and the receiving of second harmonic pulse waves. However, the circuit of previous DLPT system is complicated. Second harmonic pulse waves detection in a simpler system would be required.

In this paper, a novel detection system for second harmonic ultrasonic pulse waves using a bonded ring type double-layered piezoelectric transducer is described. Furthermore, the pulse inversion averaging method for extracting second harmonic pulse waves is described, and second harmonic pulse waves are detected in real time.

2 TRANSDUCER

The novel double-layered piezoelectric transducer (DLPT) is composed of two thickness mode piezoceramic concave disks, one is conventional type and another is ring type transducer as shown in Fig. 1. Inside and outside electrodes of bonded side in the concave transducer are output and input terminal, respectively. Resonance frequencies f_0 of these transducers are 2 MHz. These transducers are stacked and bonded to each other in the opposite direction of polarization using electroconductive silver paint as shown in Fig. 1. Ultrasonic transmission part is outside part of the transducer (the DLPT part), which is electrically connected in parallel. Ultrasonic reception part is inside part of the transducer. The frequency-admittance characteristics of the transmission part and the reception part are shown in Fig. 2(a) and 2(b), respectively. The resonance frequency of the transmission part changes from 2 MHz to 1 MHz in order to be electrically

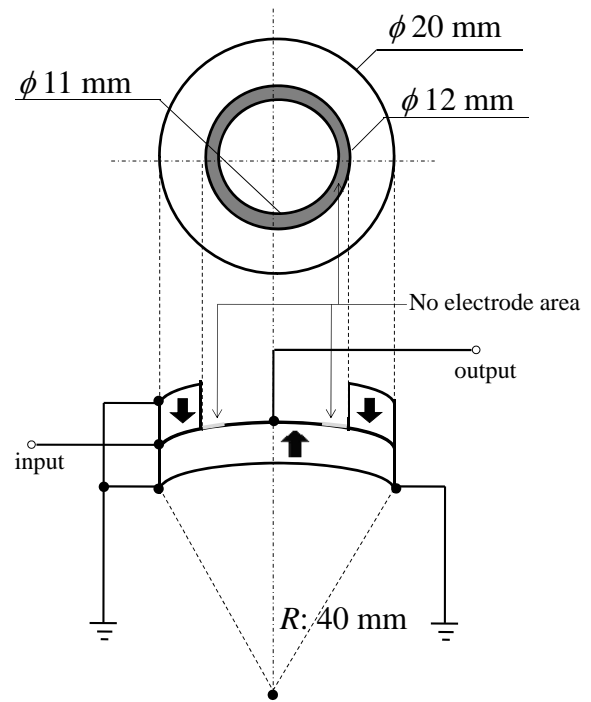


Fig. 1 A novel transducer for second harmonic pulse waves detection

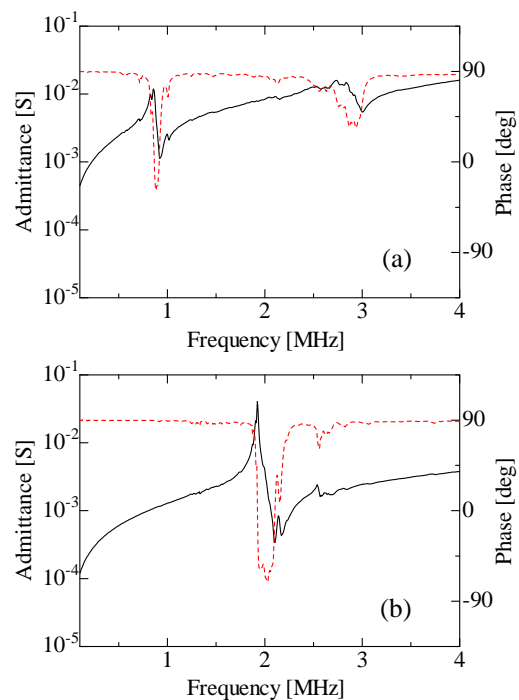


Fig. 2 Frequency-admittance characteristics of a novel transducer. (a) Transmission part. (b) Reception part.

connected in parallel. Parallel connection of DLPT has the advantages of transmitting fundamental pulse waves (1 MHz) with higher sensitivity at the fundamental frequency than single transducer [7]. The resonance frequency of the reception part remains 2 MHz, and then second harmonic pulse waves can be sensitively received.

This transducer is not required the electrical switch and the control system for switching the receiving circuit. Second harmonic detection can be carried out by simple system compared to our previous system.

In the next section, a novel transducer for detecting the second harmonic pulse waves is evaluated experimentally.

3 EXPERIMENTAL

A driving voltage signal of the DLPT was generated by an arbitrary waveform generator. For the pulse inversion averaging method [6], driving voltage waveform was designed as 20 cycles 1MHz burst sine (burst duration time: 20 μ s), and the period of the next inverted driving signal was determined to be 0.5 ms, which was much longer than the round trip time (about 50 μ s).

The experimental system for second harmonic pulse waves using the novel transducer is shown in Fig. 3. Driving signals were generated by the arbitrary waveform generator, amplified up to 150 V by a high-frequency power amplifier (the input impedance and the output impedance: 50 Ω), and electrically matched to the transducer (the impedance at resonance frequency: 100 Ω) by an electrical impedance matching circuit.

Ultrasonic pulses (1 MHz) were transmitted in water, and then pulse waves were reflected at the reflector set 40 mm away from the transducer. While ultrasonic pulse waves propagated in the water, second harmonic wave components (2 MHz) were generated by the nonlinear effect in water. The received pulse waves were averaged by an oscilloscope, and only second harmonic pulse waves were extracted by the pulse inversion averaging method. Finally, the extracted pulse waves

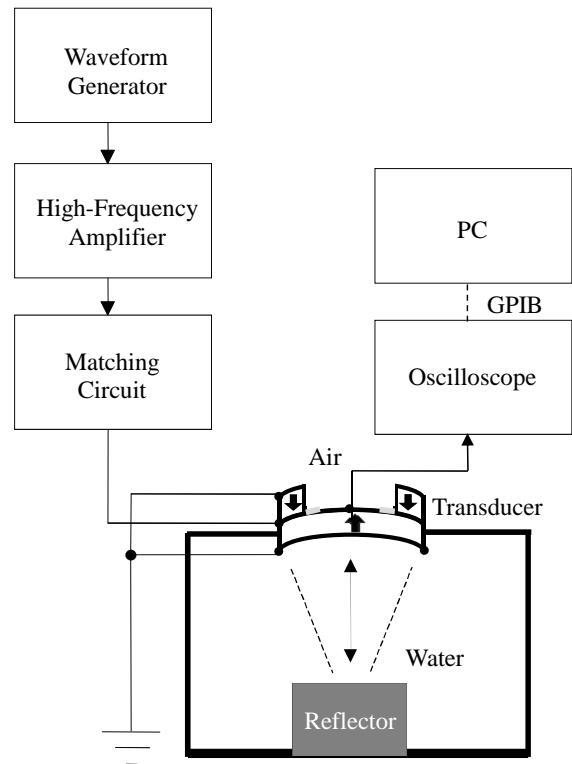


Fig. 3 Experimental set-up

were fed to a personal computer via a general purpose interface bus.

4 RESULTS AND DISCUSSION

Figure 4(a) shows the received ultrasonic pulse waves using the conventional single transducer, and spectrum of Fig. 4(a) is shown in Fig. 4(b). In Fig. 4(b), the second harmonic component is approximately 50 dB smaller than the fundamental component because the conventional single transducer has low sensitivity at 2 MHz. Figure 4(c) shows the waveform received by our system using the novel DLPT transducer. The spectrum of Fig. 4(c) is shown in Fig. 4(d). The difference between the fundamental and second harmonic amplitudes decreased to approximately 10 dB because the reception part of the transducer has a high sensitivity at 2 MHz. Figure 4(e) shows the waveform obtained by pulse inversion

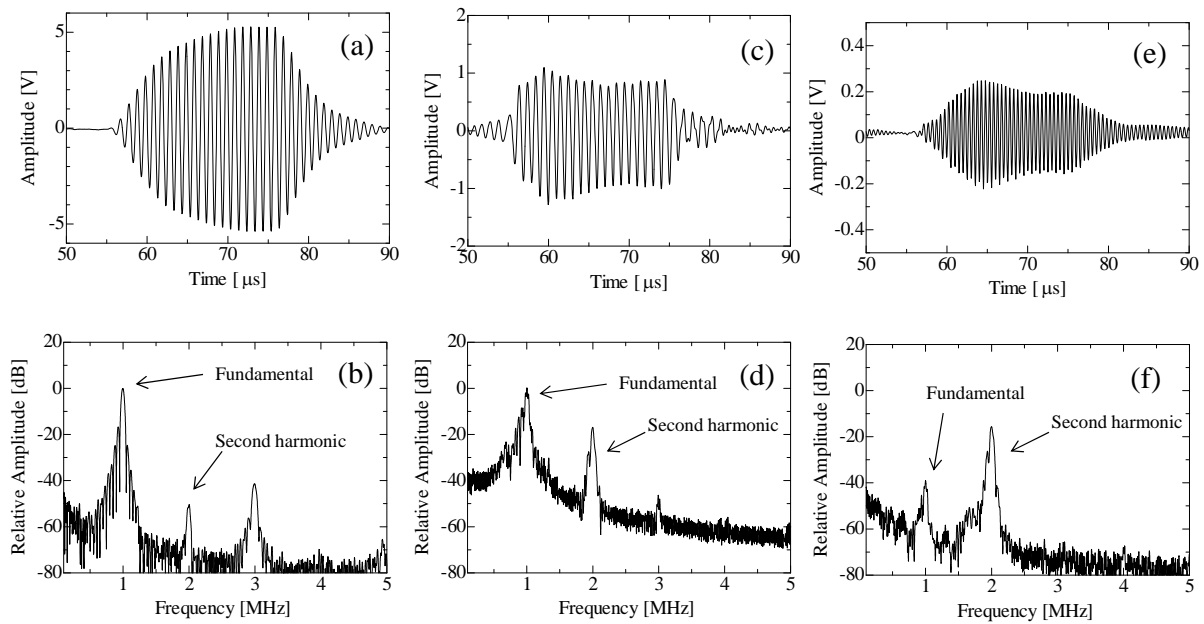


Fig. 4 Experimental results of ultrasonic pulse waveform and spectrum. (a) Waveform in conventional pulse echo system. (b) Spectrum of (a). (c) Waveform in a novel transducer without pulse inversion averaging. (d) Spectrum of (c). (e) Waveform in a novel transducer with pulse inversion averaging. (f) Spectrum of (e).

averaging method, and the spectrum of Fig. 4(e) is shown in Fig. 4(f).

In Figs. 4(b) and 4(d), the relative amplitudes of second harmonic component improved by approximately 35 dB. Furthermore, after pulse inversion averaging method is applied, as shown in Fig. 4(f), the fundamental amplitude decreases by approximately 40 dB compared to that in Fig. 4(d). Therefore, the amplitude of our system improved by approximately 75 dB compared to case of a conventional single transducer.

As observed in Fig. 4(e), the second harmonic pulse wave was extracted and displayed on the oscilloscope in real time.

5 CONCLUSIONS

A novel detection method for second harmonic pulse waves using a new type transducer of a double-layered piezoelectric transducer (DLPT) was constructed. The sensitivity of the received second harmonic pulse wave was improved by approximately 35 dB compared to the

conventional single transducer. The real time extraction of the second harmonic pulse waveform using pulse inversion averaging method was demonstrated, and the fundamental component was decreased by 40 dB. The second harmonic component was emphasized and relative improvement of 75 dB compared to conventional pulse echo.

These results indicate that our system effectively addresses the extraction of second harmonic pulse waves. We intend to apply to harmonic imaging or nondestructive testing using our transducer system in the future.

References

- [1] T. Kamakura, "Two Model Equations for Describing Nonlinear Sound Beams," *Jpn. J. Appl. Phys.*, Vol.43, No. 5B, pp.2808-2812, (2004).
- [2] D. H. Simpson, C. T. Chin and P. N. Burns, "Pulse Inversion Doppler: A New Method for Detecting Nonlinear Echoes from Microbubble Contrast Agents," *IEEE Trans.*

Ultrason. Ferroelectr. Freq. Control, Vol.46, No.2, pp.372-382, (1999).

[3] K. Nakamura, K. Fukazawa, K. Yamada and S. Saito, "Broadband Ultrasonic Transducers Using a LiNbO₃ Plate with a Ferroelectric Inversion Layer," IEEE Trans. Ultrason. Ferroelectr. Freq. Control, Vol.50, No.11, pp.1558-1562, (2003).

[4] H. Adachi, K. Wakabayashi, M. Nishio, H. Mizuno and T. Kamakura, "Fabrication of Ultrasonic Transducers with KNbO₃ Piezoelectric Single Crystal for Detecting Harmonic Signals," Jpn. J. Appl. Phys., Vol.40, No.9B, pp.5698-5702, (2001).

[5] I. Akiyama, A. Ohya and S. Saito, "Speckle Noise Reduction by Superposing Many Higher Harmonic Images," Jpn. J. Appl. Phys., Vol.44, No.6B, pp.4631-4636, (2005).

[6] M. Fukuda, M. Nishihira and K. Imano, "Real Time Extraction System Using Double-Layered Piezoelectric Transducer for Second-Harmonic Ultrasonic Pulse Waves," Jpn. J. Appl. Phys., Vol.45, No.5B, pp.4556-4559, (2006).

[7] H. Yamada and M. Onoe, "Double Frequency Ultrasonic Search Unit," Hihakai Kensa, Vol.20, No.11, pp.605-608, (1971) [in Japanese].

High resolution MFM imaging of in-plane magnetic field gradients using transient oscillation for perpendicular magnetic recording media

Genta Egawa^{a)}, Satoru Yoshimura^{a)}, Tasuku Miyazawa^{a)}, Guoqing Li^{b)},

Hitoshi Saito^{a)}

^{a)} Center for Geo-environmental Science, Faculty of Engineering & Resource Science, Akita University, Akita, 010-8502, JAPAN

^{b)} School of Physical Science and Technology, South Western University, Chongqing, 400715, CHINA

Abstract:

We developed a new MFM method which can measure the perpendicular and in-plane magnetic field gradient simultaneously with high resolution using the transient oscillation of a MFM tip. The measuring direction of in-plane magnetic field which is measured by the new frequency detection method can be easily changed only by selecting the scanning direction of a MFM tip with respect to the sample. On the same scan, perpendicular magnetic field gradient can be measured simultaneously by a conventional phase detection method. Therefore, this imaging method is useful to estimate the transition of recording bits in perpendicular magnetic recording media. We demonstrated imaging of the in-plane magnetic field gradient using transient oscillation for perpendicular magnetic recording media with high spatial resolution, and showed effectiveness of the new method for analysis of microscopic magnetic domain structure of perpendicular magnetic recording media. We also showed the frequency oscillation of a MFM tip, which is evidence about the work of the new MFM method.-

Keywords: Magnetic force microscopy (MFM), Perpendicular magnetic recording media, In-plane magnetic field gradient, Transient oscillation of MFM tip, spatial resolution

1 Introduction

Development of spatial resolution of magnetic force microscopy (MFM) is important to evaluate recorded bit patterns on the nano-scale for high density perpendicular magnetic recording media. The vector information of the magnetic field with

nano-scale is useful to estimate the recorded state of the bit edge. However, the conventional MFM can only detect the gradient of a vector component of the magnetic field determined by the direction of the MFM tip magnetization [1]. Therefore, the conventional MFM only detects the perpendicular magnetic stray field gradient

with the maximum spatial resolution of about 10 nm [2]. J. G. Zhu et al. proposed the imaging method for in-plane magnetic field gradient [3]. This method uses the change of MFM tip magnetization direction. However, the change of MFM tip magnetization direction is not effective to obtain high spatial resolution.

Here, it is known that a MFM tip coated by FePt film is very effective to obtain high resolution image for very high density recording media. The magnetized direction of the MFM tip is strongly perpendicular to the sample surface due to its very large coercivity. Therefore, the MFM imaging method which can measure the in-plane magnetic field gradient with using a MFM tip coated by hard magnetic film such as FePt have to be developed.

We developed a new MFM imaging method which can measure the perpendicular and in-plane magnetic field gradient using the transient oscillation of a MFM tip [4]. The in-plane field gradient, $\partial H_x / \partial z$ is leaded by $\partial H_z / \partial x$ [5]. This indicates that in-plane magnetic field gradient is obtained by detecting the change of vertical field gradient against the change of MFM tip position with the horizontal direction. Therefore, the direction of in-plane magnetic field gradient corresponds to the scanning direction of MFM tip with respect to the sample. In other words, the measuring direction of in-plane magnetic field gradient can be easily changed by selecting the scanning direction of the MFM tip. The in-plane components of the stray field can also be calculated from the perpendicular component image. The advantage of new technique is that has a higher spatial resolution and no post processing is necessary to obtain the in-plane component image.

With increasing the recording density for perpendicular magnetic recording media,

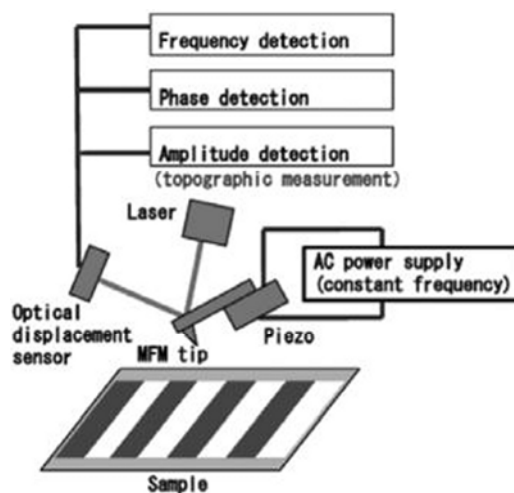


Fig. 1. Schematic diagram of the measurement setup for detection of surface morphology, perpendicular magnetic field gradient, and in-plane magnetic field gradient on a magnetic thin film.

estimation of the magnetic inhomogeneity not only in bit transition area but also at track edge will be very important. In this study, we present the MFM imaging which simultaneously measures the perpendicular and the in-plane component, utilizing the new MFM system for perpendicular magnetic recording media. We also show the frequency change of MFM tip, which is occurred by the transient oscillation of MFM tip.

2 Experiments procedure

Figure 1 shows the block diagram of the MFM measurement of the in-plane magnetic field gradient. A phase locked loop (PLL: easyPLL, Nanosurf) circuit is used to measure the frequency shift of the MFM tip resonance in a conventional phase detection MFM. Here, the MFM tip was driven at a constant frequency near the resonant frequency of the MFM tip. The frequency shift of the MFM tip is only detected when the MFM tip has moved. This shift is proportional with the in-plane component of the field gradient. The phase shift is measured to extract the perpendicular component of the magnetic field after frequency of the oscillating disappears. Therefore, the phase and frequency of the

oscillation of MFM tip were measured at the same scan, though the frequency shift and phase shift are measured at the respective time. The MFM tip-sample distance is kept constant (15 nm) after the topographic scan by using the so-called “lift mode” measurement. We used a high-coercivity MFM tip with a 20 nm $L1_0$ -FePt film whose coercivity is about 8 kOe, which is made by Nitto Optical Co., Ltd. The magnetized direction of the MFM tip was perpendicular to the sample surface by applying a magnetic field of 18 kOe in advance. The MFM tip with high-coercivity is effective to suppress the oscillation of its magnetization, and consequently to obtain microscopic magnetic domain images with high special resolution.

We observed a CoCrPt-SiO₂ perpendicular magnetic recording media which was prepared using an in-line-type magnetron sputtering system. Transmission electron microscopy shows a CoCrPt nanoparticle with a diameter of about 5.9 nm and an average interparticle distance of around 1.6 nm. Recording signals (200 or 500 or 1000 kilo flux change / inch) were written using a perpendicular single-pole inductive head. The MFM measurement was done in vacuum atmosphere. The value of Q was in the range from about 6000 to 8000. The resonant frequency of MFM tip is 280-320 kHz. The measuring time at each position was about 1ms with a data acquisition interval of 1 μ s. The detection method of frequency modulation is proposed in high Q conditions for sensitive imaging with a wide bandwidth.

3 Results and Discussions

Figure 2 shows the images of in-plane magnetic field gradient and the dependence of the average signal intensity of in-plane field at the black lines in the insets of figure 2, which is located along the writing and reading direction on the scanning angle θ for

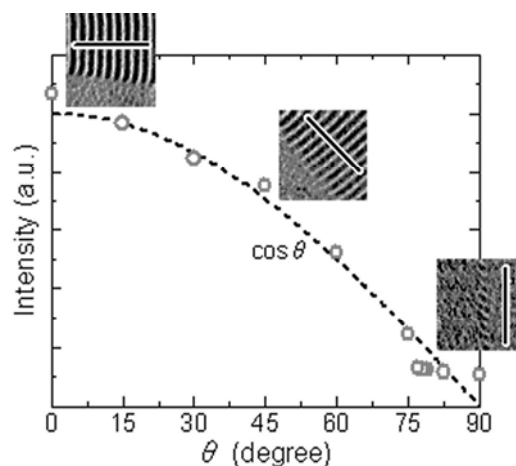


Fig. 2. Dependence of the average intensity of in-plane magnetic field on the angle between the scanning direction and the writing and reading direction for CoCrPt-SiO₂ perpendicular magnetic recording media with the recording density of 500 kfc/i.

CoCrPt-SiO₂ perpendicular magnetic recording media with the recording density of 500 kfc/i. Here the θ is assumed the angle between the scanning direction (from the left side to the right side in the images) and the writing and reading direction of the bits.

In the case of $\theta = 0$ degree (scanning direction is parallel to the writing and reading direction), largest signal intensity is obtained. With increasing θ , the signal intensity decreases following the $\cos\theta$ curve. In the case of θ of more than 75 degree, the signal intensity becomes constant. These results indicate that signal output corresponds to the in-plane magnetic field gradient along with the scanning direction, and signal output with the θ of around 90 degree is due to media noise. We can say, the in-plane magnetic field gradient with the scanning direction of $\theta = 90$ degree is effective to mask the ideally recorded signal and to observe the unintended magnetic contrasts in the track edges.

Figure 3 shows (a) the image with conventional phase detection method and (b) the image with new frequency detection method obtained by the same scan for CoCrPt-SiO₂ perpendicular magnetic recording media with the recording density of

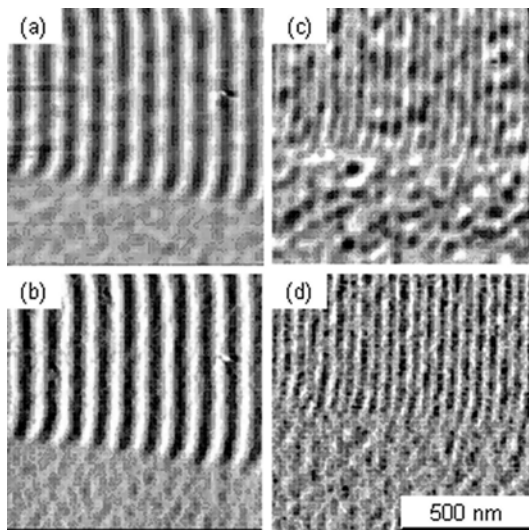


Fig. 3. Phase detection images (a) and (c), and frequency detection images (b) and (d) for a CoCrPt-SiO₂ perpendicular magnetic recording media. The recording density for (a) and (b) is 500 kfc, and the case for (c) and (d) is 1000 kfc.

500 kfc. The image of (c) and (d) also indicate the phase image and frequency image, respectively, obtained by the same scan for CoCrPt-SiO₂ perpendicular magnetic recording media with the recording density of 1000 kfc. The scanning direction of MFM tip is from the left side to the right side in the images. In the case of the phase image which indicate perpendicular magnetic field gradient image, the contrasts of white and black parts are located on recording bits. In the case of frequency image, the contrasts of white and black parts are shifted with the length of half bit compared with the case of the phase image. This indicates that the contrast for the frequency image locates on transition region between recording bits, and consequently the frequency image shows the in-plane magnetic field gradient image. Therefore, in the case of frequency image, we can estimate the recorded state on transition region between recording bits easily compared with in the case of perpendicular magnetic field gradient images.

In the case of in-plane magnetic field gradient images (b) and (d), recording patterns with 500 kfc and a very high recording

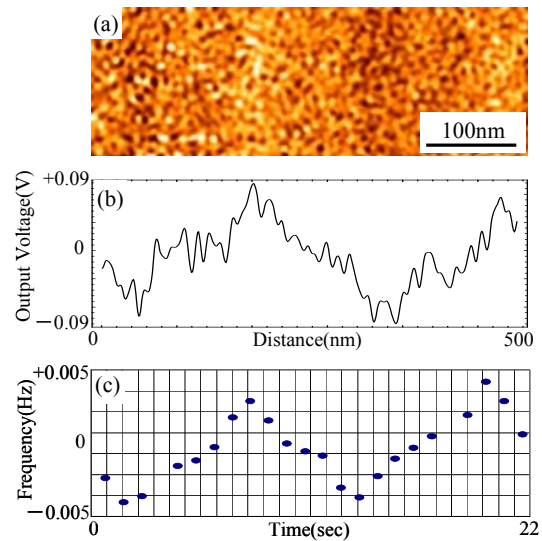


Fig. 4. Frequency detection image (a) for a CoCrPt-SiO₂ perpendicular magnetic recording media with the recording density of 200 kfc. Line profile (b) for frequency detection image of (a), and (c) frequency change of MFM tip.

density of 1000 kfc are observed clearly compared with the case of perpendicular magnetic field gradient images (a) and (c). Here, spatial resolution of the in-plane magnetic field gradient measured by the new MFM method was 9.1 nm, nevertheless the case of the perpendicular magnetic field gradient measured by same scan with conventional MFM method was 9.5 nm. These results agree with the theoretical analysis [4].

From these results, the frequency detection method to obtain in-plane magnetic field gradient image is thought to be very effective to estimate the microscopic magnetic domain structure for very high density perpendicular magnetic recording media.

Figure 4 shows (a) the frequency image which indicates in-plane magnetic field gradient image for CoCrPt-SiO₂ perpendicular magnetic recording media with the recording density of 200 kfc and (b) its line profile, respectively. The scanning direction of MFM tip is from the left side to the right side in the images. The scanning time of MFM tip for one line (500 nm) is 22 sec. The profile (c) is time dependence of frequency change of MFM tip, which is measured by frequency

counter during one line scan. The maximum change of frequency is about 0.01 Hz, while the resonant frequency of MFM tip is 280-320 kHz. This frequency change of MFM tip is due to the transient oscillation of a MFM tip. Here, “0 sec” of horizontal axis for figure (c) is the start time for MFM scan, which corresponds to the start position; “0 nm” of horizontal axis for figure (b). Moreover, “22 sec” of horizontal axis for figure (c) is also the end time for MFM scan, which corresponds to the end position; “500 nm” of horizontal axis for figure (b). The profile of frequency change of MFM tip corresponds to the line profile of the frequency image. This indicates not only theoretically [4] but also experimentally that frequency change of MFM tip, which is occurred by the transient oscillation of MFM tip corresponds to the in-plane magnetic field gradient.

Form these results, the simultaneous measurement of perpendicular and in-plane magnetic field gradient with high spatial resolution is useful for the estimation of the microscopic magnetic domain structure for very high density perpendicular magnetic recording media.

4 Conclusions

The measurement of the perpendicular and in-plane magnetic field gradient for perpendicular magnetic recording media was examined by using the new MFM method which detects the transient oscillation of a MFM tip. The obtained results can be summarized as follows:

(1) The measuring direction of in-plane magnetic field could be easily changed only by selecting the scanning direction of MFM tip with respect to the sample, and consequently we could clearly observe the unintended magnetic contrasts in the recorded bit patterns.

(2) The spatial resolution of the in-plane magnetic field gradient measured by the new MFM method was higher than the case of the perpendicular magnetic field gradient measured by same scan with conventional MFM method, and consequently we could evaluate the magnetic inhomogeneity of bit transition area.

(3) We detected the frequency change of MFM tip, which is occurred by the transient oscillation of MFM tip, and showed that the frequency change of MFM tip corresponds to the in-plane magnetic field gradient experimentally.

Acknowledgment

This research was partially supported by the Storage Research Consortium in Japan and Akita prefectural government.

References

- [1] D.rugar, H. J. Mamin, P. Guethner, S. E. Lambert, J. E. Stem, I. McFadyen, nad T. Yogi, *J. Appl. Phys.*, 68, 1169, 1990..
- [2] H. Saito, R. Sunahara, Y. Rheem, and S. Ishio, *IEEE Trans. Magn.*, 41, 4394, 2005.
- [3] J. G. Zhu, X. Lin, and R. C. Shi, *J. Appl. Phys.*, 83, 6223, 1998.
- [4] H. Saito, G. Egawa, S. Ishio, and G. Q. Li, *J. Appl. Phys.*, 103, 07D921, 2008.
- [5] D. Rugar, H. J. Mamin, P. Guethner, S. E. Lambert, J. E. Stem, I. McFadyen, and T. Yogi, *J. Appl. Phys.*, 68, 1169, 1990.

Developed a Technique to Find the Finger Joint angles Using Six Dimensional Position Sensors

**Md. Mostafizur Rahman, Kazutaka Mitobe, Masafumi Suzuki
and Noboru Yoshimura**

Department of Electrical, Electronics and Computer System Engineering, Faculty of Engineering and Resource Science,
Akita University, 1-1, Tegata-Gakuen-Cho, Akita, 010-8502 Japan
mostafiz963@yahoo.com

Abstract: In this paper the authors have developed a new technique to calculate the finger joint angles during playing piano. It is observed that during contact of the keyboard of the piano the MCP joint flexed and the IP joints extended and when the finger lifted, the MCP joint extended and the Interphalangeal (IP) joints flexed, creating a reciprocal movements and the finger joint angle varies during contact and separation period. Again we developed the high accuracy Hand Motion Capture System using electromagnetic tracker and to investigate the electromagnetic signal of magnetic six degrees of freedom sensor during operation of the piano. And then it is described a technique for using magnetic motion capture data to determine the movement of fingers, receiver position and to analyze the receiver velocity and acceleration.

Key Words: Piano, Motion capture, Velocity-acceleration, Finger joint angle, Sensor

1 INTRODUCTION

Motion capture is an extremely useful technique for animating human and human-like characters. It is widely used for virtual reality, motion acquisition for medical researches, for humanoid robots, for video games etc. Motion capture provides a unique solution for applications where animations with the characteristic qualities of human motion must be generated quickly. Real time capture techniques can be used to create immersive virtual environments for entertainment and training applications. Motion capture data retains many of the subtle elements of a performer's style making possible digital performances where the motion capture subject's unique style is recognizable in the final product.

Our hand can perform high precision movements as an actuator. Motion capture technique that can digitize a position and a posture as a time series data is widely used in order to create animation and Computer Graphics. It is very difficult to measure all hands movements because one hand has twenty seven bones and nineteen joints. The most widely used tool for a hand Motion Capture (MoCap) has been Cyber glove (Immersion) that can digitize only 80 percent of all hand movements. Therefore, it has been impossible to record the finger movements of a pianist that are high in speed and in accuracy.

The musical composition was "Sonata KV 331, Turkish March (Mozart, Wolfgang Amadeus). It was very complex music and performs an expert pianist. So we first observed the hand movement of an expert pianist and then we want to compare later with the beginners.

These all are investigated using the MoCap system, without any external meter measurements. In the world, various studied, therefore, have been done to measure the signal from human body but this MoCap technique by using

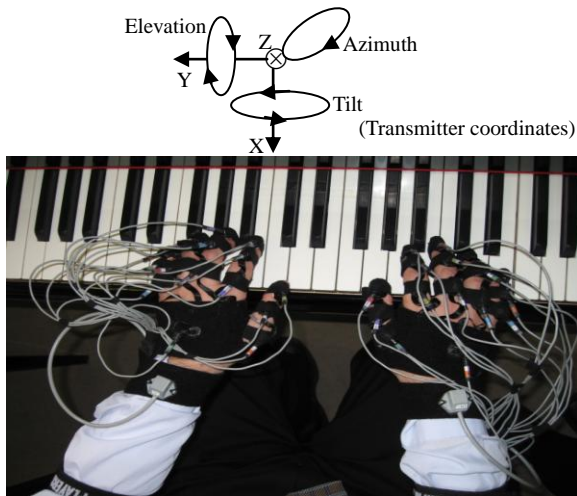
high resolution electromagnetic tracker (LIBERTY™ 16 system, Polhemus) is used in Akita University, Japan and group of researchers are investigating with this technique of magnetic six degrees of freedom sensor. Previously it was developed the hand motion capture system of a pianist [1,2] and an auto calibration method for a hand skeleton model using motion capture technique [3,4]. We observed the finger movement position, velocity, acceleration and calculated the joint angle accurately, which is very important to find the value of finger muscle force and also the vertical force of finger because velocity is directly related to the muscle force [5]. Again to calculate the joint angle is very important to find any other position of any phalanx of human body.

The motion capture of the system is also widely studied in the field of biomechanics and robotics. Biomechanics are interested in this field because the joints play a critical role in understanding both mechanics of the human body and the dynamics of human motion. Some of the works have been found of finger joint coordination but their technique is not motion capture. Those works was measured using the system electromyography (EMG) and finger joint angle was measured by miniature goniometers. Finger joint angle during typing of computer keyboard are found [6-8], they used individual miniature goniometers during tapping of computer keyboard. So they have some limitations that they can not find the phalanx position where our system is suitable to find the phalanx position.

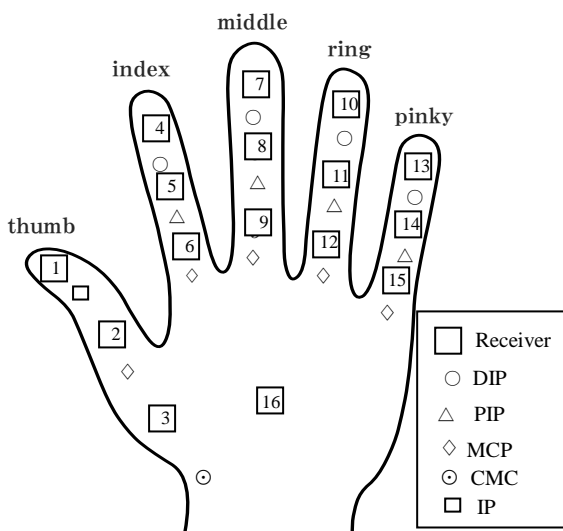
This research investigate the finger movements of six dimensions and developed a new technique to calculate the finger joint angle DIP, PIP and MCP and established the joint angle variation together with satisfactory experimental and simulation results. So this is a new technique to find any phalanx position of human body and to calculate the respective angle.

2 EXPERIMENTAL SETUP

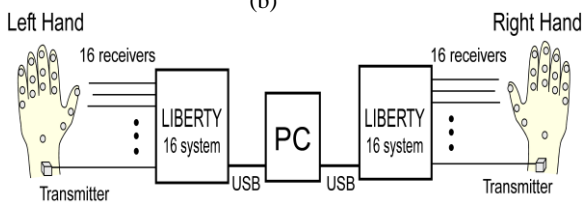
Figure 1(a) shows a photograph during playing piano. During the operation of a pianist his finger moves, as well as each phalanx MCP, PIP and DIP of a finger also moves to the direction X, Y, Z, azimuth, elevation and tilt.



(a)



(b)



(c)

Figure 1: Experimental arrangement: (a) performing with experimental setup (b) 16 sensors (channel) position (c) systematic arrangement of hand MoCap system

Table 1. Accuracy and resolution.

	Position [mm]	Angle [deg]
Accuracy	0.76	0.15
Resolution	0.0038	0.0012

The cables which are important for the experimental setup, replaced the original with special thin cables of 2 mm diameter for not to block the movements of the pianist's finger, it is also shown in the Fig. 1(a). Each receiver is processed in order to fit with the finger. Three receivers are used to measure one finger and one receiver is used for the backside of the palm. So finally sixteen receivers in one hand and totally 32 receivers are used for both hands. Additionally the adapter unit is modified with a stretch fabric band in order to fit any hand size shown in the Fig. 1(a). Figure 1(b) shows all the positions of the fingers where the sensors (receivers) are placed that are the 16 channels in the fingers in one hand. In the figure the 16 channels or receiver positions are shown by the number 1, 2, 3 - - - 16 with square symbol. Each receiver is placed tightly just on the bone that is between the joint of the fingers so it never slides, on the other hand in the optical MoCap system the receivers usually placed just on the joint of the fingers so it may slide with the movements of the finger.

The finger joints are shown using the symbol, circle is for DIP, triangle is for PIP and the diamond is for MCP. Five fingers named thumb, index, middle, ring and pinky and small and the light sensors are placed on the back side of the fingers, only one sensor is placed on the back side of the palm. Each position has also a different name and its total setup is shown in the Fig. 1(a). Figure 1(c) shows the systematic arrangement of the MoCap system for a pianist's hand. The magnetic tracker that is composed of one transmitter (23x28x16 mm) and sixteen receivers (9.6x9.6x9.6 mm) can digitize the distance (X, Y and Z) from the transmitter to receiver. Again the magnetic tracker can digitize the position and relative angles (Azimuth, Elevation, and Rotation) of receiver against a transmitter. Each receiver is called a channel and attached on the finger using kinesiotex tape and liquid type plastic in order to prevent the receiver movements. Two LIBERTY™ systems (Polhemus) are connected to a computer (ThinkPad, IBM) through a USB interfacing. It can measure the data from the experimental setup of Hand MoCap system of (six degrees of freedom) of 32 receivers at the rate of 240 Hz simultaneously. That is, it can get the data 240 per second through each receiver and each data have six directions, so we get totally (240 x 6) data per channel per second from each position of a finger of each hand. The spatial resolution and accuracy of the hand MoCap system is given in the Table1 [1-3].

3 METHODOLOGY

3.1 Velocity and acceleration

After taking the data from our experiment using MoCap system we analyzed the data using Matlab program. To find the receiver velocity and acceleration, we used simply Newton's velocity-acceleration formula. First we locate the position after taking the raw data, and then with the help of velocity-acceleration equation we observed the velocity and acceleration.

3.2 Finger joint angle

We have calculated the finger joint angle because it is very important to find the angular velocity, angular acceleration and force of the finger during plying piano. We are interested to find the angular velocity, angular acceleration and force in next time. As we used the magnetic six dimensional sensors we got the raw data like $X, Y, Z, \theta, \varphi, \psi$ where θ =Azimuth, φ =Elevation and ψ =Tilt. Now from the Euler's angle formula we can calculate from the block diagram given in the Fig. 2.

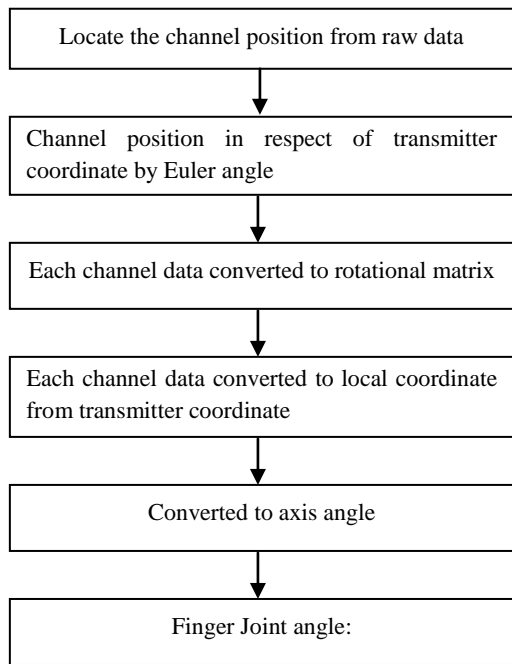


Figure 2: Block diagram for calculating finger joint angle.

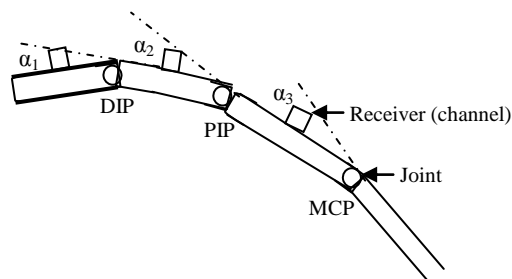


Figure 3: Schematic representation of three-link model of a finger.

Let the channel angle in respect of transmitter coordinate is:

$$R_{ch_n} = R_z(\theta_n) * R_y(\phi_n) * R_x(\psi_n) \text{ where } n = ch1 \text{ to } ch16 \text{ --- (1)}$$

$$R_{ch1}(\text{loc.co.}) = R_{ch1}(\text{rotational}) * \text{inv}(R_{ch2}(\text{rotational})) \text{ --- (2)}$$

Now if $n=1, 2$ and converted to rotational matrix then from eq. (1) we get $ch1$ and $ch2$ in a new matrix form. Then we converted the rotational matrix into local (receiver) coordinate by solving equation (2).

Now to find the axis angle we took the above equation in $[3 \times 3]$ matrix form as the following:

$$R = \begin{bmatrix} m00 & m01 & m02 \\ m10 & m11 & m12 \\ m20 & m21 & m22 \end{bmatrix} \text{ --- (3)}$$

Where $m00$ to $m22$ are the values of the angles, which contains replicated information of equation (2). And then we got the axis angles by solving equation (3) in the form, $(x, y, z \text{ and } \alpha)$.

Where, $\text{angle} = \alpha$, axis = $(x, y \text{ and } z)$ at the following equations:

$$\alpha = \text{acos}((m00 + m11 + m22 - 1)/2) \text{ --- (4)}$$

$$x = (m21 - m12) / \sqrt{((m21 - m12)^2 + (m02 - m20)^2 + (m10 - m01)^2)} \text{ --- (5)}$$

$$y = (m02 - m20) / \sqrt{((m21 - m12)^2 + (m02 - m20)^2 + (m10 - m01)^2)} \text{ --- (6)}$$

$$z = (m10 - m01) / \sqrt{((m21 - m12)^2 + (m02 - m20)^2 + (m10 - m01)^2)} \text{ --- (7)}$$

So from the axis angle we can get the finger joint angle. Similarly we can calculate each joint angle of each finger. Figure 3 shows the schematic representation of a three link model of finger joint angle.

4 RESULT AND DISCUSSION

We investigate the position, velocity, acceleration and finger joint angle. There are three components of each position, e.g. X, Y and Z. We choose Z component of position of the finger of pianist for our discussion. So before discussing, first we would like to discuss why we choose Z component. We can choose X and Y components also but from our observation Z component is suitable than other components. Figure 4 shows the left hand analysis of mean velocity and acceleration of X, Y and Z components. In this figure horizontal axis shows 16 channels position on the finger. In the figure, cross symbol shows Z component, square symbol shows Y component and diamond symbol shows the X component. In the Fig. 4(a) shows the mean velocity of all position of left hand fingers of X, Y and Z components.

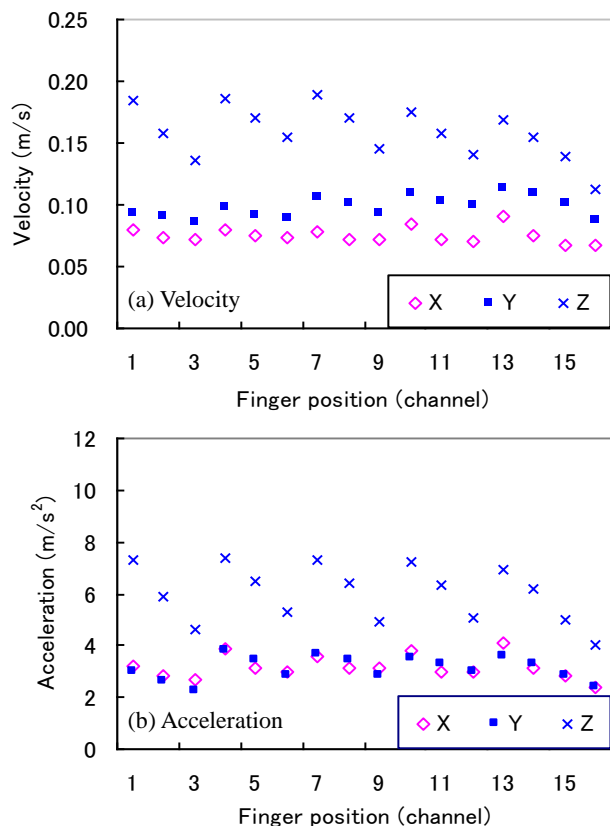


Figure 4: Mean value of left hand of X-Y-Z components

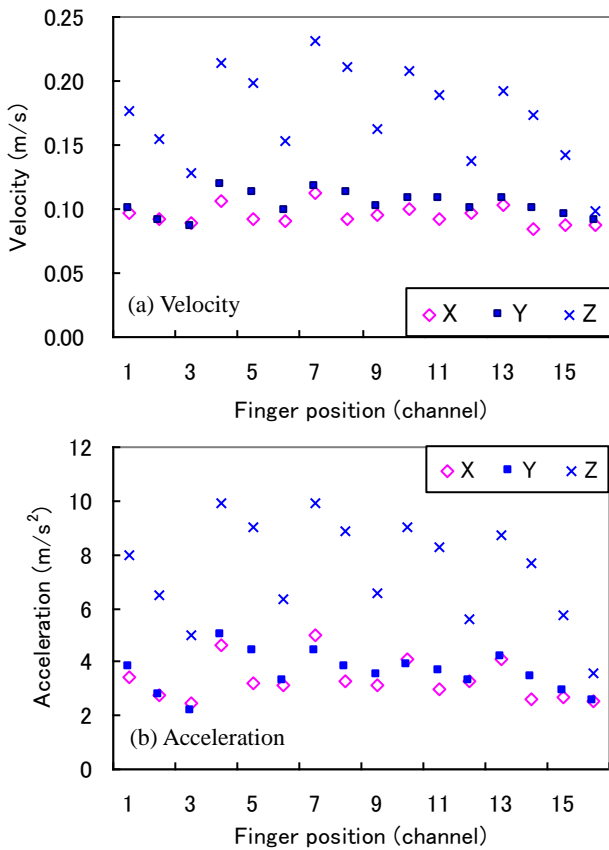


Figure 5: Mean value of right hand of X-Y-Z components

Here it is shown that velocity of Z component is greater than X and Y components as finger tip force acts more in the Z direction and X, Y are almost the same velocity. Again Fig. 4(b) shows the mean acceleration of left hand of all components and from these it is observed that Z component is higher than other components.

Figure 5 shows the right hand analysis of mean velocity and acceleration of X, Y and Z components. In this figure horizontal axis shows 16 channels position on the finger. In the figure, cross symbol shows Z component, square symbol shows Y component and diamond symbol shows the X component. In the Fig. 5(a) shows the mean velocity of all position of right hand fingers of different components. Here it is shown that velocity of Z component is greater than X and Y components. Figure 5(b) shows the mean acceleration of left hand of all components and from these it is observed that Z component is higher than other components. So it is investigated that Z component is more activated than other two components in all position during playing piano. Again, the observation is that velocity and acceleration of right hand is greater than left hand during playing piano. So further analysis we choose right hand index finger.

Mean velocity, mean acceleration and standard deviation (second line of each row) of Z component of some important positions are given in Table 2 and Table 3. From the table it is observed that index and middle fingers are higher value and almost similar characteristics though middle finger is quite high. Again everybody feels comfortable to type or play using index finger than other finger and for computer typing it is more applicable for index finger. So we considered index finger and Z component of position for further analysis though

we can choose any finger for analysis.

Figure 6 shows the movements of a receiver of distal-position of right hand index finger. In this figure we took a sample period 15.2 s to 16.2 s though we can choose any period except initial 5 s during our experiment. The pianist did not operate the regular motion in initial 5 s and it was kept for data calibration. Figure 6(a) shows position, Fig. 6(b) shows velocity and Fig. 6(c) shows acceleration of Z component. When finger position start increasing to the positive direction, acceleration also increases and goes to maximum showed in the Fig. 6(a) and Fig. 6(c) using the arrow symbol 1. When finger touches the key board then velocity is maximum shown by arrow symbol 2 in the Fig. 6(a) and Fig. 6(b) respectively. Before reaching the maximum value of position acceleration goes to negative maximum. By this way when finger position touches the keyboard in the next cycle velocity again goes to maximum.

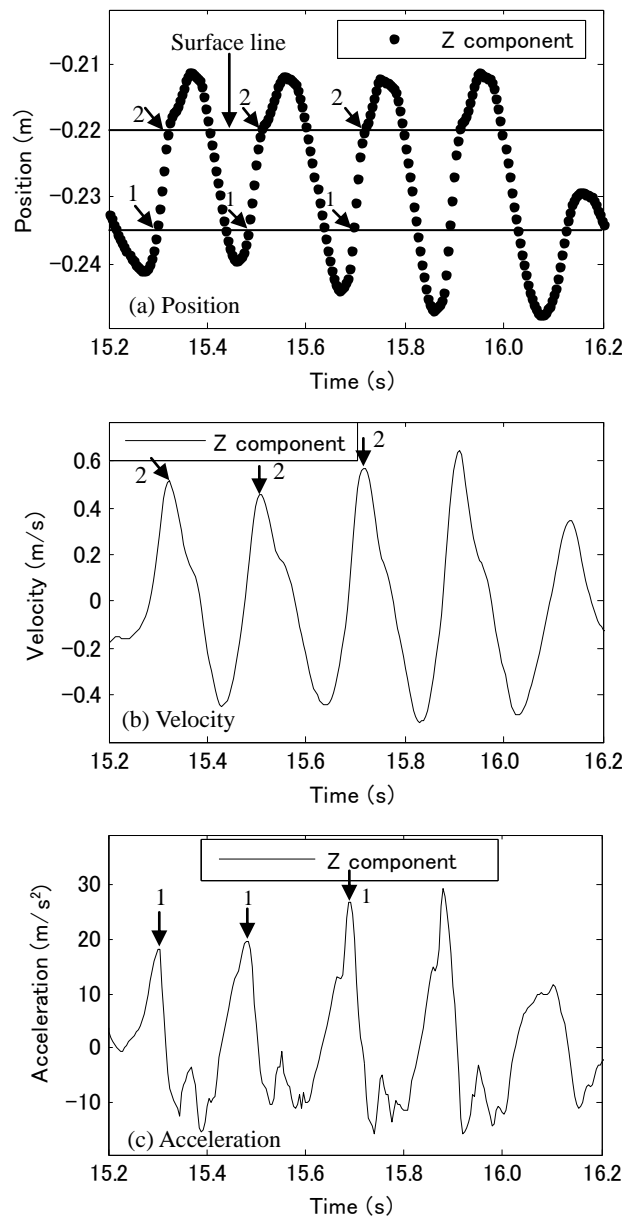


Figure 6: Movements of right hand index (distal position) finger

Table 2. Mean velocity-acceleration and standard deviation.

Left hand	Thumb (Ch1)	Index (Ch4)	Middle (Ch7)	Pinky (Ch10)	Ring (Ch13)
Velocity (m/s)	0.184 (0.227)	0.185 (0.233)	0.190 (0.229)	0.176 (0.0218)	0.169 (0.215)
Acceleration (m/s ²)	7.347 (13.36)	7.359 (11.41)	7.317 (17.95)	7.233 (11.47)	6.883 (12.13)

Table 3. Mean velocity-acceleration and standard deviation.

Right hand	Thumb (Ch1)	Index (Ch4)	Middle (Ch7)	Pinky (Ch10)	Ring (Ch13)
Velocity (m/s)	0.177 (0.216)	0.215 (0.241)	0.232 (0.250)	0.098 (0.233)	0.208 (0.220)
Acceleration (m/s ²)	8.216 (13.64)	9.878 (14.70)	9.935 (14.44)	9.010 (14.17)	8.673 (13.55)

Table 4. Relative finger joint angles.

	Pianist Joint angle (during playing piano)		Sommerich et al.1996 (Computer typist joint angle, during typing)
	Range (deg.)	Mean (deg.)	Mean (deg.)
MCP	5-43	23	28±13
PIP	26-49	32	36±11
DIP	1-38	17	-

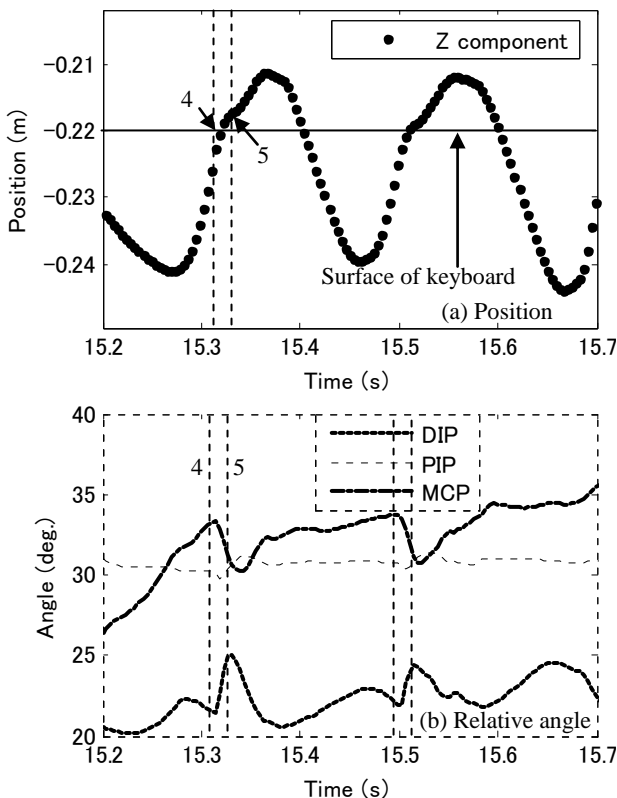


Figure 7: Finger joint angle variation (right hand index)

So it is observed that when fingertip touches the surface line of

the keyboard velocity becomes maximum value during playing piano and the surface line of the keyboard is also shown in the Fig. 6(a). This way it repeats in every cycle.

Figures 7 show the relative joint angle of right hand index finger during playing piano. This angle is very important for measuring the force of finger that performs on the keyboard of piano. Figure 7(a) shows the position of finger and Fig. 7(b) shows the joint angle variation of the finger. The arrow symbol 4 and 5 in the Fig. 7(a) shows the position of beginning of the contact of surface line of the keyboard and lift up from the keyboard during playing piano. Again Fig. 7(b) shows the beginning of the contact of the keyboard and lift up from the keyboard which is also shown by the line 4 and 5. During contact of the keyboard of the piano the MCP joint flexed and the IP joints extended before and throughout the loading phase of the contact period, so MCP joint angle increases and IP joint angle decreases and when the finger lifted up the MCP joint extended and the IP joints flexed, so MCP joint angle decreases and IP joint angle increases shown in Fig. 7(b) using the line 4 and 5. That is at the contact time of fingertip MCP joint angle increases and IP joint angle decreases again at the end of the contact from the keyboard MCP joint angle decreases and IP joint angle increases. That is MCP joint movement is the reciprocal of IP joint movement during playing piano and this is satisfied with the result Po-Ling Kuo et al.[6] though it was computer typing.

The joint angle of pianist varies wide range, as because the pianist some times moves his finger freely right and left side on the key board of piano, on the other hand the computer typist use to type on the keyboard on regular motion so their joint angle varies less than pianist. We found the variation of pianist's finger joint angle as given in the Table 4. As it is the first time to calculate the pianist finger joint angle so it is very difficult to take the reference, some of the researcher found the computer typist joint angle [7-9] though the pianist and the computer typist finger movements are not the same and it is given in the Table 4.

5 CONCLUSIONS

In this research, we have developed the high accuracy hand motion capture technique of a pianist. We observed the finger movement position, velocity and acceleration accurately, which is very important to find the value of finger muscle force. Then we investigated the surface level of the keyboard of piano. Finally we developed the new technique to calculate the finger joint angle MCP, PIP and DIP during playing piano. We established that during contact of the keyboard of the piano the MCP joint flexed and the IP joints extended and when the finger lifted, the MCP joint extended and the IP joints flexed, that is MCP joint movement is the reciprocal of IP joint movement during playing piano and the finger joint angle varies during contact period and separation period.

In future we want to observe the angular velocity, angular acceleration and fingertip force acts on the keyboard of a piano and a computer

References

- [1] Mitobe, K., Kaiga, T., Yukawa, T., Miura, T., Tamamoto, H., Al Rodgers and Yoshimura, N. "Development of a Motion Capture System for a Hand Using a Magnetic Three Dimensional Position sensor," Proc. International Conference, ACM SIGGRAPH 2006, article no. 102, Boston, Massachusetts, USA.

- [2] Rahman, M. M., Mitobe, K., Sato, J., Nikaidou, T., Suzuki, M., and Yoshimura, N. "Development of Pianist's Hand Motion Capture System Using Liberty™ 16 System, Polhemus," Proc. IEE Japan, The International Conference on Electrical Engineering, ICEE-2008, P-027, July 6-10, Okinawa, Japan.
- [3] Mitobe, K., Sato, J., Kaiga, T., Yukawa, T., Miura, T., Tamamoto, H., and Yoshimura, N. "Development of a High precision hand motion capture system and an auto calibration method for a hand skeleton model," Proc. International Conference, ACM SIGGRAPH 2007, article no. 159, San Diego, USA.
- [4] Kabir, M., Mitobe, K., Sato, J., Tamamoto, H., and Yoshimura, N. "An Approach for Calibration of Measured data Using a Magnetic Motion Capture System," IEEJ Trans. EIS, Vol. 127 No. 1, p. 88-9 (2007) [in Japanese].
- [5] Fenn, W. O. and Marsh, B. S. "Muscle force at different speeds of shortening," Journal of physiology 58, 373-395 (1935).
- [6] Kuo, P. L., Lee, D. L., Jindrich, D. L., Dennerlein, J. T., "Finger Joint coordination during tapping," Journal of Biomechanics 39, p. 2934-2942 (2006).
- [7] Jindrich, D. L., Balakrishnan, A. D., Dennerlein, J. T. "Finger Joint Impedance during tapping on a Computer Keyboard," Journal of Biomechanics 37, p.1589-1596 (2004).
- [8] Nelson, J. E., Treaster, D. E., Marras, W. S., "Finger Motion, Wrist Motion tendon travel as a function of keyboard angles," Journal of Clinical Biomechanics 15, p.489-498 (2000).
- [9] Sommerich, C. M., Marras, W. S., Parnianpour, N. "A quantitative description of typing Biomechanics," Journal of Occupational Rehabilitation 6(1), p. 33-35, (1996)

Supramolecular assembly based on thiacalix[4]arene complex with rubidium ion (Rb⁺)

Manabu Yamada,^{*} Yoshifumi Shimakawa,^{*} Yoshihiko Kondo,^{*,**} Fumio Hamada^{*,**}

^{*}Department of Material-Process and Applied Chemistry for Environments, Faculty of Engineering and Resource Science, Akita University, Akita 010-8502, Japan

^{**}Department of Life Science, Faculty of Engineering and Resource Science, Akita University, Akita 010-8502, Japan
d9507005@wm.akita-u.ac.jp, hamada@ipc.akita-u.ac.jp

Abstract: The rubidium complex forms two different thiacalix[4]arene molecular units in the crystalline state, and two pinched cone-like thiacalix[4]arene ligands exhibit a difference of intermolecular metal coordination environments. The different units are composed of two layer structures by formations of self-inclusion and intermolecular metal coordination between each thiacalix[4]arene ligand and rubidium ions. One of the same layers stabilizes an alkali metal cation- π interaction between the base layer and nearest adjacent layer with η^6 fashion. On the other hand, the interaction of other same layer exists inter-layer interactions of Rb \cdots S metal coordination and cation- π interaction with η^2 fashion between the coordinated rubidium ions of the base thiacalix[4]arene layer and the nearest adjacent thiacalix[4]arene layer. In overall crystal structures of the complex, supramolecular architecture is formed by the stacking of each unit *via* non-covalent interactions such as uncommon cation- π interactions, coordination bonds, and hydrogen bonds.

Key Words: Calix[*n*]arenes, Thiacalix[*n*]arenes, X-ray crystal structure

1 INTRODUCTION

Calixarenes are one of the most molecular scaffolds in supramolecular chemistry because of their intriguing properties such as inclusion behaviors toward many organic components and metal ions, and metal-coordination capabilities for metal ions in solution and in the solid state.¹ Their functional and conformational characteristics lead to many applications in selective metal coordination, catalytic activity, and chemical sensor. In contrast, thiacalixarenes as a counterpart of calixarenes have been found to exhibit a difference of chemical and physical properties as compared to that found in calixarenes.² In particular, one of the capabilities is preferable for infinite intermolecular interaction because their bridging sulfide moieties lead to a strongly interaction toward a wide range of metal ions. In this

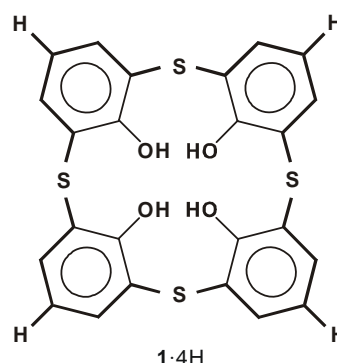


Fig. 1 Structural formula of *p*-H-thiacalix[4]arene (1·4H)

regard, the chemistry of thiacalixarenes has currently revealed various properties for metal affinities such as chelating effects,

solvent extractions, and complexation abilities for many metal ions.³ Alkali metal ion coordination chemistry involving calixarenes and thiacalixarenes has been investigated in selective extraction capabilities and structural studies.^{1,4-6} Correspondingly, our group, for example, has recently reported X-ray crystal structures of *p*-^tBu-thiacalix[4]arenes-potassium complexes.⁷ These complexes are constructed by intermolecular hydrophobic interactions of their ^tBu-moieties and metal coordination among potassium cations, phenolic and phenoxide oxygen atoms, bridging sulfur atoms of their thiacalixarene ligands. In overall crystal structures of these complexes, two fashions such as a ‘non-porous’ structure in the thiacalix[4]arene complex and ‘zeolite-like’ porous structures in the thiacalix[6/8]arenes complexes were strongly influenced hydrophobic interactions of their ^tBu-moieties at the *p*-position. For this reason, the use of *p*-H-thiacalixarenes as non-influential ligands could be extremely expected the construction of a renewed supramolecular assembly by intra- and intermolecular interactions.

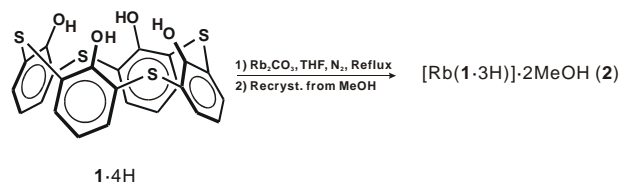
Alkali metal cation- π interactions in complexes are one of the most important non-covalent combinations, which have been attracted a significant attention because of chemical and biological relevance.⁸ The interactions have been demonstrated by many artificial receptors such as lariat ether with aromatic sidearms,⁹ calixarene derivatives,^{4a,10} and uranyl-salophen¹¹. Generally, it is well-known that alkali metal cations are included into the cavities of calixarene derivatives, although there is a few study describing the occurrence of alkali metal cation- π interactions outside aromatic rings of *p*-H-calix[4]arene cavities in the crystalline state.^{4d} Therefore, it might be possible to obtain a crystal structure by the observation of alkali metal cation- π interactions between alkali metal cations and aromatic rings of thiacalixarenes outside of the cavities. Herein we describe first structural studies of *p*-H-thiacalix[4]arene (**1·4H**, Fig. 1) complex with rubidium cation and the observation of alkali metal cation- π interaction outside aromatic rings of the thiacalix[4]arene cavities.

2. EXPERIMENTAL

2.1 Experimental Section

All reactions were carried out in nitrogen atmosphere. Tetrahydrofuran (THF) was distilled from sodium / benzophenone under nitrogen and stored over 4 Å activated molecular sieves. Methanol was commercially available and used as crystallization solvent without further purification. *p*-H-thiacalix[4]arene (**1·4H**) was obtained by de *tert*-butylation reaction of *p*-^tBu-thiacalix[4]arene¹² which was prepared according to our previously reported procedures¹³. IR spectra were recorded with a Perkin-Elmer SPECTRUM 2000 spectrophotometer. ¹H NMR spectra were taken on a Bruker DPX 300, and measured using tetramethylsilane as an internal standard and CD₃OD as a solvent, unless otherwise noted. Microanalyses were performed at the microanalysis center of Tohoku University.

2. 1 Synthesis of the complex (2)



Scheme 1 Preparation of thiacalix[4]arene complex with rubidium ions and methanol molecules

To a suspension of **1·4H** (0.5 g, 1.01 mmol) in THF (40 mL) added Rb₂CO₃ (2.33 g, 10.1 mmol), and a white suspension was obtained. The reaction mixture was stirred and refluxed for 24 h under nitrogen atmosphere. After cooling down to ambient temperature, all the solvent was removed in *vacuo*. Excess Rb₂CO₃ in the reactants was dissolved with water, and the resulting white precipitates were collected by filtration with glass filter. The precipitates were washed three times with water, dried under vacuum overnight at 150°C. The resulting solid material was dissolved in methanol (150 mL) and remained insoluble matter was filtered out. The clear solution thus obtained was allowed to stand for about two weeks to afford colorless prism crystals of the adduct (0.44 g, 75% yield): IR (KBr): ν 3420, (O-H), 1441 (C=C), 1255 (C-O) cm⁻¹. ¹H NMR (300 MHz, CD₃OD, 25 °C, TMS): δ 7.45 (d, 8H, Ar-H), 6.50 (t, 4H, Ar-H). Anal. Calcd for [Rb(**1·3H**)]·H₂O = C₂₄H₁₅O₄RbS₄·H₂O: C, 48.12; H, 2.86. Found: C, 48.08; H, 2.98. FAB-MS *m/z* 579.9 ([M]⁺, calcd for 580.5).

2. 2 Crystal data for the rubidium complex

Crystal data for complex 2: C₂₆H₂₃O₆RbS₄, *M* = 645.17, colorless prism, crystal dimensions 0.30 × 0.30 × 0.25 mm, triclinic, space group *P*-1, *a* = 9.8707(4), *b* = 12.7458(7), *c* = 21.8848(12) Å, α = 88.967(2), β = 85.6540(18), γ = 80.5530(19), *V* = 2708.1(2) Å³, *Z* = 4, Mo K α radiation (λ = 0.71075 Å), *D_c* = 1.582 g cm⁻³, *T* = 100 K, μ (Mo K α) = 2.173 mm⁻¹, 22121 measured reflections, 9854 unique reflections (*R*_{int} = 0.025), 8485 observed reflections (*I* > 2.00 σ (*I*)), 668 parameters, *R* = 0.0281, *wR* = 0.0976, GOF = 1.050. Crystallographic data of the crystals have been deposited at the Cambridge Crystallographic Data Center in CIF format CCDC no. 722470.

3 RESULTS AND DISCUSSION

Treatment of **1·4H** with Rb₂CO₃ in THF, followed by recrystallization from methanol solution, gave complex **2** as colorless prism crystals. The crystals were in a triclinic cell and the space group *P*-1. Complex **2** had an overall composition [{thiacalix[4]arene⁻} {rubidium⁺} (2MeOH)]. The asymmetric unit comprises two independent molecules of thiacalix[4]arene ligands and two rubidium cations that are coordinated to two methanol molecules each, all of which adopt the pinched cone-like conformation, namely Mol. A and Mol. B (Fig. 2A). Two conformations are stabilized by each of hydroxyl groups OH...O intramolecular hydrogen bonding of distances ranging

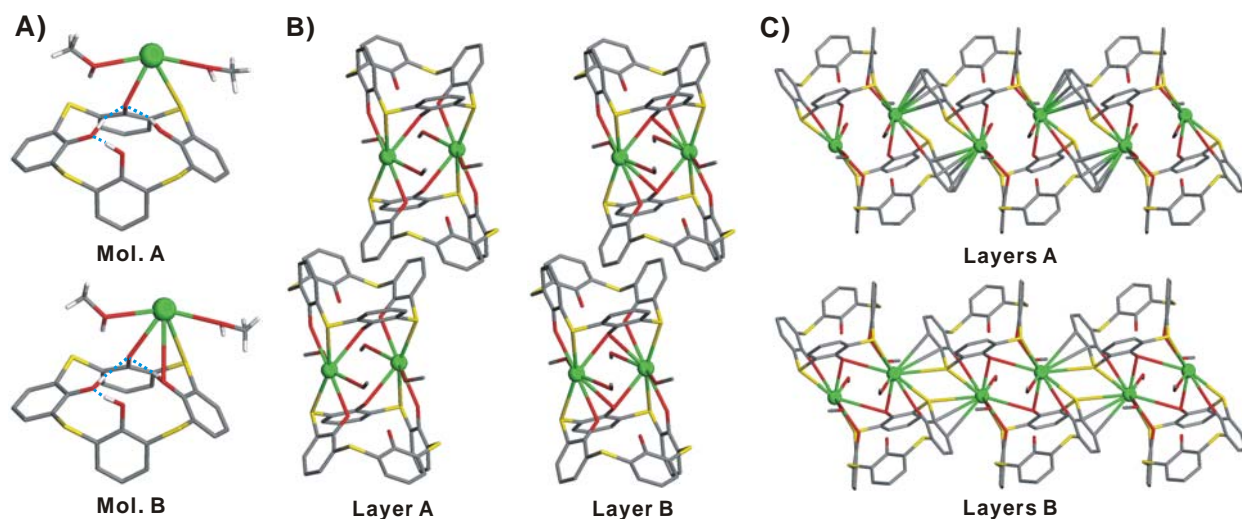


Fig. 2 Views of complex **2**. (A) The asymmetric unit showing the different coordination environments in two structural units (Mol. A and Mol. B). (B) Layer A and layer B structures showing self-inclusion and intermolecular metal coordination. (C) Extended structures of layers A and layers B showing an alkali metal cation- π interaction between the coordinated rubidium cations and thiocalix[4]arene aromatic rings (layers A), the coordination of rubidium cation to the thiocalixarene sulfur linker and part of aromatic ring (layers B).

from 1.524–2.310 Å. The distinction of two molecular structures has no enormous differences of the bond angles and bond distances, but the coordination environments between two thiocalix[4]arene ligands and two rubidium cations exist a partial difference. In the case of Mol. A, the thiocalix[4]arene molecule behaves as a bidentate ligand *via* one phenoxide oxygen atom and one bridging sulfur atom toward the rubidium ion with the Rb \cdots O and Rb \cdots S distances of 2.857 and 3.552 Å, respectively. On the other hand, the rubidium cation of Mol. B is located at the lower-rim of the thiocalix[4]arene ligand as well as Mol. A. However, the difference of coordination environments is revealed that the rubidium cation coordinates to one sulfur linker atom, phenolic, and phenoxide oxygen atoms of the thiocalix[4]arene as a tridentate ligand at the two Rb \cdots O and one Rb \cdots S distances of 3.595, 2.984, and 3.461 Å, respectively. Similarly, the different molecular units are expressly influenced by a diverse assembly formation of these thiocalix[4]arene ligands with rubidium cations as compared to extended structures of Mol. A and Mol. B. In addition, two extended structures of layer A and layer B also indicated that different coordination environments exist between each of thiocalix[4]arene molecules and rubidium cations (Fig. 2B). Layer A is comprised of Mol. A, which shows an intermolecular metal coordination between rubidium cations and the nearest adjacent thiocalix[4]arene ligands *via* two phenolic oxygen atoms and one bridging sulfur atom with two Rb \cdots O and one Rb \cdots S distances of 2.789, 3.043, and 3.471 Å, respectively. Moreover, layer A is also stabilized by two C-H \cdots π and one π -stacking interactions through a self-inclusion of the thiocalix[4]arene aromatic moieties, and the Rb \cdots Rb distance is 4.573 Å. In contrast, layer B is composed of Mol. B, which is formed by an intermolecular metal coordination between the coordinated rubidium cations and the nearest neighboring thiocalix[4]arene ligands *via* two phenolic oxygen atoms and one bridging sulfur atom at two Rb \cdots O and one Rb \cdots S distances of 2.953, 2.819, and 3.441 Å, respectively. Layer B is

also stabilized by C-H \cdots π and π -stacking interactions through a self-inclusion of the base thiocalix[4]arene aromatic ring into the cavity of the nearest adjacent thiocalix[4]arene ligand, and the Rb \cdots Rb distance is 4.402 Å. Thus, two layers are formed by each Mol. A and Mol. B, which exhibited the differences of intermolecular metal coordination environments. Although our previous reported thiocalix[4]arene-potassium complex **3** showed self-inclusion of its ^tBu-moieties by the CH- π interaction between ^tBu-moieties and thiocalix[4]arene aromatic rings^{7c}, the distinction in complex **2** changed to the self-inclusion of its aromatic ring with two types π - π interactions of face-to-face and edge-to-face contacts for comparison with complex **3**. In addition, it was clear that the coordination environments between complex **2** and complex **3** are found different fashions. This reason may contribute to factors affecting such as differences from functional group of thiocalix[4]arene ligand and the ion radius of alkali metals. The overall crystal structure was formed by the alternatively stacking of layer A and layer B, which is stabilized by several inter-layer interactions (Fig. 2C). In the extended crystal structure of layers A, an uncommon alkali metal cation- π interaction is observed between the base thiocalix[4]arene aromatic rings outside of the cavities and the coordinated rubidium cations of the nearest adjacent layer in an η^6 fashion with Rb \cdots C distance in the ranges of 3.503–3.727 Å. Surprisingly, the metal in each of layers B is coordinated to one of the thiocalix[4]arene sulfide linker as well as part of the nearest adjacent aromatic ring of the thiocalix[4]arene ligand in an η^2 fashion with typical Rb \cdots S and Rb \cdots C distances of 3.610 and 3.606–3.671 Å, respectively. This distinct phenomenon might be occurred by the location of each rubidium cation on ‘lower-rim’ of two thiocalix[4]arene molecules (*i.e.* the different Rb \cdots Rb distances strongly affect for the construction of two different layer structures). The different inter-layer interaction between layer A and layer B exists aromatic-H \cdots S hydrogen bonding with the distances of 2.661 and 2.786 Å (corresponding C \cdots S

distances of 3.603 and 3.709 Å). These results illustrate important roles on the supramolecular architecture of complex **2** that is organized by intra- and intermolecular interactions such as uncommon alkali metal cation- π interactions, metal coordination bonds, and hydrogen bonding. Furthermore, it might be suggested that the behavior of rubidium cations toward thiacalix[4]arene ligands and the intermetallic Rb \cdots Rb distances play a dominant role in important factors to obtain the intriguing architecture.

4 CONCLUSIONS

We have demonstrated two different molecular units that are formed from the reaction of rubidium carbonate and *p*-H-thiacalix[4]arene (**1-4H**). The crystal structure of complex **2** exhibited the similar conformation, but the variant coordination environments were observed in Mol. A and Mol. B. Moreover, two layer structures were constructed by on self-inclusions of the thiacalixarene aromatic rings and intermolecular metal coordination interactions. The supramolecular architecture was constructed by the identical inter-layer interactions of the alkali metal cation- π interactions and the extensive Rb \cdots S metal coordination interaction, the different inter-layer interaction of the aromatic-H \cdots S hydrogen bonding. The behavior of the metal center in the obtained structure is somewhat different from the reported potassium complex **3** that showed self-inclusions of its *t*-Bu-moieties and the complementary (O,S,O) \cdots K \cdots S intermolecular metal coordination between *p*-Bu-thiacalix[4]arene ligands and potassium cations^{7c}. This suggests that these thiacalix[4]arene ligands may exist for two different assemblies depending on functional moieties of *p*-position and solvent molecules, especially considering the distinction between alkali metal cation sizes. Further studies are focussing on studying the complexes of other alkali metal cations.

5 ACKOWLEGEEMENT

This work was supported by Grant Industrial Technology Research (Financial support to young researchers) in 2006 from New Energy and Industrial Technology Development Organization (NEDO) of Japan.

References

- [1] For example, see (a) C. D. Gutsche, *Calixarenes*; Royal Society of Chemistry: Cambridge, U. K., 1989; (b) J. Vicens, V. Böhmer, Eds.; *Calixarenes: A Versatile Class of Macrocyclic Compounds*; Kluwer Academic Publishers: Dordrecht, The Netherlands, 1991; (c) C. D. Gutsche, *Calixarenes Revisited*; Royal Society of Chemistry: Cambridge, U. K., 1998; (d) A. Ikeda and S. Shinkai, *Chem. Rev.*, 1997, **97**, 1713; (e) M. Frank, G. Maas, J. Schatz, *Eur. J. Org. Chem.*, 2004, 607; (f) Y. Obora, Y. K. Liu, S. Kubouchi, M. Tokunaga, Y. Tsuji, *Eur. J. Inorg. Chem.*, 2006, 222; (g) C. Limberg, *Eur. J. Inorg. Chem.*, 2007, 3303. (g) J. S. Kim, D. T. Quang, *Chem. Rev.*, 2007, **107**, 3780; (h) X. H. Sun, W. Li, P. F. Xia, H.-B. Luo, Y. Wei, M. S. Wong, Y. -K. Cheng, S. Shuang, *J. Org. Chem.*, 2007, **72**, 2419.
- [2] (a) H. Kumagai, M. Hasegawa, S. Miyanari, Y. Sugawa, Y. Sato, T. Hori, S. Ueda, H. Kamiyama, S. Miyano, *Tetrahedron Lett.*, 1997, **38**, 3971; (b) N. Iki, C. Kabuto, T. Fukushima, H. Kumagai, H. Takeya, S. Miyanari, T. Miyashi, S. Miyano, *Tetrahedron*, 2000, **56**, 1437; (c) N. Morohashi, F. Narumi, N. Iki, T. Hattori, S. Miyano, *Chem. Rev.*, 2006, **106**, 5291.
- [3] (a) G. Mislin, E. Graf, M. W. Hosseini, A. Bilyk, A. K. Hall, J. M. Harrowfield, B. W. Skelton, A. H. White, *Chem. Commun.*, 1999, 373; (b) H. Akdas, E. Graf, M. W. Hosseini, A. D. Cian, A. Bilyk, B. W. Skelton, G. A. Koutsantonis, I. Murray, J. M. Harrowfield, A. H. White, *Chem. Commun.*, 2002, 1042; (c) H. Katagiri, N. Iki, Y. Matsunaga, C. Kabuto, S. Miyano, *Chem. Commun.*, 2002, 2080; (d) T. Kajiwara, N. Kon, S. Yokozawa, T. Ito, N. Iki, S. Miyano, *J. Am. Chem. Soc.*, 2002, **124**, 11274; (e) H. Katagiri, N. Morohashi, N. Iki, C. Kabuto, S. Miyano, *Dalton Trans.*, 2003, 723; (f) M. Yamada, Y. Kondo, F. Hamada, *Int. J. Soc. Mater. Eng. Resor.*, 2007, **15**, 13; (g) J. Sýkora, M. Himl, I. Stibor, I. Cisarová, P. Lhoták, *Tetrahedron*, 2007, **63**, 2244; (h) D. Buccella and G. Parkin, *J. Am. Chem. Soc.*, 2008, **130**, 8617.
- [4] (a) J. M. Harrowfield, M. I. Ogden, W. R. Richmond, A. H. White, *J. Chem. Soc., Chem. Commun.*, 1991, 1159; (b) F. Hamada, K. D. Robinson, G. W. Orr, J. L. Atwood, *Supramol. Chem.*, 1993, **2**, 19; (c) M. G. Davidson, J. A. K. Howard, S. Lamb, C. W. Lehmann, *Chem. Commun.*, 1997, 1607; (d) T. A. Hanna, L. Liu, L. N. Zakharov, A. L. Rheingold, W. H. Watson, C. D. Gutsche, *Tetrahedron*, 2002, **58**, 9751.
- [5] (a) N. Iki, N. Morohashi, F. Narumi, S. Miyano, *Bull. Chem. Soc. Jpn.*, 1998, **71**, 1597; (b) N. Iki, F. Narumi, T. Fujimoto, N. Morohashi, S. Miyano, *J. Chem. Soc., Perkin Trans. 2*, 1998, 2745; (c) N. Morohashi, N. Iki, A. Sugawara, S. Miyano, *Tetrahedron*, 2001, **57**, 5557.
- [6] (a) A. Bilyk, A. K. Hall, J. M. Harrowfield, M. W. Hosseini, B. W. Skelton, A. H. White, *Inorg. Chem.*, 2001, **40**, 627; (b) J. Zeller and U. Radius, *Inorg. Chem.* 2006, **45**, 9487.
- [7] (a) K. Endo, Y. Kondo, Y. Aoyama, F. Hamada, *Tetrahedron Lett.*, 2003, **44**, 1355; (b) Y. Kondo, K. Endo, F. Hamada, *Chem. Commun.*, 2005, 711; (c) M. Yamada, Y. Kondo, N. Iki, C. Kabuto, F. Hamada, *Tetrahedron Lett.*, 2008, **49**, 3906.
- [8] (a) J. C. Ma and D. A. Dougherty, *Chem. Rev.*, 1997, **97**, 1303; (b) G. W. Gokel, S. L. De Wall, E. S. Meadows, *Eur. J. Org. Chem.*, 2000, 2967; (c) E. A. Meyer, R. K. Castellano, F. Diederich, *Angew. Chem., Int. Ed.*, 2003, **42**, 1210.
- [9] (a) S. L. De Wall, E. S. Meadows, L. J. Barbour, G. W. Gokel, *J. Am. Chem. Soc.*, 1999, **121**, 5613; (b) S. L. De Wall, L. J. Barbour, G. W. Gokel, *J. Am. Chem. Soc.*, 1999, **121**, 8405; (c) E. S. Meadows, S. L. De Wall, L. J. Barbour, G. W. Gokel, *J. Am. Chem. Soc.*, 2001, **123**, 3092; (d) J. Hu, L. J. Barbour, G. W. Gokel, *J. Am. Chem. Soc.*, 2002, **124**, 10940; (e) G. W. Gokel, L. J. Barbour, R. Ferdani, J. Hu, *Acc. Chem. Res.*, 2002, **35**, 878; (f) J. Hu and G. W. Gokel, *Chem. Commun.*, 2003, 2536; (g) G. W. Gokel, *Chem. Commun.*, 2003, 2847; (h) J. Hu, L. J. Barbour, G. W. Gokel, *New J. Chem.*, 2004, **28**, 907.
- [10] (a) R. Assmus, V. Böhmer, J. M. Harrowfield, M. I. Ogden, W. R. Richmond, B. W. Skelton, A. H. White, *J. Chem. Soc., Dalton Trans.*, 1993, 2427; (b) K. Murayama and K. Aoki, *Inorg. Chim. Acta.*, 1998, **281**, 36; (c) R. Ferdani, L. J. Barbour, G. W. Gokel, *J. Supramol. Chem.* 2002, **2**, 343; (d) A. T. Macias, J. E. Norton, J. D. Evanseck, *J. Am. Chem. Soc.*, 2003, **125**, 2351; (e) T. A. Hanna, L. Liu, A. M. Angeles-Boza, X. Kou, C. D. Gutsche, K. Ejsmont, W. H. Watson, L. N. Zakharov, C. D. Incarvito, A. L. Rheingold, *J. Am. Chem. Soc.*, 2003, **125**, 6228; (f) A. Åhman and M. Nissinen, *Chem. Commun.*, 2006, 1209.

- [11] M. Cametti, M. Nissinen, A. Dalla Cort, L. Mandolini, K. Rissanen, *J. Am. Chem. Soc.*, 2005, **127**, 3831.
- [12] (a) Higuchi, Y.; Narita, M.; Niimi, T.; Ogawa, N.; Hamada, F.; Kumagai, H.; Iki, N.; Miyano, S.; Kabuto, C. *Tetrahedron* **2000**, *56*, 4659; (b) Kabuto, C.; Higuchi, Y.; Niimi, T.; Hamada, F.; Iki, N.; Morohashi, N.; Miyano, S. *J. Incl. Phenom. Macrocycl. Chem.* **2002**, *42*, 89; (c) Kasyan, O.; Swierczynski, D.; Drapailo, A.; Suwinska, K.; Lipkowski, J.; Kalchenko, V. *Tetrahedron Lett.* **2003**, *44*, 7167.
- [13] (a) Kondo, Y.; Endo, K.; Iki, N.; Miyano, S.; Hamada, F. *J. Incl. Phenom. Macrocycl. Chem.* **2005**, *52*, 45; (b) Kondo, Y.; Hamada, F. *J. Incl. Phenom. Macrocycl. Chem.* **2007**, *58*, 123.

Synthesis and crystal structure of thiacalix[4]arene complex with cesium ions (Cs⁺)

Yoshifumi Shimakawa^a, Manabu Yamada^a, Yoshihiko Kondo^{a,b}, Fumio Hamada^{a,b}

^aDepartment of Material-Process and Applied Chemistry for Environments, Faculty of Engineering and Resource Science, Akita University, Akita 010-8502, Japan

^bDepartment of Life Science, Faculty of Engineering and Resource Science, Akita University, Akita 010-8502, Japan

m9008026@wm.akita-u.ac.jp, hamada@ipc.akita-u.ac.jp

Abstract : Supramolecular structure of the thiacalix[4]arene complex with cesium ions was determined by single-crystal X-ray diffraction studies. A 'sandwich-like' dimeric structure of the cesium complex is constructed by intermolecular coordination bonds among two thiacalix[4]arene ligands, two methanol molecules, and two cesium ions. The layer structure is formed by self-inclusion of the thiacalix[4]arene aromatic rings of each dimer, which provides evidence of an alkali metal cation- π interaction between the base layer and the neighboring layer. In overall crystal structures of complex, supramolecular architecture is formed by stacking of each unit via interactions of alkali metal cation- π interaction, coordination bonds, and hydrogen bonds.

Key Words : Thiacalixarenes, X-ray crystal structure, Cesium ion

Introduction

p-tert-Bu-calixarenes are composed of benzene rings, linked via methylene bridges, which are one of the most investigated molecular scaffolds in the supramolecular chemistry because the compound derivatives exhibit a high affinity toward a wide range of metal ions¹. In addition, thiacalixarenes which substituted a methylene bridge for sulfur, have very high metal affinity². They have been recently investigated such as a molecular recognition for metal ions and organic molecules, selective metal coordination, and chemical sensors³.

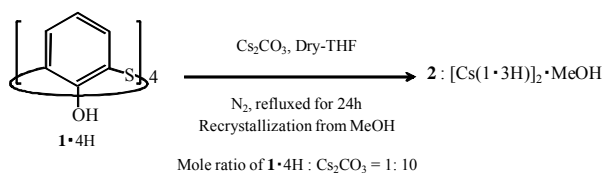
We have reported the synthesis of potassium complexes of *p-tert*-Bu thiacalix[4/6/8]arenes and X-ray crystal structures of these complexes⁴. Supramolecular formations of these complexes are strongly effected by hydrophobic interactions of their *tert*-Bu groups. *p-tert*-Bu thiacalix[4]arene potassium complexes show two dimer formations. One of the dimers is formed by hydrophobic interaction between each *tert*-Bu groups. The other was dimer made by metal coordination between neighboring *p-tert*-Bu thiacalix[4]arene and potassium.

p-tert-Bu thiacalix[6]arene potassium complexes are built from the continuous S...K...(O,S) coordination between neighboring *p-tert*-Bu thiacalix[6]arene and afford a doubly linked ladder-like polymeric 1D chain having lateral branches of *tert*-butyl groups. *p-tert*-Bu thiacalix[8]arene potassium complexes is built from the extensive (S,O)...K...(O,S) coordination between neighboring *p-tert*-Bu thiacalix[8]arene and affords a doublylinked ladder-like polymeric 1D chain having lateral branches of *tert*-butyl groups. These complexes have zeolite-like structure.

Therefore we synthesized the derivative without the *tert*-Bu groups of *p-tert*-Bu-thiacalixarenes⁵ and tried the synthesis of the metal complex with the corresponding thiacalix[4]arene and alkali metal ion. Because it is thought that thiacalixarene might be able to form another supramolecular architecture by losing of *tert*-Bu groups. As a result, we obtained the thiacalix[4]arene complex with cesium ions. Here, we report supramolecular structure of the thiacalix[4]arene complex by single-crystal X-ray diffraction studies.

Synthesis of thiacalix[4]arene complex with Cesium ions(2)

To a suspension of **1** · 4H (0.5 g, 1.01 mmol) in THF (30mL) added Cs₂CO₃(3.28g, 10.1 mmol), and a white suspension was obtained. The reaction mixture was stirred and refluxed for 24h under nitrogen atmosphere. After cooling down to ambient temperature, all the solvent was removed in vacuo. Excess Cs₂CO₃ of the reactants was dissolved with water, and the resulting white precipitates were collected by filtration with glass filter. The precipitates were washed three times with water, dried under vacuum overnight at 150°C. The resulting solid material was dissolved in methanol (300 mL) and remained insoluble matter was filtered out. The clear solution thus obtained was allowed to stand for two weeks to afford colorless block crystals of the adduct(0.32 g, 48% yield) : ¹H NMR(300 MHz, CD₃OD, 25°C, TMS) : δ 7.32(d, 8H, Ar-H), 6.38(t, 4H, Ar-H). IR(KBr) : ν 3416, 3360(O-H), 3042(C-H), 1441(C=C), 1253(C-O) cm⁻¹. Anal. Calcd for **2** · 2H₂O = C₄₈H₃₀O₈S₈Cs₂ · 2H₂O : C, 44.62 ; H, 2.65. Found : C, 44.95 ; H, 2.95. FAB-MS m/z 760.8([M + Cs⁺], calcd 760.6).



Scheme 1 Synthesis of TC4A with Cesium complexes.

Crystal structure determination of complex (2)

Single crystal of complex (**2**) decomposed rapidly from the mother liquid. The crystals containing mother liquid were drunk up with a pipette, which dropped in paraffin oil. The oil coated single crystals were picked up with on MicroMountsTM, and the crystals were placed immediately in a cold nitrogen stream at -173°C. X-ray diffraction data for complex **2** was collected on a Rigaku PAXIS RAPID imaging plate diffractometer with a graphite monochromated Mo K α radiation ($\lambda = 0.71075$ Å). Structure was solved by direct methods using SHELXS-97²¹ and refined by full-matrix least-squares on F^2 using SHELXL-97²² program. The non-hydrogen atoms were refined by anisotropically. The hydrogen atoms in these complexes were found from the residual density and refined with riding mode.

Crystal Data for complex (2) : C₅₀H₃₈O₁₀S₈Cs₂, $M = 1321.14$, colorless, block, Crystal Dimensions 0.30 x 0.25 x 0.20 mm, Space Group $P2_1/n$, $a = 13.3830(7)$, $b = 10.8649(5)$, $c = 18.3500(9)$ Å, $\beta = 112.5895(10)$, $V = 2463.5(2)$ Å³, $Z = 2$, Mo K α radiation ($\lambda = 0.71075$ Å), $D_{\text{calcd}} = 1.781$ g/cm³, $T = 100$ K, $\mu(\text{Mo K}\alpha) = 1.879$ mm⁻¹, 22826 measured reflections, 5600 unique reflections ($R_{\text{int}} = 0.032$), 5192 observed reflections ($I > 2.00\sigma(I)$), 317 parameters, $RI = 0.0225$, $wR2 = 0.0470$, refined against $|F|$, $GOF = 1.048$

Results and discussion

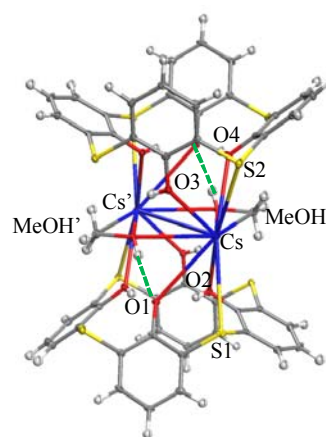


Fig. 1 Crystal structures of complex showing side view of thiacalix[4]arene complex with cesium ions and methanol molecules. Conventional atom colors of carbons, oxygen, sulfurs, cesiums, and hydrogens in complex are in gray, red, yellow, blue, and white, respectively.

Crystals as colorless blocks of [Cs(1·3H)]₂·2MeOH (**2**) complex were obtained from a treatment of **1**·4H with Cs₂CO₃ in THF, followed by recrystallization from methanol solution. The resulting complex (**2**) crystallized in the space group $P2_1/n$ and $Z = 2$ with an overall composition [$\{\text{thiacalix[4]arene}^-\}_2\{\text{cesium}^+\}_2(\text{MeOH})_2$] from single-crystal X-ray diffraction studies. Charge neutrality dictates the thiacalix[4]arene is in mono-anion form. A ‘sandwich-like’ (O,S,O)···Cs···(O,S,O) coordination dimer of complex (**2**) has centrosymmetric, is composed of two thiacalix[4]arene ligands, two cesium ions, and two methanol molecules. The pinched cone-like thiacalix[4]arene ligand behaves as a tridentate ligand *via* phenolic / phenoxide oxygen atoms and one bridging sulfur atom for cesium ion with the Cs···O(1), Cs···O(2), Cs···O(3), Cs···O(4), Cs···S(1), Cs···S(2) distances of 3.619, 3.397, 2.929, 3.151, 3.727, and 3.773 Å, respectively, and there are hydrogen bonding between the interleaved methanol molecules and phenoxide oxygen atoms of thiacalix[4]arene ligands at the MeOH···O(1) distance of 2.015 Å (Figure 1). Moreover, each of cesium ions also coordinate to one methanol molecule with the Cs···OMe(1) distance 2.344 Å, and the Cs···Cs distance is 4.886 Å. The conformation of the thiacalix[4]arene is mentioned by its hydroxyl groups OH···O intramolecular hydrogen bonds of distances ranging from 1.717 to 2.761 Å. The crystal structure of complex (**2**) is quite different from that of cesium complex with *p-tert*-Bu thiacalix[4]arene. The reason might be concerned with factors affecting such as differences from functional group of thiacalix[4]arene ligand, crystallization solvent, and anions of alkali metal sources.

The dimer forms a layer structure by the thiacalix[4]arene cavity of the base dimer includes into one aromatic ring of a neighboring dimer, and the layer structure is stabilized by C-H··· π and π -stacking interactions at the distances of 2.933, 3.292, and 3.618 Å (Figure 2).

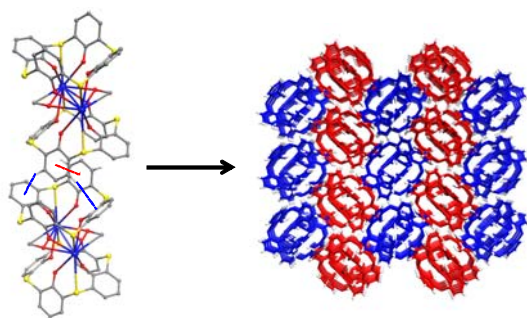


Fig. 2 Layer formations by self-inclusion of each dimer in complex(Left), and the all overall crystal structure showing alternately stacking of two different directional layers(Right).

In the extended crystal structure of layers are recognized to be involving the thiacalix[4]arene unit in two different directions, but both the thiacalix[4]arene structures adopt same conformation. The interaction between the same directional layers is observed inter-layer interactions of aromatic-H...S hydrogen bonds between the thiacalix[4]arene aromatic protons of the base layer and thioether moieties of the neighboring layer at distances ranging from 2.926 to 3.416 Å (Figure 3a). In the mixed layers, uncommon alkali metal cation- π interaction exists between the thiacalix[4]arene aromatic rings of base layer outside of its cavities and the coordinated cesium ions of the nearest adjacent layer in η^2 fashion with the aromatic centroid...Cs⁺ distance of 3.676 Å (Figure 3b). In this sort, the overall crystal structure of complex (2) constructed a supramolecular architecture by the formation both dimeric and layer structures stabilize non-covalent interactions such as metal coordination bonds, uncommon alkali metal cation- π interactions, and hydrogen bonds.

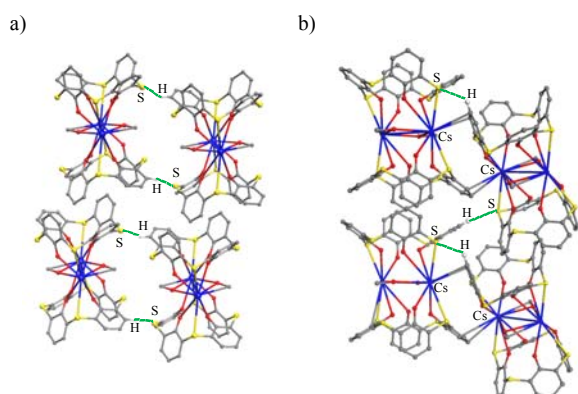


Fig. 3 Extended structures of layer in complex showing, a) Ar-H...S hydrogen bonding between same directional layers, b) the alkali metal cation- π interaction and the Ar-H...S hydrogen bonding between different directional layers.

Conclusion

In conclusion, complex (2) existed as the dimeric structure, where cesium ions and methanol molecules were interleaved. Moreover, the dimer connected with neighbouring dimer by self-inclusion of one phenol unit of the dimer into the cavity of neighbouring dimer one. It is revealed that the supramolecular architecture was constructed by hydrogen bonds and alkali metal cation- π interactions between the base layer and the nearest adjacent layer. In addition, these results might be one of important evidences for calixarenes and thiacalixarenes chemistry.

Acknowledgment

This work was supported by Grant Industrial Technology Research (Financial support to young researchers) in 2006 from New Energy and Technology Development Organization (NEDO) of Japan.

References

- [1] a) J. Vicens & V. Böhmer, *CALIXARENES A Versatile Class of Macrocyclic Compounds*, Ed. E. D. Davies, Kluwer Academic Publishers, Dordrecht **1991**; b) C. David Gutsche, *Calixarenes Revisited Monographs in Supramolecular Chemistry*, Ed. J. Fraser Stoddart, The Royal Society of Chemistry, Cambridge, **1998**
- [2] N. Morohashi, F. Narumi, N. Iki, T. Hattori, and S. Miyano, *Chem. Rev.* **106**, **2006**, 5291; b) V. Bhalla, M. Kumar, T. Hattori and S. Miyano, *Tetrahedron Lett.*, **2004**, **60**, 5881
- [3] a) T. Sone, Y. Ohba, K. Moriya, H. Kumad, K. Ito, *Tetrahedron Lett.*, **1997**, **53**, 10689; b) G. Mislin, E. Graf, W. M. Hosseini, D. A. Cian, *J. Chem. Commun* **1998** 1345; c) N. Iki, N. Morohashi, F. Narumi and S. Miyano, *Bull. Chem. Soc. Jpn.*, **1998**, **71**, 1597; d) M. Yamada, A. Shibayama, Y. Kondo, F. Hamada, *Int. J. Soc. Mater. Eng. Resour.*, Vol. **15**, **13**, **2007**
- [4] a) M. Yamada, Y. Kondo, N. Iki, C. Kabuto, and F. Hamada, *Tetrahedron Lett.*, **49**, **2008**, 3906, b) K. Endo, Y. Kondo, Y. Aoyama, and F. Hamada, *Tetrahedron Lett.*, **44**, **2003**, 1355, c) Y. Kondo, K. Endo, and F. Hamada, *Chem. Commun.*, **2005**, 711
- [5] O. Kasyan, D. Swierczynski, A. Drapailo, K. Suwinska, J. Lipkowski and V. Kalchenko, *Tetrahedron Lett.*, **44**, **2003**, 7167

Double stranded DNA discrimination by novel di-pyrene modified γ -cyclodextrins

Akane Takeda,* Noriaki Matsumura,* Yoshihiko Kondo,*^{***}
Kazuhiko Akimoto,^{***} Fumio Hamada,^{*,***}

*Department of Material-Process and Applied Chemistry for Environments, Faculty of Engineering and Resource Science, Akita University, Akita 010-8502, Japan

**Department of Life Science, Faculty of Engineering and Resource Science, Akita University, Akita 010-8502, Japan

^{***}Electronic Materials Research Laboratories, Nissan Chemical Industries, Ltd, 635 Sasakura Fuchu-Machi, Toyama 939-2792, Japan

m9008028@wm.akita-u.ac.jp, hamada@ipc.akita-u.ac.jp

Abstract: The fluorescence reagent is used to detect double stranded DNA (dsDNA). However, there are some problems such as no selectivity for single stranded DNA (ssDNA) and dsDNA because almost fluorescence dyes are cationic ones which can bind with phosphate residue of DNA. To get solution, we synthesized neutral fluorescence reagent such as novel di-pyrene modified γ -cyclodextrin(CyD) (**1**). We studied binding and selectivity of **1** for double strand DNA, which resulted that the fluorescent intensity of **1** was increased upon an intercalation into dsDNA, although the fluorescent intensity of **1** was not increased by the addition of ssDNA.

key words: Cyclodextrin, pyrene, fluorescence, double strand DNA, discrimination

1 INTRODUCTION

Recently, the genetic diagnosis has attracted significant attention as key of preventive medicine where the fluorescence reagent has been used for DNA detection. However, there are some problems such as "the distinction between ssDNA and dsDNA is difficult" and "the longevity of the fluorescence reagent is short and the handling is not easy" in detection with the fluorescence reagent. To get solution of the problems, we decided to use cyclodextrin (CyD) because CyD has many advantages such as protection of fluorescence reagent and increase of water solubility of organic molecules. We synthesized fluorescence reagent modified CyD whose intercalation capability for ssDNA and dsDNA have been studied. CyDs are torus shaped cyclic oligosaccharides composed of six, seven and eight D-glucopyranose units (α , β , γ -CyD, respectively). A variety of organic compounds can be included in their center cavities in aqueous media. Therefore fluorescence reagent can be stable by interaction with CyDs cavity. In previous paper, we reported synthesis of pyrene modified β -CyD,

which was linked between pyrene unit and CyD with amine chain. Unfortunately, this compound showed no selective

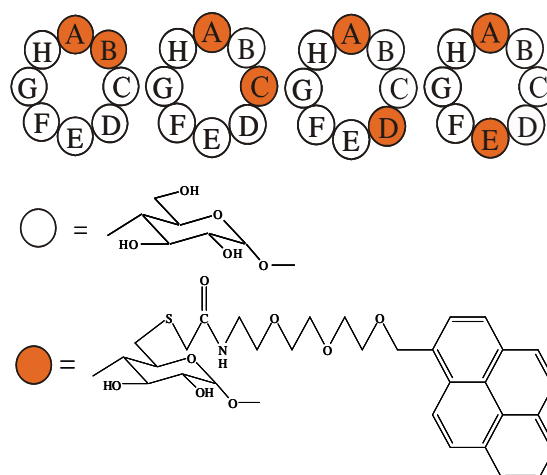


Fig. 1 Structures of di- $6^A,6^B$ -deoxy- $6^A,6^B$ -[8-(1-pyrene methoxy)-3,6-(dioxo)octa-1-amino]-(thioacetyl)]- γ -CyD, **1**

discrimination for dsDNA and ssDNA [1]. Because it might be supposed that amino group of the linker can interact with the phosphoric acid part of dsDNA and ssDNA through electrostatic interaction. To solve this problem, we synthesized the pyrene modified β -CyD with an ether chain because ether chain was hydrophilic and no interactive with the phosphoric acid residue of DNA. Unfortunately, the compound showed no interactions with dsDNA and ssDNA. We planned synthesis of another type of pyrenes modified CyD, where bis pyrene units were introduced into CyD, because particular excimer fluorescence of pyrene can work as unique recognition for dsDNA. In the synthesis, γ -CyD was used because water solubility of pyrene unit can be increased. The γ -CyD has four isomers by the substitution site of the functional group when it was modified with double functional group [2]. In this study, we synthesized the novel di-pyrene modified γ -CyD (di-6^A,6^E-deoxy-6^A,6^E-[8-(1-pyrenemethoxy)-3,6-(diox)octa-1-amino]-(thioacetyl)- γ -CyD, **1**, Fig. 1) by using the AE from which the substitution sites were away most, and examined the interaction with ssDNA and dsDNA by using a spectroscopy technique.

2 EXPERIMENTAL

2.1 Materials

Compound **2** was commercially available (TAKARA BIO INC.) [3] - [10].

2.2 Preparation of di-6^A,6^E-deoxy-6^A,6^E-[8-(1-pyrenemethoxy)-3,6-(diox)octa-1-amino]-(thioacetyl)- γ -CyD, **1**

To the solution of di-6^A,6^E-deoxy-6^A,6^E-(thioacetic acid)- γ -CyD (0.1479 g, 0.10 mmol) and 1-hydroxybenzotriazole (1-HOBt, 0.0626 g, 0.46 mmol) in a mixture dry-DMF (15 mL), N, N'-dicyclohexylcarbodiimide (DCC, 0.0879 g, 0.42 mmol) was added at 0 °C. The reaction mixture was stirred for 2h and then 8-(1-pyrenemethoxy)-3,6-(diox)octa-1-

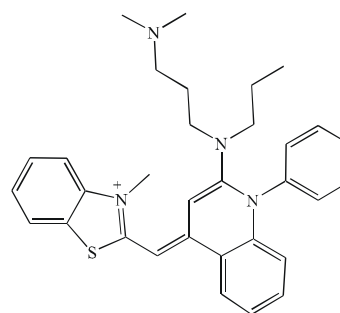


Fig. 2 Structure of intercalation reagent (**2**).

amine (0.1646 g, 0.45 mmol) was added. The reaction mixture was warmed up to a room temperature and then stirred for 3days at 80 °C. The mixture was concentrated in vacuo which was treated with 200 mL of acetone. The resulting precipitate was filtered and dried up to give crude product (0.1628 g). The crude product was dissolved in 5 mL of water and 5 mL dry-DMF. The soluble fraction was applied to a reversed - phase column (Lobar column LiChroprep RP-18, Merck Ltd., 310 mm x 10 mm). Stepwise elution with 80 - 100% aqueous methanol gave pure **1**, which was collected and dried up in vacuo to give pure **1** (0.0134 g , yield ; 6.14%) [11] - [13].

R_f : 0.56 (1-BuOH : EtOH : H₂O = 5 : 4 : 3, TLC ; silica gel 60F₂₅₄)

¹H NMR (300 MHz, DMSO-d₆) : δ = 4.5 - 4.7 (6H, m, OH of C⁶ of CyD), 4.8 - 5.0 (8H, d, H of C¹ of CyD), 5.1 - 5.3 (2H, s, CH₂ of pyrenemethoxy), 5.8 - 6.2 (16H, s, OH of C² and C³ of CyD), 7.9 - 8.0 (2H, t, H of amide), 8.0 - 8.5 (18H, m, aromatic H of pyrene) ppm.

2.3 Measurement

UV-Vis, fluorescence and CD spectra were measured using a SHIMAZU-3600 Spectrophotometer, a Perkin-Elmer LS40B Fluorescence Spectrophotometer and a JASCO J-720 Spectrophotometer, respectively. The base sequence is 1)

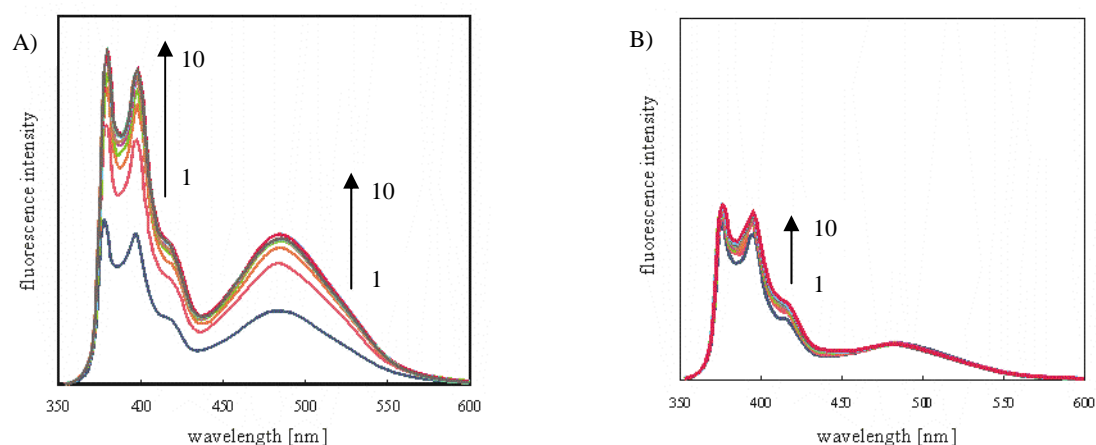


Fig. 3 Fluorescence spectra of **1** in a 10 vol.% DMSO aqueous solution (3.0×10^{-7} M) at various concentration of dsDNA or ssDNA. A) dsDNA (1:0, 2:0.9375 $\times 10^{-10}$, 3:1.875 $\times 10^{-10}$, 4:3.75 $\times 10^{-10}$, 5:7.5 $\times 10^{-10}$, 6:15 $\times 10^{-10}$, 7:30 $\times 10^{-10}$, 8:60 $\times 10^{-10}$, 9:120 $\times 10^{-10}$, 10:250 $\times 10^{-10}$ M), B) ssDNA (1:0, 2:4.6875 $\times 10^{-10}$, 3:9.375 $\times 10^{-10}$, 4:18.75 $\times 10^{-10}$, 5:37.5 $\times 10^{-10}$, 6:75 $\times 10^{-10}$, 7:150 $\times 10^{-10}$, 8:300 $\times 10^{-10}$, 9:600 $\times 10^{-10}$, 10:1200 $\times 10^{-10}$ M).

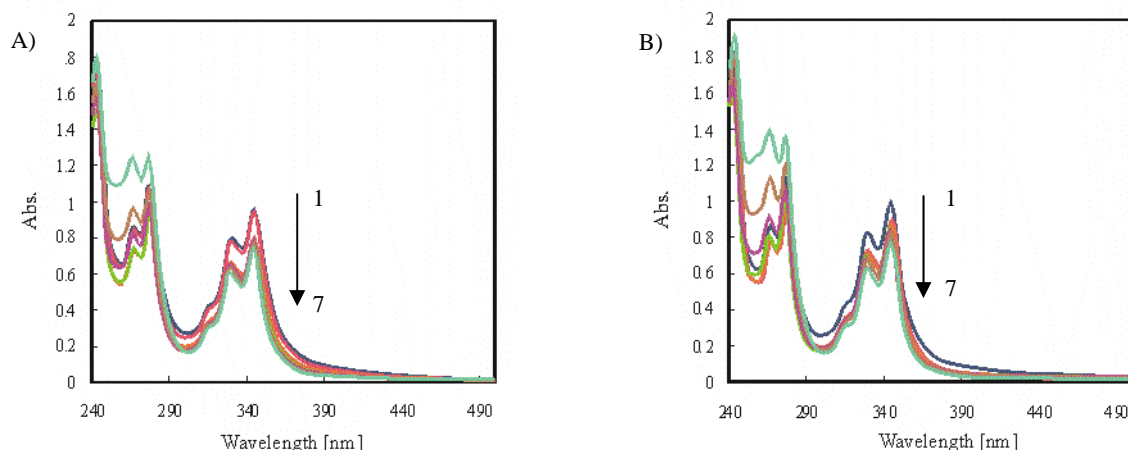


Fig. 4 UV-Vis spectra of **1** in a 10 vol.% DMSO aqueous solution (3.0×10^{-5} M) at various concentrations of dsDNA or ssDNA. A) dsDNA (1:0, 2: 9.375×10^{-9} , 3: 1.875×10^{-8} , 4: 3.75×10^{-8} , 5: 7.5×10^{-8} , 6: 1.5×10^{-7} , 7: 3.0×10^{-7} M), B) ssDNA (1:0, 2: 4.6875×10^{-8} , 3: 9.375×10^{-8} , 4: 1.875×10^{-7} , 5: 3.75×10^{-7} , 6: 7.5×10^{-7} , 7: 1.5×10^{-6} M).

ssDNA ; TAAAAATAG GCTATCCCTT ATTAAGTAAA ATAGGGAGTT (40 bp) and 2) dsDNA ; CTGAGTCCCA AATGTCCCAG CTGTTTTATG CTTTGTCTCT GTTCC CAGA GACCCTGAGT GTGGTCTAGA GTTGGGATGA GCATTGGTCT CTAATGGTTC TGAAATAATT GTATAT TCCT GCAAAAACAT TAAGTCTATT AGAAACCAGC TAATTTTATT TTGTCAITTT TATAGGTAAC ATATTCT GGT GCAGG (200 bp).

2.2.1 Spectra of 1 with DNA: For the fluorescence measurements, the excitation wavelength of the fluorescence spectra was 343 nm and excitation and emission slit were 5 nm. 10% DMSO was used as solvent for the **1** and DNA. When the DNA solution was added to the **1** solution (3.0×10^{-7} M), the spectra change was recorded. For the UV-Vis measurement, 10% DMSO was used as a solvent for the **1** and DNA. When the DNA solution was added to the **1** solution (3.0×10^{-5} M), the spectra change was recorded.

2.2.2 Spectra of intercalation reagent 2 with DNA: For the

fluorescence measurements, the excitation wavelength of the fluorescence spectra was 494 nm and excitation and emission slit were 5 nm. 10% DMSO was used as a solvent for the **2** and DNA. When the DNA solution added to the **2** solution, the spectra change was recorded.

3 RESULTS AND DISCUSSION

3.1 Interaction between 1 and DNA

Fig. 3 shows the fluorescent spectra of **1** alone and with ssDNA or dsDNA. The fluorescence intensity of monomer (at 377 nm) and excimer (at 479 nm) of the pyrene has been increased respectively when dsDNA was added to **1**. Moreover, the fluorescence intensity of **1** increased rapidly by addition of dsDNA (7.5×10^{-10} M) and then was saturated afterwards. On the other hand, an increase in the fluorescence intensity of **1** was not observed in an addition of ssDNA. The increase of the fluorescence intensity suggested the pyrene part of **1** intercalates between base

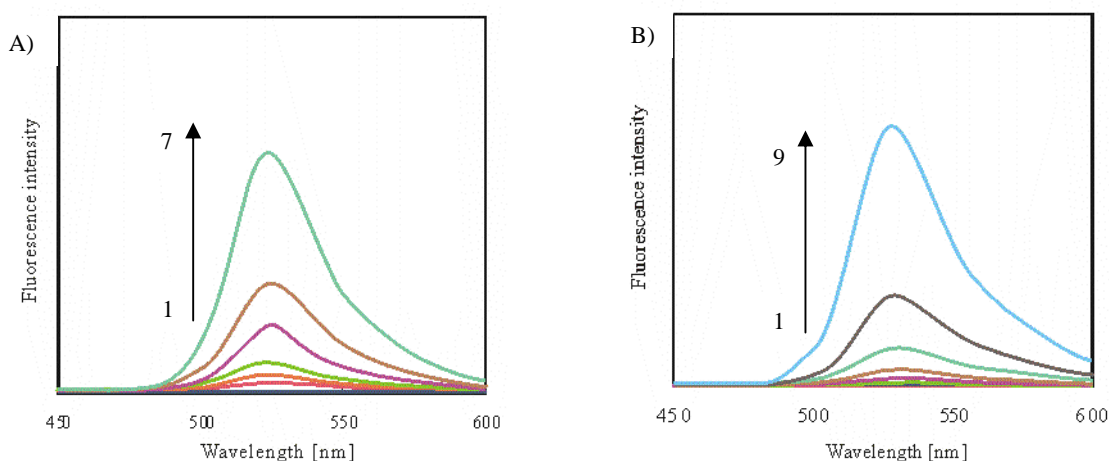


Fig. 5 Fluorescence spectra of **2** in a 10 vol.% DMSO aqueous solution at various concentrations of dsDNA or ssDNA. A) dsDNA (1:0, 2: 9.375×10^{-11} , 3: 1.875×10^{-10} , 4: 3.75×10^{-10} , 5: 7.5×10^{-10} , 6: 1.5×10^{-9} , 7: 3.0×10^{-9} M), B) ssDNA (1:0, 2: 4.6875×10^{-10} , 3: 9.375×10^{-10} , 4: 1.875×10^{-9} , 5: 3.75×10^{-9} , 6: 7.5×10^{-9} , 7: 1.5×10^{-8} , 8: 3.0×10^{-8} , 9: 6.0×10^{-8} M).

pairs of dsDNA when dsDNA was added. It also suggests that increase of the fluorescence intensity was not attributed by the inclusion with CyD cavity but by the intercalation with DNA base pairs because both monomer and excimer fluorescence intensities of pyrene were increased by the dsDNA addition.

Fig. 4 shows the UV-Vis spectra of **1** alone and with ssDNA or dsDNA. The absorbance of **1** was decreased by addition of dsDNA or ssDNA and decrease of an absorbance of dsDNA was slightly larger. It was suggested that **1** interacted with dsDNA easier than that of ssDNA.

3.2 Interaction between **2** and DNA

Fig. 5 shows the fluorescent spectra of **2** alone and with ssDNA or dsDNA. The fluorescence intensity has been increased when dsDNA was added to **2**. In addition of ssDNA, the increase of the fluorescent intensity of **2** was not seen when the DNA concentration is 7.5×10^{-10} M and after that the fluorescence intensity was increased as well as dsDNA. Thus, it has been understood that **2** can discriminate between dsDNA and ssDNA.

4 CONCLUSION

Di-pyrene modified γ -CyD **1** was synthesized, and the interaction with dsDNA and ssDNA was examined by various spectrum measurements. Fluorescence intensity of **1** increased only for dsDNA in a fluorescent spectrum measurements and it was understood that there was an interaction with DNA in the UV-Vis spectrum measurement. In addition, the discrimination ability of dsDNA and ssDNA of **1** is better than **2** when DNA concentration is high. Moreover, γ -CyD works as scaffold of the pyrene and facilitates intercalation more. From these results, di-pyrene modified γ -CyD suggested that has the intercalation ability only in dsDNA, and be effective as a new DNA discrimination reagent.

References

- [1] N. Matsumura, M. Kagaya, Y. Kondo, Y. Akagami and F. Hamada, *Int. J. Soc. Mater. Eng. Resour.*, **16**, 16, (2009).
- [2] M. Narita, F. Hamada, I. Suzuki and T. Osa, *J. Chem. Soc., Perkin Trans. 2*, 2751, (1998).
- [3] C. Schneeberger, P. Speiser, F. Kury, R. Zeillinger, *PCR Methods and Applications*, **4**, 234, (1995).
- [4] M. A. Piatyszek, N. W. Kim, S. L. Weinrich, K. Hiyama, E. Hiyama, W. E. Wriggi, and J. W. Shay, *Methods in Cell Science*, **17**, 1, (1995).
- [5] F. Karlsen, H. B. Steen, J. M. Nesland, *Journal of Virological Methods*, **55**, 153, (1995).
- [6] V. Farrelly, F. A. Rainey, E. Stackebrandt, *Applied and Environmental Microbiology*, **61**, 2798, (1995).
- [7] T. Kishida, Y. Tamaki, K. Kuroki, M. Fukuda, W. Wang, *Jpn. J. Legal Med.*, **49**, 299, (1995).
- [8] D. M. Schmidt, J. D. Ernst, *Anal. Biochem.*, **232**, 144, (1995).
- [9] J. C. Law, E. A. Facher, A. Deka, *Anal. Biochem.*, **236**,

373, (1996).

[10] J. Skeidsvoll, and P. M. Ueland, *Anal. Biochem.*, **231**, 359, (1995).

[11] A. Ueno, F. Moriwaki, T. Osa, F. Hamada and K. Murai, *Tetrahedron*, **43**, 1751, (1987).

[12] K. Fujita, T. Tahara, T. Koga, T. Imoto, *Bull. Chem. Soc. Jan*, **62**, 3150, (1989).

[13] Y. S. Klausner and M. Bodansky, *SYNTHESIS*, 453, (1972).

Extraction ability of rare metals with diethylphosphatethiacalix[6]arene

Yusuke Hashitani*, Manabu Yamada*, Yoshihiko Kondo**,
Atsushi Shibayama***, Fumio Hamada**

* Department of Material-Process and Applied Chemistry for Environments, Faculty of Engineering and Resource Science, Akita University, Akita 010-8502, Japan.

** Department of Life Science, Faculty of Engineering and Resource Science, Akita University, Japan.

*** Department of Material-Process Engineering and Applied Chemistry for Environments, Faculty of Engineering and Resource Science, Akita University, Japan.

m9008033@wm.akita-u.ac.jp

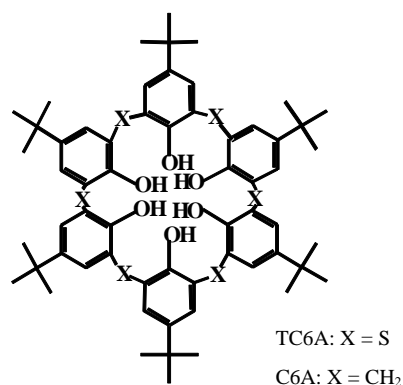
Abstract: Novel thiacalix[6]arene derivative was synthesized by an introduction of diethylphosphate group containing hetero atom at the upper rim of *p-tert*-butylthiacalix[6]arene (TC6A). The extraction ability of eight kinds of rare metals (Y, Zr, Rh, Pd, Ba, La, Ce, and Pt) was considered from liquid-liquid extraction method with diethylphosphatethiacalix[6]arene (**1**) derivative in all species (mixed) or single metal containing solutions. The titled compound showed selective extraction capabilities of Pd and Zr cations from mixed solution. On the other hands, extraction ability of only Pd cation was exhibited from single solution. The extractability of rare metals with TC6A was also compared with the extractability of ones with **1** in mixed or single solution. In single solution, the highest extractive species of the metal cations with those compounds was Pd cation. In the mixed solution, **1** showed the high selectivity of rare metal cations, but TC6A showed a small extractability of all rare metal cations examined.

Key word: Calix[*n*]arene, Thiacalix[*n*]arene, Rare metal

1 INTRODUCTION

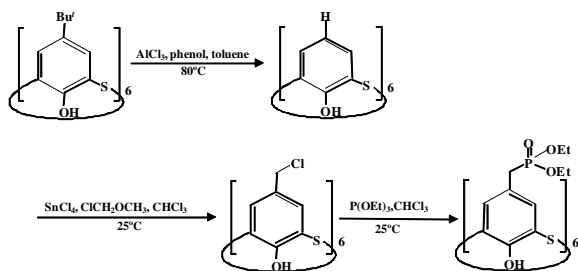
In molecular recognition chemistry and supramolecular chemistry, calixarenes and their derivatives are studied as one of the most important materials. Thiacalixarenes as a counterpart of calixarenes are versatile materials because their bridging sulfide moieties have a high affinity toward wide range of the metal cations¹, have been attracted much attention as host molecules (Scheme 1).² We have been mainly investigated thiacalix[6]arene (TC6A) possessing wide cavity, hetero atoms, oxygen atom, and sulfur atom. High selective and efficient extractability toward rare metals from platinum group metals (PGM) solution³ is shown by the modified TC6A with various functional groups containing donor atom (hetero atoms) at the lower rim (the phenolic hydroxyl groups).⁴

There are rare metals that have been used in various fields, for example, electronic materials in high-tech industry. In addition, rare metals are difficult to bring out purely as economical and technical.⁵ In our country, rare metals as original resource from mine are too less, but it is many rare metals as second resource from waste of high-tech products. Currently, developments of technology bringing out rare metals as second resource is



Scheme 1. The structure and abbreviations for Thiacalix[6]arene (TC6A) and Calix[6]arene (C6A).

well-practiced, and we have been studying for the foregoing study as extract agents. However, the lower rim modified TC6A have a problem that is difficult to keep cone conformation due to lacking of hydrogen bond between hydroxyl groups of TC6A. Therefore, the introduction of functional group containing hetero atom to the upper rim,



¹H-NMR (300 MHz, CDCl₃) : 1.21 [36H, t, CH₃], 2.95 [12H, d, CH₂-P], 3.98 [24H, m, CH₂-O], 7.49 [12H, s, Ar-H], 8.75 [6H, s, OH]
 IR : 1049.1, 1026.7 (P-O-C), 1238.7 (P=O) cm⁻¹.

Scheme 2. Synthesis of diethylphosphatethiacalix[6]arene (**1**).

para-position of TC6A, is able to discuss extractability of TC6A with cone conformation. In industrials, the extract agents containing phosphate group (e.c. TBP : tributylphosphate) are used previously, which is well-known that these extract agents have affinities for Au and Pt. In this study, we aimed the modification of phosphate group at the upper rim of TC6A (Scheme 2),⁶ and the extractability of eight kinds of rare metals (Zr, Ce, Ba, Rh, Pd, Pt, La and Y) was studied with **1** as the upper rim derivate of TC6A by using liquid-liquid extraction from single metal or all species (mixed) containing solution. The extractability of rare metals with TC6A was also compared with the extractability of ones with **1** in single or mixed solution.

2 RESULTS AND DISCUSSION

2.1 Solvent extraction

In extraction experiments, the three kinds of aqueous phase (PGM solution, single metal contained solution, all species contained solution) were used. In the solvent extraction of various metal cations with **1** or TC6A from an aqueous phase to a chloroform phase, the concentration of the metal cations extracted into organic phase, [Metal]_{org}, as **1** or TC6A complex are calculated by Eq. 1,

$$[\text{Metal}]_{\text{org}} = [\text{Metal}]_{\text{aq,init}} - [\text{Metal}]_{\text{aq}}, \quad (1)$$

where [Metal]_{aq,init} and [Metal]_{aq} are the initial and final concentration of the metal cation in the aqueous phase at $t = 0$ and 24 h, respectively. The percent extraction, $E\%$, was calculated by Eq.2.

$$E\% = [\text{Metal}]_{\text{org}} / [\text{Metal}]_{\text{aq,init}} \times 100\% \quad (2)$$

The original PGM solution was fifty times diluted with water, which was used as PGM solution in extraction (Table 1). In extraction of rare metals from the three kinds of aqueous phase, the extracting conditions was $[\mathbf{1} \text{ or TC6A}]_{\text{Total}} / [\text{Metal}]_{\text{Total}} = 1$. In single and mixed solution, concentration of one metal cation was 10 ppm, and the pH of aqueous phase was controlled from

pH 1 to 4 treated by nitric acid or hydrochloric acid and sodium hydroxide (Table 1). After solvent extraction, the total concentration of the metal species remaining in the aqueous phase, [Metal]_{aq}, was measured by inductively coupled plasma atomic emission spectrometry (ICP-AES).

All extraction experiments have done twice. The metal concentration in the aqueous phase, [Metal]_{aq}, were determined using the average of twice tried.

Table 1. The concentration of fifty times diluted PGM solution and each metal cations examined

Entry	Metal cation	mM (mmol/L)
1	50 times diluted PGM solution	2.92
2	Y (10 ppm)	0.1120
3	Zr	0.1096
4	Rh	0.0972
5	Pd	0.0940
6	Ba	0.0728
7	La	0.0720
8	Ce	0.0714
9	Pt	0.0512

2.2 Extraction of the metal cations from PGM solution

Fig. 1 shows the $E\%$ for the metal cations from PGM solution at pH 0.8. **1** had high selective and high efficiency extractability of Zr and Pd cations. In addition, it was shown that the extractability of Pd cation was the highest ($E\% = 87.43\%$), the extractability of Zr cation was the second highest ($E\% = 59.85\%$). In contrast, **1** showed small extractability of the other metal cations with under ca. 5%. On the other hand, the extractability of the metal cations with TC6A was also examined. TC6A had selective extractability of Pd cation and little selective extractability of Zr cation. The extractability of the metal cations with **1** was compared with those of ones with TC6A in PGM solution. These results showed that both **1** and TC6A had selectivity for Pd and Zr cations, where extractability of TC6A for those metal cations is very small than those of **1**.

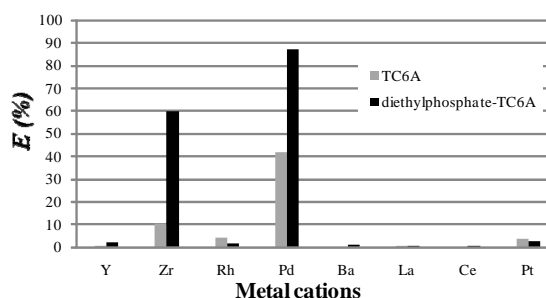


Figure 1. Extraction of the metal cations with TC6A and diethylphosphate derivate from PGM solution.

2.3 Extraction of the metal cations from solution containing single metal

Fig. 2 shows the $E\%$ for the metal cations from single solution. **1** had selective extractability of Pd cation. It was shown that the extractability of Pd cation was the highest at pH 2 ($E\% = 63.60\%$). On the other hand, the extractability of the other metal cations was under ca. 10%. In contrast, it was shown that TC6A had no selectivity for the metal cations, where extractability was under ca. 20% for other metal cations examined. On the other hand, the extractability of the metal cations with **1** was compared with the extractability of ones with TC6A in single solution. It was shown that selectivity for Pd cation by **1** was nine times. The modification of the upper rim of TC6A with diethylphosphate group seems to work for the metal extraction.

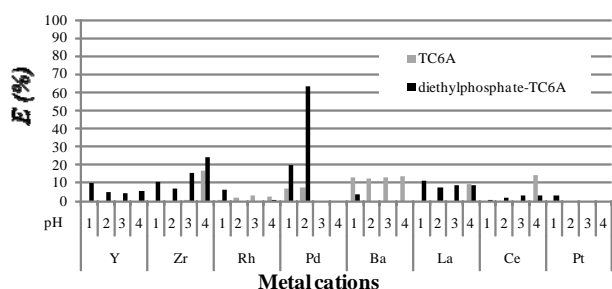


Figure 2. Extraction of the metal cations with TC6A and diethylphosphate derivate from single solution.

2.4 Extraction of the metal cations from solution containing all species

Fig. 3 shows the $E\%$ for the metal cations from mixed solution. **1** had high selective and high efficiency extractability of Pd and Zr cations. It was shown that the extractability of Pd cation was the highest at pH 3 ($E\% = 71.56\%$), the Zr cation was the second highest at pH 4 ($E\% = 68.13\%$). Additionally, the extraction rates at pH 3 and 4 are higher than those at pH 1 and 2. This is why that aqueous phase contained many hydroxide ions that work as counter anion of the metal cation more than at low pH case. On the other hand, the extractability of the metal cations with TC6A was also examined, it can be seen that TC6A had small extractability of the metal cations with under ca. 25%. The extractability of the metal cations with **1** was compared with the extractability of ones with TC6A in mixed solution. It was shown that selectivity for Pd and Zr cations rose up drastically compared with those of TC6A.

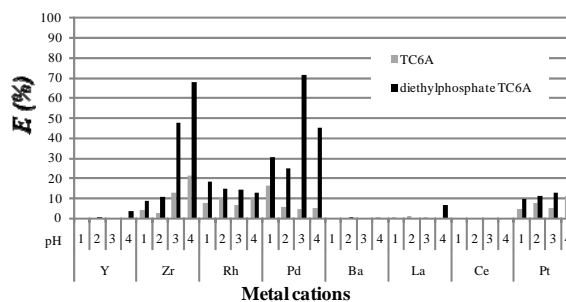


Figure 3. Extraction of the metal cations with TC6A and diethylphosphate derivate from mixed solution.

3 CONCLUSION

We have studied the extractability of **1** for rare metals containing such as single solution, mixed solution and PGM solution. It was shown that **1** had selective extractability of Pd and Zr cations. In single solution, **1** showed selectivity for Pd cation. In mixed solution and PGM solution, **1** showed selectivity for Pd and Zr cations. Additionally, the extractability of the metal cations with **1** was compared with the extractability of ones with TC6A in mixed solution, the extractability of Pd and Zr cations with **1** was up drastically. In this work, we demonstrated the useful modification at the upper rim of TC6A, which the extractability for metal cations get larger than that of native TC6A.

Acknowledgment

This study was supported by the Industrial Technology Research Grant Program in 2006 from the New Energy and Industrial Technology Development Organization (NEDO) of Japan.

References

- [1] (a) Endo, K., Kondo, Y., Aoyama, Y., Hamada, F., *Tetrahedron Lett.*, **44**, 1355, (2003); (b) Kondo, Y., Endo, K., Hamada, F., *Chem. Commun.*, 711, (2005); (c) Yamada, M., Kondo, Y., Iki, N., Kabuto, C., Hamada, F., *Tetrahedron Lett.*, **49**, 3906, (2008)
- [2] (a) Morohashi, N., Narumi, F., Iki, N., Hattori, T., Miyano, S. *Chem. Rev.*, **106**, 5291, (2006); (b) Iki, N., Morohashi, N., Narumi, F., Miyano, S., *Bull. Chem. Soc. Jpn.*, **71**, 1597, (1998); (c) Iki, N., Narumi, F., Fujimoto, T., Morohashi, N., Miyano, S., *J. Chem., Perkin Trans. 2*, 2745, (1998); (d) Morohashi, N., Iki, N., Sugawara, S., Miyano, S., *Tetrahedron*, **57**, 5557, (2001)
- [3] Harjanto, S., Cao, Y., Shibayama, A., Naitoh, I., Nanami, T., Kasahara, K., Okumura, Y., Lin, K., Fujita, T., *Materials Trans.*, **47**, 1, (2006)
- [4] Yamada, M., Shibayama, A., Kondo, Y., Hamada, F., *Int. J. Soc. Master. Eng. Resour.*, **15**, 13, (2007)
- [5] Ishikawa, I., Sato, T., *Bunseki Kagaku*, **50**, 107, (2001)
- [6] Kasyan, O., Swierczynski, D., Drapailo, A., Suwinska, K., Lipkowaki, J., Kalchenko, V., *Tetrahedron Lett.*, **44**, 7167, (2003)

H₂O₂ Oxidation of 1,4-Dihydropyridines over Mg²⁺ Ion Exchanged Clinoptilolite and Solventless Solid State Acid Decomposition of Ester to 3,5-Pyridinedicarboxylic acid

Takashi Yamashiro, Kanji Sato, Masayuki Nomura, Masataka Ogasawara, Sumio Kato and Shinichi Nakata

Department of Applied Chemistry for Environments, Faculty of Engineering and Resource Science, Akita University
1-1 Tegatagakuen-machi, Akita, 010-8502, Japan

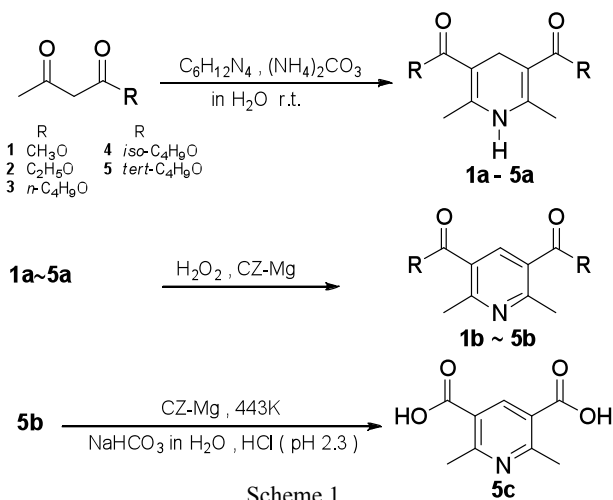
yamashiro@ac3.as.akita-u.ac.jp

Abstract: The acid property of alkali and alkaline earth cation exchanged clinoptilolites were observed by micro-calorimetry of NH₃ adsorption at 473K. The reaction rates on decomposition of *tert*-butyl acetate (TBA) over clinoptilolites was proportional to the acid strength. 1,4-Dihydropyridines were oxidized to corresponding pyridines in high yields at room temperature by H₂O₂ aqueous solution over Mg²⁺ ion exchanged clinoptilolite (CZ-Mg) in acetone. Solventless acid ester decomposition of Di-*tert*-butyl 3,5-pyridinedicarboxylate to 3,5-Pyridinedicarboxylic acid was effected using CZ-Mg at 443K.

Key Words: Mg²⁺ ion exchanged clinoptilolite, H₂O₂ oxidation, solid state acid decomposition, 1,4-Dihydropyridines

1 INTRODUCTION

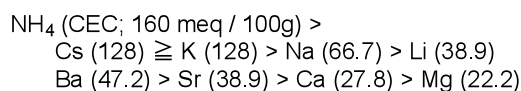
With a view to green chemistry, Hantzsch 1,4-Dihydropyridines (DHPs) were produced by the facile reaction acetoacetates with hexamethylenetetramine in aqueous ammonium carbonate solution at room temperature[1]. DHPs were oxidized to corresponding pyridines by the clean oxidizing reagent of H₂O₂ aqueous solution[2] with Mg²⁺ ion exchanged clinoptilolite (CZ-Mg) in acetone. CZ-Mg could also catalyze acid of ester decomposition of Di-*tert*-butyl 3,5-pyridinedicarboxylate for 3,5-Pyridinedicarboxylic acid in the solventless condition at 443K. The products could be readily separated and were of high purity. In this paper we report environmentally benign protocols using zeolites.



2 EXPERIMENTS and RESULTS

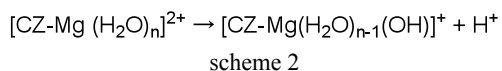
The natural clinoptilolite (CZ) of high silica zeolite, produced in Futatsui, Akita Prefecture, and its chemically treated specimens have found utility as catalysts for skeletal isomerization of cyclohexene[3] and adsorption materials for TLC[4]. The cation exchange capacities (CEC) of CZ were obtained by the easy Shollenberger's method.

A 10 g specimen (CZ-NH₄) obtained by treatment with 1 mol dm⁻³ CH₃COONH₄ solution was extracted by treatment with 80 mL of aqueous solution of 1 mol dm⁻³ alkali and alkaline earth cation chlorides under mild condition for a week at room temperature, respectively. The NH₄⁺ extracted from the specimen was analyzed and regarded as the CEC of the cation exchanged CZ. The cation exchanged behavior of CZ depends upon the nature of the alkali and alkaline earth cation hydrated ionic radius as follows:



The specimens for catalysis were filtered and washed with water and calcined at 693K for 1 hour to give alkali and alkaline earth cation exchanged CZs (CZ-M⁺ or CZ-M²⁺). The acid amount of CZs decreased relative to the original specimen owing to proton exchanged to the alkali and alkaline earth cation, in the case of CZ-NH₄ however, the acid amount increased owing to production of H⁺ by decomposition of NH₃. CZ-Mg showed strong acid point on the surface of zeolite owing to the dissociation of hydrated divalent cation[5]

(scheme2).



Some CZs were estimated for acid catalysis activity in decomposition of TBA for acid catalysis. The acid strength and amount of CZs was determined by micro-calorimetry of NH_3 adsorption, and Hammett acidity function (H_0) was additionally determined for reference. The TBA decomposition activity of the CZs was proportional to acid strength except in the case of those with little acid such as CZ-K. CZ-Mg retains a suitable amount of acid and acid strength, and is therefore superior for solid acid catalysis to the other CZs (Table 1).

Table 1. Acid properties and activity for TBA decomposition of ion-exchanged CZs

	CZ	CZ-NH ₄	CZ-K	CZ-Ca	CZ-Mg
Acid amount (mmol / g) ^{a)}	0.45	1.6	0.03	0.08	0.24
Acid strength (kJ / mol) ^{a)}	112	116	117	143	152
Hammett acidity function (H_0)	-3.0 - +1.5	-5.6 - +3.0	-5.6 - -3.0	-8.2 - -5.6	-5.6 - -3.0
Amount of 2-methylpropene ^{b)} (mL / g · min)	43	44	39	57	60

a) Determined by micro-calorimetry of NH_3 adsorption at 473 K.

b) The decomposition reaction of TBA was carried out at 473 K.

The reactions of some acetoacetates and hexamethylenetetramine in ammonium carbonate aqueous solution under stirring at room temperature gave 2,6-Dimethyl-1,4-dihydropyridines (DHPs ; **1a** - **5a**). The reagents have been utilized for oxidation of DHPs : include nitric acid, photooxidation[6], air oxidation[1], and sulfur / microwave irradiation[7]. The H_2O_2 oxidation of **2a** to **2b** was more strongly promoted by CZ-Mg than $6 \text{ mol dm}^{-3} \text{H}_2\text{SO}_4$. The rates of conversion were as follows : H_2O_2 in the absence of catalysis : 7%, 24 h ; $6 \text{ mol dm}^{-3} \text{H}_2\text{SO}_4$: 85%, 2h ; CZ-Cs : 39%, 2h ; CZ-Mg : 96%, 2h ; CZ-Mg : 100%, 3h (Fig. 1).

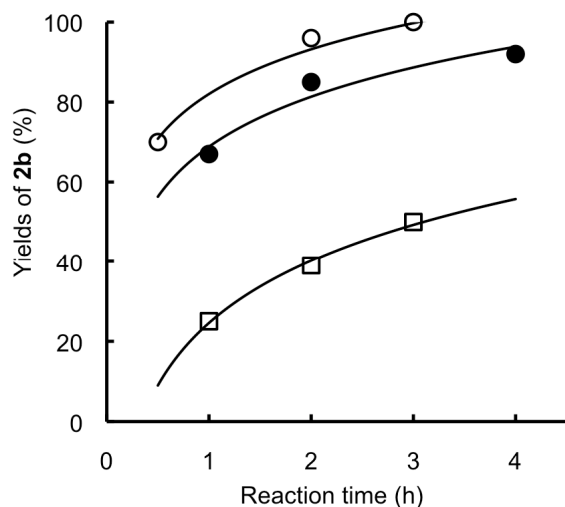


Fig. 1. The rate of H_2O_2 oxidation of **2a** to **2b**. ○: CZ-Mg, ●: $6 \text{ mol dm}^{-3} \text{H}_2\text{SO}_4$, □: CZ-Cs

General procedure for the oxidation of DHPs : A mixture of DHPs (2 mmol) in acetone 50 mL , 30% H_2O_2 aqueous solution 10 mL and CZ-Mg 0.5 g was placed in an Erlenmeyer flask and stirred with a glass sealed magnetic spin bar at room temperature for 3h , The reaction mixture was filtered and acetone was removed by evaporation. The residual mixture was poured in ice-water. The precipitate was filtered and dried to afford the corresponding pyridine derivative with colorless pure compound (Table 2).

Table 2. H_2O_2 oxidation of DHPs to pyridines with CZ-Mg

Entry	R	Product ^{a)}	Yield / %	m.p. / K
1	CH_3	1b	95 >	372 - 373
2	C_2H_5	2b	95 >	346 - 347
3	<i>n</i> - C_4H_9	3b	95 >	303 - 304
4	<i>iso</i> - C_4H_9	4b	95 >	305 - 306
5	<i>tert</i> - C_4H_9	5b	95 >	384 - 385

a) Products were accorded with the assigned structures based on elemental analyses and $^1\text{H-NMR}$ and IR spectra.

A solventless preparation of 2,6-Dimethyl-3,5-pyridine dicarboxylic acid **5c** with CZ-Mg : **5b** 1.00 g (33 mmol) and CZ-Mg 2 g was mixed thoroughly using a mortar. The mixture was transferred into a test tube and heated at 443 K for 4h. The product was dissolved in saturated sodium hydrogen carbonate aqueous solution, and filtered. The acidity of the filtrate was adjusted acidity to pH 2.3. The precipitate was filtered and dried to give the high purity **5c**, 63%. The data of **5c** are as follows : m.p. 600-601 K . IR (KBr) cm^{-1} : 2454 (COOH) , 1719 ($\nu\text{C=O}$) , 1544 (pyridine ring) , $^1\text{H-NMR}$ (DMSO) δ : 2.77 (6H, s) , 8.57 (1H, s) . Anal. Calcd for $\text{C}_9\text{H}_9\text{O}_4\text{N}$: C, 55.39; H, 4.65; N, 7.18. Found: C, 55.56; H, 4.90; N, 7.22.

References

- [1] M. Nomura, S. Nakata, F. Hamada, *Nippon Kagaku Kaishi*, **2002**, 141.
- [2] K. Sato, M. Aoki, J. Takagi, R. Noyori, *J. Am. Chem. Soc.*, **119**, 12386 (1997).
- [3] M. Nomura, G. Saito, S. Nakata, Y. Morimura, *Nippon Kagaku Kaishi*, **1994**, 524.
- [4] M. Nomura, S. Nakata, N. Abe, *Nippon Kagaku Kaishi*, **1995**, 454.
- [5] J. W. Ward, *J. Phys. Chem.*, **72**, 4211 (1968).
- [6] O. Mitunobu, S. Matumoto, M. Wada, H. Masuda, *Bull. Chem. Soc. Jpn.* **45**, 1453 (1972).
- [7] R. S. Varma, D. Kumar, *J. Chem. Soc., Perkin Trans. 1*, **1999**, 1755.

Regulation mechanisms of aryl hydrocarbon receptor by molecular chaperone HSP90

Noriko Tsuji¹⁾, Fumiaki Ohtake²⁾, Shigeaki Kato²⁾, Kei Ohtaka¹⁾,
Kazuhiro Sekine¹⁾, Hiroshi Kubota¹⁾ and Hideaki Itoh¹⁾

¹⁾ Department of Life Science, Faculty of Engineering and Resource Science, Akita University 1-1 Tegata Gakuen Town, Akita 010-8502, Japan

²⁾ Institute of Molecular and Cellular Biosciences, University of Tokyo, 1-1-1 Yayoi, Bunkyo-ku, Tokyo 113-0032, Japan

itohh@ipc.akita-u.ac.jp

Abstracts: The aryl hydrocarbon receptor (AhR) is a ligand-activated transcription factor that binds DNA in the form of a heterodimer with the AhR nuclear translocator (Arnt). It has been reported that ligand free AhR binds to molecular chaperon HSP90, XAP-2, and p23 in the cytoplasm. Although it has been shown that HSP90 regulate translocation of the AhR to the nuclear, the precise activation mechanisms of the AhR has not yet been fully understood.

At the first, we analyzed whether AhR associate to HSP90 or not, using an AhR PAS domain (may be a ligand and HSP90 binding). We have expressed and purified GST-PAS domain. On the analysis of GST-pull down assay, HSP90 was bound to the GST-PAS domain in the absence of 3-methylcholanthrene (3-MC, one of the AhR ligandan), but not in the presence of 3-MC. These results showed that PAS domain could bound to the HSP90 *in vitro*. Then, we found that AhR and HSP90 colocalized in the nuclear of HeLa cells and Neuro 2A cells in the presence of 3MC. These results suggested that ligand bound AhR may be translocated to the nuclear both with HSP90.

We are now investigating the association and dissociation mechanisms of AhR to HSP90 using recombinant domains of AhR and HSP90.

Keywords: Dioxin, Aryl hydrocarbon receptor (AhR), molecular chaperone, HSP90

1. Introduction

The aryl hydrocarbon receptor (AhR), a ligand-activated member of the basic helix-loop-helix (b-HLH) family of transcription factors, binds with high affinity to the environmental toxin, such as 2,3,7,8-tetrachlorodibenzeno-*p*-dioxin (TCDD or dioxin) [1]. The AhR mediates most of the biological and toxicological responses caused by exposure to dioxins. In the absence of ligand, the AhR is present in the cytosol as a component of a complex with a dimer of the molecular chaperone heat shock protein (Hsp90), the cochaperone p23, and XAP-2 [2]. In the absence of ligand, Hsp90 binding is thought to

maintain the AhR in an inactive state, possibly, through association in the regions that overlap AhR Arnt binding sites (bHLH and PASA/B domains) [3]. The association with Hsp90 is required for the AhR to assume a conformation that is optimal for ligand binding. Upon ligand binding, the AhR translocates from the cytosol into the nucleus and forms a heterodimer with the AhR nuclear transporter.

A critical function of hsp90 in regulating the signaling actions of many client proteins is the shuttling of AhR to the nucleus in a conformation that would become transcriptionally active. For the AhR, hsp90 appears to be an

important participant in the translocation of the ligand-bound AhR complex containing at least hsp90 and hepatitis B virus X-associated protein 2 (XAP2). Within the nucleus, processes that are not fully understood mediate the dissociation of AhR from hsp90 and the formation of a heterodimer with Aryl hydrocarbon receptor nuclear translocator (Arnt). The AhR contains two repeats of the Per-Arnt-Sim (PAS) motif, the PASA and PASB domains. The PASB domain contains a ligand binding site and one of the Hsp90 binding sites. The PASB domain has been suggested to exert an inhibitory effect on AhR transformation and its deletion results in an AhR that is constitutively active with respect to its transformation/DNA binding and transcriptional activation functions.

Hsp90 appears to bind to the ligand-binding PASB and N-terminal DNA-binding bHLH domains and following ligand binding, remains associated with the AhR during nuclear translocation. Once in the nucleus, Hsp90 dissociates or is more likely displaced by Arnt from their overlapping binding sites in the AhR leading to formation of an active transcriptional dimer of AhR/Arnt [1]. The conversion of the AhR into its high affinity DNA binding form is termed transformation and is presumably driven by a ligand binding-mediated conformational change in the AhR.

It has not yet been fully understood translocation mechanisms of AhR. It is unclear whether HSP90 and AhR both translocate from cytoplasm to the nuclear or not in the cells. We investigated the localization of AhR and HSP90 in the presence or in the absence of ligand using HeLa and Neuro2A cells. We report here that AhR may localize in the nuclear both with HSP90 under the ligand bound form.

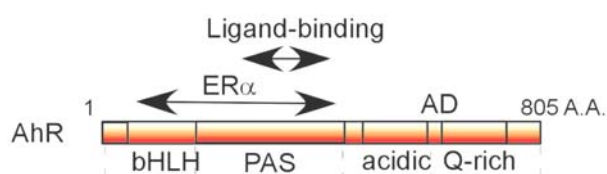


Fig. 1 Domain structure of AhR

2. Experimental

Protein Expression and GST pull-down assay. *E. coli* BL21 cells transformed by pGEX-5X-3 (GE Health Science) with GST alone, GST-PAS were cultured at 25°C in L-broth,

and GST alone or GST fusion proteins were expressed by adding 0.1 mM IPTG in the medium for 3 h. For the GST pull-down assays, GST alone, or GST fusion proteins bound to glutathione–Sepharose 4B (Nova Gen) were incubated at R.T. for 1.5 h with HSP90. The beads were recovered by centrifugation. After washing the beads, bound proteins were eluted by SDS-polyacrylamide gel electrophoresis (SDS-PAGE) sample buffer, analyzed on SDS-PAGE, and visualized by autoradiography.

Cell culture, transfection—Human cervical cancer cells -derived HeLa cells, and mouse neuroblastoma Neuro2A cells were cultured in phenol-red-free RPMI1640 containing 0.2% charcoal-stripped FBS, transfected with the receptor expression vectors. 100 IU/ml penicillin, and 0.1 mg/ml streptomycin (Sigma) at 37 °C in 95% air, 5% CO₂. Fluorescence micrographs were obtained directly from cells grown in plates that were transfected with 0.5 µg of FLAG-HA-AhR DNA using FuGENE reagent (Roche) according to the manufacturers instructions.

Cells were treated with 10 µM 3MC for 8h, after which the cells were washed with PBS and fixed with 2% (w/v) paraformaldehyde. After permeabilization, coverslips were blocked with 1% BSA, followed by incubation with goat anti-FLAG polyclonal antibody (1:500 dilutions, Santa Cruz Biotechnology) or rabbit anti-HSP90 polyclonal antibody (1:1,000 dilutions, as described previously [4]) for 2 h. After washing in PBS, the cells were incubated with secondary antibody. After washing, cells were incubated with fluorescently labeled secondary antibodies (either fluorescein, Alexa488, or Texas Red) directed at the appropriate IgG species for 1 h. Coverslips were mounted on microscope slides with Prolong Antifade. When observing colocalization with neutral lipid droplets, cells were incubated with 0.4 mM oleate complexed to 0.5% fatty acid-free BSA for 4 h before fixing them to cover-slips. Neutral lipid droplets were stained with Nile Red diluted 1:1000 for 10 min after antibody staining had been completed. After two further washes in PBS, the sections were counterstained with the DNA dye 4',6-dianidino-2-phenylindole (DAPI) at a concentration of 1 µg/ml for 5 min. The cells were finally mounted with a

mounting medium (Dako, Hamburg, Germany) and fluorescence was visualized with a Nikon ECRIPS100 inverted microscope with an argon laser delivering a wavelength of 488 nm to excite fluorescein or Alexa488 and a HeNe laser delivering 543 nm to excite Texas Red or Nile Red.

3. Results and Discussion

GST pull-down assay

At the first, we investigated whether GST-PAS binds to HSP90 using a GSR pull-down assay. In the assay, we used GST fused PAS domain of AhR and HSP90 (Fig. 2). There was no protein band on GST alone bound beads (HSP90) under the different temperature conditions (4°C and R.T.). On the contrary, we could determine the HSP90 on GST-PAS bounds beads both 4°C and R.T.

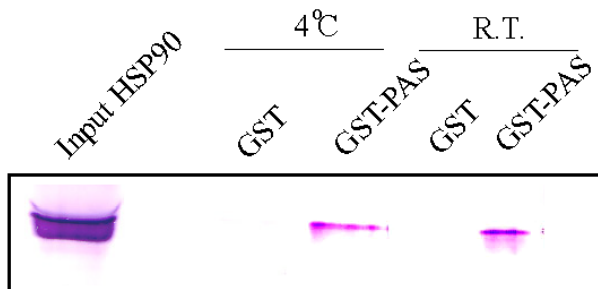


Fig. 2 GST pull-down assay

We could confirm that PAS domain of AhR might be able to bind molecular chaperone HSP90.

The Localization of AhR and HSP90

Then, we analyzed localization of AhR and HSP90 in the cells in the presence or absence of 3MC. In HeLa cells, Nuclear was faound as a blue fluorescence. AhR was localized in cytosol faound as a green fluorescence. HSP90 was also localized in the cytosol as a red fluorescence. When data were merged, localization of the AhR and HSP90 was found in the cytosol, not in the nuclear, as yellow (mixed green and red) fluorescence (Fig. 3).

However, after treatment with 3MC, AhR fluorescence was both found exclusively in the nuclear and cytosol. Treatment of the cells with 3MC exposure resulted in the AhR nuclear translocation. HSP90 was also detected in the nuclear and cytosol. We could detect the AhR and HSP90 complex as a yellow fluorescence in the nuclear under the ligand bound conditions.

Untill now, it has been thought that ligand bound AhR alone, dissociation from HSP90 after binding of ligand, may translocate to the nuclear. Our data suggested that ligand bound AhR was translocated from cytosol into nuclear with HSP90 as a complex.

We further investigated another cultured cells. In Neuro2A cells, we could obtain the same data as those of HeLa cells (Fig. 4).

In the present study, we found that AhR could translocate to nuclear both with HSP90.

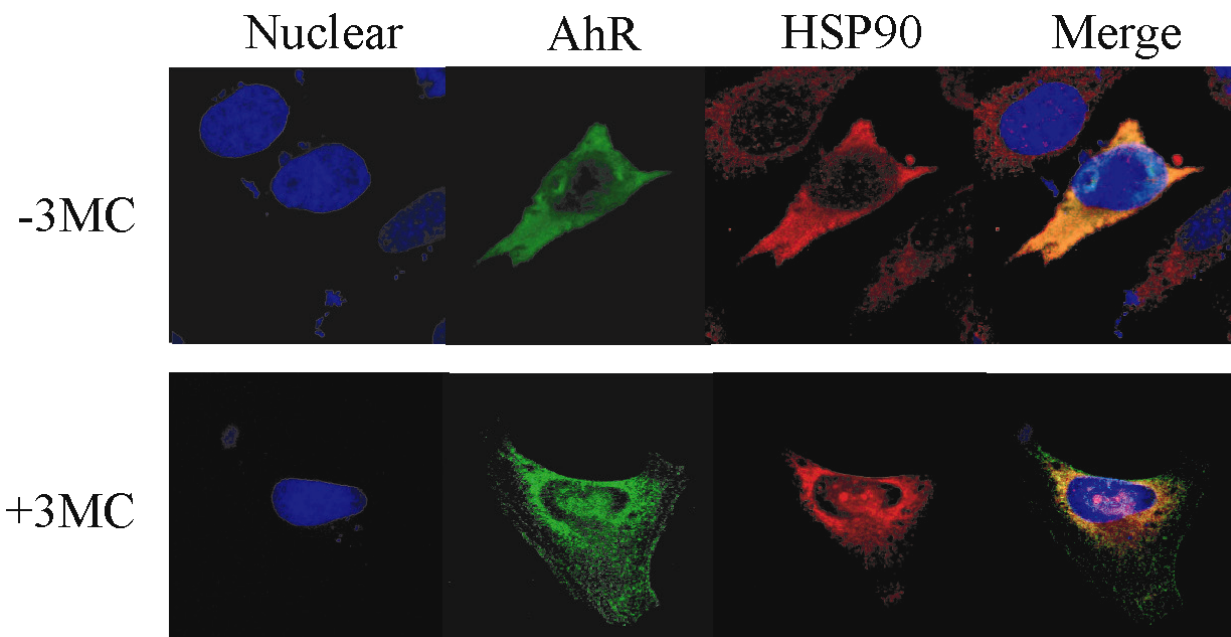


Fig. 3 Localization of the AhR and HSP90 in the HeLa cells

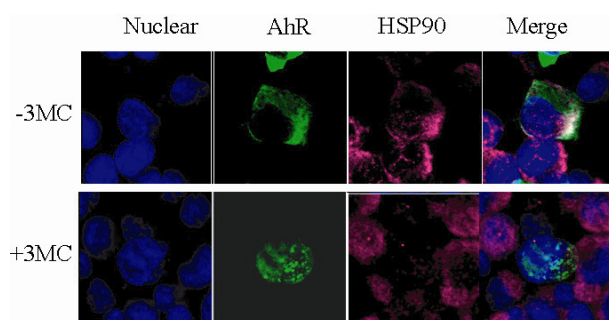


Fig. 4 Localization of the AhR and HSP90 in the Neuro2A cells

Conclusions

It has not yet been fully understood translocation mechanisms of AhR. We investigated the localization of AhR and HSP90 in the presence or in the absence of ligand using HeLa and Neuro2A cells. We report here that AhR may localize in the nuclear both with HSP90 under the ligand bound form.

References

- [1] Y. Fujii-Kuriyama, J. Mimura, "Molecular mechanisms of AhR functions in the regulation of cytochrome P450 genes" *Biochem. Biophys. Res. Commun.* 338, 311–317 (2005)
- [2] J-R. Petrusis, A. Kusnadi, P. Ramadoss, B. Hollingshead, and G-H. Perdew. "The hsp90 Co-chaperone XAP2 Alters Importin β Recognition of the Bipartite Nuclear Localization Signal of the Ah Receptor and Represses Transcriptional Activity". *J. Biol. Chem.* 278, 2677–2685, 2003
- [3] F.Ohtake, A. Baba, I. Takada, M. Okada, K. Iwasaki, H. Miki, S. Takahashi, A.Kouzmenko, K. Nohara, T. Chiba, Y. Fujii-Kuriyama, and S. Kato. "Dioxin receptor is a ligand-dependent E3 ubiquitin ligase". *Nature.* 466, 562–566, 2007
- [4] R. Ishida, .Takaoka, S. Yamamoto, T. Miyazaki, M. Otaka, S. Watanabe, A. Komatsuda, H. Wakui, K. Sawada, H. Kubota, and H. Itoh. "Cisplatin differently affects amino terminal and carboxyl terminal domains of HSP90". *FEBS Lett.* 582, 3879-83, 2008

Effect of preparation conditions of Ti ion species on structural properties of TiO₂ pillared mica.

Shigeaki Kitabayashi, Yoshitaka Ehara, Takayoshi Shindo, Sentaro Ozawa

Department of Engineering in Applied Chemistry, Faculty of Engineering and Resource Science, Akita University, 1-1,
Tegata-Gakuen-Cho, Akita, 010-8502 Japan

skv@ipc.akita-u.ac.jp

Abstract: TiO₂ pillared mica was prepared using Ti ion species as TiO₂ precursor. The titanium ion species were obtained by an addition of several titanium alkoxides to an aqueous solution of CH₃COOH, with different CH₃COOH/Ti ratios and temperatures. The structure and properties of the TiO₂ pillared mica was studied by X-ray diffraction, N₂ adsorption, FT-IR and TG-DTA. After calcined at 500°C, the BET surface area of samples varied between 250 and 460 m²/g. The sample prepared using titanium tetraethoxide as titanium source possessed well ordered structure and higher BET surface area. The basal spacing of TiO₂ pillared mica was increased with the decrease in CH₃COOH/Ti ratio and the increase in temperature of preparation of titanium ion species, while the degree of ordered structure of pillared mica was decreased.

Key words: TiO₂ pillared mica, Titanium ion species, Pillared structure

1 INTRODUCTION

Pillared clays are two-dimensional zeolite-like materials prepared by exchanging cations located between layers of clays with bulky metal polyoxyocations followed by calcination. The intercalated polycations increase the basal spacing of the clays and they are converted to metal oxide pillars by heat treatment that keep the clay layers apart. The increasing number of studies on pillared clays is in the field of applications such as heterogeneous catalysts, catalyst supports, adsorbents and environmental uses.

TiO₂ pillared clays have attracted much attention as potential materials for photocatalysts. TiO₂ has photoinduced strong oxidizing power and has been used practically as photocatalyst material. TiO₂ pillared clays show higher adsorption ability than pure TiO₂ due to its large specific surface area, and this adsorption property accelerates photocatalytic reactions. In addition, the interlayer surface of pillared clays is generally hydrophobic, which is an advantage to adsorb and enrich diluted hydrophobic organic compounds in water (Ref. [1]). Especially, using fluorine mica as host clay results in higher photocatalytic activity toward highly hydrophobic and stable organic pollutant than a conventional

pure TiO₂ photocatalyst (Ref. [2]).

The physicochemical properties of the TiO₂ pillared clays depend on several synthesis parameters, including the concentration of the metal ion, the temperature, the method of preparation, and the nature of the host clay (Ref. [3]). Titania sol or titanium ion species, *i.e.* precursors of TiO₂ pillar, have been prepared by hydrolysis of TiCl₄ or titanium alkoxide with acid (HCl, CH₃COOH etc.). Unlike the aluminum polycations, titanium ion species have no distinct metastable structure. Therefore, the preparation of TiO₂ pillared clays with well-ordered structure, which is indispensable for shape selective ability, is difficult. Additionally, TiO₂ particles in pillared clays synthesized by a conventional method are amorphous or poorly crystallized anatase, which should exhibit lower activity than highly crystallized TiO₂ anatase. For the application of TiO₂ pillared clays as photocatalysts with high activity and shape selectivity, improvements in structural and textural properties are strongly required.

In this study, TiO₂ pillared mica samples were prepared by using synthetic fluoro-tetrasilic mica as mother clay. Because of its large cation exchange capacity (CEC), it is expected that the amount and distribution of TiO₂ pillars introduced in interlayers of the mica can be widely controllable. Ti ion

species as precursors of TiO₂ pillars were obtained by hydrolyzing several titanium alkoxides in aqueous solution of acetic acid, with different CH₃COOH/Ti ratios and temperatures. In particular, higher CH₃COOH/Ti ratio was employed compared with conventional method (usually CH₃COOH/Ti=24). Effect of preparation conditions of titanium ion species on the structural properties of TiO₂ pillared mica was investigated by characterization using XRD, N₂ adsorption, FT-IR and TG-DTA.

2 EXPERIMENTAL

2.1 Preparation of TiO₂ pillared mica

Titanium tetraethoxide (Ti(O-Et)₄), titanium tetra-*i*-propoxide (Ti(O-*i*Pr)₄) and titanium tetra-*n*-butoxide (Ti(O-*n*Bu)₄) was used as Ti sources. A clear solution of titanium ion species was obtained the addition of the Ti source to an aqueous solution of acetic acid (80 wt%) at 20, 30, 40, 50, 60 or 75°C for 1.5 h. Molar ratio of acetic acid to titanium alkoxide were varied from 10 to 70. Synthetic fluoro-tetrasilic mica (NaMg_{2.5}Si₄O₁₀F₂, Topy Ind., Co.) was suspended in distilled water (1 wt%) and kept stirred at room temperature for 24 h to swell the mica. The solution of titanium ion species was added to the suspension of mica (Ti/mica=22 mmol/g, Ti/CEC=44), and the mixture was stirred for 3 h at room temperature. Then, the solid material products were separated by a centrifugation at 3700 rpm, washed several times with distilled water, and dried in vacuum. Dried samples, *i.e.* the precursor of TiO₂ pillared mica, were calcined at 500°C in air for 2 h to yield TiO₂ pillared mica samples.

2.2 Characterization

X-ray diffraction patterns were recorded on a Rigaku RAD-C system, Rigaku Co. Ltd. using CuK α radiation. Basal spacing of TiO₂ pillared mica samples was calculated from (001) reflection. Nitrogen adsorption-desorption isotherms were measured at 77K (BELSORP18, BEL JAPAN inc.). Specific surface area and pore size distribution were calculated from adsorption isotherm by B.E.T. method and MP method, respectively. The FT-IR spectra were measured on a Spectrum 2000 (Perkin Elmer Japan Co., Ltd.) using KBr technique. TG-DTA measurements were carried out at a heating rate of 10 K/min using a Rigaku TG-DTA 8120.

3 RESULTS AND DISCUSSION

Preparation and intercalation of titanium ion species into interlayers of the mica were carried out under various conditions. Typical experimental conditions and physical properties of TiO₂ pillared mica samples calcined at 500°C are

Table 1 Preparation conditions of Ti ion species, basal spacing and specific surface area of calcined TiO₂ pillared mica.

Ti precursor	CH ₃ COOH/Ti [-]	Temp. [°C]	d(001) [nm]	S(BET) [m ² /g]
Ti(O- <i>i</i> Pr) ₄	10	50	3.65	249
	25	50	2.98	281
	50	20	2.55	373
	50	30	2.39	354
	50	40	2.61	303
	50	50	2.88	292
	50	60	3.56	308
	50	75	-	-
Ti(OEt) ₄	10	50	3.18	313
	25	50	3.20	319
	50	20	2.64	363
	50	50	2.90	459
	50	60	3.07	340
	70	50	2.96	388
Ti(O- <i>n</i> Bu) ₄	10	50	3.32	283
	37	50	2.88	256
	50	50	2.71	321
	70	50	2.79	425

Temp.: hydrolysis temperature of titanium alkoxides, d(001): basal spacing, S(BET): specific surface area.

summarized in Table 1.

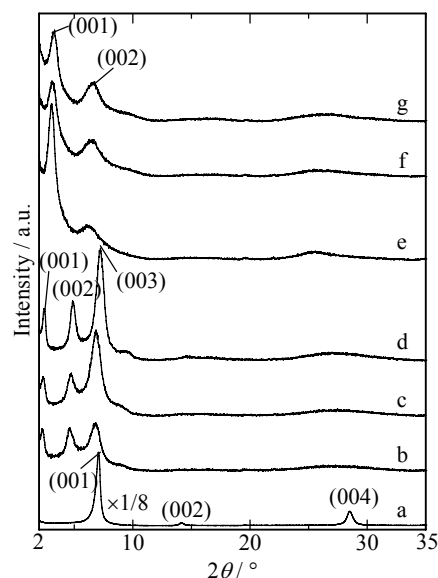


Fig. 1 XRD patterns of mica, the precursors of TiO₂ pillared mica and calcined samples with different titanium alkoxide (CH₃COOH/Ti=50, hydrolysis temperature: 50°C). The samples are a: parent mica, the precursors prepared with b: Ti(O-Et)₄, c: Ti(O-*i*Pr)₄, d: Ti(O-*n*Bu)₄, calcined samples prepared with e: Ti(O-Et)₄, f: Ti(O-*i*Pr)₄, g: Ti(O-*n*Bu)₄.

3.1 Effect of titanium alkoxide

The XRD patterns of parent mica, dried and calcined TiO₂ pillared mica samples prepared with different titanium alkoxide are shown in Fig.1. Three peaks were observed at $2\theta=2-8^\circ$ in each dried sample (Fig.1b-d). These peaks were assigned to (001), (002) and (003) reflections of layered mica intercalated with Ti ion species. This result indicates that the well-ordered layer structures were formed in intercalated samples. However, the difference in relative intensity of these three peaks were observed among titanium alkoxide precursors, implying that the amount, distribution and/or extent of dispersion of intercalated titanium ion species in interlayers of mica differ with the alkoxide used.

FT-IR spectra of parent mica and the precursors of TiO₂ pillared mica are shown in Fig.2. The broadbands between 3700 and 3000 cm⁻¹ are attributed to stretching vibration of silanol groups of external layers, adsorbed water molecules, and titanium ion species of intercalated samples. The bands around 1001 cm⁻¹ and 473 cm⁻¹ are due to asymmetric stretching vibrations of SiO₂ tetrahedra, and to bending of Si-O vibration, respectively. Four new absorption bands *i.e.* 612, 654, 1450 and 1536 cm⁻¹ are appeared after the intercalation of titanium ion species. These bands indicate the hydrolysis of titanium alkoxides with acetic acid. The bands at 612 and 654 cm⁻¹ are attributed to the formation of Ti-O-Ti bond during condensation of Ti-acetate complex. The doublet bands in 1536 and 1450 cm⁻¹ are assigned to the asymmetric and symmetric stretching vibrations of the carboxylic group coordinated to Ti as a bidentate ligand (Ref. [4]). These features are almost the same in three precursors (Fig.2b-d). These results suggest that the coordination structure of titanium ion species are unaffected by titanium alkoxide precursors.

After the samples were calcined at 500°C, sharp (001)

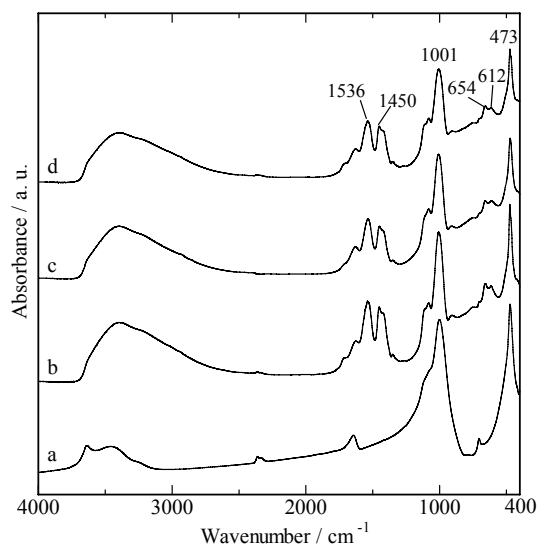


Fig. 2 FT-IR spectra of parent mica, the precursors of TiO₂ pillared mica samples with different titanium alkoxide (CH₃COOH/Ti=50, hydrolysis temperature: 50°C). a: parent mica, the precursor prepared with b: Ti(O-Et)₄, c: Ti(O-*i*Pr)₄, d: Ti(O-*n*Bu)₄.

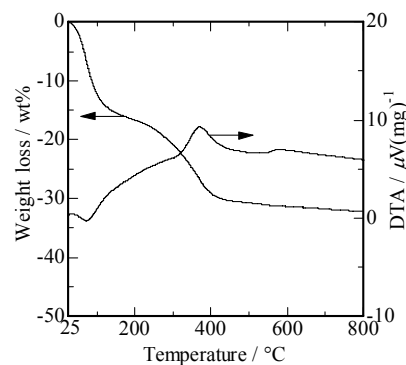


Fig. 3 TG-DTA curves of the precursors of TiO₂ pillared mica prepared with Ti(O-*i*Pr)₄ (CH₃COOH/Ti=50, hydrolysis temperature: 50°C).

peak and broad (002) peak were observed, and (003) peak was disappeared (Fig.1e-g). TG-DTA curves of the precursor of TiO₂ pillared mica prepared with Ti(O-*i*Pr)₄ are shown in Fig. 3. The main weight losses occurred in two steps, *i.e.* at 25-150°C and 150-425°C. The first weight loss (15.8 wt%) with an endothermic peak below 150°C is attributed to elimination of physically adsorbed water. The second one (13.6 wt%) with exothermic peak around 380°C is ascribed to the decomposition and combustion of organic compounds which existed in interlayers of mica. Similar TG-DTA curves were obtained on samples prepared with Ti(O-Et)₄ or Ti(O-*n*Bu)₄. These results indicate that thermal decomposition of the organic compounds contained in the titanium ion species intercalated in mica occurs during calcination at 500°C and Ti ion species are converted to TiO₂ pillars. Almost all the TiO₂ particles may exist in interlayers of mica as pillars, because no clear peaks due to anatase and rutile were found in all the samples (Fig.1). The small shift of (001) peak toward higher diffraction angles was found for TiO₂ pillared mica samples (Fig.1e-g) in the order Ti(O-Et)₄, Ti(O-*i*Pr)₄, Ti(O-*n*Bu)₄. Additionally, the sample prepared with Ti(O-Et)₄ (Fig.1e) exhibits most intense (001) reflection. The result indicates that the sample prepared with Ti(O-Et)₄ possesses well-ordered structure than other samples. This behavior may be caused by the difference in thermal stability of TiO₂ pillars.

Nitrogen adsorption-desorption isotherms of TiO₂ pillared mica samples calcined at 500°C are shown in Fig.4. Although the amount of nitrogen adsorbed were different from each other, every isotherm of the pillared mica seems to be of the type IV characteristic to solids including both micro and meso pores (BDDT classification). Small adsorption-desorption hysteresis loop due to capillary condensation in mesoporous was observed slightly. The sample prepared with Ti(O-Et)₄ exhibits higher BET surface area (459 m²/g, see Table 1) than other samples. This result also suggests that pillared structure of the sample is well-ordered which is agreement with most intense (001) reflection observed in XRD results (Fig. 1)

Castillo et al. (Ref. [5]) observed similar results, the use of Ti(O-Et)₄ as a source of titanium yielded the best textural and

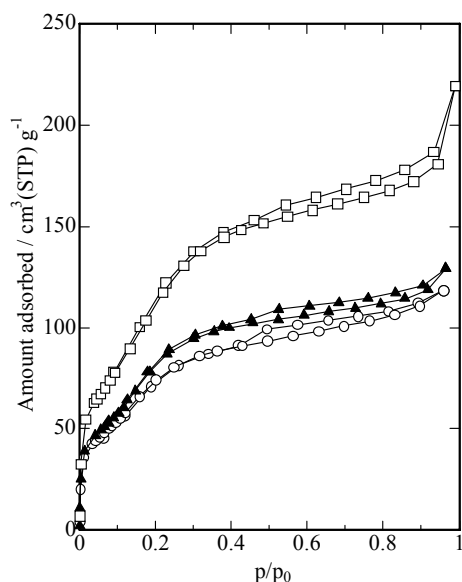


Fig. 4 Nitrogen adsorption-desorption isotherms of TiO_2 pillared mica samples with different titanium alkoxide ($\text{CH}_3\text{COOH}/\text{Ti}=50$, hydrolysis temperature: 50°C). \square : $\text{Ti}(\text{O-Et})_4$, \circ : $\text{Ti}(\text{O-}i\text{Pr})_4$, \blacktriangle : $\text{Ti}(\text{O-}n\text{Bu})_4$.

thermal stability for the preparation of TiO_2 pillared montmorillonite. They suggested that the alkoxy groups affect the ease of the hydrolysis of titanium alkoxides and a more highly ramified titanium polymer (ion) could be obtained with large alkoxy groups. In that case, diffusion in the interlayer space will be difficult, and which causes a poor distribution of the titanium polymer (pillars) between the layers of the clay. In this study, as suggested above, more stable pillared structure was formed by using $\text{Ti}(\text{O-Et})_4$ as titanium ion source.

3.2 Effect of $\text{CH}_3\text{COOH}/\text{Ti}$ ratio

XRD patterns of calcined samples with different $\text{CH}_3\text{COOH}/\text{Ti}$ ratios are shown in Fig.5. These samples were prepared using $\text{Ti}(\text{O-}i\text{Pr})_4$ as precursor of titanium ion species. The (001) peaks found around $2\theta=3^\circ$ decreased in intensity and shifted toward lower diffraction angles with a decrease in the $\text{CH}_3\text{COOH}/\text{Ti}$ ratio. The basal spacing $d(001)$ value increased from 2.87 nm at $\text{CH}_3\text{COOH}/\text{Ti}=75$ to 3.65 nm at $\text{CH}_3\text{COOH}/\text{Ti}=10$ (Table 1). These results indicate that the TiO_2 pillar size was influenced by $\text{CH}_3\text{COOH}/\text{Ti}$ ratio, and larger titanium ion species, the precursor of TiO_2 particles, were obtained at smaller $\text{CH}_3\text{COOH}/\text{Ti}$ ratio. This behavior may be attributed to a difference in the extent of condensation during hydrolysis of titanium alkoxide. However, the broadening of (001) peak was occurred, and a peak assigned to TiO_2 anatase ($2\theta=25.2^\circ$) were observed in the XRD pattern of the sample with $\text{CH}_3\text{COOH}/\text{Ti}=10$. The decrease in specific surface area (Table 1) was also observed with a decrease in the $\text{CH}_3\text{COOH}/\text{Ti}$ ratio. Under a constant Ti/mica ratio, the formation of large titanium ion species during hydrolysis resulted in a decrease in the number of them. This fact may affect to the amount of titanium ion species intercalated, and

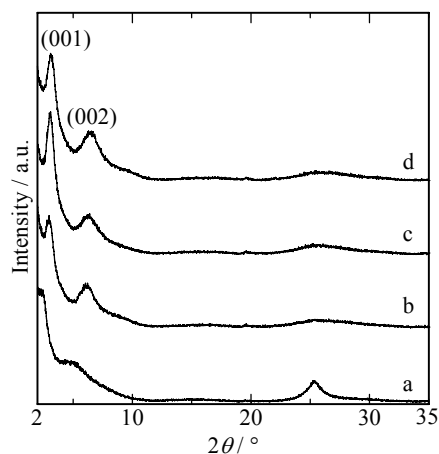


Fig. 5 XRD patterns of TiO_2 pillared mica prepared with different $\text{CH}_3\text{COOH}/\text{Ti}$ ratio ($\text{Ti}(\text{O-}i\text{Pr})_4$, hydrolysis temperature: 50°C). $\text{CH}_3\text{COOH}/\text{Ti}$ ratio is a: 10, b: 25, c: 50, d: 75.

cause a poor thermal stability which is responsible for low specific surface area. Therefore, disordered structure of TiO_2 pillared mica and large TiO_2 particles on external surface of mica were formed at $\text{CH}_3\text{COOH}/\text{Ti}=10$. The similar results were obtained with the samples prepared using $\text{Ti}(\text{O-Et})_4$ and $\text{Ti}(\text{O-}n\text{Bu})_4$.

3.3 Effect of hydrolysis temperature

XRD patterns of dried and calcined TiO_2 pillared mica samples prepared at various hydrolysis temperatures of $\text{Ti}(\text{O-}i\text{Pr})_4$ are shown in Fig.6 and Fig.7, respectively. In Fig.6, sharp peaks assignable to (001), (002) and (003) reflections of layered structure were observed at $2\theta=2-8^\circ$ for the samples prepared at $20-50^\circ\text{C}$. Whereas, only broad peaks were found for the samples prepared at 60°C and 75°C . It is reasonable to expect that the rate of hydrolysis of titanium alkoxide is faster at higher temperatures, which results in wider particle size distribution of titanium ion species. In that case, the

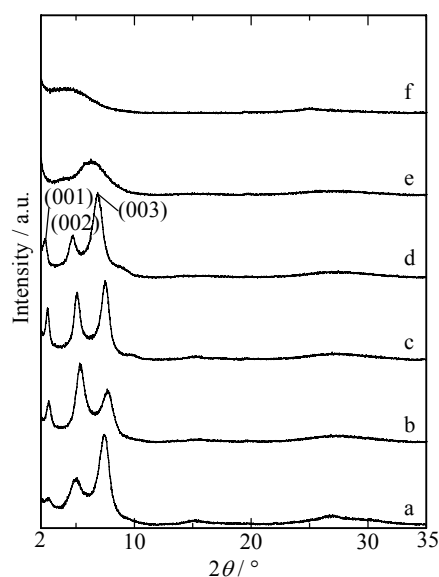


Fig. 6 XRD patterns of the precursors of TiO_2 pillared mica with different hydrolysis temperature of $\text{Ti}(\text{O-}i\text{Pr})_4$ ($\text{CH}_3\text{COOH}/\text{Ti}=50$). Hydrolyzed at a: 20°C , b: 30°C , c: 40°C , d: 50°C , e: 60°C , f: 75°C .

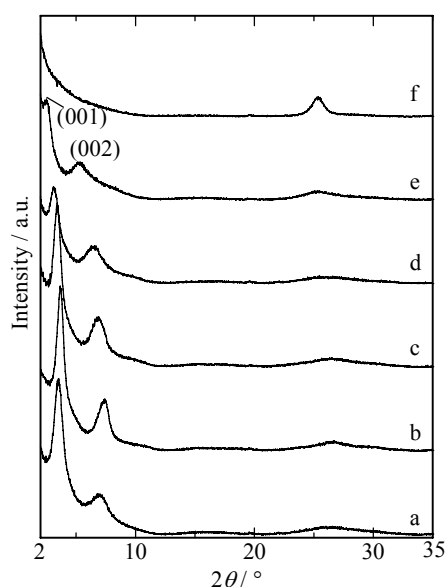


Fig. 7 XRD patterns of TiO_2 pillared mica calcined at 500°C with different hydrolysis temperature of $\text{Ti}(\text{O-}i\text{Pr})_4$ ($\text{CH}_3\text{COOH}/\text{Ti}=50$). Hydrolyzed at a: 20°C , b: 30°C , c: 40°C , d: 50°C , e: 60°C , f: 75°C .

intercalation of titanium ion species tends to proceed irregularly. The results observed above were caused by difference in size distribution and extent of dispersion of intercalated titanium ion species. After calcined at 500°C (Fig.7), two peaks due to (001) and (002) reflections were observed at $2\theta=2-7^\circ$ for the samples prepared at $20-60^\circ\text{C}$, while a decrease in intensity of (001) peaks with an increase in the hydrolysis temperature. In addition, (001) peaks were sifted toward lower diffraction angles with an increase of the hydrolysis temperature. Basal spacing increased from 2.39 nm at 30°C to 3.56 nm at 60°C (Table 1). These results indicate that the TiO_2 pillar size was affected by the hydrolysis temperature, and larger titanium ion species, the precursor of TiO_2 particles, were obtained at higher temperatures up to 60°C . However, the sample hydrolyzed at 75°C exhibited no distinct diffraction peaks of pillared structures, while a peak assigned to anatase was found at $2\theta=25.2^\circ$. Thus, to prepare the well-ordered layer structure with large TiO_2 pillars, adequate combination of temperature, time and titanium alkoxide source is important.

The micropore size distribution of TiO_2 pillared mica prepared with $\text{Ti}(\text{O-Et})_4$ is shown in Fig. 8. All samples present a unimodal peak. The center of micropore size distribution sifted from 0.7 nm to 1.0 nm with an increase in the hydrolysis temperature. However, other samples prepared with $\text{Ti}(\text{O-}i\text{Pr})_4$ or $\text{Ti}(\text{O-}n\text{Bu})_4$ exhibit almost no shift in the micropore size distribution. As mentioned above, the samples prepared with $\text{Ti}(\text{O-Et})_4$ possess more stable pillared structure. More homogeneous distribution of titanium ion species in interlayer

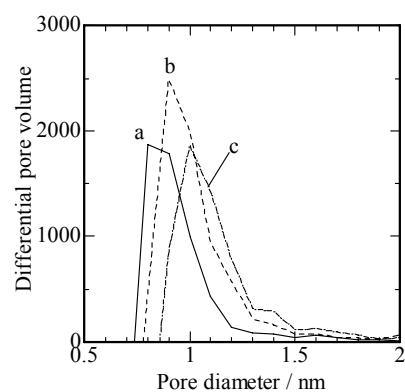


Fig. 8 Micropore size distribution of TiO_2 pillared mica with different hydrolysis temperature of $\text{Ti}(\text{O-Et})_4$ ($\text{CH}_3\text{COOH}/\text{Ti}=50$). Hydrolyzed at a: 20°C , b: 50°C , c: 60°C .

of mica could explain this behavior. In that case, intercalation of titanium ion species prepared using $\text{Ti}(\text{O-Et})_4$, with different size distribution, leads to the change in micropore size located in interlayer of pillared mica, as shown in Fig. 8. From the results of 3.2 and 3.3, there is possibility of controlling the pore size distribution by varying hydrolysis temperature together with $\text{CH}_3\text{COOH}/\text{Ti}$ ratio, when TiO_2 pillared mica samples are prepared with $\text{Ti}(\text{O-Et})_4$ as titanium ion precursor and synthetic fluoro-tetrasilicic mica as parent clay.

References

- [1] Ooka C., Yoshida H., Horio M., Suzuki K. and Hattori T., "Adsorptive and photocatalytic performance of TiO_2 pillared montmorillonite in degradation of endocrine disruptors having different hydrophobicity", *Appl. Catal. B: Environ.*, 41, pp.313-321, (2003).
- [2] Shimizu K., Murayama H., Nagai A., Shimada A., Hatamachi T., Kodama T. and Kitayama Y., "Degradation of hydrophobic organic pollutants by titania pillared fluorine mica as a substrate specific photocatalyst", *Appl. Catal. B: Environ.*, 55, pp.141-148, (2005).
- [3] Valverde J.L., Sanchez P., Dorado F., Molina C.B. and Romero A., "Influence of the synthesis conditions on the preparation of titanium-pillared clays using hydrolyzed titanium ethoxide as the pillaring agent", *Micropor. Mesopor. Mater.*, 54, pp.155-165, (2002).
- [4] Tsai M.T., "Hydrolysis and condensation of forsterite precursor alkoxides: modification of the molecular gel structure by acetic acid", *J. Non-Cryst. Solids*, 298, pp.116-130, (2002).
- [5] Castillo H.L.D., Gilt A. and Grange P., "Influence of the nature of titanium alkoxide and of the acid of hydrolysis in the preparation of titanium pillared montmorillonites", *J. Phys. Chem. Solids*, Vol.58, No.7, pp.1053-1062, (1997).

Study of electrical conduction and electric field distribution in two-layer organic electroluminescence device by impedance and optical electroabsorption measurements

Dai Taguchi, Shio Inoue, Wangcen Qin, Takaaki Manaka, and Mitsumasa Iwamoto

*Department of Physical Electronics, Tokyo Institute of Technology,
2-12-1, O-okayama Meguro-ku Tokyo, 152-8552 Japan

iwamoto@pe.titech.ac.jp

Abstract: We studied the electrical conductance of organic electroluminescence device, i.e., ITO/ α -NPD/Alq3/Al device, using an impedance analyzer, and determined the electric field across the Alq3 layer selectively using optical electroabsorption measurement. The Maxwell-Wagner model analysis showed that hole-accumulation at the α -NPD/Alq3 interface was an origin of the electric field distribution change that provoked a hysteresis in the conductance of the device.

Key Words: Maxwell-Wagner model, electroabsorption, electroluminescence device

1 Introduction

Organic devices have attracted much interest in electronics, e.g., as flexible display elements. Organic materials used therein are basically dielectric matters and they are polarized in the presence of electric field. As a nature of dielectric materials, it takes a long time to reach a thermodynamic equilibrium state [1]. Hence a study focusing on electric field distribution in organic device is helpful for understanding the device performance. By using time-resolved electric-field-induced second-harmonic generation (TRM-SHG) measurement, the authors have been developing a novel experimental technique used for probing dynamical carrier motion in organic field effect transistors (OFETs) [2]. The TRM-SHG technique allows us to visualize carrier motion, by probing the electric field migration originating from the carriers. We could show that the visualized carrier motion well traced the carrier injection, accumulation, and transportation processes in pentacene OFETs [3]. Similarly, we have been paying attention to other optical methods that are available for probing the electric field. In the present paper, we use electroabsorption (EA) measurement [4] for studying the

electric field distribution in organic electroluminescence (EL) devices. Note that EA technique has a merit in that it can easily apply to sandwich structure devices, e.g., metal-insulator-metal device. Further, spectroscopic nature of organic materials allows us to probe the electric field distribution formed in each layer of multi-layers. By using the EA measurement, Rohlfing et al. [5] determined the electric field distribution in 2-layer EL devices. However, they did not discuss the details of carrier accumulation at the interface of the 2-layer in terms of the device performance.

In our present study, we employed the EA measurement to analyze the electric field distribution in a 2-layer EL device, ITO/ α -NPD/Alq3/Al device. Then we analyzed the results using a Maxwell-Wagner (MW) effect model, with taking into account the amount of accumulated charge at the α -NPD/Alq3 interface. Further, we examined the electrical conductance using an impedance analyzer. Results showed that holes accumulated at the α -NPD/Alq3 interface made a contribution to the electric field formation in the device, and was responsible for a hysteresis generated in the electrical conductance characteristics.

2 Experimental

2.1 Sample preparation

Figure 1 illustrates the sample structure of 2-layer EL devices used here. ITO/ α -NPD/Alq3/Al device (working area: $2 \times 2 \text{ mm}^2$) was prepared, where N,N'-di-[(1-naphthyl) - N,N'-diphenyl]-(1,1'-biphenyl)-4,4'-diamine (α -NPD) and Tris (8-hydroxy quinolino) aluminum (III) (Alq3) were hole and electron transport layers, respectively. A glass substrate coated with ITO strip lines was used as the base substrate, onto which 100-nm-thick α -NPD and Alq3 layers were successively vacuum-deposited at a pressure less than 10^{-4} Pa. The deposition rate was fixed at 0.1 nm/sec, monitored using a quartz crystal microbalance. After that, Al semi-transparent electrode (thickness: 10 nm) was evaporated. Single layer devices of α -NPD and Alq3 were also prepared in the same manner, except that semi-transparent Au was deposited as the top electrode. In the EA measurements, external voltages were applied to the ITO electrode with reference to the Al (or Au) electrode.

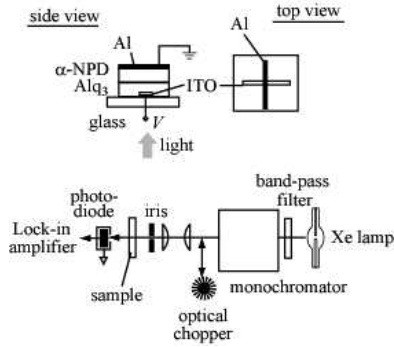


Figure 1: The 2-layer device structure and optical setup for the EA measurement.

2.2 Electroabsorption measurement

Electroabsorption (EA) measurements have been employed to study the electric field distribution in materials [4]. According to the perturbation theory, energy levels of the molecular orbital of materials shift, depending on the electric field \vec{F} applied, i.e., Stark shift. The energy shift ΔE is given as

$$\Delta E = -\frac{1}{2} \vec{F} \cdot \alpha_e \vec{F} - \vec{\mu} \cdot \vec{F} \quad (1)$$

where α_e is the electronic polarizability, $\vec{\mu}$ is the transition dipole. The absorption spectrum $A(E)$ is red- (or blue-) shifted with the energy variation ΔE . An absorption spectrum change ΔA , is approximately given in a Taylor expansion form:

$$\Delta A = \frac{dA}{dE} \Delta E + \frac{1}{2} \frac{d^2 A}{dE^2} \Delta E^2 \quad (2)$$

For isotropic materials, substituting Eq.(1) into Eq.(2) with $F = |\vec{F}|$ yields [6],

$$\Delta A = \frac{dA}{dE} \frac{1}{2} \alpha_e F^2 + \frac{d^2 A}{dE^2} \frac{1}{6} \mu^2 F^2 \quad (3)$$

Here, the third and succeeding higher order terms are discarded. For EA measurements, external voltage is $V = V_{dc} + V_{ac} \cos \omega t$. Therefore, the electric field in devices is modulated as

$$F = F_i + F_{dc} + F_{ac} \cos \omega t \quad (4)$$

where F_i is the internal electric field, $F_{dc} = V_{dc}/d$, and $F_{ac} = V_{ac}/d$ (d : layer thickness). Substituting Eq.(4) into Eq.(3), we obtain time-dependent absorption change as

$$\Delta A_\omega = \left\{ \frac{dA}{dE} \alpha_e + \frac{d^2 A}{dE^2} \frac{1}{3} \mu^2 \right\} (F_i + F_{dc}) F_{ac} \cos \omega t \quad (5)$$

at the modulation frequency ω , and

$$\Delta A_{2\omega} = \frac{1}{4} \left\{ \frac{dA}{dE} \alpha_e + \frac{d^2 A}{dE^2} \frac{1}{3} \mu^2 \right\} F_{ac}^2 \cos 2\omega t \quad (6)$$

at 2ω . Eqs. (5) and (6) suggest that EA spectrum at ω and 2ω is similar. Using the Lambert-Beer's law, the spectrum change ΔA in the presence of the external electric field is derived as

$$\Delta A = -\frac{0.43}{nd} \frac{\Delta T}{T} = -\frac{1}{nd} \frac{\Delta I_{tr}}{I_{tr}} \quad (7)$$

where T is the transmittance, n is the molecular density, and I_{tr} is the transmitted light intensity. ΔA_ω and $\Delta A_{2\omega}$ are determined individually as a function of the electric field by analyzing the transmitted light intensity. Finally, the static electric field component $F_i + F_{dc}$ is determined using ΔA_ω and $\Delta A_{2\omega}$ (see Eq.(5)) [6].

Figure 1 portrays the optical setup used for the EA measurement. Xe lamp was a light source. After passing through the band-pass filter and monochromator, the light impinged on the sample surface perpendicularly. The transmitted light intensity was detected using a photodiode connected to a Lock-in amplifier. For the EA measurement at 2ω , V_{dc} was zero, and V_{ac} was chosen 1 to 5 V. The EA spectra for α -NPD and Alq3 layers were obtained from their single layer devices. The electric field distribution F_{dc} in the 2-layer device was obtained from the EA spectra at ω , where $V_{ac}=0.5$ V. V_{dc} was changed from 0 to 10 V (forward), and then to 0 V (backward). The modulation frequency was chosen $\omega/2\pi=1$ kHz. The impedance of the device was measured using an impedance analyzer (Solartron 1260) with a modulation frequency of 5 Hz.

3 Results and Discussion

3.1 Electric field distribution

Figure 2 shows the EA spectra, i.e., the ratio of transmittance modulation and transmittance $-\Delta T/T$, for the single layer Alq3 and α -NPD devices at 2ω . They were in agreement with the second and the first derivative of the absorption spectra (solid curves) for Alq3 (a) and α -NPD (b), respectively. Eq. (6) suggests that the transition dipole dominates the EA spectrum for Alq3, whilst electronic polarization dominates the spectrum for α -NPD. Inset of Fig.2 shows the EA amplitude for the second-harmonic modulation where the $\Delta A_{2\omega}$ increases in proportion to F_{ac}^2 (see Eq.(6)). The EA spectrum for single

devices suggests that an electric field across Alq3 layer is selectively probed at 2.8 eV, where α -NPD is not activated.

Figures 3(a) and (b) show the EA spectrum for a 2-layer device at ω and the electric field across Alq3 layer estimated

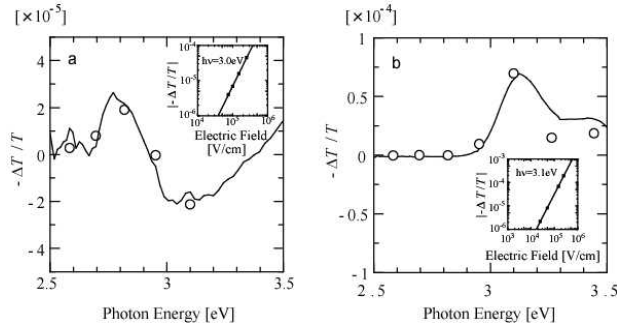


Figure 2: EA spectrum for Alq3 (a), and α -NPD (b) single-layer devices at 2ω . Inset is the amplitude dependence on the electric field F_{gc} . Solid curves are the second and the first derivatives of absorption spectrum for Alq3 and α -NPD, respectively.

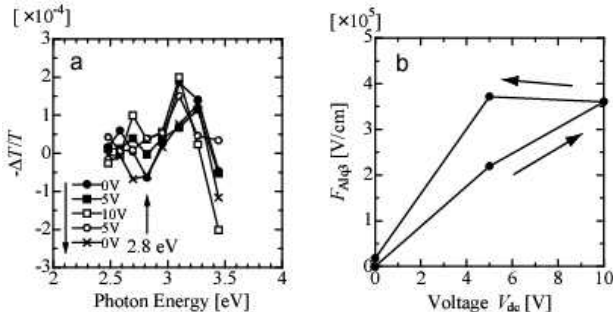


Figure 3: EA spectrum for the 2-layer ITO/ α -NPD/Alq3/Al device at the modulation frequency ω (a), and electric field across Alq3 layer (b).

from the EA measurement, respectively. The EA spectrum for $F_{dc} = 0$ was used as a reference. It was found that the electric field across the Alq3 layer showed a hysteresis behavior, i.e., Alq3 was subjected to a higher electric field when positive bias was applied in the backward direction in comparison with in the forward direction (see Fig.3(b)). Figure 4 shows the electrical conductance of the 2-layer ITO/ α -NPD/Alq3/Al device. A hysteresis was generated in accordance with the electric field applied across Alq3 layer. This result is reasonably explained by assuming that Alq3 works as a dielectric material, rather than as a semiconductor [7]. The EA and impedance measurements suggest that the high electric field remains in Alq3 layer after applying a voltage of 10 V, that is, the conductance of the 2-layer device could be regulated by the conductance of the Alq3 layer. Note that the conductance of Alq3 is 10^{-3} of the α -NPD (experimental data is not shown here).

3.2 Charge accumulation at the interface and hysteresis

On account of the MW effect [3], charge Q_s is accumulated at the α -NPD/Alq3 interface. A potential V_s is generated by this accumulated charge as

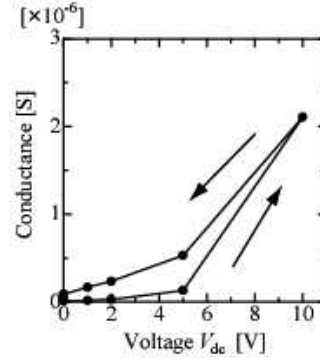


Figure 4: Electrical conductance of the 2-layer ITO/ α -NPD/Alq3/Al device.

$$V_s = \frac{Q_s}{C_1 + C_2} \quad (8)$$

where C_1 and C_2 are the capacitance of α -NPD and Alq3 layers, respectively. The average electric field across the Alq3 layer is

$$F_{Alq3} = \frac{V_s}{d_2} + \frac{1}{d_2} \frac{C_1}{C_1 + C_2} V_{dc} \quad (9)$$

Here d_2 is the thickness of Alq3 layer. The first term is the electric field caused by accumulated charge Q_s (see Eq.(8)). The second term is the external electric field (Laplace field). Figure 3(b) shows that the Alq3 layer experiences the change of an electric field of $F_{Alq3} = 2 \times 10^5$ V/cm at $V_{dc} = 5$ V during the application voltage cycle. Using Eqs. (8) and (9), we calculated that the change of accumulated charge was $\Delta Q_s = 1.1 \times 10^{-7}$ C/cm². Here, $C_1 = C_2 = \epsilon_r \epsilon_0 / d = 2.7 \times 10^{-8}$ F/cm² ($\epsilon_r = 3$; $d = d_2 = 100$ nm; ϵ_0 is the vacuum permittivity). In other words, the accumulated charge Q_s was the origin of the electric field change of Alq3 and responsible for the hysteresis in the conductance (Fig.4).

4 Conclusions

Using EA measurements, electric field distribution in 2-layer EL devices was determined. EA measurements for α -NPD and Alq3 single layer devices were conducted and showed that EA spectrum amplitude increases with F^2 . The electric field distribution in the 2-layer device was analyzed, where the electric field across the Alq3 layer was selectively determined using the EA measurements. The hysteresis behavior of the electrical conductance was explained by taking into account the change of the electric field distribution, which originated from the charge accumulation caused by the Maxwell-Wagner effect. It was suggested that holes were accumulated at the α -NPD/Alq3 interface, which was responsible for the hysteresis of the conductance.

Acknowledgement This work was supported by the Grants-in-Aid for Scientific Research (Grant 20656052 and Priority A 19206034) from Japan Society for the Promotion of Science (JSPS).

References

- [1] Brütting, W., Berleb, S., Mückl, A.G., *Org. Electron.*, Vol. 2 pp.1-36 (2001).
- [2] Manaka, T., Lim, E., Tamura, R., Iwamoto, M., "Direct imaging of carrier motion in organic transistors by optical second-harmonic generation," *Nature Photonics*, Vol.1 , pp.581-584 (2007).
- [3] Lim, E., Manaka, T., and Iwamoto, M., "Analysis of pentacene field-effect transistor with contact resistance as an element of a Maxwell–Wagner effect system," *J. Appl. Phys.*, Vol. 104, p.054511 (2008).
- [4] Cardona, M., "Modulation Spectroscopy," Academic, London, (1969).
- [5] Rohlfiing, F., Yamada, T. and Tsutsui, T., "Electroabsorption spectroscopy on tris-(8-hydroxyquinoline) aluminum-based light emitting diodes," *J. Appl. Phys.*, Vol. 86, pp.4978-4984 (1999).
- [6] Taguchi, D., Inoue, S., Miyazawa, R., Qin, W., Kawate, T., Weis, M., Manaka, T. and Iwamoto, M., "Effect of Orientational Order of Tris(8-hydroxyquinolinato)aluminum(III) on Electroabsorption," to be published in *Thin Solid Films* (2009).
- [7] Lampert, M. A., "Current Injection in Solids," Academic, New York, (1970).

Effect of Partial Reduction on Methanol Oxidation Activities of Pt Oxide Catalyst

Masami TAGUCHI * and Junichi NAKAYAMA **

* Department of Materials Science and Engineering, Faculty of Engineering and Resource Science,
Akita University, Tegata Gakuen-machi, Akita 010-8502, Japan

** Graduate School of Mining and Engineering, Akita University, Japan
taguchi@ipc.akita-u.ac.jp

Abstract: Methanol oxidation is the anodic reaction in a direct methanol fuel cell (DMFC). The development of a new catalyst, which can efficiently promote the anode reaction, is very important. In this study, a Pt thin film and two kinds of Pt oxide thin films prepared by reactive sputtering were characterized by XRD, XPS and EPMA, then their methanol oxidation activities were investigated using the rotating disk electrode method in a ($\text{H}_2\text{SO}_4 + \text{CH}_3\text{OH}$) solution. The Pt, PtO and PtO₂ thin films were obtained by sputtering a Pt target in 100% Ar, Ar - 50% O₂ and 100% O₂ plasma, respectively. Neither PtO nor PtO₂ had an excellent activity when the thin films were used as-received. However, an apparent catalytic activity of methanol oxidation was observed in the partially reduced Pt oxide thin films, whose ratios of O/Pt were significantly decreased by passing a cathodic current. On the other hand, the methanol oxidation activity of the Pt thin film was hardly changed by the electrochemical reduction. The methanol oxidation current showed that the electrocatalytic activity of the partially reduced Pt oxide thin films was about hundred times higher than that of the Pt thin film. Therefore, the partially reduced Pt oxide is a material with a significant potential for use as a catalyst for not only the DMFC, but also a fuel cell using the carbon compound as the fuel.

Key Words: Methanol oxidation, Pt oxide, Anode catalyst, Fuel cell

1 INTRODUCTION

The direct methanol fuel cell (DMFC), in which methanol is directly supplied to the anode, has been expected as a new power source for portable computers and mobile phones^{[1][2]}. However, the DMFC has several technical problems. One of the major obstacles to the practical use of the DMFC is the lack of an efficient anode catalyst, which causes a poor power density in the cell. The adsorbed carbon monoxide, which is an intermediate product of the methanol oxidation, restricts the anode reaction rate that lowers the performance of the DMFC^{[3][4]}. At present, minute Pt-Ru particles are the preferred catalyst for the DMFC anode. However, the anode catalyst does not always maintain its original state. The surface composition of the catalyst may change and the chemical binding of the catalyst may change from the metallic to oxide state during operation. Therefore, an understanding of the composition and the surface properties of the catalyst when operating is essential in order to develop an efficient anode catalyst.

The purpose of this study is to clarify the relationship

between the oxygen/noble metal ratio of the noble metal oxides as the anode catalyst of the DMFC and their electrocatalytic activities. To specifically explain the idea, the objective is to demonstrate the influence of the O / Pt ratio on the electrocatalytic activity of the Pt oxides. Therefore, a Pt thin film and two kinds of Pt oxide thin films with different compositions were prepared by reactive sputtering^[2] for characterization by XRD, XPS and EPMA. Their methanol oxidation activities were also measured using a rotating disk electrode in a ($\text{H}_2\text{SO}_4 + \text{CH}_3\text{OH}$) solution.

2 EXPERIMENTAL

2.1 Preparation of sample film

The Pt thin film and two kinds of Pt oxide thin films were prepared on a titanium rod (purity: 99.9 mass%, diameter: 5.0 mm, height: 10.0 mm) by a high frequency magnetron sputtering system (JEOL, JEC-SP360R) in order to investigate their methanol oxidation catalytic activity. The surface of the titanium rod was abraded to a grid size of 1000 using water-resistant emery papers and degreased with

acetone in an ultrasonic cleaner. The rod was then placed in a stainless holder in the vacuum chamber of the sputtering system along with a high purity platinum target (purity: 99.99 mass%, diameter: 7.62 mm). The distance between the titanium rod and the platinum target was 60 mm. The reactive sputtering was started after the pressure in the chamber reached 2×10^{-4} Pa. The reactive gas was fed through a mass flow controller and the gas pressure of the chamber was maintained at 2.0 Pa during the sputtering. The Pt thin film was obtained by sputtering of the platinum target in a 100% Ar plasma generated at 100 W. On the other hand, two kinds of Pt oxide thin films with different O / Pt ratios were deposited in a 100% O₂ plasma or 50% Ar - 50% O₂ plasma.

The sputtering products were analyzed by x-ray diffractometer (JEOL, JDX-3530) with Cu K α . The accelerating voltage and the emission current of the XRD were 40 kV and 40 mA, respectively. The spectra of the products were also measured using x-ray photoelectron spectroscopy (JEOL, JPS-9000SX) with Mg K α radiation in order to analyze the chemical binding. The accelerating voltage and the emission current of the XPS were 10 kV and 20 mA, respectively. EPMA (JEOL, JSM-5900LV) using an electron beam of 20 kV was then used to analyze the O / Pt atomic ratio of the products.

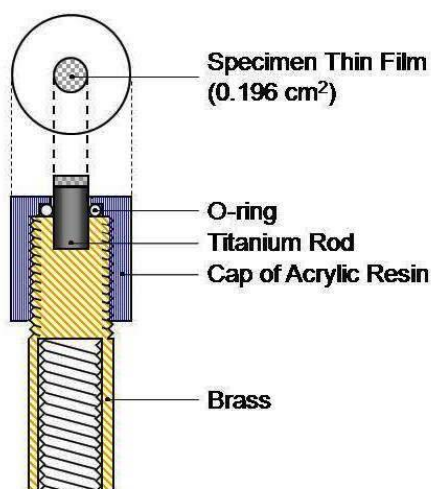


Figure 1 Rotating disk electrode.

2.2 Measurement of methanol oxidation current

Figure 1 shows the rotating disk electrode used for measuring the methanol oxidation current. The titanium rod with the sputtered product was attached to this electrode, and the electrode was attached to a rotating electrode system (Hokuto Denko, HR-200) as shown in Figure 2. The counter electrode and the reference electrode were a Pt spiral and an Ag/AgCl electrode in 3.30 kmol m⁻³ KCl, respectively. A separator was used in order to avoid the bad influence of chloride ions on the working electrode, and all measured

potentials were quoted with respect to the normal hydrogen electrode (NHE). The electrolyte solution was 1.0 kmol m⁻³ CH₃OH with 0.5 kmol m⁻³ H₂SO₄, which was saturated with argon by bubbling of the high purity gas. The temperature of the solution was changed from 298 to 323 K, but the rotation rate of the working electrode was fixed at 900 rpm. The anodic polarization curve was measured using a potentiostat (Hokuto Denko, HZ-5000) in the potential range from 0.42 to 1.22 V vs. NHE.

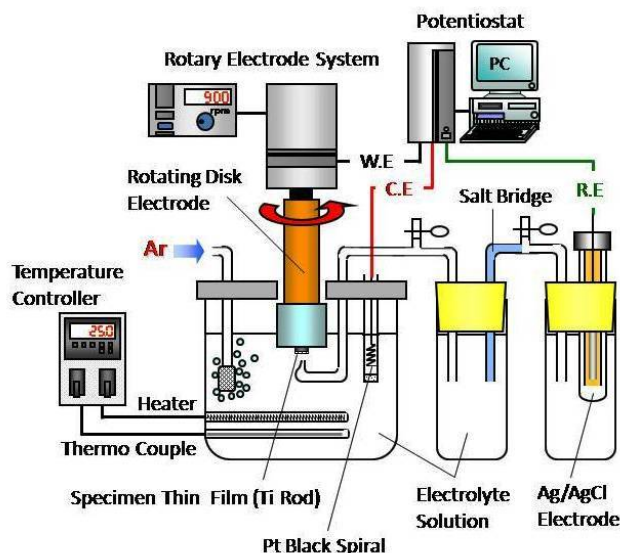


Figure 2 Measuring system of methanol oxidation activity.

3 RESULTS AND DISCUSSION

3.1 Properties of Pt and Pt oxide thin films

Figure 3 shows photographs of (a) Pt, (b) Pt oxide and (c) Pt oxide thin films prepared by sputtering a Pt target in 100% Ar, Ar - 50% O₂ and 100% O₂ plasma, respectively. The color of (a) the Pt thin film was shiny silver-grey, while (b) the Pt oxide thin film prepared by sputtering in Ar - 50% O₂ was a dull grey. On the other hand, the color of (c) the Pt oxide thin film changed to a dark brown when the reaction gas was 100 % O₂. The composition of the Pt oxide thin film prepared by sputtering in Ar - 50% O₂ was determined to be approximately PtO_{0.89}, and that in 100% O₂ was PtO_{2.15} by chemical analysis using EPMA.

Figure 4 shows the x-ray photoelectron spectra of Pt and Pt oxide thin films prepared by sputtering. The spectrum of the Pt thin film, whose peak was at the binding energy of 71.38 eV, was smaller than those of the Pt oxide thin films. The binding energy of the spectrum peak for the Pt thin film approximately corresponds to 71.3 eV, the binding energy of metallic Pt^[5]. On the other hand, the spectrum peaks of the Pt oxide thin films prepared by sputtering in Ar - 50% O₂ and

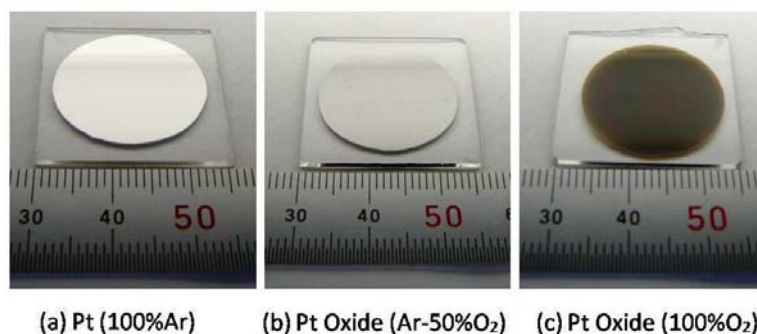


Figure 3 Photographs of (a) Pt, (b) Pt oxide and (c) Pt oxide thin films prepared by sputtering Pt target in 100% Ar, Ar - 50% O₂ and 100% O₂ plasma, respectively.

100 % O₂ were 72.1 and 74.6 eV, respectively. The former corresponds to approximately the binding energy of 72.3 eV for PtO and the latter can be assigned to that of 74.4 eV for PtO₂, which were reported by Abe et al.^[6] It is concluded from the EPMA and XPS analysis results that we can prepare the metallic Pt and two kinds of Pt oxide thin films, PtO and PtO₂, by changing the composition of the reactive gas.

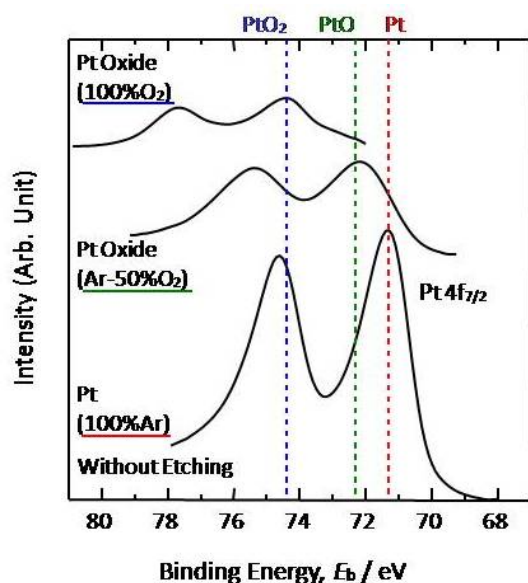


Figure 4 X-ray photoelectron spectra of Pt and Pt oxide thin films prepared by sputtering.

3.2 Activities of Pt and Pt oxide thin films as DMFC anode catalysts

Figure 5 shows the first anodic polarization curves of Pt thin film prepared using 100% Ar. The current density of the Pt thin film obviously increased with the increasing temperature in 0.5 kmol m⁻³ H₂SO₄ + 1.0 kmol m⁻³ CH₃OH. The current density was also very low in the solution without CH₃OH. Therefore, it can be confirmed that the anodic current peaks around 0.9 V vs. NHE are caused by the

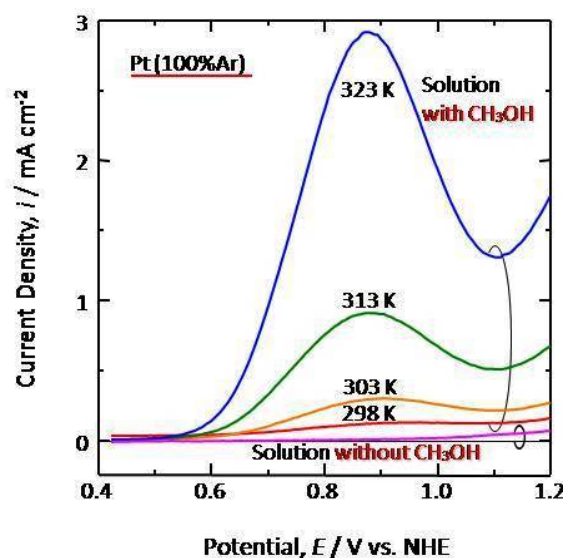


Figure 5 Anodic polarization curves of Pt thin film prepared using 100% Ar in 0.5 kmol m⁻³ H₂SO₄ + 1.0 kmol m⁻³ CH₃OH at 298 - 323 K.

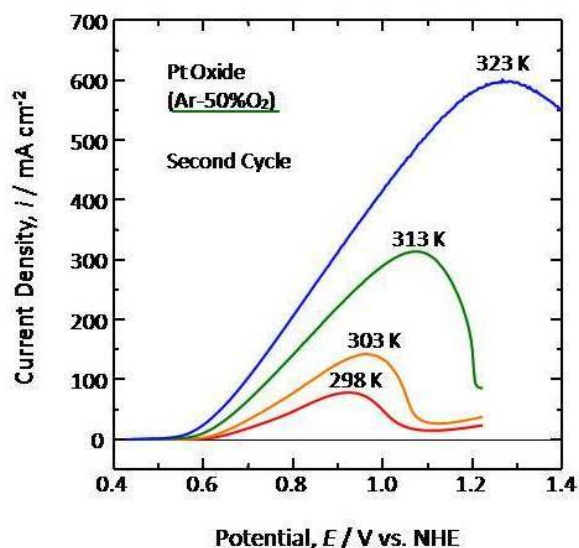


Figure 6 Anodic polarization curves of Pt thin film prepared using Ar - 50% O₂ in 0.5 kmol m⁻³ H₂SO₄ + 1.0 kmol m⁻³ CH₃OH at 298 - 323 K.

oxidation of CH₃OH.

Figure 6 shows the second anodic polarization curves of the Pt oxide thin film prepared using Ar - 50% O₂, which was identified as PtO by both the XPS and EPMA analysis, in 0.5 kmol m⁻³ H₂SO₄ + 1.0 kmol m⁻³ CH₃OH at 298 - 323 K. There is a significant difference in the activity of the methanol oxidation current between the Pt thin film in Figure 5 and the Pt oxide thin film in Figure 6. That is to say, the peak current density of the Pt oxide thin film is about 600 mA cm⁻², which is 200 times greater than that of the Pt thin film at 323 K. The current density of the Pt oxide increased and the potential at the peak current shifted to the more positive direction with the increasing temperature.

3.3 Influence of polarization on methanol oxidation activity of Pt oxide thin films

Figure 7 shows the influence of the cycle number of the anodic polarization measurement on the maximum current density of the methanol oxidation for the Pt oxide thin film prepared using Ar - 50% O₂ at 298 - 323 K. Although the Pt oxide thin film had only a slight activity for the methanol oxidation during the first polarization, the second or third repetition of the polarization measurement did abruptly increase the methanol oxidation current. However, the current density was tending downward by the fourth repetition or more.

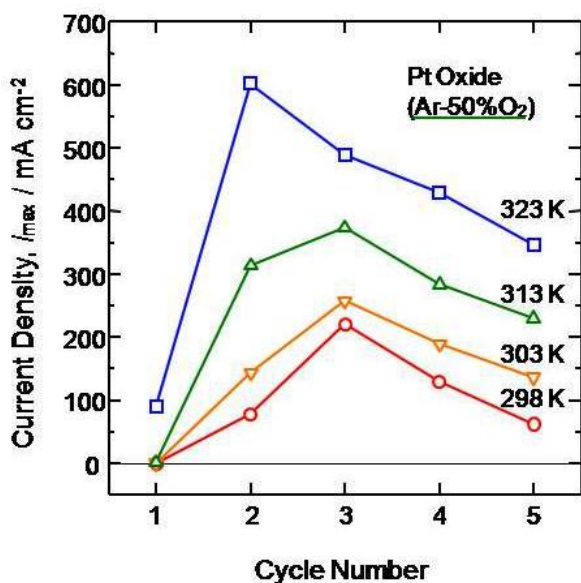


Figure 7 Influence of cyclic number of anodic polarization measurement on maximum current density of methanol oxidation for Pt oxide thin film prepared using Ar - 50% O₂ at 298 - 323 K.

Figure 8 shows the x-ray diffraction patterns of the Pt oxide thin films prepared on the Ti substrate after the third anodic polarization measurement, where the oxide thin films had the highest current density for the methanol oxidation at 298 - 313 K. It is noteworthy that there are several peaks from Pt, and not the Pt oxides in the XRD patterns. This result suggests that the Pt oxide thin films were partially reduced to a composition close to the Pt metal. In fact, the EPMA analysis showed that the O / Pt ratios of the Pt oxide thin films prepared using Ar - 50% O₂ and 100% O₂ were reduced by repeating the anodic polarization to be 0.14 and 0.37, respectively. These reductions can take place at the beginning of the anodic polarization, where a small cathodic current was observed at the potential of 0.5 V vs. NHE or lower (See Figure 5 and Figure 6).

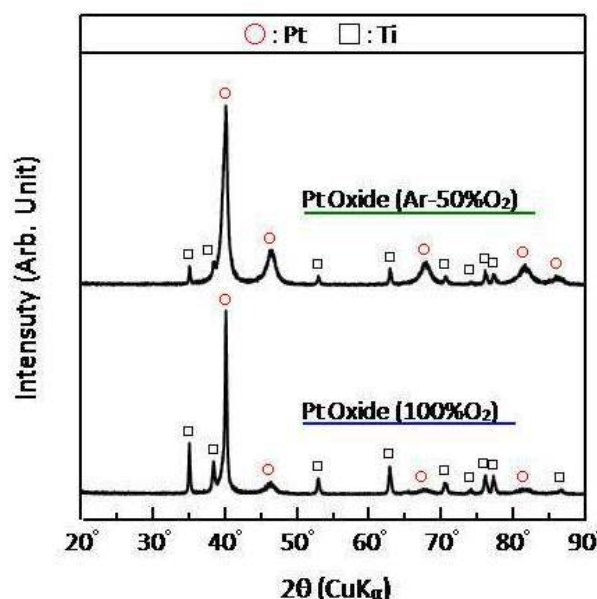


Figure 8 X-ray diffraction patterns of Pt oxide thin films prepared on Ti substrate after the third anodic polarization measurement.

3.4 Influence of cathodic reduction on methanol oxidation activity of Pt oxide thin films

The methanol oxidation of Pt oxide thin films may be activated by passing a cathodic current during the polarization measurement. In the secondary stage, the Pt thin film and two kinds of Pt oxide thin films were electrochemically reduced to investigate the activity of the methanol oxidation.

Figure 9 shows the influence of the quantity of electricity passed for the cathodic reduction on the methanol oxidation activity of the Pt thin film. After the cathodic reduction of -1.0 mA for 100 s intervals, the polarization measurement was repeated in the potential range between 0.62 to 1.2 V vs. NHE to avoid passing a useless cathodic

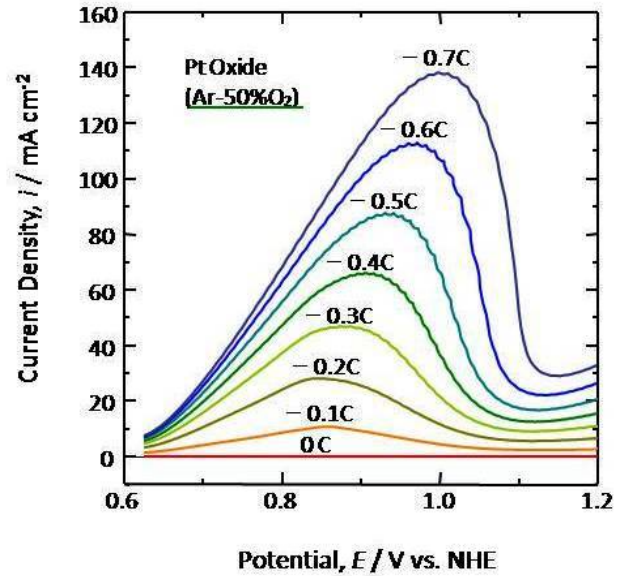
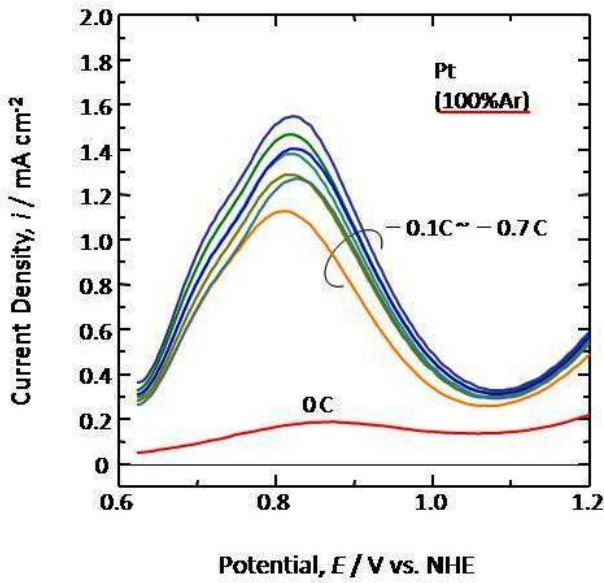


Figure 10 Influence of quantity of electricity passed for cathodic reduction on methanol oxidation activity of Pt oxide thin film prepared using Ar - 50% O₂.

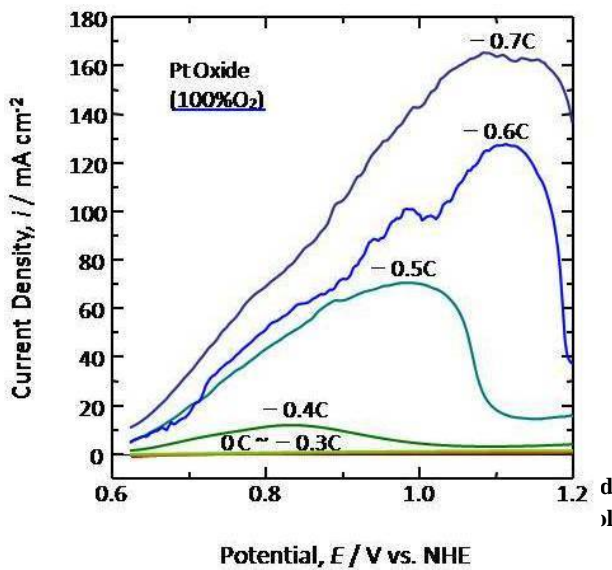


Figure 11 Influence of quantity of electricity passed for cathodic reduction on methanol oxidation activity of Pt oxide thin film prepared using 100% O₂.

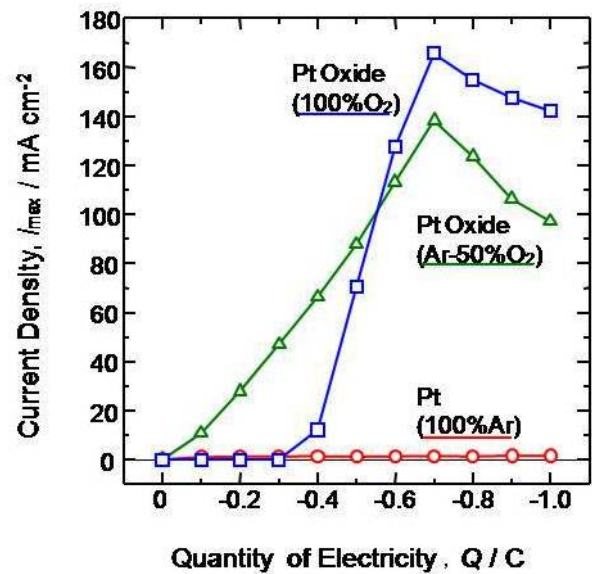


Figure 12 Relationship between cathodic electricity and peak current densities of Pt and the Pt oxide thin films.

current to the sample electrode. The peak current density of the methanol oxidation for the Pt thin film was no more than 1.6 mA cm^{-2} , regardless of the quantity of electricity passed for the cathodic reduction. On the other hand, the methanol oxidation for the two kinds of Pt oxide thin films was significantly activated by the cathodic reduction (See Figure 10 and Figure 11). The peak current density of the Pt oxide thin film prepared in the Ar - 50% O_2 plasma increased with the increasing quantity of the cathodic electricity to about 140 mA cm^{-2} at -0.7 C . The current density of about 160 mA cm^{-2} was also observed for the Pt oxide thin film prepared in the 100% O_2 plasma. These current densities of the Pt oxide thin films are nearly 100 times greater than the Pt thin film.

Figure 12 shows the relationship between the cathodic electricity and the peak current densities of the Pt and Pt oxide thin films. It is quite obvious that the cathodic reduction for the Pt thin film hardly influenced the activity of the methanol oxidation. However, the current densities of the methanol oxidation for the Pt oxide thin films were increased with the increasing cathodic electricity up to -0.7 C . By passing the cathodic electricity over -0.7 C , the current densities decreased with the increasing electricity. Based on the SEM observations, the decrease in the current density may be related to the peeling off the specimen film from the Ti substrate.

The surface analysis and the anodic polarization suggest that the electrocatalytic activity of the methanol oxidation is deeply related to the residual oxygen in the partially reduced Pt oxide thin films, because the Pt thin film without oxygen could not efficiently allow the anode reaction. Although neither PtO nor PtO₂ before the partial reduction had an excellent activity, these Pt oxide thin films may have a resistance to the catalyst poison by CO as well as a high activity for the methanol oxidation after the reduction treatment. Therefore, the partially reduced Pt oxide is a significantly active material as a catalyst for not only the DMFC, but also the fuel cell using the carbon compound as the fuel.

4 CONCLUSION

The development of a new catalyst, which can efficiently allow the methanol oxidation, is very important for the practical use of the DMFC. In this study, Pt, PtO and PtO₂ thin films were prepared by sputtering a Pt target in 100% Ar, Ar - 50% O_2 and 100% O_2 plasma, respectively. Although neither PtO nor PtO₂ had an excellent activity for the methanol oxidation when the films were as-received, an apparent catalytic activity was observed in the partially reduced Pt oxide thin films. The current density of the methanol oxidation for the Pt thin film was no more than 1.6 mA cm^{-2} , regardless of the cathodic reduction. On the other hand, these current densities of the PtO and the PtO₂ thin

films increased to $140 - 160 \text{ mA cm}^{-2}$ by the partial reduction of the cathodic current. Moreover, a surface analysis suggests that passing a cathodic current decreases the O/Pt ratio in the Pt oxide thin films and the residual oxygen in the thin film plays an important role in the activation for the methanol oxidation.

REFERENCES

- [1] M. Taguchi, H. Tamori and W. H. Smyrl : Oxygen Reduction Activity of Thermally Decomposed Tetraphenylporphyrin as Cathode Catalyst of DMFC, *Int. J. Soc. Mater. Eng. Resour.*, 13 (2006), 141-147.
- [2] M. Taguchi, J. Nakayama and K. Ito : Oxygen Reduction Properties of Co Oxide and Pt Oxide Thin Films Prepared by Reactive Sputtering, *J. Soc. Mater. Eng. Resour. Jpn.*, 21 (2008), 8-15.
- [3] H. N. Dinh, X. Ren, F. H. Garzon, P. Zelenay and S. Gottesfeld : Electrocatalysis in Direct Methanol Fuel Cells: in-situ Probing of PtRu Anode Catalyst Surfaces, *J. Electroanal. Chem.*, 491(2000), 222-233.
- [4] G. T. Burstein, C. J. Barnett, A. R. Kucernak and K. R. Williams, *Catal. Today*, 38 (1997), 425-429.
- [5] G. M. Bancroft, I. Adams, L. L. Coatsworth, C. D. Bennewitz, J. D. Brown and W. D. Westwood : ESCA study of Sputtered Platinum Films, *Anal. Chem.*, 47 (1975), 586-588.
- [6] Y. Abe, M. Kawamura and K. Sasaki : Preparation of PtO and α -PtO₂ Thin Films by Reactive Sputtering and Their Electrical Properties, *Jpn. J. Appl. Phys.*, 38 (1999), 2092-2096.

Viscoelastic Analysis of Stress Concentration around a Hole in Laminated Composite Plates by Multi-Scale Approach

Yotsugi Shibuya* and Hideki Sekine**

* Department of Mechanical Engineering, Akita University, 1-1, Tegata Gakuen-machi, Akita 010-8502, Japan

** Tohoku University, 6-6-01 Aoba-yama, Aoba-ku, Sendai 980-8579, Japan

yshibuya@gipc.akita-u.ac.jp

Abstract: Viscoelastic behavior of laminated composite plates with a hole is investigated by multi-scale approach. Effective viscoelastic properties of the laminae are evaluated by a boundary integral method at a micro-scale level, and viscoelastic analysis for laminated composite plates is performed by a finite element method at a macro-scale level using the effective viscoelastic properties of lamina obtained by the micro-scale analysis. In the micro-scale analysis and the macro-scale analysis, the Laplace transformation is adopted and the correspondence principle between elastic and viscoelastic solutions in the Laplace domain is applied. The inverse Laplace transform is formulated by the Duhamel integral, and is calculated numerically. In numerical examples, a laminated composite plate with a hole, which is made of AS4/PACM-12, is treated, and the stress concentration around the hole in the laminated composite plate is discussed.

Key Words: Multi-scale analysis, Viscoelastic behavior, Laminated composite structure, Fiber reinforced thermoplastics, Stress concentration, Homogenization theory

1 INTRODUCTION

Since the heat resistance of thermoplastic resin was improved, carbon fiber-reinforced thermoplastics have attracted attention in various industries as composites which are possible to use for applications under high thermomechanical loading, and then it has been needed to gain a better understanding of viscoelastic behavior of the composites. Matsuda et al. [1] investigated effects of fiber distribution on elastic-viscoelastic behavior of long fiber-reinforced composite laminates. Ahci and Talreja [2] characterized viscoelastic response of woven fabric polymer composites with damage by experiment and finite element analysis. Moreover, Zhang et al. [3] treated modeling of matrix crack in viscoelastic laminated composites using a smeared crack method.

Homogenization approaches are useful to assess mechanical behavior of composites taking account of their micro-structures and properties at a micro-scale level. The homogenization approach for viscoelastic analysis was attempted by Shibuya [4] and Chung et al. [5].

In the present paper, viscoelastic analysis of stress concentration around a hole in laminated composite plates is made by multi-scale approach. After effective viscoelastic properties of the laminae are evaluated by a boundary integral method at a micro-scale level, viscoelastic analysis for laminated composite plates is performed by a finite element method at a macro-scale level. In the micro-scale analysis and the macro-scale analysis, the Laplace transformation is adopted and the correspondence principle between elastic and viscoelastic solutions in the Laplace domain is applied. In

numerical examples, a laminated composite plate made of AS4/PACM-12 is treated.

2 MULTI-SCALE MODEL OF LAMINATED COMPOSITE PLATES

Consider a unidirectional fiber-reinforced polymer composite with periodic hexagonal array of fibers for laminae of laminated composite plates. The interface between the fiber and matrix is perfectly bonded. To analyze viscoelastic behavior of the unidirectional fiber-reinforced polymer composite, a hexagonal periodicity model of the composite is introduced at a micro-scale level, as shown in Fig. 1. In order to obtain the effective viscoelastic properties of the composite, a homogenization theory is applied and then two Cartesian coordinate systems x, y are adopted. The large-scale

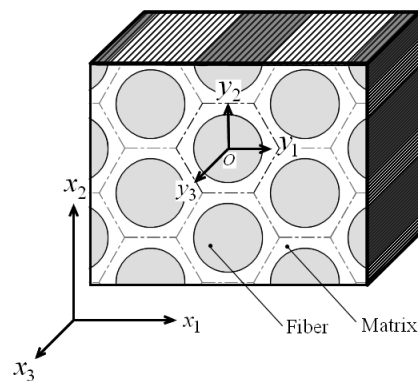


Fig. 1 Micro-structure of unidirectional fiber-reinforced polymer composite and two coordinate systems

coordinate system $\mathbf{x}=(x_1, x_2, x_3)$ is used to indicate homogenized fields. The x_1, x_2 plane is perpendicular to the fiber direction and the x_3 axis runs parallel to the fiber direction. The small-scale coordinate system $\mathbf{y}=(y_1, y_2, y_3)$ is placed in the unit cell and the origin of the coordinate system is at the center of the unit cell. The y_1, y_2 and y_3 axes run, respectively, parallel to the x_1, x_2 and x_3 axes.

A laminated composite plate with a hole is shown in Fig. 2. The laminated composite plate which consists of laminas of different angle of fiber orientation is subjected to tensile loading. In the analysis, the effective viscoelastic properties of the unidirectional fiber-reinforced polymer composite are assigned to the viscoelastic properties of the laminas at a macro-scale level. The laminated composite plate is referred to the Cartesian coordinate system $\mathbf{X}=(X_1, X_2, X_3)$. The origin of the coordinate system is located at the center of the hole. The X_1, X_3 plane coincides with the mid-plane of the laminated composite plate and the X_2 axis runs in the thickness direction of the plate. The fibers in the laminas are arranged so that the directions of the X_2 axis and the x_2 axis in the large-scale coordinate system shown in Fig. 1 are same. The width and length of the plate are denoted by W and L , respectively, the radius of the hole by a_h and the thickness of each lamina by h . The applied tensile stress is as follows: $\sigma_{33}^s = \sigma_0 H(t)$ at $X_3 = \pm L/2$. Here, σ_0 is a reference applied stress and $H(t)$ is the Heaviside step function.

3 VISCOELASTIC ANALYSIS AT THE MICRO-SCALE LEVEL

When a unidirectional fiber-reinforced polymer composite with periodic hexagonal array of fibers, which makes the laminas is referred to the two coordinate systems \mathbf{x} and \mathbf{y} as shown in Fig. 1, the viscoelastic stress-strain relations are expressed as follows:

$$\sigma_{ij}(\mathbf{x}, \mathbf{y}, t) = \int_0^t C_{ijkl}(\mathbf{y}, t-t') \frac{\partial \varepsilon_{kl}(\mathbf{x}, \mathbf{y}, t')}{\partial t'} dt' \quad (1)$$

where σ_{ij} are the stresses, ε_{ij} are the strains, C_{ijkl} are the relaxation moduli which are functions of \mathbf{y} , and t is time. When the Laplace transformation is adopted, Eq. (1) is written in the Laplace domain as

$$\hat{\sigma}_{ij}(\mathbf{x}, \mathbf{y}, p) = p \hat{C}_{ijkl}(\mathbf{y}, p) \hat{\varepsilon}_{kl}(\mathbf{x}, \mathbf{y}, p) \quad (2)$$

where the hat ^ indicates the Laplace transform of a function and p is a variable of the Laplace transform. The equilibrium

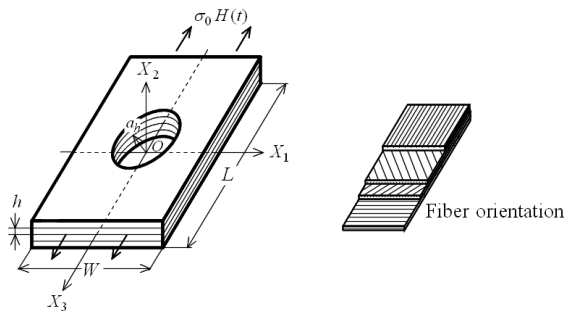


Fig. 2 Laminated composite plate subjected to tensile loading

equations and the strain-displacement relations in the Laplace domain are given by

$$\frac{\partial}{\partial x_j} \hat{\sigma}_{ij}(\mathbf{x}, \mathbf{y}, p) + \hat{F}_i(\mathbf{x}, p) = 0, \quad (3)$$

$$\hat{\varepsilon}_{ij}(\mathbf{x}, \mathbf{y}, p) = \frac{1}{2} \left[\frac{\partial \hat{u}_i(\mathbf{x}, \mathbf{y}, p)}{\partial x_j} + \frac{\partial \hat{u}_j(\mathbf{x}, \mathbf{y}, p)}{\partial x_i} \right] \quad (4)$$

where F_i are the body forces and u_i are the displacements.

Let us derive the homogenized equation of the unidirectional composite. The displacements in the Laplace domain are expressed by asymptotic expansion with a parameter λ in the forms:

$$\hat{u}_i(\mathbf{x}, \mathbf{y}, p) = \hat{u}_i^{(0)}(\mathbf{x}, \mathbf{y}, p) + \lambda \hat{u}_i^{(1)}(\mathbf{x}, \mathbf{y}, p) + \dots \quad (5)$$

where λ is the ratio of two length scales. The relation between the coordinate systems \mathbf{x} and \mathbf{y} , and their differential operators are given by

$$\mathbf{y} \rightarrow \frac{\mathbf{x}}{\lambda}, \quad \frac{\partial}{\partial x_i} \rightarrow \frac{\partial}{\partial x_i} + \frac{1}{\lambda} \frac{\partial}{\partial y_i} \quad (6)$$

By substituting Eqs. (5) and (6) into Eq. (4) and using Eq. (2), the λ^{-1} order terms of Eq. (3) is written as

$$\frac{\partial}{\partial y_j} \{ p \hat{C}_{ijkl}(\mathbf{y}, p) [\hat{\varepsilon}_{kl}^{(1)}(\mathbf{y}, p) + \hat{\varepsilon}_{kl}^*(\mathbf{x}, p)] \} = 0 \quad (7)$$

where

$$\hat{\varepsilon}_{ij}^{(1)}(\mathbf{y}, p) = \frac{1}{2} \left[\frac{\partial \hat{u}_i^{(1)}(\mathbf{y}, p)}{\partial y_j} + \frac{\partial \hat{u}_j^{(1)}(\mathbf{y}, p)}{\partial y_i} \right], \quad (8)$$

$$\hat{\varepsilon}_{ij}^*(\mathbf{x}, p) = \frac{1}{2} \left[\frac{\partial \hat{u}_i^{(0)}(\mathbf{x}, p)}{\partial x_j} + \frac{\partial \hat{u}_j^{(0)}(\mathbf{x}, p)}{\partial x_i} \right]. \quad (9)$$

Here, it is noted that $\hat{\varepsilon}_{ij}^*$ are constant in the unit cell. Henceforth, the mark * indicates a constant quantity throughout the unit cell. Moreover, the equilibrium equations referred to the coordinate system \mathbf{x} are obtained in the forms:

$$\frac{1}{V} \frac{\partial}{\partial x_j} \int_V \{ p \hat{C}_{ijkl}(\mathbf{y}, p) [\hat{\varepsilon}_{kl}^{(1)}(\mathbf{y}, p) + \hat{\varepsilon}_{kl}^*(\mathbf{x}, p)] \} dV(\mathbf{y}) + \hat{F}_i(\mathbf{x}, p) = 0 \quad (10)$$

where V is the volume of unit cell per unit length in the fiber direction. As the terms in the braces in the above equations

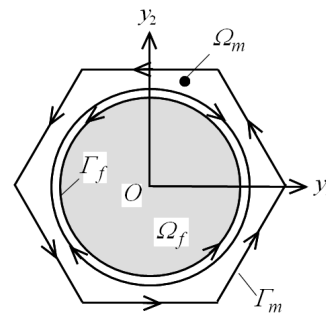


Fig. 3 Integral contours

correspond to stress fields in the unit cell, the homogenized stress-strain relations in the Laplace domain are written as

$$\begin{aligned}\hat{\sigma}_{ij}^*(p) &= pC_{ijkl}^*(p)\hat{\varepsilon}_{kl}^*(p) \\ &= \frac{1}{V} \int_V \{ p\hat{C}_{ijkl}(\mathbf{y}, p)[\hat{\varepsilon}_{kl}^{(1)}(\mathbf{y}, p) + \hat{\varepsilon}_{kl}^*(p)] \} dV(\mathbf{y})\end{aligned}\quad (11)$$

where C_{ijkl}^* are the effective relaxation moduli. Equation (11) is expressed in the forms of boundary integrals using the Gauss's theorem, as follows:

$$\begin{aligned}\hat{\sigma}_{ij}^*(p) &= \frac{1}{V} \left\{ \int_{\Gamma_f} \frac{1}{2} C_{ijkl}^f [\hat{u}_k^{f(1)}(\mathbf{y}', p) n_i \right. \\ &\quad + \hat{u}_i^{f(1)}(\mathbf{y}', p) n_k] d\Gamma(\mathbf{y}') + C_{ijkl}^f \hat{\varepsilon}_{kl}^*(p) \Omega_f \\ &\quad + \int_{\Gamma_m} \frac{1}{2} p \hat{C}_{ijkl}^m(p) [\hat{u}_k^{m(1)}(\mathbf{y}', p) n_i \\ &\quad + \hat{u}_i^{m(1)}(\mathbf{y}', p) n_k] d\Gamma(\mathbf{y}') \\ &\quad \left. + p \hat{C}_{ijkl}^m(p) \hat{\varepsilon}_{kl}^*(p) \Omega_m \right\}\end{aligned}\quad (12)$$

where n_i are the components of the normal vector on boundaries. As shown in Fig. 3, Γ denotes the integral contour on boundaries and Ω the volume per unit length in the fiber direction. The superscripts f and m indicate the fiber and matrix phases, respectively.

By dividing the unit cell region into the fiber and matrix phases, Eq. (7) is rewritten as

$$\frac{\partial}{\partial y_j} \hat{\sigma}_{ij}^\beta(\mathbf{y}, p) = 0, \quad (13)$$

$$\hat{\sigma}_{ij}^\beta(\mathbf{y}, p) = p \hat{C}_{ijkl}^\beta(p) [\hat{\varepsilon}_{kl}^{(1)}(\mathbf{y}, p) + \hat{\varepsilon}_{kl}^*(p)] \quad (14)$$

where the superscript β takes f and m .

The solution of the perturbed displacements for boundary value problems is expressed as

$$\begin{aligned}\hat{u}_j^{\beta(1)}(\mathbf{y}, p) &= \int_{\Gamma_\beta} [\hat{U}_{ij}^\beta(\mathbf{y}, \mathbf{y}', p) \hat{\tau}_i^\beta(\mathbf{y}', p) \\ &\quad - \hat{T}_{ij}^\beta(\mathbf{y}, \mathbf{y}', p) \hat{u}_i^{\beta(1)}(\mathbf{y}', p)] d\Gamma(\mathbf{y}') \\ &\quad - \int_{\Omega_\beta} \hat{S}_{ijkl}^\beta(\mathbf{y}, \mathbf{y}', p) \hat{\varepsilon}_{kl}^*(p) d\Omega(\mathbf{y}')\end{aligned}\quad (15)$$

where τ_i^β are the surface tractions on the boundary Γ_β , and U_{ij}^β , T_{ij}^β and S_{ijkl}^β are, respectively, the fundamental solutions for displacements, tractions and stresses in an infinite viscoelastic medium subjected to an instantaneous point load at the point \mathbf{y}' . These fundamental solutions are obtained using the correspondence principle between elastic and viscoelastic solutions [6].

The inverse Laplace transform is formulated by the Duhamel integral. Then, the following boundary integral equations for the fiber and matrix phases are obtained from Eq. (15).

$$\begin{aligned}\frac{1}{2} u_j^{f(1)}(\mathbf{y}, t) &= \int_{\Gamma_f} [U_{ij}^f(\mathbf{y}, \mathbf{y}', t) \tau_i^f(\mathbf{y}', t) \\ &\quad - T_{ij}^f(\mathbf{y}, \mathbf{y}') u_i^{f(1)}(\mathbf{y}', t)] d\Gamma(\mathbf{y}') \\ &\quad - \int_{\Omega_f} S_{ijkl}^f(\mathbf{y}, \mathbf{y}') \varepsilon_{kl}^*(t) d\Omega(\mathbf{y}') \quad (\mathbf{y} \in \Gamma_f),\end{aligned}\quad (16)$$

$$\begin{aligned}\frac{1}{2} \frac{\partial u_j^{m(1)}(\mathbf{y}, t)}{\partial t} &= \int_0^t \int_{\Gamma_m} [U_{ij}^m(\mathbf{y}, \mathbf{y}', t-t') \frac{\partial \tau_i^m(\mathbf{y}', t')}{\partial t'} \\ &\quad - T_{ij}^m(\mathbf{y}, \mathbf{y}', t-t') \frac{\partial u_i^{m(1)}(\mathbf{y}', t')}{\partial t'}] d\Gamma(\mathbf{y}') dt' \\ &\quad - \int_0^t \int_{\Omega_m} S_{ijkl}^m(\mathbf{y}, \mathbf{y}', t-t') \frac{\partial \varepsilon_{kl}^*(t')}{\partial t'} d\Omega(\mathbf{y}') dt' \\ &\quad (\mathbf{y} \in \Gamma_m),\end{aligned}\quad (17)$$

Moreover, the homogenized stresses of lamina are expressed from Eq. (12) as

$$\begin{aligned}\sigma_{ij}^*(t) &= \frac{1}{V} \left\{ \int_{\Gamma_f} \frac{1}{2} C_{ijkl}^f [u_k^{f(1)}(\mathbf{y}', t) n_i \right. \\ &\quad + u_i^{f(1)}(\mathbf{y}', t) n_k] d\Gamma(\mathbf{y}') + C_{ijkl}^f \varepsilon_{kl}^*(t) \Omega_f \\ &\quad + \int_0^t \int_{\Gamma_m} \frac{1}{2} C_{ijkl}^m(t-t') \left[\frac{\partial u_k^{m(1)}(\mathbf{y}', t')}{\partial t'} n_i \right. \\ &\quad + \frac{\partial u_i^{m(1)}(\mathbf{y}', t')}{\partial t'} n_k] d\Gamma(\mathbf{y}') dt' \\ &\quad \left. + \Omega_m \int_0^t C_{ijkl}^m(t-t') \frac{\partial \varepsilon_{kl}^*(t')}{\partial t'} dt' \right\}\end{aligned}\quad (18)$$

To determine the effective relaxation moduli C_{ijkl}^* , Eqs. (16) and (17) are solved with respect to $u_i^{(1)}$ for given strains $\varepsilon_{ij}^* = \varepsilon_a H(t)$ where ε_a is a reference strain, and then the homogenized stresses σ_{ij}^* are calculated.

4 VISCOELASTIC FINITE ELEMENT ANALYSIS AT THE MACRO-SCALE LEVEL

To make viscoelastic analysis of laminated composite plates, we adopt the finite element approach. The viscoelastic stress-strain relation of the lamina of laminated composite plates is written as

$$\{\sigma^s(t)\} = \int_0^t [C^s(t-t')] \frac{\partial \{\varepsilon^s(t')\}}{\partial t'} dt' \quad (19)$$

where the superscript s refers to the quantity corresponding to the lamina of laminated composite plates. The braces $\{\cdot\}$ denote a vector and the brackets $[\cdot]$ a matrix. The relaxation modulus matrix $[C^s(t)]$ is determined from the effective relaxation modulus matrix $[C^*(t)]$, as follows:

$$[C^s(t)] = [T][C^*(t)][T]^{-1} \quad (20)$$

where $[T]$ is the transformation matrix.

To implement finite element formulation, the principle of

virtual work is applied to the lamina of laminated composite plates. Then, it follows that

$$\int_{V_e} \delta \{\varepsilon^s\}^T \{\sigma^s(t)\} dV = \int_{V_e} \delta \{u^s\}^T \{F^s(t)\} dV + \int_{S_t} \delta \{u^s\}^T \{\tau^s(t)\} dS \quad (21)$$

where the superscript T denotes the transpose of a vector and the symbol δ the first variation of vector. With regard to the domain of integral, V_e is the volume of element and S_t is the boundary of element, where the surface traction vector $\{\tau^s\}$ is applied. To obtain the finite element formulas, we perform the Laplace transformation to Eqs. (19) and (21), and then we obtain

$$\int_{V_e} \delta \{\varepsilon^s\}^T [p\hat{C}^s(p)] \{\hat{\varepsilon}^s(p)\} dV = \int_{V_e} \delta \{u^s\}^T \{\hat{F}^s(p)\} dV + \int_{S_t} \delta \{u^s\}^T \{\hat{\tau}^s(p)\} dS. \quad (22)$$

The displacement vector $\{u^s\}$ and the strain vector $\{\varepsilon^s\}$ in the element are expressed, respectively, using the nodal displacement vector $\{u_n^s\}$ as follows:

$$\{u^s\} = [N] \{u_n^s\}, \quad \{\varepsilon^s\} = [B] \{u_n^s\} \quad (23)$$

where $[N]$ and $[B]$ are the matrices related to the shape function N and the strain-displacement relations, respectively. By substituting Eq. (23) into Eq. (22), the following equation is derived.

$$\int_{V_e} ([B] \delta \{u_n^s\})^T [p\hat{C}^s(p)] [B] \{\hat{u}_n^s(p)\} dV = \int_{V_e} ([N] \delta \{u_n^s\})^T \{\hat{F}^s(p)\} dV + \int_{S_t} ([N] \delta \{u_n^s\})^T \{\hat{\tau}^s(p)\} dS. \quad (24)$$

Equation (24) holds for any virtual displacement vector $\delta \{u_n^s\}$. Therefore, the finite element formula in the Laplace transform is obtained in the form

$$\int_{V_e} [B]^T [p\hat{C}^s(p)] [B] dV \{\hat{u}_n^s(p)\} = \{\hat{f}_n^s(p)\} \quad (25)$$

where

$$\{\hat{f}_n^s(p)\} = \int_{V_e} [N]^T \{\hat{F}^s(p)\} dV + \int_{S_t} [N]^T \{\hat{\tau}^s(p)\} dS. \quad (26)$$

Here, we note that the vector $\{\hat{f}_n^s(p)\}$ corresponds to the nodal force vector. The inverse Laplace transform is obtained

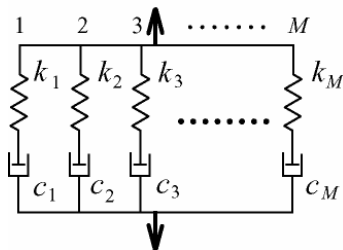


Fig. 4 A generalized Maxwell model of thermoplastic resin

by the Duhamel integral, as follows:

$$\int_0^t \left(\int_{V_e} [B]^T [C^s(t-t')] [B] dV \right) \frac{\partial}{\partial t'} \{u_n^s(t')\} dt' = \{f_n^s(t)\}. \quad (27)$$

The stress vector in the element is expressed as

$$\{\sigma^s(t)\} = \int_0^t [C^s(t-t')] [B] \frac{\partial}{\partial t'} \{u_n^s(t')\} dt'. \quad (28)$$

5 NUMERICAL RESULTS AND DISCUSSION

The composite materials used for a numerical example is a carbon fiber-reinforced composite AS4/PACM-12 whose experimental data are referred to Ref. [7]. The carbon fiber AS4 (Hercules) is transversely isotropic and the following properties [8] are used: $E_L^f = 235$ GPa, $E_T^f = 14$ GPa, $\nu_{LT}^f = 0.2$, $\nu_{TT}^f = 0.25$, $G_{LT}^f = 28$ GPa. The thermoplastic matrix PACM-12 (DuPont) is supposed to be isotropic. The creep compliance of the matrix is determined from the experimental data.

By considering a generalized Maxwell model shown in Fig. 4 for the thermoplastic matrix PACM-12, the creep compliance of matrix in the Laplace domain is given by

$$\hat{J}_m(p) = \frac{1}{p^2 \sum_{i=1}^M \frac{k_i c_i}{(k_i + p c_i)}} = \frac{\prod_{i=1}^M (k_i + p c_i)}{p^2 \sum_{i=1}^M k_i c_i \prod_{j=1, j \neq i}^M (k_j + p c_j)} \quad (29)$$

where M is the number of elements of the generalized Maxwell model, k_i is the coefficient of i th spring element and c_i is the coefficient of i th dash pot element. Equation (29) can be expanded to partial fractions with proper constants A_i and a_i , as follows:

$$\hat{J}_m(p) = \frac{A_{-1}}{p^2} + \frac{A_0}{p} + \sum_{i=1}^{M-1} \frac{A_i}{(p - a_i)} \quad (30)$$

Thus, the creep compliance of matrix is obtained from the inverse Laplace transform in the form

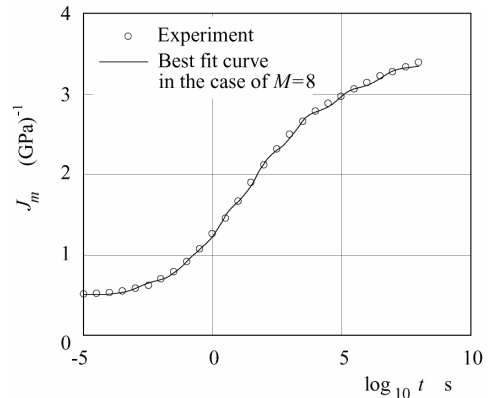


Fig. 5 Creep compliance of PACM-12 at $T = 145$ °C

$$J_m(t) = A_{-1}t + A_0 + \sum_{i=1}^{M-1} A_i \exp(a_i t) \quad (31)$$

The constants A_i and a_i are determined from a master curve of PACM-12 [9] at the glass transition temperature T_g ($=145^\circ\text{C}$) by the least square method. The best fit curve of the creep compliance in the case where the number of elements is set at $M=8$ is shown by a solid line in Fig. 5. In the figure, the circles indicate experimental data [9]. Although the best fit curve oscillates slightly, the agreement between the best fit

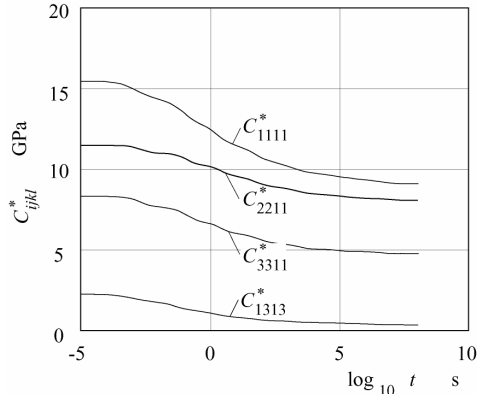


Fig. 6 Effective relaxation moduli C_{ijkl}^*

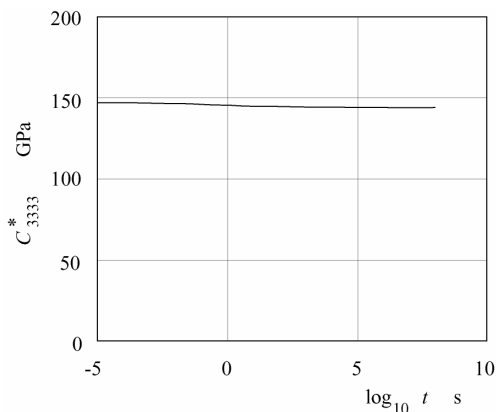


Fig. 7 Effective relaxation moduli C_{3333}^*

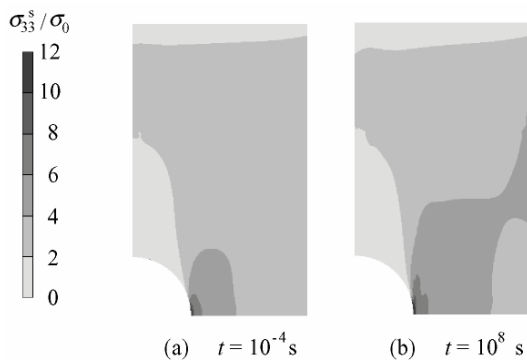


Fig. 8 Viscoelastic stress distribution of σ_{33}^s in the 0° lamina

curve and the experimental data is satisfactory. By taking account of the fact that the variation of volume of the matrix is very small during deformation, the Poisson's ratio of matrix is taken as $\nu_m = 0.495$.

The effective relaxation moduli of lamina are needed to analyze viscoelastic behavior of the laminated composite plate with a hole. The effective relaxation moduli are evaluated in the case of the fiber volume fraction $C_f = 0.6$ and the temperature $T = 145^\circ\text{C}$. Figure 6 shows the effective relaxation moduli C_{ij11}^* ($i = j = 1, 2, 3$) and C_{1313}^* versus time t . The effective relaxation moduli C_{ij11}^* ($i = j = 1, 2, 3$) are obtained from the response of the stress σ_{ij}^* under the applied strains $\varepsilon_{11}^*(t) = \varepsilon_a H(t)$ and $\varepsilon_{22}^* = \varepsilon_{33}^* = 0$, while the effective relaxation modulus C_{1313}^* is obtained from the response of the stress σ_{13}^* under the shear strain ε_{13}^* . It is seen from Fig. 6 that the effective relaxation moduli decrease with time due to the stress relaxation of matrix. Figure 7 shows the effective relaxation modulus C_{3333}^* versus time t . The effect of stress relaxation of matrix on the effective relaxation modulus is small due to the large Young's modulus of fiber in the longitudinal direction.

Let us investigate the stress concentration around the hole in the laminated composite plate. The laminate configuration is taken as $[0/45/-45/90]_s$, and the following values are set: the width $W = 60\text{mm}$, the length $L = 100\text{mm}$, the radius of the hole $a_h = 10\text{mm}$ and the thickness of lamina $h = 0.625\text{mm}$.

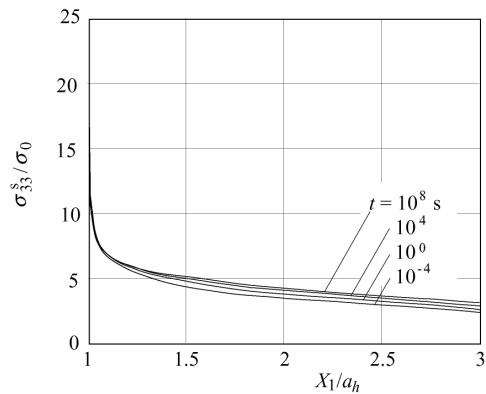


Fig. 9 Variation of σ_{33}^s in the 0° lamina along the X_1 axis

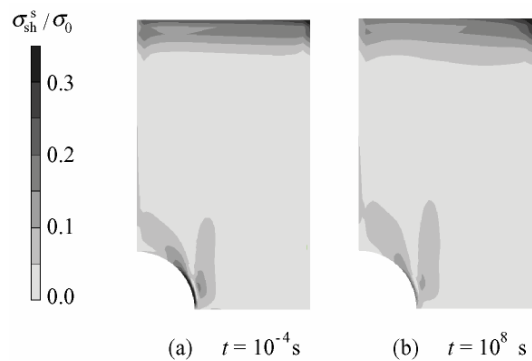


Fig. 10 Viscoelastic interlaminar stress distribution of σ_{sh}^s at the interface between the 0° and 45° lamina

Figure 8 shows the viscoelastic stress distribution of σ_{33}^s in the 0° lamina which is the outermost lamina. As can be seen from the figure, the stress concentration occurs around the hole in the lamina. Figure 9 depicts the variation of σ_{33}^s in the 0° lamina along the X_1 axis. The stress σ_{33}^s increases with time due to the stress relaxation in the 45° , -45° and 90° laminas, and the stress is remarkable at the edge of the hole, i.e., $X_1/a_h = 1.0$.

Figure 10 shows the viscoelastic interlaminar stress distribution of the shear stress $\sigma_{sh}^s [= \sqrt{(\sigma_{21}^s)^2 + (\sigma_{23}^s)^2}]$ at the interface between the 0° and 45° laminas. It is recognized from the figure that the stress concentration of σ_{sh}^s occurs near the edge of the hole. To clear the stress concentration, the interlaminar shear stress σ_{sh}^s at the interface between the 0° and 45° laminas near the hole is presented in Fig. 11 and those at the edge of the hole in Fig. 12. It is found from Figs. 11 and 12 that the interlaminar shear stress σ_{sh}^s has a peak at the edge of the hole for about $\theta = \pi/8$, which decreases with time.

Figure 13 shows the viscoelastic interlaminar stress distribution of σ_{sh}^s at the interface between the -45° and 90° laminas. It is seen from this figure that the change of the viscoelastic interlaminar stress distribution of σ_{sh}^s is not so large over the time range of 10^8 s.

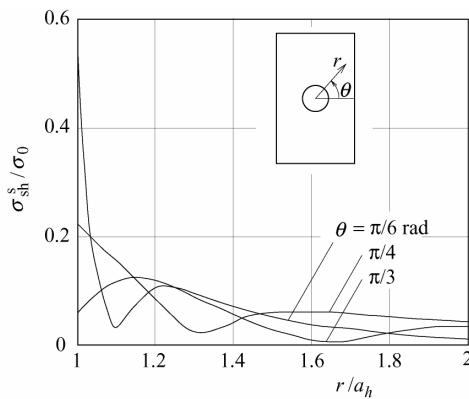


Fig. 11 Interlaminar shear stress σ_{sh}^s at the interface between the 0° and 45° laminas near the hole when $t = 10^{-4}$ s

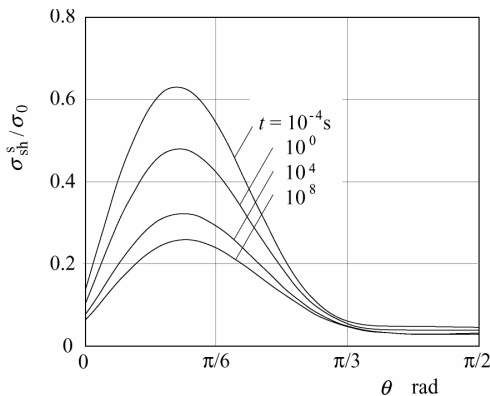


Fig. 12 Interlaminar shear stress σ_{sh}^s at the interface between the 0° and 45° laminas at the edge of the hole

6 CONCLUSIONS

Viscoelastic behavior of laminated composite plates with a hole has been examined by multi-scale approach. Effective viscoelastic properties of the laminas have been evaluated by a boundary integral method at a micro-scale level. Viscoelastic analysis for laminated composite plates has been performed by a finite element method at a macro-scale level using the effective viscoelastic properties of lamina obtained by the micro-scale analysis.

When a carbon fiber-reinforced composite AS4/PACM-12 has been used for a numerical example, we have found that the effective relaxation moduli C_{ijkl}^* decrease with time due to the stress relaxation of matrix.

From the viscoelastic analysis for the $[0/45/-45/90]_s$ laminated composite plate with a hole, we have elucidated that the stress concentration of the stress σ_{33}^s in the 0° lamina around the hole increases with time, while that of the interlaminar shear stress σ_{sh}^s decreases with time.

References

- [1] Matsuda, T., Ohno, N., Tanaka, H. and Shimizu, T., Int. J. Mech. Sci., Vol.45, pp.1583-1598, (2003).
- [2] Ahci, E. and Talreja, R., Compos. Sci. Technol., Vol.66, pp.2506-2519, (2006).
- [3] Zhang, Y., Xia, Z. and Ellyin, F., J. Compos. Mater., Vol.22, pp.2001-2022, (2005).
- [4] Shibuya, Y., JSME Int. J., Ser.A Vol.40, pp.313-319, (1997).
- [5] Chung, P. W., Tamma, K. K. and Namburu, R. R., Compos. Sci. Technol., Vol.60, pp.2233-2253, (2000).
- [6] Rizzo, F. J. and Shippy, D. J., SIAM J. Appl. Math., Vol.21, pp.321-330, (1971).
- [7] Miyase, A., Wang, S. S., Chen, A. W.-L. and Geil, P. H., J. Compos. Mater., Vol.27, pp.908-920, (1993).
- [8] Carman, G. P., J. Compos. Mater., Vol.27, pp.589-612, (1993).
- [9] Miyase, A., Chen, A. W.-L., Geil, P. H. and Wang, S. S., J. Compos. Mater., Vol.27, pp.886-907, (1993).

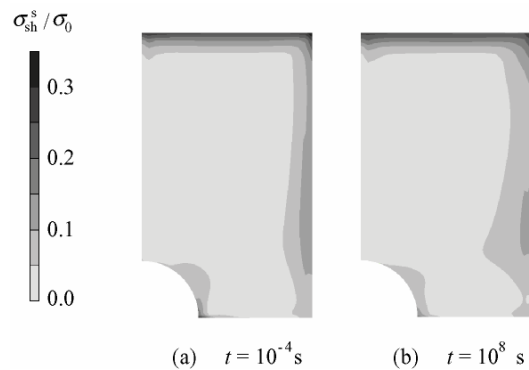


Fig. 13 Viscoelastic interlaminar stress distribution of σ_{sh}^s at the interface between the -45° and 90° laminas

Relation of High SO₂ Absorptivity and Pore Structure Changes of Hydrated Lime Depending on Slaking Conditions for Quicklime

Tetsushi Iwashita^{*}, Kyaw Choh^{**}, Yoshimi Gotoh^{**}, Mituhiro Kubota^{*} and Hitoki Matsuda^{*}

^{*}Department of Energy Engineering and Science, Nagoya University, Furo-cho, Chikusa-ku, Nagoya, 464-8603 Japan

^{**}Yabashi Industries Co., Ltd., 226 Akasaka-cho, Ogaki, 503-2213 Japan

tetsusi@re.commufa.jp

Abstract: To develop highly efficient hydrated lime for the treatment of flue gas from the municipal waste incineration plant, the authors prepared hydrated lime sample by slaking quicklime with water of 0.65 to 10 times the mass of quicklime and investigated the relation between pore structure characteristics and dry SO₂ absorptivity. The mass ratio of slaking water to quicklime is denoted as SWR. The results showed that the hydrated lime prepared with SWR = 0.9 possessed the highest pore volume and SO₂ absorptivity. Moreover, another hydrated lime was prepared by slaking quicklime with slaking water of SWR = 0.7, 0.9 and 2, that contained diethylene glycol (acronym DEG) of 0, 0.5, 2, 5 and 10 mass% of the quicklime. The results indicated that SO₂ absorptivity was highly improved by increasing DEG mass% in the range 0 to 2 mass%. It was recognized that DEG suppressed the growth of calcium hydroxide crystallite during slaking of quicklime, leading to the formation of pore structure of hydrated lime suitable for SO₂ absorption.

Key Words: hydrated lime, slaking water, diethylene glycol, pore volume, SO₂ absorptivity

1 INTRODUCTION

In Japan, hydrated lime is mostly used for removing acidic gases such as HCl and SO₂ from municipal waste incineration flue gas. For this purpose, industrial grade hydrated lime has been used so far, but there arises the shortage of landfill site for solid wastes discharged from waste incineration plants. On the other hand, we have to preserve the limestone resource and to promote saving of energy involved in handling, transportation, etc., it is essentially required to use less amount of lime. To realize these demands, development of highly efficient hydrated lime is fundamentally required. In the mid 1990s, 1st generation reactive hydrated lime with specific surface area of more than 2 times larger than that of the industrial grade hydrated lime was developed[1]. It was found that the increase in specific surface area of the hydrated lime was effective in improving the HCl absorptivity. In the early 2000s, 2nd generation highly reactive hydrated lime for removing SO₂ with pore volume of 2 to 3 times larger than that of the industrial grade hydrated lime was developed[2]. Recently, the highly efficient hydrated lime with improved HCl as well as SO₂ absorptivity has been developed.

Hydrated lime is formed when calcium oxide reacts with water as:

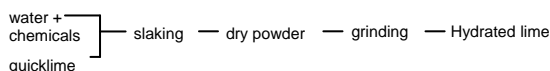


The exothermic heat is large enough to convert all the water in the reaction mass as steam. Thus, practically water in twice the stoichiometric amount is needed, so that one stoichiometric amount of water is present in the reaction mass at all times to react with quicklime throughout the reaction until the reaction reaches completion while the other stoichiometric amount of water is driven away as steam by the reaction heat.

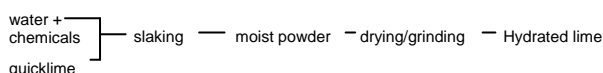
Typical hydrated lime production processes are shown in Fig. 1. Industrial grade hydrated lime is produced by slaking with water around 0.64 times the mass of quicklime, in order to produce dry hydrated lime without needing any drying operation, therefore this process is termed as Dry slaking. The 1st generation reactive hydrated lime is produced mostly by dry slaking, i.e. SWR = 0.6 to 0.8, with slaking water containing chemicals such as alcohols, glycols, etc. for increasing the specific surface area. On the other hand, the 2nd generation highly reactive hydrated lime is produced by semi-wet or wet slaking, i.e. SWR = 0.8 to 4, with slaking water containing the same type of chemicals such as alcohols, glycols, and then removing the excess water to obtain dry hydrated lime [3]-[6]. Regarding the absorption of HCl by hydrated lime, it has been reported that the overall reaction is governed by the pore diffusion[7].

For the absorption of SO₂, the study on the change in pore volume and its structure of CaO with the progress in absorption is made and it is reported that the CaO prepared from Ca(OH)₂ has slit or plate like shaped pores and the CaO prepared from CaCO₃ has cylindrical shaped pores and that the CaO prepared from Ca(OH)₂ is more effective in reacting with SO₂ [8].

Dry slaking: SWR = 0.6-0.8



Semi-Wet slaking: SWR = 0.8-1.2



Wet slaking: SWR = 1.2-10

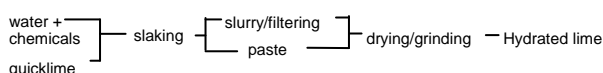


Figure 1: Hydrated lime production processes

It seems that the effect of slaking condition on the pore structure of hydrated lime needs to be investigated thoroughly. Furthermore, there is no paper on the relation between the pore structure of hydrated lime such as the pore volume, the pore size, the specific surface area and the fundamental characteristics of dry sorption of acidic gases, especially SO₂. In view of this, we prepared hydrated lime sample by slaking 1 to 90min with SWR = 0.65 to 10 of slaking water, and analyzed the respective changes in pore volume, specific surface area, crystallite size of the calcium hydroxide with the progress in slaking time and the SO₂ absorptivity of the obtained samples at 15min slaking time, then determined the optimum slaking condition for the improved SO₂ absorptivity. Similarly, we prepared hydrated lime sample by slaking 1 to 90min with SWR = 0.7, 0.9 and 2 of slaking water containing DEG of 0, 0.5, 2, 5 and 10mass% of the quicklime, then analyzed the properties as mentioned previously to evaluate the effect of DEG on the pore structure characteristics and the SO₂ absorptivity.

2 EXPERIMENT

2.1 Quicklime Raw Material

Quicklime powders obtained by grinding industrial grade quicklime of Japan Industrial Standard JIS-R9001 were used. The quicklime QL1 had the purity of CaO > 95%, the mean particle size of <45µm, the specific surface area of 2.28x10³ m².kg⁻¹ and the pore volume of 0.008x10⁻³ m³.kg⁻¹. Another quicklime QL2 had the purity of CaO > 95%, the mean particle size of <45 µm, the specific surface area of

2.45x10³ m².kg⁻¹ and the pore volume of 0.009x10⁻³ m³.kg⁻¹. The hydration reactivity *t*₆₀ of the quicklimes QL1 and QL2 were 24s and 18s respectively (According to the ASTM C110-76a, the hydration reactivity of the quicklime, noted as *t*₆₀, is the time taken by the lime slurry to reach 337K when 0.15kg of quicklime powder is added to 0.6kg of water at 293K under the agitation of 300rpm in a Dewar flask).

2.2 Slaking Experiment

The slaking of quicklime QL1 was carried out with SWR = 0.65 to 10 of slaking water using a mixer/agitator machine (Model: C138A, Maruto Manufacturer). First 1kg of quicklime was placed in the bowl of the machine and then a predetermined amount of slaking water at 313K was added as quickly as possible. After 15min, the resulting wet hydrated lime was removed, dried in a vacuum dryer (Model: Vacuum Oven ADP-21, Yamato) for 12h at 393K under reduced pressure of -0.1MPa, and the dry hydrated lime was ground to pass 75µm in an airtight pulverizer (IKA LABORTECHNIK, Type: M 20 S 8, Janke & Kunkei GmbH & Co.). In the case of SWR = 10, the resulting hydrated lime slurry was filtered using a 5C filter paper of 1µm retaining to obtain a wet hydrated lime cake which was then put through the subsequent drying and grinding treatments. The hydrated lime samples thus prepared were evaluated for physical properties such as specific surface area, pore volume, crystallite size and SO₂ absorptivity.

The slaking of quicklime QL2 was carried out exactly in the same manner as that of quicklime QL1, except that the SWR = 0.7, 0.9 and 2 of slaking water containing DEG of 0, 0.5, 2, 5 and 10mass% of quicklime and the hydration time of 1 to 90 min were used.

Hereafter, the hydrated lime samples obtained from slaking quicklime-QL1 and quicklime-QL2 were denoted as hydrated lime-HL1 and hydrated lime-HL2 respectively in the present paper.

2.3 Pore Characteristics Analyses

A high speed gas sorption analyzer (NOVA3000 of Quantachrome, Yuasa) was used for measuring specific surface area with N₂ absorption by 3 point BET method, total pore volume with the absorption of N₂ at P/P₀ = 0.9975 and pore size distribution with N₂ desorption by BJH method.

2.4 XRD Analyses

The X ray diffraction of the hydrated lime sample was carried out in the condition of XRD : Cu Kα; 40 KV, 30x10⁻³ A. For the calculation of calcium hydroxide crystallite size at (101), *d*=0.263nm, half width of the peak at 2θ= 34.1° was used. The size of the calcium hydroxide crystallite, 2θ= 34.1°(101) *d*-spacing=0.263nm, included in the hydrated lime sample was evaluated by using Scherrer's equation, Eq.(2), with potassium carbonate, 2θ=34.1° (112) *d*-spacing = 0.263, as a reference.

$$D = 0.89 \times \lambda / (\sqrt{\beta_0^2 - \beta_e^2}) \times \cos\theta \quad (2)$$

where, D is average crystallite size (nm), λ is 0.154 (nm) representing the wave length of $\text{CuK}\alpha$ used in the XRD instrument, β_0 is the half-width of the diffracted wave (rad.), β_e is the half-width of the diffracted wave at the same angle of a standard crystal (rad.) and θ is the measured angle of diffraction as $2\theta/\theta$.

2.5 SO₂ Absorptivity

A schematic diagram of SO₂ absorption column (0.04 m ϕ x 0.5 m height) used for determining the dry SO₂ absorptivity of hydrated lime is shown in Fig. 2. An amount of 0.6×10^{-3} kg of hydrated lime was placed evenly in a 100 μm glass filter of 33.5×10^{-3} m ϕ . The sample unit was then set up at the bottom of the reactor glass tube of 40×10^{-3} m ϕ x 0.5 m height maintained at 442.3 K. For temperature control, a thermocouple was placed at the middle of the reactor outside surface. After flowing N₂ gas of 2×10^{-3} m³ at STP for 10 min until the thermal equilibrium was achieved, a mixed gas of 1 % SO₂-99% N₂ of 9.1×10^{-3} m³ at STP simulating the flue gas from a municipal waste incinerator was introduced into the reactor so that the total amount of SO₂ in the simulated gas was a half of the stoichiometric amount of Ca²⁺ in the sample. Further, steam of 3.9×10^{-3} m³ at STP, heated to 443K was introduced into the reactor. The total reaction time was set 50 minutes, thereby the cross sectional flow rate of the gas was 8×10^{-3} m³ · s⁻¹. These reaction conditions were kept quite similar to that of the typical flue gas treatment operating parameters in the municipal waste incineration plants.

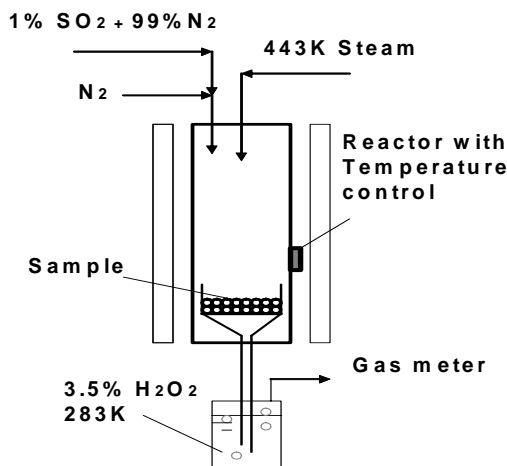


Figure 2: SO₂ absorptivity measuring apparatus

The gas from the reactor exist was scrubbed with 0.4×10^{-3} m³ of 3.5% H₂O₂ solution kept at 283 K and at the end of the experiment the amount of SO₂ dissolved was

analyzed. The SO₂ absorptivity of the hydrated lime sample was determined as-

$$\text{SO}_2 \text{ absorptivity (\%)} = (S_A - S_B) / S_A \times 100 \quad (3)$$

where, S_A = amount of SO₂ in the simulated gas
 S_B = amount of SO₂ in the H₂O₂ solution

3 RESULTS AND DISCUSSION

3.1 Pore Characteristics and SO₂ Absorptivity of Hydrated Lime-HL1

The relation of the specific surface area, pore volume and SO₂ absorptivity of the hydrated lime-HL1 are shown in Fig. 3. It can be seen that the specific surface area increases with the increase in SWR until SWR = 0.73, but decreases with larger than SWR=0.73. On the other hand, SO₂ absorptivity and pore volume increase with the increase of SWR until SWR = 0.9 and decrease with larger than SWR = 0.9. These findings suggest that SO₂ absorptivity is related directly with pore volume and is not directly related with the specific surface area.

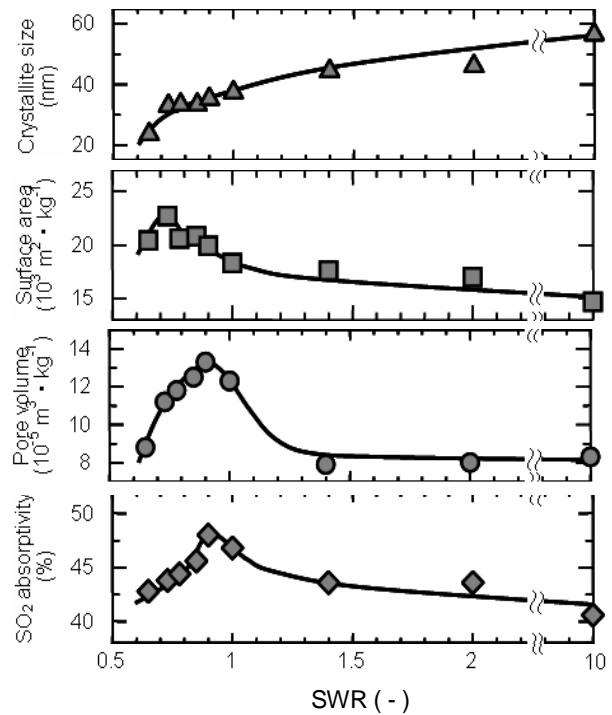


Figure 3: Effect of SWR on pore characteristics of HL1

Figure 4 shows that SO₂ absorptivity increases in an almost direct proportionality with the increase in pore volume indicating that the pore volume is of primary significance for highly efficient hydrated lime with improved SO₂ absorptivity.

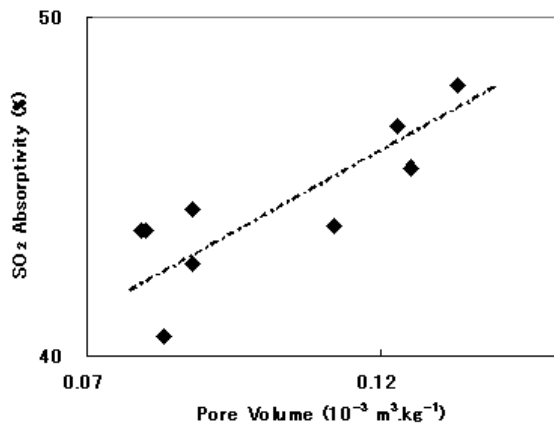


Figure 4: Relation between SO₂ absorptivity and pore volume of HL1

3.2 Relation of Crystallite Size and Pore Characteristics of Hydrated Lime-HL1

The relation of crystallite size and pore characteristics of hydrated lime-HL1 are shown in Fig. 5. It can be seen that the surface area almost directly decreases with increasing crystallite size for all crystallite sizes. On the contrary, the pore volume increases with the increase in crystallite size in the range of 20 - 35 nm only and then decreases with the increase in crystallite size in the range 35 - 59 nm. It can be suggested for a certain slaking condition, that the pore volume of the hydrated lime gives the maximum value when the crystallite size of the hydrated lime is about 35nm.

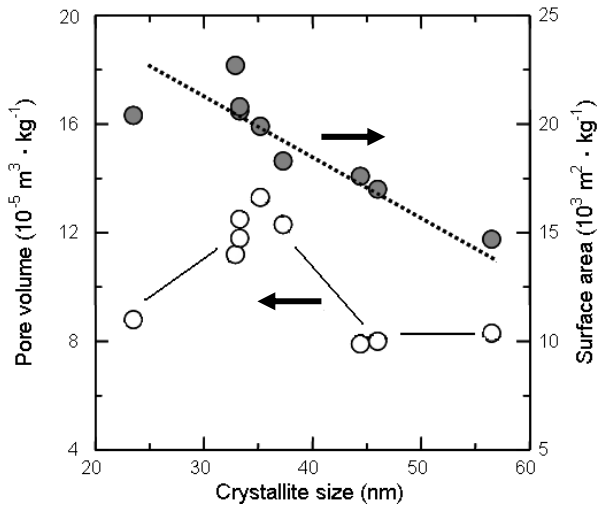


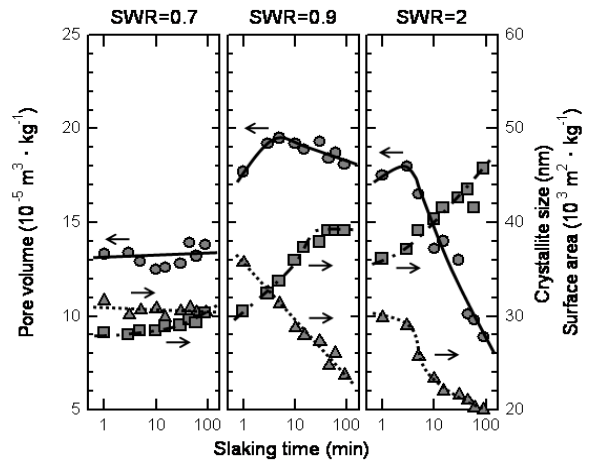
Figure 5: Relation of crystallite size with pore characteristics of HL1

3.3 Relation of Crystallite Size, Pore Characteristics and Slaking Time of hydrated lime HL2

The relation of crystallite size, pore volume and specific surface area of hydrated lime-HL2 during the slaking process of quicklime-QL2 for SWR = 0.7, 0.9 and 2, with DEG = 0 mass% are shown in Fig. 6. For SWR=0.7, the size of the

crystallite is almost constant at 28 nm for all slaking time, indicating that there is no growth in crystallite with slaking time. For SWR=0.9, the crystallite grows from 30 nm to 37 nm in 1 to 15 min of slaking time, but stops growing for further increase in slaking time. For SWR=2.0, the growth of crystallite starts at 36 nm and continues growing for all slaking time, finally reaching 46 nm at 90 min slaking time. It is clear that higher SWR and longer slaking time promote the growth of crystallite.

Thus, for SWR=0.7, where there is no growth in crystallite size with slaking time, the specific surface area of the hydrated lime-HL2 remains almost the same at $32 \times 10^3 \text{ m}^2 \cdot \text{kg}^{-1}$ for all slaking time. For SWR=0.9, where the growth of crystallite is moderate, the specific surface area of the hydrated lime is $36 \times 10^3 \text{ m}^2 \cdot \text{kg}^{-1}$ and $24 \times 10^3 \text{ m}^2 \cdot \text{kg}^{-1}$ at 1 and 90 minute slaking time, respectively. For SWR=2, where the growth of crystallite and the decrease of pore volume are more pronounced. The initial specific surface area is comparatively much smaller, $30 \times 10^3 \text{ m}^2 \cdot \text{kg}^{-1}$ at 1min. and $20 \times 10^3 \text{ m}^2 \cdot \text{kg}^{-1}$ at 90 min. slaking time.



(●:Pore volume, ■:Crystallite size, ▲:Surface area)
Figure 6: Relation of pore characteristics of HL2 for SWR = 0.7, 0.9 and 2, with DEG= 0 mass%

3.4 Relation of Pore Characteristics and SO₂ Absorptivity of Hydrated Lime-HL2 with Slaking Water containing DEG

The data of the specific surface area, pore volume, crystallite size and SO₂ absorptivity for the hydrated lime-HL2 prepared by slaking 15min with slaking water of SWR = 0.9 containing DEG of 0 to 10 mass% of quicklime are plotted in Fig.7. It can be seen that pore volume remains constant for all DEG values. However crystallite size decreases sharply from 36nm to 18nm with increasing DEG in the range DEG = 0 to 2 mass% and then decreases slowly from 18nm to 15nm with increasing DEG in the range DEG = 2 to 10 mass%. Similarly, SO₂ absorptivity increases sharply from 44% to 66% with increasing DEG in the range DEG = 2 to 10 mass% and then decreases slowly from 66% to 61% with increasing DEG in the range DEG = 2 to 10 mass%

range. This indicates that the smaller crystallite size makes the smaller pore size distribution (ex. 3 to 20nm) with being effective SO₂ absorption.

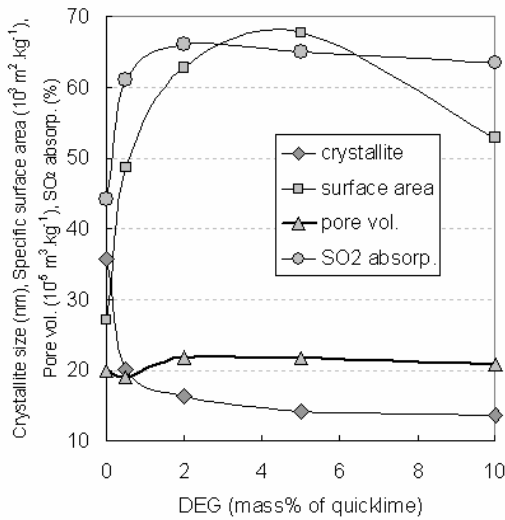


Figure 7: Effect of DEG on pore characteristics and SO₂ absorptivity of HL2 for SWR = 0.9

The data of the specific surface area, pore volume and SO₂ absorptivity for the hydrated lime-HL2 prepared by slaking 15min with slaking water of SWR = 0.7, 0.9 and 2 containing DEG of 2 mass% of quicklime are plotted in Fig.8. In this case, it can be seen that the crystallite size and pore volume increase with the increase in SWR = 0.7 to 2 and reach the respective largest value at SWR = 2. Also, SO₂ absorptivity increases with the increase in SWR from 0.7 to 0.9 and then remains constant for SWR 0.9 to 2. However the specific surface area increases with the increase in SWR = 0.7 to 0.9 and then decreases with the increase in SWR = 0.9 to 2. It can be seen that the crystallite size and the pore volume are directly related.

Based on these data, it can be concluded that the relations of pore volume, specific surface area, crystallite size and SO₂ absorptivity of the hydrated lime prepared by slaking with slaking water containing DEG are completely different from that of with slaking water without DEG.

Figure 9 shows that the pore size distribution in terms of Dv(log d), the differential of pore volume for increment in pore diameter in logarithmic value: i.e. $(v_2 - v_1) / (\log d_2 - \log d_1)$, of the three hydrated limes HL2 slaked with SWR = 0.7, 0.9 and 2 of slaking water containing DEG of 2 mass% of quicklime are all different. For SWR = 0.9, there are few pores in the pore size range of 3 to 5nm, then increases with the increase in pore size in the range of 5 to 10nm, and decreases with the increase in pore size in the range of 10 to 100nm.

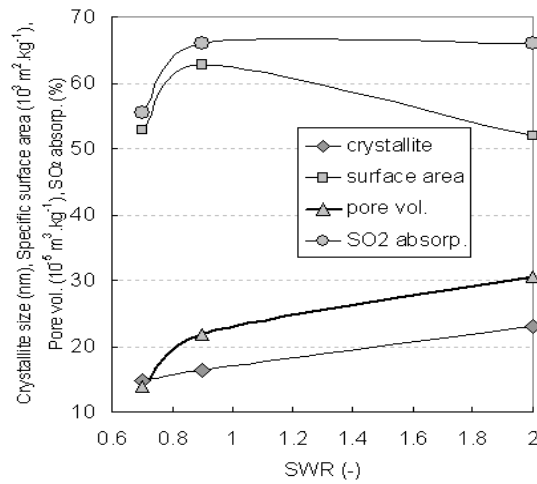


Figure 8: Effect of SWR on pore characteristics and SO₂ absorptivity for DEG of 2 mass% of QL2

Among the three samples, the sample prepared with SWR = 0.7 has the lowest pore volume and together with low number of pores for all pore sizes in its pore structure, it is naturally low in SO₂ absorptivity. The difference between the samples of SWR = 0.9 and SWR =2, although the latter posses larger pore volume, SO₂ absorptivity is the same for both samples. It is shown that even though SWR = 2 has many pores in the pore size of 10 to 100 nm which is attributed to the formation of extremely large pore volume, its SO₂ absorptivity is almost the same as that of hydrated lime prepared with SWR = 0.9 which has lower pore volume but has a larger number of pores lying in the range from 3 to 20 nm. Based on these comparison, it can be concluded that for developing highly efficient hydrated lime with efficient SO₂ absorption, hydrated lime not only with large pore volume, but also with pore size distribution having a large number of pores existed in the pore size of 3 to 20nm is required.

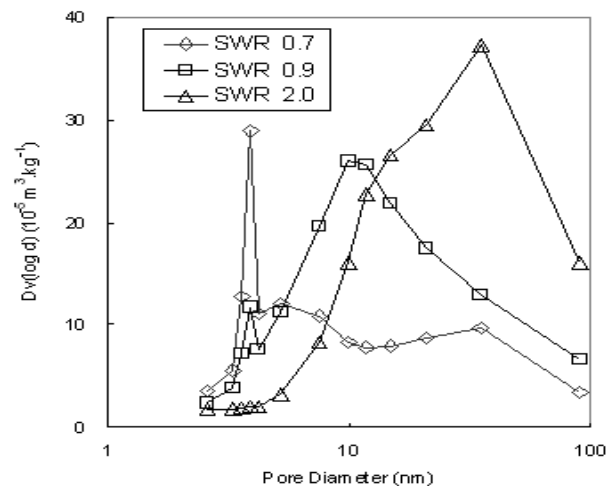


Figure 9: Effect of SWR =0.7, 0.9, 2 with DEG 2 mass% of QL2 on pore diameter

4 CONCLUSION

The results obtained by the present work can be summarized as follow:

1) The crystallite size became larger with increasing SWR (Slaking Water Ratio). The specific surface area inversely decreased with increasing SWR. However, the pore volume and SO₂ absorptivity increased with increasing SWR until SWR = 0.9, attained the maximum values, and decreased when SWR was added as SWR > 0.9. At SWR=0.9, the crystallite size of hydrated lime was about 35 nm.

2) For SWR=0.7, there was no change in crystallite size and pore volume for all slaking time. For SWR=0.9, crystallite grew to the crystallite size of 37 nm within 15 min of slaking time and almost stopped growing afterwards. On the other hand, the pore volume was almost constant for all slaking time. For SWR=2, the crystallite was 37nm even at the onset of the slaking and grew with slaking time and reached 47nm at 90min. On the contrary, pore volume decreased with increasing slaking time.

3) Diethylene glycol (acronym DEG) suppressed the growth of calcium hydroxide crystallite and improved the SO₂ absorptivity of the hydrated lime. The crystallite prepared with DEG 0.5 - 10 mass% of quicklime was about half the size of the crystallite prepared with DEG 0 mass%. Further, the SO₂ absorptivity of the hydrated lime prepared with DEG of 0.5 - 10 mass% was 1.5 times higher than that of the hydrated lime prepared without DEG.

4) The relations of pore volume, specific surface area, crystallite size and SO₂ absorptivity of the hydrated lime prepared with DEG were different from that of the hydrated lime prepared without DEG.

For a certain amount of DEG, crystallite size and pore volume increased with SWR = 0.7 to 2. The SO₂ absorptivity also increased with SWR = 0.7 to 0.9, but stopped increasing with SWR = 0.9 to 2.

5) The highly efficient hydrated lime, not only with the large pore volume, but also with the pore size distribution having a large number of pores existed in the pore size of 3 to 20nm is desirable for efficient SO₂ absorption.

The pore size distribution of the hydrated lime prepared with DEG of 2 mass% with SWR = 0.9 had the maximum number of pores in 3 to 20 nm size range and pretty large pore volume.

5 REFERENCES

- [1] T. Murakami., "Hydrated Lime for Refuse Incineration Flue Gas Cleaning," *Powder Science & Engineering*, Vol. 36, No. 12, pp. 61-68, (2004).
- [2] K. Yamashita. "Hydrated Lime for Incineration Flue Gas Treatment," *J. Soc. Inorg. Mater. Japan*, Vol.10, pp.412-419, (2003).
- [3] Japanese Patent, Disclosed, 2004-161536.
- [4] Japanese Patent No. 3379649.
- [5] Japanese Patent No. 3576160.
- [6] J. A. H. Oates. "*Lime and Limestone: Chemistry and Technology, Production and Uses*," Wiley-VCH, pp.219, (1998).
- [7] K. Michael, K. Andreas, K. Gernot, Z. Xinhai, D. Jun, X. Jingcai and G. Lingmei., "Reaction Mechanism of a Single Calcium Hydroxide Particle with Humidified HCl," *Chem. Eng. Sci.*, Vol.60, No. 21, pp.5819-5829, (2005).
- [8] B. K. Gullett and K. R. Bruce, "Pore Distribution Changes of Calcium-Based Sorbents Reacting with Sulfur Dioxide," *AIChE Journal*, Vol.33, No. 10, pp.1719-1726, (1987).

Conductive Paper prepared by Electroless Nickel Plating

Shohta Takemura*, Takeshi Ueno*, Toshihiro Takamatsu*,
Mihoko Igarashi**, Toshiyuki Tanaki*,
Masahiro Shimada** and Takayuki Okayama***

* Tama branch, Commercialization support department, Tokyo Metropolitan Industrial Technology Research Institute, 3-7-10, Akebono-cho, Tachikawa-shi, Tokyo, 190-0012, Japan

** Tokyo Metropolitan Industrial Technology Research Institute, 3-13-10 Nishigaoka, Kita-ku, Tokyo, 115-8586, Japan

*** Faculty of Agriculture, Tokyo University of Agriculture and Technology, 3-5-8 Saiwai-cho, Fuchu-shi, Tokyo, 183-8509, Japan
takemura.shohta@iri-tokyo.jp

Abstract: Conductive paper is prepared by coating its surface using an electroless nickel plating technique. In this study, we established a process for preparing conductive paper and derived optimum conditions for the process. The experimental results confirmed the relationship between the paper thickness, the coating structure and the electrical characteristics. The prepared conductive paper shields circuitry from electromagnetic waves. Therefore, the electromagnetic shielding effectiveness of samples was evaluated by the KEC method, and an electric field shielding effectiveness of 60 dB was confirmed. The proposed conductive paper can be used to achieve EMC.

Key words: EMC, Electroless Nickel Plating, Conductive Paper

1 INTRODUCTION

There is an increasing demand for medical and electronic equipment that would not malfunction when exposed to electromagnetic radiation and produce less electromagnetic radiation. The various limits are set by international standards [1,2]. The ability to operate without interfering with other devices or being interfered by other devices is called electromagnetic compatibility (EMC). Conductive paper can be used to achieve EMC.

Conductive paper is paper in which electricity flows on the surface due to a coating applied using a metal plating process. This paper can shield the equipment from electromagnetic waves. The conductive paper is pasted to electronic circuit boards and protects them from electromagnetic waves; it can also reduce the noise radiated from the wiring.

In previous studies, a nickel plating process was used in an attempt to experiment with conductive filter paper [3-5]. However, a process of plating on hardwood and softwood paper has not been reported.

In this study, conductive paper was prepared by electroless nickel plating on softwood and hardwood paper. We established a process for producing conductive paper. A practical sample was evaluated by measuring the electromagnetic shielding effect.

2 MATERIALS AND METHODS

The prepared samples are softwood paper, hardwood paper and filter paper. Softwood and hardwood paper is formed from pulp using the Japanese Industrial Standard (JIS) method [6].

The Kanigen electroless nickel plating process, which is a nickel-phosphorus alloy plating method, was used [7]. Fig. 1 shows the plating process.

Sections of plated samples were observed with a scanning electron microscope. In addition, a cross section of paper containing nickel was observed by energy dispersive X-ray spectroscopy (EDX). The volume resistivity of the sample was measured with a 4-probe conductivity meter. The prototype conductive paper in this research was placed around electronic circuits to serve as a near field radiation shield and the sample was evaluated by the KEC method, which evaluates the effectiveness of the electric and magnetic field shielding. KEC method evaluates the shielding performance of electric and magnetic field from decrement quantity of the electromagnetic waves by setting the conductive paper between the antenna. KEC method evaluates an electric field or a magnetic field individually. The shielding effect was evaluated from 80 to 1000 MHz, which is the frequency range in the RF immunity standard test (IEC61000-4-3) [1,2].

3 RESULTS AND DISCUSSION

Fig.2 shows a sample cross section of the plating process of the hardwood paper of different thickness respectively. The

sample is hardwood, about 0.2 mm thick, sandwiched in nickel. The hardwood is so thick because the plating solution did not penetrate the sample adequately. A hardwood sample that contains nickel in the paper achieved a thickness of about 0.1 mm. Cross section of softwood sample of about 0.2mm thickness was confirmed with sandwiched in nickel as well as hardwood sample by EDX.

Table 1 shows volume resistivity of the sample. The sample was compared with conductive filter paper. Volume resistivity of sample was calculated by measurements of thickness of the whole of paper. The ratio of cellulose for the whole of paper was increased by the nickel distribution as shown in Fig.2(b). Therefore the volume resistivity of hardwood paper increased as the thickness of paper became thick. The sample with thickness of about 0.1 mm (hardwood paper) showed the lowest volume resistivity.

The electric field shielding effect of the sample is shown in Fig. 3 and the sample was compared with commercial products, including chemical products, such as the Morimoto EMI-Shield, and conductive filter paper. The electric field shielding effect of the hardwood sample was 60 dB, which is a fairly typical performance[8].

4 CONCLUSION

The conductive paper process prepared by electroless nickel plating was established for hardwood and softwood materials.

In the conductive paper, the nickel distribution affected the paper thickness. The hardwood conductive paper provided 60 dB of electric field shielding, indicating that the paper will be useful in providing EMC.

References

- [1] International Electrotechnical Commission, <http://www.iec.ch/>, (2009).
- [2] Clayton, R. P., Electromagnetic Compatibility, Wiley, pp.1-983, (2005).
- [3] Takemura, S., Ueno, T. and Shimada, M., Proc. of 58th Annual Meeting of the Japan Wood Research Society, CD-ROM, PQ021, (2008).

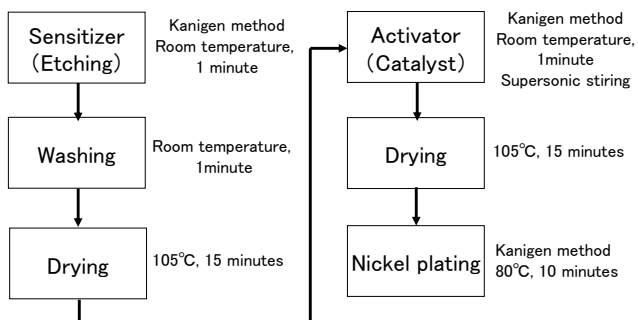


Fig. 1 Nickel Plating Process

[4] Saito, T., Irie, K., Sato, E., Tomuro, Y. and Kuwana, A., J. of the Surface Finishing Society of Japan, Vol.44, No.3, pp.53-57, (1993).

[5] Nakao, Y., J. of The Society of Fiber Science and Technology, Vol.42, No.12, pp.510-514, (1986).

[6] Japanese Standards Association, JIS handbook, 32, pp.1-885, (2007).

[7] Japan KANIGEN co., Ltd., <http://www.kanigen.co.jp/>, (2009).

[8] Kobayashi, T., J. of Engineering Materials, Vol.57, No.3, pp.6-9, (2009).

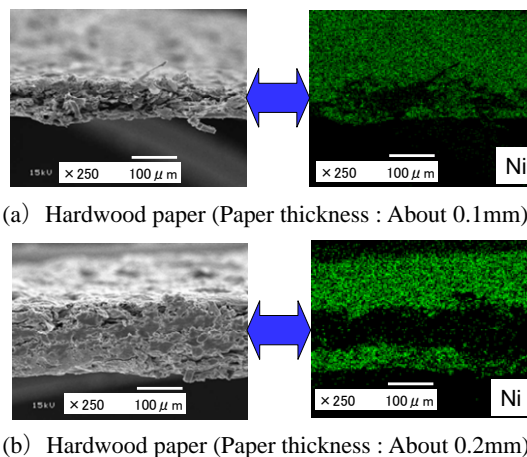


Fig. 2 Nickel distribution of samples

Table 1 Volume resistivity of samples

Samples	Thickness of paper (mm)	Volume resistivity ($\Omega \cdot \text{cm}$)
Hardwood paper	0.10	6.3×10^{-3}
	0.29	2.9×10^{-2}
	0.38	3.0×10^{-2}
Softwood paper	0.23	6.1×10^{-2}
Filter paper	0.26	2.2×10^{-2}

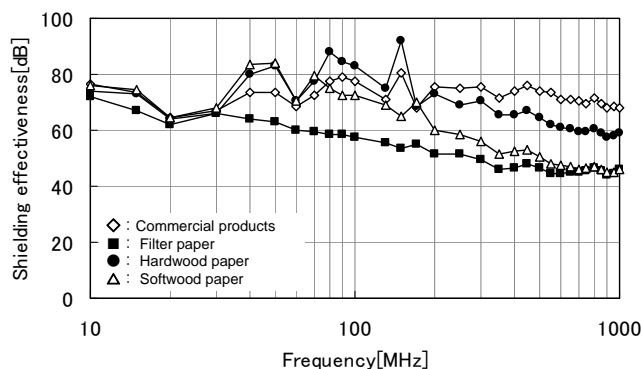


Fig. 3 Shielding effectiveness of samples (Electric field)

Oxygen storage behavior of delafossite-type CuLnO_2 (Ln=La, Y)

Sumio Kato¹, Hidenori Sato¹, Masataka Ogasawara¹, Shinichi Nakata¹,
Takashi Wakabayashi², Yuunosuke Nakahara²

1. Department of Engineering in Applied Chemistry, Faculty of Engineering and Resource Science, Akita University,
1-1 Tegatagakuen-cho, Akita 010-8502, Japan

2. Catalysts Division, Mitsui Mining & Smelting Co., Ltd., 1013-1 Ageoshibo, Ageo, Saitama 362-0025, Japan

s_kato@ipc.akita-u.ac.jp

Abstract: Delafossite-type CuLnO_2 (Ln=La,Y) was synthesized and their oxygen storage capacity (OSC) under oxidation/reduction cycle was investigated. CuLaO_2 was synthesized by heating at 1000°C for 6h in N_2 flow and CuYO_2 was synthesized by calcination of $\text{Y}_2\text{Cu}_2\text{O}_5$ at 1190°C for 1h in N_2 flow. The oxygen storage capacity values of CuLaO_2 and CuYO_2 at lower temperatures were larger than that of CeO_2 -based materials which is used as a promoter of an automobile catalyst. Structural stability of delafossite-type CuLnO_2 under cyclic oxidation/reduction atmosphere was investigated using XRD analysis. During the OSC measurement, CuLaO_2 decomposed to La_2CuO_4 and Cu_2O . CuYO_2 also decomposed partially to Y_2O_3 , $\text{Y}_2\text{Cu}_2\text{O}_5$ and Cu_2O . These results suggest that the oxidative decomposition of CuLnO_2 occurred at high temperature.

Key Words: oxygen storage, delafossite, copper oxide

1 INTRODUCTION

A three-way catalyst (TWC) composed of precious metal catalyst are widely used in order to remove pollutants in automobile exhaust gas, including carbon monoxide (CO), nitrogen oxides (NOx) and hydrocarbons (HC). In the pollutant removal process, CO and HC are oxidized to CO_2 and H_2O , and NOx is reduced to N_2 . TWC performance is lowered by the cyclic oxidative-reductive compositional fluctuation in exhaust gas. Therefore, metal oxides whose oxidation state can change easily such as CeO_2 -based solid solutions are widely used as promoters having oxygen storage capacity (OSC) [1]. CeO_2 exhibits oxygen storage/release behavior in oxidative/reductive atmosphere, which is accompanied by the redox of Ce ions between the oxidation states of Ce^{3+} and Ce^{4+} , and is stable enough during oxygen storage/release process for use in an actual exhaust gas. Improvement of catalytic performance, especially of catalytic activity at low temperature and under oxygen-rich condition, has become necessary for compliance with recent automobile emission regulations. In order to improve activity at low temperature, it would be effective to use a promoter which exhibits a large OSC in the low temperature range. To develop a material exhibiting oxygen storage/release behavior at lower temperature, we focused on Cu-containing delafossite-type oxides, CuMO_2 (M=trivalent cation), and have reported the OSC under cyclic oxidative/reductive atmosphere, for M=Fe, Mn, Cr and Al [2]. CuMO_2 has a layered structure consisting of edge-shared MO_6

octahedra and two-coordinated Cu^+ cations at the interlayer sites. For M=La, Y and Fe, there have been reported non-stoichiometric delafossite-type oxides such as CuLaO_{2+x} , CuYO_{2+x} and CuFeO_{2+x} which have extra oxide ions at the interlayer between MO_6 octahedra sheets [3,4]. This intercalation of oxide ions accompanies oxidation of Cu^+ to Cu^{2+} . Although oxygen storage and release behavior with temperature in air has been reported for CuLnO_2 (Ln: La, Y) [3], the behavior in cyclic oxidative-reductive atmosphere has not been investigated.

In this work, we synthesized delafossite-type copper oxide, CuMO_2 (M= La and Y) and investigated their OSC under cyclic oxidative-reductive atmosphere using a pulse injection method. Phase stability of the delafossite oxides against both oxidative and reductive atmosphere were also investigated in order to reveal oxygen storage/release mechanism.

2 EXPERIMENTAL

CuLnO_2 (Ln=La,Y) were synthesized by a conventional solid state reaction. Cu_2O , La_2O_3 , Y_2O_3 were used as the starting materials. The stoichiometric mixtures were obtained by ball milling using ethanol and pressed into pellets of 10mm diameter. CuLaO_2 was synthesized by heating at 1000°C for 6h in N_2 flow. CuYO_2 was synthesized by calcination of $\text{Y}_2\text{Cu}_2\text{O}_5$. $\text{Y}_2\text{Cu}_2\text{O}_5$ was synthesized by heating of a stoichiometric mixture of CuO and Y_2O_3 at 1050°C for 24h in air. Then $\text{Y}_2\text{Cu}_2\text{O}_5$ was heated at 1190°C for 1h. Phase

identification of the oxides was performed by a powder X-ray diffraction (XRD) method using Ni-filtered $\text{CuK}\alpha$ radiation. Weight change of samples was measured by thermogravimetry (heating rate $10^\circ\text{C}/\text{min}$). The OSC of each oxide was estimated by the pulse injection method according to Yao [1], using H_2 gas instead of CO . This OSC value was used as an index of reversible oxygen uptake in the oxidation/reduction cycle. The oxide sample (25mg) was placed in a quartz reactor and heated in He flow ($200\text{cm}^3/\text{min}$) at 800°C for 15min prior to pulse injection. Then, it was completely oxidized by injecting 50% O_2/He pulses until a 100% breakthrough was attained. H_2 and 50% O_2/He pulses were alternately injected into the oxide with He gas flowing at $200\text{cm}^3/\text{min}$ until constant O_2 uptake was found. The volume of a pulse was 1.16cm^3 . The amounts of O_2 and H_2 in the effluent gas were monitored with a gas chromatograph equipped with a TCD detector. OSC of the oxide was estimated from the amount of O_2 uptake at $200\text{-}800^\circ\text{C}$.

3 RESULTS AND DISCUSSION

For both CuLaO_2 and CuYO_2 , the X-ray diffraction peaks were indexed on the basis of hexagonal unit cell corresponding to 3R-type structure. The OSC of CuLnO_2 estimated by the pulse injection as a function of temperature are shown in Fig.1. Oxygen storage behavior appears in the temperature range higher than 300°C for both CuLaO_2 and CuYO_2 . The OSC values of CuLaO_2 and CuYO_2 increased with temperature up to 718 and $798 \mu\text{mol-O}_2/\text{g}$ at 700°C , respectively. During the OSC measurement at 800°C , continuous O_2 uptake was observed for both oxides. This would be due to a decomposition of the oxides in a low oxygen partial pressure. Therefore, the OSC value at 800°C could not be estimated as a constant value.

The XRD patterns of CuLaO_2 and CuYO_2 after the OSC measurement at 800°C are shown in Fig.2. La_2CuO_4 and Cu_2O were observed for CuLaO_2 and $\text{Y}_2\text{Cu}_2\text{O}_5$, Y_2O_3 and Cu_2O were observed for CuYO_2 . Although the valence state of Cu in both delafossite-type CuLaO_2 and CuYO_2 is +1, it is found that Cu^{2+} containing oxides such as La_2CuO_4 and $\text{Y}_2\text{Cu}_2\text{O}_5$ formed during OSC measurement. In the TG curves of CuLaO_2 and CuYO_2 measured in air flow, weight gains were observed in the temperature range, $300\text{-}500^\circ\text{C}$. These results suggest that decomposition of the delafossite-type oxides would be caused by oxidation of Cu^+ .

XRD patterns of oxidized and reduced CuLaO_2 samples prepared by injection of O_2 or H_2 pulse at $400\text{-}600^\circ\text{C}$. Both the oxidized and reduced samples at 400°C , the delafossite-type CuLaO_{2+x} including excess oxygen formed as a single phase, while a small amount of La_2CuO_4 were observed for samples treated at 500°C . From these results, it is found that oxygen storage/release behavior of CuLaO_2 at 400°C was caused by oxidation and reduction without a structural change and decomposition of oxygen excess delafossite phase. Therefore, CuLaO_2 would be available as an oxygen storage material at low temperature. While, these delafossite oxides decomposed under oxidation/reduction cycle above 500°C . Further investigation is needed to improve both an OSC and durability against oxidation/reduction cycle at high temperature.

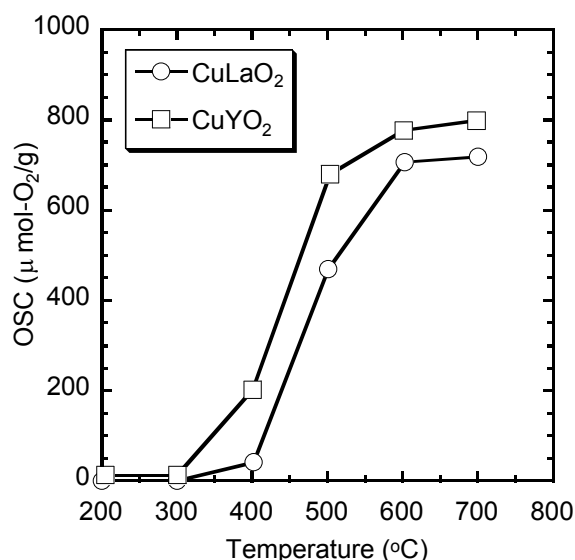


Fig.1 Oxygen storage capacity of CuLaO_2 and CuYO_2 as a function of temperature.

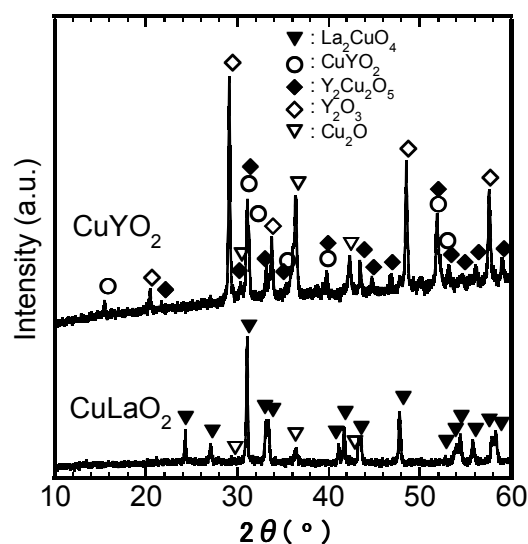


Fig.2 XRD patterns of CuLaO_2 and CuYO_2 after the OSC measurement.

REFERENCES

- [1] H.C. Yao and Y. F. Yu Yao, *Journal of Catalysis*, Vol.86, pp.254-265, (1984).
- [2] S. Kato, R. Fujimaki, M. Ogasawara, S. Nakata, T. Wakabayashi, Y. Nakahara, *Applied Catalysis. B: Environment*, Vol.89, pp.813-818, (2009).
- [3] R.J. Cava, H.W. Zandbergen, A.P. Ramirez, H. Takagi, C.T. Chen, J.J. Krajewski, W.F. Peck Jr, J.V. Waszczak, G. Meigs, R.S. Roth, L.F. Schneemeyer, *Journal of Solid State Chemistry*, Vol.104, pp.437-452, (1993).
- [4] E. Mugnier, A. Barnabe, P. Tailhades, *Solid State Ionics*, Vol.177, pp.607-612, (2006).

Mechanism of deactivity in Rh catalysts

Takashi Wakabayashi*, Yuunosuke Nakahara*,
Masataka Ogasawara**, Sumio Kato** and Shinichi Nakata**

*Catalysts Division, Mitsui Mining and Smelting Co., Ltd., 1013-1 Ageosho, Ageo, Saitama, 362-0025, Japan

** Faculty of Engineering and Resource Science, Akita University 1-1 Tegatagakuen-cho, Akita, 010-8502 Japan

t_wakabayashi@mitsui-kinzoku.co.jp

Abstract: The relationship between the catalytic activity and surface states of dispersed rhodium on ZrO_2 was studied for fresh, aged and reduced as aging condition. It was shown that the catalytic activity of aged catalyst was improved to that of fresh catalyst by reductive treatment, and the catalytic activity was found to depend on dispersion of rhodium on ZrO_2 . To evaluate dispersion of rhodium after each aging temperature, activation energy was calculated. Based on these results, it was presumed that the major factor of deactivity in rhodium catalysts was rhodium's oxidation.

Key Words: Rhodium, deactivity, Oxidation

1 INTRODUCTION

The three-way catalysts (TWCs) oxidizes hydrocarbons (HC) as well as carbon monoxide (CO) and furthermore reduces nitrogen oxides (NOx) leading to near-zero emissions for these pollutants, close to stoichiometric air-to-fuel ratio (A/F). Use of the precious metals (Pt, Pd, Rh) are well-known high activities for these pollutants. Rh is especially used as a key material to promote the reduction of NOx. Currently, TWCs is demanded from improvement of performance and need efficient use of the precious metals by the global new legislation and the fluctuation of the precious metal's price.

Therefore, investigation of the precious metal's deactivity is useful for development of high-performance TWCs. The precious metal's deactivity usually occur sintering, to be buried and dissolved into supported materials, covering the precious metal surface with oxygen by aging of high temperature and the change in A/F (atmosphere of oxidation/reduction)[1, 2]. Moreover there is catalyst poison through phosphorous, zinc, calcium etc. come from fuel and/or lubricant [3].

This paper aims for Rh that is low deposits and high demand for automotive catalyst as shown in Figure 1[4]. We then studied that the major factor of deactivity in Rh/ ZrO_2 .

2 EXPERIMENTAL

2.1 Catalyst preparation

The catalyst powder had a loading of 0.3wt.% Rh supported on commercial ZrO_2 and was prepared by impregnation of $Rh(NO_3)_3$. The catalyst used in this study was ceramics honeycomb ($\phi 25.4 \times L30$ mm, 600 cell, 4.3 mill) coated with Rh/ ZrO_2 washcoat (Fresh catalyst).

The aged catalyst was obtained by heating at 1253K for 25h in cycle for a simulated stoichiometric and fuel lean gas by using C_3H_6 , O_2 and balance N_2 . The reduced catalyst was obtained to use aged catalyst by heating at 973K for 3h in H_2 . The sample used in the measurement of dispersion of Rh was obtained by heating at 873K, 973K, 1073K and 1173K for 0.5-50h in the same atmosphere with the aged catalyst.

2.2 Catalytic activity test and Characterization

Catalytic activities were tested raising the temperature from 373K to 673K in a simulated stoichiometric (A/F=14.6) gas by using CO, C_3H_6 , NO, CO_2 , H_2 , H_2O and balance N_2 . The concentration of CO, C_3H_6 and NO in the effluent gas was continuously monitored by an on-line gas analyzer (Horiba, MEXA7100). Catalytic performance was evaluated using the temperature of 50% conversion (T_{50}) and the conversion rate at 673K (η_{400}) for fresh, aged and reduced catalysts.

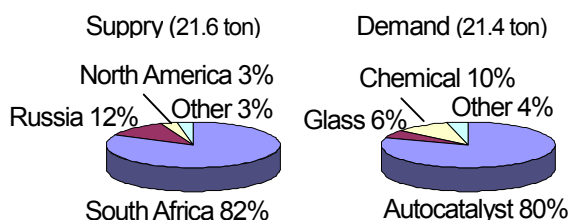


Fig. 1 Trend of supply and demand for Rhodium (2009)

The characterization of sample in each condition was carried out as follows. Chemical states of Rh on ZrO₂ was observed by X-ray photoelectron spectroscopy (XPS, ULVAC-PHI, Quantum2000) and measured Rh K-edge spectra for X-ray absorption fine structure (XAFS) in beam line BL01B1 of Spring-8. Surface states of Rh/ZrO₂ was observed by Transmission electron microscope (TEM, Hitachi, H-9000NAR). The dispersion of Rh on ZrO₂ was measured by using CO pulse method[5]. Specific surface area was measured by using Brunauer-Emmett-Teller (BET) method (Quantachrome Instrument, Quadrasorb SI).

3 RESULT AND DISCUSSION

Catalytic activities had better be low the value of T₅₀ and high the value η 400 for CO, C₃H₆ and NOx. Table 1 shows catalytic activities for each condition of Rh/ZrO₂. The value of T₅₀ for the fresh catalyst was shifted to higher temperature and the value of η 400 was remarkably declined by aging. However, it was found that the value of T₅₀ and the value of η 400 for the aged catalyst was recovered to the fresh catalyst's value by the reductive treatment.

Dispersion of Rh for these catalysts is presented in Figure 2. Dispersion of Rh for the fresh catalyst also was declined by aging, and that of the aged catalyst was improved by reductive treatment. This indicates that there is a correlation between catalytic activity and dispersion of Rh. Moreover these results imply that the process leading to Rh deactivation is not an irreversible reaction. Therefore, it is thought that the difference of dispersion of Rh between the fresh catalyst and the reduced catalyst is due to burying and dissolution of Rh into ZrO₂. In addition, it is not easy to think that the major factor of deactivity is burying and dissolution into ZrO₂, because catalytic activity was recovered to the fresh catalyst's value by reductive treatment.

Chemical states of Rh was observed in token of Rh₂O₃ in the fresh and the aged catalyst and Rh+Rh₂O₃ in the reduced catalyst. For all samples treated in the different condition, it was found that Rh₂O₃ was predominant. But the Rh particles of each sample was not able to be observed with TEM. The major factor of deactivity in Rh/ZrO₂ is thought to be sintering or oxidation of Rh from the above-mentioned result.

Then, dispersion of Rh for aging time and temperature was measured. From the activation energy calculated based on the result, it was presumed that the major factor of deactivity in Rh/ZrO₂ was oxidation of Rh, though the value of the activation energy was different according to aging time.

Table 1 Catalytic activity on Rh/ZrO₂ in a simulated exhaust gas

Sample condition	T50(°C)			η 400(%)		
	CO	C ₃ H ₆	NO	CO	C ₃ H ₆	NO
Fresh	214	282	248	100.0	98.5	95.0
Aged	322	U.D.	357	76.3	46.7	62.7
Reduced	247	312	259	100.0	97.1	89.9

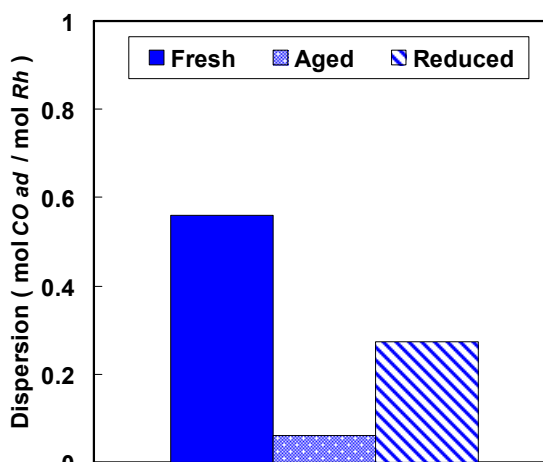


Fig. 2 Dispersion of Rh on ZrO₂ by CO pulse method

4 CONCLUSION

In the present study, to use Rh effectively, we examined the major factor of deactivity in Rh/ZrO₂. It was shown that catalytic activity for the aged catalyst was improved by a reductive the treatment, though catalytic activity for the fresh catalyst was declined by aging. In addition, there is a correlation between catalytic activity and dispersion of Rh. For all samples treated in the different condition, it was found that Rh₂O₃ was predominant by XPS and XAFS. These results showed that neither burying nor sintering into ZrO₂ were major factor of deactivity in Rh/ZrO₂. From the activation energy calculated based on the result of dispersion of Rh measurement for aging time and temperature, the deactivity in Rh/ZrO₂ was presumed to be caused by the oxidation of Rh.

REFERENCES

- [1] C.H. Bartholomew, Applied Catalysis A, General Vol.212, pp.17-60(2001)
- [2] H.C. Yao, S. Japar, M. Shelef, Journal of Catalysis, Vol.50, pp.407-418(1977)
- [3] D.E. Angove, N.W. Cant, Catalysis Today, Vol.63, pp.371-378(2000)
- [4] Johnson Matthey "Platinum 2009 Interim Review"
- [5] T. Takeguchi, S. Manabe, R. Kikuchi, K. Eguchi, T. Kanazawa, S. Matsumoto, Applied Catalysis A, Vol.91, pp.293(2005)

Synthesis and Characterization of Nb-containing Mesoporous Materials from Layered Perovskite Type Potassium Niobium Oxyfluoride

Masataka Ogasawara, Yusaku Amamoto, Hiroyuu Horiuchi,
Koichi Obara, Sumio Kato and Shinichi Nakata

Department of Engineering in Applied Chemistry, Faculty of Engineering and Resource Science,
Akita University, 1-1 Tegatagakuen-machi, Akita 010-8502 Japan

snakata@ipc.akita-u.ac.jp

Abstract: Mesoporous materials are expected to find applications in catalysts because they have ordered pores with uniform size and high specific surface area. In this study, mesoporous material containing niobium in the pore-wall was synthesized using tetraethoxysilane (TEOS), layered-perovskite type potassium niobium oxyfluoride (K_2NbO_3F) and hexadecyltrimethylammonium chloride ($C_{16}TMACl$). This mesoporous material was characterized with powder X-ray diffraction, N_2 adsorption-desorption isotherms and transmission electron microscope. In the composition ratio of starting materials was $K_2NbO_3F : C_{16}TMACl : TEOS = 1 : 1 : 7.2$, Nb-containing mesoporous material with bimodal pores was obtained.

Key Words: Mesoporous material, Layered perovskite, Niobium oxide

1 INTRODUCTION

Mesoporous silica synthesized using structure directing agent (SDA) such as long chain surfactant have attracted attention because they have ordered pores with a uniform size of 2–50 nm and a high specific surface area [1]. Mesoporous nanoparticles have large pores due to the presence of interparticle spaces, resulting in formation of bimodal porous material. It has the advantage of reducing transport limitations of reactant and adsorbate. Several synthesis methods have been reported for preparing bimodal mesopores, such as the method using two kinds of surfactants [2].

Many researches on catalytic activity of mesoporous materials containing transitional metal have been performed. Mesoporous materials containing niobium in the pore-wall have been investigated regarding catalytic activity for oxidation [3] and hydrodesulfurization [4]. Generally, Nb–mesoporous materials are synthesized using niobium chloride [5] or niobium ethoxide [4] solution as a starting material. On the other hand, it is discovered that mesostructured materials were formed from layered-perovskite type potassium niobium oxyfluoride (K_2NbO_3F) and alkyltrimethylammonium chloride (C_nTMACl) [6]. This result suggests that layered material K_2NbO_3F is useful as a starting material for a mesoporous material. In this

study, Si–Nb–mesoporous material was synthesized using tetraethoxysilane (TEOS), K_2NbO_3F and C_nTMACl and its pore property was investigated.

2 EXPERIMENTAL

K_2NbO_3F was synthesized by solid state reaction. KF , K_2CO_3 and Nb_2O_5 were weighed in the molar ratio $KF : K_2CO_3 : Nb_2O_5 = 4 : 1 : 1$ and mixed in ethanol using a mortar and pestle. The mixture was heated at 1083 K for 6 h in air. $C_{16}TMACl$ was used as the SDA. 4 cm³ of TEOS and 24 cm³ of 0.1 mol dm⁻³ $C_{16}TMACl$ aqueous solution were added to 50 cm³ of distilled water. 0.56 g of powder K_2NbO_3F was immediately dispersed in this solution. The molar ratio of the starting material was $K_2NbO_3F : C_{16}TMACl : TEOS = 1 : 1 : 7.2$. The suspension was stirred with a magnetic stirrer at 323 K for 3 h. The resulting white precipitate was recovered by filtration and drying. The dried sample was calcined in air at 753 K for 3 h in order to remove SDA.

Structural characterization of the products was performed by the powder X-ray diffraction (XRD). The pore and particle shapes were observed by transmission electron microscopy (TEM). N_2 adsorption-desorption isotherms were recorded at 77 K and the pore size distribution and pore volume were estimated by the Dollimore-Heal method.

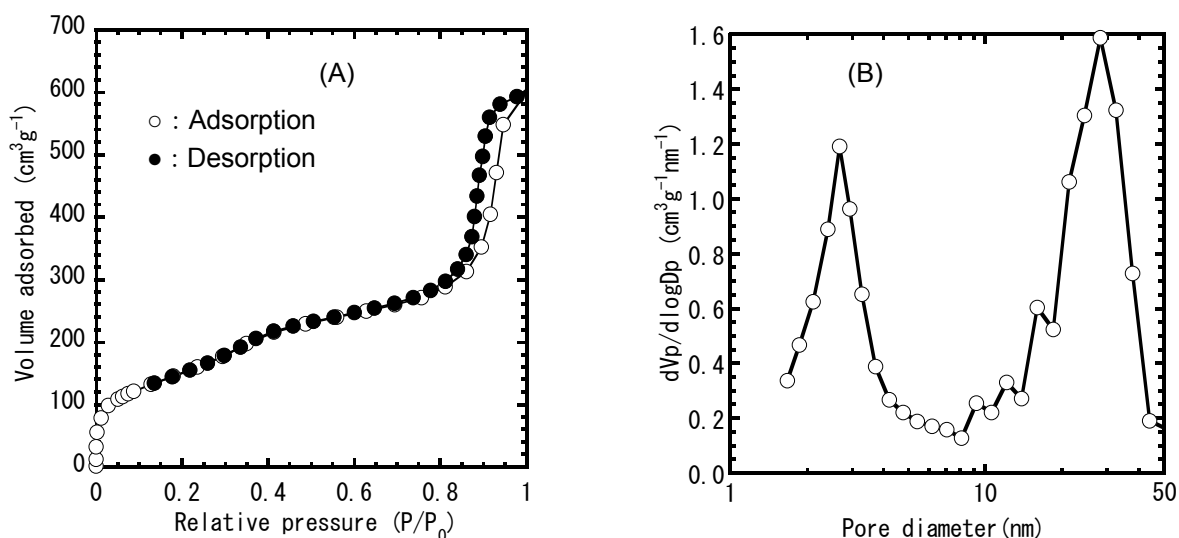


Figure 1 N_2 adsorption-desorption isotherms (left) and pore size distribution (right) of calcined products.

3 RESULTS AND DISCUSSION

The XRD pattern of product before calcination, the diffraction peak was observed at d-spacing of 5.0 nm. This peak indicates the formation of mesostructure. In the case of the product synthesized at 323 K for 3 h without K_2NbO_3F , no XRD peak indicating the formation of mesostructure was observed. This result suggests that the presence of the K_2NbO_3F induces the formation of the mesostructure. In the XRD patterns of calcined products, diffraction peak was also observed in the range $2\theta = 1.5\text{--}2^\circ$. It was revealed that the mesostructure was maintained after removal of SDA. From the TEM observation of calcined products, 2–3 nm diameter mesopores were observed. However, the pore arrangement was not uniform but worm-hole like. Additionally, it is observed that ca. 20–30 nm diameter nano-size particle including 2–3 nm mesopores was formed.

The nitrogen adsorption-desorption isotherm of product is shown in Figure 1(A). Two-step increases in nitrogen adsorption were observed in the ranges of $0.2 < P/P_0 < 0.4$ and $P/P_0 > 0.85$. This behavior indicates that the mesoporous materials have bimodal pores. The pore size distribution estimated using adsorption branch is shown in Figure 1(B). Two peaks in pore size distribution were observed at around 2–4 and 15–40 nm. From the results of TEM observation, it is considered that the small pores of around 2–4 nm are due to templating effect of $C_{16}TMA$ and the large pores of around 15–40 nm are due to interparticle spaces among the nanoparticles.

4 CONCLUSIONS

Si–Nb–mesoporous material was synthesized from TEOS, layered-perovskite type potassium niobium oxyfluoride K_2NbO_3F and $C_{16}TMACl$. The mesoporous material with bimodal pores synthesized in this study is a promising material

for catalyst dealing with nano-scale compounds such as biomolecules.

Acknowledgment

This work was supported by Grant-in-Aid for Young Scientists (B) from the Ministry of Education, Culture, Sports, Science, and Technology, Japan. (No. 19760539)

References

- [1] Yanagisawa, T., Shimizu, T., Kuroda, K., Kato, C., "The Preparation of Alkyltriethylammonium-Kanemite Complexes and Their Conversion to Microporous Materials" *Bull. Chem. Soc. Jpn.*, 63, 988 (1990)
- [2] Suzuki, K., Ikari, K., Imai, H., "Synthesis of Silica Nanoparticles Having a Well-Ordered Mesostructure Using a Double Surfactant System" *J. Am. Chem. Soc.*, 126, 462 (2004)
- [3] Ziolk, M., Lewandowska, A., Grzybowska, B., Klisiński, A., "NbMCM-41 Mesoporous Molecular Sieves in Oxidative Dehydrogenation of Ethane and Propane" *React. Kinet. Catal. Lett.*, 80, 199 (2003)
- [4] Cedeño, L., Hernandez, D., Klimova, T., Ramirez J., "Synthesis of Nb-containing mesoporous silica molecular sieves Analysis of its potential use in HDS catalysts" *Appl. Catal. A*, 241, 39 (2003)
- [5] Yang, P., Zhao, D., Margolese, D.I., Chmelka, B.F., Stucky, G.D., "Generalized syntheses of large-pore mesoporous metal oxides with semicrystalline frameworks" *Nature*, 396, 152 (1998)
- [6] Ogasawara, M., Kato, S., Tsukidate, H., Akaogi, T., Moriya, Y., Nakata, S., "Synthesis of Mesostructured Materials from K_2NbO_3F as Starting Material" *Chem. Lett.*, 33, 1138 (2004)

The study of corrosion behavior of trivalent chromium coatings with Fe³⁺

**Wei-Kun Chen¹, Chung-Ming Liu^{2,*}, Yu-Der Tsai¹,
Ming-Der Ger³**

¹Graduate School of Defense Science, Chung Cheng Institute of Technology, National Defense University,
Tao-Yuan 335, Taiwan

²Department of Chemical and Materials Engineering Lunghwa University of Science and Technology,
Taiwan, R.O.China

³Department of Applied Chemistry & Materials Science, Chung Cheng Institute of Technology, National
Defense University, Tao-Yuan 335, Taiwan, ROC

patrick.liuc@msa.hinet.net

Abstract: The main purpose of this paper is to develop the trivalent chromium conversion coatings on zinc alloy. The influence of ferric ions on the trivalent chromium conversion coatings on galvanized steel was investigated in this study. The coatings was evaluated in 3.5 wt.% NaCl at room temperature using polarization curve. The structure and valence state of the coatings were examined by scanning electron microscopy (SEM), transmission electron microscopy (TEM), and X-ray photoelectron spectroscopy (XPS), respectively. The results of polarization curves showed that when coatings with ferric ions up to $2.50 \times 10^{-3} \text{M}$, the corrosion resistance of the coatings was declined clearly. Furthermore, SEM observation demonstrated that the samples treated with ferric ions have a crack surface spread to the whole coatings. Moreover, the coating is peeling off the substrate when the ferric ions up to $5.00 \times 10^{-3} \text{M}$.

Keywords: Trivalent chromate; conversion coatings ; corrosion resistance.

1. INTRODUCTION

Conventional chromate conversion coating (CCC) has superior corrosion resistance and self-healing ability. However, the CCC treatment employs hexavalent chromium ions, Cr(VI), whose use has been limited by several environmental legislations. This is because Cr(VI) displays high toxicity for human health and causes serious environmental pollutions. On the contrary, trivalent chromium, Cr(III), has low toxicity, and the waste water and solid waste from the Cr(III) bath can be treated in a simple and efficient way. Moreover, the industrial implementation of Cr(III) conversion coating is similar to that of the chromate counterpart. Hence, the Cr(III) conversion coating treatment is one of the potential alternatives to the CCC process for zinc-coated steels[1–7]. In general, the formation of cracks deteriorates the corrosion resistance of the conversion coating. Gigandet et al. [8] and Cho et al. [4] observed that cracks form in CCCs during the immersion in the solution or the baking process. However, the CCCs have self-healing capability to repair themselves at defect sites and maintain an excellent corrosion resistance. Conversely, other metallic ions (including Cr(III)) in conversion coatings lack the capability to heal coating defects. Therefore, developing a conversion coating process to replace the CCCs progresses at a slow pace, and how to reduce the density of cracks will be the key point to impart non-chromate conversion coatings with adequate corrosion protection properties. The trivalent CCC formed in a Cr(III) bath containing transition metal ions such as Co(II), Ni(II) and Fe(II) showed superior corrosion resistance than that formed in the bath without

transition metal ions. In this paper ferric ions have been used in the conversion coating process, the concentration of iron effect were the point in this study.

2. EXPERIMENTAL

2.1. Substrate and coating solution

The substrate was $6.5 \times 10 \text{ cm}^2$ galvanized steel coated with a $8 \sim 10 \text{ }\mu\text{m}$ -thick zinc layer. Prior to trivalent chromium conversion coating, the galvanized steel were immersed in 0.5% (v/v) HNO_3 activated for 10 s, and then rinsed with deionised water. The trivalent chromium conversion treatments were performed by immersion of the galvanized steel into a coating solution containing chromium (III) nitrate, $\text{Cr}(\text{NO}_3)_3$ with 0M (Blank), $1.25 \times 10^{-3} \text{ M}$ (Case1), $2.50 \times 10^{-3} \text{ M}$ (Case2), $3.75 \times 10^{-3} \text{ M}$ (Case3), and $5.00 \times 10^{-3} \text{ M}$ (Case4) ferric ions for 60s with agitation at $60 \text{ }\square$.

2.2. Electrochemical measurement and coating characterization

The linear polarization curves were measured from -0.3 V (vs. OCP) to 0.5 V at the scanning rate of 5 mV/s . The area of the working electrode is 2.54 cm^2 , a conventional three-electrode cell was used. The surface of the coated films was observed by SEM (FESEM, JEOL, JSM-6500F). The chemical composition of the surface films formed was investigated with SIMS and XPS.

3. RESULTS AND DISCUSSION

3.1 Polarization curves

The LP spectra obtained on the different

concentrations of ferric ions is depicted in Fig. 1. Moreover, the corrosion potential, E_{corr} , and the corrosion current density, i_{corr} , were summarized in Table 1. The LP test results showed that all specimens exhibited active corrosion behavior, and corrosion rate tended to increase as a result of adding ferric ions. The corrosion resistance of the coatings began to decline strongly when coatings with ferric ions up to $2.50 \times 10^{-3} M$.

3.2 SEM observation

Fig. 2~5 shows SEM images for chromate coatings on zinc with ferric ions of 0M (Blank), $1.25 \times 10^{-3} M$ (Case1), $3.75 \times 10^{-3} M$ (Case3), and $5.00 \times 10^{-3} M$ (Case4), respectively. The morphological analysis that the sample submitted to 0M ferric ions (Blank) have a rough surface in the coating. For the samples with ferric ions more than $1.25 \times 10^{-3} M$, the length and width of crack increase with the concentration of ferric ions. Furthermore, the coating is peeling off the substrate when the ferric ions up to $5.00 \times 10^{-3} M$.

3.3 SIMS analysis of the chromate coatings

The SIMS depth profile of the chromate coatings with 0M (Blank), and $2.50 \times 10^{-3} M$ ferric ions (Case2) are shown in Fig 6 and 7. The SIMS analysis indicates that the sample submitted to Case2, the Fe signal mainly existed at the surface. Moreover, the existence of ferric ions seems to increase the depth of chromate coatings. Because of the chromate coatings is a mixture of chromium/zinc oxides. The depth of chromate coatings was determined by the maximum of elements Zn, H, Cr, and O signal. On the basis of the evidence we deduced that the

sample with ferric ions would lead the chromate coatings to destruction, hence the coating solution can react with the substrate continuously.

3.4 XPS analysis of the chromate coatings

The XPS spectra recorded during depth composition profiling of the Cr oxide films deposited on the galvanized steel are shown in Fig 8. This spectrum was obtained after sputtering for 2 min from the top surface by Ar-ion. In Fig. 8 shows major peaks appeared in 709.8 and 729.9 eV, respectively. From the XPS analysis, it was confirmed that conversion coatings have Fe_2O_3 and FeO compounds.

4. CONCLUSION

The corrosion resistance of the coatings was declined clearly when coatings with ferric ions up to $2.50 \times 10^{-3} M$.

SEM observation demonstrated that the samples treated with ferric ions have a crack surface spread to the whole coatings. Moreover, the coating is peeling off the substrate when the ferric ions up to $5.00 \times 10^{-3} M$.

The SIMS analysis indicates that the Fe signal mainly existed at the surface. Moreover, the existence of ferric ions seems to increase the depth of chromate coatings, we deduced that the sample with ferric ions would lead the chromate coatings to destruction, hence the coating solution can react with the substrate continuously.

From the XPS analysis, it was confirmed that conversion coatings have Fe_2O_3 and FeO compounds.

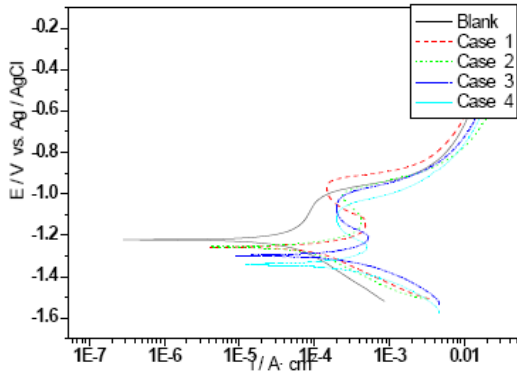


Fig. 1. The Linear polarization spectra obtained on the different concentrations of ferric ions.

Table1. The I_{corr} and E_{corr} spectra obtained on the different concentrations of ferric ions.

Sample	Ferric ions (M)	I_{corr} (A/cm^2)	E_{corr} (V)
Blank	0	3.50×10^{-6}	-1.21
Case1	1.25×10^{-3}	4.01×10^{-6}	-1.25
Case2	2.50×10^{-3}	6.14×10^{-6}	-1.25
Case3	3.75×10^{-3}	2.25×10^{-5}	-1.29
Case4	5.00×10^{-3}	3.89×10^{-5}	-1.34

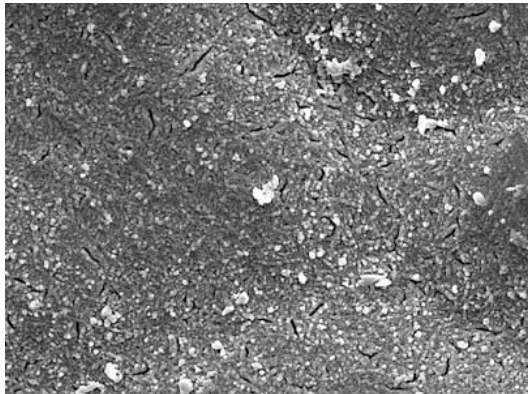


Fig. 2. SEM images for chromate coatings on zinc with ferric ions of 0M ferric ions.

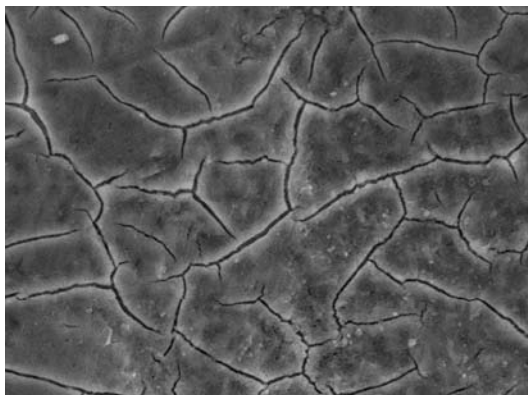


Fig. 3. SEM images for chromate coatings on zinc with ferric ions of 1.25×10^{-3} M ferric ions.

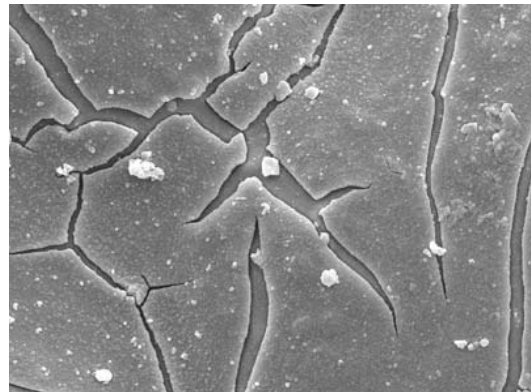


Fig. 4. SEM images for chromate coatings on zinc with ferric ions of 3.75×10^{-3} M.

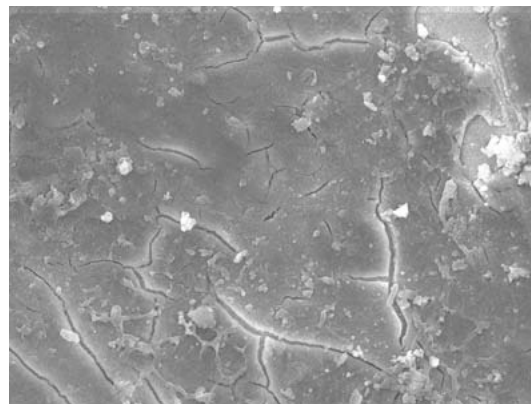


Fig. 5. SEM images for chromate coatings on zinc with ferric ions of 5.00×10^{-3} M ferric ions.

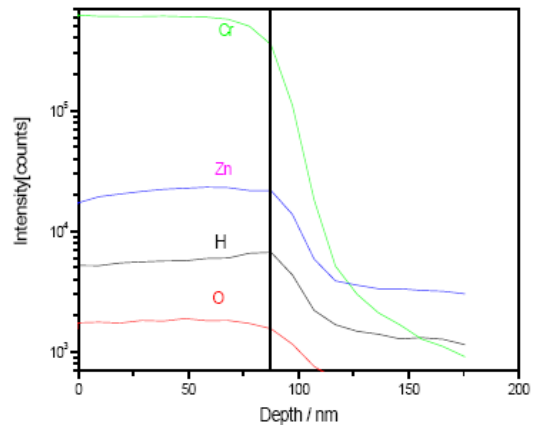


Fig. 6. The SIMS depth profile of chromate coatings with 0M ferric ions.

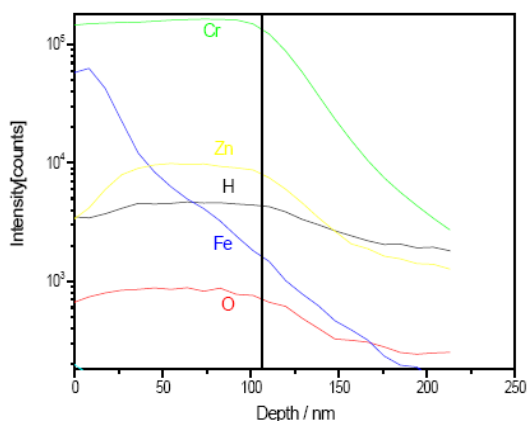


Fig. 7. The SIMS depth profile of chromate coatings with $2.50 \times 10^{-3} \text{M}$ ferric ions.

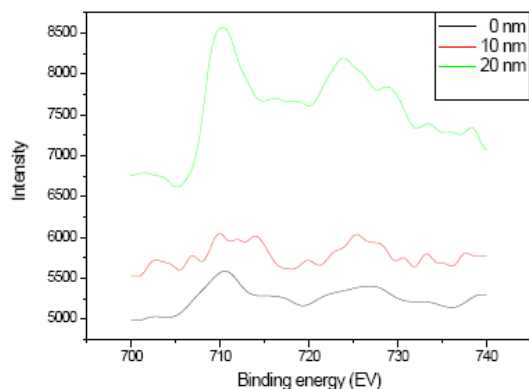


Fig. 8. The XPS spectra recorded of the Cr oxide films deposited on the galvanized steel.

References

- [1] P. Campestrini, G. Goeminne, H. Terryn, J. Vereecken and J. H. W. de Wit, *Journal of the Electrochem. Soc.*, 151 (2004) 59-70.
- [2] P. Campestrini, E. P. M. van Westing, and J. H. W. de Wit, *Electrochimica Acta*, 46 (2001) 2631-2647.
- [3] Y. Yoon, R. G. Buchheit, *Electrochemical and Solid State Letters*, 11 (2005) 65-68.
- [4] K. W. Cho, V. S. Rao and H. S. Kwon, *Electrochimica Acta*, 52 (2007) 4449-4456. [5] S. Natarajan, V. Ravikiran, *Surface Engineering*, 22 (2006) 287-293.
- [6] A. A. O. Magalhaes, B. Tribollet, O. R. Mattos, I. C. P. Margarit, and O. E. Barcia, *Journal of the Electrochem. Soc.*, 150 (2003) 16-25.
- [7] Directive 2002/95/EC of the European Parliament and the Council on the Restriction of the Use of Certain Hazardous Substances in Electrical and Electronic Equipments, *Official Journal of the European Union*, January 27, L 37/19, 2003.
- [8] M.P. Gigandet, J. Faucheu and M. Tachez, *Surface and Coatings Technology*, 89 (1997) 285-291.
- [9] Y. J. Tan, S. Bailey and B. Kinsella, *Corrosion Science*, 38 (1996) 1545-1561.
- [10] M. Dabalà, E. Ramous and M. Maqrini, *Materials and Corrosion*, 55 (2004) 381-386.
- [11] Z. yong, Z. Jin, C. Qiu and Y. Liu, *Applied Surface Science*, 225 (2008) 1672-1680.
- [12] N. T. Wen, F. J. Chen, M. D. Ger, Y. N. Pan, c, and C. S. Lin, *Electrochemical and Solid State Letters*, 11 (2008) 47-50.
- [13] N. T. Wen, C. S. Lin, C. Y. Bai and M. D. Ger. *Surface and Coatings Technology*, 203 (2008) 317-323.
- [14] Y. T. Chang, N. T. Wen, W. K. Chen, M. D. Ger, G. T. Pan and C. L. Yang, *Corrosion Science*, 50 (2008) 3494-3499.
- [16] H. C. Yu, B. Z. Chen, X. Shi, X. Sun and B. Li, *Materials letters*, 62 (2008) 2828-2831.
- [17] H. C. Yu, B. Chen, H. Wu, X. Sun and B. Li, *Electrochimica Acta*, 54 (2008) 720-726.

Influence of Boric acid on the corrosion resistance of trivalent chromium coatings on galvanized steel

Yu-Der Tsai¹, Chung-Ming Liu^{2,*}, Wei-Kun Chen¹,
Ming-Der Ger³, Ching-Yuan Bai³

¹Graduate School of Defense Science, Chung Cheng Institute of Technology, National Defense University,
Tao-Yuan 335, Taiwan

²Department of Chemical and Materials Engineering Lunghwa University of Science and Technology,
Taiwan, R.O.China

³Department of Applied Chemistry & Materials Science, Chung Cheng Institute of Technology, National
Defense University, Tao-Yuan 335, Taiwan, ROC

patrick.liuc@msa.hinet.net

Abstract: The influence of Boric acid on the Cr(III) conversion coatings on galvanized steel was investigated by CV, LP, AC, SEM, and salt spray tests. The addition of Boric acid to the chromium solution considerably improved the reactive capacity at room temperature, thus enhance the corrosion resistance. The coatings were prepared by immersion of galvanized steel in an aqueous solution composed of trivalent chromate.

The results of CV curves demonstrated that solution with Boric acid has more reactive capacity on galvanized steel. The corrosion behavior was studied by means of LP, AC, and neutral salt spray tests. SEM observation shows that coatings prepared from the solution without Boric acid have more cavities and cracks than those prepared with Boric acid.

Keywords: Trivalent chromate; conversion coatings; CV; AC; Boric acid.

1. INTRODUCTION

Zinc plating has been widely used to protect carbon steel, in the past 20 years. Be a sacrificial anode, zinc provides an excellent galvanic protection [1-4].

The corrosion resistance of galvanized steel can be improved by means of chemical conversion treatment [old1], Chromate conversion coatings (CCC) have been used for many years to protect metals, such as Zinc, Aluminum, and Magnesium from corrosion [5,6]. They are highly effective, but unfortunately chromate compounds are toxic and carcinogenic and harmful to health, must be withdrawn within a short time [7-11]. Cr(III) coatings are worth studying, because of the Cr(III) coatings are much less toxic than Cr(VI) coatings, and the corrosion resistance can be similar to the Cr(VI) coatings, therefore they are considered to be commercially acceptable alternatives to Cr(VI) treatments [12-14].

Cr(III) coatings, of course it's an excellent replacement for the Cr(VI) coatings. However, it's still a problem in Cr(III) conversion process at high temperature environment. The energy consumed and complicated equipment problems were induced by the process.

In this study, the aim is to know the influence of Boric acid on the Cr(III) conversion coatings on galvanized steel. The corrosion resistance of the coatings was investigated by salt spray test, and electrochemical measurements. The role of Boric acid will be discussed in terms of the surface morphology by scanning electron microscopy (SEM).

2. EXPERIMENTAL

The substrate is $6.5 \times 10 \text{ cm}^2$ galvanized steel coated with a $8 \sim 10\text{-}\mu\text{m}$ -thick zinc layer. Prior to Cr(III) conversion coating, the galvanized steel were immersed in HNO_3 activated for 10 s, and then rinsed with deionised water. The Cr(III) conversion treatments were performed by immersion of the galvanized steel into a coating solution containing chromium (III) nitrate, $\text{Cr}(\text{NO}_3)_3$ with (and/or) without Boric acid. The solution pH was adjusted to 2 with HNO_3 (and/or) NaOH . After activation and rinsing with deionised water, the specimens were immersed

in the conversion solution for 60s with agitation at 60°C (and/or) room temperature. The chemical conversion films that formed on the galvanized steel were dried afterwards at 90°C for 30min.

The CV measurement was executed at room temperature in $1\text{M K}_2\text{CO}_3$ with (and/or) without Boric acid using a conventional three-electrode cell. The potential was from -2V to 2V at the scanning rate of 50mV/s . The working electrode was galvanized steel, and a surface area of 2.54 cm^2 . The corrosion performance was evaluated by means of AC, LP, and salt spray test. The AC measurement was carried out at room temperature in 3.5 wt. \% NaCl using a conventional three-electrode cell. The measurement conditions were an amplitude voltage of 5mV , a frequency range of $10 \text{ mHz} \sim 100\text{kHz}$, a surface area of 2.54 cm^2 .

The linear polarization curves were measured from the potential -0.3V to 0.5V at the scanning rate of 5mV/s after a steady open circuit potential reached. The area of the working electrode was 2.54 cm^2 , a conventional three-electrode cell was used. The neutral salt spray test was performed in accordance with the ASTM standard B-633. The formation of the white corrosion products was checked by the naked eye. The surface of the coated films was observed by SEM.

3. RESULTS AND DISCUSSION

3.1 The influence of conversion temperature

The influence of the conversion temperature in the coatings solution were investigated by AC, LP, and SEM. Fig. 1 shows the LP curves in 3.5 wt. \% NaCl solution for the chromium conversion coatings prepared from $\text{Cr}(\text{NO}_3)_3$ solution at different conversion temperature. For the coatings prepared at 60°C showed more positive corrosion potential, and negative corrosion current than those prepared at room temperature. Therefore, the coatings corrosion resistance prepared at 60°C is superior to those prepared at room temperature.

Fig. 2(a) and 2(b) showed the results of Nyquist and Phase angle plots of films formed at different conversion temperature.

The Nyquist spectra measured from the coating formed at room temperature indicated a single semicircle, which is indicative of one reaction between electrolyte and specimen. The diameter of the arc can be regarded as the polarization resistance (R_p), and that in the coating formed at 60°C showed a larger semicircle which meaning the coating has a greater polarization resistance (R_p) [15]. The polarization resistance (R_p) of the coating treated at 60°C is better than treated at room temperature, in agreement with the results of LP test. The Phase angle plot showed that there are two peaks formed at different conditions. However, the peak are variations in shape from room temperature to 60°C. Namely, the structure of the conversion coatings in the two conditions is mutually different.

The AC and LP examined the films formed at different conversion temperature were showed that the conversion temperature is severe influence the reactive capacity on galvanized steel, moreover the coating formed at 60°C showed better performance than the coating formed at room temperature.

The surface observation of the coatings was performed by means of SEM. Fig. 3 shows the SEM images of the coatings prepared from different conversion temperature. The SEM images indicate that under room temperature deposit conditions, the coatings were cracks over the whole surface. However, the coatings formed at 60°C were smooth.

3.2 CV curves

The effect of Boric acid at different concentrations was examined on galvanized steel. Fig. 4 demonstrated that the CV curves in the standard solution (1M K_2CO_3) with and without Boric acid. The 0.3M Boric acid has greatly anode peak than without Boric acid. However, the anode peak of the 0.1M Boric acid was nearly close to the case of without Boric acid. Namely, the 0.3M Boric acid produced more reactive capacity on galvanized steel.

3.3 The effect of Boric acid in the trivalent chromium coatings

The effect of the Boric acid in the Cr(III) coatings was study by LP, AC, neutral salt spray tests and SEM. The LP spectra obtained on the different concentrations of Boric acid is depicted in Fig. 5. The case of without Boric acid has the lowest corrosion potential and highest corrosion current. The 0.1M Boric acid is as good as the case of without Boric acid. Nevertheless, both the 0.1M Boric acid and without Boric acid are contrary to the case of 0.3M Boric acid. For this reason, the corrosion resistance of the conversion coatings with 0.3M Boric acid is better than the others.

Fig. 6(a) and 6(b) showed the results of Nyquist and Phase angle plots of films formed from standard solution and solution with different concentrations of Boric acid.

The Nyquist spectra demonstrated that the coatings formed at 0M Boric acid is as good as 0.1M Boric acid. However, the 0.3M Boric acid showed an extremely superior impedance. The Phase angle diagram showed that two peaks are formed, Regardless of Boric acid at different concentrations. Even so, the case of the 0.3M Boric acid has the highest phase angle degree. This meaning that the films formed at 0.3M Boric acid is dense than the others.

Table1 illustrated the influence on conversion temperature (and/or) Boric acid by salt spray tests. The result indicates that the conversion temperature (and/or) concentrations of Boric acid both are absolutely affects the corrosion resistance. On the basis of the evidence we deduced that the case of conversion temperature at 60°C (and/or) 0.3M Boric acid has more powerful reactive capacity than the others on galvanized steel. Thus the corrosion resistance of the coatings formed at 60°C (and/or) 0.3M Boric acid were improved and no white rust were observed.

Representative SEM of coatings obtained in different concentrations of Boric acid baths is shown in Fig. 7. The morphological analysis indicates that the samples submitted to 0.1M Boric acid has a plenty of cavities on the surface. Nevertheless, sample submitted to 0.3M Boric acid has a uniform conversion layer.

4. CONCLUSION

The influence of Boric acid on the corrosion resistance of Cr(III) coatings on galvanized steel was investigated by means of electrochemical measurement and morphological analysis. From the data obtained from CV analysis of trivalent chromium coatings it would seem that the 0.3M Boric acid produced more reactive capacity than the others on galvanized steel.

The addition of 0.3M Boric acid to the chromium solution considerably improved the reactive capacity, thus led to the formation of Cr(III) coatings with good barrier properties even if formed at room temperature.

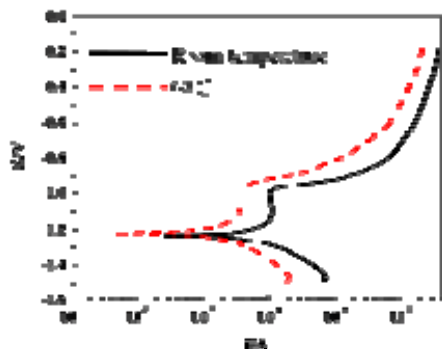


Fig. 1. Linear polarization curves for coatings formed at 60°C (and/or) room temperature in 3.5 wt.% NaCl.

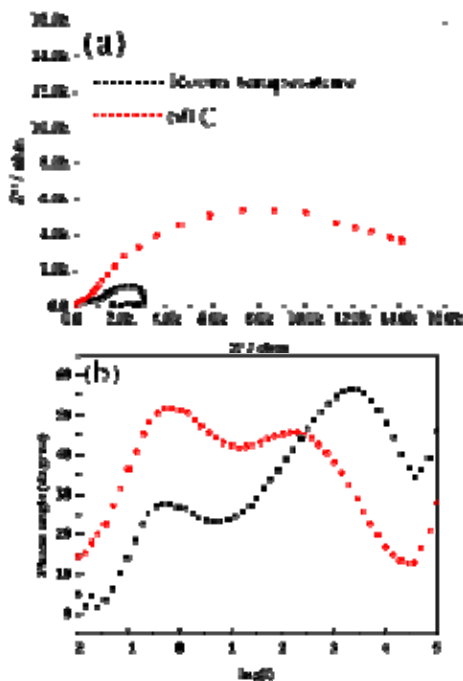


Fig. 2. AC impedance curves for coatings formed at 60°C (and/or) room temperature in 3.5 wt.% NaCl. (a) Nyquist plot and (b) Phase angle plot.

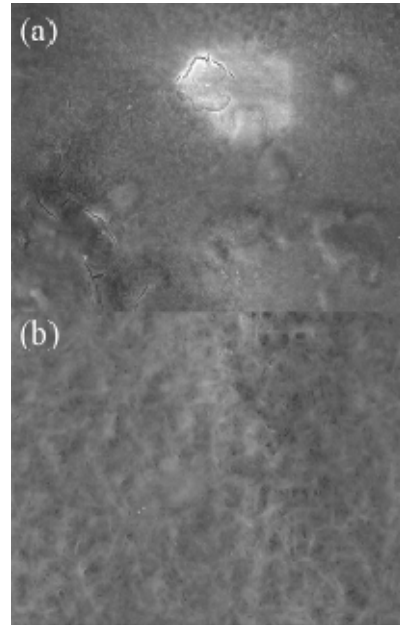


Fig. 3. SEM images of the chromium conversion coatings prepared from $\text{Cr}(\text{NO}_3)_3$ solution (a) conversion at room temperature and (b) conversion at 60°C.

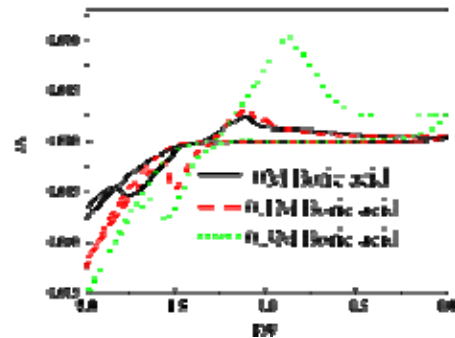


Fig. 4. CV curves for Boric acid effects on galvanized steel.

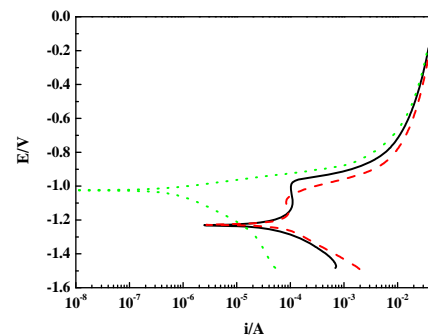


Fig. 5. Linear polarization curves for coatings formed at different concentrations of Boric acid in 3.5 wt.% NaCl.

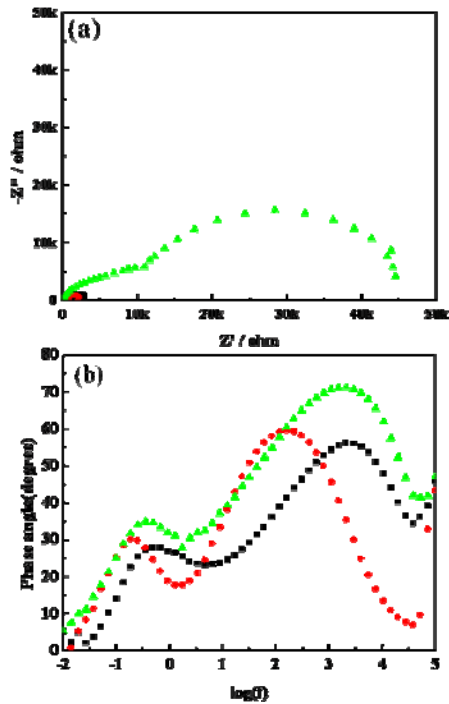


Fig. 6. AC impedance curves for coatings formed at different concentrations of Boric acid in 3.5 wt.% NaCl. (a) Nyquist plot and (b) Phase angle plot.

Table1. The influence on conversion temperature and Boric acid are examined by salt spray tests.

Case	Salt spray test's time(h)					
	12	24	48	72	96	120 ~
60°C	○	○	○	○	○	✗
35°C	○	✗				
0.1M Boric acid	○	✗				
0.3M Boric acid	○	○	○	○	○	○

Symbols:(○: whist rust inexistence, ✗: white rust appeared)

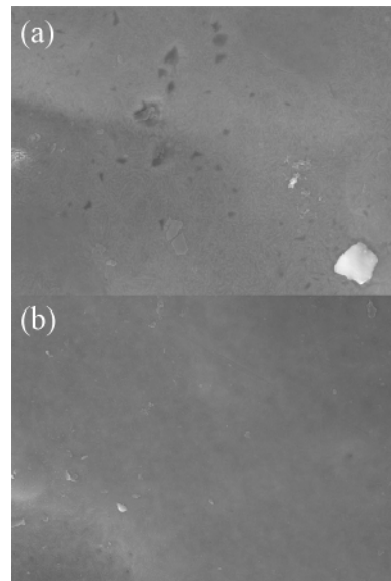


Fig. 7. SEM images of the Cr(III) coatings prepared from different concentrations of Boric acid (a) 0.1M Boric acid (b) 0.3M Boric acid.

References

- [1] H.E. Townsend, Mater. Perform. 30 (1991) 60.
- [2] F.W. Eppensteiner, M.R. Jenkins, Met. Finish. Guidebook and Directory Issue 96, 1998, p. 489.
- [3] T. E. GRAEDEL: J. Electrochem. Soc., 1989, 136, 193c–203c.
- [4] D. C. H. NEVISON: in 'ASM handbook', 755–769; 1987, Materials Park, OH, ASM International.
- [5] L.F.G. Williams, Plating (1972) 931.
- [6] K.A. Korinek, ASM Handbook, ASM International, vol. 13, 1987.
- [7] P.L. Hagans, C.M. Haas, Chromate conversion coatings, ASM Handbook, Surface Engineering, 5, ASM International, Materials Park, OH, 1994, pp. 405–411.
- [8] B.R.W. Hinton, Met. Finish. 89 (9) (1991) 55.
- [9] G. D. WILCOX and J. A. WHARTON: Trans IMF, 1997, 75, B140–B142.
- [10] c. S. JEFFCOATE, H. S. ISAACS, A. J. ALDYKIEWICZ JR and M. P. RYAN: J. Electrochem. Soc., 2000, 147, 540–547.
- [11] P. L. HAGANS: in 'ASM handbook', 405–411; 1994, Materials Park, OH, ASM International.
- [12] P. C. WYNN and C. V. BISHOP: Trans. Inst. Met. Fin., 2001, 79, B27–B30.
- [13] A. GARDNER and J. SCHARF: Soc. Automot. Eng., 2001, SP-1614, 91–95.
- [14] P.C. Wynn, C.V. Bishop, Trans. IMF 79 (2001) B27.
- [15] Yoon-Seok Choi, Jae-Joo Shim, Jung-Gu Kim, "Effects of Cr, Cu, Ni and Ca on the corrosion behavior of low carbon steel in synthetic tap water," Journal of Alloys and Compounds, 391, pp.162-169, 2005.

Effect of Resin Impregnation on Mechanical Properties of Rice Hull Silica Carbon

Jun Asano*, Mitsuhiro Kimura*, Takeshi Takahashi** and Hiroshi Iizuka***

* Master's Program of Mechanical Systems Engineering, Graduate School of Science and Engineering,
Yamagata University, Jonan 4-3-16, Yonezawa 992-8510, Japan

** Sanwa Yushi Co. Ltd., Ichinichi-cho 4-1-2, Tendo 994-0044, Japan

*** Faculty of Engineering, Yamagata University, Jonan 4-3-16, Yonezawa 992-8510, Japan

ekn29190@dipfr.dip.yz.yamagata-u.ac.jp

Abstract: New utilization of rice hull, which is one of the agricultural by-products in Japan, is required to use as an industrial resource from a viewpoint of recycling. The rice hull silica carbon (RHS carbon) material is manufactured by mixing and impregnating the rice hull with a phenol resin, and then carbonizing in a nitrogen gas atmosphere at high temperatures. The RHS carbon has the natural porous structure that is originated from the natural structure of the rice hull. Since the RHS carbon has excellent frictional properties, it is expected to be a friction element in a linear motion slider. However, the mechanical properties of the RHS carbon were dispersed largely, and were strongly affected by the making process. In this study, the impregnation rate of the phenol resin was controlled, and discussed the optimal impregnation rate to achieve the low dispersion in the mechanical properties. Moreover, the authors evaluated the effect of the molding method on the mechanical properties.

Key Words: rice hull, porous carbon materials, making process, mechanical strength, friction property

1 INTRODUCTION

The rice hull silica carbon (RHS carbon) material is manufactured by mixing and impregnating the rice hull with a phenol resin, and then carbonizing in a nitrogen gas atmosphere at high temperatures [1, 2]. The RHS carbon has been developed in order to utilize the rice hull from a viewpoint of the recycling of agricultural by-products [3-5]. Especially, the RHS carbon is expected to use as the sliding elements for linear motion bearings and so on, since it has a high mechanical strength, high water resistance and excellent low friction [6].

The dispersion of the mechanical properties is one of the most important issues for the industrial application. The present authors have investigated the mechanical properties of the RHS carbon and showed that the dispersion was large depending on the pretreatment of the rice hull, the molding method and the impregnation rate of the phenol resin [7]. In particular, the making process is considered to be the most important factor to obtain the uniform quality for the RHS carbon. The present authors have also studied the effects of the grinding pretreatment and pressure kneading on the mechanical strength [6].

In this study, the optimum impregnation rate was discussed to achieve the low dispersion of the mechanical strength and the friction properties, adding the grinding and pressure kneading processes into the original manufacturing

procedure. Moreover, the effect of the forming method on the mechanical property was evaluated using the pressure and injection molded materials.

2 EXPERIMENTAL PROCEDURE

2.1 Materials

Fig.1 shows the making process of the RHS carbon. The rice hull was ground using a grinder as a pretreatment for the even impregnation. Then, the pretreated rice hull was mixed with a resol-type phenol resin (liquid-type) using a pressurized kneader machine. The carbonization was performed in a nitrogen gas atmosphere at 1173K as the 1'st impregnation. A novolac-type phenol resin (powder-type) was further mixed with the powder of the RHS carbon for the pressure forming or injection molding, as the 2'nd impregnation. Then, the formed materials were carbonized in a nitrogen gas atmosphere at 1173K.

Table 1 lists the manufacturing conditions. The 1'st impregnation rates were 15, 20, and 25 wt.% , and those of the 2'nd impregnation were 15, 20, 25, and 30 wt.% for the pressure formed test-pieces. The impregnation rates were 25wt.% as the 1'st and the 2'nd impregnations for the original test-piece and the injection molded test-piece. The pressure formed original RHS carbon was prepared for the comparison of the mechanical properties.

Table 1 Manufacturing condition of RHS carbon

Material	Molding method	1 st impregnation rate [wt.%]	2 nd impregnation rate [wt.%]
Pretreated RHS carbon	Pressure forming	15	15,20,25,30
		20	15,20,25,30
		25	15,20,25,30
	Injection molding	25	25
Original RHS carbon	Pressure forming	25	25

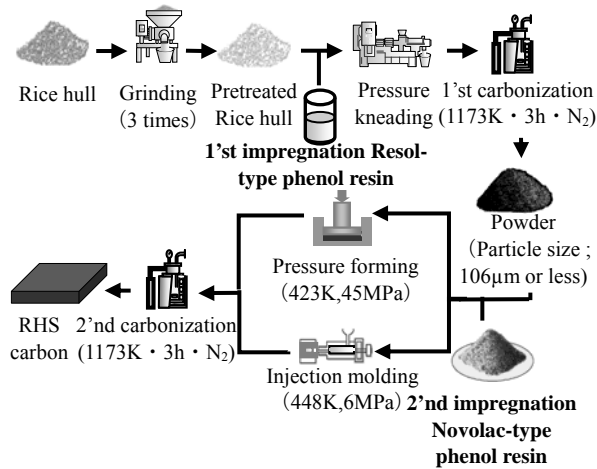


Fig.1 Making process of RHS carbon

The test-pieces for the compression test, the observation of macrostructure and the frictional test were prepared by cutting out from the pressure formed plates and injection molded plates. The geometry of the compression test-piece was $10 \times 5 \times 5 \text{ mm}^3$ for the pressure formed and $8 \times 4 \times 4 \text{ mm}^3$ for the injection molded plates. The geometry of the frictional test-piece was $3.5 \times 3.5 \times 3.5 \text{ mm}^3$.

2.2 Experimental procedure

The observation of the macrostructure was carried out using an optical microscope after polishing with some emery papers and buffing. The compression test was performed using a universal testing machine. The crosshead speed was set to be 0.5mm/min. Refer to JIS R1608. The displacement of test-piece was measured using a laser displacement measuring system.

The friction and wear tests were carried out using a pin-on-ring type testing system. The partner material was SUS304, and was rotated by a motor. The testing load was 9.8N. The friction resistance was measured using a load cell, and the coefficient of the dynamic friction was calculated from the friction resistance. A laser type displacement measuring device was attached to the upper portion of the test-piece, and measured the amount of wear. The abrasive surface was observed using a scanning electron microscope.

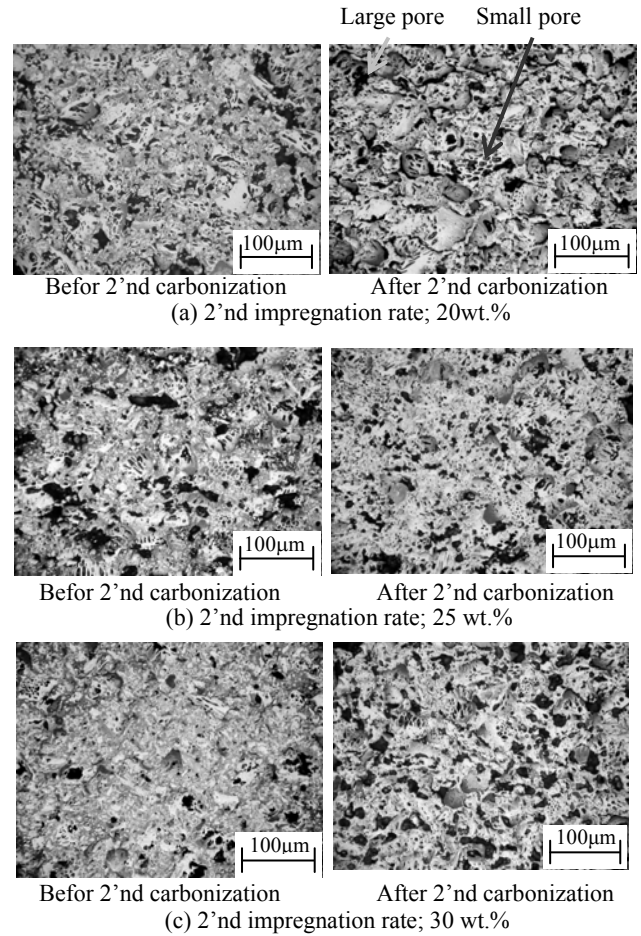


Fig.2 Macrostructures of RHS carbon with 25wt.% 1st impregnation rate

3 RESULTS AND DISCUSSION

3.1 Observation of macro-structure

Figure 2 shows the macrostructures of the test-pieces with 25wt.% for the 1st impregnation. The macrostructure has two types of pores, as shown in Figure 2(a). The small pore derives from the natural porous structure of the rice hull. The large pores are made during the carbonization of the phenol resin. The porosity decreased with increasing the 2nd impregnation rate. For the test-piece with 15wt.%, the porosity also decreased with increasing the rate of the 2nd impregnation. However, as shown in Figure 2(c), the porosity inversely increased in the structure of the 30 wt.% as the 2nd impregnation rate, because of the gas generation during the carbonization of the impregnated phenol resin.

Figure 3 shows the macrostructure of the original RHS carbon. There are many large pores. Moreover, the phenol resin is not uniformly impregnated in the rice hull porous structure. Comparing to the original structure, as shown in Figure 2, the impregnation of the phenol resin is uniformly performed in the material with the pretreatment.

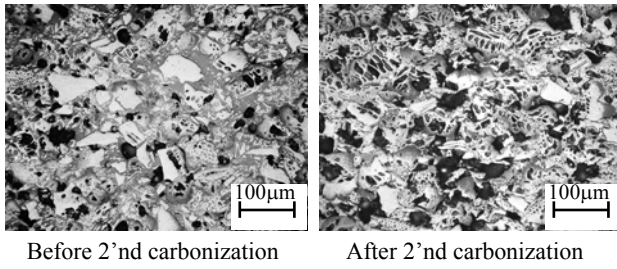


Fig.3 Macrostructures of original RHS carbon

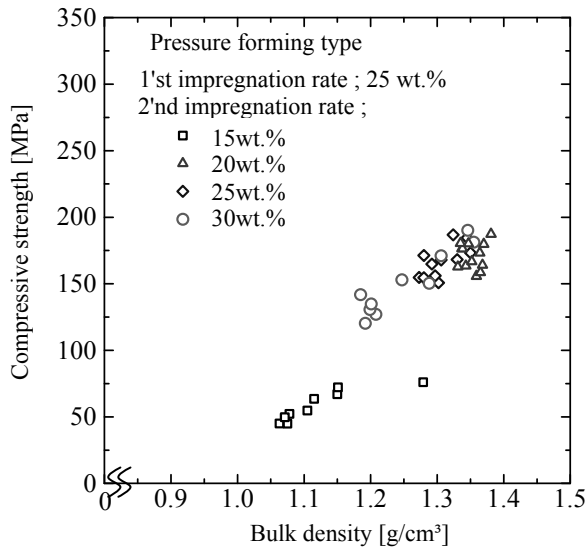


Fig.4 Effect of 2'nd impregnation rate on compressive strength and bulk density

These results show that 25wt.% is the enough impregnation rate to fill up the natural porous structure of the rice hull for the 1'st and 2'nd impregnations. Then, the macrostructure becomes fine for the combinations of 25wt%-20wt.% and 25wt%-25wt.% as the 1'st and 2'nd impregnations. However, the porosity inversely increases in the test-piece with 30wt.% impregnation rate, which is rather high because the amount of gas is increased during the carbonization.

3.2 Compressive strength

Figure 4 shows the effect of the impregnation rate on the compressive strength and the bulk density. They are increased with increasing the impregnation rate. The dispersion is small in the test-piece with 25wt.% as the 1'st impregnation. The dispersion was lowest in the test-piece with 25wt.% as the 1'st and 20 wt.% or 25wt.% as the 2'nd impregnations.

Figure 5 shows the relation between the compressive strength and the bulk density. The compressive strength is increased with increasing the bulk density. The injection molded test-piece has high bulk density and therefore achieves high compressive strength.

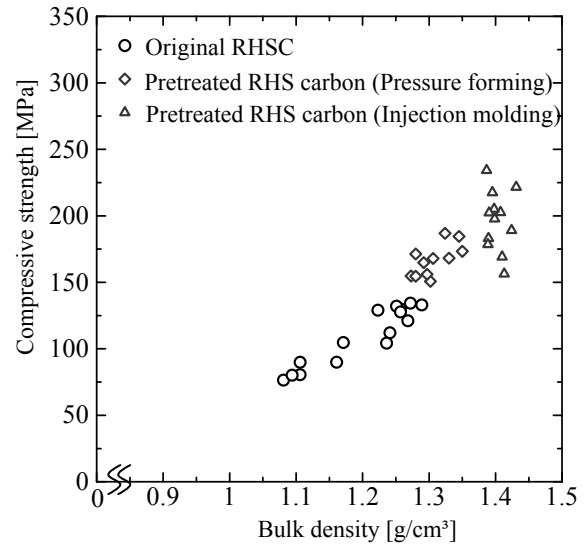


Fig.5 Relation between compressive strength and bulk density of RHS carbon

Table 2 Mechanics characteristic of pretreated RHS carbon

Molding method	Impregnation Rate [wt.%]	Bulk density [g/cm ³]	Compressive strength [MPa]	Weibull coeffi.
Pressure forming	25-20	1.35	175.5	19.1
	25-25	1.31	171.8	14.8
Injection molding	25-25	1.4	196.7	12.8

Table 2 lists the mechanics characteristic of the RHS carbon. The Weibull coefficient is a parameter of the dispersion which is based on the fracture mechanics [8]. In general, the coefficient is required to be higher than fifteen or twenty for the industrial usage. The Weibull coefficient of the two test-pieces was 19.1, 14.8, respectively. These values are tolerably high.

3.3 Frictional properties

Figure 6 shows the relation between the coefficient of dynamic friction and the sliding distance for the pressure formed type and injection molding type RHS carbon. The coefficient of dynamic friction is decreased with the sliding distance and settled within the value of 0.11-0.16. The coefficient of dynamic friction is low for the test-pieces with low impregnation rate. The coefficient of dynamic friction was 0.15 for the injection molded test-piece.

Figure 7 shows the relation between the porosity of the RHS carbon and the coefficient of dynamic friction. The coefficient of dynamic friction is low in the high porosity test-pieces. In general, the coefficient of the dynamic friction is closely related with the hardness of the material and the contact area between the both friction materials. As shown in

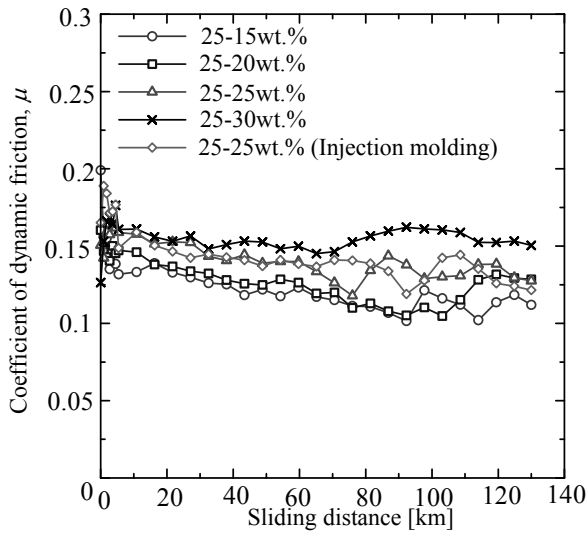


Fig.6 Relation between coefficient of dynamic friction and sliding distance in pressure forming type and injection molding type pretreated RHS carbon

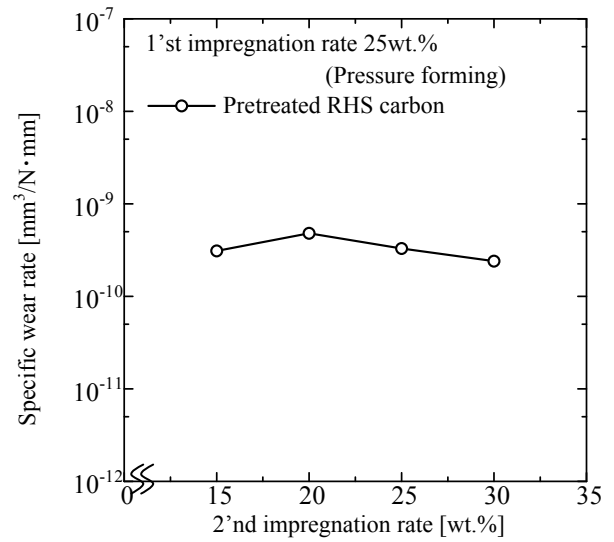


Fig.8 Relation between specific wear rate and 2'nd impregnation rate of phenol resin

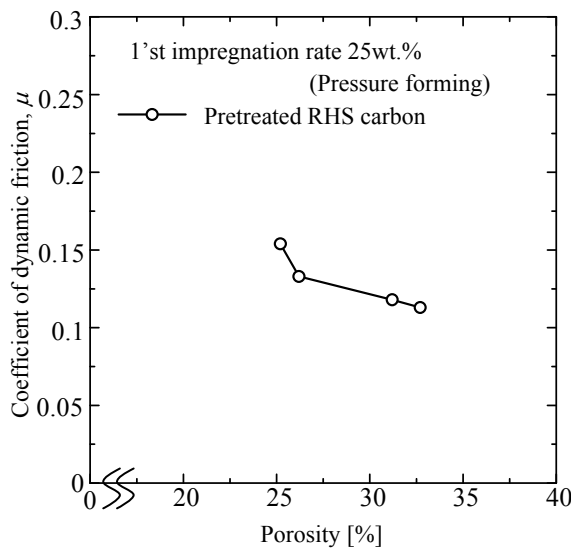


Fig.7 Relation between porosity of RHS carbon and coefficient of dynamic friction

Figure 6, the coefficient of the dynamic friction is lower in the low impregnation materials.

Figure 8 shows the relation between the specific wear rate and the 2'nd impregnation rate. The wear volumes are about 10^{-10} mm³/Nmm. Figure 9 shows the friction surface of pressure forming type RHS carbon. The sliding direction is vertical of the photo. The gray part is contact area with the partner material. The white part is the pore, such as filled with the abrasion facets. Some surface cracks and abrasion wear traces were observed at the contact surface.

The coefficient of dynamic friction of engineering ceramics, such as Al₂O₃ and SiC, is higher than about 0.2 in unlubricous condition and the specific wear rate is about 10^{-6} - 10^{-4} mm³/Nmm [9, 10]. Therefore, the RHS carbon is

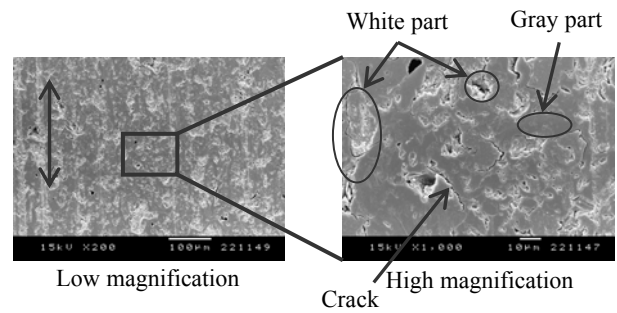


Fig.9 Morphology of interface of pressure forming type RHS carbon

considered to have excellent friction properties.

4 CONCLUSION

The impregnation rate of the phenol resin in the RHS carbon was controlled, and discussed the optimal rate to achieve the low distribution in mechanical properties. Moreover, the authors evaluated the effect of the molding method on the mechanical properties. The summary of the results is shown as follows.

- (1) The fine macrostructure was obtained by the combination of the 1'st impregnation with 25wt.% and the 2'nd impregnation with 20 or 25 wt.% .
- (2) The dispersion of the compressive strength is low in the test-piece with 25wt.% as the 1'st and 25 wt.% as the 2'nd impregnations. The Weibull coefficient was 19.1 in the test-piece with 25wt.% as the 1'st and 20wt.% as the 2'nd impregnations.
- (3) The coefficient of dynamic friction was considerably low, and was the value of 0.11-0.16. The wear volume was about 10^{-10} mm³/Nmm.

The authors wish to express their gratitude to the Ministry of Agriculture, Forestry and Fisheries of Japan for their financial support on “New technology development for activation of food industry by academic, industry, and governmental cooperation”.

REFERENCES

- [1] H.Iizuka, G.Kato, K.Hokkirigawa, S.Shikano and T.Takahashi, “Fracture Strength of a New Porous Carbon Material from Rice Bran”, Proc. Third Int. Conf. on ECOMATERIALS, Tukuba, Japan, pp.301-304 (1997).
- [2] M.Shishido, S.Kubo, T.Takahashi and H.Iizuka, “Mechanical Properties of Porous Carbon Materials made from Rice Hull” Trans. Mat. Res. Soc. Japan, Vol.31, No.4, pp.993-996 (2006).
- [3] T.Ishitani and K.Ohtsubo, “Science of Rice (in Japanese)”, (Tokyo, Asakura Shoten, 1995), p.172 (1995).
- [4] H.Iizuka, T.Noguchi and S.Shikano, A New Porous Carbon Material made from Rice Bran, J. of Mater. Engng. for Resources, Vol.11, No.1, pp.10-15 (2003).
- [5] H.Unuma, K.Niino, K.Sasaki, Y.Shibata, H.Iizuka, S.Shikano, T.Nakamura, Preparation and characterization of glass-like carbon/silica composites from rice hull and phenolic resin, J. of Mater. Sci., Vol.41, No. 17, pp.5593-5597 (2006).
- [6] K.Yoshida, H.Iizuka, Y.Shibata, H.Unuma, T.Nakamura and S.Shikano, Water Resistance of Porous Carbon Materials made from Rice Hull, Inter. J. of Mater. Engg. for Resources, Vol.13, No.2, pp.49-53(2006).
- [7] M.Kimura, S.Endo, T.Takahashi and H.Iizuka, “Effects of Pretreatment and Kneading on Mechanical Properties of RHS Carbon”, Trans. Mat. Res. Soc. Japan, Vol.33, No.4, pp.1205-1208 (2008).
- [8] G.E.Dieter, “Mechanical Metallurgy”, (Tokyo, Mc Graw-Hill, 1976), p.290 .
- [9] Edited by Japanese Society of Tribologists, “Tribology of Ceramics”, (Tokyo, Youkendou, 2003), p.60 .
- [10] Edited by Japanese Society of Tribologists, “Tribology of New Materials”, (Tokyo, Youkendou, 1991), p.10 .

Diamond film growth on the substrate of Mo-Re alloy foil

Zhiming YU*, Xiaobin WU, Jian Wang, Qiuping Wei

School of Materials Science and Engineering, Central South University, Changsha, 410083, P.R. China

zhiming@mail.csu.edu.cn

Abstract: Nano-crystalline diamond film was deposited on the substrate of Mo-Re alloy foil, by using a hot filament chemical vapor deposition (HFCVD) method. The morphology, band structures and crystalline structure of the film were analyzed by the scanning electron microscope (SEM), Raman spectroscopy and X-ray diffractometer (XRD), respectively. The results show that the thickness of the diamond film is about 350 nm by 1 hour deposition. There is a 2H-Mo₂C layer between diamond film and the Mo-Re substrate. The values of the *a* axis and the ratio of *c/a* of the Mo₂C are 3.003 Å and 1.579, respectively. This Mo₂C layer might be due to the carbon atoms in gas phase diffuse into the Mo-Re alloy.

Keywords: Mo-Re alloy, diamond film, CVD.

1 INTRODUCTION

Diamond film is one of the hardest materials and is well known for several extraordinary features such as high mechanical strength, excellent thermal conductivity, outstanding wear and friction properties, high chemical inertness etc. Recently main focus has been directed towards the synthesis and properties of nanocrystalline (NCD) and ultra-nanocrystalline diamond (UNCD) films, since these films have a superior behavior when compared with polycrystalline diamond(PCD) films and microcrystalline diamond(MCD) films[1-4]. NCD can be obtained by increasing the ratio of methane in the standard CH₄/H₂ gas mixture[5-6] or introducing inert gas (e.g.Ar,He,N₂) and/or nitrogen into the conventional gas system [7-9]. Additionally, the decrease in diamond grain size increases the grain boundaries containing non-diamond carbon in the film, therefore resulting to significant improvement in electrical properties especially the electron emission properties[10]. It is reported that the nanocrystalline diamond have been deposited on the Fe/Si substrates[11] and macroporous silicon substrate[12] in order to investigate the filed emission characteristic.

In this paper, it is reported on that nanocrystalline diamond film deposited on a foil of Mo-Re alloy for cold field electron emission.

2 EXPERIMENTAL DETAILS

The substrate is a foil of Mo-40%wt Re alloy in white with a thickness of 6 μm. The diamond film deposition was performed in a steel chamber of super high vacuum with a base pressure of less 10⁻⁵ Pa, detail of this equipment was given in previous work [13]. The hot filament CVD system consists of a process chamber equipped with a tungsten filament and a substrate stage that were employed for activation of gas-phase reactions and for the independent control of substrate temperature, respectively. The methane and hydrogen were used as the reactant and dilution, respectively. Prior to diamond deposition, the substrates were ultrasonically treated for 10 min in a slurry of acetone and nanodiamond powder, for provide high diamond nucleation density. The temperatures of the filament and the substrate were monitored by an optical pyrometer and K-type thermocouple, respectively. The technical parameters of HFCVD is given in table 1.

Table 1. Experimental parameters for the HFCVD diamond

Parameters	Values
The volume ratio of CH ₄ and H ₂ /%	1, 2, 3, 4
Total gas flow /sccm	50
Filament temperature/°C	2100 ± 50
Substrate temperature/°C	750 ± 30
Spacing between filament and substrate/mm	8
Ambient pressure/Pa	30 torr
Deposition time/min	60

The scanning electron microscopy (SEM) was carried out using FEI Sirion200 Field emission scanning electron microscope (FESEM), with 10 kV acceleration voltage. The XRD analysis was carried out by D/max2500 diffractometer, with a monochromatized Cu K α radiation of 10 kV and 20 mA. The Raman spectrum was measured using a LabRaman RH800 spectrometer (UK) with an argon laser source with a 488 nm wavelength. Laser power was set as 20 mW.

3 RESULTS AND DISCUSSION

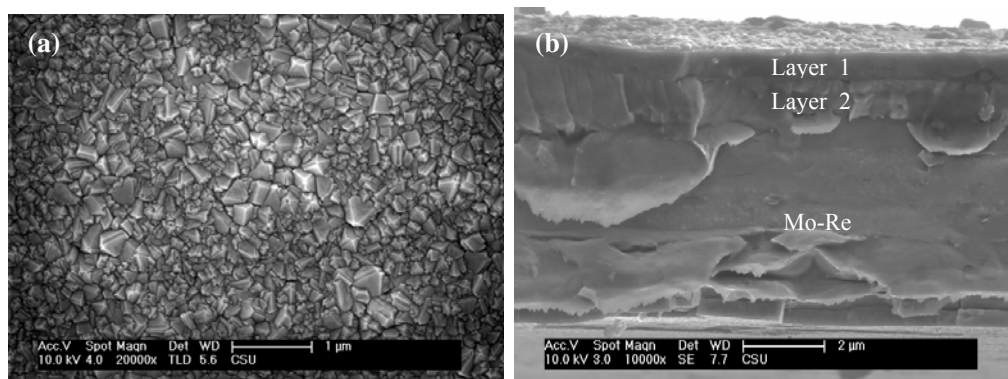


Fig.1 SEM image of diamond film on Mo-Re foil. (a) top view, (b) crossing-section view.

Fig. 2 is the Raman spectrum of the sample. Raman spectroscopy is a convenient probe to evaluate the quality of the diamond films by recording the variations of the vibration frequency of the carbon-carbon bond. In the Raman spectrum, there is a sharp Raman peak at 1332 cm⁻¹ resulting from the characteristic vibration mode of *sp*³ hybridization; a broad signal in the range from 1400 to 1600 cm⁻¹ is attributed to highly disordered carbon atoms in *sp*² hybridization. The other broad peak at 1500~1580 cm⁻¹ with a FWHM of about 80cm⁻¹ comes the amorphous graphitic component in the diamond film. The measured ratio of I_D/I_G is around in a value of 3.5. It means furthermore a high quality diamond film on the surface

Fig. 1 shows SEM images of the diamond film deposited on the Mo-Re foil with the methane concentration of 2%. It can be seen that there are two different layers on the surface of the substrate of Mo-Re foil. Fig. 1(a) is a typical morphology of polycrystalline diamond film with grain sizes from 20 ~ 400 nm. It is found two layers on the Mo-Re substrate as shown Fig. 1(b). The thicknesses of the top layer (layer 1) and the second later (layer 2) are about 350 nm and 900 nm, respectively.

layer. The two peaks at 1140 cm⁻¹ and 1480 cm⁻¹ are generally accepted as an evidence of NCD, although some assign it to the presence of transpolyacetylene in NCD films[14-15].

Fig. 3 is the XRD pattern of the sample deposited with the methane concentration of 2%. One sees the peaks at 2 θ = 44° and 75°, which are correspondent the diffractions from diamond (111) and (220) planes. It is also found the peaks of at the 2 θ = of 40.40°, 58.58°, 73.64° and 115.96°, which are correspondent the diffractions from the (110), (200), (211) and (222) of the Mo-Re alloy, respectively. It indicates that the Mo-Re alloy is also in a bcc structure and implies that the Mo atom is partly substituted by Re atom. It is interesting

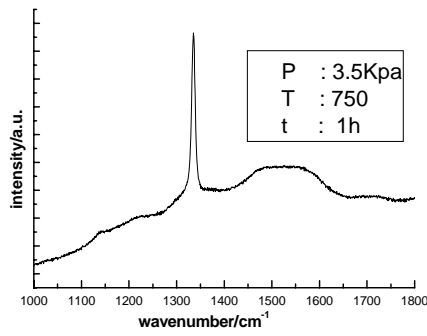


Fig.2. Raman spectrum for the diamond films

that all of the angles from the Mo-Re are less than

calculated angles considering a pure bcc Mo metal with a lattice constant $a = 3.147$ nm. It means that the lattice constant of the bcc Mo-Re alloy is larger than 3.147 nm. This probably implies the radius of Re atom in the lattice of the Mo-Re alloy is larger than 1.363 nm.

Furthermore, there at least are 15 peaks corresponds the metallic compound of Mo_2C in Fig. 3. The values of these 2θ are shown in table 2. It indicates the molybdenum carbide is in a hexagonal structure, i.e., $2\text{H-Mo}_2\text{C}$. For the metallic compound of Mo_2C , the carbon atoms insert interstitially in half octahedral sites of the HCP of molybdenum atoms. The crystalline

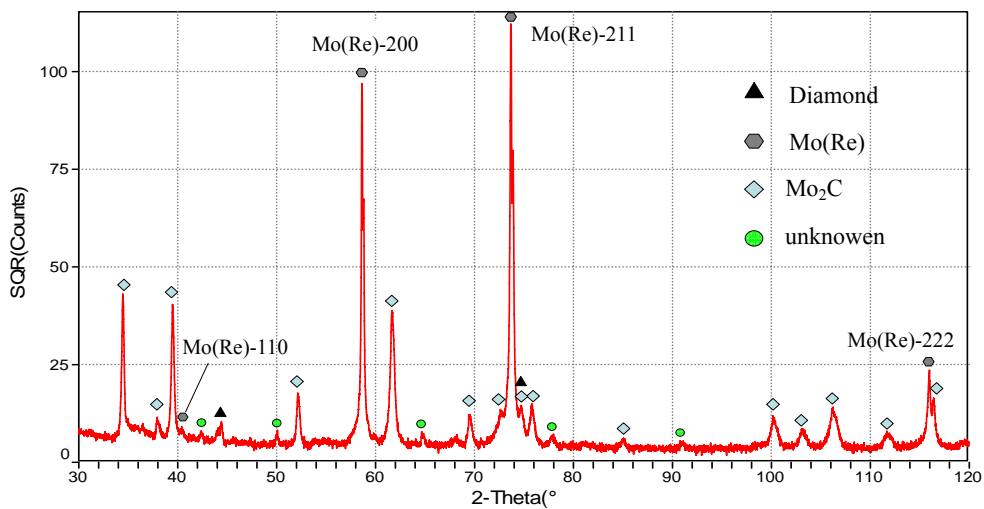


Fig. 3. XRD pattern of the sample.

structure of the $2\text{H-Mo}_2\text{C}$ is schematically shown in Fig 4. Its parking sequence is in principle $\text{AcBcAc}\dots$, where A and B denote the normal sites in the HCP lattice and c denotes the interstitial site. The diffraction angle of the $2\text{H-Mo}_2\text{C}$ is determined by $\theta = \arcsin\left(\frac{\lambda}{2} \sqrt{\frac{h^2 + hk + k^2}{a^2} + \frac{l^2}{c^2}}\right)$. It is, therefore, found from the data in table 2 that the values of the a axis and the ratio of c/a of the metallic compound are 3.003 \AA and 1.579, respectively. The measured value of the ratio of c/a is less than 1.633, meaning carbon atom in the Mo_2C attracts its nearest neighboring Mo atom. The Mo_2C formation may be due to the carbon atoms in gas phase diffuse into the Mo-Re alloys at the deposition

temperature of about $750 \text{ }^\circ\text{C}$.

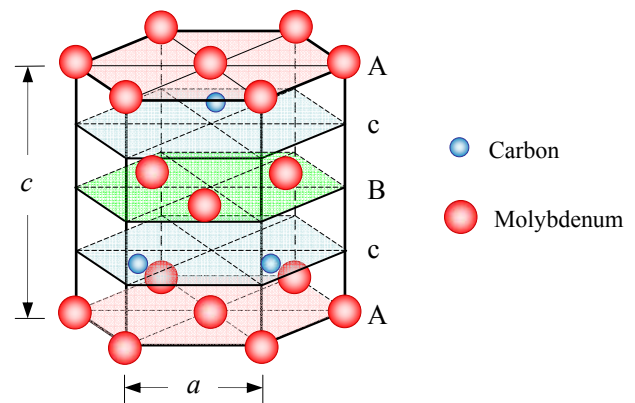


Fig. 4 Schematically crystalline structure of the $2\text{H-Mo}_2\text{C}$

Table 2. Measured 2θ values of $2\text{H-Mo}_2\text{C}$.

Planes	(100)	(002)	(101)	(102)	(110)	(013)	(200)	(112)	(201)	(202)	(023)	(210)	(211)	(114)	(212)
2θ	34.52	37.95	39.45	52.15	61.64	69.5	72.6	74.72	75.8	85.05	100.15	103.1	106.2	111.8	116.3

4 CONCLUSION

Diamond film was deposited on a Mo-Re foil substrate with a thickness of 6 μm by using hot-filament chemical vapor deposition (HFCVD). It is found that the foil of Mo-Re alloy is in substitutional solid solution. The thickness of the diamond film is about 350 nm by 1 hour deposition. It is found that there is a 2H-Mo₂C layer between diamond film and the Mo-Re substrate. The values of the *a* axis and the ratio of *c/a* of the metallic compound are 3.003 Å and 1.579, respectively. This Mo₂C layer might be due to the carbon atoms in gas phase diffuse into the Mo-Re alloy at the temperature of about 750°C.

References

- [1] F. Pinzari, P. Ascarelli, E. Capelli, G. Mattei, R. Giorgi, "Wettability of HF-CVD diamond films," *Diamond & Related Materials*, 10, pp. 781–785 (2001).
- [2] D. Pradhan, Y.C. Lee, C.W. Pao, W.F. Pong, I.N. Lin, "Low temperature growth of ultrananocrystalline diamond film and its field emission properties", *Diamond & Related Materials* 15, pp. 2001–2005(2006).
- [3] Changzhi Gu, Xin Jiang, Zengsun Jin, Weibiao Wang, "Electron emission from nanocrystalline diamond films," *J. Vac. Sci. Technol. B*, Vol. 19, No. 3, pp. 962-964(2001).
- [4] J. Philip and P., "Hess Elastic, mechanical, and thermal properties of nanocrystalline diamond films," *JOURNAL OF APPLIED PHYSICS*. Vol 93, No. 4, pp. 2164-2171(2003).
- [5] Roland Haubner, Benno Lux, "Deposition of ballas diamond and nano-crystalline diamond.," *International Journal of Refractory Metals & Hard Materials* 20, pp.93–100(2002).
- [6] Yih-Trong Jan, Hui-Chen Hsieh, Chia-Fu Chen, "Fabrication of nano-size conic diamond arrays by bias assisted PCVD," *Diamond & Related Materials*, 8, pp. 772–780 (1999).
- [7] O.J.L. Fox, J. Ma, P.W. May, M.N.R. Ashfold, Yu.A. Mankelevich, "The role of inert gas in MW-enhanced plasmas for the deposition of nanocrystalline diamond thin films," *Diamond & Related Materials*, 9, pp. 750–758 (2000).
- [8] Franz A.M. Koeck, Robert J. Nemanich, "Emission characterization from nitrogen-doped diamond with respect to energy conversion," *Diamond & Related Materials*, 15, pp. 217–220 (2000).
- [9] Chuan-Feng Shiha, Kuo-Shung Liua, I-Nan Linb, "Effect of nitrogen doping on the electron field emission properties of chemical vapor deposited diamond films," *Diamond & Related Materials*, 18, pp. 1591–1599 (2001).
- [10] H. Ji, Z. S. Jin, J. Y. Wang, X. Y. Lu, "Field emission characteristics of diamond films with different surface morphologies," *J. Vac. Sci. Technol. B* Vol. 17, No. 2, pp. 684-687(1999).
- [11] Kenji Hirakuri, Takahiro Yokoyama, and Hirofumi Enomoto, "Surface properties and field emission characteristics of chemical vapor deposition diamond grown on Fe/Si substrates," *JOURNAL OF APPLIED PHYSICS*, Vol. 89, No. 12, pp. 8253-8258(2001).
- [12] S. K. Arora, S. Chhoker, N. K. Sharma, V. N. Singh, and V. D. Vankar, "Growth and field emission characteristics of diamond films on macroporous silicon substrate. *JOURNAL OF APPLIED PHYSICS*," 104, 103524 (2008).
- [13] Z. YU, A. Flodstrom and W. Karlsson, "Influence of oxygen and nitrogen on the growth of hot-filament chemical vapor deposited diamond films," *Thin Solid Films* 342, pp. 74-82 (1999).
- [14] C. Casiraghi, F. Piazza, A.C. Ferrari, D. Grambole, J. Robertson, "Bonding in hydrogenated diamond-like carbon by Raman spectroscopy," *Diamond & Related Materials*, 14, pp. 1098–1102 (2005).
- [15] Kuzmany R. Pfeiffer, N. Salk and B. Günther, "The mystery of the 1140 cm^{-1} Raman line in nanocrystalline diamond films," *Carbon*, 42, pp. 911–917(2004).

Composite Material Produced from Rice Husk and Chopped Carbon Fiber

Seiji Kumagai, Junya Sasaki, Yuta Abe and Masaya Sugimoto

Department of Machine Intelligence and Systems Engineering, Akita Prefectural University
84-4, Tsuchiya-aza-ebinokuchi, Yurihonjo, 015-0055, Japan

kumagai@akita-pu.ac.jp

Abstract : A carbon/silica/carbon-fiber composite (CSCFC) was fabricated from agricultural waste of rice husk and industrial waste of carbon fiber (CF) ends. The powder of rice husk mixed with chopped CF ends (0 to 30 mass%) was molded into a disk by means of hot-pressing in an inert condition without using any binders. A compression of 100 MPa was intermittently applied to the mixed which was heated from room temperature to 150°C, and then at 280 °C. The molded was further heated to 300, 400, 500, or 1000 °C in an inert condition, producing a CSCFC. The CSCFC added with 10 mass% of chopped CF and heated to 300°C displayed the highest compressive strength of 120 MPa and low bulk density of 1.2 g/cm³. It was also shown that higher heat treatment temperature rather reduced the compressive strength. The CF restricted a uniform thermal shrinkage of the matrix material derived from rice husk, causing cracks and eventually reducing the compressive strength.

Key Words: Composite, rice husk, carbon fiber, hot-pressing, compressive strength.

1 INTRODUCTION

Carbon fiber-reinforced plastics (CFRPs) have been extensively utilized in advanced industrial products such as aircraft, vehicles, rockets, building and sport goods. 13,412 metric tons of carbon fiber (CF) was shipped from Japanese manufacturers in 2008 [1]. A fabrication of CFRP structures can emit CF ends of which length is insufficient for the use of other applications. A huge quantity of the emitted CF ends is now treated as industrial waste, requiring the effective recycling methodology.

Unsaturated polyester and phenolic resins are well employed for matrices of CFRPs. Those resins are derived from fossil fuel. Replacing the fossil fuel-based matrices with the biomass-based renewable matrices can contribute to a sustainable manufacture of CFRPs and to reducing environmental burden of the earth.

Wood [2-5], rice bran [6, 7] and rice husks [8, 9], which are all byproduct of forestry and agriculture, have been used as precursors of high-strength carbon-based materials. However, a fair amount of thermosetting phenolic resin to enhance moldability and to improve mechanical performance of those materials is used in the fabrication processes. The use of phenolic resin, which is produced from fossil resources, is by no means environmentally friendly.

Rice husk (RH) is one of promising biomass species in Japan because of stable and large yield (2 million metric

tons a year) and low-cost of acquisition. 63 mass% of RH is recycled for use in agricultural, livestock and other industries [10]. However, the rest is not efficiently utilized. The incineration of RHs is now discouraged because it produces ash, fumes, and toxic organic gases, leading to serious air pollution. Recycling of RH is now a socially important concern in Japanese agriculture.

An average composition of RH from various countries were reported to be as ash 20 mass% (almost silica), lignin 22 mass%, cellulose 38%, pentosans 18 mass%, and other organic matters [11]. Lignin, considered as adhesive to hold wood structure, is composed of mainly phenyl-propane units linked together by various means [12]. Lignin has a structural similarity with phenolic resins which are produced by curing the mixture of phenol and formaldehyde and have been extensively used as adhesives [13]. Because lignin could play a role of adhesive and display a thermosetting property similarly seen in phenolic resins, the authors accomplished to produce a high-strength carbon/silica composite (CSC) from RH without using any additives and binders [14].

In the present study, industrial waste of CF ends was attempted to be added into the RH-derived CSC for further enhancing its mechanical strength. The raw RH powder was mixed with the chopped CF ends having different lengths in a slurry state. Then, the mixture was dried and hot-pressed so as to produce the carbon/silica/carbon-fiber composite (CSCFC). The bulk density and the compressive strength of CSCFCs

produced in various conditions were evaluated.

2 EXPERIMENTAL METHODS

2. 1. Pulverization of raw RH and chopping of CF

The RH sample was obtained by threshing of Akita Komachi rice grown in Nishiki, Senboku City, Japan in autumn 2005. The ash was produced by heating the RH to 950 °C in air flow (200 mL/min). The ash content of the RH was 17.1 mass%. Its major constitution (91.1 mass% in ash) was SiO₂, which was measured by using a fluorescent X-ray analyzer (XRF-1700, Shimadzu Corp., Japan). The RH powder was prepared, by using a planetary ball mill (P-6, Fritsch GmbH, Germany). The average particle diameter was evaluated using a laser diffraction particle size analyzer (SALD-300V, Shimadzu Corp., Japan) and it was 15 μm.

Polyacrylonitrile (PAN) carbon fiber ends of ϕ 6 μm were pre-chopped into *ca.* 5 mm in length. The pre-chopped CF was further chopped at different operation conditions using the above planetary ball mill. Three types of the chopped CFs (CF_S, CF_M and CF_L), of which length distributions are shown in **Figure 1**, were prepared. The length of arbitrary 100 chopped CFs sandwiched between slide and cover glasses were measured by means of an optical video microscope (VH-5000; Keyence Corp., Japan). The arithmetic mean lengths of CF_S, CF_M and CF_L were 56, 242 and 363 μm, respectively.

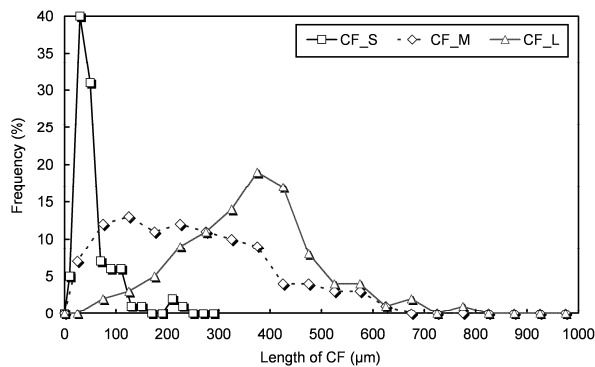


Figure 1. Length distribution of three types of chopped CFs.

2. 2. Hot-pressing procedure to fabricate CSCFCs

Slurry of a mixture of the pulverized RH and the chopped CF was produced at different ratios. The level of CF addition was not based on the mass of the produced CSCFC, but on the mass of the pulverized raw RH. The slurry was sufficiently kneaded and then dried at 105 °C, giving the completely dried mixture. Using a hot-pressing equipment, a schematic diagram of which is shown in **Figure 2**, a disk-shaped CSCFC was molded. 700 mg of the dried mixture was compressed by two SUS 304 stainless steel rods (ϕ 9.96 mm) in a stainless steel cylinder (ϕ 10.00 mm), following the specified compression and heating program shown in **Figure**

2. Nitrogen gas flowed at the rate of 1.0 L/min in order to avoid exposure of the sample mixture to ambient air. The sample mixture was compressed at a pressure of 100 MPa under the constant heating rate of 5 °C/min up to 150 °C. The heater was installed around the cylinder. The pressure was then removed and the sample was heated up to 250 °C at the heating rate of 5 °C/min and up to 280 °C at 2 °C/min, restricting the undesired outward injection of the fluidized RH through the clearance of the rods and the cylinder. The temperature was held at 280 °C and the sample was again compressed at a pressure of 100 MPa for 10 min. Then, the pressure was removed to prevent the sample from cracking. The sample was further heated to 300, 400, or 500 °C at 5 °C/min and cooled to room temperature. The maximum heating temperature for each sample is determined to be simply the heat treatment temperature.

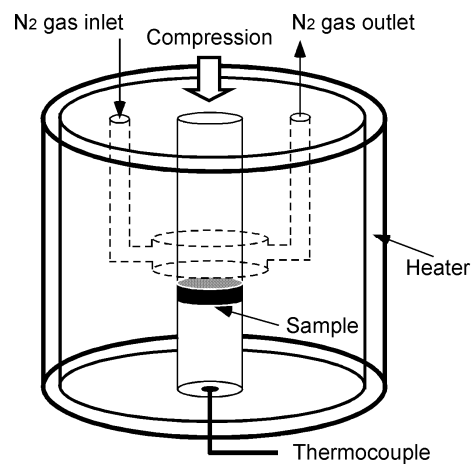


Figure 2. A schematic diagram of the hot-pressing equipment.

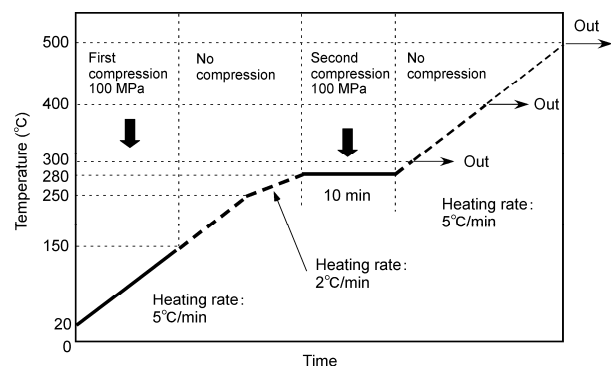


Figure 3. The compressing and heating program to fabricate CSCFCs.

A CSCFC heated up to 500 °C in the above hot-pressing equipment was once again heated to 1000 °C at the rate of 10 °C/min and held for 1 h in nitrogen flow (1.0 L/min) using a tubular electric furnace. Finally, this sample was cooled to room temperature in nitrogen flow.

2. 3. Material evaluation

The mass, diameter and thickness of the CSCFC samples, dried at 105 °C for 3 h, were measured using a slide caliper, providing values for bulk density under the assumption that the samples were a normal cylinder shape. The compressive strengths of the samples were evaluated using a universal testing machine (Ezgraph 10kN, Shimadzu Corp., Japan). Stress–strain curves were obtained, during which the compressive stroke velocity was set to be 1 mm/min and the stress was applied to the circular planes. The compressive strengths were determined based on the maximum compressive stress. The surfaces of the CSCFC samples were observed using the above-mentioned optical video-microscope. The average and standard deviation of 5 measurements are shown in the results related to the bulk density and the compressive strength of CSCFCs.

3 RESULTS AND DISCUSSION

3. 1. Impact of CF addition on compressive strength of CSCFCs

The RH powder mixed with the 10 mass% of CF_M (mean length: 242 μm) was molded into the disk-shaped CSCFC. The bulk density and the compressive strength of the CSCFCs at different heat treatment temperatures are shown in **Figure 4**. The samples added with no CF were also molded and tested in the similar manners. Without use of CF, the highest bulk density and compressive strength appeared at the heat treatment temperature of 1000 °C, which was explained by the sample densification caused by thermal shrinkage and the formation of crystalline SiO_2 [14]. The highest bulk density (1.2 g/cm^3) and compressive strength (120 MPa) of the CSCFC added with CF were observed at the heat treatment temperature of 300 °C. The higher heat treatment temperature rather reduced the bulk density and the compressive strength, which is inconsistent with the results without CF.

Figure 5 shows the surface optical micrographs of the CSCFCs fabricated at different heat treatment temperatures. More and larger cracks were found to be produced with

increasing the heat treatment temperature. The obtained results suggested that the CF addition could certainly increase the compressive strength. However, the added CF restricted the spontaneous and uniform thermal shrinkage of the matrix. The resultant crack formations led to the decrease in the bulk density and the compressive strength.

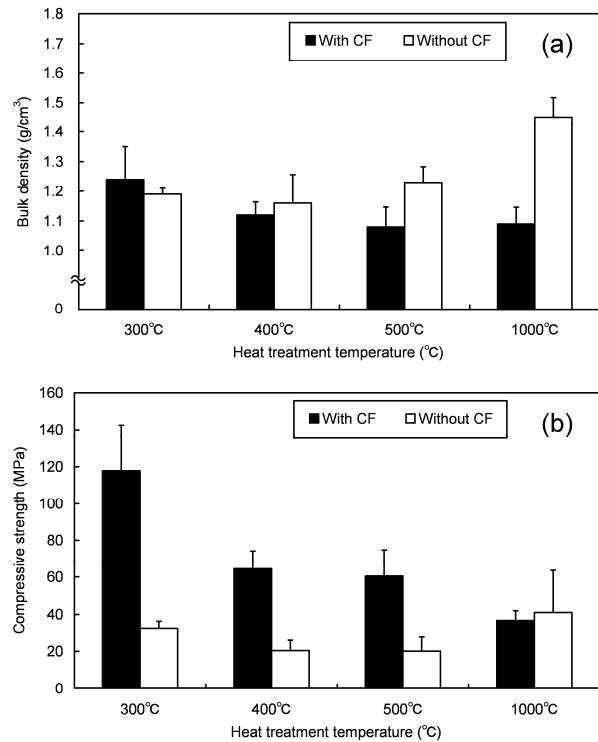


Figure 4. Impact of CF addition on the bulk density and the compressive strength of RH-derived CSC fabricated at different heat treatment temperatures. The used CF is CF_M. (a) bulk density, (b) compressive strength.

3. 2. Relation between CF level and compressive strength of CSCFCs

Fixing the heat treatment temperature to be 300 °C and 500 °C, CSCFCs with different levels of CF_M were prepared. **Figure 6** shows the bulk density and the

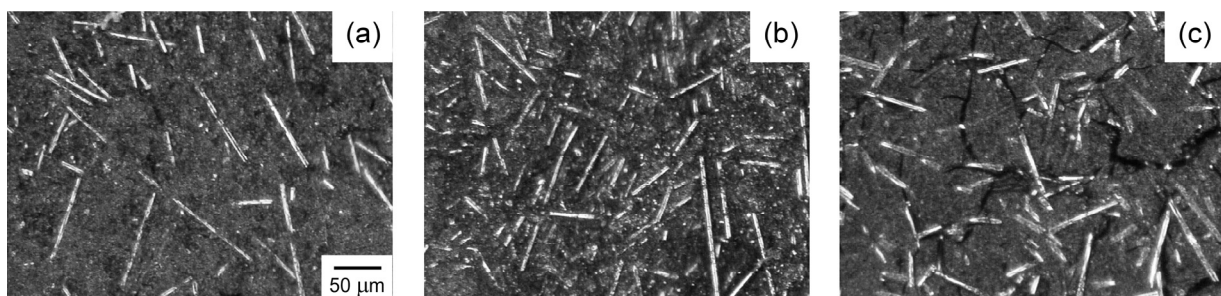


Figure 5. Surface optical micrographs of the CSCFCs fabricated at different heat treatment temperatures. CF_M was added into all the samples at 10 mass%. (a) 300 °C, (b) 500 °C, (c) 1000 °C.

compressive strength of the CSCFCs of which CF level was set to be 0-30 mass% and of which heat treatment temperatures were 300 and 500 °C. The bulk density of the CSCFC heated to 300 °C increased slightly with the CF level, while that heated to 500 °C decreased slightly. The highest compressive strengths appeared at 10 mass% for the CSCFC heated to 300 °C (120 MPa) and at 20 mass% for that heated to 500 °C (70 MPa).

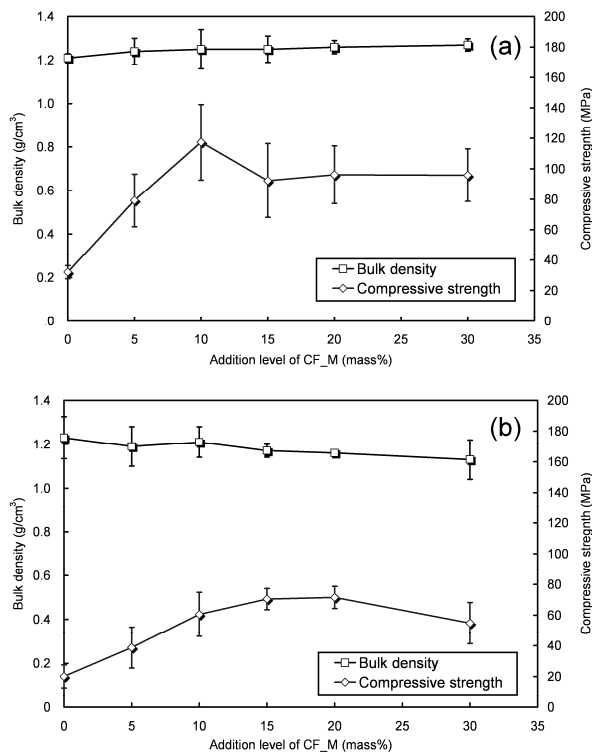


Figure 6. Impact of level of CF addition on the bulk density and the compressive strength of CSCFCs fabricated at different heat treatment temperatures. The used CF is CF_M. (a) 300 °C, (b) 500 °C.

The surface optical micrographs of the CSCFCs heated to 500 °C at different CF levels were shown in **Figure 7**. It is clearly found that the matrix portion decreased with the CF level. Cracks formations were enhanced by the

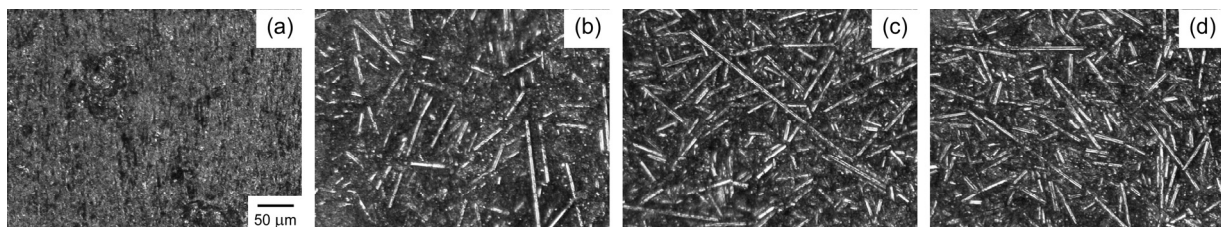


Figure 7. Surface optical micrographs of the CSCFCs fabricated at different CF levels. CF_M was added into all the samples. (a) 0 mass%, (b) 10 mass%, (c) 20 mass%, (d) 30 mass%.

high-level CF addition (>20 mass%). The results shown in **Figure 6** revealed that the CF addition at <10 mass% was useful to increase the compressive strength of the samples heated up to 500 °C. This was obviously ascribed to the reinforcement by the CF use. However, higher level of the CF addition resulted in the decrease in the matrix portion derived from RH. This is responsible for reducing the bulk portion substantially subjected to compressive loading and for weakening the adhesion between the CF and the matrix. The different CF levels leading to the maximum compressive load was likely to be related to the differences in the matrix properties. The slight decrease in the bulk density of CSCFC heated to 500 °C, with increasing the CF level, implies that cracks were more formed with the CF addition level. Thus, the CF level leading to the maximum compressive strength was dependent on the heat treatment temperature.

3. 3. Role of CF length on compressive strength of CSCFCs

Fixing the heat treatment temperature to be 300 °C and the CF addition level to be 10 mass%, three different types of the chopped CFs, of which length distributions were shown in **Figure 1**, was used. **Figure 8** shows the bulk density and the compressive strength of CSCFCs added with different lengths of CFs. It was found that the CF length had no impact on the bulk density. The change of CF_S to CF_M increased significantly the compressive strength, while the change of CF_M to CF_L hardly increased the compressive strength. The average lengths of CF_S, CF_M and CF_L were 56, 242 and 363 μm, respectively. The increase in the average length from 56 to 242 μm was supposed to be critical to enhance the adhesion between the CF and the matrix, while that from 242 to 363 μm had a weak impact on the adhesion. Although a certain length was required to attain high compressive strength, the length of *ca.* 300 μm was sufficient. Excessively long CF could reduce the sample moldability. Further study will be carried to optimize the length of CF attaining the maximum compressive strength.

3. 4. Performance improvement of CSCFC

Being different from the CSC without CF, lower heat treatment temperature was shown to be suitable to attain higher compressive strength. Appropriate fabrication conditions of the CSCFC having high compressive strength

were found to be as follows; CF length: 242 μm , CF level: 10 mass%, heat treatment temperature: 300 $^{\circ}\text{C}$. However, because of residual volatile organic matters, thermal stability of the CSCFC heated at the lower temperature should be improved. In order to accomplish both the high compressive strength and the thermal stability, higher heat treatment temperature (>500 $^{\circ}\text{C}$) is required. Much lower heating rate would be promising to alleviate crack formations caused by the restriction of uniform thermal shrinkage. The role of heating rate on the performance of CSCFC will be investigated in future. Other mechanical properties such as the tensile strength and flexural strength are also important. The hot-pressing equipment will be upgraded to produce slab or plate samples for those evaluations in future.

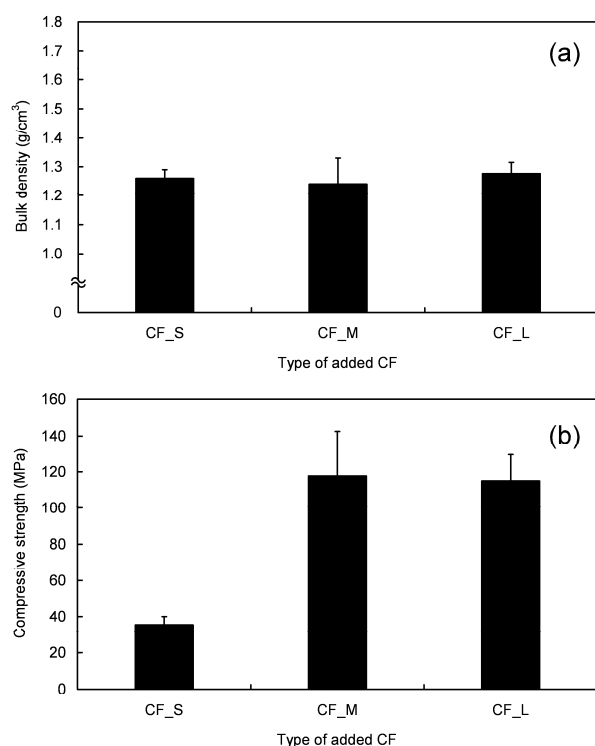


Figure 8. Bulk density and compressive strength of CSCFCs added with different lengths of CFs. (a) bulk density, (b) compressive strength.

4 CONCLUSIONS

A composite of carbon/silica/carbon-fiber was successively produced from RH and CF ends. The powder of RH mixed with the chopped CF was molded into a disk by means of hot-pressing without using any binders. The molded was further heated to 300, 400, 500, or 1000 $^{\circ}\text{C}$ in an inert condition. The following conclusions were obtained.

- (1) The composite added with the chopped CF of 242 μm in length at the level of 10 mass%, and heated to 300 $^{\circ}\text{C}$ displayed the highest compressive strength of 120 MPa and low bulk density of 1.2 g/cm^3 .

- (2) The CF restricted a uniform thermal shrinkage of the matrix derived from rice husk, causing crack formations.
- (3) Higher treatment temperature was rather unnecessary to increase the compressive strength of the CSCFC.

Acknowledgement—This research was supported in part by KAKENHI for Young Scientists A (21681011). We would like to thank Dr. Mitsuhiro Okayasu of Akita Prefectural University for their assistance in the compressive strength evaluation.

References

- [1] The Japan Carbon Fiber Manufacturers Association, 2009. <http://www.carbonfiber.gr.jp> (in Japanese).
- [2] Okabe, T., Saito, K., Hokkirigawa, K., 1996. New porous materials, woodceramics: development and fundamental properties. *J. Porous Mater.* 2, 207-213.
- [3] Hokkirigawa, K., Okabe, T., Saito, K., 1996. Friction properties of new porous carbon materials: woodceramics. *J. Porous Mater.* 2, 237-243.
- [4] Iizuka, H., Fushitani, M., Okabe, T., Saito, K., 1999. Mechanical properties of wood ceramics: a porous carbon materials. *J. Porous Mater.* 6, 175-184.
- [5] Zhao, B. Y., Hirose, T., Okabe, T., Zhang, D., Fan, T. X., Hu, K. A., 2002. Woodceramics prepared from wood powder/phenolated wood composite. *J. Porous Mater.* 9, 195-201.
- [6] Iizuka, H., Noguchi, T., Shikano, S., 2003. A new porous carbon materials made from rice bran. *Int. J. Soc. Mater. Eng. Resour.* 11, 10-15.
- [7] Zhou, Y., Hirao, K., Yamaguchi, T., Hokkirigawa, K., 2005. Preparation and tribological properties SiC/RBC composite ceramics. *J. Mater. Res.* 20, 3439-3448.
- [8] Unuma, H., Niino, K., Sasaki, K., Shibata, Y., Iizuka, H., Shikano, S., Nakamura, T., 2006. Preparation and characterization of glass-like carbon/silica composite from rice hull and phenolic resin. *J. Mater. Sci.* 41, 5593-5597.
- [9] Yoshida, K., Iizuka, H., Shibata, Y., Unuma, H., Nakamura, T., Shikano, S., 2006. Water resistance of porous carbon materials made from rice hull. *Int. J. Soc. Mater. Eng. Resour.* 13, 49-53.
- [10] New Energy and Industrial Technology Development Organization (NEDO), 2006. Estimated amount of existent and available biomass in Japan: GIS database, <http://app1.infoc.nedo.go.jp/kinds/no2.pdf> (in Japanese).
- [11] Chandrasekhar, S., Satyanarayana, K. G., Pramada, P. M., Raghavan, P., Gupta, T. N., 2003. Review: processing, properties and applications of reactive silica from rice husk - an overview. *J. Mater. Sci.* 38, 3159-3168.
- [12] Tillman, D. A., Rossi, A. J., Kitto, W. D., 1981. *Wood combustion, principle, process and economics*, Academic Press, New York.
- [13] Khan, M. A., Ashraf, S. M., 2007. Studies on thermal characterization of lignin, substituted phenol formaldehyde resin as wood adhesives. *J. Therm. Anal. Calorim.* 89, 993-1000.
- [14] Sasaki, J., Kumagai, S., Ishizawa, H., Takeda, K., 2008. Fabrication of dense and high-strength carbon/silica composite from natural rice husk by means of binderless hot-pressing. *Proceedings of the 6th Asia and Australasian Conference on Composite Materials*, 451-454.

Strength and Sliding Properties of Carbon/Silica Composite Produced from Rice Husk without Binder

Junya Sasaki, Seiji Kumagai and Masaya Sugimoto

Department of Machine Intelligence and Systems Engineering, Akita Prefectural University
84-4, Tsuchiya-aza-ebinokuchi, Yurihonjo, 015-0055, Japan
kumagai@akita-pu.ac.jp

Abstract : A carbon/silica composite (CSC) designed for use under sliding and compressive load was fabricated from rice husk (RH), an agricultural waste material, without using any binders. A compression pressure of 100 MPa was applied to the RH powder heated from room temperature to 150°C firstly, and then that heated at 280°C for 10 min secondly. The RH powder was finally heated from 280 °C to 500 °C without compression, producing the precursor of CSCs. The CSCs were produced by sintering the precursor in an electric furnace at 800, 1000, 1200, 1400 °C without compression, in nitrogen gas. The CSC sintering at 800 °C for 1 h in nitrogen gas provided the maximum bulk density of 1.52 g/cm³. The maximum compressive strength was measured to be 55.7 MPa at the sintering temperature of 1200 °C. The maximum Vickers microhardness at the surface of 476 appeared on the CSC produced at the second compression pressure of 200 MPa and then sintered at 800 °C. The CSC sintered at 1000 °C showed the static friction coefficient of 0.15 and the dynamic friction coefficient of 0.05 under the contact with SUS304 stainless steel.

Key Words: Composite, rice husk, silica, hot-pressing, sliding properties.

1 INTRODUCTION

About 2 million tons of rice husk (RH) are produced every year in the process of rice threshing in Japan. Of this, 63 mass% of RH is recycled for use in agricultural, livestock and other industries [1]. Thus, recycling of residual RH is now a socially important subject, especially in rice-growing regions in Japan.

In order to reduce agricultural waste and to promote the use of renewable resources, methods of fabricating molded carbon materials from agricultural byproducts have been widely studied [2-5]. High-strength molded carbon-based materials have been fabricated from wood [6-9], rice bran [10, 11] and rice husks [12, 13]. In this fabrication process, a fair amount of thermosetting phenolic resin is used as a molding binder, which can enhance moldability and improve mechanical performance. Unuma et al. produced RH-based materials by incorporating a resol-type phenolic resin [12]. The RH-based material, which was prepared by means of press molding at room temperature and was sintered at 900-1400 °C, had a bulk density of 1.1–1.3 g/cm³ and compressive strength of 130–150 MPa. The commercially available RH-based material, which was produced by incorporating a phenolic resin, using a press mold at room temperature and by sintering at 1000 °C, recorded a bulk

density of 1.28 g/cm³, compressive strength of 139 MPa, and Vickers hardness of 620 [13]. However, the use of these thermosetting resins, which are derived from fossil resources, is not environmentally friendly.

In the present study, RH was transformed into a densified and molded carbon/silica composite (CSC) without using any binders. One characteristic of RH that differentiates it from other types of agricultural byproducts is that it contains silica at ~20 mass%. Pulverized RH was carbonized and molded into a disk-shaped precursor by means of binderless hot-pressing with a specialized procedure. Hot-pressing and hot-extruding methods have often been used to produce molded ligneous materials [15, 16]. The precursor was sintered for further densification up to 1400 °C in inert nitrogen gas, finally producing the disk-shaped CSC. The dimensions, bulk density, compressive strength, surface hardness, and sliding properties of the RH-derived composites were evaluated. The fabricated CSCs can be used as sliding materials such as bearings and gears, and as sealing materials such as gaskets and packings.

2 EXPERIMENTAL METHODS

- 2.1. Fabrication of CSC by means of binderless hot-pressing
The RH sample was obtained by threshing of Akita

Komachi rice grown in Nishiki, Senboku City, Japan in autumn 2005. The ash was produced by heating the RH to 950 °C in air flow (200 mL/min). The ash content of the RH was 17.1 mass%. Its major constitution (91.1 mass% in ash) was SiO₂, which was measured by using a fluorescent X-ray analyzer (XRF-1700, Shimadzu Corp., Japan). The RH powder was prepared, by using a planetary ball mill (P-6, Fritsch GmbH, Germany). The average particle diameter was evaluated using a laser diffraction particle size analyzer (SALD-300V, Shimadzu Corp., Japan) and it was 15 μm.

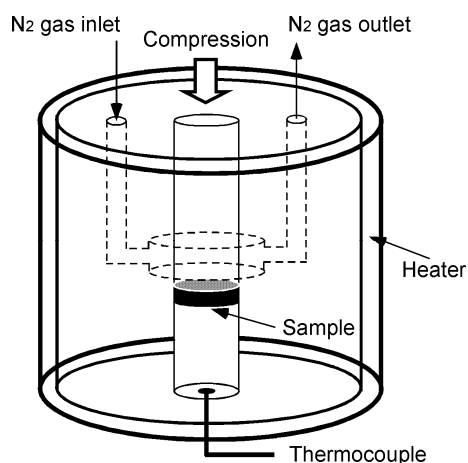


Figure 1. A schematic diagram of the hot-pressing equipment.

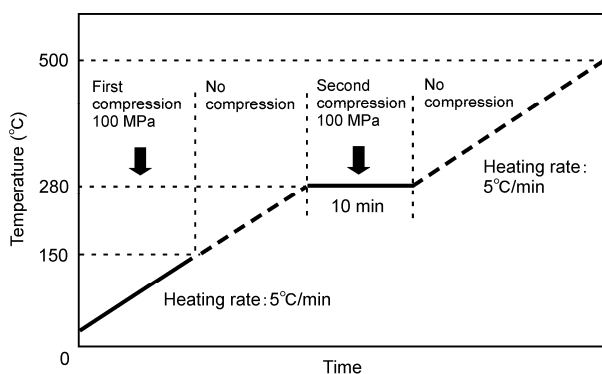


Figure 2. The compressing and heating program to fabricate a precursor of CSC.

A disk-shaped precursor material was molded from the RH powder using hot-pressing equipment, a schematic diagram of which is shown in **Figure 1**. 700 mg of RH powder dried at 105 °C for 3 h was compressed by two SUS 304 stainless steel rods (ϕ 9.96 mm) in a stainless steel cylinder (ϕ 10.00 mm), following the specified compression and heating program shown in **Figure 2**. Nitrogen gas flowed at the rate of 1.0 L/min in order to avoid exposure of the sample to ambient air. The sample was compressed at a pressure of 100 MPa under the constant heating rate of 5 °C/min up to 150 °C. The heater was installed around the cylinder. The pressure was then removed and the material was

heated at a similar rate up to 280 °C, restricting the undesired outward injection of the fluidized RH through the clearance of the rods and the cylinder. The temperature was held at 280 °C and the sample was again compressed at a pressure of 100 MPa for 10 min. Then, the pressure was removed to prevent the sample from cracking. The sample was further heated to 500 °C at 5 °C/min and naturally cooled to room temperature.

The precursor produced by the above process was once again heated to 800, 1000, 1200, 1400 °C at the rate of 10 °C/min and held for 1 h in nitrogen flow (1.0 L/min) using a tubular electric furnace. Finally, the sample was cooled naturally to room temperature in nitrogen flow.

2. 2. Material evaluation

2. 2. 1. Sample pre-treatment and bulk density evaluation

The samples fabricated were polished using an abrasive paper (1500 mesh) with water being applied prior to several evaluations. This treatment was for the removal of undesired flash and surface deposits produced as sintering byproducts. The mass, diameter and thickness of the samples, dried at 105 °C for 3 h, were measured using a slide caliper, providing values for bulk density under the assumption that the samples were a normal cylinder shape.

2. 2. 2. Compressive strength evaluation

The compressive strengths of the samples were evaluated using a universal testing machine (Ezgraph 10kN, Shimadzu Corp., Japan). Stress-strain curves were obtained, during which the compressive stroke velocity was set to be 1 mm/min and the stress was applied to the circular planes. The compressive strengths were determined based on the maximum compressive stress.

2. 2. 3. Surface hardness evaluation

The Vickers microhardness at the surface of the samples was evaluated using a microhardness tester (H100C XYp, Fisher Instruments Corp., Japan). A standard diamond pyramid was indented on the sample surface at an indentation rate of 15 mN/s, up to 300 mN in 20 s and held at 300 mN for 5 s. The Vickers microhardness of the sample was evaluated based on the maximum indentation depth. The surface hardness shown in this paper are the Vickers microhardness values. The sample surface was observed by using an optical microscope system attached to the above microhardness tester.

2. 2. 4 Evaluation of sliding and wear properties

For the evaluation of sliding and wear properties of CSCs, samples of which diameters were larger than those for the other evaluations were fabricated. 10 g of RH powder dried at 105 °C for 3 h was compressed in a stainless steel cylinder of ϕ 40.00 mm. The compression and heating program was similar to those for the other evaluations. The dynamic friction coefficient of the samples was evaluated by

using a friction and wear testing machine (EFM-III-EN/F, Orientec, Japan). A cylinder made of SUS304 stainless steel was thrust to the rotating disc-shaped sample. The testing setup, following JIS-K-7218, is shown in **Figure 3**. The sliding cross-section was 2.00 cm². The rotating speed and the pressure applied were set to be 1 m/s and 0.025 MPa. In order to evaluate the wear property of the samples, the mass change after the sliding action for 1000 m was measured. The static friction coefficient of the sample was measured by using a frictional meter (Muse 94i-II, Shinto Scientific Co., Ltd., Japan), in which a circular plate (ϕ : 26 mm) made of SUS 304 stainless steel was contacted with the sample.

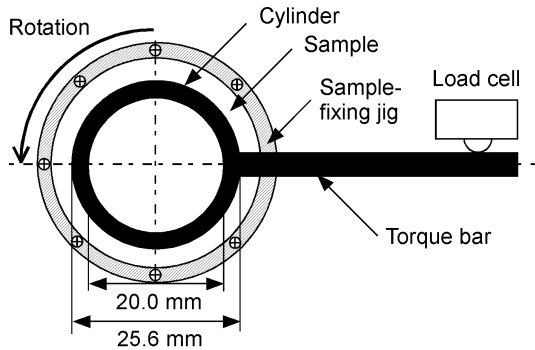


Figure 3. A schematic diagram of a system to measure the dynamic friction coefficient and sliding wear of CSCs.

3 RESULTS AND DISCUSSION

3. 1. Mass, dimension and bulk density of CSCs

The mass, dimension and bulk density of the precursor and the CSCs sintered at the different temperatures are shown in **Table 1**. It was found that a high sintering temperature lowered the mass and diameter of the CSCs. Although the mass of CSC decreased with the sintering temperature, the CSCs sintered at 800, 1000 and 1200 °C showed a similar and high level of bulk density (~ 1.5 g/cm³). Sintering at 1400 °C led to a large decrease in the mass, considerably lowering the bulk density.

3. 2. Compressive strength and surface hardness of CSCs

Figure 4 shows the relation between the compressive strength and the sintering temperature of the CSC. The higher sintering temperature of 1200 °C provided a higher compressive strength. However, the even higher sintering

temperature of 1400 °C reduced the compressive strength, which was comparable to that of the precursor. The CSCs sintered at 800, 1000 and 1200 °C showed a similar and high bulk density. However, the compressive strength of the CSC sintered at 1200 °C was about twice higher than that sintered at 800 °C.

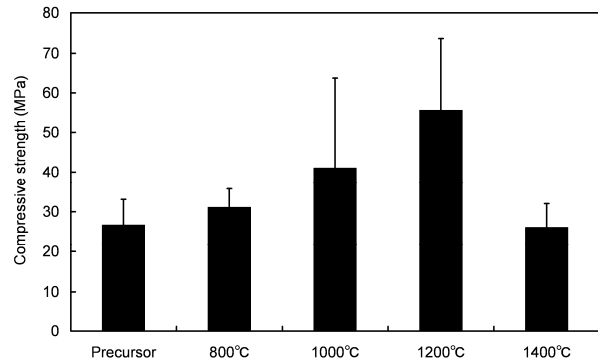


Figure 4. Relation between the compressive strength and the sintering temperature for the CSCs.

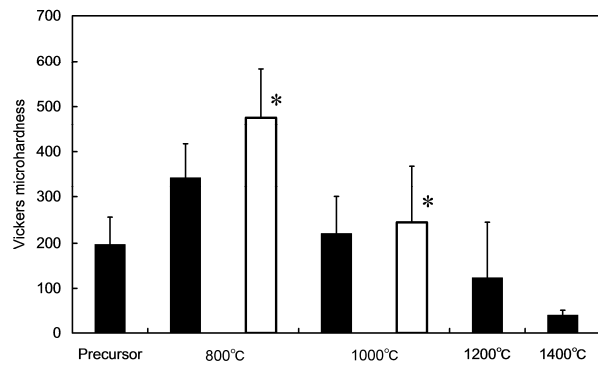


Figure 5. Vickers microhardness at the surface of the CSCs sintered at different temperatures. *: second compression pressure was 200 MPa.

The Vickers microhardness at the surface of the CSCs is shown in **Figure 5**. When the second compression was set to be 100 MPa, a high surface hardness of 343 was observed for the sintering temperature of 800 °C. The densification of the CSC caused by sintering up to 800 °C contributed to the increase in the surface hardness. However, the higher sintering temperature reduced the surface hardness. The CSCs

Table 1. Mass, dimension and bulk density of the precursor and the CSCs sintered at different temperatures.

	Precursor	800 °C	1000 °C	1200 °C	1400 °C
Mass (mg)	284±9	275±4	263±12	257±3	185±15
Diameter (mm)	9.2±0.1	8.7±0	8.6±0.2	8.6±0.1	8.3±0.2
Thickness (mm)	3.1±0.2	3.1±0.1	3.1±0.1	3.0±0.2	3.0±0.3
Bulk density (g/cm ³)	1.37±0.05	1.52±0.05	1.45±0.07	1.48±0.06	1.17±0.03

Data shown are the averages ± standard deviation

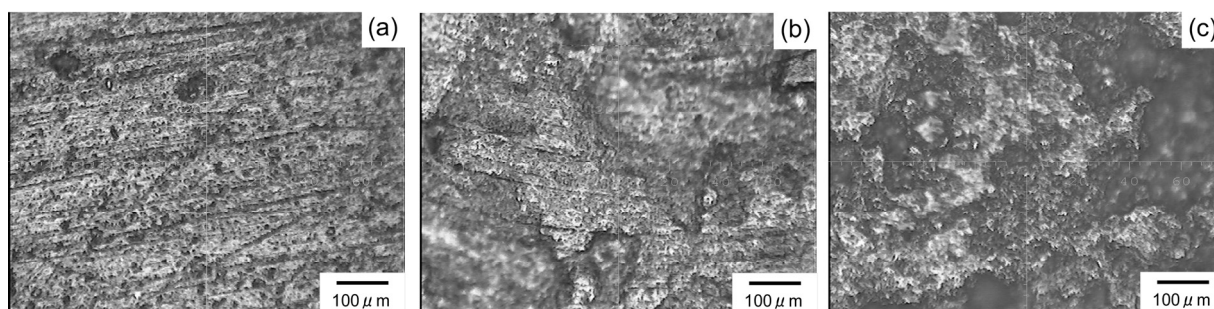


Figure 6. Surface optical micrographs of the CSCs. (a) precursor, (b) CSC sintered at 800 °C, (c) CSC sintered at 1200 °C.

sintered at 1200 and 1400 °C showed much lower surface hardness rather than that of the precursor. An increase in the second compression pressure from 100 to 200 MPa resulted in an increase in the Vickers microhardness of the CSC sintered at 800 °C, attaining the maximum value of 476. The increased pressure reduced the thickness of the CSC sintered at 800 °C, contributing to its densification and an increase in the bulk density (~10 % increment). A slight increase in the hardness was also observed for the CSC sintered at 1000 °C owing to the increased pressure, in which the densification caused by the increased pressure were also slight.

The surface optical micrographs of the precursor and the CSCs are shown in **Figure 6**. The precursor displayed a flat surface with many craters. With increasing sintering temperature, the surface flat region eroded and the asperity increased. A more extensive eroded region was observed on the CSC sintered at 1200 °C compared to that sintered at 800 °C. A wholly eroded surface was observed on the CSC sintered at 1400 °C.

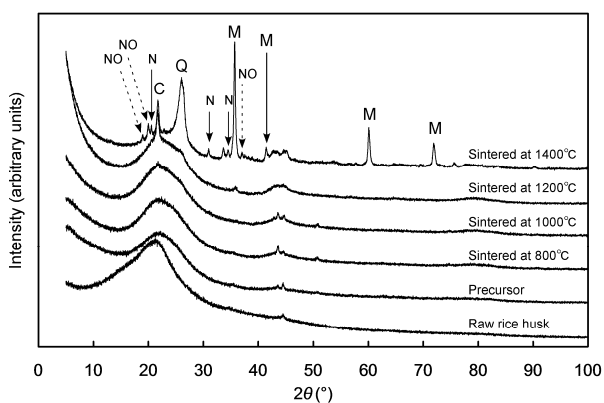


Figure 7. XRD patterns of the raw RH, the precursor and the CSC sintered at 800–1400 °C; powder-state samples were evaluated. C: cristobalite SiO₂, Q: quartz SiO₂, M: moissanite SiC, N: α-Si₃N₄, NO: Si₂N₂O.

Figure 7 depicts the XRD patterns of the raw RH, the precursor and the CSCs sintered at different temperatures. An X-ray diffractometer (CuK_α, X'Pert Pro; PANalytical, Japan) was used. X-ray output conditions were 45 kV and 40 mA.

The high diffraction intensity at the low diffraction angle ($2\theta < 10^\circ$) and the halo at $2\theta = 15\text{--}35^\circ$, which occurred in the patterns of the precursor and the CSCs sintered at 800–1400 °C, are peculiar XRD characteristics of amorphous SiO₂ with silanol (Si-OH) groups, described as SiO₂·xH₂O [17]. A peak at 22° observed on the patterns of CSCs sintered at 1000–1400 °C indicates the presence of cristobalite SiO₂ [18]. A peak due to quartz SiO₂ at 26° [19] and peaks due to moissanite SiC [20] were also observed in the patterns of CSC sintered at 1400 °C. It is noteworthy that peaks resulting from silicon nitride and silicon oxynitride appeared in the XRD pattern of the CSC sintered at 1400 °C. The N-marked peaks were attributed to the formation of α-Si₃N₄ [21] and NO-marked peaks were due to the formation of Si₂N₂O [22], which means that the CSC underwent a nitridation during the sintering at 1400 °C. The nitrogen used as the ambient inert gas for the sintering process was the source of the nitridation. The peaks around 43–45° that appeared in all the XRD patterns were not identified.

A high and similar level of bulk density (~1.5 g/cm³) appeared at the sintering temperature of 800–1200 °C. The bulk density at 1400 °C was considerably lower (1.17 g/cm³). The compressive strength increased with the sintering temperature up to 1200 °C and showed the highest value at 1200 °C. On the other hand, the highest surface hardness was observed at 800 °C. Sintering temperatures of >800 °C reduced the surface hardness.

It is supposed that the following events occurred in the CSC. At a sintering temperature of 600–800 °C, a release of residual organic matter occurred with a large thermal shrinkage. At 800–1200 °C, a release of the water of crystallization from SiO₂·xH₂O to form crystalline SiO₂ proceeded, with thermal shrinkage. The release of the water of crystallization caused an oxidation of carbon and then produced vacancies at the surface and in the bulk of the CSC. Those events at 600–1200 °C reduced the mass of the CSC. However, thermal shrinkage occurred simultaneously, thus resulting in a densified structure, producing a high bulk density (~1.5 g/cm³) at 800–1200 °C. At >1200 °C, the crystalline SiC structure was produced in the CSC, indicating that the following reaction proceeded with the oxidation of carbon.



The formation of crystalline SiC in a carbon material derived from RH and phenolic resin was also pointed out by Unuma et al. [12]. The above reaction was responsible for a large mass reduction and a reduction of the bulk density. The increase in the compressive strength is likely to be attributable to the densification of the CSC, which was related to thermal shrinkage (shown in **Table 1**) as well as to the formation of crystalline SiO₂ (shown in **Figure 7**). Being different from the bulk phase, the surface region was more subject to oxidation of carbon resulting from the release of water of crystallization and SiC formation. This produced many vacancies and finally a textural structure at the surface region, which softened the surface and decreased the surface hardness. Therefore, the surface hardness decreased with the sintering temperature at >800 °C. It was also shown that a high sintering temperature (>1200 °C) was by no means necessary to attain both the desired compressive strength and surface hardness of the CSC.

3. 3. Sliding and wear properties of CSCs

10 g of RH powder dried at 105 °C for 3 h was compressed in a stainless steel cylinder of ϕ 40.00 mm for the evaluation of sliding and wear properties. The precursor and the CSC sintered at 1000 °C were produced, in which the second compression pressure was set to be 100 MPa. It was shown in **Figure 5** that those samples produced at ϕ 10.00 mm had a similar level of the Vickers microhardness. The mass, dimension and bulk density of those samples produced at ϕ 40.00 mm were shown in **Table 2**. The bulk density of the precursor produced at ϕ 40.00 mm was lower than that at ϕ 10.00 mm. However, because of larger thermal shrinkage in the thickness direction, the bulk density of the CSC at ϕ 40.00 mm was similar to that at ϕ 10.00 mm. **Table 3** shows the dynamic and static friction coefficient and wear mass of those samples. Both the samples showed low dynamic friction coefficient (~0.05). A lower static friction coefficient and larger wear mass were observed on the CSC sintered at 1000 °C. **Figure 8** shows the optical micrographs of the sample surfaces before and after the sliding test. Before the sliding test, a more extensive eroded region was observed on the sintered CSC, which was similarly seen in the above surface observation using the sample produced at ϕ 10.00 mm. The lower static dynamic coefficient of the sintered CSC

seems to be ascribed to be the increased asperity providing the smaller area contacting with the sliding material. The surface of the sintered CSC after the sliding test seems to be more porous than that of the precursor, which is same as that before the sliding test. The larger wear mass of the sintered CSC than that of the precursor was likely to be related to its porous structure which can be readily eroded.

Table 2. Mass, dimension and bulk density of the precursor and the CSCs sintered at 1000 °C for the evaluation of sliding properties.

Sample	Mass (g)	Diameter (mm)	Thickness (mm)	Bulk density (g/cm ³)
Precursor	4.40	33.5	4.0	1.25
CSC sintered at 1000 °C	3.99	30.9	3.7	1.44

Table 3. Sliding properties of the precursor and the CSCs sintered at 1000 °C.

Sample	Dynamic friction coefficient	Static friction coefficient	Wear mass (mg)
Precursor	0.04	0.19	14
CSC sintered at 1000 °C	0.05	0.15	22

4 CONCLUSIONS

RH powder was carbonized and molded into a precursor to 500 °C by means of binderless hot-pressing, during which compression pressure of 100 MPa was intermittently applied from room temperature to 150 °C, and then to 280°C. The precursor obtained was then sintered up to 1400 °C without compression, in nitrogen gas, so as to produce the CSC. The CSC sintered at 800 °C showed the highest bulk density of 1.52 g/cm³. The maximum compressive strength was measured to be 55.7 MPa at the sintering temperature of 1200 °C. The maximum Vickers microhardness at the surface of 476 appeared on the CSC produced at second compression pressure of 200 MPa and then sintered at 800 °C. Thermal shrinkage resulting from a release of residual organic matter, and the oxidation of carbon resulting from a release of the water of crystallization from SiO₂.xH₂O and the formation of SiC structure, were thought

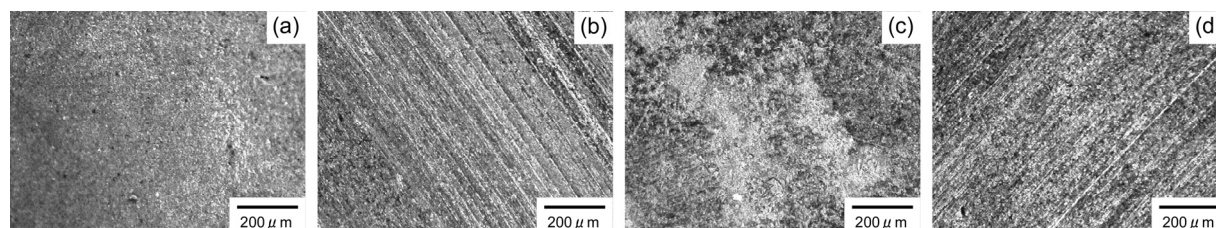


Figure 8. Surface optical micrographs of the precursor and the CSC before and after the sliding test. (a) precursor before sliding, (b) precursor after sliding, (c) CSC sintered at 1000 °C before sliding, (d) CSC sintered at 1000 °C after sliding.

to be related to the changes in the bulk density, the compressive strength and the surface hardness of the RH-derived CSC. The CSC sintered at 1000 °C showed the static friction coefficient of 0.15 and the dynamic friction coefficient of 0.05 under the contact with SUS304 stainless steel.

Acknowledgement—This research was supported in part by KAKENHI for Young Scientists A (21681011). We would like to thank Dr. Mitsuhiro Okayasu and Dr. Teruo Bito of Akita Prefectural University for their assistance in the compressive strength evaluation and the XRD analysis, respectively. Mr. Ryoetsu Shindo and Dr. Mitsuhiro Kimura of the Akita Research and Development Center are acknowledged for their help in sliding tests and surface hardness evaluation, respectively.

References

- [1] New Energy and Industrial Technology Development Organization (NEDO), 2006. Estimated amount of existent and available biomass in Japan: GIS database, <http://app1.infoc.nedo.go.jp/kinds/no2.pdf> (in Japanese).
- [2] Oya, A., Kishimoto, N., Mashio, S., Kumakura, K., Suzuki, T., Serrano-Talavera, B., Linares-Solano, A., 1995. Structure and properties of a molded carbon derived from rice hull, *J. Mater. Sci.* 30, 6249-6252.
- [3] Pendyal, B., Johns, M. M., Marshall, W. E., Ahmedna, M., Rao, R. M., 1999. The effect of binders and agricultural by-products on physical and chemical properties of granular activated carbons. *Bioresource Technol.* 68, 247-254.
- [4] Watari, T., Nakata, A., Kiba, Y., Torikai, T., Yada, M., 2006. Fabrication of porous SiO₂/C composite from rice husks. *J. Eur. Ceram. Soc.* 26, 797-801.
- [5] Amaya, A., Medero, N., Tancredi, N., Siva, H., Deiana, C., 2007. Activated carbon briquettes from biomass materials. *Bioresource Technol.* 97, 1635-1641.
- [6] Okabe, T., Saito, K., Hokkirigawa, K., 1996. New porous materials, woodceramics: development and fundamental properties. *J. Porous Mater.* 2, 207-213.
- [7] Hokkirigawa, K., Okabe, T., Saito, K., 1996. Friction properties of new porous carbon materials: woodceramics. *J. Porous Mater.* 2, 237-243.
- [8] Iizuka, H., Fushitani, M., Okabe, T., Saito, K., 1999. Mechanical properties of wood ceramics: a porous carbon materials. *J. Porous Mater.* 6, 175-184.
- [9] Zhao, B. Y., Hirose, T., Okabe, T., Zhang, D., Fan, T. X., Hu, K. A., 2002. Woodceramics prepared from wood powder/phenolated wood composite. *J. Porous Mater.* 9, 195-201.
- [10] Iizuka, H., Noguchi, T., Shikano, S., 2003. A new porous carbon materials made from rice bran. *Int. J. Soc. Mater. Eng. Resour.* 11, 10-15.
- [11] Zhou, Y., Hirao, K., Yamaguchi, T., Hokkirigawa, K., 2005. Preparation and tribological properties SiC/RBC composite ceramics, *J. Mater. Res.* 20, 3439-3448.
- [12] Unuma, H., Niino, K., Sasaki, K., Shibata, Y., Iizuka, H., Shikano, S., Nakamura, T., 2006. Preparation and characterization of glass-like carbon/silica composite from rice hull and phenolic resin. *J. Mater. Sci.* 41, 5593-5597.
- [13] Yoshida, K., Iizuka, H., Shibata, Y., Unuma, H., Nakamura, T., Shikano, S., 2006. Water resistance of porous carbon materials made from rice hull. *Int. J. Soc. Mater. Eng. Resour.* 13, 49-53.
- [14] RB&H Ouyo-kigyokumiai, 2008. RB ceramics and RH ceramics, http://www.komenuka.jp/kogyo/kog_no02 (in Japanese).
- [15] Rodriguez-Valero, M. A., Martinez-Escandell, M., Molina-Sabio, M., Rodriguez-Reinoso, F., 2001. CO₂ activation of olive stones carbonized under pressure. *Carbon* 39, 320-323.
- [16] Imanishi, H., Soma, N., Yamashita, O., Miki, T., Nakayama, K., 2005. Effect of production conditions of wood powder on bending properties of wood powder molding materials without adhesive, *JSME Int. J. A. Solid Mech.* 48, 432-436.
- [17] Sakka, F., 1983. Science of amorphous glass, Uchida Rokkakuho, Tokyo (in Japanese).
- [18] International Center for Diffraction Data (ICDD), 1986. Powder diffraction file, SiO₂ (Cristobalite) 27-605, 208.
- [19] International Center for Diffraction Data (ICDD), 1989. Powder diffraction file, SiO₂ (Quartz) 33-1161, 407.
- [20] International Center for Diffraction Data (ICDD), 1987. Powder diffraction file, SiC (Moissanite) 29-1131, 434.
- [21] International Center for Diffraction Data (ICDD), 2003. Powder diffraction file, α-Si₃N₄ 74-0554.
- [22] Dong, S., Jiang, D., Tan, S., Guo, J., 1997. Preparation and characterization of nano-structured monolithic SiC and Si₃N₄/SiC composite by hot isostatic pressing. *J. Mater. Sci.* 16, 1080-1083.

Rice Husk and Beet Sugar-based Activated Carbon Produced by Means of Extrusion Molding

Yuta Aoki, Hirotaka Ishizawa, Seiji Kumagai, Masaya Sugimoto and Yasuhiro Toida*

Department of Machine Intelligence and Systems Engineering, Akita Prefectural University
84-4, Tsuchiya-aza-ebinokuchi, Yurihonjo, 015-0055, Japan

* Petroleum Refining Research and Technology Center, Japan Energy Corporation
Niizominami, 3-17-35, Toda, 335-8502, Japan

kumagai@akita-pu.ac.jp

Abstract : An activated carbon with a high micro- and mesoporosity, as well as a high bulk density, was fabricated by activating the extrusion-molded precursor made from carbonized rice husk (RH) and beet sugar (BS) at 850°C in CO₂. The pore structure of the RH- and BS-based activated carbon (RHBSAC) was analyzed in relation to the bulk density. The extrusion molding was very useful to increase the bulk density. RHBSAC which was first activated for 1 h was immersed again in the BS syrup and then activated in CO₂ for 2 h. This two-step activation process provided both a high bulk density (0.93 g/cm³) and a micro- and mesoporous structure (BET specific surface area: 844 m²/g, total pore volume: 0.53 cm³/g, micropore volume: 0.29 cm³/g, and mesopore volume: 0.19 cm³/g).

Key Words: Rice husk, activated carbon, bulk density, pore structure

1 INTRODUCTION

About 2 million metric tons of rice husks (RHs) are produced every year as an agricultural byproduct in the process of rice threshing in Japan [1]. The most common method for disposing of RHs in Japan used to be incineration on the farm. However, the incineration of RHs is now discouraged because it produces ash, fumes, and toxic organic gases, leading to serious air pollution. Therefore, 63 mass% of the RH produced in Japan is now made use of in the agricultural, livestock, energy (fuel) and material engineering industries, but the rest is not efficiently re-utilized [1].

The failure to make use of all of the RH is due to its material properties. RHs incorporate a double layer composed of silica and cuticle to resist invasion by insects and pathogenic organisms. This protective layer slows down natural biodegradation, which discourages the re-utilization of RHs in the agricultural and livestock industries. The ash content of RHs, which mostly comprises silica, is approximately 20 mass %. This high ash content means that the carbon content is low, limiting the use of RHs as a fuel source or as a precursor for carbon materials. On the other hand, RHs do have a noteworthy advantage. Most rice grains harvested in Japan are now threshed in integrated large-scale facilities, meaning that a large quantity of RHs can be readily collected at low cost. It would be socially and industrially beneficial if RHs could be recycled into products.

The industrial importance of porous materials such as activated carbons (ACs) is well known, especially for processes such as separation, purification, catalysis, electrolysis, which require a highly porous structure [2]. Many researchers have attempted to produce RH-based porous materials by means of physical activation [3-5] and chemical activation [6-8]. A characteristic of the RH-based porous material is the simultaneous appearance of microporosity and mesoporosity resulting from carbon and silica, respectively [9].

A higher bulk density is required to better the adsorption performance of ACs in a specified volume, such as in fixed-bed reactor columns. The above-mentioned RH-based porous materials are basically powder-state. However, it is difficult for ACs to attain both a highly textured structure and a high bulk density. Pendyal et al described the bulk density and the textural properties of granular ACs produced from a RH and several types of binders [3]. They revealed that a sugar-based binder (a mass ratio of binder to RH : 1) was more useful than a conventional binder of coal tar and improved both properties. An AC made from a RH and a sugar-based binder, being completely derived from crops, would seem to be ideal for separation and purification processes requiring extremely high safety. Sugarcane and beet are major sugar crops harvested in Japan. The yield of beet sugar (BS) in Japan is about 4.3 million metric tons, which is three times larger than that of sugarcane

porous material. A gradual addition of the BS syrup into several states of the RHBSAC was useful to prevent an inflation of the BS syrup and to fabricate dense RHBSACs.

The bulk density was calculated by measuring the mass, diameter and length of the fabricated cylindrical sample. The mass yields of the one-step and two-step activations were also calculated.

Table 1. Fabricated RHBSAC samples.

Sample name	Activation condition
RHBSAC1.0	One-step activation for 1.0 h
RHBSAC1.0+1.0	First step activation for 1.0 h and second step activation for 1.0 h
RHBSAC1.0+2.0	First step activation for 1.0 h and second step activation for 2.0 h
RHBSAC1.0+2.5	First step activation for 1.0 h and second step activation for 2.5 h

2.2 Textual characterization

Nitrogen adsorption-desorption isotherms at $-196\text{ }^{\circ}\text{C}$ were obtained using a gas adsorption analyzer (Autosorb-3B; Quantachrome Instruments Inc., USA). A sample of 0.02 g was degassed at $200\text{ }^{\circ}\text{C}$ for $>3\text{ h}$ prior to isotherm measurement. BET specific surface area (BET SSA or S_{BET}) was based on the theory of Brunauer, Emmett and Teller and was calculated using the volume of N_2 adsorbed at relative pressures of 0.05-0.1 [2]. The liquid N_2 volume in relation to the N_2 volume adsorbed at a relative pressure of 0.995 was determined as the total pore volume (V_t). An AC consists of graphite-like sheets between which small slit-shaped pores exist [11]. In the present study, micropores were distinguished as either ultramicropores (width $\leq 0.7\text{ nm}$) or supermicropores ($0.7 < \text{width} \leq 2.0\text{ nm}$), in accordance with Sing et al [12]. The pore size distribution was evaluated using density functional theory (DFT) [13, 14]. The DFT software developed by Quantachrome Instruments Inc. (version 1.62) was used to obtain the pore size distribution. The volumes of ultramicropores (V_u), supermicropores (V_s), and mesopores (V_m) were obtained using these pore size distribution data. The macropore volume (V_c) was calculated as follows: $V_c = V_t - (V_u + V_s + V_m)$; V_{micro} means the volume of micropores and equals $V_u + V_s$.

3 RESULTS AND DISCUSSION

Typical nitrogen adsorption-desorption isotherms of the fabricated RHBSACs at $-196\text{ }^{\circ}\text{C}$ are shown in **Figure 3**. The sharp knees at relative pressure of <0.1 were observed for all the samples, which are typical to micropore system. A gradual increase in the isotherm slope at relative pressures of >0.1 and a hysteresis loop at a high relative pressure, indicating that capillary condensation of nitrogen gas in mesopores occurred and thus proving the existence of mesopores, were also observed for all the samples. The

hysteresis loops had no sharp knees, meaning that mesopores having specific sizes were absent. The isotherms of all the RHBSACs belong to the type IV classified by IUPAC [12]. The nitrogen uptake of the RHBSACs processed by two-step activation was greater than that of the RHBSAC produced by one-step activation, in particular at a low relative pressure (<0.1). The longer second step activation time resulted in the greater nitrogen uptake at low relative pressure (<0.1), developing micropore system. The increase in the second step activation time (2.0 to 2.5 h) hardly contributed to the increase in the nitrogen uptake, indicating that more activation ($>2.5\text{ h}$) was not required to develop the pore structure of the RHBSAC.

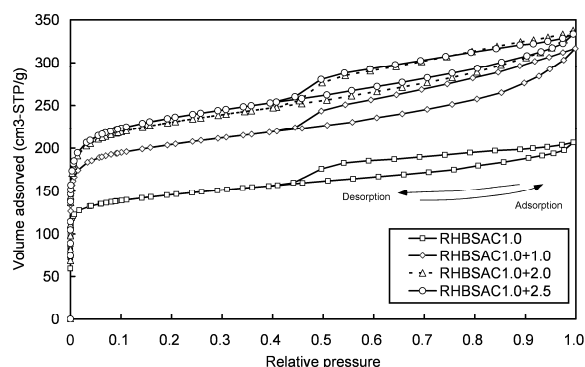


Figure 3. Typical nitrogen adsorption-desorption isotherms of the fabricated RHBSACs at $-196\text{ }^{\circ}\text{C}$.

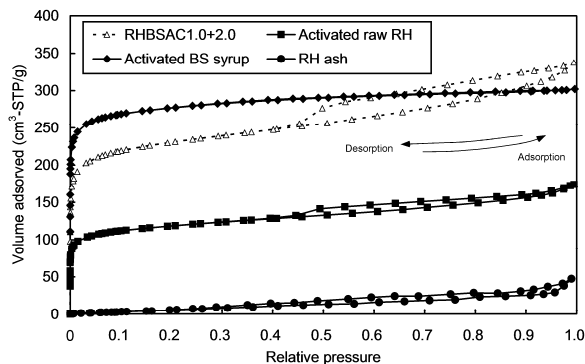


Figure 4. Nitrogen adsorption-desorption isotherms at $-196\text{ }^{\circ}\text{C}$ of the RHBSAC1.0+2.0, the raw RH activated at $850\text{ }^{\circ}\text{C}$ for 1 h, the BS syrup activated at $850\text{ }^{\circ}\text{C}$ for 1 h, the RH ash.

Nitrogen adsorption-desorption isotherms at $-196\text{ }^{\circ}\text{C}$ of the RHBSAC1.0+2.0, the activated raw RH, the activated BS syrup, the RH ash are shown in **Figure 4**. The isotherm of the activated BS syrup showed a typical isotherm of type I classified by IUPAC [12], indicating that the activated BS syrup was highly microporous. The isotherms of the RHBSAC1.0+2.0 and the activated raw RH had an analogous

Table 2. Activation mass yield, bulk density and textural properties of RHBSACs.

Sample	AMY (%)	BD (g/cm ³)	S_{BET} (m ² /g)	V_t (cm ³ /g)	V_u (cm ³ /g)	V_s (cm ³ /g)	V_m (cm ³ /g)	V_c (cm ³ /g)
RHBSAC1.0	82.4	1.13	524	0.31	0.12	0.06	0.09	0.04
RHBSAC1.0+1.0	73.1	0.98	698	0.44	0.15	0.09	0.16	0.04
RHBSAC1.0+2.0	69.5	0.93	844	0.53	0.14	0.15	0.19	0.05
RHBSAC1.0+2.5	66.4	0.89	862	0.55	0.13	0.17	0.20	0.05

The data were average of 5 separate measurements.

AMY: Activation mass yield (100%: dried state after BS syrup immersion and prior to the final activation), BD: Bulk density

Table 3. Bulk density and textural properties of RH-based porous materials produced under gas activation (from the literature), compared with results for RHBSAC1.0+2.0.

Sample	BD (g/cm ³)	S_{BET} (m ² /g)	V_t (cm ³ /g)	V_{micro} (cm ³ /g)	Reference
RHBSAC1.0+2.0	0.93	844	0.53	0.29	Present study
RH and sugar syrup based granular AC	0.35*	350	-	-	[3]
RH based silica/carbon porous composite	0.45	450	-	-	[15]
RH and grape must based AC briquette	-	386	-	0.148	[4]

BD: Bulk density, *: Filling density in a graduated cylinder, -: No data.

shape. The differences between them were the nitrogen uptake at very low relative pressure (<0.05) and the size of the hysteresis loops. Thus, higher microporosity and mesoporosity of the RHBSAC1.0+2.0 were attributed to carbon deposition impregnated from the BS syrup. A low pressure hysteresis was observed on the isotherm of the RH ash. This isotherm was the type H3 classified by IUPAC classification, suggesting a presence of slit-shaped pores [12]. Smaller nitrogen uptake and hysteresis loop on the isotherm of the RH ash implies that a template derived from inorganic matters in the RH produced scanty mesoporosity. Therefore, mesoporosity of the RHBSAC1.0+2.0 and the activated raw RH was attributed to the carbon deposition on the inorganic template. Thus, micro- and mesopores in the RHBSAC samples can be treated as slit-shaped pores having carbonaceous walls. It is supposed that ash content of RH produced a template of mesoporosity of RHBSAC and carbon content of RH and BS was connected to the development of microporosity and mesoporosity of RHBSAC.

Activation mass yield, bulk density and textural properties of the RHBSACs were summarized in **Table 2**. The very highest bulk density of 1.13 g/cm³ was observed on the RHBSAC1.0, which was exposed to the one-step activation. The RHBSAC prepared using the two-step activation process displayed a larger BET SSA and a larger total pore volume than that prepared through the one-step activation (RHBSAC1.0). The lower activation mass yield and the lower bulk density were required for the highly porous structure. The volumes of the ultramicropores, supermicropores, mesopores and macropores of the RHBSACs were also evaluated, which were calculated from the results of the DFT pore size distributions. The volume of ultramicropores of the

RHBSAC produced by two-step activation decreased with increasing the second step activation time and the decreasing the bulk density. Longer second step activation time resulted in larger volumes of supermicropores and mesopores. The reduced volume of ultramicropores, which was attributable to their pore widening, seems to be connected to the increase in the volume of supermicropores and mesopores. Although prolonging the second step activation time from 2.0 to 2.5 h hardly increased the BET SSA and the pore volumes, the bulk density decreased significantly. Neither one-step nor two-step activations increased the volume of macropores. Thus, the preparation conditions of the RHBSAC1.0+2.0 were the best to attain both high bulk density and highly porous structure.

The properties of other RH-based porous materials for which density and textural information have been reported in literature are shown in **Table 3** and compared with those of RHBSAC1.0+2.0. This clearly demonstrates that the RHBSAC1.0+2.0 displayed a higher bulk density and texture than the previous RH-based porous materials produced under gas activation did.

RHBSACs with a high micro- and mesoporosity, as well as a high bulk density, were fabricated by using RH and BS. A gradual addition of the BS syrup into several states of the RHBSACs was beneficial to prevent an inflation of the BS syrup during its carbonization and its activation, finally attaining both a high bulk density and a high porosity. Developed microporosity and mesoporosity of the RHBSACs were shown to result from carbon deposition impregnated from the BS syrup. In addition to this, the pore structure could be changed by the activation conditions: the ultramicropores degenerated, and supermicropores and mesopores developed with increasing activation time of up to 2.5 h.

4 CONCLUSIONS

Micro- and mesoporous ACs were made from the agricultural byproduct RH, using BS as a binder, by means of CO₂ gas activation. The extrusion molding was very useful to increase the bulk density. The relationship between the textural properties and the bulk density was studied. A two-step activation process, which included one more BS syrup immersion, was shown to be useful for developing supermicropores and mesopores in the RHBSAC with a small reduction of the bulk density. Finally, the RHBSAC1.0+2.0 produced by two-step activation displayed a higher bulk density and a greater textural properties than previously reported RH-based porous materials have done.

Acknowledgement—This research was supported in part by the Industrial Technology Research Grant Program in 2006 of the New Energy and Industrial Technology Development Organization (NEDO) of Japan.

References

- [1] New Energy and Industrial Technology Development Organization, Estimated Amount of Existent and Available Biomass in Japan: GIS Database, 2006. <http://appl.infoc.nedo.go.jp/kinds/no2.pdf> (in Japanese).
- [2] R.C. Bansal, M. Goyal, Activated Carbon Adsorption, CRC Press Inc., Boca Raton, Florida, USA, 2005.
- [3] B. Pendyal, M.M. Johns, W.E. Marshall, M. Ahmedna, R.M. Rao, The effect of binders and agricultural by-products on physical and chemical properties of granular activated carbons, *Bioresource Technol.* 68 (1999) 247-254.
- [4] A. Amaya, N. Medero, N. Tancredi, H. Siva, C. Deiana, Activated carbon briquettes from biomass materials, *Bioresource Technol.* 97 (2007) 1635-1641.
- [5] S. Kumagai, K. Sasaki, Y. Shimizu, K. Takeda, Formaldehyde and acetaldehyde adsorption properties of heat-treated rice husks, *Sep. Purif. Tech.* 61 (2008) 398-403.
- [6] Y. Guo, K. Yu, Z. Wang, H. Xu, Effects of activation conditions on preparation of porous carbon from rice husk, *Carbon* 41 (2000) 1645-1687.
- [7] N. Yalcin, V. Sevinc, Studies of the surface area and porosity of activated carbons prepared from rice husks, *Carbon* 38 (2000) 1943-1945.
- [8] Y. Guo, S. Yang, K. Yu, J. Zhao, Z. Wang, H. Xu, Adsorption of Cr(VI) on micro- and mesoporous rice husk-based active carbon, *Mater. Chem. Phys.* 74 (2002) 320-323.
- [9] T.H. Liou, Evolution of chemistry and morphology during the carbonization and combustion of rice husk, *Carbon* 42 (2004) 785-794.
- [10] Ministry of Agriculture, Forestry and Fisheries of Japan, Statics of Agriculture, Forestry and Fisheries: Industrial Crops, 2008. <http://www.maff.go.jp/www/info/bunrui/mono04.html> (in Japanese).
- [11] Y. El-Sayed, T.J. Bandosz, Acetaldehyde adsorption on nitrogen-containing activated carbons, *Langmuir* 18 (2002) 3213-3218.
- [12] K.S.W. Sing, D.H. Everett, R.A.W. Haul, L. Moscou, R.A. Pierotti, J. Rouquerol, T. Siemieniewska, Reporting physisorption data for gas/solid systems, *Pure Appl. Chem.* 57 (1985) 603-619.
- [13] J.P. Olivier, Improving the models used for calculating the size distribution of micropore volume of activated carbons from adsorption data, *Carbon* 36 (1998) 1469-1472.
- [14] Z. Ryu, J. Zheng, M. Wang, B. Zhang, Characterization of pore size distributions on carbonaceous adsorbent by DFT, *Carbon* 37 (1999) 1257-1264.

- [15] T. Watari, A. Nakata, Y. Kiba, T. Torikai, M. Yada, Fabrication of porous SiO₂/C composite from rice husks, *J. Eur. Ceram. Soc.* 26 (2006) 797-801.

Influence of Ultraviolet-ray Irradiation on the Mechanical and Electrical Properties of Eco-Friendly Dielectric Materials

Katsuyoshi Shinyama and Shigetaka Fujita

Department of Electronic Intelligence and Systems, Hachinohe Institute of Technology
88-1, Myo Ohbiraki, Hachinohe, 031-8501 JAPAN
shinyama@hi-tech.ac.jp

Abstract: Polylactic acid (PLA) is a biodegradable and eco-friendly plastic that is attracting more attention than any other plastics of its kind. In this study, we examined the effects of ultraviolet light (UV) on the mechanical and electrical characteristics of PLA, in order to clarify the prospect of PLA as an electrical insulator material. The curves of the tensile stress versus the elongation show the following: the stress and elongation of PLA decreased with an increase in UV irradiation hours and the decrease of the elongation was significant. The temperature dependency of the dielectric breakdown strength (E_B): with an increase in UV irradiation hours, E_B of PLA had a tendency to decrease over a wide temperature range.

Key Words: biodegradable plastics, mechanical properties, electrical properties, ultraviolet-ray irradiation

1 INTRODUCTION

One of the current issues stemming from the growing concern over the prospect of the exhaustion of oil resources is recycling wire coating materials such as vinyl chloride and polyethylene. Almost all the copper and aluminum used for electric wires are being recycled today because they are valuable substances. However, since this recycling system does not regard wire coating materials as recyclable, most of them are disposed of as industrial waste except for those used in the recycling operations of wire manufacturers. With the call for the recycle of wire coating materials, growing attention is now being paid to electrical wires that only use the polyethylene series for wire coatings since they are eco-friendly materials (EM). Since polyethylene is made from petroleum, it is clear that a replacement will be required in the near future. The authors are focusing on biodegradable plastics which are even more eco-friendly.

Biodegradable plastics can be used just like other general plastic materials and once they are thrown away, they will be decomposed by microbes, eventually being broken down into carbon dioxide and water. Among biodegradable plastics, polylactic acid (PLA), also called a biomass plastic, is drawing greater attention than other plastics of its kind, because PLA is produced by the polymerization of lactic acids derived from the fermentation of corn or other plants[1-2]. However, PLA has hardly been applied to electrical insulation due to the lack of knowledge of its electrical insulation properties. About the electrical characteristics of PLA, many are reported including

the author [3-15]. The authors have examined the mechanical and electrical characteristics of PLA in a bid to promote its application to electrical insulation materials[3-9].

We have reported that the electrical resistivity of PLA is higher than that of low-density polyethylene (LDPE) at room temperature, and the dielectric breakdown strength (E_B) of PLA at room temperature is roughly 1.4 times greater than that of LDPE[9]. In this study, as an evaluation of PLA's durability, we examined the effects of ultraviolet light (UV) on the mechanical and electrical characteristics of PLA, and also carried out a thermal analysis and surface analysis to analyze the effects.

2 EXPERIMENTAL METHODS

For the samples, we used biaxial-stretched films of PLA (Palgreen LC, thickness: 25 μ m) manufactured by Tohcello Co., Ltd. Figure 1 is the chemical structural formula of PLA.

Our previous report shows that irradiation of long-wavelength ultraviolet light (UV-A, wavelength: 365 nm) produced little effect on the electrical properties of PLA[10]. In this study, we irradiated the sample with short-wavelength

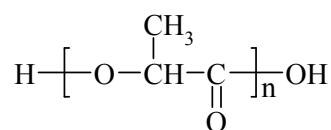


Fig. 1 Chemical structure of PLA.

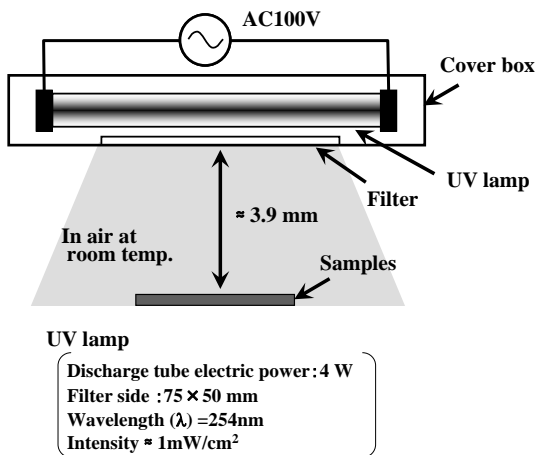


Fig. 2 UV irradiating equipment.

ultraviolet light (UV-C, wavelength: 254 nm) in air at room temperature. The sample was irradiated for up to three hours with UV light at an intensity of approximately 1 mW/cm². Figure 2 shows an outline illustration of the UV irradiating equipment.

Test pieces were prepared in accordance with JIS K 7127 for the mechanical test in air at room temperature. The test piece was 25 mm wide, 150 mm long, and had a width of 6 mm at the stretched section. Two parallel lines 25 mm apart were marked at the center of each test piece.

After the UV irradiation, aluminum film electrodes of \varnothing 25 mm were formed by vapor deposition on both sides of each test piece for the measurement of dielectric properties and electrical resistivity. The measurements were carried out while increasing the temperature of the samples in dry air.

In the dielectric breakdown strength test, a DC voltage (1 kV/sec) was applied to the test piece in silicone oil while adjusting the temperature of the oil using the same measuring system as that used in the previous report[9]. The strength was obtained by dividing the dielectric breakdown voltage by the thickness of the test piece.

We used a heat flux type differential scanning calorimeter (DSC) (Shimadzu Corporation, DSC-60) for the thermal analysis. The standard sample was α -alumina. The DSC curves of PLA were observed while increasing the temperature at the rate of 10°C/min in a nitrogen gas atmosphere from 30°C to 230°C.

We used an X-ray photoelectron spectrometer (XPS) (JEOL Ltd., JPS-9000) for the surface analysis. The X-ray source voltage was set to 10 kV, and the emission current to 10 mA.

3 RESULTS AND DISCUSSION

We carried out a thermal analysis using the differential scanning calorimeter at first. Figure 3 shows the DSC curves of UV-irradiated PLA. Figure 4 and Figure 5 show the glass transition temperatures (T_g) and the melting points (T_m) of PLA,

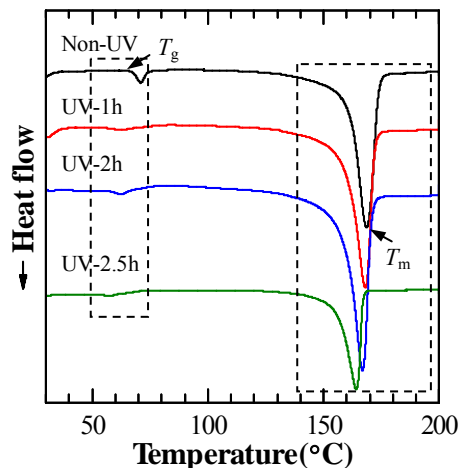


Fig. 3 DSC curves of PLA.

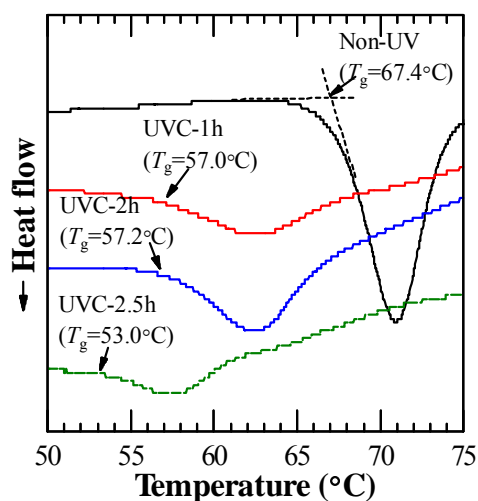


Fig. 4 Glass transition temperatures (T_g) of PLA.

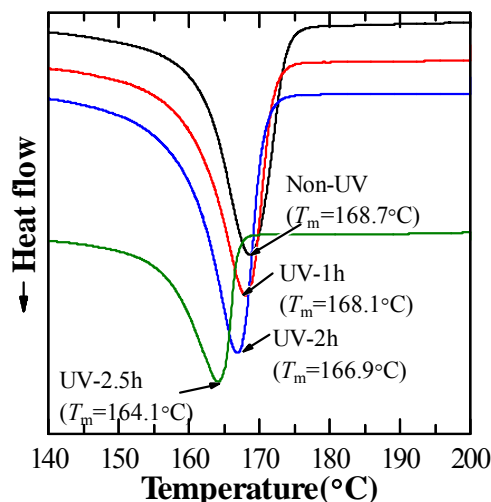


Fig. 5 Melting points (T_m) of PLA.

respectively, derived from the DSC curves. PLA's T_g and T_m had a tendency to decrease with an increase in the UV irradiation hours. This implies that the UV irradiation caused

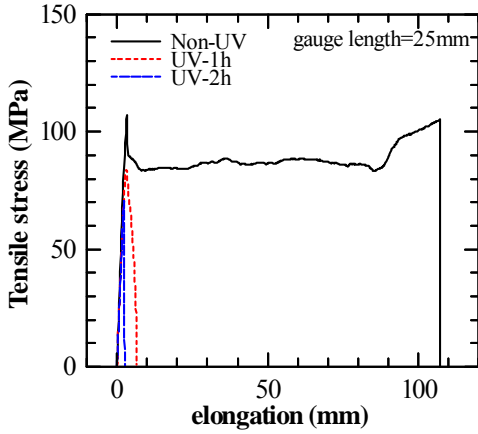


Fig. 6 Changes in the tensile stress and the elongation curve of PLA.

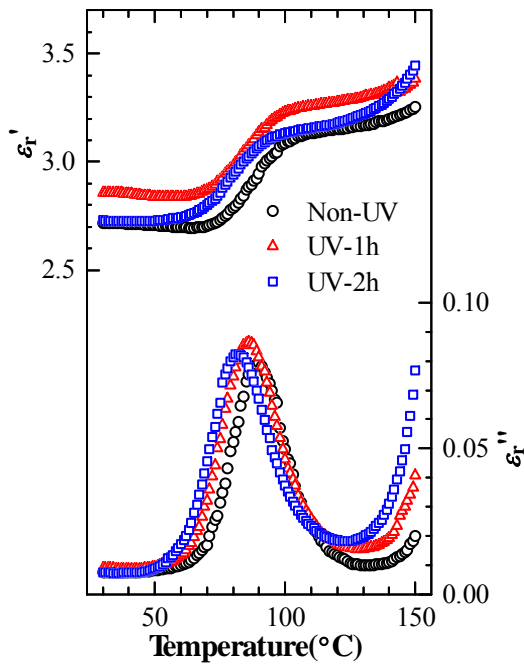


Fig. 7 Temperature dependencies of ϵ_r' and ϵ_r'' at $f = 1$ kHz..

intermolecular breaks in the PLA.

Figure 6 shows changes in the tensile stress and the elongation curve of PLA as a function of the UV irradiation hours. The tensile stress and the elongation decreased as the irradiation hours increased. The UV irradiation significantly reduced the elongation. Taking this into account along with Figure 4 and Figure 5 indicates that the mechanical strength of the PLA was reduced by intermolecular breaks in the PLA caused by the UV irradiation.

Figure 7 shows the temperature dependencies of the relative permittivity (ϵ_r') and the imaginary part of the complex relative permittivity or the dielectric loss factor (ϵ_r'') at $f = 1$ kHz. With longer UV irradiation hours, ϵ_r' and ϵ_r'' of the PLA had a tendency to increase. This reveals that the UV irradiation probably cut some of the molecular chains causing the

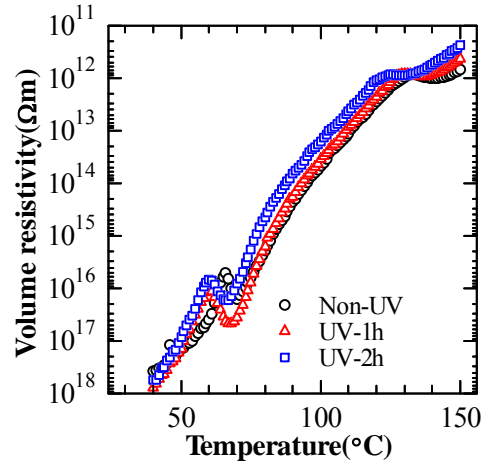


Fig. 8 Temperature dependencies of the volume resistivity of PLA.

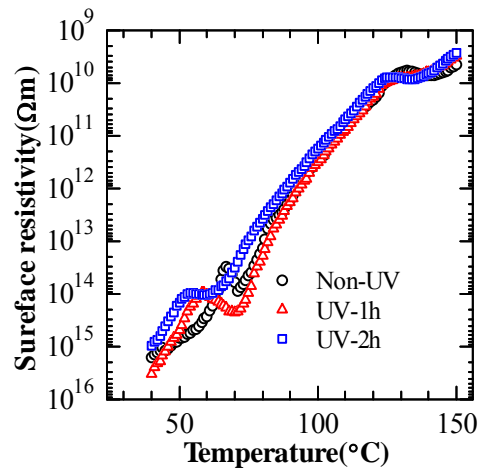


Fig. 9 Temperature dependencies of the surface resistivity of PLA.

electrical polarization to increase with time. The temperatures at which ϵ_r' and ϵ_r'' start to increase lowered with an increase in UV irradiation hours. As Figure 5 shows, the UV irradiation decreased T_g , so it decreased the temperature at which micro-Brownian motion begins, creating conditions in which orientation polarization can more easily occur.

Figure 8 and Figure 9 show the temperature dependencies of the volume resistivity and the surface resistivity of PLA, respectively, with a static electric field of 0.2 MV/cm being applied. The volume resistivity and the surface resistivity of PLA have a tendency to decrease over a wide temperature range as the UV irradiation hours increase. Figure 8 and Figure 9 agree with the results obtained by Yamaguchi et al. who reported that electric current conductivity on PLA increased after it was irradiated with UV (wavelength: 222 nm, intensity: 5.5 mW/cm²) for 30 minutes generated by a KrCl excimer lamp[15]. Both the volume resistivity and the surface resistivity curves have small peaks at around 70°C, which is close to T_g , implying that there are biased dipoles in the material. The temperature at which these peaks appear lowers

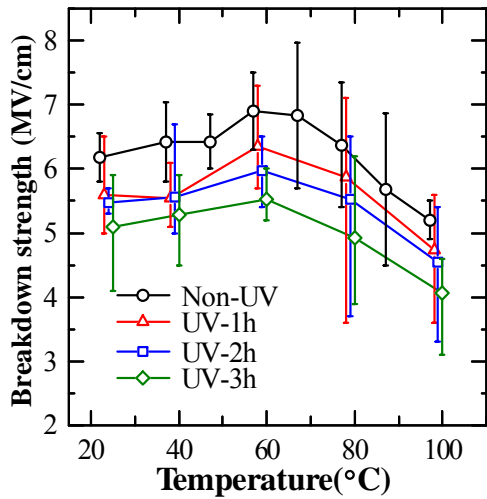


Fig. 10 Temperature dependency of the dielectric breakdown strength of PLA.

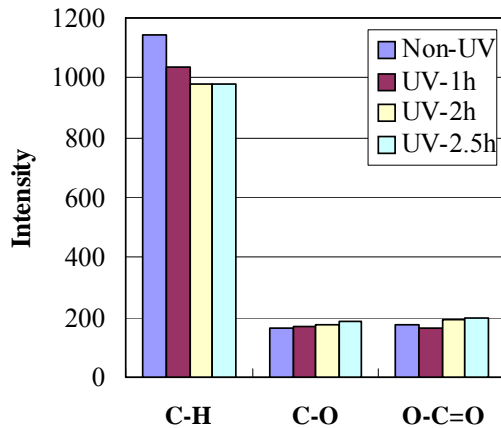


Fig. 11 Changes in strength of each molecular bond site on the surface, which were derived from waveform separation of the C1s spectrum of PLA.

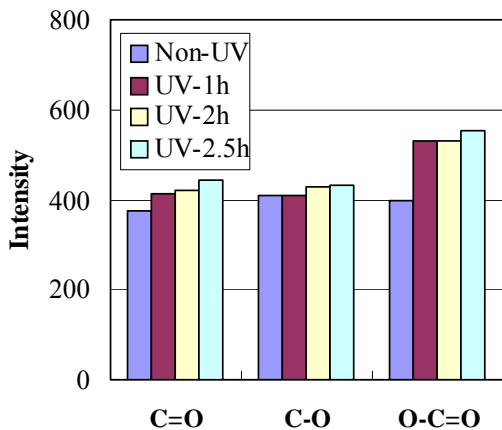


Fig. 12 Changes in strength of each molecular bond site on the surface, which were derived from waveform separation of the O1s spectrum of PLA.

as the UV irradiation hours increase. We found that the UV irradiation caused ion conduction based on these data.

Figure 10 shows the temperature dependency of the dielectric breakdown strength (E_B) of UV-irradiated PLA. E_B of PLA has a tendency to decrease over a wide temperature range as the UV irradiation hours increase, leading to the conclusion that the UV irradiation lowered the E_B of PLA.

As shown in Figure 6 through Figure 10, the mechanical and electrical properties of PLA were degraded after UV irradiation. In order to find the detailed causes, we examined the UV induced structural changes on the surface of the test pieces by performing a surface analysis with an XPS analyzer. Figure 11 shows the changes in strength of each molecular bond site on the surface, which were derived from waveform separation of the C1s spectrum of PLA. The spectrum peak of C-H bond around 285 eV decreased after the UV irradiation. Peaks of C-O and O-C=O around 287 eV and 289 eV slightly increased after the UV irradiation. Figure 12 shows the changes in strength of each molecular bond site on the surface after the UV irradiation which were derived from waveform separation of the O1s spectrum of PLA. Peaks of C=O and O-C=O around 532 eV and 533 eV increased after the UV irradiation. Bonding energies of C-O, C-H, and C=O are 3.6 eV, 4.3 eV, and 7.5 eV, respectively. Since the energy of the UV-C lamp we used in this study was 4.9 eV, the UV irradiation easily breaks the molecular bonds of C-O or C-H. Therefore we know that the UV irradiation broke some of the molecular chains on the PLA surface to generate radicals which combined with oxygen atoms producing a low-molecular weight substance and degradation reactions by oxidization were also accelerated.

4 CONCLUSIONS

Poly(lactic acid) (PLA) is a biodegradable and eco-friendly plastic that is attracting more attention than any other plastics of its kind. In this study, we examined the effects of ultraviolet light (UV) on the mechanical and electrical characteristics of PLA, in order to clarify the prospect of PLA as an electrical insulator material. The results are as follows:

- (1) The curves of the tensile stress versus the elongation show the following: the stress and elongation of PLA decreased with an increase in UV irradiation hours and the decrease of the elongation was significant.
- (2) The temperature dependencies of relative permittivity (ϵ_r') and the dielectric loss factor (ϵ_r'') at $f = 1$ kHz: with an increase in UV irradiation hours, ϵ_r' and ϵ_r'' of PLA had a tendency to increase, and the temperatures at which ϵ_r' and ϵ_r'' start to increase lowered.
- (3) The temperature dependencies of the volume resistivity and the surface resistivity of PLA with a static electric field of 0.2 MV/cm: with an increase in UV irradiation hours, the volume resistivity and the surface resistivity of PLA had a tendency to decrease over a wide temperature range.
- (4) The temperature dependency of the dielectric breakdown strength (E_B): with an increase in UV irradiation hours, E_B of PLA had a tendency to decrease over a wide temperature range.

Acknowledgments

This work was supported by a targeted research subsidy from the Hachinohe Institute of Technology. The authors would like to thank Tochello Co., Ltd. for supplying the test samples.

References

- [1] Y. Inoue et al.: "Recent Advances in Research and Development for Green Plastics", CMC Publishing Co., Ltd., Tokyo (2002) (in Japanese)
- [2] H. Tsuji: "Biodegradable Polymers", Corona Publishing Co., Ltd., Tokyo (2002) (in Japanese)
- [3] K. Shinyama and S. Fujita: "Fundamental Study on Electrical Properties of Biodegradable Plastics", Proc. of the 4th International Conference on Materials Engineering for Resources (ICMR2001), Vol. 2, pp. 284-287 (2001)
- [4] K. Shinyama and S. Fujita: "Study on the Electrical Properties of a Biodegradable Plastic", Proc. of the 7th International Conference on Properties and Applications of Dielectric Materials (ICPADM2003), Vol. 2, pp. 707-710 (2003)
- [5] K. Shinyama and S. Fujita: "Electrical Properties of Biodegradable Plastics", Proc. of the International Conference on Electrical Engineering (ICEE2004), Vol. 1, pp.357-360 (2004)
- [6] K. Shinyama and S. Fujita: "Electrical Conduction and Dielectric Properties of Biodegradable Plastics", *T. IEE Japan*, Vol. 125-A, No. 3, pp. 204-208 (2005) (in Japanese)
- [7] K. Shinyama and S. Fujita: "Mechanical and Electrical Properties of Biodegradable Plastics", Proc. of 2005 International Symposium on Electrical Insulating Materials (ISEIM2005), Vol. 3, pp. 775-779 (2005)
- [8] K. Shinyama and S. Fujita: "Mechanical and Electrical Properties of Eco-Friendly Dielectric Materials", Proceedings of the Fifth International Conference on Materials Engineering for Resources (ICMR2005), pp.291-296, (2005)
- [9] K. Shinyama and S. Fujita: "Mechanical and Dielectric Breakdown Properties of Biodegradable Plastics", *IEEJ Trans. FM*, Vol. 126-A, No. 1, pp.31-36, (2006)
- [10] K. Shinyama and S. Fujita: "Influence of Ultraviolet Irradiation on Biodegradable Plastics", 2005 National Convention Record IEE Japan, Vol. 2, p.30 (2005) (in Japanese)
- [11] T. Nakagawa, T. Nakiri, R. Hosoya and Y. Tajitsu: "Electrical Properties of Biodegradable Polylactic Acid Film", *IEEE Transactions on Industry Applications*, Vol. 40, No. 4, pp. 1020-1024 (2003)
- [12] F. Kato, M. Matsushita, S. Omori, and Y. Ohki: "Effect of Endothermic Reaction Associated with Glass Transition on the Breakdown Strength of Biodegradable Polymer Films", *IEEE Transactions on DEI*, Vol. 14, No.3, pp. 653-655, (2007)
- [13] K. Miyata, S. Fujita, Y. Ohki and T. Tanaka: "Comparison of Partial Discharge Resistance among Several Biodegradable Polymers", *IEEE Trans. DEI*, Vol. 14, No. 6, pp. 1474-1476, (2007)
- [14] Y. Ohki and N. Hirai: "Electrical Conduction and Breakdown Properties of Several Biodegradable Polymers", *IEEE Trans. DEI*, Vol. 14, No. 6, pp. 1559-1567, (2007)
- [15] Y. Yamaguchi, N. Uchibori and Y. Ohki: "Effects of Ultraviolet Photon Irradiation on the Dielectric Properties of Biodegradable Polymers", *IEEJ Trans. FM*, Vol. 127-A, No. 2, pp.115-120, (2007) (in Japanese)

Formation of Ni-Aluminide Coating Containing Zr by Synchronous Electrodeposition of Al and Zr and Cyclic-Oxidation Resistance

Tsuyoshi Yokota*, Michihisa Fukumoto** and Motoi Hara**

*Graduate School of Engineering and Resource Science, Akita University, Japan

**Department of Materials Science and Engineering, Faculty of Engineering and Resource Science, Akita University, 1-1, Tegata Gakuen-Cho, Akita,
010-8502 Japan

hara@ipc.akita-u.ac.jp

Abstract: The formation of a coating layer consisting of Ni-aluminide containing Zr on a pure Ni substrate was attempted by the synchronous electrodeposition of Al and Zr. The cyclic-oxidation resistance for the Ni covered with this coating was then evaluated in air at 1423 K. The synchronous electrodeposition of Al and Zr was carried out using a potentiostatic electrodeposition at 1023 K in an equimolar NaCl-KCl melt containing 3.5 mol% AlF_3 and 0.05 or 3.5 mol% ZrF_4 . For the specimen electrodeposited at -1.7 V in the melt containing 3.5 mol% AlF_3 and 0.05 mol% ZrF_4 , coatings consisting of Ni_2Al_3 and NiAl_3 were formed on the Ni. At the surface region of these coatings, small particles consisting of ZrAl_3 were formed. The cyclic-oxidation test showed that, for the specimen with both Al and Zr depositions, an increase in specimen mass due to the oxidation was small. The cross-sectional observation showed that, for the specimen with both Al and Zr depositions after the oxidation test, an adhesive scale consisting of Al_2O_3 was formed.

Keywords: coating, high temperature oxidation, electrodeposition, zirconium, aluminum, nickel aluminide, molten salt

1. INTRODUCTION

Ni-aluminide has been promising as a coating material for the high temperature materials because Ni-aluminide has a high oxidation resistance due to the formation of a protective Al_2O_3 scale. However, for the Al_2O_3 scale on the Ni-aluminide, spallation occurred during thermal cycling, and the oxidation resistance of the Ni-aluminide was poor [1]. It was reported that the addition of a small amount of reactive element as Zr is effective for improving the spallation of the Al_2O_3 scale on the Ni aluminide [2, 3].

In the present study, it was tried to form the Ni-aluminide layer containing small amounts of Zr by the synchronous electrodeposition of Al and Zr on the pure Ni specimen.

Although electrodeposition using an aqueous solution as the electrolyte has been widely used, Al and Zr cannot be electrodeposited from aqueous solutions because both metals have electrodeposition potentials lower than the reduction of water. We have succeeded in electrodeposition of Al on TiAl from a molten-salt and improvement in the oxidation resistance of TiAl [4]. In the present study, by means of the synchronous electrodeposition of Al and Zr using molten-salt, the coating consisting of Ni-aluminide containing Zr was prepared. For the specimens covered with this coating, the cyclic-oxidation resistance was examined in air at 1423 K.

2. EXPERIMENTAL

Pure Ni was used as the cathode substrate. A graphite rod was employed as the anodic counter electrode. The electrolytic bath was an equimolar NaCl-KCl melts containing 3.5 mol%AlF₃ and 0.05 or 3.5 mol%ZrF₄. An already reported device [5] was used for the electrolysis cell. The cell container was an alumina crucible held in a quartz tube set in a vertical electric furnace. The mixed salt was placed in the cell container equipped with a reference electrode, and then it was heated in the furnace. When the salt melted and the temperature reached the prescribed temperature, the specimen electrode and counter electrode were immersed in the molten salt. During the heating and the electrodeposition experiment, Ar gas was fed into the cell. The electrodeposition experiment was potentiostatically conducted at -1.7 V (vs. Ag/AgCl (0.1)). After the electrodeposition, the cross-section of the specimen was inspected by SEM and EPMA. The cyclic-oxidation resistance of specimen after the electrodeposition treatment was evaluated by measuring the oxidation mass gain curve in air at 1423 K. For the cyclic-oxidation test, the time of one cycle was 3.6 ks.

3. RESULTS AND DISCUSSION

3.1 Morphology and Composition of Coating

Fig. 1 shows scanning electron micrographs and the concentration profiles of Ni, Al and Zr of the cross-sections near the surface of the Ni specimens electrodeposited at -1.7 V for 0.6, 1.2 and 1.8 ks in the NaCl-KCl melt containing 3.5

mol%AlF₃ and 3.5mol%ZrF₄. For the Ni specimen electrodeposited for 0.6 ks, the deposited layer was scarcely observed. For the Ni specimen electrodeposited for 1.2 and 1.8 ks, the formation of a very thin deposited layer was observed on the surface of the Ni substrate. It is thought that the formation of the thin deposited layer resulted from the fact that ZrF₄ prevented the reduction of the Al ion because the amount of ZrF₄ added into bath was high.

Fig. 2 shows scanning electron micrographs and the concentration profiles of Ni, Al and Zr of the cross-sections near the surface of the Ni specimens electrodeposited at -1.7 V for 0.6, 1.2 and 1.8 ks in the NaCl-KCl melt containing 3.5 mol%AlF₃ and 0.05mol%ZrF₄. Coatings of 40 ~ 60 μm thickness adhering tightly to the substrate were observed. An increase in electrodeposition time led an increase in the thickness of the coating. The coating consisted mainly of Ni₂Al₃. For the Ni specimen electrodeposited for 0.6 and 1.2 ks, the surface region of the coating consisted of NiAl₃. For each specimen, particles of precipitate that looked white were observed in the topmost region of the coating. These particles were identified as ZrAl₃ from the point analysis by EPMA and the X-ray diffraction analysis. Moreover, particles of the precipitate were locally formed in the topmost region of the coating.

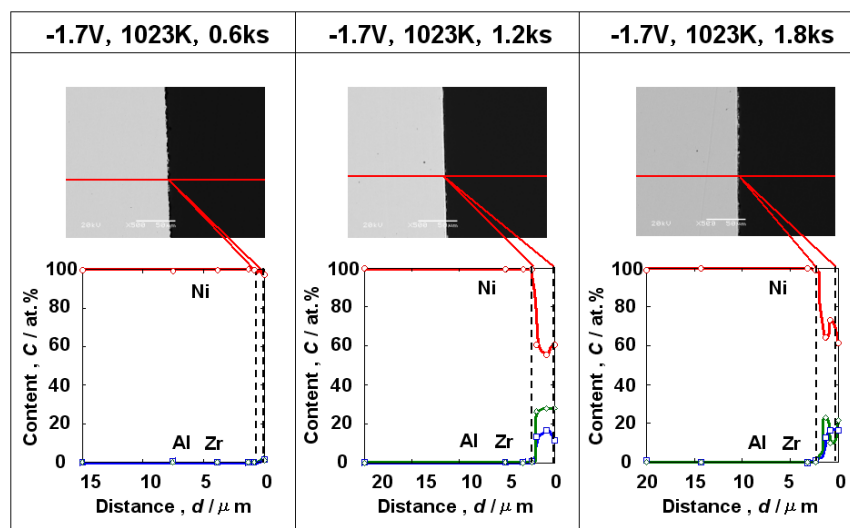


Fig.1 Cross-sectional micrographs and X-ray line scanned profiles of Ni, Al and Zr for Ni specimens electrodeposited at -1.7 V for 0.6, 1.2 and 1.8 ks in the NaCl-KCl melt containing 3.5 mol%AlF₃ and 3.5 mol%ZrF₄.

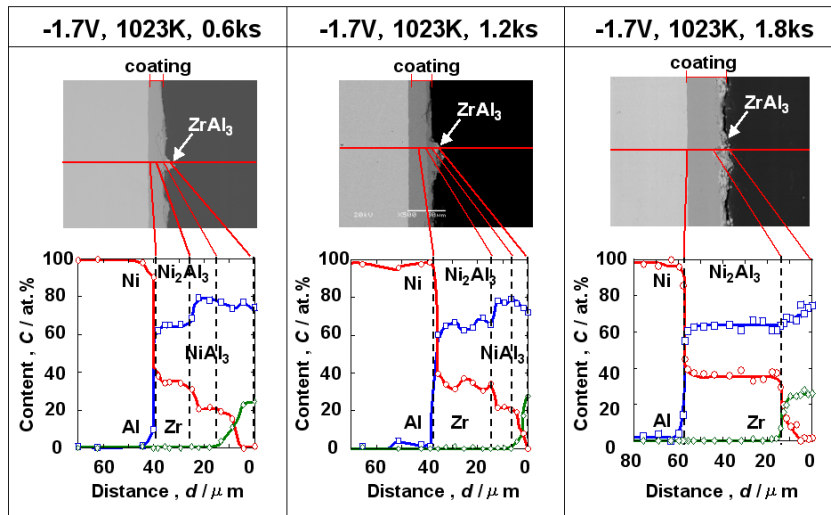


Fig.2 Cross-sectional micrographs and X-ray line scanned profiles of Ni, Al and Zr for Ni specimens electrodeposited at -1.7 V for 0.6, 1.2 and 1.8 ks in the NaCl-KCl melt containing 3.5 mol%AlF₃ and 0.05 mol%ZrF₄.

3.2 Cyclic-Oxidation Behavior of Ni Specimen with the Coating

Fig. 3 shows the results of the cyclic-oxidation test at 1423 K in air for the Ni specimens with the coatings formed by the electrodeposition in the NaCl-KCl melt containing 3.5 mol%AlF₃ and 0.05mol%ZrF₄, which are shown in Fig. 2. For comparison, this figure contains the results of the specimen of no treatment and that treated with only Al deposition. The Ni specimen treated with only Al deposition had the coating consisting of Ni₂Al₃ without ZrAl₃ particles. For the specimen of no treatment, mass gain was largely increased with a time. For the specimen treated with only Al deposition, the mass gain increased after about 20 cycles, and the mass started to decrease due to the spallation of the scale after 50 cycles. For the specimen treated with Al and Zr depositions, on the other hand, the mass gain was small, and no mass decrease due to spallation of the scale was observed. These results indicated that the ZrAl₃ particles precipitated in the topmost region of the coating played an important part in improvement in a cyclic-oxidation resistance of the coating consisting of Ni-aluminide.

Fig.4 shows that scanning electron micrographs and the concentration profiles of Ni, Al and Zr of the cross-sections near the surface of the Ni specimens electrodeposited for 0.6, 1.2 and 1.8 ks in the NaCl-KCl melt containing 3.5 mol%AlF₃ and 0.05mol% ZrF₄, after the cyclic oxidation test of 100 cycles. For each specimen, a thin, uniform scale was observed. The EPMA and XRD analysis showed that this scale consisted

of Al₂O₃. It was observed that the Al₂O₃ scale locally penetrated into the substrate metal. This indicates that the adhesion of the scale to the substrate metal was good. Therefore, the high cyclic oxidation resistance of the specimens

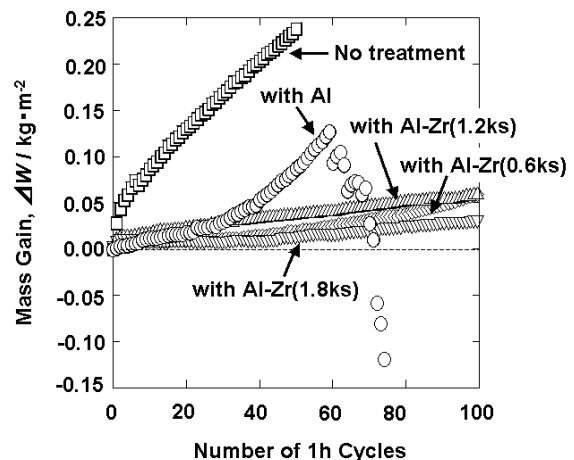


Fig.3 Mass gain-time curves of Ni specimens with Al and Zr deposits after electrodeposition at -1.7 V for 0.6, 1.2 and 1.8 ks in the NaCl-KCl melt containing 3.5 mol%AlF₃ and 0.05 mol%ZrF₄, during cyclic oxidation at 1423 K in air. For comparison, this figure contains no treated Ni specimen and Ni specimen with only Al deposit.

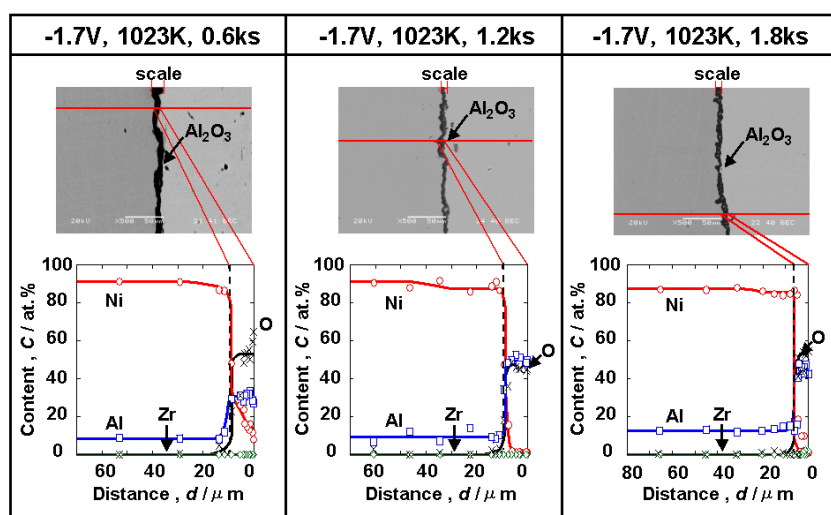


Fig.4 Cross-sectional micrographs and X-ray line scanned profiles of Ni, Al and Zr for Ni specimens electrodeposited at -1.7 V for 0.6, 1.2 and 1.8 ks in the NaCl-KCl melt containing 3.5 mol%AlF₃ and 0.05 mol%ZrF₄, after cyclic oxidation test of 100 cycles at 1423 K in air.

with Al and Zr depositions is attributable to the formation of the adhesive scale. For these specimens after the oxidation test, the Al concentration in a metal below the scale was about 10 at.%. The Ni-Al binary phase diagram shows that the metal having this Al concentration is Ni-solid solution. It is postulated that the Al concentration of Ni-Al alloy layer below the scale decreased due to the inner diffusion of Al into the metal substrate during the cyclic oxidation test. In the substrate metal after the oxidation test, the ZrAl₃ particles were not observed. This was because that the ZrAl₃ particles decomposed during the oxidation test. As a result, the Zr was contained into the surface region of the Ni-aluminide layer. Consequently, it is thought that the Zr in the surface region of the Ni-aluminide layer contributed to the formation of the adhesive Al₂O₃ scale on the Ni-aluminide layer during the oxidation test.

4. CONCLUSION

A Ni-aluminide coating containing Zr was formed on a Ni specimen by the simultaneous electrodeposition of Al and Zr using a molten salt bath. The cyclic-oxidation resistance of the Ni covered with the Ni-aluminide containing Zr was evaluated. The following conclusions can be drawn.

- (1) When the simultaneous electrodeposition of Al and Zr was carried out using the molten NaCl-KCl containing 3.5 mol%AlF₃ and 0.05mol%ZrF₄, a deposited layer consisting Ni₂Al₃ and NiAl₃ was formed. In the topmost region of the deposited layer, particles consisting of ZrAl₃ were locally formed.

- (2) The specimens covered with the Ni-aluminide layer containing the ZrAl₃ particles showed a high cyclic-oxidation resistance. On these specimens after oxidation test, an adhesive scale consisting Al₂O₃ was formed.

Acknowledgment

This study was carried out with financial support for Specially Promoted Research, No. 16001004, from a Grant-in-Aid for Science Research, Ministry of Education, Culture, Science and Technology, Japan.

References

- [1] J. L. Smialek: Metall. Trans A, Vol. 9A, pp. 309, (1978).
- [2] C. A. Barrett: Oxidation of Metals, Vol. 39, pp. 361, (1988).
- [3] B. A. Pint: Oxidation of Metals, Vol. 45, pp. 1, (1996).
- [4] M. Fukumoto, M. Hara and T. Nagataki: Oxidation of Metals, Vol. 61, pp.1, (2004).
- [5] M. Hara, Y. Matsuda, M. Fukumoto and T. Narita: Oxidation of Metals, Vol. 70, pp.295, (2008).

Experimental Studies on Evaluation of Curing Effect of Blast-Furnace Slag Cement Concrete by Using Odor Sensor

Yoshitsugu Shirokado*, Makoto Kagaya* and Noritoshi Saito*

* Department of Civil and Environmental Engineering, Faculty of Engineering and Resource Science, Akita-University, 1-1,
Tegata-Gakuencho, Akita, 010-8502 Japan
shiro715@gipc.akita-u.ac.jp

Abstract: In order to evaluate the increases of the amount of calcium hydroxide with progression of the hydration reaction of the cement used for the concrete, it was shown that the odor strength measured by using odor sensor was able to be an index of increasing in concentration of the calcium hydroxide solution. Then, the compressive strength, temperature and humidity and odor strength in ordinary concrete N and portland blast-furnace slag cement concrete BB were measured in water curing (=standard curing), indoor and outdoor atmospheric curing condition. And odor strength in slag powder concrete BP cured in water curing (=standard curing) for different period before setting in outdoor atmosphere in winter season were measured at the age of 14 days. The odor strength in the concrete N and BB was related to the change in the temperature and humidity which greatly influenced on the curing effect, and a necessity to prolong the moisture curing for the slag powder concrete BP compared with the ordinary concrete N to obtain a given curing effect was shown by measuring the odor strength.

Keywords: Blast-furnace slag cement, Water curing, Curing effect, Odor sensor, Odor strength

1 INTRODUCTION

The effective utilization of blast-furnace slag powder for replacement cement materials is very important from the view point of saving resources. However, the initial water curing period for the blast-furnace slag concrete has to prolong because the compressive strength development of the slag concrete is slower than that of ordinary concrete. It is important for the slag concrete to develop simple method of evaluation of curing effect, since the compressive strength and durability of the concrete were lowered due to drying and low-temperature environment in the early ages in comparison with standard curing [1], [2].

In this study, the relation between concentration of calcium hydroxide solution and odor strength was examined since the amount of crystallization of calcium hydroxide

increases with progress of hydration reaction of the cement in concrete by curing [3]. Then the relation between temperature and humidity and odor strength in the specimen of ordinary concrete N and B type portland blast-furnace slag cement concrete BB were examined in water curing (standard curing), indoor and outdoor atmospheric curing condition. Finally, the odor strength in concrete specimen of slag powder concrete BP cured in water curing (standard curing) for different period before setting in outdoor atmosphere in winter season were measured at the age of 14 days. The difference between odor strength in water curing and that in outdoor curing condition was defined as the difference in odor strength, and the relation between the difference and the length of water curing (standard curing) period was examined for slag powder concrete BP compared with ordinary concrete N.

2 EXPERIMENTAL OUTLINE

2.1 Materials and mixture proportions

Normal Portland cement (density: 3.16g/cm^3), B type portland blast-furnace slag cement (density: 3.04g/cm^3), blast-furnace slag powder (density: 2.91g/cm^3 and specific surface area: $6050\text{cm}^2/\text{g}$), and chemical admixture such as air-entraining agent AE (principal components: natural resinates) were used in the concrete mixtures. Natural mixed sand S as a fine aggregate (density in saturated surface-dry condition: 2.57g/cm^3 ; absorption: 3.16% and fineness modulus: 2.73) and crushed stone G as a coarse aggregate (maximum size: 20mm; density in saturated surface-dry condition: 2.68g/cm^3 and absorption: 1.34%) were used. Table 1 shows the mixture proportions of ordinary concrete: N, B type portland blast-furnace slag cement concrete: BB, and slag powder concrete (50% of normal portland cement replaced with blast-furnace slag powder): BP. Water binder ratio was 60%.

2.2 Production of test specimens

A paddle mixer with 50 liters capacity was used with a mixing time of 90 seconds after putting crushed stone, natural mixed sand, cement, water and chemical admixture in order into the mixer. After mixing, slump and air content were measured in accordance with JIS A 1101 and JIS A 1128. A steel form of 200mm depth and 100mm diameter was used for testing compressive strength, and 3 kind of forms of 150mm depth and 75, 100 and 150mm diameter for measuring temperature, humidity and odor strength in concrete. The required amount of concrete sample to fill half of the form volume was put into the form, and it was consolidated by inner vibrator. Then the remaining half of the form volume concrete was placed and consolidated by the same way. The form was removed after 24 hours.

2.3 Curing condition of specimens

Concrete N and BB shown in table 1 were cured in water bath (in standard curing at 20°C), indoor atmosphere (in the laboratory at $19.1 \pm 1^\circ\text{C}$ and $43 \pm 10\%$), and outdoor atmosphere (in the outdoor atmosphere sheltered from the rain at $7 \pm 5^\circ\text{C}$ and $68 \pm 27\%$) for 0.5, 1, 3, 7, 14, 28 and 91 days to measure compressive strength, temperature and humidity and odor strength of test specimen. The period of the outdoor atmospheric curing was 2006/11/30 to 2007/2/28 in case of ordinary concrete N and 2006/12/19 to 2007/3/19

Table 1 Mix proportions of concrete

Type	W/B (%)	s/a (%)	Slump (cm)	Air content (%)	Unit content (kg/m^3)					
					W*	C*	BFP*	S*	G*	AE*
N	60.0	44.6	8.0	6.0	175	292	-	771	1000	0.18
BB			12.0	5.5	170	283	-	776	1006	0.17
BP			12.0	5.5	175	146	146	766	994	0.18

*W, C, BFP, S, G and AE show the unit content of water, cement (normal portland cement N and B type portland blast-furnace slag cement), blast-furnace slag powder, fine aggregate, coarse aggregate and air-entraining agent.

in case of portland blast-furnace slag cement concrete BB.

Concrete N and BP shown in table 1 were cured in water bath (in standard curing at 20°C) for 7 to 14 days. After that outdoor atmospheric curing was carried out outdoors sheltered from the rain at -5.1 to 13.3°C and 37 to 97% humidity, and the specimen just after removing form was also set outdoors. The period of the outdoor atmospheric curing was 2008/12/9 to 2009/1/26. The outdoor curing was started at the same day to keep the constant influence of fluctuation of outdoor atmospheric temperature and humidity, but each specimen has finished in water curing for a required period. The odor strength in outdoor atmospheric curing was measured at the age of 14 days. All specimens were covered with the hard plastic sheet on the top surface to prevent evaporation for one day and they were set in indoor atmosphere without the influence of harmful effects.

2.4 Measurement of temperature and humidity in concrete specimen and compressive strength test

The temperature and humidity in concrete specimen with 75, 100 and 150mm diameter, and 150mm depth were measured at some ages for each curing condition. A plastic sleeve was buried to insert the temperature and humidity conversion probe at a depth of 70mm on the center of top surface of specimen just after placing concrete. At the age of measuring, the temperature and humidity conversion probe was inserted in the sleeve and the temperature and humidity in concrete specimen were measured in each curing condition. Compressive strength was measured in accordance with JIS A 1108 at the same age as that of measuring the temperature and humidity.

2.5 Measurement of odor strength

The instrument equipped odor sensor which consists of two types of highly sensitive metallic oxide semiconductors was used in this study. One semiconductor is sensitive to the odor molecule with relatively high molecular weight and another one is to that with relatively low molecular weight. When the oxidation and reduction reaction of the metallic oxide is caused by the absorption of the odor molecule, internal electrical resistance value of the semiconductor is

Table 2 Variation of odor strength in measuring atmosphere

	MIN-MAX	Average	Standard deviation	Coefficient of variation (%)
Indoor	683-949	817	86	10.5
Outdoor	647-822	741	57	7.7

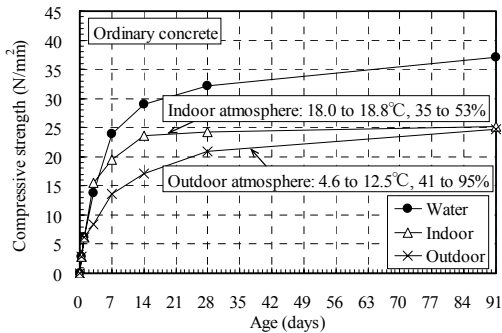


Figure 1 Compressive strength development of ordinary concrete for each curing condition

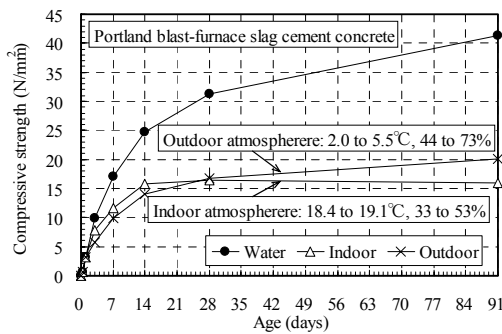


Figure 2 Compressive strength development of portland blast-furnace slag cement concrete for each curing condition

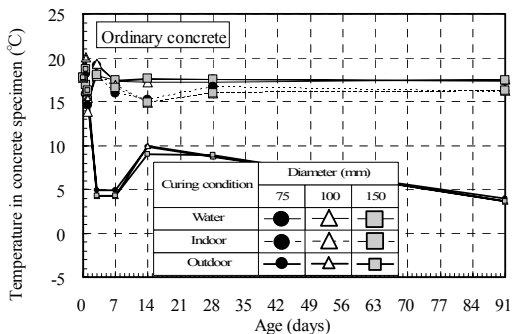


Figure 3 Temperature in ordinary concrete specimen for each curing condition versus ages

changed. The change of resistance is converted to a numerical value as odor strength.

In order to introduce the absorption pipe of the instrument into the concrete specimen, a drilled hole with 6mm diameter was made on the center of top surface of concrete specimen at a depth of 70mm for some ages in each curing condition. After removing the bored powder, the odor strength in concrete specimen was measured. As the odor strength is largely affected by aerial odor strength in the measurement environment, it was deduced from the odor strength measured in concrete specimen. The value was

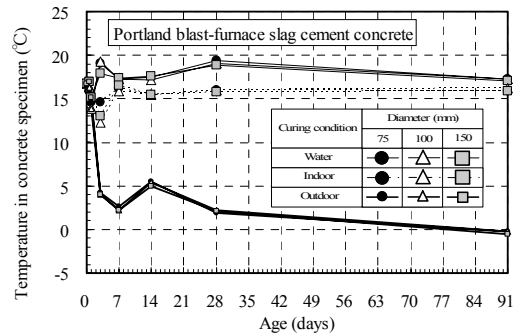


Figure 4 Temperature in portland blast-furnace slag cement concrete specimen for each curing condition versus ages

defined as the odor strength in concrete specimen. Then, the accuracy of the measured value of the odor strength was improved by washing the highly sensitive metallic oxide semiconductor by using the standard air in every measurement condition. Table 2 shows the variation of the aerial odor strength in the measurement environment.

3 RESULTS AND DISCUSSION

3.1 Strength gain, and temperature and humidity change of concrete specimen with age for each curing condition

Figures 1 and 2 show the compressive strength development of ordinary concrete and portland blast-furnace slag cement concrete in case of each curing condition. The ranges of atmospheric temperature and humidity measured in the condition were shown in these figures. In both figures, the compressive strength development after the age of 14 days cannot be observed in the indoor atmospheric curing condition because of the evaporation of the water from the specimen due to low atmospheric humidity. However, the slow strength development can be observed after the age of 14 days in the outdoor atmospheric curing condition at which the humidity is higher and the temperature is lower than the indoor atmospheric curing condition. The difference of this compressive strength development shows that structural concrete needs appropriate curing condition so as to be recognized generally.

Figures 3 and 4 show the fluctuation of temperature with ages in ordinary and portland blast-furnace slag cement concrete specimen for each curing condition. Figures 5 and 6 show that of humidity with ages in these concrete specimen for each curing condition. The internal temperature and humidity at a start were initial concrete temperature and 100% of internal humidity. The temperature of both

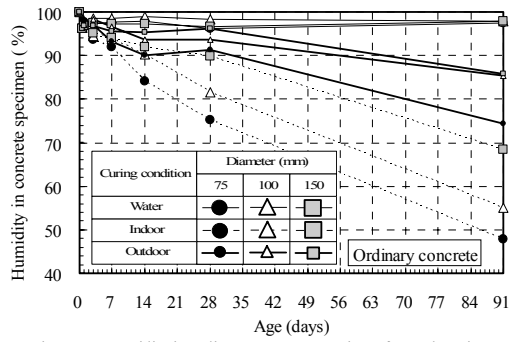


Figure 5 Humidity in ordinary concrete specimen for each curing condition versus ages

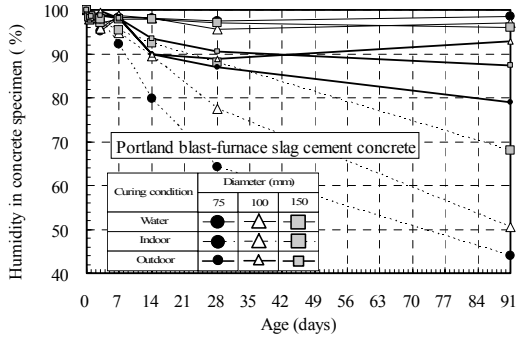


Figure 6 Humidity in portland blast-furnace slag cement concrete specimen for each curing condition versus ages

concretes was 16 to 20°C in water curing and indoor curing conditions and it was almost the same as the curing temperature. However, the temperature of both concretes has once risen at the age of 7 days in case of outdoor atmospheric curing. It has fallen after the age of 14 days with the progression of ages, and it was almost the same as the outdoor atmospheric temperature 0 to 4°C at the age of 91 days. The effect of the difference of diameter of the specimen on the temperature could not be observed. The humidity in the concrete specimen was 96 to 99% in water curing irrespective of the diameter. However, it lowered with the progression of age in indoor and outdoor atmospheric curing. The humidity in indoor atmospheric curing was much lower than that in outdoor one. The degree of lowering is depend on the size of diameter. At the age of 91 days, the humidity in the specimen with the 75mm diameter was reduced to 20 to 24% and 11 to 14% from the humidity in the specimen with the 150mm diameter in the indoor and outdoor atmospheric curing which was sheltered from the rain. This fact was caused by easily evaporation of free water from the specimen with small size of diameter.

As mentioned above, it shows that the fluctuation of the temperature and humidity in the curing condition and the difference of member size control the curing effect. It is important to develop the method to evaluate the curing effect

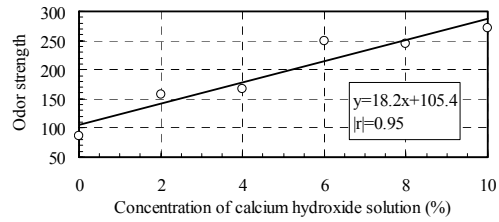


Figure 7 Relationship between concentration of calcium hydroxide solution and odor strength

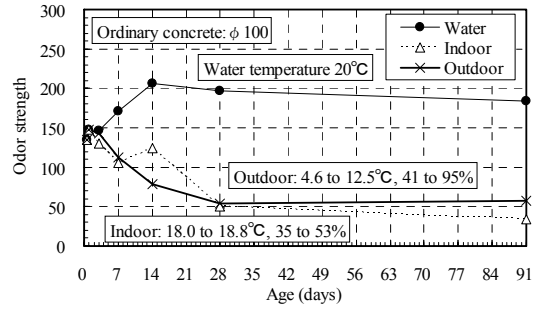


Figure 8 Relationship between odor strength of ordinary concrete for each curing condition and ages

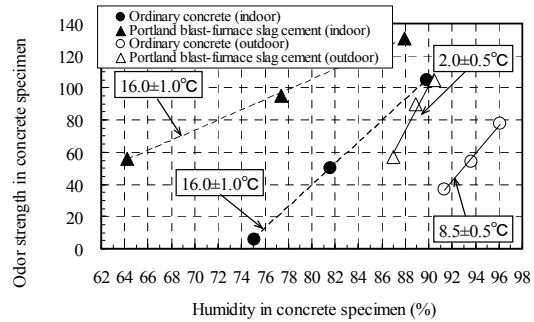


Figure 9 Relationship between humidity and odor strength in concrete specimen

easily from the viewpoint of the quality assurance of concrete structure.

3.2 Measurement results of odor strength in concrete specimen

It is generally known that the calcium hydroxide is formed with the progress of hydration reaction of the cement in concrete and the amount of crystallization of calcium hydroxide increases for curing [3]. It has been considered that the curing effect can be measured by a simple evaluation of the concentration of the calcium hydroxide solution. It was examined whether the odor strength as an index to evaluate the curing effect was appropriate or not in this section. Figure 7 shows the relationship between concentration of calcium hydroxide solution and odor strength. Though water was hard to dissolve much of the calcium hydroxide, high level concentration of calcium

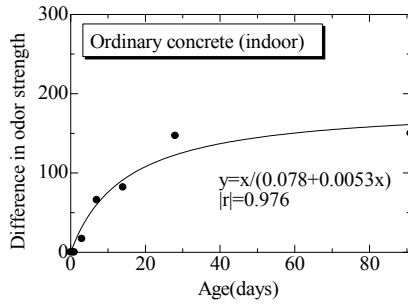


Figure 10 Difference in odor strength of ordinary concrete between water curing and indoor one versus ages

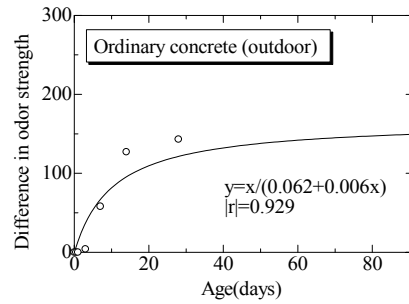


Figure 11 Difference in odor strength of ordinary concrete between water curing and outdoor one versus ages

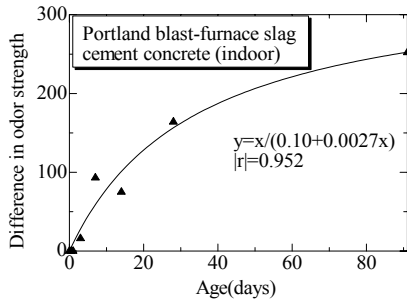


Figure 12 Difference in odor strength of portland blast-furnace slag cement concrete between water curing and indoor one versus ages

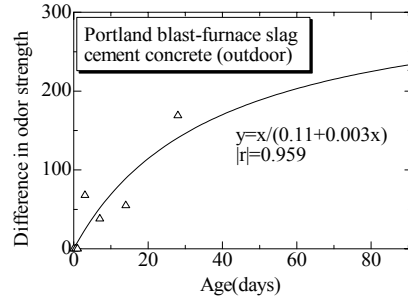


Figure 13 Difference in odor strength of portland blast-furnace slag cement concrete between water curing and outdoor one versus ages

hydroxide solution was made positively to clarify the relationship. In case of measuring the aerial odor strength in the measurement environment was deduced from the tested odor strength. The figure shows clearly that the odor strength increases with an increase in the concentration of calcium hydroxide solution and there exists a closely linear relation. It therefore was judged that the measurement of the odor strength in the concrete could evaluate the difference of the concentration of the calcium hydroxide solution formed by the difference in the progression of hydration reaction due to different curing condition.

Figure 8 shows the relationship between odor strength of ordinary concrete and ages for each curing condition as an example. The odor strength in case of the water curing tends to increase initially and approach to a constant value with an increase in age. The odor strength in case of indoor and outdoor atmospheric curing decreases with an increase in the age. In these cases, the differences between odor strength in water curing and indoor atmospheric curing, and the outdoor atmospheric curing at the ages of 91 days were 82 and 69% of the odor strength in case of the water curing. It is considered that these results were caused by the delay of hydration reaction of concrete due to the drying environment in indoor atmospheric curing and drying and

low-temperature environment in outdoor atmospheric curing.

The relationships between odor strength and temperature, and humidity were examined since the curing effect depends on the temperature and humidity in concrete as shown in 3.1. Figure 9 shows the relationship between humidity and odor strength for a given temperature in N and BB concrete specimen. The odor strength increases with an increase in the humidity in concrete specimen for a given temperature. And, the odor strength increases with an increase in the temperature in concrete specimen for a given humidity. From these results, it is considered that the odor strength in the concrete is related to the change in the temperature and humidity which greatly influences on the curing effect. The odor strength in portland blast-furnace slag cement concrete BB is higher than that in ordinary concrete N for a given humidity at $16 \pm 1^\circ\text{C}$. This fact is probably due to the odor characteristic of the blast-furnace slag powder contained the slag cement.

3.3 Evaluation of curing effect of blast-furnace slag cement concrete by measuring difference of odor strength

The difference between odor strength in water curing and that in each curing condition was defined as the

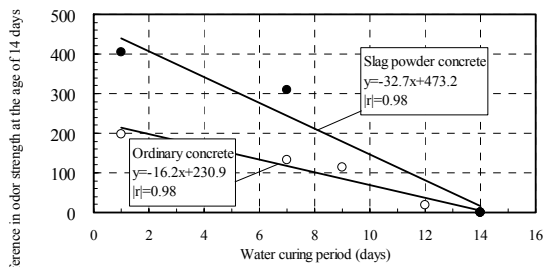


Figure 14 Relationship between water curing period and difference in odor strength at the age of 14 days

difference in odor strength, and the change of the difference with the age was examined. Figures 10 to 13 show the change of the difference in odor strength of ordinary concrete N and portland blast-furnace slag cement concrete BB with ages. The difference in odor strength increases with the age, and the values of ordinary concrete are 150 and 126 and those of portland blast-furnace slag cement concrete are 252 and 229 at the age of 91 days in indoor and outdoor atmospheric curing. The smaller the difference in odor strength is, the closer the curing condition is to water curing. Therefore, it is judged that indoor and outdoor atmospheric curing for portland blast-furnace slag cement concrete were sever rather than those for ordinary concrete. And, it was clear that the time dependent curve of this difference in odor strength could be closely approximated by a hyperbolic function for each concrete type and curing condition.

In order to evaluate the curing effect of the concrete using blast-furnace slag powder by odor strength, ordinary concrete N and slag powder concrete BP cured in water curing during different period was set in outdoor atmosphere in winter season. 50% of normal portland cement was replaced by the slag powder with 6000 cm²/g of specific surface area. The difference in odor strength of the specimen was measured at the age of 14 days. Figure 14 shows the relationship between period of water curing and the difference in odor strength of the specimen in outdoor atmosphere at the age of 14 days in winter time. The difference in odor strength decreases with an increase in the period of standard curing. As shown in this figure, it is necessary to prolong the water curing period for blast-furnace slag cement concrete compared with ordinary concrete to obtain a given difference in odor strength in winter time. Generally, an increase in the period of water curing produces curing effect. It therefore is considered that the decrease in the difference in the odor strength with an increase in the period of water curing evaluates the curing effect of the blast-furnace slag cement concrete.

4 CONCLUSIONS

An evaluation of curing effect of ordinary concrete N and portland blast-furnace slag cement concrete BB in water curing, indoor and outdoor atmospheric curing condition was examined by measuring compressive strength, temperature and humidity in concrete specimen, and odor strength in concrete specimen by using odor sensor. The slag powder concrete BP cured in water curing during different period was set in outdoor atmosphere in winter season, and the curing effect evaluated by the difference in odor strength was compared with ordinary concrete N. The following results were obtained.

(1) The fluctuation of temperature and humidity in the curing condition and the difference of member size control the curing effect.

(2) It was judged that the measurement of the odor strength in the concrete could evaluate the difference of the concentration of the calcium hydroxide solution formed by the difference in progression of hydration reaction due to different curing condition.

(3) The odor strength in the concrete N and BB was related to the change in the temperature and humidity which greatly influenced on the curing effect.

(4) The difference between odor strength in water curing and that in each curing condition was defined as the difference in odor strength. The difference in odor strength of slag powder concrete BP decreased with an increase in water curing period before setting in outdoor atmosphere.

(5) It was necessary to prolong the water curing period for slag powder concrete BP compared with ordinary concrete N to obtain a given difference in odor strength in winter time.

References

- [1] Iyoda, T. and Uomoto, T. : Progress of hydration and amount of free water in hardened cement in arid condition continuously on early curing, *Cement Science and Concrete Technology*, No.54, pp.167-173, (2000).
- [2] Shirokado, Y., Chang, D. and Kagaya, M. : Evaluation of curing effect of fly ash cement concrete by using odor sensor, *Proceedings of the Japan Concrete Institute*, Vol.30, No.2, pp.217-221, (2008).
- [3] Yamada, J. and Ariizumi, M. : Knowledges on cement and concrete properties for beginners, *Kajima Publication Association*, pp.80-81, (1982).

Investigation for Fine Grinding of Limestone with a Super Centrifugal Mill

Naoya Kotake^a, Kiyohiro Endo^b, Ikkou Sato^b, Susumu Gunji^c and Hiroaki Kezuka^c

^a Department of Chemistry and Chemical Engineering, Graduate School of Science and engineering, Yamagata University, 4-3-16, Jonan, Yonezawa, Yamagata, 992-8510 Japan

^b Department of Chemistry and Chemical Engineering, Faculty of Engineering, Yamagata University, Japan

^c Nippon Coke & Engineering Company, Limited, 1, Koh-machi, Tochigi, 328-8503 Japan

nkotake@yz.yamagata-u.ac.jp

Abstract: This study presents results from a study of fine grinding in limestone conducted using a super centrifugal mill (SC-mill), a type of circular stirred mill. The effects of the operational conditions in the SC-mill such as rotor speed, grinding time, the mass of the grinding media, and the mass of the feed sample on the fine grindability of limestone were investigated for 0.5 and 0.8 mm grinding media. The results suggest that the mass and the specific surface area of the fine particles produced by the SC-mill could be expressed as functions of the operational conditions mentioned above for the respective grinding media size.

Key Words: SC-mill, fine grinding, grinding media size, limestone, products below 1 μm

1 INTRODUCTION

Limestone is an important mineral resource in Japan, and is widely used in the steel, cement, and paper-pulp industries, in agriculture and stockbreeding, and in the food and pharmaceutical industries. These uses generally require the limestone to be ground to smaller particle sizes, with some applications demanding extremely fine grinding. This study examines the use of high performance grinding techniques to attain a very fine limestone product.

The grinding apparatus used in this experiment was a super centrifugal mill (SC-mill) [1-4], which is a circular-type, high flow stirred mill. The SC-mill was developed for fine or ultra-fine grinding in the submicron or several tens of nanometer region, where other conventional stirred media mills exhibit low grinding efficiency [5-8]. The main features of this mill are 1) the length of the grinding vessel, which is short in comparison with its diameter, and 2) the flow direction of the grinding material slurry, which is made to coincide with the direction of centrifugal force due to the rotor acting on small grinding media (ball diameter less than 1 mm), as shown in Figure 1. Thus, efficient fine or ultra-fine grinding can be achieved by an increase in the frequency of collisions between the grinding media and the particles, and by a large shearing force due to the rotor.

In this work, we have performed experiments on the fine grinding of limestone with a SC-mill, and investigated the effects of the grinding media size on the fine grindability of limestone under various operational conditions such as rotor

speed, grinding time, the mass of the grinding media, and the mass of the feed sample.

2 EXPERIMENTS

2.1 Sample material

The limestone used in this investigation was supplied by Ueda Lime Co., Ltd. For preparation of the feed sample, a jaw crusher was used to crush the large fragments of massive limestone; the crushed products were then screened with a 75 μm sieve. The physical properties and the chemical components of the limestone are listed in Table 1.

Table 1 Limestone used in this experiment.

Physical properties	Density	2680 kg/m ³
	Moh's hardness	4
	Vicker's hardness	115 kgf/mm ²
	Young's modulus	68 GPa
	Poisson's ratio	0.32
	Tensile strength	4.15 MPa
	Work index	9.4 kWh/t
Chemical components	CaO	55.1 %
	MgO	0.44 %
	SiO ₂	0.19 %
	Fe ₂ O ₃	0.01 %
	Al ₂ O ₃	0.01 %
	Ig.loss	44.25 %

2.2 Experimental method

2.2.1 Super centrifugal mill: The grinding machine is a circular-type stirred mill (SC-mill; SC100/32XZ) from Nippon Coke & Engineering Co. Ltd. Details of the grinding vessel of the mill are shown in Figure 1 and a schematic diagram of the circulating system of the mill in Figure 2. The mill consists of a rotor on the inside of a cylindrical grinding chamber and a separator in the outer part of the cylinder. The grinding vessel has an inner diameter of 0.11 m and is 0.044 m in length (inner volume: 0.42 dm³); the rotor is 0.094 m in diameter and 0.022 m in length, and is made of SUS440C stainless steel. The total volume of the grinding vessel including the separator is 0.85 dm³.

In operation, the material feed is first fed into the inner chamber of the grinding vessel via the input port, and then the rotor is actuated to rotate. As a result, the mixture of the material and the grinding media circulating within the chamber is screened by the separator, through which only the predetermined size of material particles are selectively allowed to pass, while the grinding media as well as the rest of the material feed (containing particles above the cut-off size) remain inside the grinding chamber. The slurry of partially ground products (large particles) is transported through the separator to the holding tank and re-enters the grinding vessel to collide with the grinding media, and this process is repeated by means of a circulating flow.

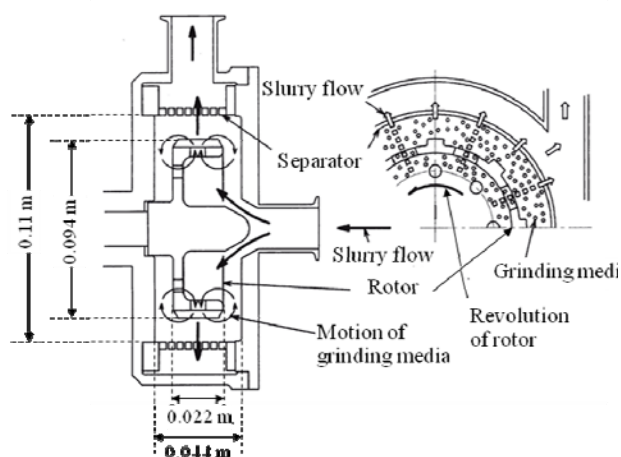


Figure 1 Grinding vessel of SC-mill.

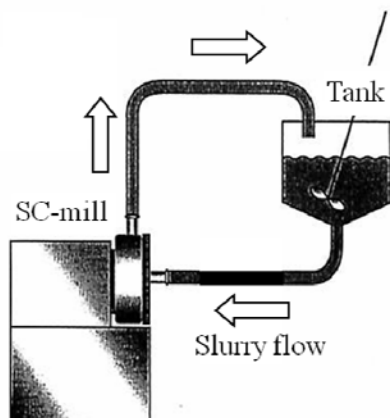


Figure 2 Circulating system of SC-mill.

2.2.2 Grinding method: Grinding media were small zirconia balls with diameters 0.5 mm and 0.8 mm (density; 6000 kg/m³, Vicker's hardness; 1280 kgf/mm²). The slurry volume of the feed sample was 4 dm³ and the circulating flow rate was 3 dm³/min. A total of 27 grinding conditions for each grinding media size were examined, varying the rotor speed, the grinding time, the mass of the grinding media, and the mass of the feed sample (slurry concentration). All experimental conditions are summarized in Table 2. Grinding experiments were carried out for 5-300 min under each grinding condition.

Table 2 Experimental conditions for fine grinding.

Slurry volume	4 dm ³
Circulating flow rate	3 dm ³ /min
Rotor speed, n	2000, 2640, 3200 rpm
Diameter of grinding media	ϕ 0.5, 0.8 mm
Mass of grinding media, W_b	570, 710, 850 g
Size of feed sample	< 75 μ m
Mass of feed sample, W_s (Slurry concentration)	430, 640, 860 g (4, 6, 8 vol.% solid) 540, 800, 1070 g (5, 7.5, 10 vol.% solid) 640, 970, 1290 g (6, 9, 12 vol.% solid)
Ratio of mass, W_s/W_b	0.75, 1.1, 1.5

The particle size distributions of the ground products were measured using a laser diffraction and scattering method (Shimadzu Corporation Co., Ltd, SALD-7000). The specific surface area of the products was determined by the BET adsorption method (Yuasa-Ionics Co., Ltd, Mono Sorb MS-21).

3 RESULTS AND DISCUSSION

3.1 Size distribution of ground products

An example of the particle size distribution of the ground products is given in Figure 3 for 0.5 mm grinding media, the rotor speed $n = 2000$ rpm, 710 g of grinding media, and 800 g of feed sample. From this figure, it is seen that the particle size of the ground products decreases with increasing grinding time.

There are several ways that have been used to describe the particle size distribution width and the fineness of the ground product. One of the simplest descriptions of the particle size distribution width is the particle size ratio, $x_{0.9}/x_{0.1}$, where $x_{0.9}$ is the 90% cumulative weight passing size and $x_{0.1}$ is the 10% cumulative weight passing size. The fineness of the product in mineral processing is most commonly expressed by the median particle size, $x_{0.5}$ (i.e., the 50% cumulative weight passing size).

Figures 4-6 show the change in the width of the particle size distribution with respect to the product size, $x_{0.5}$, obtained from the SC-mill using 0.5mm grinding media and rotor speeds

of 2000, 2640, and 3200 rpm. It can be observed from these figures that the particle size ratio, $x_{0.9}/x_{0.1}$, i.e. the width of the particle size distribution, decreased as the median particle size decreased for all rotor speeds at the 0.5 mm media size. Furthermore, the experimental results in this study confirm that a variation in the width of the particle size distribution is a common phenomenon in fine grinding with various circular-type stirred mills [9]. From these results, it is considered that the mass of the produced fine particles is proportional to the mass of the grinding media, the mass of the feed sample, and the rotor speed (or the revolution number of the rotor) in a logarithmic plot.

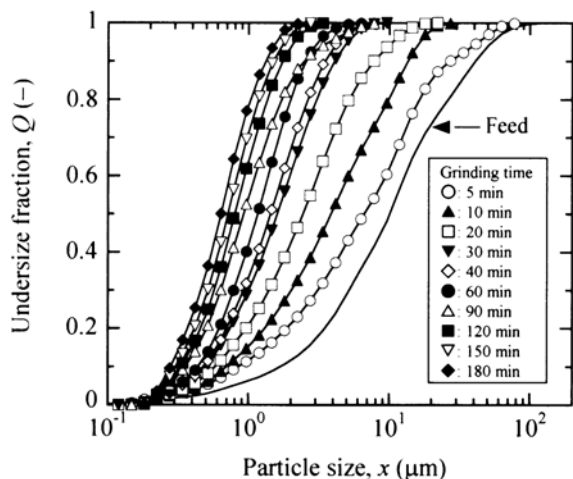


Figure 3 Particle size distribution of ground products for grinding media size, 0.5 mm, rotor speed, $n=2000$ rpm, mass of grinding media, $W_b=710$ g, mass of feed sample, $W_s=800$ g.

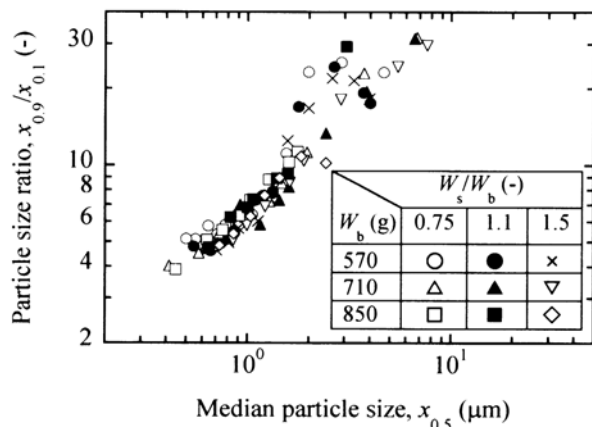


Figure 4 Relation between particle size ratio and median particle size for grinding media, 0.5 mm, rotor speed, $n=2000$ rpm.

3.2 Evaluations of fine grinding

The fine grindability of the grinding conditions in various media mills [10-13] has been evaluated by using the production of particles below $1 \mu\text{m}$. Figures 7 and 8 show an example of the relation between the mass of products below $1 \mu\text{m}$, W_1 and

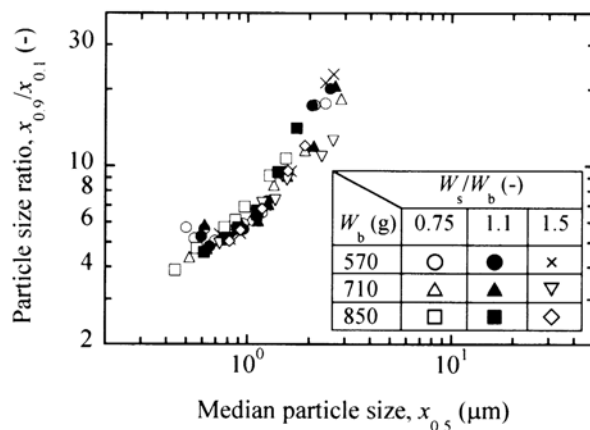


Figure 5 Relation between particle size ratio and median particle size for grinding media, 0.5 mm, rotor speed, $n=2640$ rpm.

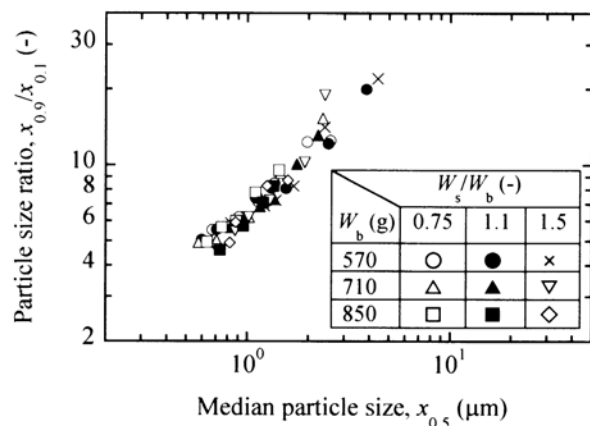


Figure 6 Relation between particle size ratio and median particle size for grinding media, 0.5 mm, rotor speed, $n=3200$ rpm.

the number of rotor revolutions, nt (n : rotor speed, t : grinding time) for media sizes 0.5 mm and 0.8 mm. The applicable relations for the respective media sizes are

$$W_1 = a(nt)^{0.45} \quad \text{for media size 0.5 mm,} \quad (1)$$

$$W_1 = a'(nt)^{0.54} \quad \text{for media size 0.8 mm,} \quad (2)$$

where a and a' are constants which depend on the ratio of the feed sample mass, W_s , to the grinding media mass, W_b , i.e., W_s/W_b .

Figures 9 and 10 show the relations between the mass ratio, W_s/W_b and the coefficients, a and a' , respectively, for three levels of grinding media mass, W_b . These relations are expressed by

$$a = C(W_s/W_b)^{0.85} \quad \text{for media size 0.5 mm,} \quad (3)$$

$$a' = C'(W_s/W_b)^{0.84} \quad \text{for media size 0.8 mm,} \quad (4)$$

where C and C' are coefficients which are dependent on the mass of the grinding media, W_b .

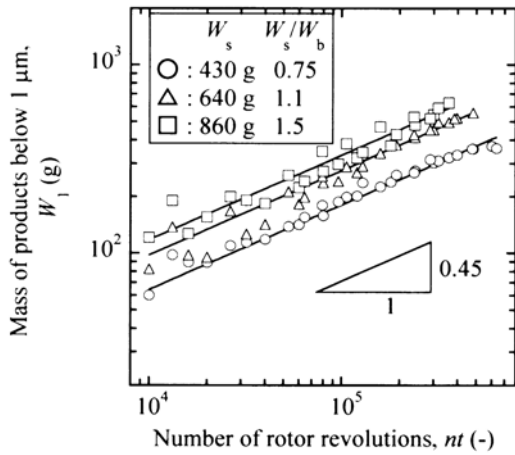


Figure 7 Relation between mass of products below 1 μm and number of rotor revolutions for grinding media, 0.5 mm, mass of grinding media, 570 g.

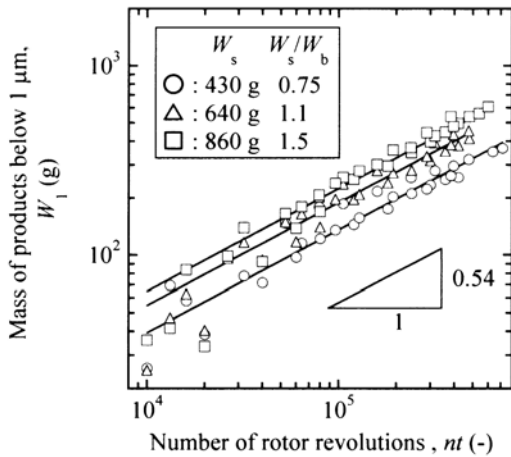


Figure 8 Relation between mass of products below 1 μm and number of rotor revolutions for grinding media, 0.8 mm, mass of grinding media, 570 g.

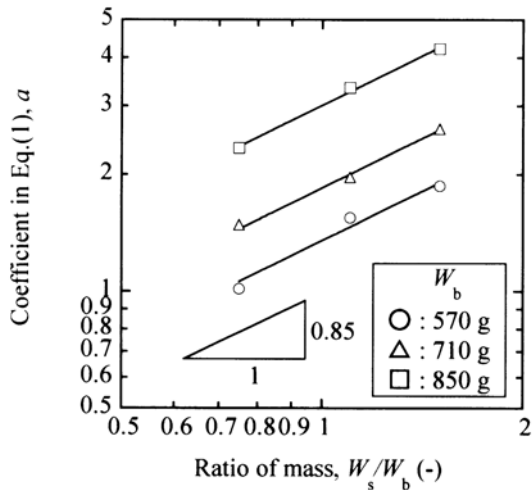


Figure 9 Relation between coefficient in Eq.(1), a and ratio of mass, W_s/W_b for grinding media, 0.5 mm.

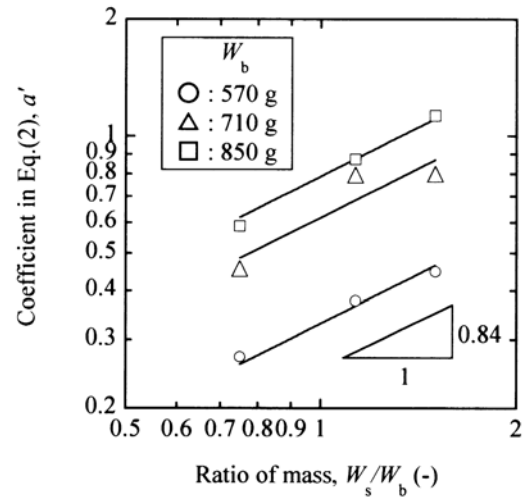


Figure 10 Relation between coefficient in Eq.(2), a' and ratio of mass, W_s/W_b for grinding media, 0.8 mm.

Figure 11 shows the relations between the coefficients C and C' given by Eqs. (3) and (4) and the mass of the grinding media, W_b , which are given by

$$C = 4.5 \times 10^{-6} W_b^{1.98} \quad \text{for media size 0.5 mm,} \quad (5)$$

$$C' = 3 \times 10^{-7} W_b^{2.2} \quad \text{for media size 0.8 mm.} \quad (6)$$

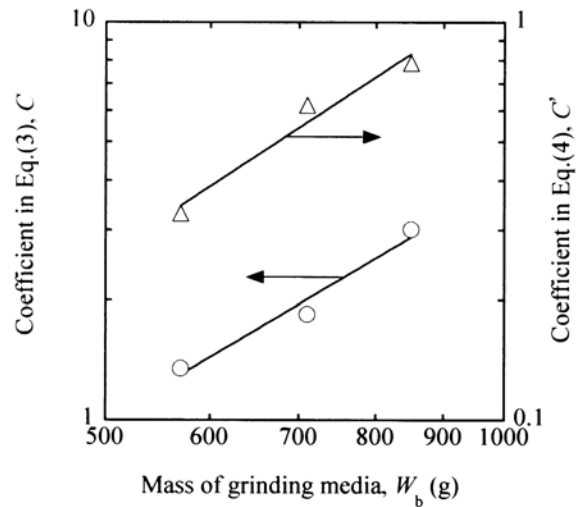


Figure 11 Relation between coefficients in Eqs.(3) and (4), C , C' and mass of grinding media, W_b .

Substituting Eqs. (3) and (5) into Eq. (1), and Eqs. (4) and (6) into Eq. (2), we obtain the following relations:

$$W_1 = 4.5 \times 10^{-6} W_b^{1.13} W_s^{0.85} (nt)^{0.45} \quad \text{for media size 0.5 mm,} \quad (7)$$

$$W_1 = 3 \times 10^{-7} W_b^{1.36} W_s^{0.84} (nt)^{0.54} \quad \text{for media size 0.8 mm,} \quad (8)$$

or

$$Q_1 = W_1/W_s = 4.5 \times 10^{-6} W_b^{1.13} W_s^{-0.15} (nt)^{0.45}$$

for media size 0.5 mm, (7)'

$$Q_1 = W_1/W_s = 3 \times 10^{-7} W_b^{1.36} W_s^{-0.16} (nt)^{0.54}$$

for media size 0.8 mm, (8)'

where Q_1 is the mass fraction of ground products below $1 \mu\text{m}$. From Eqs. (7) and (8) or Eqs. (7)' and (8)', the influence of the SC-mill operational conditions on the production of fine limestone particles can be evaluated. These equations indicate that the mass of the grinding media is the most effective operating factor for fine particle production of limestone for a given grinding media size. This means that the collision frequency of the grinding media against the sample particles in the SC-mill increases as the amount of the grinding media is increased.

Figure 12 shows the relation between the total surface area of the ground products, S ($=S_w$ (specific surface area) $\times W_s$ (mass of feed sample)) and the mass of the products below $1 \mu\text{m}$, W_1 , for all of the experimental conditions, taking the grinding media size as a parameter. An almost linear relation is found, which can be expressed by

$$S = 24.3 W_1 \quad (9)$$

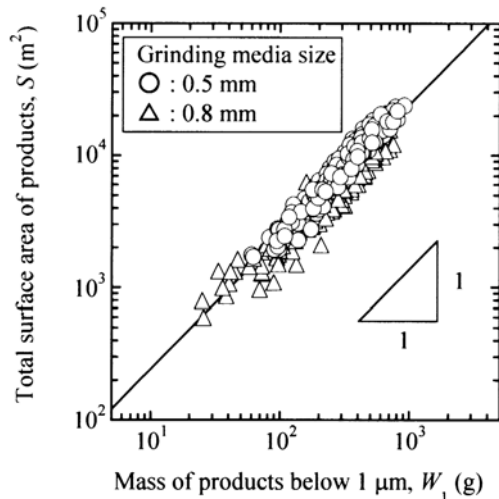


Figure 12 Relation between total surface area of products, S and mass of products below $1 \mu\text{m}$, W_1 .

From this equation, the specific surface area, S_w ($=S/W_s$) of the ground products can be estimated from the mass of the fine particles produced.

Substituting Eqs. (7) and (8) into Eq. (9), we obtain Eqs. (10) and (11).

$$S_w = S/W_s = 1.1 \times 10^{-4} W_b^{1.13} W_s^{-0.15} (nt)^{0.45}$$

for media size 0.5 mm, (10)

$$S_w = S/W_s = 7.3 \times 10^{-5} W_b^{1.36} W_s^{-0.16} (nt)^{0.54}$$

for media size 0.8 mm. (11)

From Eqs. (10) and (11), we can calculate the specific surface area of products, S_w , obtained using various operational conditions of the SC-mill. These equations should also be useful in the cement industry, where Blaine's value is presently used.

3.3 Effects of grinding media size on fine grinding

Figure 13 shows that the comparison of the mass of products below $1 \mu\text{m}$ for 0.5 and 0.8 mm grinding media under all experimental conditions. The data plotted in the figure can be fit to the following approximate linear relation.

$$W_1(0.5) = 1.17 W_1(0.8), \quad (12)$$

where $W_1(0.5)$ is the mass of ground products smaller than $1 \mu\text{m}$ obtained with 0.5 mm grinding media and $W_1(0.8)$ is that obtained using 0.8 mm grinding media.

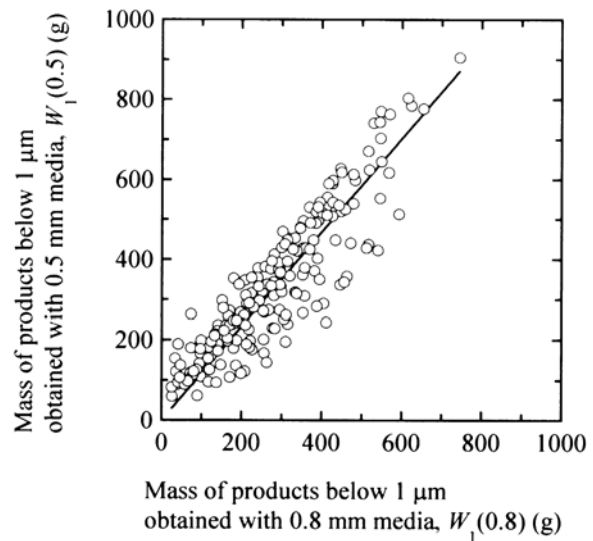


Figure 13 Comparison of mass of fine particles produced in different grinding media sizes.

Smaller grinding media is useful for the production of fine limestone particles in the SC-mill. In this experiment, the decrease in the grinding media size gave rise to an increase of 17 % in the fine particle mass produced. One reason for this improvement may be that more effective comminution in the SC-mill was achieved by an increased number of collisions between grinding media and particles, which were caused by the increased number of the media due to the decrease in media size.

4 CONCLUSIONS

In the present work, we carried out experiments on the fine grinding of limestone with a SC-mill, changing the grinding media size under the various operational conditions, in order to investigate its fine grinding performance. The results are summarized as follows;

1. The grinding conditions (rotor speed, n , grinding media mass, W_b , and feed sample mass, W_s) had only slight effects on the shape of the particle size distribution produced by fine grinding.

2. The quantitative relations between the mass of fine particle products of limestone and the operational conditions for two kinds of grinding media size can be expressed with Eqs. (7) and (8) or Eq. (7)' and (8)'.

3. A linear relation was found between the mass of fine particles and the total surface area of limestone ground with the SC-mill, irrespective of all grinding conditions tested, which is expressed by Eq. (9). By use of Eqs. (10) and (11) we could quantitatively express the effect of grinding conditions on the increase in specific surface area for the different grinding media sizes.

4. Fine grindability of the limestone in the SC-mill was improved by decreasing the grinding media size: a decrease of about 40 % in the diameter of the media caused a roughly 20% increase in the mass of fine particle product.

Acknowledgments

The authors would like to thank Ueda Lime Co., Ltd. for supplying and preparing the limestone sample.

Nomenclature

a	Coefficient in Eq. (1)
a'	Coefficient in Eq. (2)
C	Coefficient in Eq. (3)
C'	Coefficient in Eq. (4)
N	Rotor speed (rev/min)
Nt	Number of rotor revolutions (rev), (-)
Q	Cumulative undersize fraction (-)
Q_1	Mass fraction of ground products below 1 μm (-)
S	Total surface area of ground products ($=S_w \times W_s$) (m^2)
S_w	Specific surface area of ground products (m^2/g)
t	Grinding time (min)
W_1	Mass of ground products below 1 μm (g)
$W_1(0.5)$	Mass of ground products below 1 μm obtained with 0.5 mm media (g)
$W_1(0.8)$	Mass of ground products below 1 μm obtained with 0.8 mm media (g)
W_b	Mass of grinding media (g)
W_s	Mass of feed sample (g)
x	Particle size (μm)
$x_{0.1}$	10 % cumulative weight passing size (μm)
$x_{0.5}$	50 % cumulative weight passing size (median particle size) (μm)
$x_{0.9}$	90 % cumulative weight passing size (μm)

References

- [1] Ishikawa, T., "Circular-type Grinding Machine with High Flow Rate-SC-mill-", Haikan-to-Souchi (Japanese edition), Vol.38, pp.11-15 (1998).
- [2] Ishikawa, T., Japan Patent 10015411(1998).
- [3] Ishikawa, T., United States Patent 5791569 (A1) (1998).
- [4] Gunji, S. and Ishikawa, T., "Comminution and Dispersion of Particles by Stirred Media Mills", Powder Science and Engineering (Japanese edition), Vol.37, pp.69-76 (2005).
- [5] Kwade, A. and Schwedes, J., "Wet Comminution in Stirred Media Mills", KONA, No.15, pp.91-101 (1997).
- [6] Kwade, A., "Wet Comminution in Stirred Media Mills -Research and its Practical Application", Powder Technology, Vol.105, pp.14-20 (1999).
- [7] Fadhel, H. B., Frances, C., "Wet Batch Grinding of Alumina Hydrate in a Stirred Bead Mill", Powder Technology, Vol.119, pp.257-268 (2001).
- [8] Kwade, A., Schwedes, J., "Breaking Characteristics of Different Materials and their Effect on Stress Intensity and Stress Number in Stirred Media Mills", Powder Technology, Vol.122, pp.109-121 (2002).
- [9] Jankovic, A., Sinclair, S., "The shape of product size distributions in stirred mills", Minerals Engineering, Vol.19, pp.1528-1536 (2006).
- [10] Kotake, N., Shimodaira, K., Nishihara, H., Abe, Y., Kanda, Y., "Production of Submicron Particles by Ball Milling and its Evaluation", Journal of the Society of Materials Science (Japanese edition), Vol.42, pp.1265-1270 (1993).
- [11] Kanda, Y., Hasegawa, M., Matsuno, T., Koseki, K., Hayashi, Y., "Production of Submicron Particles by Autogenous Grinding with a Stirred Mill", Journal of the Society of Materials Engineering for Resources of Japan, Vol.6, pp.35-42 (1993).
- [12] Kanda, Y., Hayashi, Y., Yamaguchi, N., Hasegawa, M., "Production of Submicron Particles of Limestone by Autogenous Grinding with a Stirred Mill", Journal of the Society of Materials Engineering for Resources of Japan, Vol.8, pp.12-20 (1995).
- [13] Kotake, N., Abiko, S., Yamaguchi, S., Kanda, Y., "The Evaluation and Expression of Fine Grindability Using a Ball Mill Grinding", Journal of the Society of Powder Technology Japan, Vol.34, pp.759-766 (1997).

Adsorptive Desulfurization of Commercial Kerosene by Using Biomass-derived Activated Carbons

Hiroataka Ishizawa, Seiji Kumagai, Masaya Sugimoto and Yasuhiro Toida*

Department of Machine Intelligence and Systems Engineering, Akita Prefectural University
84-4, Tsuchiya-aza-ebinokuchi, Yurihonjo, 015-0055, Japan

* Petroleum Refining Research and Technology Center, Japan Energy Corporation
3-17-35, Niizominami, Toda, 335-8502, Japan

kumagai@akita-pu.ac.jp

Abstract : Micro- and mesoporous granular rice husk activated carbon (RHAC) and microporous granular coconut shell activated carbon (CSAC) were tested to remove aromatic sulfur compounds of benzothiophenes (BTs) and dibenzothiophenes (DBTs) from commercial kerosene. Fixed-bed flow tests were conducted, providing the breakthrough curves for BTs and DBTs. The adsorption isotherms for BTs and DBTs were also obtained in a batch-mode, correlating with the results of the fixed-bed flow test. Both the ACs were useful to remove them. RHAC showed a lower-selectivity for DBTs and a higher-selectivity for BTs, than CSAC.

Key Words: Rice husk, activated carbon, bulk density, pore structure

1 INTRODUCTION

Benzothiophene and its derivatives (BTs), and dibenzothiophene and its derivatives (DBTs) contained in fuel oils such as kerosene and diesel oil are refractory poly-aromatic sulfur compounds. Alkyl-substituted DBTs, i.e., 4-methyldibenzothiophene (4-MDBT) and 4,6-dimethyldibenzothiophene (4,6-DMDBT), are known to be highly refractory [1, 2]. Modified HDS methods using catalysts such as CoMo and NiMo [3-7] and adsorptive desulfurization using porous materials [8-10] have been proposed for the efficient removal of refractory BTs and DBTs from fuel oils. Desulfurization using activated carbons (ACs) [11-13] or catalyst-loaded ACs [14], which can be performed at ambient temperature and pressure, has been intensively studied.

Kumagai et al demonstrated that ACs with a specific pore structure could be used for the efficient and selective removal of DBTs from kerosene [15]. ACs made from agricultural waste of rice husk (RH), which were with a composite micro-mesoporous structure, were shown to be promising for the removal of DBTs from kerosene. ACs made from agricultural waste are now very profitable in view of cost and environmental friendliness.

Kerosene is widely used in Japan as a home heating fuel for portable and installed kerosene heaters, and can be readily purchased at filling stations or delivered to homes. Kerosene is a promising hydrogen source for fuel cells for

domestic use in Japan. In the present study, two-types of biomass-based ACs were used for the adsorptive removal of BTs and DBTs from commercial kerosene. The granular RH-based AC (RHAC) produced in a laboratory and the purchased granular coconut-shell AC (CSAC) were tested in fixed-bed flow tests and batch-mode adsorption tests.

2 EXPERIMENTAL METHODS

2.1. Materials

Granular RHAC was produced from RH and beet sugar. The used RH was Koshihikari rice harvested in Toyooka, Iwata City, Japan in autumn 2004. The beet sugar was a commercial product supplied from the Hokuren Agriculture Cooperative Association (Hokkaido, Japan). The detailed fabrication process of RHAC is described in [16]. RHAC used for the present study was fabricated via the two-step activation process. Commercially available granular CSAC (GW 10/32, Kuraray Chemical Co., Ltd., Japan) was used. The grain-size of RHAC and CSAC was adjusted to 1.0-2.0 mm using sieves. The samples were not subjected to any treatments, such as washing, prior to the desulfurization tests and material characterizations.

2.2. Compositional analysis

The ash content of the samples (0.1 g) was precisely determined from the residual ash ratio after incineration at 800°C for 1 h in air (100 mL/min) using a thermogravimetric analyzer (TGA-51; Shimadzu Corp., Japan). A CHN/S

analyzer (2400 I; Perkin Elmer Inc., USA) was used to determine the hydrogen, carbon, nitrogen and sulfur content of the samples. All samples were dried at 105 °C for 3 h prior to analyses. The oxygen content, excluding that in ash, was determined as the difference between the original sample weight and the weight of the hydrogen, carbon, nitrogen, sulfur, and ash. The ash content cannot be equal to the inorganic content of RHAC samples, because not all forms of inorganic matter in RHACs are oxides (e.g., hydrated compounds). Thus, it should be noted that the oxygen content might have error.

2. 3. Textual characterization

Nitrogen adsorption-desorption isotherms at -196 °C were obtained using a gas adsorption analyzer (Autosorb-3B; Quantachrome Instruments Inc., USA). A sample of 0.02 g was degassed at 200 °C for >3 h prior to isotherm measurement. The BET specific surface area (S_{BET}) is based on the BET theory and was calculated using the volume of N_2 adsorbed at relative pressures of 0.05-0.1 [17]. The liquid N_2 volume in relation to the N_2 volume adsorbed at a relative pressure of 0.995 was determined as the total pore volume (V_t). An AC consists of graphite-like sheets between which small slit-shaped pores exist [18]. In the present study, micropores were distinguished as either ultramicropores (width ≤ 0.7 nm) or supermicropores ($0.7 < \text{width} \leq 2.0$ nm), in accordance with Sing et al [19]. The pore size distribution was evaluated using density functional theory (DFT) [20]. The DFT software developed by Quantachrome Instruments Inc. (version 1.62) was used to obtain the pore size distribution. The volumes of ultramicropores (V_u), supermicropores (V_s), and mesopores (V_m) were obtained using these pore size distribution data. The macropore volume (V_c) was calculated as follows: $V_c = V_t - (V_u + V_s + V_m)$; V_{micro} means the volume of micropores and equals $V_u + V_s$.

2. 4. Concentration measurement of aromatic sulfur compounds in kerosene

Aromatic sulfur compounds in the used kerosene were identified and the sulfur in BTs and DBTs was quantified using a gas chromatograph-inductively coupled plasma mass spectrometer (GC-ICP-MS, GC 6890N; ICP-MS 7500CS;

Agilent Technologies Inc., USA). The definition of BTs and DBTs are shown in **Figure 1**. BTs are defined as sulfur compounds containing single or double aromatic rings of which molecular mass was less than that of 4-MDBT (molecular mass: 198) in the used GC-ICP-MS system. DBTs are defined as sulfur compounds containing double aromatic rings that have a molecular mass not less than that of 4-MDBT. It should be noted that dibenzothiophen (DBT) was included in BTs.

2. 5. Adsorptive desulfurization tests.

2. 5. 1. Fixed-bed flow desulfurization test

A stainless cylindrical column (length: 150 mm, volume: 13.5 cm^3) was filled with a sample which was previously dried at 130 °C in ambient air for 3 h. The storage density of the sample (mass of the filled sample / column volume) was also measured. Commercial kerosene produced in 2004 by the Japan Energy Corporation was used for the fixed-bed flow test. Concentrations of BTs and DBTs in the used kerosene were 8.4 and 3.9 mass ppm-S, respectively. Flow-rate of kerosene was adjusted at 1.0 cm^3/min using a plunger pump (NP-KX-120; Nihon Seimitsu Kagaku Co., Ltd, Japan). The effluent kerosene was separated every 10 min using a fraction collector. The test was carried out at 25 °C.

2. 5. 2. Batch adsorptive desulfurization test

A sample was immersed in 15.0 g of kerosene in a 30- cm^3 glass vessel at 10 °C for 240 h. The samples were dried at 130 °C in ambient air for 3 h prior to kerosene immersion. The kerosene used for this batch adsorption test was produced in 2007 by the Japan Energy Corporation. Concentrations of BTs and DBTs in the used kerosene were 4.5 and 1.2 mass ppm-S, respectively. The kerosene was not stirred during immersion. The adsorption time of 240 h was confirmed to be sufficient to reach equilibrium adsorption. The adsorption isotherms of the sample showing the relationship between the equilibrium concentration of BTs and DBTs in the kerosene and the adsorption capacity of the sample for BTs and DBTs were obtained, in which five different masses for each sample were tested.

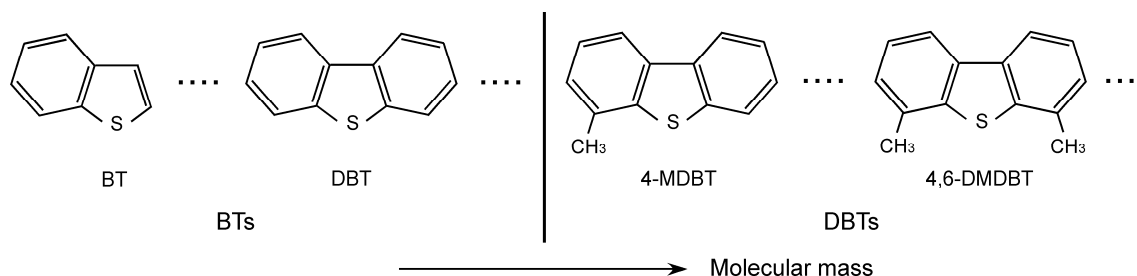


Figure 1. A definition of BTs and DBTs

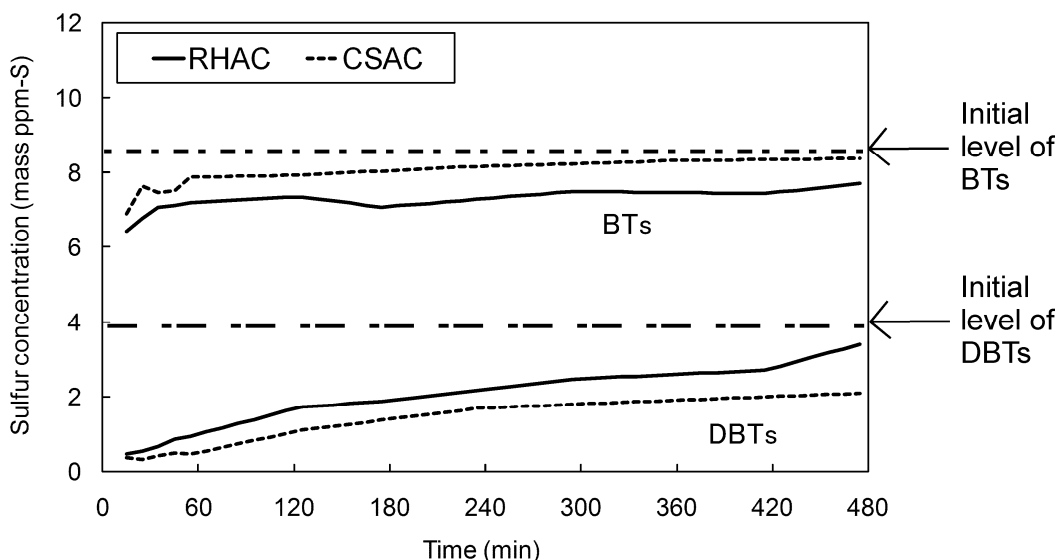


Figure 2. Breakthrough curves of RHAC and CSAC for BTs and DBTs in fixed-bed flow tests using commercial kerosene produced in 2004.

3 RESULTS AND DISCUSSION

3. 1. Results of material characterization

The elemental compositions of RHAC and CSAC are shown in **Table 1**. Higher carbon and hydrogen contents were observed in CSAC than in RHAC. The ash content of RHAC was much higher than that of CSAC. A major ingredient of the ash (~90 mass%) was SiO₂. A similar level of oxygen content was seen in both the samples. The above results indicate that more carbonaceous structure was produced on CSAC than RHAC.

Table 1. Elemental compositions of RHAC and CSAC

Sample	C	H	N	S	Ash	O*
RHAC	58.60	0.03	0.55	0.01	36.80	4.02
CSAC	94.13	0.41	0.27	0.08	0.50	4.61

Table 2. Textural properties of RHAC and CSAC

Sample	S_{BET} (m ² /g)	V_t (cm ³ /g)	V_u (cm ³ /g)	V_s (cm ³ /g)	V_m (cm ³ /g)
RHAC	943	0.56	0.15	0.17	0.19
CSAC	1169	0.56	0.21	0.22	0.06

S_{BET} : BET specific area, V_t : total pore volume, V_u : volume of ultramicropore, V_s : volume of supermicropore, V_m : volume of mesopore.

Nitrogen adsorption-desorption isotherms of RHAC and CSAC at -196 °C were measured. **Table 2** shows the BET specific surface area and the pore volumes, calculated based on the BET theory and the DFT method, respectively. A similar level of total pore volume was observed in RHAC and

CSAC. However, the BET surface area, and the volumes of ultramicropores and supermicropores of CSAC were larger than those of RHAC, which was attributed to a microporous structure of CSAC. In place of smaller volume of micropores, RHAC showed a larger volume of mesopores.

3. 2. Results of desulfurization tests

The breakthrough curves of RHAC and CSAC for BTs and DBTs in the fixed-bed flow tests are shown in **Figure 3**. The concentrations of BTs and DBTs in the first effluent kerosene treated by RHAC were respectively 6.4 and 0.5 mass ppm-S, while those by CSAC were respectively 6.9 and 0.4 mass ppm-S. BTs concentration of RHAC was maintained to be ~7 mass ppm-S at >60 min. That of CSAC was also maintained to be ~8 mass ppm-S, which was higher than that of RHAC. DBTs concentrations of both the samples were found to increase with the treated kerosene. DBTs concentration of CSAC was lower than that of RHAC.

Table 3 shows the adsorption capacities of BTs and DBTs in unit mass and volume at the time of 480 min. The adsorption capacity in unit volume was calculated using the data of storage density. Larger adsorption capacities in unit mass of both BTs and DBTs were observed on RHAC than on CSAC. The data of storage density clearly indicates that CSAC was denser than RHAC. Owing to the higher storage density, a larger adsorption capacity of DBTs in unit volume appeared on CSAC than on RHAC.

The adsorption isotherms of RHAC and CSAC for BTs and DBTs in the batch-mode desulfurization tests are shown in **Figure 3**. At the lower equilibrium concentration of DBTs (<0.2 mass ppm-S), RHAC and CSAC showed a similar level of DBTs adsorption capacity. At the higher

concentration of DBTs, a larger capacity was observed on CSAC than on RHAC, which was more pronounced in volume basis. For the BTs adsorption, RHAC showed a larger adsorption capacity at any concentration in both mass and volume basis. The adsorption isotherms in volume basis are consistent with the result of the fixed-bed flow tests.

Table 3. Adsorption capacity of BTs and DBTs on RHAC and CSAC at the time of 480 min in the fixed-bed flow tests.

	Sample	BTs	DBTs
Adsorption capacity in unit mass (mg-S/g-Ads)	RHAC	0.094	0.147
	CSAC	0.010	0.123
Storage density (g/cm ³)	RHAC	0.357	
	CSAC	0.514	
Adsorption capacity in unit volume (mg-S/cm ³ -Ads)	RHAC	0.034	0.052
	CSAC	0.005	0.063

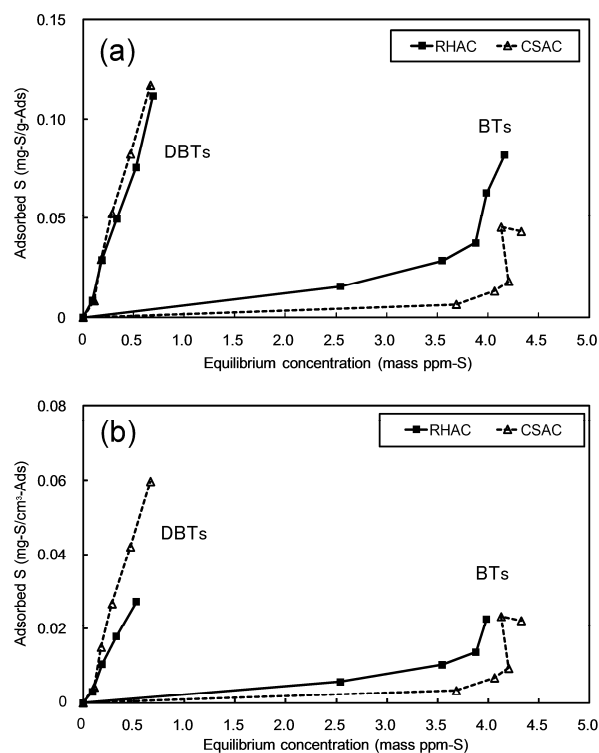


Figure 3. Adsorption isotherms of RHAC and CSAC for BTs and DBTs in batch adsorptive desulfurization tests with the use of commercial kerosene produced in 2007. (a) mass basis, (b) volume basis.

3. 3. Adsorptive desulfurization using biomass-derived ACs

The mechanisms have been proposed to explain the adsorption of organic aromatic compounds on ACs. One mechanism is the dispersion interaction mechanism including the π -electron overlap between the adsorbate and the graphene layers [21]. The mechanism of DBTs adsorption on

a catalyst was studied by Meille et al [22]. They pointed out that π electrons in the aromatic rings participate in the DBTs adsorption mechanism. DBTs include two aromatic rings and BTs include one aromatic ring, indicating that higher affinity with the ACs was expected on DBTs than on BTs. Pore-filling is also major mechanism. Ania et al showed that the volume of micropores with a width of <0.7 nm (defined as ultramicropores in the present study) governed the amount of DBT adsorbed in n-hexane, and the adsorption capacity was linearly related to the volume of these pores [12]. The size of 4,6-DMDBT molecule was reported to be 0.63 nm [11]. DBTs with a planar structure can enter slit-shaped ultramicropores. The interaction between π electrons on graphene sheets with slit-shaped pores in ACs and π electrons in DBTs further promotes entry of DBTs parallel to the wall surface of ultramicropores. Therefore, the predominant adsorption sites of DBTs in ACs are deemed to be ultramicropores. Kim et al stated that, for DBT and 4,6-DMDBT, methyl group at the aromatic ring enhances the negative electrostatic potential on the two sides of the molecular plane because methyl group is an electron donor to the aromatic rings [23]. The increased electrostatic potential is likely to enhance the π - π interaction between the graphene sheets in ultramicropore and the aromatic rings of BTs and DBTs. The mechanisms of the π - π interaction and the ultramicropore-filling are consistent with the higher-selectivity of RHAC and CSAC for DBTs than for BTs.

A higher-selectivity for DBTs and a lower-selectivity for BTs were observed on CSAC in the fixed-bed flow and the batch adsorption desulfurization tests. The compositional analysis revealed that much higher carbon content was observed on CSAC than on RHAC. The higher carbon content is likely to enhance the π - π interaction between the graphene sheets and the aromatic rings. DBTs have a stronger π - π interaction resulting from more aromatic rings and alkyl-substitution, supporting the higher-selectivity of CSAC for DBTs.

In addition to this, despite the lower carbon content and the smaller volume of ultramicropores, RHAC showed a larger BTs adsorption capacity and an acceptable DBTs adsorption capacity when compared with CSAC. Ania et al mentioned that mesopores in ACs controlled the kinetics of the DBT adsorption process [12]. Kumagai et al stated that, at low sulfur content ($<$ a few mass ppm-S), the DBTs adsorption sites in ultramicropores might not be fully filled. In such the condition, mesopores play a role of pathways to efficiently lead DBTs into ultramicropores, and the volume of mesopore affects the DBTs adsorption capacity [15]. The textural analysis indicated that RHAC had 3-fold larger mesopore volumes. It is supposed that a larger volume of mesopore in RHAC compensated for the reduced carbon content and ultramicropore volume.

4 CONCLUSIONS

Results of the fixed-bed flow tests and batch-mode adsorption tests showed that RHAC and CSAC were useful to remove aromatic sulfur compounds from kerosene. RHAC showed a lower selectivity for DBTs and a higher selectivity for BTs than CSAC. A larger adsorption capacity of DBTs in volume basis was observed on CSAC, which was attributed to its higher carbon content and larger volume of ultramicropores. Although RHAC had lower carbon content and smaller volume of ultramicropores, a larger adsorption capacity of BTs and acceptable adsorption capacity of DBTs in volume basis appeared on RHAC. This was explained by a larger volume of mesopores contributing to efficient transportation of BTs and DBTs towards their adsorption sites of ultramicropores.

Acknowledgement—This research was supported in part by the Industrial Technology Research Grant Program in 2006 of the New Energy and Industrial Technology Development Organization (NEDO) of Japan.

References

- [1] Song C, Ma X. New design approaches to ultra-clean diesel fuels by deep desulfurization and deep dearomatization, *Appl Catal B-Environ* 2003;41:207-38.
- [2] Macaud M, Milenkovic A, Schulz E, Lemaire M, Vrinat M. Hydrodesulfurization of alkylidibenzothiophenes: evidence of highly unreactive aromatic sulfur compounds. *J Catal* 2000;193:255-63.
- [3] Mochida I, Sakanishi K, Ma X, Nagao S, Isoda T. Deep hydrodesulfurization of diesel fuel: design of reduction process and catalysts. *Catal Today* 1996;29:185-9.
- [4] Farag H, Whitehurst DD, Sakanishi K, Mochida I. Carbon versus alumina as a support for Co-Mo catalysts reactivity towards HDS of dibenzothiophenes and diesel fuel. *Catal Today* 1999;50:9-17.
- [5] Sakanishi K, Nagamatsu T, Mochida I, Whitehurst DD. Hydrodesulfurization kinetics and mechanism of 4,6-dimethyldibenzothiophene over NiMo catalyst supported on carbon. *J Mol Catal A-Chem* 2000;155:101-9.
- [6] Kabe T, Ishihara A, Zhang Q. Deep desulfurization of light oil. Part 2: hydrodesulfurization of dibenzothiophene, 4-methyldibenzothiophene 4, 6- dimethyldibenzothiophene. *Appl Catal A-Gen* 1993;97:L1-9.
- [7] Bataille F, Lemberton JL, Michaud P, Perot G, Vrinat M, Lemaire M, Schulz E, Breyse M, Kasztelan S. Alkylidibenzothiophenes hydrodesulfurization-promoter effects, reactivity, and reaction mechanism. *J Catal* 2000;191:409-22.
- [8] Jayne D, Zhang Y, Haji S, Erkey C. Dynamics of removal of organosulfur compounds from diesel by adsorption of carbon aerogels for fuel cell applications. *Int J Hydrogen Energ* 2005;30:1287-93.
- [9] Ma X, Sun L, Song C. A new approach to deep desulfurization of gasoline, diesel and jet fuel by selective adsorption for ultra-clean fuels and for fuel cell applications. *Catal Today* 2002;77:107-16.
- [10] Sano Y, Choi KH, Korai Y, Mochida I. Adsorptive removal of sulfur and nitrogen species from a straight run gas oil over activated carbons for its deep hydrodesulfurization. *Appl Catal B-Env* 2004;49:219-25.
- [11] Zhou A, Xiaoling M, Song C. Liquid-phase adsorption of multi-ring thiophenic sulfur compounds on carbon materials with different surface properties, *J Phys Chem B* 2006;110:4699-707.
- [12] Ania CO, Bandosz TJ. Importance of structural and chemical heterogeneity of activated carbon surfaces for adsorption of dibenzothiophene. *Langmuir* 2005;21:7752-59.
- [13] Alhamed YA, Bamufleh HS. Sulfur removal from model diesel fuel using granular activated carbon from dates' stone activated by $ZnCl_2$. *Fuel* 2009;88:87-94.
- [14] Ania CO, Bandosz TJ. Metal-loaded polystyrene-based activated carbon as dibenzothiophene removal media via reactive adsorption. *Carbon* 2006;44:2404-12.
- [15] Kumagai S, Shimizu Y, Toida Y, Enda Y. Removal of dibenzothiophenes in kerosene by adsorption on rice husk activated carbon. *Fuel* 2009;88:1975-82.
- [16] Ishizawa H, Sasaki J, Kumagai S, Takeda K, Toida Y. Micro and mesoporous molded activated carbon made from rice husk and beet sugar. *Carbon 2008 proceedings (CD-ROM)*, 2008;P0046:6 pages.
- [17] International Organization for Standardization, ISO/DIS 9277, Determination of the specific surface area of solids by gas adsorption - BET method, 2008.
- [18] El-Sayed Y, Bandosz TJ. Acetaldehyde adsorption on nitrogen-containing activated carbons. *Langmuir* 2002;18:3213-8.
- [19] International Organization for Standardization, ISO 15901-3, Pore size distribution and porosity of solid materials by mercury porosimetry and gas adsorption - Part 3: Analysis of micropores by gas adsorption, 2007.
- [20] Zhou A, Ma X, Song C. Effects of oxidative modification of carbon surface on the adsorption of sulfur compounds in diesel fuel. *Appl Catal B:Environ* 2009;87:190-9.
- [21] Sing KSW, Everett DH, Haul RAW, Moscou L, Pierotti RA, Rouquerol J, Siemieniewska T. Reporting physisorption data for gas/solid systems. *Pure Appl Chem* 1985;57:603-19.
- [22] Meille V, Schulz E, Lemaire M, Vrinat M. Hydrodesulfurization of 4-methyl-dibenzothiophene: a detailed mechanistic study. *Appl Catal A-Gen* 1999;187:179-86.
- [23] Kim JH, Ma X, Zhou A, Song C. Ultra-deep desulfurization and denitrogenation of diesel fuel by selective adsorption over three different adsorbents: A study on adsorptive selectivity and mechanism. *Catal Today* 2006;11:74-83.

Synthesis and Properties of Poly(arylene ether) by Self-Polycondensation of Novel AB Type Monomer

Takuya Kai and Mitsutoshi Jikei*

Department of Engineering in Applied Chemistry, Akita University,
1-1, Tegatagakuen-machi, Akita-shi, Akita 010-8502, Japan
mjikei@gipc.akita-u.ac.jp

Abstract: Poly(arylene ether)s, such as poly(arylene ether sulfone)s and poly(arylene ether ketone)s, are important high performance engineering plastic and are used in electronics and biomedical applications. Commercially available poly(arylene ether)s have been prepared by polycondensation of two bi-functional monomers which are abbreviated by A-A and B-B monomers respectively from structural view point. In this work, self-polycondensation of a novel AB type monomer, 4-(4-hydroxyphenoxy)-4'-chlorodiphenylsulfone, was carried out in aprotic polar solvents at 160°C via nucleophilic aromatic substitution. GPC and viscosity measurements indicated that the polymerization in N,N-dimethylacetamide (DMAc) gave the polymer with high molecular weight up to 10^5 . Glass transition temperature determined by DSC was 208°C which is slightly higher than commercially available polysulfone (195°C) prepared from bisphenol A and 4,4'-dichlorodiphenylsulfone. The tensile tests suggest that the modulus and elongation at break are comparable with the film of commercially available polysulfone.

Key words: Poly(arylene ether), self-polycondensation, AB type monomer

1 INTRODUCTION

Poly(arylene ether)s, such as poly(arylene ether sulfone)s and poly(arylene ether ketone)s, are important engineering plastics which are used in electronics, mechanics, automobiles, coatings and biomedical applications. [1] All of the commercially available poly(arylene ether)s are prepared from the polycondensation of two bi-functional monomers which are abbreviated by A_2 and B_2 monomers. In order to prepare the polymers with high molecular weight, the strict control of the molar ratio of A and B functional groups is required, which often involves the thorough purification of monomers and other chemicals. [2] The other pathway to prepare condensation polymers is the self-polycondensation of AB type monomers. Since the A and B functional groups are connected in the same molecule, the molar ratio of A and B is automatically set to be 1. In addition, all of the propagating molecules have one A and one B functions. The defined end functions can be useful for the preparation of block copolymers and the reaction with other components.

In this paper, we report the preparation and self-polycondensation of a novel AB type monomer, 4-(4-hydroxyphenoxy)-4'-chlorodiphenylsulfone, to prepare poly(phenylene ether ether sulfone). Structure of the monomer and the resulting polymers was confirmed by spectroscopic measurements. Thermal and mechanical properties of the resulting polymers were also evaluated.

2 EXPERIMENTS

2.1 Materials

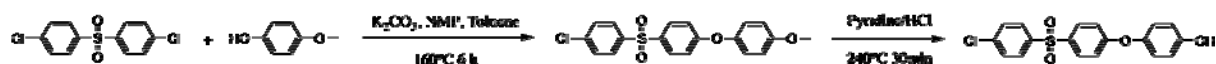
4,4'-Dichlorodiphenylsulfone, p-methoxyphenol and pyridine hydrochloride were purchased from Kanto

Chemical Co. Ltd. and used without further purification. N-Methylpyrrolidinone (NMP), dimethylacetamide (DMAc) and dimethylformamide (DMF) were purchased from Sigma-Aldrich Japan Co. and used without further purification. Other reagents and solvents were purchased from Kanto Chemical Co. Ltd. and used without further purification.

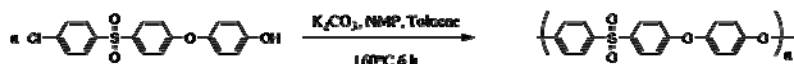
2.2 Preparation of the AB type monomer

In a three-necked flask equipped with a nitrogen inlet, a Dean-Stark trap and a condenser, 4,4'-dichlorodiphenylsulfone (7.67 g, 26.7 mmol), p-methoxyphenol (3.317 g, 26.7 mmol), potassium carbonate (4.62 g, 33.4 mmol) were charged. NMP (100 mL) and toluene (20 mL) were added to the flask and the mixture was heated at 160°C for 6 h. Water generated during the reaction was azeotropically distilled off from the mixture in the initial 2 h. After the heating step at 160°C, NMP was removed by reduced distillation. The residue was dissolved in chloroform and the chloroform solution was washed with water. The chloroform solution was dehydrated with sodium sulfate and the solvent was removed using a rotary evaporator. The residue was heated at 240°C under reduced pressure for 24 h. The crude product was purified by a column chromatography in chloroform/hexane (2/1). The yield of 4-(4-methoxyphenoxy)-4'-chlorodiphenylsulfone was 46 %.

In a flask equipped with a condenser, 4-(4-methoxyphenoxy)-4'-chlorodiphenylsulfone (5.00 g, 13.3 mmol) and pyridine hydrochloride (11.13 g, 96.3 mmol) were charged. The mixture was heated at 240°C for 1 h. After cooling, the mixture was dissolved in chloroform



Scheme 1



Scheme 2

and the chloroform solution was washed with water. After evaporation, the crude product was purified by a column chromatography in chloroform/ethyl acetate (19/1). The yield of 4-(4-hydroxyphenoxy)-4'-chlorodiphenylsulfone was 95 %.

2.3 Self-Polycondensation

In a three-necked flask equipped with a nitrogen inlet, a Dean-Stark trap and a condenser, 4-(4-hydroxyphenoxy)-4'-chlorodiphenylsulfone (0.50 g, 1.39 mmol) and potassium carbonate (0.24 g, 1.73 mmol) were charged. NMP (5 mL) and toluene (1 mL) were added to the flask and the mixture was heated at 160°C for 6 h. Water generated during the reaction was azeotropically distilled off from the mixture in the initial 2 h. After the heating step at 160°C, the mixture was poured into water (100 mL). The precipitate was recovered by filtration and dried in vacuo at 150°C for 5 h.

2.4 Measurements

NMR measurements were carried out using a Varian Mercury 300 NMR spectrometer. IR spectra were recorded using a Perkin Elmer Spectrum 2000 spectrometer. DSC and TG/DTA measurements were carried out using a Rigaku Thermoplus DSC8230 and TG8120, respectively. Gel permeation chromatography (GPC) measurements were carried out in DMF containing LiBr (0.01 mol/L) as an eluent. Polystyrene-divinylbenzene columns (Shodex KD-806M x 2 and KD-802) were used for separation. A UV detector (JASCO 875-UV) was set at 268 nm and the molecular weight was calculated on the basis of polystyrene standards. Inherent viscosity was measured at a concentration of 0.5 g/dL in NMP at 30°C.

3 RESULTS and DISCUSSION

A novel AB type monomer which contains one hydroxy and one chloride group was prepared from 4,4'-dichlorodiphenylsulfone and p-methoxyphenol as starting materials (Scheme 1). The first coupling reaction was carried out with a feed molar ratio of 1:1. The crude product contained unreacted, mono-substituted and di-substituted diphenylsulfones. Most of the unreacted diphenylsulfone was removed by heating the crude product at 240°C in vacuo. The column chromatography in chloroform/hexane mixture gave the purified 4-(4-methoxyphenoxy)-4'-chlorodiphenylsulfone in 33-46% yield. The methoxy group in 4-(4-methoxyphenoxy)-4'-chlorodiphenylsulfone was converted to the hydroxy group by heating the methoxy product with pyridine hydrochloride at 240°C. The structure of the 4-(4-hydroxyphenoxy)-4'-chlorodiphenylsulfone was confirmed by ¹H, ¹³C NMR, IR and elemental analysis.

Figure 1a shows the ¹H NMR spectrum of the 4-(4-hydroxyphenoxy)-4'-chlorodiphenylsulfone. A strong singlet peak at 9.5 ppm was attributed to the hydroxy proton. The peak at 3.8 ppm attributed to the methoxy protons completely disappeared. The peaks in aromatic region were assigned to the protons in the proposed structure. The integration ratio of the peaks also supported the assignment. In the ¹³C NMR spectrum, 12 peaks were observed from 116 to 163 ppm, which were assigned to each carbon of 4-(4-hydroxyphenoxy)-4'-chlorodiphenylsulfone. IR and elemental analysis also supported the formation of the AB type monomer.

Self-polycondensation of the AB monomer was carried out via nucleophilic substitution in aprotic polar solvents, as shown in Scheme 2. The resulting polymer was isolated by pouring the reaction mixture in water. Figure 1b shows the ¹H NMR spectrum of the polymer prepared in DMAc. The peaks at 9.5 and 7.7 ppm in Figure 1a which are attributed to the hydroxy proton and the protons ortho to the chloride group disappeared in Figure 1b. The disappearance of the peaks suggests that the molecular weight of the product is so high that the terminal groups are invisible in the ¹H NMR measurement. In the ¹³C NMR spectra, 6 peaks were observed from 117 to 161 ppm. Both ¹H and ¹³C NMR spectra indicated that the self-polycondensation proceeded efficiently to form the polymer with highly symmetric structure. Table 1 shows the results of the self-polycondensation of the AB monomer in various solvents. The polymer with the highest inherent viscosity was obtained by the polymerization in DMAc. The inherent viscosity of the polymer prepared in DMF or NMP was

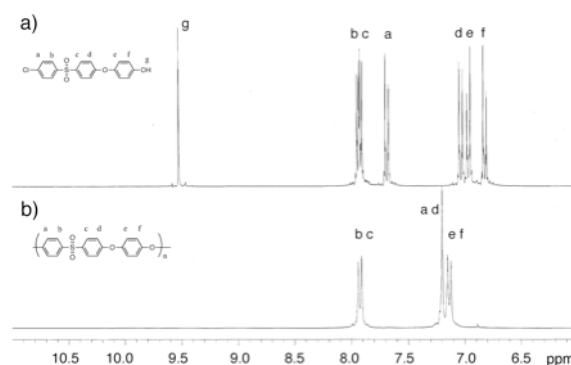


Figure 1. ¹H NMR spectra of the AB monomer (a) and the resulting polymer (b)

lower than that prepared in DMAc. The isolated yield of the polymer prepared in DMSO was much lower in comparison

Table 1. Polymerization of the AB monomer in various solvents.^{a)}

Solvent	Yield (%)	η_{inh} (dL/g) ^{b)}
NMP	100	0.43
DMAc	96	0.80
DMF	85	0.33
DMSO	54	0.32

^{a)} polymerization at 160°C for 6 h.

^{b)} measured in NMP at 30°C at a concentration of 0.5 g/dL.

Table 2. Thermal and mechanical properties of the resulting polymer.

Polymer	T_g (°C)	T_d (°C) ^{a)}	Tensile modulus (GPa)	Elongation at break (%)
this work ^{b)}	208	505	2.32	5.1
polysulfone ^{c)}	195	487	2.33	5.1

^{a)} the temperature at the weight loss of 5 %.

^{b)} prepared in DMAc, $\eta_{inh} = 0.80$ (dL/g).

^{c)} purchased from Sigma-Aldrich Co., $\eta_{inh} = 0.47$ (dL/g)

with the polymerization in the amide solvents. The amount of the solvents also influenced the polymerization. The polymerization in 8 mL of DMAc for 1.0 g of the monomer gave the polymer in high yield with the inherent viscosity in the range 0.8-1.0 dL/g. The weight average or number average molecular weight and its distribution of the polymer ($\eta_{inh} = 0.80$ (dL/g)) was 1.72×10^5 , 2.75×10^4 and 6.24, respectively. The GPC curve showed the shoulder peak in the low-molecular weight region, which resulted in the large molecular weight distribution.

The resulting polymer was soluble in chloroform, NMP, DMF, DMAc and DMSO. Thermal and mechanical properties of the polymer are listed in Table 2. Glass transition temperature of the resulting polymer was higher

than that of commercially available polysulfone derived from bisphenol A and 4,4'-dichlorodiphenylsulfone. The temperature of the weight loss of 5 % was also higher than that of the polysulfone. Both of T_g and T_d indicate that the polymer prepared in this work has slightly better thermal stability in comparison with the commercially available polysulfone. Tensile tests were carried out to evaluate the mechanical properties of the polymers. Both tensile modulus and the elongation at break of the polymer prepared in DMAc were comparable with those of the commercially available polysulfone.

4 CONCLUSION

A novel AB type monomer, 4-(4-hydroxyphenoxy)-4'-chlorodiphenylsulfone, was prepared from 4,4'-dichlorodiphenylsulfone and p-methoxyphenol. Self-polycondensation of the AB monomer was successfully carried out in aprotic polar solvents. The polymer prepared in DMAc has an inherent viscosity of 0.8 dL/g. GPC measurement suggested the formation of the high-molecular-weight polymer with broad molecular weight distribution. Thermal stability of the polymer was slightly better than the commercially available polysulfone. Mechanical properties evaluated by the tensile tests were comparable with those of the polysulfone.

Defined end functional groups (A and B) of the polymer prepared from AB type monomers can be used as reaction sites to prepare block copolymers. The study on the preparation of the block copolymers from this AB and other AB or AB₂ type monomers is in progress.

5 REFERENCES

- [1] Cotter R.J 1995A *Handbook of Polyarylethers* Gordon and Breach Science Publishers S.A.
- [2] Odian G 1991 *Principles of Polymerization Third Ed.* Wiley Interscience

Cutting Performance of Micro Saw Wire Bonded with Diamond Grains Using Metal Solder

Osamu Kamiya*, Yasuyuki Miyano**, Mamoru Takahashi*,
Hiroshi Kawase***, Kazuya Sekiguchi***, Yuichi Oga***, Minoru Suto****

*Department of Mechanical Engineering, Faculty of Engineering and Resource Science,
Akita University, 1-1, Tegata-Gakuen-Cho, Akita, 010-8502 Japan

**Faculty of Education and Human Studies, Akita University, Japan

***Graduate School of Engineering and Resource Science, Akita University, Japan

**** Diwa Industry Corporation, 58-4, Kurokawa-aza-Hiramori, Nikaho, 018-0302, Japan

kamiya@ipc.akita-u.ac.jp

Abstract: The cutting performance of the saw wires that are bonded with diamond grains using active metal solder has been studied. Based on this study, a new type of diamond grains bonded micro cutting saw wire which is capable of cutting Si crystals has been developed.

In conventional cutting of a Si crystal or hard material, a slurry containing diamond grains is poured into the cutting region. The slurry with diamond grains is consumed and contaminates drain. In order to prevent pollution, we have developed an environmentally friendly micro cutting wire to which the diamond grains are bonded directly by using metal solder. We call it AD wire, and the wire is capable of cutting the work pieces without any slurry. The performance in terms of cutting speed of AD wire is also significantly superior to those of wires made using the slurry type method.

In our AD process, diamond grains are bonded strongly to a tungsten wire, by the use of a specially developed bronze solder. These grains do not detach from the wire during cutting. We demonstrate using an application example that the new wire can cut Si crystals and can be widely used as a cutting wire with a long life.

Key words: Diamond grained saw wire, Metal bond, Solder, Cutting tool

1 INTRODUCTION

In the conventional micro-cutting process using a wire-saw for machining precision parts and cutting silicon wafers, a slurry containing diamond grains is used. Slurry loss is a major cost of the process, and the diamond grains and debris from cutting are the source of water contamination.

The purpose of this research is to develop a new type of wire saw bonded directly with diamond grains by using a metal solder. In order to develop such a micro wire saw, we used a special solder that contained a metallic compound¹⁻³⁾. In this paper, we demonstrate that using this solder, diamond grains can be bonded to tungsten wires with a good bonding strength. We also demonstrate that the diamond grained saw wire performs superior compared to other commercial cutting wires.

2 MATERIALS AND BONDING PROCESS

The grain sizes of the industrially made diamond grains used in this study were 10 to 20 μm . Tungsten wires were used as the core metal wires. The diameters of the tungsten wires were 60, 80 and 100 μm and the mechanical properties of the wire 80 μm in diameter are listed in Table 1. The metal solder

is a mixture of Cu-Sn bronze powder^{1,2)}, titanium hydride (TiH_2) and natural gel.

The first step of the bonding process was coating the wire with the mixture of solder powders and diamond grains. The coated wire was then heated to 1120 K inside a vacuum chamber with the vacuum level at 10^{-3} Pa for soldering to take place. Continuous wire bonding was made using a laboratory scale production system developed by us which is capable of continuously coating and heating/soldering thus producing the diamond grained saw wire over 1000 m in length

Table 1 Mechanical properties of a tungsten wire
80 μm in diameter.

Tensile Strength	2 GPa
Elongation	5%
Hardness	360 Hv

3 RESULTS AND DISCUSSION

3.1 Effect of TiH_2

We previously reported¹⁾ that diamond grains were able to bond to metals using a special solder which included a metal hydride, as shown in Fig.1. We evaluated a number of metal hydrides (TaH , NbH , HfH_2 , VH , ZrH_2 , TiH_2) and found that TiH_2 was most suitable for bonding diamond to metals. TiH_2 powder readily decomposes into elemental hydrogen and active Ti by heating. Hydrogen and Ti then react with oxides originally on the surface of the metal wire, allowing wetting of the surfaces of both diamond grains and the metal wire with the solder, as shown in Fig. 1.

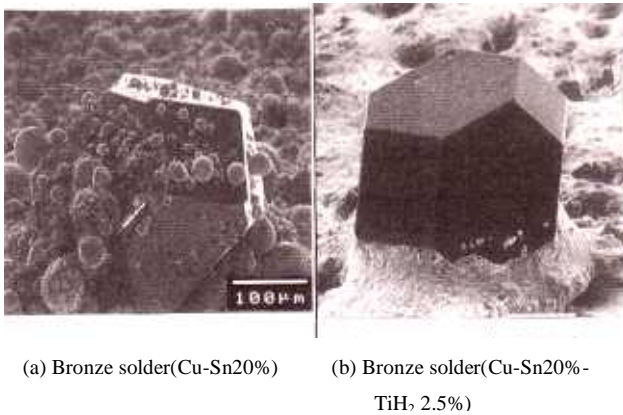


Fig.1 Effect of Titanium hydride on wet ability between Diamond surface and Bronze.

3.2 Production of saw wire

A SEM image of a typical diamond grained wire produced in the present study is shown in Figure 2(a). The diameter of the tungsten wire is 80 μm and the average size of the diamond grains is 20 μm, so that total diameter of the coated wire is about $(80 + 2 \times 20)$ 120 μm in this case. We compared it to two types of commercial cutting wires, as shown in Figure 2(b) and 2(c); wire (b) is a Ni plating type and wire (c) is a resin bonded type, respectively.

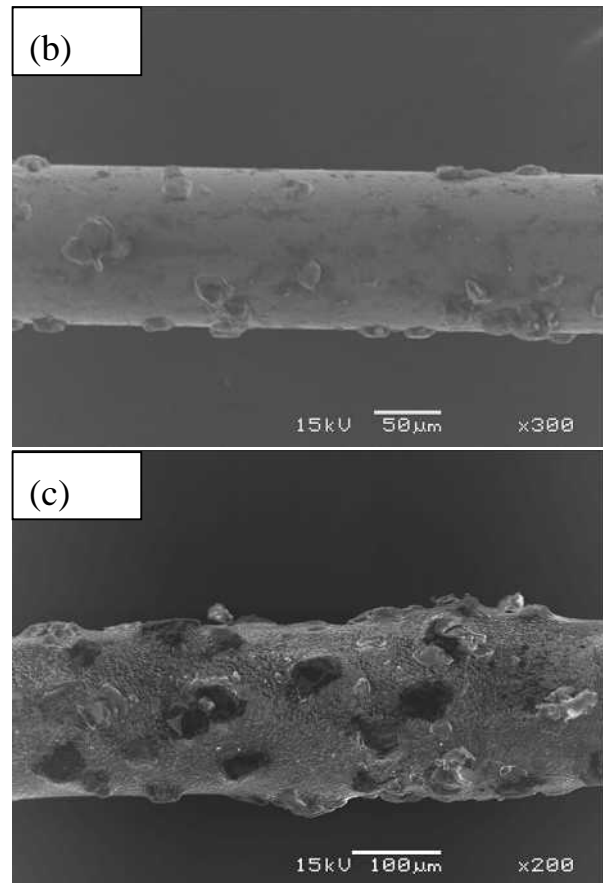
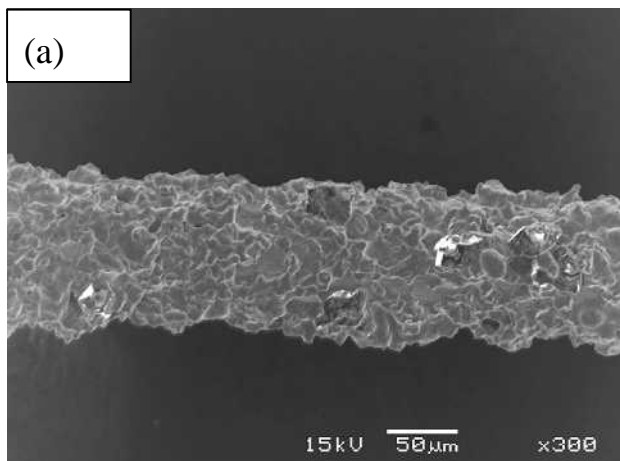


Fig.2 (a) AD saw wire type (A) 100 μm in diameter on which the diamond grain were fixed by metal solder by heating at 1120K. Commercial diamond fixed saw wires of (B) on electroplated type, and (c) a resin bonded type (C).



Fig.3 Cutting machine equipped with an AD wire.

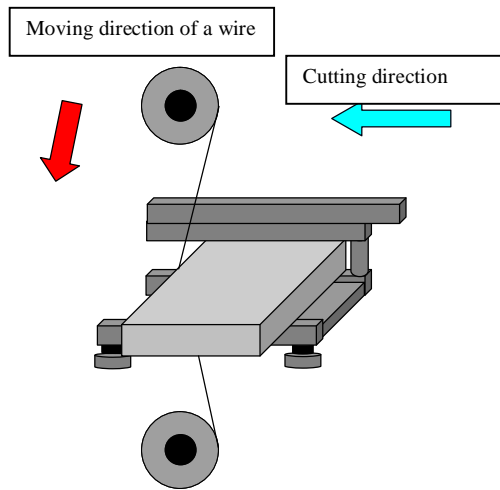


Fig.4 Mechanism of the cutting machine

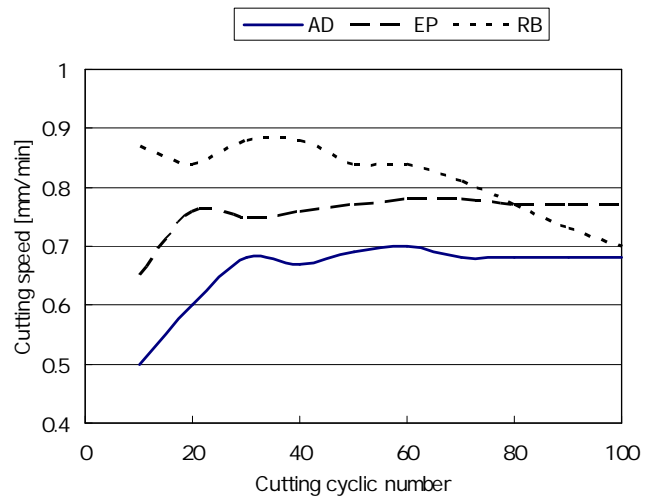


Fig.5 Cutting performance of three types of diamond saw wires. AD: our AD wire, EP: Electro plated type, RB: Resin bonded type wire.

3.3 Cutting performance

We developed an (original) cutting machine for evaluating the performance of cutting wires, as shown in Figure 3. Figure 4 indicates the mechanism of the machine. Wire speed, tension and cutting load were selected and the values are given in Table 2. The length of wire was set just at 50m and the wire was tested repeatedly until it broke.

Table 2 Conditions in cutting with an AD wire.

Wire speed [m/min]	100
Length of wire [m]	50
Tension [N]	5
Cutting load [N]	1

Table 3 Wire type used

Wire type	Diameter [mm]	Grain size [μ m]
AD wire	0.12	10-20
Electro plated, B	0.14	10-20
Resin bonded, C	0.25	40-60

Figure 5 shows the result of cutting performances of the three types of diamond grained saw wires with the wire and grain sizes listed in Table 3. Cutting tests were carried out on specimen of polycrystalline Si semiconductor for solar cells.

Figure 5 shows that the three different saw wires reached the same level of a cutting speed at 100 cycles. The value was

about 0.7 mm/min for a Si plate 10 mm in thickness. The diameters of the wire A, B and C were 120, 140, 250 μ m, respectively. Thus, if the cutting rate for each unit diameter is considered as the indication of cutting performance, AD wire performed the best. As shown in Figure 6, in AD wire, diamond particles were strongly bonded to the tungsten wire and did not easily detach from the solder during cutting. This is not the case for wire B where diamond grains were pulled out during cutting, as is evident in Figure 6.

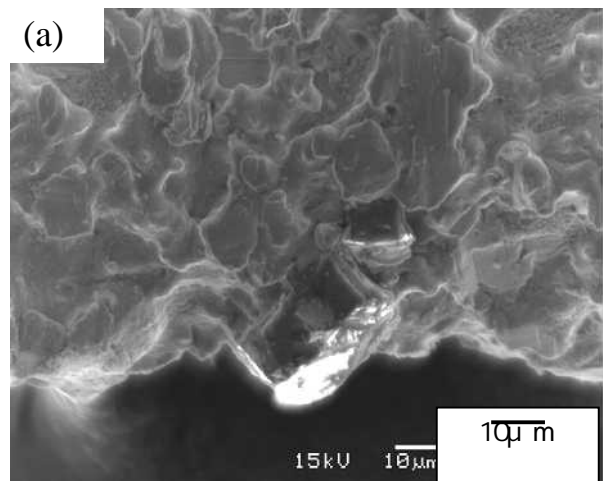


Fig.6 (a) Diamond grains remain in AD wire after cutting test. (b) Diamond grains are pull out from wire B during the cutting process of Si.

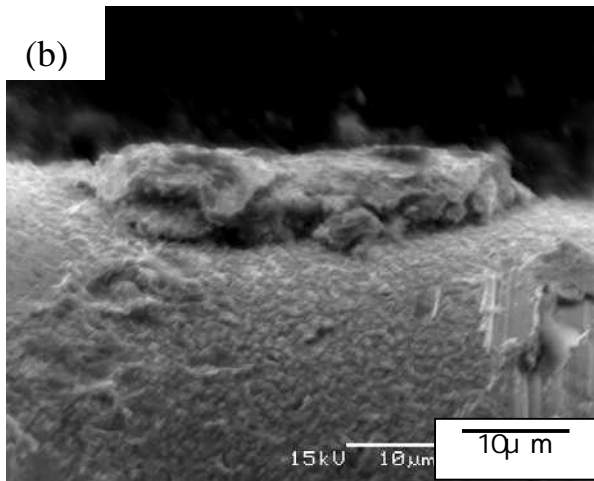


Fig.6 (a) Diamond grains remain in AD wire after cutting test. (b) Diamond grains are pull out from wire B during the cutting process of Si.

4 CONCLUTIONS

We have developed a process to bond diamond grains to a metal wire, producing saw wire. We have demonstrated using an application example of the new wire for cutting a Si crystal plate that:

- (1) Diamond grains can be bonded to a tungsten wire with the diameter as small as 0.08 mm, by the use of the specially developed bronze solder.
- (2) Cutting rate of the AD wire, based on the amount of cut per unit diameter, is higher than those of an electroplated type and a resin bonded type cutting wires.
- (3) Diamond grains bond strongly to the wires using the AD process and do not easily detach during cutting of Si plates.

Acknowledgement The author would like to express their thanks to Dr. Zhan Chen of Auckland University of Technology for his valuable suggestions.

References

- [1] Kamiya, O., Tsuji, D., Ashihara, F., Takahashi, M., Ishikawa, T., and Chen, Z.W., "Diamond and Metal Bonding by Active Solder for Micro-Cutting Wire", *International Journal of Modern Physics B.*, Vol.20, No25,26,27, pp3932-3937, (2006)
- [2] Kamiya, O., Ishikawa, T., Suzuki, K., Moritoki, H., and Kumagai, K., "Improvement of Laser Weld Joint between Sintered Diamond Tool and Steel", *Scientific and Technical Reports of the Mining College, Akita University*, 18(1997), p.37-44. (in Japanese with English abstract)
- [3] Ishikawa, T., Kida, T., Kamiya, O., and Moritoki, H., "Grinding Ability of Tungsten-Coated Diamond Composite Sintered Tool", *Transactions of JSME*, Vol.63, No.616(1997), p.2694-2700.(in Japanese with English abstract)

A Chemometrical Approach for Beer Discrimination by Near-infrared Spectroscopy

Hua Li^{*}, Masanori Kumagai^{**}, Kazuhiko Fujiwara^{*}, Ryoei Kikuchi^{*},
Noboru Yoshimura^{*}, Toshio Amano^{***}, Jinming Lin^{****} and Nobuaki Ogawa^{*}

^{*} Faculty of Engineering and Resource Science, Akita University,
Tegata Gakuencho, Akita 010-8502, Japan

^{**} Institute for Food and Brewing, Akita Prefectural Agriculture, Forestry and Fisheries Research
Center, Arayamachi, Akita 010-1623, Japan

^{***} OPT Research, Inc., 5-1-3, Minami-Aoyama, Minato-ku, Tokyo 107-0062, Japan

^{****} Department of Chemistry, Tsinghua University, Beijing 100084, China.

ogawa@ipc.akita-u.ac.jp

Thirty-eight beers from different producing areas and/or makers were distinguished by principal component analysis (PCA) of the near infrared (NIR) spectra acquired by a portable NIR spectrometer. Classification of Akita beers: beers locally produced in Akita prefecture, Japan, from other famous brand beers could be successfully performed, especially when the PCA was calculated on the standard normal variate (SNV) spectra. The classification equations use information related to water and CH₂ absorption that reflected the differences in chemical composition of beers due to different production processes. In addition, the compositions of total polyphenol and total nitrogen were estimated from NIR spectra by multiple linear regression (MLR). This study showed that NIR spectroscopy is promising for beer quality evaluation, both for identifying multifarious beers including Akita beers using PCA and for rapid in-line quality control and inspection for beer production using the quantitative MLR analysis.

Keywords: near infrared spectroscopy, principal component analysis, multiple linear regression, distinction, beer

1. Introduction

The beer industry is one of the important sectors in the food industry. According to the statistical information [1], the total global consumption of beer in 2006 was 170.1 trillion liters. In the world beer industry, more than 90% of beers are produced from using bottom zymotechnics [2]. The flavor of beers is related to the production techniques and the raw material used. The alcohol and carbon dioxide content of beer are the result of the fermentation by an organic microorganism, *Saccharomyces cerevisiae*. Microzymes are crucial for beer

quality. In Japan, some of Akita's beer (which is produced in Akita Prefecture, Japan) are the first to adopt native crude *S. cerevisiae* and natural water which is rich in mineral substances. The *S. cerevisiae* used for Akita beers is different from that used for generally and commercially available beers in Japan. It is refined from natural plants, for example cherry blossom and beech etc. and contains proteins, vitamins, various amino acids and minerals. Therefore, the smell or taste of these beers has a natural fine aroma. For general brewhouses, the *S. cerevisiae* is filtrated as the final step and it

is not retained in the beer. However, some times Akita beer producers adopt top zymotechnics for Akita beers; the zymolytic time is shorter, the temperature is higher (20–25°C) and the *S. cerevisiae* is not filtrated out. The lactobacilli which remain in the Akita beer helps to assimilate food and can control absorbed superfluous calories. Therefore, a rapid, non-destructive and convenient method is needed to determinate the innate characters, specialties and composition of these beers. It is important not only to rapidly and exactly control the beer quality, but to find out the difference between Akita beers and general beers. The traditional instrumental analysis methods normally are complicated and time-consuming and, also, the instruments are very expensive [3]. Norris and his colleagues applied statistical technologies to analyses NIR spectra [4], which was a great development in the field of NIR spectroscopy. Early examples for applying the NIR technique to beer manufacturing include the determination of the alcohol content [5], β -glucan, malt extract, α acid of hops which is related to the ferment energy of quantitative analysis [6]. Marc Maudoux performed routine laboratory analyses on beers in European markets with an NIR spectrometer [7] using an off-line inspection with the samples exhausttreated [8]. Because of the relatively weak absorption of energy with NIR wavelengths, the rays penetrate into samples and can reveal valuable information. NIR could carry out rapid, non-destructive, simple qualitative and quantitative analysis for many materials, and has been widely used in analytical chemistry [9,10]. However, compared with the developments in the application of NIR technology, there is a need to better understand the NIR spectrum as a fundamental analytical chemistry technique.

Our research group has reported the influence of alcohol and chroma on the distinction of Japanese Sakes (rice wines)[11]. In this work, the local Akita beer was studied using a portable NIR spectrometer. It was easy to assign the absorption wavelengths by using the NIR contribution ratio spectrum (loading plots), which describes the correlation between NIR spectra and chemical analysis data. The findings from this research facilitated a discussion on different aspects in NIR spectra between local beers and other normal beers sold in the market.

2. Experimental

A portable NIR spectrometer (PlaScan-SH, Systems Engineering, Tokyo, Japan) equipped with an acoustooptical tunable filter (AOTF) was used for the analysis. The NIR diffuse transreflectance spectra [$\log(1/T)$] were obtained in the wavelength region 1200–2400 nm, at a resolution of wavelength of 1 nm to give 1200 data points at $20 \pm 1^\circ\text{C}$, and a white ceramic disk was used as a reference. Using the beer analysis methods of the American Society of Brewing Chemists (ASBC) [12] we determined seven indices: bitterness units, total polyphenol, total nitrogen, $[\text{H}^+]$, chroma, apparent extract and alcohol. We obtained 23 kinds of beer including low malt and nonalcoholic beer commonly sold in the market by four famous Japanese companies (Asahi Breweries Ltd, Kirin Brewery Ltd, Suntory Ltd, Sapporo Breweries Ltd) and 15 kinds of Akita beers produced by three Akita beer factories (Aquila Brauhaus Co. Ltd, Warabiza Co. Ltd, Toast Co. Ltd). Original spectra [$\log(1/T)$] and standard normal variate (SNV) spectra in the 1200–2400 nm wavelength region were subjected to data analysis. The spectra were subjected to principal component analysis (PCA) and multiple linear regression (MLR). The JUSE-StatWorks V3.5 software program [Union of Japanese Scientists and Engineers (JUSE), Tokyo, Japan] was used for the data analysis.

3. Results and Discussion

3.1 PCA

Figures 1(a) and 1(b) show the score plots of the first two principal components (PCs) for the 38 beers samples calculated from the seven quality indices measured conventionally and from NIR original spectra, respectively. By using the quality indices, it became obvious that the beers examined were clustered into three groups: the Akita beers, four famous brand beers and the low malt beers. The arrows are immanent vectors (postulated that the sum of each index quantity equal to one) and they show the contribution of each index. These data indicated that the contribution of the bitterness unit, total nitrogen, $[\text{H}^+]$ and apparent extract were high for PC1 while the contribution of total polyphenol was high for PC2. In Figure 1(b), the contribution of PC1 to the total variance of NIR spectra was 86.3%. This is very high and reveals the substantial changes in the spectra of the measured

beers. The segregation of Akita beers from the famous brand beers led us to the assumption that NIR spectra were carrying information related to production processes. Presumably, in a similar way to those illustrated in the PC score plots for quality indices, the PC scores calculated from spectra may also carry information related to the bitterness units, total nitrogen, $[H^+]$, apparent extract and total polyphenol. This means that the PCA of the NIR spectra could be used to replace conventional analyses.

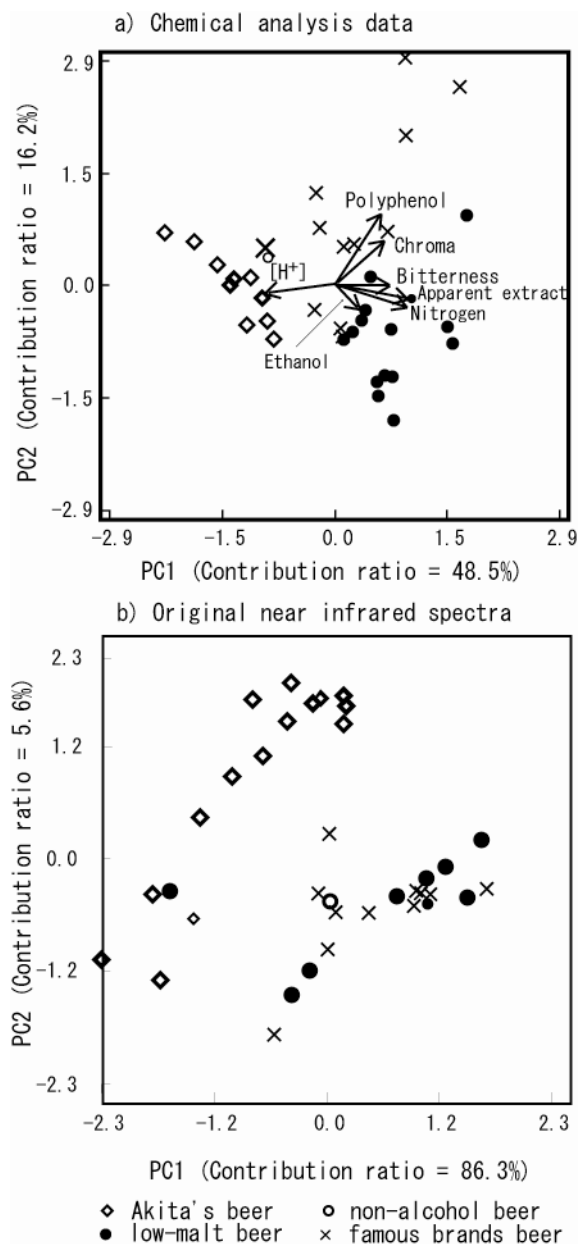


Figure 1 Score plots of PC1 versus PC2 for beer samples using (a) their quality indices measured by conventional methods and (b) their original near infrared spectra.

3.2 Quantitative analysis for quality indices

In addition to the classification, MLR has been used to develop calibration equations for the quality indices of the beers examined. Table 1 shows the calibration results using only three wavelengths selected from the original and the SNV spectra. The results indicate that the bitterness unit, total polyphenol, total nitrogen and alcohol could be predicted with fair accuracy, especially the results for the SNV spectra. It has been found that the wavelengths used for MLR calibrations for total polyphenol and total nitrogen selected from the SNV spectra were quite similar to those exhibited in the contribution rate spectra of PC2 and PC3 calculated from the same spectra. Thus there must be some relationship between the absorption of these quality indices and the ability of NIR spectroscopy to classify the beers. These results suggested that our technique can be used in the quality control of the beers on the production site, especially for total polyphenol and/or total nitrogen contents.

Our rapid and timely analyses can also be used for market research. One can also get feedback from the data during the development of new beer.

Table 1 Calibration and validation results for each parameter calculated by multiple linear regression (MLR).

Quality indices	Original spectra			SNV spectra		
	λ [nm]	R ²	SEC	λ [nm]	R ²	SEC
Bitterness	1929, 1980 2123	0.40	4.34	1256, 1307 2129	0.67	4.10
Total polyphenol	1467, 1701 2117	0.61	66.4	1455, 1997 2209	0.64	63.4
Total nitrogen	1415, 2209 2340	0.70	0.03	1923, 2209 2357	0.69	0.02
$[H^+]$	1233, 1838 2323	0.64	0.26	2123, 2209 2357	0.64	0.25
Beer colour	1347, 1364 1438	0.34	31.5	1444, 1450 2163	0.34	31.6
Apparent extract	1227, 1238 2363	0.52	0.97	1746, 2248 2363	0.53	0.96
Alcohol	1427, 1843 2266	0.54	0.66	1729, 1781 1832	0.76	0.47

SNV: Standard normal variate; R²: coefficient of determination; SEC: standard error of calibration; SEP: standard error of prediction.

4. Conclusions

This research has investigated beers using a portable near infrared (NIR) spectrometer and chemometrics. The difference in the beer production processes altered the quality indices of the beers and, therefore, contributed to the calculations of PC scores. The score plots of PC1 and PC2 calculated from original spectra that carried information related to the

bitterness units, total nitrogen, $[H^+]$, apparent extract and total polyphenol could discriminate the Akita beer from the common famous brand beers. The utilisation of SNV spectra could provide clearer discrimination results and interpretation, pointing out that the PCA of the NIR spectra could be used to replace conventional analysis. By using MLR, the composition of total polyphenol and total nitrogen can be predicted with fair accuracy. The system is useful for quality control of the beers on the production site. Our analysis can also be used for rapidly and timely market research, which will provide relevant feedback from data when developing new beer.

References

- [1] Y.Q. Cui, X.L. Dong and G.T. Zhou, *The Technique of Brewing about Miniature Beer*. Chemical Industry Press, Beijing, China (2008) (in Chinese).
- [2] D.L. Chen, *Production Technique of Beer*. Chemical Industry Press, Beijing, China (2005) (in Chinese).
- [3] G.S. Birth and K.H. Norris, "An instrument using light transmittance for nondestructive measurement of fruit maturity", *Food Technol.* 12, 592 (1958).
- [4] A.W. Brant, A.W. Otte and K.H. Norris, "Recommended standard for scoring and measuring opened egg quality", *Food Technol.* 5, 356 (1951).
- [5] A.G. Coventry and M.J. Hunston, "Application of nearinfrared spectroscopy to analysis of beer samples", *Cereal Food World* 29, 715 (1984).
- [6] C.F. McGuire, "Near-infrared reflectance estimates of malt extract", *Cereal Chem.* 59, 510 (1982).
- [7] M. Maudoux, S.H. Yan and S. Collin, "Quantitative analysis of alcohol, real extract, original gravity, nitrogen and polyphenols in beers using NIR Spectroscopy", *J. NearInfrared Spectrosc.* 6, A 363 (1998).
- [8] F.A. Inon, R. Llarío, S. Garrigues and M. Guardia, "Development of a PLS based method for the determination of the quality of beers by use of NIR: spectral ranges and sample introduction considerations", *Anal. Bioanal. Chem.* 382, 1549 (2005).
- [9] H.W. Siesler, "Introduction", in *Near-Infrared Spectroscopy: Principles, Instruments, Applications*, Ed by H.W. Siesler, Y. Ozaki, S. Kawata, and H.M. Heise. Wiley-VCH Verlag, Weinheim, Germany. 1-3 (2002).
- [10] D.A. Burns and E.W. Ciurczak, *Handbook of Near-Infrared Analysis*. Marcel Dekker, New York, USA (2001).
- [11] T. Sato, M. Kumagai, T. Amano and N. Ogawa, "Discrimination of Japanese sake using a portable nearinfrared spectrometer and chemometrics", *Bunseki Kagaku* 52(9), 653 (2003) (in Japanese).
- [12] *Methods of Analysis* (8th Edn). American Society of Brewing Chemists, St Paul, MN, USA (1992).

Application of Low Ground Vibration, Low Noise Fracturing
Method Using GANSIZER

Kenji MURATA , Yasuyuki Mochizuki and Yukio KATO

Nippon koki. Co., Ltd.2-1 Dobu, Nagasaka, Nishigo-mura,
Nishishirakawa-gun, Fukushima,961-8686, JAPAN

Kmurata@nippon-koki.co.jp

abstract : GANSIZER is non-explosive gas generant. GANSIZER is composed of thermit composition and compound containing crystallization water. Reaction of thermit composition generates high temperature and vaporizes crystallization water. Reaction of GANSIZER produces very rapidly high pressure, high temperature vapor without emitting shock wave. Ground vibration and noise generated by fracturing method using GANSIZER is considerably lower than those generated by controlled blasting.

We successfully applied low ground vibration, low noise fracturing method using GANSIZER to the excavation of deep big hole for bridge construction in close vicinity of Shinkansen rail line. We also applied fracturing method using GANSIZER to rock fracturing in close vicinity of houses.

Key word: Constraction Materials, Rock fracturing method, Lwo vibration and noise

Experimental Studies for The Possible Friction Stir Welding of High Nitrogen-containing Austenitic Stainless Steel

Yasuyuki Miyano¹, Hidetoshi Fujii², Sun Yufeng², Kouichi Ieko³,
Yasuyuki Katada⁴ and Osamu Kamiya³

1. Faculty of Educational Systems and Studies, Akita University, Japan

2. Joining and Welding Research Institute, Osaka University, Japan

3. Faculty of Mechanical Engineering, Akita University, Japan

4. National Institute for Materials Science, Japan

y.miyano@gipc.akita-u.ac.jp

Abstract: To develop the practical use of high nitrogen-containing austenitic stainless steels, the possible friction stir welding (FSW) of high nitrogen-containing stainless steels was examined. In this report, the butt-welding of 2 mm thick HNS plates was performed using a load-controlled FSW machine. Two types of welding tools were used in this study, namely, a Si₃N₄-based material and a WC-Co-based material. For the FSW with Si₃N₄, full-penetrated and defect-free butt welding joints were successfully produced. On the other hand, for the FSW with WC-Co, the tool was deformed and the stir zone did not completely reach the bottom sufficiently. The stir zone produced by the Si₃N₄ tool showed a Vicker's hardness higher than the base metal and showed a fine microstructure due to recrystallization. The yield strength and the tensile strength of the welds produced by the Si₃N₄ tool exceeded that of the base metal.

Key words: Electro-slag remelting methods, Friction stir welding, Butt-welding, Austenite, α formation

1. INTRODUCTION

Although high nitrogen-containing austenitic stainless steel (HNS) is known as a superior material, having high strength, high toughness, and high corrosion resistance, there are some problems to be solved, such as blowhole generation or nitride precipitation, caused by heat input during the welding process due to the high nitrogen content [1-6]. Based on such information, the application of a solid state joining process for HNS, which can be performed under its melting points, is significantly demanded [7, 8].

Friction stir welding (FSW), a new solid state welding process developed by TWI (The Welding Institute, England) in 1991 [9], is considered an effective technique. However, reliable FSW HNS joints and butt welding joints have not yet been successfully obtained [8].

In this study, FSW was applied to HNS under various welding conditions. To examine the effect of the FSW tool on

the HNS, the performances of two types of welding tools, a WC-Co-based material and a Si₃N₄-based material, were investigated. To determine the optimum conditions to create reliable HNS FSW joints, some welding parameters, i.e., the tool rotation speed, welding speed and the welding load, were examined.

2. EXPERIMENTAL PROCEDURE

2.1. Test materials

The material used in this study was 1 mass% nitrogen-containing austenitic stainless steel produced by pressurized electro-slag remelting methods (ESR) [10]. Its chemical composition was 23Cr-0Ni-1Mo-1N (mass %). The plates were 2mm thick, 30mm wide and 300mm long.

2.2. Welding conditions

Butt-welding experiments were performed using a load controlled FSW machine. Two types of welding tools, Si₃N₄ and WC-Co based materials were examined. A water-cooled

holder was installed and argon gas was employed to prevent oxidation of the plates. The conditions utilized in this study are listed in Table.1.

Table 1. FSW conditions applied in this experiment.

	Tool Materials	Rotation Speed (rpm)	Welding Speed (mm/min)
Condition A	Si ₃ N ₄	400	200
Condition B	WC-Co	400	100

2.3. Metallurgical inspections

The joints were evaluated on the basis of surface appearance, macrostructure and microstructure observation. The metallurgical inspections were performed on a cross section of the joint after polishing and etching with aqua regia.

2.4. Evaluation of joints properties

The mechanical properties were evaluated using the Vicker's hardness test and transverse tensile test. The hardness profiles of the transverse section of the joints were measured in the middle section of the welded plates with a load of 4.9N for 15s. The transverse tensile specimens were cut perpendicular to the welding directions, as shown in Fig.1 (a). Configuration of the tensile specimen is shown in Fig.1 (b). Before the test, the specimen was thoroughly mechanically finished to remove any ripples and flash. The tensile tests were carried out at room temperature at a crosshead speed of 1 mm/s. After the test, the fracture surfaces were examined by scanning electron microscopy (SEM). The crystal structures of the base metal and the stir zone were identified by XRD.

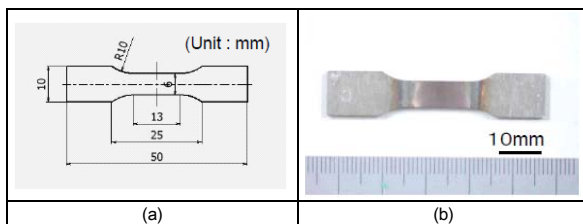


Figure 1. Configuration of transverse tensile specimen used in this study. (a) Specifications (b) Appearance

3. RESULT AND DISCUSSIONS

For the FSW joints produced under Condition A, defects, such as voids and cracks, were not observed on the surface. The top surfaces had a very smooth quality and there were almost no protrusions or depressions. On the other hand, for the joints under Condition B, tool deformations were observed during welding process, and the stir zone did not penetrate to the bottom.

The low magnification cross sections of the FSW joints under Condition A are shown in Fig. 2. The left and right sides of the weld center are consistent with the advancing and retreating sides, respectively. The stir zone is clearly observed around the weld center and thoroughly penetrated to the back sides. The presence of a high degree of continuity and no defects in the weld interior indicate the production of sound weld joints.

The optical microstructures of 3 regions (labeled A, B and C shown in Fig. 3) are presented in Fig. 3. Region A is located

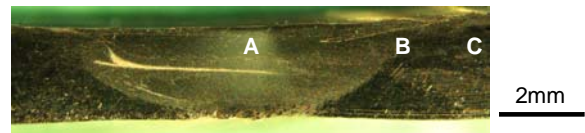


Figure 2. Cross section images of the friction stir welding joints of Condition A.

on the weld center, region B is on the border of the stir zone and the heat affected zone (HAZ), and region C is on the base metal. The average grain size of the base metal is estimated to be more than 100μm. On the other hand, the size of grain is extremely fine in the stir zone. This result would be due to recrystallization during the FSW process.

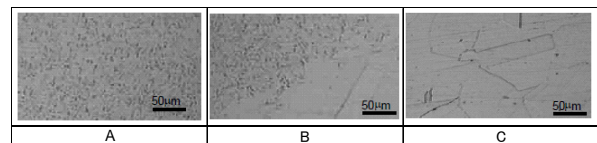


Figure 3. Optical microstructures of regions A, B and C shown in Figure 2.

The hardness profiles across the stir zones of the welded joints are shown in Fig. 4. The hardening of the stir zone in HNS during the FSW was also observed in this study [8]. The stir zone exhibits about a 1.5 times higher hardness than the base metal. No remarkable differences in hardening depending on the conditions were observed. A good relationship between the increase in hardness and the refinement of the grain were observed in this study.

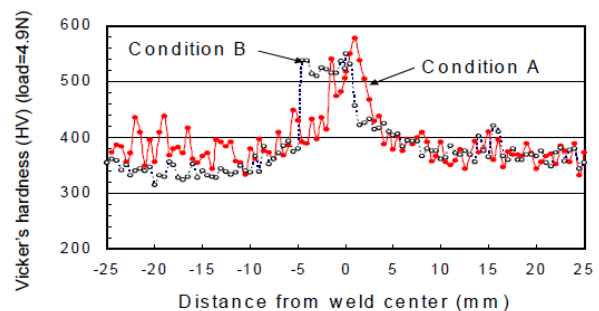


Figure 4. Hardness distribution of friction stir welding joints.

The stress and elongation relationship of welding products are shown in Fig. 5. Both welding products show higher strength than the base metals. The tensile strength and the yield strength of joints of Condition A show the highest values. However, the elongation of joints of Condition A is inferior to that of Condition B.

The SEM observations of the fracture surfaces of the weld joints and the base metal are shown in Fig. 6. The base metal shows a clear dimple pattern over the entire viewing field. Although fractures occurred in the HAZ in both Conditions A

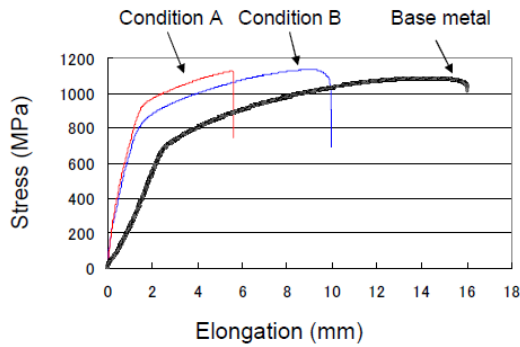


Figure 5. The stress and elongation relationship of HNS friction stir welding joints.

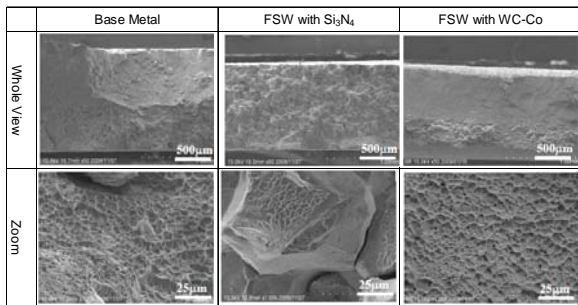


Figure 6. SEM images of the fracture surfaces of the base metal and the FSW joints.

and B, the fracture morphology is completely different. The fracture surface of the joints under Condition A shows a small dimple portion related to the fine grain, on the other hands that of Condition B shows the characteristic feature of brittle fracture failure. The difference in failure shown here is probably due to the α phase formation identified in Fig. 7.

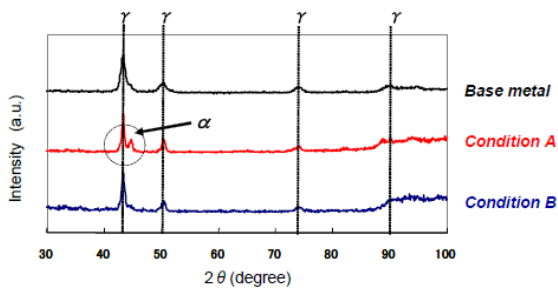


Figure 7. XRD patterns of the base metal and the fractured surface of FSW joints.

Fig. 8 shows typical changes in the temperatures of the work piece during the process. Thermocouples were embedded on the bottom surface at the center line [11], thus the heat input in the upper zone should be estimated to be higher value. In this case, the peak temperatures under Condition B showed a lower value than that of Condition A. Although the difference recorded here is small, it was suspected that the FSW under Condition B was performed in α formation zone shown in Fig.

9. This suggests that the heat input should exceed the α formation zone to produce sound HNS joints.

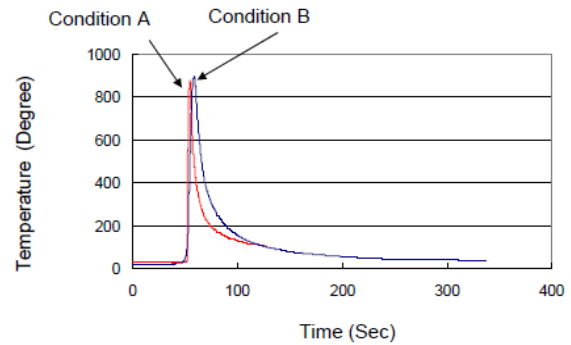


Figure 8. Temperature cycles for thermocouples located on the bottom surface.

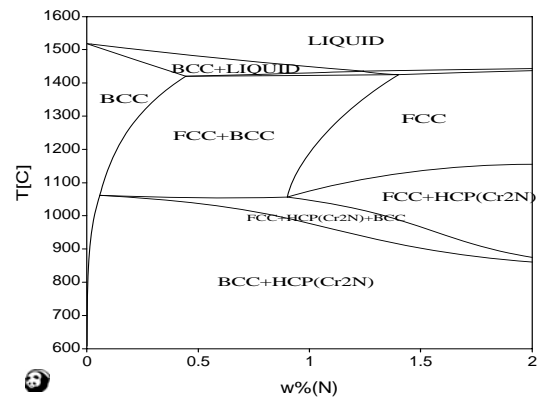


Figure 9. Thermo dynamics phase diagram of HNS (Fe-23Cr-1Mo-N) depending on nitrogen contents, calculated by the multi-component phase diagram calculation software: Pandat, Materials Design Technology Co., Ltd..

4. CONCLUSION

The friction stir welding to obtain butt-welding joints of 1 mass % nitrogen-containing austenitic stainless steel was successfully performed without welding defects and tool deformation utilizing Si_3N_4 under the condition involving the rotation speed of 400 rpm, the welding speed of 200mm/min. The stir zones consist of very fine grain structures and show an increase in the Vicker's hardness. These joints also show higher tensile strength and yield strength than the base metals. The present study shows that FSW is one of the efficient joining processes that can produce sound HNS weld joints.

Acknowledgements

The authors wish to thank Mr. M. Kato, Akita Industrial Research Institute, and Mr. R. Kato, Akita University, for their technical assistance. The financial supports from the Japanese

Ministry of Education, Science, Sports and Culture with a Grant-in-Aid for Young Scientists (Start-up, No.20860019-00) and a Grant-in-Aid for Scientific Research (B) (No.00247230) are gratefully acknowledged.

Reference

- [1] Kamiya, Z. W. Chen, Y. Kikuchi and T. Ohyoshi: Weldability Study of High Nitrogen Austenitic Stainless Steels Proceedings of Int. Conf. on AMDP2002, SD-file, Metal-paper 3-10. SD-file, Metal-paper 3-10, (2002).
- [2] Kamiya, Y. Kikuchi and Z. W. Chen., "Welding of High Nitrogen Stainless Steel and the Microstructure on Fracture Toughness of the welds", Proceeding of ICMR Akita, 215-220, (2001).
- [3] I. Woo, Y. Kikuchi., "Welderbility of High Nitrogen Stainless Steel", ISIJ International, 42-12: 1334-1343, (2002).
- [4] T. Ogawa, K. Hiraoka, Y. Katada, M. Sagara and C. Shiga., "Nitride Precipitation Behavior of High Nitrogen-bearing Stainless HAZ and its Corrosion Resistance: Study on Properties of Welded Joints for High Nitrogen-bearing Stainless Steel", Q. J. Japan Welding Soc., 20-1: 96-104, (2002).
- [5] T. Ogawa, K. Hiraoka, Y. Katada, M. Sagara S. Tsukamoto and C. Shiga., "Nitride Precipitation Behavior of High Nitrogen-bearing Stainless HAZ and its Corrosion Resistance: Study on Properties of Welded Joints for High Nitrogen-bearing Stainless Steel", Q. J. of Japan Welding Soc., 20-1: 107-113, (2002).
- [6] I. Woo, T. Horinouchi, Y. Miyano and Y. Kikuchi., " Role of precipitated Cr₂N on the HAZ impact toughness of High-nitrogen Ni-free stainless steel. J. Steel and Related Materials", 2: 187-196, (2004).
- [7] I. Woo, M. Aritoshi and Y. Kikuchi., "Metallurgical and Mechanical Properties of High Nitrogen Stainless Steel Friction Welding", ISIJ Intern., 42-4: 401-406, (2002).
- [8] S.H.C. Park, Y.S. Sato, H. Kokawa, K. Okamoto, S. Hirano and M. Inagaki., "Microstructure of Friction-Stir-Welded High Nitrogen Stainless Steel, Materials Science Forum", 539-543: 3757-3762, (2007).
- [9] W. M. Thomas, E. D. Nicholas, J. C. Needhman, M. G. Murch, P. Temple-Smith and C. J. Dawes., "International Patent Application PCT/GB92/02203 and GB Patent Application 9125978.8", UK Patent Office, London, Decwmbler 6, (1991).
- [10] W. Holzgruber., "Austrian Pat. No. 333.327", S12, (1974).
- [11] L. Cui, H. Fujii, N. Tsuji and K. Nogi., "Friction Stir Welding of a High Carbon Steel", Scripta Mater., 56: 637-640, (2007).

Heat flux of a transferred arc driven by AC magnetic field

N. Matsumoto, T. Yamamoto, M. Sugimoto, S. Kumagai and K. Takeda

Department of Machine Intelligence and Systems Engineering, Akita Prefectural University
84-4, Tsuchiya-aza-ebinokuchi, Yurihonjo, 015-0055, Akita Prefecture, JAPAN
kumagai@akita-pu.ac.jp

Abstract : Plasma arcs are widely used for welding, cutting, spraying and refining of molten metals, because of their high energy density. Characteristic property of the arc is concentration of heat flux in narrow area. However, for some applications of heating or melting metals over large area, wide arcs with expanded heat flux are often required. By applying transverse AC magnetic field to the arc, the authors have developed a wide heat source, where the arc oscillates back and forth at a high speed synchronized with applied field frequency.

Theoretical and experimental analyses revealed that the energy density of the arc deflected by DC transverse magnetic field reduced with the increase of the field flux density in previous work.

In present work, the authors consider the energy density profile of the expanded arc oscillated by AC magnetic field theoretically. The distribution of the heat flux can be controlled by adjusting a wave form of the electric current through the magnetic field coil.

Key Words: heat flux, transferred arc, magnetic field, arc root

1 INTRODUCTION

Plasma arcs have been widely used for cutting or welding metals because they can supply a dense energy flow in a small area of an arc spot. However, it is not a convenient heat source to treat a wide area. To expand a plasma arc, various trials have been attempted [1], [2], [3], [4]. Takeda et al. [3], [4] developed a magnetically driven arc by imposing an alternating magnetic field perpendicular to a transferred

arc. The arc oscillates because of the interaction between the electric arc current and the external magnetic field. Typical plasma arc profiles are presented in Fig. 1. An arc in no magnetic field, as shown in Fig. 1(a), deforms to a DC magnetic field, as portrayed in Fig. 1(b). By imposing an AC magnetic field, the arc oscillates as depicted in Fig. 1(c).

For practical applications of such a magnetically driven arc, precise understanding of the heat flux distribution is necessary. Experimental observation by T. Yamamoto et al. [5] revealed that the heat flux decreased near the edge of the

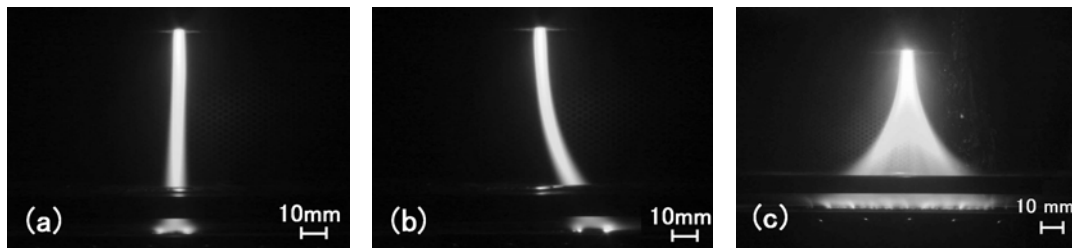


Fig.1 Various plasma arcs: no magnetic field (a), in a DC magnetic field (b),and in an AC magnetic field (c).

oscillatory amplitude. T. Toh et al. ⁽⁶⁾ has attempted to predict the heat flux distribution theoretically using a 3D MHD model. The present study develops a simple but practical model to predict heat flux variations with various waveforms of the imposed magnetic field, using the assumption of a one-dimensional heat source.

2 THEORETICAL CONSIDERATION OF THE HEAT FLUX VARIATION WITH DC MAGNETIC FLUX DENSITY

2.1 Displacement of the arc root by imposing magnetic flux density

A schematic of the setup used to produce a magnetically driven arc is presented in Fig. 2. As depicted therein, the following coordinate system (x, y, z) is used in this study. A plasma torch is located on the z axis; the anode expands in the x - y plane. An external magnetic field is generated perpendicular to the arc by DC electric current running through a two-turn rectangular field coil. The magnetic field is imposed in the direction of x . The arc current's interaction with the external magnetic field results in arc movement in the y direction. Without any imposed magnetic field, the center of the arc root is located at the origin $(0, 0, 0)$. With a magnetic field, it moves to $(0, Y, 0)$.

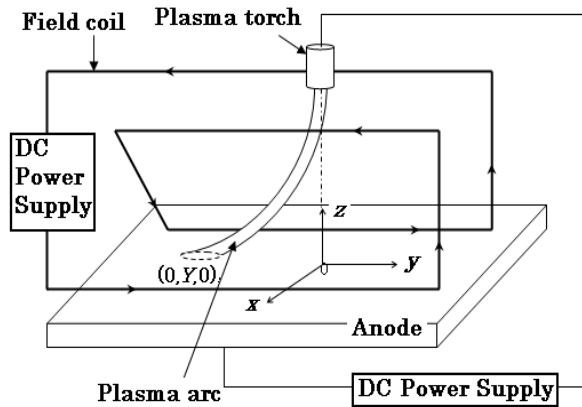


Fig.2 Schematic illustration of a system used to produce a magnetically driven arc

In a uniform magnetic field, it is known that displacement Y is expressed as [3]

$$Y = R - \sqrt{R^2 - L^2}, \quad (1)$$

where L denotes the standoff distance between a torch orifice and an anode plane. A radius of curvature R varies inverse proportionally to an imposed magnetic flux density B .

2.2 Deformation of the arc root with its displacement

The arc at $Y=0$ is assumed to be cylindrically symmetric. As presented in Fig. 3, the cross section of the arc on the anode changes its shape from a circle with diameter d_0 to an ellipse with minor diameter d_0 and major diameter d_Y in an imposed magnetic field.

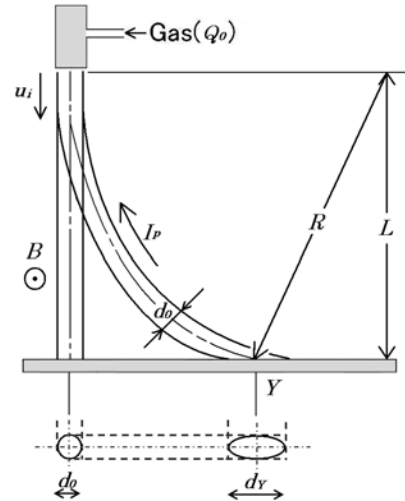


Fig. 3 Schematic illustration on the arc root deformation

Considering Eq.1, geometrical considerations engender the following relation:

$$\frac{d_Y}{d_0} = \frac{L^2 + Y^2}{L^2 - Y^2}. \quad (2)$$

The heat flux distribution function in the arc root is introduced as $h_Y(x, y)$, where subscript Y represents that its center position is located at Y . As described later, the heat flow from the arc to the anode remains constant independent of the imposed magnetic flux density. Under such a condition, the following ratio on the heat flux is satisfied:

$$\frac{h_Y(0, Y)}{h_0(0, 0)} = \frac{d_0}{d_Y} = \frac{L^2 - Y^2}{L^2 + Y^2}. \quad (3)$$

In that equation, $h_0(0, 0)$ and $h_Y(0, Y)$ respectively denote the heat flux at the center of the arc root in no magnetic field and that in imposed magnetic field, according to the definition of $h_Y(x, y)$.

As portrayed in Fig. 4, the heat flux decreases concomitantly with increased Y or B .

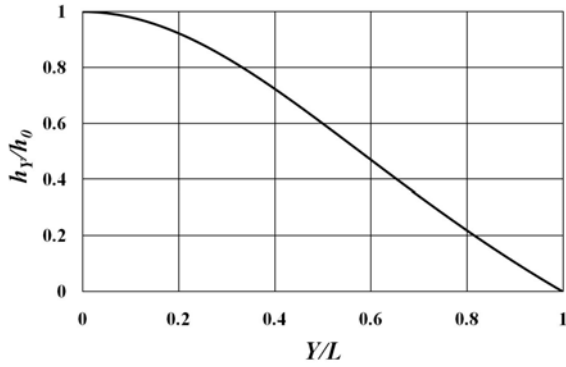


Fig. 4 Variation of the heat flux at the center of the arc root with Y

2.3 Transformation of 2D heat flux distribution to 1D heat flux distribution

To simplify the theoretical considerations, the two-dimensional heat flow is transformed into one-dimensional heat flow, regarding the arc root as a linear heat source varying its length with the imposed magnetic flux density. One dimensional heat flux is expected to satisfy the following relation.

$$H_Y(y) = \int_{-\infty}^{+\infty} h_y(x, y) \cdot dx \quad (4)$$

In no magnetic field, it is expressed as $H_0(y)$ because the arc root center is located at $Y=0$. Considering the experimental observation that the heat flux of the arc has a maximum value at the center of the arc-root and decreases its value with distance from the center, the following assumption is adopted in the present work for the one-dimensional distribution function.

$$H_0(y) = \frac{2P_o}{d_0} \left\{ 1 - \left| \frac{2y}{d_0} \right| \right\} \quad \text{for } 0 \leq |y| < \frac{d_y}{2}, \quad (5)$$

$$H_0(y) = 0 \quad \text{for } |y| \geq \frac{d_y}{2}. \quad (6)$$

Therein, P_o represents the total power transferred from the arc to the anode. Under the imposed magnetic field, the distribution function for the heat flux centered on $y=Y$ is expressed as shown below.

$$H_Y(y) = \frac{2P_o}{d_Y} \left\{ 1 - \left| \frac{2(y-Y)}{d_Y} \right| \right\} \quad \text{for } 0 \leq |y-Y| < \frac{d_Y}{2} \quad (7)$$

$$H_Y(y) = 0 \quad \text{for } |y-Y| \geq \frac{d_Y}{2} \quad (8)$$

In those equations, d_Y denotes the one-dimensional heat source length, which varies with Y according to the relation of Eq. (2).

3 DETERMINATION OF d_0 AND CONFIRMATION OF THE ASSUMPTIONS' VALIDITY

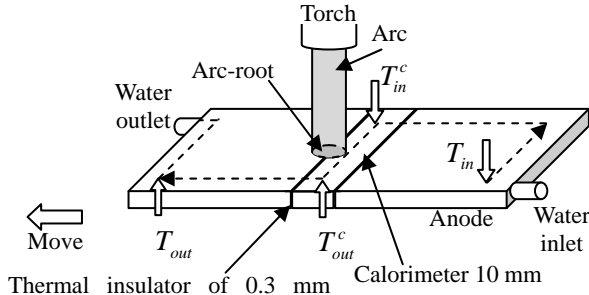
3.1 Experiment using a calorimeter

To determine d_0 and to confirm the validity of the assumptions used in the theoretical model, an experiment was conducted using a similar experimental arrangement to that shown in Fig. 2. A transferred arc was produced between a plasma torch with a tungsten cathode and a water-cooled copper anode. The standoff distance between the torch orifice and the anode was fixed at 70 mm. A power supply was connected to the torch; the anode was operated in a constant current mode. The arc current was adjustable up to 130 A. The open circuit voltage of the power supply was 280 V. Argon gas was fed to the torch as a plasma forming gas at the flow rate of 4.5×10^{-4} kg/s. An external magnetic field was generated perpendicular to the arc using DC electric current through a two-turn rectangular field coil. The maximum magnetic flux density in the coil center was 2.22 mT at the coil current of 300 A.

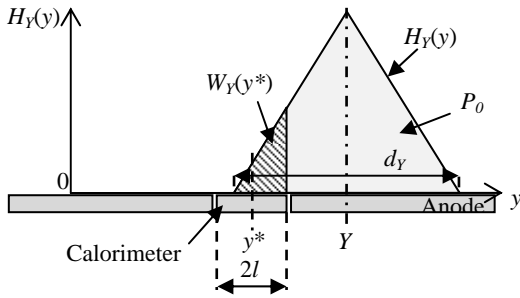
In this experiment, a special anode assembly was developed to estimate the heat flux distribution in the arc root. As depicted in Fig. 5, it consisted of three water-cooled copper blocks. The 10-mm-wide, 10-mm-thick and 100-mm-long center block is designated as a calorimeter hereinafter. The calorimeter was thermally insulated from the others. It was moved by a motor drive mechanism in the direction of the arc displacement at 0.33 mm/s. The heat flow to the calorimeter was estimated as the temperature increase ($T_{out}^C - T_{in}^C$) in the cooling water flowing through this block. We must bear in mind that the distribution of the heat flux in the anode root can not be measured directly by the calorimeter. As portrayed in Fig. 5(b) the heat flow into the calorimeter having the width of $2l$, $W_Y(y^*)$ is expressed in the following equation:

$$W_Y(y^*) = \int_{y^*-l}^{y^*+l} H_Y(y) dy, \quad (9)$$

where y^* represents the center position of the calorimeter, and $H_Y(y)$ denotes the one-dimensional heat flux distribution function in the arc root centered at Y .



(a) Anode assembly and a calorimeter



(b) Heat flow to the calorimeter

Fig. 5 Anode assembly (a) and schematic illustration of the heat flow to the calorimeter (b)

3.2 Determination of d_0

Without an imposed magnetic field, the heat flow into the calorimeter located at $y^*=0$ is expressed as

$$W_0(0) = \frac{4l(d_0 - l)}{d_0^2} P_0. \quad (10)$$

The total heat flow P_0 in Eq. 10 was determined according to the measurement of temperature difference ($T_{out} - T_{in}$) through the anode assembly. Experimental measurements revealed that P_0 kept constant independent of the magnetic flux density. In the present experimental condition, the obtained P_0 was 7.2 kW. Without any imposed magnetic field, the heat flow to the calorimeter at $y^* = 0$ was 3.3 kW. From Eq. 10, d_0 was estimated as $d_0 = 38.4$ mm.

3.3 Confirmation on the validity of the assumptions

Theoretical variation of $W_Y(y^*)$ can be calculated using the experimental data of d_0 and P_0 obtained in 3.2, in two different cases of Y , theoretical predictions of $W_Y(y^*)$ were compared with measured variations of the heat flow to the calorimeter.

Figure 6 presents a comparison between theoretical predictions and experimental results for various y^* for $Y=0$. The theoretical predictions closely match the experimental profile.

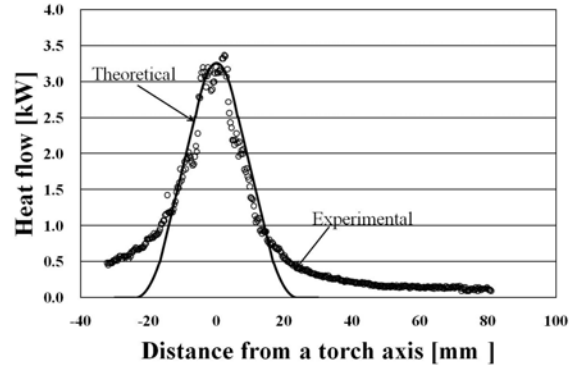


Fig. 6 Comparison between theoretical result and experimental results without an external magnetic field

A similar comparison at $Y=29$ mm is portrayed in Fig. 7. In this case, the agreement was also good, meaning that the assumptions used in the theoretical model are confirmed as valid.

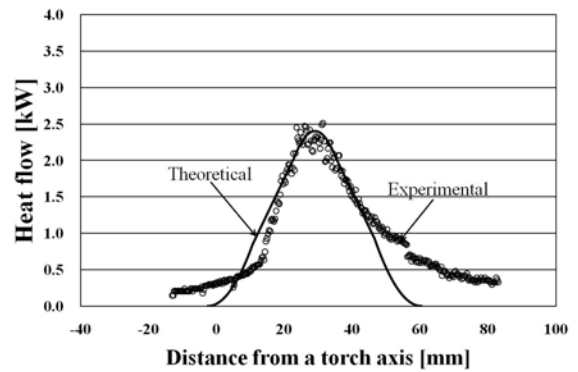


Fig. 7 Comparison between theoretical result and experimental result with a DC magnetic field at $Y=29$ mm

After the impact on the anode, the hot plasma gas travels to the large y direction. Its heat flow to the anode may result in the deviation of the experimental results from the theoretical prediction. The agreement of theoretical predictions with

experimental results is good despite the rough assumptions used for theoretical considerations.

4 THEORETICAL PREDICTION ON THE HEAT FLUX DISTRIBUTION IN AC MAGNETIC FIELD

In the practical applications of magnetic driven arc, the frequency range of the AC field is 10~100 Hz. In such a low frequency condition, it is known that the eddy current effect is negligibly small. In present theory, it is not considered.

If the imposed AC magnetic flux density (B) is expressed in the following arbitrary form as

$$B(t) = B_o f(t), \quad (11)$$

then the arc root center position (Y) is reasonably assumed to be in a similar form of

$$Y(t) = Y_o f(t), \quad (12)$$

where B_o and Y_o respectively represent the amplitude of the AC magnetic flux density and that of the arc root movement. Function $f(t)$ represents the waveform varying between -1 and 1. In a small distance dy for a short time interval dt , the heat flow around a position y and a time t is defined as shown below.

$$dq(y,t) = H_Y(y) dy \cdot dt, \quad (13)$$

During the half period of the AC magnetic field, the heat flow into dy can be expressed as

$$dQ(y) = \left\{ \int_0^\tau dq(y,t) dt \right\} dy = \left\{ \int_{-Y_o}^{Y_o} H_Y(y) \frac{dt}{dY} dY \right\} dy, \quad (14)$$

where τ represents the half period of the imposed field. Then the heat flux averaged over the half period of the AC field is obtained as shown in Eq. 15.

$$\langle H(y) \rangle = \frac{1}{\tau} \frac{dQ(y)}{dy} = \frac{1}{\tau} \int_{-Y_o}^{Y_o} H_Y(y) \frac{dt}{dY} dY \quad (15)$$

In that equation, $\langle H(y) \rangle$ can be calculated numerically. For example, if the imposed AC magnetic field varies in a sinusoidal form, Eq. 12 can be expressed as shown below.

$$Y = Y_o \cos\left(\frac{\pi}{\tau} t\right) \quad (16)$$

Consequently, Eq. 16 can then be rewritten as

$$\langle H(y) \rangle = \pi \int_{-Y_o}^{Y_o} H_Y(y) \frac{dY}{\sqrt{Y_o^2 - Y^2}}. \quad (17)$$

Numerical calculations were conducted for three different AC waveforms. In all cases, Y_o , P_o , and d_o were assumed, respectively, as 4.0×10^{-2} m, 7.2 kW and 38.4×10^{-3} m. Figure 8 shows a heat flux distribution in the AC magnetic field with a sinusoidal waveform.

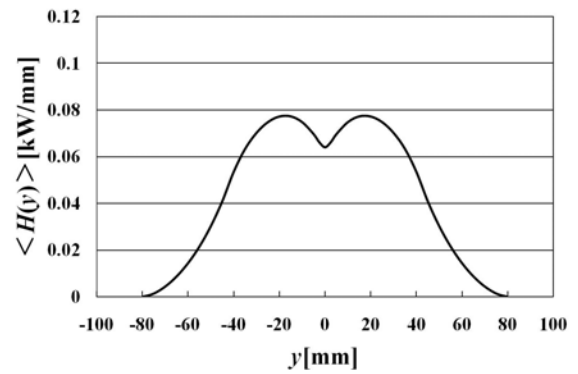


Fig. 8 Heat flux distribution with a sinusoidal magnetic field

Figure 9 shows the heat flux distribution in a triangular magnetic field.

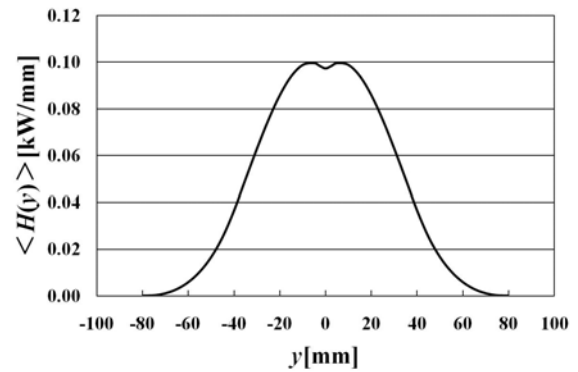


Fig. 9 Heat flux distribution with a triangular magnetic field

Comparison of Fig. 8 and Fig. 9 clearly shows that the heat flux distribution depends on the external magnetic waveform, meaning that the heat flux distribution on the

anode can be controlled by changing the waveform of the imposed magnetic field.

5 CONCLUSIONS

Theoretical examinations were performed to predict the heat flux distribution of a magnetically driven arc. Conclusions can be summarized as follows.

- (1) Experimental results revealed that transformation of the 2D heat flux inside the arc root to 1D heat flux was useful to simplify the model and estimate a heat flux distribution on the anode.
- (2) Results of the experiment confirmed that the assumption of triangle-shape distribution was reasonable for the 1D arc root model.

Numerical calculations revealed that the heat flow profile along the oscillatory motion was controlled by changing the waveform of the imposed magnetic field.

NOMENCLATURE

B	Magnetic flux density [T]
B_0	Amplitude of magnetic flux density [T]
$H_Y(y)$	One-dimensional heat flux in DC magnetic field [W/m]
$\langle H(y) \rangle$	Time averaged heat flux in AC magnetic field [W/m]
L	standoff distance between arc torch and anode [m]
P_o	Total heat flow from the arc to the anode [W]
$dQ(y)$	Heat transferred to the small distance dy during a half period [J]
R	Radius of curvature of the deflected arc [m]
T_{in}	Temperature of cooling water at the inlet of the anode [K]
T_{out}	Temperature of cooling water at the outlet of the anode [K]
T_{in}^c	Temperature of cooling water at the inlet of the calorimeter [K]
T_{out}^c	Temperature of cooling water at the outlet of the calorimeter [K]
Y	Position of arc root center [m]
Y_o	Amplitude of the arc center oscillation [m]
$W_Y(y^*)$	Heat flow to the calorimeter at y^* [W]
d_o	Minor diameter of the arc root [m]
d_Y	Major diameter of the arc root [m]
$f(t)$	Waveform varying with time [-]

l	Half width of the calorimeter [m]
$dq(y,t)$	Heat transferred to a small distance dy for short time interval dt [J]
t	Time [s]
x,y,z	Coordinate [m]
y^*	Center position of the calorimeter [m]
τ	Half period of the oscillation [s]

REFERENCES

- [1] Y. Arata and H. Maruo, Technology Reports of the Osaka University, 22 (1972) 135.
- [2] J.E. Harry and D. Goodwin, Surface heat treatment using a plasma torch with a magnetically traversed arc, Proc. of 4th Int. Conf. on Advances in Welding Processes, England, 1978, 181.
- [3] K. Takeda, Oscillating plasma arc by external AC magnetic field, Proc. Int. Workshop on Plasma Jet in the Development of New Materials Technology, Frunze, (1990) 485-492.
- [4] K. Takeda, Generation of magnetically oscillating plasma arc and its properties, High Temperature Society (Japanese) 16 (1990) 357.
- [5] T. Yamamoto, K. Takeda, T. Toh, and J. Tanaka, Distribution of heat flux transported by using a magnetically driven arc, Thin Solid Films, 515 (2007) 4228.
- [6] T. Toh, J. Tanaka, Y. Maruki, T. Yamamoto, and K. Takeda, Magneto-hydrodynamic Simulation of DC Arc Plasma under AC Magnetic Field, ISIJ Int., 45-7 (2005), 947-953.
- [7] M. Tanaka, H. Terasaki, R. Narita, K. Kobayashi, H. Fujii, and M. Ushio, Anode Heat Transfer in TIG Arc and its Effect on Weld Penetration, Quarterly J. JWS, 23-3 (2005), 398-404. (in Japanese)

Production of Aluminum Using Arc Electrode

Kensuke Horiuchi, Mitsuru Hironaka, Seiji Kumagai, Masaya. Sugimoto, and Koichi Takeda

Department of Machine Intelligence and Systems Engineering, Akita Prefectural University
84-4, Tsuchiya-aza-ebino-kuchi, Yurihonjo, 015-0055, Akita Prefecture, JAPAN
m10a012@akita-pu.ac.jp

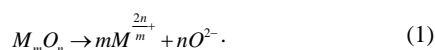
Abstract : Obtaining metals with high affinity for oxygen is difficult using conventional smelting with a carbon reductant. Molten salt electrolysis, which is free from carbon dioxide emissions, is often used. Although no carbon dioxide emissions are expected, huge amounts of CO₂ are generated in actual molten salt electrolysis, where graphite electrodes are used as anodes. This is why carbon is an indispensable material for high-temperature molten salt. For example, more than 1.2 tons CO₂ are emitted from a molten salt electrolysis bath to produce one ton of aluminum. We are developing a CO₂-free process using arc electrodes. Alumina (Al₂O₃) mixed cryolite and AlF₃ are used as test materials. Electrolysis is conducted in a stainless steel chamber under an inert Ar atmosphere. The arc is generated as a gaseous anode using a water-cooled plasma torch in constant current mode. It is confirmed from the experiment results that electrolysis proceeded with no carbon dioxide gas emissions using the plasma arc electrode.

Key Words: Molten salt, Electrolysis, Anode, Plasma arc, Al₂O₃

1 INTRODUCTION

Obtaining metals with high affinity for oxygen by conventional smelting processes using carbon reductant is not easy. Molten salt electrolysis methods are often used for smelting of such metals. Although no emission of carbon dioxide is expected in molten salt electrolysis, huge amounts of CO₂ are generated in actual processing, where graphite electrodes are used as anodes. This is why carbon has been considered as an indispensable material for use with high-temperature molten salt.

In a molten salt bath of metallic oxide, M_mO_n is dissociated as



Under an applied electric field, metallic ions and oxygen ions move respectively toward negative poles and positive poles.

At cathodic electrodes



At anodic electrodes, which comprise carbon materials,



and / or



Thereby more than 1.2 tons of CO₂ are emitted from production of one ton of Al using electrolysis processes.

This work is intended to develop a CO₂-free process, thereby replacing solid anodes with gaseous anodes. Conventional solid graphite electrode process and gaseous arc electrode process are depicted respectively in Fig. 1 and Fig. 2.

Few studies have described such trials. Taylor and Wang [1] investigated smelting of Cr₂O₃; in addition, Larson and Eager [2] proposed Ti production processes. A US patent filed by Donahue et al. [3] described a similar concept.

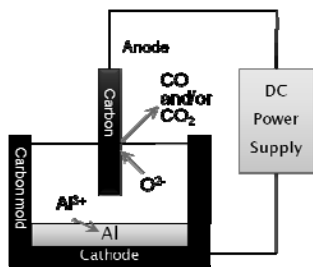


Fig. 1 Graphite electrode process

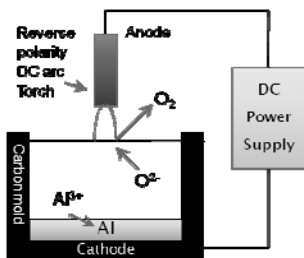


Fig. 2 Arc electrolysis process

gas was introduced as the plasma gas into the torch at the flow rate of 0.45 g/sec. The torch was mounted on the top of the stainless chamber.

The 90-mm-deep graphite mold had 100 mm inner diameter and 120 mm outer diameter. Figure 4 shows that it was thermally insulated by ceramic fiber wool. A 6-mm-diameter copper rod was placed in the mold in contact with the mold bottom for starting the arc. The plasma torch and the graphite mold were electrically connected respectively to the positive and negative poles of the DC power supply (SS-120P; Daiden), the maximum outputs of which were 120 A and 180 V.



Fig. 4 Mold

2 EXPERIMENTS

2.1 Experimental Arrangement

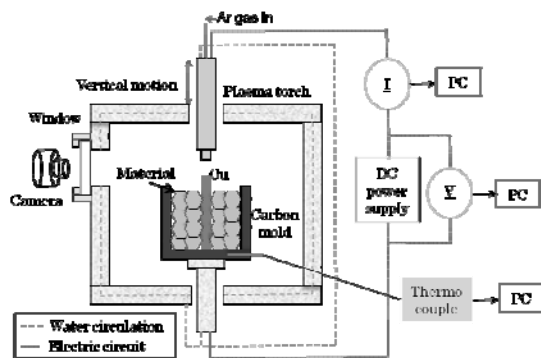


Fig. 3 Experimental apparatus

Figure 3 portrays a schematic illustration of experimental arrangement consisting of the reactor assembly and the reverse polarity DC arc assembly. All experiments were performed in a water-cooled stainless steel chamber to maintain the inert atmosphere.

The water-cooled plasma torch comprises a tungsten rod electrode (anode) and a ceramic nozzle with a 6-mm-diameter orifice, which give the arc definition and serve to direct the arc to an external cathode (molten salt). This torch was operated in a DC transferred arc mode. Argon

2.2 Material

The starting material was a mixture of reagent grade α type- Al_2O_3 powder (certified purity, 99.0%), reagent grade cryolite, Na_3AlF_6 , (certified purity, 90.0%) and reagent grade of aluminum trifluoride, AlF_3 (certified purity, 98.0%). As depicted in Fig. 5, the addition of cryolite decreases the alumina melting temperature. In addition, AlF_3 reduces the melting temperature further. The melting temperatures of copper and the slag were, respectively, 1357 K and 1050 K.

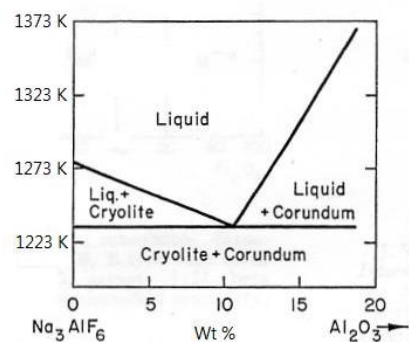


Fig. 5 Material (binary phase diagram)

The slag was prepared by weighing the three reagents and mixing them, with sintering at 1000 K. Because the alumina was in a solid state, it is electrically an insulator.

Consequently, the arc cannot form between the torch and the solid alumina or the arc does not serve as an anode. In our experiment, the arc was first generated between the torch and the copper rod. During heating and melting of the copper rod, the slag was intended to be in molten state by heat conduction from the copper, as portrayed in Fig. 6.

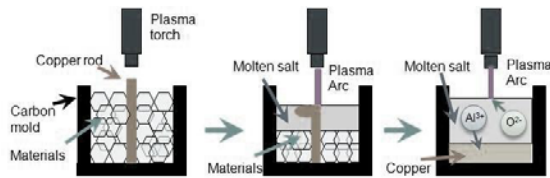


Fig. 6 Preparation of molten slag

Finally, a molten copper layer is formed at the mold bottom. The arc serves as an anode on the molten slag pool surface. The slag composition was determined as presented in Table 1 to ensure melting.

Table 1 Composition of material used in experiments

Substance	Chemical formula	Mass fraction
Cryolite	Na_3AlF_6	0.90
Aluminum fluoride	AlF_3	0.05
Alumina	Al_2O_3	0.05

2.3 Experimental Procedure

The sintered slag was crushed into small pieces and put into the mold. The air in the reaction chamber was replaced with argon gas before the arc started. After adjusting the torch position at 2 mm above the top of the copper rod, the arc was ignited at 30 A. Immediately thereafter, the torch position was adjusted to 40 mm above the top of the mold; then the arc current was increased to 80 A. Subsequently, the current and position were kept constant at these values.

The variation of the arc current and the arc voltage were recorded with time. The stability of the arc was observed through the chamber viewing windows. After a certain time of operation, the arc was shut off; then the mold was cooled and metal product (copper-aluminum alloy) was extracted from the slag.

An aqua-regia solution dissolved the product metal. The diluted solution was then analyzed using inductively coupled plasma mass spectroscopy (iCAP 6500; Thermo Fisher Scientific Corp.). The amount of metallic aluminum produced by electrolysis was evaluated from measurements of Al concentration in the alloy product.

3 EXPERIMENTAL RESULTS AND DISCUSSION

After ignition, the reverse polarity arc was observed stably, as presented in Fig. 7. Typical characteristic time variations of arc current and voltage are portrayed in Fig. 8. The arc was ignited at the current of 30 A and 50 s after, the arc voltage increased suddenly from 50 V to more than 100 V. From that time, white fumes emitted from the molten salt surface filled the reaction chamber interior. The increased arc voltage might be attributed to the fumes' existence.

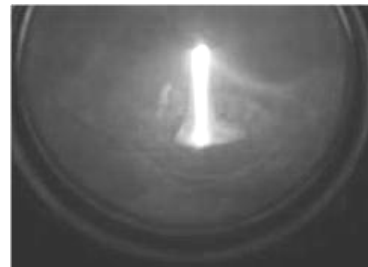


Fig. 7 Reverse polarity arc observed through the viewing window

The golden metallic product obtained for 290 s operation of the arc is portrayed in Fig. 9. The increased mass from the original copper rod of 15.69 g to the final product of 16.64 g indicates that the amount of metal produced by the electrolysis was 0.95 g. Table 2 portrays results of chemical analysis for Al and Na obtained using ICP mass spectroscopy. The estimated amount of Al produced by electrolysis from Table 2 was 0.98 g. Agreement between the weight measurement and chemical analysis was good.

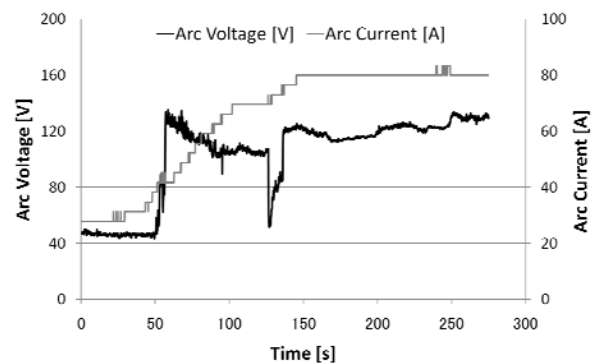


Fig. 8 Current and voltage variation with time

Table 2 Chemical composition of the metallic product analyzed by ICPM

Al	Na
5.69 [mass%]	0.055 [mass%]

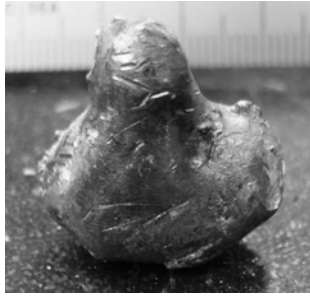


Fig. 9 Al-Cu alloy

The current efficiency of the arc-driven electrolysis can be estimated from Fig. 8. The amount (W) of Al extracted by charges (Q) of the aluminum ions transferred through the molten salt is represented as the following.

$$W = \frac{M}{n_o \cdot F} \cdot Q \quad (6)$$

In that equation, M is the aluminum molar mass, n_o is the aluminum ionic valency, and F is the Faraday constant. If the efficiency of current contributed to the electrolysis is expressed as η , then

$$Q = \eta \int I dt \quad (7)$$

Therefore,

$$W = \eta \frac{M}{n_o \cdot F} \cdot \int I dt \quad (8)$$

As shown in Fig. 8, the electrolysis is assumed to start at 50 s after the arc ignition and end at 290 s. The total charge driven by the arc was predicted as 18150 Coulombs according to the integral of Eq. (7) from $t=50$ s to $t=290$ s. Using the experimental result of $W=0.95$ g, the current efficiency η was estimated as 0.56. Low current efficiency might result from the frequent termination of the arc on the graphite mold or on the copper rod.

4 CONCLUSIONS

Fundamental experiments of the arc driven electrolysis were carried out for alumina base molten slag. A consumable solid electrode of a graphite cathode was replaced by a gaseous arc using a plasma torch. Results confirmed that electrolysis proceeded with no carbon dioxide gas emissions.

The intense energy concentration of the arc evaporated of molten slag, which might increase the arc voltage. Further studies should be undertaken to suppress evaporation. Proper adjustment of slag composition to increase the melting temperature might be useful. Oscillatory motion of an arc column using an external magnetic field is expected to reduce the molten slag's surface temperature. Stable operation to prevent the arc from termination on the mold is important to increase the current efficiency.

References

1. P.R. Taylor, W. Wang, A Laboratory Investigation of Reduction of Chromium Oxide by a Reverse-Polarity DC Plasma-Driven Molten Oxide Electrolysis Process, Plasma chemistry and Plasma Processing, (2002), vol.22. 387-400
2. H.R. Larson, T.M. Eager, Method and apparatus for producing titanium by the electrolysis of titanate slags, JOM, 3 (1998) 56-57.
3. R.J. Donahue, W.G. Hsterberg, G. William, T.M. Cleary, Method and apparatus for producing titanium, US Patent No. 4,964,973 (1990).

Preparation of chiral poly(diacetylene) film by using circularly polarized light

Hideki Kohn, Tatsunori Shino, Yuki Ohshima,
Takaaki Manaka, and Mitsumasa Iwamoto

*Department of Physical Electronics, Tokyo Institute of Technology,
2-12-1, O-okayama Meguro-ku Tokyo, 152-8552 Japan

iwamoto@pe.titech.ac.jp

Abstract: By irradiating evaporated 10,12-pentacosadiynoic acid (*p*-DA) monomer film with circularly polarized light (CPL), we prepared chiral poly(diacetylene) [PDA] film. The induced chirality was dependent on the rotational direction of the CPL. It was shown that the induced chirality increased with the PDA domain size, regulated by the substrate temperature.

Key Words: chirality, poly(diacetylene), circularly polarized light

1 Introduction

Chiral organic materials have received much attention in medicine and biochemistry [1], and have been motivated by possible device applications in electronics [2-4]. Chiral materials can be directly prepared by using physical and chemical process [5]. On the other hand, we proposed a novel preparation method [6-7], and showed the successful preparation of chiral poly(diacetylene) [PDA] film. That is, the chiral PDA films were prepared by introducing circularly polarized light (CPL) during the photopolymerization process from achiral diacetylene (DA) monomer films. The process

needed no chiral dopants, but the rotational direction of the CPL regulated induced circular dichroism (CD). Hence, chiral organic films prepared using this technique have a merit in device application. In this paper, we discuss the controllability of the induced chirality by using amphiphilic DA monomer ($\text{CH}_3(\text{CH}_2)_{11}\text{C}\equiv\text{C}-\text{C}\equiv\text{C}(\text{CH}_2)_8\text{COOH}$: *p*-DA). The substrate temperature was controlled during evaporation of these DA monomers. It was found that the intensity of CD signal strongly depended on the substrate temperature.

2 Sample preparation

Amphiphilic *p*-DA monomers were purchased from Tokyo Chemical Industry Co., Ltd., and used without further purification (see Fig. 1 for chemical structure of polymer). The DA monomers were deposited on glass substrate by the vacuum evaporation. The deposition rate was controlled to 0.6 ~ 0.7 Å/sec using a quartz crystal microbalance. The process pressure was kept at less than 1.0×10^{-4} Pa during the evaporation, and the substrate temperature was 333 K or 273 K. The film thickness of deposited monomers was approximately 100 nm. After the monomer deposition, the substrate temperature was lowered to 293 K, and the substrate was immediately removed from the vacuum chamber for

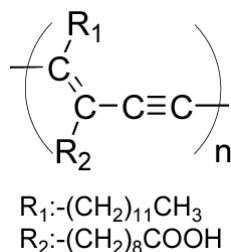


Figure 1: Chemical structure of PDA.

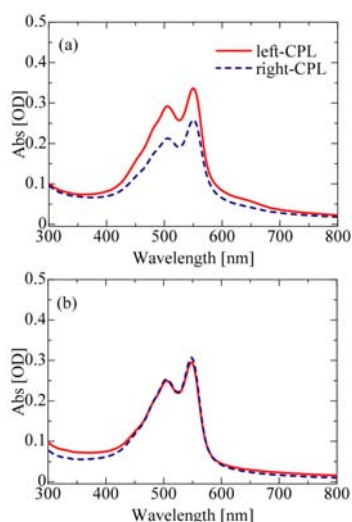


Figure 2: UV-vis spectra of evaporated PDA films. Sample prepared on (a) 333 K substrate, (b) on 273 K substrate. Solid and dashed lines represent the spectrum for the film polymerized with left and right-CPL, respectively.

polymerization in air. The deposited monomer films were photopolymerized using UV-CPL with a wavelength of 314 nm from a high-pressure Hg lamp (HAMAMATSU L-8333). The intensity of CPL was approximately 27.2 mW/cm^2 , and the irradiation time was 25 min. Then, the monomers films were transformed into blue-phase PDA films. The red-phase PDA films were obtained by further annealing at 353 K for 10 min. CD spectrum was measured using JASCO CD spectrometer J-715, and spot area of incident light was $7 \times 7 \text{ mm}^2$.

3 Results and Discussion

Figure 2 shows the UV-vis absorption spectra of red-phase PDAs obtained from the *p*-DA monomers at different substrate temperature. Red-phase PDA films showed a prominent

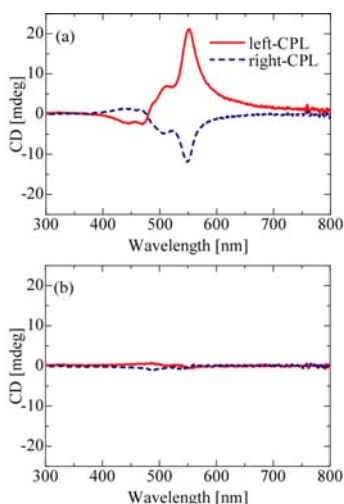


Figure 3: CD spectra of evaporated PDA films. Sample prepared on (a) 333 K substrate, (b) on 273 K substrate. Solid and dashed lines represent the spectrum for the film polymerized with left and right-CPL, respectively.

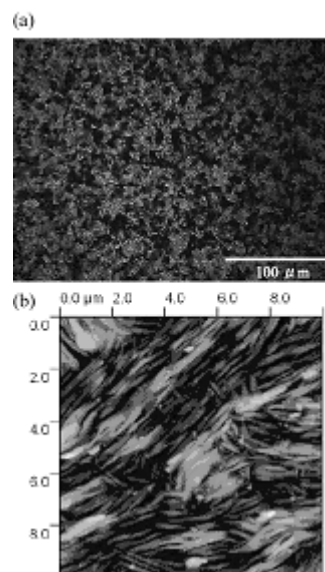


Figure 4: (a) Polarizing microscopy and (b) AFM images of PDA film that was deposited at 333 K and polymerized with right-CPL.

absorption peak around 550 nm and small shoulder peak at 500 nm, respectively. The CD spectra of red-phase PDA films were shown in Fig. 3, and, left- and right-handed chirality were selectively induced in the absorption region (above 500 nm), depending on the rotational direction of the CPL used for the polymerization. Similar results were obtained for other amphiphilic DA, $\text{CH}_3(\text{CH}_2)_9\text{C}\equiv\text{C}-\text{C}\equiv\text{C}(\text{CH}_2)_8\text{COOH}$: *t*-DA, and the chirality was also selectively induced by choosing the direction of the CPL employed [8]. Figure 4 shows polarizing microscope and AFM images of the red-phase PDA films polymerized with right-CPL at a substrate temperature of 333 K. The evaporated DA monomer film was comprised of numerous domains, while its polymerization proceeded accompanying without any changes of crystal structure of the monomer film, i.e., topochemical reaction [9]. As a result of the polymerization, large conjugated system was formed perpendicularly to the long axis of monomers [10]. As shown in Fig. 4(a), crystalline grain with large domain size was formed on a substrate at 333 K, whereas small on a substrate at 273 K (not shown here). Tanaka et al. reported that the molecular orientation of *n*-paraffin was dependent on the substrate temperature [11]. The structure similarity between the side-chain structure of PDA and *n*-paraffin suggested that the film structure of the diacetylene monomer with a rod shape would be affected by the substrate temperature. Further, many fibrils were formed from the backbone [see Fig. 4(b)]. It should be noted that no significant difference was observed between the left- and right-handed chiral PDA in the macroscopic observation. Interestingly, compared with the CD spectrum obtained from PDA films at high temperature [see Fig. 3], the CD signal was negligibly small for the films prepared at 273 K. Consequently, the CD signal intensity increased in accordance with the domain size as the substrate temperature increased within the limit of our experiments.

4 Conclusions

We studied the induced chirality of PDA polymerized from DA monomer. The CD of chiral PDA was observed, and the polarity of the CD signal was dependent on the rotational direction of the CPL used for the polymerization. Further, we measured CD spectrum at different substrate temperature, and showed that stronger chirality was induced at higher substrate temperature.

Acknowledgement—This work was partly supported by Global COE Program, "Photonics Integration-Core Electronics", MEXT, Japan.

References

- [1] Suh, I. H., Park, K. H., Jensen, W. P., and Lewis, D. E., "Molecules, Crystals, and Chirality" *Journal of Chemical Education*, Vol.74, No.7, pp.800-805, (1997).
- [2] Yashima, E., Maeda, K., and Okamoto, Y., "Memory of Macromolecular Helicity Assisted by Interaction with Achiral Small Molecules" *Nature*, Vol.399, pp.449-451, (1999).
- [3] Akagi, K., Piao, G., Kaneko, S., Higuchi, I., Shirakawa, H., and Kyotani, M., "Helical Polyacetylene Synthesized under Chiral Nematic Liquid Crystals" *Synthetic Metals*, Vol.102, pp.1406-1409, (1999).
- [4] Akagi, K., Guo, S., Mori, T., Goh, M., Piao, G., and Kyotani, M., "Synthesis of Helical Polyacetylene in Chiral Nematic Liquid Crystals Using Crown Ether Type Binaphthyl Derivatives as Chiral Dopants" *Journal of the American Chemical Society*, Vol.127, pp.14647-14654, (2005).
- [5] Pasteur, L., "Sur les relations qui peuvent exister entre la forme cristalline, la composition chimique et le sens de la polarisation rotatoire" *Annales de chimie et de physique*, Vol.24, pp.442-459, (1848).
- [6] Manaka, T., Kon, H., Ohshima, Y., Zou, G., and Iwamoto, M., "Preparation of Chiral Polydiacetylene Film from Achiral Monomers Using Circularly Polarized Light" *Chemistry Letters*, Vol.35, No. 9, pp.1028-1029, (2006).
- [7] Kohn, H., Ohshima, Y., Manaka, T., and Iwamoto, M., "Induced Optical Chirality of Poly(diacetylene) Film by Circularly Polarized Light and Its Control by Changing Substrate Temperature" *Japanese Journal of Applied Physics*, Vol.47, No.2, pp.1359-1362, (2008).
- [8] Kohn, H., Ohshima, Y., Manaka, T., and Iwamoto, M., "Optical Chirality Induced in Evaporated Poly(diacetylene) Film by Circularly Polarized Light" *Macromolecular Symposia*, Vol.268, Issue 1, pp.77-80 (2008).
- [9] Enkelmann, V., Wegner, G., "Crystallographic Analysis of a Topochemical Polymerization" *Angewandte Chemie, International Edition in English*, Vol.16, No.6, p.416, (1977).
- [10] Shufang, Y., Huilin, Z., and Pingsheng, H., "X-ray Diffraction Analysis of 10,12-Pentacosadiynoic Acid Langmuir-Blodgett Films during Polymerization" *Journal of Materials Science*, Vol.34, No.13, pp.3149-3154, (1999).
- [11] Tanaka, K., Okui, N., and Sakai, T., "Molecular Orientation Behavior of Paraffin Thin Films Made by Vapor Deposition" *Thin Solid Films* Vol.196, Issue 1, pp.137-145, (1991).

Synthesis of Diamond Films on Tungsten Carbide Surface by Step Synthesis Method using Combustion Flame

Mamoru Takahashi*, Osamu Kamiya* and Tadashi Ohyoshi*

*Department of Mechanical Engineering, Faculty of Engineering and Resource Science, Akita University,
1-1 Tegatagakuen-machi, Akita, 010-8502, Japan

mtaka@ipc.akita-u.ac.jp

Abstract: Diamond is widely used for industry, such as cutting tools. A combustion flame method is able to synthesize diamond by an acetylene-oxygen (C_2H_2/O_2) combustion flame in atmosphere. The method has various advantages, for example, the synthesis speed is very fast as compared with other methods. In recently, tungsten carbide (WC) is used as cutting tools in the machining industry. The deposition of diamond films on tungsten carbide surfaces is possible to increase the tool life and tool performance. In this study, the combustion flame method was used to synthesize diamond films on tungsten carbide surfaces. However, it was difficult to produce the diamond films that adhere to the WC substrate surfaces. Therefore, in order to improve the adherent strength, a step synthesis method was proposed. During synthesis by this method, temperatures of the film surface and distances of the flame inner cone from the surface for each step were changed. A chemical pretreatment on the WC substrate surface and the distance of the flame inner cone from the substrate were investigated as influence factors of the synthesis diamond and delamination. Synthesized films were investigated by scanning electron microscopy (SEM) and X-ray diffraction equipment system (XRD), and its were discussed. The results showed that diamond films were synthesized and the better adhesion of the diamond films was obtained on the WC surfaces by presented method.

Key words: Synthesized diamond films, Combustion flame, Tungsten carbide, Delamination

1 INTRODUCTION

Diamond is widely used for industry, such as cutting tools and polish tools. Because it has excellent properties of high thermal conductivity, high hardness and high wear resistance. Moreover, a diamond film has been considered dental cutting tools [1], and the diamond has been studied for use as coatings on medical devices [2].

In recently, tungsten carbide (WC) is used as cutting tools in the machining industry. The deposition of diamond films on tungsten carbide surfaces is possible to increase the tool life and tool performance. The CVD method that diamond was deposited on the WC surface has been developed. There were any problems that adherent strength between the synthesized film and the substrate surface was low and nuclear density on the surface was low. Thus, it was difficult to produce the diamond films that adhere to the WC surfaces. Moreover, the equipment of CVD method was very large, and the synthesis speed was very slow.

A combustion flame method [3, 4] is able to synthesize by an acetylene-oxygen (C_2H_2/O_2) combustion flame in atmosphere. The method has various advantages, for example, the synthesis speed is very fast as compared with other methods, the equipment is safe and cheap and electric power is

unnecessary, etc. The method has advantageous feature on industrial markets. In the combustion flame method, enlargement of area of the synthesized diamond [5], synthesis of large single crystal diamond [6] and synthesis of the diamond film for application in electronic devices [7] have been investigated. We have synthesized the diamond films on the Molybdenum (Mo) surface by the combustion flame method [8-14]. In this case, during cooling process, most synthesized diamond films delaminated. Therefore, a three-step synthesis method was proposed [8] to prevent the film delamination, to synthesize good diamond films. The delamination could be prevented to some extent.

In this study, the combustion flame method was used to synthesize diamond films on tungsten carbide surfaces. However, it was difficult to produce the diamond films that adhere to the WC substrate surfaces. Therefore, in order to improve the adherent strength, the method and synthetic conditions for the Mo substrate surface were applied, a step synthesis method for the WC surface was proposed. During the synthesis by this method, temperatures of the film surface and distances of the flame inner cone from the surface for each step were changed. A chemical pretreatment on the WC substrate surface and a distance of the flame inner cone from the substrate were investigated as influence factors of the synthesis diamond

and delamination. Synthesized films were investigated by scanning electron microscopy (SEM) and X-ray diffraction equipment system (XRD), and its were discussed. The results showed that diamond films were synthesized and the better adhesion of diamond films was obtained on the WC surfaces by presented method.

2 EXPERIMENTAL

2.1 Substrate

The substrate used for synthesizing the diamond was tungsten carbide (WC). A WC rod of 10mm diameter was used, and it was cut in thickness of about 3mm, its shape was a disk. As a pretreatment, to synthesize the diamond and prevent the delamination, chemical processing was performed. Moreover, as growth nuclei of the diamond synthesis, the diamond seed particles of about 0.25 μm in diameter were dispersed in acetone, the WC substrate was put into inside, and seed attachment processing was performed for 30 minutes with the ultrasonic syringe.

2.2 Experimental equipment

Experimental equipment is shown in Fig. 1. The $100 \times 100 \times 55\text{mm}$ copper box was used for cooling. Cooling water was poured into this box and the film surface temperature was kept constant. A non-contact infrared radiation thermometer was used for measurement of the film surface temperature during the synthesis. As a support for cooling, a tungsten (W) rod of 10mm diameter was stood in the center of a box right through, and it was fixed to the table by the flange. The WC substrate was attached on this W rod. In order to cool efficiently, thermally conductive Ag paste was applied between the WC substrate and the W rod. They were glued in the furnace at 473K.

The cooling box was put on a stage. Since it was capable of moving in the vertical direction, the distances from a cooling waterside to the film surface were changed, and the film surface temperature was controlled. A stepping motor was set to the stage, and it was controlled by the stage controller.

Acetylene and oxygen were used for fuel of the synthesis,

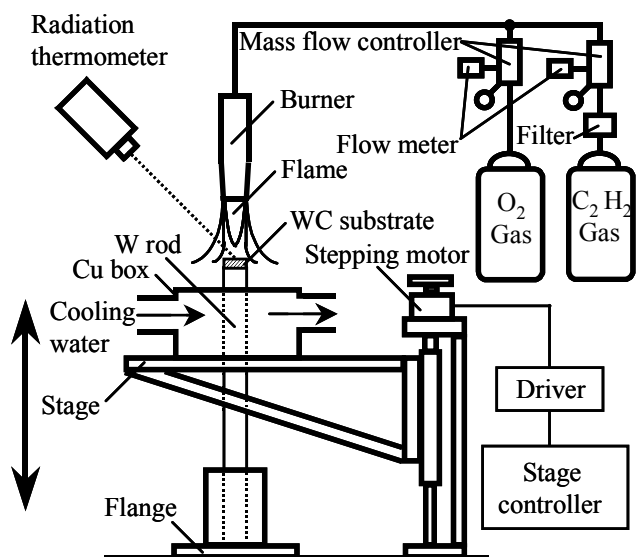


Figure 1 Experimental set up for synthesizing diamond by acetylene-oxygen combustion flame.

Table 1 Conditions for synthesizing diamond.

Reaction gas	$\text{C}_2\text{H}_2 + \text{O}_2$
Film surface temperature	1223~1423[K]
Pressure	$10^5[\text{Pa}]$
C_2H_2 Flow rate, F_a	70.9[cm^3/s]
O_2 Flow rate, F_o	63.8[cm^3/s]
Flow ratio, $R_f = F_o / F_a$	0.90

and a burner was used welding burner, mixed gas was introduced into the burner, and it was burned. The diameter of an exit of the burner was 1mm. In addition, for the gas flow meter, a mass flow controller was used. It can control flow quantity of gas precisely and can display flow quantity digitally.

2.3 Three-step synthesis method

A three-step synthesis method for Mo substrate surface was proposed to prevent the film from the delamination [10]. In this method, the film surface temperature was changed into three steps during the synthesis. The first step of the method was set to 1423K. This was caused that good diamond films were not synthesized but high bonding strength could be obtained at high temperature. The intermediate layer which works as the buffer phase for thermal stress reduction was synthesized on the Mo substrate in the first step. High bonding strength was then realized by the layer, and the delamination was prevented. The second step was set to 1223K, because the good diamond phase could be synthesized. To obtain thickness of the film, the third step was set to 1323K. In the first step synthesis, the diamond was synthesized, and the Mo_2C was also deposited on a substrate. Thus, the first step layer had the diamond and Mo_2C phases (multi-layer). In the second and third step synthesis, the diamond was synthesized. The boundary between the first layer and the second layer were confirmed, because crystal conditions were different. However, the boundary between the second layer and the third layer were not confirmed. This was caused that synthesized diamond of the second layer and the third layer were similar properties. In addition, average thickness of synthesized film by the three-step method was 30 μm per 1 hour.

In this study, this method for the Mo substrate surface was applied the WC substrate surface to synthesize the diamond film.

2.4 Synthetic conditions

The synthetic conditions are shown in Table 1. A flow ratio of oxygen flow rate F_o to acetylene flow rate F_a was set to $R_f = F_o / F_a = 0.90$, because a delamination-free crystal growth could be realized at the flow ratio $R_f = 0.90$ for the Mo substrate surface [13].

We have previously determined [11, 12] that the surface roughness by pretreatments on the substrate surface affected on the delamination, therefore diamond films were synthesized on pretreated substrate surfaces. WC substrates were pretreated to roughen the substrate surface and to modify the surface composition [1, 16]. As etching step, using Murakami's reagent ($\text{K}_3[\text{Fe}(\text{CN})_6]:10\text{g} + \text{KOH}:10\text{g}$ in 100ml water) was carried out in an ultrasonic bath to roughen the WC substrate surface. Next etching step was performed using an acid solution of hydrogen peroxide ($\text{H}_2\text{SO}_4:3\text{ml} + \text{H}_2\text{O}_2:88\text{ml}$), to remove cobalt (Co) from the substrate surface. WC contain Co as a binder, Co present at

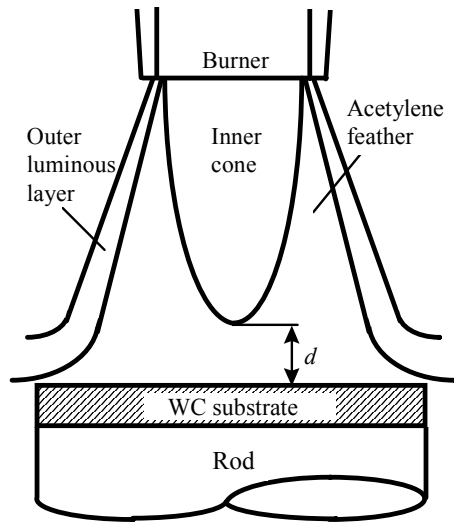


Figure 2 An outline figure of a combustion flame.

the substrate surface has negative effect on the nucleation of diamond. It catalyses the formation of graphite and other non-diamond carbon [15].

An outline figure of a combustion flame is shown in Fig. 2. The combustion flame consists of flame inner cone, acetylene feather and outer luminous layer. The diamond was able to synthesize in acetylene feather area. A distance of the flame inner cone from the substrate: d is shown in Fig. 2. During the synthesis, when the distance was changed, synthesized diamond films and the delamination were affected, because acetylene feather area was changed. The changing distance was an important factor to synthesize the diamond and prevent the delamination. Here, the distance d was measured by a scale. The scale was set to the burner in the equipment that the burner was capable of moving in the vertical direction. In the first, the top of the flame inner cone was touched the substrate surface. Next, the top of the flame inner cone was moved in upper direction by the burner with the scale in the equipment. Thus, the distance d was controlled manually. When the distance was short, a diamond growth speed was fast, and when the distance was long, the diamond growth speed was slow [11, 12]. Therefore, we have considered changing the distances to investigate as influence factors of the synthesis diamond and delamination.

Synthetic times for each step of the three-step method were set to 1200s, and synthesizing total time of the three-step was set to 1 hour [10, 11].

3 EXPERIMENTAL RESULTS AND DISCUSSION

3.1 Synthesis for no pretreated WC substrate

The synthetic method and conditions for the Mo substrate surface were applied the WC substrate surface to synthesize the diamond film. In the first, the synthesis for no pretreated WC substrate was performed by the combustion flame method with the three-step method. In this case, the distance was set to $d=1.5\text{mm}$, this distance was the optimal distance for the Mo substrate surface. But, diamond films were not synthesized on most synthesized specimen substrates. Next, the distance was set to $d=2.0\text{mm}$, diamond films were not synthesized. And, the distance was set to $d=3.0\text{mm}$, diamond films were not

Table 2 Conditions of the three-step synthesis method for the WC substrate surface.

	Synthesized time
1 st . step 1273[K]	1200[s]
2 nd . step 1173[K]	1200[s]
3 rd . step 1223[K]	1200[s]

Table 3 Results of WC surface roughness after pretreatment.

Time [min]	0	1	5	10	20
Ra [μm]	0.07	0.12	0.19	0.22	0.38

synthesized as well as $d=1.5$ and 2.0mm . This was caused that WC substrates were not pretreated to roughen the substrate. And the distances were not optimum. The distances $d=1.5$, 2.0 and 3.0mm for the WC substrate were close to the substrate surface, because the temperature of the WC substrate was very high and the WC substrate became red. Rapid temperature rising occurred, and temperatures could not control. So, the synthesis was not able to continue. We considered that this phenomenon was contributed by the material property that recrystallization temperature. This temperature was nearly 1300K . Therefore, we considered that the distance should be long, and temperatures of the synthesized film surface for each step should be changed as shown in Table 2. In this condition, the first step was set to 1273K , the second step was set to 1173K and the third step was set to 1223K , respectively.

3.2 Synthesis for pretreated WC substrate

Films were synthesized on the pretreated WC substrate surface. WC substrates were pretreated to roughen the substrate surface. As etching step, using Murakami's reagent was carried out in the ultrasonic bath to etch and roughen the WC substrate surface. The treatment times were 1, 5, 10 and 20min. Surface roughness for each pretreatment time were measured. The measured surface roughness: Ra (Arithmetical mean deviation of the assessed profile) of the treatment time 1min was $Ra=0.12\ \mu\text{m}$, the treatment time 5min was $Ra=0.19\ \mu\text{m}$, the treatment time 10min was $Ra=0.22\ \mu\text{m}$ and the treatment time 20min was $Ra=0.38\ \mu\text{m}$, respectively. Here, the surface roughness of no pretreated substrate was measured that the measured surface roughness was $Ra=0.07\ \mu\text{m}$. During the synthesis, the distance was set long and set to $d=5.0\text{mm}$, because the distances $d=1.5$, 2.0 and 3.0mm were close to the substrate surface. According to the results, synthesized films were not deposited on the 1min pretreated WC substrate. This caused that the surface roughness of the 1min pretreated substrate was small. But, synthesized films were deposited on 5, 10 and 20min pretreated WC substrates. Here, the comprehensive condition of the adhesion and morphology of the synthesized film on the 10min pretreated substrate was good compared with 5 and 20min. Though synthesized films were not deposited on no pretreated substrate, synthesized films were deposited on pretreated substrate. But, the synthesis did not sometimes go well.

3.3 Synthesis for pretreated WC substrate with removing Co

After the WC substrate was pretreated by using 10min

Murakami's reagent treatment, the synthesis for the pretreated WC substrate surface with removing cobalt (Co) was performed. WC substrates were pretreated to modify the substrate surface composition. WC contain Co as the binder, Co present at the substrate surface has negative effect on the nucleation of diamond. It catalyses the formation of graphite and other non-diamond carbon [15]. Thus, the adhesion strength between the film and substrate was very poor. In order to obtain good adhesion, Co was removed. Here, the using WC substrate in this experiment contains 5-6 wt. % Co binder. As etching step was performed using the acid solution of hydrogen peroxide, in order to remove Co from the WC substrate surface. The treatment times were 10sec [1, 16]. We confirmed that Co was removed from the WC substrate in the acid solution. During the synthesis, the distance was set to $d=5.0\text{mm}$. Synthesized films were deposited on the pretreated WC substrate with removing Co. This caused that Co was removed and adhesion was obtained. However, the film could be synthesized to some extent, but it was not well.

When synthesized films for the pretreated WC substrate surface with removing cobalt at the distance $d=5.0\text{mm}$ were obtained, the temperature control on the film surface was very difficult. This cause was the material property. Consequently, the distance should be changed one after another, and the distance was set to the long distance as $d=7.0\text{mm}$. Next, the distance was set to the more long distance as $d=7.5\text{mm}$ and the distance was set to the more long distance as $d=8.0\text{mm}$,

Table 4 Conditions of the two-step synthesis method for the WC substrate surface.

	Case 1	Case 2	Case 3
1 _{st} .step	1273[K]:1200[s]	7.0[mm]	7.5[mm]
2 _{nd} .step	1223[K]:1200[s]	7.0[mm]	7.0[mm]

respectively. The results showed that the temperature control on the film surface at the distance $d=7.0$, 7.5 and 8.0mm was easy compared with the distance $d=5.0\text{mm}$, respectively. However, rapid temperature rising still occurred and the synthesis was not able to continue. So, we thought that this phenomenon was caused by the distance, the synthesis time and material property. Moreover, at the distances $d=8.0\text{mm}$, synthesized crystals did not grow and the synthesized film was not obtained. This reason was that the distance was too long to synthesize the diamond. The diamond was able to synthesize in acetylene feather area, and there were many radical to synthesize the diamond in this area. At the distance $d=8.0\text{mm}$, the condition of acetylene feather area in combustion flame was not good.

Therefore, new synthesis condition was proposed as shown in Table 4. In this condition, synthesis steps are decreased as two steps, and distances were changed for each step. The first step of this condition was set to 1273K, the second step was set to 1223K. Case 1 condition was that the distance of the first step was set to $d=7.0\text{mm}$ and the distance of the second step was to $d=7.0\text{mm}$. Case 2 condition was that the distance of the first

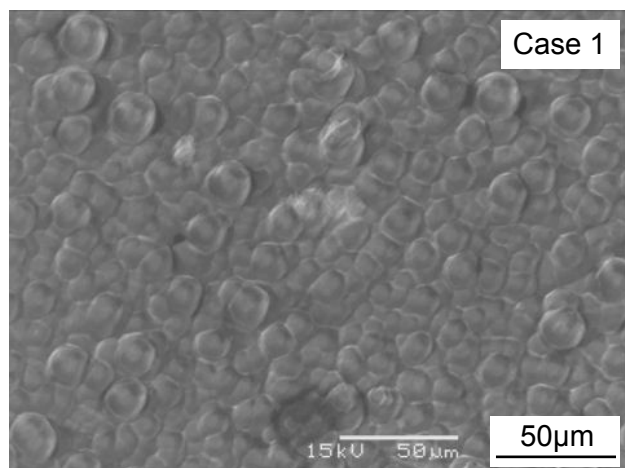


Figure 3 SEM micrograph of the synthesized film at Case 1.

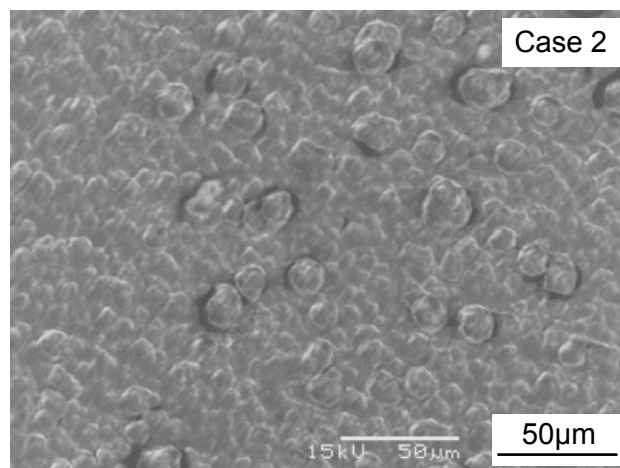


Figure 5 SEM micrograph of the synthesized film at Case 2.

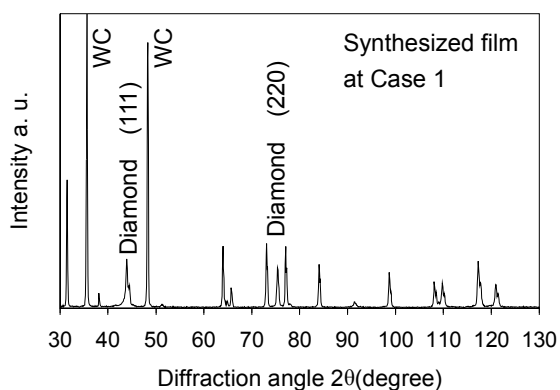


Figure 4 XRD patterns of the synthesized film at Case 1.

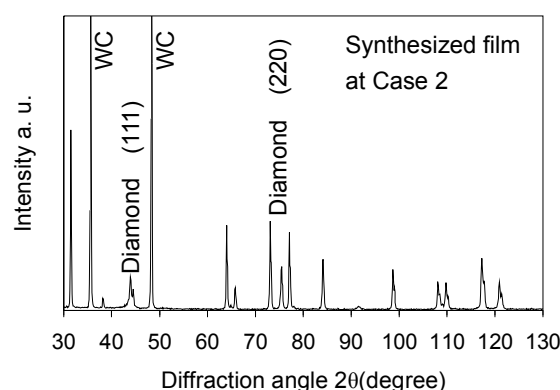


Figure 6 XRD patterns of the synthesized film at Case 2.

step was set to $d=7.0\text{mm}$ and the distance of the second step was to $d=7.5\text{mm}$. Case 3 condition was that the distance of the first step was set to $d=7.5\text{mm}$ and the distance of the second step was to $d=7.0\text{mm}$.

3.3.1 Synthesis for pretreated WC substrate with removing cobalt at Case 1: Synthesized films were deposited on the pretreated WC substrate with removing cobalt at Case 1 condition. The temperature control on the film surface was easy compared with $d=5.0\text{mm}$ (constant). Rapid temperature rising did not occur. The delamination of synthesized film did not occur. This reason was that WC substrate surface was etched by pretreatment and attached area was large between synthesized film and substrate surface. And Co on the WC substrate surface was removed by acid treatment and generation of graphite was prevented. The SEM micrograph and the result of XRD for the synthesized film are shown in Fig. 3 and 4, respectively. From Fig. 3, the synthesized film was smooth, and sizes of synthesized crystals were stable. In Fig. 4, peaks that show existence of the diamond could be confirmed. The peak that shows existence of diamond (111) side especially was confirmed and diamond was synthesized.

3.3.2 Synthesis for pretreated WC substrate with removing cobalt at Case 2: Synthesized films were deposited on the pretreated WC substrate with removing cobalt at Case 2 condition. The temperature control on the film surface was easy as same as Case 1. The delamination of the synthesized film did not occur. This reason was same as Case 1. The SEM

micrograph and the result of XRD for the synthesized film are shown in Fig. 5 and 6, respectively. From Fig. 5, the synthesized film was smooth. Sizes of synthesized crystals were stable, and size was a little small compared with Case 1. This cause was that when the distance of the second step was long, the growth diamond could be confirmed. The peak that shows existence of diamond (111) side was confirmed and diamond was synthesized.

3.3.3 Synthesis for pretreated WC substrate with removing cobalt at Case 3: Synthesized films were deposited on the pretreated WC substrate with removing cobalt at Case 3 condition. The temperature control on the film surface was easy as same as Case 1 and 2. However, the delamination of the synthesized film occurred. This reason was that the distance of the first step was set to $d=7.5\text{mm}$. When the distance was set long, growth rate was slow. Consequently, synthesized crystals of the first step were small, the attached area between the film and the substrate was small, the combination of each crystal was weak, and the bonding strength became poor. The SEM micrograph and the result of XRD for the synthesized film are shown in Fig. 7 and 8, respectively. From Fig. 7, the synthesized film was obtained and it was smooth. In Fig. 8, peaks that show existence of the diamond could be confirmed. The peak that shows existence of diamond (220) side was confirmed. But the peak that shows existence of diamond (111) side was little confirmed, thus, good diamond was not synthesized.

4 CONCLUSIONS

In order to get a good adhesion of the diamond film on tungsten carbide surfaces, the combustion flame method was used to synthesize diamond films. During the synthesis by this method, temperatures of the film surface and distances of the flame inner cone from the surface for each step were changed. A chemical pretreatment on the WC substrate surface and the distance of the flame inner cone from the substrate were investigated as influence factors of the synthesis diamond and delamination. Synthesized films were investigated by scanning electron microscopy (SEM) and X-ray diffraction equipment system (XRD), and its were discussed. The results showed that the diamond films was synthesized and the better adhesion of the diamond films was obtained on the tungsten carbide surfaces by the presented method. The first step of this method was set to 1273K, the second step was set to 1223K. Synthesis steps were two step, and distances were changed for each step. (Case 1 ; the first step : $d=7.0\text{mm}$, the second step : $d=7.0\text{mm}$, Case 2 ; the first step : $d=7.0\text{mm}$, the second step : $d=7.5\text{mm}$, Case 3 ; the first step : $d=7.5\text{mm}$, the second step : $d=7.0\text{mm}$) Here, the WC substrate was pretreated by using 10min Murakami's reagent treatment and 10sec acid solution treatment. This reason was that the WC substrate surface was etched by pretreatment and attached area was large between the synthesized film and substrate surface. And Co on the WC substrate surface was removed by acid treatment and generation of graphite was prevented. In the Case 1 and 2, the delamination-free diamond film was synthesized. In the Case 3, the good diamond film was not synthesized and the delamination of synthesized film occurred. This reason was that the distance of the first step was set to $d=7.5\text{mm}$. When the distance was long, growth rate was slow. Therefore, synthesized crystals of the first step were small, the attached area between the film and the substrate was small, the combination of each

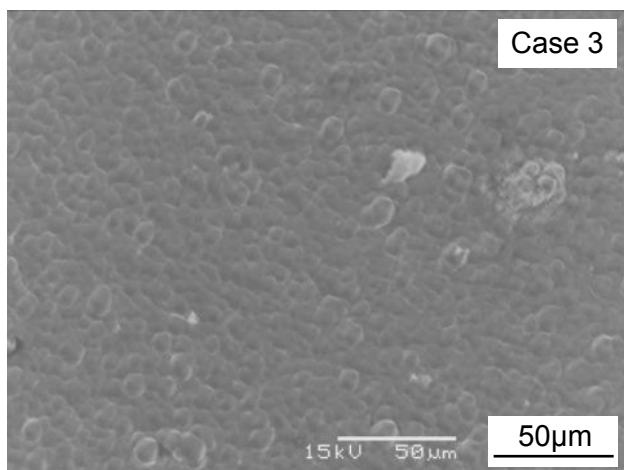


Figure 7 SEM micrograph of the synthesized film at Case 3.

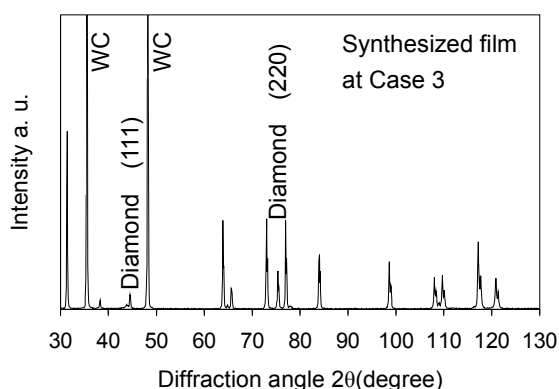


Figure 8 XRD patterns of the synthesized film at Case 3.

crystal was weak, and the bonding strength became poor.

It concludes that the delamination-free crystal growth can be realized by the presented method.

Acknowledgement This work was supported by Grant-in-Aid for Young Scientists (B) (18760073) from the Ministry of education, Science, Sports and Culture of Japan.

References

- [1] Polini, R., Allegri, A., Guarino, S., Quadrini, F., Sein, H. and Ahmed, W., "Cutting Force and Wear Evaluation in Peripheral Milling by CVD Diamond Dental Tools", *Thin Solid Films*, Vols. 469-470, pp. 161-166, (2004).
- [2] Narayan, R. J., Wei, W., Jin, C., Andara, M., Agarwal, A., Gerhardt, R. A., Shih, C. C., Shih, C. M., Lin, S. J., Su, Y. Y., Ramamurti, R. and Singh, R. N., "Microstructural and Biological Properties of Nanocrystalline Diamond Coatings", *Diamond and Related Materials*, Vol. 15, Nos. 11-12, pp. 1935-1940, (2006).
- [3] Hirose, Y., Okada, N. and Koike, H., "Synthesis of Diamond Using Combustion Flame in the Atmosphere (in Japanese)", *Journal of Combustion Society of Japan*, No. 80, pp. 1-17, (1989).
- [4] Hirose, Y., "Synthesis of Diamond Film in Combustion Flame (in Japanese)", *Journal of Japan Institute of Energy*, Vol. 73, No.11, pp. 973-979, (1994).
- [5] Ando, Y., Tobe, S., Saito, T., Sakurai, J., Tahara, H. and Yoshikawa, T., "Enlargement of the Diamond Deposition Area in Combustion Flame Method by Traversing Substrate", *Thin Solid Films*, Vol. 457, No.1, pp. 217-223, (2004).
- [6] Donnet, J. B., Oulanti, H., Le Huu, T. and Schmitt, M., "Synthesis of Large Single Crystal Diamond Using Combustion-flame Method", *Carbon*, Vol. 44, No. 2, pp. 374-380, (2006).
- [7] Okumura, Y., Kanayama, K., Tabaru, M. and Kawabata, S., "Combustion Synthesis of High-quality Diamond Film Suitable for Application in Electronic Devices", *Proceedings of the Combustion Institute*, Vol. 31, No. 2, pp. 1831-1838, (2007).
- [8] Kamiya, O., Kumagai, K. and Yama, T., "Synthesize of Diamond-film on Mo and Stainless Steel Surface by Combustion-flame (in Japanese)", *Journal of Japan Thermal Spraying Society*, Vol. 33, No. 1, pp. 1-7, (1996).
- [9] Kamiya, O., Horikane, H. and Ishikawa, K., "Crystal Morphology and Bonding Strength of Diamond Film Synthesized Using Combustion Flame on Molybdenum Base Metal (in Japanese)", *Journal of High Temperature Society*, Vol. 26, No. 4, pp. 154-161, (2000).
- [10] Takahashi, M., Ito, S., Kamiya, O. and Ohyoshi, T., "Synthesis of Diamond Film on Molybdenum Substrate Surface by Combustion Flame Considering the Delamination of the Interface(in Japanese)", *Trans. Japan Society of Mechanical Engineers, Series A*, Vol. 71, No. 703, pp. 578-583, (2005).
- [11] Takahashi, M., Kamiya, O. and Ohyoshi, T., "Influences for the Delamination of the Interface of Diamond Film Synthesized Using Combustion Flame on Molybdenum Substrate Surface (in Japanese)", *Journal of High Temperature Society*, Vol. 31, No.3, pp. 154-159, (2005).
- [12] Takahashi, M., Kamiya, O. and Ohyoshi, T., "Relationship between the Bonding Strength and the Structure of Initial Growth Film for Synthesized Diamond by the Three-step Method Using Combustion Flame (in Japanese)", *Journal of High Temperature Society*, Vol. 32, No. 5, pp. 295-304, (2006).
- [13] Takahashi, M., Kamiya, O. and Ohyoshi, T., "Effects of Flow Ratio on the Delamination of Diamond Films Synthesized by the Three-step Method Using Combustion Flame on Molybdenum Substrate Surface (in Japanese)", *Trans. Japan Society of Mechanical Engineers, Series A*, Vol. 73, No. 725, pp. 125-130, (2007).
- [14] Takahashi, M., Harada, Y., Kamiya, O. and Ohyoshi, T., "Prevention of Delamination of Synthesized Diamond Films by the Three Stepwise Combustion Flame Method -Effect of Distances of the Flame Inner Cone from the Substrate of Each Step and Substrate Surface Profiles on Delamination- (in Japanese)", *Journal of High Temperature Society*, Vol. 34, No. 3, pp. 136-143, (2008).
- [15] Neto, M. A. and Pereira, E., "Influence of Oxygen and Nitrogen Addition During Growth of CVD Diamond on Pure Cobalt Substrate", *Diamond and Related Materials*, Vol. 15, Nos. 4-8, pp. 465-471, (2006).
- [16] Geng, C. L., Tang, W. Z., Hei, L. F., Liu, S. T. and Lu, F. X., "Fracture Strength of Two-step Pretreated and Diamond Coated Cemented Carbide Microdrills", *International Journal of Refractory Materials and Hard Materials*, Vol. 25, No. 2, pp. 159-165, (2007).

New Imaging Method for Electrophoresis by Sub-Terahertz Wave

Hongbing Zhang*, Kazutaka Mitobe**, Masafumi Suzuki** and Noboru Yoshimura***

*Venture Business Laboratory, Akita University, 1-1 Tegata-Gakuen-Cho, Akita, 010-8502 Japan

**Department of Electrical and Electronic Engineering, Faculty of Engineering and Resource Science, Akita University, 1-1 Tegata-Gakuen-Cho, Akita, 010-8502 Japan

*** Akita University, 1-1 Tegata-Gakuen-Cho, Akita, 010-8502 Japan

hozeliz@hotmail.com

Abstract: A new imaging method of analyzing the results of cellulose acetate electrophoresis is proposed by sub-THz wave (THz). By improving the spatial resolution, we demonstrate the THz imaging about the distribution of medical molecules in cellulose acetate of low-concentration amino acid. Using the THz imaging system, we obtained THz images of the cellulose acetate with a glycine sensitivity of 0.88 $\mu\text{g}/\text{mm}^2$ and an L-methionine sensitivity of 0.63 $\mu\text{g}/\text{mm}^2$. Comparison of the THz and staining images showed that the new imaging method using the THz imaging system has a good possibility for cellulose acetate membrane electrophoresis analysis even for relatively low-concentration electrophoresis.

Key words: THz imaging, Cellulose acetate electrophoresis

1 INTRODUCTION

The use of cellulose acetate microbiology filters as solid supports for zone electrophoresis and the separation of hemoglobin phenotypes on cellulose acetate membranes was reported first by Kohn in 1956.¹⁾ Since then, it has been adapted to a wide range of applications involving, for example, the separation of hemoglobins,²⁾ and whey proteins,³⁾ the rapid detection of viral antibodies,⁴⁾ and the separation of basic, neutral, and acidic amino acids in proteins.⁵⁾ Cellulose acetate electrophoresis has been shown to be an accurate and simple method for protein quantification. Cellulose acetate electrophoresis nowadays not only plays an important role in routine clinical diagnostic procedures, but has also been effective in the investigation of a broad range of subjects in life science research. The advantages of this technique are its simplicity, rapidity, possibility of processing several samples at the same time, and low cost. However, there are some limitations of cellulose acetate electrophoresis. The main limitation of this technique is its low resolving power; it is impossible to discriminate variants that have almost the same mobility and materials for which the staining method is not effective.

The THz region lies between the infrared and microwave regions. It has not been well explored compared with other

electromagnetic spectral regions owing to the difficulties in the generation and detection of the wave. In recent years, as THz generators and detectors have become not only available but also affordable and easier to use, THz technology has attracted a great deal of interest for many important applications and technologies, for example, the detection of high explosives, the nondestructive detection of illicit drugs, and the pulse THz spectroscopy of DNA, bovine serum albumin, and collagen. Recently, the THz spectra of many chemical materials have been established with the development of THz techniques.^{6,7)} From the THz spectra, we can discriminate variants with almost same mobility. The study of electrophoresis by THz imaging techniques has not been reported until now. Here, we have proposed, for the first time, an analysis method for cellulose acetate electrophoresis using the THz imaging technique.

In this paper, we describe the details of the THz imaging method for analyzing cellulose acetate electrophoresis. We will also provide THz and staining images of glycine and L-methionine after cellulose acetate electrophoresis.

2 EXPERIMENTAL PROCEDURE

2.1 Apparatus for cellulose acetate electrophoresis

The experimental device for cellulose acetate membrane electrophoresis is a Toyo EPC105AA, which is composed of two parts. One is a constant current power source and the other

is an apparatus comprising a tank, two supporting plates, two pressing plates, two electrodes, filter paper, a cellulose acetate membrane strip, and a lid. The cellulose acetate membrane is placed on the apparatus crossing over the central compartment with its ends on both supporting plates and fixed with the pressing plate. The sample solutions are applied on the cellulose acetate strip. Then, electrophoresis is performed at a constant current. After electrophoresis, THz imaging is carried out on the cellulose acetate membrane strip.

2.2 Experimental setup of THz imaging system

The THz imaging system is composed of a THz generator, an optical imaging system, a detector, a lock-in amplifier, and a personal computer. Using a tunnel injection transit time (TUNNETT) oscillator that uses the tunnel effect as a THz illuminant, the TUNNETT diode,⁸⁻¹⁰⁾ which oscillates by allowing electric current flow, the THz is discharged to the free space by the horn antenna. The frequency is 0.189 THz (λ : about 1.58 mm). Two polyethylene lenses are used to collimate and focus the generated THz beam. The THz is detected by a Schottky barrier diode (SBD) and that can be operated at room temperature. The signal is read by the lock-in amplifier from the detector at 4 kHz and is fed into the computer. The details of the THz imaging system can be found elsewhere.¹¹⁾

3 METHOD

Electrophoresis was carried out for glycine and L-methionine with cellulose acetate membranes. First, we placed 200 ml of electrophoresis buffer into two compartments of the electrophoresis tanks. Two pieces of Toyo Roshi No. 131 filter paper (80 x 150 mm², was cut from a piece of 80 x 300 mm²) were thoroughly wetted with buffer solution and placed over the edges of the shoulder pieces. One edge of the paper ran parallel to the edge of the shoulder and the other was immersed in the buffer.

A cellulose acetate membrane 60 x 220 mm² was cut into strips of 30 x 110 mm² and placed on the surface of the other compartment of buffer evenly for 5 min. It is essential that this procedure is followed exactly since it prevents the trapping of air bubbles in the pores of the membrane. The excess buffer on the strips was lightly removed with filter paper, so that the strips were not over-dried. The strips were placed in the electrophoresis apparatus crossing over the central compartment with their ends on both supporting plates and fixed with the pressing plate. 4 strips were used at a time. To achieve the best results, we supplied power for 10 min to make the membrane surface uniform before applying the sample solution. Then, we applied 0.5 μ l of the sample solution to the surface of each of the strips using a pipette along a length of 10 mm. After that, the apparatus was covered with the lid. The power supply was connected and electrophoresis was performed at a constant current of 0.75 mA/cm for 20, 40, 60, and 80 min.

Two strips were used for the same sample during electrophoresis. One was used for staining and the other was used for THz imaging. To reduce the diffusion of the material

in the cellulose acetate after electrophoresis, we dried it by wrapping it with two sheets of filter paper, which was used for THz imaging.

4 RESULTS AND DISCUSSION

The cellulose acetate with a glycine solution of 0.64 mol/l, an application volume of 0.5 μ l, an application width of about 4 mm, and a length of about 10 mm, was subjected to electrophoresis for 20, 40, 60, and 80 min. The staining and THz images for different electrophoresis times are shown in Fig. 1. Here, the THz images were processed with MatLab software. The left (at the 1 min of staining) and middle (the over-dried) parts of Fig. 1 show the staining images and the right part shows the THz images. From the staining and THz images, we found that the area over which glycine spread was 254.40 mm² during electrophoresis. From the applied volume, we calculated the glycine distribution quantity to be 0.88 μ g/mm². The cellulose acetate membrane absorbed the solution uniformly. The absorption rates of the THz in cellulose acetate and glycine are different. Thus, the glycine distribution can be observed by THz imaging even if the amount of glycine on the cellulose acetate is small.

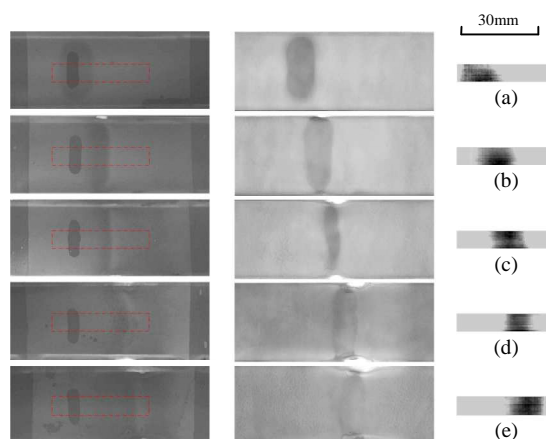


Fig. 1. Images obtained by staining (left and middle) and THz imaging (right) of the glycine sample at different electrophoresis times: (a) the applied solution seeps into the cellulose acetate completely before electrophoresis for (b) 20, (c) 40, (d) 60 and (e) 80 min.

The same experiment was carried out with L-methionine solution. Here, the concentration of the solution was 0.32 mol/l, the application volume was 0.5 μ l, the application length was about 10 mm, and the width was about 4 mm. Electrophoresis was performed for the cellulose acetate for 20, 40, 60, and 80 min. The staining and THz images for the different electrophoresis periods are shown in Fig. 2. The left and middle parts of the figure show the staining images and the right part shows the THz images. From the staining and THz images, we also found that the area over which L-methionine spread was 189.62 mm² during electrophoresis. From the applied volume, we calculated the L-methionine distribution quantity to be 0.63 μ g/mm². Unlike the staining method, the THz imaging can

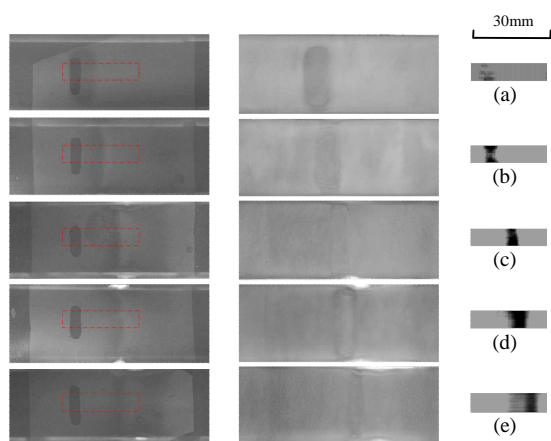


Fig. 2. Images obtained by staining (left and middle) and THz imaging (right) of the L-methionine sample at different electrophoresis times: (a) the applied solution seeps into the cellulose acetate completely before electrophoresis for (b) 20, (c) 40, (d) 60 and (e) 80 min.

detect even a small amount of sample, which is clear from the images. From our observations, it is reconfirmed that some medical molecules cannot be detected by the staining method, whereas the THz imaging technique can easily detect these molecules because the absorption rate is different for different materials.

The staining image process is not effective for the observation of medical molecules that have similar mobilities in cellulose acetate. Sometimes, staining itself is difficult for some molecules. Along with the development of the THz technique, many THz spectra of biological materials have been observed in previous studies. We consider the THz imaging technique to be a new tool for recognizing medical molecules in lieu of the staining method. In addition, from the results of other studies, it is clear that the collective vibration modes of many biomolecules occur in the THz range, and the refractive index and absorption coefficients of biomolecules differ from each other in the THz region.^{12,13} THz images can be obtained for the migration of different materials that can be distinguished by changing THz frequency.

5 Conclusions

A THz imaging technique has been developed, which connects the world of THz imaging to that of scientific and commercial applications. In the fields of medical diagnosis and biological analysis with THz radiation, THz imaging is used more and more widely. In this paper, we have proposed a new THz imaging method for cellulose acetate electrophoresis. We used the cellulose acetate apparatus and THz imaging system to obtain the staining and THz images of glycine and L-methionine. From the two types of images, we also measured electrophoresis migrations of the samples, and the migration distances obtained by the two methods are the same. In addition, we can easily observe the distribution of samples in the cellulose acetate by THz imaging. THz imaging may be an essential tool for imaging molecules even where the staining

method is ineffective. Comparison between the staining and THz images demonstrated that the THz imaging has a good possibility for the analysis of cellulose acetate electrophoresis results.

Acknowledgement This work was supported by a Grant-in-Aid for Scientific Research B (18360130) from the Japan Society for the Promotion of Science.

References

- [1] Rocco, R. M., "Joachim Kohn (1912–1987) and the Origin of Cellulose Acetate Electrophoresis," *Clin. Chem.* Vol. 51, pp.1896-1901, (2005).
- [2] Bartlett, R. C., "Rapid Cellulose Acetate Electrophoresis," *Clin. Chem.* Vol. 9 pp.325-329, (1963).
- [3] Levitt, N. H., Amsler, K. R. and Mckinney, R. W., "Rapid detection of viral antibody by cellulose acetate electrophoresis," *Appl. Microbiol.* Vol. 22 pp.143-144, (1971).
- [4] Bell, J. W. and Stone, W. K., "Rapid Separation of Whey Proteins by Cellulose Acetate Electrophoresis," *J. Dairy Sci.* Vol. 62, pp. 502-504, (1979).
- [5] Hiratsuka, N., Shiba, K., Shinomura, K., Hosaka, S., Cho, H., Nagasaki, A. and Kobayashi, S., "Evaluation of hematuria using the urinary albumin-to-total-protein ratio to differentiate glomerular and nonglomerular bleeding," *Biol. Pharm. Bull.* Vol. 17, pp. 1355-1357, (1994).
- [6] Wang, S., Ferguson, B., Abbot, D. and Zhang, X. C., "T-ray Imaging and Tomography," *J. Biol. Phys.* Vol. 29, pp. 247-256, (2003).
- [7] Nishizawa, J., Sasaki, T., Suto, K., Yamada, T., Tanabe, T., Tanno, T., Sawai, T. and Y. Miura, "THz imaging of nucleobases and cancerous tissue using a GaP THz-wave generator," *Opt. Commun.* Vol. 244, pp. 469-474, (2005).
- [8] Plotka, P., Nishizawa, J., Kurabayashi, T. and Makabe, H., "240-325 GHz GaAs fundamental-mode TUNNETT diodes fabricated with molecular layer epitaxy," *IEEE Trans. Electron Devices* Vol. 50, pp. 867-873, (2003).
- [9] Nishizawa, J., Murai, A., Makabe, H., Ito, O., Kimura, T., Suto, K. and Oyama, Y., "100 -thick tunnel junction by double impurity doping liquid phase epitaxy for V-band TUNNETT oscillation," *Solid-State Electron.* Vol. 48, pp. 2251-2254, (2004).
- [10] Nishizawa, J., Plotka, P., Makabe, H. and Kurabayashi, T., "GaAs TUNNETT Diodes Oscillating at 430-655 GHz in CW Fundamental Mode," *IEEE Microwave And Wireless Components Letters*, Vol. 15, pp. 597-599, (2005).
- [11] Zhang, H. B., Mitobe, K. and Yoshimura, N., "Application of Terahertz Imaging to Water Content Measurement," *Jpn. J. Appl. Phys.* Vol. 47 pp. 8605-8070, (2008).
- [12] Yamamoto, K., Tominaga, K., Sasakawa, H., Tamura, A., Murakami, H., Ohtake, H. and Sarukura, N., "Terahertz Time-Domain Spectroscopy of Amino Acids and Polypeptides," *Biophys. J. Biophys. Lett.* Vol. 89, pp. L22-L25, (2005).
- [13] Nishizawa, J., Sasaki, T. and Tanno, T., "Coherent terahertz-wave generation from semiconductors and its applications in biological sciences," *J. Phys. Chem. Solids* Vol. 69, pp. 693-701, (2008).

Development of Hybrid Magnetic Responsive Fluid for Vibration Damper

Katsuaki Sunakoda*, Hiroshi Kawasaki**, and Toshiyuki Hakata**

**Department of Mechanical Engineering, Faculty of Engineering and Resource Science, Akita University,
1-1 Tegatagakuen-machi, Akita, 010-8502, Japan*

** *Research & Development Division Toda Kogyo Corporation
1-4 Meijishinnkai, Otake, Hiroshima 739-0652 Japan
sunakoda@ipc.akita-u.ac.jp*

Abstract: Magneto-rheological fluid (MR fluid) is well known as a magnetic responsive fluid, and many application fields have been announced. In particular, the MR fluid damper has been studied as a semi-active control device in automobiles and for protecting constructions and bridges from earthquake and wind hazards. However, the MR fluid is inherently somewhat abrasive, and as with any micron-scale particulate suspension in which a density mismatch between the particulate and fluid exists, settling in MR fluids must be considered.

A new intelligent fluid is studied and developed. The developed fluid is a hybrid type fluid, and it consists of carbonyl irons and super fine magnetite. Average diameters of carbonyl iron and super fine magnetite are a size in the order of a few microns and about 10 nano-meters respectively. Special treatment is made by coating the surface of carbonyl iron with super fine magnetite. Physical properties such as dispersion stability and thixotropic characteristics are examined. A small capacity damper is made, and damping tests are performed using the new fluids and also commercial MR fluid. Dynamic properties of the damper are evaluated. As a result of a series of studies, the developed hybrid magnetic responsive fluid is expected to be used as an intelligent fluid.

Key words: hybrid magnetic responsive fluid, MR fluid, carbonyl iron, magnetite, damper

1 INTRODUCTION

Magnetic responsive fluid such as MR fluid have been investigated and applied as automobile suspensions[1]. A feature of Magnetic responsive fluid is its dramatic change in viscosity under a magnetic field, in comparison with electro-rheological fluid (ER) and magnetic fluid. This advantageous feature has led to much research and application studies in the academic world and industry [2]-[7]. In particular, the MR fluid damper has been studied as a semi-active control device in automobiles and for protecting constructions and bridges from earthquake and wind hazards.

Although it is said that the response time of MR fluid in magnetic field is in the order of 10^{-3} seconds and is sufficient for seismic or wind motion problems, the response time of the MR damper is about tens ~ hundreds micro seconds. To solve the difficulties in this lag time, a special electric circuit design is required for the semi-active controller [8]. Also, micron-sized (1-10 μ m) magnetizable particles are used in the carrier fluid, separation is observed between particles and the carrier fluid with time passage when the semi-active MR damper is not in

operation . Settlement of particles is problematic. To prevent settlement, small sized particles such as magnetite and application of a high thixotropic tendency to the fluid seem to be effective, but thus far the authors have not found a perfect solution.

In this paper we will introduce a few of our recent studies which include the development of a new intelligent fluid and magnetic properties as well as damping properties of the new fluid. Basic aims of the development of the new intelligent fluid are stability against settlement and strong magnetization. To achieve the above goals, magnetization particles are designed to be within a narrow small diameter particle (1~4 μ m) distribution band with a high density of particles in fluid (35vol%), and with each particle consisting of carbonyl iron and super fine magnetites. The surface of carbonyl iron is coated by super fine magnetites having a size of about 10 nm.

The newly developed intelligent fluid (Hereinafter referred to as "Hybrid Magnetic Responsive Fluid," or "HMRF") was evaluated by testing of settlement stability and magnetic field functions. Then, a shear mode flow test and pressure driven mode flow test were also performed on the HMRF[9]. After the above tests were finished, two types of small damper, (i.e.

semi-active damper and passive damper) were designed, and damping properties of the HMRF were examined. For the test of passive damper, commercial MR fluid and conventional oil were compared.

After a series of tests, it is clear that HMRF has a strong Bingham fluid tendency and it will be usable as an intelligent fluid, not only for the semi-active damper but also for the passive damper.

2 DEVELOPMENT OF HMRF

The development of the intelligent fluid is planned so as : 1) the fluid has a proper viscosity, under an assumption of using it as a functional oil for dampers and hydraulic equipment; 2) the fluid is superior in settlement of particles; and 3) the characteristics in a magnetic field or non-magnetic field are equal or superior to the commercial MR fluid.

2.1 Size and Density of Particle

To maintain a proper viscosity of fluid, we concentrated on the distribution of diameter and density of the particles. The size of particles was set at 1~4 μ m, and the density was optimized. Carbonyl irons were made spherical in shape (Photo. 1). Various densities were made. Finally, 35Vol.% of density was selected as a MFRF.

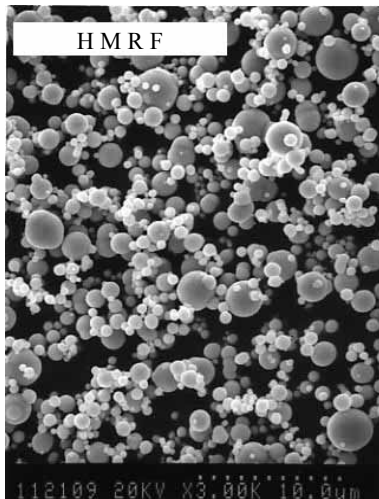


Photo.1 SEM Photo. of HMRF

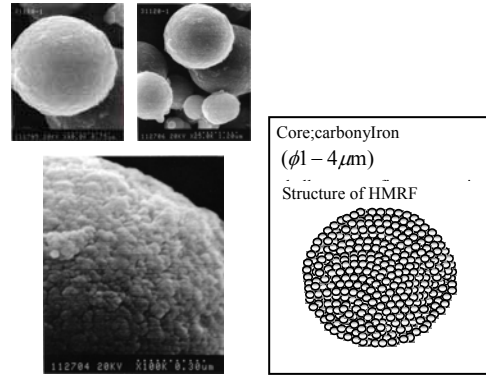


Photo.2 Surface of Particle Fig.1 Ideal figure of particle

Table.1 Physical properties of HMRF

Particles		No.1 HMRF	No.2 HMRF	No.3 HMRF
		Carbonyl Iron + Magnetite	Carbonyl Iron + Magnetite	Carbonyl Iron + Magnetite
Carrier Liquid		Hydrocarbon	Hydrocarbon	Hydrocarbon
Density(Vol.%)		35.0	35.0	35.0
Magnetic Field				
Hc	(kA/m)	0.8	0.8	0.2
Bm	(mT)	726	714	727
Br	(mT)	2.7	3.1	1.3
r/s	—	0.004	0.004	0.002
Thixotropy.index		4.0	4.7	3.2

Thixotropy.index: 3.83/38.3 s⁻¹,

No.1,No.2 : Deaeration treatment, No.3 : No-deaeration treatment

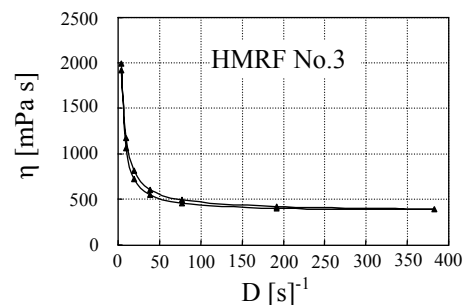


Fig.2 Shear rate and viscosity

2.2 Stability against settlement

To improve settlement as well as magnetizability and de-magnetizability, special treatment was done by coating the surface of carbonyl iron with super fine magnetite with a size of about 10 nm. Photograph 2 shows the surface of the iron particle coated by magnetite.

2.3 Physical Properties of HMRF

Magnetic properties, thixotropic properties, and settlement tendencies of the HMRF were examined. Physical properties of HMRF are listed in Table 1. Shear rate versus viscosity change were also examined, and thixotropy index were detected. Figure 2 shows an example of the detected thixotropic graph. Figure 3 shows the detected settlement tendency, In Table 1, No.1 HMRF and No.2 HMRF are the same fluid, but different lot Nos., which are deaeration treatment fluids and No.3 is the no-deaeration fluid.

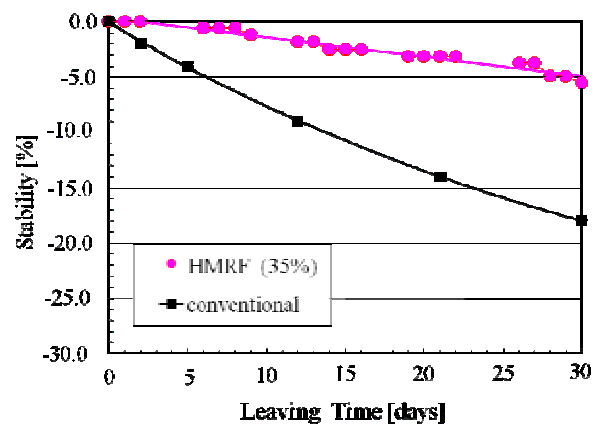


Fig. 3 Settlement observation

3 VIBRATION TEST BY USING SEMI-ACTIVE DAMPER & PASSIVE DAMPER

The damper's performances were examined by using small semi-active and passive dampers which were designed and manufactured for the estimation of HMRF. In the passive test, a commercial type of MR fluid and hydraulic oil were also examined for comparison.

3.1 Vibration test using semi-active damper

Figure 4 shows the cutting view of semi-active damper. The damper has an inside diameter of 45mm, a stroke of ± 40 mm, and outer diameter of 41mm. The damper uses a particularly simple geometry in which the outer cylindrical housing is part of the magnetic circuit (See Fig.5.). The effective fluid orifice is the annular space between the outside of the piston and the inside of the damper cylinder housing. A small pressurized accumulator is provided to accommodate thermal expansion of the fluid.

Cyclic loading tests with various input conditions were carried out to investigate the fundamental dynamic characteristics of the developed HMRF fluid. As typical examples of the test results, displacement-force hysteresis loops obtained under the sinusoidal displacement are shown in Fig. 6. The test was performed under input electric current of 0A, 0.2A, 0.4A, 0.6A, 0.8A, and 1.0A.

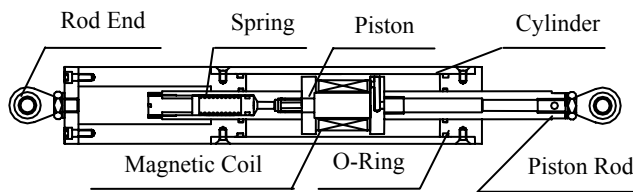


Fig.4 Semi-active Damper

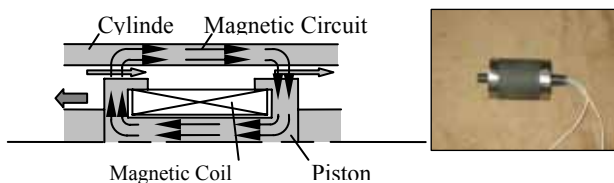


Fig.5 Schematic view of magnetic circuit and piston

From the hysteresis loops, this damper has a tendency similar to a friction type damper which can often be seen in a Bingham fluid damper. Saturation occurred with increasing input of electric current.

3.2 Vibration test using passive damper

Although semi-active dampers using MR fluid have been investigated in detail for a long time, the paucity of reports on passive type dampers using intelligent fluid encouraged us to research them. If they have the advantages of being able to utilize intelligent fluids, such as MR fluid and/or HMRF type fluid in the passive damper used as a seismic damper, the application field will change completely, and we will be able to expect to eliminate problems such as settlement and heater effect on magnetic circuits.

Figure 7 shows a schematic view of the passive damper. Figure 8 shows the details of the orifices. The permanent arrangement and exterior of the piston are shown in Fig. 9.

Cyclic loading tests with and without permanent magnetism were carried out to investigate the fundamental dynamic characteristics of the developed HMRF fluid. In the case without permanent magnetism, hydraulic oil was used in the test together with the commercial type of MR fluid.

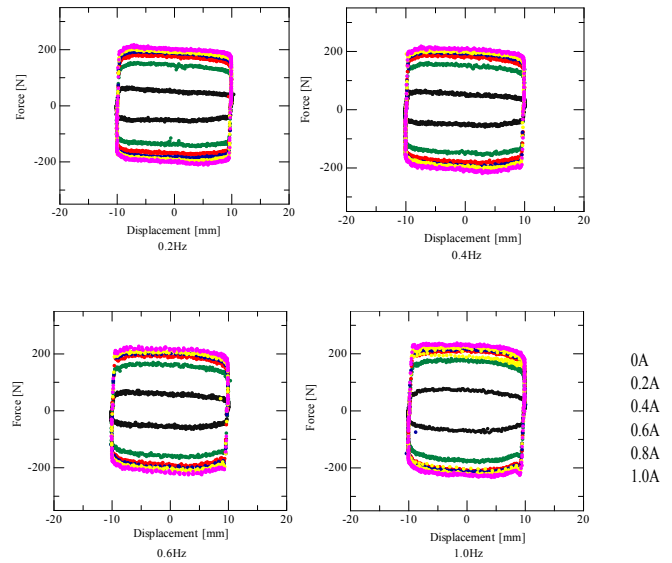


Fig.6 Displacement-force hysteresis loops

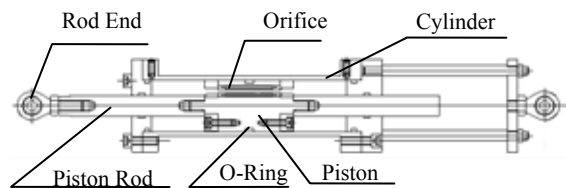


Fig.7 Passive damper

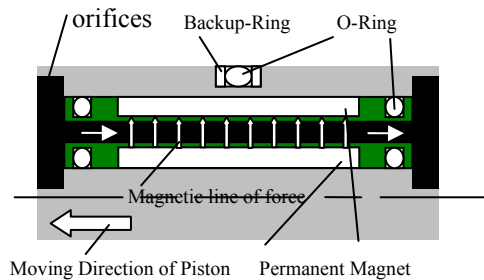


Fig. 8 Details of the Orifices

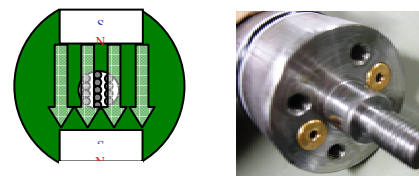


Fig.9 Permanent magnet arrangement and Photo. of the piston

1) Vibration test results without permanent magnet

As typical examples of the test results, displacement-force hysteresis loops obtained under the sinusoidal displacement are shown in Table 2, Figs. 10 and 11.

Table.2 Test results without magnetic field

Frequency [Hz]	HMRF Damper [N]	MR Damper [N]	Oil Damper [N]	Friction [N]
0.2	384 (190)	295 (101)	251 (57)	194
0.4	668 (480)	405 (217)	331 (143)	188
0.6	925 (754)	527 (356)	418 (247)	171
0.8	1171 (1014)	686 (529)	503 (346)	157
1	1364 (1217)	848 (701)	584 (437)	147
1.2	1547 (1403)	1017 (873)	646 (502)	144
1.4	1771 (1631)	1203 (1063)	731 (591)	140
1.6	1912 (1778)	1381 (1247)	808 (674)	134
1.8	-	1607 (1479)	882 (754)	128
2	-	1839 (1714)	970 (845)	125

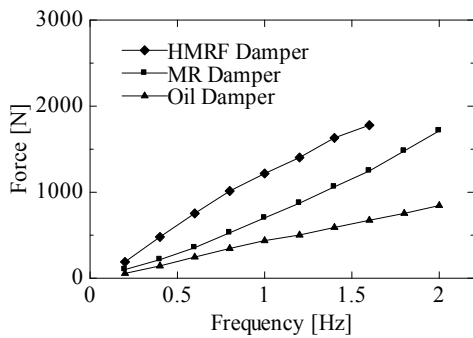


Fig.10 Force-Frequency relation (without permanent magnet)

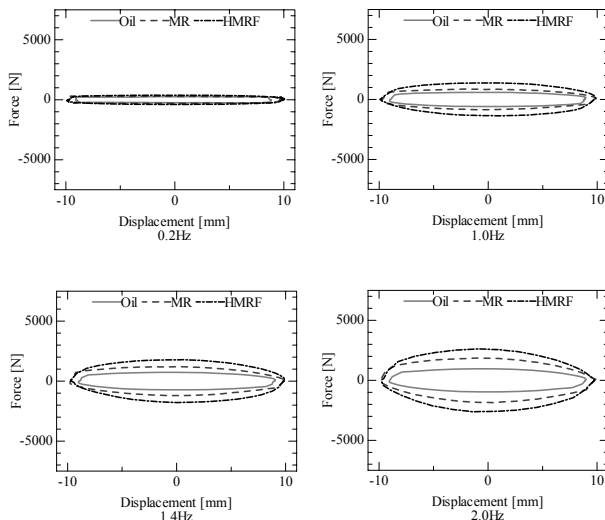


Fig.11 Displacement-force hysteresis loops (without permanent magnet)

In the case without permanent magnetism, it is clear that the passive damper which uses the HMRF produces the largest resistance force.

2) Vibration test results with permanent magnetism

Displacement-force hysteresis loops obtained under the sinusoidal displacement are shown in Table 3, Figs. 12 and 13.

From these data, the damper which uses the HMRF has a large energy absorbing capacity and it will be effective for using of low frequency domain. In the passive damper tests, the resistance force using HMRF is about 1.5 times the resistance force using commercial type MR fluid.

Table.3 Experimental result in magnetic field

Frequency [Hz]	HMRF damper [N]	MR damper [N]	Oil damper [N] (No magnetic field)
0.2	3746	2437	251
0.4	4088	2656	331
0.6	4599	2825	418
0.8	5265	3005	503
1	5572	3417	584
1.2	5613	3515	649
1.4	5288	3591	731
1.6	5616	3757	808
1.8	5561	3775	882
2	5731	4038	970

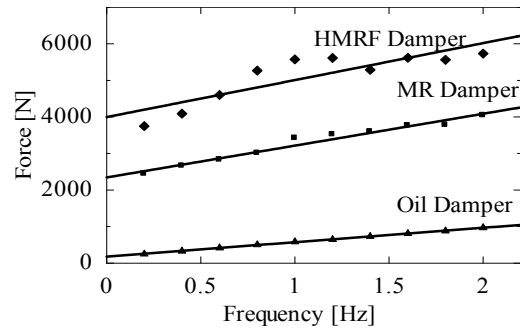


Fig.12 Force-Frequency relation (without permanent magnet)

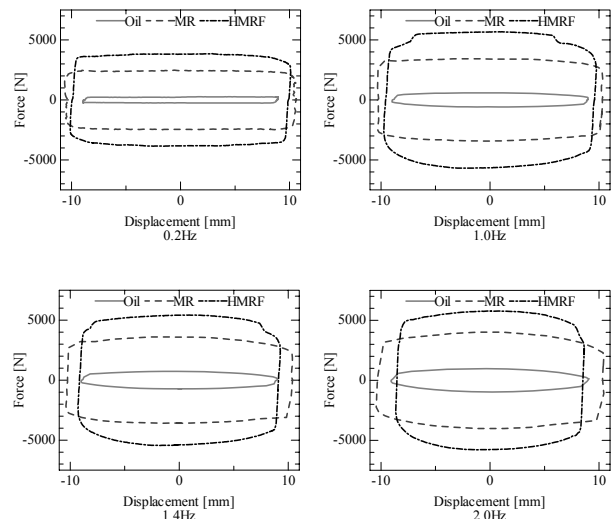


Fig.13 Displacement-force hysteresis loops (with permanent magnet)

4 CONCLUSIONS

As a result of a series of studies, the following conclusions have been obtained.

- 1) A new intelligent fluid which consists of hydrocarbon oil and carbonyl irons coating with super fine magnetite has been developed.
- 2) The developed fluid shows a strong Bingham fluid tendency.
- 3) The characteristics of the developed fluid are similar to the conventional MR fluid and the new fluid can be used as a semi-active damper oil.
- 4) From vibration test results without permanent magnetism, the developed fluid can be used as well as the conventional MR fluid as a hydraulic oil. Further, in such a case the developed fluid has an energy absorption effect 3~ 4 times that of oil in the same device.
- 5) A passive damper which uses the developed fluid and permanent magnetism, shows a strong energy absorption effect. This fact suggests that the damper using the developed fluid has a possibility of becoming a simplified and a compact damper.

Acknowledgements

The authors would like to thank Prof. S. Morishita at the School of Environment & Information Science, Yokohama National University for his help and cooperation, and the authors also would like to thank Mr. S. Takahashi, Managing Director, Corporate Administration, Toda Corporation, for his helpful advices.

References

- [1] SAE, *Automotive Engineering International Online*, 2000, pp. 2.
- [2] Spencer, B. F., Jr., and Sain, M. K., 1997, "Controlling Buildings: A New Frontier in Feedback", *Special Issue of the IEEE Control Syst. Mag.*, **17**-6, pp.19-35.
- [3] Spencer, B. F. Jr., Yang, G., Carlson, J. D., and Sain, M. K., 1998, "Smart damper for Seismic Protection of Structure: A Full-Scale Study", *Proc., 2nd World Conference on Structure Cotrol*, pp. 589-594.
- [4] Sunakoda, K., Sodeyama, H., Iwata, N., Fujitani, H., Soda, S., 2000, "Dynamic Characteristics of Magneto-Rheological Fluid Damper", *Proc. SPIE's 7th Annual International Symposium on Smart Structures and Materails*, **3989**, pp. 194-203.
- [5] Sodeyama, H., Suzuki, K., Sunakoda, K., 2004, "Development of Large Capacity Semi-Active Seismic Damper Using Magneto-Rheological Fluid", *ASME Journal of Pressure Vessel and Piping Technology*, **126**, pp.105-109.
- [6] Sodeyama, H., Sunakoda, K., Fujitani, H., Soda, S., Iwata, N., 2000, "Development of a Magneto-Rheological Fluid Damper for Semi-Active Vibration Control Systems of Rea l Building Structures", *MoVic 2000*, **2**, pp. 725-730.
- [7] Sunakoda, K., Sodeyama, H., 2000, "A Basic Study on Dynamic Characteristics of MR Damper," (in Japanese), *Proc. 2nd Japan National Symposium on Structural Control*, pp. 27-30.
- [8] Yang, G., Spencer, B.F. Jr., 2002, "Practical Design and Dynamic Performance Considerations in Development of

Full-Scale MR Dampers", *Workshop on Smart Structural Systems Organized for U.S.-Japan Cooperative Research Programs on Smart Structural Systems and Urban Earthquake Disaster Mitigation*, pp. 129-140.

[9] Shiraishi, T., Morishita, S., 2004, "Measurements of Typical Characteristics of MR Fluids and Their Application to Design of MR Devices Considering Working Modes," (in Japanese), *Trans. Japan Society of Mechanical Engineers, Series C*, **70**-696. pp. 2308-2314.

Ultra High Voltage Power Transmission in China

Li Guang-fan *, Li Bo*, Zhou Yuan-xiang **, Li Jin-zhong*

* China Electric Power Research Institute, Haidian District, Beijing, China 100192;

** State Key Lab of Control and Simulation of Power Systems and Generation Equipments,

Dept of Electrical Engineering, Tsinghua University, Beijing, China 100084

ligf@epri.ac.cn

Abstract: Due to the unbalanced distribution of energy and electric load in China, power transmission has to transmit large block of electric energy over a long distance. Consequentially, ultra high voltage (UHV) power transmission has to be developed in China. By now, 1000 kV UHV AC power transmission line has been under commercial operation since Jan 2009 and ± 800 UHV DC power transmission line is being constructed meanwhile in China. To meet the demands of studying UHV technologies, the State Grid Corporation of China has built a test system with the highest voltage level of the world at present. In this paper, UHV power transmission lines and UHV test bases of China are introduced.

Key Words: UHV Transmission, UHV Test and Demonstration Line, UHV Test Base

1. INTRODUCTION

The need of electric energy is synchronized with the economic growth of the nation. Similarly, along with the expansion of the scale of power grid and increasing demand of remote power transmission, the voltage level should be upgraded. The development of ultra high voltage (UHV) power transmission in China is consequential to the need of the increasing economy of China. The first commercial 1000 kV UHV AC Test and Demonstration Project in the world has just been built in China, and Xiangjiaba-Shanghai ± 800 kV UHV DC Demonstration Project is under construction now. To meet the needs of studying UHV transmission technologies, State Grid Corporation of China has built several test bases including UHV AC Test Base in

Wuhan, UHV DC Test Base in Beijing, UHV Tower Test Base in Beijing, and High Altitude Test Base in Tibet. A series of studies have been done in these test bases and needed test data is provided for the construction and operation of UHV power transmission. China is occupying a leading position in UHV power transmission.

2. CURRENT STATUS OF UHV TRANSMISSION IN THE WORLD

Since 1960s, due to increasing demand for electricity, increasing capacity of power transmission, increasing difficulty for power transmission corridor, limitation of short-circuit current by switch, and other reasons, the former Soviet Union, Japan, America, Italy

and other countries began to study UHV AC transmission technologies. UHV laboratories and test bases were successively built. Many technical problems of UHV power transmission, such as over-voltage, audible noise, radio interference and ecological effects were studied. The million volts level transformation projects were successfully constructed by the former Soviet Union and Japan.

At present, UHV transmission technologies are being studied actively in some countries with rapid economic growth, such as India, Brazil and South Africa.

The former Soviet Union began to construct 1150 kV UHV AC transmission project in 1982. And in Aug 1985 the first 1150kV transmission line was established and put into operation at the rated voltage, in which the line of Ekibastuz- Kokchetav- Kostanay was 900 km long. However, after the former Soviet Union collapsed, its economic stagnated and the power demand was greatly decreased. Those transmission lines mentioned above started to operate at a lower voltage of 500 kV since Jan 1992, and the extra UHV transmission lines according to the original plan also failed to construct. Besides, since 1990, the former Soviet Union started to construct $\pm 750\text{kV}/6000\text{MW}$ DC transmission project and had finished parts of the lines. The DC facilities also passed the type tests. However, for the same reason of the UHV AC project, UHV DC transmission project was also forced to give up in 1992 [1].



Fig. 1. UHV Transmission in former Soviet Union.

Due to the difficulty for the power transmission corridor arrangement, and the purpose to limit the 500 kV short-circuit current, Japan planed to construct three 1000 kV AC double circuit transmission lines to supply electric energy to Tokyo power grid after technical and economic verification. And these transmission lines were

run paratactically with several 500 kV transmission lines built at the preliminary stage of the power plants. Since the beginning of UHV transmission constructions in 1988, Japan had successively constructed 427 km AC double circuit transmission lines from 1992 to 1999, which were operated at 500 kV and were planned to be operated at higher voltage level in 2002. Moreover, Japan had built Shin-Haruna test station in 1996. However, due to the economic recession, the nuclear power plant project was postponed as well as the UHV projects[2, 3].



Fig. 2. Shin-Haruna test station for UHV facilities in Japan.

American Electric Power Company (AEP), Allmanna Svenska Elektriska Aktiebolaget (ASEA), Bonneville Power Administration (BPA), Electric Power Research Institute (EPRI) and General Electric Company (GE) have built a series of UHV test bases successively on a certain scale, in which electromagnetic environment, power frequency voltage, switching impulse, lightning impulse, mechanical properties were studied. However, because the electric energy growth decelerates, resources such as natural gas are sufficient and nuclear power technologies are mature, they haven't programmed any practical UHV transmission project.

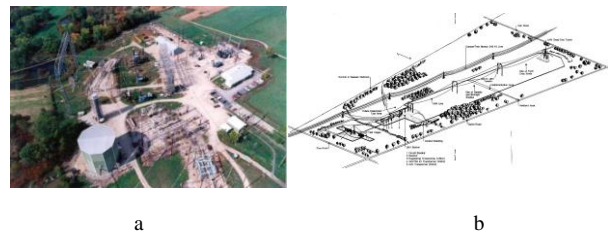


Fig. 3. a. Lenox outdoor high voltage test base of American
b. AEP-ASEA UHV test base

In Italy, a large capacity nuclear power station was planned in 1960s to supply electric energy to the load

center in the north. And 1000 kV was chosen as the rated voltage level after research. Later, natural gas power stations were constructed in load center instead of building nuclear power plant far away. In the other hand, the growth of electric load was much lower than expected. Therefore, Italy has built no UHV AC transmission project[4].

3. THE NECESSITY AND DEVELOPMENT PLAN OF UHV TRANSMISSION IN CHINA

In recent years, the economy of China develops fast and the power load gets a rapid growth. During the year 1987 to 1994, the power generation capacity raised from 1 hundred million kW to 2 hundred million kW in 7 years. During the year 1994 to 2005, the power generation capacity raised from 2.4 hundred million kW to 5.1 hundred million kW in 11 years. 10 million kW power generation capacity has been newly added to the power grid every year since 1988 and 20 million kW power generation capacity has been newly added to the grid every year since 1998. The total power generation capacity of China has reached 7.3 hundred million kW in the year 2008, and the electricity consumption of China has reached 3.43 trillion kWh. The requirement of power supply keeps increasing [5].

The development of power source and productive forces has a contrary distribution in China. The coal power and water power will be the main power supply in a long period. 75% of water power resources which can be developed economically distribute in the southwest of China, two thirds of coal power resources distribute in the northwest of China. However, two thirds of power load of China centralizes in the east of China and the growth of load will keep the same tendency. The distance of the west power resource bases and the east power load centers is about 500 km to 2000 km. The long distance and huge capacity power transmission will be inevitable in the development of power grid in China.

The 500 kV power grids in China have already got some problems, such as shortage of transportation ability, lack of transmission corridors, short current exceeding standard, insufficient of power switching ability between

large regional grids. The present extra high voltage (EHV) transmission technology can not satisfy the needs of power transmission, thus the development and technology innovation of power grid have to be speeded up.

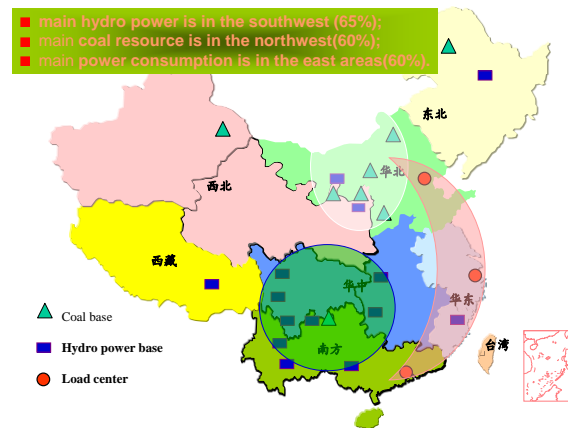


Fig. 4. Distribution of electric energy and load in China.

According to the general rules of constructing a higher voltage class, once the current power load increases to 4 times of the load when the present voltage level was built, the construction of a higher voltage level power system will be economic and reasonable. Compared to the 500 kV EHV system, the UHV system has many advantages such as larger capacity, longer transportation distance, lower losses and fewer transmission corridor. The UHV system will break through the technical bottleneck of the 500 kV EHV system, improve the power transportation ability and meet the requirement of the sustained and rapid growth of power. Generally, the power project construction cost of transmission capacity per unit is in inverse proportion to the voltage class. The investment of per unit capacity for 1000 kV AC system is 73% of that for 500 kV, and the investment of per unit capacity for ± 800 kV DC system is 72% of that for ± 500 kV DC system.

The State Grid Corporation of China put forward the construction strategy that taking the UHV system as the backbone grid and developing the other levels of power grid in harmony. The plan will promote the intensive exploitation of large-scale coal power bases, large-scale water power bases, and large-scale renewable energy bases. Moreover, the plan will optimize the configuration of power resources in larger scale.

According to the present plan, the construction of 1000 kV AC synchronous power grid in Northern China-Central China-Eastern China area will be finished in the year 2020, the implement of long distance power transmission by ± 800 kV DC system will be achieved, too. The transmission capacity of UHV system will exceed 200 GW. The construction of UHV system will improve the use efficiency of power resource, relieve the difficulty of coal transportation, reduce the environmental pollution of Eastern China, and promote the economic development of Western China. Meanwhile, the interconnected power grids will be improved in safety, reliability, flexibility and economy.

The State Development and Reform Commission approved the 1000 kV AC demonstration project in the Jindongnan-Nanyang-Jingmen area in August, 2006 and approved the ± 800 kV DC demonstration project between Fulong, Sichuan and Nanhui, Shanghai in April, 2007.

4. JINDONGNAN-NANYANG-JINGMEN 1000 kV UHV AC TEST AND DEMONSTRATION TRANSMISSION PROJECT [6]

The first test and demonstration project of 1000 kV UHV AC transmission in China consists of 2 electric substations and a switch station. Originated from the electric substation in Changzhi, southeast of Shanxi province, the project takes the Nanyang switch station as the middle part and the Jingmen electric substation as the tail. It is set up by using a single circuit which is 640km long and steps over the Yellow River and the Hanjiang River. Big capacity (1000 kV, 3000 MVA) monocoque type autotransformer is used. The autotransformer has 2 \times 3000 MVA transformation capacity, 1000 kV gas-insulated metal-enclosed switch gear and double-circuit-breaker. The rated voltage is 1000 kV, the maximum operating voltage is 1100 kV, and the current conveying capacity is 2800 MW. The main transformer has a capacity of 2 \times 3000 MVA every single phase. GIS/HGIS switches, high-voltage shunt-wound reactors and high performance surge arresters are used in this project. All equipment is mainly made in China.



Fig. 5. 1000 kV UHV AC test and demonstration transmission line.

Electric substation of the Southeast of Shanxi province is located in Changzhi, Shanxi province, set up with a transformer which has a capacity of 3 \times 1000 MVA currently. There is one 1000 kV circuit connected to the substation, which is equipped with GIS equipment and a 3 \times 320 Mvar high-voltage reactor. And there are five 500 kV circuits connected to the substation, too, equipped with HGIS equipment. The 110 kV side of the transformer is equipped with two 240 Mvar reactors and four 210 Mvar capacitors.

Nanyang switch station is located in Nanyang, Henan province and used as a switch station currently. There are two 1000 kV circuits connected to the switch station equipped with HGIS equipment and two 3 \times 240 Mvar high-voltage reactors.

Jingmen electric substation is located in Jingmen, Hubei province, set up with a 3 \times 1000 MVA transformer currently. There is one 1000 kV circuit connected to the substation, equipped with HGIS equipment and a 3 \times 320 Mvar high-voltage reactor. And there are five 500 kV circuits connected to the substation too, equipped with HGIS equipment. The 110 kV side of the transformer is equipped with two 240 Mvar reactors and four 210 Mvar capacitors.

The whole line project is 640 km long. The section between the southeast of Shanxi province and Nanyang is 359 km long, and the other section between Nanyang and Jingmen is 281 km long. There are more than 1200 towers in the whole line, and the average height of the towers is 77 m. 8-split aluminium conductor steel reinforced is used at most of the line, and 6-split

aluminium alloy conductor steel reinforced with special strength is used for long-span lines. The long-span of the Yellow River is located in Mengzhou, Henan Province, and the strain section is 3651 m long with a 1220 m main span. The long-span of the Hanjiang River is located in Zhongxiang, Hubei province, and the strain section is 2956 m long with a 1650 m main span.

The construction of the 3 electric substation earthworks and the 2 long-span was started in Dec 2006 and finished with system debugging in Dec 2008. The 168-hour demonstration run was begun at 22:00, Dec. 30th, 2008. After that the system was putting into operation on Jan. 6th, 2009. By now it runs steadily, and all the facilities are in good condition. The result of the actual measurements of this project shows that all the electromagnetic environment data has reached the requirement of China Environmental Protection Administration, and is equal to the result of 500 kV AC transmission project.

5. XIANGJIABA-SHANGHAI ± 800 kV UHV DC DEMONSTRATION PROJECT [6]

Demonstration project of Xiangjiaba-Shanghai ± 800 kV UHV DC transmission consists of 2 substations and 1 transmission line, lying in 8 provinces. It is 2000 km long, stepping over the Long River 4 times. The rated transmission power is 6,400,000 kW, and the maximum transmission power is 7,000,000 kW.



Fig. 6. ± 800 kV UHV DC demonstration project.

The project has two poles with two 12-impulse convertors in series for each pole. The voltage is set as “400 kV+400 kV”. 6-inch electricity triggered thyristor valves are used and the capacity of each current convertor reaches 1,750,000 kW. The construction was

built in stages and is flexible with good reliability.

Fulong convertor station is located in Yibing, Sichuan province. The high voltage and low voltage valve halls are located face to face, and 28 convertor transformers of which each capacity is 321 MVA are set up. 500 kV GIS equipment is used in the 9 outlets currently. The total capacity of AC filter and reactive compensation are designed to be 3080 Mvar and divided into 4 groups.

Fengxian convertor station, which is the receiving end, is located in Fengxian, Shanghai. The high and low voltage valve halls are located face to face, and 28 convertor transformers of which each capacity is 297 MVA are set up. 500 kV GIS equipment is used in the 3 outlets currently. The total capacity of AC filter and reactive compensation are designed to be 3900 Mvar and divided into 4 groups.

The earthwork of the project and construction of the transmission line, as well as the development of the equipment are being processed tensely now.

6. UHV TEST BASES [6]

UHV power transmission technologies represent the highest level of electric technologies today. Due to the unique climate and environment of China, line corona, environmental electromagnetic properties, as well as insulation properties which is affected by the high-altitude, ice layer, heavy pollution and other harsh natural causes, require to be studied in depth. UHV equipment test and live assessment also require the necessary facilities and conditions. To meet the requirements of the special high-voltage engineering design, construction and operational needs, the State Grid Corporation of China calls on independent innovation and has built the UHV AC Test Base (Wuhan), UHV DC Test Base (Beijing), UHV Tower Test Base (Beijing), High Altitude Test Base (Tibet) as the main body, with the leading level of the world.

UHV AC Test Base of China is located in Wuhan, Hubei Province. It lies in the south of the Phoenix Mountain with an elevation of 36m, covering an area of 239960 m². UHV tests include power sources, 1 km

single circuit UHV AC transmission line, 1 km double-circuit UHV AC transmission line, laboratory measurements of electromagnetic environment, environmental climate test room, live UHV AC test equipment field, outdoor long wave front impulse test site, etc. It has the ability of studying UHV AC transmission line electromagnetic environment, as well as outdoor insulation under special natural environment conditions (high-altitude, pollution, ice, strong radiation). It can also carry out long-term transmission line live researches, double circuit transmission line researches, compact transmission line researches, air gap insulating properties and live-line working researches, electromagnetic environmental studies, UHV power transmission facilities researches, UHV measurement technology researches. Training of UHV equipment operation, maintenance, test and live line work can be carried out in this test base too.



Fig. 7. UHV AC Test Base of China

UHV DC Test Base of China is located in Changping Park, Zhongguancun Science Park, Beijing and covers an area of 260130 m². It includes UHV DC test line, corona cage, outdoor test field, testing hall, laboratory of insulators, surge arrester laboratory, electromagnetic environment simulating test field, pollution laboratory, environment laboratory, and UHV valve laboratory. It is able to carry out studies on UHV electromagnetic environment of DC transmission lines or AC/DC transmission lines in same corridor, technologies of multi-circuit on the same tower, technologies of AC/DC transmission lines in the same corridor, the air gap insulating properties and live-line working technology, characteristics of the outdoor insulation, and other special features. These meet the requirements of UHV DC transmission projects [7, 8].



Fig. 8. UHV DC Test Base of China

UHV Tower Test Base is the only research base of China in which tower used in real transmission lines is studied. Based on the needs of the UHV 1000 kV double-circuit tower, it can cover long-term development of UHV power grid appears 1000kV with double-circuit tower, ± 1000 kV single-circuit and ± 800 kV double-circuit transmission line tower with a large-scale tower, such as size and design loads for the new tower structure, components and the overall test pilot research platform structures.



Fig. 9. UHV Tower Test Base of China

Tibet high altitude test base is located at an altitude of 4300 m in Yangbajing town, Dangxiong, Lhasa, covering about 44,000 m², and is the world highest power research base. It is composed of the outdoor test site, contamination laboratory, and test segment. It is not only able to meet the high elevation (4000 m or above) power transmission lines, equipment of insulation and electromagnetic properties, but also to enhance China's high altitude EHV/UHV test ability in order to provide solutions to the elevation problems. It provides the strong technical support to the high-altitude regions of China's power transmission project. It also will be formed by a group of world-leading level with independent intellectual property rights of research

results, to fill the world UHV Experimental study on high-altitude gaps.



Fig. 10. High Altitude Test Base in Tibet

The facilities in the UHV test bases have become domestic. The experimental conditions and the other abilities have already created a number of records of the world. It also obtained more than 100,000 series of valid test data. Surge arresters used in UHV AC test and demonstration project, CVT, fittings and various types of substation equipment have experienced live tests. Facilities of UHV DC test demonstration project including smoothing reactor have passed tests, too, which ensures UHV constructions and safe operation.

7. CONCLUSIONS

Under the organization of State Grid Corporation of China, based on the domestic abilities of research, design, manufacture and construction, China UHV transmission has taken only several years to finish many tasks from feasibility assessment in technology and economy, fundamental study, test means to programming and design, manufacture, construction, debugging and successful commissioning. Many world-class results have been achieved and the technologies of domestic manufacturing of China have been upgraded greatly. Via the practice of UHV power transmission, China has mastered key technologies of UHV power transmission and is occupying a leading position in UHV power transmission.

References

[1] State Grid Corporation of China, "UHV transmission construction, operation, and maintain, the report of training in Russia," Beijing: State Grid Corporation of China, (2005).

- [2] State Grid Corporation of China, "Abroad report of Japan Consulting on UHV AC pilot project," Beijing: State Grid Corporation of China, (2006).
- [3] State Grid Corporation of China, "The investigation report of the UHV transmission technology in Japan," Beijing: State Grid Corporation of China, (2005).
- [4] Ardito A., de Nigris M., Giorgi A., et al, "The Italian 1000 kV project," International Workshop on UHVAC Transmission Technology, Beijing, China, (2005).
- [5] Liu Z.Y., "UHV Power Grid," China Economy Press, Beijing, China, (2005).
- [6] Liu Z.Y., "UHV AC Transmission Technologies," China Electric Power Press, Beijing, China, (2005).
- [7] GB311.1-1997, "Insulation co-ordination for high voltage transmission and distribution equipment," Beijing, China, (1998).
- [8] IEC60071-1: 1993 "Insulation for co-ordination high voltage transmission and distribution equipment" .